

IUPAC Series on Analytical and Physical Chemistry  
of Environmental Systems, Volume 10

---

# **Environmental Colloids and Particles**

## **Behaviour, Separation and Characterisation**

---

*Edited by*

**KEVIN J. WILKINSON**

*University of Montreal, Montreal, Canada*

**JAMIE R. LEAD**

*The University of Birmingham, Birmingham, UK*



John Wiley & Sons, Ltd



---

# **Environmental Colloids and Particles**

## **Behaviour, Separation and Characterisation**

---

IUPAC SERIES ON ANALYTICAL AND PHYSICAL CHEMISTRY  
OF ENVIRONMENTAL SYSTEMS

**Series Editors**

**Jacques Buffle**, *University of Geneva, Geneva, Switzerland*

**Herman P. van Leeuwen**, *Wageningen University, Wageningen, The Netherlands*

Series published within the framework of the activities of the IUPAC Commission on Fundamental Environmental Chemistry, Division of Chemistry and the Environment.

INTERNATIONAL UNION OF PURE AND APPLIED CHEMISTRY (IUPAC)  
Secretariat, PO Box 13757, 104 T. W. Alexander Drive, Building 19,  
Research Triangle Park, NC 27709-3757, USA

Previously published volumes (Lewis Publishers):

**Environmental Particles** Vol. 1 (1992) ISBN 0-87371-589-6

*Edited by Jacques Buffle and Herman P. van Leeuwen*

**Environmental Particles** Vol. 2 (1993) ISBN 0-87371-895-X

*Edited by Jacques Buffle and Herman P. van Leeuwen*

Previously Published volumes (John Wiley & Sons, Ltd):

**Metal Speciation and Bioavailability in Aquatic Systems** Vol. 3 (1995)

ISBN 0-471-95830-1

*Edited by André Tessier and David R. Turner*

**Structure and Surface Reactions of Soil Particles** Vol. 4 (1998)

ISBN 0-471-95936-7

*Edited by Pan M. Huang, Nicola Senesi and Jacques Buffle*

**Atmospheric Particles** Vol. 5 (1998)

ISBN 0-471-95935-9

*Edited by Roy M. Harrison and René van Grieken*

**In Situ Monitoring of Aquatic Systems** Vol. 6 (2000)

ISBN 0-471-48979-4

*Edited by Jacques Buffle and George Horvai*

**The Biogeochemistry of Iron in Seawater** Vol. 7 (2001)

ISBN 0-471-49068-7

*Edited by David R. Turner and Keith A. Hunter*

**Interactions between Soil Particles and Microorganisms** Vol. 8 (2002)

ISBN 0-471-60790-8

*Edited by Pan M. Huang, Jean-Marc Bollag and Nicola Senesi*

**Physicochemical Kinetics and Transport at Biointerfaces** Vol. 9 (2004)

ISBN 0-471-49845-9

*Edited by Herman P. van Leeuwen and Wolfgang Köster*

**Forthcoming titles:**

**Biophysical Chemistry of Fractal Structures and Processes  
in Environmental Systems** Vol. 11 (2007)

ISBN 0-470-01474-1

*Edited by Nicola Senesi and Kevin J. Wilkinson*

IUPAC Series on Analytical and Physical Chemistry  
of Environmental Systems. Volume 10

---

# Environmental Colloids and Particles

## Behaviour, Separation and Characterisation

---

*Edited by*

**KEVIN J. WILKINSON**

*University of Montreal, Montreal, Canada*

**JAMIE R. LEAD**

*The University of Birmingham, Birmingham, UK*



John Wiley & Sons, Ltd

Copyright © 2007 IUPAC

Published in 2007 by John Wiley & Sons Ltd, The Atrium, Southern Gate, Chichester,  
West Sussex PO19 8SQ, England

Telephone (+44) 1243 779777

Email (for orders and customer service enquiries): cs-books@wiley.co.uk  
Visit our Home Page on [www.wiley.com](http://www.wiley.com)

All Rights Reserved. No part of this publication may be reproduced, stored in a retrieval system or transmitted in any form or by any means, electronic, mechanical, photocopying, recording, scanning or otherwise, except under the terms of the Copyright, Designs and Patents Act 1988 or under the terms of a licence issued by the Copyright Licensing Agency Ltd, 90 Tottenham Court Road, London W1T 4LP, UK, without the permission in writing of the Publisher. Requests to the Publisher should be addressed to the Permissions Department, John Wiley & Sons Ltd, The Atrium, Southern Gate, Chichester, West Sussex PO19 8SQ, England, or emailed to permreq@wiley.co.uk, or faxed to (+44) 1243 770620.

Designations used by companies to distinguish their products are often claimed as trademarks. All brand names and product names used in this book are trade names, service marks, trademarks or registered trademarks of their respective owners. The Publisher is not associated with any product or vendor mentioned in this book.

This publication is designed to provide accurate and authoritative information in regard to the subject matter covered. It is sold on the understanding that the Publisher is not engaged in rendering professional services. If professional advice or other expert assistance is required, the services of a competent professional should be sought.

The TEM image used on the front cover was kindly supplied  
by Didier Perret, Denis Mavrocordatos and Charles-Philippe Leinemann.

***Other Wiley Editorial Offices***

John Wiley & Sons Inc., 111 River Street, Hoboken, NJ 07030, USA

Jossey-Bass, 989 Market Street, San Francisco, CA 94103-1741, USA

Wiley-VCH Verlag GmbH, Boschstr. 12, D-69469 Weinheim, Germany

John Wiley & Sons Australia Ltd, 42 McDougall Street, Milton, Queensland 4064, Australia

John Wiley & Sons (Asia) Pte Ltd, 2 Clementi Loop #02-01, Jin Xing Distripark, Singapore 129809

John Wiley & Sons Canada Ltd, 6045 Freemont Blvd, Mississauga, ONT, L5R 4J3, Canada

Wiley also publishes its books in a variety of electronic formats. Some content that appears in print may not be available in electronic books.

***Library of Congress Cataloging-in-Publication Data:***

Wilkinson, Kevin J.

Environmental colloids and particles : behaviour, separation, and characterisation / Kevin J. Wilkinson, Jamie R. Lead.

p. cm.

Includes index

ISBN-13: 978-0-470-02432-4

ISBN-10: 0-470-02432-1

1. Colloids. 2. Water chemistry. 3. Nanoparticles—Environmental aspects. I. Lead, Jamie R. II. Title.

QD549.W446 2006

541'.345—dc22

2006020351

***British Library Cataloguing in Publication Data***

A catalogue record for this book is available from the British Library

ISBN-13: 978-0-470-02432-4 (HB)

ISBN-10: 0-470-02432-1 (HB)

Typeset in 10/12pt Times by Laserwords Private Limited, Chennai, India

Printed and bound in Great Britain by Antony Rowe Ltd, Chippenham, Wiltshire

This book is printed on acid-free paper responsibly manufactured from sustainable forestry  
in which at least two trees are planted for each one used for paper production.

---

# Contents

---

List of Contributors . . . . .	ix
Series Preface . . . . .	xi
Preface . . . . .	xiii
<b>1 Environmental Colloids and Particles: Current Knowledge and Future Developments . . . . .</b>	<b>1</b>
<i>Jamie R. Lead and Kevin J. Wilkinson . . . . .</i>	
<b>2 Colloidal Properties of Submicron Particles in Natural Waters . . . . .</b>	<b>17</b>
<i>Montserrat Filella . . . . .</i>	
<b>3 Colloid–Trace Element Interactions in Aquatic Systems . . . . .</b>	<b>95</b>
<i>Frederic J. Doucet, Jamie R. Lead and Peter H. Santschi . . . . .</i>	
<b>4 Ultrafiltration and its Applications to Sampling and Characterisation of Aquatic Colloids . . . . .</b>	<b>159</b>
<i>Laodong Guo and Peter H. Santschi . . . . .</i>	
<b>5 Characterisation of Aquatic Colloids and Macromolecules by Field-flow Fractionation . . . . .</b>	<b>223</b>
<i>Martin Hassellöv, Frank von der Kammer and Ronald Beckett . . . . .</i>	
<b>6 Modern Electrophoretic Techniques for the Characterisation of Natural Organic Matter . . . . .</b>	<b>277</b>
<i>Philippe Schmitt-Kopplin and Jens Junkers . . . . .</i>	
<b>7 Electrophoresis of Soft Colloids: Basic Principles and Applications . . . . .</b>	<b>315</b>
<i>Jérôme F. L. Duval . . . . .</i>	
<b>8 Strategies and Advances in the Characterisation of Environmental Colloids by Electron Microscopy . . . . .</b>	<b>345</b>
<i>Denis Mavrocordatos, Didier Perret and Gary G. Leppard . . . . .</i>	
<b>9 Force Microscopy and Force Measurements of Environmental Colloids . . . . .</b>	<b>405</b>
<i>Eric Balnois, Georg Papastavrou, and Kevin J. Wilkinson . . . . .</i>	
<b>10 Laser Scanning Microscopy for Microbial Flocs and Particles . . . . .</b>	<b>469</b>
<i>John R. Lawrence and Thomas R. Neu . . . . .</i>	
<b>11 Study of Environmental Systems by Means of Fluorescence Correlation Spectroscopy . . . . .</b>	<b>507</b>
<i>Nicolas Fatin-Rouge and Jacques Buffe . . . . .</i>	
<b>12 Laser-induced Breakdown Detection . . . . .</b>	<b>555</b>
<i>Jae-il Kim and Clemens Walther . . . . .</i>	
<b>13 Probing Environmental Colloids and Particles with X-rays . . . . .</b>	<b>613</b>
<i>Jean-François Gaillard . . . . .</i>	
<b>Index . . . . .</b>	<b>667</b>





**Kevin J. Wilkinson** received a Ph.D. in Environmental Chemistry from the National Water Research Institute of the University of Quebec (*INRS-Eau*) in 1993. After his Ph.D., he joined the research group of Prof. Jacques Buffle at the University of Geneva, where he began to examine some of the important biophysical properties of environmental biopolymers and colloids. Following the establishment of his own research group in 1994, he focused his research on relating the structure of environmental colloids to their function in addition to initiating a research programme designed to develop a fundamental

understanding of the chemical mechanisms of trace metal bioavailability. In 2005, he was appointed Associate Professor of Chemistry at the University of Montreal. His teaching includes (bio)analytical and environmental chemistry. His current research interests include: (i) improving our understanding of the role(s) of microorganisms on the biophysicochemistry of trace elements and colloids; (ii) development and optimisation of novel analytical techniques for quantifying bioavailability and colloidal/aggregate structure; (iii) characterising environmental biopolymers; and (iv) determining the role of diffusion in complex environmental media (biofilms, flocs, sediments). He is currently a member of the editorial boards of *Environmental Toxicology and Chemistry* and *Environmental Chemistry* and a titular member of the IUPAC Chemistry and Environment Division.



**Jamie R. Lead** is an aquatic chemist who received his first degree in Environmental Science from the University of Sussex, U.K. He obtained his Ph.D. in 1994 from Lancaster University, U.K., investigating lanthanide and actinide speciation in relation to humic substances from aquatic and terrestrial systems. He subsequently undertook postdoctoral research at Lancaster University, working on colloid-metal interactions using field-flow fractionation, and at the University of Geneva, Switzerland applying fluorescence correlation spectroscopy to quantify the diffusion coefficients of organic colloids and nanoparticles. He

subsequently took up an academic position in the School of Geography, Earth and Environmental Sciences at the University of Birmingham, U.K. (2000), where he was made a Senior Lecturer in Water Chemistry (2004) and is currently a Reader in Aquatic Chemistry. His major current research interests are: (i) the development and application of new analytical and fractionation techniques in the area of metal speciation and colloid structure; (ii) quantifying the structure of aquatic colloids and nanoparticles and the relationship structure has to their role in trace pollutant fate and behaviour; and (iii) the fate and behaviour of manufactured nanoparticles in the aquatic environment. He has published extensively in the area of colloid structure and the interactions of colloids with metals. He heads a current knowledge transfer network on aquatic colloids (AQUANET) and on manufacture nanoparticles (NANONET), and as such, has organised and chaired several recent international conferences and workshops in these areas.



---

# List of Contributors

---

**Eric Balnois**

*Laboratoire Polymères, Propriétés aux Interfaces et Composites (L2PIC), Université de Bretagne Sud, rue de St Maudé, BP 92116, F-56321 Lorient Cedex, France*

**Ronald Beckett**

*Water Studies Centre, School of Chemistry, Monash University (Clayton Campus), Melbourne, Victoria 3800, Australia*

**Jacques Buffle**

*Analytical and Biophysical Environmental Chemistry (CABE), Department of Inorganic, Analytical and Applied Chemistry, University of Geneva, 30 quai Ernest Ansermet, CH-1211 Geneva 4, Switzerland*

**Frederic J. Doucet**

*University of Nottingham, Sutton Bonington Campus, Loughborough LE12 5RD, UK*

**Jérôme F. L. Duval**

*Environment and Mineralogy Laboratory, UMR INPL-CNRS 7569, Research Center François Fiessinger, 15 avenue du Charmois, BP 40, F-54501 Vandoeuvre-lès-Nancy cedex, France*

**Nicolas Fatin-Rouge**

*Laboratoire de Chimie des Matériaux et Interfaces, 16 route de Gray, F-25030 Besançon cedex, France*

**Montserrat Filella**

*Analytical and Biophysical Environmental Chemistry (CABE), Department of Inorganic, Analytical and Applied Chemistry, University of Geneva, 30 quai Ernest-Ansermet, CH-1211 Geneva 4, Switzerland*

**Jean-François Gaillard**

*Departments of Civil and Environmental Engineering, Northwestern University, 2145 Sheridan Road, Evanston, IL 60208-1309, USA*

**Laodong Guo**

*Department of Marine Science, University of Southern Mississippi, 1020 Balch Boulevard, Stennis Space Center, MS 39529, USA*

**Martin Hassellöv**

*Department of Chemistry, Göteborg University, S-412 96 Gothenburg, Sweden*

**Jens Junkers (deceased)**

*GSF–National Research Center for Environment and Health, Institute for Ecological Chemistry, Molecular BioGeoanalysis, Ingolstädter Landstraße 1, D-85764 Neuherberg, Germany*

**Jae-II Kim**

*Institut für Nukleare Entsorgung, Forschungszentrum Karlsruhe, PO 3640, D-76021  
Karlsruhe, Germany*

**John R. Lawrence**

*National Water Research Institute, 11 Innovation Boulevard, Saskatoon, Saskatchewan,  
Canada, S7N 3H5*

**Jamie R. Lead**

*Division of Environmental Health and Risk Management, School of Geography, Earth  
and Environmental Sciences, University of Birmingham, Birmingham, B15 2TT, UK*

**Gary G. Leppard**

*National Water Research Institute, 867 Lakeshore Road, PO Box 5050, Burlington,  
Ontario, Canada L7R 4A6*

**Denis Mavrocordatos (deceased)**

*Swiss Federal Institute for Environmental Science and Technology, EAWAG Urban Water  
Management, 133 Überlandstrasse, CH-8600 Dübendorf, Switzerland*

**Thomas R. Neu**

*Department of River Ecology, UFZ Centre for Environmental Research Leipzig-Halle,  
Brückstrasse 3a, D-39114 Magdeburg, Germany*

**Georg Papastavrou**

*Laboratory of Colloid and Surface Chemistry (LCSC), Department of Inorganic,  
Analytical and Applied Chemistry, University of Geneva, Sciences II, 30 quai Ernest  
Ansermet, CH-1211 Geneva 4, Switzerland*

**Didier Perret**

*Section of Chemistry, University of Geneva, 30 quai Ernest Ansermet, CH-1211 Geneva  
4, Switzerland*

**Peter H. Santschi**

*Departments of Marine Sciences and Oceanography, Laboratory for Oceanographic and  
Environmental Research, Texas A&M University at Galveston, 5007 Avenue U,  
Galveston, TX 77551, USA*

**Philippe Schmitt-Kopplin**

*GSF-National Research Center for Environment and Health, Institute for Ecological  
Chemistry, Molecular BioGeoanalysis, Ingolstädter Landstraße 1, D-85764 Neuherberg,  
Germany*

**Frank von der Kammer**

*Institute for Geological Sciences, Environmental Geosciences, Vienna University, A-1090  
Vienna, Austria*

**Clemens Walther**

*Institut für Nukleare Entsorgung, Forschungszentrum Karlsruhe, PO 3640, D-76021  
Karlsruhe, Germany*

**Kevin J. Wilkinson**

*Department of Chemistry, University of Montreal, CP 6128, Succ. centre-Ville, Montreal,  
Canada, H3C 3J7*

---

# Series Preface

---

The main purpose of the IUPAC Series on Analytical and Physical Chemistry of Environmental Systems is to make chemists, biologists, physicists and other scientists aware of the most important biophysicochemical conditions and processes that define the behaviour of environmental systems. The various volumes of the Series thus emphasise the fundamental concepts of environmental processes, taking into account specific aspects such as physical and chemical heterogeneity, and interaction with the biota. Another major goal of the series is to discuss the analytical tools that are available, or should be developed, to study these processes. Indeed, there still seems to be a great need for methodology developed specifically for the field of analytical/physical chemistry of the environment.

This volume in the series focuses on the nature and properties of aquatic colloids and, in particular, the various recent instrumental techniques which can be used for their characterisation. It can be seen to follow the first two volumes of the series (*Environmental Particles*, vols. 1 and 2, 1992–93). It is noteworthy that the techniques of surface, colloid, polymer and gel characterisation, as well as the related scientific information that the techniques provide, have largely improved over the past 10–15 years. It is thus an opportune moment to perform a critical assessment of their capabilities for environmental applications.

This volume was realised within the framework of the activities of the IUPAC Division of Chemistry and the Environment. We thank IUPAC for its administrative and financial support and assistance with this project. With their help, it was possible to organize a discussion meeting of the full team of chapter authors in Birmingham (U.K.) in 2004 which was an essential step in the preparation and harmonisation of the various chapters in this book.

The Series is well received and is growing prosperously. A new volume on the fractal properties of soil particles will be published soon. As with all books in this series, it will present critical reviews reflecting the current state-of-the-art and provide guidelines for future research in the field.

Jacques Buffle and Herman P. van Leeuwen  
*Series Editors*



---

# Preface

---

In spite of decades of research, the precise role of colloids and nanoparticles in environmental systems is still poorly understood. For example, in soils and sediments, colloid-facilitated transport is a well-known, though rarely quantified, process. The bioavailability of pollutants is likely to be strongly modified by interactions with colloids, though few studies are able to discriminate between adsorption and the direct effects of the colloid on the organism. Recent indications suggest that the introduction of engineered nanoparticles into the environment may be cause for concern due to their toxicity and potential ability to influence contaminant and, perhaps, pathogen behaviour. Unfortunately, a majority of research papers describe qualitatively or semi-quantitatively the above phenomena, using parameters such as partition coefficients that cannot be generalised across environmental media. In addition, although it is commonly accepted that the fate of trace elements depends to a large extent on their adsorption to colloidal phases, values of 0–100% binding are typically reported. While such large variations can often be attributed to the trace element that has been examined or the nature of the medium in which it occurred, a large variability is often introduced by the analytical technique used to make the determination and (unfortunately) the experience of the research group. Therefore, this book was written in order to (i) identify some of the common problems still needing study in colloid research (Chapter 1); (ii) summarise our current understanding of environmental colloids and their reactions (Chapters 2 and 3); and (iii) carefully and critically describe a number of important techniques to characterise colloidal physical and chemical properties (Chapters 4–13). In this volume, the focus has been placed on modern and novel applications of techniques that have not been previously examined in detail or on techniques that have seen vast methodological improvements over the past 10 years. Furthermore, as is often the case for colloidal researchers, the characterisation techniques have been approximately divided into those looking at whole samples (Chapters 4–7) and those examining properties of a given sample fraction (Chapters 8–13).

This book is the result of the efforts of a number of authors, collaborators and students. It came about from the initiative of Professor D. Turner, following his organisation of a European research conference on aquatic colloids. The International Union of Pure and Applied Chemistry (IUPAC) then provided much of the structure and funding which allowed this project to come to fruition. The role of the Series Editors, Professors H. P. van Leeuwen and J. Buffle is also greatly appreciated. In addition, the Technical Editor, Professor R. M. Town, is acknowledged for her thoroughness and her extremely impressive turnaround times on each of the chapters. Finally, on a tragic note, we must announce that during the preparation of this book, two of our young chapter authors were lost prematurely. The contributions of Jens Junkers (Chapter 6) and Denis Mavrocordatos (Chapter 8) to their respective chapters were greatly appreciated. Their future contributions to the characterisation of colloidal systems and to science, in general, will be greatly missed. Both were young scientists who succeeded in leaving their mark in the field of

environmental colloids, in spite of relatively short careers. Both left behind numerous friends, colleagues and family who will miss them greatly.



Jens Junkers  
(1970–2004)



Denis Mavrocordatos  
(1968–2003)

K. J. Wilkinson and J. R. Lead

---

# 1 Environmental Colloids and Particles: Current Knowledge and Future Developments

---

JAMIE R. LEAD

*Division of Environmental Health and Risk Management, School of Geography, Earth and Environmental Sciences, University of Birmingham, Birmingham B15 2TT, UK*

KEVIN J. WILKINSON

*Department of Chemistry, University of Montreal, P.O. Box 6128, Succ. Centre-ville, Montreal, Canada H3C 3J7*

1	Definitions . . . . .	1
2	The Importance of Size . . . . .	3
3	Non-size-based measurements of colloids and particles . . . . .	9
4	Strategies for advancing our understanding of colloidal systems . . . . .	10
5	Future perspectives . . . . .	11
	References . . . . .	12

## 1 DEFINITIONS

The precise definition of environmental colloids or environmental colloidal systems was discussed in the first volume of this series [1], but still remains a matter of some debate, years later. In a number of areas, including environmental chemistry, the idea of phase has been excluded from common usage and we now often talk of colloids rather than colloidal systems. This procedure will be followed here, but it should be remembered that environmental colloids are relatively dilute dispersions of solid (sometimes liquid or gas) phases within a water or atmospheric gas phase. Although a great deal of discussion revolves around the exact meanings of the terms ‘colloids’ and ‘particles’, to some extent, these problems are trivial, in that they primarily relate to nomenclature differences amongst different disciplines and different researchers that could be avoided by the careful and systematic use of appropriate terms. For instance, a size-based definition was first developed in the field of colloid chemistry [2], however, water engineers frequently use membrane filters with nominal pore sizes of about 5–10 µm, while aquatic chemists commonly use 0.2 or 0.45 µm pore sizes. Even within the broadly defined environmental sciences, different definitions are employed. For example, membranes with a *ca.*, 1 nm (1 kDa) nominal pore

size are often used to discriminate, somewhat arbitrarily, between the truly dissolved and the non-aqueous phases. Finally, further confusion has recently occurred due to the now common use of terms such as macromolecules and nanoparticles. Generally, macromolecule refers to a small polymeric colloid while the term nanoparticle is also applied to the very smallest colloids [3], usually below 100 nm.

In this chapter and throughout the book, the lower size limit for colloids is set in a similar manner to traditional colloid chemistry, *i.e.*, any organic or inorganic entity large enough to have a supramolecular structure and properties that differ markedly from those of the aqueous phase alone, *e.g.*, possibility of conformational changes or the development of an electrical surface field. This limit coincides with the environmentally relevant condition that aquatic colloids are generally small enough that, in the absence of aggregation, Brownian motion is sufficient to keep them suspended in the water column for long periods (>hours–days). Similarly, the upper size limit corresponds to the point where interfacial phenomena are qualitatively less important due to the smaller relative surface to volume ratio of the colloid/particle, although interfacial phenomena are important in all environmental systems. From the preceding constraints has evolved the more practical IUPAC definition that the colloidal size range will typically have at least one dimension in the 1 nm to 1  $\mu\text{m}$  size range [1,4], while particles are defined as materials whose dimensions are  $>1 \mu\text{m}$ .

Clearly, there are limitations on the usefulness of these definitions, for both practical and theoretical reasons. Due to both the chemical and physical complexity of environmental colloids and particles and a lack of standardisation of analytical techniques, including fractionation and sizing methods (especially filtration [5]), experimental data can rarely be rigorously related to even the operational IUPAC definitions. For example, it is not yet possible to determine direct, systematic and rigorous relationships between the physico-chemical properties of membrane permeates or retentates and their environmental function. The current size-based definitions are essentially operational; greater understanding may be gained from definitions that are based on colloidal structure or function (environmental role), in an analogous manner to biological macromolecules. Unfortunately, it is not yet clear that any such attempt would be successful, again due to the complexity of environmental colloids and particles.

Nevertheless, the search for more fundamental definitions of colloids is in progress [6]. For example, it has been argued that colloids should be defined as those species for which no chemical potential can be defined [7]. In a view that was developed further by Gustafsson and Gschwend [6], Buffle and Leppard considered that colloids were dominated by aggregation processes whereas particles were dominated by sedimentation [8]. According to Gustafsson and Gschwend, a colloid in one water body could behave as a particle in another water body, depending on the precise physicochemistry of the medium. This implies that the distinction between colloids and particles may be both site and time specific. Gustafsson and Gschwend [6] distinguished the colloidal from the dissolved phase by the presence or absence of an internal milieu with properties, such as a dielectric constant, that are substantially different from those of the bulk solution. In such a case, a polyelectrolyte with no internal spaces could be considered as being a dissolved species, although this view has been challenged [9]. Clearly, the requirement for an internal milieu poses some problems and neglects the importance of the surface binding of pollutants.

Although these definitions are relatively comprehensive, it must be recognised that they are limited when applied to the environment. For example, sedimentation is surely of less importance in groundwaters than it is in surface waters. Second, as noted above, the surface properties of colloids and particles are extremely important. Third, colloids are not at equilibrium but rather exist as a dynamic system with respect to aggregation processes, pollutant binding and biological uptake. Finally, even if the conceptual models provide a good starting point for further understanding the role and impact of colloids and particles, it is currently extremely difficult to validate the models with rigorous analytical results. Despite important progress over the past few decades of research, we are only at the very beginnings of a comprehensive understanding in this field.

## 2 THE IMPORTANCE OF SIZE

As mentioned above, between 1 nm and 1  $\mu\text{m}$ , solid-phase materials are dominated by surface properties, including surface area and electrical charge, rather than bulk properties such as the chemical composition of the colloids. Interfacial properties are particularly important at the lower end of the size scale. For example, about 50% of the mass (or atoms) is found at the surface of a 3 nm colloid compared with about 5% of the mass for a 30 nm colloid [3]. Colloidal surface properties are therefore extremely important to understanding environmental function since colloidal aggregation and the sorption of trace pollutants, nutrients and pathogens are dependent on the nature of the colloid–colloid and colloid–water interfaces [10–12]. At the upper end of the colloidal size scale (*ca.* 1  $\mu\text{m}$ ), not only do surface properties become less relevant, but also gravitational forces begin to exceed forces due to Brownian motion, with a resulting sedimentation of the particles/aggregates [13].

Historically, filtration through a 0.45  $\mu\text{m}$  filter has been used to distinguish the particulate and dissolved phases. The filtration step has also been used to reduce sample complexity, partially to sterilise the dissolved phase through removal of a majority of the microorganisms and to improve analytical sensitivity, *e.g.* by reducing fouling on electrode or other surfaces. More recently, additional filtration steps have been introduced [5,14] such that filtration is now typically performed with several nominal pore sizes in order to define dissolved, colloidal and particulate phases. Nevertheless, it must be emphasised that these phases are purely operational and are not necessarily related to real differences in structure or to environmental or chemical behaviour. In addition, quantitative comparisons between data sets are difficult due to a variability in the nominal pore sizes that are used and to artefacts that are inherent in the filtration method [4,15–17]. Nonetheless, filtration has produced a wealth of data and greatly advanced our understanding of environmental colloids and particles. However, as stressed later in this volume, confidence in filtration and ultrafiltration data requires that rigorous protocols are implemented, including calculation of mass balances and quantification of the particle size distributions in the sample, retentate and permeate using appropriate microscopic techniques. These verifications are rarely performed and therefore a large proportion of literature data must be critically re-evaluated.

Very little is known, in detail and with accuracy, about the true size distribution of naturally occurring colloids and particles, either as isolated entities or as aggregates, in any environmental compartment. A simplified size distribution of several key biological, organic and mineral phases is given in Figure 1. A key observation from this figure is

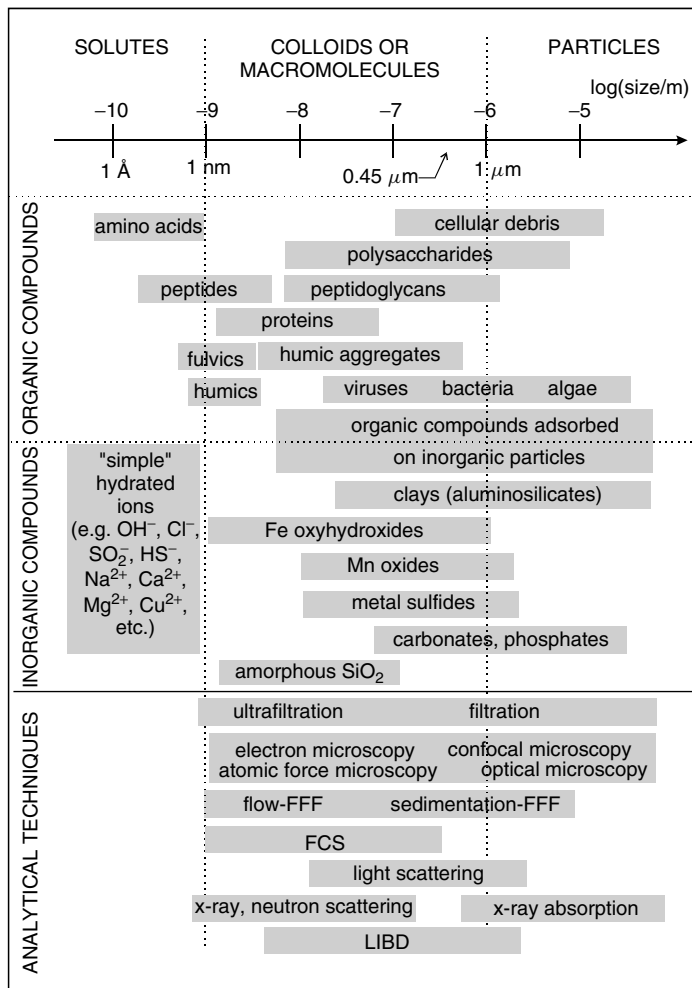


**Figure 1.** Size distributions of various types of environmental colloids and particles and several of the analytical techniques that are used to characterize them. Abbreviations: FFF = field-flow fractionation (Chapter 5); FCS = fluorescence correlation spectroscopy (Chapter 11); LIBD = laser-induced breakdown spectroscopy (Chapter 12). Adapted from [1] with permission from Taylor and Francis

that the sizes of each of the apparently homogeneous colloid types are often spread over several orders of magnitude. Furthermore, the categorisation of different colloid types is somewhat artificial since, in natural systems, colloid groups are rarely found in purified forms but most often are components of complex heteroaggregates. Even a ‘homogeneous’ colloid class such as the humic substances are better described as a complex mixture that includes recognisable biomolecules [18]. Figure 1 also indicates the approximate size ranges in which several of the key colloidal characterisation techniques operate.

Several examples of some colloidal and particulate size distributions, measured using different techniques on unperturbed natural waters, are given in Figure 2. Interestingly,

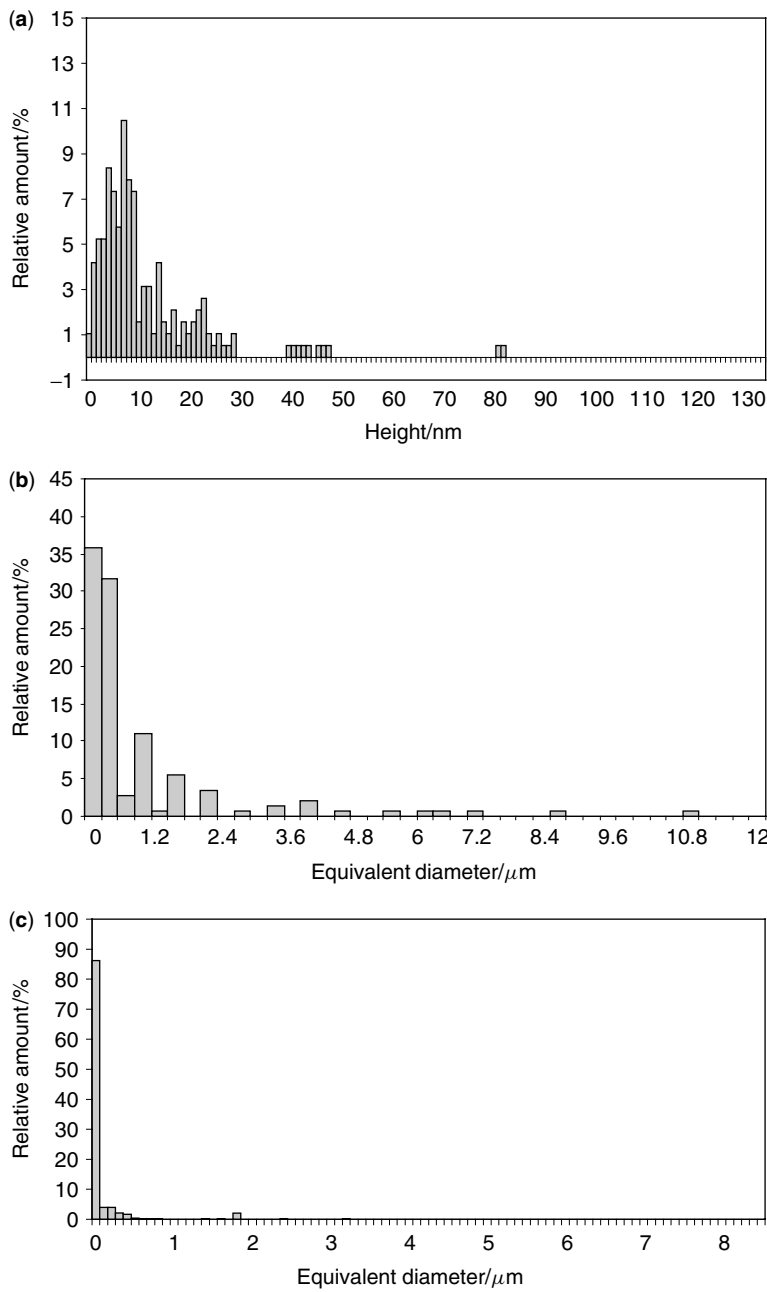


**Figure 2.** Particle size distributions calculated from AFM, ESEM, SEM [15] and SdFFF [19]. Parts (a)–(c) from *Journal of Environmental Monitoring*, 2005, 7, 115–121. Reproduced by permission of The Royal Society of Chemistry

observed sizes are often distributed roughly normally (usually skewed with a long tail) within the analytical window of the technique being employed [15], strongly suggesting an important limitation of the individual techniques and the need to use several characterisation techniques simultaneously, a theme which we will return to later in this chapter. Indeed, Figure 3 shows comparative images using scanning electron microscopy (SEM) and environmental scanning electron microscopy (ESEM) of the same sample with considerably different observed morphologies. The variability of the distributions demonstrates both the difficulty of producing reliable data and the fundamentally different nature of data collected by different techniques. Nevertheless, this situation allows a number of techniques to be applied to produce representative data on the nature of colloids and their interactions.

Although average measures are most often quantified, environmental colloids are always polydisperse, often with undefined size distributions. Size distributions can be determined experimentally by field-flow fractionation (FFF) [21,22], electron microscopy [15,23,24] and atomic force microscopy (AFM) [15,25,26] and calculated from fluorescence correlation spectroscopy (FCS) [27–29] and dynamic light scattering [30]. Nevertheless, the techniques each have different detection limits and detection windows corresponding to different size ranges (Figure 1). Some techniques are simply incapable of measuring accurately the whole range of data on polydisperse samples, a factor which may both skew the data collected and invalidate their interpretation. In addition, size distributions may be related to the mass, number or surface area of the colloids as described by the number-, weight- or  $z$ -averages (Table 1). Unfortunately, a large proportion of literature values do not specify which average is determined, in spite of the fact that for polydisperse samples, the different averages will have very different numerical values (Figure 4). Furthermore, most of the colloidal sizing techniques do not measure size directly but rather a different physicochemical property from which the size is derived. For example, whereas physical (number-average) dimensions are determined by microscopic techniques [15,24], diffusion coefficients are generally determined from light scattering, size-exclusion chromatography, flow field-flow fractionation (F1FFF) [21,28] and FCS [27,29]. Charge/size ratios are derived from electrophoretic mobilities [31] and buoyant mass from sedimentation FFF [21] and other centrifugation-based techniques such as analytical ultracentrifugation. Although molecular dimensions and molar masses can be estimated from diffusion coefficients (and eventually electrophoretic mobilities when coupled to titration data), the calculations are based on a large number of (sometimes unwarranted) assumptions (sphericity, permeability, homogeneous charge distribution, absence of aggregates, *etc.*) [32]. Although each of the above points refers to current and important problems, they will be discussed but not solved in this volume; future good-quality science will need to meet these challenges in appropriate ways.

Consequently, numerous, largely unsupported, assumptions have often been accepted by the environmental sciences community. For instance, the importance of colloids is often ascribed to an increase in specific surface area with decreasing size resulting in the exposure of a greater number of functional groups at the solid–aqueous interface and thus a greater uptake of trace pollutants. Furthermore, sizes are generally held to follow a Pareto or other (*e.g.* log-normal [33]) distribution (Figure 2). However, the actual high-quality experimental data to support these beliefs (in particular those employing

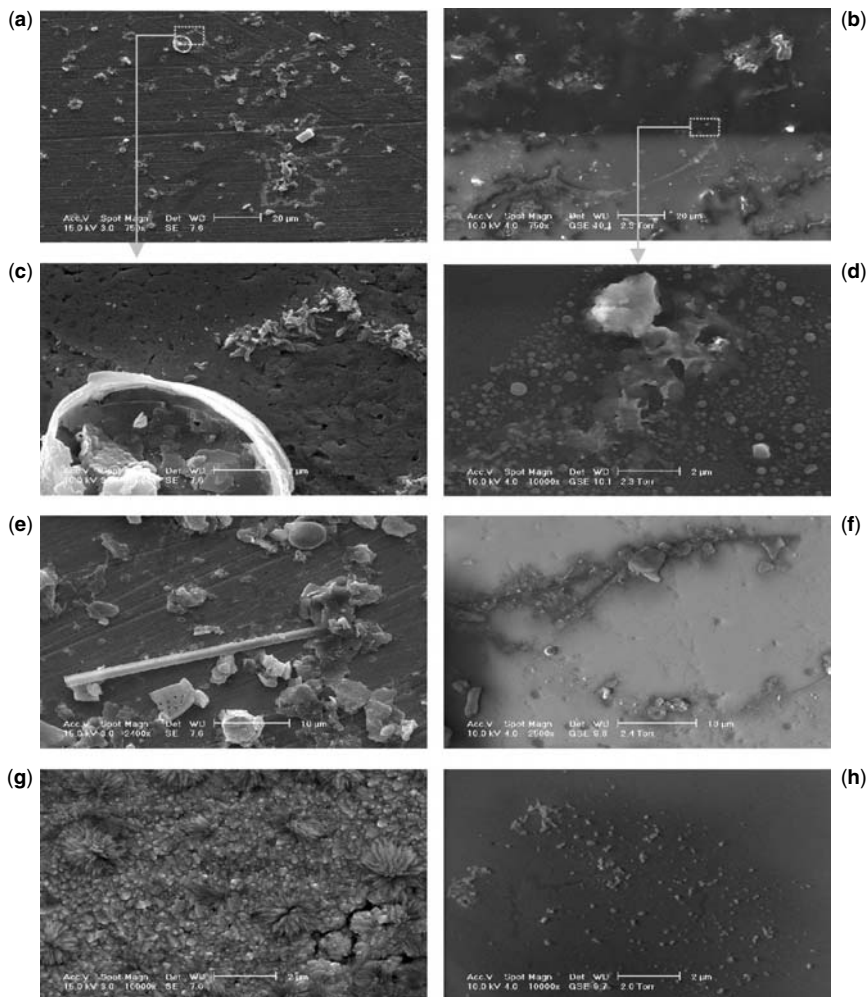


**Figure 3.** Images of the Tamar Estuary taken by both SEM (a, c, e, g) and ESEM (b, d, f, h) [20]. The images are taken from water from the same sample bottle, but a–b, c–d, e–f and g–h are not image pairs of exactly the same sample. Reprinted from Doucet, F. J., Maguire, L. and Lead, J. R., Size fractionation of aquatic colloids and particles by cross-flow filtration, analysis by scanning electron and atomic force microscopy, *Analytica Chimica Acta*, **522**, 59–71, Copyright 2004, with permission from Elsevier

several different techniques) are extremely small. In addition, it is highly likely that many types of environmental colloids are permeable to both water [34] and trace pollutants so that simply taking into account surface complexation reactions would result in an underestimation of colloidal binding. Indeed, following their adsorption on the surface of the colloidal particle, it is likely, in many cases, that pollutants are taken up into the body of the colloid or particle [35]. A final related point is that very few studies have been performed *in situ*: most results have been extrapolated from partially

**Table 1.** Equations for number-, weight- and  $z$ -average molar masses and diameters. Several techniques allow for the near direct determination of these average values (*e.g.* electron or transmission electron microscopy: number-average diameters; fluorescence correlation spectroscopy: number-(single fluorophore) or weight-(several fluorophores) average diameters; dynamic light scattering<sup>a</sup>:  $z$ -average diameters). For monodisperse samples ( $M_w/M_n \approx 1$ ), average values will be similar for all of the calculations whereas for a typical polydisperse sample values can vary by several orders of magnitude (cf. Figure 4)

	Number-average	Weight-average <sup>b</sup>	$z$ -Average
Molar mass	$M_n = \frac{\sum n_i M_i}{\sum n_i}$	$M_w = \frac{\sum n_i M_i^2}{\sum n_i M_i}$	$M_z = \frac{\sum n_i M_i^3}{\sum n_i M_i^2}$
Diameter	$d_n = \frac{\sum n d_i}{\sum n}$ $d_n = \frac{\sum w_i / d_i}{\sum w_i / d_i^2}$	$d_w = \frac{\sum n_i d_i^4}{\sum n_i d_i^3}$ $d_w = \frac{\sum w_i d_i}{\sum w_i} = \frac{\sum n_i d_i M_i}{\sum n_i M_i}$	$d_z = \frac{\sum n_i d_i^6}{\sum n_i d_i^5}$ $d_z = \frac{\sum c_i d_i M_i}{\sum c_i M_i}$

<sup>a</sup> Dynamic light scattering calculates the  $z$ -average diameter for Rayleigh scatterers ( $d \ll \lambda$ ) and for particles where measurements have been extrapolated to a scattering angle of 0.

<sup>b</sup> Calculations of diameter averages assume that  $n_i d^3$  is proportional to the weight of the particles through the density and that the density is constant for all size ranges.

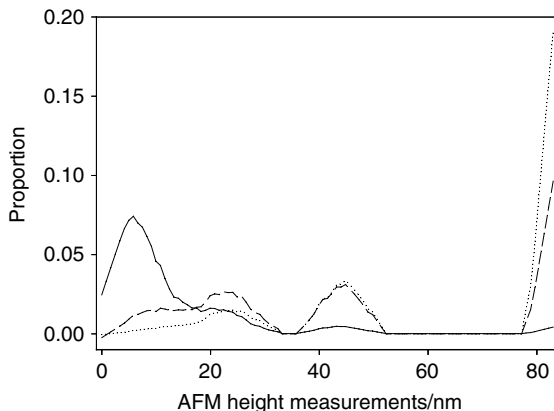


**Figure 4.** Number-(solid line), weight-(dashed line) and  $z$ -average (dotted line) diameters calculated from the AFM colloidal size (heights) distribution given in Figure 2a using the equations provided in Table 1. In this case of a natural, polydisperse sample, the number-average mean was calculated as 12.2 nm, the weight-average diameter as 58.5 nm and the  $z$ -average diameter as 75.8 nm. The example illustrates that even for the same sample, techniques that are based on different principles will provide a substantially different indication of the particle size distributions. In addition, the analytical bias of the technique (*e.g.* detection window, Figure 1) will significantly influence what is recorded by the scientist. To facilitate comparison, data have been smoothed using a negative exponential

processed or model systems under controlled laboratory conditions. In order to overcome some of the major difficulties that remain in this field, adequate and reliable methods for sampling, sample handling, fractionation, analysis and modelling will need to be developed.

Finally, when considering the size of a colloid or particle of particular shape, it is essential to ask two questions. First, why are the size-based measurements being performed, i.e. what does this analysis reveal about environmental processes such as trace element uptake to biota? Second, are there ways of performing more revealing analyses? The first question is idealistic and forces us to consider the link between size and the relevant processes. There is no doubt that size is a useful parameter for considering colloidal behaviour. It affects processes such as the transport and biouptake of trace pollutants in sediments, soils, waters and the atmosphere. Furthermore, colloidal size is a standard parameter that can, with reservations, be used to compare data sets. Nevertheless, the reliance on size as a primary measurement is limiting, as discussed in the next section. The second question is more practical. More revealing parameters can indeed be measured. A significant current challenge in the study of environmental colloids and particles is to develop these methods and to apply them in order to produce non-trivial results that are based on parameters other than size.

### 3 NON-SIZE-BASED MEASUREMENTS OF COLLOIDS AND PARTICLES

Although size is a useful and frequently measured parameter, it is limited in the extent to which it can be used to gain detailed understanding of environmental behaviour. For instance, larger particles often dominate the sedimentation process. Since the larger particles generally, but not always [36,37], dominate particle mass distributions [1], a mass distribution may be the most relevant means to present sedimentation data. In contrast, insight into aggregation processes will likely benefit more from considering particle number distributions, which are likely to be dominated by the smaller colloids. Finally, surface area may be the most relevant parameter when considering pollutant uptake by colloids and particles. Like particle number, surface area is likely to be dominated by smaller colloids, albeit not in an identical manner. Since these three processes, i.e. uptake, aggregation and sedimentation, are interrelated, *e.g.* through the colloidal pumping model [38], a thorough understanding of the entire process will likely require accurate determinations of the mass, number and specific surface area distributions.

For a number of processes, size can be considered as a proxy for other parameters. In particular, knowledge of the diffusion coefficients of colloidal complexes with trace elements and organic pollutants is vital to understanding: (i) their transport in soils, sediments and the diffusive boundary layer around surfaces; (ii) their mass transport to biological organisms [39] and (iii) their quantitative analytical determination using important *in situ* metal speciation techniques such as diffusive gradients in thin films (DGT) and voltammetry. Although a number of techniques measure colloidal diffusion coefficients (Table 2), data are most often converted to size, as in the case of FIFFF [21,22,40] by assuming that the colloids are impermeable and spherical (Stokes–Einstein equation). Clearly, in natural systems, there is a range of colloidal morphologies, many of extreme complexity. Although the conversion to equivalent radii is helpful for making comparisons, diffusion coefficients are arguably a more powerful indicator of colloidal activity (aggregation, reactivity, *etc.*) and should be retained, whenever possible. In addition, other parameters such as fractal dimensions (aggregates) [41,42], colloidal form factors [24], gyration radii or contour or persistence lengths (*e.g.* fibrils) [43] may also provide structural information that is more easily related to environmental function. Similar arguments are valid

**Table 2.** Comparison of most probable (mean or median) diffusion coefficients ( $\text{m}^2\text{s}^{-1} \times 10^{10}$ ) for the Suwannee River standard fulvic acid. Figures in parentheses are standard deviations. For FCS, poor accuracy was obtained at high ionic strength ( $n = 3$ ); for FIFFF, no values were measurable at low pH and high ionic strength ( $n = 3$ ); for PFG NMR, data for regions 1–4 (corresponding to 0.8–1.9, 1.9–3.5, 3.5–4.3, 6.3–8.1 ppm) have been collapsed to give the most probable diffusion coefficients. For PFG-NMR, standard deviations for all individual data in all cases were 0.2. Reprinted with permission from *Environmental Science and Technology*, **34**, 3508–3513. Copyright 2000 American Chemical Society

	Ionic strength/mmol dm <sup>-3</sup>	pH or pD		
		4	5.5	7.0
FCS	5	2.21 (0.07)	2.52 (0.02)	2.71 (0.06)
	50	2.05 (0.02)	2.40 (0.04)	2.61 (0.04)
	500	2–3	2–3	2–3
FIFFF	5	–	3.0 (0.08)	2.9 (0.03)
	50	–	1.9 (0.05)	2.2 (0.02)
	500	–		
PFG-NMR	Low	2.8–3.6	2.5–3.7	2.4–3.5
	500	2.6–3.8	2.5–3.7	2.5–3.5

for other colloidal characterisation techniques such as electrophoresis [34], which provides an estimate of the charge/size ratio of the colloids [34,44], although conversions of electrophoretic mobilities often require significant and complex interpretation [45].

#### 4 STRATEGIES FOR ADVANCING OUR UNDERSTANDING OF COLLOIDAL SYSTEMS

Based on the above considerations, it is clear that to enhance further our understanding of environmental colloids and their impacts, there is a need to (i) employ *in situ* methods [46]; (ii) use non-perturbing methods [7]; (iii) use a variety of methods for comparative purposes [23,27,28,47]; and (iv) take great care in sampling and sample processing and use appropriate checks including the measurement of standard materials, where appropriate [48]. The use of standard materials is discussed in Chapter 3 in relation to ultrafiltration and cross-flow filtration (CFF) techniques, but is nevertheless a continuing limitation in the nanoparticle range where few appropriate standards are available [24,25]. The simultaneous use of a number of methods is another key point. Indeed, a number of studies have demonstrated that a reliance on any single technique may introduce substantial distortions of our view of the colloidal structure [15,28,33,36,47] and their effects on pollutant uptake [10]. When analysing the same colloidal sample, agreement between several techniques will provide increased confidence in the result [28] while disagreement will require the differences to be rationalised appropriately. This type of comparison can also mitigate the analytical uncertainties that normally occur when analysing unknown samples in the absence of certified reference materials.

An example that demonstrates the importance of using several techniques in parallel is given in Table 2. For diffusion coefficients of the reasonably monodisperse and purified Suwannee River standard fulvic acid, good agreement was obtained by FCS, nuclear magnetic resonance (NMR) and FIFFF [28]. In contrast, some multi-method studies to

evaluate colloidal properties have shown only partial agreement (and indeed often substantial differences) in size distributions, metal binding properties and colloidal morphologies, especially for natural samples (*e.g.* AFM, transmission electron microscopy (TEM) and FCS [49]; AFM and ESEM [15]; AFM and TEM [47]; and CFF and FIFFF [10]). In addition to the size distributions provided in Figure 2, comparative SEM and ESEM images obtained from a single sampling from a freshwater sample are given in Figure 4. Substantially different conformations and surface coverages are shown. Similarly, for the same site, AFM images [15] were very different from EM images. Interestingly, TEM and AFM images were generally more similar [47] than images from AFM and ESEM, even though the experimental conditions were nearly identical for the AFM and ESEM acquisition (*i.e.* relative humidity of *ca.* 50–60%). Although TEM images are generally obtained under high vacuum, the use of hydrophilic resins and multi-method TEM sample preparation techniques [24] may be sufficient to stabilise the three-dimensional structure of the colloids and colloidal aggregates [23]. In a final example that clearly demonstrates the complementary nature of three colloidal characterisation techniques, intrinsic viscosity measurements convincingly demonstrated an increase in the diameter of humic substances with increasing pH [50] whereas FCS demonstrated the opposite trend [28] and AFM height measurements showed no trend [26]. In this case, the differences occurred because each of the techniques probed different parameters. The story of the blind men trying to define an elephant by touch may be useful here. One man finds the tail and thinks it is a snake, another finds a leg and thinks it is a tree and so on. Similarly, in the above example, the intrinsic viscosity measurements evaluated *molecular* volumes (but ignored aggregates) whereas FCS measured an average diffusion coefficient that takes into account the effect of aggregation in solution. The AFM measurements evaluated adsorbed (molecular or aggregate) heights following interaction with a substrate (and possible reorganisation at the solid–water interface).

Clearly, the analytical uncertainty associated with multi-method measurements of natural systems is increased because it is difficult to know *a priori* whether the analyses are incorrect or rather whether different aspects of the same structure have been revealed. The development of certified reference materials, although difficult due to colloidal complexity and instability, may nonetheless be helpful for checking instrument operation. In addition, relevant materials, including synthetic manganese or iron oxides, standard humic substances (HS; *e.g.* International Humic Substances Society standards) or microbial exudates are being used more often and with greater success. Future research will therefore require the investigation of ‘standard’ or reference colloids in addition to minimally perturbed colloids from real systems.

## 5 FUTURE PERSPECTIVES

Over the past 15 years, enormous progress has been made towards an understanding of environmental colloidal systems, including the development and application of fractionation and analysis techniques; the development of models; the elucidation of colloidal structure and their interaction with trace elements, nutrients and pathogens; and the impact of colloids on the fate and behaviour of the trace elements, nutrients and pathogens.

The development of powerful techniques by which colloids and particles can be fractionated and analysed has been the primary, unambiguous improvement of recent years.

As detailed in the chapters that follow, the (continuing) development and optimisation of novel, minimally perturbing (ideally *in situ*) methods has immensely improved our ability to quantify colloidal and particulate structures and their behaviour in the environment. In addition, sophisticated models for quantifying colloidal structure and predicting pollutant binding to colloids and colloidal transport have been developed. Nevertheless, further improvements are still required before the majority of models can be used with confidence in the real environment. Hence the iterative development and application of techniques and models to real systems is a key future development. Further discussion of this point is found in each of the individual chapters, although it should be noted that many of the most recent methods have only rarely been used on unperturbed colloidal environmental samples.

Significant developments into the analysis of colloidal structure and their impact on pollutant, nutrient and pathogen fate and behaviour have occurred in the last 15 years, although this field is also still at an early stage. Many of the colloidal characterisation techniques (AFM, ESEM, FCS, CE, FFF, etc.) have not been fully or appropriately deployed in the environment and therefore our current understanding of natural colloidal structures is tentative and only partially quantitative. Significant improvements are expected over the next 15 years once we are better able to couple the nanoscopic characterisation obtained by using FFFF, AFM, TEM and other methods with conceptual models of colloid structure and their interactions. A more systematic determination of parameters, such as diffusion coefficients and fractal dimensions, will also be useful to gain greater understanding at a fundamental, mechanistic and quantitative level. Our understanding of colloidal systems has greatly evolved since the production of the first volume of *Environmental Particles* [1], 15 years ago. The next 15 years are certain to be extremely promising with exciting developments of fundamental knowledge in this vital area.

## REFERENCES

1. Buffe, J. and van Leeuwen, H. P., eds (1992). *Environmental Particles*. IUPAC Series on Analytical and Physical Chemistry of Environmental Systems, Vol. 1. Lewis, Boca Raton, FL.
2. Goodwin, J. (2004). *Colloids and Interfaces with Surfactants and Polymers*. John Wiley & Sons, Ltd, Chichester.
3. Dowling, A. (2005). *Nanoscience and Nanotechnologies: Opportunities and Uncertainties*. Royal Society/Royal Academy of Engineering, London.
4. Lead, J. R., Davison, W., Hamilton-Taylor, J. and Buffe, J. (1997). Characterizing colloidal material in natural waters *Aquat. Geochem.*, **3**, 213–232.
5. Guo, L. and Santschi, P. H. (2006). Ultrafiltration and its application to sampling and Characterisation of aquatic colloids. In *Environmental Colloids and Particles: Behaviour, Structure and Characterisation*, eds Wilkinson, K. J. and Lead, J. R. IUPAC Series on Analytical and Physical Chemistry of Environmental Systems, Vol. 10. John Wiley & Sons, Ltd, Chichester, Chapter 4.
6. Gustafsson, O. and Gschwend, P. M. (1997). Aquatic colloids: concepts, definitions, and current challenges, *Limnol. Oceanogr.*, **42**, 519–528.
7. Stumm, W. (1993). Aquatic colloids as Chemical reactants: surface structure and reactivity, *Colloids Surf. A*, **73**, 1–18.
8. Buffe, J. and Leppard, G. G. (1995). Characterization of aquatic colloids and macromolecules: Part I. Structure and behaviour of colloidal material, *Environ. Sci. Technol.*, **29**, 2169–2175.

9. Doucet, F. J., Lead, J. R. and Santschi, P. H. (2006). Colloids–trace element interactions in aquatic systems. In *Environmental Colloids: Behaviour, Structure and Characterisation*, eds Wilkinson, K. J. and Lead, J. R. IUPAC Series on Analytical and Physical Chemistry of Environmental Systems, Vol. 10. John Wiley & Sons, Ltd, Chichester, Chapter 3.
10. Benedetti, M. F., Ranville, J. F., Allard, T. and Bednar, A. J. (2003). The iron status in colloidal matter from the Rio Negro, Brazil, *Colloids. Surf. A*, **217**, 1–9.
11. Foster, A. L., Brown, G. E. and Parks, G. A. (2003). X-ray absorption fine structure study of As(V) and Se(IV) sorption complexes on hydrous Mn oxides, *Geochim. Cosmochim. Acta*, **67**, 1937–1953.
12. Campbell, P. G. C., Twiss, M. R. and Wilkinson, K. J. (1997). Accumulation of natural organic matter on the surfaces of living cells: implications for the interaction of toxic solutes with aquatic biota, *Can. J. Fish. Aquat. Sci.*, **54**, 2543–2554.
13. Gustafsson, O., Duker, A., Larsson, J., Andersson, P. and Ingri, J. (2000). Functional separation of colloids and gravitoids in surface waters based on differential settling velocity: coupled cross-flow filtration–split flow thin-cell fractionation (Cff-Splitt), *Limnol. Oceanogr.*, **48**, 1731–1742.
14. Heathwaite, L., Haygarth, P., Matthews, R., Preedy, N. and Butler, P. (2005). Evaluating colloidal phosphorus delivery to surface waters from diffuse agricultural sources, *J. Environ. Qual.*, **34**, 287–298.
15. Doucet, F. J., Maguire, L. and Lead, J. R. (2004). Size fractionation of aquatic colloids and particles by cross flow filtration: analysis by scanning electron and atomic force microscopy, *Anal. Chim. Acta*, **522**, 59–71.
16. Horowitz, A. J., Lum, K. R., Garbarino, J. R., Hall, G. E., Lemieux, C. and Demas, C. R. (1996). Problems associated with using filtration to define dissolved trace element concentrations in natural water samples, *Environ. Sci. Technol.*, **30**, 954–963.
17. Buffe, J., Perret, D. and Newman, M. (1992). The use of filtration and ultrafiltration for size fractionation of aquatic particles. In *Environmental Particles*, Vol. 1, eds Buffe, J. and van Leeuwen, H. P. Lewis, Boca Raton, FL, p. 554.
18. Sutton, R. and Sposito, G. (2005). Molecular structure in soil humic substances: the new view, *Environ. Sci. Technol.*, **39**, 9009–9015.
19. Gimbert, L. J., Haygarth, P. M., Beckett, R. and Worsfold, P. J. (2005). Comparison of centrifugation and filtration techniques for the size fractionation of colloidal material in soil suspensions using sedimentation field-flow fractionation, *Environ. Sci. Technol.*, **39**, 1731–1735.
20. Doucet, F. J., Lead, J. R., Maguire, L., Achterberg, E. and Millward, G. (2005). Visualisation of natural aquatic colloids and particles – a comparison of conventional high vacuum SEM and environmental scanning electron microscopy, *J. Environ. Monit.*, **7**, 115–121.
21. Hassellöv, M., von der Kammer, F. and Beckett, R. (2006). Characterisation of aquatic colloids in macromolecules by field-flow fractionation. In *Environmental Colloids: Behaviour, Structure and Characterization*, eds Wilkinson, K. J. and Lead, J. R. IUPAC Series on Analytical and Physical Chemistry of Environmental Systems, Vol. 10. John Wiley & Sons, Ltd, Chichester, Chapter 5.
22. Lyven, B., Hasselöv, M., Turner, D. R., Haraldsson, C. and Andersson, K. (2003). Competition between iron- and carbon-based carriers for trace metals in a freshwater assessed using flow field-flow fractionation coupled to ICP-MS, *Geochim. Cosmochim. Acta*, **67**, 3791–3802.
23. Liss, S. N., Droppo, I. G., Flanagan, S. T. and Leppard, G. G. (1996). Floc architecture in wastewater and natural riverine systems, *Environ. Sci. Technol.*, **30**, 680–686.
24. Mavrocordatos, D., Perret, D. and Leppard, G. G. (2007). Strategies and advances in the characterisation of environmental colloids by electron microscopy. In *Environmental Colloids: Behaviour, Structure and Characterisation*, eds Wilkinson, K. J. and Lead, J. R., IUPAC Series on Analytical and Physical Chemistry of Environmental Systems, Vol. 10. John Wiley & Sons, Ltd, Chichester, Chapter 8.
25. Balnois, E., Papastavrou, G. and Wilkinson, K. J. (2006). Force microscopy and force measurements of environmental colloids. In *Environmental Colloids: Behaviour, Structure and Characterisation*, eds Wilkinson, K. J. and Lead, J. R. IUPAC Series on Analytical and Physical Chemistry of Environmental Systems, Vol. 10. John Wiley & Sons, Ltd, Chichester, Chapter 9.

26. Balnois, E., Wilkinson, K. J., Lead, J. R. and Buffle, J. (1999). Atomic force microscopy of humic substances: effects of pH and ionic strength, *Environ. Sci. Technol.*, **33**, 1311–1317.
27. Lead, J. R., Wilkinson, K. J. and Starchev, K. (2003). Diffusion coefficients of humic substances in agarose gel and in water, *Environ. Sci. Technol.*, **37**, 482–487.
28. Lead, J. R., Wilkinson, K. J., Balnois, E., Cutak, B., Larive, C., Assemi, S. and Beckett, R. (2000). Diffusion coefficients and polydispersities of the Suwannee River fulvic acid: comparison of fluorescence correlation spectroscopy, pulsed-field gradient nuclear magnetic resonance and flow field-flow fractionation, *Environ. Sci. Technol.*, **34**, 3508–3513.
29. Fatin-Rouge, N. and Buffle, J. (2007). Study of environmental systems by means of fluorescence correlation spectroscopy. In *Environmental Colloids and Particles: Behaviour, Structure and Characterisation*, eds Wilkinson, K. J. and Lead, J. R. IUPAC Series on Analytical and Physical Chemistry of Environmental Systems, Vol. 10. John Wiley & Sons, Ltd, Chichester, Chapter 11.
30. Schurtenberger, P. and Newman, M. E. (1993). Characterization of biological and environmental particles using static and dynamic light scattering. In *Environmental Particles*, eds Buffle, J. and van Leeuwen, H. P. IUPAC Series on Analytical and Physical Chemistry of Environmental Systems, Vol. 2. Lewis, Boea Raton, FL.
31. Schmitt-Kopplin, P. and Junkers, J. (2006). Modern electrophoretic techniques for the characterisation of natural Organic matter. In *Environmental Colloids: Behaviour, Structure and Characterisation*, eds Wilkinson, K. J. and Lead, J. R. IUPAC Series on Analytical and Physical Chemistry of Environmental Systems, Vol. 10. John Wiley & Sons, Ltd, Chichester, Chapter 6.
32. Buffle, J. (1998). *Complexation Reactions in Aquatic Systems: an Analytical Approach*. Ellis Horwood, New York.
33. Droppo, I. G., Flannigan, D. T., Leppard, G. G., Jaskot, C. and Liss, S. N. (1996). Floc stabilization for multiple microscopic techniques, *Appl. Environ. Microbiol.* **62**, 3508–3515.
34. Duval, J., Wilkinson, K. J., Buffle, J. and van Leeuwen, H. P. (2005). Humic substances are soft and permeable: evidence from their electrophoretic mobilities, *Environ. Sci. Technol.* **39**, 6435–6445.
35. Villalobos, M., Bargar, J. and Sposito, G. (2005). Mechanisms of Pb(II) sorption on a biogenic manganese Oxide, *Environ. Sci. Technol.*, **39**, 569–576.
36. Lead, J. R., Davison, W., Hamilton-Taylor, J. and Harper, M. (1999). Trace metal sorption by natural particles and coarse colloids, *Geochim. Cosmochim. Acta*, **63**, 1661–1670.
37. Moran, S. B. and Moore, R. M. (1989). The distribution of colloidal aluminium and organic carbon in coastal and open ocean waters off Nova Scotia, *Geochim. Cosmochim. Acta*, **53**, 2519–2527.
38. Honeyman, B. D. and Santschi, P. H. (1992). The role of particles and colloids in the transport of radionuclides and trace metals in the oceans. In *Environmental Particles*, Vol. 1, (Buffle, J. and van Leeuwen, H. P., eds.), pp. 554, Lewis Publishers.
39. Wilkinson, K. J. and Buffle, J. (2004). Critical evaluation of physicochemical parameters and processes for modeling the biological uptake of trace metals in environmental (aqueous) systems. In *Physicochemical Kinetics and Transport at Chemical–Biological Interphases*, eds van Leeuwen, H. P. and Koester, W. John Wiley & Sons, Ltd, Chichester, pp. 533.
40. Thang, N. M., Geckes, H., Kim, J. I. and Beck, H. P. (2001). Application of the flow field-flow fractionation (fFFF) to the characterization of aquatic humic colloids: evaluation and optimization of the method. *Colloids Surf. A*, **181**, 289–301.
41. Redwood, P. S., Lead, J. R., Harrison, R. M. and Stoll, S. (2005). Characterization of humic substances by environmental scanning electron microscopy, *Environ. Sci. Technol.*, in press.
42. Rizzi, F. R., Stoll, S., Senesi, N. and Buffle, J. (2004). A transmission electron microscopy study of the fractal properties and aggregation processes of humic acids, *Soil Sci.*, **169**, 765–775.
43. Balnois, E. and Wilkinson, K. J. (2002). Sample preparation techniques for the observation of environmental biopolymers by atomic force microscopy, *Colloids Surf. A*, **207**, 229–242.
44. Radko, S. P. and Charambach, A. (2002). Separation and characterization of sub-mm- and mm-sized particles by capillary zone electrophoresis, *Electrophoresis*, **23**, 1957–1972.

45. Duval, J. F. L. (2006). Electrophoresis of soft colloids: basic principles and applications. In *Environmental Colloids and Particles: Behaviour, Structure and Characterisation*, eds Wilkinson, K. J. and Lead, J. R. IUPAC Series on Analytical and Physical Chemistry of Environmental Systems, Vol. 10. John Wiley & Sons, Ltd, Chichester, chapter 7.
46. Buffe, J. and Horvai, G. (2000). *In-Situ Monitoring of Aquatic Systems*. John Wiley & Sons, Ltd, Chichester.
47. Wilkinson, K. J., Balnois, E., Leppard, G. G. and Buffe, J. (1999). Characteristic features of the major components of freshwater colloidal organic matter revealed by transmission electron and atomic force microscopy, *Can. J. Fish. Aquat. Sci.*, **155**, 287–310.
48. Muirhead, D. and Lead, J. R. (2003). Physico-chemical characteristics of natural colloids in a heavily-polluted, urban watershed: analysis by atomic force microscopy, *Hydrobiologia* **454**, 65–69.
49. Lead, J. R., Balnois, E., Hosse, M., Menghetti, R. and Wilkinson, K. J. (1999). Characterization of Norwegian natural organic matter: size, diffusion coefficients and electrophoretic mobilities, *Environ. Int.*, **25**, 245–258.
50. Avena, M. J., Vermeer, A. W. P. and Koopal, L. K. (1999). Volume and structure of humic acids studied by viscometry pH and electrolyte concentration effects, *Colloids Surf. A*, **151**, 213–224.



---

## 2 Colloidal Properties of Submicron Particles in Natural Waters

---

MONTSERRAT FILELLA

*Department of Inorganic, Analytical and Applied Chemistry, University of Geneva, 30 quai Ernest-Ansermet, CH-1211 Geneva 4, Switzerland*

1	Introduction . . . . .	17
2	Conceptual and Experimental Approaches . . . . .	19
3	Global Properties of Environmental Colloids . . . . .	21
3.1	Size . . . . .	21
3.2	Charge . . . . .	24
3.3	Efficiency of Aggregation . . . . .	24
3.4	Fractal Dimension . . . . .	33
4	Physical Fractionation Data . . . . .	38
5	Main Homologous Compounds . . . . .	40
5.1	Inorganic Colloids . . . . .	42
5.1.1	Sources . . . . .	42
5.1.2	Main Types . . . . .	48
5.1.2.1	Aluminosilicates . . . . .	48
5.1.2.2	Iron Oxides . . . . .	49
5.1.2.3	Manganese Oxides . . . . .	51
5.2	Organic Macromolecules . . . . .	51
5.2.1	Fulvic and Humic Compounds . . . . .	52
5.2.2	Carbohydrates . . . . .	53
5.2.2.1	Fibrils . . . . .	55
5.2.2.2	Transparent Exopolymer Particles . . . . .	55
5.3	Organic Coatings of Inorganic Colloids . . . . .	56
5.4	Living Organisms . . . . .	58
6	Conclusions . . . . .	60
	List of Symbols and Abbreviations . . . . .	61
	References . . . . .	63

### 1 INTRODUCTION

Colloids may be defined as particles that are sufficiently small that the surface free energy of the particle dominates the bulk free energy. As discussed in the Introduction to this

book, this includes particles roughly sized between 1 and 1000 nm. The word ‘colloid’ was coined by Graham (1805–69) [1] and comes from the Greek  $\kappa\omega\lambda\lambda\alpha$ , which means ‘glue’. Use of this term has persisted, even if a substantial part of colloid chemistry does not deal with glue-type materials. Traditionally, the term ‘colloid’ has been used to refer to the system of the dispersed phase in the dispersing medium. A colloidal dispersion is then defined as a system in which particles of colloidal dimensions are dispersed in a continuous phase of a different composition. The dispersed particles may be small solid particles, organic macromolecules, small gas bubbles or small droplets of liquid. The phase in which these particles are dispersed may be a solid, a liquid or a gas. However, in environmental sciences any material which can be brought into a colloidal solution is nowadays often referred to as a ‘colloid’. Although this chapter will adopt this common practice, it will soon become clear to the reader that the properties of a particle that make it behave like a ‘colloid’ are often inseparable from the physical and chemical characteristics of the water medium. For instance, the upper limit of the colloidal size range itself is defined by the size at which particles sediment, and this is directly dependent upon the kinetic energy of the system [2]. It may range from 5  $\mu\text{m}$  in a karstic aquifer characterised by very high water velocities, as compared with lakes or other groundwater systems [3], to 2  $\mu\text{m}$  or less in the surface of the ocean [4]. At the same time, the capacity of particles to sediment depends on their size and thus on their ability to coagulate, which in turn depends on the ionic strength of the water media.

Information on the characteristics of compounds that behave as colloids in natural water systems has been gathered for over a century, although it has not always been aimed at understanding possible colloidal behaviour. It was soil scientists who pioneered the application of colloidal concepts. As discussed by Bertsch and Seaman [5], the idea that surface-reactive phases in soils are colloidal and include  $\text{Al(OH)}_3$ ,  $\text{Fe(OH)}_3$  and  $\text{SiO}_2$  hydrogels was put forward over a century ago [6] and evidence of the existence of positively and negatively charged colloids was gathered in the 1920s and 1930s by Mattson [7,8 and the series on “The laws of soil colloidal behavior”]. The application of the principles of colloid chemistry to natural waters is probably more recent. It was largely inspired by the work of atmospheric scientists in the case of marine systems [9–11] and, in the case of freshwaters, greatly boosted by waste water engineers [12–15]. The first edition of Stumm and Morgan’s [16] classic book on aquatic chemistry already stated that ‘The significance of the solid–solution interface in natural waters becomes apparent when one considers the state of subdivision of the solids typically presented in natural waters. The dispersed phase in a natural body of water consists predominantly of inorganic colloids, such as clays, metal oxides, metal hydroxides and metal carbonates, and of organic colloidal matter of detrital origin, as well as living organisms (algae and bacteria)’. This statement could have been written now, 35 years later, for the introduction of this chapter. For years, however, the operational distinction between ‘dissolved’ and ‘particulate’ matter in natural waters, separated on the basis of filtration through a 0.45  $\mu\text{m}$  (or 0.22  $\mu\text{m}$ ) membrane filter, has jeopardised the general application of colloidal concepts to the study of natural waters. Although it has repeatedly been pointed out that the distinction between particulate and dissolved is arbitrary and of uncertain value, it is now included in most standard analytical methodologies. Ironically, however, recent years have seen a shift, at least within the domain of research, from colloids being

generally ignored, and mostly included in the so-called ‘dissolved’ fraction, to being considered as particles with a maximum size of 0.45 µm (or even 0.22 µm, depending on the investigator). This phenomenon is closely linked to the increasingly widespread use of various versions of ultrafiltration techniques, particularly in coastal and open ocean environments. In this chapter, colloids will follow the IUPAC definition [17]: colloids are “molecules or polymolecular particles dispersed in a medium that have at least in one direction a dimension roughly between 1 nm and 1 µm”.

Although the study of the behaviour and role of colloids in environmental systems has developed significantly over recent years, much is still unknown. The main reasons for this are: (i) the intrinsic complexity of natural colloids; (ii) the traditional lack of appropriate experimental techniques, a problem which, as this book shows, is progressively being overcome; and (iii) a significant gap between the coagulation theory that environmental systems inherited, which was developed to describe simple systems containing identical, spherical, non-living particles, and the ‘reality’ of natural systems that contain heterogeneous mixtures of particles from many sources [18].

Given that this chapter deals with an extremely broad subject with data that come from very different fields, it is not intended as an exhaustive review of all published data but rather (i) to provide a conceptual framework that allows for the integration of what is already known about natural colloids *under* environmentally relevant conditions and (ii) to highlight particular aspects that merit further development. In this sense, it should mainly be considered as an invitation to further reading and as a basis for discussion. An extensive literature review is provided for this purpose. The chapter begins by looking at the different conceptual and experimental approaches that have so far been applied to the study of environmental colloids (Figure 1) and then focuses on the global properties of unfractionated environmental colloids in natural systems (size, charge, sticking coefficients, porosity), because this kind of data has rarely been reviewed. This is followed by a discussion of some of the main types of compounds present in natural waters in the colloidal size range. The chapter does not include a detailed compilation of published data on the colloidal properties (size, Hamaker constants, charge) of these compounds.

## 2 CONCEPTUAL AND EXPERIMENTAL APPROACHES

When studying real natural systems, characterised not only by molecular-level chemical heterogeneity but also by natural structural complexity at the macroscopic scale, two different conceptual approaches exist. The system can be considered either as a whole, with properties that vary in a continuous manner, or as a large but finite collection of different components that can be isolated and studied separately.

The first approach (approach A in Figure 1) is theoretically better: the properties of a rather complex mixture can rarely be summarised as the sum of the properties of each individual component because of the multiple interactions which often exist between them [19]. For instance, microscopic investigations [20–25] have shown that, in natural conditions, hydrous oxides and high molecular mass natural organic matter (NOM) form intimate structures in natural waters. The aggregation of these entities leads to a more complicated structure in which small colloids may, in turn, not only be scavenged at the surface, but also be embedded in the mineral–organic moieties. However, although

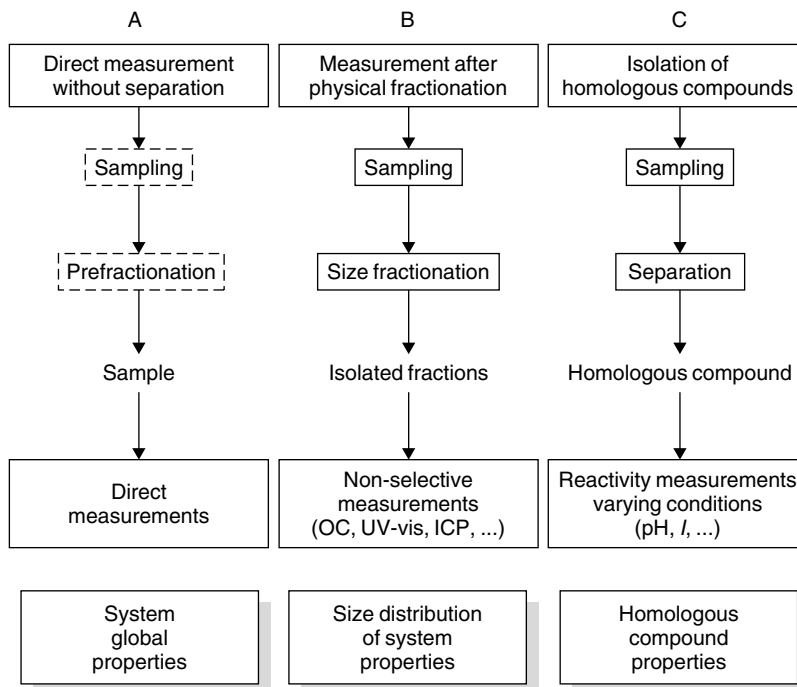


**Figure 1.** Schematic representation of the three approaches used to study colloids in natural waters. Dashed boxes, optional steps

preferable, the characterisation and the study of the properties of natural particle assemblages without perturbing them is challenging because it is virtually impossible to isolate the aggregates free of artefacts. In practice, a more common approach is to study the global colloidal properties of the particles present in a given system without attempting to isolate individual colloids or assemblages first. Published data on properties such as size, charge, coagulation efficiency and porosity gained by taking this approach are collated and discussed in Section 3.

However, nowadays the more widely applied methods are based either on the use of operationally defined physical fractionation procedures, followed by the measurement of variables such as organic carbon and trace metal concentrations in the different size classes, (approach B in Figure 1) or on the isolation of so-called homologous compounds (i.e. groups of compounds with similar operationally defined physicochemical characteristics), such as clays, iron oxides and humic substances and the subsequent study of their properties (approach C in Figure 1). Over the past few years, approach B has become increasingly popular, thanks mainly to the extensive use of cross-flow filtration (CFF), which is by far the most widely used approach in colloid-related studies. This approach is discussed in Section 4. The validity of approach C relies on two premises: (i) the representativeness of the homologous compounds studied and (ii) the additivity of the properties of the different classes of particles. Neither of these hypotheses has been fully proved.

### 3 GLOBAL PROPERTIES OF ENVIRONMENTAL COLLOIDS

The following sections focus on four properties that are relevant to the colloidal behaviour of any particle: size, charge, ability to coagulate (sticking coefficients) and porosity (fractal dimension) of the aggregates. As explained in Section 1, size is an inherent part of identifying any environmental particle as a colloid.

#### 3.1 SIZE

The circulation and removal of particles from surface waters, soils and groundwaters is size dependent. Hence the behaviour of and the role played by colloidal particles in the biogeochemical cycles of trace metals and organic micropollutants are intrinsically linked to their size. The size distribution of suspended particles is a function of several variables, including source and nature of the particles, physical and biological processes of aggregation and ‘age’ of the suspension. It has been commonly accepted for many years that the number concentration of colloidal particles increases logarithmically with decreasing size, implying a continuum of particulate matter ranging from nanometre-sized material to the large particulate matter settling out of the water column. This power-law distribution paradigm arose from initial observations by aerosol physicists [26–29] and oceanographers [9–11, 30–33] for particles in the  $>1\text{ }\mu\text{m}$  size range. Most of the observed particle size distributions in ocean waters in the 1970s and early 1980s were such that they showed equal particle volumes in logarithmically increasing size ranges [34]. It was suggested that these flat distributions resulted from the combination of the distributions of individual components that are log-normal by number [35] and of aggregation processes. Friedlander [26,27] suggested that, for distributions with production of particles at the fine end and removal by sedimentation at the coarse end, the form of the distribution is determined by the parameters describing the coagulation and sedimentation mechanisms and the flux of matter through the spectrum. In equilibrium, the size spectrum would display several subranges, each dominated by a single coagulation mechanism (Brownian motion, shear and differential sedimentation). Hunt [36,37] calculated a different slope of the power-law exponent as a function of the predominant coagulation mechanism by using dimensional analysis: Brownian motion, 2.5; shear collisions, 4.0; differential sedimentation, 4.0; and gravitational settling, 4.75. Hunt’s calculations did not include the fractal nature of the natural aggregates (see Section 3.4). According to Friedlander’s hypothesis, a flux of particulate matter through the distribution would then exist from smaller to larger sizes ending in the sedimentation of the larger particles. The result would be the observation of quasi-stationary distributions (so-called Junge distributions [38]) [36]. In practice, at proximity to a source, size distributions might not be flat but show various peaks. Peaks may also be related to aggregation, for example the formation of peaks related to a faster collision by Brownian motion as compared with elimination by shear. McCave argued that oceans are not mixed as rapidly as the atmosphere and that only away from direct sources and a long time after the introduction of particles to the ocean do ocean spectra become flat [34]. It is important to point out that all of the above considerations were developed for particles larger than  $1\text{ }\mu\text{m}$  and that, although commonly accepted for colloidal-size particles, the number of measurements of particle size spectra for natural waters in the colloidal size range is, in fact, relatively low.

Table 1 shows results from studies in which the dependence of the number of particles on their size was quantified in terms of a power-law dependence. The scarcity of values probably stems from the difficulties involved in measuring them. In fact, sizing polydisperse samples in the colloid range remains a difficult task for which no single method has proved to be totally adequate. Sequential gravimetric analysis following filtration or centrifugation is the traditional method for measuring particle size distributions in colloidal systems and is still used today. However, determining size distributions of particles of size  $<1\text{ }\mu\text{m}$  using this technique is still not reliable because of the difficulty involved in isolating enough material to weigh. The sizing of natural polydisperse samples often requires the use of a method that incorporates a preliminary separation step (ultrafiltration, ultracentrifugation) in order to reduce sample polydispersity and heterogeneity prior to detection and analysis by techniques such as dynamic light scattering (DLS) or transmission electron microscopy (TEM) (Chapter 8, this volume). Light scattering techniques have the advantage of being non-destructive, they involve minimal sample alteration and they are rapid. However, although they are very powerful for colloidal samples that do not vary greatly in size, the measurement of polydisperse samples becomes difficult without prefractionation [39,40]. The need for prior separation is overcome in single particle counters [e.g. electrosensing zone (ESZ), light obscuration (LO), single particle counter (SPC)] by simply passing very dilute suspensions through the detector. Apart from the SPC [41,42], the minimum size for such methods is limited to about  $0.5\text{ }\mu\text{m}$  by the detector's sensitivity.

The measured particle size distributions rarely contain data below 60 nm. When present, they deviate from the expected power law, with a tendency towards lower than expected particle numbers. One possible explanation might be the analytical limitations of the methods used. For instance, incomplete collection of low-density small colloids under centrifugation conditions is to be expected [46,47], particularly when existing evidence shows that most of the very small colloids observed in natural waters are either organic in nature [50–53] or are inorganic colloids interbridged with polysaccharidic-like materials [21,24,54]. Moreover, many detection techniques either do not 'see' very small inorganic particles (SPC) [42] or cannot detect them in the presence of larger particles (DLS) [39]. A technique that is particularly well suited to measuring inorganic nanoparticle sizes, laser induced breakdown detection (LIBD) [55] (Chapter 12, this volume), does not detect organic particles in natural conditions.

When considering the stability of very small colloids, the effect of particle concentration should also be taken into account. According to the power-law paradigm, very small colloids would be present in very high numbers. Since the colloid aggregation rate is proportional to the square of the particle concentration [16], the collision frequency in nanosystems will be many orders of magnitude higher than for larger colloid particles.

### 3.2 CHARGE

Most colloidal particles are charged. The three main origins of surface charge are [56] (i) chemical reactions at the surface (i.e. silica, iron oxyhydroxides, humics, bacteria), (ii) lattice imperfections at the solid surface and isomorphous replacements within the lattice (aluminosilicates) and (iii) ion adsorption. At pH values close to neutral, most natural particles, such as aluminosilicates, and most insoluble oxides, organic compounds, bacteria and algae are characterised by a negative surface potential, as indicated by negative

**Table 1.** Literature-reported power law dependence<sup>a</sup> of particle number on particle size in the colloidal size range for environmentally relevant systems

System	$\beta^a$	Size range	Method	Reference
Foraminifera and diatoms, near-surface south Indian Ocean	$4.5 \pm 0.3$	100 nm–100 $\mu\text{m}$	Calculated from previously published data	[43]
Gulf of Mexico	$2.65^b$	<2 $\mu\text{m}$	TEM	[4]
Lake Zürich, Switzerland, 2.5 m depth	3.79	1–20 $\mu\text{m}$	ESZ	[44]
Grimsel test site groundwater, Switzerland	4.17	10 nm–10 $\mu\text{m}$	TEM, SEM, SPC, GRAV	[45]
Coastal surface waters, California, US	$\geq 6^b$	40–120 nm	TEM	[46]
River water, Water of Leith, Dunedin, New Zealand	$2.6 \pm 0.3$	5–400 nm	TEM	[47]
Transitgas tunnel (Aar valley, Switzerland)	2.5 – 4	30 nm–3 $\mu\text{m}$	SEM, SPC	[41]
Leuggern, Switzerland	2.6			
Zurzach, Switzerland	3.1			
Bied brook (karstic system), Switzerland	$2.74 \pm 0.35$ (n = 34)	500 nm–60 $\mu\text{m}$	LO	[3]
Noiraigue spring (karstic system), Switzerland	$2.82 \pm 0.39$ (n = 43)			
Alpine river (flood), Switzerland	2.71	200 nm–15 $\mu\text{m}$	SPC	[48]
Lake Lugano, Switzerland	3.00			
Aare River above lake Biinne, Switzerland	3.03			
Aare River below Lake Biinne, Switzerland	3.00			
Marl groundwater, Wellenberg, Switzerland	4	50 nm–5 $\mu\text{m}$	SPC	[49]
Lake Léman, Switzerland:		50 nm–2 $\mu\text{m}$	SPC	[42]
Hypolimnion, 30 m depth	$4.06 \pm 0.08$			
Epilimnion, 5 m depth	$4.01 \pm 0.10$			
Versoix River, Switzerland	$3.53 \pm 0.08$			

<sup>a</sup> Slope of the power-law distribution:  $n(d_p) = dN/dd_p = Ad_p^{-\beta}$ , where  $n(d_p)$  = particle size distribution function (diameter basis),  $N$  = particle number,  $d_p$  = particle diameter,  $A$  = coefficient related to the total number concentration of particles,  $\beta$  = power-law slope. <sup>b</sup> Slope value for a cumulative distribution in the original = ( $\beta - 1$ ).

values for their electrophoretic mobility. It is therefore not surprising that, irrespective of their composition, colloidal particles in surface waters [57–60] and in groundwater aquifers [61,62] are almost always observed to have a negative surface charge. There are very few exceptions to this rule [63–65] and these are usually related to the presence of iron oxides in the system. For example, in a study conducted in a deep, strongly weathered aquifer, very low in organic matter content, positively charged colloids, consisting mainly of iron and aluminium oxides were found [66].

Despite the fact that natural colloids consist of a varied mixture of mineral, organic and microbiological materials, it has been widely observed that natural particles in suspension in estuarine and marine waters [57–59,63,64,67–69] and in freshwaters [60,63,70–74] display an unusually narrow range of electrophoretic mobilities. This is consistent with the hypothesis that all the particles are coated with NOM [57–59,67,68,75,76]. NOM is ubiquitous in natural aquatic systems and adsorbs on most colloidal particles (see Section 5.2.4). Adsorbed NOM seems to dominate the surface properties of natural particles and can have a significant effect on colloidal stability and consequently can affect the transport and fate of colloids in aquatic environments. Observed differences in mean mobility between samples from different aquatic systems [60,67,68,76] depend on the small concentration of divalent cations in the water [76]. This is true even for estuarine samples in which the major cation ( $\text{Na}^+$ ) plays only a minor role in determining the surface charge.

The extent of colloid transport in subsurface systems is generally described in terms of the magnitude of the surface charge of the colloids and aquifer surfaces. However, spatial heterogeneity in surface charge can make the average surface charge on the grains (as measured by the zeta potential) irrelevant for transport predictions. This has been very effectively illustrated by Elimelech *et al.* [77], who created patchwise heterogeneity in colloidal particles by modifying the surface chemistry of a fraction of the quartz sand grains via reaction with aminosilane (charge reversed).

Information on colloidal and suspended matter charge can also be obtained by potentiometric proton titrations. This simple approach has made it possible to differentiate samples containing mostly clays, such as kaolinite (flat titration curves), from others rich in heterogeneous compounds such as humic substances (non-flat, continuous titration curve shape) [78].

### 3.3 EFFICIENCY OF AGGREGATION

The rate of colloid aggregation depends on both the frequency of particle collisions and the efficiency of particle contacts. The efficiency of particle contacts is controlled primarily by surface forces which introduce an energetic barrier that determines the probability of successful interparticle collisions. This energetic barrier is influenced by the ionic strength and composition of the water, and also by the adsorption of surface-active species. The collision frequency was theoretically solved by von Smoluchowski [79], and the basis for an evaluation of the collision efficiency was formulated by Fuchs [80]. The effect of dispersion forces was explained by Hamaker [81], Bradley [82] and De Boer [83]; electrostatic repulsion can be evaluated on the basis of the Derjaguin-Landau-Verwey-Overbeek (DLVO) theory [84,85].

In practice, the stability of particles in an aqueous suspension is usually described by an empirical sticking factor,  $\alpha$ , defined as

$$\alpha = \text{interparticle attachment rate}/\text{interparticle collision rate} \quad (1)$$

The sticking factor is, therefore, the ratio of collisions producing aggregates to the total number of collisions that occur by physical processes. For a perfectly stable suspension, all collisions are unsuccessful and  $\alpha = 0$ . For a completely destabilised suspension, all collisions produce aggregation and  $\alpha = 1$ . The sticking factor is measured experimentally by the fraction of collisions leading to permanent aggregation and corresponds to the inverse of the stability ratio,  $W (W = \alpha^{-1})$ , as defined by Fuchs [16]. Solutions for the calculation of the collision efficiency based on the DLVO theory are available, but large discrepancies are usually observed between experimental and theoretical predictions [86–88] in the presence of repulsive double-layer interactions in model systems and of NOM in natural systems. Wide particle size distributions and surface charge heterogeneity—plus wide pore distributions, complex pore geometry and rough matrix surfaces in the case of porous media – preclude, for the time being, the application of the DLVO theory to predict collision efficiencies in natural media.

The  $\alpha$  values can be determined in a laboratory reactor where the physical interparticle contact rate is controlled. Two methods have generally been used: one based on the control of the Brownian coagulation through the addition of salt, and the other on the control of the coagulation by shear. In the latter method, a Couette reactor is normally used. This reactor consists of a fixed inner and a rotating outer cylinder and provides a quantifiable two-dimensional laminar shear in the annular space between the cylinders [89–91]. Alternatively, a Jar-test (paddle-mixing) device can be used [92]. When a suspension of particles which are uniform in size at the onset of the aggregation is allowed to coagulate, the denominator of equation (1) can be described by analytical equations for contacts by fluid shear (orthokinetic flocculation) and by Brownian diffusion (perikinetic flocculation). Alternatively, it can be measured experimentally by setting conditions that force Brownian coagulation, such as very high salt concentration. The numerator in equation (1) is then determined experimentally by following the decrease in particle concentration with time. The sticking factor is calculated from the ratio of measured changes in particle concentration to calculated contact rates for the laboratory reactor used or measured at high electrolyte concentrations. The methods available have some limitations. For instance, Kiørboe and Hansen [93] documented an inverse relationship between shear rates and measured coagulation efficiencies. A comparison of  $\alpha$  values obtained from experiments that are run at different shear rates might therefore have no meaning. According to Alldredge and McGillivray [94], the method that is most commonly used may tend to underestimate  $\alpha$ .

Few sticking factor values have been published for natural colloids, and even fewer for unfractionated natural suspensions. Published values are shown in Table 2. Results for latex particles have not been considered. Data for homologous compounds are of little value for environmental prediction purposes due to the high level of variation in the origin and treatment of the particles and the wide range of conditions and techniques used for the measurements. It is difficult to establish any general trends from the published data, except that, as expected, values for a given system show the positive effect of calcium on colloid destabilisation. As mentioned in Section 3.2, adsorbed NOM can dominate the surface properties of natural particles and can have a significant effect on colloidal stability [95–99]. As NOM contains many acidic functional groups, its adsorption produces a uniformly negative surface charge on the colloids in natural waters. This charge should

**Table 2.** Literature-reported sticking factors,  $\alpha$ , for environmentally relevant systems

System	$\alpha$	Conditions <sup>a</sup>	Method	Reference
Clays (1.5–6 $\mu\text{m}$ , mean = 4.2 $\mu\text{m}$ )		pH = 7.8–8.2 NaCl	Shear $G = 52 \text{ s}^{-1}$ Couette device	[100]
Kaolinite	0.0245 ± 0.007 0.0308 ± 0.004 0.0724 ± 0.007	0.05 0.09 0.3	Microscopy, ESZ	
Illite	0.0128 ± 0.003 0.0275 ± 0.005 0.0455 ± 0.007	0.05 0.09 0.3		
Montmorillonite	0.075 ± 0.009 0.089 ± 0.006 0.125 ± 0.005	0.05 0.09 0.3		
Kaolinite	0.0445 ± 0.002 0.0915 ± 0.006 0.138 ± 0.009	Synthetic sea water 0.036 0.087 0.343		
Illite	0.0180 ± 0.003 0.0701 ± 0.007 0.0740 ± 0.009	0.036 0.087 0.343		
Montmorillonite	0.0943 ± 0.003 0.113 ± 0.019 0.148 ± 0.006	0.036 0.087 0.343		
Estuarine sediments (clay size fraction of Pamlico sediments) <sup>b</sup>	0.05 0.08 0.09 0.10 0.13 0.17 0.13 0.18 0.22	Fresh water sediment 1.8 ppt (salinity) 4.4 ppt 17.5 ppt Upper estuary sediment 1.8 ppt (salinity) 4.4 ppt 17.5 ppt Lower estuary sediment 1.8 ppt (salinity) 4.4 ppt 17.5 ppt		
Alumina	0.01 – 0.063 0.086	$\text{Ca}^{2+}$ Filtered lake water	Shear	[101]
Haematite (300 nm)	0.01–1 <sup>c</sup>	$[\text{Ca}^{2+}] = 0.001–0.5$ , $[\text{HA}] = 1, 5, 20$ pH = 6.6	Brownian Dark field Microscopy	[102]
Amazon river sediments (27% montmorillonite, 24% illite, 38% kaolinite)	0.70 0.82	2% salinity Organic coating Organic coating removed	Shear Couette device Microscopy (200 particles)	[103,104]

**Table 2.** (*continued*)

System	$\alpha$	Conditions <sup>a</sup>	Method	Reference
Yukon river sediments (20% montmorillonite, 29% illite, 45% chlorite)	0.23 0.77	0.6% salinity Organic coating Organic coating removed		
Continental shelf off Guiana sediments (45% montmorillonite, 18% illite, 30% kaolinite)	0.19 0.26	0.9% salinity Organic coating Organic coating removed		
Delaware Bay sediments (2–4 $\mu\text{m}$ )	0.077  0.145  0.171 0.177  0.207 0.216	1.1% salinity Organic coating Organic coating removed  4.4% salinity Organic coating Organic coating removed  17.5% salinity Organic coating Organic coating removed	Blade-type reactor Microscopy counting (200 particles)	
Freshwater suspended particles	0.01–0.08	$[\text{Ca}^{2+}] = 5 \times 10^{-4}$ , TOC = 2 (natural conditions)	Shear $G = 50 \text{ s}^{-1}$	[105]
Epilimnion Loch Raven reservoir, US	0.035–0.2  0.035–0.006  0.025–0.058	$[\text{FA}] = 0$ , $[\text{Ca}^{2+}] = 0$ – $1 \times 10^{-3}$  $[\text{Ca}^{2+}] = 0$ , $[\text{FA}] = 0$ –20  $[\text{FA}] = 5$ , $[\text{Ca}^{2+}] = 1 \times 10^{-4}$ – $1 \times 10^{-3}$	Stirred tank ESZ	
Kaolinite (3.7 $\mu\text{m}$ )	0.058	$[\text{CaCl}_2] = 5 \times 10^{-3}$ (ccc)	Shear $G = 700 \text{ s}^{-1}$	[95]
Silica (4 $\mu\text{m}$ )	0.034  Increasing concentrations of aquatic HA stabilize the suspensions	$[\text{CaCl}_2] = 1 \times 10^{-2}$ (ccc)	Magnetic stirring	
Turbid impoundment	0.0085 <sup>b</sup> 0.015 <sup>b</sup>	Added $[\text{Ca}^{2+}] = 1 \times 10^{-3}$ $= 1.2 \times 10^{-3}$	Brownian DLS	[106]

(Continued overleaf)

**Table 2.** (*continued*)

System	$\alpha$	Conditions <sup>a</sup>	Method	Reference
Chuckwa Creek, OK, US	0.09 <sup>b</sup> 0.35 <sup>b</sup>	$= 1.6 \times 10^{-3}$ $= 2 \times 10^{-3}$		
Haematite (<100 nm)	Values depending on conditions: sharp initial decrease in stability (100-fold) within a factor of 10 increase in the concentration of OM followed by a sharp increase in particle stability when OM increased beyond the ccc point	Varying pH (2–12), $I$ (0.001–0.084), electrolyte (CaCl <sub>2</sub> , NaCl, MgCl <sub>2</sub> , Na <sub>2</sub> SO <sub>4</sub> , phosphate), OM (fatty acid, laureate, polyaspartate, FA, HA)	Brownian DLS W	[107]
Freshwater sediments	0.15 0.30	Freshwater Seawater	Shear	[108]
Lake suspended particles (1–12 $\mu\text{m}$ )	0.07–0.13  0.009–0.11  0.055  0.047	Lake Zürich: DOC $\approx$ 1 $[\text{Ca}^{2+}] \approx$ $1.2 \times 10^{-3}$  Lake Sempach: DOC = 4 $[\text{Ca}^{2+}] \approx$ $1.2 \times 10^{-3}$  Lake Luzern: DOC = 1, $[\text{Ca}^{2+}] \approx$ $0.9 \times 10^{-3}$  Lake Greifen: DOC = 4, $[\text{Ca}^{2+}] \approx$ $2 \times 10^{-3}$	Shear $G = 50 \text{ s}^{-1}$ Blade-type reactor ESZ	[109]
Haematite (100 nm)	$1 \times 10^{-5}$ – $1^b$	$[\text{KCl}] =$ $(5\text{--}300) \times 10^{-3}$	Brownian DLS W	[96]
Haematite	0.01– $1^b$  0.005– $1^b$	$[\text{FA}] = 1$ , $[\text{KCl}] =$ $(3\text{--}100) \times 10^{-3}$  $[\text{FA}] = 2.5$ , $[\text{KCl}] =$ $(3\text{--}100) \times 10^{-3}$	Brownian DLS W	[97]
Haematite (60 nm)	0.0003–1	$0.005 < I < 0.2$ , 4.0 $< \text{pH} < 6.3$	Brownian DLS	[98]

**Table 2.** (*continued*)

System	$\alpha$	Conditions <sup>a</sup>	Method	Reference
	All types of OM enhance haematite stability when $I$ is low	$[\alpha\text{-Fe}_2\text{O}_3] = 10$ Addition of polyaspartic acid, polyacrylic acid and swamp NOM		
Alumina (1.33 $\mu\text{m}$ )	0.001 0.06 0.17	$[\text{Ca}^{2+}] = 0$ $[\text{Ca}^{2+}] = 2 \times 10^{-3}$ $[\text{Ca}^{2+}] = 4 \times 10^{-3}$ $[\alpha\text{-Al}_2\text{O}_3] = 5$ , $[\text{SRFA}] = 2.60 \text{ mg OC dm}^{-3}$ , $\text{pH} = 6.5$	Shear $G = 55 \text{ s}^{-1}$ Jar test ESZ	[110]
Deep crystalline water	Values in figures, difficult to extract	$\text{pOC} < 4.3$ , $\text{pH} = 8.0$	Brownian Batch experiments SPC	[111,112]
Na-montmorillonite (100 nm)		Variation of $[\text{Na}^+]$ ( $0\text{--}2 \times 10^{-2}$ ) and $[\text{Ca}^{2+}]$ ( $0\text{--}1 \times 10^{-3}$ )		
Haematite (70 nm)	$1 \times 10^{-4}\text{--}2 \times 10^{-4}$ These values include hydrodynamic interactions	$I = 0.005$ , $\text{pH} = 5.0\text{--}8.2$	Brownian Laser diffraction Particle size analyser (0.48–180 $\mu\text{m}$ )	[113]
Kaolinite (<1 $\mu\text{m}$ )	Values depending on conditions: $\alpha = 1$ at pH 4 at any $I$ ; $\alpha < 1$ at pH > edge surface PZNPC,	$[\text{NaClO}_4] = 0.001\text{--}1$ , $\text{pH} = 4\text{--}10$ , $[\text{soil HA}] = 0\text{--}6 \text{ mg OC dm}^{-3}$	Brownian DLS W	[114]
Kaolinite (179 nm $\times$ 11 nm)	$1.6 \times 10^{-5}\text{--}1^b$ Kaolinite particles were stable in $[\text{NaCl}] < 0.1$	$[\text{NaCl}] = 0.1\text{--}0.5$ , $\text{pH} = 7.8$ , $T = 27.5$	Brownian DLS W	[115]
Brook that drains peat areas	0.17 $1.7 \times 10^{-4}$	$\text{TOC} = 21.4\text{--}35.4$ , $[\text{Ca}^{2+}] = 71\text{--}82.7$	Brownian Shear LO	[116]
Kaolinite Montmorillonite Coarse Hanford sediment, US	$8.26 \times 10^{-4}$ $5.02 \times 10^{-4}$ $1.42 \times 10^{-3}$	$\text{pH} = 10$ , $T = 22$	Brownian DLS	[117]
Fine Hanford sediment, US	$1.41 \times 10^{-3}$			

(Continued overleaf)

**Table 2.** (*continued*)

System	$\alpha$	Conditions <sup>a</sup>	Method	Reference
Kaolinite (<1 $\mu\text{m}$ )	Values depending on conditions: increase in metal concentration resulted in increased $\alpha$ , plateau at $\alpha = 0.56$	[Kaolinite] = 25–200 mg $\text{dm}^{-3}$ , [FA] = 0.15–1.2 mg $\text{dm}^{-3}$ (constant ratio = 500 : 3), [Pb(II)], [Cu(II)], [Ca(II)] = $1 \times 10^{-4} - 1 \times 10^{-2}$ , $I = 0.01$ NaNO <sub>3</sub> , pH = 4, 6, $T = 25$	Brownian DLS	[118]

<sup>a</sup> Element concentrations are expressed in mol  $\text{dm}^{-3}$  and FA, TOC and DOC concentrations in mg  $\text{dm}^{-3}$  except where stated otherwise. Temperatures are expressed in °C. <sup>b</sup> Scanned from published figures by using Un-Scan-It <sup>c</sup> Estimated from the coagulation rate constants published in the paper.

impart stability to the particles by producing repulsive electrostatic double-layer forces, at least at low ionic strength. In addition, some NOM has a high molecular mass and hence could impart stability through repulsive steric forces, which arise when segments of adsorbed NOM are confined to a smaller volume during particle collisions. The results in Table 2 show that inorganic colloids exhibit a higher colloidal stability in the presence of humic substances. However, it has been suggested that the effect of NOM on the coagulation of mineral particles depends on the type of NOM: humic-type compounds and rigid polysaccharide-rich fibrils would have opposite effects [119].

Much attention has been paid to the study of the role of coagulation processes in diatom blooms [120–125]. Diatom blooms provide a convenient way of studying marine aggregation because they are characterised by high particle concentrations and undergo rapid aggregation relatively free from competing processes such as grazing [18]. Although diatoms are not colloids according to size criteria, published results are of some interest and are shown in Table 3. Interpreting these results is not a straightforward process because phytoplankton stickiness can vary according to species and physiological state [126].

It is generally accepted that sticking factors are independent of the mode of particle transport [131] but conclusive evidence is lacking. For instance, Gibbs [104] found that  $\alpha$  increased with particle size for some types of natural sediments but not for others; Burban *et al.* [108] assumed that  $\alpha$  decreased as the floc size of sediments increased; Atteia *et al.* [116] estimated two  $\alpha$  values, one for Brownian coagulation and another for perikinetic coagulation by using aggregation experiments performed on natural suspensions of organic-rich waters in a brook which drained peat areas. The two  $\alpha$  values, which differed by a factor of 1000, were estimated by applying a model previously developed by the author [132] to particle size distributions determined by an LO technique (50 nm – 10  $\mu\text{m}$ ) in stirred solutions. In practice, most of the models of aggregation in natural waters assume  $\alpha$  to be constant across all sizes of aggregating particles and independent of collision velocity [34,105,109,133–138].

**Table 3.** Literature-reported sticking factors,  $\alpha$ , for diatom cells

Species	$\alpha$	Conditions	Method	Reference
<i>Thalassiosira pseudonana</i>	<0.005 ≈0.1	Nutrient depleted Cell growth stopped, cells nutrient limited	Device incorporating a vertically oscillating grid $G = 50 \text{ s}^{-1}$	[126]
<i>Skeletonema costatum</i>	>0.1	Transition between exponential and stationary growth phase		
Marine snow (200–7600 $\mu\text{m}$ in diameter)	0.60–0.88	Seawater	Differential settling, video recording	[94]
<i>Skeletonema costatum</i> (non-axenic)	0.02–0.25	$\alpha$ decreases with age of culture	Couette device $G = 50 \text{ s}^{-1}$	[93]
<i>Skeletonema costatum</i> (axenic)	0.00–0.98	$\alpha$ decreases with age of culture		
<i>Thalassiosira pseudonana</i> (non-axenic)	0.00–0.08	$\alpha$ increases with age of culture		
<i>Thalassiosira weissflogi</i>	0.00–0.01			
<i>Chaetoceros affinis</i>	0.04–0.61			
<i>Phaeodactylum tricornutum</i>	0.15–0.20	$\alpha$ independent of culture age		
<i>Rhodomonas baltica</i>	0.00–0.05			
<i>Dunaliella marina</i>	0.00–0.04			
<i>Skeletonema costatum</i>	0.001–0.13	34 days	Couette device $G = 5.7 \text{ s}^{-1}$	[91]
Mixed diatom bloom, shallow Danish fjord	0.01–0.3	$\alpha$ decreases along the bloom (3 weeks)	Couette device $G = 30 \text{ s}^{-1}$	[127]
Phytoplankton bloom in a mesocosm	0.80 (day 7)–0.03 (day 11)	$\alpha$ decreases during bloom event	Couette device $G = 5 \text{ s}^{-1}$ ESZ	[128]
Phytoplankton TEP	0.015 0.21	Saltwater mesocosm, 14 day experiment	Microscopy, photography	[129]
Diatoms in Benguela upwelling current	Up to 0.4	$\alpha$ followed on 8 consecutive days	Couette device $G = 10 \text{ s}^{-1}$	[130]

As for surface waters, colloid deposition during flow through porous media, such as soils and groundwater, is commonly assumed to take place in two rate-limiting steps [139]: transport of colloidal particles to matrix surfaces by Brownian diffusion, interception or gravitational sedimentation resulting in colloid–matrix collisions and the attachment of colloidal particles to the matrix surfaces. The proportion of colloid–matrix collisions that

result in the attachment of the colloidal particles is also described by an attachment (or collision) efficiency factor  $\alpha$  [140]. Principles and examples of colloid deposition kinetics in model and real systems can be found in [139].

### 3.4 FRACTAL DIMENSION

As the coagulation of solid particles proceeds, fluid is taken into pores in the aggregates that are formed. As the process continues, aggregate density decreases, while total aggregate volume increases. The result is an increase in the cross-section of the aggregate, thereby increasing the rate of interparticle contact. Observation of natural systems indicates that the aggregates in such systems are fractal objects whose structure remains self-similar during a change of scale [141–143]. In other words, a portion of the aggregate, regardless of its characteristic length dimension,  $L$ , is statistically equivalent to the structure of the entire aggregate. This self-similarity leads to a power-law relationship between the mass of the aggregate,  $m$ , and the dimension of the portion of the aggregate:

$$m \propto L^D \quad (2)$$

where  $D$  is called the fractal dimension. For a Euclidean object such as a sphere,  $D = 3$ .

Numerical and physical experimentation has identified regimes of colloid aggregation that tend to produce porous aggregates of given fractal dimensions. Nearly 20 years ago, Meakin [144] published an excellent review of research in this area. In the diffusion-limited aggregation (DLA) regime, aggregate growth is produced by Brownian transport and irreversible adhesion of contacting aggregates. These aggregates have a fractal dimension of around 1.8 ([141] and references therein) and their average mass increases with time in a linear fashion. In the reaction-limited aggregation (RLA regime), only a fraction of the contact between aggregates results in irreversible adhesion between the colliding aggregates. These aggregates have a more compact structure with values between 1.9 and 2.1 ([141] and references therein) and their average mass increases exponentially [145]. These two regimes of colloidal aggregation are accepted as universal, irrespective of the chemical nature of particular colloid systems [145].

However, not all natural aggregates are fractal. For instance, Chin *et al.* [146] formed aggregates by passing bubbles through seawater containing NOM. These aggregates had a gel structure that must be characterised by a different sizing scale than that of fractals because of the ‘annealing’ that combines them.

Strictly, the fractal relationship [equation (2)] is limited to monodisperse systems. Natural systems are strongly heterodisperse, making it difficult to use fractal scaling to describe the relationship between mass and length. However, the properties of aggregates in such systems can be described by an extension to fractal scaling that expresses it as a geometric property [147]. Jackson [148] derived a quantity related to length,  $\lambda$  ( $\lambda = L^D$ , where  $L$  is the particle length), that is conserved in the same way as mass during coagulation.

Jiang and Logan [149] extended Hunt’s work ([36]; see Section 3.1) in such a way that the fractal dimension of the aggregates could be inferred from the observed slope of the particle size spectrum in steady-state conditions. Using dimensional analysis, they

predicted that the slope of the cumulative particle size distributions would be  $-D/2$  for Brownian motion,  $-\frac{1}{2}(D+3)$  for fluid shear and  $-\frac{1}{2}(1+2D)$  for differential sedimentation (Stoke's settling,  $D \geq 2$ ).

The fractal dimensions are calculated using power-law relationships between the volume of the aggregates and the characteristic length raised to the power  $D$ . They can be derived from relationships with measured aggregate properties (i.e. porosity, density, turbidity), from settling velocity relationships or from particle size spectra [150]. Different techniques have often been used specifically for the determination of fractal dimensions: static light scattering (SLS) [97,151–155], DLS [154,156], small-angle neutron scattering (SANS) [157–159], small-angle X-ray scattering (SAXS) [160–162] and microscopy image analysis [154,163,164]. A two-dimensional fractal dimension,  $D_2$ , has sometimes been defined by a power-law relationship between projected area [i.e. from microscopic and/or charge-coupled device (CCD) images] and the characteristic length of the aggregates [165]. The coalesced sphere assumption corresponds to  $D_2 = 2$ .

Numerous studies have been carried out on polystyrene latex beads, which will not be considered here. The majority of the studies involving 'environmental' particles have used synthetic laboratory particles such as goethite [151], haematite [97,113,154], montmorillonite [166] or fractionated organic compounds [158–165,167–169]. The few examples of fractal concepts being applied to non-fractionated environmental samples concern the characterisation of marine snow [170,171], aggregates formed in a mesocosm diatom bloom [172,173] and estuarine and marine suspended particles [174–177]. Some relevant published results are collated in Table 4. The techniques used are also given. It is important to underline the fact that most of these results have been obtained for aggregates that largely exceed the colloidal domain. For instance, the *Zoogloea ramifera* aggregates studied by Logan and Wilkinson [170] are in the size range 0.4–1.4 mm! Fractal dimension concepts have also been applied to the characterisation of particle aggregation processes in engineered environments, such as water and wastewater treatment plants [166,178].

Avnir *et al.* [179] questioned the fractal character reported for many systems based on experimentally derived scaling exponents. They pointed out that a fractal object, in the purely mathematical sense [180], requires many orders of magnitude of power-law scaling, and therefore to conclude that the experimental results indicate fractality requires 'many' orders of magnitude. They found that the reported experimental fractality in a wide range of physical systems was typically based on a scaling range spanning only 0.5–2 decades. The combination of SAXS and SLS attempted by Rice *et al.* [162] constituted a first attempt to determine whether fractal behaviour was actually observed over a wide scaling range in an environmental-related sample: fulvic and humic compounds. Their SLS results seemed to show that at a long characterisation length scale, humic acid is not fractal. Jackson and Lochmann [122] also noted that an aggregate composed of algal cells is not, strictly a fractal because equation (2) is not satisfied for particles smaller than the algal cell. They pointed out that some authors highlight the difference by talking about such aggregates as having a 'cluster fractal dimension' [181]. However, regardless of the 'true' fractal nature of environmental colloids, the application of the fractal approach to data analysis may still provide a useful methodology to describe the porosity and structure of natural colloids.

**Table 4.** Literature-reported fractal dimension estimates for environmentally relevant aggregates<sup>a</sup>

System	D	Method	Reference
Soil (kaolinite, trace hallosite)	$2.92 \pm 0.02$	Adsorption	[182]
Soil (mainly feldspars, quartz and limonite)	$2.29 \pm 0.06$		
Silica	2.1		[183]
Aluminium suspension	1.4–1.7	SAXS	[184]
Yeast flocs	1.79–2.25	Microscopy	[185]
Al-pillard montmorillonite	$1.94 \pm 0.10$	Adsorption	[186]
Kaolin–polymer flocs	1.31–1.42	Light scattering, image analysis	[187]
Goethite (plate-like, $60 \times 18 \times 11$ nm)	1.6 2.0	SLS DLA RLA Analysis of published data on settling tests and size–density relationships:	[151] [188]
Activated sludge flocs	1.45–2.0	Data from [189]	
Ferric aggregates	2.61–2.85	Data from [190]	
Alum aggregates	2.302–2.324	Data from [191]	
Alum aggregates	1.59–1.97	Data from [192]	
Activated sludge flocs	1.4		
Clay–iron flocs	1.92		
Activated sludge flocs	1.44–1.49	Data from [193]	
Activated sludge flocs	1.70–2.07	Data from [194]	
River sediment	$2.75 \pm 0.10$	SAXS	[195]
Ferric chloride ( $>0.5$ $\mu\text{m}$ )	2.3	ESZ (floc volume-particle volume relationship)	[196]
Haematite (100 nm) destabilized with salt	$2.3 \pm 0.1$	DLS (D estimated assuming $R \propto t^{1/D}$ (valid for [salt] > ccc))	[96]
<i>Zoogloea ramigera</i>	$1.8 \pm 0.3$	Light microscopy, cell counting (number of cells per floc-floc length relationship)	[170]
Marine snow (0.4–20 mm)	$1.39 \pm 0.15^{\text{A}}$ $1.26 \pm 0.06^{\text{B}}$	Size–porosity (A) and settling velocity (B) data from [197]	
Diatom aggregates (7–20 mm)	$1.52 \pm 0.19$	Size–porosity data from [198]	
Activated sludge	1.0–1.3	Size–porosity data from [192]	
Estuarine aggregates	1.78	Settling velocity data from [199]	

**Table 4** (*continued*)

System	D	Method	Reference
Lacustrine aggregates	1.39–1.69	Settling velocity data	
Oceanic aggregates	2.14	from [200]	
Oceanic aggregates	1.94		
<i>Zoogloea ramigera</i>	$1.79 \pm 0.28^A$ $2.99 \pm 0.36^B$	Light microscopy, cell counting (number of cells per floc-floc length relationship)	[201]
<i>Saccharomyces cerevisiae</i>	$2.66 \pm 0.34^A$	Rotating test tubes (A), bench-top fermenter (B)	
Haematite and IHSS FA	2.93 ([KCl] = 0.01, [FA] = 1 mg dm <sup>-3</sup> ) 2.83 ([KCl] = 0.05, [FA] = 2.5 mg dm <sup>-3</sup> )	SLS	[97]
IHSS HA and soil HA	$2.3 \pm 0.1$	SANS (dependence of scattering intensity on the scattering vector) $I = 0.1$ , pH = 5.0, T = 21	[158]
Stream sediment HA (6.7 g dm <sup>-3</sup> in 0.1 mol dm <sup>-3</sup> NaOH)	2.5	SAXS (dependence of scattering intensity on the scattering vector)	[160]
Aquatic humus (45 mg C dm <sup>-3</sup> )	1.6		
Marine snow (1–60 mm)	$1.72 \pm 0.07$	$D_2$ estimated <i>in situ</i> by microscope and image analysis	[171]
Marine snow composed of one type of particle marine snow formed by:	$1.28 \pm 0.11$		
Feecal pellets	$1.34 \pm 0.16$		
Diatoms	$1.86 \pm 0.13$		
No identifiable particles	$1.63 \pm 0.72$		
Larvacean houses	$2.21 \pm 0.17$		
HA extracted from a mud–clay soil (A1 horizon)	1.8 (T = 4–8) 2.35 (after 40 h of T increase at 21)	SANS (dependence of scattering intensity on the scattering vector) pH = 5.0, I = 0.1	[159,167]
Stream sediment HA	$2.2 \pm 0.1$	SAXS (dependence of scattering intensity on the scattering vector)	[168]
Stream sediment FA	$2.3 \pm 0.1$		
Peat HA	$2.7 \pm 0.1$		
Soil FA	$2.5 \pm 0.1$		
Lignite HA	$2.3 \pm 0.1$		
Lignite FA	$2.8 \pm 0.1$		
Groundwater humus	$2.5 \pm 0.1$		
HA extracted from a ultisol	2.71 (pH = 3) 2.73 (pH = 4) 2.43 (pH = 5) 1.34 (pH = 6)	Turbidity (log–log plots of turbidity versus wavelength)	[169]

(continued overleaf)

**Table 4** (continued)

System	D	Method	Reference
Mesocosm	2.33	ESZ, photography, image analysis	[173]
Phytoplankton bloom in a mesocosm (initial size: 2–50 µm; final: 50–300 µm)	2.49 ± 0.41 (day 7) 1.68 ± 0.08 (day 12)	ESZ (volume), CCD-video camera (length)	[172]
Haematite (25 nm)	1.87 ± 0.07 1.68 ± 0.04 1.83 ± 0.07 2.2 ± 0.1	DLA regime ([KCl] > 0.1): Dynamic scaling of DLS data TEM image analysis SLS RLA regime: SLS	[154]
Suspended particles in Monterey Bay, USA (1 µm–10 mm)	2.26–2.36	ESZ, photographic camera, confocal TV, IR laser-light sheet video system	[174]
Haematite (70 nm)	1.25–1.5	No shear applied. Estimation by fitting von Smoluchowski equation to experimental aggregation data	[113]
Marine particles (15–200 µm): Non-aggregating phytoplankton bloom	2.59 ± 0.17	ESZ, image analysis (Acridine Orange-stained particles) (particle equivalent diameter–average length relationship)	[175]
Old diatom flocs and marine snow aggregates	1.77 ± 0.34		
Estuarine flocs (>150 µm)	~2.5	INSSEV ( <i>in situ</i> settling velocity) device	[176]
Severn estuary intertidal mudflats (28 samples)	1.93 ± 0.43		
Humber estuary intertidal mudflats (4 samples)	2.06 ± 0.27		
Soil FA	2.3 ± 0.1	SAXS (dependence of scattering intensity on the scattering vector)	[162]
Soil HA	2.6 ± 0.1		
Peat FA	2.2 ± 0.1		
Peat HA	2.5 ± 0.1		
Aggregates formed by addition of alum [Al <sub>2</sub> (SO <sub>4</sub> ) <sub>3</sub> .18H <sub>2</sub> O] to: lake water (different coagulation stages)	2.93 ± 0.20 2.57 ± 0.20 2.12 ± 0.50	Mixing jar with stroboscopic light, CCD camera	[166]
Montmorillonite suspension (different coagulation stages)	2.71 ± 0.20 2.51 ± 0.20 2.39 ± 0.30		

**Table 4** (*continued*)

System	D	Method	Reference
NOM aggregates in Mediterranean waters:		TEM image analysis as described in [154]	[177]
Linear parts	1.44		
Compact parts	1.73		

<sup>a</sup> Concentrations are expressed in mol dm<sup>-3</sup> except where stated otherwise. Temperatures are expressed in °C.

#### 4 PHYSICAL FRACTIONATION DATA

As mentioned in Section 3.1, the use of prefractionation techniques is a prerequisite to many of the existing particle counting techniques. Prefractionation techniques have the advantage of reducing the polydispersity of each fraction, thereby facilitating the interpretation of the measurements. This separation step also provides the opportunity to collect fractions during the course of the separation. Subsequent analysis of these fractions can provide a detailed characterisation of the particle composition across the size range of the separations (approach B in Figure 1). On-line measurement of some properties in the fractions has also been implemented.

Traditional physical separation methods for natural waters include settling, membrane filtration and centrifugation. Filtration is the most commonly used method in studies of aquatic colloids, despite its many shortcomings [202]. Of the numerous problems encountered when using frontal filtration for size fractionation, the two most serious are the non-quantitative changes in effective pore size caused by the loading of particles on the filter surface and the low resolution of the technique. High-speed centrifugation, mostly used by soil scientists, averts the problem of clogging that is encountered in filtration, but does not avert the problem of relatively low resolution. Centrifugation is also very time consuming due to long run times, the need for multiple sample transfers and the numerous repetitions needed to obtain satisfactory cut-offs [203]. Continuous-flow centrifugation has been developed, which may reduce analysis times, but has been shown to suffer from aggregation within the centrifuge which may alter particle size distributions [74]. Different separation techniques have sometimes been combined in prefractionation schemes. Illustrative examples in surface waters can be found in [204] (settling, CFF and centrifugation), [205,206] (single-bowl continuous-flow high-speed centrifugation and ultrafiltration) and [21] (sedimentation, centrifugation, filtration). Nowadays, new physical fractionation methods such as reverse osmosis, cross-flow filtration (CFF) and field-flow-fractionation (FFF) are widely applied to fractionate colloidal material from natural waters. When coupled with the measurement of parameters such as organic carbon, trace metal concentrations, etc, in the different size classes, these fractionation techniques become powerful tools in the study of colloids in natural waters.

Of the existing fractionation methods, CFF has become increasingly popular and is by far the most widely used technique in colloid-related studies. In CFF, also known as tangential-flow-filtration (TFF), a prefiltered sample flows parallel to a CFF membrane and hydrostatic pressure drives solutes with an effective molecular size less than the cut-off of the membrane through the membrane (permeate). The remaining solution (retentate),

containing both smaller solute molecules and larger colloids, is swept along the membrane surface and recycled through the retentate reservoir. Compounds that are rejected by the membrane are thus increasingly concentrated in the retentate over time. The total flow of permeate through the membrane is controlled by the transmembrane pressure and the hydraulic resistance of both the membrane and the concentration polarisation layer.

Most of the existing studies couple CFF separation with the determination of the elements present in each fraction by inductively coupled plasma mass spectrometry (ICP-MS) or by other techniques measuring trace metal concentrations. Hundreds of such studies now exist. The use of CFF to characterise the composition of the colloids themselves is much less widespread, with the exception of the contents of organic carbon (OC). In effect, CFF has been used extensively to study marine water, freshwater and groundwater NOM (see Chapter 4).

In spite of the fact that the published data are so widely dispersed, the authors of a critical compilation of CFF data for NOM in freshwaters [207] were able to establish some trends using the published values. For rivers and lakes with low dissolved organic matter (DOM) contents (less than 7 mg OC dm<sup>-3</sup>), the proportion of large colloidal (0.450 µm – 100 000 Da) and small colloidal and ‘dissolved’ (<100 000 Da) organic components is ca. 30 and 70%, respectively. Lakes with higher DOM content have a greater relative amount of DOM in the larger size fraction. The authors concluded that high and low DOM rivers differ only in the concentration of smaller size pedogenic DOM, whereas for lakes, a high DOM content would generally indicate a greater contribution from larger size aquagenic components.

There is no similar critical compilation of NOM CFF data for oceans. However, several trends can be identified from selected studies: (i) the lower molar mass (LMM) fraction is the major fraction of DOM (in seawater studies, DOM is usually defined by filtration at 0.22 µm) through the whole water column in the ocean; (ii) the higher molecular mass (HMM) fraction of DOM is more abundant on the surface. This would suggest that HMM-DOM is relatively reactive whereas the LMM-DOM is the major form of refractory DOM in the ocean. The results of degradation experiments [208,209] and <sup>14</sup>C age measurements [210] of different size classes of seawater DOM seem to support this hypothesis. Results from estuarine, continental shelf and slope waters indicate that >10 kDa NOM is contemporary in age (more recent than 1950) with residence times 1–30 days, whereas the 1–10 kDa fraction is much older (>1 kDa is 380 – 4500 years old) [211]. HMM-NOM cycles rapidly within estuarine and coastal regions, with the most refractory NOM persisting in oceans for thousands of years. These results provide indirect evidence of the size-reactivity continuum hypothesis, which suggests that the diagenetic state of NOM (understood as the extent of degradation) decreases with increasing size [209]. Although these results suggest that compositional differences do exist, detailed chemical data that might explain such differences remain sparse [212–215].

Although the application of CFF in aquatic environments is now widespread, uncertainty regarding the consistency in molecular mass-based fractionation and possible discrimination of organic constituents warrant cautious interpretation. Potential problems, including contamination, the breakthrough of high molecular mass compounds, the retention of lower molecular mass molecules and adsorptive losses to the membrane itself, could affect the reliability of size-based fractionations. The technique and the membranes used have been the object of many assessments. See Chapter 4 for a more detailed discussion.

Since marine colloids are predominantly organic, the development of CFF applications to marine environments is linked to important developments in OC measuring techniques [216]. When evaluating published results, it is important to remember that controversy surrounding the measurement of DOC concentrations in seawater was prevalent during the late 1980s and early 1990s (corresponding chapter in [217]). The high-temperature (catalytic) combustion (HTC) method introduced by Sugimura and Suzuki [218] led to an argument about the existence of a much larger reservoir of DOC in the ocean than had been estimated by the conventional method based on wet chemical oxidation [219]. After 1992, further examination of the HTC technique [220–225] showed that HTC measurements included a potentially high system blank relative to the DOC level in seawater (e.g. [226,227]). Eventually, the DOC values obtained from the HTC method in the early stage were retracted [228]. Thereafter, the HTC method was reassessed and improved [229]. Details of DOC measurement can be found in a review by Sharp [230]. Oceanic DOC concentrations measured by HTC after 1994 can be found in Ogawa and Tanoue [231].

Ultrafiltration has been used in the study of inorganic colloids, such as iron and manganese, in freshwaters, estuaries and oceans. However, as discussed in detail by Town and Filella [207], the process of interpreting iron ultrafiltration data is far from straightforward and results should be viewed with caution. In freshwaters at least, it is not clear whether the large colloidal species detected by ultrafiltration are ‘real’ iron oxy-hydroxides or are complexed or associated with NOM [232–237]. EPR applied to CFF fractionated samples showed that, at least in some cases, both forms coexist [78,238]. Manganese seems to be present in smaller colloidal fractions than iron and aluminium, probably because of the well-known slow oxidation kinetics of Mn(II) to insoluble Mn(IV) [239,240].

Elution methods such as FFF (see [241] and Chapter 5) and size-exclusion chromatography (SEC) have the advantage of allowing narrow size range fractions to be collected at points across the distribution for subsequent observation and analysis. FFF is a family of separation techniques based on the principle of combining a field perpendicular to a laminar flow in thin channels. FFF has been used to investigate particle composition, morphology and mineralogy by X-ray diffraction (XRD), ICP-MS, graphite furnace atomic absorption spectrometry (GF-AAS), scanning electron microscopy (SEM), LIBD and multiangle laser light scattering (MALLS). SEC has also been coupled with light scattering detectors [242–244] and ICP-MS [245]. FFF has been applied to the study of marine waters, freshwaters, groundwaters and soil solutions (see Chapter 5). Although useful, these techniques do have limitations. A major drawback of the FFF techniques is that the eluted fractions are significantly diluted compared with the injected colloid, making it more difficult to measure the resultant size fractionation. This also implies that highly sensitive detection techniques are required [246].

## 5 MAIN HOMOLOGOUS COMPOUNDS

As explained in Section 2, the study of environmental colloids can be approached through the investigation of the colloidal properties of so-called homologous compounds, i.e.

groups of compounds which have a similar composition and similar properties (approach C in Figure 1). In this section, some of the main groups of natural colloids will be discussed.

Traditionally, hydrous colloidal systems have been classified into two major classes: 'hydrophobic' and 'hydrophilic' colloids [247]. The so-called 'hydrophobic' colloids are liquid dispersions of small solid particles, each consisting of a large number of atoms and molecules. They are considered to be a two-phase system with a large total interfacial area where the properties of the particle surfaces play a dominant role. In environmental systems, they traditionally include all inorganic colloids. However, the term 'hydrophobic' colloid is somewhat misleading. Clearly, inorganic particles in water are not hydrophobic at all; they are certainly wetted by water, and usually one or two monolayers of water are fairly strongly adsorbed on the particle surface. Historically, the term 'hydrophobic' colloids was introduced to distinguish these colloids from those which were referred to as 'hydrophilic' colloids. The latter were made up of the colloidal solutions of gums, which have a high affinity for water. Hydrophilic colloids can, however, be considered true solutions of macromolecules and, consequently, the terms 'macromolecular colloids' or 'polyelectrolyte solutions' are often preferred. Their 'colloidal' properties would be the result of the large size of the dispersed molecules with respect to the size of the molecules of water. In environmental systems, they include NOM. Some authors (e.g. [248]) prefer not to consider hydrophilic colloids as colloids and reserve the name for the 'hydrophobic' colloids. It is important to mention that a third class of colloidal system is often distinguished from the original group of lyophilic colloids, namely the systems in which an equilibrium exists between truly dissolved simple molecules and large kinetic units consisting of associated molecules. These units are called micelles and are only formed beyond a certain minimum concentration. Under certain conditions, some types of NOM exhibit micellar behaviour [249–251].

In this chapter, both inorganic and organic have been included in the generic term colloids, but they will be discussed separately. Although the main types of inorganic and organic colloids present in natural waters have been known for many years, non-perturbing methods allowing the characterisation and the *quantification* of the different types of particles and their associations in a given systems are still needed.

To study the characteristics of the different families of compounds, they either first have to be isolated from a natural system or synthetic compounds have to be used as surrogates. Unfortunately, the methods used to isolate homologous compounds are often particularly aggressive. In soil samples, the methods used to concentrate and isolate clay minerals involve the dispersion of the clay fraction via treatment with harsh reagents designed to alter surface charge properties significantly and destroy complex mineral assemblages present in the original material [5]. Similarly, the isolation of the so-called humic and fulvic fractions involves treating the sample with strongly basic and acidic solutions [252], which certainly will not preserve the original conformation of these macromolecules. Alternatively, synthetic compounds have frequently been used in place of their natural counterparts (i.e. synthetic haematite instead of 'real' iron oxides) in the study of the colloidal properties of environmental particles. However, it is becoming increasingly clear [5,253,254] that these model colloids are not necessarily representative of the complex shapes and surface characteristics of natural environmental colloids. Their use should be treated with caution.

## 5.1 INORGANIC COLLOIDS

Studies which attempt to identify inorganic colloids in whole samples are mostly based on electron microscopy. Electron microscopy allows the direct observation of particle sizes and shapes and provides chemical information when coupled with energy-dispersive X-ray spectroscopy (EDS) and mineralogical information when coupled with selected area diffraction (SAED) [255]. Table 5 shows some selected examples of inorganic colloid identification in natural waters. Colloid characterisation in these studies has often been limited to qualitative particle surveys describing the dominant morphology and composition of an unspecified number of colloids. There is a general lack of quantitative studies which actually characterise the composition and mineralogy of undisturbed natural colloid suspensions.

### 5.1.1 Sources

There are various potential sources of inorganic colloidal particles in natural surface waters: *in situ* mobilisation of colloidal particles in soils and subsurface waters, formation of colloidal particles by chemical precipitation from supersaturated solutions, biota and external sources such as waste disposal.

In the absence of a direct external source, such as glacial erosion in glacial lakes and rivers, the main source of mineral colloids in surface waters is detachment from soil surfaces. Extensive detachment occurs when raindrops impinge the soil surface. Otherwise, the formation of solid phases by chemical precipitation is a widely observed phenomenon [256]. For instance, calcite precipitates in lakes and oceans, extensive iron and manganese formation takes place in the redox transition layers of eutrophic lakes and sediments [136,239,240,257,258] and metal sulfides precipitate in anoxic waters. Many of the numerous kinds of aquatic particles rich in calcium [259,260] or silicon [260,261] are of biogenic origin.

The most common source of colloids in soils and groundwaters is *in situ* release as a result of changes in solution chemistry [62,262–269]. The dispersion and release of particles in most soils are favoured by high pH, low ionic strength or high sodium saturation conditions [267,270–272]. For instance, chemical conditions that lead to the release of colloidal particles can occur during heavy rainfall or the irrigation of soils with sodium-rich waters (e.g. roadside soils receiving de-icing salts [273]). Some field observations suggest that *in situ* mobilisation of colloidal particles may also result from the dissolution of cementing agents [61,274].

Since most groundwater colloids are composed of minerals that occur naturally in the aquifer, aluminosilicates are ubiquitous in most of the systems (see McCarthy and Deguelde [62] for an extensive review). Fewer studies are available on the abundance of colloidal particles in rock fractures. In a field investigation on granitic groundwater at the Grimsel Test Site in Switzerland, the particles ( $0.2 \text{ mg dm}^{-3}$  of particles larger than 10 nm) were primarily made up of silica and phyllosilicate minerals [41,45,111,275,276].

Colloid precipitation is of little importance in most natural subsurface environments because soil solutions tend either to be undersaturated or to be in equilibrium with respect to the mineral phases present. However, human activities such as waste disposal, groundwater pumping and artificial recharge can bring about drastic changes in water chemistry and create conditions that favour the formation of colloids [277,278]. Some radionuclides,

**Table 5.** Some selected examples of identification of mineral colloids in natural water samples

System	Minerals	Method	Reference
Settling particles in Lake Zürich, Switzerland	Main phases: calcite and quartz. Others: clays (kaolinite)	TEM, SEM, EDS, XRD	[279]
Redox transition layer in anoxic soft water lake	Iron oxyhydroxide, spherical/ellipsoidal particles, 0.05–0.5 µm diameter, poorly crystalline ferrihydrite, composition: $\text{Fe P}_{0.055-0.14}\text{Ca}_{0.012-0.02}$ , high C content, appreciable Si and Mn	TEM–EDX, XRD, wet chemistry	[280]
Nepheloid layer of the ocean (GEOSECS Atlantic cruise)	Classification of particles on the basis of the Si/Al ratio Main particles: opal + quartz, clay, Ca. Less abundant: Fe, organics, S. Rare: Al, P, K	Computer-evaluated SEM image, 2000 particles (1–20 µm) analysed/sample	[281]
Surface waters, soft water lake	Iron hydroxide, spherical/cylindrical particles, <0.5 µm, composition: variable Ca, ≤Fe, Si, P, S	Electron microscopy–EDX	[282]
Anoxic waters soft water lake	Iron sulfide: $\text{FeS}_{0.4-0.7}$	Mössbauer, wet chemistry, XRD	[283]
Ems estuary	Geochemically different particle types	Samples filtered (0.4 µm Nuclepore filter), retained particles analysed (300 particles/sample); sizes 1–6 µm Automated EPXMA, multivariate analysis	[284]
Suspended sediments in an ice-contact proglacial lake (Briksdal Lake, Norway)	Biotite-type mica (48% 0.2–1.0; 39% 1–3), Na-feldspar (30% 0.2–1.0, 34% 1–3), K-feldspar (19% 0.2–1.0; 15% 1–3), Ti-contaminated quartz (3% 0.2–1, 10% 1–3); >90% biotite in the deposited sediment	Filtration through capillary pore (Nuclepore) filters: 3, 1, 0.8, 0.6, 0.4, 0.2, 0.1 µm TEM-EDS, TEM-EDAX	[72]
Groundwaters collected near a secondary-sewage infiltration site on Cape Cod, MA, USA	Population of monodisperse 100 nm particles, composition: P 1.86 Fe:1.0	SEM and SEM-EDAX	[277]

**Table 5.** (*continued*)

System	Minerals	Method	Reference
Baltic Sea and North Sea	Particles classified into 10 types More abundant particles: 80% Si-rich particles (quartz, K-rich, Fe-rich aluminosilicates) Less abundant: Ba + S, Fe, Mn, Ca, P + S, Ti, Al	Samples filtered (0.4 µm Nuclepore filter), retained particles analysed Automated SEM–EDS, multivariate analysis	[285]
Redox transition boundary layer in a eutrophic lake (Lake Bret, Switzerland)	Fe-rich particles that contain Fe, P and Ca exclusively	TEM–EDS, macroscopic analysis	[286]
Mississippi River and main tributaries, US	Major components: illite and kaolinite. Minor component in all rivers: montmorillonite. Smectite present in different proportions in some rivers. Quartz and rutile ubiquitous in all rivers	Ultrafiltration, XRD	[73]
Groundwater in the vicinity of a coal ash, US	Si (always), Ca and Mg (variable amounts)	SEM–EDS	[274]
Two Atlantic coastal plain aquifers, US	Swamp Deep: kaolinite, chamosite, goethite Upland Deep: kaolinite Swamp shallow: quartz, gibbsite, $\text{Fe(OH)}_3$ Lc42-01: kaolinite, muscovite, amorphous $\text{Fe(OH)}_3$ , rutile	SEM–EDS	[61]
Groundwater, Whiteshell Research area, CA, US	10–450 nm range: $\text{Na}-\text{Ca}-\text{HCO}_3$ waters: aluminosilicate, carbonate, OC, Fe oxide; deeper saline waters: aluminosilicate, Fe oxide, carbonate 1–10 nm range: OC, some carbonate, Fe oxide	CFF, SEM–EDS, XRD	[287]
Natural iron oxides (sediments, 8 oligotrophic Canadian lakes)	Poorly ordered ferrihydrite (spherical and ellipsoidal), lepidocrocite (lath type)	Teflon collection, TEM-EDS-ED, XRD	[20]

*(Continued overleaf)*

**Table 5.** (*continued*)

System	Minerals	Method	Reference
Darling River, Australia	Illite, kaolinite, smectite, quartz	SdFFF–ICP–MS The mineralogical composition was already known, the plot of atomic ratios allowed the examination of mineralogy trends across size classes	[242]
Aquifer underlying seepage basins, US	Clay platelets (5–10 µm diameter), rod-shaped particles (5 µm length), more common spherical particles (0.1 µm diameter)	Morphology classification according to SEM–EDS measurements	[288]
Acidic seepage basin, US	Four categories: phase containing only Si (quartz), a K-rich aluminosilicate (mica or hydroxyl-interlayered vermiculite; a 1:1 Al:Si aluminosilicate (kaolinite); a Ti-rich Fe-oxide	SEM–EDS	[289]
Suspended matter in flow event (Elbe River) (<63 µm)	Particles classified into 12 groups. Most abundant groups: >40% Si (77% of all particles). Important groups: Fe-enriched aluminosilicate. Remaining 23% particles are: Fe-rich (iron oxide and iron phosphate)	EPXMA	[290]
Groundwaters from a granitic site (El Berrocal, Spain)	Silica, aluminosilicates (mainly K-feldspars), Fe, Ti, Al oxyhydroxides In carbonated, oxic waters, carbonate (Ca, Zn) also present; in carbonated, less oxic waters, sulfur with Cu, Zn, Fe identified	Ultrafiltration, SEM, EDS	[291]
Diagenetic Fe and Mn oxyhydroxides from two geochemically different lakes (Sudbury, CA)	Fe-rich material: predominantly ferrihydrite and poorly crystallised lepidocrocite Mn-rich material: mixture of poorly crystallised Mn oxyhydroxides	Teflon collection, TEM, XRD	[22]

**Table 5.** (*continued*)

System	Minerals	Method	Reference
Different granitic groundwaters (Grissel, Zurzach, Leuggern, Transigtas, Switzerland)	Clay, SiO <sub>2</sub> , illite	Large (>500 nm) colloids isolated by filtration, SEM–EDS	[41]
Subsurface colloids mobilised from Southeastern Coastal Plain sediments, US	Soil mobile colloids (200–300 nm): Al-rich goethite, goethite-armored kaolinite, crandallite	Leaching in column experiments, SEM–EDS–SAED	[5,292]
Karstic aquifer, Switzerland	Quartz, phyllosilicates and some feldspars, calcite, dolomite, and ankerite; no crystallised Fe oxides	Ultrafiltration, SEM–EDS, XRD	[293]
Drained peat bog to a river (karstic watershed)	Fe–C-rich globular colloids with a carbon core	TEM (TEM–EDS, STEM–EDS, EF–TEM)	[294]
Southern Bight of the North Sea	13 particle types, classified in 7 groups: terrigenous (aluminosilicate and calcium carbonate); terrigenous–biogenic (silica), terrigenous–hydrogenous (Fe-rich), biohenic–authogenic (S-containing), terrigenous–anthropogenic (Ti- and Al-rich), biogenic–anthropogenic (organic), terrigenous–anthropogenic– authogenous (heavy metal rich)	EPXMA, STEM–EDS–SAED Samples filtered (0.45 µm Nuclepore filter); retained particles analysed	[295]
Oxic–anoxic interface of a eutrophic lake (Lake Lugano, Switzerland)	Iron colloids with a [PO <sub>4</sub> ] <sub>part</sub> :[Fe] <sub>part</sub> ratio of 0.48 ± 0.11	TEM–EDS (1096 particles)	[23]
Subsurface colloids mobilised from Southeastern Coastal Plain Sediments, USA	Kaolinite, vermiculite, illite	SdFFF–ICP–MS	[251]

*(Continued overleaf)*

**Table 5.** (*continued*)

System	Minerals	Method	Reference
Nyong basin (Cameroon, Africa)	Colourless waters: Particulate fraction (>0.45 µm): poorly ordered kaolinite, quartz, goethite Colloidal fraction euhedral kaolinite, amorphous iron oxyhydroxides Coloured water: Particulate fraction before plus phytoliths and biogenic opal Colloidal fraction NOM and Fe oxyhydroxides associated with NOM	CFF, XRD, TEM, FTIR, EPR, DRS	[233]
Watershed (peat, drains, river, karst spring), Vallée-des-Points, Switzerland	Fe–Ca(–C <sub>org</sub> )-rich colloids	STEM-EDS, TEM-EELS	[296]
Deep meromictic lake (Lake Lugano, Switzerland)	10–50 nm granules attached to EPS network	TEM, TEM-EDS	[24]
Shallow meromictic lake (Paul Lake, US)	Ill-defined Fe–EPS intimate mixtures		
Peat-land crossed by a river (Vallée des Ponts, Switzerland)	100–500 nm spherical and drop-like globules with C-rich core		
Fe-rich particles formed at the oxic–anoxic layer of a meromictic lake (Lake Paul, US)	Hydrous iron oxides form complex aggregates with NOM	TEM, TEM-EDS	[25]
Almeria–Oran front in the eastern Alboran Sea (SW Mediterranean Sea)	Three morphotypes (10 nm–5 µm): Globules (10–200 nm), 5 m deep, contained Ca, P, S and Cl Rounded entities (50 globules, >200 nm), contained linear and compact parts, 40 m deep, Fe–P-rich Spherulitic aggregates (crystalline), 40 m, Mg-rich	TEM, TEM-EDS	[177]

**Table 5.** (continued)

System	Minerals	Method	Reference
Suspended particles, River Don, UK (8 sites)	High flow samples: Clays: illite, chlorite, kaolin, hydroxy-interlayered vermiculite, regularly interstratified mica-vermiculite Non-clays: quartz, feldspars, amphibole, goethite Base flow samples: same composition + talc, calcite	XRD, VATIR	[297]
US Geological Survey's Cape Cod Toxic Substances Hydrology research site	Quartz, feldspar, kaolinite along with small amounts of smectite and illite/muscovite, sizes 50 nm–5 µm	Colloids collected on filters and sediments ground to <10 µm by mortar and pestle Powder X-ray diffraction	[298]
Synthetic HFO and biotic iron oxides ( <i>Bacillus subtilis</i> and <i>Bacillus licheniformis</i> )	Biotic iron oxides occurred as small particles (5–10 nm) and were identified as 2-line ferrihydrite	TEM, TEM-SAED, TEM-PEELS	[299]
Gotlan Deep, Baltic Sea	Two different morphotypes of Mn-rich particles: amorphous particles (92%) and <i>Metallogenium</i> -like particles	SEM-EDS	[300]

such as the actinides, are highly likely to undergo hydrolysis and form colloidal particles by precipitation [301,302]. In this field, some authors have made a distinction between ‘true colloids’ and ‘pseudo-colloids’. Intrinsic or true colloids would be those generated by the products of actinide hydrolysis. Pseudo-colloids would originate from the sorption of actinide ions or intrinsic colloids onto natural aquatic colloids. This distinction is not made in other fields of study.

### 5.1.2 Main Types

**5.1.2.1 Aluminosilicates.** Aluminosilicates are by far the most abundant colloids in aquatic systems. The release of elements into aqueous environments through the weathering of aluminosilicate rocks is an important geochemical phenomenon. It controls the composition of natural waters and contributes to the formation of secondary solids. Many authors have carried out studies on the weathering of aluminosilicates (e.g. [303–306; 307] and references therein). The difference in mineralogy observed between mobile colloid fractions and the total or water dispersible clay fractions in soils has been explained, at least in part, by the different size distributions of total clay and mobile colloidal particles [267,308]. Much less attention has been paid to the size distribution, in the colloidal size range, of the different types of aluminosilicates in natural waters.

Aluminosilicates can be distinguished from other colloidal materials by their highly anisometric and often irregular particle shape, their broad particle size distribution, the flexibility of their layers, their pronounced cation-exchange capacity and the different types of charges present (structural permanent charges on the faces, from isomorphous substitutions within the aluminosilicate structure, and variable, pH-dependent charges at the edges) with the associated different modes of aggregation [309,310]. Aluminosilicate particles show different modes of particle aggregation: plane to plane, edge to plane and edge to edge. The stability of clay particles in natural waters is mainly determined by a pH-dependent charge heterogeneity in combination with double-layer compression. Clay particle coagulation is complicated because the edge and plane sometimes carry opposing net charges which may lead to spontaneous aggregation through edge-to-plane association [309,311]. However, electrostatic shielding as a result of proton desorption or anion adsorption can lead to charge reversal along the edge, producing an almost homogeneously charged clay particle. The double-layer interaction with other clay particles would be repulsive, and the suspension stable [115,312,313].

It is important to note that, although the electrokinetic, surface and reactivity properties of aluminosilicates have been the subject of a large number of studies, the extent to which the results of most of the studies can be applied to the aluminosilicates present in natural waters in the colloidal size range remains largely unknown. The main reasons for this are as follows. (i) The extensive use of a wide panoply of particle pretreatments, such as drying and grounding procedures, hydration,  $\text{Na}^+$  saturation, removal of carbonates, NOM and iron coatings, most of which are characterised by their capacity to modify irreversibly the surface properties of the particles. For instance, it has been suggested that published conclusions regarding the surface chemistry of feldspars might not have properly accounted for the electrolyte salt and dissolution effects because the charge and stoichiometry of the surface depends on the type of pretreatment [314]. (ii) The widespread use of particles that are much bigger than colloids in many studies (e.g. [315–317]). It has been shown that increasing the edge surface fraction by particle size reduction (dry milling), in order to mimic natural wear and physical weathering, results in an increase in the surface specific area and the cation-exchange capacity [318]. This was interpreted by the creation of new, positively charged edge surfaces. These sites at the edges are considered to be the major reactive sites in aluminosilicate surfaces [319]. (iii) The different surface nature of ‘natural’ aluminosilicates compared with ‘pure’ minerals. According to some authors [320,321], natural clays behave in natural waters as if they were amorphous on their outermost surface layers due to the continuous processes of partial dissolution and reprecipitation of clay components at the solid–aqueous interface (aluminium and silicon oxides). These particles would continue to exhibit a specific internal crystalline structure.

**5.1.2.2 Iron Oxides.** Iron(III), which is stable in the presence of oxygen, is hydrolysed to insoluble oxyhydroxides, whereas iron(II), which is stable in the absence of oxygen, is soluble and relatively free from complexation. The interchange between these two iron oxidation states leads to the production and removal of particles in the different environmental compartments. These processes of interconversion, which are highly dependent on pH, are influenced and controlled by microorganisms. The basic biological and chemical interactions of iron in natural waters have been known for years [322,323]. Davison and De Vitre [258], Stumm and Sulzberger [324] and Davison [239] have published excellent

reviews on iron cycling and particles in freshwaters. The biogeochemistry of iron in seawater has been the subject of a book in this series [325] and the formation and occurrence of biogenic iron-rich minerals have recently been extensively discussed [326].

In recent years, a great deal of attention has been paid to iron oxides, particularly in relation to ocean productivity issues [327–331]. Iron is unique among biologically essential trace metals in that it has a higher particulate than dissolved concentration in ocean surface waters. Recently, many studies on iron speciation in seawater seem to indicate that the low concentration of dissolved iron present in oceanic surface water is generally associated with an excess concentration of iron-binding organic ligands [332–335]. The high Fe(III) solubility found in some surface waters might be due to the production of natural Fe(III)-complexing organic ligands, such as siderophores [335–337]. However, the higher iron solubility level observed in mid-depth waters (100–3000 m depth), especially in subarctic waters, seems to be associated primarily with humic-type fluorescent material [335].

Iron and aluminium oxides were generally thought to act as cementing or coagulating agents in soils and geological formations because they possess a net positive charge in many relevant environmental conditions, and their presence was thought to stabilise negatively charged, phyllosilicate clay systems against the dispersive effect of high exchangeable sodium levels. Nowadays, it is known that iron oxide coatings play a more active role in controlling a number of environmentally important soil, freshwater and groundwater processes, including the transport of groundwater colloids, the attenuation of bacteria and viruses and the behaviour of contaminant trace metals [338–340,298].

Naturally occurring iron particles are by no means simple. They are often present alongside bacteria and other mineral particles, and their surface properties are affected by the adsorption of NOM. Moreover, iron particles are found under different crystalline and/or amorphous chemical phases. For instance, iron oxides may exist as haematite ( $\alpha\text{-Fe}_2\text{O}_3$ ), goethite ( $\alpha\text{-FeOOH}$ ), lepidocrocite ( $\gamma\text{-FeOOH}$ ), maghaemite ( $\gamma\text{-Fe}_2\text{O}_3$ ), magnetite ( $\text{Fe}_3\text{O}_4$ ) and ferrihydrite [258]. The last phase is the collective name for X-ray amorphous Fe(III) phases which are thought to be formed during the oxidative hydrolysis of Fe(II). Ferrihydrites are metastable and may, for example, be transformed into lepidocrocite and haematite in sediments. The surfaces of amorphous iron are less well defined than those of the crystalline hydrous oxides. The metastable, low-crystallinity iron oxyhydroxide two-line ferrihydrite (2LFh) is frequently found as the dominant inorganic iron-colloid species in aquatic systems. Ferrihydrite consists of spherical particles, 10–20 nm in diameter, with a large surface area ( $100\text{--}300 \text{ m}^2 \text{ g}^{-1}$ ) and a defective haematite structure in which some O ions are replaced by water and some iron positions are vacant [341]. Moreover, iron oxides formed in natural waters are not ‘pure’ oxides but contain significant amounts of other elements. For instance, the application of an interdisciplinary sampling and analytical strategy to characterise the particulate species found in the different compartments of a watershed (peat, drains, river, karst spring) in the Vallée-des-Points, Switzerland, showed the formation, in abundance, of a class of Fe–Ca( $-\text{C}_{\text{org}}$ )-rich colloids, which are then scavenged during their transport into karst [296]. Further examples of the complexity of ‘real’ iron oxides can be found in [24].

Most laboratory studies on iron oxides have been carried out with synthetic particles. For example, reproducible, monodisperse, spherical haematite particles of varying sizes

have often been produced using the Matijevic and Schreiner [342] method, also described in [97].

**5.1.2.3 Manganese Oxides.** In natural waters, the biogeochemical cycle of manganese is essentially controlled by redox reactions between dissolved Mn(II) and insoluble oxides and oxyhydroxides of Mn(III, IV). Although the oxidation of Mn(II) to Mn(III, IV) is thermodynamically possible at neutral pH and atmospheric oxygen concentrations, the activation energy is high and the process is very slow. It has been stated that bacteria-mediated manganese oxidation is the only process of manganese oxidation in freshwater, marine, estuarine and soil environments [343–345]. Naturally occurring manganese oxyhydroxides are essentially X-ray amorphous. By using extended X-ray absorption fine structure (EXAFS) spectroscopy, it has been found that todorokite and H<sup>+</sup>-birnessite are the dominant phases in sediment trap material collected in the eutrophic lake Sempach [346]. Vernadite ( $\delta$ -MnO<sub>2</sub>), which has been identified in the Black Sea chemocline [347], is now also considered as H<sup>+</sup>-birnessite ([343] and references therein). Using TEM–EDS analysis, the presence of amorphous manganese-rich particles of bacterial origin was reported in the chemocline of a small meromictic lake, Paul Lake (MI, USA) [348]. Two different morphotypes of manganese-rich particles were identified by SEM–EDX in the Gotland Basin (Baltic Sea) thermocline [300]: amorphous particles (92%) and stellate structures (*Metallogenium*-like particles, [349]). Their morphologies resembled those already described in meromictic lakes [348,350]. Amorphous particles had a spherical radius of between 1.25 and 2.5  $\mu\text{m}$ , whereas the equivalent spherical radius of stellate particles was in the range 2.5–6.6  $\mu\text{m}$ . The majority of both types of particles, about 68% of all manganese-rich particles, were associated with large aggregates containing an organic matrix. Manganese represented more than 60% of the total elemental composition of the particles: calcium, iron and silica were also detected. Therefore manganese-rich particles essentially consisted of manganese oxides and oxyhydroxides. It is important to point out that the method of separation used by these authors only allowed for the analysis of particles with a mean diameter of between 1 and 50  $\mu\text{m}$ , outside the colloidal size range.

Excellent reviews on manganese particles in freshwaters have been published by Davison [239] and De Vitre and Davison [240].

## 5.2 ORGANIC MACROMOLECULES

Colloidal and particulate NOM are highly heterogeneous in size and chemical and isotopic composition. It has long been asserted, and is still accepted today, that most dissolved organic matter (DOM) in natural systems is uncharacterised at the molecular level [351]. The contribution of the major biochemical constituents, i.e. proteins, carbohydrates and lipids, may not exceed 30% of bulk DOM [19]. In contrast, more than 80% of organic carbon in particulate organic matter (POM) is made up of these three biochemical constituents [352]. The rest of the NOM is highly resistant to degradation and includes products that are the result of the decomposition of plant and animal residues. This refractory fraction of NOM (ROM) is often known as the fulvic and/or humic fraction. Although, strictly, these terms should refer only to coloured NOM extracted from soils using alkali, they are commonly used for aquatic NOM in environmental studies, and will be used in this chapter.

The abundance and characteristics of NOM vary among the different environmental compartments. Organic colloids seem to represent the highest percentage in oceans: colloidal organic matter could account for 30–40% of the conventionally defined DOM in oceanography (<0.22 µm) of the world's ocean, of which about half is made up of carbohydrates.

DOM represents a continuum of biological lability [353], from refractory material turning over on a time-scale of centuries to millennia [354,355] to very labile material turning over on a time-scale of minutes to days [356–358]. A third type of DOC, one that can be utilised by microbes but turns over on a time-scale of months to years [359–362], has been also identified. The most biologically reactive organic components in natural waters include dissolved free compounds such as neutral monosaccharides and free amino acids. Rapid turnover maintains these compounds at nanomolar concentrations. Colloidal organic compounds will mostly be in the biologically semi-labile and refractory categories.

Only two main categories of NOM will be described in this chapter, the humic-type compounds and the carbohydrates. Other compounds, such as proteins and lipids, are present at much lower concentrations in the different environmental systems and very little is known about their colloidal properties in natural waters. It is important to bear in mind that humic-type compounds and carbohydrates cannot be considered as two classes that belong to a single classification: whereas humics are a group of compounds which are defined, in theory, by their resistance to biological and chemical degradation, and in practice, operationally by the isolation procedure used, carbohydrates constitute a wide, but well-defined, biochemical class and show variable lability properties.

### 5.2.1 Fulvic and Humic Compounds

ROM is omnipresent in soils, sediments and water. It makes up about 75% w/w of the NOM in most soils and may represent more than 50% of the OC in some freshwaters. ROM is composed of complex heterogeneous mixtures of organic compounds, has a high relative molecular mass and is resistant to degradation. It cannot be described in terms of unique chemical structures and is operationally defined by the technique used for its extraction and fractionation [363,364]. Many of the problems encountered when studying the ROM in natural systems are linked to the fact that it is polydisperse, poly-electrolytic and polyfunctional; its three-dimensional structure is affected by pH and ionic strength.

When dealing with ROM in natural waters, it is important to bear in mind that the environment clearly influences humic substance formation, not only by dictating the range of possible precursors but also by influencing the type of processes that are possible. Thus, the principal source of seawater NOM is planktonic and bacterial excretion and degradation whereas terrestrial biomass and NOM production is mainly provided by higher plants. A major problem in understanding environmental influences is that humic-type substances are often isolated from environments other than those in which they were formed. For example, of all aquatic systems, lakes present one of the most complex mixtures of NOM because they accumulate organic matter from several different sources within a limited space: primary autochthonous productivity similar to that of oceanic

pelagic zones, allochthonous inputs and the release of sediment organic matter. A classification of humic materials based on the origin of the compounds (aquagenic, pedogenic) would probably be more environmentally sound than the current separation schemes based purely on analytical factors [19].

Methods used to determine the sources of NOM and to distinguish between terrestrial and aquagenic contributions in aquatic systems include analyses of stable carbon isotope ratios [211,365] and specific bioindicators such as carbohydrates, amino acids, lipids and lignin residues [365–374]. However, many single-biomarker studies follow the production or fate of a small suite of compounds that may represent only a small percentage of bulk DOM. Coupling spectroscopic measurements (e.g. UV and fluorescence) with DOC monitoring has also been used to extract information about the nature and variability of NOM [375–380].  $^{13}\text{C}$  nuclear magnetic resonance (NMR) spectroscopy has mainly been used to study humic substances isolated from the natural environment, but a few studies have also addressed the spectroscopic characteristics of bulk DOM and its potential source materials [381–383].

It is common practice to isolate hydrophobic fraction of ROM in natural waters by adsorption on non-ionic resins and elution with alkali [363,384–386] and the subsequent study of the properties of the isolated fractions. Whether the isolation procedure significantly modifies the properties of the humic substances, particularly size and structure, has remained an open question for years. On the other hand, the quantitative determination of ROM is rare [375]. For instance, applications of the resin-based isolation method for this purpose do exist [387,388] but the procedure is time consuming and examples are scarce.

### 5.2.2 Carbohydrates

Carbohydrates are excreted by algae and bacteria or released during cell lysis. Organic substances are released from phytoplankton cells during all phases of growth, as has been consistently observed in laboratories for over 70 years. Carbohydrates, especially polysaccharides, sometimes comprise 80–90% of the total extracellular release [389–393]. The amount and composition of the exudates depend on nutrient status [394–397], light [398,399] and growth phase [393,400], and are often highly species specific [401]. Large amounts of dissolved polysaccharides are released during phytoplankton blooms [402] and the composition changes during the bloom [403], but no correlation seems to exist between carbohydrate concentrations and chlorophyll-*a* [402–404]. The accumulation of gelatinous masses due to extracellular release by algae has been observed in different seawaters, e.g. the Adriatic Sea [405–409], the southern North Sea and the English Channel [410,411]. Bacteria have been shown to produce copious amounts of fibrillar material in marine snow, influencing the structure of the predominantly algae-derived matrix [412]. Excretion from zooplankton is a further source of dissolved carbohydrates [413,414].

More than 100 different sugar species and sugar derivatives are present as monomeric constituents in polysaccharides [415]. The complexity of polysaccharides is further increased by the different possible linkages (including branching linkages) and the variable

molar mass (up to millions of daltons) within a single family of polysaccharides species [416]. Furthermore, large variations in the secondary structure and molecular associations are possible. The colloidal behaviour of polysaccharides depends on their macromolecular structure, varying from totally linear (cellulose) to strongly branched (spherocolloids such as amylopectin or gum arabic) compounds. Due to minimal steric hindrance, the former have a strong tendency to pack into thick, water-insoluble fibres, whereas the latter are usually highly hydrated (hydrocolloids) and form gels that can contain up to 99.5% water. All types of sugars are present in natural systems: neutral sugars [214,404,417–420], amino sugars [417,419,421] and acidic sugars [422–427]. They also exist in combination with other biochemicals (e.g. lipopolysaccharides and glycoproteins).

For years the study of polysaccharides in natural waters has received much less attention than the study of ROM. Possible reasons are (i) a lack of adequate methods of characterisation, (ii) the majority degrade rapidly and (iii) no well-defined environmental role. The situation has largely changed over recent years, thanks mainly to the attention paid to NOM in oceans where a significant proportion consists of carbohydrates. Although studied much less frequently than carbohydrates in seawater, carbohydrates also constitute a large component (1–30%) of the dissolved organic matter in freshwater environments.

Current methods for determining carbohydrates in natural waters include chromatographic methods [428–433] and colorimetric assays. The most popular colorimetric methods are the MBTH (3-methyl-2-benzothiazolinone hydrochloride) method [427,434–436] and the TPTZ method [437]. Chromatographic and colorimetric methods are based on the measurement of the monosaccharides liberated after acid hydrolysis. Chromatographic methods allow the qualitative and quantitative identification of individual sugars in seawater, but desalting of the samples is necessary prior to anion-exchange chromatography and often causes the loss of a large percentage of charged sugars. It is known that carbohydrate measurements in seawater by using colorimetric methods give higher concentrations of reducing sugars than those observed using separation methods such as HPLC–PAD [404,427,433]. On the other hand, colorimetric methods do not provide information on the composition of the saccharides. Neither method allows the identification of the exact polysaccharides present, and neither gives any indication of the size of the polysaccharides, except when coupled with a size fractionation technique [213,214,418,421,438,439]. Some classes of compounds, predominantly carbohydrate in nature, have been defined either by microscopic observation (fibrils, Section 5.2.2.1) or by the application of staining techniques (TEP, Section 5.2.2.2). Their exact structure and composition are not known but both seem to play environmental roles linked to their colloidal features.

It is important to note that, in contrast to humic compounds, environmental polysaccharides cannot be isolated easily from natural waters. This means that the study of their colloidal properties can only be done by using model polysaccharides, normally produced in cultures of bacteria and phytoplankton. This is the case for polysaccharides, such as alginic acid, dextran, polygalacturonic acid, schizophylan, succinoglycan, and xanthan, that have been used in a number of studies [440–442,454,489,514]. Whether the results obtained from studies performed with these compounds can be extrapolated to natural aquatic systems remains questionable.

**5.2.2.1 Fibrils.** Fibrils of bacterial, algal and plant origin make up a very substantial part, on a seasonal basis, of OC in surface waters [443–447]. This type of colloid has the appearance of a twisted ribbon with the diameter tending towards 5 nm and the length being much greater than the diameter (sometimes more than 100-fold greater) [448,449]. Their major component is polysaccharide [450], some of it acid polysaccharide. Fibrils can be synthesised by several kinds of aquatic organisms [446,451,452] and by the roots of a terrestrial plant of major agricultural significance [453].

Individual fibrils cannot be seen by optical microscopy, although large aggregations can be detected as an ‘amorphous’ material stained by basic dyes [454]. They usually require high-resolution TEM for visualisation. For the physical characterisation of these delicate structures in a native state, particular attention to sample handling and sample stabilisation techniques is required [54,448,449,455,456–459]. Recently they have also been observed by atomic force microscopy (AFM) [447].

Freshwater fibrils have mainly been studied in freshwaters by Leppard and co-workers. Fibrils can act as floc formers (which can enhance particle sedimentation) and thus play a role in hydrophobic colloid scavenging [119], form matrix components of biofilms and facilitate microbial adhesion to surfaces [460]. Far fewer studies have been devoted to the characterisation of fibrils in seawater [447,455]. Fibrillar colloids, which are abundant in productive surface water, are much rarer in deep water [447]. This confirms that they are probably generated primarily by phytoplankton.

**5.2.2.2 Transparent Exopolymer Particles.** Transparent exopolymer particles (TEP) are a class of organic particles present in seawater and freshwater systems and in some microalgae cultures that consist predominantly of polysaccharides [125,129,461,462]. They are operationally defined by the colorimetric method used for their detection. These particles are transparent on clear slides and can only be directly observed on slides via a relatively cumbersome process involving sample filtration on specific filters, staining with Alcian Blue and transferring back again to clear slides using an FTF (filter–transfer–freezer) technique described by Passow and co-workers [462,463]. An alternative spectrophotometric method has been proposed for detecting TEP in freshwaters [464].

TEP exists at concentrations of  $10\text{--}10^6 \text{ cm}^{-3}$ . In general, the highest concentrations of TEP *in situ* are found after the peak of diatom blooms [464–468]. TEP are large, sticky, transparent, discrete particles (they are filterable on to 0.4  $\mu\text{m}$  filters and are usually between 1  $\mu\text{m}$  and 1 mm in length) or are attached to other particles. Therefore, although their size range greatly exceeds the colloidal size domain, it covers an important colloidal range.

The monomer composition of TEP remained fairly constant, despite changes in algae composition, and all TEP analysed to date consists of strongly sulfated polysaccharides enriched in desoxysugars and galactose [422,469]. TEP and their precursors appear to be a chemically distinct group of polysaccharides whose production and standing stocks are uncoupled from bulk carbohydrates [422].

Presumably they are formed abiotically from polysaccharides excreted by phytoplankton and bacterioplankton [93,461,463]. TEP can be formed from various abiotic processes: adsorption on surfaces [466], aggregation and/or coagulation under shear conditions in the water column [470] and bubble scavenging [422,463,467,469].

The formation of TEP may potentially constitute a way in which DOC released by phytoplankton is removed from the euphotic zone. TEP helps to glue smaller particles together to form larger aggregates known as marine or lake snow [471]. The matrix of all marine snow aggregates examined to date, regardless of their origin and composition, consists of TEP [472]. TEP can sediment rapidly [463].

In laboratory studies of seawater, a continuous and rapid assembly of polymer chains into microgels was observed [146]. The same observation has recently been made in the surface microlayer of open water in the central Arctic Ocean in summer by TEM [473].

Relatively few studies exist on the presence of TEP in freshwaters. Worm and Søndergaard [474] used a neutral solution of Alcian Blue to stain transparent particles in the eutrophic Lake Frederiksborg Slotsso, Denmark. The abundance, size spectra and bacterial colonisation of their Alcian Blue-stained particles were close to those of marine TEP. Logan *et al.* [129] and Grossart *et al.* [475] reported high concentrations of TEP in Lake Constance and indicated that the formation of sinking aggregates following blooms of mucous-producing diatoms is primarily controlled by TEP. Carrias *et al.* [476] reported the presence of TEP in the oligomesotrophic Lake Pavin, France, and in the eutrophic Lake Aydat, France. Nano-TEP were significantly higher in Lake Aydat than in Lake Pavin.

### 5.3 ORGANIC COATINGS OF INORGANIC COLLOIDS

It is widely accepted that adsorption of organic material masks the properties of the underlying mineral particles in surface waters, in soils and in groundwater aquifers. The clearest demonstration of the importance of surface coatings in natural waters comes from the measurements of electrophoretic mobility already discussed in Section 3.2. Direct observation of NOM coating in natural systems is less abundant. A combination of staining of organic matter with RuO<sub>4</sub> and observing particles from the North Sea by STEM–EDS revealed that all suspended particles were coated with organic matter [295]. The amount of organic matter present in the particles varied with the season. The application of Fourier transform infrared (FTIR) spectroscopy to natural suspended matter and colloids evidenced the association of NOM with iron and manganese in some natural waters [233,238]. In recent years, synchrotron scanning transmission X-ray microscopy (STXM) combined with near-edge x-ray absorption fine structure (NEXAFS) spectroscopy has opened up new possibilities for the observation and characterisation of NOM associations with mineral surfaces [477–480].

Many studies have been carried out into the sorption of different types of OM on synthetic and natural mineral particles. The most widely studied inorganic particles have probably been oxides, mainly, haematite (e.g. 98,102,441,481–494), goethite (e.g. [495–499]) and amorphous iron oxyhydroxides (e.g. [500–503]). Some studies have also been devoted to other oxides such as manganese oxides [71,496], alumina (e.g. [110,484,495,503–511]), δ-Al<sub>2</sub>O<sub>3</sub> [512], gibbsite [485,495] and silica [512,513]. Aluminosilicates have also been the object of some interest for a long time [440,454,514–521]. Most of the work published has been on kaolinite (e.g. [118,512,513,522–529]) and montmorillonite (e.g. [512,523,524,526–528,530]). Much less has been published on other aluminosilicates such as vermiculite [484], chlorite [484], illite [531] and smectite [496]. The most extensively studied OM has been ROM from different origins: coal [523], peat [522,527,528], soil [118,486,495,498,499,525,526,529],

lake [70,71,75,102,487,488,500,504,509,512], river [110,489,490,503,505,522,510] and ocean [502]. A limited number of studies have focused on the behaviour of polysaccharides as adsorbents [440,454,489,491,501,514,532,533]. The effects of NOM on colloid deposition kinetics have also been studied in column experiments [99,534–539]. It has been generally observed that (i) OM adsorption produces a charge reversal in oxides and in some clays [70,71,110,490,495,508–510,525] and (ii) adsorption increases with increasing ionic strength and decreases with increasing pH [489,490,492,493,505,525,531,540].

NOM can adsorb via several mechanisms [541,542,543], including hydrophobic interactions, hydrogen bonding, electrostatic interactions, cation bridging [485,505], water bridging and ligand exchange–surface complexation [485,487,490,492,494,505,522,541,544, 545–549]. Ligand exchange seems to be the preferred sorption mechanism for explaining sorption of humic substances by ferric and aluminium oxide [487,505,522,545] and formation of cation bridges the preferred mechanism for explaining the sorption by aluminosilicates [528]. However, different binding mechanisms seem to operate for different clays [550].

Measuring the distance dependence of forces acting between the particle surfaces determines which forces dominate particle interactions. The recent development of colloid probes for AFM has made it possible to measure these forces under a range of solution conditions [502,503,551,552]. Greater application of this technique will allow a better understanding of the mechanisms involved in OM adsorption.

Interestingly, not all NOM behaves in the same way. Sorption acts to fractionate the organic matter present in the system [98,487,488,496,497,511,527,553,554–558]. Organic molecules with higher molecular mass and a greater content of aromatic moieties, carboxylic acids, N- and S-containing groups and amino residues are preferentially sorbed. However, most observations on preferential adsorption are indirect [496,522,559]; they do not directly analyse compounds that are sorbed on the mineral surface, but measure the remaining compounds in the supernatant. It has been suggested that soils act as a chromatographic system, and that the sorption process of NOM leads to fractionation of compounds according to sorption intensity [560]. More hydrophobic DOM would be strongly adsorbed and thus more refractory to degradation. Nevertheless, it is still difficult to generalise. For instance, using solid- and liquid-state  $^{13}\text{C}$  NMR, Wang and Xing [561] observed that, contrary to the above observations, the aliphatic fractions of Amherst humic acids were preferentially adsorbed by montmorillonite and kaolinite whereas aromatic fractions remained in solution, with the humic fractions adsorbed on kaolinite surfaces being more aliphatic than those adsorbed on montmorillonite. The higher preference of montmorillonite for aromatic adsorption, as compared with kaolinite, has been confirmed by Feng *et al.* [528].

As mentioned earlier, the adsorption of NOM plays a dominant role in determining the interparticle forces and thus the stability of natural water colloids [97,102,103,544,562, 563]. NOM sorption can also enhance colloid mobilisation through dissolution processes. For example, sediment grain dissolution and the mobilisation of clay colloids by sorption of humic substances have been observed [564–566]. Enhanced Fe(III) solubility at some depths in the ocean has been attributed to humic-type fluorescent organic matter [567].

Soil NOM is strongly sorbed on the mineral phase in soils. On contact with mineral soil horizons rich in aluminium and iron oxides and hydroxides, DOC concentrations decrease sharply due to sorption in most soils [568,569] and the export of DOC to riverine systems is higher from soils that lack effective sorbents for NOM [570,571]. Sorption of DOM is considered to be a major process in the preservation of organic matter in soils [572–574]. Similarly, NOM can be rapidly removed from stream waters by adsorption on particles in the streambed [553,575,576]. NOM desorbed from sediments is mineralised by the microbial community present in seawater at a rate five orders of magnitude faster than sorbed NOM [577]. Thus association of NOM with minerals provides protection against rapid microbial decay.

#### 5.4 LIVING ORGANISMS

Although most phytoplankton and bacterioplankton are larger than 1  $\mu\text{m}$  [578], a significant amount falls within the colloidal size range. Phytoplankton is composed of prokaryotes (cyanobacteria and prochlorophytes) and eukaryotes. An inverse relationship exists between phytoplankton population abundance,  $P$ , and organism size,  $O$ , such that

$$P = kO^b \quad (3)$$

where  $k$  is a proportionality factor and  $b$  takes a constant value around  $-0.75$  [579]. This relationship can be explained in terms of how individual organisms acquire resources as a function of body size [580].

Algal blooms offer a relatively simple system for studying the role of aggregation in aquatic systems. Typical algal blooms occur when nutrient and light conditions allow the rapid growth of a phytoplankton population near the surface. A bloom usually ends when the algae deplete their nutrient supply and slow their growth while they continue to sediment out of the surface layer or to be consumed by zooplankton. Coagulation has been invoked as the primary removal process of algal material in the sea [581–583] and in lakes [138]. Coagulation theory has been applied to the understanding of algal blooms [120–122,584].

Pelagic bacteria are abundant ( $10^6 \text{ cm}^{-3}$ ) [585], accounting for most oceanic biomass and metabolism [586]. They eluded detection for years due to their size and the fact that they are uncultivable. Oceanographers have therefore devised cultivation-independent methods of study [587]. Photosynthetic bacteria *Prochlorococcus* and *Synechococcus* are the most abundant oceanic primary producers. Bacteria have isoelectric points ranging from about 2 to 4, depending on species and growth stage [588], giving them a negative surface charge at the pH of most natural waters. The ionisable functional groups on bacterial cell walls that are thought to contribute most to surface charge are phosphate, either in phosphodiester bridges, as in teichoic acids, or at the end of a polymer, as in phospholipids, protein or peptidoglycan-associated and polysaccharide-associated carboxylates, monohydrogenphosphate and peptidoglycan or protein-associated ammonium.

The colloidal chemistry of bacteria is greatly affected by the presence of surface polysaccharides. Widely varying sizes for these polysaccharides have been reported.

Simoni *et al.* [589] estimated from TEM imaging that bacterial polysaccharides for *Pseudomonas* sp. B13 extended only 20 nm from the surface at neutral pH, but Hermansson [590] concluded that bacteria have extracellular material on the scale of  $10^3$  nm. Frank and Belfort [591] used AFM to measure interaction forces between bacterial polysaccharides from *Pseudomonas atlantica* adsorbed on a surface and the AFM tip and found forces extending more than 1200 nm from the surface. They deduced from light scattering measurements that the maximum extended length of the polymer was 4000 nm. The equilibrium lengths of surface polysaccharides in *Pseudomonas putida* KT2442 and *Burkholderia cepacia* G4, determined by measuring the interaction forces between bacteria and silicon nitride by AFM and applying a steric repulsion model by AFM, ranged from 230 to 1040 nm [592]. Based on these literature values, it seems that the size of the polysaccharide layer can vary depending on the microbial species, growth conditions and suspending phase. The presence of extended surface polymers may explain why the DLVO theory predicts weaker forces and shorter distances for the adhesion of bacteria to surfaces than those measured by AFM [592].

Viruses were not studied until recently, yet are the most abundant biological entities in the sea. They are also abundant in freshwaters. Viruses are small particles, usually about 20–200 nm long [593], consisting of genetic material (DNA or RNA, single- or double-stranded) surrounded by a protein coat (some have lipids). Viruses were not regarded as quantitatively important components of marine food webs until they were shown by direct counts to be abundant [594]. The ultracentrifugation and TEM method currently used to collect and visualise marine viruses and prokaryotes is adapted only slightly from the original technique published in 1949 [595]. Nowadays it is possible to use epifluorescence microscopy with nucleic acid stains such as 4,6-diamino-2-phenylindole (DAPI), Yo-Pro and SYBR to count viruses accurately, rapidly and inexpensively compared with TEM [595–598]. Fluorescence counts are always systematically higher than those obtained by TEM [594,598]. The first reports of high viral abundance [599–601] awakened interest in the topic. Viral abundances are typically  $10^{10}$  dm $^{-3}$  in surface waters (about 5–25 times the bacterial abundance), and follow the same abundance patterns as bacteria. Marine viral diversity has also been examined by morphology and size distribution; cultures and natural samples show a broad array of sizes and shapes [602]. Viruses can form aggregates under certain conditions, as described by Floyd and Sharp [603,604] and Floyd [605] and modelled by Grant [606]. An excellent review on viruses in aquatic ecosystems has been published [607].

An area of research that has received some attention is the transport of pathogenic enteric viruses in groundwater because it is considered to be a serious threat to the safety of many drinking water supplies. Viral behaviour in ground water appears to be controlled by the properties of viruses [608–610], the properties of the porous medium [340,611,612] and the properties of the water transporting the virus [611,613–616]. In particular, viral attachment has been shown to be a function of water pH [613,614,616], the isoelectric point of the porous medium [611] and the isoelectric point of the virus [608–610]. This suggests that electrostatic interactions are an important factor controlling virus attachment and detachment [140,340]. Viruses and inorganic colloids respond similarly to changes in solution and surface chemistry as they migrate through porous media [269,617]. Previous studies had already shown that electrostatic forces dominate the interaction between virus and mineral grains [611,617–620]. Organic matter of natural and anthropogenic origin

hinders virus attachment to mineral surfaces [621–625], presumably by adsorbing to and masking virus attachment sites. Virus isoelectric points can differ considerably (e.g. 3.9 for bacteriophage MS2 and 7.3 for bacteriophage PM2). When virus particles are more than 60 nm in diameter, viral dimensions may become the overriding factor in explaining virus behaviour in aquifers [608].

## 6 CONCLUSIONS

This chapter is the result of a comprehensive, although not exhaustive, literature search (more than 2500 papers were collected) on colloids in natural waters. The wealth of the research activities undertaken in this field is reflected not only in the growing number of papers being published, but also in the breadth of the research. However, as underlined by this chapter, many aspects of the subject have yet to be explored. The main reason for this is probably the particularly idiosyncratic nature of these particles, which makes them especially difficult to study. In effect, colloids in natural waters are characterised by being heterogeneous and dynamic systems and the fact that they are present in low concentrations. In spite of these difficulties, many interesting techniques have been developed or adapted for their study, some of which are described in this book. Unfortunately, the technical developments have not always been accompanied by the parallel development of new conceptual approaches. Articles that attempt to foster new ways of thinking (e.g. [2,119]) are rare.

As discussed in this chapter, two different strategies dominate past and current work on environmental colloids: a holistic approach that tends to emphasise the complexity and heterogeneity of aquatic colloids and attempts to describe their behaviour by using global descriptors, and a second, reductionist approach that targets selected fractions of the ‘mixture’ for detailed analysis of specific features that might be meaningfully extrapolated back to the bulk pool. However, understanding the structures and dynamics of complex systems such as natural colloids can rarely be done simply by assembling the parts. Nearly 20 years ago, Tipping [626] already recognised that drawing the different approaches together was the major, ‘perhaps insurmountable’, challenge in the field.

Some colloidal properties of submicron particles (size, porosity) have been described by empirical power laws. Power laws are emergent general features of complex systems. The study of scaling has proved an extremely effective way not only of simplifying complexity in ecology and biology [627–629], but also of understanding the underlying physical and chemical principles that regulate it. Moreover, it has been shown that empirical power laws can lead to the formulation and testing of mechanistic hypotheses [630]. The exploration of this pathway may provide the much needed link between the holistic and reductionist approaches to the study of natural colloid science. This would require further studies of the properties of unfractionated systems described in terms of power laws, and not of mean values, and also improved identification and quantification of the ‘fundamental parts’ that constitute the systems. A comprehensive and critical evaluation of what has been published so far on the properties of environmentally meaningful homologous compounds would be an ideal guide for further research.

## LIST OF SYMBOLS AND ABBREVIATIONS

### SYMBOLS

$\alpha$	Sticking factor
$\beta$	Exponent of the power-law dependence of number and size of particles
$\lambda$	Variable expressing fractal scaling ( $= L^D$ )
$b$	Exponent of the power law dependence of number and size of phytoplankton
$d_p$	Particle diameter
$D$	Fractal dimension of an aggregate
$D_1$	One-dimensional fractal dimension
$D_2$	Two-dimensional fractal dimension
$G$	Mean velocity rate ( $s^{-1}$ ); $G$ is related to the dissipation rate, $\varepsilon$ , and to the molecular viscosity, $\nu$ , through $G = (\varepsilon/\nu)^{\frac{1}{2}}$
$L$	Characteristic length dimension of an aggregate
$m$	Mass of an aggregate
$N$	Number of particles
$O$	Plytoplankton size
$P$	Phytoplankton population abundance
$R$	Particle or aggregate radius
$W$	Stability ratio defined by Fuchs ( $W = \alpha^{-1}$ )

### ABBREVIATIONS

AFM	Atomic force microscopy
ccc	critical coagulation concentration
CCD	Charge-Coupled Device
CFF	Cross-flow filtration
DAPI	4,6-Diamino-2-phenylindole
DLA	Diffusion-limited aggregation
DLS	Dynamic light scattering
DLVO	Derjaguin–Landau–Verwey–Overbeek
DOC	Dissolved organic carbon
DOM	Dissolved organic matter
DRS	Diffuse reflectance spectroscopy
ED	Electron diffraction
EDS	Energy-dispersive X-ray spectroscopy
EELS	Electron-energy loss spectrometry
EF-TEM	Energy-filtered transmission electron microscopy
EM	Electrophoretic mobility
EPR	Electron paramagnetic resonance
EPS	Exopolymeric substances
EPXMA	Electron probe X-ray microanalysis
ESZ	Electrosensing zone (Coulter principle)
EXAFS	Extended X-ray absorption fine structure

FA	Fulvic acid
FFF	Field-flow fractionation
FTF	Filter-transfer-freezer
FTIR	Fourier transform infrared
GF-AAS	Graphite furnace atomic absorption spectrometry
GPC	Gel-permeation chromatography
GRAV	Gravimetry
HA	Humic acid
HMM	High molar mass
HPLC-PAD	High-performance liquid chromatography–pulsed amperometric detection
HTC	High-temperature combustion
ICP-MS	Inductively coupled plasma mass spectrometry
IHSS	International Humic Substance Society
INSSEV	<i>in situ</i> settling velocity
IR	Infrared
LIBD	Laser induced breakdown detection
LMM	Low molar mass
LO	Light obscuration
MALLS	Multiangle laser light scattering
MBTH	3-Methyl-2-benzothiazolinone hydrochloride
NEXAFS	Near-edge X-ray absorption fine structure
NMR	Nuclear magnetic resonance
NOM	Natural organic matter
OC	Organic carbon
PEELS	Parallel electron energy-loss spectrometry
PZNPC	Point zero net proton charge
POM	Particulate organic matter
RLA	Reaction-limited aggregation
ROM	Refractory organic matter
SAED	Selected-area electron diffraction
SANS	Small-angle neutron scattering
SAXS	Small-angle X-ray scattering
SEC	Size-exclusion chromatography
SdFFF	Sedimentation field-flow fractionation
SEM	Scanning electron microscopy
SLS	Static light scattering
SPC	Single particle counter
STEM	Scanning transmission electron microscopy
STXM	Synchrotron scanning transmission X-ray microscopy
TEM	Transmission electron microscopy
TEP	Transparent exopolymer
TFF	Tangential flow filtration
TOC	Total organic carbon
TPTZ	2,4,6-Tripyridyl-1,3,5-triazine
VATIR	Vertically attenuated infrared spectroscopy
XRD	X-ray diffraction

## REFERENCES

1. Graham, T. (1861). Liquid diffusion applied to analysis, *Philos. Trans. R. Soc. London*, **151**, 183–224.
2. Gustafsson, Ö. and Gschwend, P. M. (1997). Aquatic colloids: Concepts, definitions, and current challenges, *Limnol. Oceanogr.*, **42**, 519–528.
3. Atteia, O. and Kozel, R. (1997). Particle size distributions in waters from a karstic aquifer: from particles to colloids, *J. Hydrol.*, **201**, 102–119.
4. Harris, J. E. (1977). Characterization of suspended matter in the Gulf of Mexico—II Particle size analysis of suspended matter from deep water, *Deep-Sea Res.*, **24**, 1055–1061.
5. Bertsch, P. M. and Seaman, J. C. (1999). Characterization of complex mineral assemblages: Implications for contaminant transport and environmental remediation, *Proc. Natl. Acad. Sci. USA*, **96**, 3350–3357.
6. Van Bemmelen, J. M. (1888). Die Absorptionsverbindungen und das Absorptionsvermögen der Ackererde, *Landwirtsch. Vers. Station*, **35**, 69–136.
7. Mattson, S. (1926). Electrodialysis of the colloidal soil material and the exchangeable bases, *J. Agric. Res.*, **33**, 553–567.
8. Mattson, S. (1929). The laws of soil colloidal behavior. I, *Soil Sci.*, **28**, 179–230.
9. Brun-Cottan, J.-C. (1971). Etude de la granulométrie des particules marines. Mesures effectuées avec un compteur Coulter, *Cahiers Océanogr.*, **23**, 193–205.
10. Sheldon, R. W., Prakash, A. and Sutcliffe, W. H. (1972). The size distribution of particles in the ocean, *Limnol. Oceanogr.*, **17**, 327–340.
11. Lerman, A., Carder, K. L. and Betzer, P. R. (1977). Elimination of fine suspensoids in the oceanic water column, *Earth Planet. Sci. Lett.*, **37**, 61–70.
12. Stumm, W. and Morgan, J. J. (1962). Chemical aspects of coagulation, *J. Am. Water Works Assoc.*, **54**, 971–992.
13. Stumm, W. and O'Melia, C. R. (1968). Stoichiometry of coagulation, *J. Am. Water Works Assoc.*, **60**, 514–539.
14. Hahn, H. H. and Stumm, W. (1970). The role of coagulation in natural waters, *Am. J. Sci.*, **268**, 354–368.
15. Kavanagh, M. C. and Leckie, J. O., eds (1980). *Particulates in Water. Characterization, Fate, Effects, and Removal*, ACS Advances in Chemistry Series, Vol. 189, American Chemical Society, Washington, DC.
16. Stumm, W. and Morgan, J. J. (1970). *Aquatic Chemistry. An Introduction Emphasizing Chemical Equilibria in Natural Waters*. Wiley-Interscience, New York.
17. Everett, D. H. (1972). Manual of symbols and terminology for physicochemical quantities and units. Appendix II. Definitions, terminology and symbols in colloid and surface chemistry. Part I, *Pure Appl. Chem.*, **31**, 577–638.
18. Alldredge, A. L. and Jackson, G. A. (1995). Aggregation in marine systems, *Deep-Sea Res. II*, **42**, 1–7.
19. Buffe, J. (1988) *Complexation Reactions in Aquatic Systems: An Analytical Approach*. Ellis Horwood, Chichester.
20. Fortin, D., Leppard, G. G. and Tessier, A. (1993). Characteristics of lacustrine diagenetic iron oxyhydroxides, *Geochim. Cosmochim. Acta*, **57**, 4391–4404.
21. Perret, D., Newmann, M. E., Nègre, J.-C., Chen, Y. and Buffe, J. (1994). Submicron particles in the Rhine River – I. Physico-chemical characterization, *Water Res.*, **28**, 91–106.
22. Tessier, A., Fortin, D., Belzile, N., De Vitre, R. R. and Leppard, G. G. (1996). Metal sorption to diagenetic iron and manganese oxyhydroxides and associated organic matter: Narrowing the gap between field and laboratory measurements, *Geochim. Cosmochim. Acta*, **60**, 387–404.

23. Lienemann, C.-P., Monnerat, M., Dominik, J. and Perret, D. (1999). Identification of stoichiometric iron–phosphorus colloids produced in a eutrophic lake, *Aquat. Sci.*, **61**, 133–149.
24. Perret, D., Gaillard, J.-F., Dominik, J. and Atteia, O. (2000). The diversity of natural hydrous iron oxides, *Environ. Sci. Technol.*, **34**, 3540–3546.
25. Taillefert, M., Lienemann, C.-P., Gaillard, J.-F. and Perret, D. (2000). Speciation, reactivity, and cycling of Fe and Pb in a meromictic lake, *Geochim. Cosmochim. Acta*, **64**, 169–183.
26. Friedlander, S. K. (1960). On the particle-size spectrum of atmospheric aerosols, *J. Meteorol.*, **17**, 373–374.
27. Friedlander, S. K. (1960). Similarity considerations for the particle-size spectrum of a coagulating, sedimenting aerosol, *J. Meteorol.*, **17**, 479–483.
28. Twomey, S. (1977). *Atmospheric Aerosols*. Elsevier, Amsterdam.
29. Pruppacher, H. R. and Klett, J. D. (1978). *The Microphysics of Clouds and Precipitation*. Reidel, Dordrecht.
30. Sheldon, R. W. and Parsons, T. R. (1967). A continuous size spectrum for particulate matter in the sea, *J. Fish. Res. Bd. Can.*, **24**, 909–915.
31. McCave, I. N. (1975). Vertical flux of particles in the ocean, *Deep-Sea Res.*, **22**, 491–502.
32. Pak, H., Zaneveld, J. R. V. and Kitchen, J. (1980). Intermediate nepheloid layers observed off Oregon and Washington, *J. Geophys. Res.*, **85**, 6697–6708.
33. McCave, I. N. (1983). Particulate size spectra, behavior, and origin of nepheloid layers over the Nova Scotian continental rise, *J. Geophys. Res.*, **88**, 7647–7666.
34. McCave, I. N. (1984). Size spectra and aggregation of suspended particles in the deep ocean, *Deep-Sea Res.*, **31**, 329–352.
35. Lambert, C. E., Jehanno, C., Silverberg, N., Brun-Cottan, J. and Chesselet, R. (1981). Log-normal distributions of suspended particles in the open ocean, *J. Mar. Res.*, **39**, 77–98.
36. Hunt, J. R. (1980). Prediction of oceanic particle size distributions from coagulation and sedimentation mechanisms. In *Particulates in Water. Characterization, Fate, Effects, and Removal*, eds Kavanaugh, M. C. and Leckie, J. O. ACS Advances in Chemistry Series, Vol. 189, American Chemical Society, Washington, DC, pp. 243–257.
37. Hunt, J. R. (1982). Self-similar particle-size distributions during coagulation: theory and experimental verification, *J. Fluid Mech.*, **122**, 169–185.
38. Junge, C. E. (1969). Comments on “Concentrations and size distribution measurements of atmospheric aerosols and a test of the theory of self-preserving size distributions”, *J. Atmos. Sci.*, **26**, 603–608.
39. Filella, M., Zhang, J., Newman, M. E. and Buffe, J. (1997). Analytical applications of photon correlation spectroscopy for size distribution measurements of natural colloidal suspensions: capabilities and limitations, *Colloids Surf. A*, **120**, 27–46.
40. Schurtenberger, P. and Newmann, M. E. (1993). Characterization of biological and environmental particles using static and dynamic light scattering. In *Environmental Particles*, eds Buffe, J. and van Leeuwen, H. P. IUPAC Series on Analytical and Physical Chemistry of Environmental Systems, Vol. 2. Lewis, Boca Raton, FL, pp. 37–115.
41. Degueldre, C., Pfeiffer, H.-R., Alexander, W., Wernli, B. and Bruetsch, R. (1996). Colloid properties in granitic groundwater systems. I: Sampling and characterization, *Appl. Geochem.*, **11**, 677–695.
42. Rossé, P. and Loizeau, J.-L. (2003). Use of single particle counters for the determination of the number and size distribution of colloids in natural surface waters, *Colloids Surf. A*, **217**, 109–120.
43. Lal, D. and Lerman, A. (1975). Size spectra of biogenic particles in ocean water and sediments, *J. Geophys. Res.*, **80**, 423–430.
44. Osman-Sigg, G. K. and Stumm, W. (1982). Partikelgrößenverteilung und natürliche Koagulation im Zürichsee, *Schweiz. Z. Hydrol.*, **44**, 405–421.

45. Degueldre, C. (1990). *Grimsel Colloid Exercise – An International Intercomparison Exercise on the Sampling and Characterization of Groundwater Colloids*. Report EUR 12660 en. Commission of the European Communities, Luxembourg.
46. Wells, M. L. and Goldberg, E. D. (1992). Marine submicron particles, *Mar. Chem.*, **40**, 5–18.
47. Kim, J. P., Lemmon, J. and Hunter, K. A. (1995). Size-distribution analysis of sub-micron colloidal particles in river water, *Environ. Technol.*, **16**, 861–868.
48. Boller, M. and Blaser, S. (1998). Particles under stress, *Water Sci. Technol.*, **37**, 9–29.
49. Degueldre, C., Bilewicz, A., Hummel, W. and Loizeau, J. L. (2001). Sorption behaviour of Am on marl groundwater colloids, *J. Environ. Radioact.*, **55**, 241–253.
50. Wells, M. L. and Goldberg, E. D. (1993). Colloid aggregation in seawater, *Mar. Chem.*, **41**, 353–358.
51. Wells, M. L. and Goldberg, E. D. (1994). The distribution of colloids in the North Atlantic and Southern Oceans, *Limnol. Oceanogr.*, **39**, 286–302.
52. Benner, R., Biddanda, B., Black, B. and McCarthy, M. (1997). Abundance, size distribution, and stable carbon and nitrogen isotopic compositions of marine organic matter isolated by tangential-flow filtration, *Mar. Chem.*, **57**, 243–263.
53. Stolpe, B., Hassellöv, M., Andersson, K. and Turner, D. R. (2005). High resolution ICPMS as an on-line detector for flow field-flow fractionation; multi-element determination of colloidal size distributions in a natural water sample, *Anal. Chim. Acta*, **535**, 109–121.
54. Filella, M., Buffe, J. and Leppard, G. G. (1993). Characterization of submicrometre colloids in freshwaters: evidence for their bridging by organic structures, *Water Sci. Technol.*, **27**, 91–102.
55. Walther, C., Büchner, S., Filella, M., and Chanudet, V. (2006). Probing particle size distributions in natural surface waters from 15 nm to 2 µm by a combination of LIBD and Single Particle Counting, *J. colloid Interface Sci.*, **301**, 532–537.
56. Sposito, G. (1992). Characterization of particle surface charge. In *Environmental Particles*, eds Buffe, J. and van Leeuwen, H. P. IUPAC Series on Analytical and Physical Chemistry of Environmental Systems, Vol. 1. Lewis, Boca Raton, FL, pp. 291–314.
57. Neihof, R. A. and Loeb, G. I. (1972). The surface charge of particulate matter in seawater, *Limnol. Oceanogr.*, **17**, 7–16.
58. Neihof, R. A. and Loeb, G. I. (1974). Dissolved organic matter in seawater and the electric charge of immersed surfaces, *J. Mar. Res.*, **32**, 5–12.
59. Hunter, K. A. (1980). Microelectrophoretic properties of natural surface-active organic matter in coastal seawater, *Limnol. Oceanogr.*, **25**, 807–822.
60. Gerritsen, J. and Bradley, S. W. (1987). Electrophoretic mobility of natural particles and cultured organisms in freshwaters, *Limnol. Oceanogr.*, **32**, 1049–1058.
61. Ryan, J. N. and Gschwend, P. M. (1990). Colloid mobilization in two Atlantic Coastal plain aquifers: field studies, *Water Resour. Res.*, **26**, 307–322.
62. McCarthy, J. F. and Degueldre, C. (1993). Sampling and characterization of colloids and particles in groundwater for studying their role in contaminant transport. In *Environmental Particles*, eds Buffe, J. and van Leeuwen, H. P. IUPAC Series on Analytical and Physical Chemistry of Environmental Systems, Vol. 2. Lewis, Boca Raton, FL, pp. 247–315.
63. Loder, T. C. and Liss, P. S. (1982). The role of organic matter in determining the surface charge of suspended particles in estuarine and oceanic waters, *Thalassia Jugosl.*, **18**, 433–447.
64. Loder, T. C. and Liss, P. S. (1985). Control by organic coatings of the surface charge of estuarine suspended particles, *Limnol. Oceanogr.*, **30**, 418–421.
65. Newton, P. P. and Liss, P. S. (1987). Positively charged suspended particles: Studies in an iron-rich river and its estuary, *Limnol. Oceanogr.*, **32**, 1267–1276.

66. Kaplan, D. I., Bertsch, P. M. and Adriano, D. C. (1995). Facilitated transport of contaminant metals through an acidified aquifer, *Ground Water*, **33**, 708–717.
67. Hunter, K. A. and Liss, P. S. (1979). The surface charge of suspended particles in estuarine and coastal waters, *Nature*, **282**, 823–825.
68. Hunter, K. A. and Liss, P. S. (1982). Organic matter and the surface charge of suspended particles in estuarine waters, *Limnol. Oceanogr.*, **27**, 322–335.
69. Newton, P. P. and Liss, P. S. (1989). Surface charge characteristics of oceanic suspended particles, *Deep-Sea Res.*, **36**, 759–767.
70. Tipping, E. and Cooke, D. (1982). The effects of adsorbed humic substances on the surface charge of goethite ( $\alpha$ -FeOOH) in freshwaters, *Geochim. Cosmochim. Acta*, **46**, 75–80.
71. Tipping, E. and Heaton, M. J. (1983). The adsorption of aquatic humic substances by two oxides of manganese, *Geochim. Cosmochim. Acta*, **47**, 1393–1397.
72. Bryant, R. and Williams, D. J. A. (1987). The electrochemistry of colloidal particles from a proglacial lake, *Chem. Geol.*, **62**, 291–305.
73. Rees, T. F. and Ranville, J. F. (1989). *Characterization of Colloids in the Mississippi River and its Major Tributaries*. Water Resources Investigations, USGS 88–4220, US Geological Survey, Washington, DC, pp. 513–522.
74. Rees, T. F., Leenheer, J. A. and Ranville, J. F. (1991). Use of a single-bowl continuous-flow centrifuge for dewatering suspended sediments: effect on the sediment physical and chemical characteristics, *Hydrol. Process.*, **5**, 201–214.
75. Tipping, E. (1981). Adsorption by goethite ( $\alpha$ -FeOOH) of humic substances from three different lakes, *Chem. Geol.*, **33**, 81–89.
76. Beckett, R. and Le, N. P. (1990). The role of organic matter and ionic composition in determining the surface charge of suspended particles in natural waters, *Colloids Surf.*, **44**, 35–49.
77. Elimelech, M., Nagai, M., Ko, C.-H. and Ryan, J. N. (2000). Relative insignificance of mineral grain zeta potential to colloid transport in geochemically heterogeneous porous media, *Environ. Sci. Technol.*, **34**, 2143–2148.
78. Allard, T., Ponthieu, M., Weber, T., Filizola, N., Guyot, J.-L. and Benedetti, M. (2002). Nature and properties of suspended solids in the Amazon Basin, *Bull. Soc. Géol. Fr.*, **173**, 67–75.
79. von Smoluchowski, M. (1918). Versuch einer mathematischen Theorie der Koagulationskinetik kolloider Lösungen. *Z. Phys. Chem. (Leipzig)*, **92**, 129–168.
80. Fuchs, N. (1934). Über die Stabilität und Aufladung der Aerosole, *Z. Phys.*, **89**, 736–742.
81. Hamaker, H. C. (1937). The London–van der Waals attraction between spherical particles, *Physica*, **4**, 1058–1072.
82. Bradley, R. S. (1936). The cohesion between smoke particles, *Trans. Faraday Soc.*, **32**, 1088–1090.
83. De Boer, J. H. (1936). The influence of van der Waals' forces and primary bonds on binding energy, strength and orientation, with special reference to some artificial resins, *Trans. Faraday Soc.*, **32**, 10–38.
84. Verwey, E. J. W. and Overbeek, J. Th. G. (1948). *Theory of the Stability of Lyophobic Colloids*. Elsevier, Amsterdam.
85. Derjaguin, B. V. and Landau, L. (1941). Theory of the stability of strongly charged lyophobic sols and of the adhesion of strongly charged particles in solution of electrolytes, *Acta Physicochim. USSR*, **14**, 633–662.
86. Kihira, H., Ryde, N. and Matijević, E. (1992). Kinetics of heterocogulation. 1. A comparison of theory and experiment, *Colloids Surf.*, **64**, 317–324.
87. Litton, G. M. and Olson, T. M. (1993). Colloid deposition rates on silica bed media and artifacts related to collector surface preparation methods, *Environ. Sci. Technol.*, **27**, 185–193.

88. Elimelech, M. and O'Melia, C. R. (1990). Kinetics of deposition of colloidal particles in porous media, *Environ. Sci. Technol.*, **24**, 1528–1536.
89. Van Duuren, F. A. (1968). Defined velocity gradient model flocculator, *J. Sanit. Eng. Div. Proc. Am. Soc. Civil Eng.*, **94**, 671–682.
90. Donnelly, R. (1991). Taylor–Couette flow: the early days, *Phys. Today*, **44**, 32–39.
91. Drapeau, D. T., Dam, H. G. and Grenier, G. (1994). An improved flocculator design for use in particle aggregation experiments, *Limnol. Oceanogr.*, **39**, 723–729.
92. Li, X. and Logan, B. E. (1997). Collision frequencies between fractal aggregates and small particles in a turbulently sheared fluid, *Environ. Sci. Technol.*, **31**, 1237–1242.
93. Kiørboe, T. and Hansen, J. L. S. (1993). Phytoplankton aggregate formation: observations of patterns and mechanisms of cell sticking and the significance of exopolymeric material, *J. Plankton Res.*, **15**, 993–1018.
94. Alldredge, A. L. and McGillivray, P. (1991). The attachment probabilities of marine snow and their implications for particle coagulation in the ocean, *Deep-Sea Res.*, **38**, 431–443.
95. Jekel, M. R. (1986). The stabilization of dispersed mineral particles by adsorption of humic substances, *Water Res.*, **20**, 1543–1554.
96. Amal, R., Coury, J. R., Raper, J. A., Walsh, W. P. and Waite, T. D. (1990). Structure and kinetics of aggregating colloidal haematite, *Colloids Surf. A*, **46**, 1–19.
97. Amal, R., Raper, J. A. and Waite, T. D. (1992). Effect of fulvic acid adsorption on the aggregation kinetics and structure of hematite particles, *J. Colloid Interface Sci.*, **151**, 244–257.
98. Tiller, C. L. and O'Melia, C. R. (1993). Natural organic matter and colloidal stability: models and measurements, *Colloids Surf. A*, **73**, 89–102.
99. Kretzschmar, R., Robarge, W. P. and Amoozegar, A. (1995). Influence of natural organic matter on colloid transport through saprolite, *Water Resour. Res.*, **31**, 435–445.
100. Edzwald, J. K., Upchurch, J. B. and O'Melia, C. R. (1974). Coagulation in estuaries, *Environ. Sci. Technol.*, **8**, 58–63.
101. Osman-Sigg, G. K. (1982). *Kolloidale und suspendierte Teilchen in natürlichen Gewässern: Partikelgrößenverteilung und natürliche Koagulation im Zürichsee*. Eidgenössische Technische Hochschule Zürich, Ph.D dissertation No. 6986; cited in [105].
102. Tipping, E. and Higgins, D. C. (1982). The effect of adsorbed humic substances on the colloid stability of haematite particles, *Colloids Surf.*, **5**, 85–92.
103. Gibbs, R. J. (1983). Effect of natural organic coatings on the coagulation of particles, *Environ. Sci. Technol.*, **17**, 237–240.
104. Gibbs, R. J. (1983). Coagulation rates of clay minerals and natural sediments, *J. Sediment. Petrol.*, **53**, 1193–1203.
105. Ali, W., O'Melia, C. R. and Edzwald, J. K. (1984). Colloidal stability of particles in lakes: measurement and significance, *Water Sci. Technol.*, **17**, 702–712.
106. Gallegos, C. L. and Menzel, R. G. (1987). Submicron size distribution of inorganic suspended solids in turbid waters by photon correlation spectroscopy, *Water Resour. Res.*, **23**, 596–602.
107. Liang, L. (1988). *Effect of Surface Chemistry on Kinetics of Coagulation of Submicron Size Iron Oxide Particles ( $\alpha\text{-Fe}_2\text{O}_3$ ) in Water*. Ph.D thesis, California Institute of Technology, Pasadena, CA.
108. Burban, P.-Y., Lick, W. and Lick, J. (1989). The flocculation of fine-grained sediments in estuarine waters, *J. Geophys. Res.*, **94**, 8323–8330.
109. Weilenmann, U., O'Melia, C. R. and Stumm, W. (1989). Particle transport in lakes: models and measurements, *Limnol. Oceanogr.*, **34**, 1–18.
110. Chandrakanth, M. S. and Amy, G. L. (1996). Effects of ozone on the colloidal stability and aggregation of particles coated with natural organic matter, *Environ. Sci. Technol.*, **30**, 431–443.

111. Degueldre, C., Grauer, R., Laube, A., Oess, A. and Silby, H. (1996). Colloid properties in granitic groundwater systems. II: Stability and transport study. *Appl. Geochem.*, **11**, 697–710.
112. Degueldre, C., Triay, I., Kim, J.-I., Vilks, P., Laaksoharju, M. and Miekeley, N. (2000). Groundwater colloid properties: a global approach, *Appl. Geochem.*, **15**, 1043–1051.
113. Gardner, K. H., Theis, T. L. and Young, T. C. (1998). Colloid aggregation: numerical solution and measurements, *Colloids Surf. A*, **141**, 237–252.
114. Kretzschmar, R., Holthoff, H. and Sticher, H. (1998). Influence of pH and humic acid on coagulation kinetics of kaolinite: a dynamic light scattering study, *J. Colloid Interface Sci.*, **202**, 95–103.
115. Aurell, C. A. and Wistrom, A. O. (2000). Coagulation of kaolinite colloids in high carbonate strength water, *Colloids Surf. A*, **168**, 277–285.
116. Atteia, O., Mondi, C. and Perret, D. (2001). Aggregation rates of natural particle populations, *Water Res.*, **35**, 2429–2434.
117. Czigány, S., Flury, M. and Harsh, J. B. (2005). Colloids stability in vadose zone Hanford sediments, *Environ. Sci. Technol.*, **39**, 1506–1512.
118. Heidmann, I., Christl, I. and Kretzschmar, R. (2005). Aggregation kinetics of kaolinite-fulvic acid colloids as affected by the sorption of Cu and Pb, *Environ. Sci. Technol.*, **39**, 807–813.
119. Buffe, J., Wilkinson, K. J., Stoll, S., Filella, M. and Zhang, J. (1998). A generalized description of aquatic colloidal interactions: The three-colloidal component approach, *Environ. Sci. Technol.*, **32**, 2887–2899.
120. Jackson, G. A. (1990). A model of the formation of marine algal flocs by physical coagulation processes, *Deep-Sea Res.*, **37**, 1107–1211.
121. Hill, P. S. (1992). Reconciling aggregation theory with observed vertical fluxes following phytoplankton blooms, *J. Geophys. Res.*, **97**, 2295–2308.
122. Jackson, G. A. and Lochmann, S. E. (1992). Effect of coagulation on nutrient and light limitation of an algal bloom, *Limnol. Oceanogr.*, **37**, 77–89.
123. Riebesell, U. (1992). The formation of large marine snow and its sustained residence in surface waters, *Limnol. Oceanogr.*, **37**, 63–76.
124. Riebesell, U. and Wolf-Gadrow, D. A. (1992). The relationship between physical aggregation of phytoplankton and particle flux: a numerical model, *Deep-Sea Res.*, **39**, 1085–1102.
125. Jackson, G. A. (1995). TEP and coagulation during a mesocosm experiment, *Deep-Sea Res. II*, **42**, 215–222.
126. Kiørboe, T., Andersen, K. P. and Dam, H. G. (1990). Coagulation efficiency and aggregate formation in marine phytoplankton, *Mar. Biol.*, **107**, 235–245.
127. Kiørboe, T., Lundsgaard, C., Olesen, M. and Hansen, J. L. S. (1994). Aggregation and sedimentation processes during a spring phytoplankton bloom: A field experiment to test coagulation theory, *J. Mar. Res.*, **52**, 297–323.
128. Dam, H. G. and Drapau, D. T. (1995). Coagulation efficiency, organic-matter glues and the dynamics of particles during a phytoplankton bloom in a mesocosm study, *Deep-Sea Res. II*, **42**, 111–123.
129. Logan, B. E., Passow, U., Alldredge, A. L., Grossart, H.-P. and Simon, M. (1995). Rapid formation and sedimentation of large aggregates is predictable from coagulation rates (half-lives) of transparent exopolymer particles (TEP), *Deep-Sea Res. II*, **42**, 203–214.
130. Kiørboe, T., Tiselius, P., Mitchell-Innes, B., Hansen, J. L. S., Visser, A. M. and Mari, X. (1998). Intensive aggregate formation with low vertical flux during an upwelling-induced diatom bloom, *Limnol. Oceanogr.*, **43**, 104–116.
131. Delichatsios, M. A. and Probstein, R. F. (1975). Coagulation in turbulent flow: theory and experiment, *J. Colloid Interface Sci.*, **51**, 394–405.

132. Atteia, O. (1998). Evolution of size distributions of natural particles during aggregation: modelling versus field results, *Colloids Surf. A*, **139**, 171–188.
133. O'Melia, C. R. and Bowman, K. S. (1984). Origins and effects of coagulation in lakes, *Schweiz. Z. Hydrol.*, **46**, 64–85.
134. Farley, K. J. and Morel, F. M. M. (1986). Role of coagulation in the kinetics of sedimentation, *Environ. Sci. Technol.*, **20**, 187–195.
135. Filella, M. and Buffle, J. (1993). Factors controlling the stability of submicron colloids in natural waters, *Colloids Surf. A*, **73**, 255–273.
136. Pizarro, J., Belzile, N., Filella, M., Leppard, G. G., Nègre, J.-C., Perret, D. and Buffle, J. (1995). Coagulation/sedimentation of submicron iron particles in a eutrophic lake. *Water Res.*, **29**, 617–632.
137. Hofmann, A. and Filella, M. (1999). Transport of suspended matter in the hypolimnion of Lake Lugano: a comparison of field observations and model predictions, *J. Great Lakes Res.*, **25**, 865–882.
138. Hofmann, A., Filella, M., Lallier-Vergès, E. and Dominik, J. (2001). The role of aggregation in the rapid sedimentation of diatoms in lake water: a case study in the north basin of Lake Lugano (Switzerland, Italy), *Arch. Hydrobiol. Suppl.*, **139**, 85–116.
139. Kretzschmar, R., Borkovec, M., Grolimund, D. and Elimelech, M. (1999). Mobile subsurface colloids and their role in contaminant transport, *Adv. Agron.*, **66**, 121–193.
140. Elimelech, M., Gregory, J., Jia, X. and Williams, R. A. (1995). *Particle Deposition and Aggregation: Measurement, Modelling, and Simulation*. Butterworth-Heinemann, Woburn, MA.
141. Jullien, R. and Botet, R. (1987). *Aggregation and Fractal Aggregates*. World Scientific, Singapore.
142. Avnir, D. (ed.) (1989) *The Fractal Approach to Heterogeneous Chemistry*. Surfaces, Colloids and Polymers, John Wiley & Sons, Inc., New York.
143. Vicsek, T. (1992). *Fractal Growth Phenomena*, 2nd edn. World Scientific, Singapore.
144. Meakin, P. (1988). Fractal aggregates, *Adv. Colloid Interface Sci.*, **28**, 249–331.
145. Lin, M. Y., Lindsay, H. M., Weitz, D. A., Ball, R. C., Klein, R. and Meakin, P. (1989). Universality in colloid aggregation, *Nature*, **339**, 360–362.
146. Chin, W.-C., Orellana, M. V. and Verdugo, P. (1998). Spontaneous assembly of marine dissolved organic matter into polymer gels, *Nature*, **391**, 568–572.
147. Jackson, G. A. and Burd, A. B. (1998). Aggregation in the marine environment, *Environ. Sci. Technol.*, **32**, 2805–2814.
148. Jackson, G. A. (1998). Using fractal scaling and two-dimensional particle size spectra to calculate coagulation rates for heterogeneous systems, *J. Colloid Interface Sci.*, **202**, 20–29.
149. Jiang, Q. and Logan, B. E. (1991). Fractal dimensions of aggregates determined from steady state size distributions, *Environ. Sci. Technol.*, **25**, 2031–2038.
150. Logan, B. E. (1999). *Environmental Transport Processes*. John Wiley & Sons, Inc., New York.
151. Hackley, V. A. and Anderson, M. A. (1989). Effects of short-range forces on the long-range structure of hydrous iron oxide aggregates, *Langmuir*, **5**, 191–198.
152. Rarity, J. G., Seabrook, R. N. and Carr, R. J. G. (1989). Light-scattering studies of aggregation, *Proc. R. Soc. London, Ser. A*, **423**, 89–102.
153. Klein, R., Weitz, D. A., Lin, M. Y., Lindsay, H. M., Ball, R. C. and Meakin, P. (1990). Theory of scattering from colloidal aggregates, *Prog. Colloid Polym. Sci.*, **81**, 161–168.
154. Zhang, J. and Buffle, J. (1996). Multi-method determination of the fractal dimension of hematite aggregates, *Colloids Surf. A*, **107**, 175–187.
155. Weitz, D. A., Huang, J. S., Lin, M. Y. and Sung, J. (1984). Dynamics of diffusion-limited kinetic aggregation, *Phys. Rev. Lett.*, **53**, 1657–1660.

156. Zhang, J. and Buffle, J. (1995). Kinetics of hematite aggregation by polyacrylic acid: importance of charge neutralization, *J. Colloid Interface Sci.*, **174**, 500–509.
157. Teixeira, J. (1988). Small-angle scattering by fractal systems, *J. Appl. Crystallogr.*, **21**, 781–785.
158. Österberg, R. and Mortensen, K. (1992). Fractal dimension of humic acids. A small angle neutron scattering study, *Eur. Biophys. J.*, **21**, 163–167.
159. Österberg, R., Szajdak, L. and Mortensen, K. (1994). Temperature-dependent restructuring of fractal humic acids: A proton-dependent process, *Environ. Int.*, **20**, 77–80.
160. Rice, J. A. and Lin, J.-S. (1993). Fractal nature of humic materials. *Environ. Sci. Technol.*, **27**, 413–414.
161. Malekani, K., Rice, J. A. and Lin, J.-S. (1997). The effect of sequential removal of organic matter on the surface morphology of humin, *Soil Sci.*, **162**, 333–342.
162. Rice, J. A., Tombácz, E. and Malekani, K. (1999). Applications of light and X-ray scattering to characterize the fractal properties of soil organic matter, *Geoderma*, **88**, 251–264.
163. Weitz, D. A. and Oliveira, M. (1984). Fractal structures formed by kinetic aggregation of aqueous gold colloids, *Phys. Rev. Lett.*, **52**, 1433–1436.
164. Tence, M., Chevalier, J. P. and Jullien, R. (1986). On the measurement of the fractal dimension of aggregated particles by electron microscopy: experimental method, corrections and comparison with numerical models, *J. Phys. (Paris)*, **47**, 1989–1998.
165. Chakraborti, R. K., Gardner, K. H., Atkinson, J. F. and Van Benschoten, J. E. (2003). Changes in fractal dimension during aggregation, *Water Res.*, **37**, 873–883.
166. Chakraborti, R. K., Atkinson, J. F. and Van Benschoten, J. E. (2000). Characterization of alum floc by image analysis, *Environ. Sci. Technol.*, **34**, 3969–3976.
167. Österberg, R. and Mortensen, K. (1994). Fractal geometry of humic acids. Temperature-dependent restructuring studied by small-angle neutron scattering. In *Humic Substances in the Global Environment and Implications on Human Health*, eds Senesi, N. and Miano, T. M. Elsevier, Amsterdam, pp. 127–132.
168. Rice, J. A. and Lin, J. S. (1994). Fractal dimensions of humic materials. In *Humic Substances in the Global Environment and Implications on Human Health*, eds Senesi, N. and Miano, T. M. Elsevier, Amsterdam, pp. 115–120.
169. Senesi, N., Lorusso, G. F., Miano, T. M., Maggipinto, G., Rizzi, F. R. and Capozzi, V. (1994). The fractal dimension of humic substances as a function of pH by turbidity measurements. In *Humic Substances in the Global Environment and Implications on Human Health*, eds. Senesi, N. and Miano, T. M. Elsevier, Amsterdam, pp. 121–126.
170. Logan, B. E. and Wilkinson, D. B. (1990). Fractal geometry of marine snow and other biological aggregates, *Limnol. Oceanogr.*, **35** 130–136.
171. Kilps, J. R., Logan, B. E. and Alldredge, A. L. (1994). Fractal dimensions of marine snow determined from image analysis of *in situ* photographs, *Deep-Sea Res. I*, **41**, 1159–1169.
172. Li, X. and Logan, B. E. (1995). Size distributions and fractal properties of particles during a simulated phytoplankton bloom in a mesocosm, *Deep-Sea Res. II*, **42**, 125–138.
173. Jackson, G. A., Logan, B. E., Alldredge, A. L. and Dam, H. G. (1995). Combining particle size spectra from a mesocosm experiment measured using photographic and aperture impedance (Coulter and Elzone) techniques, *Deep-Sea Res. II*, **42** 139–157.
174. Jackson G. A., Maffione, R., Costello, D. K., Alldredge, A. L., Logan, B. E. and Dam, H. G. (1997). Particle size spectra between 1  $\mu\text{m}$  and 1 cm at Monterey Bay determined using multiple instruments, *Deep-Sea Res. I*, **44**, 1739–1767.
175. Li, X., Passow, U. and Logan, B. E. (1998). Fractal dimensions of small (15–200  $\mu\text{m}$ ) particles in Eastern Pacific coastal waters, *Deep-Sea Res. I*, **45**, 115–131.
176. Dyer, K. R. and Manning, A. J. (1999). Observation of the size, settling velocity and effective density of flocs, and their fractal dimensions, *J. Sea Res.*, **41**, 87–95.

177. Grout, H., Sempere, R., Thill, A., Calafat, A., Prieur, L. and Canals, M. (2001). Morphological and chemical variability of colloids in the Almeria–Oran Front in the eastern Alboran Sea (SW Mediterranean Sea), *Limnol. Oceanogr.*, **46**, 1347–1357.
178. Gorczyca, B. and Ganczarczyk, J. (1996). Image analysis of alum coagulated mineral suspension, *Environ. Technol.*, **17**, 1361–1369.
179. Avnir, D., Biham, O., Lidar, D. and Malcai, O. (1998). Is the geometry of nature fractal?, *Science*, **279**, 39–40.
180. Mandelbrot, B. B. (1982). *The Fractal Geometry of Nature*, rev. ed. Freeman, New York.
181. Feder, J. (1988). *Fractals*. Plenum Press, New York.
182. Avnir, D., Farin, D. and Pfeifer, P. (1984). Molecular fractal surfaces, *Nature*, **308**, 261–263.
183. Schaefer, D. W., Martin, J. E., Wiltzius, P. and Cannell, D. S. (1984). Fractal geometry of colloidal aggregates, *Phys. Rev. Lett.*, **52**, 2371–2374.
184. Axelson, M., Tchoubar, D., Bottero, J. and Fiessinger, F. (1985). Détermination par DPAX de la structure fractale d’agrégats obtenus par collage d’amas. Etude de deux solutions d’hydroxyde d’aluminium  $\text{Al(OH)}_x$  avec  $x = 2.5$  et  $3$ . *J. Phys. Fr. (Paris)*, **46**, 1587.
185. Davis, R. H. and Hunt, T. P. (1986). Modelling and measurement of yeast flocculation. *Biotechnol. Progr.*, **2**, 91–97.
186. Farin, D. and Avnir, D. (1989). The fractal nature of molecule–surface interactions and reactions, In *The Fractal Approach to Heterogeneous Chemistry*, Surfaces, Colloids and Polymers, ed. Avnir, D. John Wiley & Sons, Ltd, Chichester, pp. 271–293.
187. Glasgow, L. A. (1989). Effects of the physicochemical environment on floc properties, *Chem. Eng. Prog.*, **85**, 51–55.
188. Li, D. and Ganczarczyk, J. (1989). Fractal geometry of particle aggregates generated in water and wastewater treatment processes, *Environ. Sci. Technol.*, **23**, 1385–1389.
189. Li, D. H. and Ganczarczyk, J. J. (1987). Stroboscopic determination of settling velocity, size and porosity of activated sludge flocs, *Water Res.*, **21**, 257–262.
190. Lagvankar, A. L. and Gemmell, R. S. (1968). A size–density relationship for flocs, *J. Am. Water Works Assoc.*, **60**, 1040–1046.
191. Broadway, J. D. (1978). Dynamics of growth and breakage of alum floc in presence of fluid shear. *J. Environ. Eng. Div. (Am. Soc. Civ. Eng.)*, **104**, 901–915.
192. Tambo, N. and Watanabe, Y. (1979). Physical characteristics of flocs – I. The floc density function and aluminium floc, *Water Res.*, **13**, 409–419.
193. Magara, Y., Nambu, S. and Utosawa, K. (1976). Biochemical and physical properties of an activated sludge on settling characteristics, *Water Res.*, **10**, 71–77.
194. Mitani, T., Unno, H. and Akekata, T. (1983). A structure model for activated sludge flocs. *Jpn. Water Res.*, **6**, 69–75.
195. Schmidt, P. W. (1989). Use of scattering to determine the fractal dimension, In *The Fractal Approach to Heterogeneous Chemistry*, Surfaces, Colloids and Polymers, ed. Avnir, D. John Wiley & Sons, Ltd, Chichester, pp. 67–79.
196. Wiesner, M. R. and Mazounie, P. (1989). Raw water characteristics and the selection of water treatment configurations for particle removal, *J. Am. Water Works Assoc.*, **81**, 80–89.
197. Alldredge, A. L. and Gotschalk, C. C. (1988). *In situ* settling behavior of marine snow, *Limnol. Oceanogr.*, **33**, 339–351.
198. Logan, B. E. and Alldredge, A. L. (1989). Potential for nutrient uptake by flocculating diatoms, *Mar. Biol.*, **101**, 443–450.
199. Gibbs, R. J. (1985). Estuarine flocs: their size, settling velocity and density, *J. Geophys. Res.*, **90**, 3249–3251.
200. Hawley, N. (1982). Settling velocity distribution of natural aggregates, *J. Geophys. Res.*, **87**, 9489–9498.

201. Logan, B. E. and Wilkinson, D. B. (1991). Fractal dimensions and porosities of *Zoogloea ramigera* and *Saccharomyces cerevisiae* aggregates. *Biotechnol. Bioeng.*, **38**, 389–396.
202. Buffle, J., Perret, D. and Newmann, M. (1992). The use of filtration and ultrafiltration for size fractionation of aquatic particles, colloids, and macromolecules. In *Environmental Particles*, eds Buffle, J. and van Leeuwen, H. P. IUPAC Series on Analytical and Physical Chemistry of Environmental Systems, Vol. 1. Lewis, Boca Raton, FL, pp. 171–230.
203. Chittleborough, D. J., Hotchin, D. M. and Beckett, R. (1992). Sedimentation field-flow fractionation: a new technique for the fractionation of soil colloids, *Soil Sci.*, **153**, 341–348.
204. Ranville, J. F., Harnish, R. A. and McKnight, D. M. (1991). Particulate and colloidal organic material in Pueblo Reservoir, Colorado: influence of autochthonous source on chemical composition. In *Organic Substances and Sediment in Water*, Vol. I, Humics and Soils ed. Baker, R. A. Lewis, Chelsea, MI, pp. 47–73.
205. Rostad, C. E., Rees, T. F. and Daniel, S. R. (1998). Colloid particle sizes in the Mississippi River and some of its tributaries, from Minneapolis to below New Orleans, *Hydrol. Process.*, **12**, 25–41.
206. Rostad, C. E., Leenheer, J. A. and Daniel, S. R. (1997). Organic carbon and nitrogen content associated with colloids and suspended particulates from the Mississippi River and some of its tributaries, *Environ. Sci. Technol.*, **31**, 3218–3225.
207. Town, R. M. and Filella, M. (2002). Size fractionation of trace metals in freshwaters: implications for understanding their behaviour and fate, *Re/Views Environ. Sci. Bio/Technol.*, **1**, 277–297.
208. Amon, R. M. W. and Benner, R. (1994). Rapid cycling of high-molecular-weight dissolved organic matter in the ocean, *Nature*, **369**, 549–552.
209. Amon, R. M. W. and Benner, R. (1996). Bacterial utilization of different size classes of dissolved organic matter, *Limnol. Oceanogr.*, **41**, 41–51.
210. Guo, L., Santschi, P. H., Cifuentes, L. A., Trumbore, S. B. and Southon, J. J. (1996). Cycling of high-molecular-weight dissolved organic matter in the Middle Atlantic Bight as revealed by carbon isotopic ( $^{13}\text{C}$  and  $^{14}\text{C}$ ) signatures, *Limnol. Oceanogr.*, **41**, 1242–1252.
211. Santschi, P. H., Guo, L., Baskaran, M., Trumbore, S., Southon, J., Bianchi, T. S., Honneyman, B. and Cifuentes, L. (1995). Isotopic evidence for the contemporary origin of high-molecular-weight organic matter in oceanic environments, *Geochim. Cosmochim. Acta*, **59**, 625–631.
212. Hedges, J. I., Cowie, G. L., Richey, J. E., Quay, P. D., Benner, R., Strom, M. and Forsberg, B. R. (1994). Origins and processing of organic matter in the Amazon River as indicated by carbohydrates and amino acids, *Limnol. Oceanogr.*, **39**, 743–761.
213. Skoog, A. and Benner, R. (1997). Aldoses in various size fractions of marine organic matter: Implications for carbon cycling, *Limnol. Oceanogr.*, **42**, 1803–1813.
214. Mannino, A. and Harvey, H. R. (2000). Biochemical composition of particles and dissolved organic matter along an estuarine gradient: sources and implications for DOM reactivity, *Limnol. Oceanogr.*, **45**, 775–788.
215. Harvey, H. R. and Mannino, A. (2001). The chemical composition and cycling of particulate and macromolecular dissolved organic matter in temperate estuaries as revealed by molecular organic tracers, *Org. Geochem.*, **32**, 527–542.
216. Sharp, J. H. (1973). Size classes of organic carbon in seawater, *Limnol. Oceanogr.*, **18**, 441–447.
217. Hansell, D. A. and Carlson, C. A., eds (2002). *Biogeochemistry of Marine Dissolved Organic Matter*. Academic Press, San Diego, CA.
218. Sugimura, Y. and Suzuki, Y. (1988). A high-temperature catalytic oxidation method for the determination of non-volatile dissolved organic carbon in seawater by direct injection of a liquid sample, *Mar. Chem.*, **24**, 105–131.

219. Menzel, D. W. and Vaccaro, R. F. (1964). The measurement of dissolved and particulate carbon in seawater, *Limnol. Oceanogr.*, **9**, 138–142.
220. Hedges, J. I., Bergamaschi, B. A. and Benner, R. (1993). Comparative analysis of DOC and DON in natural waters, *Mar. Chem.*, **41**, 121–134.
221. Sharp, J. H., Benner, R., Bennett, L., Carlson, C. A., Dow, R. and Fitzwater, S. (1993). Re-evaluation of high temperature combustion and chemical oxidation measurements of dissolved organic carbon in seawater, *Limnol. Oceanogr.*, **38**, 1774–1782.
222. Sharp, J. H., Benner, R., Bennett, L., Carlson, C. A., Fitzwater, S. E., Peltzer, E. T. and Tupas, L. M. (1995). Analyses of dissolved organic carbon in seawater: the JGOFS EqPac methods comparison, *Mar. Chem.*, **48**, 91–108.
223. Ogawa, H. and Ogura, N. (1992). Comparison of two methods for measuring dissolved organic carbon in sea water, *Nature*, **356**, 696–698.
224. Tanoue, E. (1992). Vertical distribution of dissolved organic carbon in the North Pacific as determined by the high-temperature catalytic oxidation method, *Earth Planet. Sci. Lett.*, **111**, 201–216.
225. Cauwet, G. (1994). HTCO method for dissolved organic carbon analysis in seawater: influence of catalyst on blank estimation, *Mar. Chem.*, **47**, 55–64.
226. Williams, P. M. (1992). Measurement of dissolved organic carbon and nitrogen in natural waters, *Oceanography*, **5**, 107–116.
227. Benner, R. and Strom, M. (1993). A critical evaluation of the analytical blank associated with DOC measurements by high-temperature catalytic oxidation, *Mar. Chem.*, **41**, 153–160.
228. Suzuki, Y. (1993). On the measurement of DOC and DON in seawater. *Mar. Chem.*, **41**, 287–288.
229. Sharp, J. H. (1997). Marine dissolved organic carbon: are the older values correct?, *Mar. Chem.*, **56**, 265–277.
230. Sharp, J. H. (2002). Analytical methods for total DOM pools. In *Biogeochemistry of Marine Dissolved Organic Matter*, eds Hansell, D. A. and Carlson, C. A. Academic Press, San Diego, CA, pp. 35–90.
231. Ogawa, H. and Tanoue, E. (2003). Dissolved organic matter in oceanic waters, *J. Oceanogr.*, **59**, 129–147.
232. Santschi, P. H., Guo, L., Means, J. C. and Ravichandran, M. (1999). Natural organic matter binding of trace metals and trace organic contaminants in estuaries. In *Biogeochemistry of Gulf of Mexico Estuaries*, eds Bianchi, T. S., Pennock, J. R. and Twilley, R. R. John Wiley & Sons, Inc., New York, pp. 347–380.
233. Gustafsson, Ö., Widerlund, A., Andersson, P.S., Ingri, J., Roos, P. and Ledin, A. (2000). Colloid dynamics and transport of major elements through a boreal river – brackish bay mixing zone, *Mar. Chem.*, **71**, 1–21.
234. Olivie-Lauquet, G., Allard, T., Bertaux, J. and Muller, J.-P. (2000). Crystal chemistry of suspended matter in a tropical hydrosystem, Nyong basin (Cameroon, Africa), *Chem. Geol.*, **170**, 113–131.
235. Crerar, D. A., Means, J. L., Yuretich, R. F., Borcsik, M. P., Amster, J. L., Hastings, D. W., Knox, G. W., Lyon, K. E. and Quiett, R. F. (1981). Hydrogeochemistry of the New Jersey coastal plain. 2. Transport and deposition of iron, aluminum, dissolved organic matter, and selected trace elements in stream, ground- and estuary water, *Chem. Geol.*, **33**, 23–44.
236. Fox, L. E. (1988). The solubility of colloidal ferric hydroxide and its relevance to iron concentrations in river water, *Geochim. Cosmochim. Acta*, **52**, 771–777.
237. Benoit, G. and Rozan, T. F. (1999). The influence of size distribution on the particle concentration effect and trace metal partitioning in rivers, *Geochim. Cosmochim. Acta*, **63**, 113–127.

238. Olivié-Lauquet, G., Allard, T., Benedetti, M. and Muller, J.-P. (1999). Chemical distribution of trivalent iron in riverine material from a tropical ecosystem: a quantitative EPR study, *Water Res.*, **33**, 2726–2734.
239. Davison, W. (1993) Iron and manganese in lakes, *Earth Sci. Rev.*, **34**, 119–163.
240. De Vitre, R. and Davison, W. (1993). Manganese particles in freshwaters. In *Environmental Particles II*, eds Buffle, J. and van Leeuwen, H. P. Lewis, Boca Raton, FL, pp. 317–352.
241. Gimbert, L. J., Andrew, K. N., Haygarth, P. M. and Worsfold, P. J. (2003). Environmental applications of flow field-flow fractionation (FFF), *Trends Anal. Chem.*, **22**, 615–632.
242. Hussain, S., Mehta, M. S., Kaplan, J. I. and Dubin, P. L. (1991). Experimental evaluation of conflicting models for size exclusion chromatography, *Anal. Chem.*, **63**, 1132–1138.
243. Waggoner, D. B. and Christman, R. F. (1998). Molar masses and radii of humic substances measured by light scattering, *Acta Hydrochim. Hydrobiol.*, **26**, 191–195.
244. Waggoner, D. B., Christman, R. F., Cauchon, G. and Paulson, R. (1997). Molar mass and size of Suwannee River natural organic matter using multi-angle laser light scattering, *Environ. Sci. Technol.*, **31**, 937–941.
245. Schmitt, D., Müller, M. B. and Frimmel, F. H. (2000). Metal distribution in different size fractions of natural organic matter, *Acta Hydrochim. Hydrobiol.*, **28**, 400–410.
246. Beckett, R. and Hart, B. T. (1993). Use of field-flow fractionation techniques to characterize aquatic particles, colloids, and macromolecules. In *Environmental Particles*, eds Buffle, J. and van Leeuwen, H. P. IUPAC Series on Analytical and Physical Chemistry of Environmental Systems, Vol. 2. Lewis, Boca Raton, FL, pp. 165–205.
247. Lyklema, J. (1991). *Fundamentals of Interface and Colloid Science. Volume I: Fundamentals*. Academic Press, London.
248. Munk, P. (1989). *Introduction to Macromolecular Science*. John Wiley & Sons, Inc., New York.
249. Kerner, M., Hohenberg, H., Ertl, S., Reckermann, M. and Spitz, A. (2003). Self-organization of dissolved organic matter to micelle-like microparticles in river water, *Nature*, **422**, 150–154.
250. Terashima, M., Fukushima, M. and Tanaka, S. (2004). Influence of pH on the surface activity of humic acid: micelle-like aggregate formation and interfacial adsorption, *Colloids Surf. A*, **247**, 77–83.
251. Sutton, R. and Sposito, G. (2005). Molecular structure on soil humic substances: the new view, *Environ. Sci. Technol.*, **39**, 9009–9015.
252. Filella, M., Buffle, J. and Parthasarathy, N. (2005). Humic and fulvic compounds. In *Encyclopedia of Analytical Science*, 2nd edn, eds Worsfold, P. J., Townshend, A. and Poole, C. F., Vol. 4. Elsevier, Oxford, pp. 288–298.
253. Sholkovitz, E. R. and Copland, D. (1982). The chemistry of suspended matter in Esthwaite Water, a biologically productive lake with seasonally anoxic hypolimnion, *Geochim. Cosmochim. Acta*, **46**, 393–410.
254. McCarthy, J. F. and McKay, L. D. (2004). Colloid transport in the subsurface: past, present, and future challenges, *Vadose Zone J.*, **3**, 326–337.
255. Chanudet, V. and Filella, M. (2006). A non-perturbing scheme for the mineralogical characterisation of colloids in natural waters, *Environ. Sci. Technol.*, **40**, 5045–5051.
256. Stumm, W. and Morgan, J. J. (1996). *Aquatic Chemistry. Chemical Equilibria and Rates in Natural Waters*, 3rd edn. Wiley-Interscience, New York.
257. Davison, W. (1985). Conceptual models for transport at a redox boundary. In *Chemical Processes in Lakes*, ed. Stumm, W. Wiley-Interscience, New York, pp. 31–53.
258. Davison, W. and De Vitre, R. (1992) Iron particles in freshwater. In *Environmental Particles*, eds Buffle, J. and van Leeuwen, H. P. IUPAC Series on Analytical and Physical Chemistry of Environmental Systems, Vol. 1. Lewis, Boca Raton, FL, pp. 315–355.

259. Morse, J. W. (1986). The surface chemistry of calcium carbonate minerals in natural waters. An overview. *Mar. Chem.*, **20**, 91–112.
260. Wetzel, R. G. (2001). *Limnology: Lake and River Ecosystems*, 3rd edn. Academic Press, San Diego, CA.
261. Dodge J. D. (1973). *The Fine Structure of Algal Cells*. Academic Press, London.
262. Bertrand A. R. and Sor K. (1962). The effects of rainfall intensity on soil structure and migration of colloidal materials in soils, *Soil Sci. Soc. Am. Proc.*, **26**, 297–300.
263. Nightingale, H. I. and Bianchi, W. C. (1977). Ground-water turbidity resulting from artificial recharge, *Ground Water*, **15**, 146–152.
264. Kaplan, D. I., Bertsch, P. M., Adriano, D. C. and Miller, W. P. (1993). Soil-borne mobile colloids as influenced by water flow and organic carbon, *Environ. Sci. Technol.*, **27**, 1193–1200.
265. Ryan, J. N. and Gschwend, P. M. (1994). Effect of solution chemistry on clay colloid release from an iron oxide-coated aquifer sand, *Environ. Sci. Technol.*, **28**, 1717–1726.
266. Seaman, J. C., Bertsch, P. M. and Miller, W. P. (1995). Chemical controls on colloid generation and transport in a sandy aquifer, *Environ. Sci. Technol.*, **29**, 1808–1815.
267. Kaplan, D. I., Sumner M. E., Bertsch, P. M. and Adriano, D. C. (1996). Chemical conditions conductive to the release of mobile colloids from Ultisol profiles, *Soil Sci. Soc. Am. J.*, **60**, 269–274.
268. Roy, S. B. and Dzombak, D. A. (1996). Colloid release and transport processes in natural and model porous media, *Colloids Surf.*, **107**, 245–262.
269. Ryan, J. N. and Elimelech, M. (1996). Colloid mobilization and transport in groundwater, *Colloids Surf. A*, **107**, 1–56.
270. Suarez D. L., Rhoades J. D., Lavado R. and Grieve C. M. (1984). Effect of pH on saturated hydraulic conductivity and soil dispersion, *Soil Sci. Soc. Am. J.*, **48**, 50–55.
271. Chiang, S. C., Radcliffe, D. E., Miller, W. P. and Newman K. D. (1987). Hydraulic conductivity of three southeastern soils as affected by sodium, electrolyte concentration, and pH, *Soil Sci. Soc. Am. J.*, **51**, 1293–1299.
272. Seta A. K. and Karathanasis A. D. (1996). Water dispersible colloids and factors influencing their dispersibility from soil aggregates, *Geoderma*, **74**, 255–266.
273. Amrhein C., Mosher P. A. and Strong J. E. (1993). Colloid-assisted transport of trace metals in road side solid receiving deicing salts, *Soil Sci. Soc. Am. J.*, **57**, 1212–1217.
274. Gschwend, P. M., Backhus, D. A., MacFarlane, J. K. and Page, A. L. (1990). Mobilization of colloids in groundwater due to infiltration of water at a coal ash disposal site, *J. Contam. Hydrol.*, **6**, 307–320.
275. Degueldre, C., Baeyens, B., Goerlich, W., Riga, J., Verbist, J. and Stadelmann, P. (1989). Colloids in water from a subsurface fracture in granitic rock, Grimsel Test Site, Switzerland, *Geochim. Cosmochim. Acta*, **53**, 603–610.
276. Smith, P. A. and Degueldre C. (1993). Colloid-facilitated transport of radionuclides through fractured media, *J. Contam. Hydrol.*, **13**, 143–166.
277. Gschwend, P. M. and Reynolds, M. D. (1987). Monodispersed ferrous phosphate colloids in an anoxic groundwater plume, *J. Contam. Hydrol.*, **1**, 309–327.
278. Liang, L., McCarthy, J. F., Jolley, L. W., McNabb, J. A. and Mehlhorn, T. L. (1993). Iron dynamics: Transformation of Fe(II)/Fe(III) during injection of natural organic matter in a sandy aquifer, *Geochim. Cosmochim. Acta*, **57**, 1987–1999.
279. Giovanoli, R., Brütsch, R., Diem, D., Osman-Sigg, G. and Sigg, L. (1980). The composition of settling particles in Lake Zürich, *Schweiz. Z. Hydrol.*, **42**, 89–100.
280. Tipping, E., Woof, C. and Cooke, D. (1981). Iron oxide from a seasonally anoxic lake, *Geochim. Cosmochim. Acta*, **45**, 1411–1419.
281. Bishop, J. K. B. and Biscaye, P. E. (1982). Chemical characterization of individual particles from the nepheloid layer in the Atlantic Ocean. *Earth Planet. Sci. Lett.*, **58**, 265–275.

282. Tipping, E., Woof, C. and Ohnstad, M. (1982). Forms of iron in the oxygenated waters of Esthwaite Water, UK. *Hydrobiologia*, **92**, 383–393.
283. Davison, W. and Dickson, D. P. E. (1984). Mössbauer spectroscopic and chemical studies of particulate iron material from a seasonally anoxic lake, *Chem. Geol.*, **42**, 177–187.
284. Bernard, P. C., Van Grieken, R. E. and Eisma, D. (1986). Classification of estuarine particles using automated electron microprobe analysis and multivariate techniques, *Environ. Sci. Technol.*, **20**, 467–473.
285. Bernard, P. C., Van Grieken, R. E. and Brügmann, L. (1989). Geochemistry of suspended matter from the Baltic Sea. 1. Results of individual particle characterization by automated electron microprobe, *Mar. Chem.*, **26**, 155–177.
286. Buffle, J., De Vitre, R. R., Perret, D. and Leppard, G. G. (1989). Physico-chemical characteristics of a colloidal iron phosphate species formed at the oxic–anoxic interface of a eutrophic lake, *Geochim. Cosmochim. Acta*, **53**, 399–408.
287. Vilks, P., Miller, H. G. and Doern, D. C. (1991). Natural colloids and suspended particles in the Whiteshell Research Area, Manitoba, Canada, and their potential effect on radiocolloid formation, *Appl. Geochem.*, **6**, 565–574.
288. Newman, M. E., Elzerman, A. W. and Looney, B. B. (1993). Facilitated transport of selected metals in aquifer material packed columns, *J. Contam. Hydrol.*, **14**, 233–246.
289. Kaplan, D. I., Bertsch, P. M., Adriano, D. C. and Orlandini, K. A. (1994). Actinide association with groundwater colloids in a coastal plain aquifer, *Radiochim. Acta*, **66/67**, 181–187.
290. Van Put, A., Van Grieken, R., Wilken, R.-D. and Hudec, B. (1994). Geochemical characterization of suspended matter and sediment samples from the Elbe River by EPXMA, *Water Res.*, **28**, 643–655.
291. Turrero, M.-J., Gómez, P., Pérez del Villar, L., Moulin, V., Magonthier, M.-C. and Menager, M.-T. (1995). Relation between colloid composition and the environment of their formation: application to the El Berrocal site (Spain), *Appl. Geochem.*, **10**, 119–131.
292. Seaman, J. C., Bertsch, P. M. and Strom, R. N. (1997). Characterization of colloids mobilized from Southeastern Coastal Plain sediments, *Environ. Sci. Technol.*, **31**, 2787–2790.
293. Atteia, O., Perret, D., Adatte, T., Kozel, R. and Rossi, P. (1998). Characterization of natural colloids from a river and spring in a karstic basin, *Environ. Geol.*, **34**, 257–269.
294. Couture, C., Mavrocordatos, D., Atteia, O. and Perret, D. (1998). The genesis and transformation of organo-mineral colloids in a drained peatland area, *Phys. Chem. Earth*, **23**, 153–157.
295. Jambers, W., Dekov, V. and Van Grieken, R. (1999). Single particle characterisation of inorganic and organic North Sea suspension, *Mar. Chem.*, **67**, 17–32.
296. Mavrocordatos, D., Mondi-Couture, C., Atteia, O., Leppard, G. G. and Perret, D. (2000). Formation of a distinct class of Fe–Ca( $-C_{org}$ )-rich particles in a complex peat–karst system, *J. Hydrol.*, **237**, 234–247.
297. Hillier, S. (2001). Particulate composition and origin of suspended sediment in the R. Don, Aberdeenshire, UK, *Sci. Total Environ.*, **265**, 281–293.
298. Bunn, R. A., Magelky, R. D., Ryan, J. N. and Elimelech, M. (2002). Mobilization of natural colloids from an iron-oxide-coated sand aquifer: effect of pH and ionic strength, *Environ. Sci. Technol.*, **36**, 314–322.
299. Mavrocordatos, D. and Fortin, D. (2002). Quantitative characterization of biotic iron oxides by analytical electron microscopy, *Am. Mineral.*, **87**, 940–946.
300. Neretin, L. N., Pohl, C., Jost, G., Leipe, T. and Pollehne, F. (2003). Manganese cycling in the Gotland Deep, Baltic Sea, *Mar. Chem.*, **82**, 125–143.
301. Champ D. R., Young J. L., Robertson D. E. and Abel K. H. (1984). Chemical speciation of long-lived radionuclides in a shallow groundwater flow system, *Water Pollut. Res. J. Can.*, **19**, 35–54.

302. Lieser, K. H., Gleitsmann, B., Peschke, S. and Steinkopff, Th. (1986). Colloid formation and sorption of radionuclides in natural systems, *Radiochim. Acta*, **40**, 39–47.
303. Berner, R. A. and Holdren, G. R. (1979). Mechanism of feldspar weathering II. Observations of feldspars from soils, *Geochim. Cosmochim. Acta*, **43**, 1173–1186.
304. Aagaard, P. and Helgeson, H. C. (1982). Thermodynamic and kinetic constraints on reaction rates among minerals and aqueous solutions; I. Theoretical considerations, *Am. J. Sci.*, **282**, 237–285.
305. Wieland, E., Wehrli, B. and Stumm, W. (1988). The coordination chemistry of weathering: III. A generalization on the dissolution rates of minerals, *Geochim. Cosmochim. Acta*, **52**, 1969–1981.
306. Blum, A. E. and Stillings, L. L. (1995). Feldspar dissolution kinetics, In *Chemical Weathering Rates of Silicate Minerals*, eds White, A. F. and Brantley, S. L. Reviews in Mineralogy, **31**, pp. 291–351.
307. Helgeson, H. C., Murphy, W. M. and Aagaard, P. (1984). Thermodynamic and kinetic constraints on reaction rates among minerals and aqueous solutions. II. Rate constants, effective surface area, and the hydrolysis of feldspar, *Geochim. Cosmochim. Acta*, **48**, 2405–2432.
308. Kaplan, D. I., Bertsch, P. M. and Adriano, D. C. (1997). Mineralogical and physicochemical differences between mobile and nonmobile colloidal phases in reconstructed pedons, *Soil Sci. Soc. Am. J.*, **61**, 641–649.
309. van Olphen, H. (1991). *Clay Colloid Chemistry. For Clay Technologists, Geologists and Soil Scientists*, 2nd edn. Krieger, Malabar, FL.
310. Lagaly, G. and Ziesmer, S. (2003). Colloid chemistry of clay minerals: the coagulation of montmorillonite dispersions, *Adv Colloid Interface Sci.*, **100–102**, 105–128.
311. Heil, D. and Sposito, G. (1993). Organic matter role in illitic soil colloids flocculation: I. Counter ions and pH, *Soil Sci. Soc. Am. J.*, **57**, 1241–1246.
312. Secor, R. B. and Radke, C. J. (1985). Spillover of the diffuse double layer on montmorillonite particles, *J. Colloid Interface Sci.*, **103**, 237–244.
313. Chang, F.-R. C. and Sposito, G. (1996). The electrical double layer of a disk-shaped clay mineral particle: effects of electrolyte properties and surface charge density, *J. Colloid Interface Sci.*, **178**, 555–564.
314. Mukhopadhyay, B. and Walther, J. V. (2001). Acid–base chemistry of albite surfaces in aqueous solutions at standard temperature and pressure, *Chem. Geol.*, **174**, 415–443.
315. Aldahan, A., Haiping, Y. and Possnert, G. (1999) Distribution of beryllium between solution and minerals (biotite and albite) under atmospheric conditions and variable pH. *Chem. Geol.*, **156**, 209–229.
316. Liu, W., Sun, Z., Forsling, W., Du, Q. and Tang, H. (1999). A comparative study of surface acid–base characteristics of natural illites from different origins, *J. Colloid. Interface Sci.*, **219**, 48–61.
317. Arnold, T., Zorn, T., Zänker, H., Bernhard, G. and Nitsche, H. (2001). Sorption behavior of U(VI) on phyllite: experiments and modeling, *J. Contam. Hydrol.*, **47**, 219–231.
318. Sondi, I. and Pravdić, V. (1996). Electrokinetics of natural and mechanically modified ripidolite and beidellite clays, *J. Colloid Interface Sci.*, **181**, 463–469.
319. Morris, H. D., Shelton, B. and Ellis, P. D. (1990).  $^{27}\text{Al}$  NMR spectroscopy of iron-bearing montmorillonite clays. *J. Phys. Chem.*, **94**, 3121–3129.
320. Schulthess, C. P. and Sparks, D. L. (1989). Competitive ion exchange behavior on oxides, *Soil Sci. Soc. Am. J.*, **53**, 366–373.
321. Schulthess, C. P. and Huang, C. P. (1990). Adsorption of heavy metals by silicon and aluminum oxide surfaces on clay minerals, *Soil Sci. Soc. Am. J.*, **54**, 679–688.
322. Mortimer, C. H. (1941) The exchange of dissolved substances between mud and water in lakes: I and II, *J. Ecol.*, **29**, 280–329.

323. Mortimer, C. H. (1942). The exchange of dissolved substances between mud and water in lakes: III and IV, *J. Ecol.*, **30**, 147–201.
324. Stumm, W. and Sulzberger, B. (1992). The cycling of iron in natural environments: Considerations based on laboratory studies of heterogeneous redox processes, *Geochim. Cosmochim. Acta*, **56**, 3233–3257.
325. Turner, D. R. and Hunter, K. A., eds (2001). *The Biogeochemistry of Iron in Seawater*. John Wiley & Sons, Ltd, Chichester.
326. Fortin, D. and Langley, S. (2005). Formation and occurrence of biogenic iron-rich minerals, *Earth Sci. Rev.*, **72**, 1–19.
327. Martin, J. H. and Fitzwater, S. E. (1988). Iron deficiency limits phytoplankton growth in the north-east Pacific subarctic, *Nature*, **331**, 341–343.
328. Martin, J. H., Coale, K. H., Johnson, K. S., Fitzwater, S. E., Gordon, R. M., Tanner, S. J., Hunter, C. N., Elrod, V. A., Nowicki, J. L., Coley, T. L., Barber, R. T., Lindley, S., Watson, A. J., Van Scoy, K., Law, C. S., Liddicoat, M. I., Ling, R., Stanton, T., Stockel, J., Collins, C., Anderson, A., Bidigare, R., Ondrusek, M., Latasa, M., Millero, F. J., Lee, K., Yao, W., Zhang, J. Z., Friederich, G., Sakamoto, C., Chavez, F., Buck, K., Kolber, Z., Greene, R., Falkowski, P., Chisholm, S. W., Hoge, F., Swift, R., Yungel, J., Turner, S., Nightingale, P., Hatton, A., Liss, P. and Tindale, N. W. (1994). Testing the iron hypothesis in ecosystems of the equatorial Pacific Ocean, *Nature*, **371**, 123–129.
329. Coale, K. H., Johnson, K. S., Fitzwater, S. E., Gordon, R. M., Tanner, S., Chavez, F. P., Ferioli, L., Sakamoto, C., Rogers, P., Millero, F., Steinberg, P., Nightingale, P., Cooper, D., Cochlan, W. P., Landry, M. R., Constantinou, J., Rollwagen, G., Trasvina, A. and Kudela, R. (1996). A massive phytoplankton bloom induced by an ecosystem-scale iron fertilization experiment in the equatorial Pacific Ocean, *Nature*, **383**, 495–501.
330. Behrenfeld, M. J. and Kolber, Z. S. (1999). Widespread iron limitation of phytoplankton in the South Pacific Ocean, *Science*, **283**, 840–843.
331. Boyd, P. W., Watson, A. J., Law, C. S., Abraham, E. R., Trull, T., Murdoch, R., Bakker, D. C. E., Bowie, A. R., Buesseler, K. O., Chang, H., Charette, M., Croot, P., Downing, K., Frew, R., Gall, M., Hadfield, M., Hall, J., Harvey, M., Jameson, G., LaRoche, J., Liddicoat, M., Ling, R., Maldonado, M. T., McKay, R. M., Nodder, S., Pickmere, S., Pridmore, R., Rintoul, S., Safi, K., Sutton, P., Strzepek, R., Tanneberger, K., Turner, S., Waite, A. and Zeldis J. (2000). A mesoscale phytoplankton bloom in the polar Southern Ocean stimulated by iron fertilization, *Nature*, **407**, 695–702.
332. Kuma, K., Nishioka, J. and Matsunaga, K. (1996). Controls on iron(III) hydroxide in seawater: The influence of pH and natural organic chelators, *Limnol. Oceanogr.*, **41**, 396–407.
333. Johnson, K. S., Gordon, R. M. and Coale, K. H. (1997). What controls dissolved iron concentrations in the world ocean?, *Mar. Chem.*, **57**, 137–161.
334. Nakabayashi, S., Kusakabe, M., Kuma, K. and Kudo, I. (2001). Vertical distributions of iron(III) hydroxide solubility and dissolved iron in the northwestern North Pacific Ocean, *Geophys. Res. Lett.*, **28**, 4611–4614.
335. Takata, H., Kuma, K., Iwade, S., Yamajyo, Y., Yamaguchi, A., Takagi, S., Sakaoka, K., Yamashita, Y., Tanoue, E., Midorikawa, T., Kimura, K. and Nishioka, J. (2004). Spatial variability of iron in the surface water of the northwestern North Pacific Ocean, *Mar. Chem.*, **86**, 139–157.
336. Macrellis, H. M., Trick, C. G., Rue, E. L., Smith, G. and Bruland, K. W. (2001). Collection and detection of natural iron-binding ligands from seawater, *Mar. Chem.*, **76**, 175–187.
337. McCormak, P., Worsfold, P. J. and Gledhill, M. (2003). Separation and detection of siderophores produced by marine bacterioplankton using high-performance liquid

- chromatography with electrospray ionization mass spectrometry. *Anal. Chem.*, **75**, 2647–2652.
338. Murphy, D. M., Garbarino, J. R., Taylor, H. E., Hart, B. T. and Beckett, R. (1993). Determination of size and element composition distributions of complex colloids by sedimentation field-flow fractionation–inductively coupled plasma mass spectrometry, *J. Chromatogr.*, **642**, 459–467.
339. Tessier, A., Carignan, R., Dubrueil, B. and Rapin, F. (1989). Partitioning of zinc between the water column and the oxic sediments in lakes, *Geochim. Cosmochim. Acta*, **53**, 1511–1522.
340. Ryan, J. N., Elimelech, M., Ard, R. A., Harvey R. W. and Johnson P. R. (1999). Bacteriophage PRD1 and silica colloid transport and recovery in an iron oxide-coated sand aquifer, *Environ. Sci. Technol.*, **33**, 63–73.
341. Schwertmann, U., Fischer, W. R. and Taylor R. M. (1974). New aspects of iron oxide formation in soils, *Trans. 10th Int. Congr. Soil Sci.*, **6**, 237–249.
342. Matijević, E. and Scheiner, P. (1978). Ferric hydrous oxide sols. III. Preparation of uniform particles by hydrolysis of Fe(III)-chloride, -nitrate, and – perchlorate solutions, *J. Colloid Interface Sci.*, **63**, 509–523.
343. Tebo, B. M., Ghiorse, W. C., van Waasbergen, L. G., Siering, P. L. and Caspi, R. (1997). Bacterially mediated mineral formation: Insights into manganese(II) oxidation from molecular genetic and biochemical studies, In *Geomicrobiology: Interactions between Microbes and Minerals*, eds Banfield, J. F. and Nealson, K. H. Reviews in Mineralogy 35, Mineralogical Society of America, Washington, DC, pp. 225–266.
344. Nealson, K. H. (1999). The manganese-oxidizing bacteria. In *The Prokaryotes: An Evolving Electronic Resource for the Microbiological Community*, 3rd edn, ed. Dworkin, M. Springer-Verlag, New York, Release 3.g.
345. Ehrlich, H. L. (2002). *Geomicrobiology*, 4th edn. Marcel Dekker, New York.
346. Hug, S. J., Johnson, A., Friedl, G., Lichtensteiger, T., Belevi, H. and Sturm, M. (1997). Characterization of environmental solids and surfaces, *Chimia*, **51**, 884–892.
347. Rozanov, A. G., Neretin, L. N. and Volkov, I. I. (1998). Redox nepheloid layer (RNL) of the Black Sea: its location, composition and origin. In *Ecosystem Modeling as a Management Tool for the Black Sea*, Vol. 1, eds Ivanov, L. I. and Oguz, T. Kluwer, Dordrecht, pp. 77–91.
348. Liemann, C.-P., Taillefert, M., Perret, D. and Gaillard, J.-F. (1997). Association of cobalt and manganese in aquatic systems: Chemical and microscopic evidence, *Geochim. Cosmochim. Acta*, **61**, 1437–1446.
349. Dubinina, C. E. (1970). Untersuchungen über die Morphologie von *Metallogenium* und die Beziehungen zu Mycoplasma, *Z. Allg. Mikrobiol.*, **10**, 309–320.
350. Ghiorse, W. C. (1984). Biology of iron- and manganese-deposition bacteria, *Ann. Rev. Microbiol.*, **38**, 515–550.
351. Hedges, J. I., Eglinton, G., Hatcher, P. G., Kirchman, D. L., Arnosti, C., Derenne, S., Ever-shed, R. P., Kögel-Knabner, I., De Leeuw, J. W., Littke, R., Michaelis, W. and Rullkötter, J. (2000). The molecularly-uncharacterized component of nonliving organic matter in natural environments, *Org. Geochem.*, **31**, 945–958.
352. Wakeham, S. G., Lee, C. and Hedges, J. I. (2000). Fluxes of major biochemicals in the equatorial Pacific Ocean. In *Dynamics and Characterization of Marine Organic Matter*, eds Handa, N., Tanoue, E. and Hama, T. Terra Scientific Publishing Company, Tokyo/Kluwer, Dordrecht, pp. 117–140.
353. Carlson, C. A. (2002). Production and removal processes. In *Biogeochemistry of Marine Dissolved Organic Matter*, eds Hansell, D. A. and Carlson, C. A. Academic Press, San Diego, CA, pp. 91–151.

354. Williams, P. M., and Druffel, E. R. M. (1987). Radiocarbon in dissolved organic matter in the central North Pacific Ocean, *Nature*, **330**, 246–248.
355. Bauer, J. E., Williams, P. M. and Druffel, E. R. M. (1992).  $^{14}\text{C}$  activity of dissolved organic carbon fractions in the north-central Pacific and Sargasso Sea, *Nature*, **357**, 667–670.
356. Fuhrman, J. A., and Ferguson, R. L. (1986). Nanomolar concentrations and rapid turnover of dissolved free amino acids in seawater: agreement between chemical and microbiological measurements, *Mar. Ecol. Prog. Ser.*, **33**, 237–242.
357. Keil, R. G. and Kirchman, D. L. (1991). Contribution of dissolved free amino acids and ammonium to the nitrogen requirements of heterotrophic bacterioplankton, *Mar. Ecol. Prog. Ser.*, **73**, 1–10.
358. Rich, J., Gosselin, E. M., Sherr, M., Sherr, B. and Kirchman, D. L. (1997). High bacterial production, uptake and concentrations of dissolved organic matter in the Central Arctic Ocean, *Deep Sea Res. II*, **44**, 1645–1663.
359. Ogura, N. (1972). Rate and extent of decomposition of dissolved organic matter in the surface water, *Mar. Biol.*, **13**, 89–93.
360. Kirchman, D. L., Lancelet, C., Fasham, M., Legendre, L., Radach, G. and Scott, M. (1993). Dissolved organic matter in biogeochemical models of the ocean. In *Towards a Model of Ocean Biogeochemical Processes*, eds Evans, G. T. and Fasham, M. J. R. Springer-Verlag, Berlin, pp. 209–225.
361. Carlson, C. A. and Ducklow, H. W. (1996). Growth of bacterioplankton and consumption of dissolved organic carbon in the Sargasso Sea, *Aquat. Microb. Ecol.*, **10**, 69–85.
362. Cherrier, J., Bauer, J. E. and Druffel, E. R. M. (1996). Utilization and turnover of labile dissolved organic matter by bacterial heterotrophs in eastern North Pacific surface waters, *Mar. Ecol. Prog. Ser.*, **139**, 267–279.
363. Thurman, E. M. and Malcolm, R. L. (1981). Preparative isolation of aquatic humic substances, *Environ. Sci. Technol.*, **15**, 463–466.
364. Swift, R. S. (1996). Organic matter characterization. In *Methods of Soil Analysis. Part 3. Chemical Methods*, eds Sparks, D. L., et al. Soil Science Society of America, Madison, WI, pp. 1011–1070.
365. van Heemst, J. D. H., Megens, L., Hatcher, P. G., de Leeuw, J. W. (2000). Nature, origin and average age of estuarine ultrafiltered dissolved organic matter as determined by molecular and carbon isotope characterization, *Org. Geochem.*, **31**, 847–857.
366. Hedges, J. I., Clark, W. A., Quay, P. D., Richey, J. E., Devol, A. H. and Santos, U. d. M. (1986). Compositions and fluxes of particulate organic material in the Amazon River, *Limnol. Oceanogr.*, **31**, 717–738.
367. Yunker, M. B., Macdonald, R. W., Veltkamp, D. J. and Cretney, W. J. (1995). Terrestrial and marine biomarkers in a seasonally ice-covered Arctic estuary – integration of multivariate and biomarker approaches, *Mar. Chem.*, **49**, 1–50.
368. Budge, S. M. and Parrish, C. C. (1998). Lipid biogeochemistry of plankton, settling matter and sediments in Trinity Bay, Newfoundland. II. Fatty Acids *Org. Geochem.*, **29**, 1547–1559.
369. Fahl, K. and Stein, R. (1999). Biomarkers as organic-carbon-source and environmental indicators in the Late Quaternary Arctic Ocean: problems and perspectives, *Mar. Chem.*, **63**, 293–309.
370. Goñi, M. A., Yunker, M. B., Macdonald, R. W. and Eglinton, T. I. (2000). Distribution and sources of organic biomarkers in arctic sediments from the Mackenzie River and Beaufort Shelf, *Mar. Chem.*, **71**, 23–51.
371. Benner, R. and Opsahl, S. (2001). Molecular indicators of the sources and transformations of dissolved organic matter in the Mississippi River plume, *Org. Geochem.*, **32**, 597–611.
372. Saliot, A., Derieux, S., Sadouni, N., Bouloubassi, I., Filliaux, J., Dagaut, J., Momzikoff, A., Gondry, G., Guillou, C., Breas, O., Cauwet, G. and Deliat, G. (2002). Winter and

- spring characterization of particulate and dissolved organic matter in the Danube–Black Sea mixing zone, *Estuarine Coastal Shelf Sci.*, **54**, 355–367.
373. Saliot, A., Parrish, C. C., Sadouni, N., Bouloubassi, I., Filliaux, J. and Cauwet, G. (2002). Transport and fate of Danube Delta terrestrial organic matter in the Northwest Black Sea mixing zone, *Mar. Chem.*, **79**, 243–259.
374. Wang, X.-C., Chen, R. F. and Gardner, G. B. (2004). Sources and transport of dissolved and particulate organic carbon in the Mississippi River estuary and adjacent coastal waters of the northern Gulf of Mexico, *Mar. Chem.*, **89**, 241–256.
375. Zumstein, J. and Buffle, J. (1989). Circulation of pedogenic and aquagenic organic matter in an eutrophic lake, *Water Res.*, **23**, 229–239.
376. Chin, Y.-P., Aiken, G. and O'Loughlin, E. (1994). Molecular weight, polydispersity, and spectroscopic properties of aquatic humic substances, *Environ. Sci. Technol.*, **28**, 1853–1858.
377. Coble, P. G. (1996) Characterization of marine and terrestrial DOM in seawater using excitation–emission matrix spectroscopy, *Mar. Chem.*, **51**, 325–346.
378. Krasner, S. W., Croué, J.-P., Buffle, J. and Perdue, E. M. (1996). Three approaches for characterizing NOM, *J. Am. Water Works Assoc.*, **88**, 66–79.
379. Peuravuori, J. and Pihlaja, K. (1997). Molecular size distribution and spectroscopic properties of aquatic humic substances, *Anal. Chim. Acta*, **337**, 133–149.
380. Abbt-Braun, G., Lankes, U. and Frimmel, F. H. (2004). Structural characterization of aquatic humic substances – The need for a multiple method approach, *Aquat. Sci.*, **66**, 151–170.
381. Orem, W. H. and Hatcher, P. G. (1987). Solid state  $^{13}\text{C}$  NMR studies of dissolved organic matter in pore waters from different depositional environments, *Org. Geochem.*, **11**, 73–82.
382. Benner, R., Pakulski, J. D., McCarthy, M., Hedges, J. I. and Hatcher, P. G. (1992). Bulk chemical characteristics of dissolved organic matter in the ocean, *Science*, **255**, 1561–1564.
383. Engelhardt, E. and Bianchi, T. S. (2001). Sources and composition of high-molecular-weight dissolved organic carbon in a southern Louisiana tidal stream (Bayou Trepagnier), *Limnol. Oceanogr.*, **46**, 917–926.
384. Thurman, E. M. (1985). *Organic Geochemistry of Natural Waters*. Martinus Nijhoff/Dr W. Junk, Dordrecht.
385. Leenheer, J. A. (1981) Comprehensive approach to preparative isolation and fractionation of dissolved organic carbon from natural waters and wastewaters, *Environ. Sci. Technol.*, **15** 578–587.
386. G. R. Aiken (1985), Isolation and concentration techniques for aquatic humic substances in: G. R. Aiken, D. M. McKnight, R. L. Wershaw, P. McCarthy, eds, *Humic Substances in Soil, Sediment and Water. Geochemistry, Isolation and Characterization*. Wiley-Interscience, New York, pp. 363–385.
387. Ertel, J. R., Hedges, J. I., Devol, A. H., Richey, J. E. and Ribeiro, M. N. G. (1986). Dissolved humic substances of the Amazon River system, *Limnol. Oceanogr.*, **31**, 739–754.
388. Aiken, G. and Leenheer, J. (1993). Isolation and chemical characterization of dissolved and colloidal organic matter, *Chem. Ecol.*, **8**, 135–151.
389. Fogg, G. E. and Westlake, D. F. (1955). The importance of extracellular products of algae in freshwater, *Verh. Int. Verein. Limnol.*, **12**, 219–232.
390. Fogg, G. E. (1971). Extracellular products of algae in freshwater, *Arch. Hydrobiol. Beih. Ergeb. Limnol.*, **5**, 1–25.
391. Myklestad, S. (1977). Production of carbohydrates by marine planktonic diatoms. II. Influence of the  $N/P$  ratio in the growth medium on the assimilation ratios growth rate, and production of cellular and extracellular carbohydrates by *Chaetoceros affinis* var. *willei*

- (Gran) Hustedt and *Skeletonema costatum* (Grev.) Cleve, *J. Exp. Mar. Biol. Ecol.*, **29**, 161–179.
392. Fogg, G. E. (1983). The ecological significance of extracellular products of phytoplankton photosynthesis, *Bot. Mar.*, **26**, 3–14.
393. Myklestad, S., Holm-Hansen, O., Vårum, K. M. and Volcani, B. E. (1989). Rate of release of extracellular amino acids and carbohydrates from the marine diatom *Chaetoceros affinis*, *J. Plankton Res.*, **11**, 763–774.
394. Hellebust, J. A. (1974). Extracellular products. In *Algal Physiology and Biochemistry*, ed. Stewart, W. D. P. Blackwell, Oxford, pp. 838–863.
395. Wangersky, P. J. (1978). Production of dissolved organic matter. In *Marine Ecology, Vol. IV. Dynamics*, ed. Kinne, O. Wiley, Chichester, pp. 115–220.
396. Ignitiades, L. and Fogg, G. E. (1973). Studies on the factors affecting the release of organic matter by *Skeletonema costatum* (Greville) Cleve in culture, *J. Mar. Biol. Assoc., UK*, **53**, 937–956.
397. Bratbak, G. (1987). Carbon flow in an experimental microbial ecosystem, *Mar. Ecol. Prog. Ser.*, **36**, 267–276.
398. Hellebust, J. A. (1965). Excretion of some organic compounds by marine phytoplankton, *Limnol. Oceanogr.*, **10**, 192–206.
399. Mague T. H., Friberg E., Hughes D. J. and Morris I. (1980). Extracellular release of carbon by marine phytoplankton; a physiological approach, *Limnol. Oceanogr.*, **25**, 262–279.
400. Myklestad, S. and Haug, A. (1972). Production of carbohydrates by the marine diatom *Chaetoceros affinis* var. *willei* (Gran) Hustedt. I. Effect of the concentration of nutrients in the culture medium, *J. Exp. Mar. Biol. Ecol.*, **9**, 125–136.
401. Myklestad, S. (1974). Production of carbohydrates by marine planktonic diatoms. I. Comparison of nine different species in culture, *J. Exp. Mar. Biol. Ecol.*, **15**, 261–274.
402. Ittekot, V., Brockmann, U., Michaelis, W. and Degens, E. T. (1981). Dissolved free and combined carbohydrates during a phytoplankton bloom in the Northern North Sea, *Mar. Ecol. Prog. Ser.*, **4**, 299–305.
403. Ittekot, V. (1982). Variations of dissolved organic matter during a plankton bloom: qualitative aspects, based on sugar and amino acid analyses, *Mar. Chem.*, **11**, 143–158.
404. Borch, N. H. and Kirchman, D. L. (1997). Concentration and composition of dissolved combined neutral sugars (polysaccharides) in seawater determined by HPLC-PAD, *Mar. Chem.*, **57**, 85–95.
405. Herndl, G. J. and Peduzzi, P. (1988). The ecology of amorphous aggregations (marine snow) in the northern Adriatic Sea: I. General considerations, *Mar. Ecol.*, **9**, 79–90.
406. Herndl, G. J. (1992). Marine snow in the Northern Adriatic Sea: possible causes and consequences for a shallow ecosystem, *Mar. Microb. Food Web*, **6**, 149–172.
407. Vollenweider, R. A., Rinaldi, A. and Montanari, G. (1992). Eutrophication, structure and dynamics of a marine coastal system: results of ten-year monitoring along the Emilie-Romagna coast (Northwest Adriatic Sea). In *Marine Coastal Eutrophication*, eds Marchetti, R., Wollenweider, R. A., and Viviani, R. Elsevier, Amsterdam, pp. 63–106.
408. Alldredge, A. L. and Crocker, K. M. (1995). Why do sinking mucilage aggregates accumulate in the water column?, *Sci. Total Environ.*, **165**, 15–22.
409. Penna, N., Capellacci, S., Ricci, F. and Kovac, N. (2003). Characterization of carbohydrates in mucilage samples from the northern Adriatic Sea, *Anal. Bioanal. Chem.*, **376**, 436–439.
410. Boalch, G. T. and Harbour, D. S. (1977). Unusual diatom off the coast of south-west England and its effect on fishing, *Nature*, **269**, 687–688.
411. Lancelot, C. (1995). The mucilage phenomenon in the continental coastal waters of the North Sea, *Sci. Total Environ.*, **165**, 83–102.
412. Heissenberger, A., Leppard, G. G. and Heendl, G. J. (1996). Ultrastructure of marine snow. II. Microbiological considerations, *Mar. Ecol. Prog. Ser.*, **135**, 299–308.

413. Klok, J., Cox, H. C., Baas, M., Schuyl, P. J. W., de Leeuw, J. W. and Schenck, P. A. (1984). Carbohydrates in recent marine sediments – I. Origin and significance of deoxy- and *O*-methyl-monosaccharides, *Org. Geochem.*, **7**, 73–84.
414. Lee, C. and Henrichs, S. M. (1993). How the nature of dissolved organic matter might affect the analysis of dissolved organic carbon, *Mar. Chem.*, **41**, 105–120.
415. Lindberg, B. (1981). Structural studies of polysaccharides, *Chem. Soc. Rev.*, **10**, 409–434.
416. Aspinall, G. O., ed. (1982). *The Polysaccharides*. Vol. 1. Academic Press, New York.
417. Kerhervé, P., Charrière, B. and Gadel F. (1995). Determination of marine polysaccharides by high-pH anion-exchange chromatography with pulsed amperometric detection, *J. Chromatogr. A*, **718**, 283–289.
418. McCarthy, M., Hedges, J. and Benner, R. (1996). Major biochemical composition of dissolved high molecular weight organic matter in seawater, *Mar. Chem.*, **55**, 281–297.
419. Boon, J. J., Klap, V. A. and Eglinton, T. I. (1998). Molecular characterization of microgram amounts of oceanic colloidal organic matter by direct temperature-resolved ammonia chemical ionization mass spectrometry, *Org. Geochem.*, **29**, 1051–1061.
420. Kirchman, D. L., Meon, B., Ducklow, H. W., Carlson, C. A., Hansell, D. A. and Steward, G. F. (2001). Glucose fluxes and concentrations of dissolved combined neutral sugars (polysaccharides) in the Ross Sea and Polar Front Zone, Antarctica, *Deep-Sea Res. II*, **48**, 4179–4197.
421. Kaiser, K. and Benner, R. (2000). Determination of amino sugars in environmental samples with high salt content by high-performance anion-exchange chromatography and pulsed amperometric detection, *Anal. Chem.*, **72**, 2566–2572.
422. Mopper, K., Zhou, J., Ramana, K. S., Passow, U., Dam, H. G., and Drapeau, D. T. (1995). The role of surface-active carbohydrates in the flocculation of a diatom bloom in a mesocosm, *Deep-Sea Res. II*, **42**, 47–73.
423. Bergamaschi, B. A., Walters, J. S. and Hedges, J. I. (1999). Distribution of uronic acids and *O*-methyl sugars in sinking and sedimentary particles in two coastal marine environments, *Geochim. Cosmochim. Acta*, **63**, 413–425.
424. Hung, C.-C. and Santschi, P. H. (2001). Spectrophotometric determination of total uronic acids in seawater using cation-exchange separation and pre-concentration by lyophilization, *Anal. Chim. Acta*, **427**, 111–117.
425. Hung, C. C., Tang, D., Warnken, K. W. and Santschi, P. H. (2001). Distributions of carbohydrates, including uronic acids, in estuarine waters of Galveston Bay, *Mar. Chem.*, **73**, 305–318.
426. Hung, C.-C., Guo, L., Santschi, P. H., Alvarado-Quiroz, N. and Haye, J. M. (2003). Distributions of carbohydrate species in the Gulf of Mexico, *Mar. Chem.*, **81**, 119–135.
427. Hung, C. C., Warnken, K. W. and Santschi, P. H. (2005). A seasonal survey of carbohydrates and uronic acids in the Trinity River, Texas, *Org. Geochem.*, **36**, 463–474.
428. Mopper, K. (1977). Sugars and uronic acids in sediment and water from the Black Sea and North Sea with emphasis on analytical techniques, *Mar. Chem.*, **5**, 585–603.
429. Cowie, G. L. and Hedges, J. I. (1984). Determination of neutral sugars in plankton, sediments, and wood by capillary chromatography of equilibrated isometric mixtures, *Anal. Chem.*, **56**, 497–504.
430. Wicks, R. J., Moran, M. A., Pittman, L. J. and Hodson, R. E. (1991). Carbohydrate signatures of aquatic macrophytes and their dissolved degradation products as determined by a sensitive high-performance ion chromatography method, *Appl. Environ. Microbiol.*, **57**, 3135–3143.
431. Mopper, K., Schultz, C. A., Chevolot, L., Germaine, C., Revuelta, R. and Dawson, R. (1992). Determination of sugars in unconcentrated seawater and other natural waters by

- liquid chromatography and pulsed amperometric detection, *Environ. Sci. Technol.*, **26**, 133–138.
432. Jørgensen, N. O. G. and Jensen, R. E. (1994). Microbial fluxes of free monosaccharides and total carbohydrates in freshwaters determined by PAD–HPLC, *FEMS Microb. Ecol.*, **14**, 79–94.
433. Gremm, T. J. and Kaplan, L. A. 1997 Dissolved carbohydrates in streamwater determined by HPLC and pulsed amperometric detection, *Limnol. Oceanogr.*, **42**, 385–393.
434. Johnson, K. M. and Sieburth, J. McN. (1977). Dissolved carbohydrates in seawater. I. A precise spectrophotometric analysis for monosaccharides, *Mar. Chem.*, **5**, 1–13.
435. Johnson, K. M., Burney, C. M. and Sieburth, J. McN. (1981). Doubling the production and precision of the MBTH spectrophotometric assay for dissolved carbohydrates in seawater, *Mar. Chem.*, **10**, 467–473.
436. Pakulski, J. D. and Benner, R. (1992). An improved method for the hydrolysis and MTBH analysis of dissolved and particulate carbohydrates in seawater, *Mar. Chem.*, **40**, 143–160.
437. Myklestad, S. M., Skånoy, E. and Hestmann, S. (1997). A sensitive and rapid method for analysis of dissolved mono- and polysaccharides in seawater, *Mar. Chem.*, **56**, 279–286.
438. Hama, T. and Handa, N. (1980). Molecular weight distribution and characterization of dissolved organic matter from lake waters, *Arch. Hydrobiol.*, **90**, 106–120.
439. Hama, T. and Handa, N. (1987). Pattern of organic matter production by natural phytoplankton population in a eutrophic lake. 2. Extracellular products, *Arch. Hydrobiol.*, **109**, 227–243.
440. Parfitt, R. L. and Greenland, D. J. (1970). Adsorption of polysaccharides by montmorillonite, *Soil Sci. Soc. Am. Proc.*, **34**, 862–865.
441. Mavrocordatos, D., Lienemann, C.-P. and Perret, D. (1994). Energy filtered transmission electron microscopy for the physico-chemical characterization of aquatic submicron colloids, *Mikrochim. Acta*, **117**, 39–47.
442. Wilkinson, K. J., Balnois, E., Leppard, G. G. and Buffle, J. (1999). Characteristic features of the major components of freshwater colloidal organic matter revealed by transmission electron and atomic force microscopy, *Colloids Surf. A*, **155**, 287–310.
443. Massalski, A. and Leppard, G. G. (1979). Morphological examination of fibrillar colloids associated with algae and bacteria in lakes, *J. Fish Res. Bd. Can.*, **36**, 922–938.
444. Burnison, B. K. and Leppard, G. G. (1983). Isolation of colloidal fibrils from lake water by physical separation techniques, *Can. J. Fish. Aquat. Sci.*, **40**, 373–381.
445. Leppard, G. G. and Burnison, B. K. (1983). Bioavailability, trace element associations with colloids and an emerging interest in colloidal organic fibrils. In *Trace Element Speciation in Surface Waters and its Ecological Implications*, ed. Leppard, G. G. Plenum Press, New York, pp. 105–122.
446. Leppard, G. G., Massalski, A. and Lean, D. R. S. (1977). Electron opaque microscopic fibrils in lakes: their demonstration, their biological derivation and their potential significance in the redistribution of cations, *Protoplasma*, **92**, 289–309.
447. Santschi, P. H., Balnois, E., Wilkinson, K. J., Zhang, J. and Buffle, J. (1998). Fibrillar polysaccharides in marine macromolecular organic matter as imaged by atomic force microscopy and transmission electron microscope, *Limnol. Oceanogr.*, **43**, 896–908.
448. Leppard, G. G., Burnison, B. K. and Buffle, J. (1990). Transmission electron microscopy of the natural organic matter of surface waters, *Anal. Chim. Acta*, **232**, 107–121.
449. Perret, D., Leppard, G. G., Müller, M., Belzile, N., De Vitre, R. and Buffle, J. (1991). Electron microscopy of aquatic colloids: non-perturbing preparation of specimens in the field, *Water Res.*, **25**, 1333–1343.
450. Burnison, B. K. (1978). High molecular weight polysaccharides isolated from lake water, *Verh. Internat. Verein. Limnol.*, **20**, 353–355.

451. Strycek, T., Acreman, J., Kerry, A., Leppard, G. G., Nermut, M. V. and Kushner, D. J. (1992). Extracellular fibril production by freshwater algae and cyanobacteria, *Microb. Ecol.*, **23**, 53–74.
452. Brown, D. L., Massalski, A. and Leppard G. G. (1976). Fine structure of excystment of the quadriflagellate alga *Polytomella agilis*, *Protoplasma*, **90**, 155–171.
453. Leppard G. G. and Ramamoorthy S. (1975). The aggregation of wheat rhizoplane fibrils and the accumulation of soil-bound cations, *Can. J. Bot.*, **53**, 1729–1735.
454. Olness, A. E. and Clapp, C. E. (1975). Influence of polysaccharide structure on dextran adsorption by montmorillonite, *Soil Biol. Biochem.*, **7**, 113–118.
455. Leppard, G. G., West, M. M., Flannigan, D. T., Carson, J. and Lott, J. N. A. (1997). A classification scheme for marine organic colloids in the Adriatic Sea: colloid speciation by transmission electron microscopy, *Can. J. Fish. Aquat. Sci.*, **54**, 2334–2349.
456. Perret, D., Lienemann, C.-P. and Mavrocordatos, D. (1995). EELS-ESI identification of heterogeneous suspensions of aquatic microparticles, *Microsc. Microanal. Microstruct.*, **6**, 41–51.
457. Liss, S. N., Droppo, I. G., Flannigan, D. T. and Leppard, G. G. (1996). Floc architecture in wastewater and natural riverine systems, *Environ. Sci. Technol.*, **30**, 680–686.
458. Droppo, I. G., Flannigan, D. T., Leppard, G. G., Jaskot, C. and Liss, S. N. (1996). Floc stabilization for multiple microscopic techniques, *Appl. Environ. Microbiol.*, **62**, 3508–3515.
459. Lienemann, C.-P., Mavrocordatos, D. and Perret, D. (1997). Enhanced visualization of polysaccharides from aqueous suspensions, *Mikrochim. Acta*, **126**, 123–129.
460. Leppard, G. G. (1997). Colloidal organic fibrils of acid polysaccharides in surface waters: electron-optical characteristics, activities and chemical estimates of abundance, *Colloids Surf. A*, **120**, 1–15.
461. Alldredge, A. L., Passow, U. and Logan, B. E. (1993). The abundance and significance of a class of large, transparent organic particles in the ocean, *Deep-Sea Res. I*, **40**, 1131–1140.
462. Passow, U. and Alldredge, A. L. (1995). A dye-binding assay for the spectrophotometric measurement of transparent exopolymer particles (TEP), *Limnol. Oceanogr.*, **40**, 1326–1335.
463. Passow, U., Alldredge, A. L. and Logan, B. E. (1994). The role of particulate carbohydrate exudates in the flocculation of diatom blooms, *Deep-Sea Res. I*, **41**, 335–357.
464. Arruda Fatibello, S. H. S., Henriques Vieira, A. A. and Fatibello-Filho, O. (2004). A rapid spectrophotometric method for the determination of transparent exopolymer particles (TEP) in freshwater, *Talanta*, **62**, 81–85.
465. Passow, U. and Alldredge, A. L. (1995). Aggregation of a diatom bloom in a mesocosm: the role of transparent exopolymer particles (TEP), *Deep-Sea Res. II*, **42**, 99–109.
466. Passow, U. and Wassmann, P. (1994). On the trophic fate of *Phaeocystis pouchetti* (Hariot): IV. The formation of marine snow by *P. pouchetti*, *Mar. Ecol. Prog. Ser.*, **104**, 153–161.
467. Passow, U. (2002). Production of TEP by phyto- and bacterioplankton, *Mar. Ecol. Prog. Ser.*, **236**, 1–12.
468. Engel, A. (2000). The role of transparent exopolymer particles (TEP) in the increase in apparent particles stickiness ( $\alpha$ ) during the decline of a diatom bloom, *J. Plankton Res.*, **22**, 485–497.
469. Zhou, J., Mopper, K. and Passow, U. (1998). The role of surface-active carbohydrates in the formation of transparent exopolymer particles by bubble adsorption of seawater. *Limnol. Oceanogr.*, **43**, 1860–1871.
470. Passow, U. (2000). Formation of transparent exopolymer particles, TEP, from dissolved precursor material, *Mar. Ecol. Prog. Ser.*, **192**, 1–11.

471. Worm, J. and Søndergaard, M. (1998). Dynamics of heterotrophic bacteria attached to *Microcystis* spp. (Cyanobacteria), *Aquat. Microbiol. Ecol.*, **14**, 19–28.
472. Passow, U., Shipe, R. F., Murray, A., Pak, D. K., Brzezinski, M. A. and Alldredge, A. L. (2001). The origin of transparent exopolymer particles (TEP) and their role in the sedimentation of particulate matter, *Cont. Shelf Res.*, **21**, 327–346.
473. Bigg, E. K., Leck, C. and Tranvik, L. (2004). Particulates of the surface microlayer of open water in the central Arctic Ocean in summer, *Mar. Chem.*, **91**, 131–141.
474. Worm, J. and Søndergaard, M. (1998). Alcian Blue-stained particles in a eutrophic lake, *J. Plankton Res.*, **20**, 179–186.
475. Grossart, H.-P., Simon, M. and Logan, B. E. (1997). Formation of macroscopic organic aggregates (lake snow) in a large lake: the significance of transparent exopolymer particles, phytoplankton, and zooplankton, *Limnol. Oceanogr.*, **42**, 1651–1659.
476. Carrias, J.-F., Serre, J.-P., Sime-Ngando, T. and Amblard, C. (2002). Distribution, size, and bacterial colonization of pico- and nano-detrital organic particles (DOP) in two lakes of different trophic status, *Limnol. Oceanogr.*, **47**, 1202–1209.
477. Myneni, S. C. B., Brown, J. T., Martinez, G. A. and Meyer-Ilse, W. (1999). Imaging of humic substance macromolecular structures in water and soils, *Science*, **286**, 1335–1337.
478. Schäfer, T., Claret, F., Bauer, A., Griffault, L., Ferrage, E. and Lanson, B. (2003). Natural organic matter (NOM)–clay association and impact on Callovo-Oxfordian clay stability in high alkaline solution: spectromicroscopic evidence, *J. Phys. IV*, **104**, 413–416.
479. Geckeis, H., Schäfer, T., Hauser, W., Rabung, Th., Missana, T., Degueldre, C., Möri, A., Eikenberg, J., Fierz, Th. and Alexander W. R. (2004). Results of the colloid and radionuclide retention experiments (CRR) at the Grimsel Test Site (GTS), Switzerland – impact of reaction kinetics and speciation on radionuclide migration, *Radiochim. Acta*, **92**, 765–774.
480. Schumacher, M., Christl, I., Scheinost, A. C., Jacobsen, C. and Kretzschmar, R. (2005). Chemical heterogeneity of organic soil colloids investigated by scanning transmission X-ray microscopy and C-1s NEXAFS microspectroscopy, *Environ. Sci. Technol.*, **39**, 9094–9100.
481. Murphy, E. M., Zachara, J. M. and Smith, S. C. (1990). Influence of mineral-bound humic substances on sorption of hydrophobic organic compounds, *Environ. Sci. Technol.*, **24**, 1507–1516.
482. Verrall, K. E., Warwick, P., Fairhurst, A. J. (1999). Application of the Schulze-Hardy rule to haematite and haematite/humate colloid stability, *Colloids Surf. A*, **150**, 261–273.
483. Wang, L., Chin, Y.-P. and Traina, S. J. (1997). Adsorption of (poly)maleic acid and an aquatic fulvic acid by goethite, *Geochim. Cosmochim. Acta*, **61**, 5313–5324.
484. Zhou, J. L., Rowland, S., Fauzi, R., Mantoura, C. and Braven, J. (1994). The formation of humic coatings on mineral particles under simulated estuarine conditions – a mechanistic study, *Water Res.*, **28**, 571–579.
485. Parfitt, R. L., Fraser, A. R. and Farmer, V. C. (1977). Adsorption on hydrous oxides. III. Fulvic and humic acid on goethite, gibbsite and imogolite, *J. Soil Sci.*, **28**, 289–296.
486. Filius, J. D., Hiemstra, T. and van Riemsdijk, W. H. (1997). Adsorption of small weak organic acid on goethite: modeling of mechanisms. *J. Colloid Interface Sci.*, **195**, 368–380.
487. Gu, B., Schmitt, J., Chen, L., Liang, J. F. and McCarthy, J. F. (1994). Adsorption and desorption of natural organic matter on iron oxide: mechanisms and models, *Environ. Sci. Technol.*, **28**, 38–46.
488. Gu, B., Schmitt, J., Chen, Z., Liang, L. and McCarthy, J. F. (1995). Adsorption and desorption of different organic matter fractions on iron oxide, *Geochim. Cosmochim. Acta*, **59**, 219–229.

489. Au, K.-K., Penisson, A. C., Yang, S. and O'Melia, C. R. (1999). Natural organic matter at oxide/water interfaces: complexation and conformation, *Geochim. Cosmochim. Acta*, **63**, 2903–2917.
490. Day, G. McD., Hart, B. T., McKelvie, I. D. and Beckett, R. (1994). Adsorption of natural organic matter onto goethite, *Colloids Surf. A*, **89**, 1–13.
491. Chen, K. L., Mylon, S. E. and Elimelech, M. (2006). Aggregation kinetics of alginate-coated hematite nanoparticles in monovalent and divalent electrolytes, *Environ. Sci. Technol.*, **40**, 1516–1523.
492. Fairhurst, A. J., Warwick, P. and Richardson, S. (1995) The influence of humic acid on the adsorption of europium onto inorganic colloids as a function of pH, *Colloids Surf. A*, **99**, 187–199.
493. Vermeer, A. W. P., van Riemsdijk, W. H. and Koopal, L. K. (1998). Adsorption of humic acid to mineral particles. 1. Specific and electrostatic interactions, *Langmuir*, **14**, 2810–2819.
494. Schmitt, J., Gu, B., Schorer, M., Flemming, H.-C. and McCarthy, J. J. (1996). The role of natural organic matter as a coating on iron oxide and quartz, *Arch. Hydrobiol. Spec. Issues Adv. Limnol.*, **47**, 315–322.
495. Vermöhlen, K., Lewandowski, H., Narres, H.-D. and Schwuger, M. J. (2000). Adsorption of polyelectrolytes onto oxides – the influence of ionic strength, molar mass, and  $\text{Ca}^{2+}$  ions, *Colloids Surf. A*, **163**, 45–53.
496. Chorover, J. and Amistadi, M. K. (2001). Reaction of forest floor organic matter at goethite, birnessite and smectite surfaces, *Geochim. Cosmochim. Acta*, **65**, 95–109.
497. Meier, M., Namjesnik-Dejanovic, K., Maurice, P. A., Chin, Y.-P. and Aiken, G. R. (1999). Fractionation of aquatic natural matter upon sorption to goethite and kaolinite, *Chem. Geol.*, **157**, 275–284.
498. Filius, J. D., Lumsdon, D. G., Meeussen, J. C. L., Hiemstra, T. and van Riemsdijk, W. H. (2000). Adsorption of fulvic acid on goethite, *Geochim. Cosmochim. Acta*, **64**, 51–60.
499. Filius, J. D., Meeussen, J. C. L., Lumsdon, D. G., Hiemstra, T. and van Riemsdijk, W. H. (2003). Modeling the binding of fulvic acid by goethite: the speciation of adsorbed FA molecules, *Geochim. Cosmochim. Acta*, **67**, 1463–1474.
500. Edwards, M., Benjamin, M. M. and Ryan, J. N. (1996). Role of organic matter acidity in sorption of natural organic matter (NOM) to oxide surfaces, *Colloids Surf. A*, **107**, 297–307.
501. Jones, F., Cölfen, H. and Antonietti, M. (2000) Iron oxyhydroxide colloids stabilized with polysaccharide, *Colloid Polym. Sci.*, **278**, 491–501.
502. Mosley, L. M., Hunter, K. A. and Ducker, W. A. (2003). Forces between colloid particles in natural waters, *Environ. Sci. Technol.*, **37**, 3303–3308.
503. Sander, S., Mosley, L. M. and Hunter, K. A. (2004). Investigation of interparticle forces in natural waters: effects of adsorbed humic acids on iron oxide and alumina surface properties. *Environ. Sci. Technol.*, **38**, 4791–4796.
504. Žutić, V. and Tomaić, J. (1988). On the formation of organic coatings on marine particles: interactions of organic matter at hydrous alumina/seawater interfaces, *Mar. Chem.*, **23**, 51–67.
505. Schlautman, M. A. and Morgan, J. J. (1994). Adsorption of aquatic humic substances on colloidal-size aluminum oxide particles: influence of solution chemistry, *Geochim. Cosmochim. Acta*, **58**, 4293–4303.
506. Varadachari, C., Chattopadhyay, T. and Ghosh, K. (1997). Complexation of humic substances with oxides of iron and aluminium, *Soil Sci.*, **162**, 28–34.

507. Tombácz, E., Filipcsei, G., Szekeres, M. And Gingl, Z. (1999). Particle aggregation in complex aquatic systems, *Colloids Surf. A*, **151**, 233–244.
508. Davis, J. A. (1982). Adsorption of natural dissolved organic matter at the oxide/water interface, *Geochim. Cosmochim. Acta*, **46**, 2381–2393.
509. Davis, J. A. and Gloor, R. (1981). Adsorption of dissolved organics in lake water by aluminium oxide: effect of molecular weight, *Environ. Sci. Technol.*, **15**, 1223–1229.
510. Chandranth, M. S., Honeyman, B. D. and Amy, G. L. (1996). Modeling the interactions between ozone, natural organic matter, and particles in water treatment, *Colloids Surf. A*, **107**, 321–342.
511. Ochs, M., Cosovic, B. and Stumm, W. (1994). Coordinative and hydrophobic interaction of humic substances with hydrophylic  $\text{Al}_2\text{O}_3$  and hydrophobic mercury surfaces, *Geochim. Cosmochim. Acta*, **58**, 639–650.
512. Schulthess, C. P. and Hunag, C. P. (1991). Humic and fulvic acid adsorption by silicon and aluminum oxide surfaces on clay minerals, *Soil Sci. Soc. Am. J.*, **55**, 34–42.
513. Amy, G. L., Collins, M. R., Kuo, C. J., Chowdhury, Z. K. and Bales, R. C. (1989). Effects of humic substances on particle growth, and removal during coagulation. In *Aquatic Humic Substances. Influence on Fate and Treatment of Pollutants*, eds. Suffet, I. and MacCarthy, P. American Chemical Society, Washington, DC, pp. 443–471.
514. Olness, A. E. and Clapp, C. E. (1973). Occurrence and collapsed and expanded crystals in montmorillonite–dextran complexes, *Clays Clay Miner.*, **21**, 289–293.
515. Sen, B. C. (1960). Studies on adsorption of humic acids on H-clays and the role of metal ions in humic metal adsorption, *J. Indian Chem. Soc.*, **37**, 793–797.
516. Sen, B. C. (1964). Studies on the effect of different constituents of soil humic acid in the formation of clay–humus complexes, *J. Indian Chem. Soc.*, **41**, 145–149.
517. Schnitzer, M. and Kodama, H. (1966). Montmorillonite: effect of pH on its adsorption of a soil humic compound, *Science*, **153**, 70–71.
518. Rashid, M. A., Buckley, D. E. and Robertson, K. R. (1972). Interactions of a marine humic acid with clay minerals and a natural sediment, *Geoderma*, **8**, 11–27.
519. Orlov, D. S., Pivovarova, I. A. and Gorbunov, N. I. (1973). Interaction of humic substances with minerals and the nature of their bonds – a review. *Agrokhimiya*, **9**, 140–153.
520. Preston, M. R. and Riley, J. P. (1982). The interactions of humic compounds with electrolytes and three clay minerals under simulated estuarine conditions, *Estuar. Coastal Shelf Sci.*, **14**, 567–576.
521. Theng, B. K. (1982). Clay–polymer interactions: summary and perspectives, *Clays Clay Mineral.*, 1–10.
522. Murphy, E. M., Zachara, J. M. and Smith, S. C. (1990). Influence of mineral-bound humic substances on sorption of hydrophobic organic compounds, *Environ. Sci. Technol.*, **24**, 1507–1516.
523. Tombácz, E., Filipcsei, G., Szekeres, M. and Gingl, Z. (1999). Particle aggregation in complex aquatic systems, *Colloids Surf. A*, **151**, 233–244.
524. Baham, J. and Sposito, G. (1994). Adsorption of dissolved organic carbon extracted from sewage sludge on montmorillonite and kaolinite in the presence of metal ions, *J. Environ. Qual.*, **23**, 147–153.
525. Kretzschmar, R., Hesterberg, D. and Sticher, H. (1997). Effects of adsorbed humic acid on surface charge and flocculation of kaolinite, *Soil Sci. Soc. Am. J.*, **61**, 101–108.
526. Tombácz, E., Szekeres, M., Baranyi, L. and Michéli, E. (1998). Surface modification of clay minerals by organic polyions, *Colloids Surf. A*, **141**, 379–384.

527. Specht, C. H., Kumke, M. U. and Frimmel, F. H. (2000). Characterization of NOM adsorption to clay minerals by size exclusion chromatography, *Water Res.*, **34**, 4063–4069.
528. Feng, X., Simpson, A. J. and Simpson, M. J. (2005) Chemical and mineralogical controls on humic acid sorption to clay mineral surfaces. *Org. Geochem.*, **36**, 1533–1566.
529. Heidmann, I., Christl, I. and Kretzschmar, R. (2005) Sorption of Cu and Pb to kaolinite–fulvic acid colloids: assessment of sorbent interactions. *Geochim. Cosmochim. Acta*, **69**, 1675–1686.
530. Nayak, D. C., Varadachari, C. and Ghosh, K. (1990). Influence of organic acidic functional groups of humic substances in complexation with clay minerals, *Soil Sci.*, **149**, 268–271.
531. Du, Q., Sun, Z., Forsling, W. and Tang, H. (1999). Complexations in illite–fulvic acid–Cu<sup>2+</sup> systems. *Water Res.*, **33**, 693–706.
532. Mavrocordatos, D., Lienemann, C.-P. and Perret, D. (1994). Energy filtered transmission electron microscopy for the physico-chemical characterization of aquatic submicron colloids. *Mikrochim. Acta*, **117**, 39–47.
533. Jardine, P. M., Weber, N. L. and McCarthy, J. F. (1989). Mechanisms of dissolved organic carbon adsorption on soil, *Soil Sci. Soc. Am. J.*, **53**, 1378–1385.
534. Dunnivant, F. M., Jardine, P. M., Taylor, D. L. and McCarthy, J. F. (1992). Transport of naturally occurring dissolved organic carbon in laboratory columns containing aquifer material, *Soil Sci. Soc. Am. J.*, **56**, 437–443.
535. Amirbahman, A. and Olson, T. M. (1993). Transport of humic matter-coated hematite in packed beds, *Environ. Sci. Technol.*, **27**, 2807–2813.
536. Amirbahman, A. and Olson, T. M. (1995). Deposition kinetics of humic-coated hematite in porous media in the presence of Ca<sup>2+</sup>, *Colloids Surf. A*, **99**, 1–10.
537. Kretzschmar, R. and Sticher, H. (1997). Transport of humic-coated iron oxide colloids in a sandy soil: influence of Ca<sup>2+</sup> and trace metals, *Environ. Sci. Technol.*, **31**, 3497–3504.
538. Kretzschmar, R., Barmettler, K., Grolimund, D., Yan, Y. D., Borkovec, M. and Sticher, H. (1997). Experimental determination of colloid deposition rates and collision efficiencies in natural porous media, *Water Resour. Res.*, **33**, 1129–1137.
539. Guo, M. and Chorover, J. (2003). Transport and fractionation of dissolved organic matter in soil columns, *Soil Sci.*, **168**, 108–118.
540. Varadachari, C., Mondal, A. H., Nayak, D. C. and Ghosh, K. (1994). Clay–humus complexation: effect of pH and the nature of bonding, *Soil Biol. Biochem.*, **26**, 1145–1149.
541. Greenland, D. J. (1971). Interactions between humic and fulvic acids and clays, *Soil Sci.*, **111**, 34–41.
542. Sposito G. (1984). *The Surface Chemistry of Soils*. Oxford University Press, New York.
543. Huang, P. M. and Schnitzer, M., eds (1986). *Interactions of Soil Minerals with Natural Organics and Microbes*. Soil Science Society of America, Madison, WI.
544. Liang, L. and Morgan, J. J. (1990). Chemical aspects of iron oxide coagulation in water: Laboratory studies and implications for natural systems, *Aquat. Sci.*, **52**, 32–55.
545. Stumm, W., Kummert, R. and Sigg, L. (1980) A ligand exchange model for the adsorption of inorganic and organic ligands as hydrous oxide interfaces. *Croat. Chem. Acta*, **53**, 291–312.
546. Schnitzer, M. and Hanson, E. H. (1970). Adsorption on hydrous oxides, *Soil Sci.*, **109**, 333–340.
547. Kummert, R. and Stumm, W. (1980). The surface complexation of organic acids on hydrous  $\gamma$ -alumina. *J. Colloid Interface Sci.*, **75**, 373–85.
548. Mortland, M. M. (1986). Mechanisms of adsorption of nonhumic organic species by clays. In *Interactions of Soil Minerals with Natural Organics and Microbes*, eds Huang, P. M. and Schnitzer, M. Soil Science Society of America, Madison, WI, pp. 59–76.

549. Tombácz, E., Libor, Z., Illés, E., Majzik, A. and Klumpp, E. (2004). The role of reactive surface sites and complexation by humic acids in the interaction of clay mineral and iron oxide particles, *Org. Geochem.*, **35**, 257–267.
550. Wattel-Koekkoek, E. J. W., van Genuchten, P. P. L., Buurman, P. and van Lagen, B. (2001). Amount and composition of clay-associated soil organic matter in a range of kaolinitic and smectitic soils, *Geoderma*, **99**, 27–49.
551. Assemi, S., Hartley, P. G., Scales, P. J. and Beckett, R. (2004). Investigation of adsorbed humic substances using atomic force microscopy, *Colloids Surf. A*, **248**, 17–23.
552. Lead, J. R., Muirhead, D. and Gibson, C. T. (2005). Characterization of freshwater natural aquatic colloids by atomic force microscopy (AFM), *Environ. Sci. Technol.*, **39**, 6930–6936.
553. McKnight, D. M., Bencala, K. E., Zellweger, G. W., Aiken, G. R., Feder, G. L. and Thorn, K. A. (1992). Sorption of dissolved organic carbon by hydrous aluminum and iron oxides occurring at the confluence of Deer Creek with the Snake River, Summit County, Colorado, *Environ. Sci. Technol.*, **26**, 1388–1396.
554. Gu, B., Melhorn, T. L., Liang, L. and McCarthy, J. F. (1996). Competitive adsorption, displacement, and transport of organic matter on iron oxide: I. Competitive adsorption, *Geochim. Cosmochim. Acta*, **60**, 1943–1950.
555. Gu, B., Melhorn, T. L., Liang, L. and McCarthy, J. F. (1996). Competitive adsorption, displacement, and transport of organic matter on iron oxide: II. Displacement and transport, *Geochim. Cosmochim. Acta*, **60**, 2977–2992.
556. Kaiser, K., Guggenberger, G., Haumaier, L. and Zech, W. (1997). Dissolved organic matter sorption on sub soils and minerals studied by  $^{13}\text{C}$ -NMR and DRIFT spectroscopy, *Eur. J. Soil Sci.*, **48**, 301–310.
557. McCarthy, J. F. (2001). Subsurface transport of dissolved humic substances and associated contaminants. In *Humic Substances and Chemical Contaminants*, eds Clapp, C. E., Hayes, M. H. B., Senesi, N. Bloom, P. R. and Jardine, P. M. Soil Science Society of America, Madison, WI, Chapter 21, pp. 429–448.
558. Korshin, G. V., Benjamin, M. M. and Sletten, R. S. (1997). Adsorption of natural organic matter (NOM) on iron oxide: effects on NOM composition and formation of organo-halide compounds during chlorination, *Water Res.*, **31**, 1643–1650.
559. Collins, M. J., Bishop, A. N. and Farrimond, P. (1995). Sorption by mineral surfaces: Rebirth of the classical condensation pathway for kerogen formation? *Geochim. Cosmochim. Acta*, **59**, 2387–2391.
560. Kaiser, K. and Zech, W. (1997). Competitive sorption of dissolved organic matter fractions to soils and related mineral phases, *Soil Sci. Soci. Am. J.*, **61**, 64–69.
561. Wang, K. and Xing, B. (2005) Structural and sorption characteristics of adsorbed humic acid on clay minerals. *J. Environ. Qual.*, **34**, 342–349.
562. O'Melia, C. R. and Tiller, C. L. (1993) Physicochemical aggregation and deposition in aquatic environments. In *Environmental Particles*, eds Buffe, J. and van Leeuwen, H. P. IUPAC Series on Analytical and Physical Chemistry of Environmental Systems, Vol. 2. Lewis, Boca Raton, FL, pp. 353–386.
563. O'Melia, C. R. (1980). Aquasols: the behaviour of small particles in aquatic systems, *Environ. Sci. Technol.*, **14**, 1052–1060.
564. Kodama, H. and Schnitzer, M. (1973). Dissolution of chlorite minerals by fulvic acid, *Can. J. Soil Sci.*, **53**, 240–243.
565. Kodama, H., Schnitzer, M. and Jaakkimainen, M. (1983). Chlorite and biotite weathering by fulvic acid solutions in closed and open systems. *Can. J. Soil Sci.*, **63**, 619–629.
566. Swartz, C. H. and Gschwend, P. M. (1998). Mechanisms controlling release of colloids to groundwater in a Southeastern Coastal Plain aquifer sand, *Environ. Sci. Technol.*, **32**, 1779–1785.

567. Tani, H., Nishioka, J., Kuma, K., Takata, H., Yamashita, Y., Tanoue, E. and Midorikawa, T. (2003). Iron(III) hydroxide solubility and humic-type fluorescent organic matter in the deep water column of the Okhotsk Sea and the northwestern North Pacific Ocean, *Deep-Sea Res. I*, **50**, 1063–1078.
568. McDowell, W. H. and Likens, G. E. (1988). Origin, composition, and flux of dissolved organic carbon in the Hubbard Brook valley, *Ecol. Monogr.*, **58**, 177–195.
569. Kaiser, K., Guggenberger, G. and Zech, W. (1996). Sorption of DOM and DOM fractions to forest soils, *Geoderma*, **74**, 281–304.
570. McLaughlin, J. W., Lewin, J. C., Reed, D. D., Trettin, C. C., Jurgensen, M. F. and Gale, M. R. (1994). Soil factors related to dissolved organic carbon concentrations in a black spruce swamp, Michigan. *Soil Sci.*, **158**, 454–464.
571. Hagedorn, F., Kaiser, K., Feyen, H. and Schleppi, P. (2000). Effects of redox conditions and flow processes on the mobility of dissolved organic carbon and nitrogen in a forest soil. *J. Environ. Qual.*, **29**, 288–297.
572. Haider, K. (1992). Problems related to the humification processes in soils of temperate climates. In *Soil Biochemistry*, Vol. 7, eds Stotzky, G. and Bollag, J.-M. Marcel Dekker, New York, pp. 55–94.
573. Kaiser, K. and Guggenberger, G. (2000). The role of DOM sorption to mineral surfaces in the preservation of organic matter in soils, *Org. Geochem.*, **31**, 711–725.
574. Wattel-Koekkoek, E. J. W. and Buurman, P. (2004). Mean residence time of kaolinite and smectite-bound organic matter in Mozambiquan soils, *Soil Sci. Soc. Am. J.*, **68**, 154–161.
575. McDowell, W. H. M. (1985) Kinetics and mechanisms of dissolved organic carbon retention in a headwater stream, *Biogeochemistry*, **1**, 329–352.
576. McKnight, D. M. and Bencala, K. E. (1990). The chemistry of iron, aluminum and dissolved organic material in three acidic metal-enriched, mountain stream processes *Water Resour. Res.*, **26**, 3087–3100.
577. Keil, R. G., Montluçon, D. B., Prahl, F. G. and Hedges, J. I. (1994). Sorptive preservation of labile organic matter in marine sediments, *Nature*, **370**, 549–552.
578. Serra, T., Colomer, J., Cristina, X. P., Vila, X., Arellano, J. B. and Casamitjana, X. (2001). Evaluation of laser *in situ* scattering instrument for measuring concentration of phytoplankton, purple sulfur bacteria, and suspended inorganic sediments in lakes, *J. Environ. Eng.*, **127**, 1023–1030.
579. Damuth, J. (1981). Population density and body size in mammals, *Nature*, **290**, 699–700.
580. Enquist, B. J., Brown, J. H. and West, G. B. (1998). Allometric scaling of plant energetics and population density, *Nature*, **395**, 163–165.
581. Wassmann, P., Vernet, B. G., Mitchell, B. G. and Rey, F. (1990). Mass sedimentation of *Phaeocystis pouchetii* in the Barents Sea during spring, *Mar. Ecol. Prog. Ser.*, **66**, 183–195.
582. Riebesell, U. (1991). Particle aggregation during a diatom bloom. I. Physical aspects, *Mar. Ecol. Prog. Ser.*, **69**, 273–280.
583. Riebesell, U. (1991). Particle aggregation during a diatom bloom. II. Biological aspects, *Mar. Ecol. Prog. Ser.*, **69**, 281–291.
584. Jackson, G. A. and Lochmann, S. (1993). Modeling coagulation of algae in marine ecosystems. In *Environmental Particles*, eds Buffal, J. and van Leeuwen, H. P. IUPAC Series on Analytical and Physical Chemistry of Environmental Systems, Vol. 2. Lewis, Boca Raton, FL, pp. 387–414.
585. Hobbie, J. E., Daley, R. J. and Jasper, S. (1977). Use of Nuclepore filters for counting bacteria by fluorescence microscopy, *Appl. Environ. Microbiol.*, **33**, 1225–1228.

586. Azam, F. (1998). Microbial control of oceanic carbon flux: the plot thickens, *Science*, **280**, 694–696.
587. Azam, F. and Worden, A. Z. (2004). Microbes, molecules, and marine ecosystems, *Science*, **303**, 1622–1624.
588. Harden, V. P. and Harris, J. O. (1953). The isoelectric point of bacterial cells, *J. Bacteriol.*, **65**, 198–202.
589. Simoni, S. F., Harms, H., Bosma, T. N. P. and Zehnder, A. J. (1998). Population heterogeneity affects transport of bacteria through sand columns at low flow rates, *Environ. Sci. Technol.*, **32**, 2100–2105.
590. Hermansson, M. (1999). The DLVO theory in microbial adhesion, *Colloids Surf. B*, **14**, 105–119.
591. Frank, B. P. and Belfort, G. (1997). Intermolecular forces between extracellular polysaccharides measured using the atomic force microscope, *Langmuir*, **13**, 6234–6240.
592. Camesano, T. A. and Logan, B. E. (2000). Probing bacterial electrosteric interactions using atomic force microscopy, *Environ. Sci. Technol.*, **34**, 3354–3362.
593. Bitton, G. (1975). Adsorption of viruses onto surfaces in soil and water, *Water Res.*, **9**, 473–484.
594. Fuhrman, J. A. (1999). Marine viruses and their biogeochemical and ecological effects, *Nature*, **399**, 541–548.
595. Sharp, D. G. (1949). Enumeration of virus particles by electron micrography, *Proc. Soc. Exp. Biol. Med.*, **70**, 54–59.
596. Hara, S., Terauchi, K. and Koike, I. (1991). Abundance of viruses in marine waters: assessment by epifluorescence and transmission electron microscopy, *Appl. Environ. Microbiol.*, **57**, 2731–2734.
597. Hennes, K. P. and Suttle, C. A. (1995). Direct counts of viruses in natural waters and laboratory cultures by epifluorescence microscopy, *Limnol. Oceanogr.*, **40**, 1050–1055.
598. Weinbauer, M. G. and Suttle, C. A. (1997). Comparison of epifluorescence and transmission electron microscopy for counting viruses in natural marine waters, *Aquat. Microb. Ecol.*, **13**, 225–232.
599. Sieburth, J. M., Johnson, P. W. and Hargraves, P. E. (1988). Ultrastructure and ecology of *Aureococcus anophagefferens* gen. et sp. nov. (Chrysophyceae): The dominant picoplankter during a bloom in Narragansett Bay, Rhode Island, summer 1985, *J. Phycol.*, **24**, 416–425.
600. Bergh, Ø., Børshøj, K. Y., Bratbak, G. and Heldal, M. (1989). High abundance of viruses found in aquatic environments, *Nature*, **340**, 467–468.
601. Proctor, L. M. and Fuhrman, J. A. (1990). Viral mortality of marine bacteria and cyanobacteria, *Nature*, **343**, 60–62.
602. Proctor, L. M. (1997). Advances in the study of marine viruses, *Microsc. Res. Technol.*, **37**, 136–161.
603. Floyd, R. and Sharp, D. G. (1978). Viral aggregation: quantitation and kinetics of the aggregation of poliovirus and reovirus, *Appl. Environ. Microbiol.*, **35**, 1079–1083.
604. Floyd, R. and Sharp, D. G. (1978). Viral aggregation: effects of salts on the aggregation of poliovirus and reovirus at low pH, *Appl. Environ. Microbiol.*, **35**, 1084–1094.
605. Floyd, R. (1979). Viral aggregation: mixed suspensions of poliovirus and reovirus, *Appl. Environ. Microbiol.*, **38**, 980–986.
606. Grant, S. B. (1994). Virus coagulation in aqueous environments, *Environ. Sci. Technol.*, **28**, 928–933.
607. Wommack, K. E. and Colwell, R. R. (2000). Viriplankton: viruses in aquatic ecosystems, *Microbiol. Mol. Biol. Rev.*, **64**, 69–114.

608. Dowd, S. E., Pillai, S. D., Wang, S. and Corapcioglu, M. Y. (1998). Delineating the specific influence of virus isoelectric point and size on virus adsorption and transport through sandy soils, *Appl. Environ. Microbiol.*, **64**, 405–410.
609. Deborde, D. C., Woessner, W. W., Kiley, Q. T. and Ball, P. (1999). Rapid transport of viruses in a floodplain aquifer, *Water Res.*, **33**, 2229–2238.
610. Woessner, W. W., Ball, P. N., DeBorde, D. C. and Troy, T. L. (2001). Viral transport in a sand and gravel aquifer under field pumping conditions, *Ground Water*, **39**, 886–894.
611. Loveland, J. P., Ryan, J. N., Amy, G. L. and Harvey, R. W. (1996). The reversibility of virus attachment to mineral surfaces, *Colloids Surf. A*, **107**, 205–221.
612. Pieper, A. P., Ryan, J. N., Harvey, R. W., Amy, G. L., Illangasekare, T. H. and Metge, D. W. (1997). Transport and recovery of bacteriophage PRD1 in a sand and gravel aquifer: Effect of sewage-derived organic matter, *Environ. Sci. Technol.*, **31**, 1163–1170.
613. Bales, R. C., Li, S., Maguire, K. M., Yahya, M. T. and Gerba, C. P. (1993). MS-2 and poliovirus transport in porous medium: hydrophobic effects and chemical perturbations, *Water Resour. Res.*, **29**, 957–964.
614. Bales, R. C., Li, S., Yeh, T.-C. J., Lenczewski, M. E. and Gerba, C. P. (1997). Bacteriophage and microsphere transport in saturated porous media: force-gradient experiment at Borden, Ontario, *Water Resour. Res.*, **33**, 639–648.
615. Redman, J. A., Grant, S. B., Olson, T. M., Adkins, J. M., Jackson, J. L., Castillo, M. S. and Yanko, W. A. (1999). Physicochemical mechanisms responsible for the filtration and mobilization of a filamentous bacteriophage in quartz sand, *Water Res.*, **33**, 43–52.
616. Guan, H., Schulze-Makuch, D., Schaffer, S. and Pillai, S. D. (2003). The effect of critical pH on virus fate and transport in saturated porous medium, *Ground Water*, **41**, 701–708.
617. Gerba, C. P. (1984). Applied and theoretical aspects of virus adsorption to surfaces, *Adv. Appl. Microbiol.*, **30**, 133–168.
618. Murray, J. P. and Parks, G. A. (1980). Polyvirus adsorption on oxide surfaces. Correspondence with the DLVO–Lifshitz theory of colloid stability. In *Particulates in Water. Characterization, Fate, Effects, and Removal*, eds Kavanaugh, M. C. and Leckie, J. O. ACS Advances in Chemistry Series, Vol. 189. American Chemical Society, Washington, DC, pp. 97–133.
619. Penrod, S. L. and Olson, T. M. and Grant, S. B. (1996). Deposition kinetics of two viruses in packed beds of quartz granular media, *Langmuir*, **12**, 5576–5587.
620. Redman, J. A., Grant, S. B., Olson, T. M., Hardy, M. E. and Estes, M. K. (1997). Filtration of recombinant Norwalk virus particles and bacteriophage MS2 in quartz sand: importance of electrostatic interactions, *Environ. Sci. Technol.*, **31**, 3378–3383.
621. Moore, R. S., Taylor, D. H., Sturman, L. S., Reddy, M. M. and Fuhs, G. W. (1981). Poliovirus adsorption by 34 minerals and soils, *Appl. Environ. Microbiol.*, **42**, 963–975.
622. Gerba, C. P., Goyal, S. M., Cech, I. and Bogdan, G. F. (1981). Quantitative assessment of the adsorptive behavior of viruses to soils, *Environ. Sci. Technol.*, **15**, 940–944.
623. Moore, R. S., Taylor, D. H., Reddy, M. M. M. and Sturman, L. S. (1982). Adsorption of reovirus by minerals and soils, *Appl. Environ. Microbiol.*, **44**, 852–859.
624. Atherton, J. G. and Bell, S. S. (1983). Adsorption of viruses on magnetic particles – I. Adsorption of MS2 bacteriophage and the effect of cations, clay and polyelectrolyte, *Water Res.*, **17**, 943–948.
625. Fuhs, G. W., Chen, M., Sturman, L. S. and Moore, R. S. (1985). Virus adsorption to mineral surfaces is reduced by microbial overgrowth and organic coatings, *Microb. Ecol.*, **11**, 25–39.
626. Tipping, E. (1988). Colloids in the aquatic environment, *Chem. Ind.*, 485–490.
627. Harte, J., Kinzig, A. and Green, J. (1999). Self-similarity in the distribution and abundance of species, *Science*, **284**, 334–336.

628. Maurer, B. A. (1999). *Untangling Ecological Complexity: the Macroscopic Perspective*. University of Chicago Press, Chicago.
629. Brown, J. H. and West, G. B., eds. (2000). *Scaling in Biology*. Oxford University Press, New York.
630. Brown, J. H., Gupta, V. K., Li, B.-L., Milne, B. T., Restrepo, C. and West, G. B. (2002). The fractal nature of nature: power laws, ecological complexity and biodiversity. *Philos. Trans. R. Soc. London B*, **357**, 619–626.



---

# 3 Colloid–Trace Element Interactions in Aquatic Systems

---

**FREDERIC J. DOUCET**

*School of Biosciences, University of Nottingham, Sutton Bonington Campus,  
Loughborough LE12 5RD, UK*

**JAMIE R. LEAD**

*Division of Environmental Health and Risk Management, School of Geography, Earth and  
Environmental Sciences, University of Birmingham, Birmingham B15 2TT, UK*

**PETER H. SANTSCHI**

*Departments of Marine Sciences and Oceanography, Laboratory for Oceanographic and  
Environmental Research, Texas A&M University, 5007 Avenue U, Galveston, TX 77551,  
USA*

1	Introduction—Aquatic Colloids as Chemical Reactants . . . . .	96
1.1	Recognition and Importance of the Colloidal Pool . . . . .	96
1.1.1	Recognition of the Colloidal Pool . . . . .	96
1.1.2	Importance of the Colloidal Pool . . . . .	97
1.2	Importance of Colloid Size in Trace Element Complexation . . . . .	99
1.3	Impact of Colloid Binding on Trace Element Fate and Behaviour . . . . .	100
2	Laboratory Experiments on Trace Element Binding by Colloids . . . . .	102
2.1	Binding to Inorganic Colloids . . . . .	102
2.2	Binding to Organic Colloids . . . . .	105
2.3	Binding to Biological Cells . . . . .	107
2.4	Organic–Inorganic and Ternary Interactions . . . . .	108
3	Trace Element Binding by Freshwater Colloids . . . . .	110
3.1	Relevance of Pure Phases to Colloidal Systems . . . . .	110
3.1.1	Heterogeneity of Binding Ligands on Natural Colloids . . . . .	110
3.1.2	Kinetics of Metal–Colloid Reactions . . . . .	111
3.1.3	Strength of Binding and Mechanisms of Association . . . . .	112
3.1.4	Surface Coatings . . . . .	113
3.2	Distribution Coefficients . . . . .	113
3.3	The Importance of the Colloidal Phase . . . . .	115
3.4	Phases and Mechanisms Responsible for Trace Element Binding . . . . .	117
4	Interactions Between Trace Metals and Colloids in Marine and Estuarine Environments . . . . .	122

4.1	Colloidal Trace Metals and Ligands: Concentrations, Stability and Significance for Solution-Phase Speciation . . . . .	125
4.1.1	Thorium . . . . .	127
4.1.2	Iron . . . . .	130
4.1.3	Copper . . . . .	131
4.1.4	Other Trace Metals . . . . .	132
4.2	Trace Metal Binding and Colloidal Carrier Phases . . . . .	132
4.2.1	Reversibility versus Irreversibility of Metal Binding to Colloidal Macromolecular Ligands . . . . .	134
4.2.2	Relationships Between Colloidal Metal or Ligand Concentrations and Their Chemical and Physicochemical Properties . . . . .	135
4.2.3	Sources and Sinks of Metal-binding Colloids: Relationships to Thiol and Acid Polysaccharide Production . . . . .	136
4.3	The Significance of Surface-active Colloidal Ligands on Particle-Water Partition Coefficients and Kinetic Removal Rate Constants . . . . .	137
5	Some Perspectives and Research Directions . . . . .	138
	Acknowledgements . . . . .	140
	List of Abbreviations and Symbols . . . . .	140
	References . . . . .	141

## 1 INTRODUCTION-AQUATIC COLLOIDS AS CHEMICAL REACTANTS

### 1.1 RECOGNITION AND IMPORTANCE OF THE COLLOIDAL POOL

Colloids are important, often dominant, ligands affecting the speciation, fate, transport, biogeochemistry, bioavailability and toxicity of trace elements (nutrients or contaminants) in aquatic systems [1–3]. They are therefore central to understanding the toxic and nutrient status of trace elements and the processes affecting their transport in the aquatic environment. However, the study of colloids and their role in the biogeochemistry of trace elements is often hindered by their instability (due to their propensity to undergo conformational changes, aggregate and then sediment), their small size and low concentration and their complex, heterogeneous compositions, involving an intimate association between chemical, mineralogical and/or biological phases, such as organic humic substances and polysaccharides, inorganic oxides of aluminium, iron, manganese and silicon, as well as carbonate and clay minerals, and microbes including viruses and bacteria (see Chapters 1 and 2). Their study therefore requires the use of suitable analytical and sampling techniques, which must be sensitive, non-perturbing (ideally *in situ*) and quantitative, providing information on both average values (*e.g.* mean size) and values of complexity (*e.g.* size distributions or polydispersity of sampled colloids). Such appropriate techniques have only become available in recent years (see Chapter 4 and succeeding chapters).

#### 1.1.1 Recognition of the Colloidal Pool

Prior to the development of these techniques, most studies on trace element partitioning between solid and aqueous phases used standard membrane filtration (hereafter called ‘filtration’) to produce ‘particulate’ (>0.2, 0.4 or 0.45 µm in size) and ‘dissolved’ (<0.2, 0.4

or  $0.45\text{ }\mu\text{m}$  in size) fractions. Filtration is an operationally defined separation method [4], the use of which was, in part, justified by (i) its simplicity, (ii) the reduction in the chemical complexity of the filtrate (i.e. removal of suspended sediment such as silt, sand and large clay particles, and of large natural organic matter), (iii) the preservation of the samples via their partial sterilisation (i.e. through the removal of bacteria and other microorganisms that may promote biological transformations in the water samples during transport and storage), increasing allowable storage times [5], and (iv) improved data quality from many analytical techniques, *e.g.* by prevention of the sorption of particles to electrode surfaces. The use of filtration was also encouraged by the generally accepted belief that the colloidal mass was relatively low [6] and that colloids had a composition and behaviour very similar to those of larger particles [7]. To date, this basic separation method is still included in chemical analysis procedures used by regulatory organisations to determine water quality levels [8–11]. This is surprising, both because the so-called ‘dissolved’ fraction is now recognised to generally include a large proportion of colloids [12–16] (Table 1), which may be even larger in mass than the sum of particles of micron size [17,18], and because of the known artefacts inherent to filtration [6]. Indeed, most organic carbon and trace elements (up to 89% for Fe) in the ‘dissolved’ fraction of the Venice Lagoon and Galveston Bay were found to be associated with colloidal material [2,13]. In samples from the Gulf of Mexico, up to 50% of ‘dissolved’  $^{234}\text{Th}$  was shown to be colloidal with sizes between 1 kDa and  $0.2\text{ }\mu\text{m}$  [19]. Similar observations were also made for other trace metals (*e.g.* Ag, Cd, Cr, Cu, Hg, Pb) using ultrafiltration [12–15,20] (see Chapter 4) and sedimentation field-flow fractionation coupled to GF-AAS and ICP-MS [21] (see Chapter 5). Other field studies also attributed the consistently short residence times of toxic metals in ground and surface waters to colloid-facilitated transport [22–24]. For instance, residence times of  $^{234}\text{Th}$ -carrying colloids in the water column of the Gulf of Mexico ranged from 1 to 14 days for the  $>10\text{ kDa}$  colloidal fraction and from 5 to 65 days for the  $>1\text{ kDa}$  colloidal fraction [25]. Further, controlled laboratory experiments have shown that colloidal material can accelerate the migration of cationic and anionic trace elements through porous and fractured media [24,26]. This colloidal pool has not been accounted for in studies that used filtration as a separation technique, implying that the arbitrary classification of trace elements into particulate and dissolved fractions is inadequate to understand their detailed biogeochemical cycling [27]. Although the IUPAC definition of colloids has lower and upper limits of 1 nm and  $1\text{ }\mu\text{m}$ , respectively, relating these to environmental processes and mechanisms remains problematic (see Chapters 1 and 2). In particular, the lower size cut-off at 1–3 nm is more problematic and, in practice, is usually defined by ultrafiltration membranes with a nominal pore size of 1–10 kDa [28], with sizes based on standards such as vitamin B<sub>1</sub>. However, the relationship between this cut-off and conceptual definitions of the colloid–solution boundary [29,30] is not yet clear (see Chapter 1).

### 1.1.2 Importance of the Colloidal Pool

The ubiquitous occurrence and the large magnitude of the colloidal pool are significant for several reasons. First, the number of small colloids are orders of magnitude greater than the larger particles (*e.g.*  $10^6$  times more 10 nm colloids than  $1\text{ }\mu\text{m}$  particles) [31]. Indeed, recent studies have used AFM to indicate that colloids smaller than 50 nm represent the bulk of the colloidal fraction, when expressed in particle number (see Chapter 1). Recent

**Table 1.** Examples of percentage of colloidally bound metals<sup>a</sup> in natural waters

River/region	Colloidally bound metal% <sup>b</sup>						
	Al	Cu	Fe	Mn	Ni	Pb	Zn
1. Northern Britain [325]	15–100	20–60	30–100	10–50	3–60	30–90	5–50
2. Nova Scotia (Canada) [273]	75–85	n.d.	83–95	43–64	n.d.	n.d.	n.d.
3. Ochlockonee (USA) [326]	n.d.	n.d.	>65	30	n.d.	n.d.	n.d.
4. Silone Channel (Italy) [2]	n.d.	44	82	24	8.2	49	n.d.
5. Ob/Yenisey (Russia) [327]	n.d.	n.d.	89–97	n.d.	n.d.	22–52	n.d.
6. San Joaquin/Sacramento (USA) [275]	99	17	84–88	20	n.d.	n.d.	2
7. Garonne (France) [328]	n.d.	n.d.	69	5	n.d.	n.d.	34
8. New Jersey Pinelands (USA) [329]	55–85	48–71	63–96	25–35	n.d.	80–91	20–50
9. West Neck Bay (USA) [15]	n.d.	58	n.d.	n.d.	n.d.	85	22
10. Thur River (Switzerland) [330]	n.d.	5–30	n.d.	<10	1–12	n.d.	1–40
11. Kagamigaike pond (Japan) [331]	>6	>8	>14	>10	n.d.	>16	>9
12. Rivers in Amazon basin [201]	35–91	17–35	35–91	n.d.	n.d.	n.d.	n.d.
13. Several waters (Germany) [332]	n.d.	43	68	n.d.	45	100	15
14. Delsjö Creek (Sweden) [205]	12	40	89	1.4	12	83	13

<sup>a</sup> Colloidally bound metals (CM) are defined as follows: 1, 1 kDa < CM < 0.1 µm; 2, 10 kDa < CM < 1 µm; 3, 1 kDa < CM < 0.4 µm; 4, 10 kDa < CM < 0.7 µm; 5, 3 nm < CM < 0.4 µm; 6, 10 kDa < CM < 0.2 µm; 7, 10 kDa < CM < 0.4 µm; 8, 10 kDa < CM < 0.45 µm; 9, 1 kDa < CM < 0.45 µm; 10, 10 kDa < CM < 0.45 µm; 11, 0.05 µm < CM < 0.4 µm; 12, 5 kDa < CM < 0.22 µm; 13, 1 kDa < CM < 0.45 µm; 14, 1 kDa < CM < 0.45 µm. <sup>b</sup> n.d., not determined.

work has shown the potential importance of the very fine (ca 50 nm) fraction [32–35], although quantitative work is hampered by method limitations (see Chapter 1). Second, colloidal material is particularly important due to the likelihood of it having a higher specific surface area (SSA) than the particulate fraction and, hence, a larger number of functional groups potentially available to complex with trace elements and mediate the partitioning of trace elements between dissolved and particulate phases [36,37]. Indeed, a greater SSA is believed to expose greater numbers of reactive functional groups to the solution phase. For an assumed constant mass and density of the solid phase over the size range, total SSA is thought to increase as size decreases, resulting in a greater density of binding sites per unit mass. Although this relationship is likely to be valid for colloids of

constant mass and density over the colloidal size range, the lack of suitable techniques for the investigation of complex and diverse colloid morphology means that this inverse relationship between size and SSA is assumed [18]. Although reasonable, little or no direct experimental evidence for this assumption exists. In aquatic systems, natural colloids, which consist of various combinations of inorganic and organic materials varying in size and also in densities and geometries, may not have SSAs that follow the inverse relationship with particle size. To date, the precise relationship between SSA, as determined by, *e.g.*, the BET method, and the density of functional groups is not fully understood. As a result, variations in the colloid composition or microstructure with apparent size may be more responsible for the significance of colloids for trace element binding. Indeed, it is known that binding site densities, binding constants and mineralogy all vary as a function of size within the colloidal fraction [18,38,39]. It is conceivable that many inorganic and organic components of colloids (*e.g.* amorphous mineral oxides, humic aggregates) have a large proportion of internal surfaces, implying that their SSA may be less dependent upon apparent ‘size’ than is often assumed. Also, such inorganic phases have a porous gel-like structure where the physical size of individual gel flocs may not greatly influence the SSA as most surface would be internal. In addition, macromolecular colloids (*e.g.* humic substances), which tend to be more significant in smaller size fractions, are known to have amongst the largest site densities of colloid components. The importance of the size–SSA relationship may therefore often be overstated, and it may therefore be more realistic to rather concentrate on the relationship between size, SSA and composition. However, as discussed in Chapter 1, the parameter of size is perhaps less relevant to understanding environmental behaviour than others such as diffusion coefficient, and composition is proxy for more fundamental parameters such as equilibrium or rate constants. Clearly, a great deal of further work is needed before we can understand the role of these colloids in a fully quantitative manner. Third, the behaviour of colloids is significantly different from those of dissolved and particulate phases [29]. For instance, colloids have a fate quite distinct from that of particulate material since their residence times in the aquatic environment are estimated to be orders of magnitude lower [7] and are dominated by aggregation rather than sedimentation in surface waters [31]. Similarly, colloid-associated trace elements behave differently, both chemically and biologically, from species that are truly dissolved or associated with large settleable particles. For instance, the rate of uptake of Fe by diatoms was shown to be significantly higher for Fe bound with small colloids (1–10 kDa) than when bound to large colloids (10 kDa–0.2 µm) [40], although the extent to which colloid binding influences the uptake of metals (*e.g.* Ag, Cd, Cr, Zn) by aquatic organisms depends on the nature of the metal and the biota [41–43]. What is particularly important is the types and quantity of trace element complexing sites present in each pool (*i.e.* dissolved, colloidal and particulate) and the intensity with which trace elements interact with each site type. Our knowledge of this area is severely limited.

## 1.2 IMPORTANCE OF COLLOID SIZE IN TRACE ELEMENT COMPLEXATION

As colloids are primarily defined by size, it is worth considering the potential impact of colloids on trace element complexation. The fact that colloid size may influence a range of characteristics [30] that can affect trace element speciation has been covered in the previous section. However, the intrinsic importance of size *per se* has been overestimated due to the apparent ease with which that parameter can be measured, primarily

by filtration. This apparent ease derives essentially from the fact that filter manufacturers specify a size cutoff and the assumption that a defined filter pore size will lead to a ‘neat’ cutoff in terms of actual particle/colloid size. However, practical difficulties such as microbial degradation from the filter and non-size-based fractionation [34,44] mean that any reasonably accurate filtration must be more complicated, involving careful control of the experimental conditions and subsequent checks on filter and colloid behaviour [6,34]. Nevertheless, the size of colloid–metal complexes is an important parameter in itself, especially in helping to conceptualise the behaviour of trace elements during processes such as diffusion, aggregation and sedimentation ([30] and Chapter 1). Indeed, such is the importance that colloid size has attained, even in studies using methods such as flow field-flow fractionation (FFF; see Chapter 5), which directly quantifies the arguably more important parameter of diffusion coefficient, results are usually presented in terms of an estimate of colloid size, based on an assumed, usually spherical, particle geometry [37,45]. However, some studies have interpreted data differently to better understand environmental behaviour. For instance, data were produced on particles from split thin-flow fractionation (SPLITT), distinguishing a number of chemical phases by different settling velocities [46]. Nevertheless, colloid size (and related parameters) plays an important role in helping us to understand trace element bioavailability, cycling and transport. For instance, bioavailability of a trace element may depend critically on the diffusion of the complex from the bulk solution to the cell wall of an aquatic organism [47], particularly for colloids smaller than 50 nm. Speciation has been shown to determine critically the bioavailability and uptake of metals in a variety of organisms [42,48–51]. In the case of bioavailability, complex lability also needs to be accounted for [52] and this, in turn, may be related to size, through changes in chemistry and mineralogy. In addition, sedimentation and resuspension rates are both dependent on colloid size, and sedimentation is a major removal mechanism of trace elements from the water column [53,54]. Aggregation rates are also related to size due to increased mobility and therefore collision frequencies at smaller sizes [55].

### 1.3 IMPACT OF COLLOID BINDING ON TRACE ELEMENT FATE AND BEHAVIOUR

Colloids are of great importance in the quantitative binding of trace elements, in many cases dominating their fate and behaviour in natural waters. A better understanding of the strong affinity between colloids and trace elements is essential since the environmental fate and behaviour of these colloid-bound metals will be different from those of either dissolved metals or particle-bound metals. In particular, transport through surface and ground waters and biological uptake and availability to aquatic organisms will be affected. Although somewhat outside the scope of this chapter, we will briefly consider the importance of colloids on both transport and bioavailability.

As stated earlier, colloids and particles are formally differentiated on the basis of size largely because of practicalities and by extension of traditional colloid chemistry definitions. This has relevance to the environment because this cut-off between colloids and particles can be taken as the limit either side of which either aggregation or sedimentation processes dominate. Above sizes of  $\sim 1 \mu\text{m}$ , macro- and microparticle transport is dominated by settling under gravitation, whereas below this, transport of nanoparticles and

macromolecules (i.e. colloids) is dominated by aggregation and disaggregation [29,31,55]. Binding of metals to settling particles and their removal by sedimentation are a major process by which metal concentrations in the water column are regulated [53,54]. Of course, these two processes (aggregation and sedimentation) and the different pools of solid-phase material are interrelated. Indeed, the concept of colloidal pumping [7,56,57] has been introduced to explain and link the coupled processes of adsorption, coagulation and removal by sedimentation. Metals primarily bound to colloids because of their high reactivity are transferred over time to the particulate phase, which sediments.

In the past decade, extensive research has been carried out on the mobility of radioactive nuclides in surface and subsurface waters ([58] and references therein, [59]). Despite potential problems with experimental techniques, the mobility of colloid-bound radionuclides has been demonstrated and is generally attributed to adsorption by negatively charged silicate [60–63] and/or humic colloids [59,64].

A recent chapter in an earlier volume in this series [65] thoroughly reviewed trace element biouptake, by evaluating the role of colloidal complexation on metal availability, including constraints on diffusion, dissociation kinetics and biological processes. A great deal of research has been performed in this area, although few authors have investigated the role of colloids in metal biouptake in a quantitative and mechanistic manner [42,66]. A number of studies have investigated the impacts of size fractionated colloids on metal uptake to filter and deposit feeders [40,51,67], with different availabilities depending on a variety of biological and physico-chemical processes (diffusive uptake, direct ingestion, *etc.*). For instance, one study investigating Zn and Cd uptake to mussels [68] found that direct ingestion of colloid-associated Zn and Cd by filter-feeding organisms was an important process, but that the efficiency of the process was related to the distribution coefficient describing the metal–surface interaction. Current models of metal toxicity, such as the biotic ligand model (BLM) [66,69], used as research tools or likely to be used in US and EU regulations do not currently contain realistic sub-models which account for the behaviour of aquatic colloids in trace metal behaviour.

A clear understanding of the mechanisms underlying trace element association with aquatic colloids is essential for elucidating thermodynamic and kinetic aspects of the range of interactions occurring in aquatic systems and for predicting the fate and behaviour of these trace elements in such systems. As a result, a considerable amount of data on trace element binding by colloids has been gathered from both laboratory experiments (using model colloids that were either artificially synthesised or isolated from natural waters) and field observations. In this chapter, we will first review the current knowledge on the chemical and physicochemical aspects of the binding of trace elements with pure and extracted (i.e. model) colloids before discussing to what extent the information derived on ‘model’ phases is relevant to trace element binding to natural colloids. This will be followed by a discussion on our present knowledge of colloid–metal interactions in both fresh and marine waters. Modelling of speciation among dissolved, colloidal and particle-bound trace elements in waters is also a key aid to understanding their biogeochemical cycles and toxicity [56] and this will briefly be reviewed. The same authors have pointed out that our ability to model trace element transport is largely limited by a lack of detailed understanding of the distribution of trace elements between dissolved and particulate phases in natural systems. However, increasingly sophisticated models of element binding to colloids and particles have been developed in recent years [70–72], which simulate the

distribution of particle-bound metals among solid phases. The advantages and limitations of current models will be briefly discussed later in the chapter.

## 2 LABORATORY EXPERIMENTS ON TRACE ELEMENT BINDING BY COLLOIDS

A great deal of information has been collected by studying single- and multicomponent systems in carefully controlled laboratory experiments using environmentally relevant pure or extracted phases such as oxides, humic substances (HS) or bacteria. Such an approach with pure phases, which may be used to ‘model’ environmental colloid systems, can provide detailed information on the mechanistic, thermodynamic and kinetic aspects of the binding processes. However, we must question the relevance of the outputs to real environmental systems and to natural aquatic colloids. The use of biological systems and extracted phases increases the complexity of the system and consequently the depth of knowledge that can be attained. For instance, we do not have an in-depth knowledge of the mechanisms (i.e. bond types, kinetics of binding) of metal binding to HS due to the complex structure of natural HS. However, such model systems (i.e. pure or extracted phases) do approach the real environment to a limited extent and are therefore necessary. The study of natural samples that have been minimally perturbed during sampling and fractionation, on the other hand, provides a more realistic description of the environment [3,18,73,74], but these studies provide much less insight into the mechanisms involved due to the complexity of natural colloidal phases. As a result, an iterative combination is needed between the fully mechanistic determination of metal binding to pure phases and a more poorly constrained (but more relevant) determination of metal binding by real natural colloids [75,76]. Careful interpretation of such approaches serves as an indispensable aid to understanding chemical, physicochemical and biological processes controlling interactions between colloids and trace elements [77].

### 2.1 BINDING TO INORGANIC COLLOIDS

Inorganic colloids are commonly occurring mobile phases in the aquatic environment [78] and have been shown to be quantitatively important in binding trace cations [37], despite the current predominant focus on organic phases (*e.g.* humic substances, EPS). In particular, iron and manganese oxyhydroxides [54,72,79,80], in addition to aluminium oxides and silicates [72,81–85], have been implicated in metal binding because of their large SSA and binding constants. In addition, many studies have examined the interaction of trace elements, inorganic phases and a third phase such as HS, their analogues or biological cells [81,86,87].

Models of these interactions have been developed, of which the standard one is the surface complexation model (SCM) [79,88]. This model postulates surface reactions as occurring via equilibria that can be described mathematically by mole balance equations directly analogous to solution equilibrium expressions (with electrostatic correction). The model splits an experimentally accessible apparent equilibrium constant,  $K_{\text{app}}$  (or change in Gibbs free energy,  $\Delta G$ ) into an intrinsic constant  $K_{\text{int}}(\Delta G_{\text{int}})$  and a correction factor based on coulombic interactions,  $K_{\text{coul}}(\Delta G_{\text{coul}})$ . However, even for well-characterised

**Table 2.** Surface complexes and definition of the corresponding intrinsic equilibrium constants for the 2-p*K* basic Stern model with ion-pair formation. Reprinted from Christl, I. and Kretzschmar, R., Competitive sorption of copper and lead at the oxide–water interface: Implications for surface site density, *Geochimica et Cosmochimica Acta*, **63**, 2929–2938, Copyright 1999, with permission from Elsevier

Surface complex	Reaction or type of complex	Intrinsic equilibrium constant
$\text{SOH}_2^+$	Protonation/deprotonation of surface site	$K_1 = \frac{c_{\text{SOH}^0} c_{\text{H}^+}}{c_{\text{SOH}_2^+}} \exp(-F\Psi_0/RT)$
$\text{SOH}$		$K_2 = \frac{c_{\text{SO}^-} c_{\text{H}^+}}{c_{\text{SOH}^0}} \exp(-F\Psi_0/RT)$
$\text{SO}^-$		
$\text{SO}^- \cdot \text{Na}^+$	Ion-pair	$K_{\text{Na}} = \frac{c_{\text{SO}^- \cdot \text{Na}^+}}{c_{\text{SO}^-} \cdot c_{\text{Na}^+}} \exp(F\Psi_d/RT)$
$\text{SOH}_2^+ \cdot \text{NO}_3^-$	Ion-pair	$K_{\text{NO}_3} = \frac{c_{\text{SOH}_2^+ \cdot \text{NO}_3^-}}{c_{\text{SOH}_2^+} c_{\text{NO}_3^-}} \exp(-F\Psi_d/RT)$
$\text{SOM}^+$	Inner-sphere	$K_{\text{SOM}} = \frac{c_{\text{SOM}^+} c_{\text{H}^+}}{c_{\text{SOH}^0} c_{\text{M}^{2+}}} \exp(F\Psi_0/RT)$
$\text{SO-M}^+$	Outer-sphere	$K_{\text{SO-M}} = \frac{c_{\text{SO-M}^+} c_{\text{H}^+}}{c_{\text{SOH}^0} c_{\text{M}^{2+}}} \exp[F(2\Psi_d - \Psi_0)/RT]$
$\text{SO-MOH}^0$	Outer-sphere	$K_{\text{SO-MOH}} = \frac{c_{\text{SO-MOH}} (c_{\text{H}^+})^2}{c_{\text{SOH}^0} c_{\text{M}^{2+}}} \exp[F(\Psi_d - \Psi_0)/RT]$

pure phases, various types of chemical and physical interactions are possible. Furthermore, data fitting from sorption edge-type experiments can be ambiguous. Non-unique fits to surface complexation models are possible [83], despite (or because of) their complexity (Table 2). Consequently, a number of different variations of SCMs have been developed explaining data equally well. Recently, the combination of X-ray or other spectroscopic methods (see Chapter 11) and quantum mechanical modelling has helped to constrain the SCMs and produce somewhat more rigorous mass action quotients [89–93]. An example of the surface complexes derived from such studies which model interactions between vanadium and goethite is given in Figure 1 [89].

Well-constrained and powerful models have been developed describing, for example, the interactions of As with amorphous iron oxides and schwertmannite [94,95], cadmium, copper, nickel, lead and a variety of oxyanions such as selenate with goethite [90–92,96, 97] and uranium with haematite [98]. Similar models have been developed describing the interactions of nickel with amorphous manganese oxide [99], metal oxyanions and lead with birnessite [93]. In addition, metal sorption to other phases such as calcite [85] and clay [81,100] have also been studied. Interestingly, the study by Rouff *et al.* [85] measured Pb sorption on calcite as a function of metal to solid ratio and reaction time. Pb was found to bind to calcite surfaces only moderately (distribution coefficient  $K_D \approx 10^3$ ) and binding under the conditions studied ( $\text{pH} = 8.2$ ;  $0.15 \text{ mol dm}^{-3} \text{ NaNO}_3$ ) was likely to be reversible with little Pb incorporated into the solid phase. This finding is in agreement

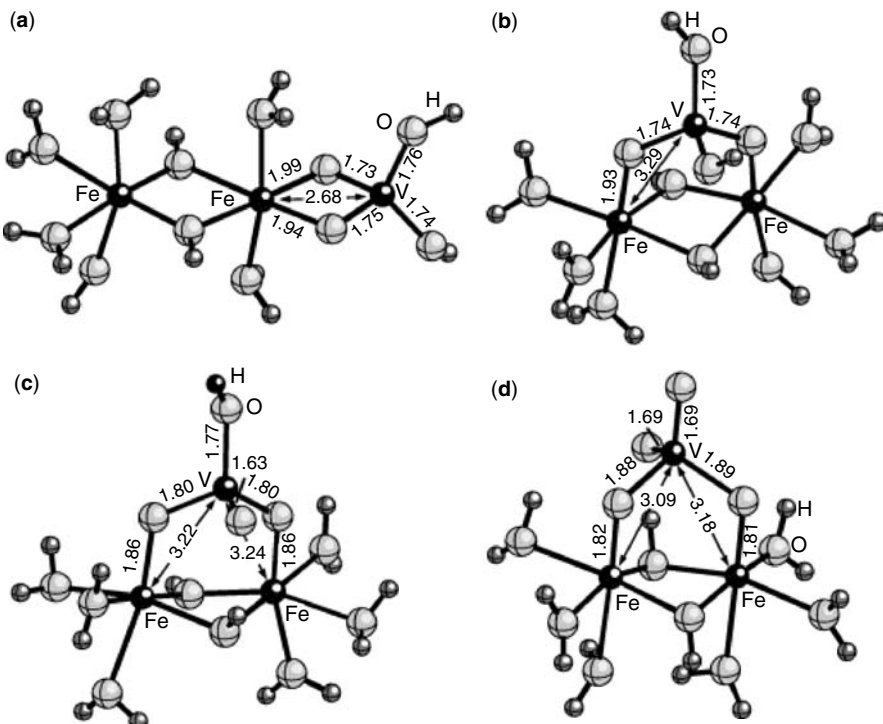


**Figure 1.** V(V) *ab initio* molecular geometry clusters: (a)  $\text{VO}_2(\text{OH})_2$  bidentate edge-sharing (210); (b)  $\text{VO}_2(\text{OH})_2$  bidentate corner-sharing (110); (c)  $\text{VO}_3(\text{OH})$  on bidentate corner (110); (d)  $\text{VO}_4$  on bidentate corner (110). Bond lengths shown in Å. Clusters (b) and (c) are favoured energetically and give V–Fe and V–O bond lengths in good agreement with those observed in the EXAFS. Reprinted from Peacock, C. L. and Sherman, D. M., Vanadium(V) adsorption onto goethite (alpha-FeOOH) at pH 1.5 to 12: A surface complexation model based on *ab initio* molecular geometries and EXAFS spectroscopy, *Geochimica et Cosmochimica Acta*, **68**, 1723–1733, Copyright 2004, with permission from Elsevier

with field studies [54] which indicate that carbonates are not significant metal carriers in lake water.

These studies generally indicate that pH is an important variable, as with natural colloids. Indeed, pH simultaneously affects competition between  $\text{H}^+$  and metal ions for surface sites on the colloid, the surface charge of colloids and the speciation of the adsorbing species. For instance, natural Fe oxides have been identified with both positive or negative surface charges, depending on solution pH [101] and organic matter coating [102]. Also, a low pH increases the affinity of dissolved phosphate for Fe oxide colloids in both freshwater and seawater [103]. The authors explained their observations in terms of the simultaneous dependence of the speciation of phosphorus and the surface charge of the Fe hydroxide with pH. In addition, effects of other cations and anions have also been observed. For instance, adsorption of phosphate, a negatively charged molecule with a high affinity for Fe hydroxide surfaces [104,105], on hydrous Fe oxides is known to have a positive influence on the adsorption of Zn [106] and Cd [80] (Figure 2). This effect was explained by the presence of phosphate decreasing the electrostatic potential

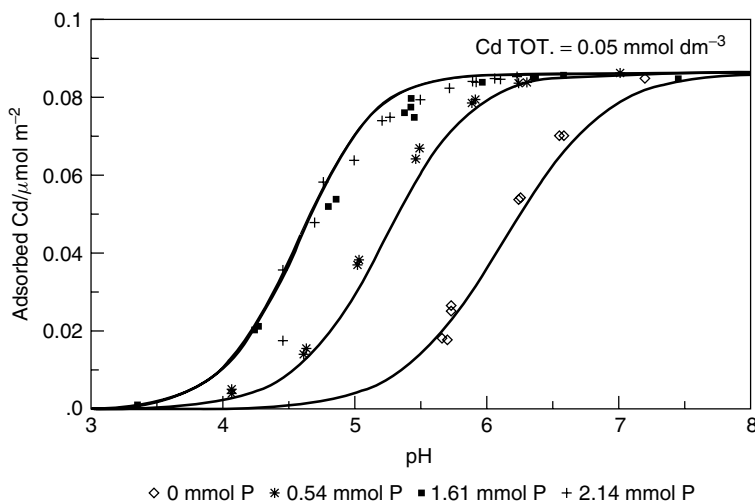


**Figure 2.** Cadmium absorption data for goethite ( $570 \text{ m}^2 \text{ dm}^{-3}$ ) in  $0.1 \text{ mol dm}^{-3} \text{ NaNO}_3$  and  $0.05 \text{ mmol dm}^{-3} \text{ Cd}$  in the system. The symbols represent data with different amounts of phosphate in the system. The solid lines represent the model calculations. At these low cadmium concentrations, carbonate species have no influence. According to the model, most cadmium is adsorbed on the 021 face for the low phosphate concentrations. For the two highest phosphate concentrations, the cadmium monodentate surface complex (110 face) is far dominant. Reprinted from Venema, P., Hiemstra, T. and van Riemsdijk, W. H., Interaction of cadmium with phosphate on goethite, *Journal of Colloid and Interface Science*, **192**, 94–103, Copyright 1997, with permission from Elsevier

near the goethite surface, which promotes the presence of higher overall Cd concentration near the surface with the subsequent increased Cd surface loading [80].

## 2.2 BINDING TO ORGANIC COLLOIDS

As shown in Chapter 2, the main types of recalcitrant organic colloids present in natural waters are HS and polysaccharide- and peptidoglycan-rich microbial products of cell wall ‘sloughing’ (herein called ‘exudates’).

A large literature exists on the binding of HS and metals, partly because of the extraction methodologies available and partly because of their intrinsic environmental importance. The literature is too voluminous to review here, and has been reviewed elsewhere [107], while recent models of metal binding have also reviewed and recalculated metal binding data [108–111]. However, much has been published on HS–metal binding since these reviews (Table 3). In general, solution pH, and also the heterogeneous nature of HS, are the primary parameters affecting HS interactions with trace elements, whereas material charges have a secondary effect. The two currently most important and widely used models of HS–metal binding are Model VI and its predecessors [109,112] and NICCA and its variants [113]. Both models have been taken up and used substantially by researchers as a means of interpreting data gathered experimentally [114] and have been incorporated into fuller speciation codes such as WHAM [115] and ECOSAT [116,117], which contain descriptions of solution and other speciation. A brief summary of the models and their implications is given below.

**Table 3.** Recent studies on HS-metals binding

Reference	Type of HS-metals binding system studied
[334]	Technetium binding to groundwater HS
[335]	Copper binding to N-containing sites in stream water HS
[272]	Copper binding to marine water HS
[336]	Cadmium binding to stream water HS
[337]	Lead binding to soil HS
[338]	Americium binding to a peat HS
[129]	Surfact compounds or Np(IV/V) sorbed to fulvates and clays

The models of the interaction of HS with cations have their origin in basic principles that are similar to SCMs (i.e. mole balance expressions for equilibria), but the electrostatic corrections applied in these models are based on principles distinct from those typically employed in SCMs. For instance, Model V/VI use a semi-empirical form of electrostatic correction originally employed to describe the electrostatics of proteins, whereas NICCA uses a Donnan gel formulation. The large heterogeneity of potential specific binding sites including carboxylate-type groups, primarily important at low to neutral pH values, and weaker basic groups such as phenolates, primarily important at neutral to high pH values, has been stressed in both models. In Model VI, heterogeneity is expressed by expansion of a small number of fitting parameters to characterise several hundred discrete metal and proton binding site types (Table 4). In the NICCA model, binding site heterogeneity is incorporated through a continuous distribution approach. Both models have been shown to provide excellent fits to a good deal of independent literature data [118,119]. For instance, both models mimic very well the effects of pH, ionic strength and competition over a wide range of HS types and solution conditions, and their main strength is the existence of a database with, *e.g.*,  $pK_a$  values for use in Model VI. Nonetheless, despite their complexity and sophistication, these models contain the possibility of non-unique solutions and cannot be considered as predictive, largely because of the complexity of the HS structures. However, although the determination of binding sites by spectroscopic means has been impossible to date, some assumptions and simplifications about the nature and interactions of HS with metals will always be required in a model, regardless of the quality of the measurements upon which it is based. For humic substances, it is believed that their heterogeneity is quantitatively more important than electrostatic effects, and more work is required in this area.

In addition, the structures of exudates and their implications for stability and aggregation of colloids have been examined [120]. In addition, their roles in aggregation processes have also been shown to differ from those of HS, in that they appear essentially to promote bridging and aggregation, whereas HS are often responsible for charge repulsion effects and stabilisation [121]. However, there are very few studies that have investigated their interactions with trace metals [122–124]. They have found that (i) exuded ligands include a number of potential metal binding sites (*e.g.* sulfur and carboxyl groups) and (ii) the composition and concentration of exudates influence metal uptake, with subsequent effects on the biological availability of these metals. However,

**Table 4.** Summary of parameters in Humic Ion-Binding Model VI. Reprinted from Tipping, E., ed. (2002), *Cation Binding by Humic Substances*, with permission from Cambridge University Press

Parameter	Description	How found
$n_A$	Abundance of type A sites ( $\text{mol g}^{-1}$ )	Fitted
$n_B$	Abundance of type B sites ( $\text{mol g}^{-1}$ )	$= 0.5n_A$
$pK_A$	Intrinsic proton dissociation constant for type A sites	Fitted
$pK_B$	Intrinsic proton dissociation constant for type B sites	Fitted
$\Delta pK_A$	Distribution term that modified $pK_A$	Fitted
$\Delta pK_B$	Distribution term that modified $pK_B$	Fitted
$pK_{MHA}$	Intrinsic equilibrium constant for metal binding at type A sites	Fitted
$pK_{MHB}$	Intrinsic equilibrium constant for metal binding at type B sites	Fitted, or correlated with $pK_{MHA}$
$P$	Electrostatic parameter	Fitted
$K_{\text{sel}}$	Selectivity coefficient for counterion accumulation	Fitted, or set to unity
$f_{\text{pr}}$	Fraction of proton sites that can make bidentates sites	Calculated from geometry
$M$	Molecular weight	Estimated from literature
$r$	Molecular radius	Estimated from literature

the extent to which polysaccharide-rich exudates can compete with humic substances to bind metals is unclear.

### 2.3 BINDING TO BIOLOGICAL CELLS

Although phytoplankton cells are generally too large to be considered as colloids, viruses and usually bacteria can be classified as such and can potentially make an important contribution to trace element binding because of their ubiquity, high reactivity and high concentration. To our knowledge, there is very little work that has reported strong field evidence that bacterial surfaces may play a significant role in trace element fate and behaviour in certain natural environments (acid rock drainage waters) [125]. As with mineral surfaces, surface complexation modelling has been used extensively to interpret the binding of metals to bacterial surfaces as a function of pH, ionic strength and metal to solid ratios. In general, a minimum of three sites have been necessary to accurately explain metal binding by surface complexation [126,127], tentatively identified as carboxylate, phosphate and either hydroxyl or amino groups. However, these sites have generally not been confirmed by secondary means such as spectroscopy. X-ray spectrometry has been used to provide further evidence for the uniqueness of surface complexes formed [128,129], where Cd binding to a Gram-positive bacterium was explained primarily by sorption to a phosphoryl group at low pH, to a carboxyl group at circumneutral pH and possibly to a different phosphoryl group at high pH.

The NICCA model used to interpret metal binding to HS has also been successfully applied to Cd and Zn binding to a Gram-positive soil bacterium [130], explaining pH dependence and Ca competition, although Fowle and Fein [131] argued that the use of NICCA was not warranted by the relatively simple (compared with HS) bacterial cell wall.

These authors also reported the pH dependence of Cd, Cu and Pb binding to a Gram-positive bacterium using a relatively simple SCM, with binding by bacteria insignificant below pH 4 but virtually complete above pH 6 [131]. Cox *et al.* [132] used a linear programming method to mimic the binding of protons (but not trace metals) to a bacterial surface. The model, which has similarities to the ‘mixture models’ previously used to explain ion binding to HS [111], identified two extra sites, in addition to those mentioned above, i.e. carboxylic, phosphodiesters, phosphoric, amine and hydroxyl, based on their data fitting and the likely available binding sites present in bacteria.

All of the studies reported above examined a single type of bacteria (usually the Gram-positive *Bacillus subtilis*) and Yee and Fein [133] argued that Cd sorption to bacteria is not dependent on the bacterial species. However, the extent to which this observation from a small number of cultured, inactive species in isolation can be applied to real systems with microbial consortia in a range of metabolic states is not clear. It can be expected that bacterial trace element retention and affinities are element and bacterial surface specific, which suggests that the corresponding processes of sorption will be specific to the element in question and the functional groups at the surface of the bacteria. They may, however, also be affected by other factors, such as the presence of EPS and the types of uptake mechanisms taking place. The complexity of trace metal complexation by living organisms is illustrated by the uptake of Cd into the cell or on the surface of the freshwater bacterium *Rhodospirillum rubrum*, which can be inhibited by Zn but is enhanced in the presence of Mn and Cu [134].

Quantitative examination of trace element uptake rates by aquatic bacteria is also important to understanding their role in trace element transport and to verifying the validity of trace element uptake models such as the FIAM and biotic ligand model (BLM) [134]. For bacteria, cell uptake rates have not generally been determined, except in two recent studies for Cd [134] and Zn [50]. However, using the simpler phytoplankton, both surface binding and cell uptake rates are commonly calculated [66,135,136]. In this chapter on aquatic colloids, these will not be considered further.

The single phase (and often single metal) studies mentioned above are of great importance in understanding metal speciation in the natural environment because they provide in-depth knowledge of possible mechanisms, equilibria and kinetics. However, the main factors complicating our understanding of the role of colloid–metal interactions are the complexity of the ligands involved and the increasing recognition that inorganic surfaces in the environment will most often be coated with organic and inorganic nanoparticles (see Section 2.4). Single-component studies therefore provide a limited insight into metal complexation in natural (environmental) systems. Increasingly, a number of studies have investigated the interaction between colloids of varying composition and several trace elements. This is a further important step towards more realistic systems, although still limited in its overall relevance to ‘real’ systems.

## 2.4 ORGANIC-INORGANIC AND TERNARY INTERACTIONS

As mentioned earlier, inorganic colloids are rarely present as bare surfaces, and are instead coated to some extent by natural organic matter (NOM), such as the ubiquitous humic and fulvic substances [33,111,137–139]. In addition, coatings of inorganic phases such as iron oxides are possible (see Chapter 2). NOM coatings alter the surface characteristics

of inorganic colloids, which, in turn, alter their stability, mobility and interactions with trace elements [140–142]. It may therefore be arguable to what extent studies on trace metal interactions with inorganic colloid bare surfaces are relevant to the understanding of chemical processes occurring in natural systems. In addition, several classes of NOM have been identified in natural waters, such as humic and fulvic acids, polysaccharides, peptidoglycans and complex cell wall residues of microorganisms [120]. These organic matter components have distinctively different physicochemical structures and properties, and will therefore sorb on to inorganic surfaces differently. It is therefore also essential to distinguish between these different classes of NOM in order to understand better the mechanistic and kinetic aspects of their adsorption onto mineral surfaces, and elucidate their effects on trace element binding to minerals. However, attempts to isolate different NOM classes into ‘relatively pure’ fractions is still fraught with experimental difficulties. This is the primary reason why the majority of studies have been undertaken with either commercial humic and fulvic acids or with natural unfractionated NOM. This also explains why our current knowledge on the principal binding mechanisms and other processes involved in the adsorption of organic matter on inorganic colloid surfaces is severely limited, although several parallel, competitive processes are likely to take place. Potential mechanisms for HS adsorption are summarised in Table 5.

The occurrence of organic coatings on inorganic surfaces can affect the uptake of trace elements (*e.g.* Eu [143], Zn [144,145], U and Th [146–148]) by inorganic colloids. Uptake also depends upon a number of other factors, such as the speciation of the trace element considered, the pH of the aquatic system and the presence of competing trace elements or other ligands including colloidal surfaces. The main types of organic molecules that adsorb on oxide surfaces are those with greater content of aromatic moieties, carboxylic acid groups, N- and S-containing groups and amino residues [16]. Future work is essential to understand better ternary interactions between inorganic colloids,

**Table 5.** Principal binding mechanisms and other processes involved in the adsorption of humic substances at inorganic colloid surfaces. Reprinted (modified) from, Tipping, E., ed. (2002), *Cation Binding by Humic Substances*, with permission from Cambridge University Press

Mechanism	Cause/Significance
1. Electrostatic binding	Attraction and repulsion, and consequent changes in co-ion and counterion distributions
2. Ligand exchange	Exchange of surface hydroxyl groups for acid functional groups
3. Hydrophobic effect	Removal of apolar moieties from contact with water
4. Hydrogen bonding	Exchange of hydrogen bonds with water for those with the surface, significant for polar groups in hydrophobic environments
5. Van der Waals interactions	Important for large adsorbates, making many contacts
6. Conformational change	Change in size, shape, flexibility of the organic molecules
7. Co-adsorption	Adsorption of entities associated with humic substances, <i>e.g.</i> bound protons and metal cations
8. Competition	Diminishment of adsorption due to competition by another compound, <i>e.g.</i> $\text{SO}_4^{2-}$
9. Fractionation	Adsorption of some components favoured over others
10. Element release	Dissolution of the solid engendered by the adsorbed humic matter

organic matter and trace elements as a step towards understanding the more complex ‘real’ systems.

### 3 TRACE ELEMENT BINDING BY FRESHWATER COLLOIDS

#### 3.1 RELEVANCE OF PURE PHASES TO COLLOIDAL SYSTEMS

As shown in Section 2, considerable research has been performed on trace element binding to pure or extracted phases. On these pure phases, molecular level surface speciation can be characterised by spectroscopic methods (often X-ray spectrometry, see Chapter 10), quantum chemistry modelling, or both [89]. The understanding derived from these studies can be used to produce and quantify fundamental mechanistic and thermodynamic explanations of metal–surface interactions. Again, as discussed in Section 2, binding between metals and surfaces is most often explained in terms of equilibrium surface complexation reactions. However, a significant question remains as to what extent the information derived on pure phases is relevant to trace element binding to natural aquatic surfaces and colloids.

Similarities exist between conditional equilibrium constants measured using model phases (Mn and Fe oxyhydroxides and NOM) and those measured from natural freshwaters [149,150] and between Mn and Fe hydrous oxides and a variety of natural freshwater particles [73]. In addition, plots of conditional equilibrium constants and complexation capacities derived from laboratory experiments on both HS and biological cells are, in general, consistent with similar plots for natural waters [151]. However, agreement here is only semi-quantitative, largely due to method dependence of the measurements. Indeed, an inter-laboratory study found good agreement between complexation capacities but  $\log K$  values varied between regions from 7 to 12 for the same natural waters [152]. There are many reasons (detailed below) to assume that links between the laboratory and environmental systems cannot be made directly. Indeed, while the concepts for models (*e.g.* surface complexation) may be transferred from the laboratory to the environment, it is possible that quantitative transfer of the models themselves cannot take place directly [75]. It is also likely that surface complexation model concepts may only be transferable with great caution due to the complexity of aquatic systems. For instance, non-surface sorption reactions, precipitation, dissolution and other processes may occur as physicochemical or biological parameters such as pH or oxygen content (redox potential) are changed [73]. However, in many cases, adsorption is the most likely reaction mechanism [3]. Despite these caveats, the pure phases coated with organic material discussed in Section 2 are likely to represent the most important colloidal phases in natural waters. Some complexities of natural aquatic systems and the limitations of our knowledge are briefly discussed hereafter.

##### 3.1.1 Heterogeneity of Binding Ligands on Natural Colloids

As discussed in Chapter 2, natural aquatic colloids are composed of many possible phases, with a large number and variety of chemical binding sites. In addition, chemically similar or even identical sites may behave differently from one another based on their physical and chemical environment. Most commonly, the electrostatic component of binding

is considered to modify chemical binding (as in surface complexation modelling). The sorption or desorption of elements may be hindered by steric effects, *e.g.* the physical unavailability of binding sites (in clays and postulated in organics [153]). This physical and chemical complexity is seen in pure phases such as Fe (oxy)hydroxides to a limited extent, but the heterogeneity of natural colloids currently prevents full mechanistic knowledge of these systems. In the absence of this knowledge, models will only be semi-empirical and not fully predictive.

### 3.1.2 Kinetics of Metal–Colloid Reactions

Data collected on pure phases are (usually) interpreted by surface complexation models based on thermodynamic equilibrium (*e.g.* [154]). However, in real environmental systems, slow rates of reactions may preclude equilibrium. Although much kinetic data are still lacking and the default assumption is of thermodynamic equilibrium, chemical reactions in natural waters may not be complete after months or longer [155], whereas equilibrium on pure phases may be reached in a matter of hours or days, depending on the nature of the sorbent and solution conditions (*e.g.* solution pH, ionic strength, temperature) and initially occurring reactions [156,157]. For instance, slow Zn sorption kinetics on low surface area gibbsite was caused by the formation of Zn–Al layered double hydroxide at the surface of the mineral phase, whereas Zn sorption kinetics were rapid on silica and high surface area gibbsite where inner-sphere adsorption complexes formed at the surface [157]. However, sorption usually shows a fast initial reaction, followed

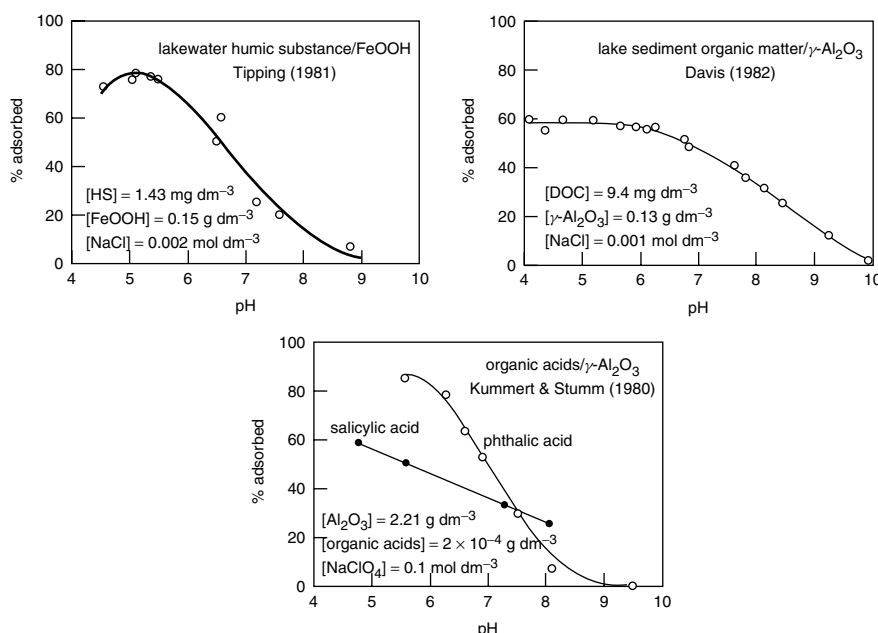


**Figure 3.** Adsorption of organic acids by oxides. The lines are for guidance only. For the references cited, see the original. Reproduced from Tipping, E., ed. (2002), *Cation Binding by Humic Substances*, with permission from Cambridge University Press

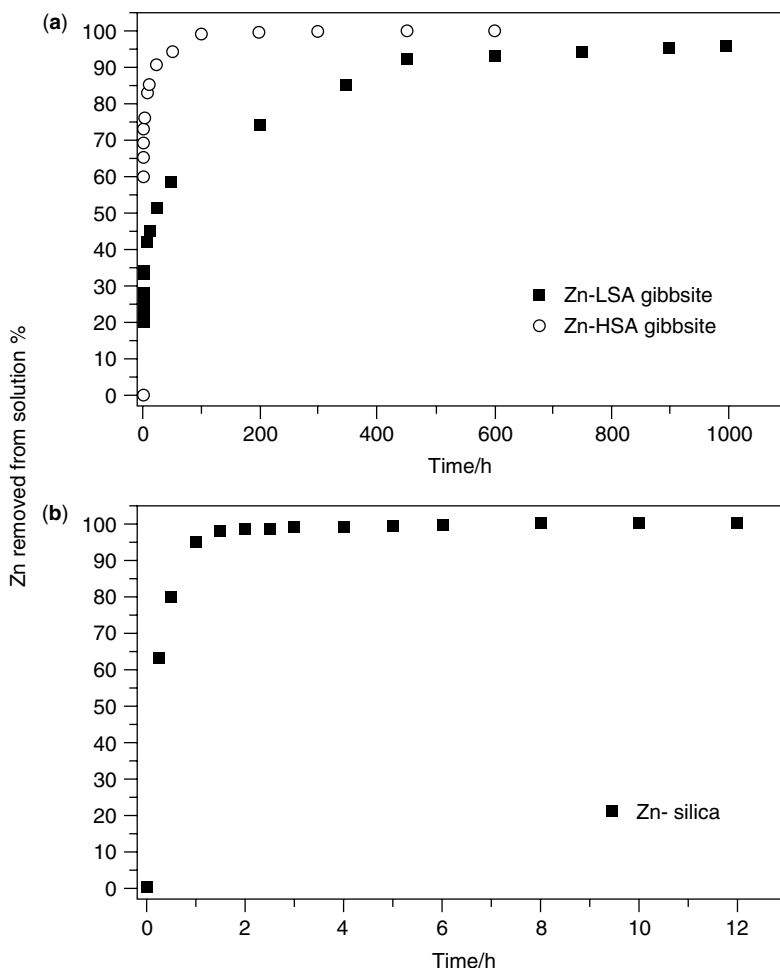


**Figure 4.** Zn sorption kinetics on low-surface-area gibbsite and high-surface-area gibbsite (a) and amorphous silica (b). Reprinted from Roberts D. R., Ford R. G., Sparks D. L., Kinetics and mechanisms of Zn complexation on metal oxides using EXAFS spectroscopy, *Journal of Colloid and Interface Science*, **263**, 364–376, Copyright 2003, with permission from Elsevier

by slow continuous adsorption processes [158,159] (Figure 3 [111] Figure 4 [157]), such as diffusion through micropores. In environmental systems, equilibrium models may be valid if the chemical reactions are rapid in relation to other processes being studied, such as flow of water through compartment of interest. Thus, on practical grounds, equilibrium models may be applied to non-equilibrium systems. Nevertheless, modelling of the kinetics of metal–colloid systems is progressing [160].

### 3.1.3 Strength of Binding and Mechanisms of Association

Binding of metals in the environment is likely to be stronger than in laboratory experiments on HS or biota [161]. This is probably due to a combination of effects, including steric

occlusion, non-attainment of equilibrium in the laboratory and the higher metal to ligand ratios used in most laboratory experiments, as compared with environmental systems. While some studies have now been performed at relevant ratios [18], these are often at higher overall concentrations of metals and ligands, potentially in the presence of physicochemical processes that will not occur in the field and most certainly complicating data interpretations.

As the surface complexation model implies, metal association with surfaces is via a sorption mechanism (specifically adsorption to surface groups and electrostatic accumulation adjacent to the molecule or mineral surface). However, in anoxic waters (not specifically considered in this chapter), precipitation by sulfides is a major control on metal behaviour [162]. Additionally, natural colloids may undergo other non-sorption reactions, such as dissolution and aggregation. Again, while these different mechanisms occur with pure phases, there are many processes/interactions involving natural colloids which are not understood at present.

### 3.1.4 Surface Coatings

The importance of surface coatings of HS has long been recognised in terms of the stability of colloids and prevention of aggregation [141,163], through the alteration of colloidal surface charges [164–167]. An important insight into the mechanism of colloidal stabilisation by NOM in natural waters (involving both electrostatic and steric repulsive forces) has also been gained recently through the measurement of interparticle forces using AFM [168,169]. The importance of HS coatings has also been widely regarded as an important mechanism of bacterial adhesion and biofilm formation. It has been shown to affect the binding of pesticides to inorganic surfaces [138]. In addition, it has been postulated as an important mechanism by which metals bind to colloids [18]. This coverage, if a general property of environmental surfaces indicates that surface complexation modelling depends primarily on the surface film on a colloid and this may not be related to its bulk chemical composition.

## 3.2 DISTRIBUTION COEFFICIENTS

Partitioning between an arbitrarily defined (usually retention by or permeation through a 0.45 µm pore-size filter) solution and a particulate phase has been commonly represented by distribution coefficients ( $K_D$ , expressed in  $\text{dm}^3 \text{ g}^{-1}$ ), which are defined as follows:

$$K_D = \frac{c_{M_p}}{c_{M_d}} \quad (1)$$

where  $c_{M_p}$  and  $c_{M_d}$  represent the total trace metal concentrations in the particulate and dissolved phases, respectively.

Literature values of  $K_D$  have been summarised [170–173]. It should be noted that these coefficients are not simple thermodynamic constants and in fact are the summation of reactions (or their equilibrium constants) of the many individual reactions occurring in each term, and often contain unrecognised terms of other phases due to the presence of colloidal ligands in the filter-passing phase ([56] and references therein). This often leads to what had been called the ‘particle concentration effect’ (p.c.e.) (Figure 5),

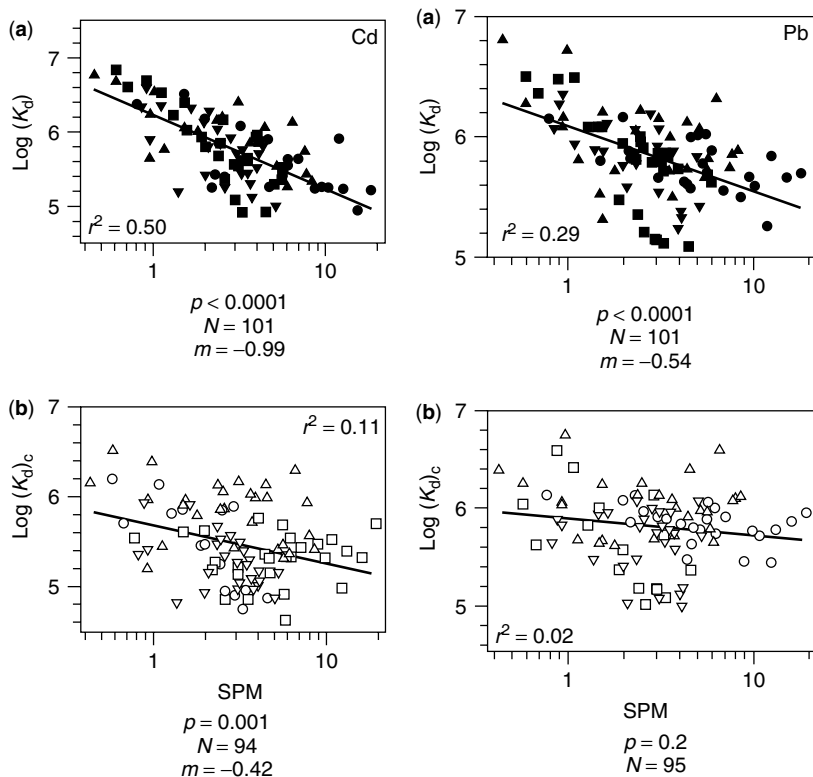


**Figure 5.** The particle concentration effect is clearly evident for the metals Cd and Pb when data are pooled from all sites. Nearly all individual sites also have statistically significant linear regressions for the log-normalised data. (b) Including colloidal forms of metals in the particulate metal fraction causes the slopes of the lines to flatten and the significance of the regressions to decline for Cd and Pb (according to the colloidal model, the slope of all the regression lines should become zero when plotted in this way). Reprinted from Benoit, G. and Rozan, T., The influence of size distribution on the particle concentration effect and trace metal partitioning in rivers, *Geochimica et Cosmochimica Acta*, **63**, 113–127, Copyright 1999, with permission from Elsevier

documented in both laboratory ([7,20,56,174,175] and references therein) and field experiments ([14,19,56,176–179] and references therein). In the field, trace elements in both the dissolved and particulate phases can be separated using filtration or sediment traps. Alternatively, the particulate phase may be collected from the environment and then re-suspended and spiked with known concentrations of metals in the laboratory. The dissolved and particulate fractions can then be separated and the trace element concentrations measured. Based on the discussion in the last section, it is likely that the laboratory and field investigations themselves may give different results, due to the nature of the binding groups investigated.

Despite their common use, distribution coefficients are operational values that are known to be dependent on many factors, including pH, ionic strength and the nature and quantity of ligand groups in both the solution and particulate phases.  $K_D$  values are

considered here because of their importance in the literature, their continued use [180], their use in transport models and the indirect evidence that they have provided to determine the importance of the colloidal phase (the particle concentration effect, see below). If  $K_D$  was a thermodynamic constant, one might expect clear trends with pH and the concentration of suspended particulate material. For instance, one would expect  $K_D$  to increase with increase in pH in the lower pH range [although not necessarily at higher pH due to competition between particles/colloids and solution ligands (*e.g.* carbonates)] and to be independent of the concentration of suspended matter. However, in practice, although  $K_D$  usually follows this trend with pH, a number of studies have shown the opposite relationship (summarised in [172]). In addition,  $K_D$  is usually seen to decrease with increase in the concentration of suspended matter, contrary to any thermodynamic prediction. This behaviour has generally been interpreted in terms of the ‘particle concentration effect’ [7]. This effect is due to the presence of complexing colloidal ligands in the filter-passing solution, and this has therefore been considered to be an experimental artefact of the filtration procedure utilised, but has led to useful insights into the role of colloids. Essentially, colloidal material and associated metals pass through the filter membrane and are included in the ‘dissolved’ phase. The concept of the particle concentration effect and its consequences have been reviewed for marine systems [7,181–183], but it has since been shown to also occur in freshwaters [178,179]. Additionally, it has been observed that under comparable conditions, values of  $K_D$  decrease in the order Pb > Zn > Cd > Cu [173]. However, according to known binding strengths of metal to colloids and particles [18,109,184], we might expect the order of  $K_D$  values to be Pb > Cu > Cd > Zn. The different order may be due to competition between colloids and particles, rather than between solution- and solid-phase material.

Although distribution coefficients have been useful in identifying the importance of colloids in dissolved phases, they provide no *direct* further information regarding the colloidal phase and its importance in trace metal binding [16] (Figure 5a, and b [179]) [178], and will add nothing further to our understanding of colloidal systems. Their determination should therefore be discontinued.

### 3.3 THE IMPORTANCE OF THE COLLOIDAL PHASE

The importance of the colloidal phase in binding elements in freshwaters has become recognised over the last decade or more and evidence has come from a number of studies. As mentioned earlier, reinterpretation of  $K_D$  values has provided only a single source of evidence. For instance, the recalculation of ‘true’ partition constants from literature distribution coefficients for Pb [178] indicated that the partition coefficient was greater than  $10^{7.4}$ , demonstrating that almost all Pb was associated with either colloids or particles. As mentioned earlier, based solely on geometric considerations, colloids are assumed to dominate binding because of their greater SSA and therefore potentially higher number of reactive functional groups [31,44]. Therefore, we expect a majority of Pb to be bound by the colloidal phase. This was illustrated by Lofts and Tipping [185], who indirectly showed the presence of iron oxide in the filtered (<0.45 µm) phase of UK river waters, by association of Pb with this oxide, as predicted by modelling of the overall Pb partitioning.

Direct evidence of the importance of colloidal binding has primarily come from filtration data experiments, often in the cross-flow mode (see Chapter 4), and initially used in

marine waters (see Section 4). An ultrafiltration step has been added to the initial filtration to give three fractions that are nominally defined as dissolved (trace elements in ultrafilter permeate), particulate (filter retentate) and colloidal (filter permeate; ultrafilter retentate). Other definitions of the three fractions were also made through the combination of the retentates and permeates of the different pore sizes in different ways. Several methods have been used to calculate the colloidal fractions [186] (summarised in Table 6). However, recent work [186] has shown that significant discrepancies may occur when calculating concentrations of Ca present in the dissolved, colloidal and particulate phases using different methods. Such discrepancies are likely due to anion rejection of the membrane [187] and/or  $\text{CaCO}_3$  precipitation upon warming of the sample in the laboratory. In addition, for trace elements, retention of material smaller than the nominal pore size and permeation of material larger than the material pore size may occur (see Chapter 4 and [34]). The ultrafiltration step is usually performed at 1–10 kDa. Although the lack of standardisation, along with well-known filtration artefacts (*e.g.* membrane clogging, selective membrane retention of molecules and ions) [6,187], make quantitative comparison difficult, it is clear that the colloidal fraction is significant in trace element binding (Table 1). In addition, other size-based separation schemes exist, based on SPLITT (see Chapter 5), field-flow fractionation (FFF, see Chapter 5) and centrifugation, or mixtures of these techniques [188].

**Table 6.** The main calculation methods for the concentration of the colloidal fraction. Reprinted from Dahlqvist, R., Benedetti, M. F., Andersson, K., Turner, D., Larsson, T., Stolpe, B. and Ingri, J., Association of calcium with colloidal particles and speciation of calcium in the Kalix and Amazon rivers, *Geochimica et Cosmochimica Acta*, **68**, 4059–4075, Copyright 2004, with permission from Elsevier

Method 1 (most common)	Colloidal fraction calculated total metal concentrations (determined using ICP-AES) from the 1 kDa retentate and permeate:  $[\text{colloidal}] = \frac{[\text{1 kDa retentate}]_{\text{ICP}} - [\text{1 kDa permeate}]_{\text{ICP}}}{CF}$ where $CF$ is the concentration factor $CF = \frac{\text{volume of retentate} + \text{volume of permeate}}{\text{volume of retentate}}$
Method 2	Colloidal fraction calculated using total metal concentrations from the 0.22 $\mu\text{m}$ permeate and the 1 kDa permeate solutions:  $[\text{colloidal}]_{1 \text{ kDa}-0.22 \mu\text{m}} = [< 0.22 \mu\text{m}]_{\text{ICP}} - [< 1 \text{kDa}]_{\text{ICP}}$
Method 3	Colloidal fraction calculated using both ICP-AES and ISE analyses in the same <0.22 $\mu\text{m}$ fraction:  $[\text{colloidal}]_{<0.22 \mu\text{m}} = [<0.22 \mu\text{m}]_{\text{ICP}} - [<0.22 \mu\text{m}]_{\text{ISE}}$
Method 4	Colloidal fraction calculated using ICP and ISE results from the 1 kDa and the 0.22 $\mu\text{m}$ retentate solutions:  $[\text{colloidal}]_{1 \text{ kDa}-0.22 \mu\text{m}} = \frac{[1 \text{ kDa retentate}]_{\text{ICP}} - [1 \text{ kDa retentate}]_{\text{ISE}}}{CF}$

### 3.4 PHASES AND MECHANISMS RESPONSIBLE FOR TRACE ELEMENT BINDING

Data described in the previous section do little to elucidate the mechanisms and phases responsible for trace metal complexation/sorption. A number of possible phases exist which may contribute to binding, including inorganic (hydrous oxides of Fe and Mn, Al and Si, carbonates, phosphates) and organic matter (HS, microbial exudates and debris and microbial cells). These phases contain metal binding ligands such as hydroxyl, carboxyl amino and thiol groups. Of these, materials such as carbonates appear not to be overly involved in trace element chemistry, possibly because of their low SSA [54]. Particular attention has been focused on several phases: Fe oxides, Mn oxides and HS. More recently, attention has also been focused on polysaccharide microbial exudates and whole cells [57,122–124]. In addition, sulfides and thiols may well be important phases constraining free metal ion concentrations, even in oxygenated waters [189–192].

A number of lines of evidence have been developed to infer the responsible phases and mechanisms of binding, of which data on pure phases were examined in Section 2. Chemical extractions have been used extensively [149,172,193], although primarily in the analysis of sediments rather than suspended material. In this method, specific extractants such as acidic oxalic acid and basic NaOH have been used to extract specific materials such as Fe oxyhydroxides and HS, respectively. Although operational, these extractions have provided a great deal of insight, once again indicating the importance of organic carbon and Fe and Mn phases. Hlavay *et al.* [194] found that for all metals studied (Cu, Zn, Pb, Ni, Cr, As), the majority was bound to a residual acid-soluble phase, but metals were also bound to organic matter and sulfur phases. Tessier *et al.* [149] provided circumstantial evidence for the association between common metals (Cd, Cu, Ni, Pb, Zn) and Mn and Fe oxyhydroxides in circumneutral waters and oxyhydroxides/organic matter in more acidic lakes. Lead *et al.* [193] used sequential extractions to gain insight into how spiked Cu and Cd interacted with fractionated colloids and particles. The Mn oxide phase dominated Cd binding whereas all phases affected Cu behaviour. However, it was found that sorption decreased with each successive extraction due to a loss of mass and was less influenced by the exposure of new binding sites. TEM images of the material remaining after successive extraction steps did not relate well to the nominal phases in the fractions. In particular, biological cells were lysed during the first step of the extraction procedure, resulting in the release of cellular material into the water samples. Such evidence indicates that the operational extraction steps do not relate well to the nominal phases dissolved.

Several studies have extracted suspended particulate matter (SPM) from freshwaters without further chemical treatments in order to perform controlled laboratory experiments investigating the effect of pH, competition between metals, metal to SPM ratio, reaction time, particle size and source [3,18,73,74]. Generally, very simple models (single binding site, no electrostatic component to binding) have been used to describe fairly successfully the observed behaviour. For instance, Ferreira *et al.* [74] used modelled values of  $-\log nK$  for riverine and estuarine SPM (roughly colloids and particles combined) and pure phases, where  $n$  is the concentration of suspended material (colloids and particles) and  $K$  is the exchange constant of the metal for a protonated site of the solid phase. Along with the estimated proportion of each phase in the SPM, Ferreira *et al.* [74] tentatively estimated  $\text{MnO}_2$  to be the primary binding phase for Cd and Pb, despite comprising only a few percent of natural SPM. Both  $\text{MnO}_2$  and HS were thought to be the most

likely binding phases of Cu and Zn. In addition, algae were considered to be important potential binding sites. In a similar study, Hamilton-Taylor *et al.* [3] studied the sorption behaviour of Cu, Pb and Cd in a eutrophic lake and concluded that Cu was likely dominated by HS binding, Zn by planktonic binding and Pb by binding to HS and hydrous Fe oxides. However, these assignments were tentative and dependent on conditions. Muller and Duffek [73] speculated to a lesser extent on the nature of binding sites, but found affinity constants that were very similar over a wide range of surface types and that were primarily metal dependent. This behaviour was ascribed to either the surface sites being relatively uniform, at least over small variations of the metal to SPM ratio, or to differences in binding site affinity being averaged out over the particle-size spectrum. However, this study was conducted at a single pH of 8. Although this has the advantage of making conditional constants comparable and reducing side reactions such as dissolution, it nonetheless limits the wider significance of the results. Lead *et al.* [18] measured Cu and Cd binding to size-fractionated SPM, by centrifugation, in the range 0.05–0.5, 0.5–1.0 and >1.0 µm. Differences in both metal affinity and in the affinity of each metal for a specific size varied. However, only small differences between the different size fractions were observed and these were significantly less than would be expected due to surface considerations alone. The authors explained the small variation in size as a consequence of complex morphology, porosity and surface films developed on the SPM surfaces. In these studies, the nature of the metal ion had a great effect on binding strength when compared with the nature of the surface, possibly due to an averaging of the site types on colloids and particles. Generally, binding strength decreased in the order Pb > Cu > Cd > Zn, although this is somewhat sample dependent (Table 7).

**Table 7.** Apparent surface complexation constants  $\log K_{\text{ads}}$  for  $\text{Zn}^{2+}$ ,  $\text{Pb}^{2+}$ ,  $\text{Cd}^{2+}$  and  $\text{Cu}^{2+}$  and various natural aquatic particles for the reaction  $\text{M}^{2+} + \equiv \text{L}-\text{H} = \equiv \text{L}-\text{M}^+ + \text{H}^+$ ; the type of particles is also given

$\text{Zn}^{2+}$	$\text{Pb}^{2+}$	$\text{Cd}^{2+}$	$\text{Cu}^{2+}$	Particles	Reference
0.29	1.50	0.40	1.68	Average of 12 different sites	[73]
-1.27 to -0.13	-0.57 to 0.57	-0.6 -1.960	1.3 0.24, 0.46 -0.766	Algae (lake) Bacteria River sediment	[135] [339] [340]
-1.3	-0.85	-1.5	-0.9	Estuary suspended matter	[341]
-4.09	-2.74 -4.94	-4.77 -6.22	-2.99 -5.57	River surface sediment Freshwater particles	[342] [3]
-6.0	-3.5 -3.0 -2.8 -4.3 -4.2 -4.6	-6.6 -6.9 -5.8 -4.2 -3.5 -3.8	-3.8 -4.6 -4.2 -3.9 -3.5 -3.8	River Trent Ouse estuary River Ouse River Mersey (0.05–0.5 µm) River Mersey (0.5–1.0 µm) River Mersey (>1.0 µm)	[74] [74] [74] [18] [18] [18]

A different approach to evaluate potential colloidal binding phases is the use of gel electric focusing or 2-D PAGE (polyacrylamide gel electrophoresis), which allows ligand separation according to its isoelectric point ( $\text{pH}_{\text{IEP}}$ ) and molecular mass. For example, Santschi *et al.* [57] found that colloidal plutonium extracted from Rocky Flats surficial soils (Colorado, USA) was essentially bound as Pu(IV) to a negatively charged organic macromolecule with a  $\text{pH}_{\text{IEP}}$  of  $\sim 3$  and a molar mass of 10–15 kDa, but containing some organically bound Fe colloids as well (Figure 6).

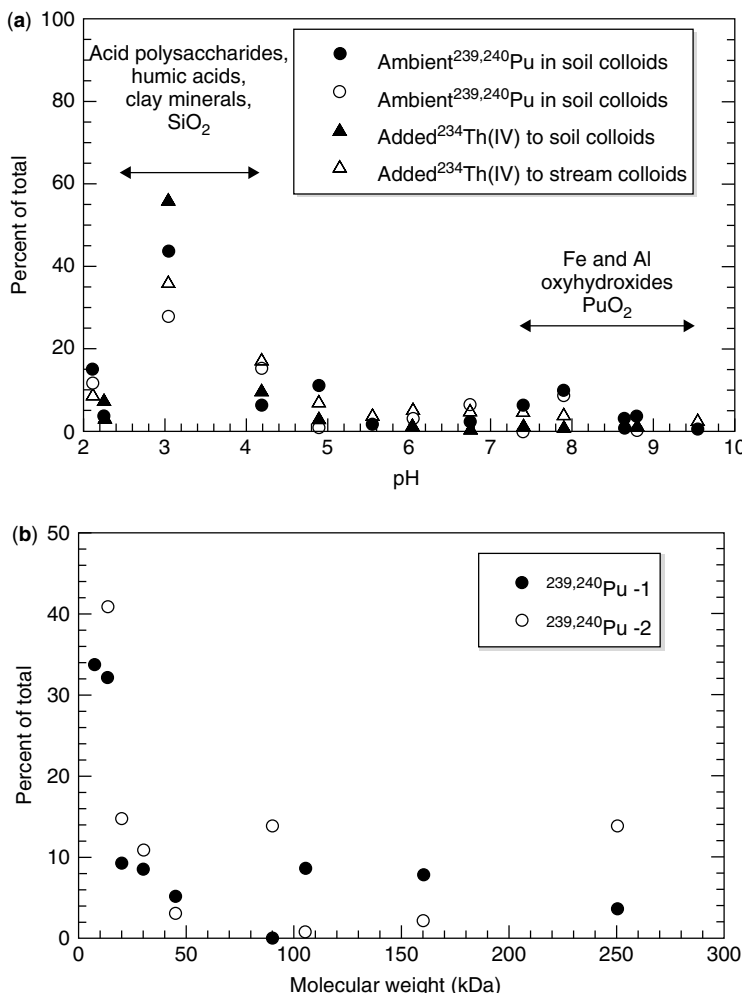
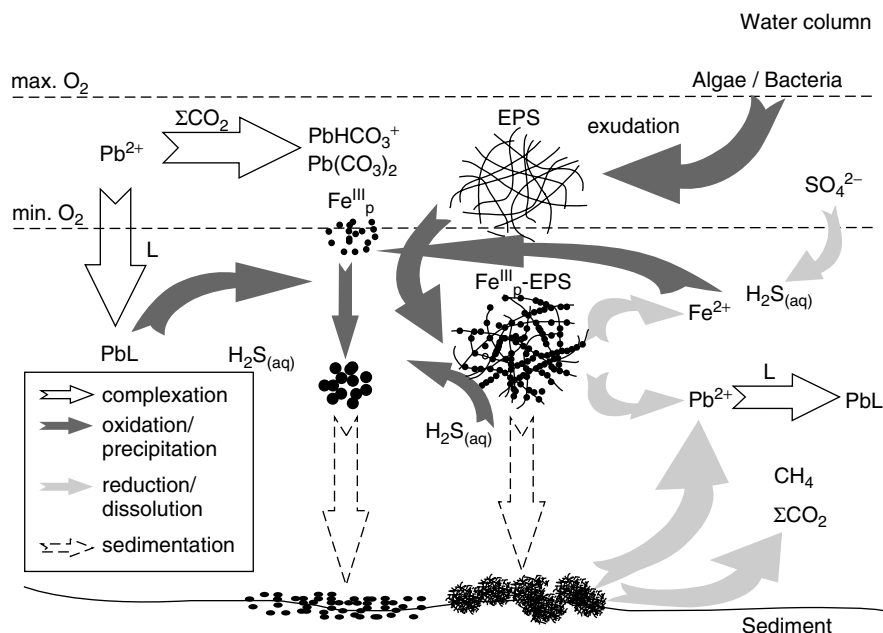


**Figure 6.** (a) Isoelectric focusing results showed that ambient colloidal  $^{239,240}\text{Pu}$  in the Rocky flats soil colloids followed more the  $^{14}\text{C}$  laws essentially associated with negatively charged organic matter. (b) The gradient SDS-PAGE electrophoresis results suggested that the organic macromolecule was of medium molar mass (i.e. 10–15 kDa). Reprinted in part with permission from Santschi, P. H., Roberts, K. A. and Guo, L., Organic nature of colloidal actinides transported in surface water environments, *Environmental Science and Technology*, **36**, 3711–3719. Copyright 2002 American Chemical Society

The studies mentioned above did not, however, include any rigorous attempts to model trace metal complexation with natural organic ligands in both solution and solid phases. However, the speciation models developed for specific phases (specifically HS, reported in Section 2) have been further developed and other simpler models applied to natural colloids and particles. Data from a study [74] were fitted to a much more complex model [72], which incorporated an ‘assemblage’ of Model V (Section 2.2) and various idealised hydrous oxides of Al, Mn, Fe, Si, colloidal HS and a cation exchanger. This additive model (assuming no interaction between components in the model), accounting for inorganic speciation in solution and competition among surfaces and among metals, indicated that Mn oxides were the dominant phase at low concentrations of free metal, whereas HS and Fe oxides were dominant at higher free metal concentrations. Although these are reasonable conclusions, which are comparable to previously mentioned data, it was noted that they were collected at high metal loadings and there are few values of constants for  $\text{MnO}_2$  available for modelling.

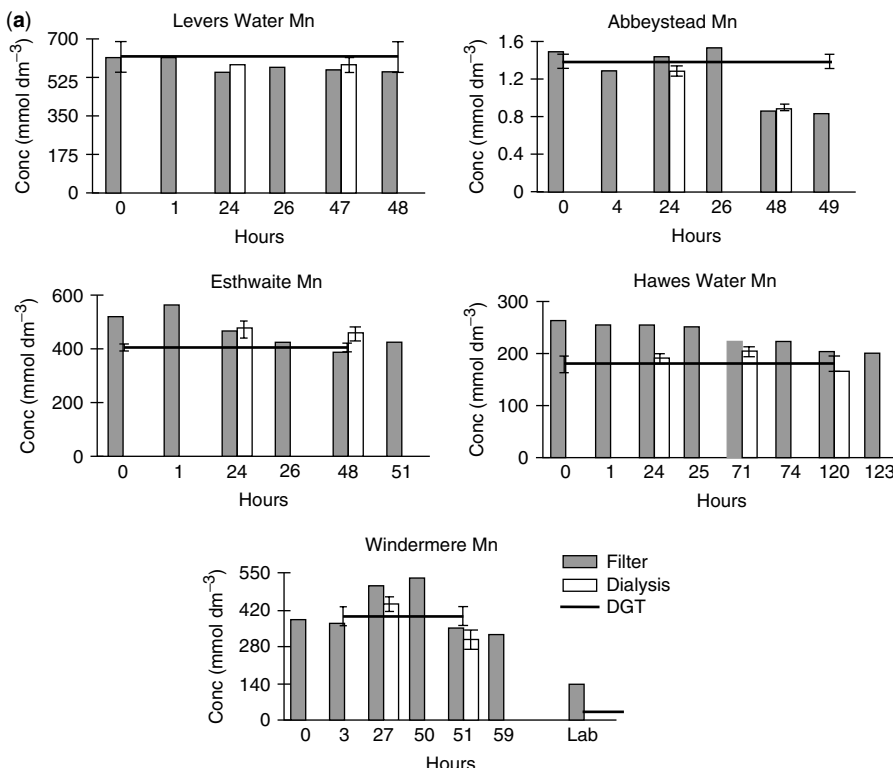
Ligand exchange reactions [195], usually coupled with adsorptive stripping voltammetry (AdSV, or sometimes referred to as cathodic stripping voltammetry, CSV) [196], and sometimes in comparison with other relevant methods [197,198], have been used to attempt to determine metal speciation. Generally, Cu and Ni have been found to be almost completely (>99.9%) complexed by organic matter [197,198]. Cd and Zn, although still dominated by organic complexation, were also present as the free (hydrated) metal ions [198,199]. Measurements of AdSV and diffusive gradients in thin films (DGT, considered later in this section) labile metal [198] gave values of labile complexes for Cu and Ni several orders of magnitude different, while widely spread values were also obtained for Cd and Zn. The differences may have been due to sample handling artefacts (DGT was performed *in situ* and AdSV in the laboratory), although the two techniques measure essentially different sets of complexes. Indeed, AdSV is a bulk equilibrium technique whereas DGT is dynamic, based on steady-state fluxes. Modelling of these AdSV data, as with similar studies in marine waters, has led to the hypothesis that certain unidentified strong ligands, probably of biological origin, are responsible for these strong metal complexes. To date, these ligands have not been identified unambiguously, although some progress has been made [200]. However, it has also been suggested that there is no need to invoke these strong ligands [151,161] and that data can be explained in terms of the different conditions (in particular the kinetic windows) at which measurements are made, the use of different techniques (i.e. with different analytical conditions and therefore different detection windows) and the heterogeneity of natural ligands. Certainly, modelling studies of HS have now included small concentrations of strong binding sites ([72]; Model VI), although their nature and importance are still unresolved.

A number of very recent studies have been performed using either *in situ* methods (DGT) or non-perturbing methods with minimal sample preparation [117,201,202]. These studies have indicated both the quantitative importance of the small, labile metal complexes [201–203] and the importance of the organics (HS and bacterial polysaccharide-rich microbial exudates), Fe oxyhydroxides and their associations in trace metal speciation [117,202]. Somewhat ambiguous results have been found for the speciation of Pb, which may be explained either by the results being technique dependent or due to real differences in the nature of the samples. However, in general, either Fe hydrous oxides or Fe–organic associations were indicated as the dominating binding phases. Taillefert



**Figure 7.** Schematic diagram of the Pb cycling in Paul Lake (MI, USA). Reprinted from Taillefert, M., Lienemann, C. P., Gaillard, J. F. and Perret, D., Speciation, reactivity, and cycling of Fe and Pb in a meromictic lake, *Geochimica et Cosmochimica Acta*, **64**, 169–183, Copyright 2000, with permission from Elsevier

*et al.* [204] showed that Pb in a small, stratified lake was primarily bound to organic material, probably EPS, although colloidal Fe was probably contained within the same complex or aggregate (Figure 7). Allard *et al.* [117] have also found substantial interactions between organic carbon and Fe oxide phases in the Amazon river and tributaries. However, Lyven *et al.* [205] examined colloids in the River Kalix (Sweden) by FIFFF (see Chapter 5) and found that organic carbon colloids (ca 1 nm) and Fe-based colloids (ca 5 nm) were the two major phases for trace element transport (see Figure 16 in Chapter 5). Whereas most metals were correlated with organic carbon or distributed between carbon and Fe phases, Pb was primarily associated with the Fe phase only. In fact, mass balance calculations demonstrated that the majority of metals (>80% in most cases) were associated with these small colloids. This study was in agreement with another paper [201] which compared cross-flow filtration (CFF) (see Chapter 4) and FIFFF. Substantially smaller sizes of Fe species were measured by FIFFF compared with CFF. More precisely, the colloidal fraction, as measured by CFF (1 nm–0.45 µm), was found to reside primarily in the size range of a few nanometres. Gimpel *et al.* [202] used DGT with other techniques to examine metal speciation and the influence of colloids. DGT is one of the very few methods that can be used to infer metal speciation *in situ* without a sampling step. In a study of freshwater lakes situated in the Lake District (UK), Gimpel *et al.* [202] compared DGT with filtration and dialysis. No significant differences were revealed in acidic lake waters or for Mn (Figure 8a), indicating a lack of colloid complexation. However, differences were significant for Fe, Cu, and Zn in circumneutral lakes

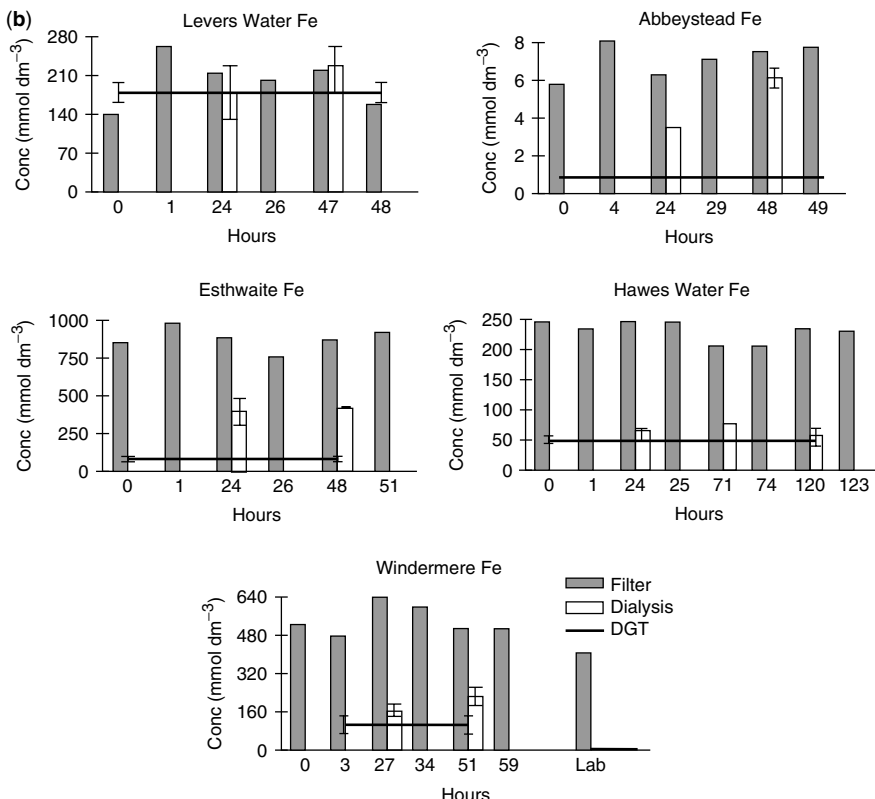
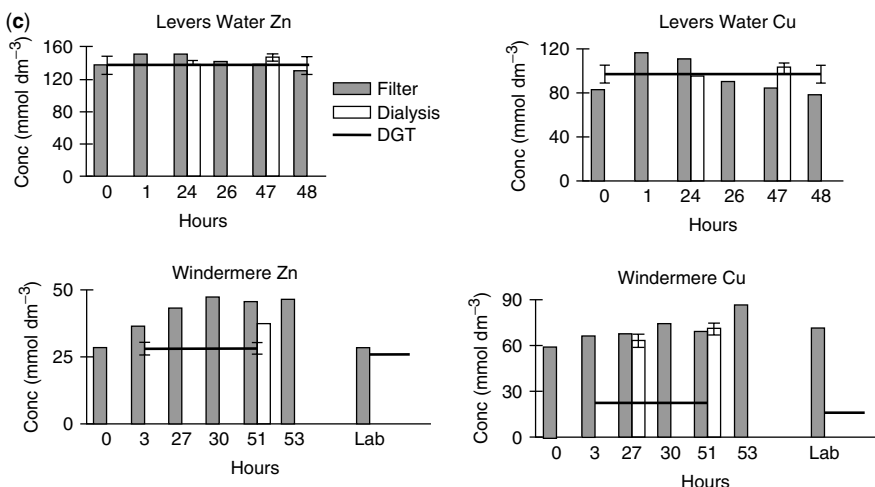


**Figure 8.** Concentrations of (a) Mn and (b) Fe in five lakes measured *in situ* by DGT (line for whole deployment time), dialysis (bar represent time on retrieval), and filtration (bar represents time at sampling). (c) Concentrations of Cu and Zn in two lakes measured by DGT (48-h deployment) (line for whole deployment time), dialysis (bar represent time on retrieval), and filtration (bar represents time at sampling). In each case, an additional DGT (36-h deployment) and filtration measurement was made on a sample of Windermere water returned to the laboratory. All filtration bars are for single measurements. Error symbols give the standard deviation from eight DGT devices and two dialysis units. Reprinted with permission from Gimpel, J., Zhang, H., Davison, W. and Edwards, A. C. (2003), *In situ* trace metal speciation in lake surface waters using DGT, dialysis and filtration, *Environ. Sci. Technol.*, **37**, 138–146. Copyright 2003 American Chemical Society

(Figure 8b and c). Again, the implications are that metals are in general quantitatively bound to the most labile and mobile colloids.

#### 4 INTERACTIONS BETWEEN TRACE METALS AND COLLOIDS IN MARINE AND ESTUARINE ENVIRONMENTS

Whereas there are a number of authoritative reviews of trace metal speciation in the ocean (*e.g.* [206–208]) and/or of the role of colloidal organic carbon, phytoplankton exudates and interfacial processes in the oceanic carbon cycle [209–211], there are only a few reviews on colloidal trace metals in marine environments [212]. Our review will extend and update older reviews, and will focus on more recent developments in the field. It will

**Figure 8.** (continued)**Figure 8.** (continued)

also make use of concepts developed in other fields such as biology, environmental science and engineering and food science. The review is organised around pertinent questions one might ask about trace metal association with marine colloids.

The marine colloidal pool contains biologically resistant heteropolycondensates such as humic-type molecules that act as soaps, surfactants and dispersants [213], and products of carbon fixation and consumption such as exopolymeric substances (EPS) that act as glues, biosurfactants bioemulsifiers and coagulants [214]. The surface-active, glue-like biopolymers also contain strong metal-binding ligand groups. Therefore, colloids in the ocean may act as agents of metal removal and of solubilisation, depending on the biomolecule, and as modifiers of metal bioavailability. In addition to questions of metal bioavailability, marine colloids are also important in their response to global change, as they provide one of the conveyor belts of global carbon cycling, as most of the organic matter in the ocean is in the dissolved state, and 20–30% of the marine dissolved organic matter (DOC) is colloidal in nature and subject to rapid turnover ([19,176,177,215] and references therein).

There are many potential binding sites in aquatic biomacromolecules, with most of them occupied by major seawater cations, not trace metals. Binding sites include carboxyl, hydroxyl, phosphate, sulfate, amino and sulfhydryl groups, with hard metal ions preferring O rather than N and S binding sites, and soft metal ions preferring S (or N) rather than O binding sites [30,216]. Although many of these sites are not exceptionally strong when acting alone, the particular steric environment of the macromolecule can provide strongly chelating binding sites for trace metals when acting in concert. For example, in the ‘egg-box’ chelating environment [217–219],  $\text{Ca}^{2+}$  is known to stabilise the  $\alpha$ -helix of alginic acid, and can, in part, be exchanged for trace metals. It has become evident in recent years that colloid–metal associations can be attributed to specific and strong metal complexation rather than non-specific metal sorption to colloidal surfaces. Also, one would expect to find metal enrichments to follow the Irving–Williams series for stability constants of transition metal complexes, which has indeed been documented for marine colloids [220] and for bacterial EPS [221].

One of the functions of major cations (*e.g.*  $\text{Ca}^{2+}$ ) is thus to hold together macro-molecular aggregates at external sites of flexible (*e.g.* HS) and rigid (*e.g.* exopolymers) biopolymers at internal helical sites. Even  $1 \times 1000$  nm fibrillar EPS biopolymers [222] have internal sites that can be occupied by trace metals, which contradicts the chemcentric view of Gustafsson and Gschwend [29], which states that rigid linear biopolymers such as the fibrillar EPS colloids should not be classified as true colloids, as they would not contain microenvironments with non-aqueous behaviour. However, since fibrils obtain their rigidity through  $\text{Ca}^{2+}$  binding of double  $\alpha$ -helical regions, with  $\text{Ca}^{2+}$  being exchangeable by other hard metal ions, they do have internal sites that are sterically very different from the external sites. Because much more is known about biopolymers such as acid polysaccharides (APS) that are used in food science or biomedical science, where they are used as emulsifiers, stabilisers and coagulants (or anticoagulants) through their amphiphilic properties, the concepts and approaches in these scientific disciplines may become very useful here. APS include alginates, carrageenans or hyaluronic acids, which contain building blocks that are also found in marine colloids and transparent exopolymeric particles (TEP) [223,224]. It may therefore be possible to apply knowledge from these scientific disciplines to the biomolecular complexants in the marine colloidal pool, which are not as well studied. The physicochemical properties of EPS molecules are important, as they

can provide ‘hideouts’ for micronutrients such as trace metals. These EPS molecules contain not only APS, but also proteins or lipids, which make the molecules amphiphilic (or amphiphatic). The amphiphilicity is caused by the generally hydrophilic properties of their acid polysaccharidic regions, while their more hydrophobic properties are due to the protein or lipid-rich regions [225]. Many of these EPS biopolymers also form gels and, as a result, are hydrocolloids. It is still unclear if strong binding sites in marine colloids are really metal specific or if apparent metal specificity is due to sheltering effects at interior sites due to aggregate binding (*e.g.* HS) or stabilisation of a helical structure (*e.g.* EPS).

TEP-like biopolymers may not only control the scavenging of metals and radionuclides and the coagulation/flocculation of particles in marine systems [57,226], but also facilitate the early development of biofilms [227], which is largely due to their surface-active nature. TEP can also initiate or modify precipitation of MnO<sub>2</sub> and FeOOH [228], SiO<sub>2</sub> [229] and CaCO<sub>3</sub> [230]. Moreover, acid polysaccharide-rich particles function in the extracellular milieu not only by forming flocs [231,232], but also by binding extracellular enzymes in their active forms. This enzymatic activity allows trace metal binding [226,233,234] and modifies the solubility of associated molecules [227,235].

In order to minimise potential artefacts, experimental approaches in laboratory studies of trace metal complexation to macromolecular ligands have often used low-pH conditions or high metal ion concentrations, for instance in laboratory titration studies of hard metal ions (*e.g.* Th(IV) [236–238]). These approaches might this not be directly relevant to marine systems. Studies at low, near-ambient concentrations under seawater conditions, apart from colloidal fraction determinations using ultrafiltration techniques (see Chapter 4), are much rarer.

#### 4.1 COLLOIDAL TRACE METALS AND LIGANDS: CONCENTRATIONS, STABILITY AND SIGNIFICANCE FOR SOLUTION-PHASE SPECIATION

There is a large amount of information from trace metal studies, which use microbial cultures and isolated exopolymeric ligands excreted by marine organisms, where large binding capacities for trace metals have been documented. For example, the surfactant and micellar nature of HS has been addressed [213], and the biosurfactant nature of EPS has also been covered [214]. Adsorption densities of metals in exopolymers can reach 2–25% of their mass as metal ions such as Cu, Cd, Co, Ni and Pb, as summarised and reviewed previously [223].

Most observations of colloidal associations of trace metals utilised cross-flow ultrafiltration (CFUF) and a few applied FIFFF techniques [239–241]. However, because of unaccounted for blanks, questions about incomplete mass balance, sorption losses, actual versus nominal molar mass cut-off membrane and sub-optimal concentration factors, published results can still contain experimental artefacts and outdated concepts. For example, reported results on colloidal fractions of metals and radionuclides in different oceanographic environments, summarised by Wells [212] and in Chapter 4 of this volume, often range between nearly 0 and nearly 100% for the same metal. Therefore, a more rigorous approach is needed to sort through the different observations using different experimental approaches, separation techniques, ultrafiltration membranes and cleaning techniques.

Although observed differences in colloidal partitioning for a given metal are obvious, differences in sampling protocols, even when using the same type of membrane with the same pore size, can make data comparison misleading. For example, <sup>234</sup>Th is a widely used

radionuclide tracer for studying POC fluxes and trace element scavenging in the ocean. Reported colloidal fractions of  $^{234}\text{Th}$  in the total dissolved (<0.2, 0.4 or 0.45  $\mu\text{m}$ ) fraction range from 0.04% in the Gulf of Maine to 75–78% in the Gulf of Mexico and in the Bedford Basin (see Chapter 4). Another example is from Dai *et al.* [242], who reported a colloidal  $^{234}\text{Th}$  (>1 kDa) of 4–16% in the Atlantic, off Bermuda, which is as low as the >10 kDa fraction reported in the same area [243], whereas Guo *et al.* [25] reported up to  $47 \pm 12\%$  for the same fraction in the Middle Atlantic Bight. The percentage of colloidal Cu (*e.g.* >1 kDa fraction), on the other hand, varied from ~0 to >60% in the Pacific seawater off Hawaii (see Chapter 4). In addition, the percentages of colloidal Zn in the total dissolved fraction also differ considerably between reported data sets. For example, colloidal Zn was <10% in Narragansett Bay and >90% in Galveston Bay (Chapter 4 and references therein). As is obvious from these comparisons, the colloidal data and large differences between different studies are likely beyond those expected from natural variability. Clearly, sampling protocols and procedural artefacts must be partly responsible for these variations.

However, there also seems to be almost as much variability in colloidal fractions of trace metals at one particular location in a given investigator's study (*e.g.* [244,245]) as across studies from different investigators, suggesting that in addition to procedural problems, sources, residence times, seasonal differences, *etc.*, all contribute to the variability in published results on colloidal associations of trace metals. Despite such a variability, one consistent trend appears in datasets with well-calibrated ultrafiltration systems: a significant correlation between the percentage of colloidal metals (*e.g.* Ag, Cu, Th) and percentage of colloidal DOC (*i.e.* COC; reviewed previously [19,151,183]) or colloidal trace-metal binding ligands (*e.g.* [246]). Furthermore, even though there are many more observations from coastal zones than from the open ocean, it appears that the proportions of colloid-associated trace metals generally decrease from riverine-dominated regions of estuaries to the open ocean (*e.g.* [13,247]). That the role of marine colloids in trace metal speciation is greatest in estuarine and coastal marine environments would be expected, as their surface-active nature results in short turnover times compared with other reaction and transport rates.

Diafiltering and desalting eliminate about 50% of the Cu, 64% of the Zn, 68% of the Ni and 91% of the Pb in the colloidal fraction [220]. The lower trace metal contents of isolated colloids confirm the contention of other work [187,248] that entrainment effects of low molecular mass molecules into the retained colloidal fraction caused by concentration polarisation effects can be a major procedural artefact. The entrainment process mostly affects molecules that have similar molar masses and sizes to the size cutoff of the ultrafiltration membranes. Other potential artifacts include membrane molar mass cut-offs that are different than those specified by the manufacturer (see Chapter 4). In a comprehensive study of marine colloids from three marine environments (Galveston Bay, the Gulf of Mexico and the Middle Atlantic Bight), Guo *et al.* [220] characterised the organic carbon and metal contents of diafiltered, freeze-dried colloidal isolates (Tables 8–10). Bioactive metals such as Cu, Zn, Ni and Fe had average concentrations greater than  $10 \mu\text{g g}^{-1}$ , Pb, Al, Mn, V, Ba and Ti between 1 and  $10 \mu\text{g g}^{-1}$  and Cd, Co and Be  $\leq 1 \mu\text{g g}^{-1}$  colloidal mass (Table 8). In most cases, the average colloidal metal concentrations were higher in the Middle Atlantic Bight than in the Gulf of Mexico, suggesting higher terrestrial and aerosol inputs to the North Atlantic Ocean. Most importantly, colloids had a metal composition and metal/OC ratio (M/C) similar to HS and marine plankton (Table 9), indicating

**Table 8.** Comparison of average trace metal concentrations in marine colloids. Reprinted from Guo, L., Santschi, P. H., and Warnken, K.W., Trace metal composition of colloidal material in estuarine and marine environments, *Marine Chemistry*, **70**, 257–275, Copyright 2000, with permission from Elsevier

Metal	Concentration/ $\mu\text{g g}^{-1}$ <sup>a,b</sup>			
	Galveston Bay (this study)	Galveston Bay (Benoit <i>et al.</i> , 1994)	Chesapeake Bay (Sigleo and Helz 1981)	Middle Atlantic Bight (this study)
Al	17 ± 16	$(3\text{--}56) \times 10^3$	$(3.6\text{--}1.40) \times 10^3$	7.8 ± 3.6
Fe	$(3 \pm 2) \times 10^2$	$(3\text{--}24) \times 10^3$	$(3.4\text{--}71) \times 10^3$	539 ± 807
Mn	5.1 ± 3.4	80–145	125–10190	5.1 ± 3.7
Cu	47 ± 18	13–33	—	13 ± 4
Pb	0.47 ± 0.26	29–69	—	2.7 ± 2.6
Zn	19 ± 8	270–650	—	16 ± 7
Cd	0.19 ± 0.05	—	—	0.82 ± 0.76
Co	2.5 ± 12	—	3.4–116	0.65 ± 0.32
Ni	28 ± 14	—	—	34 ± 32
Cr	18 ± 8	—	—	128 ± 165
V	2.5 ± 2.1	—	—	1.9 ± 2.6
Ba	26 ± 44	—	45–1290	1.2 ± 0.8

<sup>a</sup> —, Not measured. <sup>b</sup> For the references cited, see the original paper.

that marine colloids largely originate from planktonic sources. The M/C ratios of Galveston Bay estuarine colloids with riverine metal and DOC sources followed the sequence Cu > Ni, Cr, Zn > Mn > Co > Pb, Cd, which is similar to the Irving–Williams order except for Mn, suggesting that the interaction of metals with organic colloids is determined by the affinity of metals for specific ligands. A few metals (*e.g.* Th, Fe, Cu) for which significant literature is available are discussed below.

#### 4.1.1 Thorium

Thorium, a tetravalent ion, forms polyhydroxy colloidal complexes in organic-free solutions, but also forms strong complexes with humic acids [249] and with acid polysaccharides [233] (Figure 9), and is one of the elements that generally shows very high colloidal fractions in marine environments [25]. Indeed, the observed particle–water partitioning of colloids or pure polysaccharide fractions in marine environments was described by partitioning coefficients [233]. Hirose *et al.* [236] reported a thorium complexation capacity (ThCC) or Th(IV) binding ligand concentration of 25 nmol dm<sup>-3</sup> in suspended particles of the surface ocean, ~0.3 nmol dm<sup>-3</sup> in the deep ocean and in the filtrate, of ~3–4 nmol dm<sup>-3</sup> in surface waters and ~2–3 nmol dm<sup>-3</sup> in deep waters of the Pacific, [250]. The concentration of the relatively strong organic ligands for Th(IV) is thus about three orders of magnitude higher in the ocean than that of colloidal or particulate Th [238] (Figure 10), which occurs at concentrations of 0.1–1.5 pmol dm<sup>-3</sup> [176,251]. On the other hand, the Th(IV)-binding ligand concentration is present at only about 2–5% of the total organic carbon concentration in the colloidal or particulate phases. For example, given that the COC concentration in the ocean is about 15 μmol dm<sup>-3</sup> in surface

**Table 9.** Comparison of average metal/aluminium (M/Al) atomic ratios between marine colloids, average soil, upper crust, humic substances, marine plankton and Galveston Bay suspended particles. Reprinted from Guo, L., Santschi, P. H., and Warnken, K.W., Trace metal composition of colloidal material in estuarine and marine environments, *Marine Chemistry*, **70**, 257–275, Copyright 2000, with permission from Elsevier

Element	Me/Al concentration ratio <sup>a,b</sup>					
	Galv Bay colloids	GOM colloids	MAB colloids	Average solids	Upper crust	Humic substance
Cu	2.1 ± 1.9	1.2 ± 1.1	0.82 ± 0.32	0.00018	0.000078	0.06–0.29
Pb	0.0058 ± 0.0036	0.07 ± 0.08	0.043 ± 0.031	0.000033	0.000029	0.001–0.003
Zn	0.77 ± 0.57	1.2 ± 1.0	0.85 ± 0.16	0.00052	0.00028	0.014–0.14
Cd	0.0054 ± 0.005	0.0086 ± 0.0094	0.026 ± 0.024	0.000001	<0.000001	0.00023–0.0004
Co	0.10 ± 0.07	0.05 ± 0.04	0.043 ± 0.02	0.000058	0.000069	—
Ni	1.21 ± 1.12	1.03 ± 1.07	1.92 ± 0.99	0.00032	0.00011	0.019
Cr	0.93 ± 0.72	1.59 ± 1.16	7.8 ± 6.2	0.00051	0.00023	0.03
Be	0.04 ± 0.03	0.05 ± 0.05	0.50 ± 0.54	0.000035	0.0001	—
Fe	13.9 ± 10.7	14.2 ± 13.5	27.7 ± 27.8	0.27	0.19	7.1
Mn	0.20 ± 0.13	0.15 ± 0.18	0.29 ± 0.15	0.0038	0.0033	—
V	0.13 ± 0.11	0.12 ± 0.11	0.12 ± 0.09	0.00067	0.00036	—
Ba	0.40 ± 0.68	0.018 ± 0.01	0.033 ± 0.02	0.00138	0.0016	0.00012
Ti	0.35 ± 0.21	0.86 ± 0.74	0.80 ± 0.59	0.039	0.022	0.033

<sup>a</sup> Me/Al atomic ratios are calculated from metal concentrations in the average soils (Bowen, 1966), upper continental crust (Wedepohl, 1995), humic solutes (Raspor *et al.*, 1984; Degens, 1965; Taylor and Garbarino, 1995), marine plant material (Bowen, 1966; Martin and Knauer, 1973), and suspended particles (Wen, 1996). For the references cited, see the original paper. <sup>b</sup> GOM, Gulf of Mexico; MAB, Middle Atlantic Bight; GB, Galveston Bay.

**Table 10.** Colloidal M/C atomic ratios ( $\times 10^5$ ) in marine environments compared with those of continental crust, humic substances, marine plankton and suspended particles. Reprinted from Guo, L., Santschi, P. H., and Warnken, K.W., Trace metal composition of colloidal material in estuarine and marine environments, *Marine Chemistry*, **70**, 257–275, Copyright 2000, with permission from Elsevier

Element	Me/C atomic ratio <sup>a</sup>						
	Galveston Bay colloids	Gulf of Mexico colloids	MAB colloids	Continental crust	Suspended particles	Humic substances	Marine plants
Cu	49 ± 1.1	1.93 ± 0.40	2.5 ± 1.9	13	38	10	0.61
Pb	0.016 ± 0.006	0.078 ± 0.03	0.11 ± 0.09	4.7	4.1	0.19	0.14
Zn	2.0 ± 0.7	8.8 ± 6.7	2.8 ± 2.6	45	92	2.9	8.1
Cd	0.014 ± 0.007	0.013 ± 0.008	0.059 ± 0.052	0.05	0.26	0.034	0.063
Co	0.28 ± 0.07	0.083 ± 0.053	0.12 ± 0.10	11	8.2	—	0.042
Ni	2.9 ± 0.7	1.6 ± 1.0	5.5 ± 4.3	18	36	0.29	0.18
Cr	2.7 ± 1.8	2.6 ± 1.1	20 ± 24	38	—	0.46	0.068
Be	0.14 ± 0.08	0.095 ± 0.032	1.2 ± 1.3	20	—	—	—
Fe	41 ± 32	22 ± 9	82 ± 11	$3.2 \times 10^4$	$2.7 \times 10^4$	107	44
Al	4.2 ± 3.6	2.8 ± 2.5	3.3 ± 2.6	$1.6 \times 10^5$	$8.4 \times 10^4$	145	7.8
Mn	0.62 ± 0.3	0.23 ± 0.18	1.1 ± 1.2	$1.4 \times 10^4$	$4.6 \times 10^2$	—	3.4
V	0.35 ± 0.31	0.26 ± 0.31	0.34 ± 0.39	59	—	—	0.14
Ba	1.2 ± 2.3	0.031 ± 0.014	0.084 ± 0.050	$2.8 \times 10^2$	—	0.0017	0.77
Ti	1.0 ± 0.4	1.3 ± 0.1	1.6 ± 0.2	$3.7 \times 10^3$	—	0.50	3.5

<sup>a</sup> Me/C ratios ( $\times 10^5$ , or numbers of metal atoms in every 100 000 OC atoms) are calculated for the upper continental crust from data of Wedepohl (1995), for humic substances from Degens (1965), Raspor *et al.* (1984), and Taylor and Garbarino (1995); for marine plants from Bowen (1966) or Martin and Knauer (1973); and for suspended particles from Martin and Windom (1991). For the references cited, see the original paper.

waters and 8  $\mu\text{mol dm}^{-3}$  in deep waters [252], and particulate organic matter (POC) about 10  $\mu\text{mol dm}^{-3}$  in surface waters and 0.5  $\mu\text{mol dm}^{-3}$  in deep waters [250], this gives ratios of 3 nmol colloidal ligand/15  $\mu\text{mol C}$  = 0.2 mmol ligand/mol C in the surface ocean, 3 nmol colloidal ligand/8  $\mu\text{mol C}$  = 0.4 mmol ligand/mol C in the deep ocean, 5 nmol particulate ligand/10  $\mu\text{mol dm}^{-3}$  C POC = 0.5 mmol ligand/mol C in the surface ocean, 0.3 nmol  $\text{dm}^{-3}$  particulate ligand/0.5  $\mu\text{mol dm}^{-3}$  C in deep waters = 0.5 mmol ligand/mol C in deep waters, or uniformly 0.2–0.5 mmol ligand/mol C. These ratios are similar to those determined directly for bacteria [237], where they are directly proportional to the SSA to volume ratios of the organisms. If the ligand is an acid polysaccharide-like molecule with about 1 meq  $\text{g}^{-1}$  ≈ 12 meq/mol C of carboxylic acid groups, this would result in about 2–5% of the colloidal OC belonging to the Th(IV)-binding macromolecular ligand. In agreement with this assessment, Alvarado-Quiroz [253] obtained directly a 1–2% yield during the 2D-PAGE separation isolation for the Th(IV)-binding ligand that was first separated using alcohol precipitation from a number of cultured microorganisms.

Ligands other than carboxylic groups, *e.g.* phosphate and sulfur, probably also contribute to binding of Th(IV) [233,234,253]. The observation of two or three functional groups coinciding with the Th(IV) peak in laboratory systems with COM and EPS harvested from marine phytoplankton and bacteria, in addition to the variability in molecular masses of the Th(IV)-binding ligand in the isoelectric focusing system [253], makes it likely that a family of clustered chelating ligands exist with varying molar mass and functional groups. However, more work still needs to be carried out to obtain structural information on these novel macromolecular ligands.

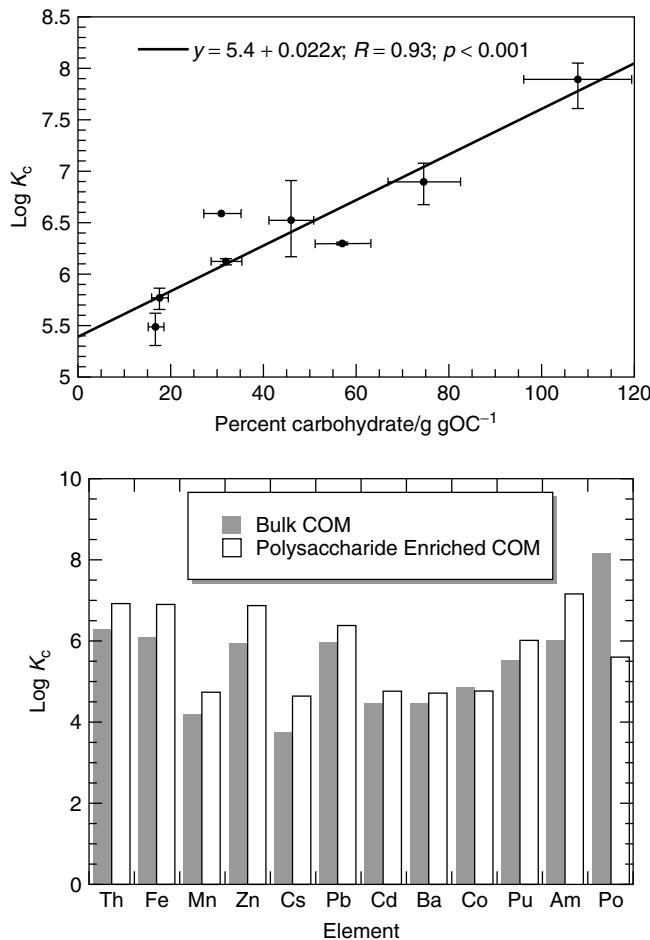


**Figure 9.** This figure [233] shows an enhanced partitioning of Th(IV) to marine colloids, in proportion to the polysaccharide content. Many other metals, except Po, which behaves more like a sulfur analogue, also show enhanced partitioning (COM stands for colloidal organic matter, OC for organic carbon and  $K_c$  for colloid/water partition coefficient, in  $\text{dm}^3 \text{kg}^{-1}$ ). Reproduced with permission from the American Society of Limnology and Oceanography

Given the similar ionic radii of Th(IV) and Ca(II) [119 pm for Th(IV), 126 pm for Ca(II) at 8-fold coordination; 108 pm for Th(IV), 114 pm for Ca(II) at 6-fold coordination], it is possible that Th(IV) exchanges for Ca(II) in the egg-box coordination environment. Other possibilities might include exchange for Mg(II) in the ATP and DNA coordination environment, where Mg(II) and Ca(II), and also other metal ions, can play a critical role in stabilising the conformation [256,257].

#### 4.1.2 Iron

The biogeochemistry, i.e. bioavailability and bioaccumulation, distributions, sources, analytical methods and thermodynamics, of the Fe system in the ocean has been reviewed

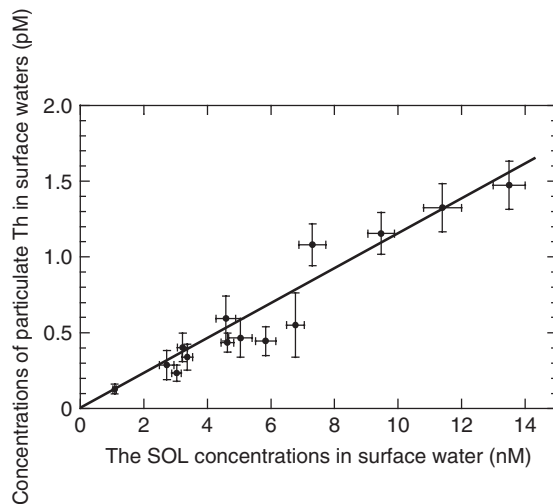


**Figure 10.** Correlation between particulate  $^{232}\text{Th}$  concentrations and strong organic ligand concentrations in the Pacific Ocean. Reproduced from [238] with permission from Professor K. Hirose

by Turner and Hunter [258], and the following review will be more focused on the importance and role of colloidal Fe in marine systems. The colloidal fraction of Fe is considerable, ranging from 10 to 50% in the North Atlantic, North Pacific and equatorial Pacific [212,259,260]. The solubility of Fe(III) in 0.7 mol  $\text{dm}^{-3}$  NaCl is 0.01 nmol  $\text{dm}^{-3}$  [261,262], whereas in DOC-free seawater at 25 °C, extrapolated from concentrations as a function of DOC concentrations, the Fe(III) solubility, as defined by Fe(III) found in the <3 kDa fraction, is 0.02 nmol  $\text{dm}^{-3}$  [263], close to that in 0.7 mol  $\text{dm}^{-3}$  NaCl [262]. The solubility of Fe(III) in oxic seawater, calculated by Millero *et al.* [264] for hydrous ferric oxide [ $\text{Fe(OH)}_3$ ], goethite and hematite ( $\text{Fe}_2\text{O}_3$ ) are 12, 0.38 and 0.22 nmol  $\text{dm}^{-3}$  at 25 °C, respectively, is, however, substantially higher, probably due to unrecognised colloidal fractions. This strongly suggests that the majority of the 0.5  $\mu\text{m}$  filter-passing Fe is bound to organic ligands [263,265–267]. Iron solubility not only increases with increasing DOC and exudate concentrations [263] or humic acid concentrations [261], but also with the concentration of heterotrophic bacteria and with humic-type fluorescence intensity [268]. In contrast to freshwater [204,205,269] and estuarine and coastal systems [13,270], most of the iron contained in organic ligands in open ocean settings is lower molecular (*e.g.* <10 kDa) [263,267], with the concentrations of total organic ligands being 0.16–0.93 and 0.36–0.96 nmol  $\text{dm}^{-3}$  for the <3 kDa and <10 kDa fractions, respectively [263].

#### 4.1.3 Copper

Copper is a typical soft metal, with Cu(I) having a high binding affinity to thiolic ligands such as phytochelatins, metallothioneins and some siderophores. Cu(II) is believed to be reduced to Cu(I) during complexation reactions with sulphydryl ligands [271]. The highest values of stability constants were obtained for colloidal ligands in Galveston Bay [190], and Cu concentrations were closely correlated with glutathione and the sum

of Cu, Ni, and Zn concentrations with total reduced sulfur concentrations, suggesting complexation to reduced sulfur moieties. High stability constants have also been reported for colloidal ligands in coastal environments in England [244–246]. Interestingly, and contrary to accepted dogma, one does not necessarily need aquagenic ligands produced by microorganisms to obtain strong ligands. Strong Cu-binding behaviour has also been documented for terrestrial HS in seawater, which are, according to our definition, colloidal [272]. However, Cu speciation is probably not dominated by colloidal ligands in the open ocean. Owing to their surface-active nature, they are likely removed by coagulation. Indeed, Cu was suggested to be bound by low molar mass ligands [255,271,273–277], whereas colloidal Cu concentration of  $9 \text{ nmol dm}^{-3}$ , representing 63% of the total  $0.4 \mu\text{m}$  filter-passing Cu, was reported for Pacific waters off Hawaii [278]. The discrepancy might be readily explained by the observations made by Guo *et al.* [220], who showed that 83% of the sulfur ligand containing glutathione with a molar mass of 612 Da can be retained by a 1 kDa ultrafiltration membrane, thus making it likely that the relatively high colloidal fractions of Cu in the open ocean could be caused by low molar mass thiols.

#### 4.1.4 Other Trace Metals

Colloidal fractions of Al are not as high as one might expect from their importance in freshwater systems, where 80–90% can be colloidal [205,269]. Indeed, Moran and Moore [17] reported a 1–15% colloidal fraction for Al in the North Atlantic surface waters, and Reitmeyer *et al.* [279] reported 0–11% (see Chapter 4).

The colloidal fractions of Ni, Cu, Cd and Pb range from near 0 to 67%, depending on author, site and metal (see Chapter 4). The range is large to such an extent that any differences between coastal and open ocean sites are not evident from these data.

The inverse correlation between the ratio of colloidal Pb-binding and the colloidal Cu-binding ligand (as a fraction of the total metal-binding ligand concentration) [244] (Figure 11) suggests the existence of distinctive pools of specific ligands for Cu and Pb. The positive correlation between filter-passing Cu, Pb or Cd with glutathione concentrations, as reported by Tang *et al.* [191] for the Galveston Bay estuary, and the close to 1:1 correlation between the sum of Ni, Cu and Zn (and Pb, Cd) concentrations and total reduced sulfur concentrations, suggest complexation of these metals with reduced sulfur ligands. Such reduced sulfur compounds also can reduce metal species such as Cu(II) to Cu(I) [276,280]. Complexation reactions are probably also coupled to redox reactions for a number of other trace metals, often mediated by microbial enzymes [281].

## 4.2 TRACE METAL BINDING AND COLLOIDAL CARRIER PHASES

The most abundant potential carrier phases  $\text{SiO}_2$ ,  $\text{CaCO}_3$  and  $\text{Al}_2\text{O}_3$  are not strong metal complexants, and appear mainly to act as ballast [282] to accelerate the sinking out of aggregating exopolymers secreted by phytoplankton and/or bacteria. However, metal binding to exopolymers that are associated with microbial cells can explain, as in the case of Th(IV), binding to marine particulate matter [233,283]. Most of the trace metals in marine systems, however, pass a  $0.5 \mu\text{m}$  filter and are found in the ‘dissolved’ phase that also contains colloidal carriers for these metals.

Except for organic carbon, most other elements would probably form pseudo-colloids, i.e. they would associate with colloids formed by other elements (*e.g.* metal oxides and

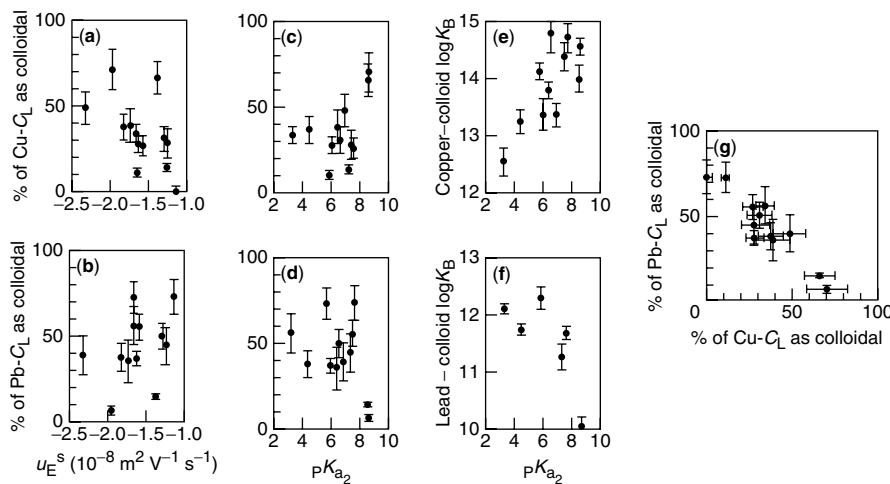


**Figure 11.** Relationships between metal-binding parameters [(a)–(d)] colloid–solution partitioning of metal-binding ligands; (e) and (f) stability constant for the binding of the metal by the colloids and surface ionisation characteristics ( $u_E$  and  $pK_{a_2}$ ) of the colloidal matter. Reprinted from Muller F. L. L., Colloid/solution partitioning of metal-selective organic ligands, and its relevance to Cu, Pb and Cd cycling in the Firth of Clyde, *Estuarine Coastal and Shelf Science*, **46**, 419–437, Copyright 1998, with permission from Elsevier

silicates). Fe and DOC are known carriers for trace elements, and a significant fraction of both ‘dissolved’  $0.4 \mu\text{m}$  filter-passing Fe(III) and DOC exist in a colloidal state in marine environments. Therefore, it might be interesting to compare their concentrations to investigate the variability of their ratios in oceanic environments. Colloidal concentrations of Al and Fe in open ocean waters are low:  $0.5 \text{ nmol dm}^{-3}$  of Fe [284] and  $0.1\text{--}0.5 \text{ nmol dm}^{-3}$  of Al [17]. It is often not clear whether trace metals are bound directly to Fe oxyhydroxides or organic carbon ligands in Fe–OC colloidal associations such as humic acids or APS fibrils coated with FeOOH [204]. SAXS, EXAFS and XANES techniques have, however, the potential to make such distinctions [285,286].

Marine colloidal organic matter, COM  $\geq 1 \text{ kDa}$ , which ranges in concentration from  $20$  to  $30 \mu\text{mol dm}^{-3}$  C in the surface ocean, and about half of that in the deep ocean [19,215, 287–289], comprises about 30% of the DOC pool. COM contains about  $2\text{--}12 \mu\text{mol dm}^{-3}$  C of total polysaccharides,  $\leq 3 \mu\text{mol dm}^{-3}$  C of APS,  $0.4\text{--}1 \mu\text{mol dm}^{-3}$  C of total uronic acids,  $0.05\text{--}0.5 \mu\text{mol dm}^{-3}$  C of total lipids and  $5\text{--}50 \text{ nmol dm}^{-3}$  C of phospholipids [290–293]. While arguing that the largest fraction of marine DOM is composed of acyl polysaccharidic biopolymers, Aluwihare *et al.* [291] and Repeta *et al.* [294] reported that most of the carbohydrates in the colloidal macromolecular fraction are also composed of neutral polysaccharides, with identifiable uronic acid (URA) compounds (glucuronic and galacturonic acid) making up only about 2–5% of the total carbohydrate content, and the total acyl group carbon amounting for 10% or less of the total organic carbon content, despite the fact that the acyl-C containing biopolymer appears to make up a major fraction of the total macromolecular carbon.

A major fraction of macromolecular carbon is made up by surface-active EPS, hence exopolymer binding of trace metals can be important in the downward transport of metals

in the ocean. A variety of metals have been found closely associated with bacterial exopolymers in the water column [228]. Other important carrier phases are metal oxides such as iron oxyhydroxides, which are usually closely associated with the three orders of magnitude more abundant organic matter.

The Pacific Ocean surface data indicates  $\sim 5 \text{ nmol dm}^{-3}$  colloidal Fe and Deep Pacific Ocean data  $\sim 0.5 \text{ nmol dm}^{-3}$  colloidal Fe. Assuming COC concentrations of about  $20 \mu\text{mol dm}^{-3}$  C in surface waters and  $10 \mu\text{mol dm}^{-3}$  C in deep waters, this would give a C:Fe mass ratio of about 800 in surface waters and 4000 in deep waters. Similarly, Guo *et al.* [220] measured these ratios directly in diafiltered and freeze-dried colloids taken from surface waters of different oceanographic environments: in the Middle Atlantic Bight the C:Fe mass ratio was 1300, in the Gulf of Mexico surface waters it was 800–1800 and in Galveston Bay it was 250, regardless of salinity. Wen *et al.* [13] reported colloidal Fe concentrations in Galveston Bay, sampled at a different period, of  $3\text{--}227 \text{ nmol dm}^{-3}$  at salinities  $\geq 10$ , and COC concentrations of  $60\text{--}190 \mu\text{mol dm}^{-3}$  C, resulting in C:Fe ratios of 4000–620. Hence C:Fe ratios appear to be very consistent in different marine environments, i.e. about  $10^3$ : 1, about an order of magnitude lower than ratios found in marine phytoplankton [295]. This is contrary to the freshwater environment, where Fe-rich colloids have been documented by a number of studies [205,269], and where C:Fe ratios are likely of the order of 1:1, rather than consisting of pure Fe oxyhydroxides [205]. The organic carbon content of the Fe-rich colloids has often not been determined, but it can be argued that peak shapes of organic carbon in FIFFF systems of Lyven *et al.* [205] allow for 10% of the much more abundant organic carbon to be associated with Fe oxyhydroxides. The observed mobility of these Fe-rich colloids also requires low  $\text{pH}_{\text{IEP}}$  values, which can only be imparted by adsorbed organic matter. Indeed, Pokrovsky and Schott [269] provided more direct evidence for the existence of these Fe-rich organic colloids in freshwater systems.

#### 4.2.1 Reversibility versus Irreversibility of Metal Binding to Colloidal Macromolecular Ligands

Quigley and co-workers [233,296] observed irreversible binding of Th(IV) to Fe hydroxide colloids and marine colloidal organic matter. Buckau *et al.* [297] reported similar observations for Th(IV) desorption from humic colloids of the Gorleben groundwater aquifer, where most of the Th(IV) was also reported to be irreversibly sorbed. Honeyman and Santschi [56] and Mackey and Zirino [298] explained the apparent irreversibility of trace metal binding to natural organic ligands in seawater by invoking a ‘strawberry’ or ‘onion’ model, whereby metals are sheltered inside an aggregate, leading to very limited desorption. Field observations of trace metal complexation to solution ligands have also invoked limited desorption of metals bound to ‘aged’ colloids [244]. However, experimental results by reported Guo *et al.* [42] show that some recently sorbed trace metals can dissociate from colloids. Muller [244] proposed that newly formed colloidal ligands are generally weaker than pre-existing ones, whereby metals become less exchangeable with time. This is also borne out by observations by Wells *et al.* [299], which indicated that kinetically inert complexes closely paralleled the distribution of colloidal Cu in Narragansett Bay. However, this apparent irreversibility of trace metal binding, as deduced from limited or no desorption of pre-adsorbed metal, usually does not preclude

the attainment of a pseudo-equilibrium during the forward, i.e. the adsorption phase of the reaction. During this uptake phase, a plateau stage is usually reached within hours, days or months, depending on metal ions and experimental conditions, after which the colloid–particle–water distribution does not change any longer [12,20,297,300].

#### 4.2.2 Relationships Between Colloidal Metal or Ligand Concentrations and Their Chemical and Physicochemical Properties

What do we know about the physicochemical parameters of colloidal organic matter in the ocean, *e.g.* proton reactive sites, their  $pK_a$  values, electrophoretic mobilities and relative hydrophobicities? Santschi *et al.* [215] reported a total concentration of  $1.4 \text{ meq g}^{-1}$  of proton-reactive sites in marine colloids from the Gulf of Mexico, which is intermediate between that of HS ( $10\text{--}16 \text{ meq g}^{-1}$ ) and acid polysaccharides such as alginic acid (*ca.*  $5 \text{ meq g}^{-1}$ ) [301]. These proton-reactive sites have been assumed to be represented by  $pK_a$  values of 2, 4, 6, 8 and 10 [146], although these values may be arbitrary. Actual values of  $pK_{a_1}$  have been determined for aquatic colloids as  $\leq 3$  [222,233,244,245,298,302,303], which could suggest dicarboxylic acids, sulfate or polyphosphate as possible ligands. Values for  $pK_{a_2}$  are more variable, and increase from about 4 to 8.7 across the salinity gradient in the Firth of Clyde estuary [244,245], suggesting that the nature of colloids changes most dramatically in the estuarine mixing zone. Interestingly,  $\log K$  values, and also concentrations of metal-specific ligands ( $c_L$ ) in the colloidal fraction (colloidal  $c_L$ /total  $c_L$ ) of selected metals were significantly related to the  $pK_{a_2}$  of the colloids, with Cu showing a positive relationship for both  $\log K$  and % colloidal  $c_L$  with  $pK_{a_2}$ , whereas for Pb a negative relationship was found [244] (Figure 11). This is possibly due to the different affinities of these two metals for the two predominant forms of freshwater colloids [205], *i.e.* the smaller organic carbon rich colloids (Cu enrichments) and Fe-rich colloids (Pb enrichments), which can also be found in coastal waters [304].

In agreement with the  $pK_a$  values, measured electrophoretic mobilities of aquatic colloids are negative. Electrophoretic mobilities,  $u_E$ , determined by laser Doppler velocimetry in a ZetaSizer instrument at a pH of 8, were measured as about  $-2.5 \times 10^{-8} \text{ m}^2 \text{ V}^{-1} \text{ s}^{-1}$ , ranging from about  $-2 \times 10^{-8}$  to  $-3.4 \times 10^{-8} \text{ m}^2 \text{ V}^{-1} \text{ s}^{-1}$  [18,244,245]. Their values were weakly related to the colloidal fraction of metal-specific ligands, with Cu and Pb again relating in opposite ways. Further information on the interpretation of electrophoretic mobilities can be found in Chapter 6.

Isoelectric points of marine colloids of about 2–3 were determined by Quigley *et al.* [233] and Alvarado-Quiroz *et al.* [253], in agreement with the  $pK_{a_1}$  values of marine colloids of  $\sim 3$  [244,245] or below [222], suggesting that the surface charge is dominated by strongly acidic groups, and that basic, positively charged ligand groups such as amino groups are considerably rarer.

Although marine colloids are negatively charged, suggesting hydrocolloid-like behaviour, it does not preclude coexistence with more hydrophobic sites, as has been said before. Indeed, EPS and APS have been described as amphiphilic [153,225,305]. Furthermore, it is likely that more hydrophobic ligands would be more particle reactive, and thus have a shorter residence time in the water. However, this has not been demonstrated in the field. Laboratory studies on bacterial attachment, however, show a clear relationship between attachment probability and relative hydrophobicity of the bacterial surfaces [305,306], which are composed of EPS.

#### 4.2.3 Sources and Sinks of Metal-binding Colloids: Relationships to Thiol and Acid Polysaccharide Production

Sources and sinks of strongly complexing ligands that control metal speciation in seawater are not well understood. Both eukaryotes and prokaryotes produce thiolic and acid polysaccharide-rich ligands under nutrient or trace metal stress (see reviews in [218,223, 224,227,307]). Marine prokaryotes are known to release siderophores (Fe-complexing) with stability constants that agree with the strong L1 ligand for Fe [308–310]. Some low molar mass ( $\leq 700$  Da) metal complexes are by-products of intracellular metal detoxification [311,312]. Sources of colloidal complexes include exopolymer excretion, cell lysis, protozoan excretion, sloppy feeding by grazers, viral infection or breakdown of biogenic detrital particulates and, in the coastal zone, terrestrial inputs. Trace metals such as Cu appear to be complexed by thiolic ligands in response to phytoplankton metabolism [190,191,277].

The positive relationships between  $^{234}\text{Th}/\text{POC}$  and the abundance of APS and total URA compounds in Gulf of Mexico waters, reported by Guo *et al.* [220] and Santschi *et al.* [234], suggest Th(IV) binding by acid polysaccharide compounds (Figure 12). The relatively low abundance but high surface activity of these metal-binding biopolymers [234] could reconcile the decade-old enigma of contradictory findings, and rapid coagulation of Th nuclides that are bound to colloidal organic matter into large particles, of carbon flow from high molar mass to low molar mass molecules (or vice versa) [215,231,313], by allowing for a major fraction of  $^{234}\text{Th}$  to bind to the minority APS compounds and be transferred by coagulation up the particle size spectrum into large particles, without having a dominant effect on the carbon flow, which is from the breakdown of large to small molecules. Interestingly, this coagulation process is further modified by the enzymatic release of smaller fragments of fibrillar acidic polysaccharides [222,234,314] into the ‘dissolved’ phase, where they are still able to complex with freshly produced  $^{234}\text{Th}$  and coagulate back into the particulate size fraction [234,296]. The relatively low and

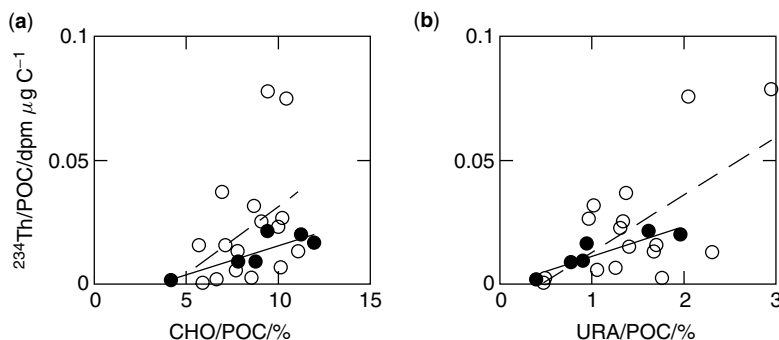


**Figure 12.** Correlation of the  $^{234}\text{Th}/\text{POC}$  ratio with percentage of carbohydrates (CHO/POC) and uronic acids (URA/POC) in suspended particles (open circles) and sinking particles caught in sediment traps (filled circles), taken from oligotrophic Gulf of Mexico waters. Reproduced (modified) by permission of the American Geophysical Union from Santschi, P. H., Hung, C. C., Schultz, G., Alvarado-Quiroz, N., Guo, L., Pinckney, J. and Walsh, I. Control of acid polysaccharide production and  $^{234}\text{Th}$  and POC export fluxes by marine organisms, *Geophys. Res. Lett.*, **30**, art. no. 1044, 2003. Copyright 2003 American Geophysical Union

constant percentage of particulate polysaccharides as APS compounds also explains the tight correlation that was reported by Quigley *et al.* [233] between the logarithm of the conditional binding constant of  $^{234}\text{Th}$  and the polysaccharide content of the macromolecular organic matter, making the total polysaccharide content of suspended matter a good predictor of both APS and  $^{234}\text{Th}$  contents. However, specific APS compounds could be important in controlling rates and amounts of  $^{234}\text{Th}$  sorption, and also rates of coagulation of particles, but their role is largely unknown [234,283].

Correlations between POC normalised polysaccharide fractions (CHO, URA and APS) and  $^{234}\text{Th}/\text{POC}$  in the Gulf of Mexico were significant at the 90–99% confidence level, but correlation coefficients were highest (with  $p \leq 0.02$ ) for sinking particles [234] (Figure 11b), suggesting that they provide a more sorted assembly of particles for calculating POC and APS flux. The fact that average URA/POC and APS/POC ratios in sinking particles were similar to those in large ( $>53 \mu\text{m}$ ) suspended particles, but that  $^{234}\text{Th}/\text{POC}$  ratios were, on average, higher in  $>53 \mu\text{m}$  particles, agrees with the notion that  $^{234}\text{Th}$  is transported by coagulation up the size spectrum, whereas the  $^{234}\text{Th}$  content in sinking particles may be decreased by enzymatic degradation of Th(IV)-binding APS compounds. It is important to note that the range of  $^{234}\text{Th}/\text{POC}$  ratios in the  $>53 \mu\text{m}$  particles that were observed by Santschi *et al.* [234] is similar to that in the Pacific Ocean [315] and Arabian Sea [282].

A number of photosynthetic organisms are known to produce APS compounds. However, significant correlations between the abundance of phytoplankton species, APS or URA abundance, and  $^{234}\text{Th}/\text{POC}$  ratios varied with sampling season and locations [234, 316]. It is very likely that a variety of phytoplankton species excrete Th(IV)-binding APS-rich mucilage, thus facilitating the removal of  $^{234}\text{Th}$  from the water column, albeit at different efficiencies. In addition to phytoplankton, bacteria also produce abundant APS compounds [227], especially when attached to particles as a ‘micro-biofilm’. Indeed, significant relationships between APS concentrations and heterotrophic bacterial production (BP), and  $^{234}\text{Th}/\text{POC}$  ratios and BP, were observed, which strongly suggest microbial involvement through production of Th(IV)-binding APS compounds, while their enzymatic activities can produce smaller but more stable filter-passing fragments that also bind Th(IV).

It therefore appears that the role of photosynthesising microorganisms in this process is mainly to produce metal [*e.g.* Th(IV)]-binding APS-containing ligand macromolecules, whereas that of attached heterotrophic bacteria is to reduce the size of algae-produced APS-macromolecule and release these enzymatically degraded smaller filter-passing fragments from the filterable aggregates into the surrounding solution [234,317]. Since both phytoplankton and bacterial activities are closely coupled, one therefore needs to consider both groups of microorganisms when evaluating their contributions to the standing crop of  $^{234}\text{Th}$ -binding APS compounds. Filter-feeding zooplankton and bacterivorous plankton organisms [318,319] also need to be considered. However, they may simply act as biological amplifiers of coagulation.

#### 4.3 THE SIGNIFICANCE OF SURFACE-ACTIVE COLLOIDAL LIGANDS ON PARTICLE-WATER PARTITION COEFFICIENTS AND KINETIC REMOVAL RATE CONSTANTS

Particle concentration effects (see Section 3.2) on  $K_D$  and kinetic constants ( $k_i$ ) for removal from the filter-passing phase of trace metals or radionuclides have been reported

in the literature for many years, and indicate the presence of colloidal ligands in the filter-passing fraction ( $K_D$ ) that have surface active properties ( $k_i$ ) and can be removed by coagulation [56,174]. Such particle concentration effects disappear, however, when one corrects for the presence of colloidal ligands [183,191]. While values of the partition coefficients of the A-metal  $^{234}\text{Th}(\text{IV})$  to colloids ( $K_c$ ) are generally similar to  $K_D$  values for particles, this is not necessarily the case for B-metals such as Cu [246,320], where  $K_c$  is generally found to be larger than  $K_D$ .

Aggregation rates of colloidally complexed metals show two distinctive reaction rates, with the faster rate consistent with Brownian ‘colloidal pumping’ [56] that occurs at a uniform rate and is faster at higher particle concentrations, and a slower rate that varies for each metal [175,321].

$^{234}\text{Th}$ , which is generated *in situ* from the radioactive decay of  $^{238}\text{U}$ , and which can be used to derive residence times of Th(IV)-binding colloids, provides colloidal residence times (with respect to coagulation) that vary from fractions of days in estuaries to a few weeks in the surface ocean [25,215]. Similar results are obtained in controlled laboratory coagulation experiments using radioactive metals bound to estuarine COM [175,321]. These laboratory results also confirmed particle concentration effects on removal rate constants, previously demonstrated for Th(IV) [56,174]. Residence times that reflect colloidal organic carbon ages are longer, as much of the carbon is recycled. For example, Santschi and co-workers [215,222] and Guo and co-workers [25,289] obtained mostly modern (i.e. younger than 55 years – produced since about 1950) apparent radiocarbon ages for high molar mass colloids  $\geq 10$  kDa, but mostly older ages (*e.g.* 400–4500 years) for low molar mass COM  $\geq 1$  kDa in surface waters containing mostly biopolymers [215]. Benthic nepheloid layers of estuaries and continental shelf or slope areas of the Gulf of Mexico and the Middle Atlantic Bight contained mostly geopolymers generated through hydrodynamic and physicochemical fractionation processes occurring near the sediment–water interface during sediment resuspension [289,322]. In that case, the age distribution observed above was reversed, *e.g.* with apparent radiocarbon ages up to 10 000 years for  $\geq 10$  kDa colloids, and younger ages for  $\geq 1$  kDa colloids, indicating fundamental differences between biopolymers and geopolymers.

It therefore appears that whenever colloids are generated by microorganisms in surface and bottom waters, their importance to trace metal binding and removal might be disproportionately higher than would be expected from the observed colloidal fractions of trace metals.

## 5 SOME PERSPECTIVES AND RESEARCH DIRECTIONS

The study of the interactions between colloids and trace elements in aquatic systems remains a challenge upon which research must continue. The last 10 years have witnessed the development of important techniques for the separation (*e.g.* FIFFF, SPLITT, CFF), visualisation and characterisation (*e.g.* AFM, ESEM) of colloids and for the speciation of trace elements (*e.g.* voltammetry, DGT). This progress is an important step forward in a better understanding of the roles of colloids in the behaviour and fate of trace elements in the aquatic environment. However, substantial efforts should still be directed towards the development of new techniques which are both quantitative and non-perturbing, and ideally used *in situ*. Application of these newly established techniques to real systems is

now needed to collect systematic data sets, including mechanistic and kinetic, in addition to thermodynamic information.

At present, the detailed characterisation of colloidal material should be pursued with greater vigour. Indeed, we have previously discussed the several assumptions made about SSA, but information on the quantitative SSAs and colloid microstructures and surface charges as a function of environmental conditions (*e.g.* solution pH, ionic strength) for different types of colloids is still lacking. This is essential to improve our mechanistic understanding of, for instance, the reversibility of trace element sorption kinetics. The main problem lies in collecting sufficient colloidal material for analysis. It is therefore imperative to make further advances in sampling and separation methods for obtaining sufficient amounts of material in the colloidal size range.

There are too few coherent laboratory studies in the literature concerning the characteristics and reactivity of mixtures of oxides [323], which may be very different from those of their component parts. This leads to an inability to predict  $K_D$  values for natural colloids because the additive and non-additive effects of component oxide systems and organic matter have not been accounted for [324]. There is also a need to improve our understanding of ternary systems (*i.e.* inorganic colloids with organic material and trace elements). Our knowledge of this area is severely limited. In addition, rather than focusing almost exclusively on humic and fulvic substances as model organic colloids, and whole microorganisms (with a myriad cell wall molecules as potential binding sites) as model solids, it will be important in the future to use more realistic colloidal model carrier phase biomolecules, such as open ocean and/or lake colloids, and purified EPS harvested from phytoplankton or bacteria, in order to study the processes of metal ion adsorption, coagulation and/or flocculation, either individually or as coupled reactions of ‘colloidal pumping’ [56]. Furthermore, since EPS are often associated or coated with mineral fragments, especially in lake water [204], it will be important to know more about their combined properties with regard to metal ion sorption.

An improved understanding of the effect of aquatic colloids (quantitatively) on the bioavailability and bioaccumulation of toxic substances and nutrients is also essential. It has recently been suggested that the colloidal fraction smaller than 30 nm may represent one of the main carrying phases in the aquatic environments [32–35]. The mechanistic and kinetic aspects whereby colloids in this size range are taken up and processed by aquatic microorganisms are largely unknown.

The powerful models currently available (*e.g.* Model VI/NICCA) can be viewed as syntheses or integrations of laboratory knowledge, which can be applied to field data in a broad sense to prove the extent to which knowledge on ‘pure’ phases is applicable. In this broader interpretation of model use, ‘failure’ (*i.e.* significant disagreement between model and measurements) is at least as important as ‘success’ since it prompts questions about why ‘failure’ occurs, thus possibly leading to emphasis on particular aspects of the measurements and further development of the model. Modelling and measurements are therefore in a two-way relationship, where the results of each can in principle be used to improve the other. It is expected that models will be increasingly applied to field measurements of colloid structure, function and reactivity in the next few years. The development of further, more sophisticated models will also be essential in the future, but this will depend on the collection of quality data, which in turn depends on the establishment of reliable techniques.

Last, but not least, our review has pointed out that one-step filtration is inappropriate for determining trace element partitioning in aquatic systems, but is still included in chemical analysis procedures used by regulatory organisations to determine water quality levels. There is therefore an immediate need for environmental managers and modellers in public health and environmental conservation services to utilise data and derivative information which have been assessed using appropriate methods and techniques. Indeed, the nature and behaviour of aquatic colloids, and their interactions with trace elements, have important practical values to these organisations since up to 100% of trace elements in natural waters are present as colloids [13,301], and the transport, bioavailability and/or toxicity of trace elements depend on whether they are present as truly dissolved, colloid or particle forms.

## ACKNOWLEDGEMENTS

The writing of this review was supported, in parts, by grants from the UK Natural Environment Research Council (NER/B/5/2002/00544 and NER/A/S/2000/01112) to J.R.L., and by grants from the US National Science Foundation (NIRT-0210865 and OCE-0351559) and the Texas Institute of Oceanography to P.H.S.. We are grateful for the careful reviews of the manuscript by six anonymous reviewers.

## LIST OF ABBREVIATIONS AND SYMBOLS

AdSV	Adsorptive stripping voltammetry
AFM	Atomic force microscopy
APS	Acid polysaccharides
$\beta$	Binding constant
BLM	Biotic ligand model
BP	Bacterial production
$c_{BS}$	Concentration of binding sites
CFF	Cross-flow filtration
CFUF	Cross-flow ultrafiltration
$c_L$	Concentration of metal-specific ligand
COC	Colloidal organic carbon
COM	Colloidal organic matter
DGT	Diffusive gradients in thin films
DOC	Dissolved organic carbon
DP	Differential pulse
ECOSAT	A computer program for the calculation of chemical speciation and mass transport in soil-water systems
EPS	Exopolymeric substances
EXAFS	Extended X-ray absorption fine structure
FIAM	Free ion activity model
FICFFF	Flow field-flow fractionation
$\Delta G$	Gibbs free energy

GF-AAS	Graphite furnace atomic absorption spectrometry
HS	Humic substances
ICP-MS	Inductively coupled plasma mass spectrometry
$K_{app}$	Apparent equilibrium constant
$K_{coul}$	Coulombic constant
$K_D$	Distribution coefficient
$K_i$	Kinetic constant
$K_{int}$	Intrinsic constant
NICCA	Non-ideal consistent competitive adsorption model
NOM	Natural organic matter
OC	Organic carbon
PAGE	Polyacrylamide gel electrophoresis
p.c.e.	Particle concentration effect
POC	Particulate organic carbon
SAXS	Small-angle X-ray scattering
SCM	Surface complexation model
SPLITT	Split thin-flow fractionation
SPM	Suspended particulate matter
SSA	Specific surface area
TEP	Transparent exopolymeric particles
URA	Uronic acid
WHAM	Windermere humic aqueous model
XANES	X-ray absorption near-edge structure

## REFERENCES

1. Rees, T. F. (1991). Transport of contaminants by colloid-mediated processes. In *The Handbook of Environmental Chemistry*, Vol. 2, ed. Hutzinger, O. Springer, Heidelberg, pp. 165–184.
2. Martin, J. M., Dai, M. H. and Cauwet, G. (1995). Significance of colloids in the biogeochemical cycling of organic carbon and trace metals in a coastal environment—example of the Venice Lagoon (Italy), *Limnol. Oceanogr.*, **40**, 119–131.
3. Hamilton-Taylor, J., Giusti, L., Davison, W., Tych, W. and Hewitt, C. N. (1997). Sorption of trace metals (Cu, Pb, Zn) by suspended lake particles in artificial (0.005 M NaNO<sub>3</sub>) and natural (Esthwaite Water) freshwaters, *Colloids Surf. A*, **120**, 205–219.
4. Goldberg, E. D., Baker, M. and Fox, D. L. (1952). Microfiltration in oceanographic research, *J. Mar. Res.*, **11**, 194–204.
5. Morrison, M. A. and Benoit, G. (2001). Filtration artifacts caused by overloading membrane filters, *Environ. Sci. Technol.*, **35**, 3774–3779.
6. Buffle, J., Perret, D. and Newman, M. (1992). The use of filtration and ultrafiltration for size fractionation of aquatic particles, colloids and macromolecules. In *Environmental Particles*, eds Buffle, J. and van Leeuwen, H. P. IUPAC Series on Analytical and Physical Chemistry of Environmental Systems, Vol. 1. Lewis, Boca Raton, FL, pp. 171–230.
7. Honeyman, B. D. and Santschi, P. H. (1992). The role of particles and colloids in the transport of radionuclides and trace metals in the oceans. In *Environmental Particles*, eds Buffle, J. and van Leeuwen, H. P. IUPAC Series on Analytical and Physical Chemistry of Environmental Systems, Vol. 1. Lewis, Boca Raton FL, pp. 379–423.
8. USEPA (1983). *Methods for Chemical Analysis of Water and Wastes*. EPA-600 4-79-020. Environmental Protection Agency, Washington, DC.

9. OWDC (1984). *National Handbook of Recommended Methods for Water-Data Acquisition*. US Geological Survey, Reston, VA, Chapter 5.
10. APHA, AWWA and WEF (1989). *Standard Methods for the Examination of Water and Wastewater*, 20th edn. American Public Health Association, American Water Works Association and Water Environment Association, Washington, DC.
11. ASTM (1989). *Annual Book of ASTM Standards*. American Society for Testing and Materials, Philadelphia, PA.
12. Wen, L. S., Santschi, P. H., Gill, G. and Paternostro, C. (1997). Colloidal and particulate silver in river and estuarine waters of Texas, *Environ. Sci. Technol.*, **31**, 723–731.
13. Wen, L. S., Santschi, P. H., Paternostro, C. and Gill, G. (1999). Estuarine trace metal distributions in Galveston Bay. I: Importance of colloidal forms in the speciation of the dissolved phase, *Mar. Chem.*, **63**, 185–212.
14. Wen, L. S., Santschi, P. H., Gill, G. A. and Tang, D. G. (2002). Silver concentrations in Colorado, USA, watersheds using improved methodology, *Environ. Toxicol. Chem.*, **21**, 2040–2051.
15. Sanudo-Wilhelmy, S. A., Rossi, F. K., Bokuniewicz, H. and Paulsen, R. J. (2002). Trace metal levels in uncontaminated groundwater of a coastal watershed: importance of colloidal forms, *Environ. Sci. Technol.*, **30**, 1575–1581.
16. Town, R. M. and Filella, M. (2002). Size fractionation of trace metal species in freshwaters: implications for understanding their behaviour and fate, *Rev. Environ. Sci. Biotechnol.*, **1**, 277–297.
17. Moran, S. B. and Moore, R. M. (1989). The distribution of colloidal aluminium and organic carbon in coastal and open ocean waters off Nova Scotia, *Geochim. Cosmochim. Acta*, **53**, 2519–2527.
18. Lead, J. R., Hamilton-Taylor, J., Davison, W. and Harper, M. (1999). Trace metal sorption by natural particles and coarse colloids, *Geochim. Cosmochim. Acta*, **63**, 1661–1670.
19. Guo, L. and Santschi, P. H. (1997). Composition and cycling of colloids in marine environments, *Rev. Geophys.*, **35**, 17–40.
20. Stordal, M. C., Gill, G. A., Wen, L. S. and Santschi, P. H. (1996). Mercury phase speciation in the surface waters of selected Texas estuaries: importance of colloidal forms, *Limnol. Oceanogr.*, **40**, 52–61.
21. Contado, C., Blo, G., Fagioli, F., Dondi, F. and Beckett, R. (1997). Characterisation of river Po particles by sedimentation field-flow fractionation coupled to GFAAS and ICP-MS, *Colloids Surf. A*, **120**, 47–59.
22. Magaritz, M., Amiel, A. J., Ronen, D. and Wells, M. C. (1990). Distribution of metals in a polluted aquifer: a comparison of aquifer suspended material to fine sediments of the adjacent environment, *J. Contam. Hydrol.*, **5**, 333.
23. Penrose, W. R., Polzer, W. L., Essington, E. H., Nelson, D. M. and Orlandini, K. A. (1990). Mobility of plutonium and americium through a shallow aquifer in a semiarid region, *Environ. Sci. Technol.*, **24**, 228–234.
24. Ryan, J. N. and Elimelech, M. (1996). Colloid mobilisation and transport in groundwater, *Colloids Surf. A*, **107**, 1–56.
25. Guo, L., Santschi, P. H. and Baskaran, M. (1997). Interactions of thorium isotopes with colloidal organic matter in oceanic environments, *Colloids Surf. A*, **120**, 255–271.
26. Puls, R. W. and Powell, R. M. (1992). Surface charge repulsive effects on the mobility of inorganic colloids in subsurface systems, *ACS Symp. Ser.*, **491**, 40–54.
27. Ran, Y., Fu, J. M., Sheng, G. Y., Beckett, R. and Hart, B. T. (2000). Fractionation and composition of colloidal and suspended particulate materials in rivers, *Chemosphere*, **41**, 33–43.
28. Eyrolle, F. and Benaim, J. Y. (1999). Metal available sites on colloidal organic compounds in surface waters (Brazil), *Water Res.*, **33**, 995–1004.
29. Gustafsson, O. and Gschwend, P. M. (1997). Aquatic colloids: concepts, definitions, and current challenges, *Limnol. Oceanogr.*, **42**, 519–528.
30. Stumm, W. and Morgan, J. J., eds (1996). *Aquatic Chemistry: Chemical Equilibria And Rates in Natural Waters*. John Wiley & Sons Inc., New York.

31. Buffle, J. and Leppard, G. G. (1995). Characterisation of aquatic colloids and macromolecules. I. Structure and behaviour of colloidal material, *Environ. Sci. Technol.*, **29**, 2169–2175.
32. Plaschke, M., Romer, J. and Kim, J. I. (2002). Characterisation of Gorleben groundwater colloids by atomic force microscopy, *Environ. Sci. Technol.*, **36**, 4483–4488.
33. Muirhead, D. and Lead, J. R. (2003). Measurement of the size and structure of natural aquatic colloids in an urbanised watershed by atomic force microscopy, *Hydrobiologia*, **494**, 65–69.
34. Doucet, F. J., Maguire, L. and Lead, J. R. (2004). Size fractionation of aquatic colloids and particles by cross-flow filtration: analysis by scanning electron and atomic force microscopy, *Anal. Chim. Acta*, **522**, 59–71.
35. Doucet, F. J., Maguire, L. and Lead, J. R. (2005). Assessment of cross-flow filtration for the size fractionation of freshwater colloids and particles, *Talanta*, **67**, 144–154.
36. Moran, S. B., Yeats, P. A. and Balls, P. W. (1996). On the role of colloids in trace metal solid-solution partitioning in continental shelf waters: a comparison of model results and field data, *Cont. Shelf Res.*, **16**, 397–408.
37. Geckes, H., Ngo, M. T., Bouby, M. and Kim, J. I. (2003). Aquatic colloids relevant to radionuclide migration: characterisation by size fractionation and ICP-mass spectrometric detection, *Colloids Surf. A*, **217**, 101–108.
38. Taylor, H. E., Garbarino, J. R., Murphy, D. M. and Beckett, R. (1992). Inductively coupled plasma mass spectrometry as an element-specific detector for field-flow fractionation particle separation, *Anal. Chem.*, **64**, 2036–2041.
39. Eyrolle, F., Benedetti, M. F., Benaim, J. Y. and Fevrier, D. (1996). The distributions of colloidal and dissolved organic carbon, major elements, and trace elements in small tropical catchments, *Geochim. Cosmochim. Acta*, **60**, 3643–3656.
40. Chen, M. and Wang, W. X. (2001). Bioavailability of natural colloid-bound iron to marine plankton: influences of colloidal size and aging, *Limnol. Oceanogr.*, **46**, 1956–1967.
41. Wang, W. X. and Guo, L. (2000). Influences of natural colloids on metal bioavailability to two marine bivalves, *Environ. Sci. Technol.*, **34**, 4571–4576.
42. Guo, L., Santschi, P. H. and Ray, S. M. (2002). Metal partitioning between colloidal and dissolved phases and its relation with bioavailability to American oysters, *Mar. Environ. Res.*, **54**, 49–64.
43. Pan, J. F. and Wang, W. X. (2004). Influences of dissolved and colloidal organic carbon on the uptake of Ag, Cd and Cr by the marine mussel *Perna viridis*, *Environ. Pollut.*, **129**, 467–477.
44. Lead, J. R., Davison, W., Hamilton-Taylor, J. and Buffle, J. (1997). Characterising colloidal material in natural waters, *Appl. Geochem.*, **3**, 213–232.
45. Beckett, R. and Hart, B. T. (1993). Use of field-flow fractionation techniques to characterise aquatic particles, colloids and macromolecules. In *Environmental Particles*, eds Buffle, J. and van Leeuwen, H. IUPAC Series on Analytical and Physical Chemistry of Environmental Systems, Vol. 2. Lewis, Boca Raton, FL, pp. 165–205.
46. Gustafsson, O., Duker, A., Larsson, J., Andersson, P. and Ingri, J. (2000). Functional separation of colloids and gravitoids in surface waters based on differential settling velocity: coupled cross-flow filtration–split flow thin-cell fractionation (CFF–SPLITT), *Limnol. Oceanogr.*, **45**, 1731–1742.
47. Tessier, A., Carignan, R. and Belzile, N. (1994). Processes occurring near the sediment water interface: emphasis on trace elements. In *Chemical and Biological Regulation of Aquatic Processes*, eds Buffle, J. and De Vitre, R. R., Lewis, Boca Raton, FL, pp. 139–175.
48. Carvallho, R. A., Benfield, M. C. and Santschi, P. H. (1999). Comparative bioaccumulation studies of colloidally complexed and free-ionic heavy metals in juvenile brown shrimp *Penaeus aztecus* (Crustacea: Decapoda: Penaeidae), *Limnol. Oceanogr.*, **44**, 403–424.
49. Schlekat, C. E., Decho, A. W. and Chandler, G. T. (1999). Dietary assimilation of cadmium associated with bacterial exopolymer sediment by the estuarine amphipod *Leptocheirus plumulosus*: effects of Cd concentration and salinity, *Mar. Ecol. Prog. Ser.*, **183**, 205–216.
50. Mirimanoff, N. and Wilkinson, K. J. (2000). Regulation of Zn accumulation by a freshwater gram-positive bacterium (*Rhodococcus opacus*), *Environ. Sci. Technol.*, **34**, 616–622.
51. Guo, L., Hunt, B. J., Santschi, P. H. and Ray, S. M. (2001). Effect of dissolved organic matter on the uptake of trace metals by American oysters, *Environ. Sci. Technol.*, **35**, 885–893.

52. Van Leeuwen, H. P. (1999). Metal speciation dynamics and bioavailability: inert and labile complexes, *Environ. Sci. Technol.*, **33**, 3743–3748.
53. Santschi, P. H. (1984). Particle flux and trace metal residence times in natural waters, *Limnol. Oceanogr.*, **29**, 1100–1108.
54. Sigg, L. (1994). Regulation of trace elements in lakes: the role of sedimentation. In *Chemical and Biological Regulation of Aquatic Processes*, eds Buffe, J. and deVitre, R. R., Lewis, Boca Raton, FL, pp. 99–138.
55. Jackson, G. A. and Burd, A. B. (1998). Aggregation in the marine environment, *Environ. Sci. Technol.*, **32**, 2805–2814.
56. Honeyman, B. D. and Santschi, P. H. (1989). A Brownian-pumping model for trace metal scavenging: evidence from Th isotopes, *J. Mar. Res.*, **47**, 950–995.
57. Santschi, P. H., Roberts, K. A. and Guo, L. (2002). Organic nature of colloidal actinides transported in surface water environments, *Environ. Sci. Technol.*, **36**, 3711–3719.
58. Warner, F. and Harrison, R. M., eds (1993). *Radioecology after Chernobyl—SCOPE 50. Biogeochemical Pathways of Artificial Radionuclides*. Scientific Committee on Problems of the Environment (SCOPE) of the International Council of Scientific Unions (ICSU). John Wiley & Sons Inc., New York.
59. Moulin, V. and Moulin, C. (2001). Radionuclide speciation in the environment: a review, *Radiochim. Acta*, **89**, 773–778.
60. Kirsting, A. B., Efurd, D. W., Finnegan, D. L., Rokop, D. J., Smith, D. K. and Thompson, J. L. (1999). Migration of plutonium in groundwater at the Nevada Test Site, *Nature*, **397**, 56–59.
61. Smith, P. A. and Degueldre, C. (1993). Colloid-facilitated transport of radionuclides through fractured media, *J. Contam. Hydrol.*, **13**, 143–166.
62. Degueldre, C., Pfeiffer, H. R., Alexander, W., Wernli, B. and Bruetsch, R. (1996). Colloid properties in granitic groundwater systems. 1. Sampling and characterisation, *Appl. Geochem.*, **11**, 677–695.
63. Degueldre, C., Triay, I., Kim, J. I., Vilks, P., Laaksoharju, M. and Miekeley, N. (2000). Groundwater colloid properties: a global approach, *Appl. Geochem.*, **15**, 1043–1051.
64. Moulin, V., Amekraz, B., Barre, N., Planque, G., Mercier, F., Reiller, P. and Moulin, C. (2004). The role of humic substances in trace element mobility in natural environments and applications to radionuclides. In *Humic Substances. Nature's Most Versatile Materials*, eds Ghabbour, E. and Davies, G. Taylor and Francis, New York, pp. 275–286.
65. Taylor, M. G. and Simkiss, K. (2004). Transport of colloids and particles across biological membranes. In *Physicochemical Kinetics and Transport at Biointerfaces*, eds van Leeuwen, H. P. and Köster, W. IUPAC Series on Analytical and Physical Chemistry of Environmental Systems, Vol. 9. John Wiley & Sons Ltd, Chichester, pp. 357–400.
66. Wilkinson, K. J. and Buffe, J. (2004). Critical evaluation of physicochemical parameters and processes for modelling the biological uptake of trace metals in environmental (aquatic) systems. In *Physicochemical Kinetics and Transport at Biointerfaces*, eds van Leeuwen, H. P. and Köster, W. IUPAC Series on Analytical and Physical Chemistry of Environmental Systems, Vol. 9. John Wiley & Sons, Ltd, Chichester pp. 445–533.
67. Schlekat, C. E., Decho, A. W. and Chandler, G. T. (2000). Bioavailability of particle-associated silver, cadmium, and zinc to the estuarine amphipod *Leptocheirus plumulosus* through dietary ingestion, *Limnol. Oceanogr.*, **45**, 11–21.
68. Davies, N. A., Taylor, M. G. and Simkiss, K. (1997). The influence of particle surface characteristics on pollutant metal uptake by cells, *Environ. Pollut.*, **96**, 179–184.
69. Paquin, P. R., Gorsuch, J. W., Apte, S., Batley, G. E., Bowles, K. C., Campbell, P. G. C., Delos, C. G., Di Toro, D. M., Dwyer, R. L., Galvez, F., Gensemer, R. W., Goss, G. G., Hogstrand, C., Janssen, C. R., McGeer, J. C., Naddy, R. B., Playle, R. C., Santore, R. C., Schneider, U., Stubblefield, W. A., Wood, C. M. and Wu, K. B. (2002). The biotic ligand model: a historical overview, *Comp. Biochem. Physiol. C Toxicol. Pharm.*, **133**, 3–35.
70. Koopal, L. K., Van Riemsdijk, W., Dewit, J. and Benedetti, M. (1994). Analytical isotherm equations for multicomponent adsorption to heterogeneous surfaces, *J. Colloid Interface Sci.*, **166**, 51–60.

71. Koelmans, A. A. and Radovanovic, H. (1998). Prediction of trace metal distribution coefficients ( $K_d$ ) for aerobic sediments, *Water Sci. Technol.*, **37**, 71–78.
72. Loftis, S. and Tipping, E. (1998). An assemblage model for cation binding by natural particulate matter, *Geochim. Cosmochim. Acta*, **62**, 2609–2625.
73. Muller, B. and Duffek, A. (2001). Similar adsorption parameters for trace metals with different aquatic particles, *Appl. Geochem.*, **7**, 107–126.
74. Ferreira, J. R., Lawlor, A. J., Bates, J. M., Clarke, K. J. and Tipping, E. (1997). Chemistry of riverine and estuarine suspended particles from the Ouse Trent system, UK, *Colloids Surf. A*, **120**, 183–198.
75. Westall, J. C., Cernik, M. and Borkovec, M. (1998). Modelling metal speciation in aquatic systems. In *Metals in Surface Waters*, eds Allen, H. E., Gartison, E. W. and Luther, G. W. Ann Arbor Press, Ann Arbor, MI, pp. 191–216.
76. Ledin, M. (2000). Accumulation of metals by microorganisms—processes and importance for soil systems, *Earth Sci. Rev.*, **51**, 1–31.
77. Balistrieri, L. S. and Murray, J. W. (1981). The surface chemistry of goethite (alpha-FeOOH) in major ion seawater, *Am. J. Sci.*, **281**, 788–806.
78. Newman, M. E., Filella, M., Chen, Y., Nègre, J. C., Perret, D. and Buffle, J. (1994). Submicron particles in the Rhine river. II. Comparison of field observations and model predictions, *Water Res.*, **28**, 107–118.
79. Buffle, J. and de Vitre, R. R., eds (1994). *Chemical and Biological Regulations in Aquatic Systems*. Lewis, Boca Raton, FL.
80. Venema, P., Hiemstra, T. and van Riemsdijk, W. H. (1997). Interaction of cadmium with phosphate on goethite, *J. Colloid Interface Sci.*, **192**, 94–103.
81. Schmitt, D., Taylor, H. E., Aiken, G. R., Roth, D. A. and Frimmel, F. H. (2002). Influence of natural organic matter on the adsorption of metal ions onto clay minerals, *Environ. Sci. Technol.*, **36**, 2932–2938.
82. Alonso, U. and Degueldre, C. (2003). Modelling americium sorption onto colloids: effect of redox potential, *Colloids Surf. A*, **217**, 55–62.
83. Painter, S., Cvetkovic, V., Pickett, D. and Turner, D. R. (2002). Significance of kinetics for sorption on inorganic colloids: modelling and experiment interpretation issues, *Environ. Sci. Technol.*, **36**, 5369–5375.
84. Evanko, C. R. and Dzombak, D. A. (1998). Influence of structural features on sorption of NOM-analogue organic acids to goethite, *Environ. Sci. Technol.*, **32**, 2846–2855.
85. Rouff, A. A., Reeder, R. J. and Fisher, N. S. (2002). Pb(II) sorption with calcite: a radiotracer study, *Aq. Geochem.*, **8**, 203–228.
86. Au, K. K., Penisson, A. C., Yang, S. and O'Melia, C. R. (1999). Natural organic matter at oxide/water interfaces: complexation and conformation, *Geochim. Cosmochim. Acta*, **63**, 2903–2917.
87. Templeton, A. S., Spormann, A. M. and Brown, G. E., Jr, (2003). Speciation of Pb(II) sorbed by *Burkholderia cepacia*/Goethite composites, *Environ. Sci. Technol.*, **37**, 2166–2172.
88. Davis, J. A. and Kent, D. B. (1990). Surface complexation modelling in aqueous geochemistry. In *Mineral-Water Interface Geochemistry*, eds Hochella, M. F. and White, A. F. Mineralogical Society of America, Washington, DC, pp. 177–260.
89. Peacock, C. L. and Sherman, D. M. (2004). Vanadium(V) adsorption onto goethite (alpha-FeOOH) at pH 1.5 to 12: a surface complexation model based on *ab initio* molecular geometries and EXAFS spectroscopy, *Geochim. Cosmochim. Acta*, **68**, 1723–1733.
90. Rietra, R. P. J. J., Hiemstra, T. and van Riemsdijk, W. H. (1999). The relationship between molecular structure and ion adsorption on variable charge minerals, *Geochim. Cosmochim. Acta*, **63**, 3009–3015.
91. Collins, C. R., Ragnarsdottir, K. V. and Shierman, D. M. (1999). Effect of inorganic and organic ligands on the mechanism of cadmium sorption to goethite, *Geochim. Cosmochim. Acta*, **63**, 2989–3002.
92. Eizinga, E. J., Peak, D. and Sparks, D. L. (2001). Spectroscopic studies of Pb(II)-sulfate interactions at the goethite–water interface, *Geochim. Cosmochim. Acta*, **65**, 2219–2230.

93. Foster, A. L., Brown, G. E. and Parks, G. A. (2003). X-ray absorption fine structure study of As(V) and Se(IV) sorption complexes on hydrous Mn oxides, *Geochim. Cosmochim. Acta*, **67**, 1937–1953.
94. Dixit, S. and Hering, J. G. (2003). Comparison of arsenic(V) and arsenic(III) sorption onto iron oxide minerals: implications for arsenic mobility, *Environ. Sci. Technol.*, **37**, 4182–4189.
95. Fukushi, K., Sato, T. and Yanase, N. (2003). Solid–solution reactions in As(V) sorption by schwertmannite, *Environ. Sci. Technol.*, **37**, 3581–3586.
96. Buerge-Weirich, D., Behra, P. and Sigg, L. (2003). Adsorption of copper, nickel, and cadmium on goethite in the presence of organic ligands, *Appl. Geochem.*, **9**, 65–85.
97. Randall, S. R., Shierman, D. M., Ragnarsdottir, K. V. and Collins, C. R. (1999). The mechanism of cadmium surface complexation on iron oxyhydroxide minerals, *Geochim. Cosmochim. Acta*, **63**, 2971–2987.
98. Liger, E., Charlet, L. and van Cappellen, P. (1999). Surface catalysis of uranium(VI) reduction by iron(II), *Geochim. Cosmochim. Acta*, **63**, 2939–2955.
99. Kennedy, C., Smith, D. S. and Warren, L. A. (2004). Surface chemistry and relative Ni sorptive capacities of synthetic hydrous Mn oxyhydroxides under variable wetting and drying regimes, *Geochim. Cosmochim. Acta*, **68**, 443–454.
100. Chen, C. C. and Hayes, K. F. (1999). X-ray absorption spectroscopy investigation of aqueous Co(II) and Sr(II) sorption at clay–water interfaces, *Geochim. Cosmochim. Acta*, **63**, 3205–3215.
101. Newton, P. P. and Liss, P. S. (1987). Positively charged suspended particles: studies in an iron-rich river and its estuary, *Limnol. Oceanogr.*, **32**, 1267–1276.
102. Kretzschmar, R. and Sticher, H. (1997). Transport of humic-coated iron oxide colloids in a sandy soil: influence of Ca<sup>2+</sup> and trace metals, *Environ. Sci. Technol.*, **31**, 3497–3504.
103. Crosby, S. A., Millward, G. E., Butler, E. I., Turner, D. R. and Whitfield, M. (1984). Kinetics of phosphate adsorption by iron oxyhydroxides in aqueous systems, *Estuar. Coast. Shelf Sci.*, **19**, 257–270.
104. Torrent, J., Schwertmann, U. and Barron, V. (1994). Phosphate sorption by natural hematites, *Eur. J. Soil Sci.*, **45**, 45–51.
105. Hiemstra, T. and Van Riemsdijk, W. H. (1996). A surface structural approach to ion adsorption: the charge distribution (CD) model, *J. Colloid Interface Sci.*, **179**, 488–508.
106. Diaz-Barrientos, E., Madrid, L., Contreras, M. C. and Morillo, E. (1990). Simultaneous adsorption of zinc and phosphate on synthetic lepidocrocite, *Aust. J. Soil Res.*, **28**, 549–557.
107. Jones, M. N. and Bryan, N. D. (1998). Colloidal properties of humic substances, *Adv. Colloid Interface Sci.*, **78**, 1–48.
108. Turner, D. R. (1995). Problems in trace metal speciation modelling. In *Metal Speciation and Bioavailability in Aquatic Systems*, eds Tessier, A. and Turner, D. R., Vol. 5, IUPAC Series on Analytical and Physical Chemistry of Environmental Systems, Vol. 3. John Wiley & Sons, Ltd, Chichester, pp. 149–204.
109. Tipping, E. and Hurley, M. A. (1996). A unifying model of cation binding by humic substances, *Geochim. Cosmochim. Acta*, **56**, 3627–3641.
110. Milne, C. J., Kinniburgh, D. G. and Tipping, E. (2001). Generic NICA–Donnan model parameters for proton binding by humic substances, *Environ. Sci. Technol.*, **35**, 2049–2059.
111. Tipping, E., ed. (2002). *Cation Binding by Humic Substances*. University of Cambridge Press, Cambridge.
112. Tipping, E., Loftis, S. and Lawlor, A. J. (1998). Modelling the chemical speciation of trace metals in the surface waters of the Humber system, *Sci. Total Environ.*, **210**, 63–77.
113. Kinniburgh, D. G., Milne, C. J., Benedetti, M. F., Pinheiro, J. P., Filius, J., Koopal, L. K. and van Riemsdijk, W. H. (1996). Metal ion binding by humic acid: application of the NICA–Donnan model, *Environ. Sci. Technol.*, **30**, 1687–1698.
114. Meylan, S., Odzak, N., Behra, R. and Sigg, L. (2004). Speciation of copper and zinc in natural freshwater: comparison of voltammetric measurements, diffusive gradients in thin films (DGT) and chemical equilibrium models, *Anal. Chim. Acta*, **510**, 91–100.
115. Tipping, E. (1994). WHAM—a chemical equilibrium model and computer code for waters, sediments and soils incorporating a discrete site electrostatic model of ion binding by humic substances, *Comput. Geosci. UK*, **20**, 973–1023.

116. Keizer, M. G. and van Riemsdijk, W. H., eds (1994). *ECOSAT: Equilibrium Calculation of Speciation and Transport*. Wageningen Agricultural University, Wageningen.
117. Allard, T., Menguy, N., Salomon, J., Calligaro, T., Weber, T., Calas, G. and Benedetti, M. F. (2004). Revealing forms of iron in river-borne material from major tropical rivers of the Amazon Basin (Brazil), *Geochim. Cosmochim. Acta*, **68**, 3079–3094.
118. Benedetti, M. F., Van Riemsdijk, W. H., Koopal, L. K., Kinniburgh, D. G., Goodey, D. C. and Milne, C. J. (1996). Metal ion binding by natural organic matter: from the model to the field, *Geochim. Cosmochim. Acta*, **60**, 2503–2513.
119. Cheng, T., De Schamphelaere, K., Loftis, S., Janssen, C. and Allen, H. E. (2005). Measurement and computation of zinc binding to natural dissolved organic matter in European surface waters, *Anal. Chim. Acta*, **542**, 230–239.
120. Wilkinson, K. J., Nègre, J. C. and Buffle, J. (1997). Coagulation of colloidal material in surface waters: the role of natural organic matter, *J. Contam. Hydrol.*, **26**, 229–243.
121. Buffle, J., Wilkinson, K. J., Stoll, S., Filella, M. and Zhang, J. (1998). A generalized description of aquatic colloidal interactions: the three-colloidal component approach, *Environ. Sci. Technol.*, **32**, 2887–2899.
122. Vasconcelos, M. T. S. D. and Leal, M. F. C. (2001). Adsorption and uptake of Cu by *Emiliania huxleyi* in natural seawater, *Environ. Sci. Technol.*, **35**, 508–515.
123. Vasconcelos, M. T. S. D., Leal, M. F. C. and van den Berg, C. M. G. (2002). Influence of the nature of the exudates released by different marine algae on the growth, trace metal uptake and exudation of *Emiliania huxleyi* in natural seawater, *Mar. Chem.*, **77**, 187–210.
124. Scoullos, M., Plavsic, M. and Karavoltos, S. (2004). Speciation studies of copper in the Gulf of Elefsis: the role of the macroalgae *Ulva rigida*, *Mar. Chem.*, **86**, 51–63.
125. Haack, E. A. and Warren, L. A. (2003). Biofilm hydrous manganese oxyhydroxides and metal dynamics in acid rock drainage, *Environ. Sci. Technol.*, **37**, 4138–4147.
126. Fein, J. B., Daughney, C. J., Yee, N. and Davis, T. A. (1997). A chemical equilibrium model for metal adsorption onto bacterial surfaces, *Geochim. Cosmochim. Acta*, **61**, 3319–3328.
127. Daughney, C. J., Siciliano, S. D., Rencz, A. N., Lean, D. and Fortin, D. (2002). Hg(II) adsorption by bacteria: a surface complexation model and its application to shallow acidic lakes and wetlands in Kejimkujik National Park, Nova Scotia, Canada, *Environ. Sci. Technol.*, **36**, 1546–1553.
128. Boyanov, M. I., Kelly, S. D., Kemner, K. M., Bunker, B. A., Fein, J. B. and Fowle, D. A. (2003). Adsorption of cadmium to *Bacillus subtilis* bacterial cell walls: a pH-dependent X-ray absorption fine structure spectroscopy study, *Geochim. Cosmochim. Acta*, **67**, 3299–3311.
129. Prange, A. and Modrow, H. (2002). X-ray adsorption spectroscopy and its applications in biological, agricultural and environmental research, *Rev. Environ. Sci. Biotechnol.*, **1**, 259–276.
130. Plette, A. C. C., Benedetti, M. F. and van Riemsdijk, W. H. (1996). Competitive binding of protons, calcium, cadmium and zinc to isolated cell walls of a Gram-positive soil bacterium, *Environ. Sci. Technol.*, **30**, 1902–1910.
131. Fowle, D. A. and Fein, J. B. (1999). Competitive adsorption of metal cations onto two Gram positive bacteria: testing the chemical equilibrium model, *Geochim. Cosmochim. Acta*, **63**, 3059–3067.
132. Cox, J. S., Scott Smith, D., Warren, L. A. and Ferris, F. G. (1999). Characterising heterogeneous bacterial surface functional groups using discrete affinity spectra for proton binding, *Environ. Sci. Technol.*, **33**, 4514–4521.
133. Yee, N. and Fein, J. (2001). Cd adsorption onto bacterial surfaces: a universal adsorption edge?, *Geochim. Cosmochim. Acta*, **65**, 2037–2042.
134. Smiejan, A., Wilkinson, K. J. and Rossier, C. (2003). Cd bioaccumulation by a freshwater bacterium, *Rhodospirillum rubrum*, *Environ. Sci. Technol.*, **37**, 701–706.
135. Xue, H. B., Stumm, W. and Sigg, L. (1988). The binding of heavy metals to algal surfaces, *Water Res.*, **22**, 917–926.
136. Knauer, K., Behra, R. and Sigg, L. (1997). Adsorption and uptake of copper by the green alga *Scenedesmus subspicatus* (Chlorophyta), *J. Phycol.*, **33**, 596–601.
137. Tipping, E. and Heaton, M. J. (1983). The adsorption of aquatic humic substances by 2 oxides of manganese, *Geochim. Cosmochim. Acta*, **47**, 1393–1397.

138. Day, G. M., Hart, B. T., McKelvie, I. D. and Beckett, R. (1994). Adsorption of natural organic matter onto goethite, *Colloids Surf. A*, **89**, 1–13.
139. Gu, B. H., Schmitt, J., Chen, Z. H., Liang, L. Y. and McCarthy, J. F. (1994). Adsorption and desorption of natural organic matter on iron oxide—mechanisms and models, *Environ. Sci. Technol.*, **28**, 38–46.
140. Ledin, A., Karlsson, S. and Allard, B. (1993). Effects of pH, ionic strength and a fulvic acid on size distribution and surface charge of colloidal quartz and hematite, *Appl. Geochem.*, **8**, 409–414.
141. Stumm, W. (1993). Aquatic colloids as chemical reactants—surface structure and reactivity, *Colloids Surf. A*, **73**, 1–18.
142. Murphy, E. M., Zachara, J. M., Smith, S. C., Phillips, J. L. and Wietsma, T. W. (1994). Interaction of hydrophobic organic compounds with mineral-bound humic substances, *Environ. Sci. Technol.*, **28**, 1291–1299.
143. Fairhurst, A. J., Warwick, P. and Richardson, S. (1995). The influence of humic acid on the adsorption of europium onto inorganic colloids as a function of pH, *Colloids Surf. A*, **99**, 187–199.
144. Ledin, A., Karlsson, S., Duker, A. and Allard, B. (1994). Measurements *in situ* of concentration and size distribution of colloidal matter in deep groundwaters by photon correlation spectroscopy, *Water Res.*, **28**, 1539–1545.
145. Duker, A., Ledin, A., Karlsson, S. and Allard, B. (1995). Adsorption of zinc on colloidal (hydr)oxides of Si, Al and Fe in the presence of a fulvic acid, *Appl. Geochem.*, **10**, 197–205.
146. Murphy, R. J., Lenhart, J. J. and Honeyman, B. D. (1999). The sorption of thorium(IV) and uranium(VI) to hematite in the presence of natural organic matter, *Colloids Surf. A*, **157**, 47–62.
147. Lenhart, J. J. and Honeyman, B. D. (1999). Uranium(VI) sorption to hematite in the presence of humic acid, *Geochim. Cosmochim. Acta*, **63**, 2819–2901.
148. Lenhart, J. J., Cabaniss, S. E., McCarthy, P. and Honeyman, B. D. (2000). Uranium(VI) complexation with citric, humic and fulvic acids, *Radiochim. Acta*, **88**, 345–353.
149. Tessier, A., Fortin, D., Belzile, N., DeVitre, R. R. and Leppard, G. G. (1996). Metal sorption to diagenetic iron and manganese oxyhydroxides and associated organic matter: narrowing the gap between field and laboratory measurements, *Geochim. Cosmochim. Acta*, **60**, 387–404.
150. Tessier, A., Rapin, F. and Carignan, R. (1985). Trace metals in oxic lake sediments: possible adsorption onto iron oxyhydroxides, *Geochim. Cosmochim. Acta*, **49**, 183–194.
151. Town, R. M. and Filella, M. (2000). Dispelling the myths: is the existence of L1 and L2 ligands necessary to explain metal ion speciation in natural waters?, *Limnol. Oceanogr.*, **45**, 1341–1357.
152. van Veen, E., Gardner, M. and Comber, S. (2001). Temporal variation of copper and zinc complexation capacity in the Humber estuary, *J. Environ. Monit.*, **3**, 322–323.
153. Buffie, J., ed. (1990). *Complexation Reactions in Aquatic Systems: an Analytical Approach*. Ellis Horwood, Chichester.
154. Jeon, B. H., Dempsey, B. A., Burgos, W. D., Royer, R. A. and Roden, E. E. (2004). Modeling the sorption kinetics of trivalent metal ions to hematite, *Water Res.*, **38**, 2499–2504.
155. Geckeis, H., Rabung, T., Ngo Manh, T., Kim, J. I. and Beck, H. P. (2002). Humic colloid-borne natural polyvalent metal ions: dissociation experiment, *Environ. Sci. Technol.*, **36**, 2946–2952.
156. Scheinost, A. C., Abend, S., Pandya, K. I. and Sparks, D. L. (2001). Kinetic controls on Cu and Pb sorption by ferrihydrite, *Environ. Sci. Technol.*, **35**, 1090–1096.
157. Roberts, D. R., Ford, R. G. and Sparks, D. L. (2003). Kinetics and mechanisms of Zn complexation on metal oxides using EXAFS spectroscopy, *J. Colloid Interface Sci.*, **263**, 364–376.
158. Strawn, D. G., Scheidegger, A. M. and Sparks, D. L. (1998). Kinetics and mechanisms of Pb(II) sorption and desorption at the aluminium oxide water interface, *Environ. Sci. Technol.*, **32**, 2596–2601.

159. van Beinum, W., Hofmann, A., Meeussen, J. C. L. and Kretzschmar, R. (2005). Sorption kinetics of strontium in porous hydrous ferric oxide aggregates. I. The donnan diffusion model, *J. Colloid Interface Sci.*, **283**, 18–28.
160. McLaren, R. G., Backes, C. A., Rate, A. W. and Swift, R. S. (1998). Cadmium and cobalt desorption kinetics from soil clays: effect of sorption period, *Soil Sci. Soc. Am. J.*, **62**, 332–337.
161. Town, R. M. and Filella, M. (2002). Crucial role of the detection window in metal ion speciation analysis in aquatic systems: the interplay of thermodynamic and kinetic factors as exemplified by nickel and cobalt, *Anal. Chim. Acta*, **466**, 285–293.
162. Wang, F. and Tessier, A. (1999). Cadmium complexation with bisulfide, *Environ. Sci. Technol.*, **33**, 4270–4277.
163. Tipping, E. and Cooke, D. (1982). The effects of adsorbed humic substances on the surface charge of goethite (alpha-FEOOH) in freshwaters, *Geochim. Cosmochim. Acta*, **46**, 75–80.
164. Neihof, R. A. and Loeb, G. I. (1974). Dissolved organic matter in seawater and the electric charge of immersed surfaces, *J. Mar. Res.*, **32**, 5–12.
165. Hunter, K. A. and Liss, P. S. (1979). The surface charge of suspended particles in estuarine and coastal waters, *Nature*, **282**, 823–825.
166. Hunter, K. A. (1980). Microelectrophoretic properties of natural surface active organic matter in coastal seawater, *Limnol. Oceanogr.*, **25**, 807–822.
167. Hunter, K. A. and Liss, P. S. (1982). Organic matter and the surface charge of suspended particles in estuarine waters, *Limnol. Oceanogr.*, **27**, 322.
168. Mosley, L. M., Hunter, K. A. and Ducker, W. A. (2003). Forces between colloidal particles in natural waters, *Environ. Sci. Technol.*, **37**, 3303–3308.
169. Sander, S., Mosley, L. M. and Hunter, K. A. (2004). Investigation of interparticle forces in natural waters: effects of adsorbed humic acids on iron oxyde and alumina surface properties, *Environ. Sci. Technol.*, **38**, 4791–4796.
170. IAEA (1985). *Sediment K<sub>d</sub>'s and Concentration Factors for Radionuclides in the Marine Environment*. Technical Report Series 247. IAEA, Vienna.
171. Santschi, P. H. and Honeyman, B. D. (1989). Radionuclides in aquatic environments, *Radiat. Phys. Chem.*, **34**, 213–240.
172. Tessier, A. (1992). Sorption of trace elements on natural particles in oxic environments. In *Environmental Particles*, eds Buffle, J. and van Leeuwen, H. P., IUPAC Series on Analytical and Physical Chemistry of Environmental Systems, Vol. 1. Lewis, Boca Raton, FL, pp. 425–454.
173. Sigg, L. (1998). Partitioning of metals to suspended particles. In *Metals in Surface Waters*, eds Allen, H., Garrison, A. and Luther, G. Ann Arbor Press, Ann Arbor, MI pp. 217–240.
174. Honeyman, B. D. and Santschi, P. H. (1991). Coupling of trace metal adsorption and particle aggregation: kinetic and equilibrium studies using <sup>59</sup>Fe-labeled hematite, *Environ. Sci. Technol.*, **25**, 1739–1747.
175. Wen, L. S., Santschi, P. H. and Tang, D. (1997). Interactions between radioactively labeled colloids and natural particles: evidence for colloidal pumping, *Geochim. Cosmochim. Acta*, **62**, 2867–2878.
176. Baskaran, M., Santschi, P. H., Benoit, G. and Honeyman, B. D. (1992). Scavenging of Th isotopes by colloids in seawater of the Gulf of Mexico, *Geochim. Cosmochim. Acta*, **56**, 3375–3388.
177. Baskaran, M. and Santschi, P. H. (1993). The role of particles and colloids in the transport of radionuclides in coastal environments of Texas, *Mar. Chem.*, **43**, 95–114.
178. Benoit, G. (1995). Evidence of the particle concentration effects for lead and other metals in fresh waters based on ultraclean technique analysis, *Geochim. Cosmochim. Acta*, **59**, 2677–2687.
179. Benoit, G. and Rozan, T. (1999). The influence of size distribution on the particle concentration effect and trace metal partitioning in rivers, *Geochim. Cosmochim. Acta*, **63**, 113–127.
180. Zhou, J. L., Liu, Y. P. and Abrahams, P. W. (2003). Trace metal behaviour in the Conwy estuary, North Wales, *Chemosphere*, **51**, 429–440.
181. Honeyman, B. D. and Santschi, P. H. (1988). Metals in aquatic systems, *Environ. Sci. Technol.*, **22**, 862–871.

182. Honeyman, B. D. (1999). Colloidal culprits in contamination, *Nature*, **397**, 23–24.
183. Santschi, P. H., Lenhart, J. and Honeyman, B. D. (1997). Heterogeneous processes affecting trace contaminant distribution in estuaries: the role of natural organic matter, *Mar. Chem.*, **58**, 99–125.
184. Milne, C. J., Kinniburgh, D. G., de Wit, J. C. M., van Riemsdijk, W. H. and Koopal, L. K. (1995). Analysis of proton binding by a peat humic acid using a simple electrostatic model, *Geochim. Cosmochim. Acta*, **59**, 1101–1112.
185. Loftis, S. and Tipping, E. (2000). Solid–solution metal partitioning in the Humber rivers: application of WHAM and SCAMP, *Sci. Total Environ.*, **251–252**, 381–399.
186. Dahlqvist, R., Benedetti, M. F., Andersson, K., Turner, D., Larsson, T., Stolpe, B. and Ingrı, J. (2004). Association of calcium with colloidal particles and speciation of calcium in the Kalix and Amazon rivers, *Geochim. Cosmochim. Acta*, **68**, 4059–4075.
187. Guo, L., Hunt, B. and Santschi, P. H. (2001). Ultrafiltration behavior of major ions (Na, Ca, Mg, F, Cl, and SO<sub>4</sub>) in natural waters, *Water Res.*, **35**, 1500–1508.
188. Assemi, S., Newcombe, G., Hepplewhite, C. and Beckett, R. (2004). Characterization of natural organic matter fractions separated by ultrafiltration using flow field-flow fractionation, *Water Res.*, **38**, 1467–1476.
189. Rozan, T. F. and Benoit, G. (1999). Geochemical factors controlling free Cu ion concentrations in river water, *Geochim. Cosmochim. Acta*, **63**, 3311–3319.
190. Tang, D., Warnken, K. W. and Santschi, P. H. (2001). Organic complexation of copper in surface waters of Galveston Bay, *Limnol. Oceanogr.*, **46**, 321–330.
191. Tang, D., Warnken, K. W. and Santschi, P. H. (2002). Distribution and partitioning of trace metals (e.g., Ni, Cu, Cd, Pb, Zn) in Galveston Bay waters, *Mar. Chem.*, **78**, 29–45.
192. Sukola, K., Wang, F. and Tessier, A. (2005). Metal–sulfide species in oxic waters, *Anal. Chim. Acta*, **528**, 183–195.
193. Lead, J. R., Hamilton-Taylor, J. and Davison, W. (1998). The effect of sequential extractions of suspended particulate matter on trace metal sorption and microbial cell stability, *Sci. Total Environ.*, **209**, 193–199.
194. Hlavay, J., Polyak, K. and Weisz, M. (2001). Monitoring of the natural environment by chemical speciation of elements in aerosol and sediment samples, *J. Environ. Monit.*, **3**, 74–80.
195. Sekaly, A. L. R., Murimboh, J., Hassan, N. M., Mandal, R., Ben Younes, M. E., Chakrabarti, C. L., Back, M. H. and Gregoire, D. C. (2003). Kinetic speciation of Co(II), Ni(II), Cu(II) and Zn(II) in model solutions and freshwaters: lability and the d electron configuration, *Environ. Sci. Technol.*, **37**, 68–74.
196. Xue, H., Gachter, R. and Sigg, L. (1997). Comparison of Cu and Zn cycling in eutrophic lakes with oxic and anoxic hypolimnion, *Aquat. Sci.*, **59**, 176–189.
197. Xue, H. and Sunda, W. G. (1997). Comparison of [Cu<sup>2+</sup>] measurements in lake water determined by ligand exchange and cathodic stripping voltammetry and by ion-selective electrode, *Environ. Sci. Technol.*, **31**, 1902–1909.
198. Odzak, N., Kistler, D., Xue, H. and Sigg, L. (2002). *In situ* trace metal speciation in a eutrophic lake using the technique of diffusion gradients in thin films (DGT), *Aquat. Sci.*, **64**, 292–299.
199. Xue, H. and Sigg, L. (1998). Cadmium speciation and complexation by natural organic ligands in freshwater, *Anal. Chim. Acta*, **363**, 249–259.
200. McCormack, P., Worsfold, P. J. and Gledhill, M. (2003). Separation and detection of siderophores produced by marine bacterioplankton using high-performance liquid chromatography with electrospray ionization mass spectrometry, *Anal. Chem.*, **75**, 2647–2652.
201. Benedetti, M. F., Mounier, S., Filizola, N., Benaim, J. and Seyler, P. (2003). Carbon and metal concentrations, size distributions and fluxes in major rivers of the Amazon basin, *Hydrol. Process.*, **17**, 1363–1377.
202. Gimpel, J., Zhang, H., Davison, W. and Edwards, A. C. (2003). *In situ* trace metal speciation in lake surface waters using DGT, dialysis and filtration, *Environ. Sci. Technol.*, **37**, 138–146.
203. Hasselov, M., Lyven, V., Haraldsson, C. and Sirinawin, W. (1999). Determination of continuous size and trace element distribution of colloidal material in natural water by on-line coupling of flow field-flow fractionation with ICPMS, *Anal. Chem.*, **71**, 3497–3502.

204. Taillefert, M., Lienemann, C. P., Gaillard, J. F. and Perret, D. (2000). Speciation, reactivity, and cycling of Fe and Pb in a meromictic lake, *Geochim. Cosmochim. Acta*, **64**, 169–183.
205. Lyven, B., Hasselov, M., Turner, D. R., Haraldsson, C. and Andersson, K. (2003). Competition between iron- and carbon-based colloidal carriers for trace metals in a freshwater assessed using flow field-flow fractionation coupled to ICP-MS, *Geochim. Cosmochim. Acta*, **67**, 3791–3802.
206. Bruland, K. W. (1983). Trace metals in seawater. In *Chemical Oceanography*, Vol. 2, eds Riley, J. and Chester, R. Academic Press, New York, pp. 157–220.
207. Donat, J. R. and Bruland, K. W. (1995). Trace elements in the oceans. In *Trace Metals in Natural Waters*, eds Salbu, B. and Steinnes, E. CRC Press, Boca Raton, FL, pp. 247–281.
208. Hunter, K. A. and Boyd, P. (1999). Biogeochemistry of trace metals in the ocean, *Mar. Freshwater Res.*, **50**, 739–753.
209. Kepkay, P. E. (2000). Colloids and the ocean carbon cycle. In *Marine Chemistry*, ed. Wangersky, P. The Handbook of Environmental Chemistry. Springer Verlag, New York, pp. 35–56.
210. Myklestad, S. M. (2000). Dissolved organic carbon from phytoplankton. In *Marine Chemistry*, ed. Wangersky, P. The Handbook of Environmental Chemistry. Springer Verlag, New York, pp. 111–148.
211. Zutic, V. and Svetlicic, V. (2000). Interfacial processes. In *Marine Chemistry*, ed. Wangersky, P. The Handbook of Environmental Chemistry. Springer Verlag, New York, pp. 149–166.
212. Wells, M. L. (2002). Marine colloids and trace metals. In *Biogeochemistry of Marine Dissolved Organic Matter*, eds Hansell, D. and Carlson, C. Academic Press, New York, pp. 347–404.
213. Guetzloff, T. F. and Rice, J. A. (1996). Micellar nature of humic colloids. In *Humic and Fulvic Acids, Isolation, Structure, and Environmental Role*, eds Gaffney, J. S., Marley, N. A. and Clark, S. B. ACS Symposium Series, Vol 651. American Chemical Society, Washington, DC, pp. 18–25.
214. Ron, E. Z. and Rosenberg, E. (2001). Natural roles of biosurfactants, *Environ. Microbiol.*, **3**, 229–236.
215. Santschi, P. H., Guo, L., Baskaran, M., Trumbore, S., Southon, J., Bianchi, T. S., Honneyman, B. and Cifuentes, L. (1995). Isotopic evidence for contemporary origin of high-molecular weight organic matter in oceanic environments, *Geochim. Cosmochim. Acta*, **59**, 625–631.
216. Ahrlund, S., Chatt, S. J. and Davies, W. R. (1958). The relative affinities of ligand atoms for acceptor molecules and ions, *Quant. Rev.*, **12**, 265–276.
217. Rees, D. A. (1972). Polysaccharide gels. A molecular view, *Chem. Ind.*, **19**, 630–635.
218. Geesey, G. G. and Jang, L. (1989). Interactions between metal ions and capsular polymers. In *Metal Ions and Bacteria*, eds Beveridge, T. and Doyle, R. John Wiley & Sons, Inc., New York, pp. 325–357.
219. Moe, S. T., Draget, K. I., SkjÅk-Bræk, G. and Smidrød, O. (1995). Alginates. In *Food Polysaccharides and Their Application*, ed. Stephen, A. Marcel Dekker, New York, pp. 245–286.
220. Guo, L., Santschi, P. H. and Warnken, K. W. (2000). Trace metal composition of colloidal materials in estuarine and marine environments, *Mar. Chem.*, **70**, 257–275.
221. Rudd, T., Sterritt, R. M. and Lester, J. N. (1984). Formation and conditional stability constants of complexes formed between heavy metals and bacterial extracellular polymers, *Water Res.*, **18**, 379–384.
222. Santschi, P. H., Balnois, E., Wilkinson, K. J., Zhang, J. W., Buffe, J. and Guo, L. D. (1998). Fibrillar polysaccharides in marine macromolecular organic matter as imaged by atomic force microscopy and transmission electron microscopy, *Limnol. Oceanogr.*, **43**, 896–908.
223. Decho, A. W. (1990). Microbial exopolymer secretions in the ocean environments their role(s) in food webs and marine processes, *Oceanogr. Mar. Biol. Annu. Rev.*, **28**, 73–153.
224. Leppard, G. G. (1995). The characterization of algal and microbial mucilages and their aggregates in aquatic ecosystems, *Sci. Total Environ.*, **165**, 103–131.
225. Dickinson, E. (2003). Hydrocolloids at interfaces and the influence on the properties of dispersed systems, *Food Hydrocolloids*, **17**, 25–39.

226. Guo, L., Hung, C. C., Santschi, P. H. and Walsh, I. D. (2002).  $^{234}\text{Th}$  scavenging and its relationship to acid polysaccharide abundance in the Gulf of Mexico, *Mar. Chem.*, **78**, 103–119.
227. Leppard, G. G. (1997). Colloidal organic fibrils of acid polysaccharides in surface water: electron-optical characteristics, activities and chemical estimates of abundance, *Colloids Surf. A*, **120**, 1–15.
228. Cowen, J. P. and Bruland, K. W. (1985). Metal deposits associated with bacteria – implications for Fe and Mn marine biogeochemistry, *Deep-Sea Res.*, **32**, 253–272.
229. Kinrade, S. D., Gillson, A. M. E. and Knight, C. T. G. (2002). Silicon-29 NMR evidence of a transient hexavalent silicon complex in the diatom *Navicula pelliculosa*, *J. Chem. Soc., Dalton Trans.*, 307–309.
230. Leveille, R. J., Fyfe, W. S. and Longstaffe, F. J. (2000). Geomicrobiology of carbonate-silicate microbialites from Hawaiian basaltic sea caves, *Chem. Geol.*, **169**, 339–355.
231. Alldredge, A. L., Passow, U. and Logan, B. E. (1993). The abundance and significance of a class of large, transparent organic particles in the ocean, *Deep-Sea Res. I*, **40**, 1131–1140.
232. Mopper, K., Zhou, J. A., Ramana, K. S., Passow, U., Dam, H. G. and Drapeau, D. T. (1995). The role of surface-active carbohydrates in the flocculation of a diatom bloom in a mesocosm, *Deep-Sea Res. II*, **42**, 47–73.
233. Quigley, M. S., Santschi, P. H., Hung, C. C., Guo, L. and Honeyman, B. D. (2002). Importance of polysaccharides for  $^{234}\text{Th}$  complexation to marine organic matter, *Limnol. Oceanogr.*, **47**, 367–377.
234. Santschi, P. H., Hung, C. C., Schultz, G., Alfarado-Quiroz, N., Guo, L. D., Pinckney, J. and Walsh, I. (2003). Control of acid polysaccharide production and Th-234 and POC export fluxes by marine organisms, *Geophys. Res. Lett.*, **30**, art. no. 1044.
235. Costerton, J. W., ed. (1984). *Current Perspectives in Microbial Ecology*. American Society of Microbiology, Washington, DC.
236. Hirose, K. (1996). Determination of a strong organic ligand dissolved in seawater: thorium-complexing capacity of oceanic dissolved organic matter, *J. Radioanaly. Nucl. Chem.*, **204**, 193–204.
237. Hirose, K. and Tanoue, E. (2001). Strong ligand for thorium complexation in marine bacteria, *Mar. Environ. Res.*, **51**, 95–121.
238. Hirose, K. (2004). Chemical speciation of thorium in marine biogenic particulate matter, *Sci. World J.*, **4**, 67–76.
239. Ratanathanawongs, W. S. K. and Keil, R. G. (1997). Monitoring the biological and physical reactivity of dextran carbohydrates in seawater incubations using flow field-flow fractionation, *J. Liq. Chromatogr. Relat. Technol.*, **20**, 2815–2834.
240. Zanardi-Lamardo, E., Clark, C. D. and Zika, R. G. (2001). Frit inlet/frit outlet flow field-flow fractionation: methodology for colored dissolved organic material in natural waters, *Anal. Chim. Acta*, **443**, 171–181.
241. Zanardi-Lamardo, E., Clark, C. D., Moore, C. A. and Zika, R. G. (2002). Comparison of the molecular mass and optical properties of colored dissolved organic material in two rivers and coastal waters by flow field-flow fractionation, *Environ. Sci. Technol.*, **36**, 2806–2814.
242. Dai, M., Buesseler, K. O., Ripple, P., Andrews, J., Belastock, R. A., Gustafsson, O. and Moran, S. B. (1998). Evaluation of two cross-flow ultrafiltration membranes for isolating marine organic colloids, *Mar. Chem.*, **62**, 17–36.
243. Moran, S. B. and Buesseler, K. O. (1992). Short residence time of colloids in the upper ocean estimated from  $^{238}\text{U}$ - $^{234}\text{Th}$  disequilibria, *Nature*, **359**, 221–223.
244. Muller, F. L. L. (1998). Colloid/solution partitioning of metal-selective organic ligands, and its relevance to Cu, Pb, and Cd cycling in the Firth of Clyde, *Estuar. Coast. Shelf Sci.*, **46**, 419–437.
245. Muller, F. L. L. (1999). Evaluation of the effects of natural dissolved and colloidal organic ligands on the electrochemical lability of Cu, Pb, and Cd in the Arran Deep, Scotland, *Mar. Chem.*, **67**, 43–60.
246. Muller, F. L. L. (1996). Interactions of copper, lead and cadmium with the dissolved, colloidal and particulate components of estuarine and coastal waters, *Mar. Chem.*, **52**, 245–268.

247. Sholkovitz, E. R., Boyle, E. A. and Price, N. B. (1978). The removal of dissolved humic acids and iron during estuarine mixing, *Earth Planet. Sci. Lett.*, **40**, 130–136.
248. Guo, L., Wen, L., Tang, D. and Santschi, P. H. (2000). Re-examination of cross-flow ultra-filtration for sampling aquatic colloids: evidence from molecular probes, *Mar. Chem.*, **69**, 75–90.
249. Nash, K. L. and Choppin, G. R. (1980). Interaction of humic and fulvic acids with Th(IV), *J. Inorg. Nucl. Chem.*, **42**, 1045–1050.
250. Hirose, K. and Tanoue, E. (1998). The vertical distribution of the strong ligand in particulate organic matter in the North Pacific, *Mar. Chem.*, **59**, 235–252.
251. Huh, C. A., Moore, W. S. and Kadko, D. C. (1989). Oceanic  $^{232}\text{Th}$ : a reconnaissance and implications of global distribution from manganese nodules, *Geochim. Cosmochim. Acta*, **53**, 1357–1366.
252. Benner, R. (2002). Chemical composition and reactivity. In *Biogeochemistry of Marine Dissolved Organic Matter*, eds Hansell, D. and Carlson, C. Academic Press, New York, pp. 59–90.
253. Alvarado Quiroz, N. A., Hung, C.-C. and Santschi, P. H. (2005). Binding of thorium(IV) to carboxylic acid, phosphate and sulfate functional groups from marine exopolymeric substances (EPS), *Mar. Chem.*, submitted.
254. Means, J. C. and Wijayaratne, R. D. (1989). Sorption of benzedrine, toluidine, and azobenzene on colloidal organic matter. In *Aquatic Humic Substances*, eds Suffet, I. and MacCarthy, P. American Chemical Society, Washington, DC, pp. 209–221.
255. Moffett, J. W., Zika, R. G. and Brand, L. E. (1990). Distribution and potential sources and sinks of copper chelators in Sargasso Sea, *Deep-Sea Res.*, **37**, 27–36.
256. Ahmad, R., Arakawa, H. and Tajmir-Riahi, H. A. (2003). A comparative study of DNA complexation with Mg(II) and Ca(II) in aqueous solution: major and minor grooves bindings, *Biophys. J.*, **84**, 2460–2466.
257. Deng, H., Bloomfield, V. A., Benevides, J. M. and Thomas, G. J. J. (2000). Structural basis of polyamine–DNA recognition: spermidine and spermine interactions with genomic B-DNAs of different GC content probed by Raman spectroscopy, *Nucleic Acids Res.*, **28**, 3379–3385.
258. Turner, D. R. and Hunter, K. A., eds (2001). *The Biogeochemistry of Iron in Seawater*. John Wiley & Sons, Inc., New York.
259. Nishioka, J., Takeda, S., Wong, C. S. and Johnson, W. K. (2001). Size-fractionated iron concentrations in the northeast Pacific Ocean: distribution of soluble and small colloidal iron, *Mar. Chem.*, **74**, 157–179.
260. Wu, J. and Luther, G. W. (1994). Size-fractionated iron concentration in water column of the Northwest Atlantic Ocean, *Limnol. Oceanogr.*, **38**, 1119–1129.
261. Liu, X. and Millero, F. J. (1999). The solubility of iron hydroxide in sodium chloride solutions, *Geochim. Cosmochim. Acta*, **63**, 3487–3497.
262. Liu, X. and Millero, F. J. (2002). The solubility of iron in seawater, *Mar. Chem.*, **77**, 43–54.
263. Chen, M., Wang, W. X. and Guo, L. D. (2004). Phase partitioning and solubility of iron in natural seawater controlled by dissolved organic matter, *Global Biogeochem. Cycles*, **18**, GB4013.
264. Millero, F. J., Yao, W. S. and Alcher, J. (1995). The speciation of Fe(II) and Fe(III) in natural waters, *Mar. Chem.*, **50**, 21–39.
265. Rue, E. L. and Bruland, K. W. (1995). Complexation of Fe(III) by natural organic ligands in the central North Pacific as determined by a new competitive ligand equilibration adsorptive cathodic stripping voltammetric method, *Mar. Chem.*, **50**, 117–138.
266. Kuma, K., Nishioka, J. and Matsunaga, K. (1996). Controls on iron(III) hydroxide solubility in seawater: the influence of pH and natural organic chelators, *Limnol. Oceanogr.*, **41**, 396–407.
267. Rue, E. L. and Bruland, K. W. (1997). The role of organic complexation on ambient iron chemistry in the equatorial Pacific Ocean and the response of a mesoscale iron addition experiment, *Limnol. Oceanogr.*, **42**, 901–910.
268. Takata, H., Kuma, K., Iwade, S. and Yamajyo, Y. (2004). Spatial variability of iron in the surface water of the northwestern North Pacific Ocean, *Mar. Chem.*, **86**, 139–157.

269. Pokrovsky, O. S. and Schott, J. (2002). Iron colloids/organic matter associated transport of major and trace elements in small boreal rivers and their estuaries (NW Russia), *Chem. Geol.*, **190**, 141–179.
270. Bruland, K. W. and Rue, E. L. (2001). Analytical methods for the determination of concentrations and speciation of iron. In *The Biogeochemistry of Iron in Seawater*, eds Turner, D. R. and Hunger, K. A. John Wiley & Sons, Inc., New York, pp. 255–290.
271. van den Berg, C. M. G., Merks, A. G. and Duursma, E. K. (1987). Organic complexation and its control of the dissolved concentrations of copper and zinc in the Scheldt estuary, *Estuar. Coast. Shelf Sci.*, **24**, 785–797.
272. Kogut, M. B. and Voelker, B. M. (2001). Strong copper-binding behavior of terrestrial humic substances in seawater, *Environ. Sci. Technol.*, **35**, 1149–1156.
273. Whitehouse, B. G., Yeats, P. A. and Strain, P. M. (1990). Cross-flow filtration of colloids from aquatic environments, *Limnol. Oceanogr.*, **35**, 1368–1375.
274. Greenamoyer, J. M. and Moran, S. B. (1996). Evaluation of an Osmonics spiral-wound cross-flow ultrafiltration system for sub- $\mu\text{m}$  sampling of Cd, Cu, and Ni in seawater, *Mar. Chem.*, **55**, 153–163.
275. Sanudo-Wilhelmy, S. A., Rivera-Duarte, I. and Flegal, A. R. (1996). Distribution of colloidal trace metals in the San Francisco Bay estuary, *Geochim. Cosmochim. Acta*, **60**, 4933–4944.
276. Leal, M. F. C. and van den Berg, C. M. G. (1998). Evidence for strong copper(I) complexation by organic ligands in seawater, *Appl. Geochem.*, **4**, 49–75.
277. Leal, M. F. C., Vasconcelos, M. T. S. D. and van den Berg, C. M. G. (1999). Copper induced release of complexing ligands similar to thiols by *Emiliania huxleyi* in seawater cultures, *Limnol. Oceanogr.*, **44**, 1750–1762.
278. Wen, L. S., Stordal, M. C., Gill, G. A. and Santschi, P. H. (1996). An ultra-clean cross-flow ultrafiltration technique for the study of trace metal phase speciation in sea water, *Mar. Chem.*, **45**, 129–152.
279. Reitmeyer, R., Powell, R. T., Landing, W. M. and Measure, C. I. (1996). Colloidal aluminum and iron in seawater: an intercomparison between various cross-flow ultrafiltration systems, *Mar. Chem.*, **55**, 75–91.
280. Al-Farawati, R. and van den Berg, C. M. G. (1999). Metal–sulfide complexation in seawater, *Mar. Chem.*, **63**, 331–352.
281. Lloyd, J. R. (2003). Microbial reduction of metals and radionuclides, *FEMS Microbiol. Rev.*, **27**, 411–425.
282. Buesseler, K. O. (1998). The decoupling of production and particulate export in the surface ocean, *Global Biogeochem. Cycles*, **12**, 297–310.
283. Santschi, P. H., Murray, J. W., Baskaran, M., Benitez-Nelson, C. R., Guo, L., Hung, C.-C., Lamborg, C., Moran, S. B., Passow, U. and Roy-Barman, M. (2005). Thorium speciation in seawater, *Mar. Chem.*, **100**, 250–268.
284. Wu, J. F., Boyle, E., Sunda, W. and Wen, L. S. (2001). Soluble and colloidal iron in the oligotrophic North Atlantic and North Pacific, *Science*, **293**, 847–849.
285. Gaillard, J. F., Webb, S. M. and Quintana, J. P. G. (2001). Quick x-ray absorption spectroscopy for determining metal speciation in environmental samples, *J. Synchrotron Radiat.*, **8**, 928–930.
286. Van Hullebusch, E. D., Zandvoort, M. H. and Lens, P. N. L. (2003). Metal immobilisation by biofilms: mechanisms and analytical tools, *Rev. Environ. Sci. Biotechnol.*, **2**, 9–33.
287. Benner, R., Pakulski, J. D., McCarthy, M., Hedges, J. and Hatcher, P. (1992). Bulk chemical characteristics of dissolved organic matter in the ocean, *Science*, **255**, 1561–1564.
288. Guo, L., Coleman, L. C. H. J. and Santschi, P. H. (1994). The distribution of colloidal and dissolved organic carbon in the Gulf of Mexico, *Mar. Chem.*, **45**, 105–119.
289. Guo, L., Santschi, P. H., Cifuentes, L. A., Trumbore, S. and Southon, J. (1996). Cycling of high molecular weight dissolved organic matter in the Middle Atlantic Bight as revealed by carbon isotopic ( $^{13}\text{C}$  and  $^{14}\text{C}$ ) signatures, *Limnol. Oceanogr.*, **41**, 1242–1252.
290. Liu, Q., Parrish, C. C. and Helleur, R. (1998). Lipid class and carbohydrate concentrations in marine colloids, *Mar. Chem.*, **60**, 177–188.
291. Aluwihare, L. I., Repeta, D. J. and Chen, R. F. (2002). Chemical composition and cycling of dissolved organic matter in the Mid-Atlantic Bight, *Deep-Sea Res. II*, **49**, 4421–4437.

292. Verdugo, P., Alldredge, A. L., Azam, F., Kirchman, D. L., Passow, U. and Santschi, P. H. (2004). The oceanic gel phase: a bridge in the DOM–POM continuum, *Mar. Chem.*, **92**, 67–95.
293. Hung, C. C., Tang, D. G., Warnken, K. W. and Santschi, P. H. (2001). Distributions of carbohydrates, including uronic acids, in estuarine waters of Galveston Bay, *Mar. Chem.*, **73**, 305–318.
294. Repeta, D. J., Quan, T. M., Aluwihare, L. I. and Accardi, A. M. (2002). Chemical characterisation of high molecular weight dissolved organic matter in fresh and marine waters, *Geochim. Cosmochim. Acta*, **66**, 955–962.
295. Ho, T. Y., Quigg, A., Finkel, Z. V., Milligan, A. J., Wyman, K., Falkowski, P. G. and Morel, F. M. M. (2003). The elemental composition of some marine phytoplankton, *J. Phycol.*, **39**, 1145–1159.
296. Quigley, M. S., Santschi, P. H., Guo, L. and Honeyman, B. D. (2001). Sorption irreversibility and coagulation behavior of  $^{234}\text{Th}$  with surface-active marine organic matter, *Mar. Chem.*, **76**, 27–45.
297. Buckau, G., Wolf, M., Geyer, S., Artinger, R. and Kim, J. I. (2004). Influence of humic substances on the migration of actinides in groundwater. In *Humic Substances. Nature's Most Versatile Materials*, eds Ghabbour, E. and Davies, G. Taylor and Francis, New York, pp. 287–296.
298. Mackey, D. J. and Zirino, A. (1994). Comments on trace metal speciation in seawater or do onions grow in the sea?, *Anal. Chim. Acta*, **284**, 635–647.
299. Wells, M. L., Smith, G. J. and Bruland, K. W. (2000). The distribution of colloidal and particulate bioactive metals in Narragansett Bay, RI, *Mar. Chem.*, **71**, 143–163.
300. Nyffeler, U. P., Li, Y. H. and Santschi, P. H. (1984). A kinetic approach to describe trace element distribution between particles and solution in natural aquatic systems, *Geochim. Cosmochim. Acta*, **48**, 1513–1522.
301. Buffle, J. and van Leeuwen, H. P., eds (1992). *Environmental Particles*. IUPAC Series on Analytical and Physical Chemistry of Environmental Systems, Vol. 1. Lewis, Boca Raton, FL.
302. Murphy, E. M. and Ginn, T. R. (2000). Modelling microbial processes in porous media, *Hydrogeol. J.*, **8**, 142–158.
303. Leenheer, J. A., Weshaw, R. L., Brown, G. K. and Reddy, M. M. (2003). Characterization and diagenesis of strong-acid carboxyl groups in humic substances, *Appl. Geochem.*, **18**, 471–482.
304. Wen, L. S., Shiller, A., Santschi, P. H. and Gill, G. (1999). Trace metal behavior in Gulf of Mexico estuaries. In *Biogeochemistry of Gulf of Mexico Estuaries*, eds Bianchi, T., Pennock, J. and Twilley, R. John Wiley & Sons, Inc., New York, pp. 303–346.
305. Sternström, T. A. (1989). Bacterial hydrophobicity, an overall parameter for the measurement of adhesion potential to soil particles, *Appl. Environ. Microbiol.*, **55**, 142–147.
306. Ahimou, F., Paquot, M., Jacques, P., Thonart, P. and Rouxhet, P. G. (2001). Influence of electrical properties on the evaluation of the surface hydrophobicity of *Bacillus subtilis*, *J. Microbiol. Methods*, **45**, 119–126.
307. Singh, N., Asthana, R. K., Kayastha, A. M., Pandey, S., Chaudhary, A. K. and Singh, S. P. (1999). Thiol and exopolysaccharide production in a cyanobacterium under heavy metal stress, *Process Biochem.*, **35**, 63–68.
308. Lewis, B. L., Holt, P. D., Taylor, S. W., Wilhelm, S. W., Trick, C. G., Butler, A. and Luther, G. W. L. (1995). Voltammetric estimation of iron(III) thermodynamic stability constants from catecholate siderophores isolated from marine bacteria and cyanobacteria, *Mar. Chem.*, **50**, 179–188.
309. Reid, R. T. and Butler, A. (1991). Investigation of the mechanisms of iron acquisition by the marine bacterium *Alteromonas luteoviolaceus*: characterisation of siderophore production, *Limnol. Oceanogr.*, **36**, 1783–1792.
310. Reid, R. T., Live, D. H., Faulkner, D. J. and Butler, A. (1993). A siderophore from a marine bacterium with an exceptional ferric ion affinity constant, *Nature*, **366**, 455–458.
311. Huges, M. N. and Poole, R. K., eds (1989). *Metals and Micro-organisms*. Chapman Hall, London.

312. Olafson, R. W., McCubbin, W. D. and Kay, C. M. (1988). Primary- and secondary-structural analysis of a unique prokaryotic metallothionein from a *Synechococcus* sp. Cyanobacterium, *Biochem. J.*, **251**, 691–699.
313. Amon, R. M. W. and Benner, R. (1994). Rapid cycling of high-molecular weight dissolved organic matter in the ocean, *Nature*, **369**, 549–552.
314. Passow, U. (2002). Production of transparent exopolymer particles (TEP) by phyto- and bacterioplankton, *Mar. Ecol. Prog. Ser.*, **236**, 1–12.
315. Benitez-Nelson, C., Buesseler, K. O., Karl, D. M. and Andrews, J. (2001). A time-series study of particulate matter export in the North Pacific Subtropical Gyre based on Th-234:U-238 disequilibrium, *Deep-Sea Res. I*, **48**, 2595–2611.
316. Hung, C. C., Guo, L. D., Santschi, P. H., Alvarado-Quiroz, N. and Haye, J. M. (2003). Distributions of carbohydrate species in the Gulf of Mexico, *Mar. Chem.*, **81**, 119–135.
317. Bacon, J. S. D. (1979). Factors limiting the action of polysaccharide degrading enzymes. In *Microbial Polysaccharides and Polysaccharases*, ed. Berkeley, R. Academic Press, New York, pp. 269–284.
318. Barbeau, K. and Moffett, J. W. (2001). Remineralization and recycling of iron, thorium and organic carbon by heterotrophic marine protozoa, *Aquat. Microb. Ecol.*, **24**, 69–81.
319. Kerner, M., Hohenberg, H., Ertl, S., Reckermann, M. and Spitz, A. (2003). Self-organisation of dissolved organic matter to micelle-like microparticles in river water, *Nature*, **422**, 150–154.
320. Wells, M. L., Kozelka, P. B. and Bruland, K. W. (1998). The complexation of ‘dissolved’ Cu, Zn, Cd and Pb by soluble and colloidal organic matter in Narragansett Bay, RI, *Mar. Chem.*, **62**, 203–217.
321. Stordal, M. C., Santschi, P. H. and Gill, G. A. (1996). Colloidal pumping: evidence for the coagulation process using natural colloids tagged with  $^{203}\text{Hg}$ , *Environ. Sci. Technol.*, **30**, 3335–3340.
322. Guo, L. and Santschi, P. H. (2000). Sedimentary sources of old high molecular weight dissolved organic matter from the ocean margin benthic nepheloid layer, *Geochim. Cosmochim. Acta*, **64**, 651–660.
323. Anderson, P. R. and Benjamin, M. M. (1990). Surface and bulk characteristics of binary oxide suspensions, *Environ. Sci. Technol.*, **24**, 692–698.
324. Vermeer, A. W. P., McCulloch, J. K., van Riemsdijk, W. H. and Koopal, L. K. (1999). Metal ion adsorption to complexes of humic acid and metal oxides: deviations from the additivity rule, *Environ. Sci. Technol.*, **33**, 3892–2897.
325. Hill, D. M. and Aplin, A. C. (2001). Role of colloids and fine particles in the transport of metals in rivers draining carbonate and silicate terrains, *Limnol. Oceanogr.*, **46**, 331–344.
326. Powell, R. T., Landing, W. M. and Bauer, J. E. (1996). Colloidal trace metals, organic carbon and nitrogen in a Southeastern U.S. estuary, *Mar. Chem.*, **55**, 165–176.
327. Dai, M. H. and Martin, J. M. (1995). First data on trace metal level and behaviour in two major Arctic river-estuarine systems (Ob and Yenisey) and in the adjacent Kara Sea, Russia, *Earth Planet. Sci. Lett.*, **131**, 127–141.
328. Kraepiel, A. M., Chiffolleau, J. F., Martin, J. M. and Morel, F. M. M. (1997). Geochemistry of trace metals in the Gironde estuary, *Geochim. Cosmochim. Acta*, **61**, 1421–1436.
329. Ross, J. M. and Sherrell, R. M. (1999). The role of colloids in trace metal transport and adsorption behaviour in New Jersey Pinelands streams, *Limnol. Oceanogr.*, **44**, 1019–1034.
330. Sigg, L., Xue, H., Kistler, D. and Schonenberger, R. (2000). Size fractionation (dissolved, colloidal and particulate) of trace metals in the Thur river, Switzerland, *Appl. Geochem.*, **6**, 413–434.
331. Itoh, A., Nagasawa, T., Zhu, Y., Lee, K. H., Fujimori, E. and Haraguchi, H. (2004). Distributions of major to ultratrace elements among the particulate and dissolved fractions in natural water as studied by ICP-AES and ICP-MS after sequential fractionation, *Anal. Sci.*, **20**, 29–36.
332. Vogl, J. and Heumann, K. G. (1997). Determination of heavy metal complexes with humic substances by HPLC/ICP-MS coupling using on-line isotope dilution technique, *Fresenius' J. Anal. Chem.*, **359**, 438–441.

333. Christl, I. and Kretzschmar, R. (1999). Competitive sorption of copper and lead at the oxide-water interface: implications for surface site density, *Geochim. Cosmochim. Acta*, **63**, 2929–2938.
334. Maes, A., Geraedts, K., Bruggeman, C., Vancluysen, J., Rossberg, A. and Hennig, C. (2004). Evidence for the interaction of technetium colloids with humic substances by X-ray absorption spectroscopy, *Environ. Sci. Technol.*, **38**, 2044–2051.
335. Croué, J. P., Benedetti, M. F., Violleau, D. and Leenheer, J. A. (2003). Characterisation and copper binding of humic and nonhumic organic matter isolated from the South Platte river: evidence for the presence of nitrogenous binding site, *Environ. Sci. Technol.*, **37**, 328–336.
336. Otto, W. H., Carper, W. R. and Larive, C. K. (2001). Measurement of cadmium(II) and calcium(II) complexation by fulvic acids using  $^{113}\text{Cd}$  NMR, *Environ. Sci. Technol.*, **35**, 1463–1468.
337. Christl, I. and Kretzschmar, R. (2001). Relating ion binding by fulvic and humic acids to chemical composition and molecular size. 1. Proton binding, *Environ. Sci. Technol.*, **35**, 2505–2511.
338. Peters, A. J., Hamilton-Taylor, J. and Tipping, E. (2001). Americium binding to humic acid, *Environ. Sci. Technol.*, **35**, 3495–3500.
339. Goncalves, M. L. S., Sigg, L., Reutlinger, M. and Stumm, W. (1987). Metal ion binding by biological surfaces: voltammetric assessment in the presence of bacteria, *Sci. Total Environ.*, **60**, 105–119.
340. Wen, X., Du, Q. and Tang, H. (1998). Surface complexation model for the heavy metal adsorption on natural sediment, *Environ. Sci. Technol.*, **32**, 870–875.
341. Bourg, A. C. M. and Mouvet, C. (1984). A heterogeneous complexation model of the adsorption of trace metals on natural particulate matter. In *Complexation of Trace Metals in Natural Waters*, eds Kramer, C. and Duinker, J. Martinus Nijhoff/Dr Junk Publishers, The Hague, pp. 137–152.
342. Wang, F., Chen, J. and Forsling, W. (1997). Modelling sorption of trace metals on natural sediments by surface complexation model, *Environ. Sci. Technol.*, **31**, 448–453.



---

# 4 Ultrafiltration and its Applications to Sampling and Characterisation of Aquatic Colloids

---

**LAODONG GUO**

*Department of Marine Science, University of Southern Mississippi 1020 Balch Boulevard, Stennis Space Center, MS 39529, USA*

**PETER H. SANTSCHI**

*Departments of Marine Sciences and Oceanography, Laboratory for Oceanographic and Environmental Research (LOER), Texas A&M University at Galveston, 5007 Avenue U, Galveston, TX 77551, USA*

1	Introduction . . . . .	160
2	Ultrafiltration Devices and Membrane Calibrations . . . . .	162
2.1	Definition of Aquatic Colloids . . . . .	162
2.2	Ultrafiltration Devices . . . . .	164
2.3	Nominal Molecular Weight (Molar Mass) Cut-off of Membrane . . . . .	168
2.4	Membrane Calibration and Operational Aspects . . . . .	169
3	Ultrafiltration Behaviour of Chemical Species . . . . .	172
3.1	Ultrafiltration Permeation Models . . . . .	172
3.2	Permeation Behaviour of Macromolecules . . . . .	173
3.3	Permeation Behaviour of Trace Metals and Radionuclides . . . . .	177
3.4	Permeation Behaviour of Major Ions . . . . .	181
3.5	Optimum Concentration Factor . . . . .	183
4	Applications to Field Studies of Aquatic Colloids . . . . .	185
4.1	Natural Organic Matter . . . . .	185
4.1.1	Size Distribution of Natural Organic Matter . . . . .	185
4.1.1.1	Fresh Waters . . . . .	185
4.1.1.2	Estuarine Waters . . . . .	188
4.1.1.3	Coastal and Oceanic Waters . . . . .	191
4.1.2	Elemental, Isotopic and Molecular Characterisation of Colloidal Organic Matter . . . . .	193
4.2	Colloidal Trace Metals . . . . .	196
4.3	Radionuclides . . . . .	200
4.3.1	Colloidal Thorium . . . . .	200

4.3.2 Colloidal Uranium . . . . .	202
4.3.3 Colloidal Plutonium and Americium . . . . .	203
4.4 Persistent Organic Pollutants . . . . .	205
5 Summary and Future Research . . . . .	206
Acknowledgements . . . . .	207
List of Symbols and Abbreviations . . . . .	207
References . . . . .	208

## 1 INTRODUCTION

Colloids, conventionally defined as macromolecules and nanoparticles with sizes ranging between 1 and 1000 nm, are known to be abundant in aquatic systems. In fact, the mass concentrations of colloids can outweigh those of suspended particulate matter (SPM), especially in coastal and oceanic environments where particles are mostly organic in nature (Table 1). In other aquatic environments, such as river, estuarine and groundwater systems, mass concentrations of colloids or colloidal organic matter (COM) can also be higher than or comparable to those of SPM or particulate organic matter (POM), respectively [1–8]. For example, a relationship between the mass concentration of colloidal organic carbon (COC, >1 nm) and SPM (>0.45 µm) was described for seawater [2] as

$$[\text{COC}] = 2.73 \times [\text{SPM}] + 946(\mu\text{g dm}^{-3})$$

**Table 1.** Comparisons between mass concentration of colloidal organic carbon (COC) and particulate organic carbon (POC) and suspended particulate matter (SPM) in aquatic environments, showing the significance of colloids<sup>a</sup>

Location	COC/ µmol dm <sup>-3</sup>	POC/ µmol dm <sup>-3</sup>	COM/ µg dm <sup>-3</sup>	SPM/ µg dm <sup>-3</sup>	Reference
Yukon River	508–2825	70–309	15 240–84 750	53 000–331 000 (5500–9270) <sup>b</sup>	[8]
Rhone Delta	7–43 <sup>c</sup>	17–102	210–1290	–	[4]
Estuarine waters of Galveston Bay	82–327	18–78	2460–9810	3200–15 400	[5]
Estuarine waters of Chesapeake Bay	67–133	100–186	2010–3990	6060–14 675	[5]
River/bay waters	52–103	13–25	1560–3090	1400–2380	[109]
Gulf of Mexico	20–69	–	600–2070	62–282	[2]
Gulf of Mexico	14–36	0.6–10	420–1080	70–117	[3]
Atlantic Ocean	13–33	0.4–9	390–990	53–345	[3]
Cigar Lake Groundwater	–	–	460–10 300 <sup>d</sup>	630–20 500	[1]

<sup>a</sup> Mass concentrations of colloidal organic matter (COM, 1 kDa–0.2 µm) are calculated from COC assuming [COM] = 2.5 × [COC] [182]. <sup>b</sup> Organic fraction. <sup>c</sup> Colloids here are the >10 kDa fraction. <sup>d</sup> Mass concentration only without organic data.

Due to their high abundance and high specific surface areas and because they contain amphiphilic and polyfunctional groups, colloids play a central role in regulating the concentration and speciation, and hence the fate, transport and bioavailability of many trace elements in aquatic environments [9–16]. Indeed, recent studies have shown that the environmental behaviour and bioavailability of colloidal sized particles and their associated trace elements could be considerably different from those in particulate and free ionic dissolved phases [17–25].

Knowledge of the distribution or partitioning of chemical species between dissolved, colloidal and particulate phases is important for a better understanding of the biogeochemical cycles of organic and inorganic components that serve as carriers, and many trace elements and contaminants that are associated with such carrier phases. Although the morphology, chemical composition, sources and environmental behaviour of colloids are still poorly understood, aquatic colloids have long been recognised as important intermediaries in the removal of trace elements through coagulation, thus facilitating contaminant transport, organic carbon cycling and micronutrient bioavailability [16,25–41]. A thorough understanding of colloids is important if we wish to understand the fate, transport and bioavailability of chemical species, but there are few methods currently available for the fast and reliable separation of colloids from the dissolved phase.

Recent applications of ultrafiltration to the sampling of aquatic colloids have advanced our understanding of the abundance, distributions, physical conformations, chemical composition and environmental behaviours of colloids in aquatic systems, including freshwater, seawater and ground waters. For example, determinations of COC and colloidal metals have been reported for freshwaters, including river and lake waters, with the number of reports increasing dramatically in recent years [8,42–50]. Applications of ultrafiltration to marine systems dates back to the 1970s and 1980s, when mostly stirred-cell ultrafiltration units with membrane discs were used [51–56]. Applications of large-volume cross-flow ultrafiltration systems to sampling marine colloids started in the late 1980s/early 1990s [2,28,33,34,57–59] and became a commonly used method, especially after a sampling intercomparison exercise ([60] and accompanying papers).

In estuarine and coastal waters, metals such as Cu, Fe, Hg and Zn have been shown to be mostly present in the colloidal form [17,45,53,61–76]. In marine environments, studies indicated that high molecular weight (HMW, usually  $>1$  kDa or  $>10$  kDa) dissolved organic matter (DOM) has high biological and chemical reactivity and short residence times in the water column [28,30,31,33,35,36,77]. Therefore, colloids are also important intermediaries in organic carbon cycling in aquatic environments. Recent advances in sampling techniques now permit the rapid isolation of large quantities (*e.g.* hundreds of milligrams) of colloidal materials from large volumes of natural waters for elemental, isotopic and molecular characterisation [30,34,77–97], although there is still a debate about optimal sampling procedures [16,98]. Other recent advances include the identification of ground water and surface water colloids that are believed to play an important role in the transport of nuclear waste nuclides such as plutonium and americium [7,40,99–101].

Despite recent advances, fast and unbiased sampling of aquatic colloids remains a challenge, limiting our understanding of the role of colloids in biogeochemical and environmental processes. In this chapter, we will discuss recent advances in the application of ultrafiltration methods to the fractionation and subsequent characterisation of aquatic colloids. We will first focus on the permeation and retention behaviours of macromolecules,

major ions and trace elements during ultrafiltration. We will then provide documented examples of colloid behaviour in natural waters, particularly as it may affect the characterisation of dissolved organic matter and the cycling of trace metals and radionuclides.

## 2 ULTRAFILTRATION DEVICES AND MEMBRANE CALIBRATIONS

### 2.1 DEFINITION OF AQUATIC COLLOIDS

Aquatic colloids are any organic or inorganic/mineral entity with supramolecular structure and properties, but small enough to remain in suspension ([102] and references therein). Nevertheless, the definition of aquatic colloids is generally based on operational techniques, primarily by size (see also Chapters 1 and 2) and the ability to scatter light. Conventionally, aquatic colloids are operationally defined as the particle size fraction between 1 nm and 1  $\mu\text{m}$ , and therefore include nanoparticles and macromolecules [9,103,104]. In aquatic systems, physical techniques such as diffusion, permeation, light scattering and viscosity measurements can be used to characterise colloidal systems, chemical techniques can help to unravel their compositional complexities and biological techniques can give insights into degradability, bioavailability and stability.

In addition to the conventional definition by size, Gustafsson and Gschwend [12] took a chemcentric point of view by introducing a functional colloid definition that might be more meaningful under certain circumstances. They argued that aquatic colloids should be defined based upon both thermodynamic and hydrodynamic parameters [6,12], as opposed to physical parameters alone. The sole use of a physical definition of colloids may be a factor contributing to a poor prediction of thermodynamic equilibrium constants such as distribution (or partitioning) coefficients between dissolved, colloidal and particulate phases ([26] and references therein). According to the chemcentric concept, aquatic colloids are those constituents with a molecular milieu into/on to which chemicals can escape from the dissolved phase, and with an environmental fate governed predominantly by coagulation-peptisation processes [12].

From the chemcentric point of view, however, organic macromolecules with a very high molecular weight, such as carbohydrates and non-globular proteins, might be considered to be more in the dissolved phase if one disregard the role  $\text{Ca}^{2+}$  (and other ions) plays in stabilising the alphahelical regions of acid polysaccharides [105] and/or facilitating gel formation [19]. On the other hand, the upper colloidal size boundary is determined by the entity's environmental fate and transport conditions [12].

The size spectrum of chemical species in aquatic systems is depicted in Figure 1. The upper size limit for a colloidal suspension can be considered the point at which Brownian motion is no longer the dominant process for particle-particle interactions. In some cases, small living organisms such as viruses, bacteria, protozoa and algae, frequently termed hydrophilic biocolloids, may be included in the colloidal fraction [106]. The lower limit for colloids is less well defined [107], with a vague boundary between dissolved and colloidal phases depending on the chemical species (Figure 1). Thus, the types of organic colloids present in aquatic environments include macromolecular organic matter, microorganisms, viruses, biocolloids, aggregates of exudates and nanoparticles such as clay minerals and oxides of iron, aluminium and manganese coated with or sorbed

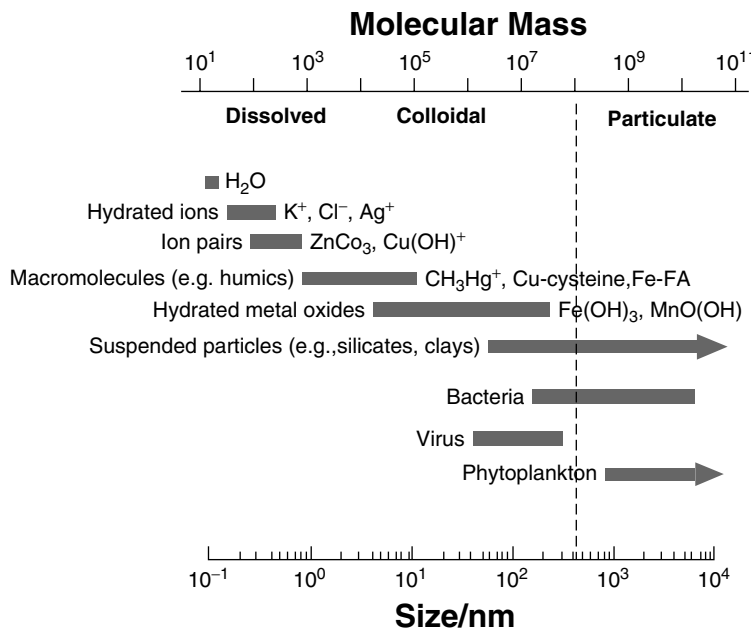


**Figure 1.** Size spectrum of chemical species in aquatic systems. Reproduced from [68] with permission from John Wiley & Sons, Inc.

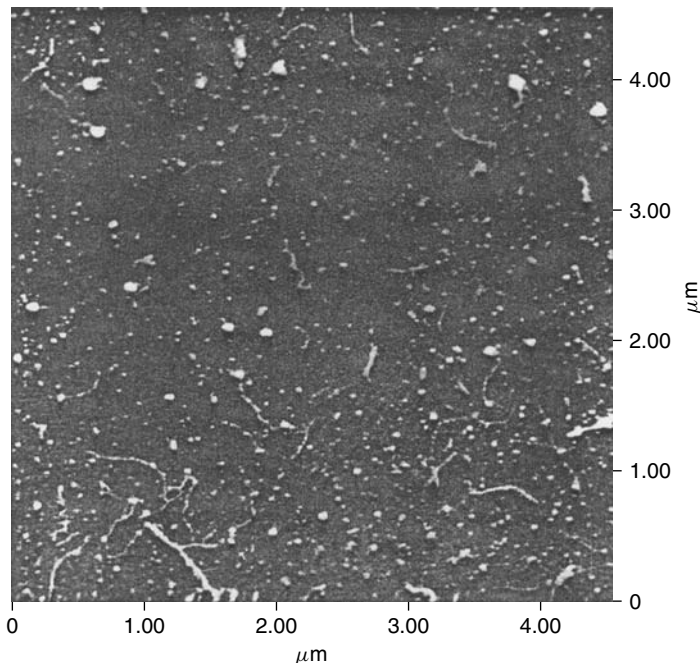


**Figure 2.** Atomic force micrographic images of estuarine colloidal organic matter. Reproduced from [80] with permission from the American Society of Limnology and Oceanography

on organic matter [9,11,102,108–110]. Depending on research purposes, it is difficult to reach an universal definition for aquatic colloids.

Isolated COM (>1 kDa) exhibits a heterogeneous nature, containing not only spherical particles but also fibrillar materials (Figure 2), as has been shown recently for freshwater and seawater colloids characterised *in situ* [80,102,111–114]. Images of freeze-dried COM generally show cotton-like, white, fluffy and fibrillar materials and also darker coloured materials, consistent with the heterogeneous nature shown by atomic force microscopic images of COM samples (Figure 2).

## 2.2 ULTRAFILTRATION DEVICES

In most field studies, colloids are based on operational definitions and calibrations, usually between ~1 nm or 1 kDa at the lower limit and 1 µm at the upper end of the size spectrum [11]. Different prefilter pore sizes between 0.2 m and 1 µm and different ultrafiltration membranes with different molecular weight cut-offs (MWCOs) have been employed for sampling aquatic colloids (Table 2). As a result, concentrations of colloidal materials reported in the aquatic science literature are not always directly comparable. Depending on research purposes and the nominal MWCO of the membrane used, colloidal chemical species reported in the literature can refer to the fraction between 10 kDa and 0.4 µm, between 3 kDa and 0.4 µm or between 1 kDa and 0.4 µm [11,16].

A variety of methods have been used for studying and isolating colloids from aquatic systems. The isolation of aquatic colloids is typically accomplished by filtration of samples through 0.2–1 µm pore-size filters, followed by different separation and isolation techniques, such as ultrafiltration [59,60,115], C<sub>18</sub> solid-phase extraction [116–118], XAD resin columns [119–121], ultracentrifugation [122,123], field-flow fractionation [124–126], gel filtration [127], size-exclusion chromatography [94,128], reversed phase chromatography [129] and a combination of ultrafiltration and field-flow fractionation [6,130]. Conventional methods using XAD resins can only extract about 10–15% of the dissolved organic matter (DOM) in seawater and require a pH adjustment [120,131]. On the other hand, ultrafiltration requires no pretreatment and can extract at least twice as much DOM from seawater [3,30,34]. Hence, ultrafiltration has become one of the most widely used techniques in recent years [11,15,16,60].

A major advantage of the cross-flow ultrafiltration (CFUF) technique is that large quantities of COM can be isolated in a relatively short time. This technique is particularly useful for the preconcentration of marine colloids from large volumes of seawater [2,58,59], as other methods are either less efficient or do not allow large quantities of pure COM to be isolated for further characterisation. For example, CFUF with 1 kDa cartridges has been used to extract several hundred milligrams of COM from freshwater and seawater for biochemical and isotopic characterisation and molecular size determinations of DOM [3,5,30,34,77,78,81–83,85,87–90,93,94,118,132–137].

Table 2 summarises some of the recent applications of ultrafiltration methods along with selected separation techniques for sampling aquatic colloids. These applications cover natural water systems from freshwater to marine environments, including lakes, rivers, streams and ground waters as well as estuarine, coastal and oceanic waters, and from sediment pore waters to podzols. Measured chemical species span a range from organic to

**Table 2.** Applications of ultrafiltration methods for isolating colloidal materials in natural waters, including lake water, river water, ground water, estuarine water and seawater

Water type or location	UF device <sup>a</sup>	MWCO <sup>a</sup> /kDa	Chemical species	References
Lake Trawsynyd	CFUF	3, 30, 100	Actinides	[252]
Lake water	UF	1, 5, 10, 100	OC	[253]
Lake water	CFUF	1 and 100	OC	[254]
Lake Pavin	CFUF	1 and 10	Uranium	[255]
Lake water	CFUF	1	OC	[45]
Lake water	CFUF	10	OC and Hg	[256,257]
Lake Biwa	CFUF	5	OC	[258]
Ground water	CFUF	10 and 100	Radionuclides	[259]
Ground water	UF	100	Pu	[40]
Ground water	CFUF	10	U/Th series	[260]
Ground water	CFUF	1	Pu	[100]
Ground water	CFUF	0.45	Metals	[261]
River water	Stirred-cell UF	1, 10, 25, 100	OC/metals	[262]
River water	CFUF	1	Ag	[18]
River water	CFUF	1, 5, 300	Metals/isotopes	[172]
Amazon River	CFUF	1 and 0.1 μm	OC	[132,137]
River water	CFUF	3	REE	[263]
River water	CFUF–FFF	3–200 nm	Metals	[44]
River water	CFUF	1	Metals	[174]
River water	CFUF	1	OC	[45]
Chena River	CFUF	1	OC	[89]
Vistula River	CFUF	1	Metals	[47]
Yukon River	CFUF	1	OC	[8,264]
Sahan River	Stirred-cell UF	1 and 10	<sup>239,240</sup> Pu, <sup>241</sup> Am, <sup>90</sup> Sr	[101]
Kalix River/seawater	CFUF	3 and 10	U	[265]
Lake Pontchartrain estuary	CFUF	3	OC	[188]
River/estuarine/ seawaters	CFUF-hf	5 and 100	Artificial radionuclides	[191]
River/bay waters	CFUF	3	OC/metals	[109]
Tidal stream	CFUF	1	OC	[207]
Freshwater	CFUF	~1	Metals	[266]
Freshwater	CFUF	5, 20, 100	OC/metals	[267]
Freshwater	CFUF	10, 100	OC and Hg	[256,268]
Freshwater	CFUF	3	Pu and Am	[7]
Freshwater	CFUF	1	OC	[49]
Freshwater	UF–FFF	3, 10, 30	OC	[130]
Estuarine water	Stirred-cell UF	20	OC	[52]
Estuarine water	Stirred-cell UF	10	OC	[54]
Estuarine water	UF and CFUF	5	OC	[200]
Estuarine water	CFUF	10	OC	[181]
Estuarine water	CFUF	10	OC/metals	[4,63]

(continued overleaf)

**Table 2** (*continued*)

Water type or location	UF device <sup>a</sup>	MWCO <sup>a</sup> /kDa	Chemical species	References
Estuarine water	CFUF	10	OC/metals	[62]
Estuarine water	CFUF	10	U	[227]
Estuarine water	CFUF	1	Hg	[17]
Estuarine water	CFUF	1 and 10	OC	[5]
Estuarine water	CFUF	1	Metals	[68,215]
Estuarine water	CFUF	10	Radionuclides (U, Th, Ra)	[149]
Estuarine water	CFUF	1 and 30	OC	[161,162]
Estuarine water	CFUF	1 and 8	Metals	[71]
Estuarine water	CFUF	1	OC	[93]
Estuarine water	CFUF	3	Uranium	[235]
Estuarine water	CFUF	1 and 10	Hg	[74,75,146]
Estuarine water	CFUF	1	OC	[94]
Estuarine/coastal waters	CFUF	10	Th isotopes	[233]
Coastal seawater	UF	5, 10, 100	OC	[190]
Coastal seawater	CFUF	~500	OC	[269]
Seawater	Stirred-cell UF	1	OC	[56]
Seawater	CFUF	10	Al	[57]
Seawater	CFUF	10	OC	[58]
Seawater	CFUF	0.5	OC	[270]
Seawater	CFUC	10	Th isotopes	[28]
Seawater	CFUF	10	<sup>234</sup> Th	[33,271]
Seawater	CFUF	1	OC	[34]
Seawater	CFUF	1 and 10	OC	[2]
Seawater	CFUF	1, 3, 10	OC	[3,30]
Seawater	CFUF	10	OC and <sup>234</sup> Th	[77]
Seawater	CFUF	1	OC, nutrients, Fe, Al	[60]
Seawater	CFUF	1	OC	[85]
Seawater	CFUF	1	OC	[133]
Seawater	CFUF	1 and 10	<sup>234</sup> Th	[31]
Seawater	CFUF	10	<sup>234</sup> Th	[228,229]
Seawater	CFUF– SPLITT	3	OC/metals	[6]
Seawater	CFUF	1	OC/Th/Pu	[230,238]
NW Pacific	CFUF	200	Fe	[272,273]
Seawater	CFUF	5, 10, 100, 1000	OC/metals	[147]
Seawater	CFUF	1	OC	[274]
Seawater	CFUF	10	Th	[227]
Seawater	CFUF	1	Fe	[25]
Seawater	CFUF	1, 5, 10, 100	Metals/OC	[76]
Sediment pore water	UF	–	OC	[275]
Sediment pore water	UF/SEC	3	OC	[128]
Sediment pore water	UF/SEC	3	OC	[129]

**Table 2** (*continued*)

Water type or location	UF device <sup>a</sup>	MWCO <sup>a</sup> /kDa	Chemical species	References
Sediment pore water	UF	3 and 100	OC	[276]
Spike/seawater	Centricon UF stirred-cell UF	5	C, <sup>109</sup> Cd, <sup>51</sup> Cr, <sup>65</sup> Zn	[213,214]
Spike/seawater	CFUF, stirred-cell UF	1	<sup>51</sup> Cr, <sup>57</sup> Co, <sup>59</sup> Fe, <sup>65</sup> Zn, <sup>109</sup> Cd, <sup>110m</sup> Ag, <sup>203</sup> Hg	[22,23]
Spike/seawater	CFUF-dialysis	1 and 10	<sup>59</sup> Fe	[24,148]

<sup>a</sup> MWCO = nominal molecular weight cut-off; CFUF = cross-flow ultrafiltration; UF = ultrafiltration; FFF = field-flow fractionation SEC = size-exclusive chromatography.

inorganic, from trace metals to radionuclides, from nutrients to major ions and from isotopes to rare earth elements (REEs). Representative results from these applications will be discussed in later sections.

Commonly used ultrafiltration devices include stirred-cell ultrafiltration units, centrifugal ultrafiltration tubes and CFUF membranes, such as hollow-fibre and spiral-wound ultrafiltration cartridges. A schematic diagram showing a typical CFUF system is shown in Figure 3. A typical ultrafiltration system is normally composed of an ultrafiltration membrane, pump(s), reservoir, tubing and fittings and a container for collecting the permeate solution. In addition, a prefiltration system is also required. For most research purposes, it is generally best to use Teflon materials for the reservoir, tubing and fittings, especially when working with trace metals, radionuclides and some organic species. Membranes are available in different materials that may have different sorptive capacities and

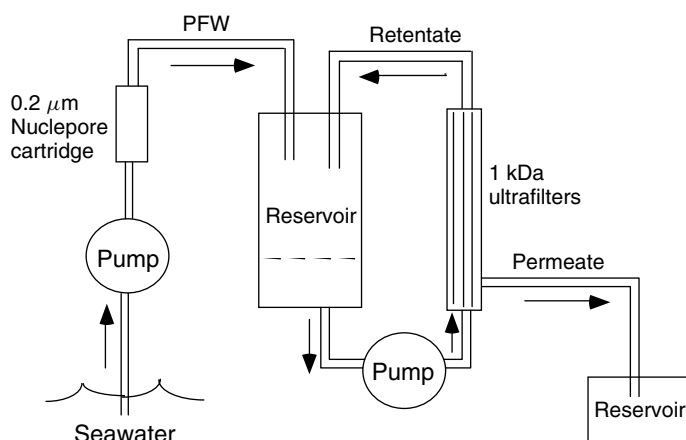


**Figure 3.** Schematic diagram showing a typical ultrafiltration system [including a prefiltration, cartridge pump(s), ultrafiltration membrane(s) and reservoirs] [285]

may interact with certain chemical species. Thus, membrane materials need to be examined and selected according to the purposes of the study. Membranes with a small surface area and thus a small dead volume may be more suitable for trace metal work and for processing small volumes of samples.

In addition to ultrafiltration, microfiltration using 0.02 µm filters (both syringe filter and disc membranes) has also been used for isolating large colloids from dissolved phase, especially for small-volume trace element studies [138–141]. However, it should be noted that colloids above the 0.02 µm size cut-off are only a small sub-fraction of colloids >1 kDa.

### 2.3 NOMINAL MOLECULAR WEIGHT (MOLAR MASS) CUT-OFF OF MEMBRANE

The rated pore size for ultrafiltration membranes is usually a nominal molecular weight cut-off (NMWCO) in kDa or atomic (molar) mass units (amu) such as 1, 3, 10, 100 kDa, etc. The term MWCO was developed for ultrafiltration membranes to define the equivalent spherical size of macromolecules that can be retained by a specific membrane [142,143]. In general, the nominal ratings are based upon a rejection rate of ~90% for specific globular molecules (Figure 4). However, the rejection rate is not necessarily the same for other molecules having the same MW but different molecular properties and configurations. According to the membrane pore size distribution (Figure 4), a 1 kDa rated ultrafiltration membrane could have ~20% pore sizes ranging from less than 1 kDa (*e.g.* 0.5 kDa) and the other 20% pore sizes larger than 1 kDa (*e.g.* 1.3 kDa), or even larger, with the majority at ~1 kDa [98,143]. Therefore, a small portion of HMW molecules (with an MW slightly higher than membrane's NMWCO), may pass through the membrane and a portion of low molecular weight (LMW) molecules (with an MW slightly lower than membrane's MWCO) could be retained by the membrane (Table 3).

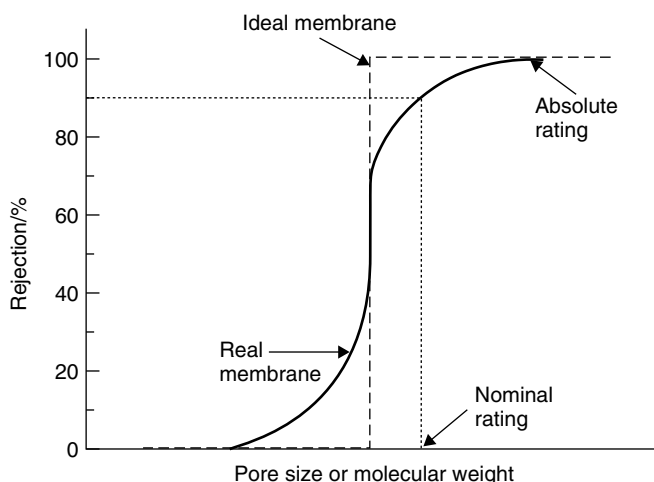


**Figure 4.** Membrane pore size distribution and ratings of ideal and real membranes. Copyright 1999, from *Ultrafiltration and Macrofiltration Handbook* by Cheryan, M. Reproduced by permission of Routledge/Taylor & Francis Group, LLC

**Table 3.** Permeation coefficient ( $P_c$ ) and/or retention coefficient ( $R_c$ ) of natural dissolved organic carbon (DOC) and standard macromolecules during ultrafiltration using a 1 kDa membrane

Macromolecule	MW/kDa	Membrane MWCO	$P_c^a$	$R_c^b$	Reference
Rhodamine	0.49	1	0.60	0.40	[98]
Raffinose	0.59	1	0.31	0.69	[144]
Glutathione	0.6	1	0.16	0.84	[98]
Vitamin B <sub>12</sub>	1.33	1	0.15	0.85	[98]
Dextran	3	1	0.03	0.97	[98]
Dextran	10	1	0.01	0.99	[98]
Dextran <sup>c</sup>	14.5	1	—	0.99	[153]
Albumin	66	1	<0.03	0.97	[144]
Seawater DOC	—	1	0.48	0.52	[144]
Vitamin B <sub>12</sub>	1.3	10	0.99	0.01	[146]
Dextran	4	10	0.43	0.57	[146]
Dextran	20	10	0.08	0.92	[146]
Dextran <sup>c</sup>	40	10	—	0.85	[149]

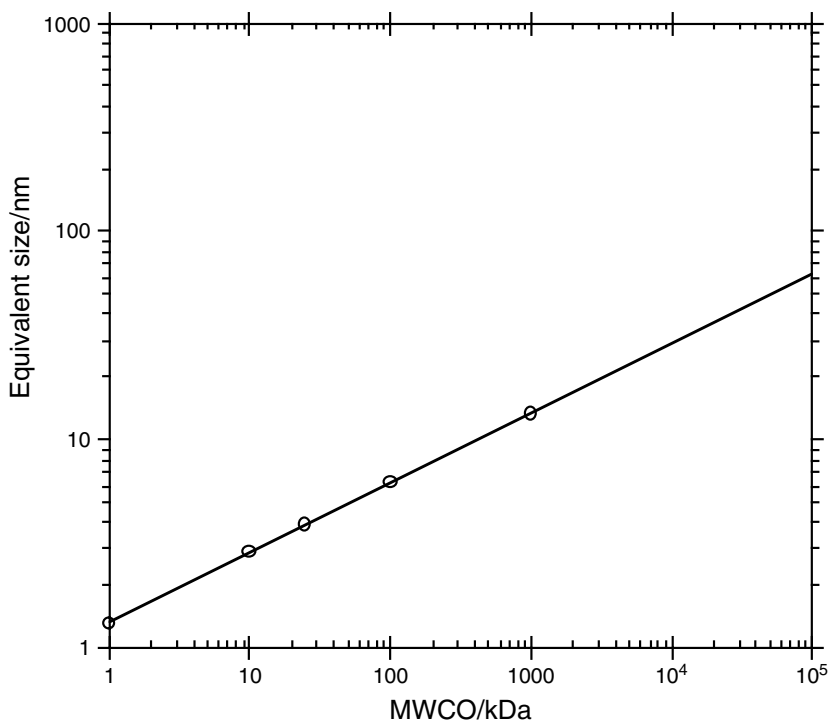
<sup>a</sup> Permeation coefficients ( $P_c$ ) listed here are either derived from permeation model [see equation (1)] or estimated from concentrations between initial solution and integrated permeate. <sup>b</sup> Retention coefficients ( $R_c$ ) are either calculated from  $1 - P_c$  or from concentrations measured in ultrafiltered samples (apparent  $R_c$ ). <sup>c</sup>  $P_c$  calculated but not derived from model is an apparent  $P_c$ .

Figure 5 shows the relationship between the membrane's MWCO and equivalent pore size. A 1 kDa MWCO corresponds to about 1.3 nm in membrane pore size, whereas a 10 kDa membrane has a pore size of about 2.9 nm. As shown in Figure 5, a 0.02  $\mu$ m (20 nm) membrane corresponds to an MWCO of over 3000 kDa (or >3 000 000 amu).

As stated above, the MWCO of a membrane is defined as the size of globular macromolecules that can be almost quantitatively retained according to filtration theory [143]. When different macromolecules are used for membrane calibration, the rejection rate could be significantly different from that of ideal globular macromolecules. Using a 1 kDa ultrafiltration membrane as an example, the typical relationship between membrane's rejection rate and molecular weight is shown for different macromolecules in Figure 6. These rejection rates were very close to those reported by the manufacturer. However, a 90% rejection rate translated into an MWCO of ~2 kDa for that membrane. The difference between observed and nominal MWCO was not unexpected, since the macromolecules used were not ideal, i.e. globular. Periodically testing the rejection rates for one's preferred membrane is a necessary procedure to ensure that the separation efficiency resembles the manufacturer's specifications and that the manufacturer's rating is indeed close to the membrane's actual MWCO under experimental conditions [98,144–147].

## 2.4 MEMBRANE CALIBRATION AND OPERATIONAL ASPECTS

Although the CFUF technique for sampling macromolecular organic matter seems promising, consistently applied rigorous cleaning and handling protocols are critical for obtaining unbiased and reliable colloidal sampling results. Frequent calibrations of ultrafiltration membranes are indispensable before sampling [98,144] because ultrafiltration membranes have a limited lifetime (or shelf time) and even new cartridges could have a different average pore size than the one given by the manufacturer [145]. For example, a manufacturer's



**Figure 5.** Relationship between MWCO (kDa) and equivalent pore size ( $\mu\text{m}$ ) (data from Amicon Inc., personal communication)

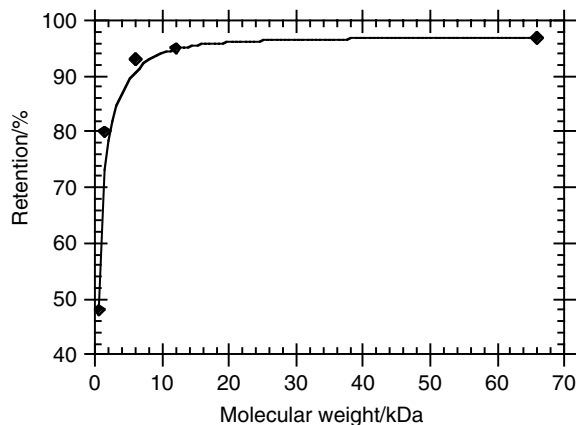


**Figure 6.** Rejection rates of a 1 kDa ultrafiltration membrane (Amicon S10N1) determined using different macromolecular organic compounds, including raffinose (MW = 0.595 kDa), vitamin B<sub>12</sub> (1.33 kDa), insulin (6 kDa), cytochrome c (12 kDa) and albumin (66 kDa). Reprinted from Guo, L. D., and Santschi, P.H. A critical evaluation of cross-flow ultrafiltration technique for sampling colloidal organic carbon in seawater, *Marine Chemistry*, **55**, 113–127, Copyright 1996, with permission from Elsevier

rated 1 kDa membrane has been shown to have an apparent MWCO of >50 kDa, even at 50% retention [145]. On the other hand, a 0.02  $\mu\text{m}$  filter which corresponds to  $\sim$ 3000 kDa can have an actual MWCO of  $\sim$ 3 kDa [148]. Frequent calibration is even more critical when ultrafiltration membranes are in prolonged use, as the integrity of membranes may be significantly altered after prolonged use or improper handling.

Proper ultrafiltration methodology consumes more time and demands greater attention to detail than previously realised, especially for oligotrophic aquatic environments. For example, time series ultrafiltration studies have shown that concentrations of organic carbon and trace metals in the permeate (or ultrafiltrate) change with time or the concentration factor (CF) as a consequence of retention of LMW materials by the membrane [67,98,144,146,149–151]. Larsson *et al.* [147] found that the ratio of retentate to permeate flux (i.e. cross-flow ratio) influenced the recovery of colloids in coastal waters. They recommended a cross-flow ratio of >15 and a CF of >10 for isolating colloids. Therefore, variable CFs and cross-flow ratios and discrete sampling of the permeate fraction can lead to a biased determination of the partitioning of chemical species between dissolved and colloidal phases. This may explain why most of the earlier ultrafiltration results had a large variability (see the next section). Hence appropriate and consistent sampling protocols for all fractions, including the retentate (colloids), permeate (ultrafiltrate), and cartridge cleaning are required during ultrafiltration in order to assess properly the mass balance (the amount of a chemical species recovered from permeate and retentate compared with that in the initial solution). In addition, consistent CFs and cross-flow ratios are critical in order to ensure reproducible and comparable colloidal data [98,147]. Another factor complicating comparison between results from different investigators is the use of many different ultrafiltration membranes from different manufacturers (Table 2), with different nominal MWCOs and varying retention characteristics [145,147]. In addition, different sampling protocols, such as storage and processing times [67,98,146], the cleaning of cartridges, rigour in obtaining mass balance, maintaining redox conditions [100,152], cross-flow ratio of retentate to permeate flux [147] and concentration factors [98,144,147] employed during ultrafiltration, in addition to varying prefiltration techniques, may lead to significantly different results in terms of molecular weight distributions and chemical composition of colloidal species in natural waters (see discussion in later sections).

Overall, important criteria for using ultrafiltration methods are (1) integrity of ultrafiltration membranes, (2) operating conditions, such as CF and cross-flow ratio and (3) mass balance (or recovery) of a specific chemical species. Damage to ultrafiltration membranes occurs readily by bacterial activity, improper preservation and operating conditions or prolonged use. Therefore, it is important to know if the membrane is intact and meets the manufacturer's specifications before sampling (see the next section). Regarding the mass balance, the amount of a specific chemical species recovered from the permeate and retentate (colloidal) fractions should be equal or close to the amount of that chemical species in the initial solution. Although a perfect recovery may not be a guarantee for the success of ultrafiltration [58,60], a recovery of >100% is indicative of contamination, while a mass balance of <100% points to a loss of a specific chemical species during ultrafiltration [144]. This point along with the concentration factor will be discussed further in a later section.

### 3 ULTRAFILTRATION BEHAVIOUR OF CHEMICAL SPECIES

Cross-flow ultrafiltration has become one of the most commonly used techniques for isolating aquatic colloids (Table 2). However, the ultrafiltration behaviour of chemical species remains poorly understood. It is very important to understand the permeation and retention behaviours of chemical species in order to understand the ultrafiltration process and to interpret size fractionation data correctly [98,150]. Recently, the ultrafiltration behaviour of chemical species, including macromolecular organic compounds with different MWs, trace metals, radionuclides and major ions, has received increasing attention [67,98,144–147,149–151,153]. For example, the permeation and retention behaviour of both lower and higher MW (compared with the NMWCO of ultrafiltration membranes) molecules have been investigated through controlled laboratory experiments and using molecular probes. Variations of chemical species in the permeate during ultrafiltration and their permeation/retention behaviour have been reported for trace metals [67,98], <sup>234</sup>Th and U in coastal seawater ([149] and Guo *et al.*, unpublished results), and major ions, such as  $\text{Na}^+$ ,  $\text{Cl}^-$ ,  $\text{F}^-$ ,  $\text{Ca}^{2+}$ ,  $\text{Mg}^{2+}$ ,  $\text{SO}_4^{2-}$  [150,154,155]. These recent advances will be summarised and discussed in the following sections using the available literature.

#### 3.1 ULTRAFILTRATION PERMEATION MODELS

If chemical species (metal ions, organics and complexes) with dimensions or sizes larger than the MWCO of a specific ultrafiltration membrane (i.e. the HMW fractions) were quantitatively retained, and those with MWs lower than the MWCO (i.e. the LMW fractions) passed through the membrane with no retention, concentrations of LMW chemical species in the discrete permeate samples would be constant with time or CF. However, this is mostly not the case. At any given ultrafiltration time, the relationship between the concentration of a given chemical species in the permeate ( $C_p$ ) and the CF (defined here as the volume ratio of initial solution,  $V_0$ , to the retentate solution,  $V_r$ , i.e.  $\text{CF} = V_0/V_r = V_0/(V_0 - V_p)$ ) can be described by the following equation [156,157]:

$$\ln C_p = \ln(P_c \times C_f^0) + (1 - P_c) \times \ln(\text{CF}) \quad (1)$$

where  $P_c$  is the permeation coefficient, defined as the ratio of  $C_p$  to  $C_f$  (feed concentration) at any given point during the ultrafiltration (i.e.  $P_c = C_p/C_f$ ), and  $C_f^0$  is the initial concentration of permeable species in the upstream feed solution. The permeation model assumes negligible sorption and constant retention characteristics of the membrane and constant partitioning across the membrane for high and low MW solutes, i.e. a constant permeation coefficient,  $P_c$ , which is related to rejection coefficient,  $R_c$ , by  $P_c = 1 - R_c$ .

A linear relationship between  $\log C_p$  and  $\log \text{CF}$  indicates a constant permeation behaviour. If the value of  $P_c$  for a chemical species is equal to 1, the concentration of that chemical species in the permeate should be equal to that in the feed solution at any given time during ultrafiltration. This means that there is no or little retention for that chemical species. On the other hand, if a chemical species has a  $P_c$  value  $< 1$ , this indicates a retention for that chemical species at each ultrafiltration cycle. The smaller the  $P_c$  value, the more retention the chemical species will experience. As a result of retention, the concentration of any chemical species in the permeate will increase with increasing CF.

The  $P_c$  value of a given chemical species can be calculated from the slope  $(1 - P_c)$ , derived from the linear relationship between  $\log C_p$  and  $\log CF$  described in equation (1).

According to membrane filtration theory [143,158], any particle with a gyration radius,  $R_p$ , less than the membrane's pore size,  $R_m$ , can pass through the membrane at a rate (permeation) which is proportional to  $(R_m - R_p)^2/R_m^2$ . Since  $R_p$  is always  $>0$ , the ratio of  $(R_m - R_p)^2/R_m^2$  will be always  $<100\%$  for the LMW case. In other words,  $P_c$  values for macromolecules will always be  $<1$  during the ultrafiltration process except for free ionic species such as  $\text{Na}^+$ ,  $\text{K}^+$  and  $\text{Cl}^-$  (see later sections). Hence, all (macro-)molecules will be retained to a certain extent.

At any point of the ultrafiltration process, the rejection (or retention) coefficient ( $R_c$ ) is defined as the fractional reduction in the feed concentration ( $C_f$ ) across the membrane [157]:

$$R_c = 1 - C_p/C_f \quad (2)$$

where  $C_p$  is the concentration of a specific chemical species in the permeate. The relationship between  $R_c$  and  $P_c$  can also be written as  $R_c = 1 - P_c$ .

From the ultrafiltration permeation model, the  $P_c$  value of a given permeable species can be calculated from the slope  $(1 - P_c)$ , derived from a linear relationship between  $\log C_p$  and  $\log CF$ , as shown in Figure 7. A combination of the values of the intercept,  $\log(P_c \times C_f^0)$ , and the slope  $(1 - P_c)$  allows an estimate of the initial feed concentration ( $C_f^0$ ) of the LMW or permeable chemical species, which can be used to determine the initial colloidal fraction [144]. Therefore, the colloidal (or retainable) fraction (i.e.  $1 - C_f^0/C_T^0$ ) of a specific chemical species can be predicted from the initial LMW concentration ( $C_f^0$ ) derived from time-series permeate data and the measured total dissolved concentration,  $C_T^0$  ([67,98,144]; see also the examples in the next sections).

### 3.2 PERMEATION BEHAVIOUR OF MACROMOLECULES

An important question with regard to how macromolecules from natural waters are isolated during ultrafiltration is what kinds of possible artifacts, if any, exist under given operating conditions. To answer such questions fully, a better understanding of permeation and retention behaviour of macromolecules is critically necessary.

Typical ultrafiltration behaviour of seawater DOC is shown in Figure 7. Concentrations of DOC in time-series permeate samples show an increase in permeate DOC concentration with increasing CF during ultrafiltration. This relationship between  $C_p$  and CF has been reported previously [98,144,146,149]. Questions raised from Figure 7 might include (1) what causes the increase of DOC concentration in the permeate (ultrafiltrate) with increasing CF, a behaviour that seemingly contradicts what one would expect from conventional macro-filtration?; (2) what is the permeation behaviour of LMW materials?; (3) how do macromolecules and their associated trace elements behave during ultrafiltration?; (4) can HMW materials break through the membrane when the membrane is intact?; and (5) what optimum CF should be used for ultrafiltration when isolating aquatic colloids for characterisation purposes?

The cause of the increase in permeate concentration with increasing CF has been a matter of contention, and could theoretically be due either to the retention of LMW materials [98,144,146,149–151,159] or the breakthrough of HMW materials [67,153]. To

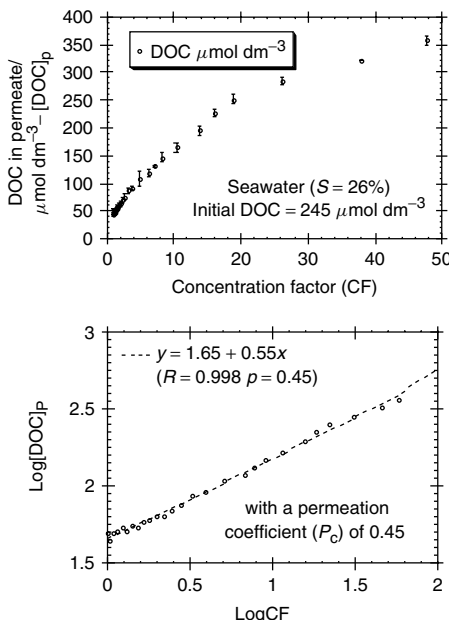


**Figure 7.** Typical ultrafiltration behaviour of dissolved organic carbon (DOC) in seawater, showing an increase in DOC concentration in permeate with increasing concentration factor and a linear relationship between  $\log C_p$  and  $\log CF$ . From the slope and intercept values, a  $P_c$  value of 0.45 and an initial LMW DOC concentration of  $\sim 99 \mu\text{mol dm}^{-3}$  can be calculated, which can be used to estimate the colloidal organic carbon (COC) as 60% of the bulk DOC ( $245 \mu\text{mol dm}^{-3}$ ) in this seawater sample. Reprinted (modified) from Guo, L. D., Wen, L., Tang, D. and Santschi, P. H. Re-examination of cross flow ultrafiltration for sampling aquatic colloids: evidence from molecular probes, *Marine Chemistry*, **69**, 75–90, Copyright 2000, with permission from Elsevier

explain quantitatively the ultrafiltration behaviour of macromolecules in natural waters, controlled laboratory experiments using standard macromolecules with known MWs and molecular probes have recently been conducted [98,144–146,150]. If the increase in permeate DOC concentration with increasing concentration factor was due to the breakthrough of HMW materials [153], one should see the increased concentration of standard HMW molecules in the permeate with increasing CF. In contrast, if the increase in permeate DOC concentration with increasing CF is due to the retention of LMW molecules, the ultrafiltration behaviour of standard LMW molecules should provide a model for understanding the permeation behaviour of natural DOC.

Using molecular probes and standard macromolecules, Figure 8 demonstrates a consistent increase in the permeate concentration of standard LMW molecules with increasing CF during ultrafiltration [98,144,146,149,151]. Whereas LMW molecules can be retained during ultrafiltration, the permeation of HMW materials occurs only for those with an MW close to membrane's MWCO. The retention of macromolecules increases significantly with increasing MW of the macromolecules (Table 3). The permeation coefficient of macromolecules decreases significantly with increasing MW of macromolecules. Although these data came from different membranes, the evidence of decreasing permeation coefficients with increasing macromolecules MW is compelling.

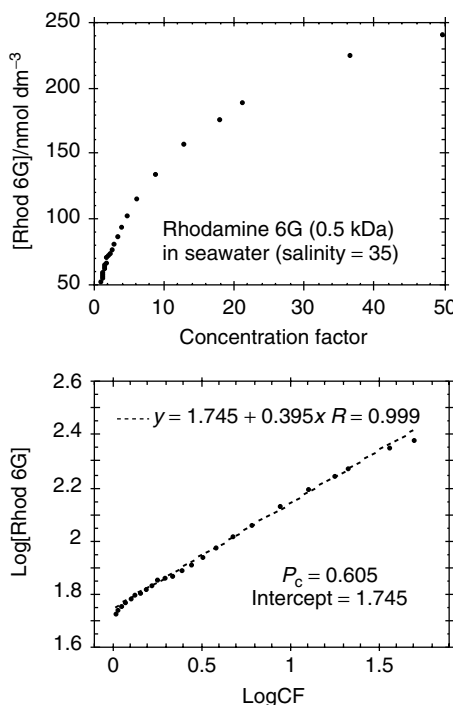


**Figure 8.** Permeation behaviour of LMW Rhodamine 6G (0.495 kDa) in seawater on a 1 kDa ultrafiltration membrane, exhibiting ultrafiltration behaviour similar to that of DOC in seawater as shown in Figure 7. Reprinted (modified) from Guo, L. D., Wen, L., Tang, D. and Santschi, P. H. Re-examination of cross flow ultrafiltration for sampling aquatic colloids: evidence from molecular probes, *Marine Chemistry*, **69**, 75–90, Copyright 2000, with permission from Elsevier

These experimental results indicate that the permeation of natural DOC results from LMW DOC passing through the ultrafiltration membrane, and the increase in DOC concentration in the permeate is indeed largely due to the LMW DOM in seawater [98,144, 146,149,151,159], as opposed to the breakthrough of HMW DOM materials as suggested by Dai *et al.* [153]. It is the constant permeation rate and a permeation coefficient  $<1$  for LMW molecules that cause the increase of a specific LMW molecule in the permeate during ultrafiltration (Figure 8).

Results of controlled laboratory experiments show that significant fractions (>40%) of LMW Rhodamine 6G (with an MW of 0.5 kDa) and glutathione (with an MW of 0.6 kDa) can be retained by a 1 kDa ultrafiltration membrane, even with a CF of  $\leq 50$  ([98] and Figure 8). Therefore, the retention of LMW molecules in the retentate can give rise to an overestimate of the colloidal fraction, especially with lower CFs [98,144,147]. The percentage of HMW molecules passing through the 1 kDa membrane decreases rapidly with increasing size or MW (Table 3). On average,  $\sim 15\%$  of vitamin B<sub>12</sub> (1.3 kDa) and  $\sim 3\%$  of a 3 kDa dextran pass through the 1 kDa membrane, while permeation of a 10 kDa dextran through the 1 kDa membrane becomes negligible ( $<0.6\%$ ).

In summary, the permeation of HMW molecules is minimal during ultrafiltration through 1 kDa MWCO membrane, even with high CFs [98]. The percentage of HMW molecules

that permeate through the ultrafiltration membrane actually decreases as the CF increases, most likely due to fouling of the membrane [143]. Therefore, small losses of HMW macromolecules (with molar masses near the membrane MWCO) to the permeate may be seen at lower CFs, but not at higher CFs [98]. For membranes with higher MWCO (*e.g.* 10 kDa), it is, however, possible that HMW (>10 kDa) non-spherical macromolecules (*e.g.* fibrils) pass through for geometric reasons [80].

The ultrafiltration behaviour of natural DOC and standard macromolecules can be well predicted by the permeation model discussed in the previous section, which consistently shows an increasing concentration in the permeate with increasing CFs (Figure 7). Comparing the model results for seawater and standard macromolecules, it seems that the permeation behaviour of natural DOC in seawater follows that of the LMW standard macromolecule. This indicates that the permeate fraction contains mostly lower MW DOC and the HMW DOC in seawater can indeed be retained during the ultrafiltration of seawater. The percentage of COC for this specific example can be calculated as 60% of the bulk DOC from the permeation model, with a  $P_c$  value of 0.45, an initial total [DOC] of 245  $\mu\text{mol dm}^{-3}$  and a model derived initial LMW DOC concentration ( $C_f^0$ ) of 99  $\mu\text{mol dm}^{-3}$ , calculated from an intercept of 1.65 in the relationship between  $\log C_p$  and  $\log \text{CF}$  (Figure 7). This is the preferred way to determine the colloidal percentage of a specific chemical species in natural waters. Measurements of the colloidal fraction from starting solution, retentate and permeate, as often reported in literature, are apparent values, which are always higher than the model predicted values due to the retention of LMW materials [98,144].

Guo *et al.* [98] showed that both standard macromolecules such as dextrans and Rhodamine 6G, and natural DOC are recovered with a mass balance of 92–95% during ultrafiltration through 1 kDa MWCO membranes, while losses of glutathione and vitamin B<sub>12</sub> to the membrane can be significant. Sorptive losses and the overall mass balance are thus dominated by the physicochemical properties of the molecules, but not their MWs. Most retained LMW DOC can be further removed during diafiltration, whereas losses of HMW DOC during diafiltration are minimal. Therefore, retention of LMW molecules rather than permeation of HMW molecules is the main problem in isolating aquatic colloids using cross-flow ultrafiltration. Artifacts from LMW compounds are minimised when high CFs are used to extract large quantities of colloids for chemical and isotopic characterisation. Indeed, high CFs have been widely used in many recent studies of colloidal macromolecular organic matter [30,31,34,35,77,78,80–85,88–93,95,96,118,133,134,160–163]. While low concentration factors overestimate the colloidal fraction, high CFs may cause other unknown effects during ultrafiltration of small volume samples. More studies are necessary to determine an optimum CF for sampling specific colloidal species using ultrafiltration. In practice, high CFs are needed for processing large volumes of water samples. To determine the colloidal percentage when only a small sample size is required, it is important to use similar CFs and the same operating conditions for all samples in order to compare colloidal fraction estimates of major and trace components among samples or among investigators. Ideally, the true colloidal fraction of a specific chemical species is obtainable only by making time-series measurements in the permeate as a function of CF, which allows one to determine the permeate coefficient needed to calculate the colloidal percentage [98,144].

### 3.3 PERMEATION BEHAVIOUR OF TRACE METALS AND RADIONUCLIDES

This section summarises recent studies on selected trace metals such as Cu, Fe, Mn, Co, Zn, Cd and Ba and radionuclides such as  $^{234}\text{Th}$  and  $^{238}\text{U}$ .

Wen *et al.* [67] demonstrated that Cu concentrations in discrete permeate samples increased with increasing permeate volume or CF (Figure 9), and the corresponding colloidal percentage of Cu decreased from  $\sim 42\%$  of the total dissolved Cu at a CF of  $\sim 11$  to  $\sim 25\%$  when the CF approached  $\sim 23$ . Similarly to Cu, trace metals such as Cd, Ni, Mn and Pb showed a behaviour consistent with the permeation model, as a result of which metal concentrations in the permeate are expected to increase (Figure 9). Cu, Cd, Ni, Mn and Pb all followed the permeation model fairly well, whereas contamination-sensitive metals such as Fe, Hg and Zn, showed an inconsistent ultrafiltration behaviour (Figure 9). Deviation from the permeation model for Fe, Hg and Zn probably resulted from the ultra-low levels of these metals and difficulties during sampling, handling and processing (see the discussion below for comparisons with radioactive metals).

The ultrafiltration behaviour of Cu could be equally well predicted by the permeation model as that of macromolecules or natural DOM. The time-series permeate data resulted in a constant permeation coefficient ( $P_c$ ) of 0.56 for the LMW complexed Cu fraction [67]. This indicates that only 56% of the LMW complexed Cu permeates through the membrane during each cycle of the ultrafiltration. To remove the LMW complexed metals, higher CFs are required for isolating colloidal metals when a fraction of metal binds strongly to LMW organic ligands.

Using radioactive metals in a dilute EDTA solution to maintain metals in an LMW complexed form, Guo *et al.* [98] examined the permeation behaviour of radioactive metals, including  $^{59}\text{Fe}(\text{III})$ ,  $^{54}\text{Mn}(\text{II})$ ,  $^{60}\text{Co}(\text{II})$ ,  $^{65}\text{Zn}(\text{II})$ ,  $^{109}\text{Cd}(\text{II})$ ,  $^{110m}\text{Ag}(\text{I})$ ,  $^{133}\text{Ba}(\text{II})$  and  $^{234}\text{Th}(\text{IV})$ . Similarly to the ultrafiltration behaviour of stable trace metals such as Cu shown in Figure 9, Guo *et al.* [98] found that concentrations of radioactive metals in the permeate ( $C_p$ ) also increased with increasing CF (Figure 10), as expected from a permeation model with a  $P_c$  value  $<1$ . While the permeation behaviour of some stable metals such as Fe, Hg and Zn in natural waters departed slightly from the permeation model (Figure 9), all radioactive metals in model solutions, including  $^{59}\text{Fe}$  and  $^{65}\text{Zn}$ , showed a linear relationship between  $\log C_p$  and  $\log \text{CF}$ , indicating a constant  $P_c$  value during the entire ultrafiltration process (Figure 10). Since there are less contamination problems for radioactive metals, the results presented in Figure 10 support the conclusion that the permeation model (Section 4.1) can be universally applied not only to macromolecules, but also to trace elements complexed with organic ligands.

Similarly to the situation for macromolecules, if LMW metals passed through the ultrafiltration membrane without being concentrated, the concentration of metals in the permeate would be constant with CF, resulting in  $P_c = 1$ . However, the opposite is true. From the values of the slopes in Figure 10,  $P_c$  values ranged from  $\sim 0.1$  to 0.72, depending on the metal. Constant  $P_c$  values for each metal and  $P_c$  values less than 1 imply that varying fractions of LMW complexed trace metals can be retained during ultrafiltration [98]. Therefore, a low CF may result in significant overestimation of colloidal abundance of certain metals as it does during ultrafiltration of natural DOC. To avoid using high CFs, permeate data are required as a function of CF to determine the colloidal metal abundance.

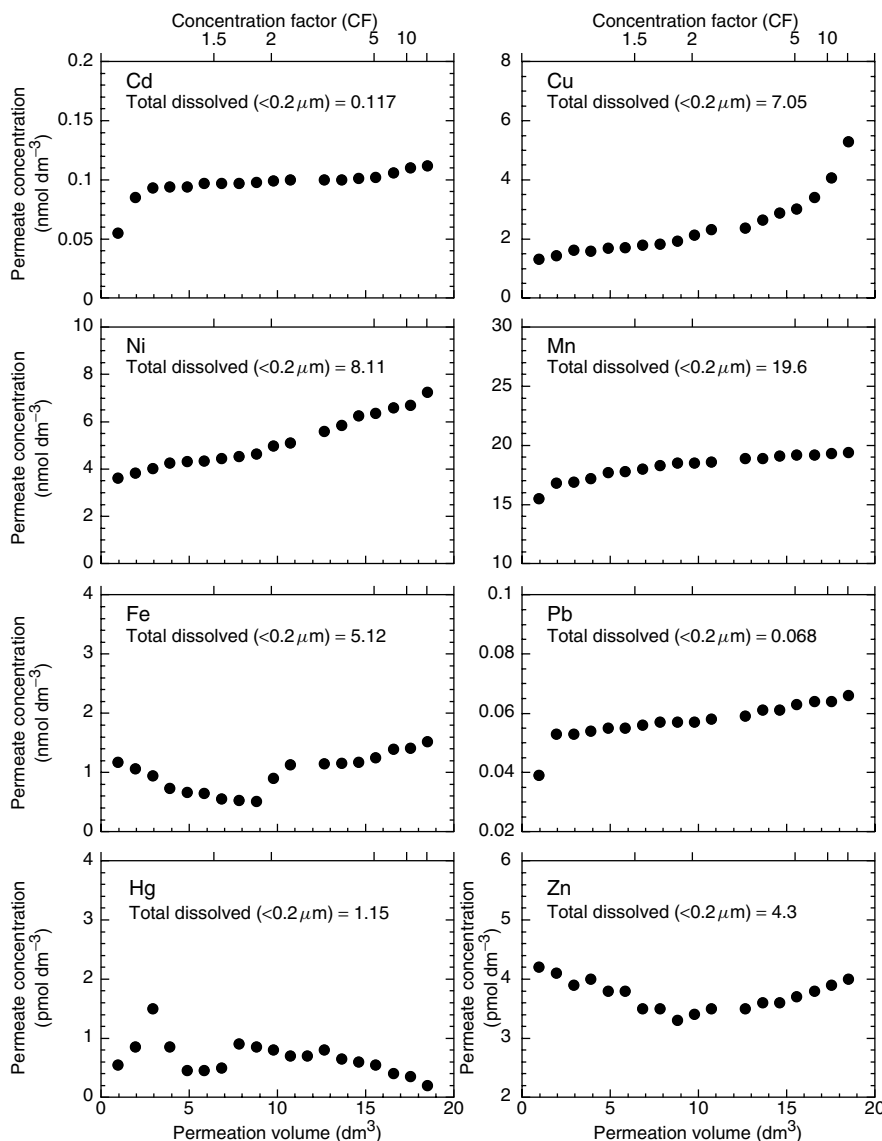


**Figure 9.** Changes of permeate concentrations of trace metals during seawater ultrafiltration. Reprinted from Wen, L. S., Stordal, M. C., Tang, D., Gill, G. A. and Santschi, P. H. An ultra-clean cross-flow ultrafiltration technique for the study of trace metal phase speciation in seawater, *Marine Chemistry*, **55**, 129–151, Copyright 1996, with permission from Elsevier

Variations of natural uranium [U(VI)] concentrations in discrete permeate time series samples are shown as a function of CF in Figure 11. Permeate U(VI) concentrations (<1 kDa in this case) in an estuarine water sample consistently increased with increasing CF. Again, these time-series permeate data could be well described by the permeation model and a permeation coefficient of 0.62. In other words, 38% of the LMW U(VI) in

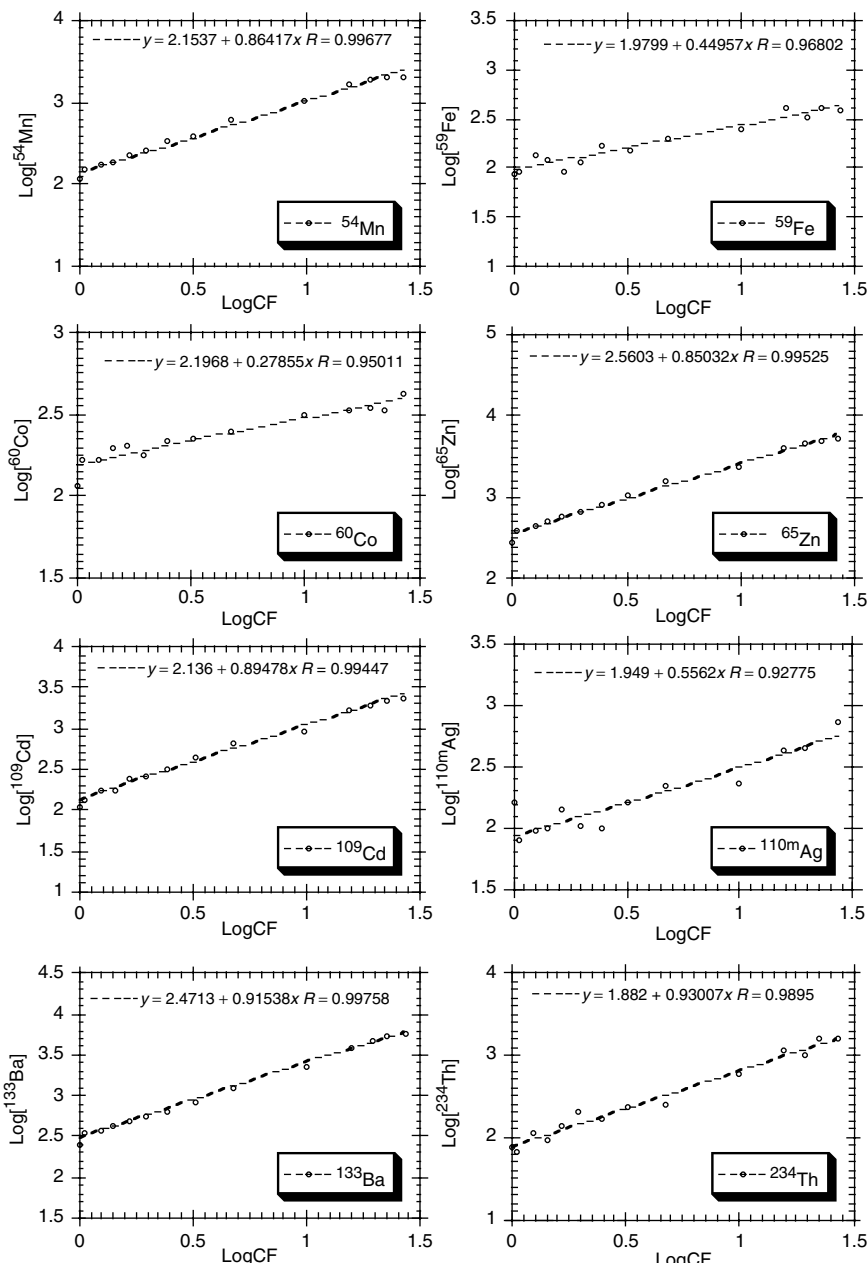


**Figure 10.** Examples of using radioactive metals to examine the permeation behaviour of metals. Reprinted from Guo, L. D., Wen, L., Tang, D. and Santschi, P. H. Re-examination of cross flow ultrafiltration for sampling aquatic colloids: evidence from molecular probes, *Marine Chemistry*, **69**, 75–90, Copyright 2000, with permission from Elsevier

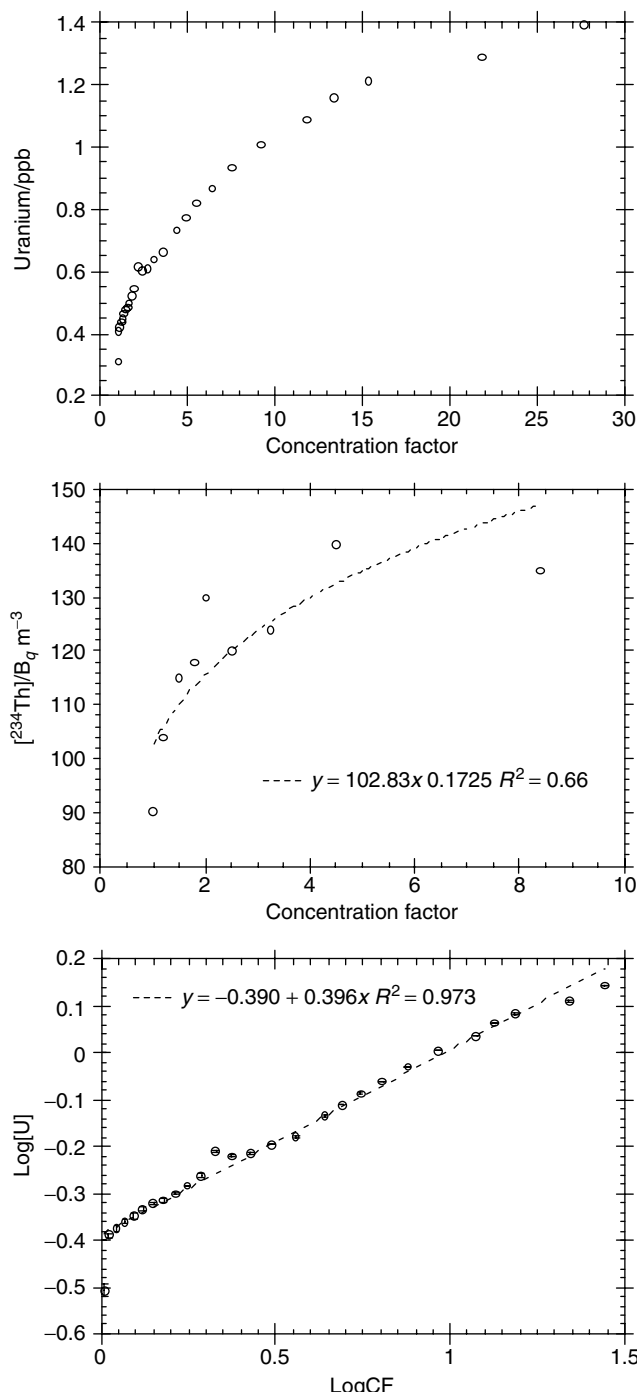


**Figure 11.** Variations of uranium ( $<1$  kDa) and  $^{234}\text{Th}$  ( $<10$  kDa) concentrations in permeate with concentration factor during ultrafiltration ( $^{234}\text{Th}$  data are from [149] with permission, and uranium data are from Guo *et al.*, in preparation)

this specific water sample could be retained by a 1 kDa ultrafiltration membrane during each ultrafiltration cycle. Uranium is a soluble element present in seawater as a carbonato complex. The extent of complexation of U(VI) with inorganic and organic ligands changes substantially along the mixing gradient between freshwater and seawater in an estuary. Due to its anionic character, it is also subject to anion rejection by the membrane (see later section), increasing its apparent colloidal fraction. Differences in U chemical speciation will give rise to a different permeation behaviour and thus different colloidal percentage of U between different water types (see also Section 4.3).

Figure 11 also shows an example of ultrafiltration behaviour for a particle-reactive  $^{234}\text{Th}(\text{IV})$  spiked in a coastal seawater sample using a 10 kDa hollow-fiber ultrafiltration membrane [149]. Similarly to both seawater DOC and trace metals, the concentration of  $^{234}\text{Th}$  in the permeate also increased with increasing CF. The relationship between  $\log[^{234}\text{Th}]$  in the permeate and logCF could be described as

$$\log[^{234}\text{Th}] = 2.012 + 0.17 \times \log \text{CF} \quad (3)$$

with a  $P_c$  value of 0.83 and an initial concentration of added LMW  $^{234}\text{Th}$  of 123  $\text{Bq m}^{-3}$  [149].

Thorium, a particle-reactive element, is usually present mostly in a colloidal/particulate form in a purely inorganic system [26,27]. The fact that up to 50% of the traditionally defined dissolved Th(IV) can be present in a <1 kDa LMW form [31,77] indicates that Th(IV) can be associated with a wide spectrum of natural organic ligands in seawater, although the complexation is often found to be specific to colloidal organic ligands [164–169]. Therefore, the observed permeation behaviour of Th(IV) can be variable, largely as a result of Th(IV) complexation with natural organic and inorganic ligands of different MWs.

### 3.4 PERMEATION BEHAVIOUR OF MAJOR IONS

Ultrafiltration is a purely physical separation technique provided that interactions between membrane materials and individual chemical species are negligible. As stated above, the retention of trace elements by ultrafiltration membranes largely results from the complexation of trace elements with organic ligands in natural waters. Thus, chemical species such as metals, nutrients, radionuclides and major ions in a free ionic form should freely permeate through membranes without significant retention during ultrafiltration. Nevertheless, the permeation behaviour of major ions in natural waters is largely unknown. For those with little complexation potential, such as  $\text{Na}^+$ ,  $\text{K}^+$  and  $\text{Cl}^-$  in seawater [170,171], a permeation behaviour similar to that for macrofiltration could be expected [150]. For other major ions such as  $\text{Ca}^{2+}$  and  $\text{Mg}^{2+}$ , it is possible that, in addition to ion rejection, a small fraction may be associated with natural organic matter such as humic substances, and would show a permeation behaviour similar to that of natural organic matter.

Figure 12 shows an example of the ultrafiltration behaviour of major ions using water samples collected across a salinity gradient of 0–20 in an estuarine environment. Concentrations of major ions in the permeate increase with increasing CF during the ultrafiltration, especially  $\text{Ca}^{2+}$ ,  $\text{Mg}^{2+}$  and  $\text{SO}_4^{2-}$ . Those major ions that are present mainly in free ionic or inorganically complexed forms in natural waters are expected to pass through a 1 kDa ultrafiltration membrane, so that their concentrations in the permeate should be constant

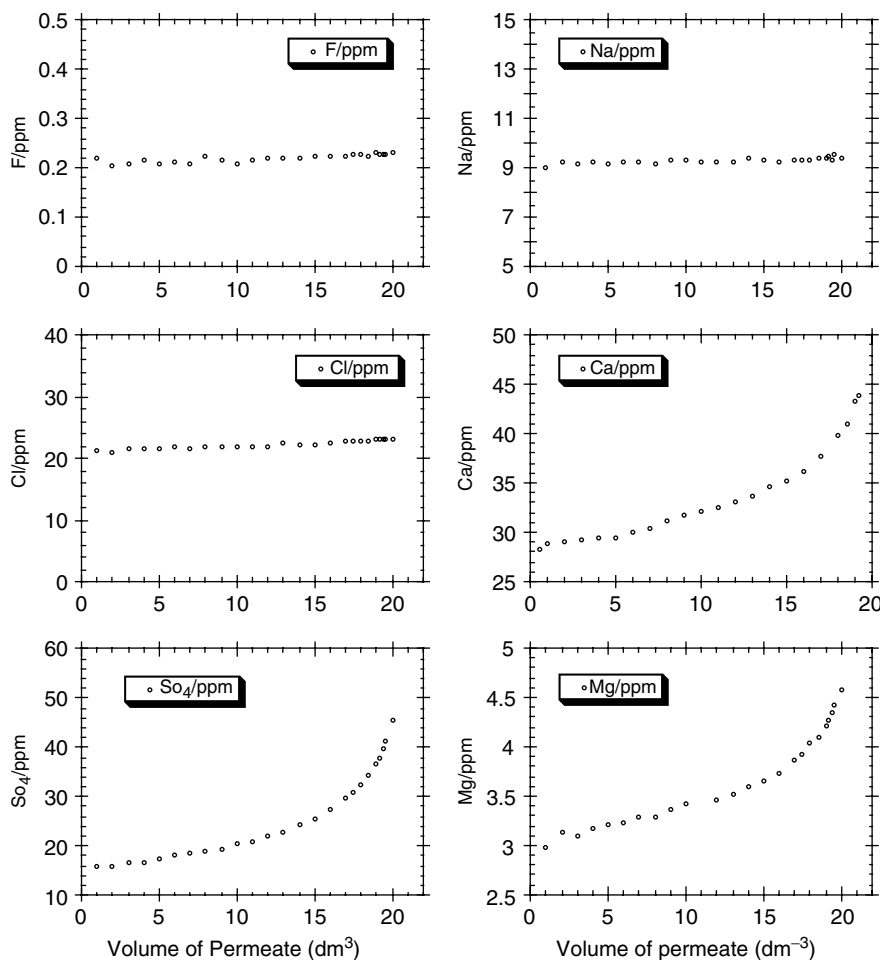


**Figure 12.** Variations of concentrations of major ions ( $\text{F}^-$ ,  $\text{Cl}^-$ ,  $\text{SO}_4^{2-}$ ,  $\text{Na}^+$ ,  $\text{Ca}^{2+}$  and  $\text{Mg}^{2+}$ ) in time-series permeate samples collected during the ultrafiltration of Trinity River water. Reprinted from Guo, L. D., Hunt, B. J. and Santschi, P. H. Ultrafiltration behavior of major ions ( $\text{Na}^+$ ,  $\text{Ca}^{2+}$ ,  $\text{Mg}^{2+}$ ,  $\text{F}^-$ ,  $\text{Cl}^-$ ,  $\text{SO}_4^{2-}$ ) in natural waters, *Water Research*, 35, 1500–1508. Copyright 2001, with permission from Elsevier

as the CF increases during the ultrafiltration. Indeed, concentrations of  $\text{F}^-$ ,  $\text{Cl}^-$ ,  $\text{Na}^+$  and  $\text{K}^+$  in the permeate change little with increasing CF, indicating that these major ions are mostly in a free ionic form in natural waters, in agreement with predictions from thermodynamic and speciation models [170,171]. In contrast, concentrations of  $\text{SO}_4^{2-}$ ,  $\text{Ca}^{2+}$  and  $\text{Mg}^{2+}$  in the permeate consistently increase to a different extent with increasing permeate volume or CF (Figure 12), probably through anion rejection, which causes cations to be rejected for reasons of electroneutrality.

The permeation behaviour of all major ions can be well presented by the permeation model discussed in Section 4.1, resulting in a constant permeation coefficient for each ion. The value of the model-derived permeation coefficient ( $P_c$ ) was 0.99 for  $\text{Na}^+$ , 0.97 for

$\text{Cl}^-$  and 0.95 for  $\text{F}^-$ . Significant (14–36%) retention was observed for  $\text{SO}_4^{2-}$ ,  $\text{Ca}^{2+}$  and  $\text{Mg}^{2+}$  during ultrafiltration, with  $P_c$  values of 0.64, 0.82 and 0.86, respectively. Nearly constant concentrations of  $\text{F}^-$ ,  $\text{Cl}^-$ , and  $\text{Na}^+$  in the permeate time-series samples confirm that there was little interaction between these ions and natural organic matter, or the ultrafiltration membrane. Thus, F, Cl, Na and K can pass through the membrane almost freely without significant retention during ultrafiltration. However, increasing permeate concentrations for  $\text{SO}_4^{2-}$ ,  $\text{Ca}^{2+}$  and  $\text{Mg}^{2+}$  are a testimony to significant retention of these ions, suggesting that there is electrostatic interaction between these ions and the membrane surface [150]. The alternative that significant fractions of these ions were associated with macromolecular colloidal materials, was less likely, due to their relatively high concentrations. These laboratory results are consistent with field ultrafiltration studies. For example, Dupre *et al.* [172] observed that  $\leq 5\%$  of  $\text{Ca}^{2+}$ ,  $\text{Mg}^{2+}$  and  $\text{Na}^+$  were complexed with organic material in wetland waters, while significant apparent colloidal  $\text{SO}_4^{2-}$  fractions were observed in fresh waters [173]. Conversely, Hill and Aplin [174] reported apparent colloidal percentages of 25% for  $\text{Ca}^{2+}$  and  $\text{Mg}^{2+}$  and 15% for  $\text{Na}^+$  and  $\text{K}^+$  in northern Britain river waters.

Guo *et al.* [150] reported that the percentage retention of major ions during ultrafiltration decreased with increasing salinity or ionic strength in water samples. This retention can be largely attributed to electrostatic repulsion by the negatively charged cartridge membrane, i.e. the interaction between major ions and membrane surfaces, such as electrostatic and electrokinetic effects [175], which can result in the selective retention of major ions during ultrafiltration. This retention mechanism for  $\text{SO}_4^{2-}$  is consistent with an increase in the  $P_c$  value of  $\text{SO}_4^{2-}$  with increasing salinity [150]. Furthermore, the retained major ions can further permeate through the 1 kDa membrane, and thus be eliminated from the retentate during diafiltration of the retentate with ultra-pure water, confirming their co-retention for electroneutrality reasons. Selective retention of major and minor ions during ultrafiltration may significantly affect the size fractionation of trace elements when using ultrafiltration techniques, and therefore needs to be taken into account.

Interestingly, even stable oxygen isotopes (expressed as  $\delta^{18}\text{O}$ ) in distilled water show a detectable fractionation during ultrafiltration ([176, and Guo *et al.*, unpublished data]: an increase in the  $\delta^{18}\text{O}$  values in permeate samples was recorded with increasing permeate volume (Figure 13). The oxygen isotope fractionation was up to 0.8%. This isotope fractionation probably results from kinetic fractionation effects caused by selective adsorption and molecular diffusion through the ultrafiltration membrane [176].

### 3.5 OPTIMUM CONCENTRATION FACTOR

As discussed before, three important issues when using cross-flow ultrafiltration are (1) the integrity of membranes, (2) ultrafiltration mass balance and (3) optimal operating conditions such as CF and cross-flow ratio. The integrity of membranes after prolonged use can be calibrated using molecular probes or standard macromolecules with known MWs [98,144,146]. A simple test is to use coloured vitamin B<sub>12</sub> solution (MW = 1.3 kDa) to check a 1 kDa membrane's integrity. If a 1 kDa membrane is intact, there should be no noticeable pink vitamin B<sub>12</sub> molecules in the permeate solution. This check can be performed quantitatively by absorbance measurements or can be done visually. Both HMW and LMW macromolecules can be used for the calibration of different membrane MWCOs.

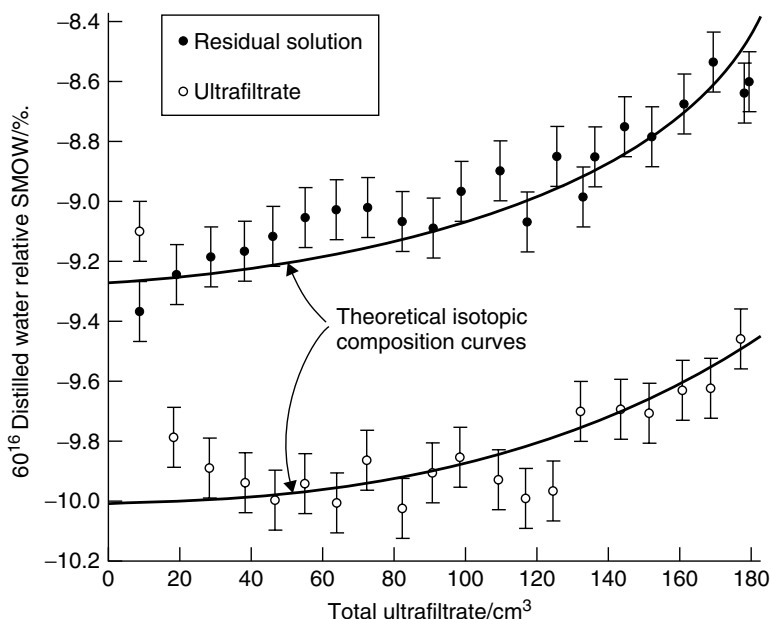


**Figure 13.** Variations of  $\delta^{18}\text{O}$  value in permeate samples with total accumulated ultrafiltrate for the distilled water experiment. Reprinted from Coplen, T. B., and Hawshaw, B. B. Ultrafiltration by a compacted clay membrane—I. Oxygen and hydrogen isotope fractionation, *Geochimica et Cosmochimica Acta*, **37**, 2295–2310, Copyright 1973, with permission from Elsevier

Mass balances can be determined by monitoring all ultrafiltration fractions, including the initial solution, permeate and retentate for each chemical species. Mass balance results are not always a perfect indicator of optimal performance. However, they give investigators an indication of possible contamination or losses to the membrane and sampling devices.

Regarding the optimum CF for ultrafiltration, it is very clear from the previous discussion of the permeation and retention behaviour of chemical species, including macromolecules, natural DOM, trace metals, radionuclides and major ions, that high CF values give more representative colloidal fraction data. Ideally, time-series permeate samples are required to calculate the colloidal fraction of a specific chemical species. As discussed before, modeling the permeate data as a function of CF allows the determination of a permeation coefficient that is representative of the entire ultrafiltration process.

Dai *et al.* [153] argued that high CF causes HMW materials to break through a membrane, contributing to an increase in concentration in the permeate with increasing CF. It seems unlikely that a membrane retaining the LMW chemical species would concurrently allow the HMW materials to break through. This situation occurs only for those macromolecules with a MW similar to the NMWCO of the membrane, i.e. very close to the membrane rated MWCO, but not for HMW molecules considerably larger than the MWCO. As stated in previous sections, the pore size of ultrafiltration membranes are not as well defined as for barrier filters such as Nuclepore polycarbonate membranes. Instead, the distribution of membrane pore sizes includes both neighboring

LMW and HMW MWCOs [143]. This allows a small fraction of macromolecules with an MW slightly higher than the membrane's MWCO to permeate through the membrane, as in the case of vitamin B<sub>12</sub> (with an MW of 1.3 kDa) passing through a 1 kDa membrane. Nevertheless, macromolecules much larger than the MWCO are efficiently retained [144,146].

## 4 APPLICATIONS TO FIELD STUDIES OF AQUATIC COLLOIDS

Recent applications of ultrafiltration for studying the composition or partitioning of aquatic colloids, along with other analytical techniques, have greatly advanced our understanding of the cycling of natural macromolecular organic matter and its associated trace substances, including metals, radionuclides and hydrophobic organic pollutants in aquatic environments. This section focuses on recent advancements regarding the roles of aquatic colloids in governing the fate, transport and bioavailability of trace elements, organic carbon cycles and geochemical and environmental behaviours of chemical species.

### 4.1 NATURAL ORGANIC MATTER

Dissolved organic carbon (DOC) is one of the largest reduced carbon pools on Earth and plays a central role in the biogeochemistry of many trace elements and organic pollutants in aquatic environments, including lake, river, estuarine, oceanic and ground water systems [177–180]. Organic carbon can be categorised as three different physically defined pools: particulate organic carbon (POC), colloidal organic carbon (COC) and DOC. These fractions are operationally defined by physical parameters, especially the pore size of the membrane. Part of the DOC is composed of colloidal macromolecular organic matter [3,8,34,45,56,89,132,181], also sometimes referred to as ultrafiltered dissolved organic matter (UDOM), which plays an important role in the carbon cycle, trace metal scavenging and biogeochemical processes in aquatic systems [10–12,15,16,27,41,43,108,111]. However, colloidal organic matter remains a poorly quantified component of natural organic matter in both freshwater and seawater systems.

A better understanding of the role of colloids in the natural organic carbon cycle depends on a detailed knowledge of the size fractionation of organic matter together with the chemical composition and the reactivity of each size class. Improvement of colloidal sampling techniques, especially ultrafiltration methods in recent years, has resulted in a growing body of literature describing the abundance, molecular weight/size distribution, elemental, isotopic and molecular composition and geochemical behaviour of COM in aquatic environments (Tables 2, 4 and 5).

#### 4.1.1 Size Distribution of Natural Organic Matter

*4.1.1.1 Fresh Waters.* The molecular weight distribution of DOC in natural waters has been examined using various ultrafiltration methods. Early research on natural organic matter (NOM) and its size or molecular weight distribution has been summarised and reviewed by a number of authors [11,14,56,182,183]. Table 4 lists recent results on DOC

**Table 4.** Examples of the percentage of colloidal organic carbon (COC) in the bulk DOC in different aquatic environments

Location (or water type)	Prefilter/ μm	MWCO <sup>a</sup> / kDa	DOC/ (μmol dm <sup>-3</sup> )	COC/DOC/%	Reference
Mackenzie River	0.45	10	50–300	5–30	[181]
Mississippi River	0.2	1	271–333	~45	[186]
Amazon River	0.1	1	399	76	[184]
Trinity River	0.2	1	495	68	[5]
Delaware River	0.2	1	136–330	28–43	[161,162]
Lake Geneva	1.2	1	59–125	36–58	[45]
Vistula River	1.2	1	392–650	36–86	[45]
Chena River	0.45	1	482	69	[89]
Yukon River	0.45	1	508–2825	73 ± 3	[8]
Soil profiles	0.45	1	–	39–80	[277]
Soil solution	–	1	–	98	[210]
Rhone Delta	0.7	500	92–179	7–49	[269]
N. Atlantic	0.45	10	45–75	10–15	[57]
Estuarine waters	0.2	10	80–400	8–19	[181]
Seawater	NA	10	42–60	<10	[58]
Pacific Ocean	0.45	10	51–64	4–5	[194]
Bedford Basin	0.2	10	70–158	4–16	[278]
Gulf of Mexico	0.4	10	50–130	8–14	[2]
Rhone Delta	0.4	10	82–148	8–30	[4]
Atlantic	0.2	10	50–90	5–10	[3]
Gulf of Mexico	0.2	10	45–86	3–5	[3]
Vinice Lagoon	0.4	10	116–312	10–26	[62]
Bedford Basin	0.2	10	56–101	3–17	[189]
Galveston Bay	0.2	10	139–495	6–11	[5]
Chesapeake Bay	0.2	10	118–205	10–16	[5]
Gulf of Mexico	0.2	3	45–70	10–16	[3]
Atlantic	0.2	3	69–90	20–24	[3]
Kalix River/Bothnic Bay	0.2	3	190–420	15–54	[109]
Seawater	0.7	1	45–416	10–64	[56]
Mississippi plume	0.2	1	83–333	27–45	[186]
Pacific Ocean	0.2	1	38–82	25–35	[34]
Pacific Ocean	0.45	1	51–64	30–37	[194]
Gulf of Mexico	0.4	1	50–131	46 ± 6	[2]
Atlantic	0.2	1	47–90	20–44	[3]
Gulf of Mexico	0.2	1	45–86	14–36	[3]
Seawater	0.2	1	30–120	0–67	[60]
Gulf of Maine	1	1	56–128	16–25	[230]
Adour Estuary	1.2	1	76–316	2–45	[45]
Bering Sea shelf	0.7	1	61–90	40 ± 7	[279]

<sup>a</sup> MWCO = nominal molecular weight cut-off.

molecular weight distributions. Examples of total organic carbon (TOC) partitioning between dissolved, colloidal and particulate phases are depicted in Figure 14 for freshwaters, Figure 15 for estuarine waters and Figure 16 for oceanic waters.

Using a 1 kDa membrane, Benner and Hedges [184] found a high COC percentage (76%) for Amazon River waters compared with that found in salt water systems. Guo

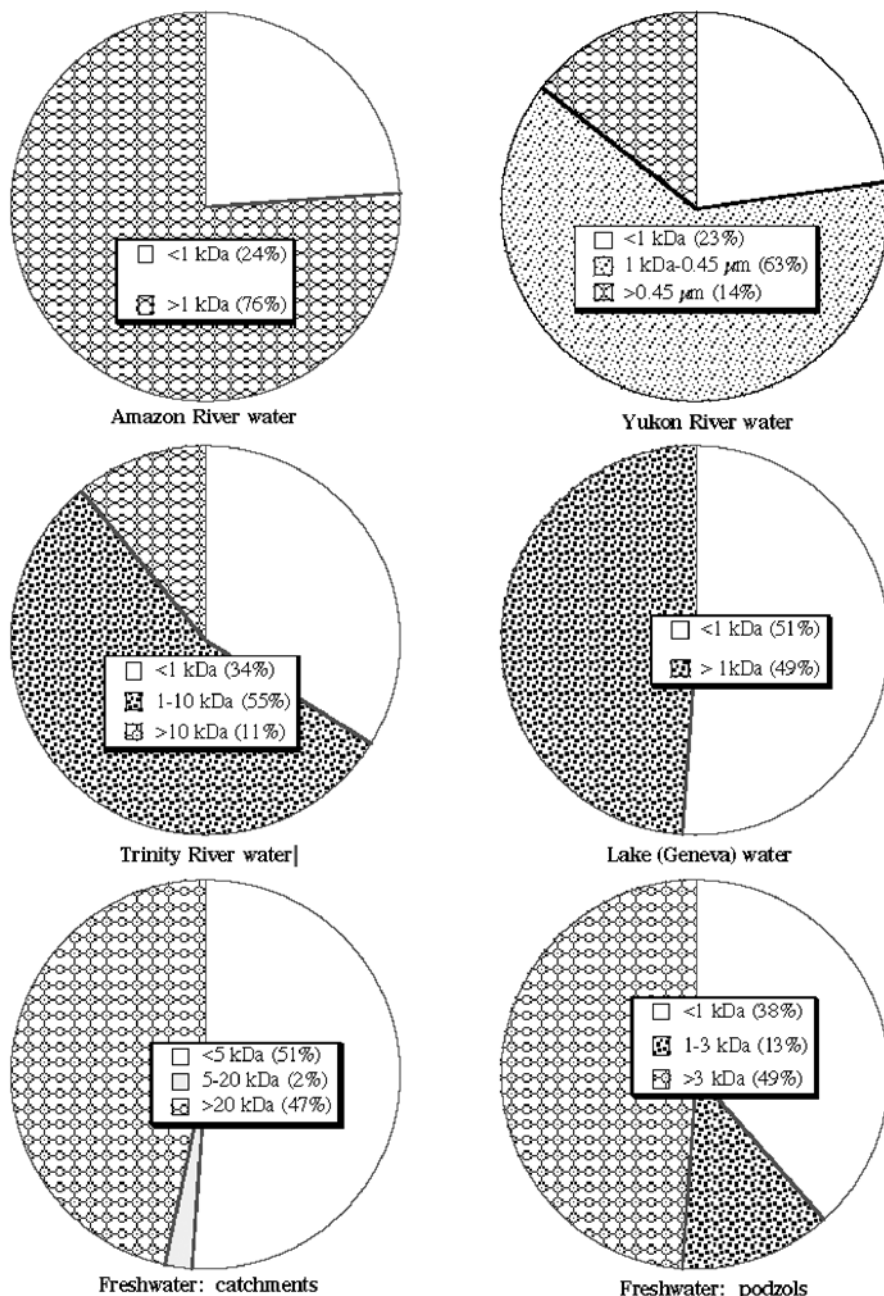


**Figure 14.** Examples of organic carbon size distribution between dissolved, colloidal and particulate phases in freshwater systems (river, lake, catchment and podzols) (data from the Amazon River [184], Yukon River [8,97], Trinity River [5], Lake Geneva [45] tropical catchments [267] and podzols [277])

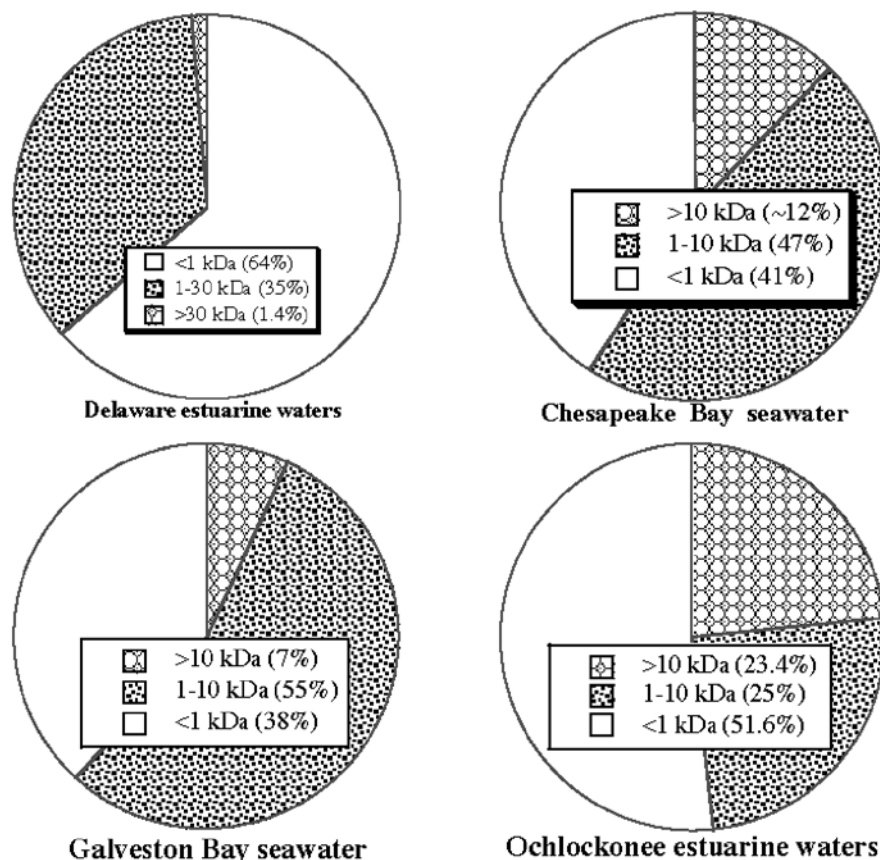


**Figure 15.** Examples of size distributions of dissolved organic carbon in estuarine environments, plotted from data of Delaware Estuary [161], Chesapeake Bay and Galveston Bay [5] and Ochlockonee Estuary [65]

and Santschi [5] reported that 66% of the bulk DOC was found as COC in Trinity River waters. Subsequently, high COC concentrations and percentages have been reported for river waters, freshwater catchments, lake waters and soil solutions (Table 4 and Figure 14 and references therein). For example, Guéguen *et al.* [8] reported an average COC percentage of  $73 \pm 3\%$  for Yukon River waters, similar to percentages reported for major world rivers. Figure 14 shows that freshwater systems, such as rivers and lakes, contain a relatively higher percentage of COC in the bulk DOC pool compared with that found in estuarine and oceanic waters (Figures 16 and 17). High percentages of COC in river waters and low salinity regions [91,132,182] probably result from high concentrations of humic substances and terrestrial organic matter fractions that enhance colloidal stability [185].

**4.1.1.2 Estuarine Waters.** Figure 15 and Table 4 provide examples of DOC molecular weight distributions in estuarine waters. Using a 1 kDa membrane, Benner *et al.* [186]

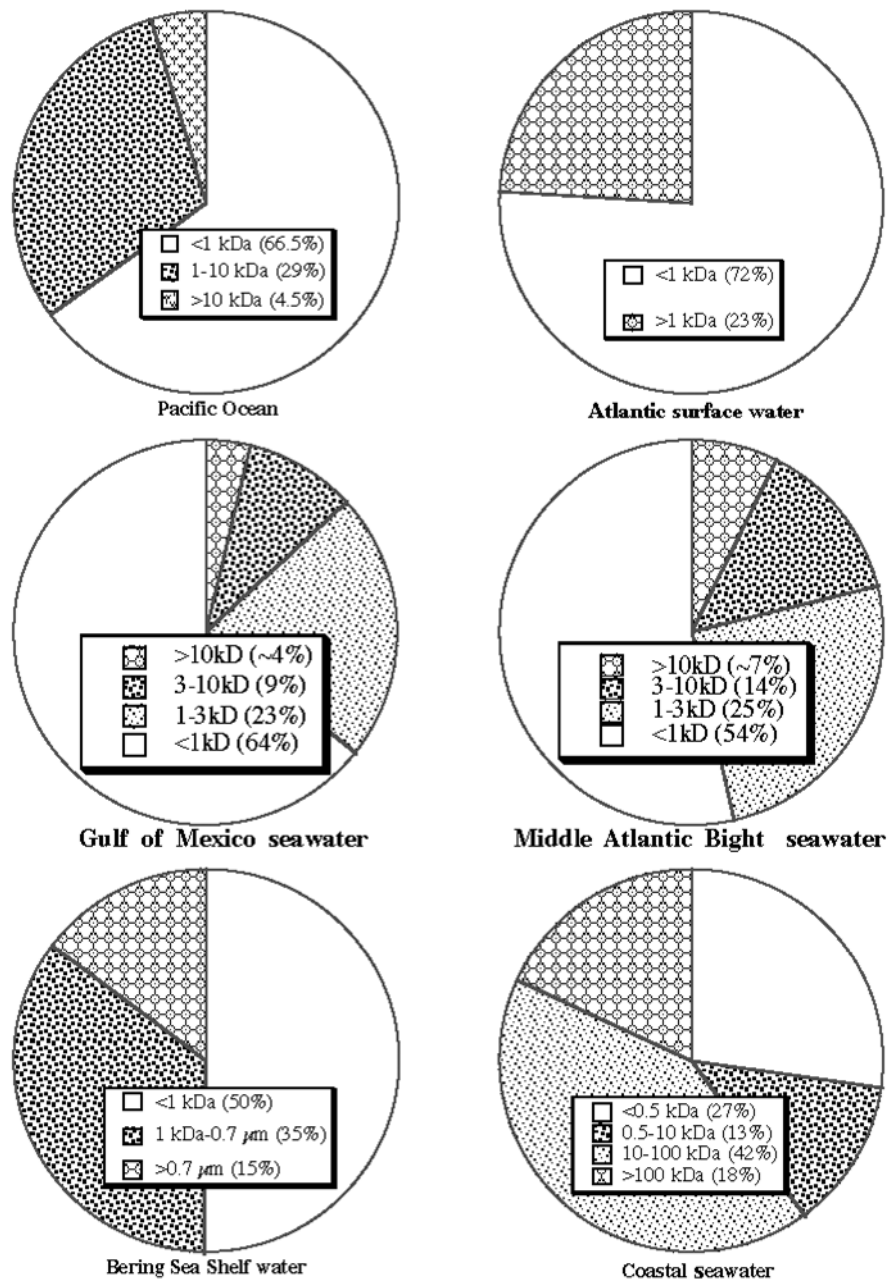


**Figure 16.** Examples of organic carbon distribution between dissolved, colloidal and particulate phases in oceanic environments, from data of the Pacific [194] and Atlantic surface waters [133], the Gulf of Mexico and Middle Atlantic Bight [3], the Bering Sea shelf [279], and coastal seawater [190]

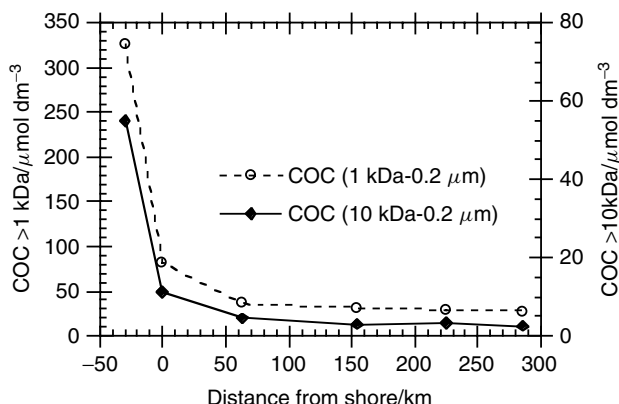


**Figure 17.** Variations of colloidal organic carbon (COC) concentration with distance from shore, showing a decrease in concentration with increasing distance consistent with colour changes of the colloidal solution shown in Figure 3. Reproduced with permission from the American Society of Limnology and Oceanography

examined the distribution of COC in the Mississippi River plume and found concentrations of COC<sub>1</sub> (1 kDa–0.2  $\mu\text{m}$ ) and COC<sub>1</sub>/DOC fractions consistently decreased from freshwater to seawater. The percentage of COC<sub>1</sub> in the bulk DOC pool was ~45% at the Mississippi River freshwater station and decreased to ~27% in open Gulf of Mexico waters. There was little variation in the percentages of COC<sub>1</sub> isolated between summer and winter [186]. Guo and Santschi [5] reported that the percentage of COC<sub>1</sub> in bulk DOC decreased from 66% in the Trinity River to 59–62% in estuarine waters of Galveston Bay (with salinities between 15 and 33). In the Sabine-Neches estuary, the COC<sub>1</sub>/DOC fraction changed from a range of 37–42% at the freshwater stations to 14–27% at salinities between 15 and 25 [17,187]. In Corpus Christi Bay, the COC<sub>1</sub>/DOC fraction ranged from 16 to 48% [17,187]. Powell *et al.* [65] reported for Ochlockonee estuarine waters with salinities from 0.03 to 28.5% that, on average, ~48% of the bulk DOC was in a colloidal fraction (1 kDa–0.4  $\mu\text{m}$ ), whereas the COC<sub>10</sub> (10 kDa–0.4  $\mu\text{m}$ ) fraction was ~23% of the bulk DOC. In the low (<1) salinity regions, COC<sub>10</sub> was up to 50% of the bulk DOC, with DOC concentrations as high as 1550  $\mu\text{mol dm}^{-3}$  [65].

Using a 3 kDa membrane, Argyrou *et al.* [188] reported only ~4–11% of bulk DOC in a colloidal fraction between 3 kDa and 0.2  $\mu\text{m}$  (COC<sub>3</sub>) in the Lake Pontchartrain estuary, with DOC concentrations of 425–700  $\mu\text{mol dm}^{-3}$ . Therefore, large quantities of the COC in Lake Pontchartrain estuary could be present in the medium MW (*e.g.* 1–3 kDa) colloidal fraction. Concentrations of the COC<sub>3</sub> decreased from the river to the mouth of the estuary [188]. In Kalix River and Bothnic Bay, Gustafsson *et al.* [109] found a COC<sub>3</sub>/DOC ratio that ranged from 15 to 54%.

In addition to membranes with 1 and 3 kDa MWCOs, the other commonly used membrane is a 10 kDa MWCO (Tables 2 and 4). Whitehouse *et al.* [181] reported 8–19% of COC<sub>10</sub> in an estuarine environment. Many other investigators have used the 10 kDa membrane for studying estuarine colloidal organic matter [4,5,62,63,65,68,189]. The HMW COC fraction (COC<sub>10</sub>, 10 kDa–0.2  $\mu\text{m}$ ) comprises about 10% of the bulk DOC depending on the estuarine environment (Table 4 and Figure 15). For example, the percentage

of COC<sub>10</sub> was 11% in the Trinity River, 6–8% in Galveston Bay waters, 10–16% in Chesapeake Bay waters [5] and up to 30–50% measured in lower salinity waters [4,65]. Other membranes such as 30 and 100 kDa have also been used to examine DOC molecular weight distributions [92,161,190,191], although using such membranes yields much lower COC values (Tables 2 and 4).

As discussed here, aquatic colloids are generally operationally defined. Different pore size membranes will result in different COC and LMW DOC values in the same water. Therefore, this also applied to the truly dissolved fraction, since both COC and LMW DOC fractions will change with sampling protocols.

**4.1.1.3 Coastal and Oceanic Waters.** Examples of the use of ultrafiltration to quantify COC concentrations and the MW distributions of DOC in seawater are summarised in Table 4 and Figure 16. Results from an ultrafiltration inter comparison study show that concentrations and percentages of COC can vary considerably for the same water when different types of membranes are used, or even worse when using the same type of membranes [60]. Nevertheless, more recent studies have produced some consistent spatial patterns of COC concentrations and MW distributions of DOC in seawater (Table 4 and Figures 17–19), although almost all colloidal data so far are apparent numbers since they were estimated from measurements of the retentate and permeate samples at low CFs.

The first attempts to quantify the concentrations of COC in seawater using ultrafiltration methods date back to the 1970s [51,52,190,192,193]. As summarised by Carlson *et al.* [56], most of the earlier studies suffered from contamination problems, yielding large potential uncertainties in the COC fractions, without consistent trends in molecular weight distributions of DOC between surface and deeper waters, or between nearshore and offshore waters [56]. In addition to the contamination problems, quantifying the COC fraction by concentration difference between the initial solution and the permeate (or retentate) may have further increased the variability in colloidal data. Since the permeation behaviour of macromolecular organic matter was not quantified, certain procedural artifacts were possible and could have resulted from sampling discrete rather than integrated permeate samples [11,60].

Attention to detail and quality assurance and control made examination of DOC molecular weight distributions in different marine environments possible, allowing more consistent measurements of the DOC molecular weight distributions in natural waters [2,3, 34,194]. Ogawa and Ogura [194] reported 4.5% of bulk DOC in the HMW COC fraction (>10 kDa), 29% in the 1–10 kDa COC fraction and 66% in the <1 kDa LMW DOC fraction in the Pacific Ocean. Comparably, Benner *et al.* [34] recovered 23–35% of the bulk DOC as the >1 kDa COC in the Pacific Ocean and Atlantic Ocean (Figure 16). In the Gulf of Mexico and the Middle Atlantic Bight, Guo *et al.* [3] reported that, on average, ~4% of the bulk DOC was in the >10 kDa COC fraction, ~9% in the 3–10 kDa COC fraction and ~23% in the 1–3 kDa COC fraction, leaving ~64% in the LMW fraction (<1 kDa) in Gulf of Mexico waters. Similarly, in seawater from the Middle Atlantic Bight, ~7% of the bulk DOC was in the >10 kDa COC fraction, ~14% in the 3–10 kDa COC fraction and ~25% in the 1–3 kDa fraction, leaving ~54% in the <1 kDa LMW fraction (Figure 16). From these results describing DOC molecular weight distribution, it is clear that the COC (>1 kDa) fraction usually comprises ~30–50% of the bulk DOC, with the variability dependent on location and depth in the water column. The majority of

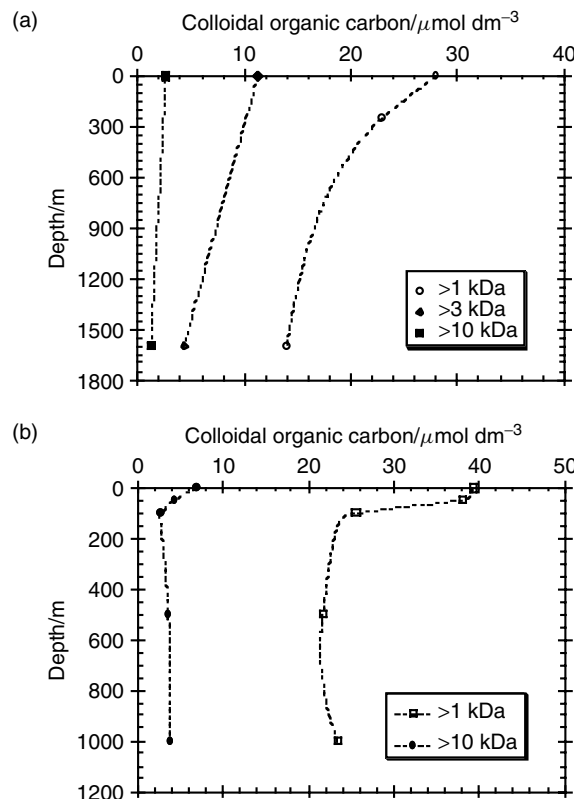


**Figure 18.** Vertical distributions of colloidal organic carbon (COC) concentrations in the Gulf of Mexico (a) and the Middle Atlantic Bight (b), showing a general decrease with increasing water depth. Reproduced with permission from the American Society of Limnology and Oceanography

the bulk DOC in oceanic environments is partitioned in the LMW fraction (Figure 16), whereas the opposite occurs in river waters (Figure 14). Possibilities exist, however, that the MW of fibrillar exopolymeric substances such as polysaccharides are not accurately assessed by ultrafiltration due to their specific molecular conformation [80,195].

Figure 17 shows that concentrations of COC, both 1 kDa–0.2  $\mu\text{m}$  and 10 kDa–0.2  $\mu\text{m}$ , decrease from nearshore to offshore waters, suggesting terrestrial inputs as important sources of COM to the ocean [3,34]. The vertical distribution of COC, on the other hand, shows both concentrations and percentages of COC decreasing from surface to deep waters (Figure 18) in the Pacific [34], in the Gulf of Mexico [2,3] and in the Middle Atlantic Bight [3]. Whereas the percentage of the HMW organic matter decreased from surface to bottom waters, the percentage of the LMW fraction (*e.g.* the <1 kDa fraction) increased from surface to deep waters [3,34]. The decrease in COC from river to sea and from surface to deeper water suggests the transport of HMW organic matter, a reactive component, from nearshore to offshore, with production in the upper water column and consumption during transport to deep waters [30].

#### 4.1.2 Elemental, Isotopic and Molecular Characterisation of Colloidal Organic Matter

Large ultrafiltration systems enable the extraction of sufficient quantities of COM samples from natural waters for elemental, isotopic and molecular characterisation. Recent reviews of advancements in the characterisation of DOM and COM are available for both freshwater and seawater systems [11,36,41,180,196,197]. Table 5 summarises recent results describing elemental (in terms of C/N ratio) and stable isotope composition of natural COM.

**Table 5.** Reported C/N ratios and stable isotope composition of colloidal organic mater (COM) in aquatic environments

Location	COM size	C/N ratio	$\delta^{13}\text{C}/\text{‰}$	$\delta^{15}\text{N}/\text{‰}$	Reference
Patuxent Estuary	5 kDa–0.4 $\mu\text{m}$	9–12	–24.8	8.5–10.8	[280,281]
Mississippi River plume	1 kDa–0.2 $\mu\text{m}$	15–23	–25.0 to –21.3	3 to 9	[186]
Pacific (near Hawaii)	1 kDa–0.2 $\mu\text{m}$	19	–22.7 $\pm$ 0.24	–	[144]
Vineyard Sound	1 kDa–0.2 $\mu\text{m}$	20	–23.9 $\pm$ 0.01	–	[144]
Pacific Ocean	1 kDa–0.2 $\mu\text{m}$	15–23	–21.63 $\pm$ 0.17	7.93 $\pm$ 0.69	[133]
Atlantic Ocean	1 kDa–0.2 $\mu\text{m}$	15–18	–22.0 $\pm$ 0.26	8.0 $\pm$ 1.2	[133]
Gulf of Mexico	1 kDa–0.2 $\mu\text{m}$	17–18	–21.3	9.85 $\pm$ 0.49	[133]
Loch Vale watershed	100 kDa–0.45 $\mu\text{m}$	8.5–11.3	–23.3 to –22.5	–	[42]
Amazon River	1 kDa–0.1 $\mu\text{m}$	27.5 $\pm$ 4.5	–27.74 $\pm$ 1.20	2.76 $\pm$ 0.95	[137]
Potomac River	1.2–400 nm	10–12	–25.98 $\pm$ 1.51	7.30 $\pm$ 0.30	[280]
Chesapeake Bay	1.2–400 nm	11–12	–24.08 $\pm$ 0.42	8.83 $\pm$ 0.19	[280]
San Francisco Bay	1.2–400 nm	–	–26.70 $\pm$ 0.72	7.92 $\pm$ 0.84	[280]
Chena River	1 kDa–0.45 $\mu\text{m}$	48 $\pm$ 0.9	–27.47 $\pm$ 0.06	1.6 $\pm$ 0.5	[89]
Chesapeake Bay	1 kDa–0.2 $\mu\text{m}$	20 $\pm$ 1	–24.85 $\pm$ 1.0	7.09 $\pm$ 0.65	[83]
Galveston Bay	1 kDa–0.2 $\mu\text{m}$	20.4 $\pm$ 1.8	–25.22 $\pm$ 0.86	8.14 $\pm$ 1.03	[83]
Gulf of Mexico	1 kDa–0.2 $\mu\text{m}$	16.6 $\pm$ 0.4	–21.67 $\pm$ 0.76	3.87 $\pm$ 0.65	[83]
Middle Atlantic Bight	1 kDa–0.2 $\mu\text{m}$	12.9 $\pm$ 2.4	–21.2 $\pm$ 0.15	5.49 $\pm$ 0.77	[83]
Yukon River	1 kDa–0.45 $\mu\text{m}$	45.8 $\pm$ 3.2	–27.44 $\pm$ 0.19	–0.66 $\pm$ 0.24	[97]
Boston Harbor	1 kDa–0.2 $\mu\text{m}$	14.8	–30.1 to –23.7	2.8 to 5.7	[95,96]
Delaware/ Chesapeake Bay	1 kDa–0.2 $\mu\text{m}$	12.9	–25.1 to –23.1	4.4 to 8.9	[95,96]
San Diego Bay	1 kDa–0.2 $\mu\text{m}$	10.7	–25.1 to –22.2	5.3 to 8.1	[95,96]
San Francisco Bay	1 kDa–0.2 $\mu\text{m}$	14.2	–26.1 to –23.1	5.1 to 6.4	[95,96]
Arctic Ocean	1 kDa–0.4 $\mu\text{m}$	17–19	–23.42 to –21.16	3.8 to 5.4	Guo <i>et al.</i> <sup>a</sup>

<sup>a</sup> Unpublished results.

Values of the C/N molar ratio are in the range 10–20 for COM from estuarine and marine environments and 23–50 in river water COM (Table 5.). For example, Guo and Macdonald [97] reported a high C/N ratio of  $46 \pm 3$  for Yukon River COM compared with  $27 \pm 5$  for the <1 kDa DOM and  $15 \pm 1$  for POM. High C/N ratios in river waters probably resulted from the high concentration of humic substances in river waters [8,91,120,198]. The relatively low C/N of marine COM shows consistency with its source and production pathways ([179] and references therein). The increase in COM C/N ratios from surface to bottom water in the ocean indicates that COM is being produced in the upper water column and undergoes modification through aggregation, degradation and diagenesis during transport from surface to deep waters [5,30,83].

The stable C and N isotope composition of COM clearly shows an increase for both  $\delta^{13}\text{C}$  and  $\delta^{15}\text{N}$  from terrestrial/freshwater to marine environments (Table 5). For example, values of COM  $\delta^{13}\text{C}$  range from  $-23$  to  $-27\text{\textperthousand}$  for river waters and from  $-23$  to  $-21\text{\textperthousand}$  for marine environments. For COM  $\delta^{15}\text{N}$ , values range from  $-0.6$  to  $3\text{\textperthousand}$  for river waters and from  $3$  to  $9\text{\textperthousand}$  for seawater. Overall, marine COM has a higher  $\delta^{15}\text{N}$  and  $\delta^{13}\text{C}$  than terrestrial COM; this characteristic can be used to identify DOM sources and biogeochemical cycles in aquatic environments. Recent studies have reported stable isotope composition at the compound specific and compound class level [49,95,96], allowing a better understanding of DOM cycling at the molecular level.

Earlier studies characterised isolated NOM from estuarine and coastal seawaters, finding carbohydrates (polysaccharides and sugars), proteins and lipids as the major organic components, although up to 60% of DOC still remains uncharacterised [51,54,193,199,200]. More recent characterisations of HMW organic material (>1 kDa), isolated from seawater using ultrafiltration followed by diafiltration indicates that polysaccharides could account for  $\sim 50\%$  of COM in marine environments [34,80,85,86,88].

In addition to the stable isotope composition, radiocarbon and  $^{234}\text{Th}$  have also been used as complementary tracers to examine the biogeochemical cycling of marine colloids [5,30,77,81] and organic carbon dynamics in terrestrial [89,97,118] and marine systems [80,86,88,201]. Fairly young HMW marine COM compared with its LMW counterparts points to a high turnover rate of colloids in the ocean, broadly consistent with the results derived from the  $^{234}\text{Th}/^{238}\text{U}$  disequilibrium method [28,31,33,77]. In waters affected by sediment resuspension, such as bottom nepheloid layers in the ocean or estuarine environments, HMW COM is, however, the oldest fraction [30,81]. Conversely, COM and DOM from Arctic rivers are predominantly young [97,118], indicating that old soil organic carbon stored in peatlands and permafrost regions is not remobilised in the form of DOM. Under current warming conditions in the north, the remobilisation of old soil organic carbon in Arctic terrestrial regions occurs through the transport of particulate phases [97,202]. Indeed, suspended POM in Arctic river waters is predominantly old [97,203] in contrast to the contemporary COM and DOM. Furthermore, very old organic carbon, up to 14000 yBP (years before present), has been determined in sediments from the vast Siberian Arctic coastline [202], supporting the export of terrestrial organic carbon to the Arctic Ocean under current climatic and environmental conditions.

A growing number of studies characterise organic molecular composition of isolated COM using HPLC, GC–MS, DT-MS and other analytical techniques [82,91,92,94,95,132,134,137,161,162,204–210]. Other molecular characterisation methods of COM includes

the use of  $^1\text{H}$  NMR [85,86,88,211],  $^{13}\text{C}$  NMR [34,93,120,207,212],  $^{15}\text{N}$  NMR [90,134], and  $^{31}\text{P}$  NMR [135,136,163]. These molecular level characterisations have considerably advanced our understanding of composition, reactivity and biogeochemical cycling of NOM in aquatic environments. A recent review on chemical composition and reactivity of marine DOM can be found in Benner [36].

Using pyrolysis–GC–MS, a semi-quantitative technique, the relative organic molecular composition shows significant differences between dissolved, colloidal and particulate organic phases in river waters, with COM containing the highest polysaccharide component (Figure 19). The high carbohydrate content and young  $^{14}\text{C}$  age of river COM suggest a high reactivity and fast turnover rate for COM compared with LMW and particulate organic phases [89,97]. In estuarine environments, variations of aromatic and carbohydrate components of COM, characterised by pyrolysis–GC–MS, show an increase of polysaccharide index and a decrease in aromatic index from river to nearshore to offshore stations in the Mississippi River plume (Figure 20).

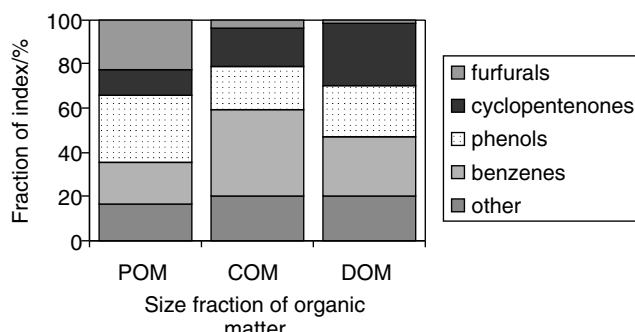


**Figure 19.** Distributions of index compounds between particulate (POM), colloidal (COM) and LMW-dissolved organic matter (LMW-DOM, <1 kDa) from Chena River waters. Figure created with data from Guo, L. D., Lehner, J. K., White, D. M. and Garland, D. S. Heterogeneity of natural organic matter from the Chena River, Alaska, *Water Research*, **37**, 1015–1022, Copyright 2003, with permission from Elsevier

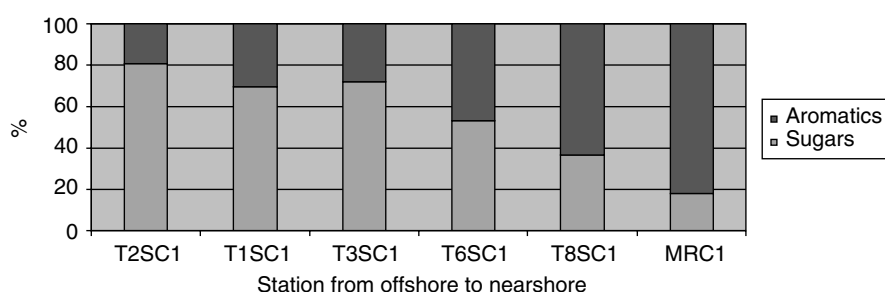


**Figure 20.** Variations of aromatics and carbohydrates in colloidal organic matter, characterised by pyrolysis–GC–MS, from offshore station to nearshore station in Mississippi River plume (Guo *et al.*, unpublished results)

## 4.2 COLLOIDAL TRACE METALS

Table 6 gives a compilation of the percentages of dissolved metals found in colloidal form in natural waters. The application of ultrafiltration methods has allowed for more detailed studies on phase speciation of trace metals in natural waters. Published results show that most trace metals, including Ag, Al, Cu, Cd, Co, Cr, Fe, Hg, Mn, Ni, Pb and Zn, are to some extent associated with colloids, regardless of the membrane's cut-offs (Table 6). Although the actual colloidal percentage may be different, these results probably have much broader significance.

Among those metals measured, Fe and Hg show the highest colloidal fractions in natural waters, although published data vary considerably. For example, colloidal Fe could account for up to 70–100% of 'dissolved' Fe in both freshwater and seawater, regardless of the MWCOs of membranes used (Table 6). Considerable fractions of dissolved Hg were also found to be associated with COM. Other trace metals that complex with COM to different extents include Al, Ag, Pb, Cu, Zn, Co, Cr, Ni and Cd (Table 6). Despite a high variability in the colloidal fraction, the partitioning of trace metals between LMW dissolved and colloidal phases measured for natural waters seems to agree well with results from laboratory experiments. For example, metal partitioning experiments using radioactive metals consistently show high colloidal fractions of Fe and Hg, intermediate colloidal fractions of Ag, Zn and Cr and relatively low colloidal fraction for Cd and Co [17,22–24,148,213,214].

It is interesting that some investigations of river water colloids noted a bimodal size distribution of organic carbon fractions and associated metals. For example, iron-enriched colloids are larger (>10 kDa) and contain most of the Ag, Pb, Al, Ga, V, Cr, W, Ti, Ge, Zr, Th, U and REEs, while iron-poor colloids are smaller (1–10 kDa) and are enriched with most of the transition metals, *e.g.* Cu, Cd, Ni, Zn and Co [48,50,68,215]. These observations were also confirmed for stream colloids by Lyven *et al.* [126], who used field-flow fractionation techniques coupled with ICP-MS to separate and identify the two types of colloids.

Thermodynamically, the solubility of iron is extremely low in oxygenated organic-free seawater due to hydrolysis [9,216]. If only inorganic Fe species are considered, an extremely small fraction of the total Fe concentration is expected to be truly dissolved [*e.g.* the  $K_{sp}$  value for  $\text{Fe(OH)}_3$  is  $4 \times 10^{-38}$ ]. It has been proposed that the presence of biologically produced LMW siderophores (<1 kDa), one of the strongest known Fe-binding ligands, greatly increases the solubility of Fe in seawater [217–219]. However, the chemical nature and molecular composition of these Fe-binding organic ligands in seawater remain largely unknown [220,221]. In some cases, almost all dissolved Fe was found in the HMW fraction in estuarine and oceanic waters [25,62,65,67–71,109,139]. The high percentage of dissolved Fe found in HMW or COM seems contradictory to the fact that LMW siderophores are among the strongest Fe-binding ligands in natural waters. In addition, it is unclear whether Fe complexes with macromolecules or exists as organically coated iron oxyhydroxides. Interestingly, dissolved Fe concentrations correlate significantly with DOC concentrations in seawater when a radioactive  $^{59}\text{Fe}$  tracer is used [148], as has also been shown for freshwater systems [222]. Whether dissolved Fe is mostly complexed with LMW organic ligands such as siderophores or HMW organic ligands (or colloids) in seawater remains to be further studied.

**Table 6.** Recent studies reporting colloidal trace metals in aquatic environments

Water type	Metal	Prefilter/ $\mu\text{m}$	MWCO/kDa	Colloidal/%	Reference
Medway River	Al	1	10	66	[58]
	Fe			73	
	Mn			45	
	Cu			64	
Ob/Yenisey Estuaries/shelf	Fe	0.4	10	30–97	[63]
	Ni			50–60	
	Cu			17–65	
	Cd			1–76	
	Pb			22–52	
Rhone Delta	Cd	0.4	10	0–38	[4]
	Cu			20–39	
	Ni			0–18	
	Cd	0.4	10	1.2–63	[62]
Venice Lagoon (Italy)	Cu			21–59	
	Fe			67–99	
	Ni			1.1–34	
	Pb			3.1–94	
	Mn			24–76	
Amazon River/shelf	U	0.2	10	15–92	[234]
	Hg	0.4	1	37–88	[64]
Ochlockonee Estuary			10	30–40	
	Fe	0.4	1	71–97	[65]
	Mn			1–30	
	Ni			5–78	
	Cu			15–66	
	Cd			5–66	
	Fe	0.4	10	14–86	[65]
	Mn			0–30	
	Ni			4–45	
	Cu			1–15	
San Francisco Bay	Cd			5–48	
	Al	0.2	10	3–99	[66]
	Ag			0–93	
	Cd			0–9	
	Cu			1–18	
	Fe			4–88	
	Mn			2–20	
	Ni			0–2	
	Sr			0	
Estuarine waters	Zn			1–3	
	Hg	0.4	1	47 ± 20	[17]
	Ag	0.4	1	25–85	[18]
			10	20–60	
Danube Estuary	Fe	0.2	10	0–88	[282]
	Mn			3–70	
	Cu			10–45	
	Cd			0–43	
	Cu	0.4	3	39–73	[283]
Clyde Estuary	Cd			0–31	

(continued overleaf)

**Table 6** (*continued*)

Water type	Metal	Prefilter/ $\mu\text{m}$	MWCO/kDa	Colloidal/%	Reference
Narragansett Bay	Pb	0.2	1	0–85	[70,71]
	Fe			93–99	
	Mn			1–5	
	Cu			35–53	
	Ni			19–40	
	Pb			35–41	
	Cd			3–37	
New Jersey Stream	Zn	0.45	10	2–14	[69]
	Al			65	
	Fe			82	
	Mn			29	
	Cu			66	
	Zn			31	
	Cd			46	
Galveston Bay	Pb	0.4	1	88	[68]
	Cu			48–66	
	Ni			12–47	
	Pb			52–88	
	Cd			23–61	
	Co			6–31	
	Zn			82–97	
Galveston Bay	Fe	0.4	10	49–99	[68]
	Cu			1–23	
	Ni			12–26	
	Pb			2–57	
	Cd			9–41	
	Co			4–16	
	Zn			14–73	
Freshwater	Hg	0.4	10	38–98	[256]
	MeHg			8–70	
Bothnic Bay spiked seawater	Fe	0.2	3	46–88	[109]
	<sup>51</sup> Cr			84–96	
	<sup>65</sup> Zn			60	
	<sup>109</sup> Cd			63–64	
	Fe			6–10	
	Al			30–100	
	Mn			15–100	
Rivers in northern Britain	Cu	0.1	1	10–50	[174]
	Zn			20–60	
	Pb			5–50	
	Ni			30–90	
	Fe			3–60	
	Al			30–100	
	Mn			15–100	
Pacific Ocean Spiked seawater	Cu	0.2	200	10–50	[272]
	Zn			13–52	
	<sup>51</sup> Cr			13–32	
	<sup>65</sup> Zn			14–30	
	<sup>75</sup> Se			13–28	
	<sup>109</sup> Cd			5–10	
	Fe			42 ± 1	
Spiked seawater	<sup>57</sup> Co	0.2	1	99 ± 5	[23]
	<sup>59</sup> Fe			42 ± 1	

**Table 6** (*continued*)

Water type	Metal	Prefilter/ $\mu\text{m}$	MWCO/kDa	Colloidal/%	Reference
Ground water	$^{65}\text{Zn}$			$40 \pm 3$	
	$^{110m}\text{Ag}$			$75 \pm 6$	
	$^{109}\text{Cd}$			$33 \pm 3$	
	$^{203}\text{Hg}$			$94 \pm 2$	
	Cu	0.45	1	70	[261]
	Al			70	
	Mn			30	
	Cd			42	
Spiked seawater	Ag			100	
	$^{59}\text{Fe}$	0.2	1	94	[24,148]
Estuarine water	Hg	0.45	1	38–57	[74]
Estuarine water	Me-Hg	0.45	1	34–56	[75]
Mississippi River <sup>a</sup>	Ce	0.4	0.02 $\mu\text{m}$	74	[141]
	Cr			9	
	Fe			50	
	Mn			52	
	Pb			21	
Pacific Ocean	Fe	0.4	1	60–100	[25]

<sup>a</sup> Colloidal percentages in the 0.02–0.45  $\mu\text{m}$  range were calculated from concentration differences for those elements with positive colloidal numbers.

While significant amounts of trace metals can be found in the colloidal fraction, the fact that inorganic ion concentrations are usually low in this fraction allows one to conclude that it is the macromolecular organic matter that is the main carrier phase for trace metals. For example, a strong linear relationship between COC and colloidal Hg was found in Galveston Bay [17] and between COC and colloidal  $^{234}\text{Th}$  in marine environments [31]. Significant relationships between colloidal metals (*e.g.* Ag, Hg, Ni, Cu, Zn and Co) and COM were also observed in estuarine waters [17,68,215]. Powell *et al.* [65] reported a linear correlation between Ni and Cu with carbon in the medium MW colloidal fraction in the Ochlockonee estuary in the Gulf of Mexico. Town and Filella [41] showed similar relationships between colloidal metals and COC concentrations in a review paper. The correlation between  $[\text{Me}]_{\text{c}}/[\text{Me}]_{\text{d}}$  (ratio of metal concentration in colloidal to that in dissolved phase) and COC/DOC suggests a relatively even distribution of organic ligand groups over the size (or molecular weight) spectrum, as evidenced from the data shown for Hg, Ag, Cu and Th [17,18,31,215]. Plots of the colloidal fraction of metals ( $[\text{Me}]_{\text{c}}/[\text{Me}]_{\text{c+d}}$ ) agree, within the scatter of the measurements, with plots of the colloidal fraction of DOC (*i.e.* COC/DOC).

Studies on the size fractionation of metals allow for the calculations of distribution coefficients between particles and the dissolved phase ( $K_{\text{d}}$ ), particles and the LMW dissolved phase ( $K_{\text{p}}$ ) and colloids and the LMW dissolved phase ( $K_{\text{c}}$ ) in different estuarine environments. The values of the logarithms of  $K_{\text{d}}$ ,  $K_{\text{p}}$  and  $K_{\text{c}}$  of trace metals such as Ag, Hg, Ni, Cu, Zn and Co in estuaries and coastal waters, ranging from 4.4 to 7.8, are very similar for a given element [67,68,74]. The similarity between values of  $K_{\text{d}}$ ,  $K_{\text{p}}$  and  $K_{\text{c}}$  suggest that the complexing strength of particles and colloids is similar for trace elements. This result is surprising, considering specific surface areas or site concentrations increase

with decreasing size of the particles or colloids. It therefore appears that the density of strong and specific metal-complexing ligands decreases with decreasing colloidal or particle size [31,164], or coagulation of amphiphilic ligands disproportionately affects the distribution of surface-active substances [167]. In addition, specific complexing sites for metals may change as a function of the molecular composition [165,169]. To understand this fully, more basic studies of the molecular and functional group composition of COM are needed [223].

#### 4.3 RADIONUCLIDES

##### 4.3.1 Colloidal Thorium

The naturally occurring thorium isotopes, especially  $^{234}\text{Th}$ , have been used as powerful tracers for studying particle dynamics and trace element scavenging in seawater because of their strong chemical reactivity to particle surfaces and suitable decay time-scale (*e.g.* half-life of 24.1 days for  $^{234}\text{Th}$ ) [26,224–226]. Marine colloids are primarily organic in nature and have different surface sites with a high affinity for hydrolytic trace elements such as Th(IV) [77,164–168]. Th isotopes of different half-lives (*e.g.* 24 days for  $^{234}\text{Th}$ , 1.9 years for  $^{228}\text{Th}$ ,  $7.5 \times 10^4$  years for  $^{230}\text{Th}$ , and  $1.4 \times 10^{10}$  years for  $^{232}\text{Th}$ ) may be used as natural tracers for the cycling of a large fraction of DOM in marine environments [28,31,33,149,227–230]. Therefore, the partitioning of Th between dissolved and colloidal phases has received increased attention in the past decade (Table 7).

Baskaran *et al.* [28] and Moran and Buesseler [33] conducted the first studies to measure colloidal Th(IV) isotopes and to estimate the residence times of a fraction of HMW

**Table 7.** Reported colloidal thorium ( $^{234}\text{Th}$ ,  $^{228}\text{Th}$ ,  $^{230}\text{Th}$  and  $^{232}\text{Th}$ ) in seawater and estimated residence time of marine colloids

Location	Isotope	MWCO/ kDa	Dissolved concentration (dpm kg $^{-1}$ )	Colloidal/%	Residence time/days <sup>a</sup>	Reference
Atlantic	$^{234}\text{Th}$	>10	1.62	11	10	[33]
Gulf of Mexico	$^{234}\text{Th}$	10	0.36–1.98	10–78	4–26	[28]
Gulf of Main	$^{234}\text{Th}$	10	1.5–2.3	0.04–1	NA	[271]
Pacific	$^{234}\text{Th}$	10	1–2	13	6	[228,229]
Bedford Basin	$^{234}\text{Th}$	10	0.1–0.54	6–75	NA	[189]
Gulf of Mexico	$^{234}\text{Th}$	10	0.5–1.9	3–9	1–20	[77]
Atlantic	$^{234}\text{Th}$	10	0.5–2.12	7–17	1–14	[31]
Gulf of Mexico	$^{234}\text{Th}$	1	0.5–2.0	54 ± 9	7–65	[31]
Middle Atlantic Bight	$^{234}\text{Th}$	1	0.5–2.12	47 ± 12	5–53	[31]
Atlantic off Bermuda	$^{234}\text{Th}$	1	1.4–2.5	4–16	–	[153]
Gulf of Maine	$^{234}\text{Th}$	1	1.29–1.52	7–36	14–41	[230]
Arctic Ocean	$^{234}\text{Th}$	10	0.13–2.81	3–26 (12.4 ± 7.9)	1–68	[227]
Gulf of Mexico	$^{232}\text{Th}$	10	$25–50 \times 10^{-6}$	60 ± 7	–	[28]
Jiulong River Estuary	$^{228}\text{Th}$	10	0.03–0.18	16	–	[233]
Jiulong River Estuary	$^{230}\text{Th}$	10	0.003–0.042	17	–	[233]
Jiulong River Estuary	$^{232}\text{Th}$	10	0.005–0.016	11	–	[233]

<sup>a</sup> Not applicable.

organic matter in seawater with respect to coagulation. Baskaran *et al.* [28] determined colloidal (10 kDa–0.4  $\mu\text{m}$ )  $^{234}\text{Th}$  in seawater from the Gulf of Mexico. Moran and Bues-seler [33] evaluated colloidal (10 kDa–0.2  $\mu\text{m}$ )  $^{234}\text{Th}$  in seawater near Bermuda. These and subsequent studies (Table 7) contributed significantly to our knowledge of the interaction of Th isotopes with DOM in seawater.

The results in Table 7 show a large range of the HMW colloidal  $^{234}\text{Th}$  fraction ( $>10$  kDa) as a percentage of the total dissolved  $^{234}\text{Th}$ . However, colloidal residence times derived from  $^{234}\text{Th}/^{238}\text{U}$  disequilibrium are consistently short for both colloidal fractions ( $>10$  and  $>1$  kDa) [28,31,33,77]. Short residence times indicate that the HMW COM turns over in the ocean on a much shorter time-scale than the bulk DOC, which has an apparent  $^{14}\text{C}$  age of 3000–6000 years [231,232].

Santschi *et al.* [77] and Guo *et al.* [31] have argued that turnover times of COM derived from  $^{234}\text{Th}$  using the current thorium scavenging models [28,33] are lower than those derived from radiocarbon, and therefore might give different values for colloid residence times in the ocean. A colloidal residence time of 1 day for HMW COM ( $>10$  kDa), as has often been calculated for the Middle Atlantic Bight, the Gulf of Mexico and the Gulf of Maine, is compatible with that calculated from the colloidal pumping model in the serial formulation of Honeyman and Santschi [26]. Although  $^{234}\text{Th}$  is probably an appropriate tracer for the coagulation dynamics of particles and HMW COM (the  $>10$  kDa fraction) in the upper water column, it may not be as good a tracer for the dissolved and LMW colloidal fractions (e.g. 1–10 kDa) if this fraction were to turn over on time-scales of  $\geq 10$  years. As an extreme example, the  $^{234}\text{Th}$ -derived residence time will be  $\leq 10$  years if  $^{234}\text{Th}/^{238}\text{U}$  is 0.99 in the LMW fraction. However, 10 years is still a contemporary age for  $^{14}\text{C}$  (i.e. younger than  $\sim 50$  years since the beginning of atomic bomb tests). Clearly, both  $^{234}\text{Th}$  and  $^{14}\text{C}$  possess limitations as tracers for those organic carbon fractions, which may turn over on decadal time-scales. Probably, these isotopes trace different processes, with  $^{234}\text{Th}$  tracing coagulation time-scales and  $^{14}\text{C}$  tracing long-term carbon turnover times.

Many consistent colloidal  $^{234}\text{Th}$  data emerged from studies with rigorous controls on mass balance and membrane integrity. For example, Santschi *et al.* [77] reported that 3–9% of the total dissolved  $^{234}\text{Th}$  occurred in the  $>10$  kDa colloidal fraction and Huh and Prahl [228] reported a mean percentage colloidal fraction ( $>10$  kDa) of  $^{234}\text{Th}$  of  $\sim 13\%$  in the NE Pacific. Guo *et al.* [31] also reported that 4–11% of  $^{234}\text{Th}$  was colloidal ( $>10$  kDa) in the Gulf of Mexico and 7–17% in the Middle Atlantic Bight. Hence around 10% of conventional dissolved  $^{234}\text{Th}$  is in the colloidal size range 10 kDa–0.2 or 0.4  $\mu\text{m}$ , which is similar to that of COM in the bulk DOC in seawater of  $\sim 10\%$  [2,3,30,77].

Very few of the Th isotopic studies have examined the degree to which Th complexes with the LMW fraction ( $<1$  kDa) or in the 1–10 kDa colloidal fraction. Indeed,  $^{234}\text{Th}$  in the 1 kDa–0.2  $\mu\text{m}$  fraction generally shows significantly higher values than that in the 10 kDa–0.2  $\mu\text{m}$  fraction. For example, the  $>1$  kDa colloidal  $^{234}\text{Th}$  was  $54 \pm 9\%$  in the Gulf of Mexico vs 3–9% for the  $>10$  kDa fraction, and the  $>1$  kDa colloidal  $^{234}\text{Th}$  was  $47 \pm 12\%$  for the  $>1$  kDa vs 7–17% for the  $>10$  kDa fraction in the Middle Atlantic Bight [31]. More variable colloidal  $^{234}\text{Th}$  fractions were recorded in the Gulf of Maine, with 7–36% for the 1 kDa  $^{234}\text{Th}$  fraction and 0.04–1% for the  $>10$  kDa fraction (Table 7). A typical size distribution of  $^{234}\text{Th}$  in marine environments is shown in Figure 21.

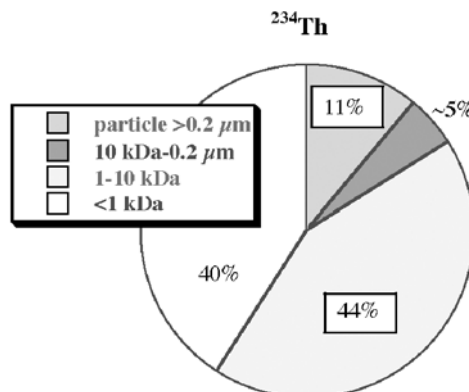


**Figure 21.** An example of  $^{234}\text{Th}$  partitioning between dissolved, colloidal and particulate phases. Reprinted from Guo, L. D., Santschi, P. H. and Baskaran, M. Interaction of thorium isotopes with colloidal organic matter in oceanic environments, *Colloids and Surfaces A*, **120**, 255–272, Copyright 1997, with permission from Elsevier

Most studies of colloid associated Th(IV) have focused on  $^{234}\text{Th}$ . Very few colloidal data are available for other Th isotopes, such as  $^{228}\text{Th}$ ,  $^{230}\text{Th}$  and  $^{232}\text{Th}$ . Baskaran *et al.* [28] reported a few colloidal  $^{232}\text{Th}$  data in the Gulf of Mexico. Zhang *et al.* [233] reported measurements on colloidal  $^{228}\text{Th}$ ,  $^{230}\text{Th}$  and  $^{232}\text{Th}$  in Jiulong River estuarine waters. They found colloidal  $^{228}\text{Th}$ ,  $^{230}\text{Th}$  and  $^{232}\text{Th}$  in the 10 kDa–0.45  $\mu\text{m}$  fraction ranging from 11 to 17% of the dissolved  $^{228}\text{Th}$ ,  $^{230}\text{Th}$  and  $^{232}\text{Th}$ , similar to values reported for  $^{234}\text{Th}$  and listed in Table 7.

#### 4.3.2 Colloidal Uranium

The application of ultrafiltration has led to many recent investigations of colloidal uranium in natural waters, as summarised in Table 8. Using a 10 kDa ultrafiltration membrane, Swarzenski *et al.* [234] first measured colloidal U in the Amazon River and its shelf waters. They found a high percentage of colloidal U in the freshwater end-member of the Amazon River (up to 90% in the >10 kDa fraction) and a decreasing fraction of colloidal U with increasing salinity in the shelf area, with 14% colloidal U in the seawater end-member [234]. However, the percentage of colloidal U in the Jiulong River estuary was only <2%, using a similar 10 kDa ultrafiltration membrane [149]. Using a lower MW cutoff membrane (1 kDa), the colloidal U (>1 kDa) in Trinity River waters was ~38% (Guo *et al.*, unpublished results). Andersson *et al.* [235] also reported colloidal U in the >3 kDa fraction in the Kalix River estuary (see also Table 7).

Using 10 and 100 kDa membranes, Harnish *et al.* [236] reported very low colloidal U (a few percent of total U activity) in surface and ground waters at the Rocky Flats Environmental Technology Site in Colorado. It seems that the partitioning of U in the colloidal fraction is highly variable and may depend on specific water chemistry parameters and concentration and composition of organic matter, and also anion rejection characteristics of ultrafiltration membranes. So far, almost all colloidal U results were calculated by concentration difference between initial solution and permeate or retentate. Therefore,

**Table 8.** Reported colloidal uranium in natural waters

Location	Salinity	Size fraction	U concentration/ ( $\mu\text{g dm}^{-3}$ )	Colloidal U/%	Reference
Amazon River	0.31	10 kDa–0.45 $\mu\text{m}$	0.12	83	[234]
Amazon River plume	9.74	10 kDa–0.45 $\mu\text{m}$	0.44	34	[234]
Amazon Shelf	35.44	10 kDa–0.45 $\mu\text{m}$	3.28	14	[234]
Surface and ground waters	–	10 kDa–5 $\mu\text{m}$	1.33 pCi $\text{dm}^{-3}$	<3	[236]
Kalix River	–	10 kDa–0.45 $\mu\text{m}$	0.11–0.18	20–90	[265]
Lake Pavin	–	>1 kDa	0.0405	78	[255]
Lake Pavin	–	>10 kDa	0.0405	18	[255]
Jiulong River estuary	29.6	10 kDa–0.22 $\mu\text{m}$	3.047	<2	[149]
Kalix River estuary <sup>a</sup>	~3	3 kDa–0.2 $\mu\text{m}$	0.327	4–6	[235]
Kalix River estuary	~2	3 kDa–0.2 $\mu\text{m}$	0.236	19–41	[235]
Kalix River estuary	0.8–1.4	3 kDa–0.2 $\mu\text{m}$	0.158	33–88	[235]
Ground water	–	10 kDa–0.45 $\mu\text{m}$	$(1–12) \times 10^{-3}$ dpm $\text{kg}^{-1}$	47–94	[260]
Trinity River/ Galveston Bay	<0.2	1 kDa–0.2 $\mu\text{m}$	0.74	38	Guo <i>et al.</i> unpubl. results

<sup>a</sup> Low numbers of colloidal U in the Kalix River estuary are the direct measurements from retentate and the high numbers are from concentration difference between initial solution and permeate (<3 kDa).

these values are probably overestimated due to the retention of LMW uranium. From the limited colloidal U data resulting from studies using different ultrafiltration membranes, conjecture of generalised conclusions regarding colloidal U in natural waters becomes difficult. Further studies are required.

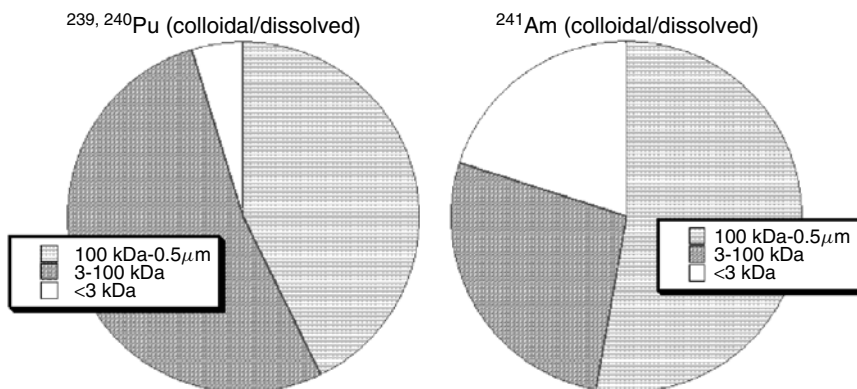
#### 4.3.3 Colloidal Plutonium and Americium

Aquatic colloids possess the potential to facilitate the transport of sparingly soluble contaminants in surface waters and ground waters [99,237]. A significant example is the colloidal actinides, such as plutonium and americium, in areas of nuclear waste disposal [7,40,236,238] and/or contamination [101].

Recent results on colloidal  $^{239,240}\text{Pu}$ ,  $^{241}\text{Am}$  and other radionuclides are summarised in Table 9. Figure 22 shows examples of size distributions of Pu and Am in surface waters. Colloidal  $^{239,240}\text{Pu}$  and  $^{241}\text{Am}$  concentrations display high variability, not only changing with different aquatic environments, but also differing considerably within the same aquatic system. Using ultrafiltration membranes with 10 and 100 kDa MWCO, Harnish *et al.* [236] examined the partitioning of Pu and Am in both surface and ground water samples at Rocky Flats. They reported a colloidal fraction of 40% for  $^{239,240}\text{Pu}$  and 47% for  $^{241}\text{Am}$ . In some cases, however, this colloidal fraction occurred mostly in the 0.45–5  $\mu\text{m}$  fraction of the surface water [236]. Kersting *et al.* [40] reported a colloidal  $^{239,240}\text{Pu}$  of up to 80% based on colloidal size between 0.007 and 1  $\mu\text{m}$ . Dai *et al.* [238]

**Table 9.** Compilation of colloidal radionuclides (Pu, Am and others) in natural waters

Location/water type	Colloidal size	Nuclide	Colloidal/%	Reference
Ground water	>100 kDa	Rb <sup>137</sup> Cs	28 >11	[259]
Lake	>100 kDa	<sup>239,240</sup> Pu <sup>241</sup> Am	>50 >50	[252]
Ground water	10 kDa–0.45 μm	<sup>239,240</sup> Pu <sup>241</sup> Am	0–40 —	[236]
Ground water	0.007–1 μm	<sup>239,240</sup> Pu <sup>137</sup> Cs	~80	[40]
Seawater	1 kDa–1 μm	<sup>239</sup> Pu <sup>240</sup> Pu <sup>241</sup> Pu	1–8	[238]
Gulf of Maine				
Pond sediments	<2 μm	<sup>239,240</sup> Pu	~25	[284]
Freshwater sediments	1 kDa–0.2 μm	<sup>239</sup> Pu <sup>240</sup> Pu	<4	[100]
Surface (stream) waters	3 kDa–0.5 μm	<sup>239,240</sup> Pu <sup>241</sup> Am	>80	[7]
Sahan River near Chernobyl	1 kDa–0.2 μm	<sup>239,240</sup> Pu <sup>241</sup> Am <sup>90</sup> Sr	49–83 76 12–15	[101]

**Figure 22.** Size distributions of <sup>239,240</sup>Pu and <sup>241</sup>Am in surface water (Santschi *et al.*, unpublished data)

measured colloidal <sup>239</sup>Pu and <sup>240</sup>Pu in the Gulf of Maine, with a <sup>240</sup>Pu/<sup>239</sup>Pu atomic ratio of 0.18. They reported 1–8% of dissolved Pu in the colloidal size range between 1 kDa and 1 μm, with higher colloidal fractions in surface seawater and lower ones in deep waters. Similarly, Dai *et al.* [100] also reported low colloidal Pu (<4%) in acidic sandy freshwater sediments, and their results suggested a refractory nature for the colloidal materials in the sediments. Using a 3 kDa membrane, Santschi *et al.* [7] measured colloidal <sup>239,240</sup>Pu and <sup>241</sup>Am in surface waters at Rocky Flats. They reported the partitioning of a large fraction

of the  $^{239,240}\text{Pu}$  and  $^{241}\text{Am}$  in the particulate phase ( $> 0.45 \mu\text{m}$ ), with 80–90% of the filter-passing fraction in the colloidal fraction depending on sampling time and locations (Figure 22), mostly bound to a 10 kDa macromolecule with an isoelectric point of about 3. They further carried out soil resuspension laboratory experiments to mimic storm and erosion events, confirming that up to 80% of filter-passing Pu existed in the colloidal fraction [7]. Matsunaga *et al.* [101] reported 49–83% of colloidal  $^{239,240}\text{Pu}$  and 76% of  $^{241}\text{Am}$  in the 10 kDa–0.2  $\mu\text{m}$  fraction. In contrast,  $^{90}\text{Sr}$  was found mostly in the LMW ( $< 1 \text{ kDa}$ ) dissolved phase in Sahan River water at the highly contaminated area close to the Chernobyl nuclear power plant [101].

Overall, association of radionuclides with the colloidal phase may considerably enhance the remobilisation of nuclides in surface and ground water environments. Further studies are needed for pollutant identification, remediation and management.

#### 4.4 PERSISTENT ORGANIC POLLUTANTS

Persistent organic pollutants (POPs) are a group of toxic chemicals that are slow to degrade and tend to bioaccumulate in the aquatic environment. The fate, transport and toxicological impact of organic contaminants, such as polycyclic aromatic hydrocarbon (PAHs), polychlorinated biphenyls (PCBs) and polychlorinated naphthalenes have received increased attention owing to their potential impacts on large regions of, if not the whole of, the planet [239–245]. Although the literature on interactions between POPs and NOM is vast, little quantitative work on colloidal POPs associated with colloidal macromolecular organic matter has been carried out. The main reason is that the majority of that work was carried out by extraction on non-ionic resins such as XAD. Therefore, only a brief discussion is given here.

The fate of organic pollutants in aquatic environments depends largely on their partitioning behaviour to colloids and particles. Dynamic colloid–water partitioning can significantly influence the speciation, and therefore the transport and bioavailability of hydrophobic organic contaminants (HOCs) [10,55,200,243,246–249].

Natural organic matter in aquatic systems is amphiphilic. Trace organics can sorb on NOM through van der Waals and hydrophobic interactions on hydrophobic parts and electrostatic interactions on more hydrophilic parts. The sorption of HOCs in aquatic systems can usually be characterised based on the partition coefficient between organic carbon (OC) or black carbon (BC) and water ( $K_{\text{OC}}$  or  $K_{\text{BC}}$ ), which are related to the octanol–water partition coefficient ( $K_{\text{ow}}$ ) of the organic contaminant and also the OC and BC concentrations [250]. Means and Wijayaratne [200] found that colloidal material has considerably higher sorptive capacity for herbicides compared with mineral particles in sediments or soil organic matter. Wijayaratne and Means [239] showed that the regression of aqueous solubilities for several PAHs versus colloidal organic matter  $K_{\text{DOC}}$  values yielded results parallel to those obtained for sediment. In the Mississippi River, significant portions of the atrazine and other herbicides were found in association with colloidal phases [251]. Interestingly, Gustafsson *et al.* [248] found a good correlation between  $K_{\text{COC}}$  and COM concentration in a coastal environment. This suggests that COM concentration and properties, i.e. the quality aspect of the macromolecules, are important in quantifying and predicting HOC phase partitioning in natural waters.

## 5 SUMMARY AND FUTURE RESEARCH

Colloids, including macromolecules and nanoparticles, are operationally defined entities sized between 1 and 1000 nm in diameter in the aquatic environment. Aquatic colloids have long been recognised as an important intermediary in the removal of trace elements from surface waters, or as a agent facilitating the transport of strongly sorbed contaminants. Colloidal processes also affect organic carbon cycling and thus the availability of trace elements to microorganisms. Therefore, sources, morphology, chemical composition and environmental behaviours of aquatic colloids are the subject of active investigations. Recent applications of ultrafiltration methods to the sampling of aquatic colloids have advanced our understanding of the abundance, distribution, physical conformation, chemical composition and environmental behaviours of colloids in aquatic systems, including river water, lake water, estuarine and coastal seawater and ground waters. Despite recent advances, fast and unbiased sampling of aquatic colloids remains a challenge that is limiting our understanding of the role of colloids in biogeochemistry and environmental sciences.

One of the most common colloidal sampling techniques is cross-flow ultrafiltration, ideally for isolating sufficient quantities of environmental colloids for biological, chemical, isotopic and molecular characterisation and for experimentation. Results of both laboratory experiments and field studies have also advanced our understanding of the permeation and retention behaviours of chemical species, including organic molecules, trace metals, radionuclides, nutrients and major ions, which in turn improve our interpretation of size fractionation data when ultrafiltration is used. Optimum operational conditions for ultrafiltration may continue to be an issue of debate. Although NOM is too complex to be represented by a single model macromolecule, many recent laboratory studies have documented the retention of LMW species, discounting the apparent breakthrough of HMW materials during ultrafiltration except possibly for fibrillar molecules. Strict calibration of ultrafiltration membranes before sampling remains important for understanding the performance of ultrafiltration systems, even though calibration results are largely dependent on a specific molecule. Regardless of research purposes, consistent concentration factors, cross-flow ratios and other operational conditions should be used for colloidal data comparisons since both colloidal size and ultrafiltration (retention and permeation) fractions are highly operational.

Ultrafiltration enables large quantities of environmental colloidal materials, which are to a large extent NOM, to be isolated from both freshwater and seawater for elemental, isotopic and molecular characterisation. As summarised in this chapter, reported data on colloidal fractions of trace species can be highly variable. Although differences in sampling locations, times and membranes used can explain part of the variability of colloidal data, many data sets are beyond acceptable natural variability. Therefore, aspects of quality control discussed here and in other chapters are essential to an improved understanding of the role of colloids in the aquatic environment. Despite the operational difficulties, ultrafiltration methods, especially cross-flow ultrafiltration, will continue to be one of the most effective ways of sampling aquatic colloids from large volumes of waters, especially for isolating sufficient amounts of freeze-dried and powdered colloidal samples. However, quantifying the LMW and colloidal fractions should be carried out through time-series permeate samples and the ultrafiltration permeation model.

## ACKNOWLEDGEMENTS

The writing of this work was supported, in part, by NSF and DOE grants (OCE-0627820 and EAR-0554781 to L.G. and OCE-0351559, DE-FG04ER63899 and NIRT-0210865 to P.H.S.), the International Arctic Research Center/University of Alaska Fairbanks and the Texas Institute of Oceanography.

## LIST OF SYMBOLS AND ABBREVIATIONS

amu	Atomic mass unit
$C_f$	Concentration of chemical species in the upstream feed solution
$C_f^0$	Initial concentration of permeable species in the upstream feed solution
CF	Concentration factor
CFUF	Cross-flow ultrafiltration
COC	Colloidal organic carbon, operationally defined
COM	Colloidal organic matter, operationally defined
$C_p$	Concentration of chemical species in the permeate
DOC	Dissolved organic carbon, conventionally <0.45 or < 0.7 $\mu\text{m}$
DOM	Dissolved organic matter, conventionally <0.45 or < 0.7 $\mu\text{m}$
DT-MS	Direct temperature-resolved mass spectrometry
FFF	Field-flow fractionation
GC-MS	Gas chromatography-mass spectrometry
HMW	High molecular weight, usually operationally defined
HOC	Hydrophobic organic contaminant
HPLC	High-performance liquid chromatography
ICP-MS	Inductively coupled plasma mass spectrometry
IUPAC	International Union of Pure and Applied Chemistry
LMW	Low molecular weight, usually operationally defined
MWCO	Molecular weight (molar mass) cut-off
NMWCO	Nominal molecular weight cut-off
NMR	Nuclear magnetic resonance
NOM	Natural organic matter
PAH	Polycyclic aromatic hydrocarbon
$P_c$	Permeate coefficient
PCB	Polychlorinated biphenyl
POC	Particulate organic carbon, conventionally >0.45 or > 0.7 $\mu\text{m}$
POM	Particular organic matter, conventionally >0.45 or > 0.7 $\mu\text{m}$
POP	Persistent organic pollutant
$R_c$	Retention coefficient
REE	Rare earth element
SPM	Suspended particulate matter
TOC	Total organic carbon
UDOM	Ultrafiltered dissolved organic matter

## REFERENCES

1. Vilks, P., Cramer, J. J., Bachinski, D. B., Doern, D. C. and Miller, H.G. (1993). Studies of colloids and suspended particles, Cigar Lake uranium deposit, Saskatchewan, Canada, *Appl. Geochem.*, **8**, 605–616.
2. Guo, L. D., Coleman, C. H., Jr and Santschi, P. H. (1994). The distribution of colloidal and dissolved organic carbon in the Gulf of Mexico, *Mar. Chem.*, **45**, 105–119.
3. Guo, L. D., Santschi, P. H. and Warnken, K. W. (1995). Dynamics of dissolved organic carbon (DOC) in oceanic environments, *Limnol. Oceanogr.*, **40**, 1392–1403.
4. Dai, M. H., Martin, J.-M. and Cauwet, G. (1995). The significant role of colloids in the transport and transformation of organic carbon and associated trace metals (Cd, Cu, and Ni) in the Rhone delta (France), *Mar. Chem.*, **51**, 159–175.
5. Guo, L. D., and Santschi, P. H. (1997). Isotopic and elemental characterization of colloidal organic matter from the Chesapeake Bay and Galveston Bay, *Mar. Chem.*, **59**, 1–15.
6. Gustafsson, O., Duker, A., Larsson, J., Andersson, P. and Ingri, J. (2000). Functional separation of colloids and gravitoids in surface waters based on differential settling velocity coupled cross-flow filtration–split flow thin cell fractionation (CCF–SPLITT), *Limnol. Oceanogr.*, **45**, 1731–1742.
7. Santschi, P. H., Roberts, K. A. and Guo, L. D. (2002). The organic nature of colloidal actinides transported in surface water environments, *Environ. Sci. and Technol.*, **36**, 3711–3719.
8. Guéguen, C., Guo, L.D., Wang, D., Tanaka, N. and Hung, C. C. (2006). Chemical characteristics and origin of dissolved organic matter in the Yukon River, *Biogeochemistry*, **77**, 139–155.
9. Stumm, W., and Morgan, J. J. (1981). *Aquatic Chemistry*. Wiley-Interscience, New York.
10. Sigleo, A. C., and Means, J. C. (1990). Organic and inorganic components in estuarine colloids: implications for sorption and transport of pollutants, *Rev. Environ. Contam. Toxicol.*, **112**, 123–147.
11. Guo, L. D., and Santschi, P. H. (1997). Composition and cycling of colloids in marine environments, *Rev. Geophys.*, **35**, 17–40.
12. Gustafsson, O., and Gschwend, P. M. (1997). Aquatic colloids: concepts, definitions, and current challenges, *Limnol. Oceanogr.*, **42**, 519–528.
13. Santschi, P. H., Lenhart, J. J. and Honeyman, B. D. (1997). Heterogeneous process affecting trace contaminant distribution in estuaries: the role of natural organic matter, *Mar. Chem.*, **58**, 99–125.
14. Burba, P., Aster, B., Nifant'eva, T., Shkinev, V. and Spivakov, B. Y. (1998). Membrane filtration studies of aquatic humic substances and their metal species: a concise overview. Part 1. Analytical fractionation by means of sequential-stage ultrafiltration, *Talanta*, **45**, 977–988.
15. Santschi, P. H., Guo, L. D., Means, J. C. and Ravichandran, M. (1999). Natural organic matter binding of trace metals and trace organic contaminants in estuaries. In *Biogeochemistry of Gulf of Mexico Estuaries*, eds Bianchi, T. S., Pennock, J.R. and Twilley, R.R. John Wiley & Sons, Inc., New York, pp. 347–380.
16. Wells, M. L., and Goldberg, E. D. (2002). Marine colloids and trace metals. In *Biogeochemistry of Marine Dissolved Organic Matter*, ed. Hansell, D. A. Academic Press, New York, 367–404.
17. Stordal, M., Gill, G., Wen, L.S. and Santschi, P. H. (1996). Mercury phase speciation in the surface waters of three Texas estuaries: importance of colloidal forms, *Limnol. Oceanogr.*, **41**, 52–61.
18. Wen, L.-S., Santschi, P. H., Gill, G. and Paternostro, C. (1997). Colloidal and particulate silver in river and estuarine waters of Texas, *Environ. Sci. Technol.*, **31**, 723–731.
19. Chin, W. C., Orellana, M. V. and Verdugo, P. (1998). Spontaneous assembly of marine dissolved organic matter into polymer gels, *Nature*, **391**, 568–572.
20. Carvalho, R. A., Benfield, M. C., Santschi, P. H. (1999). Comparative bioaccumulation studies of colloidally complexed and free-ionic heavy metals in juvenile brown shrimp *Penaeus aztecus* (Crustacea: Decapoda: Penaeidae), *Limnol. Oceanogr.*, **44**, 403–414.

21. Roditi, H. A., Fisher, N. S. and Sanudo-Wilhelmy, S. A. (2000). Uptake of dissolved organic carbon and trace metals by zebra mussels, *Nature*, **407**, 78–80.
22. Guo, L. D., Hunt, B. J., Santschi, P. H. and Ray, S. M. (2001). Effect of dissolved organic matter on the metal uptake by American oysters, *Environ. Sci. Technol.*, **35**, 885–893.
23. Guo, L. D., Santschi, P. H. and Ray, S. (2002). Metal partitioning between colloidal and dissolved phases and its relation with bioavailability to American oysters, *Mar. Environ. Res.*, **54**, 49–64.
24. Chen, M., Dei, R. C. H., Wang, W. -X. and Guo, L. (2003). Marine diatom uptake of iron bound with natural colloids of different origins, *Mar. Chem.*, **81**, 177–189.
25. Wells, M. L., and Goldberg, E. D. (2003). The level of iron enrichment required to initiate diatom blooms in HNLC waters, *Mar. Chem.*, **82**, 101–114.
26. Honeyman, B. D., and Santschi, P. H. (1989). Brownian-pumping model for oceanic trace metal scavenging: evidence from Th isotopes, *J. Mar. Res.*, **47**, 951–992.
27. Honeyman, B. D., and Santschi, P. H. (1992). The role of particles and colloids in the transport of radionuclides and trace metals in the oceans. In *Environmental Particles*, ed. Buffe, J. and van Leeuwen, H. P. IUPAC Series on Analytical Chemistry of Environmental systems, Vol. 1. Lewis, Boca Raton, FL, pp. 379–423.
28. Baskaran, M., Santschi, P. H., Benoit, G. and Honeyman, B. D. (1992). Scavenging of Th isotopes by colloids in seawater of the Gulf of Mexico, *Geochim. Cosmochim. Acta*, **56**, 3375–3388.
29. Guo, L. D., Santschi, P. H., Baskaran, M. and Zindler, A. (1995). Distribution of dissolved and particulate  $^{230}\text{Th}$  and  $^{232}\text{Th}$  in seawater from the Gulf of Mexico and off Cape Hatteras as measured by SIMS, *Earth Planet. Sci. Lett.*, **133**, 117–128.
30. Guo, L. D., Santschi, P. H., Cifuentes, L. A., Trumbore, S. and Southon, J. (1996). Cycling of high molecular weight dissolved organic matter in the Middle Atlantic Bight as revealed by carbon isotopic ( $^{13}\text{C}$  and  $^{14}\text{C}$ ) signatures, *Limnol. Oceanogr.*, **41**, 1242–1252.
31. Guo, L. D., Santschi, P. H. and Baskaran, M. (1997). Interaction of thorium isotopes with colloidal organic matter in oceanic environments, *Colloids Surf. A*, **120**, 255–272.
32. Koike, I., Hara, S., Terauchi, K. and Kogure, K. (1990). Role of sub-micrometer particles in the ocean, *Nature*, **345**, 242–244.
33. Moran, S. B., and Buesseler, K. O. (1992). Short residence time of colloids in the upper ocean estimated from  $^{238}\text{U}$ - $^{234}\text{Th}$  disequilibria, *Nature*, **359**, 221–223.
34. Benner, R., Pakulski, J. D., McCarthy, M., Hedges, J. I. and Hatcher, P. G. (1992). Bulk chemical characteristics of dissolved organic matter in the ocean, *Science*, **255**, 1561–1564.
35. Amon, R. M. W., and Benner, R. (1994). Rapid cycling of high-molecular-weight dissolved organic matter in the ocean, *Nature*, **369**, 549–552.
36. Benner, R. (2002). Chemical composition and reactivity. In *Biogeochemistry of Marine Dissolved Organic Matter*, eds Hansell, D. A., and Carlson, C.A. Academic Press, New York, pp. 59–90.
37. Moulin, V., and Ouzounian, G. (1992). Role of colloids and humic substances in the transport of radio elements through the geosphere, *Appl. Geochem.*, **1**, 179–186.
38. Wotton, R. S. (1996). Colloids, bubbles, and aggregates—a perspective on their role in suspension feeding, *J. North Am. Benthol. Soc.*, **15**, 127–135.
39. Lead, J. R., Davison, W., Hamilton-Taylor, J. and Buffe, J. (1997). Characterizing colloidal material in natural waters, *Aquat. Geochem.*, **3**, 213–232.
40. Kersting, A. B., Efurd, D. W., Finnegan, D. L., Rokop, D. J., Smith, D. K. and Thompson, J. L. (1999). Migration of plutonium in ground water at the Nevada Test Site, *Nature*, **397**, 56–59.
41. Town, R. M., and Filella, M. (2002). Size fractionation of trace metal species in freshwaters: implications for understanding their behaviour and fate, *Rev. Environ. Sci. Biotechnol.*, **1**, 277–297.
42. McKnight, D. M., Harnish, R., Wershaw, R. L., Baron, J. S. and Schiff, S. (1997). Chemical characteristics of particulate, colloidal and dissolved organic materials in Loch Vale watershed, Rocky Mountain National Park, *Biogeochemistry*, **36**, 99–124.

43. Wilkinson, K. J., Joz-Roland, A. and Buffle, J. (1997). Different roles of pedogenic fulvic acids and aquagenic biopolymers on colloid aggregation and stability in freshwaters, *Limnol. Oceanogr.*, **42**, 1714–1724.
44. Ran, Y., Fu, J. M. and Sheng, G. Y. (2000). Fractionation and composition of colloidal and suspended particulate materials in rivers, *Chemosphere*, **41**, 33–43.
45. Guéguen, C., Belin, C. and Dominik, J. (2002). Organic colloid separation in contrasting aquatic environments with tangential flow filtration, *Water Res.*, **36**, 1677–1684.
46. Guéguen, C., Wang, D. and Guo, L.D. (2003). Optical properties of natural organic matter in the Yukon River Basin, *Tohoku Geophys. J.*, **36**, 434–438.
47. Guéguen, C., and Dominik, J. (2003). Partitioning of trace metals between particulate, colloidal and truly dissolved fractions in a polluted river: the Upper Vistula River (Poland), *Appl. Geochem.*, **18**, 457–470.
48. Prokovsky, O. S., and Schott, J. (2002). Iron colloids/organic matter associated transport of major and trace elements in small boreal rivers and their estuaries (NW Russia), *Chem. Geol.*, **190**, 141–179.
49. Wang, Y., Hsieh, Y., Landing, W. M., Choi, Y. H., Salter, V. and Campbell, D. (2002). Chemical and carbon isotopic evidence for the source and fate of dissolved organic matter in the northern Everglades, *Biogeochemistry*, **62**, 269–289.
50. Wen, L. S., Santschi, P. H., Gill, G. and Tang, D. (2002). Silver concentrations in Colorado watersheds using improved methodology, *Environ. Toxicol. Chem.*, **21**, 2040–2051.
51. Maurer, L. G. (1976). Organic polymers in seawater: changes with depth in the Gulf of Mexico, *Deep-Sea Res.*, **23**, 1059–1064.
52. Zsolnay, A. (1979). Coastal colloidal carbon: A study of its seasonal variation and the possibility of river input, *Estuarine Coast. Mar. Sci.*, **9**, 559–567.
53. Sigleo, A. C., and Helz, G. R. (1981). Composition of estuarine colloidal material: major and trace elements, *Geochim. Cosmochim. Acta*, **45**, 2501–2509.
54. Sigleo, A. C., Hoering, T. C. and Helz, G. R. (1982). Composition of estuarine colloidal material: organic components, *Geochim. Cosmochim. Acta*, **46**, 1619–1626.
55. Means, J. C., and Wijayarathne, R. D. (1982). Role of colloids in the transport of hydrophobic pollutants, *Science*, **215**, 968–970.
56. Carlson, D. J., Brann, M. L., Mague, T. H. and Mayer, L. M. (1985). Molecular weight distribution of dissolved organic materials in seawater determined by ultrafiltration: a re-examination, *Mar. Chem.*, **16**, 155–171.
57. Moran, S. B., and Moore, R. M. (1989). The distribution of colloidal aluminum and organic carbon in coastal and open ocean waters off Nova Scotia, *Geochim. Cosmochim. Acta*, **53**, 2519–2527.
58. Whitehouse, B. G., Yeats, P. A. and Strain, P. M. (1990). Cross-flow filtration of colloids from aquatic environments, *Limnol. Oceanogr.*, **35**, 1368–1375.
59. Benner, R. (1991). Ultra-filtration for the concentration of bacteria, viruses, and dissolved organic matter. In *Marine Particles: Analysis and Characterization*, ed. Hurd, D. C. American Geophysical Union, Washington, DC, pp. 181–185.
60. Buesseler, K. O., Bauer, J., Chen, R., Eglinton, T., Gustafsson, O., Landing, W., Mopper, K., Moran, S. B., Santschi, P. H., Vernon-Clark, R. and Wells, M. (1996). An inter-comparison of cross-flow filtration techniques used for sampling marine colloids: overview and organic carbon results, *Mar. Chem.*, **55**, 1–32.
61. Benoit, G., Oktay, S., Cant, A., Hood, M. O., Coleman, C. H., Corapcioglu, O. and Santschi, P. H. (1994). Partitioning of Cu, Pb, Ag, Zn, Fe, Al and Mn between filter-retained particles, colloids and solution in 6 Texas estuaries, *Mar. Chem.*, **45**, 307–336.
62. Martin, J. M., Dai, M. H. and Cauwet, G. (1995). Significance of colloids in the biogeochemical cycling of organic carbon and trace metals in a coastal environment—example of the Venice Lagoon (Italy), *Limnol. Oceanogr.*, **40**, 119–131.
63. Dai, M. H., and Martin, J. M. (1995). First data on trace metal level and behaviour in two major Arctic river—estuarine systems (Ob and Yenisey) and in the adjacent Kara Sea, Russia, *Earth Planet. Sci. Lett.*, **131**, 127–141.

64. Guentzel, J. L., Powell, R. T., Landing, W. M. and Mason, R. P. (1996). Mercury associated with colloidal material in an estuarine and an open-ocean environment, *Mar. Chem.*, **55**, 177–188.
65. Powell, R. T., Landing, W. M. and Bauer, J. E. (1996). Colloidal trace metals, organic carbon and nitrogen in a southeastern US estuary, *Mar. Chem.*, **55**, 165–175.
66. Sanudo-Wilhelmy, S., Rivera-Duarte, I. and Flagal, A. R. (1996). Distribution of colloidal trace metals in the San Francisco Bay estuary, *Geochim. Cosmochim. Acta*, **60**, 4933–4944.
67. Wen, L. S., Stordal, M. C., Tang, D., Gill, G. A. and Santschi, P. H. (1996). An ultraclean cross-flow ultrafiltration technique for the study of trace metal phase speciation in seawater, *Mar. Chem.*, **55**, 129–151.
68. Wen, L. S., Santschi, P. H., Paternostro, C. and Gill, G. (1999). Estuarine trace metal distributions in Galveston Bay I: importance of colloidal forms in the speciation of the dissolved phase, *Mar. Chem.*, **63**, 185–212.
69. Ross, J. M. and Sherrell, R. M. (1999). The role of colloids in trace metal transport and adsorption behavior in New Jersey Pineland streams, *Limnol. Oceanogr.*, **44**, 1019–1034.
70. Wells, M. L., Kozelka, P. B. and Bruland, K. W. (1998). The complexation of ‘dissolved’ Cu, Zn, Cd and Pb by soluble and colloidal organic matter in Narragansett Bay, RI, *Mar. Chem.*, **62**, 203–217.
71. Wells, M. L., Smith, G. J. and Bruland, K. W. (2000). The distribution of colloidal and particulate bioactive metals in Narragansett Bay, RI, *Mar. Chem.*, **71**, 143–163.
72. Tang, D., Warnken, K. W. and Santschi, P. H. (2001). Organic complexation of copper in surface waters of Galveston Bay, *Limnol. Oceanogr.*, **46**, 321–330.
73. Tang, D., Warnken, K. W. and Santschi, P. H. (2002). Distribution and partitioning of trace metals (e.g. Ni, Cu, Cd, Pb, Zn) in Galveston Bay waters, *Mar. Chem.*, **78**, 29–45.
74. Choe, K., Gill, G. A. and Lehman, R. (2003). Distribution of particulate, colloidal, and dissolved mercury in San Francisco Bay estuary. 1. Total mercury, *Limnol. Oceanogr.*, **48**, 1547–1556.
75. Choe, K., Gill, G. A. and Lehman, R. (2003). Distribution of particulate, colloidal, and dissolved mercury in San Francisco Bay estuary. 2. Monomethyl mercury, *Limnol. Oceanogr.*, **48**, 1547–1556.
76. Ingri, J., Nordling, S., Larsson, J., Ronnegard, J., Nilsson, N., Rodushkin, I., Dahlqvist, R., Andersson, P. and Gustafsson, O. (2004). Size distribution of colloidal trace metals and organic carbon during a coastal bloom in the Baltic Sea, *Mar. Chem.*, **91**, 117–130.
77. Santschi, P. H., Guo, L. D., Baskaran, M., Trumbore, S., Southon, J., Bianchi, T., Honeyman, B. and Cifuentes, L. (1995). Isotopic evidence for the contemporary origin of high-molecular weight organic matter in oceanic environments, *Geochim. Cosmochim. Acta*, **59**, 625–631.
78. Bianchi, T. S., Lambert, C., Santschi, P. H., Baskaran, M. and Guo, L. (1995). Plant pigments as biomarkers of high-molecular-weight dissolved organic carbon, *Limnol. Oceanogr.*, **40**, 422–428.
79. Bianchi, T., Lambert, C., Santschi, P. and Guo, L. (1997). Sources and transport of land-derived particulate and dissolved organic matter in the Gulf of Mexico (Texas shelf/slope): the use of lignin-phenols and loliolides as biomarkers, *Org. Geochem.*, **27**, 65–78.
80. Santschi, P. H., Balnois, E., Wilkinson, K., Buffe, J. and Guo, L. D. (1998). Fibrillar polysaccharides in marine macromolecular organic matter as imaged by atomic force microscopy and transmission electron microscopy, *Limnol. Oceanogr.*, **43**, 896–908.
81. Guo, L. D., and Santschi, P. H. (2000). Sedimentary source of old high molecular weight dissolved organic carbon from the ocean margin benthic nepheloid layer, *Geochim. Cosmochim. Acta*, **64**, 651–660.
82. Mitra, S., Bianchi, T. S., Guo, L. D. and Santschi, P. H. (2000). Terrestrially derived dissolved organic matter in the Chesapeake Bay and the Middle Atlantic Bight, *Geochim. Cosmochim. Acta*, **64**, 3547–3557.
83. Guo, L. D., Tanaka, N., Schell, D. M. and Santschi, P. H. (2003). Nitrogen and carbon isotopic composition of high-molecular-weight dissolved organic matter in marine environments, *Mar. Ecol. Prog. Ser.*, **252**, 51–60.

84. Bertine, K. K., and Vernon-Clark, R. (1996). Elemental composition of the colloidal phase isolated by cross-flow filtration from coastal seawater samples, *Mar. Chem.*, **55**, 189–204.
85. Aluwihare, L. I., Repeta, D. J. and Chen, R. F. (1997). A major biopolymeric component to dissolved organic carbon in surface seawater, *Nature*, **387**, 166–169.
86. Aluwihare, L. I., Repeta, D. J. and Chen, R. F. (2002). Chemical composition and cycling of dissolved organic matter in the Mid-Atlantic Bight, *Deep-Sea Res. II*, **49**, 4421–4437.
87. Aluwihare, L. I., Repeta, D.J., Pantoja, S. and Johnson, C.G. (2005). Two chemically distinct pools of organic nitrogen accumulate in the ocean, *Science*, **308**, 1007–1010.
88. Repeta, D. J., Quan, T. M., Aluwihare, L. I. and Accardi, A. (2002). Chemical characterization of high molecular weight dissolved organic matter in fresh and marine waters, *Geochim. Cosmochim. Acta*, **66**, 955–962.
89. Guo, L. D., Lehner, J. K., White, D. M. and Garland, D. S. (2003). Heterogeneity of natural organic matter from the Chena River, Alaska, *Water Res.*, **37**, 1015–1022.
90. McCarthy, M., Pratum, T., Hedges, J. and Benner, R. (1997). Chemical composition of dissolved organic nitrogen in the ocean, *Nature*, **390**, 150–154.
91. Opsahl, S., and Benner, R. (1997). Distribution and cycling of terrigenous dissolved organic matter in the ocean, *Nature*, **386**, 480–482.
92. Mannino, A., and Harvey, H. R. (1999). Lipid composition in particulate and dissolved organic matter in the Delaware estuary, *Geochim. Cosmochim. Acta*, **63**, 2219–2235.
93. van Heemst, J. D. H., Megens, L., Hatcher, P. G. and de Leeuw, J. W. (2000). Nature, origin and average age of estuarine UDOM as determined by molecular and carbon isotopic characterization, *Org. Geochem.*, **31**, 847–857.
94. Minor, E. C., Simjouw, J. P., Boon, J. J., Kerkhoff, A.E. and van der Horst, J. (2002). Estuarine/marine UDOM as characterized by size-exclusion chromatography and organic mass spectrometry, *Mar. Chem.*, **78**, 75–102.
95. Zou, L., Wang, X. C., Culp, R. A., Callahan, J., Chen, R. F., Altabet, M. and Sun, M. Y. (2003). Bacterial roles in the formation of high molecular weight dissolved organic matter in estuarine and coastal waters: Evidence from lipids and compound-specific isotopic ratios, *Limnol. Oceanogr.*, **49**, 297–302.
96. Wang, X. C., Altabet, M. A., Callahan, J. and Chen, R. F. (2004). Stable carbon and nitrogen isotopic compositions of higher molecular weight dissolved organic matter from four U.S. estuaries, *Geochim. Cosmochim. Acta*, **68**, 2681–2691.
97. Guo, L. D., and Macdonald, R.W. (2006). Sources and transport of terrigenous organic matter in the upper Yukon River: evidence from isotope ( $^{13}\text{C}$ ,  $^{14}\text{C}$  and  $^{15}\text{N}$ ) composition of dissolved, colloidal and particulate phases, *Global Biogeochem. Cycles*, **20**, art number, GB2011.
98. Guo, L. D., Wen, L., Tang, D. and Santschi, P. H. (2000). Re-examination of cross flow ultrafiltration for sampling aquatic colloids: evidence from molecular probes, *Mar. Chem.*, **69**, 75–90.
99. Honeyman, B. D. (1999). Colloidal culprits in contamination, *Nature*, **397**, 23–24.
100. Dai, M., Kelly, J. M. and Buesseler, K. O. (2002). Sources and migration of plutonium in groundwater at the Savannah River site, *Environ. Sci. Technol.*, **36**, 3690–3699.
101. Matsunaga, T., Nagao, S., Ueno, T., Takeda, S., Amano, H. and Tkachenko, Y. (2004). Association of dissolved radionuclides released by the Chernobyl accident with colloidal materials in surface water, *Appl. Geochem.*, **19**, 1581–1590.
102. Buffle, J., Wilkinson, K. J., Stoll, Serge, Filella, M. and Zhang, J. (1998). A generalized description of aquatic colloidal interactions: the three-colloidal component approach, *Environ. Sci. Technol.*, **32**, 2887–2899.
103. Vold, R. D., and Vold, M. J. (1983). *Colloid and Interface Chemistry*. Addison-Wesley, London.
104. Buffle, J., and Leppard, G. G. (1995). Characterization of aquatic colloids and macromolecules. 1. structure and behavior of colloidal material, *Environ. Sci. Technol.*, **29**, 2169–2175.
105. Rees, D. A. (1972). Polysaccharide gels, a molecular view, *Chem. Ind. (London)*, **19**, 630–635.

106. Ogura, N. (1977). High molecular weight organic matter in seawater, *Mar. Chem.*, **5**, 535–549.
107. Prost, J., and Rondelez, F. (1991). Structures in colloidal physical chemistry, *Nature*, **350**, 11–23.
108. Tipping, H. (1988). Colloids in the aquatic environment, *Chem. Ind. (London)*, **15**, 485–490.
109. Gustafsson, O., Widerlund, A., Anderson, P., Ingri, J., Roos, P. and Ledin, A. (2000). Colloid dynamics and transport of major elements through a boreal river–brackish bay mixing zone, *Mar. Chem.*, **71**, 1–21.
110. Taillefert, M., Lienemann, C. P., Gaillard, J. F. and Perret, D. (2000). Speciation, reactivity, and cycling of Fe and Pb in a meromictic lake, *Geochim. Cosmochim. Acta*, **64**, 169–183.
111. Wilkinson, K. J., Balnois, E., Leppard, G. G., and Buffe, J. (1999). Characteristic features of the major components of freshwater colloidal organic matter revealed by transmission electron and atomic force microscopy, *Colloids Surf. A*, **155**, 287–310.
112. Hannah, D. M., Muirhead, D. and Lead, J. R. (2003). Imaging of suspended macromolecules and colloids in glacial and alpine streams by atomic force microscopy, *J. Glaciol.*, **49**, 607–609.
113. Muirhead, D., and Lead, J. (2003). Measurement of the size and structure of natural aquatic colloids in an urbanised watershed by atomic force microscopy, *Hydrobiologia*, **494**, 65–69.
114. Doucet, F. J., Maguire, L., and Lead, J. R. (2004). Size fractionation of aquatic colloids and particles by cross-flow filtration: analysis by scanning electron and atomic force microscopy, *Anal. Chim. Acta*, **522**, 59–71.
115. Buffe, J., Perret, D. and Newman, M. (1993). The use of filtration and ultrafiltration for size fractionation of aquatic particles, colloids and macromolecules. In *Environmental Particles*, eds Buffe, J. and van Leeuwen, H. R. IUPAC Series in Analytical and Physical Chemistry of Environmental Systems, Vol. 2. Lewis, Boca Raton, FL, pp. 171–230.
116. Louchoourn, P., Opsahl, S. and Benner, R. (2000). Isolation and quantification of dissolved lignin from natural waters using solid-phase extraction and GC/MS, *Anal. Chem.*, **2**, 2780–2787.
117. Kim, S., Simpson, A. J., Kujawinski, E. B., Freitas, M. A. and Hatcher, P. G. (2003). High resolution electrospray ionization mass spectrometry and 2D solution NMR for the analysis of DOM extracted by C-18 solid phase disk, *Org. Geochem.*, **34**, 1325–1335.
118. Benner, R., Benitez-Nelson, B., Kaiser, K. and Amon, R. M. W. (2004). Export of young terrigenous dissolved organic carbon from rivers to the Arctic Ocean, *Geophys. Res. Lett.*, **31**.
119. Druffel, E. R. M., Williams, P. M., Bauer, J. E. and Ertel, J. R. (1992). Cycling of dissolved and particulate organic matter in the open ocean, *J. Geophys. Res.*, **97**, 15639–15659.
120. Hedges, J. I., Hatcher, P. G., Ertel, J. R. and Meyers-Schulte, K. J. (1992). A comparison of dissolved humic substances from seawater with Amazon River counterparts by <sup>13</sup>C-NMR spectrometry, *Geochim. Cosmochim. Acta*, **56**, 1753–1757.
121. Lara, R. J., and Thomas, D. N. (1994). Isolation of marine dissolved organic matter: evaluation of sequential combinations of XAD resins 2, 4, and 7, *Anal. Chem.*, **66**, 2417–2419.
122. Wells, M. L., and Goldberg, E. D. (1991). Occurrence of small colloids in seawater, *Nature*, **353**, 342–344.
123. Lead, J. R., Hamilton-Taylor, J., Davidon, W. and Harper, M. (1999). Trace metal sorption by natural particles and coarse colloids, *Geochim. Cosmochim. Acta*, **63**, 1661–1670.
124. Beckett, R., Jue, Z. and Giddings, J. C. (1987). Determination of molecular weight distributions of fulvic and humic acids using field flow fractionation, *Environ. Sci. Technol.*, **21**, 289–295.
125. Vaillancourt, R. D., and Balch, W. M. (2000). Size distribution of marine submicron particles by flow field-flow fractionation, *Limnol. Oceanogr.*, **45**, 485–492.
126. Lyven, B., Hasselqvist, M., Turner, D. R., Haraldsson, C. and Andersson, K. (2003). Competition between iron- and carbon-based colloidal carriers for trace metals in a freshwater assessed using flow field-flow fractionation coupled to ICPMS, *Geochim. Cosmochim. Acta*, **67**, 3791–3802.
127. Sakugawa, H., and Handa, N. (1985). Isolation and chemical characterization of dissolved and particulate polysaccharides in Mikawa Bay, *Geochim. Cosmochim. Acta*, **49**, 1185–1193.

128. Chin, Y.-P., and Gschwend, P. M. (1991). The abundance, distribution, and configuration of porewater organic colloids in recent sediments, *Geochim. Cosmochim. Acta*, **55**, 1309–1317.
129. Burgess, R. M., McKinney, R. A., Brown, W. A. and Quinn, J. G. (1996). Isolation of marine sediment colloids and associated polychlorinated biphenyls: an evaluation of ultrafiltration and reverse-phase chromatography, *Environ. Sci. Technol.*, **30**, 1923–1932.
130. Assemi, S., Newcombe, G., Hepplewhite, C. and Beckett, R. (2004). Characterization of natural organic matter fractions separated by ultrafiltration using flow field-flow fractionation, *Water Res.*, **38**, 1467–1476.
131. Town, R. M., and Powell, H. K. (1993). Limitations of XAD resins for the isolation of the non-colloidal humic fraction in soil extracts and aquatic samples, *Anal. Chim. Acta*, **271**, 195–202.
132. Hedges, J. I., Cowie, G. L., Richey, J. E., Quay, P. D., Benner, R., Strom, M. and Forsberg, B. R. (1994). Origins and processing of organic matter in the Amazon River as indicated by carbohydrates and amino acids, *Limnol. Oceanogr.*, **39**, 743–761.
133. Benner, R., Biddanda, B., Black, B. and McCarthy, M. (1997). Abundance, size distribution, and stable carbon and nitrogen isotopic compositions of marine organic matter isolated by tangential flow ultrafiltration, *Mar. Chem.*, **57**, 243–263.
134. McCarthy, M., Hedges, J. and Benner, R. (1998). Major bacterial contribution to marine dissolved organic nitrogen, *Science*, **281**, 231–234.
135. Clark, L. L., Ingall, E. D. and Benner, R. (1998). Marine phosphorus is selectively remineralized, *Nature*, **393**, 426.
136. Clark, L. L., Ingall, E. D. and Benner, R. (1999). Marine organic phosphorus cycling: novel insights from nuclear magnetic resonance, *Am. J. Sci.*, **299**, 724–737.
137. Hedges, J. I., Mayorga, E., Tsamakis, E., McClain, M. E., Aufdenkampe, A., Quay, P., Richey, J. E., Benner, R., Opsahl, S., Black, B., Pimentel, T., Quintanilla, J. and Maurice, L. (2000). Organic matter in Bolivian tributaries of the Amazon River: a comparison to the lower mainstream, *Limnol. and Oceanogr.*, **45**, 1449–1466.
138. Kuma, K., Nishioka, J. and Matsunaga, K. (1996). Controls on iron(III) hydroxide solubility in seawater: the influence of pH and natural organic chelators, *Limnol. Oceanogr.*, **41**, 396–407.
139. Wu, J., Boyle, E., Sunda, W. and Wen, L. S. (2001). Soluble and colloidal Fe in the oligotrophic North Atlantic and North Pacific, *Science*, **293**, 847–849.
140. Nakabayashi, S., Kuma, K., Sasaoka, K., Saitoh, S., Mochizuki, M., Shiga, N. and Kusakabe, M. (2002). Variation in iron(III) solubility and iron concentration in the northwestern North Pacific Ocean, *Limnol. Oceanogr.*, **47**, 885–892.
141. Shiller, A. M. (2003). Syringe filtration methods for examining dissolved and colloidal trace element distributions in remote field locations, *Environ. Sci. Technol.*, **37**, 3953–3957.
142. Amicon (1995). *Membrane Filtration/Chromatography Catalog*. Amicon Inc., Beverly, MA.
143. Cheryan, M. (1998). *Ultrafiltration and Macrofiltration Handbook*. Technomic, Lancaster.
144. Guo, L. D., and Santschi, P. H. (1996). A critical evaluation of cross-flow ultrafiltration technique for sampling colloidal organic carbon in seawater, *Mar. Chem.*, **55**, 113–127.
145. Gustafsson, O., Buesseler, K. O. and Gschwend, P. M. (1996). Tests on the integrity of cross-flow filtration for marine colloids, *Mar. Chem.*, **55**, 93–111.
146. Choe, K., and Gill, G. A. (2001). Isolation of colloidal monomethyl mercury in natural waters using cross-flow ultrafiltration techniques, *Mar. Chem.*, **76**, 305–318.
147. Larsson, J., Gustafsson, O. and Ingri, J. (2002). Evaluation and optimization of two complementary cross-flow ultrafiltration systems toward isolation of coastal surface water colloids, *Environ. Sci. Technol.*, **36**, 2236–2241.
148. Chen, M., Wang, W. X. and Guo, L. (2004). Phase partitioning and solubility of iron in natural seawater controlled by dissolved organic matter, *Global Biogeochem. Cycles*, **18**, GB4013.
149. Chen, M., Guo, L., Huang, Y., Gao, Z., Cai, Y. and Cai, M. (2000). Application of the cross-flow ultrafiltration technique to examining colloidal uranium, thorium, radium isotopes and organic carbon in seawater, *Acta Oceanol. Sin.*, **22**, 51–59.
150. Guo, L. D., Hunt, B. J. and Santschi, P. H. (2001). Ultrafiltration behavior of major ions (Na, Ca, Mg, F, Cl, SO<sub>4</sub>) in natural waters, *Water Res.*, **35**, 1500–1508.

151. Wilding, A., Liu, R.X. and Zhou, J.L. (2004). Validation of cross-flow ultrafiltration for sampling of colloidal particles from aquatic systems, *J. Colloid Interface Sci.*, **280**, 102–112.
152. Buesseler, K. O., Hasselov, M. and Dai, M. (2003). Comment on ‘Trace metal levels in uncontaminated groundwater of a coastal watershed: importance of colloidal forms’, *Environ. Sci. Technol.*, **37**, 667–668.
153. Dai, M., Buesseler, K. O., Ripple, P., Andrews, J., Belastock, R. A., Gustafsson, O. and Moran, S. B. (1998). Evaluation of two cross-flow ultrafiltration membranes for isolating marine organic colloids, *Mar. Chem.*, **62**, 17–136.
154. Dahlqvist, R., Benedetti, M. F., Andersson, K., Turner, D., Larsson, T., Stolpe, B. and Ingri, J. (2004). Association of calcium with colloidal particles and speciation of calcium in the Kalix and Amazon rivers, *Geochim. Cosmochim. Acta*, **68**, 4059–4075.
155. Dahlqvist, R., and Ingri, J. (2002). Behaviour of Ca during ultrafiltration of river water, *Geochim. Cosmochim. Acta*, **66**, Suppl., A165.
156. Logan, B., and Jiang, Q. (1990). Molecular size distributions of dissolved organic matter, *J. Environ. Eng.*, **116**, 1046–1062.
157. Kilduff, J., and Weber, Jr. W. J. (1992). Transport and separation of organic macromolecules in ultrafiltration processes, *Environ. Sci. Technol.*, **26**, 569–577.
158. Johnson, B. D., and Wangersky, P. J. (1985). Seawater filtration: particle flow and impact considerations, *Limnol. Oceanogr.*, **30**, 966–971.
159. Pantoja, S., and Lee, C. (1999). Molecular weight distribution of proteinaceous material in Long Island Sound sediments, *Limnol. Oceanogr.*, **44**, 1323–1330.
160. Guo, L. D., Santschi, P. H. and Warnken, K. W. (2000). Trace metal composition of colloidal organic matter in marine environments, *Mar. Chem.*, **70**, 257–275.
161. Mannino, A., and Harvey, H. R. (2000). Biochemical composition of particles and dissolved organic matter along an estuarine gradient: sources and implications for DOM reactivity, *Limnol. Oceanogr.*, **45**, 775–788.
162. Mannino, A., and Harvey, H. R. (2000). Terrigenous dissolved organic matter along an estuarine gradient and its flux to the coastal ocean, *Org. Geochem.*, **31**, 1611–1625.
163. Kolowith, L. C., Ingall, E. D. and Benner, R. (2001). Composition and cycling of marine organic phosphorus, *Limnol. Oceanogr.*, **46**, 309–320.
164. Guo, L. D., Hung, C. C., Santschi, P. H. and Walsh, I. D. (2002).  $^{234}\text{Th}$  scavenging and its relationship to acid polysaccharide abundance in the Gulf of Mexico, *Mar. Chem.*, **78**, 103–119.
165. Quigley, M. S., Santschi, P. H., Hung, C., Guo, L. D. and Honeyman, B. D. (2002). Importance of acid polysaccharides for  $^{234}\text{Th}$  complexation to marine organic matter, *Limnol. Oceanogr.*, **47**, 367–377.
166. Santschi, P. H., Hung, C. C., Schultz, G., Alvarado-Quiroz, N., Guo, L. D., Pinckney, J. and Walsh, I. (2003). Control of acid polysaccharide production and  $^{234}\text{Th}$  and POC export fluxes by marine organisms, *Geophys. Res. Lett.*, **30**, 1044.
167. Santschi, P. H., Murray, J.W., Baskaran, M., Benitez-Nelson, C.R., Guo, L.D., Hung, C.-C., Lamborg, C., Moran, S.B., Passow, U. and Roy-Barman, M. (2006). Thorium speciation in seawater, *Mar. Chem.*, **100**, 250–268.
168. Alvarado-Quiroz, N. A., Hung, C.-C. and Santschi, P.H. (2006). Binding of thorium(IV) to carboxylate, phosphate and sulfate functional groups from marine exopolymeric substances (EPS), *Mar. Chem.*, **100**, 337–353.
169. Guo, L. D., Chen, M. and Guèguen, C. (2002). Control of Pa/Th ratio by particulate chemical composition in the ocean, *Geophys. Res. Lett.*, **29**, 1960.
170. Garrels, R. M., and Tompson, M. E. (1962). A chemical model for sea water at 25 °C and one atmosphere total pressure, *Am. J. Sci.*, **260**, 57–66.
171. Millero, F. J. (2001). *Physical Chemistry of Natural Waters*. Wiley-Interscience, New York.
172. Dupre, B., Viers, J., Dandurand, J., Polve, M., Benzeth, P., Vervier, P. and Braun, J. (1999). Major and trace elements associated with colloids in organic-rich river waters: ultrafiltration of natural and spiked solutions, *Chem. Geol.*, **160**, 63–80.
173. Viers, J., Dupre, B., Polve, M., Schott, J., Dandurand, J. and Braun, J. (1997). Chemical weathering in the drainage basin of a tropical watershed (Nsimi-Zoetele site, Cameroon): comparison between organic-poor and organic-rich waters, *Chem. Geol.*, **140**, 181–206.

174. Hill, D. M., and Aplin, A. C. (2001). Role of colloids and fine particles in the transport of metals in rivers draining carbonate and silicate terrains, *Limnol. Oceanogr.*, **46**, 331–344.
175. Buffle, J. (1990). *Complexation Reactions in Aquatic Systems: an Analytical Approach*. Ellis Horwood, New York.
176. Coplen, T. B., and Hawshaw, B. B. (1973). Ultrafiltration by a compacted clay membrane—I. Oxygen and hydrogen isotope fractionation, *Geochim. Cosmochim. Acta*, **37**, 2295–2310.
177. Hedges, J. I. (2002). Why dissolved organics matter? In *Biogeochemistry of Marine Dissolved Organic Matter*, eds Hansell, D. A. and Carlson, C. A. Academic Press, New York, pp. 1–33.
178. Neff, J. C., and Asner, G. P. (2001). Dissolved organic carbon in terrestrial ecosystems: synthesis and a model, *Ecosystems*, **4**, 29–48.
179. Hansell, D. A., and Carlson, C. A., eds (2002). *Biogeochemistry of Marine Dissolved Organic Matter*. Academic Press, New York.
180. Findlay, S. E. G., and Sinsabaugh, R. L. (2003). *Aquatic Ecosystems: Interactivity of Dissolved Organic Matter*. Academic Press, New York.
181. Whitehouse, B. G., Macdonald, R. W., Iseki, K., Yunker, M. B. and McLaughlin, F. A. (1989). Organic carbon and colloids in the Mackenzie river and Beaufort Sea, *Mar. Chem.*, **26**, 371–378.
182. Guo, L. D., Santschi, P. H. and Bianchi, T. S. (1999). Dissolved organic matter in estuaries of the Gulf of Mexico. In *Biogeochemistry of Gulf of Mexico Estuaries*, eds Bianchi, T. S., Pennock, J.R. and Twilley, R.R. John Wiley & Sons, Inc., New York. pp. 269–299.
183. Daffner, E. V., and Wangesky, P. J. (2002). A brief overview of modern directions in marine DOC studies, *J. Environ. Monit.*, **4**, 48–669.
184. Benner, R., and Hedges, J. I. (1993). A test of the accuracy of fresh water DOC measurements by high-temperature catalytic oxidation and UV-promoted persulfate oxidation, *Mar. Chem.*, **41**, 161–165.
185. Tiller, C. L., and O'Melia, C. R. (1993). Natural organic matter and colloidal stability – models and measurements, *Colloids Surf. A*, **73**, 89–102.
186. Benner, R., Chin-Leo, C., Gardner, W., Eadie, B., and Cotner, J. (1992). The fates and effects of riverine and shelf-derived DOM on Mississippi River plume/Gulf shelf processes. In *Nutrient Enhanced Coastal Ocean Productivity*. NOAA-Coastal-Ocean-Program. NECOP Workshop Proceedings, pp. 84–94.
187. Stordal, M. C., Santschi, P. H. and Gill, G. A. (1996). Colloidal pumping: evidence for the coagulation process using natural colloids tagged with  $^{203}\text{Hg}$ , *Environm. Sci. Technol.*, **30**, 3335–3340.
188. Argyrou, M. E., Bianchi, T. S. and Lambert, C. D. (1997). Transport and fate of dissolved organic carbon in the Lake Pontchartrain estuary, Louisiana, U.S.A., *Biogeochemistry*, **38**, 207–226.
189. Niven, S. E. H., Kepkay, P. E. and Boraie, A. (1995). Colloidal organic carbon and colloidal  $^{234}\text{Th}$  dynamics during a coastal phytoplankton bloom, *Deep-Sea Res. II*, **42**, 257–273.
190. Ogura, N. (1974). Molecular weight fractionation of dissolved organic matter in coastal seawater by ultrafiltration, *Mar. Biol.*, **24**, 305–312.
191. Eyrolle, F., and Charmasson, S. (2000). Ultrafiltration of large volumes for the determination of colloidally bound artificial radionuclides in natural waters, *Appl. Radiat. Isot.*, **52**, 927–936.
192. Sharp, J. H. (1973). Size classes of organic carbon in seawater, *Limnol. Oceanogr.*, **18**, 441–447.
193. Wheeler, J. R. (1976). Fractionation of molecular weight of organic substances in Georgia coastal water, *Limnol. Oceanogr.*, **21**, 846–852.
194. Ogawa, H., and Ogura, N. (1992). Comparison of two methods for measuring dissolved organic carbon in sea water, *Nature*, **356**, 696–698.
195. Leppard, G. G., West, M. M., Flannigan, D. T., Carson, J. and Lott, J. N. A. (1996). A classification scheme for marine organic colloids in the Adriatic Sea: colloid speciation by transmission electron microscopy, *Can. J. Fish. Aquat. Sci.*, **54**, 2334–2349.

196. Bauer, J. E. (2002). Carbon isotope composition of DOM. In *Biogeochemistry of Marine Dissolved Organic Matter*, eds Hansell, D. A. and Carlson, C. A. Academic Press, New York, pp. 405–455.
197. Cauwet, G. (2002). DOM in the coastal zone. In *Biogeochemistry of Marine Dissolved Organic Matter*, eds Hansell, D. A. and Carlson, C. A. Academic Press, New York, pp. 579–611.
198. McKnight, D. M., and Aiken, G. R. (1998). Sources and age of aquatic humus. In *Aquatic Human Substances*, ed. Hessen, D. O. Springer, New York, pp. 7–40.
199. Sigleo, A. C., Hare, P. E. and Helz, G. R. (1983). The amino acid composition of estuarine colloidal material, *Estuar. Coastal Shelf Sci.*, **17**, 87–96.
200. Means, J. C., and Wijayaratne, R. D. (1984). Chemical characterization of estuarine colloidal organic matter: implications for adsorptive processes, *Bull. Mar. Sci.*, **35**, 449–461.
201. Loh, A. N., Bauer, J. E. and Druffel, E.R.M. (2004). Variable ageing and storage of dissolved organic components in the open ocean, *Nature*, **430**, 877–881.
202. Guo, L. D., Semiletov, I., Gustafsson, O., Ingri, J., Andersson, P., Dudarev, O. and White, D. (2004). Characterization of Siberian Arctic estuarine sediments: implications for terrestrial organic carbon export, *Global Biogeochem. Cycles*, **18**, GB1036.
203. Goni, M. A., Yunker, M.B., Macdonald, R.W., and Eglington, T.I. (2005). The supply and preservation of ancient and modern components of organic carbon in the Canadian Beaufort Shelf of the Arctic Ocean, *Mar. Chem.*, **93**, 53–73.
204. Liu, Q., Parrish, C. C. and Helleur, R. (1998). Lipid class and carbohydrate concentrations in marine colloids, *Mar. Chem.*, **60**, 177–188.
205. McCarthy, M., Hedges, J. I. and Benner, R. (1996). Major biochemical composition of dissolved high molecular weight organic matter in seawater, *Mar. Chem.*, **55**, 281–297.
206. Skoog, A., and Benner, R. (1997). Aldoses in various size fractions of marine organic matter: Implications for carbon cycling, *Limnol. Oceanogr.*, **42**, 1803–1813.
207. Engelhardt, E., and Bianchi, T. S. (2001). Sources and composition of high-molecular weight dissolved organic carbon in a Southern Louisiana tidal stream (Bayou Trepagnier), *Limnol. Oceanogr.*, **46**, 917–926.
208. Benner, R., and Opsahl, S. (2001). Molecular indicators of the sources and transformations of dissolved organic matter in the Mississippi river plume, *Org. Geochem.*, **32**, 597–611.
209. Benner, R., and Kaiser, K. (2003). Abundance of amino sugars and peptidoglycan in marine particulate and dissolved organic matter, *Limnol. Oceanogr.*, **48**, 118–128.
210. Li, L., Zhao, Z., Huang, W., Peng, P., Sheng, G. and Fu, J. (2004). Characterization of humic acids fractionated by ultrafiltration, *Org. Geochem.*, **35**, 1025–1037.
211. Kovac, K., Bajt, O., Faganeli, J., Sket, B. and Orel, B. (2002). Study of macroaggregate composition using FT-IR and  $^1\text{H}$ -NMR spectroscopy, *Mar. Chem.*, **78**, 205–215.
212. Bianchi, T. S., Filley, T., Dria, K. and Hatcher, P.G. (2004). Temporal variability in sources of dissolved organic carbon in the lower Mississippi River, *Geochim. Cosmochim. Acta*, **68**, 959–967.
213. Wang, W., and Guo, L. D. (2000). Influence of natural colloids on metal bioavailability to two marine bivalves, *Environ. Sci. Technol.*, **34**, 4571–4576.
214. Wang, W., and Guo, L. D. (2001). Production of colloidal organic carbon and trace metals by phytoplankton decomposition, *Limnol. Oceanogr.*, **46**, 278–286.
215. Wen, L. S., Santschi, P. H. and Tang, D. (1997). Interactions between radioactively labeled colloids and natural particles: evidence for colloidal pumping, *Geochim. Cosmochim. Acta*, **62**, 2867–2878.
216. Waite, T. D. (2001). Thermodynamics of iron system in seawater. In *The Biogeochemistry of Iron in Seawater*, eds. Turner, D. R. and Hunter, K. A. John Wiley & Sons, Inc., New York, pp. 291–342.
217. Reid, R. T., Live, D. H., Faulkner, D. J. and Butler, A. (1993). A siderophore from a marine bacterium with an exceptional ferric ion affinity constant, *Nature*, **366**, 455–458.
218. Hutchins, D. A., Witter, A. E., Butler, A. and Luther, G. W., III (1999). Competition among marine phytoplankton for different chelated iron species, *Nature*, **400**, 858–861.
219. Barbeau, K., Moffett, J. W., Caron, D., Croot, P. L. and Erdner, D. (1996). Role of protozoan grazing in relieving iron limitation of phytoplankton, *Nature*, **380**, 61–64.

220. Bruland, K. W., and Rue, E. L. (2001). Analytical methods for the determination of concentrations and speciation of iron. In *The Biogeochemistry of Iron in Seawater*, ed. Turner, D. R. John Wiley & Sons, Inc., New York, pp. 255–289.
221. Macrellis, H. M., Trick, C. G., Rue, E. L., Smith, G. and Bruland, K. W. (2001). Collection and detection of natural iron-binding ligands from seawater, *Mar. Chem.*, **76**, 175–187.
222. Maranger, R., and Pullin, M. J. (2003). Elemental complexation by dissolved organic matter in Lakes: implications for Fe speciation and the bioavailability of Fe and P. In *Aquatic Ecosystems: Interactivity of Dissolved Organic Matter*, ed. Findlay, S. E. G. Academic Press, New York, pp. 186–214.
223. Perdue, E. M., Reuter, H.H. and Ghosal, M. (1980). The operational nature of acidic functional group analyses, and its impact on mathematical descriptions of acid–base equilibria in humic substances, *Geochim. Cosmochim. Acta*, **44**, 1841–1851.
224. Coale, K. H., and Bruland, K. W. (1987). Oceanic stratified euphotic zone as elucidated by Th-234–U-238 disequilibria, *Limnol. and Oceanogr.*, **32**, 189–200.
225. Buesseler, K. O., Andrews, J. A., Hartman, M. C., Belastock, R., and Chai, F. (1995). Regional estimates of the export flux of particulate organic carbon derived from thorium-234 during the JGOFS EQPAC program, *Deep-Sea Res. II*, **42**, 777–804.
226. Quigley, M. S., Honeyman, B. D. and Santschi, P.H. (1996). Thorium sorption in the marine environment: equilibrium partitioning at the hematite/water interface, sorption/desorption kinetics and particle tracing, *Aquat. Geochem.*, **1**, 277–301.
227. Baskaran, M., Swarzenski, P. W. and Porcelli, D. (2003). Role of colloidal material in the removal of  $^{234}\text{Th}$  in the Canada Basin of the Arctic Ocean, *Deep-Sea Res. II*, **50**, 1353–1373.
228. Huh, C. A., and Prahl, F. G. (1995). Role of colloids in upper ocean biogeochemistry in the northeast Pacific elucidated from  $^{238}\text{U}$ – $^{234}\text{Th}$  disequilibria, *Limnol. Oceanogr.*, **40**, 528–532.
229. Huh, C. A. (1997). Upper ocean distribution of  $^{234}\text{Th}$  in the Northeast Pacific: temporal variation and the role of colloids, *J. Oceanogr.*, **53**, 481–488.
230. Dai, M., and Benitez-Nelson, C. R. (2001). Colloidal organic carbon and  $^{234}\text{Th}$  in the Gulf of Maine, *Mar. Chem.*, **74**, 181–196.
231. Williams, P. M., and Druffel, E. R. M. (1987). Radiocarbon in dissolved organic matter in the central North Pacific Ocean, *Nature*, **330**, 246–248.
232. Bauer, J., Williams, P. M. and Druffel, E. R. M. (1992).  $^{14}\text{C}$  activity of dissolved organic carbon fractions in the northcentral Pacific and Sargasso Sea, *Nature*, **357**, 667–670.
233. Zhang, L., Chen, M., Yang, W. F., Xing, N., Li, Y. P., Qiu, Y. S. and Huang, Y. P. (2005). Size fractionated thorium isotopes ( $^{228}\text{Th}$ ,  $^{230}\text{Th}$ ,  $^{232}\text{Th}$ ) in surface waters in Jiulong River estuary, *Chin. J. Environ. Radioact.*, **78**, 199–216.
234. Swarzenski, P. W., McKee, B. A. and Booth, J. G. (1995). Uranium geochemistry on the Amazon shelf: chemical phase partitioning and cycling across a salinity gradient, *Geochim. Cosmochim. Acta*, **59**, 7–18.
235. Andersson, P. S., Porcelli, D., Gustafsson, O., Ingri, J. and Wasserburg, G. J. (2001). The importance of colloids for the behavior of uranium isotopes in the low-salinity zone of a stable estuary, *Geochim. Cosmochim. Acta*, **65**, 13–25.
236. Harnish, R. A., McKnight, D. M., Ranville, J. F., Stephens, V. C. and Orem, W. H. (1996). US Geological Survey, Boulder, CO. *Particulate, Colloidal and Dissolved-phase Associations of Plutonium, Americium, and Uranium in Water Samples from Well 1587 and Surface-water sites SW-51 and SW-53 at the Rocky Flats Plant, Colorado*. Water-Resources Investigations Report 96–4067.
237. Levi, B. G. (1999). Plutonium may be hitching a ride on colloids, *Phys. Today*, **52**, 19–20.
238. Dai, M., Buesseler, K. O., Kelley, J. M., Andrews, J. E., Pike, S. and Wacker, J. F. (2001). Size-fractionated plutonium isotopes in a coastal environment, *J. Environ. Radioact.*, **53**, 9–25.
239. Wijayaratne, R. D., and Means, J. C. (1984). Sorption of polycyclic aromatic hydrocarbons (PAHs) by natural colloids, *Mar. Environ. Res.*, **11**, 77–89.
240. Wijayaratne, R. D., and Means, J. C. (1984). Affinity of hydrophobic pollutants for natural estuarine colloids in aquatic environments, *Environ. Sci. Technol.*, **18**, 121–123.

241. Means, J. C., and Wijayaratne, R.D. (1989). Sorption of benzidine, toluidine and azobenzene with natural estuarine colloids. In *Aquatic Humic Substances*, eds. Suffett, I. H. and MacCarthy. American Chemical Society, Washington, DC, pp. 209–222.
242. Chiou, C. T., Malcolm, R. L., Brinton, T. I., and Kile, D. E. (1986). Water solubility enhancement of some organic pollutants and pesticides by dissolved humic and fulvic acids, *Environ. Sci. Technol.*, **20**, 502–508.
243. Chin, Y. P., and Gschwend, P. M. (1992). Partitioning of polycyclic aromatic hydrocarbons to marine porewater organic colloids, *Environ. Sci. Technol.*, **26**, 1621–1626.
244. Means, J. C. (1995). Influence of salinity upon sediment–water partitioning of aromatic hydrocarbons, *Mar. Chem.*, **51**, 3–16.
245. Richnow, H. H., Seifert, R., Heftner, J., Link, M., Francke, W., Schaefer, G. and Michealis, W. (1997). Organic pollutants associated with macromolecular soil organic matter: mode of binding, *Org. Geochem.*, **26**, 745–758.
246. Gschwend, P. M., and Wu, S. (1984). On the constancy of sediment–water partition coefficient of hydrophobic organic pollutants, *Environ. Sci. Technol.*, **19**, 90–96.
247. Kordel, W., Hennecke, D., and Franke, C. (1997). Determination of the adsorption coefficients of organic substances on sewage sludges, *Chemosphere*, **35**, 107–119.
248. Gustafsson, O., Nilsson, N. and Bucheli, T. D. (2001). Dynamic colloid–water partitioning of pyrene through a coastal Baltic spring bloom, *Environ. Sci. Technol.*, **35**, 4001–4006.
249. Chin, Y. P. (2003). The speciation of hydrophobic organic compounds by dissolved organic matter. In *Aquatic Ecosystems: Interactivity of Dissolved Organic Matter*, ed. Findlay, S. E. G. Academic Press, New York, pp. 161–185.
250. Gustafsson, O., and Gschwend, P.M. (1997). Soot as a strong partition medium for polycyclic aromatic hydrocarbons in aquatic systems. In *Molecular Markers in Environmental Geochemistry*, ed. Eganhouse, R. P. American Chemical Society Symposium Series 671. American Chemical Society, Washington, DC, pp. 365–381.
251. Periera, W., and Rostad, C. E. (1990). Occurrence, distribution and transport of herbicides and their degradation products in the lower Mississippi River and its tributaries, *Environ. Sci. Technol.*, **24**, 1400–1408.
252. Orlandini, K. A., Penrose, W. R., Harvey, B. R., Lovett, M. B. and Findlay, M. W. (1990). Colloidal behavior of actinides in an oligotrophic lake, *Environ. Sci. Technol.*, **24**, 706–712.
253. Burba, P., Shkinev, V. and Spivakov, B. Y. (1995). Online fractionation and characterization of aquatic humic substances by means of sequential-stage ultrafiltration, *Fresenius' J. Anal. Chem.*, **351**, 74–82.
254. Tranvik, L. J., and Jorgensen, N. O. G. (1995). Colloidal and dissolved organic matter in lake water: carbohydrate and amino acid composition, and ability to support bacterial growth, *Biogeochemistry*, **30**, 77–97.
255. Alberic, P., Viollier, E., Jezequel, D., Grosbois, C. and Michard, G. (2000). Interactions between trace elements and dissolved organic matter in the stagnant anoxic deep layer of a meromictic lake, *Limnol. Oceanogr.*, **45**, 1088–1096.
256. Babiarz, C. L., Hoffmann, S. R., Shafer, M. M., Hurley, J. P., Andren, A. W. and Armstrong, D. E. (2000). A critical evaluation of tangential-flow ultrafiltration for trace metal studies in freshwater systems. 2. Total mercury and methylmercury, *Environ. Sci. Technol.*, **34**, 3428–3434.
257. Babiarz, C. L., Hurley, J. P., Krabbenhoft, D. P., Gilmour, C. and Branfireun, B. A. (2003). Application of ultrafiltration and stable isotopic amendments to field studies of mercury partitioning to filterable carbon in lake water and overland runoff, *Sci. Total Environ.*, **304**, 295–303.
258. Wu, F. C., Tanoue, E. and Liu, C. Q. (2003). Fluorescence and amino acid characteristics of molecular size fractions of DOM in the waters of Lake Biwa, *Biogeochemistry*, **65**, 245–257.
259. Buddemeier, R. W., and Hunt, J. R. (1988). Transport of colloidal contaminants in groundwater: radionuclide migration at the Nevada Test Site, *Appl. Geochem.*, **3**, 535–548.
260. Tricca, A., Wasserburg, G. J., Porcelli, D. and Baskaran, M. (2001). The transport of U- and Th-series nuclides in a sandy unconfined aquifer, *Geochim. Cosmochim. Acta*, **65**, 1187–1210.

261. Sanudo-Wilhelmy, S. A., Rossi, F. K., Bokuniewicz, H. and Paulsen, R. J. (2002). Trace metal levels in uncontaminated groundwater of a coastal watershed: importance of colloidal forms, *Environ. Sci. Technol.*, **36**, 1435–1441.
262. Hoffmann, M., Yost, E. C., Eisenreich, S. J. and Maier, W. J. (1981). Characterization of soluble and colloidal-phase metal complexes in river water by ultrafiltration: a mass balance approach, *Environ. Sci. Technol.*, **15**, 655–661.
263. Ingri, J., Widerlund, A., Land, M., Gustafsson, O., Anderson, P. and Ohlander, B. (2000). Temporal variations in the fractionations of the rare earth elements in a boreal river; the role of colloidal particles, *Chem. Geol.*, **166**, 23–45.
264. Belzile, C., and Guo, L.D. (2006). Optical properties of low molecular weight and colloidal organic matter: application of the ultrafiltration permeation model to DOM absorption and fluorescence, *Mar. Chem.*, **98**, 183–196.
265. Porcelli, D., Andersson, P. S., Wasserbürg, G. J., Ingri, J. and Baskaran, M. (1997). The importance of colloids and mires for the transport of uranium isotope through the Kalix River watershed and Baltic Sea, *Geochim. Cosmochim. Acta*, **61**, 4095–4113.
266. Gounaris, V., Anderson, P. R. and Holsen, T. M. (1993). Characteristics and environmental significance of colloids in landfill leachate, *Environ. Sci. Technol.*, **27**, 1381–1387.
267. Eyrolle, F., Benedetti, F. M., Benaim, Y. J. and Ferevrier, D. (1996). The distributions of colloidal and dissolved organic carbon, major elements, and trace elements in small tropical catchments, *Geochim. Cosmochim. Acta*, **60**, 3643–3656.
268. Hoffmann, S. R., Shafer, M. M., Babiarz, C. L. and Armstrong, D. E. (2000). A critical evaluation of tangential-flow ultrafiltration for trace metal studies in freshwater systems. 2. Organic carbon, *Environ. Sci. Technol.*, **34**, 3420–3427.
269. Sempere, R., Cauwet, G. and Randon, R. (1994). Ultrafiltration of seawater with a zirconium and aluminum oxide tubular membrane: application to the study of colloidal organic carbon distribution in an estuarine bottom nepheloid layer, *Mar. Chem.*, **46**, 49–60.
270. Brownawell, B. J. (1991). Methods for isolating colloidal organic matter from seawater: general considerations and recommendations. In *Marine Particles: Analysis and Characterization*, ed. Hurd, D. C. American Geophysical Union, Washington, DC, pp. 187–194.
271. Moran, S. B., and Buesseler, K. O. (1993). Size fractionated  $^{234}\text{Th}$  in continental shelf waters off New England: implications for the role of colloids in oceanic trace metal scavenging, *J. Mar. Res.*, **51**, 893–922.
272. Nishioka, J., Takeda, S., Wong, C. S. and Johnson, W. K. (2000). Size-fractioned iron concentrations in the northeast Pacific Ocean: distribution of soluble and small colloidal iron, *Mar. Chem.*, **74**, 157–179.
273. Nishioka, J., Takeda, S., Kudo, I., Tsunune, D., Yoshimura, T., Kuma, K. and Tsuda, A. (2003). Size-fractionated iron distribution and iron-limitation processes in the subarctic NW Pacific, *Geophys. Res. Lett.*, **30**, 1730.
274. Grzybowski, W., and Pempkowiak, J. (2003). Preliminary results on low molecular weight organic substances dissolved in the waters of the Gulf of Gdańsk, *Oceanologia*, **45**, 693–704.
275. Krom, M. D., and Sholkovitz, E. R. (1977). Nature and reactions of dissolved organic matter in the interstitial waters of marine sediments, *Geochim. Cosmochim. Acta*, **41**, 1565–1573.
276. Burdige, D. J., and Gardner, K. G. (1998). Molecular weight distribution of dissolved organic carbon in marine sediment pore waters, *Mar. Chem.*, **62**, 45–64.
277. Riise, G., Van Hees, P., Lundstrom, U. and Strand, L.T. (2000). Mobility of different size fractions of organic carbon, Al, Fe, Mn and Si in podzols, *Geoderma*, **94**, 237–247.
278. Kepkay, P. E., Niven, S.E.H., and Milligan, T.G. (1993). Low-molecular-weight and colloidal DOC production during a phytoplankton bloom, *Mar. Ecol. Prog. Ser.*, **100**, 233–244.
279. Guo, L. D., Tanaka, T., Wang, D., Tanaka, N. and Murata, A. (2004). Distributions, speciation and stable isotope composition of organic matter in the southeastern Bering Sea, *Mar. Chem.*, **91**, 211–226.
280. Sigleo, A. C., and Macko, S. A. (1985). Stable isotope and amino acid composition of estuarine dissolved colloidal material. In *Marine and Estuarine Geochemistry*, ed. Sigleo, A. C. Lewis, Chelsea, MI, pp. 29–46.
281. Sigleo, A. C. (1996). Biochemical components in suspended particles and colloids: carbohydrates in the Potomac and Patuxent Estuaries, *Org. Geochem.*, **24**, 83–93.

282. Guieu, C., Martin, J.M., Tankere, S.P.C., Mousty, F., Trincherini, P., Bazot, M., and Dai, M. (1998). On trace metal geochemistry in the Danube River and western Black Sea, *Estuar. Coastal Shelf Sci.*, **47**, 471–485.
283. Muller, F. L. L. (1998). Colloid/solution partitioning of metal-selective organic ligands, and its relevance to Cu, Pb and Cd cycling in the Firth of Clyde, *Estuar. Coastal Shelf Sci.*, **46**, 419–437.
284. Loyland, S. M., Lamont, S. P. and Clark, S. B. (2001). Plutonium partitioning to colloidal and particulate matter in an acidic, sandy sediment: implications for remediation alternatives and plutonium migration, *Environ. Sci. and Technol.*, **35**, 2295–2300.
285. Guo, L. D. (1995). *Cycling of Dissolved and Colloidal Organic Matter in Oceanic Environments as Revealed by Carbon and Thorium Isotopes*. Ph.D Thesis, Texas A&M University, College Station, TX.



---

# 5 Characterisation of Aquatic Colloids and Macromolecules by Field-flow Fractionation

---

**MARTIN HASSELLÖV**

*Department of Chemistry, Göteborg University, S-412 96 Gothenburg, Sweden*

**FRANK VON DER KAMMER**

*Department for Environmental Geosciences, Center for Earth Sciences Vienna University,  
1090 Vienna, Austria*

**RONALD BECKETT**

*Water Studies Centre, School of Chemistry, Monash University (Clayton Campus),  
Melbourne, Victoria 3800, Australia*

1	Introduction . . . . .	224
2	Theoretical Aspects and Instrumentation . . . . .	226
2.1	Separation Principle of FFF . . . . .	226
2.2	Retention Theory . . . . .	228
2.3	Modes of Retention . . . . .	230
2.4	Field-flow Fractionation Subtechniques . . . . .	233
2.4.1	Flow Field-flow Fractionation . . . . .	233
2.4.1.1	Symmetrical Flow FFF (sFFF) . . . . .	234
2.4.1.2	Asymmetric Flow FFF (aFFF) . . . . .	235
2.4.2	Sedimentation Field-flow Fractionation . . . . .	238
2.5	Prefractionation of Steric Particles . . . . .	239
2.6	Detection . . . . .	240
2.7	Calibration of Channel Dimensions . . . . .	244
2.7.1	Injection of Non-retained Sample to Obtain Void Volume . . . . .	245
2.7.2	Breakthrough Volume Method . . . . .	245
2.7.3	Back Calculation Using a Standard of Known Size . . . . .	245
2.7.4	Calibration of Channel Dimensions Using Multiple Standards . . . . .	245
2.8	Constant or Programmed Field Runs . . . . .	246
2.9	Conversion of Fractograms to Particle Size Distributions . . . . .	246
2.9.1	Element Content Distributions . . . . .	247
2.9.2	Element Atomic Ratio Distributions . . . . .	247
2.10	Sample Recovery . . . . .	247

3	Size Fractionation of Macromolecules . . . . .	247
3.1	Collection and Preconcentration of Colloidal Organic Matter . . . . .	248
3.2	Determination of Size and Molar Mass Distributions of Colloidal Organic Matter Using FlFFF . . . . .	249
3.3	Operating Conditions: Flow-rates, Membranes, Carrier . . . . .	250
3.4	Molar Mass Calibration . . . . .	252
3.5	Validation with Other Methods . . . . .	253
3.6	Aggregation Studies of Humic Substances . . . . .	254
3.7	Trace Element Associations with Macromolecular Organic Matter and Other Nanophases . . . . .	254
4	Fractionation of Inorganic Particles . . . . .	261
4.1	Differentiation of Inorganic Particles and Organic Macromolecules . . . . .	262
4.2	Sample Preconcentration . . . . .	263
4.3	Element-Based Size Distributions . . . . .	264
4.4	Non-Spherical Particles and Particle Shape . . . . .	264
4.5	Application to Natural Sediment Particles . . . . .	267
5	Conclusions . . . . .	267
	List of Symbols and Abbreviations . . . . .	269
	References . . . . .	271

## 1 INTRODUCTION

Colloids are traditionally defined as particles having at least one dimension in the range 1 nm–1 µm. Colloids in natural waters have received increasing attention in recent years, mainly due to their impact on the transport and fate of contaminants in the environment (Chapters 1 and 3). Since colloids are transported in most aqueous systems as if they are truly dissolved, they generally enhance the transport of the associated contaminants due to high partitioning to the colloidal phase [1]. Colloids have also been shown to function as a very efficient intermediary in the transfer of elements from the truly dissolved to particulate fraction in seawater where trace elements may be removed from surface waters by aggregation and settling [2]. Sensitive analytical techniques for the determination of contaminants and trace constituents at low concentrations are continuously being developed for environmental fields. However, to understand the interaction of these solutes with the colloidal continuum, suitable fractionation techniques are needed to decrease the level of complexity in the analysis (i.e. in order to reduce matrix effects, polydispersity or the number of phases that bind the analytes). Furthermore, if the fractionation occurs according to a physical or chemical property, then it adds a further dimension to the analytical results.

The size distributions of aquatic colloids will reflect certain physicochemical processes such as aggregation and adsorption, which in turn influences element speciation, biological uptake, transport and the fate of particles and their associated contaminants. For this reason, it is important to have proper techniques for sizing and fractionating colloidal

particles. Even in cases where particle size is not the most important factor in itself, size fractionation of the sample with selective detection can resolve material which is chemically different. Since the widely used methods of filtration and centrifugation have limitations in terms of their accuracy or convenience, new techniques are being sought by environmental scientists [3]. Field-flow fractionation (FFF) is one of the techniques that have been tested and used quite frequently and shown to have great potential for characterising environmental colloids.

Scientific folklore has it that in 1965, while returning from a river trip in Wyoming, Calvin Giddings stayed overnight in a hotel and during a disturbed sleep envisioned the separation principle that would become known as field-flow fractionation. The method was outlined in a brief article in 1966 [4]. The method was so named due to the separation principle that forces particles towards a channel wall by a 'field'. Near the wall, the particles are 'fractionated' in the laminar 'flow' of the channel since different particles are affected to various extents by the field.

Following his return to the University of Utah, Giddings directed some of his team of chromatographers to search for proof of the new methodology. Notable among these were Marcus Myers, who was responsible for designing and building much of the instrumentation that is still used today, and Karin Caldwell, who performed or supervised numerous experiments aimed at advancing FFF theory and demonstrating new applications. The first successful retention reported from Giddings' laboratory described the separation of polystyrene polymers of different molar mass in a 3 m long channel using a thermal gradient field (thermal FFF or ThFFF) [5].

Giddings and co-workers continued developments on sedimentation FFF (SdFFF) [6], and channel cross-flow (flow FFF or FlFFF) [7] and electrical field (electrical FFF) [8] were soon to follow. FlFFF has become the most widely used of the FFF subtechniques, whereas, despite its potential, electrical FFF has been virtually neglected for 30 years due to a number of practical difficulties. This method is likely to be revived with Caldwell's recent introduction of a superior channel design [9]. Other FFF fields that have been tested include gravitational, magnetic, dielectric, shear and acoustic types.

The initial environmental applications of FFF again spring from the Giddings group. In 1982, a brief study of suspended colloidal particles from several Utah rivers was reported [10]. This study demonstrated to environmental scientists that a new set of separation and sizing techniques were available for characterising natural aquatic colloids and organic macromolecules. As a result of this work, Beckett and Giddings began a collaboration, which resulted in methods for determining the particle size distribution of colloidal aquatic particles using SdFFF [11] and molar mass distributions of humic substances using FlFFF [12].

Karaiskakis *et al.* [10] demonstrated an important principle when they analysed various size fractions collected for their elemental composition using energy-dispersive X-ray analysis (EDXA). Although this method was tedious and lacked precision, it demonstrated an important principle, that FFF combined with sensitive analytical techniques could generate detailed size-based elemental speciation data.

This idea was extended to include FFF-EDXA analysis of individual particles in fractions collected after SdFFF separation, but this was even more time consuming [13]. Giddings suggested the use of ICP-AES as a detector for FFF (J. C. Giddings, personal

communication) but an on-line ICP-MS elemental analyser was first instigated by Howard Taylor at USGS [14]. Subsequent studies by various workers have demonstrated that this is a powerful approach for characterising element composition distributions in colloidal and macromolecular samples.

## 2 THEORETICAL ASPECTS AND INSTRUMENTATION

This chapter will focus on the development and application of FFF that have been published over the last 12 years for the separation and characterisation of environmental colloids. The detailed theory of FFF has been covered in several reviews [15–17] and in the FFF Handbook [18]. For a general background and summary of the first environmental applications, the reader is advised to examine corresponding chapter in Volume 2 in this series, *Environmental Particles* [19].

We will use the term *particles* throughout the chapter for entities which can be separated by FFF; most of these fulfil the IUPAC definition of *colloids* except that they may reach sizes up to 100 µm. In this chapter, we also use the term truly dissolved (<0.001 nm or 1000 g mol<sup>-1</sup>) to distinguish from traditionally dissolved (<0.45 or <0.22 µm filterable) fractions.

### 2.1 SEPARATION PRINCIPLE OF FFF

FFF is a family of flow-driven separation techniques that provide a continuous separation applicable to particles of size from about 1 nm to 50 µm. The fractionation is achieved by the interaction of particles with an external field or gradient, which applies a force acting perpendicular to the channel flow. This results in a non-uniform distribution of the particles over the laminar flow profile that exists across the thin, ribbon-like fractionation channel. The system set-up is similar to liquid chromatography with some significant differences (Figure 1); most importantly, in FFF there is no stationary phase.

The family of FFF separation systems is divided into subtechniques according to the type of external field that is applied. A size-dependent separation is generally achieved by the physical size parameter (*e.g.* diffusion coefficient or buoyant mass) that is responsible for the different subtechniques (Table 1). Thus other particle parameters, in addition to size, may also be involved in the separation process.

To date, most environmental studies on colloids or macromolecules have been performed with either SdFFF or FIFFF. These two FFF techniques are the most commonly used for the separation of environmental particles and, consequently, this chapter will focus on these techniques.

Since FIFFF retention depends solely on the diffusion coefficient of the particles, the hydrodynamic diameter can be calculated directly. Importantly, the measurement is independent of the particle density. In SdFFF, retention is related to the buoyant mass of the particles and hence the density is required if the particle diameter is to be calculated. It should be noted that the particle size determined by FFF is always an equivalent spherical particle diameter. Thus values obtained for non-spherical particles from different subtechniques will differ from each other to some extent (Chapter 1).

As has been emphasised in this book, characterisation of the colloidal continuum in natural waters is a daunting task with many pitfalls. Nevertheless, it will be shown that FFF

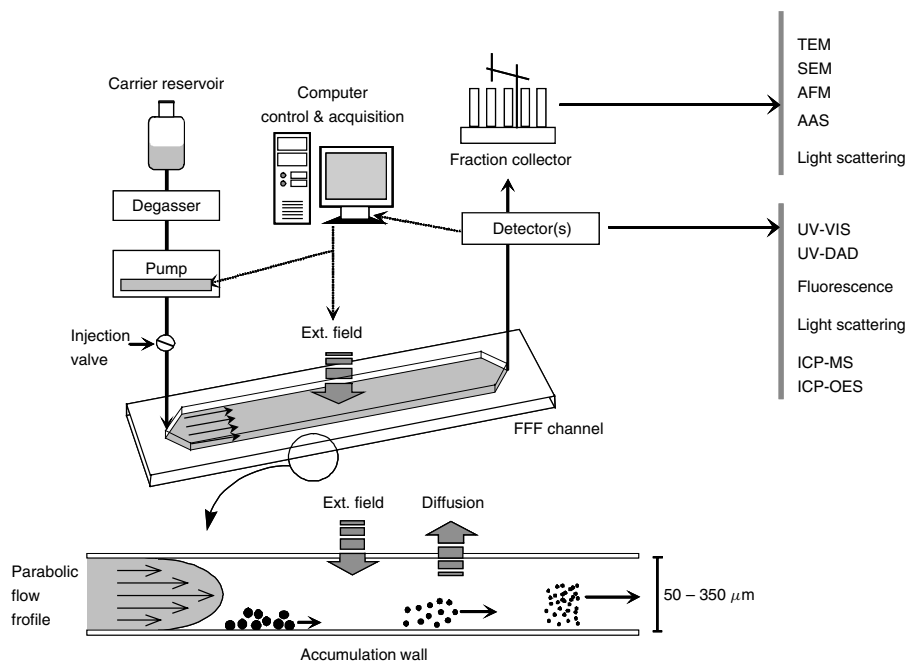


**Figure 1.** Schematic diagram of an FFF system including the channel (with enlarged view of the Brownian mode separation principle), channel flow pump, detection system and control. The detection systems to the right are a list of the most commonly used. The instrumentation has many similarities with liquid chromatography systems. From von der Kammer (2005) [20]

**Table 1.** Fields applied in common FFF subtechniques for the separation of colloids and the corresponding particle parameter causing fractionation

FFF subtechnique	Applied field/gradient	Fractionation parameter	Comments
SdFFF	Centrifugal	Buoyant mass	Assumes constant density; the particle volume is determined and transferred to an equivalent spherical diameter
Symmetrical FIFFF	Cross-flow	Diffusion coefficient	Used to calculate equivalent hydrodynamic or Stokes diameter
Asymmetric FIFFF	Cross-flow	Diffusion coefficient	

can simplify complex samples by fractionation. By combination with various detection systems, FFF can also provide distributions of both physical and chemical properties. For example, with an element-selective detector, element-based size distributions can be produced.

Additional measurements on the eluate can be used to confirm the calculated particle size or to calculate some other particle characteristic such as density or shape. For example,

light scattering detectors can deliver independent size parameters such as the root mean square (RMS) radius (given a number of assumptions).

## 2.2 RETENTION THEORY

In FFF, the separation is generally achieved by the retention of particles relative to the average flow velocity of the carrier liquid in the ribbon-like fractionation channel.

There are two different elution modes, Brownian and steric/hyperlayer. In the Brownian mode, retention is achieved due to the combined influence of (1) the field force acting on the particles that drives them in the direction of the accumulation wall and (2) their diffusive flux back into the channel due to the concentration gradient that is created (Figure 2).

When dynamic equilibrium is established, a cloud of particles is formed with the particle concentration decreasing exponentially as a function of the distance from the wall into the channel. The mean cloud thickness,  $l$ , depends on the particle properties (i.e. diffusion coefficient, mass, etc.) and the field strength. In most cases, this results in smaller particles forming a cloud that reaches further into the channel than the cloud formed by the larger particles. The mean cloud thickness is generally expressed as the dimensionless retention parameter,  $\lambda$  [equation (1)], which is the ratio of the cloud thickness,  $l$ , to the channel thickness,  $w$ :

$$\lambda = l/w = kT/Fw \quad (1)$$

To a first approximation, the cloud is pushed along the channel by the fluid flow velocity vector, which is at a distance  $l$  from the accumulation wall. Thus the smaller particles will be transported at higher velocities and experience lower retention than the larger particles. It has to be emphasised that in contrast to the schematic diagram shown in Figure 2, the particle clouds usually occupy only a few percent of the full channel height and the processes responsible for fractionation take place in the near vicinity of the accumulation wall [18]. For a channel thickness of 200  $\mu\text{m}$ ,  $l$  is typically 1–10  $\mu\text{m}$  and  $\lambda$  is 0.005–0.05. It can be shown that the retention parameter,  $\lambda$ , can be related to the force  $F$  exerted on the particles by equation (1), where  $T$  is the absolute temperature and  $k$  is Boltzmann constant. Since the interaction of the particles with the field or gradient

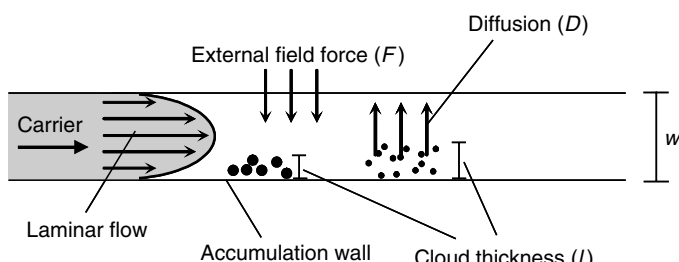


**Figure 2.** Separation principle of a normal mode FFF separation, showing the parabolic flow profile of the laminar flow and the balance between the two fluxes driven by the field and the molecular diffusion. The particle concentration in the formed particle cloud will decrease exponentially from the accumulation wall upwards in the channel and have a mean cloud thickness,  $l$ . Note that the clouds actually occupy about 1–10% of the channel thickness. From von der Kammer (2005) [20]

generates a force which is related to the relevant physical properties of the particles (i.e. size density, mass, *etc.*), these properties can then be derived from the FFF experiment.

The experimental information retrieved from a simple FFF run is the degree of retention of a sample component relative to the mean flow velocity of the carrier. The retention ratio,  $R$ , of a sample component is defined as

$$R = \frac{M_{1,v}}{M_{1,r}} \quad (2)$$

where  $M_{1,v}$  is the first moment of the void peak, which is due to the elution of non-retained substances and occurs at the channel void time  $t^0$  with a corresponding void volume  $V^0$ , and  $M_{1,r}$  is the first moment of a retained analyte peak, which is given as the sample retention time or volume ( $t_r$  or  $V_r$ , respectively). When a concentration signal is obtained from the detector, the first moment  $M_1$  of the peak corresponds to the median of its concentration profile as defined by

$$M_1 = \frac{\int_{t_i}^{t_f} t c(t) dt}{\int_{t_i}^{t_f} c(t) dt} \quad (3)$$

where  $c(t)$  is the concentration of a sample component as a function of time  $t$  and  $t_i$  and  $t_f$  refer to the start and the end of the elution profile, respectively. In the case of Gaussian peaks, the peak maximum can be used instead of the first moment and  $R$  reduces to a peak maximum retention ratio:

$$R = \frac{t_v^0}{t_r} = \frac{V^0}{V_r} \quad (4)$$

The retention ratio  $R$  is related to the retention parameter by the fundamental relationship

$$R = 6\lambda \coth\left(\frac{1}{2\lambda}\right) - 12\lambda^2 \quad (5)$$

Some approximations have been developed which are applicable for limited regions of  $R$ . Three of the more recognised approximations are as follows:

$$R = 6\lambda - 12\lambda^2 \quad (6)$$

$$R = 6\lambda \quad (7)$$

$$\lambda = \frac{R}{6\sqrt[3]{(1-R)}} \quad (8)$$

Plots for the approximations are compared to the exact solution, equation (5), in Figure 3. For a retention ratio of  $R < 0.5$  where the component is eluting at least at twice the channel void volume, the error for the different approximations is better than  $-21.4\%$  for equation (7)  $<0.1\%$  for equation (6) and  $<0.7\%$  for equation (8). Hence equation (8) gives sufficient accuracy for the calculation of  $\lambda$  from  $R$  without the use of numerical computational routines.

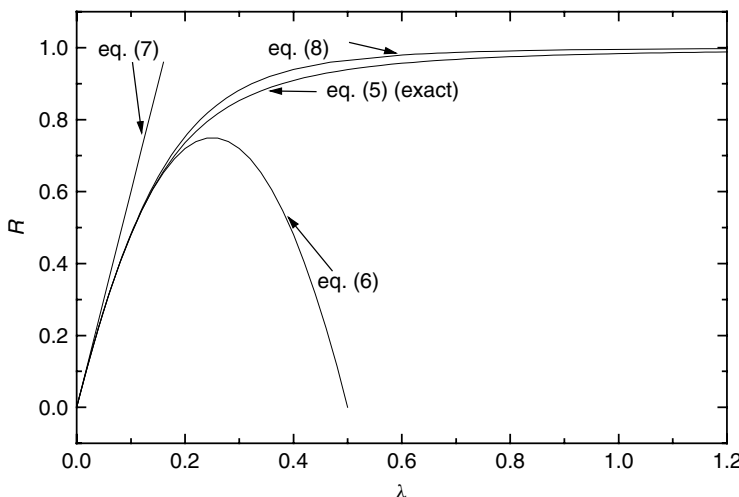


**Figure 3.** Functions of the retention ratio  $R$  over the retention parameter  $\lambda$  for the exact solution and the relevant approximations [equations (5)–(8)]. From von der Kammer (2005) [20]

In the case of  $R > 0.5$ , the determination of  $R$  may be hindered by the possible overlap of the sample peak with the void peak.

### 2.3 MODES OF RETENTION

In FFF, two different modes of operation are known, the diffusion dominated *Brownian mode* described in Section 2.2 and the *steric/hyperlayer mode*. The latter occurs for larger particles ( $d > 1 \mu\text{m}$ ) where diffusion is negligible and hydrodynamic lift forces acting on particles travelling close to the accumulation wall are significant. For this reason the term *lift/hyperlayer mode* is often preferred (Figure 4).

The Brownian mode generally applies to the fractionation of colloids that are much smaller than the mean thickness of the diffusive sample cloud formed in the channel (i.e.  $d_p \ll l$ ) such that particles can be treated as point masses. With increasing particle size, the fractionation gradually changes from Brownian to steric/hyperlayer mode (Table 2) as the Brownian mode assumption, that the particles are point masses with no physical size, becomes less valid.

It is crucial to be aware of the elution mode operating in a given FFF run as the elution order is reversed in steric/hyperlayer ( $R$  increases with  $d_p$ ) compared with the Brownian mode ( $R$  decreases with  $d_p$ ). This means that samples containing particle sizes spanning across the so-called *steric inversion point* (typically around  $0.5\text{--}2 \mu\text{m}$ ) cannot be fractionated unambiguously in a single FFF run. In addition, theoretical equations cannot be used to directly calculate particle sizes from FFF retention times in the steric/hyperlayer mode due to the complexity of the hydrodynamic lift forces. Instead, an empirical calibration with appropriate standards is required.

Hence the particle centres can no longer approach the accumulation wall to infinitely small distances. For real particles, the minimum distance of approach of the particle centre

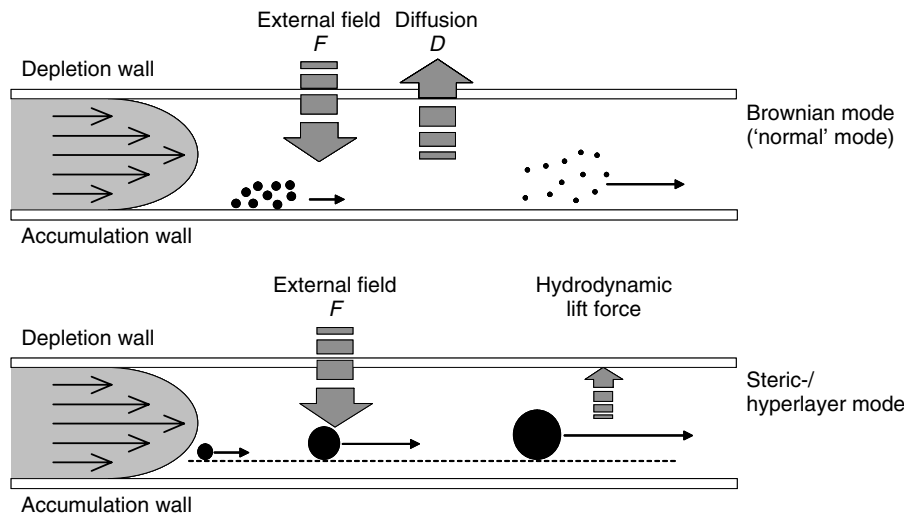


**Figure 4.** Schematic plot of the two different fractionation modes observed in FFF: the normal Brownian mode and the steric/hyperlayer mode. In the steric/hyperlayer mode, particle diffusion is negligible. Typical particle size ranges for the different modes are given in Table 2. From von der Kammer (2005) [20]

**Table 2.** Elution modes in FFF and the approximate diameter ranges

	Brownian	Steric/hyperlayer
Elution order	<i>Increasing size</i>	<i>Decreasing size</i>
FlFFF diameter range/ $\mu\text{m}$	0.001–2	0.8–50
SdFFF diameter range/ $\mu\text{m}$	0.05–2	0.8–50

equals the particle radius. This means that the effective channel thickness,  $w_{\text{eff}}$ , is reduced by twice the particle radius (or one diameter,  $d$ ), i.e.  $w_{\text{eff}} = w - d$ . Giddings and Myers introduced a modified retention expression for the Brownian mode to take into account this steric perturbation [21].

By applying this modified retention expression,  $R$  values for particles can be derived which span across the steric inversion point. Any given  $R$  value corresponds to two different particle sizes, the larger eluting in the steric/hyperlayer mode and the smaller in the Brownian mode (Figure 5). Both appear simultaneously at the outlet of the channel and can not be distinguished by most detection systems (Figure 6). Therefore, the samples must first be prefractionated (*e.g.* filtration or centrifugation) to ensure that no supermicron particles coexist with the colloids in the sample.

A number of important trends can be noted from Figure 5:

- The particle size at the steric inversion point depends on the channel height, run parameters such as the field strength and channel flow rate and particle characteristics such as size and mass which determine the field induced force.

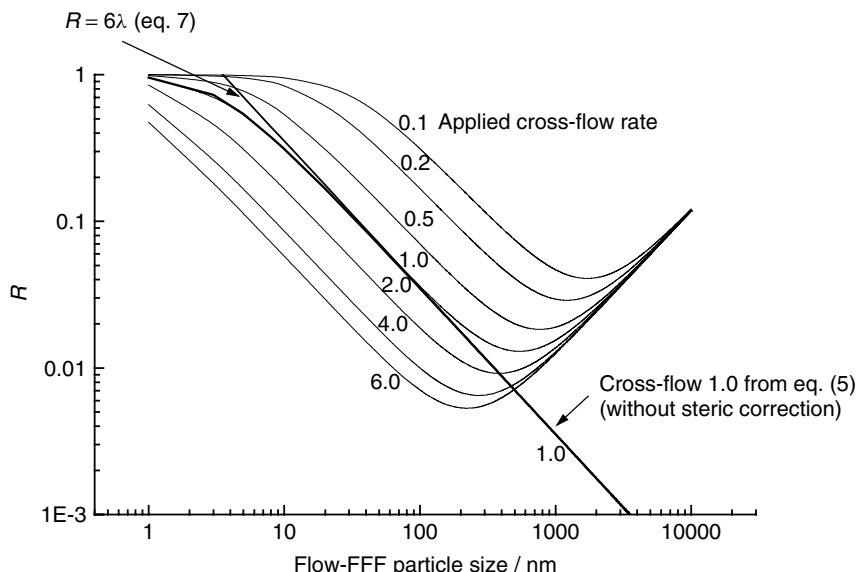


**Figure 5.** Comparison of  $R$  as a function of particle size for the standard expression without steric correction and the corresponding including steric effects. The numbers denote field strength as cross-flow rates in  $\text{cm}^3 \text{ min}^{-1}$  in a symmetric FIFFF channel with length 25 cm, breadth 2 cm and thickness 250  $\mu\text{m}$  at 25 °C. It is clear that two different particle sizes correspond to the same  $R$  value, hence these particles will elute at the same time if they are present in the sample. To avoid this situation, a sample should contain only particles above or below the steric inversion point, which is the minimum of the curves shown. It should also be recognised that for every field strength applied there is a limited region over which  $\log R$  is linearly related to  $\log d_p$ . From von der Kammer (2005) [20]

- A correct fractionation in constant field Brownian mode is restricted to the linear region of the  $R(d_p)$  function, limiting the size range to  $\sim 10\text{--}20$ -fold greater than the particle size of components which are sufficiently separated from the void peak.
- The lower size limit for an FFF analysis can be decreased by increasing the field strength, but this may also produce undesirable effects by decreasing the size where steric perturbations begin to be significant.

Although direct calculation of particle size is not possible, impressive fractionations in the pure steric/hyperlayer mode have been performed with analytes such as latex beads [22], chromatographic silica [23], red blood cells [24], yeast cells [25] and starch granules [26]. These are relatively simple systems compared with the complexity of the density, shape and size of natural aquatic colloids.

Steric SdFFF calibrated with polystyrene latex has been used to determine supermicron size distributions of sediment particles and pure clays [27]. The difference in density between the sample and calibration particles must be accounted for in this procedure [28]. Particle shape has a considerable influence on the hydrodynamic lift force and this will cause errors if spherical particles are used for calibration [29].

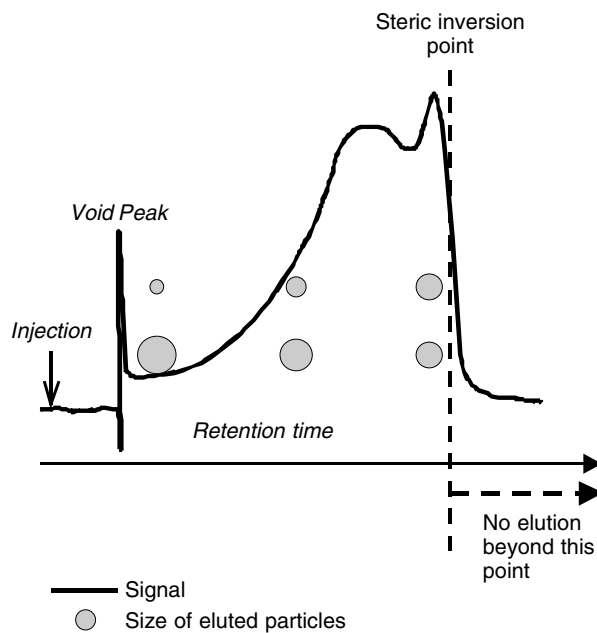


**Figure 6.** Schematic view of an FFF fractogram on a sample spanning across the steric inversion diameter. At a certain retention time both small and large particles elute, each migrating down the channel using a different mode as shown also in (*cf.* Figure 5). Therefore, it is generally necessary to ensure that the sample only contains particles below or above the steric inversion diameter

## 2.4 FIELD-FLOW FRACTIONATION SUBTECHNIQUES

Various types of fields can be used in FFF and the force exerted on samples will be related to sample properties. This fact can be used in order to gain information about the physicochemical properties of the sample components. As stated previously, the majority of FFF applications dealing with environmental colloids are based on two techniques, FIFFF and SdFFF, which use either fluid cross-flow or centrifugation to create the fields.

### 2.4.1 Flow Field-flow Fractionation

Flow-FFF utilises a secondary flow perpendicular to the axial carrier flow stream in the channel in order to generate an external force on the sample components. This is achieved by replacing the bottom and top walls of the channel by flat permeable frits and through the use of additional pumps to provide the cross-flow. The frit in the accumulation wall (cross-flow outlet) is covered by a membrane (minimum pore size  $\sim 0.5\text{--}1\text{ nm}$ ), which prevents sample compounds from leaving the channel. The technique can be further divided into two categories: symmetrical and asymmetric FIFFF. In asymmetrical FIFFF (aFIFFF, sometimes also termed AF4 or AF<sup>4</sup>), the top frit is replaced by an impermeable wall and the cross-flow is generated by operating the inflow at higher flow-rates than the outflow, thus forcing some of the fluid to exit through the lower frit. The asymmetric

variant has attracted much interest in the last decade and is today commercially available from three manufacturers in different set-ups using channel materials suitable for both aqueous and organic solvents.

All FIFFF techniques follow the same fractionation principles. The cross-flow drives the sample components to the accumulation wall; from there they also diffuse back into the channel thus establishing a dynamic equilibrium with a characteristic relative mean cloud thickness  $\lambda$  [equation (1)] depending on the component properties, cross-flow rates (field force) and channel dimensions. In FIFFF,  $\lambda$  can be determined:

$$\lambda = \frac{kTV^0}{fV_c w^2} = K_e/f \quad (9)$$

where  $V^0$  is the channel volume,  $V_c$  the cross-flow rate and  $f$  the friction coefficient, which accounts for the drag force transmitted to the compound from the cross-flow. In a FIFFF run with a constant cross-flow rate then  $k$ ,  $T$ ,  $V^0$ ,  $V_c$  and  $w^2$  are experimental constants ( $K_e$ ) and  $\lambda$  is therefore inversely proportional to the friction coefficient  $f$  as shown in equation (9). The friction coefficient can be related to the physicochemical properties of the sample by using either Stokes law, equation (10), or the Einstein equation, equation (11):

$$f_{\text{Stokes}} = 3\pi\eta d_h \quad (10)$$

$$f_{\text{Einstein}} = \frac{kT}{D} \quad (11)$$

where  $\eta$  is the dynamic viscosity of the carrier fluid and  $d$  the diameter of the particle. Substituting  $f$  in equation (9) yields

$$\lambda = \frac{kTV_0}{3\pi n V_c w^2 d_h} \quad (12)$$

$$\lambda = \frac{V_0 D}{V_c w^2} \quad (13)$$

Thus, the retention parameter  $\lambda$  is determined by the diffusion coefficient  $D$  of the respective particles or their equivalent Stokes diameter,  $d_h$ . The measured retention ratio  $R$  can therefore be directly transformed into the diffusion coefficient or the hydrodynamic diameter from first principles, ideally without external calibration. Equation (12) delivers only the equivalent spherical hydrodynamic diameter, which means the size of a sphere having the same hydrodynamic behaviour as the measured particle which is related to friction force experienced as well as the type (sticky–non-sticky) and thickness of the hydration shell.

**2.4.1.1 Symmetrical Flow FFF (sFIFFF).** The commercially available sFIFFF instruments originate from designs drawn by Myers and Giddings [7]. The channel is made out of two Perspex blocks in which flat ceramic frits are mounted (Figure 7). The blocks are separated by an accumulation wall membrane and a spacer, which defines the channel geometry and height.

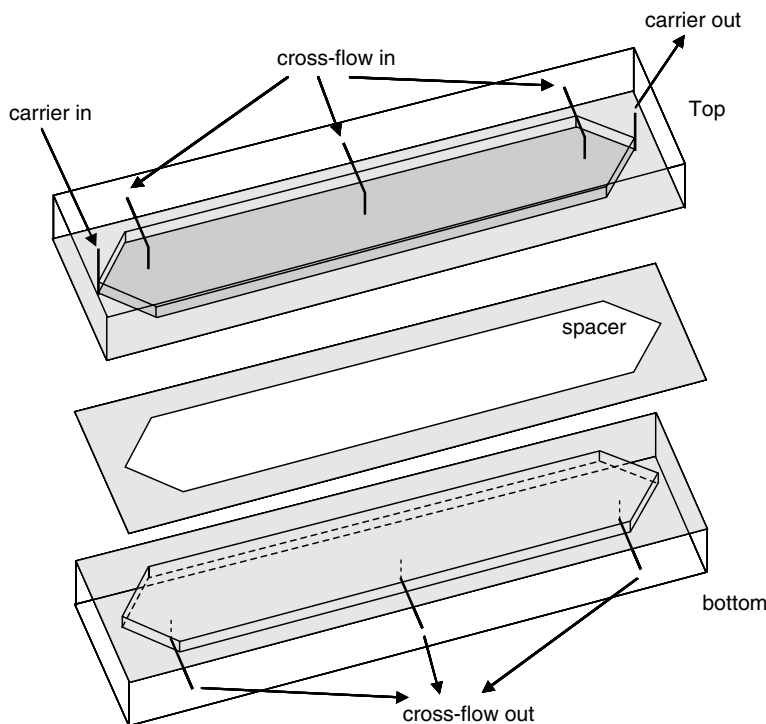


**Figure 7.** A cross-sectional view of an sFIFFF channel assembly, showing the upper and lower acrylic blocks with porous ceramic frits inserted, the spacer with the channel geometry cut out and the ultrafiltration membrane placed over the lower frit. The complete assembly is clamped together. From von der Kammer (2005) [20]

The carrier flow is usually delivered by an HPLC pump and the cross-flow can be maintained by a double-piston syringe pump or by an independent HPLC pump. Closed-circuit cross-flow delivery by a double-piston pump has the advantage of recirculation of the cross-flow with high precision in the flow-rate and a reduction of carrier liquid consumption. The serious disadvantage that may arise is that substances that pass the membrane are recycled into the channel via the top frit, which in turn may cause instability of the baseline and changes in the dissolved solute composition (*e.g.* ionic strength, pH, major or trace elements).

**2.4.1.2 Asymmetric Flow FFF (aFIFFF).** In aFIFFF, there is no upper frit or an independent supply of cross-flow (Figure 8). The cross-flow must be generated by a surplus of carrier flow entering the channel, which then leaves the channel via the cross-flow outlet ( $V_{in} = V_{out} + V_c$ , where  $V_{in}$  is the inlet,  $V_{out}$  the outlet and  $V_c$  the cross-flow volumetric flow-rate). The flow-rates are thus no longer independent of each other and must be carefully controlled. aFIFFF can be realised with either a flat channel [30,31] or a hollow-fibre FFFF [32,33]. Other specific differences with respect to sFIFFF are the sample injection procedure often employed and the spacer geometry. The conventional procedure of stopping the channel flow and only applying cross-flow to relax the sample is not feasible in

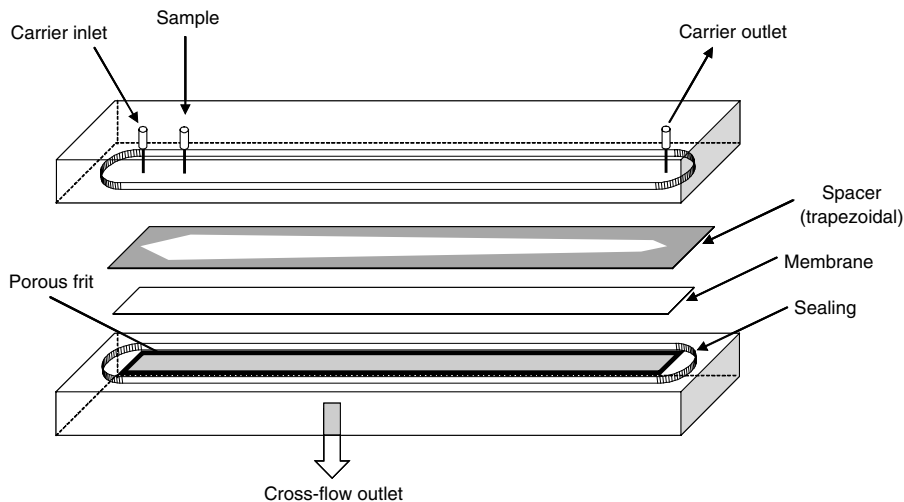


**Figure 8.** An example of an aFFF channel design (other designs exist) utilising a channel top made of glass or acrylic with ports for the carrier inlet, sample injection and detector outlet. From von der Kammer (2005) [20]

aFFF, where the use of injection into two opposing flows is used (Figure 9). During injection and relaxation, fluid is pumped into the channel from both ends, the normal outlet port becoming a second inlet port during this procedure. The injection of the sample can be done through either of the two opposing flow inlets or via an additional port slightly downstream of the channel flow input port. These focussing techniques [31] have the advantage of focusing the sample into a narrow zone and the injection of large sample volumes without losses in fractionation performance due to zone spreading often observed with sFFF.

A recent technical development in aFFF is a modified sample introduction technique where the sample is injected via the inlet port. The new injection port slightly downstream is used to feed additional carrier volume, which generates the focusing zone between these two inlets. Excess flow not exiting through the membrane is directed towards the outlet port creating the normal flow towards the detectors.

Since the cross-flow is extracted from the carrier flow along the channel, the carrier flow velocity decreases along the channel length from inlet to outlet. This can be minimised by choosing different spacer geometries (usually trapezoidal) with decreasing channel breadth from the injection point to the outlet. In some designs, the cross-flow drains freely, driven only by the pressure differences between the channel and atmosphere; alternatively, it may be controlled by a suction pump (*e.g.* a syringe pump). If the cross-flow drains freely, the control of either the channel outflow rate  $V_{\text{out}}$  or the cross-flow outlet stream  $V_c$  is required. This can be achieved by monitoring the flows and adjusting  $V_{\text{out}}$  or  $V_c$  with needle valves. If the cross-flow rate is changed during the FFF run, both the inlet flow ( $V_{\text{in}}$ ) and either the outlet or cross-flow flow-rates ( $V_{\text{out}}$  or  $V_c$ ) must be actively controlled. Whereas the inlet flow-rate is easily controlled by HPLC pumps, in one of the other two flow streams, either a syringe pump or a metering/control device must be employed. By adjusting the two opposing flow-rates, in a manner that is possible to define a certain zone

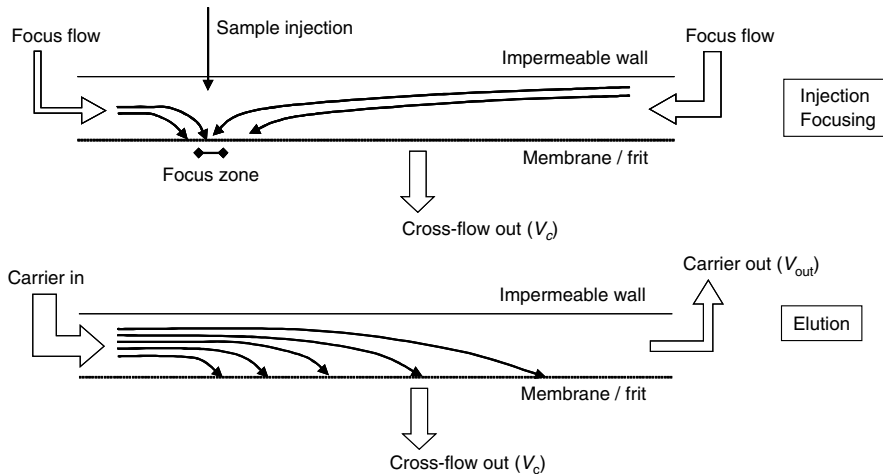


**Figure 9.** Sample injection and focusing are shown for the channel design given in Figure 8. The focus zone is created by balancing two opposing flows (one large and one small). The sample can be injected in either of these flows or in a separate flow entering in the vicinity of the focus zone. From von der Kammer (2005) [20]

in the channel where the lateral flow is virtually zero, all flow vectors in the channel are directed towards this zone. The sample will be focused into a thin starting line independent of the sample volume injected. Figure 9 shows an example of sample focusing and elution in aFIFFF.

Another recent development is the slot-outlet or smart stream splitting at the outlet. This is comparable to the frit-outlet technique in sFIFFF and allows preconcentration of the sample by removing a fraction of the carrier liquid through the top-wall near the end of the channel. The design differs among manufacturers and the preconcentration factor achievable depends on  $\lambda$  (and hence the thickness of the zone not occupied by the sample) and comes at the cost of small outlet flow-rates. In aFIFFF analysis, the void time  $t^0$  may be obtained by equation (14) [34]:

$$t^0 = \frac{V^0}{V_c} \ln \left\{ 1 + \frac{V_c}{V_{out}} \left[ 1 - \frac{w \left( b_0 z' - \frac{b_0 - b_L}{2L} z'^2 - y \right)}{V^0} \right] \right\} \quad (14)$$

The parameters in equation (14) are obtained from the geometry of the spacer (Figure 10), where  $y$  is the area of the tapered inlet section.

When compared to the symmetric channel, the asymmetric technique provides some important advantages:

- The channel can be observed through the transparent top-wall so that flow streams and focusing can be verified using coloured polymers such as dextran blue.
- When focusing is employed, sample volume does not affect fractionation, which results in increased resolution.

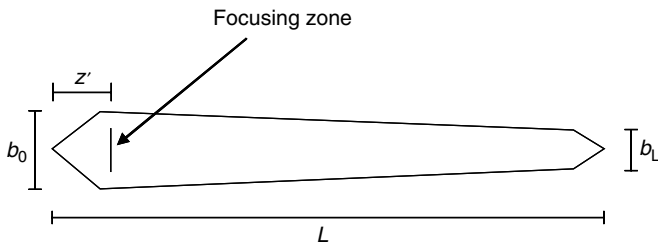


**Figure 10.** The most common geometry of the spacer used in aFICFFF. The trapezoidal shape is used to reduce the effect of a non-constant channel and cross-flow along the channel (due to non-independent supply of cross-flow). The parameters used in equation (14) are shown. From von der Kammer (2005) [20]

- On-channel preconcentration of dilute samples is an inherent feature.

Nonetheless, there are also some drawbacks of aFICFFF:

- Steric inversion is reported to start at lower particle diameters and extends into the submicron range (>ca. 500 nm).
- The theoretical treatment of the fractionation is considerably more complicated.
- At low cross-flow rates (<1 cm<sup>3</sup> min<sup>-1</sup>), focusing is slow whereas at higher focusing flows, and consequently higher cross-flow rates, sample recovery is reduced for larger (>200 nm) particles.
- When the valves and pumps switch from focus to elution mode, there may be a critical time-span where the flow conditions in the channel are not ideal. This has been overcome in a newer commercial system by using the same total flow-rates for the channel inlet during both focusing and fractionation. This eliminates pressure transients when the flows are switched, although this does put some restrictions on the selection of flow-rates.

#### 2.4.2 Sedimentation Field-flow Fractionation

The layout of a centrifugational FFF channel, which applies centrifugal force as the field, is shown in Figure 11 [6]. Such a set-up permits a large enhancement of the limited gravitational FFF due to the higher field forces that are available. In this case, the channel is placed in a centrifuge drum and spun at speeds of up to about 20 000 rpm (although 3000 rpm is the upper limit used in most work). The only commercially available instrument has capabilities up to about 3000 rpm, which allows particles as small as 50 nm to be separated.

In contrast to FICFFF, where the sample components are fractionated according to their diffusion coefficient, the SdFFF system fractionates according to the effective (or buoyant) mass ( $m_e$ ), i.e. the product of particle volume,  $V_p$ , and the density difference between the particle and the carrier medium ( $\rho_p - \rho_c$ ).

The centrifugal force acting on the sample components is described by

$$F = m_e \omega^2 r_c \quad (15)$$

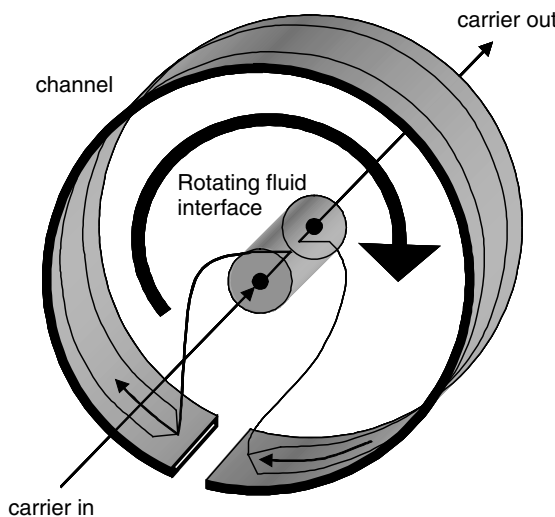


**Figure 11.** Schematic diagram of an SdFFF channel, where the channel is bent around a centrifuge basket and the channel flow enters and exits the channel through seals and the centrifuge axis. From von der Kammer (2005) [20]

where  $\omega$  is the angular rotation frequency and  $r_c$  the radius of the centrifuge from the rotation axis to the channel;  $\omega$  is defined as  $\omega = 2\pi f_c$ , with  $f_c$  being the rotation frequency where  $f_c = \text{rpm}/60$ . An expression for the retention parameter  $\lambda$  can be derived from equations (1) and (15):

$$\lambda = \frac{kT}{m_e \omega^2 r_c w} \quad (16)$$

Equation (17) is then obtained for spherical particles in SdFFF:

$$\lambda = \frac{6kT}{\pi d^3 |\rho_p - \rho_c| \omega^2 r_c w} \quad (17)$$

using  $V_p = \pi d^3 / 6$ , where  $d$  is the equivalent spherical particle diameter. SdFFF retention depends on the particle diameter cubed, which gives SdFFF an outstanding fractionation power, and hence resolution, with respect to particle size.

## 2.5 PREFRACTIONATION OF STERIC PARTICLES

To avoid errors due to larger particles eluting in steric mode, particles above the steric inversion ( $\sim 1 \mu\text{m}$ ) must be removed before FFF analysis of submicron particles. The most common methods are filtration or settling (gravitational or centrifugation), for which great care has to be taken to ensure that the prefractionation does not change the colloidal size distribution. For example, it has been found that colloidal particles much smaller than the nominal pore size of the filters can be retained by the filtration membranes. This is explained by trapping of colloids in the pores and by concentration polarisation followed

by membrane surface coagulation [35]. This effect is enhanced for smaller pore sizes. It should also be noted that the pore size of commercial filters is generally given as the size of the largest particle that is quantitatively retained. The membranes also retain large amounts of particles below the pore size [36]. Therefore, it is recommended to use the largest pore size membrane possible (*e.g.* 1–5 µm) that will still retain most of the steric particles. Biological particles such as bacteria and algae are most efficiently removed by filtration as opposed to centrifugation due to the small density differences between the cells and water. On the other hand, due to the above constraints of filtration, gravitational settling and centrifugation are preferred methods for particle prefractionation.

## 2.6 DETECTION

Since the main goal of the FFF analysis is to produce particle size distributions, the detector should respond to particle volume, mass or number in the eluting size fractions (Table 3).

Detection systems can be either on-line detectors such as those used in HPLC or off-line systems which are applied to characterise fractions after collecting volume fractions from the eluent (Figure 1).

Detectors may also be used to validate the particle size distribution of the sample or to retrieve additional size-resolved physicochemical parameters including particle morphology (Table 3). The general techniques used for conversion of the fractograms into particle size or molecular weight distributions are discussed in Section 2.9.

Other external detectors can deliver additional information about the sample fractions eluting from the channel. For example, ICP-MS determines major and trace element concentrations as a function of particle size [14,37–40]. Light scattering detectors after FFF fractionation can provide independently acquired particle size or molar mass distributions [41,42].

UV detectors are the most commonly used detectors for FFF applications due mainly to their availability, simplicity and low cost. On the other hand, the quantification of the separated particles or macromolecules is not always straightforward since the UV signal is actually a superposition of an absorption and turbidimetric measurement, which is a combination of absorbance, light scattering (particle sizes less than or equal to the wavelength of the light used) and light obscuration (particle size  $\gg$  wavelength). The absorbance contribution follows Beer's law, but there is a more complicated relationship involved with the scattering and obstruction contributions. In general, large particles scatter light more effectively than smaller particles, and particles with varying composition and refractive indices give rise to further complications. Hence the signal will be dependent on specific light absorption (if present) particle size and particle properties in addition to the concentration. A recent approach uses a fluorescence spectrometer as a simple light scattering detector by setting the excitation and emission wavelengths to identical values. This allows the measurement of particle turbidity at 90° (nephelometry) at a freely selected wavelength (280–750 nm). The signal obtained is selective for inorganic or biological particles and very insensitive to natural macromolecules such as DOC. An increased sensitivity compared with UV–VIS spectrometers has been observed for soil-type colloids [43,20].

When fractionating environmental samples with a large heterogeneity in shape (for FlFFF) and chemical composition (for SdFFF), FFF elution may not necessarily follow FFF theory exactly. In such cases, it is advisable to include an independent size

**Table 3.** Detection systems used for environmental FFF applications and the parameter that is determined

Detector	Parameter determined	Comments
<b>Online</b>		
UV-VIS	Absorbance	Requires sample to have a chromophore
	Scattering/turbidity	Requires particles to be large enough to scatter light, signal is depending on concentration and several particle properties incl. size
Fluorescence	Fluorescence	For fluorescing organic matter; Humic-like: $\lambda_{\text{ex}}/\lambda_{\text{em}}$ 330–350/420–480 nm Fulvic-like: $\lambda_{\text{ex}}/\lambda_{\text{em}}$ 220–240/420–450 nm <sup>a</sup>
	Nephelometric turbidity	For $\lambda_{\text{ex}} = \lambda_{\text{em}}$ : detector optics must be suitable (low stray light)
ICP-MS	Elemental concentrations for major/trace elements	Elemental distributions; elemental content in colloidal fraction
ICP-AES	Elemental concentrations for major elements	Elemental distributions; elemental content in colloidal fraction
Static light scattering	Root mean square radius of gyration	In the limits of Rayleigh–Gans–Debye approximation
Dynamic light scattering	Diffusion coefficient/hydrodynamic radius	On-line for particles <10–25 nm $R_h$ ; stop flow-bypass for larger particles
Differential refractive index (DRI)	DRI $\propto$ mass concentration	Provided $dn/dc$ (refractive index increment) is known
Laser-induced breakdown detection (LIBD)	Breakdown probability proportional to number concentration $\times$ particle size	FFF provides particle size information to retrieve number concentration; limited by similarity of breakdown response between standards and sample particles
<b>Offline</b>		
Electron microscopy	Morphology, particle size	Mainly used for validation of FFF
Isotope labelling	Obtain adsorption density distributions	Potential to be an on-line detector
ICP-MS; ICP-OES GF-AAS; TXRF	Elemental concentrations for major/trace elements	Option if instrumentation is not at place; risk of contamination; time consuming/tedious

<sup>a</sup>  $\lambda_{\text{ex}}$ ,  $\lambda_{\text{em}}$  denote excitation and emission wavelength selection of the fluorescence detector, respectively.

measurement after the fractionation (*e.g.* light scattering). The advantage of using on-line light scattering detectors is that the FFF provides enough reduction in polydispersity for the light scattering detectors to determine accurate size distributions [42,20]. In combination with FFF-derived size parameters or by combining static and dynamic light scattering techniques, information about molecular conformations, particle density or shapes can be obtained [42,47,48,20].

Laser-induced breakdown detection (LIBD, Chapter 11) is also a promising detection method for FFF. Very briefly, the principle of detection is that when a colloid particle

**Table 4.** Approximate detection limits with various detection systems exemplified from experience with organic and inorganic colloids<sup>a</sup>

Detector	Organic colloids	Reference	Inorganic colloids	Reference
UV-VIS	1 mg dm <sup>-3</sup>	[44]	~0.8 mg dm <sup>-3</sup>	[42,20,45]
Q-ICP-MS	e.g. Fe: 100 µg dm <sup>-3</sup> , La: 5 µg dm <sup>-3</sup>	[37]	e.g. Fe: ~400 µg dm <sup>-3</sup>	[45]
HR-ICP-MS	e.g. Fe: 20 µg dm <sup>-3</sup> , La: 0.2 µg dm <sup>-3</sup>	[40]	e.g. Fe: ~100 µg dm <sup>-3</sup>	[46]
SLS	1 to 20 µg dm <sup>-3</sup>		1 mg dm <sup>-3</sup> ~200 µg dm <sup>-3</sup>	
LIBD	~5 µg dm <sup>-3</sup> Polystyrene	[45]	Iron oxyhydroxide	[45]

<sup>a</sup> Assumptions: stop-flow injection using 0.075 cm<sup>3</sup> sample loop.

passes through the focal volume of the focused, pulsed laser, then the power density to induce breakdown of the dielectric properties of the solvent is lower than that for pure water. Therefore, if the laser energy is correctly tuned, plasma formation will only occur when a colloid passes through the focal volume of the optical cell. The parameter that is measured is the breakdown probability, which depends both on particle concentration and on size (Table 4). The main advantage of LIBD is that it is extremely sensitive even to small colloids (Table 4).

The first paper that was published used sFIFFF coupled to LIBD and compared this with sFIFFF-MALLS [49]. The detection limit for polystyrene standards (19–102 nm) was 2–3 orders of magnitude lower for sFIFFF-LIBD than for a corresponding light scattering detector. They concluded that the main limitations on the detection were due to impurities in the carrier and particles that was leaching from the ceramic frit in the sFIFFF channel. Therefore, they optimised the method by changing to an aFIFFF system with no upper frit and improving the flow cell of the LIBD [45]. These modifications resulted in a 2–10-fold further reduction in detection limit.

When comparing polystyrene with iron oxyhydroxide colloids, they also found that the breakdown probability depended not only on concentration and size but also on composition. This point needs to be investigated further before LIBD can be routinely used as an FFF detector but it shows great potential for the detection of the often very low concentrations of colloids found in many aquatic environments.

The recent development of an on-line DOC detector for FIFFF, which is based on wet chemical oxidation (persulfate) assisted by UV irradiation, could result in a breakthrough for the characterisation of macromolecular organic matter with FFF [50].

It is also possible to collect fractions for off-line analysis (e.g. electron microscopy), which can complement on-line detection [51–53].

In conventional FFF, only small volumes of sample (0.025–0.1 cm<sup>3</sup>) are injected and the sample is extensively diluted with carrier during the fractionation. Therefore, in order to have an eluted concentration that exceeds the detection limit, the first priority is to use the most sensitive detectors available (Table 4). For some environmental samples, (e.g. sediment particles), it is possible to vary the concentration of the injected sample, but in many other cases this is not practical due to concentration constraints (e.g. DOM, low suspended solids in natural waters). If the original sample concentration is

not high enough to exceed the detection limit, then there is the possibility of using preconcentration or post-channel concentration methods. The preconcentration methods can be external [11,54] or internal (on-channel preconcentration) [44].

The on-channel preconcentration approach can be used both for aFIFFF and for sFIFFF to study chromophoric organic matter in fresh and marine waters. In this case, a sample injection is employed in either the forward or backward focusing flow streams [44,55]. Lyvén *et al.* [44] showed that almost quantitative recovery could be achieved for the preconcentration of low molar mass polymers and natural water colloids with sample injection volumes ranging from 1.7 to 100 cm<sup>3</sup> [44]. The molar mass of the samples was similar to the membrane cut-off. Injection flows, membrane type and carrier were optimised. Injections in both the forward and backward focusing flow streams were evaluated: recoveries were slightly better for backward injection. However, there is a larger risk of incomplete focusing with backward loading due to the longer distances that the samples need to travel. An experimental approach was used to determine the minimal time required for sample loading and focusing. To ensure sufficient focusing time for all colloids, the focusing time was increased until a stable retention time was attained for the largest reference standard. This on-channel preconcentration method was later used in sFIFFF coupling with ICP-MS for determining trace element size distributions for natural water colloids [37–40,56]. Due to the very low concentrations of both colloids and trace metals found in natural waters, these determinations of size-dependent trace element associations with colloids as a function of particle size would not have been possible without the preconcentration procedure.

The sample peak width also influences the detection limits of the original sample. A very broad peak (*e.g.* for high size polydispersity and the use of high field strengths) will result in more dilution of the eluted peak and hence a higher sample detection limit than a narrower peak with the same injected sample mass and peak area.

In coupling FFF to ICP-MS, it has recently been observed that the use of a volatile electrolyte, such as NH<sub>4</sub>NO<sub>3</sub>, in the carrier causes less problems of salt deposition in the ion source of the ICP-MS as compared with the use of, for example, NaCl [40]. Ideally, an absence of electrolyte present in the carrier would be best for ICP-MS, but the FFF separation needs some electrolyte (*e.g.* 10<sup>-3</sup> mol dm<sup>-3</sup>) in order to minimise wall repulsion effects. Ionic dispersant and a buffer are often also desirable for stabilisation of the colloids.

For the determination of trace compounds associated with colloids (*e.g.* trace elements using ICP-MS coupling), it is important to be aware that the colloids are continuously washed with clean carrier during the fractionation so the sample is exposed to sorption disequilibria during the analysis. Therefore, only slowly dissociating compounds associated with the colloids are determined and weakly associated, labile colloidal compounds dissociating on the time-scale of the analysis (minutes to an hour) will be underestimated. In FIFFF, both the desorbed and the truly dissolved fraction permeate the ultrafiltration membrane on the accumulation wall and are never recorded by the detector, whereas in SdFFF both of these fractions will stay in the channel and either elute in the void peak (unretained) or be slightly retained if desorption is slow (minutes). The advantage of using an on-channel preconcentration instead of an external ultrafiltration procedure is mainly due to the short time that the sample is subject to modified conditions and the simplicity of adding the preconcentration step to the FIFFF method. In recent commercial FIFFF

systems, on-channel post-concentration methods have been applied by reducing excess carrier from the upper wall of the channel just before the outlet (frit-outlet or slot-outlet). There have been some difficulties in the production, maintenance and precision of some of these devices. However, there are now systems commercially available for symmetrical FIFFF using the frit-outlet system and for aFIFFF using a slot-outlet for removal of excess liquid. These can result in up to a fivefold increase in the concentration of the eluent passing through the detector, which yields correspondingly lower detection limits.

If the particle concentration is sufficiently high, particle–particle overlap may occur (overloading) [57]. Under such conditions, the sample will not be properly relaxed (i.e. attain its equilibrium particle cloud thickness) and therefore particles will extend further into the channel and elute faster than predicted by theory. Caution must be taken when injecting large amounts of material with any injection technique. During the on-channel preconcentration and stop-flow relaxation steps, overloading may become a problem. Overloading effects can be identified by an earlier eluting peak with a fronting peak shape.

Fortunately, for FFF separations, detector sensitivity is usually sufficiently high to detect the separated components at sample concentrations well below the overloading concentration. However, for further characterisation of the particulate material by other detection systems, *e.g.* mass spectrometry, or the subsequent analysis of collected fractions, it is often necessary to inject large amounts of sample material in order to exceed the detection limits. In these cases it is likely that overloading effects affect the resulting size distribution.

The best way to rule out overloading is to inject various amounts of sample in order to follow any changes in the retention times and peak shapes. The applied field in stop-flow relaxation or focusing flows in on-channel preconcentration could also have an affect on non-ideal behaviour. This causes the sample component clouds to be compressed during high-field periods, causing both higher local concentrations and a potential interaction with the accumulation wall. When working with sample amounts near the overloading point, a variation of the field strength acting on the analytes can be used to find conditions where overloading starts.

To achieve low detection limits, it is very important not to have system contamination or carry-over from previous analysis. Contamination can include leaching from the membrane and particles from the upper frit (FIFFF) or centrifuge seals (SdFFF). Therefore, it is essential to clean the membrane and channel with a suitable cleaning protocol after assembly and to rinse the system continuously with a low carrier flow between analyses. Following fractionation, it is also best practice to turn the cross-flow off in order to wash out any material that may have adhered to the accumulation wall. By injecting a suitable wash solution between runs, it is possible to wash out adsorbed material; however, the time to get back to equilibrium conditions can be quite long. Therefore, it is often more practical to carry out a wash each day rather than between every run.

## 2.7 CALIBRATION OF CHANNEL DIMENSIONS

If FFF theory is to be used to calculate particle parameters such as size, then it is essential first to determine the channel parameters (void volume, channel height, external volumes, *etc.*).

The critical parameter is the channel height,  $w$ , which must be measured very accurately. Even in SdFFF, where the channel height is equal to the spacer thickness, deviations

usually occur. In FlFFF, the membrane covering the accumulation wall may protrude into the channel and consequently reduce the nominal channel height given by the spacer thickness. The extent of this protrusion can vary with membrane material and method of production and also with the cross-flow rate applied. There are several different methods of calibrating the channel volume or the channel thickness, summarised below.

### 2.7.1 Injection of Non-retained Sample to Obtain Void Volume

It is possible to inject a truly dissolved substance that is highly diffusive and therefore will travel at the average channel flow velocity (void volume). For precise work, fairly low flow-rates should be used ( $<0.5 \text{ cm}^3 \text{ min}^{-1}$ ) and the first moment of the peak used. Accurate estimates of the inlet and outlet dead volumes are also required. This method works reasonably well in SdFFF but in FlFFF most of injected substances will permeate the membrane and therefore not be measurable.

### 2.7.2 Breakthrough Volume Method

A method that is complementary to that in Section 2.7.1 is the breakthrough volume method [58]. This relies on the injection of a colloidal or particulate probe with very slow diffusion and without any field. In such a case, the particles will be somewhat randomly distributed across the vertical axis of the channel. Particles that will be situated in the centre of the channel will travel along the apex of the parabola of the laminar flow profile at a velocity that is 1.5 times as fast as the average flow velocity [58]. Reasonably high flow-rates are used ( $1\text{--}3 \text{ cm}^3 \text{ min}^{-1}$ ) to reduce the residence time in the channel, thus minimising diffusion away from the centre line of the channel.

### 2.7.3 Back Calculation Using a Standard of Known Size

The most reliable method is probably to fractionate narrowly distributed standards of known size and to tune the value of the channel thickness to back calculate the correct size. It is important that the size parameter specified for the standard particles (*e.g.* hydrodynamic diameter or buoyant mass) matches the primary sizing parameter of the particular FFF method involved.

### 2.7.4 Calibration of Channel Dimensions Using Multiple Standards

Channel dimensions may be calculated from a single injection of a spherical standard of known size using basic FFF theory or the appropriate approximations given in equations (6)–(8). Due to statistical errors, the possible effects of steric inversion or lift forces for the larger particles, and limitations due to approximations of equations (6)–(8), it is advisable to use multiple standards which span the size region of interest. Having established a plot with at least three particle diameters over a range of elution volumes, it is possible to generate a simple calibration function.

Finally, in aFlFFF it is also important to determine the focusing point (either experimentally or theoretically) and to correct the channel volume for that before calibrating the channel thickness [59].

## 2.8 CONSTANT OR PROGRAMMED FIELD RUNS

If a constant field sufficient to separate the smallest particles is applied to a sample containing a wide particle size range, the elution time for the separation of the largest particles becomes very long. Therefore, in practice, a high field is applied initially, which is then reduced over time. Several field decay algorithms (or programs) have been used, including ones where the field is reduced with a linear, parabolic or exponential function. Field programming is often essential in SdFFF due to the very high selectivity (i.e. 3). It is less crucial in other forms of FFF where the selectivity may be lower (i.e. 1 in FlFFF). In certain cases field programming is also effective in increasing resolution for these techniques [60,61].

An effective program for reducing the field with time is known as the power decay approach [62]. In SdFFF, it involves applying a constant speed,  $\omega_0$  for an initial period,  $t_1$ , after which the speed is decayed according to a power equation:

$$\omega = \omega_0 \left( \frac{t_1 - t_a}{t - t_a} \right)^4 \quad (18)$$

where  $\omega$  is the angular speed of the centrifuge after time  $t$  from the start of the SdFFF run and  $t_1$  and  $t_a$  are constants that control the field decay rate. This approach has the advantage of providing a nearly constant level of fractionating power over the size range required [62].

## 2.9 CONVERSION OF FRACTOGRAMS TO PARTICLE SIZE DISTRIBUTIONS

The raw data obtained from an SdFFF instrument is a plot of a detector signal versus elution time or volume and is referred to as a fractogram. The equivalent spherical particle diameter corresponding to a given elution time or volume can be computed as discussed above. In the case of field decay FFF runs, numerical computations can be carried out in a series of short time intervals so that the particle diameter can be calculated for each elution time [19,62]. This provides the  $x$ -axis of the particle size distribution (PSD).

The UV detector response, which is designated  $UV_i$  at point  $i$  along the elution profile, is assumed to be proportional to the mass concentration of the sample in the eluent ( $dm_i^c/dV_i$ ), which can be converted to the appropriate  $y$ -axis for a particle size distribution ( $dm_i^c/dd_i$ ) by

$$\frac{dm_i^c}{dd_i} \approx \frac{dm_i^c}{dV_i} \cdot \frac{\delta V_i}{\delta d_i} \propto UV_i \frac{\delta V_i}{\delta d_i} \quad (19)$$

where  $m_i^c$  is the cumulative mass of sample eluted up to elution volume  $V_i$ ,  $d_i$  is the particle diameter eluting at  $V_i$  and  $\delta d_i$  is the increment in  $d_i$  corresponding to increment  $\delta V_i$  in  $V$  at point  $i$  along the fractogram. The quantity  $\delta V_i/\delta d_i$  can be calculated by applying the FFF retention theory as described above.

The PSD is a plot of  $dm_i^c/dd_i$  versus  $d_i$ . This form of the PSD, which is taken as the area under the curve between given diameters, is proportional to the mass of sample in that size range. Since the  $x$ -axis is not in absolute units but is only proportional to  $dm_i^c/dd_i$ , it is often necessary to normalise the PSD. Areas for a given size range are typically plotted as fraction or percentage of mass of particles in that range.

### 2.9.1 Element Content Distributions

If the FFF eluent is fed into an element analysis detector such as an ICP-MS instrument, an ion current  $I_{E_i}$  is generated for each element  $E$  of interest, where  $I_{E_i}$  is proportional to the mass concentration of the element present in the eluent ( $dm_{E_i}^c/dV_i$ ). Then the element fractogram is converted to an element-based particle size distribution using the equation

$$\frac{dm_{E_i}^c}{dd_i} \approx \frac{dm_{E_i}^c}{dV_i} \cdot \frac{\delta V_i}{\delta d_i} \quad (20)$$

where  $m_{E_i}^c$  represents a cumulative mass of element  $E$  eluted up to the digitised point  $i$  on the fractogram. The  $dm_{E_i}^c/dV_i$  is the element concentration in the eluent and is obtained from  $I_{E_i}$  by calibration with standard solutions. The element-based particle size distributions are obtained by plotting  $dm_{E_i}^c/dd_i$  against particle diameter  $d$ .

### 2.9.2 Element Atomic Ratio Distributions

Element atomic ratio distributions indicate changes in chemical composition across the entire size range of the sample. By selecting two appropriate elements [ $E_{(a)}$  and  $E_{(b)}$ ], the ratios of their molar concentrations can be computed from the equation

$$\frac{n_{E_{(a)i}}}{n_{E_{(b)i}}} = \frac{dm_{E_{(a)i}}^c}{dV_i} \cdot \frac{dV_i}{dm_{E_{(b)i}}^c} \cdot \frac{AW_{(b)}}{AW_{(a)}} \quad (21)$$

where quantities (moles) of the different elements are represented by  $n_{E_{(a)i}}$  and  $n_{E_{(b)i}}$  and their atomic masses are indicated by  $AW_{(a)}$  and  $AW_{(b)}$ , respectively. This ratio can then be plotted against particle diameter  $d_i$ .

## 2.10 SAMPLE RECOVERY

A simple recovery test can be performed by diluting the sample to a suitable concentration and injecting it into the system without a relaxation procedure and without any field. The sample plug will generate a short and high signal trace, which is evaluated for its peak area and compared with the signal area after normal fractionation. A more sophisticated approach uses an extra tube to bypass the channel. It is an advantage to use long tubes of large inner diameter to generate some sample dispersion, which makes the signal slightly broader and less high. If there is a low recovery of the sample, then the sample should initially be injected with no field or a very low field and no relaxation with a successive increase first of the relaxation time and then of the field. The integrated detector signal can be monitored for decreases in sample recovery.

## 3 SIZE FRACTIONATION OF MACROMOLECULES

In most aquatic environments, natural organic matter (NOM) is an important phase involved in many biogeochemical cycles and responsible for the fate and transport of many trace constituents. Truly dissolved and colloidal forms of NOM in surface waters

result to a significant extent from the degradation of terrestrial plants and other soil leachates. The most studied group of compounds is the humic substances (HS). This material is known to be old, refractory material that is microbially available to only a small extent. In rivers, lakes and especially seawater, biological production may also produce new organic matter. This aquagenic organic matter is believed to be transformed and recycled more rapidly than terrestrial organic matter.

Colloidal NOM (nominally defined as macromolecules or aggregates with size 1 nm–1 µm) has been extensively studied largely due to its high binding capacity for trace constituents (*e.g.* metals and organic contaminants) (Chapter 3) and for its optical properties. The binding of trace constituents affects its transport properties and bioavailability. Colloidal organic matter contains some important aromatic structures with light-absorbing and fluorescing properties. This chromophoric or coloured NOM increases the light attenuation (thus affecting photosynthesis) and is involved in various photochemical transformations in surface waters.

### 3.1 COLLECTION AND PRECONCENTRATION OF COLLOIDAL ORGANIC MATTER

Colloidal NOM is present in rather low concentrations in most natural waters (less than 1 mg dm<sup>-3</sup> in seawater; up to 100 mg dm<sup>-3</sup> in some rivers), so in order to characterise the material the common approach has been to isolate and sometimes also desalinate the sample. For FFF analyses, extremely organic-rich waters have been analysed without any preconcentration [12], but generally the NOM must first be concentrated.

The most common isolation methods for NOM are various solid-phase extraction protocols with different pH and solvent treatments. Fractions are often operationally defined as humic acids (soluble above pH 2), fulvic acids (soluble at all pH). Both humic acid and fulvic acid isolates have been characterised with FIFFF. The advantage of these isolation protocols is that large quantities of material can be isolated and freeze-dried. The main disadvantage is that it is not clear to what extent the material is changed and how relevant the fulvic and humic fractions are compared with its unperturbed aqueous state.

The second most common method of preconcentration is cross-flow ultrafiltration (CFF) (Chapter 4), where a ultrafiltration membrane of *ca.* 1000 g mol<sup>-1</sup> molecular weight cut-off (MWCO) is most often used. CFF is fairly simple to set up and it can also allow the processing of large volumes of water (concentration factors from 20 to 100), but it is time consuming (sample is recirculated over the membrane surfaces for many hours). Another disadvantage of CFF is that the MWCO of the membrane is not very precise. For example, some of the material above the MWCO will permeate the membrane and some of the smaller molecules will be retained (also true for FIFFF). One advantage of the combination of CFF preconcentration with FIFFF analysis is that the same type of ultrafiltration membrane can be used with both techniques. FIFFF has been used to study NOM which was fractionated by ultrafiltration membranes. It was found that the ultrafiltration separation was not strictly size or charge selective, but rather the material was fractionated based on chemical composition [63,64]. FIFFF has also been used to study membrane fouling [65].

An effective method of concentrating colloidal NOM for FIFFF utilises the various variants of on-channel preconcentration that can be used in both sFIFFF and aFIFFF

(Section 2.6). On-channel preconcentration has many similarities to cross-flow filtration (CFF); however, in addition, it can be done quickly with the analysis directly following the concentration step under very similar conditions to the FFF. Due to the quick (*ca.* 30 min) preconcentration step, it is easy to vary the conditions in order to optimise the method. On-line concentration has been applied for several studies of colloidal NOM [37–40,56,66,67]. On a few occasions the method has been used for large sample volume injection in aFICFFF for colloidal NOM [68].

### 3.2 DETERMINATION OF SIZE AND MOLAR MASS DISTRIBUTIONS OF COLLOIDAL ORGANIC MATTER USING FLFFF

Beckett and co-workers published the first applications of sFICFFF on fulvic and humic acids starting in 1987 [12,69]. They reported molar mass distributions calculated from FFF fractograms based on calibrations with polystyrene sulfonate standards. Following those initial studies, many applications of FICFFF on isolated HS and non-isolated chromophoric dissolved organic matter (DOM) from rivers, lakes, groundwater, soils, compost and landfill leachates and sediments have been published [44,68,70–78].

The consensus has been that the molar mass of HS is much lower than was earlier believed. Generally, the molar mass of fulvic acids is in the range 700–1500 g mol<sup>-1</sup> and that of humic acids 1500–5000 g mol<sup>-1</sup>. The weight- and number-average molar masses have been calculated and also the polydispersities (the ratio of the two), which was generally lower for fulvic than for humic acids.

With the application of their new on-line DOC detector for FICFFF, Ressat and Hendry [50] presented molar mass distributions of both UV absorbance and DOC, but most importantly by their ratio or normalised intensity comparison (NIC), the so-called specific UV absorbance (SUVA), as a function of molar mass was derived. It has been shown previously that the SUVA at 254 nm correlates with the aromaticity of the sample. Therefore, with this method it is possible to study aromaticity as a function of molar mass. The NIC or SUVA increased as a function of molar mass for Suwannee River and for another surface water NOM, which indicates a larger relative aromaticity for larger molecules (Figure 12).

If used in combination with a fluorescence detector, it should be possible also to increase the understanding of the fluorescence properties of natural organic matter as a function of molar mass. Fluorescence of NOM is often used for analysis and characterisation [79].

In seawater, colloidal organic matter of both terrestrial and marine origin is present. Its absorbance properties limit the penetration depth of sunlight, which in turn affects primary production. Photodegradation coupled with microbial recycling and flocculation in estuaries represent the most important removal pathways for the colloidal organic matter. There are a few exploratory examples where FFF with UV and fluorescence detection have been shown to be a valuable tool to study the size-dependent optical properties of the colloidal organic matter [44,55,67,75,76].

A study of two Florida rivers and estuaries using sFICFFF (with frit-inlet, frit-outlet) concluded that conservative mixing (dilution) was the dominant process in one river estuary, while photodegradation was also important in the other [76]. Light exposure incubations followed by molar mass distribution determinations by UV and fluorescence

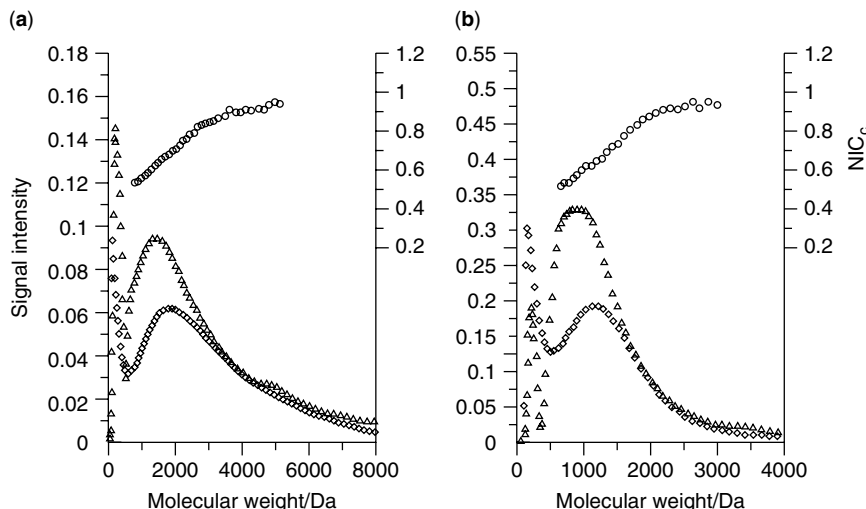


**Figure 12.** Continuous molecular weight-specific NIC analysis ( $\text{NIC}_c$ ) on representative samples: (a) SRNOM and (b) King Site 2.2 m. UV analyses are represented by (M), DOC detector results by (8) and NIC values by (O). Reprinted from Ressat, T. N. and Hendry, M. J. *Analytical Chemistry*, **77**, 4194–4200. Characterizing dissolved organic carbon using asymmetrical flow field-flow fractionation with on-line UV and DOC detection. Copyright 2005 American Chemical Society

detection showed an 85% decrease in UV and a 94% decrease in fluorescence but only a very small shift in molar mass distributions (Figure 13).

FIFFF with UV and fluorescence detection was used to characterise the molar mass distributions of coloured DOM in the brackish Baltic sea and the oceanic Skagerrak sea [55]. The peak area of UV and fluorescence detection gave two different measurements of macromolecular organic matter. Weight- and number-average molar masses were calculated from the fractograms. Coloured DOM decreased with salinity but was not conservatively mixed (non-linear relation). The ratio of the UV and fluorescence peak areas followed different mixing lines for the different water masses.

Ratanathanawongs Williams and Keil used FIFFF to measure the biological and physical reactivity of dextran carbohydrates in seawater incubations [80]. Vaillancourt and Balch explored the use of FIFFF with a power-law decay programme on preconcentrated (2200-fold) seawater sample to cover the size range 0.01–1 µm [81].

### 3.3 OPERATING CONDITIONS: FLOW-RATES, MEMBRANES, CARRIER

Sufficient retention of colloidal NOM (*e.g.* HS) so as to separate it from the void peak in order to determine accurately diffusion coefficient, size or molar mass distributions requires the use of a high cross-flow rates (typically  $3\text{--}6 \text{ cm}^3 \text{ min}^{-1}$ ). This is due to these macromolecules being highly diffusive. In order to improve resolution, the channel flow is reduced so that a higher cross-flow to channel-flow ratio is achieved (typically 6–10). The result of such high cross-flow rates is that parts of the sample are in very close vicinity to the membrane, with an increased risk of losing these sample components through the membrane or by absorption to it. The recovery of NOM in FIFFF can be adversely affected by permeation of the low molar mass components through the membrane.

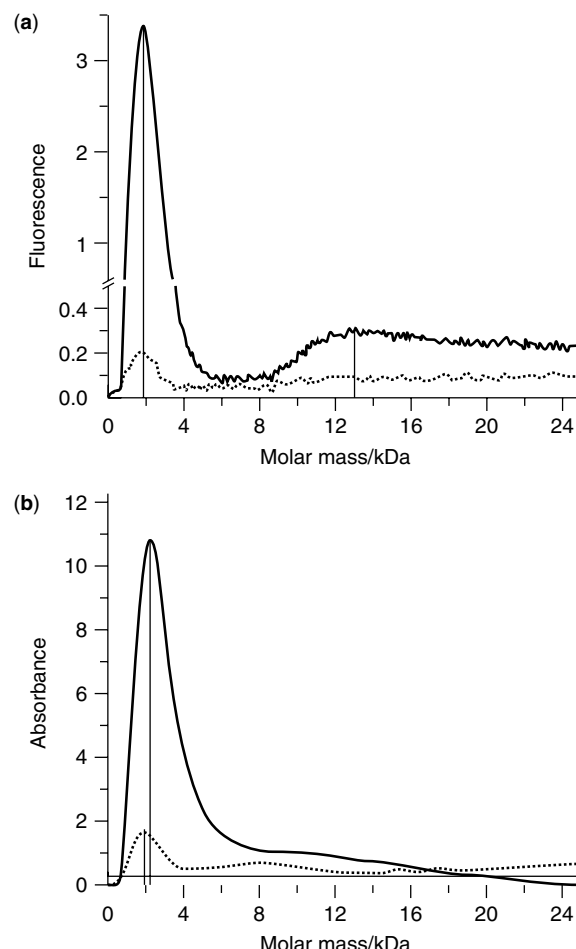


**Figure 13.** Spectra as a function of molar mass ( $\text{kDa} = 1000 \text{ g mol}^{-1}$ ) in a photodegradation study of a fresh CR sample (No. 55, salinity 1.3), before (solid line) and after (dashed line) 7 days of sunlight exposure. (a) Fluorescence (350/450 nm); (b) absorbance (330 nm). Reprinted from Zanardi-Lamardo, E., Clark, C. D., Moore, C. A. and Zika, R. G. *Environmental Science and Technology*, **36**, 2806–2814. Comparison of the molar mass and optical properties of colored dissolved organic material in two rivers and coastal waters by flow field-flow fractionation. Copyright 2002 American Chemical Society

The fulvic acid fraction of colloidal NOM is negatively charged and is also very hydrophilic in nature, hence adsorption to the membrane is a lesser problem than for larger mineral colloids. On the other hand, the humic acid fraction is less hydrophilic, has a higher molar mass and is more easily aggregated.

Indeed, it has been observed that for humic acids, aggregation and adsorption on the membrane reduce the recovery [77,82]. Thang *et al.* [82] found that the ionic strength and pH of the carrier had the largest effect on humic acid recovery and that membrane material or MWCO had only a small influence. However, a similar comparison on non-isolated

colloidal NOM showed that different membrane materials had large effects and that the carrier composition had less effect [44]. The two main loss mechanisms (adsorption and permeation) are likely to be different for different fractions of the colloidal NOM.

A comprehensive list of membranes used in FIFFF studies has been compiled by Gimbert *et al.* [83]. The most commonly used membranes in FIFFF for colloidal NOM analysis are either cellulose-based or polyether sulfone-based membranes. Even though a significant fraction of NOM components (especially fulvic acids) have molar masses around  $1000 \text{ g mol}^{-1}$ , membranes with a higher molar mass MWCO (*e.g.*  $3000\text{--}10\,000 \text{ g mol}^{-1}$ ) have often been used for these types of samples [69,70,77]. Sample losses have been observed and carrier optimisation has been performed to minimise sample losses, but generally the use of a membrane with smaller pore size is the best solution for improved recovery. A membrane with a  $1000 \text{ g mol}^{-1}$  MWCO will cause a high back-pressure in the channel. Leaking channels were mainly a problem for the older FIFFF systems, but less so with the newer systems.

Ionic strength has been shown to have a large influence on the recovery of colloidal NOM. The most common carrier composition is a pH buffer [*e.g.* tris(hydroxymethyl) aminomethane, phosphate, borate, ammonium], and sometimes with the addition of a monovalent salt (*e.g.* NaCl or  $\text{NH}_4\text{NO}_3$ ). Even though the molecular conformation of random coil-type colloids can be affected by ionic strength, the most likely cause of the decreased recovery with increasing ionic strength for NOM is that the repulsive force between the molecules and the membrane is shielded. This may result in more colloids being forced through the membrane and greater adsorption on the membrane. Surfactants are not as important in the carrier to stabilise the NOM as they are for other types of particles. In fact, for the common  $1000 \text{ g mol}^{-1}$  MWCO membrane, the use of a surfactant can disturb the analysis since it can be partly retained by the membrane.

### 3.4 MOLAR MASS CALIBRATION

In order to convert the fractogram to a diffusion coefficient or hydrodynamic diameter distribution, according to FIFFF theory, only the channel dimensions (the thickness) need to be calibrated using the approaches described in Section 2.7. For colloidal NOM, it is often desirable to convert the fractogram to a molar mass distribution in order to compare results with other studies using different methods (*e.g.* SEC). Since molar mass is not a primary parameter of FIFFF, this requires a calibration with standards. Since there are no good standards for NOM, different analogues have been considered. For HS, polystyrene sulfonate (PSS) molar mass standards were shown to have more similar diffusive properties than globular proteins [51] and subsequently have been extensively used.

Severe overloading effects of PSS have been reported at the low ionic strength of  $1 \text{ mmol dm}^{-3}$  in sFIFFF [82] and  $0.1 \text{ mmol dm}^{-3}$  using hollow-fibre FIFFF [84], but not for the higher value of  $10 \text{ mmol dm}^{-3}$ . Therefore, PSS standards are probably useful for molar mass calibrations but should not be used at very low ionic strength. Furthermore, the PSS concentration should be as close to the detection limit as possible while still producing an adequate detector signal-to-noise ratio.

The relationship between  $D$  and molar mass,  $M$ , for PSS is given by

$$D = a/M^b \quad (22)$$

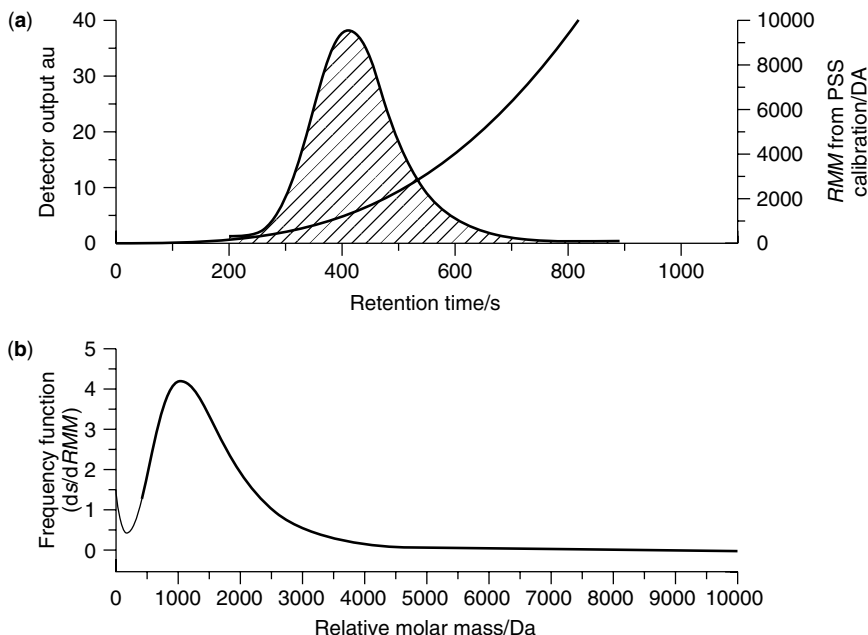


**Figure 14.** Conversion of a fractogram (a) to a molar mass distribution (b). The relationship between retention time and molar mass for polystyrenesulfonate standards is also given in (a). Reprinted with permission from Hassellöv, M. Relative molar mass distributions of chromophoric colloidal organic matter in coastal seawater determined by flow field-flow fractionation with UV absorbance and fluorescence detection, *Marine Chemistry*, **94**, 111–123, Copyright 2005, with permission from Elsevier

Typical values for the constants in equation (22) are  $a = 1.5 \times 10^{-8}$  and  $b = 0.6$ , which are close to the values for a random coil in a good solvent. However, this should not be taken to prove that HS are linear molecules, as other spectroscopic evidence suggests that this is not the case.

Since the diffusion coefficient (which is almost inversely proportional to the retention volume) is not linearly related to the molar mass [equation (22)], it is necessary to correct the y-axis when converting the fractogram to a molar mass distribution [12]. This procedure is analogous to the non-linear conversion of retention times to equivalent spherical diameter in SdFFF. The fractogram of a marine colloidal NOM is shown together with the molar mass function obtained from PSS calibration as shown in Figure 14a. The molar mass distributions with the corrected frequency function are shown in Figure 14b [55].

### 3.5 VALIDATION WITH OTHER METHODS

In a first study of the molar mass distribution of HS, a good correlation was found between the average MW found from FlFFF and the values obtained using vapour pressure osmometry and low-angle X-ray scattering [12]. Subsequently, a strong validation of the diffusion coefficient determination of fulvic acids by FlFFF was also obtained through an intercalibration exercise with fluorescence correlation spectroscopy (FCS) and pulsed-field gradient nuclear magnetic resonance (PFG-NMR) [78]. FlFFF agreed well with FCS

and slightly less with PFG-NMR, which yielded slightly larger  $D$  values (Chapter 11, Figure 6). The diffusion coefficients ranged from  $1.9 \times 10^{-10}$  to  $3.5 \times 10^{-10} \text{ m}^2 \text{ s}^{-1}$ , corresponding to hydrodynamic diameters for the majority of the Suwannee River fulvic acid molecules between 1.5 and 2.5 nm.

In a comparison of SEC with FIFFF for the determination of NOM molar mass distributions, some overall similarities were found but differences were observed in the lower and higher molar mass regions [85]. The discrepancies can partly be explained by differences in the two methods. SEC has a higher size resolution than FIFFF in the lower molar mass region, whereas the opposite is true for the higher molar mass region studied. Furthermore, SEC showed some signs of gel–solute interactions, which could explain some of the differences. However, it should be recognised that corresponding interactions could also occur with the FIFFF membrane. Such interactions could shift the molar mass distributions obtained by the two techniques significantly, particularly since the elution orders are opposite for SEC and FFF.

### 3.6 AGGREGATION STUDIES OF HUMIC SUBSTANCES

Using FIFFF-UV, Amarasiriwardena *et al.* investigated the aggregation behaviour of isolated humic acids upon addition of  $\text{Ca}^{2+}$  [38]. Shifts in the molar mass distributions obtained indicated that the humic acids were increasingly aggregated when higher  $\text{Ca}^{2+}$  concentrations were added. The hypothesis was that  $\text{Ca}^{2+}$  formed bridges between individual humic acid molecules. They also found that the aggregation was a function of the equilibrium time. Subsequently, Siripinyanond *et al.* used aFIFFF coupled to ICP-MS to study HS aggregation behaviour following the addition of  $\text{Ca}^{2+}$  to a humic acid that was spiked with metals [86]. As above, a similar behaviour was found, indicating a significant shift to larger sizes for  $\text{Ca}^{2+}$  additions of  $1.6 \text{ g dm}^{-3}$  and aggregation times of up to 3 days (Figure 15). Furthermore, they found that some of the added metals (Cu and Cd) were complexed to smaller sized molecules whereas Pb was adsorbed by larger molecules. After aggregation, Cu, and especially Cd, showed a bimodal size distribution.

### 3.7 TRACE ELEMENT ASSOCIATIONS WITH MACROMOLECULAR ORGANIC MATTER AND OTHER NANOPHASES

Macromolecular organic matter such as HS has a high binding capacity for most trace elements (Chapter 3, [87]). It is often of interest to determine the fraction of the total metals bound to organic matter, as this has implications for the bioavailability and diffusion of the metals. Such a distinction can be performed directly with CFF or using measurements of truly dissolved metals (*e.g.* by electrochemical methods or diffusion gradients in thin films). If the metal concentration as a function of the molar mass or diffusion coefficient of the metal species is required, then it is possible to use FIFFF coupled to ICP-MS [37–39,40,56,66].

Hassellöv *et al.* developed an FIFFF–ICP-MS method for freshwater NOM, using on-channel preconcentration [37]. The initial work was conducted using a first-generation quadrupole ICP-MS instrument with which 32 elements could be determined in a freshwater sample. Some examples of the element-based fractograms obtained for a Swedish

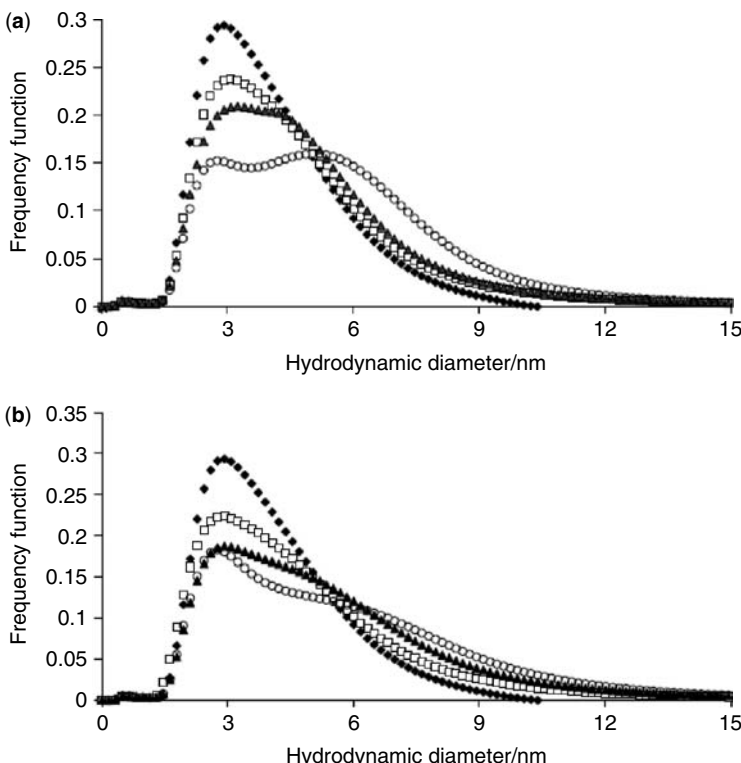


**Figure 15.** Hydrodynamic diameter distributions of humic acids exposed to (a)  $1600 \text{ mg dm}^{-3}$   $\text{Ca}^{2+}$  and (b) seawater at increasing contact times: 0 min ( $\diamond$ ), 60 min ( $\square$ ), 180 min ( $\blacktriangle$ ) and 4320 min ( $\circ$ ). The figures show varying degrees of aggregation on addition of salt. Reprinted from Siripinyanond, A., Worapanyanond, S. and Shiowatana, J. *Environmental Science and Technology*, **39**, 3295–3301. Field-flow fractionation-inductively coupled plasma mass spectrometry: An alternative approach to investigate metal–humic substances interaction, Copyright 2005 American Chemical Society

Creek are given in Figure 16. It was found that most elements were mainly associated with organic- and iron-rich (probably dominated by iron oxyhydroxides) colloidal phases [39]. For example, Cu and U were mainly associated with organic matter, Pb was only associated with iron oxyhydroxides and other metals were found in both phases (*e.g.* Zn and La).

The apparent phase partitioning between the organic- and iron-rich phases was quantified by peak deconvolution, since the two phases, with obviously different chemical properties, overlapped in their size distribution. This deconvolution method is illustrated in Figure 17.

The experimental results of the partitioning between organic matter- and iron-rich colloids were compared with thermodynamic modelling. The model was assembled from Tipping's WHAM-V computer program and iron oxyhydroxide surface complexation modelling [88]. The trends in the experimental data (without any fitting) were predicted

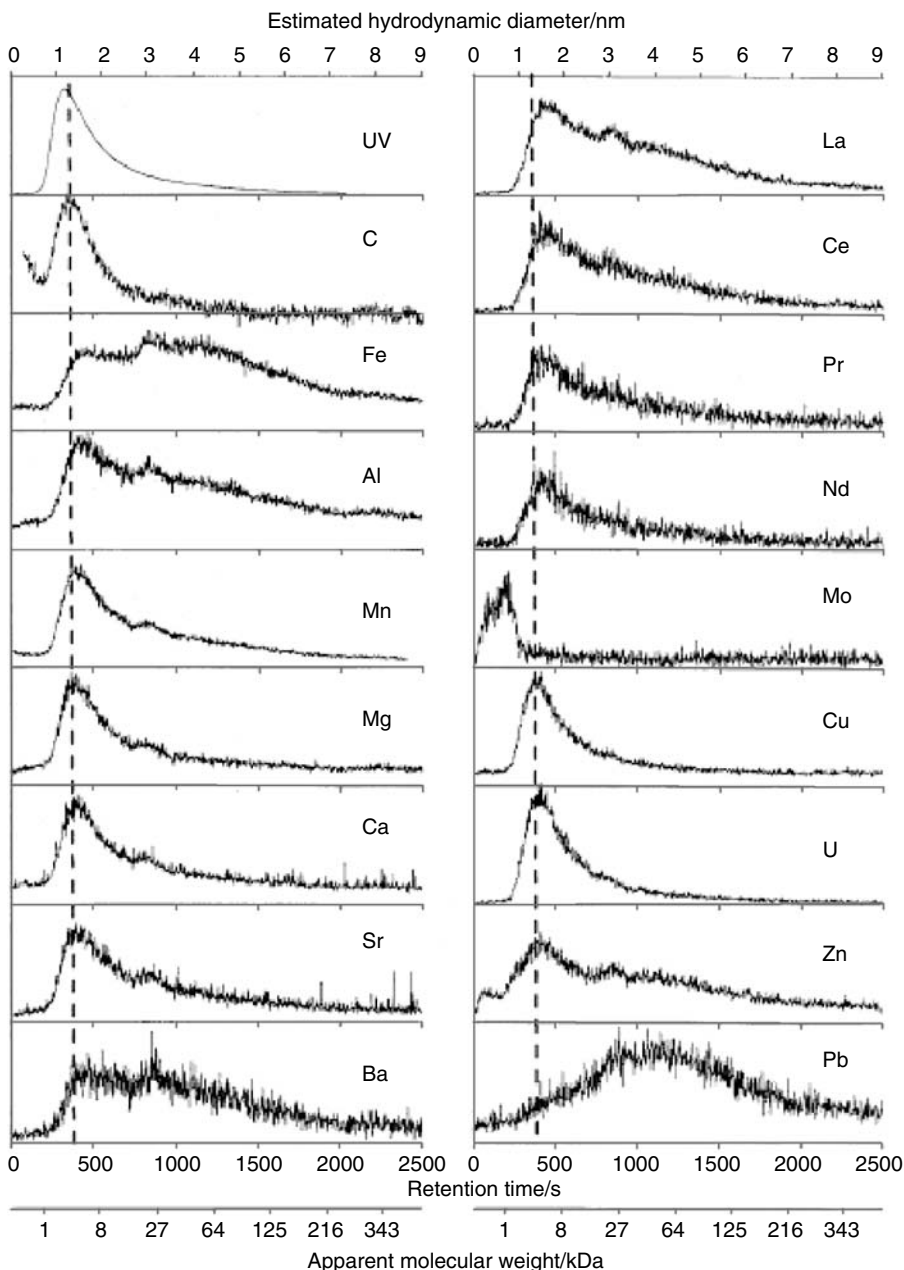


**Figure 16.** FIFFF-ICP-MS size distributions for selected elements in colloidal material from Delsjö Creek, Gothenburg, Sweden. The retention time and corresponding hydrodynamic diameter are shown together with marks of molar mass from polystyrene sulfonate calibrations. The vertical dashed lines mark the peak retention time of carbon. Reprinted from Lyvén, B., Hassellöv, M., Turner, D. R., Haraldsson, C. and Andersson, K. Competition between iron- and carbon-based colloidal carriers for trace metals in a freshwater assessed using flow field-flow fractionation coupled to ICPMS, *Geochimica et Cosmochimica Acta*, **67**, 3791–3802, Copyright 2003, with permission from Elsevier

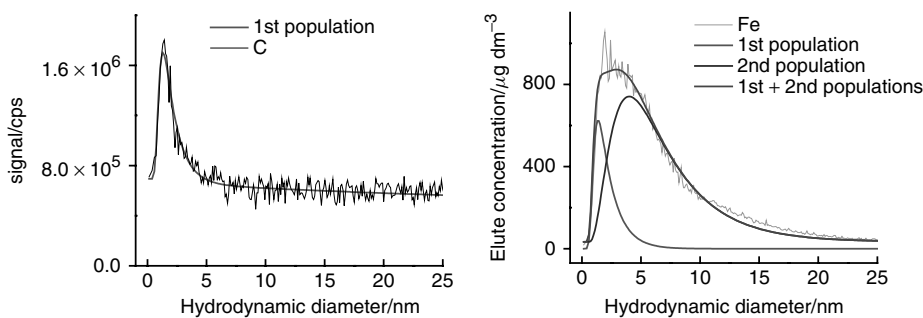


**Figure 17.** (a) Carbon- and (b) Fe-based colloidal size distributions in Delsjö Creek water sample. The Fe distribution has been deconvoluted into two fractions attributed to Fe associated with organic matter [based on the C distribution in (a)] and Fe oxyhydroxide colloids based on the distribution of Pb since Pb does not have any affinity to organic colloids in this sample [39,40]

fairly well by the model and pH was shown to be a dominant factor in the competition between the organic and the iron phases. At low pH (<6) the metals were preferentially bound to HS.

Subsequently, the method was significantly improved by the application of a state-of-the-art high-resolution ICP-MS (HR-ICPMS) system [40]. The HR-ICP-MS instrument has a higher sensitivity and a lower background, giving much lower detection limits. With this instrumentation, 46 elements could be quantified and at least 15 more qualitatively identified. Partitioning between mainly iron-bound (*e.g.* P), mainly carbon-bound (*e.g.* As, Cd and I) and mixed phases (*e.g.* V), were quantified for elements not previously studied with the method by peak deconvolution (Figure 17).

Further improvements of the coupled technique should be aimed at further lowering the background of some metals. For example, exchanging symmetrical for asymmetric FIFFF resulted in a considerable improvement in LIBD detection [45].

FIFFF–HR-ICP-MS has been applied to a seasonal study of the Kalix River in northern Sweden, where ICP-MS metal partitioning to iron and organic colloids was determined [56] (Figure 18). It was found that during winter conditions, the low river flow (under ice) was dominated by iron-rich colloids coming from groundwater. On the other hand, during snowmelt and spring flood periods, the river was dominated by organic colloids from leaching of the upper soil layers.

FIFFF–ICP-MS has also been applied to determine size distributions of Cu, Zn and Pb bound to soil HS [38] and for Fe, Mn and Al in compost and in a waste water stream [89]. For the HS, the elemental distributions followed the UV fractogram, whereas in the waste water, Cu, Mn and Zn followed different patterns.

The size distribution and elemental distribution of Fe, U, Ca, Th, La and Ce were determined by FIFFF–ICP-MS for isolated HS (0.1 mol dm<sup>-3</sup> NaOH extraction) and groundwater from the Gorleben aquifer [66]. There were both similarities and differences between the groundwater and the isolated material. The hydrodynamic diameter of the UV peak was smaller (~1 nm) for the isolated HS than for the groundwater sample

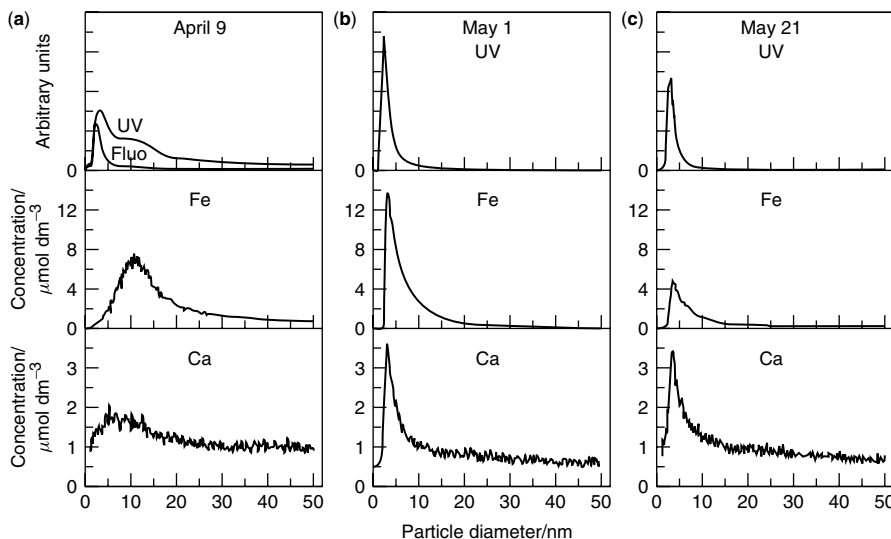


**Figure 18.** Comparison of the size distribution of organic material (UV and fluorescence signals),  $[\text{Fe}]$  and  $[\text{Ca}]$  (a) before the spring flood, (b) during peak discharge and (c) after the spring flood in the Kalix River during 2002. In the 9 April sample the UV signal exhibits a double peak. The first peak is UV absorbance of humic material (as seen with the fluorescence signal) and the second peak is due to light scattering from the larger Fe colloids (the latter peak correlates very well with the size distribution of Fe). Reprinted from Dahlqvist, R., Benedetti, M. F., Andersson, K., Turner, D., Larsson, T., Stolpe, B. and Ingri, J. Association of calcium with colloidal particles and speciation of calcium in the Kalix and Amazon rivers, *Geochimica et Cosmochimica Acta*, **68**, 4059–4075, Copyright 2004, with permission from Elsevier

(2–3 nm). In addition, there were very different iron signals for the two (Figure 19): in the groundwater there was some iron in the humic peak but in the isolated sample a large iron signal was eluted from the channel after the cross-flow was turned off.

Changes in the UV and elemental size distributions were observed using FIFFF–ICP-MS when anoxic river sediment porewater was oxidised [90]. Both the UV and elemental signals in Figure 20 indicate increases in the amount of colloidal material after oxidation. For most elements measured there was an increase in size during the oxidation whereas for the UV signal there was a small decrease in size.

FIFFF–AES was used to measure the iron distribution of material previously isolated by tangential flow ultrafiltration from the Rio Negro River, Brazil [91]. Iron was shifted just slightly to higher molar masses compared with the UV signal.

Quantification of the amount of the analyte that was present in the colloidal peaks of the fractograms requires that the detector signal is converted to a concentration. The simplest way is to acquire a calibration curve by introducing several standard samples just after the FFF–ICP-MS run. That approach is illustrated for  $^{147}\text{Sm}$  in Figure 21, where the ICP-MS signal (Figure 21a) is converted to concentration ( $\mu\text{g dm}^{-3}$ ) and plotted as a function of elution volume ( $\text{dm}^3$ ) (Figure 21c). By integrating the peak to obtain the total area, the amount of colloidal  $^{147}\text{Sm}$  ( $\mu\text{g}$ ) is obtained. Two experimental approaches can be used for this calibration. A standard injection valve with a large loop gives a flat-topped peak,

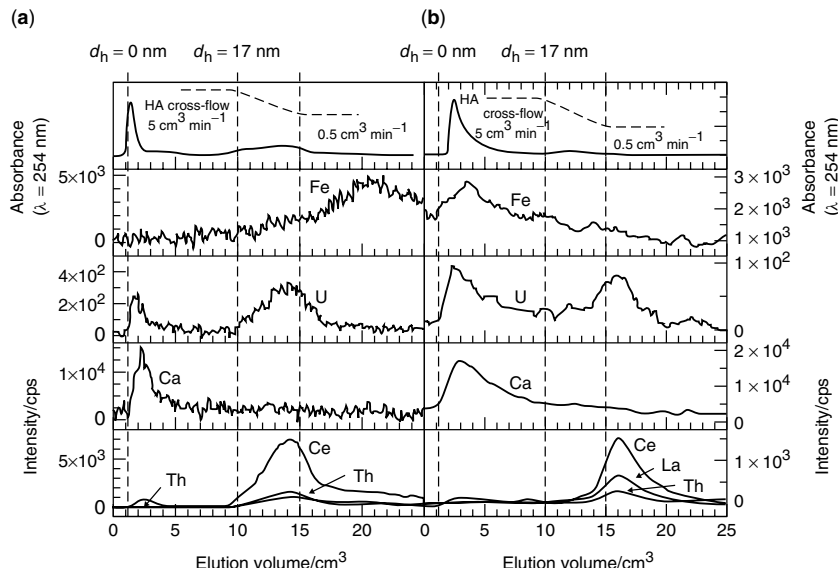


**Figure 19.** FIFFF-ICP-MS fractograms of (a) humic/fulvic colloids extracted from Goerleiben sediment by  $0.1 \text{ mol dm}^{-3}$  NaOH solution and (b) a groundwater (Gohy 2227). Reprinted from Geckeis, H., Manh, T. N., Bouby, M. and Kim, J. I. Aquatic colloids relevant to radionuclide migration: characterization by size fractionation and ICP-mass spectrometric detection, *Colloids and Surfaces A-Physicochemical and Engineering Aspects*, **217**, 101–108, Copyright 2003, with permission from Elsevier

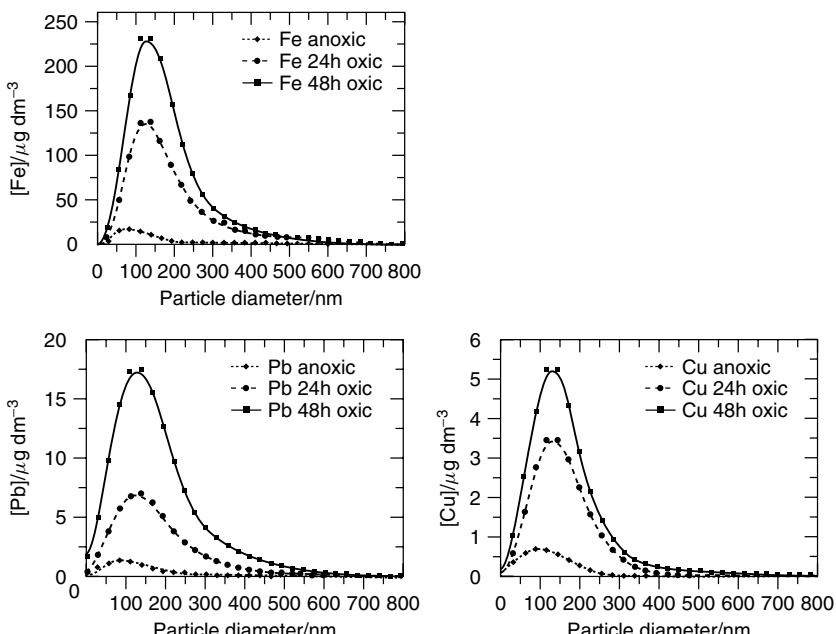


**Figure 20.** Fe-, Pb- and Cu-based size distributions obtained by aFIFFF-ICP-MS during oxidation of anoxic sediment porewaters from the river Elbe. Reproduced with permission from Wiley-VCH.

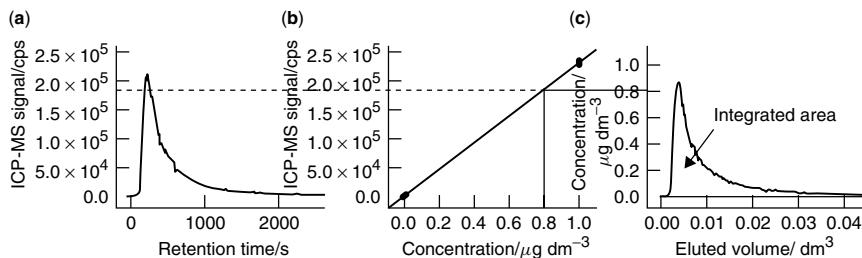


**Figure 21.** Quantification of the results from a  $^{147}\text{Sm}$  fractogram. The y-axis on the FIFFF-HR-ICP-MS fractogram (corrected for dilution) is converted from the ICP-MS signal (cps) (a) to concentration ( $\mu\text{g dm}^{-3}$ ) (c) via the external calibration plot (b). Peak integration of each element in the concentration vs elution volume fractogram gives the total mass ( $\mu\text{g}$ ) of the element in the sample associated with the colloidal phase. Reprinted from Stolpe, B., Hassellöv, M., Andersson, K. and Turner, D. R. High resolution ICPMS as an on-line detector for flow field-flow fractionation; multi-element determination of colloidal size distributions in a natural water sample, *Analytica Chimica Acta*, **535**, 109–121, Copyright 2005, with permission from Elsevier

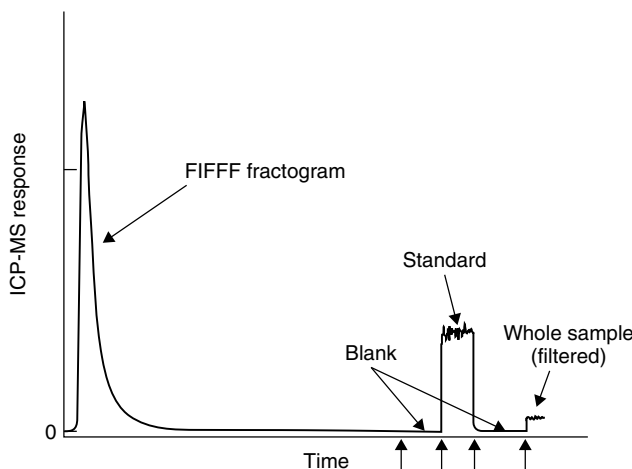


**Figure 22.** Elemental quantification sequence in FIFFF-ICP-MS using an injection valve with a large volume loop [37,40]. Vertical arrows indicate switching of the ICP-MS input stream

where the peak height corresponds to the concentration (Figure 22). Alternatively, a small loop is used, giving a peak that can be integrated to give the amount of element for a known injection volume. It is important to prepare the ICP-MS standards and blanks in the FFF carrier so that they have the same response in the metal standards as during the FFF run. The addition of an internal standard to the stream eluting from the FFF channel is valuable for monitoring changes in sensitivity and as a quality check of the analysis. The internal standard signal should be constant and any sudden change indicates problems with perhaps the flow control in the FFF or the sample introduction system in the ICP-MS system.

#### 4 FRACTIONATION OF INORGANIC PARTICLES

In the last decade, improvements in FFF methodology for the analysis of inorganic particles have mainly been attributed to emerging detection technologies. The most important are the coupling to IC spectrometers for the determination of element-based size distributions (see Section 4.3), the application of light scattering techniques to inorganic particles to obtain independent information on particle size [41], density [48] and shape [20] and the introduction of LIBD as a highly sensitive detection method for polystyrene and inorganic colloids [82].

In the case of sFIFFF–LIBD, Bouby *et al.* found detection limits to be 2, 40 and 240 µg dm<sup>-3</sup> for 20, 50 and 100 nm diameter polystyrene nanosphere particles respectively [45]. With coupling of LIBD to aFIFFF, the detection limits even decreased to 1, 4 and 20 µg dm<sup>-3</sup> for the same particle sizes. This was due to the fact that aFIFFF showed less background concentrations in the carrier. The higher background in sFIFFF was attributed to corrosion and particle leaching from the top frit in the sFIFFF instrument. This is a problem which is also well known in ICP-MS coupling of sFIFFF. For the fractionation of ferrihydrite colloids by aFIFFF, the authors reported higher detection limits, most probably due to the higher laser energy required for the dielectric breakdown of the ferrihydrite colloids in LIBD. The detection limits reported for 5–20 nm ferrihydrite colloids were ~240 µg dm<sup>-3</sup> for LIBD, ~380 µg dm<sup>-3</sup> for ICP-MS (detected on Fe-57) and ~800 µg dm<sup>-3</sup> for UV–VIS detection (at 210 nm).

Another promising development has been the correction of the turbidity signal for particle size effects for micrometre-sized particles [92] and its extension to nanometre-sized particles [93]. The turbidity coefficient or extinction efficiency  $\tau$  for spherical particles detected in turbidity in a UV–DAD or UV–VIS detector can be described as [93]

$$\tau = \log K c \quad (23)$$

where  $K$  is the sample-specific extinction coefficient and  $c$  the sample mass concentration. The extinction efficiency for monodisperse spheres can also be described as [93]

$$\tau = \frac{\pi}{4} d^2 N Q \quad (24)$$

where  $d$  is the sphere diameter,  $N$  the number concentration of particles and  $Q$  the dimensionless extinction efficiency.  $Q$ , however, is a function of the size parameter  $x$  and the relative refractive index  $m$ . At constant  $m$ , which is the case for a homogeneous sample,  $Q(x,m)$  simplifies to  $Q(x)$ . The size parameter is given by  $x = \pi d/\lambda$ . Hence the extinction coefficient depends on the diameter/wavelength ratio. More details are given in the paper [93]; the model is restricted to monodisperse and homogeneous spherical particles. Calculations for particle diameters larger than the applied detection wavelength were not presented.

The effects of particle size and applied wavelength on UV–VIS detection have been demonstrated in theory and experiment [43].

#### 4.1 DIFFERENTIATION OF INORGANIC PARTICLES AND ORGANIC MACROMOLECULES

Since organic and inorganic particles will typically show different behaviour and play different roles in environmental processes, it is of importance to differentiate them. Unfortunately, it is difficult to obtain a clear, specific and quantitative distinction between the two types of colloids if they coexist in a single sample. With typical environmental samples, it is expected that the smallest fractions (a few nanometres in diameter) will be dominated by organic substances whereas in the  $>10$  nm fraction inorganic (mineral) particles will predominate. This does not imply that, *e.g.*, clay or iron oxides are not present in the smaller size range, or that organic particles, such as large aggregates of HS, viruses or bacteria, are absent in the larger size range. A certain differentiation of organic/inorganic particles may be achieved by a careful choice of FFF subtechnique, run conditions and detection systems. For example, in SdFFF runs that are optimised for inorganic particles  $>20$  nm, organic particles with density similar to water and sizes below  $\sim 50$  nm will elute in or near the void peak. Detection methods such as light scattering or fluorescence systems in nephelometric mode are insensitive to light absorption and particles below  $\sim 20$  nm and can therefore provide an acceptable differentiation from light-absorbing organic macromolecules [43]. Petteys and Schimpf [41] used UV–VIS detection at 280 nm to distinguish between haematite colloids [small signal-to-particle mass concentration ratio (turbidity)] and humic/fulvic acids [high signal-to-particle mass concentration ratio (absorbance)].

Another example of the distinction between light-absorbing organic substances and light-scattering inorganic particles is shown in Figure 23 [20]. This illustrates the selectivity of light-scattering detection for mineral particles over DOM. The sample contained colloids that were extracted from a natural soil sample and filtered at  $0.45\text{ }\mu\text{m}$ . The sample contained  $11\text{ mg dm}^{-3}$  of DOC and only  $9\text{ mg dm}^{-3}$  of inorganic colloids.

As is obvious from the two graphs in Figure 23, the UV–VIS detector was not able to generate meaningful data from which a size distribution could have been generated reflecting both the organic and inorganic colloids correctly. The signal from the strongly light-absorbing DOM overwhelmed the signal contribution (turbidity) of inorganic particles. On the other hand, the use of a fluorescence detector in the nephelometric mode, where the

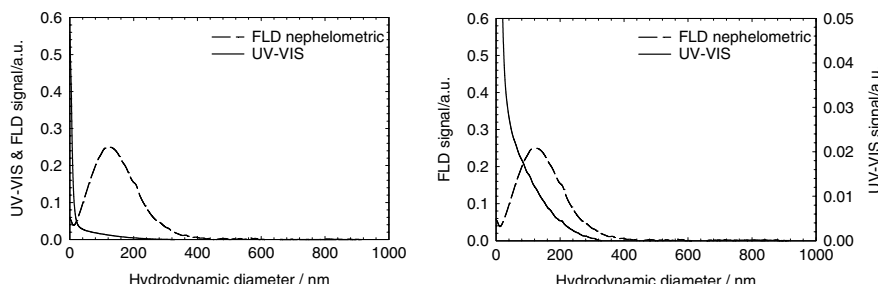


**Figure 23.** FIFFF fractograms of the  $<0.45\text{ }\mu\text{m}$  fraction of soil colloids. The fluorescence detector was set to 320 nm for both excitation and emission wavelengths (nephelometric mode); the UV–VIS wavelength was 260 nm. (a) The UV–VIS signal scaled to its maximum value in the void peak; (b) UV–VIS signal zoomed for better visibility of the shape of the fractogram in the region of the inorganic particles (nephelometric signal). From von der Kammer (2005) [20]

excitation and emission wavelengths are set to the same value, reveals clearly the underlying signal from the inorganic particles. The theoretical background of using HPLC-fluorescence detectors as turbidity detectors is covered elsewhere [43].

#### 4.2 SAMPLE PRECONCENTRATION

The concentrations of naturally occurring inorganic colloids may not always be high enough for a direct FFF analysis. Colloid mass concentrations may vary between a few  $\mu\text{g dm}^{-3}$  and in some special cases  $>100 \text{ mg dm}^{-3}$  [94]. As in the case of natural organic matter, a preconcentration may be desired, no matter whether is performed externally (sFIFFF, SdFFF) or internally (aFIFFF). However, extreme caution has to be exercised with respect to artefacts produced by any technique which increases the colloidal concentration above the natural value of the sample. The techniques applied to preconcentrate samples containing inorganic particles usually remove the excess of water by centrifugation, aggregation and resuspension or by ultrafiltration membrane techniques where the colloid concentration is increased in the retentate [51,52,54]. The characteristics of the sample will determine the maximum preconcentration which can be achieved without producing artefacts, mainly due to aggregations of the sample. Inorganic particles are much more prone to aggregation than organic macromolecules due to the typically lower electrostatic repulsion. Aggregation may additionally be forced by the presence of destabilising macromolecules (fibrils) that are often present in, e.g., surface water samples. Figure 24 shows experimental results from the enrichment of soil colloids. The experiments involved the

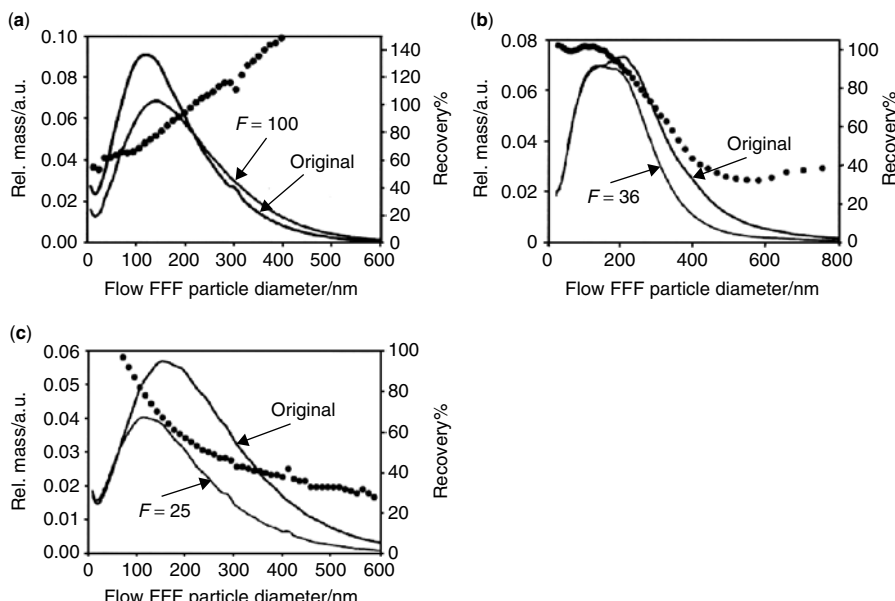


**Figure 24.** Sample preconcentration results with respect to recovery (●) over size, preconcentration factor  $F$  and potential distortions of the size distribution. (a) Sartorius VivaSpin centrifuge concentrators, 10 kDa PES membrane; (b) Schleicher & Schuell hollow-fibre cross-flow filtration units, 10 kDa regenerated cellulose membrane, (c) Sartorius VivaFlow cross-flow filtration unit, 10 kDa regenerated cellulose membrane. From von der Kammer (2005) [20]

dilution of an existing soil colloid dispersion and reconcentration to the former value. The two samples (original and diluted–reconcentrated) were compared by sFICFFF analysis. Cross-flow techniques provide good recoveries for the smallest size fraction with virtually complete losses for the larger particles, whereas centrifuge membrane concentrators cause aggregation of the smaller colloids, thereby generating new larger colloids.

It is recommended that preconcentration is thoroughly evaluated by varying the fractionation conditions or by independent methods such as light scattering or electron microscopy.

#### 4.3 ELEMENT-BASED SIZE DISTRIBUTIONS

As shown in Section 3.7, the combination of FFF with detectors delivering absolute or relative element concentration information allows the generation of element-based size distributions. There is no other technique available which delivers element-based particle size distributions with comparable resolution and size range. The technique was first developed by sampling discrete fractions from the FFF outlet and analysing them by ICP-MS [95] or AAS [52,96]. However, the compatibility of flow-rates in the FFF separation and nebuliser inlets of ICP spectrometers allows for direct coupling and true on-line analysis [14].

The analysis of solid nanometre-sized particles by ICP spectrometers without prior digestion has raised the question of whether complete combustion, dissociation and ionisation in the plasma are obtained. Comparisons of digested and non-digested samples showed that the results were nearly identical in GF-AAS and ICP-MS [52]. Schmitt *et al.* [97] reported a slight underestimation of Al when a suspension of montmorillonite was directly injected into the ICP-MS system. However, in their experiment, the total colloid concentration was  $326 \text{ mg dm}^{-3}$ , which is orders of magnitude higher than those typically found at the outlet of an FFF channel. In any case, calibration standards that are used to obtain absolute concentration values instead of relative ion currents or count rates in ICP-MS should match the composition of the carrier solution [98]. In another interesting study, Murphy *et al.* demonstrated the differentiation of illite and kaolinite particles in a mixture by determining the Rb trace of illite, an element which was not present in the kaolinite particles [14].

Apart from giving information on how major and trace elements are distributed across the size spectrum of a sample, additional information may be generated by constructing molar elemental ratios as a function of size [14,52,46,98,99].

Changes in the molar elemental ratios with size indicate a change in mineral composition or specific surface area across the size spectrum. For example, as it is known that iron forms particle coatings on clay minerals, it is expected that Fe/Al ratios should increase with decreasing size due to the corresponding increase in surface area of the particles as shown in Figure 25c. Finally, in adsorption experiments, surface sorption densities may be calculated by relating the element concentration to the total particle concentration (approximated by the UV–VIS trace) [53].

#### 4.4 NON-SPHERICAL PARTICLES AND PARTICLE SHAPE

It was recognised fairly early that particle shape may have an effect on the fractionation process in FFF [100]. In addition to the influence of particle shape on the retention

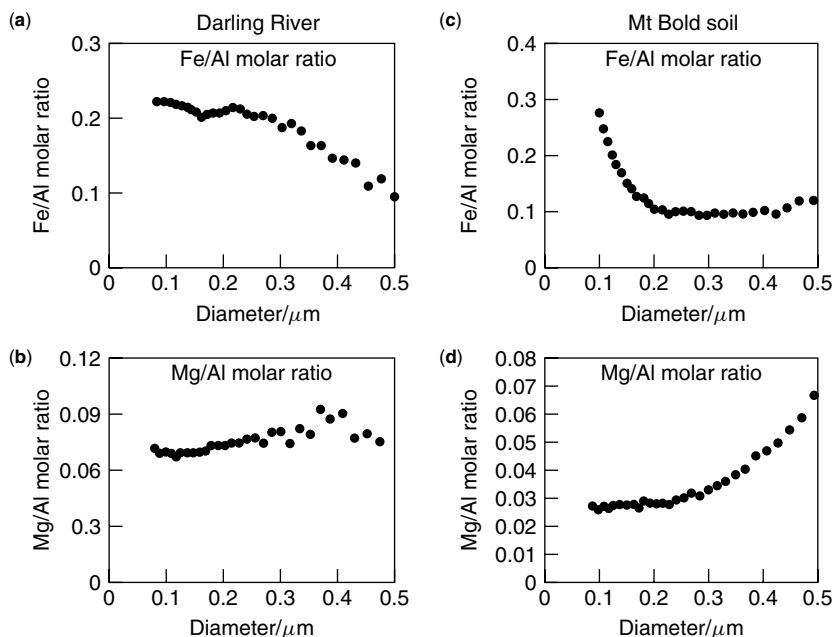


**Figure 25.** Element molar ratio versus particle diameter for Darling River colloids: (a) Fe/Al; (b) Mg/Al and Mt Bold soil colloids; (c) Fe/Al; (d) Mg/Al. Al is assumed to be proportional to the mass concentration of the particles. Smaller particles are assumed to have higher specific surface area so enrichment in the molar ratio towards smaller particles is taken as evidence for surface coatings while other trends in the curves can be interpreted as changes mineralogy. Reprinted from Van Berkem, J. and Beckett, R., Determination of adsorption characteristics of the nutrient orthophosphate to natural colloids by sedimentation field-flow fractionation, *Journal of Chromatography A*, **733**, 105–117, Copyright 1996, with permission from Elsevier

of the particles in the channel [101], it should be recognised that the particle diameter determined by FFF necessarily becomes an equivalent spherical diameter (as in most other techniques). The calculated equivalent diameter depends on the subtechnique used. FlFFF yields the Stokes diameter and, in the case of non-spherical particles, the diameter reported by FlFFF is that of a sphere experiencing the same friction force as the analysed particles. This can be termed the equivalent hydrodynamic diameter or, since the concept of FlFFF is based on translational diffusion, the equivalent translational diffusion diameter [102]. In SdFFF, retention is dependent on the effective or buoyant mass of the particle. For a particle with known density, the diameter that is determined corresponds to the equivalent volumetric diameter, or the diameter of a sphere having the same volume as the analysed particle.

A consequence of the considerations above is that size distributions generated from different methods, including various FFF subtechniques, which refer to a different equivalent diameter do not correspond and a straightforward conversion between these particle size distributions is only possible if the particles have a known geometry (Chapter 1). This restriction also holds true for the conversion of different types of distributions such as particle number, particle surface area or particle mass/volume distributions.

Van Berkel and Beckett [99] found that the application of a spherical particle geometry for the calculation of particle surface area and the corresponding surface adsorption density distribution fails when particles differ significantly from a spherical shape (*e.g.* platelet form of clay particles). A correction for particle shape is necessary to obtain accurate results.

What at first glance seems to be a serious drawback of FFF analysis is in fact one of the strengths of the technique, since it permits the determination of particle shapes. The combination of SdFFF with microscopic techniques, such as SEM and TEM, allows the calculation of particle thickness and aspect ratios. The procedure involves separation and then determination of the particle projected area by SEM and combining this with the particle volume, which is provided by the SdFFF elution time [103]. Aspect ratios determined in a kaolinite sample ranged from 2.8 to 5.4 (fraction <0.5  $\mu\text{m}$ ) and between 5.3 and 5.9 (fraction >0.5  $\mu\text{m}$ ). For illite clay, aspect ratios ranging from 11.3 to 24.3 were determined.

Since SdFFF and FFFFF give different equivalent spherical particle sizes, the use of both techniques on the same sample would deliver the particle shape directly if the resulting size distributions are linked via a geometric model [20,102].

Another approach is to use external detectors for the independent determination of particle size. Modern light-scattering photometers allow the simultaneous determination of particle sizes on the basis of static light scattering (SLS, MALLS) and dynamic light scattering (DLS). For the determination of larger particles, it is of the outmost importance, however, to check if the data treatment used in the supplier's software is correctly adapted to the properties of the analysed particles. Furthermore, in DLS analysis it may be necessary to operate the detector in a stop-flow mode. The combination of FFF–MALLS–DLS delivers up to three different particle radii (FFF, RMS radius from MALLS and hydrodynamic radius from DLS).

The applicability of MALLS has been demonstrated for polystyrene spheres [104], haematite colloids [41], iron hydroxide, phosphate and silicate particles [48] and complex environmental samples such as soil extracted colloids [42,105].

In Figure 26, the independently determined RMS radii which are calculated from the MALLS data are shown for the same sample fractionated under different field conditions. Although the data retrieved in vicinity of the void peak are not easily interpreted, the

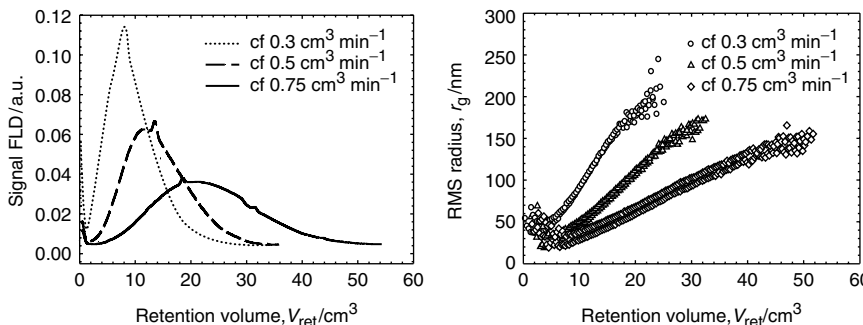


**Figure 26.** Fractionation of soil colloids applying different cross-flows (cf). Calculation of RMS radii from MALLS data using linear Zimm fitting. From von der Kammer (2005) [20]

linear increase in particle size with elution volume follows the FFF theory. Also the particle sizes obtained from MALLS are in a very reasonable range compared with the FFF data [42]. The maximum size determined by MALLS decreases with increasing cross-flow, which indicates some selective losses of larger particles with the higher field forces. The utilisation of MALLS or MALLS–DLS for the independent determination of particle size can provide a direct check on the FFF results and can be used to identify the presence of non-ideal behaviour in the FFF separation. Additionally, FFF band broadening and the resulting overestimation of the width of the size distribution have no effect if FFF–MALLS analysis is employed. This was demonstrated by Petteys and Schimpf, who analysed haematite particles with FFF–MALLS and observed substantially narrower distribution functions than from FFF [41].

It must be emphasised that MALLS-derived RMS radii are not directly comparable to radii determined by FFF. For a homogeneous spherical particle, the RMS radius equals  $0.775 \times$  the physical radius of the sphere and this factor varies with particle geometry and the mass distribution within the particle itself.

Linking results from MALLS with the volumetric diameter obtained by SdFFF can provide estimates of the particle density [48] or particle shape [20]. For particle shape determination, SdFFF is ideally coupled to both static and dynamic light scattering (MALS–DLS), allowing the simultaneous determination of the radius of gyration and the hydrodynamic radius in a single run for each eluting fraction. It was demonstrated on akaganeite particles that a combination of SdFFF–DLS or SdFFF–MALLS–DLS provides a good estimate of aspect ratios of particles provided that the geometry can be described by an appropriate model, in this case a prolate ellipsoid [20].

#### 4.5 APPLICATION TO NATURAL SEDIMENT PARTICLES

Determination of the particle size distribution of natural sediment samples (grain size analysis) can pose a major challenge to the FFF procedure. These samples often cover a very broad size range from a few nanometres to hundreds of micrometres [27,90,106] and the particles may be heterogeneous in shape, density and surface characteristics. Such samples need to be prefractionated in order to split the size range into at least two fractions that can be separated with the normal and steric/hyperlayer modes of FFF [27,46]. In a study of pure clays and marine sediment samples, it was found that a  $1\text{ }\mu\text{m}$  centrifugal split, followed by normal and lift hyperlayer fractionations using sedimentation FFF, gave similar size distributions to a conventional sieving/settling method. However, the submicron particles were disproportionately lost in the  $1\text{ }\mu\text{m}$  split [27] (Figure 27).

Even in the colloidal size range it is often not possible to cover the complete size distribution in one fractionation run, despite the use of field programming (decaying field). If a high enough initial field is applied to retain the  $30\text{--}50\text{ nm}$  colloids, then the steric inversion is shifted downwards from  $\sim 0.8\text{ }\mu\text{m}$  to less than  $0.5\text{ }\mu\text{m}$  (see the example for FlFFF in Figure 5).

#### 5 CONCLUSIONS

FFF offers some analytical possibilities that no other technique can deliver. In this chapter we have outlined the information that can be obtained by applying this method to environmental samples. FFF is a high-resolution sizing and separation technique which is

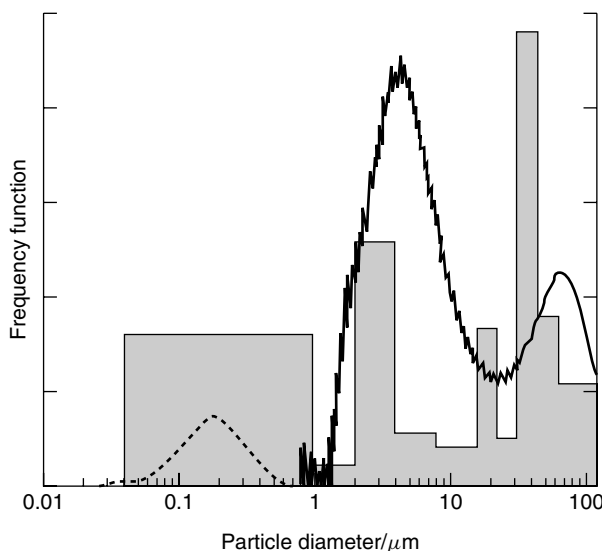


**Figure 27.** Particle size distributions for Skagerrak sediment sample. The solid bars show the distribution derived from conventional sieving/settling grain size analysis, the dotted line that from normal mode FFF and the full line that from hyperlayer mode FFF. Reproduced from Hassellöv, M., Lyven, B., Bengtsson, H., Jansen, R., Turner, D. R. and Beckett, R. Particle size distributions of clay-rich sediments and pure clay minerals: A comparison of grain size analysis with sedimentation field-flow fractionation, *Aquatic Geochemistry*, 7, 155–171. Copyright 2001, with kind permission of Springer Science and Business Media

applicable to a large range of environmentally important samples. However, to take full advantage of the capabilities of FFF, the analyst must be aware of certain limitations and have the knowledge to optimise the experimental conditions in order to produce quality data on the sample of interest. A major objective of this chapter has been to provide the essential information required in order to make informed choices about the FFF subtechnique and run conditions best suited for various classes of environmental samples.

The samples that can be processed by FFF covers the size range from roughly 1 nm to 50  $\mu\text{m}$ , but any given run will be limited to about a 20-fold variation in diameter and particle sizes can not cross the steric inversion boundary at about 1  $\mu\text{m}$ . Field programming is advantageous in some circumstances and this is usually easy to achieve experimentally with FFF. Different fields (or subtechniques) are best suited to certain size ranges and classes of samples.

FFF is a powerful measurement device and the elution time can directly yield information such as the size and mass-distribution, depending on the subtechnique used. Since it involves continuous separation of the sample, this means that size-based distributions of a given parameter can be obtained. If other measurements are made on the fractionated components, then further quantities such as particle density and shape parameters can be evaluated. This may be achieved either by collecting discrete fractions at points across the distribution or by employing online detectors such as MALLS.

A particularly powerful combination is FFF–ICP-MS, which enables element-based size distributions to be plotted. These composition distribution data can be used to evaluate

the transport and fate of colloids and their contaminant load in aquatic, terrestrial and atmospheric environments.

Many factors can affect the resolution of FFF separations and the accuracy of the measurements obtained with it. Factors such as sample–wall interactions, concentration effects and secondary relaxation during field programming must be considered in striving to achieve maximum performance. However, to put this in its correct perspective, similar considerations also apply to other sizing and separation methods.

When analysing complex environmental samples and comparing results from different FFF subtechniques or FFF results with other techniques, the user should consider that the majority of available techniques refers to an equivalent particle size and that size distributions must not match each other. From the differences, however, information about the particle shape can be deduced.

As has been discussed thoroughly in this chapter, FFF is an extremely versatile method. Many subtechniques are available, due to the different fields that can be utilised, and each is capable of being run under a range of field and flow conditions. For this reason, FFF is applicable to a wide range of materials and particle sizes. However, this versatility comes at a price and there is no simple recipe that can be followed to obtain an optimal set of run conditions.

In the case of environmental colloids, almost every sample must be considered as an unknown and consequently the FFF method used needs to be verified for its applicability and the absence of perturbations in the fractionation process. The first consideration will be the sample collection, storage and preparation method to be used. Environmental scientists will be well aware of this problem, as it is common to all field studies. For FFF analysis, the aspect which must receive particular attention is preservation of the particle size distribution. Any procedure that causes aggregation or disruption of the particles or molecules must either be avoided or at least taken into account when interpreting the data. A particular issue for many environmental samples is the effect of concentrating the collected sample. It is hoped that more sensitive detectors such as light scattering and LIBD will eliminate the need for sample concentration.

In this chapter, some sample preparation procedures and run conditions have been given that have been applied successfully to the analysis of various types of environmental samples. These may be used as a starting point for the development of an FFF analysis method. However, a much more important lesson to be learned from this chapter is the necessity of a fundamental understanding of the principles of FFF so that the starting methods can then be successfully modified and tested in a logical manner to produce accurate and reliable results for the particular sample at hand.

## LIST OF SYMBOLS AND ABBREVIATIONS

$\omega$	Angular rotation frequency; angular speed
$\rho$	Density
$\eta$	Dynamic viscosity
$\lambda$	Retention parameter $\lambda = l/w$ (dimensionless)
$\Delta\rho$	Density difference particle – carrier medium ( $\rho_p - \rho_c$ )
$\lambda_{\text{em}}$	Emission wavelength in fluorescence spectroscopy

$\lambda_{\text{ex}}$	Excitation wavelength in fluorescence spectroscopy
$\rho_c$	Density of the carrier
$\rho_p$	Density of particle
AAS	Atomic absorption spectrometry
CFF	Cross-flow ultrafiltration
$D$	Diffusion coefficient
$d$	Diameter
$d_p$	particle diameter
DAD	Diode-array detection
DLS	Dynamic light scattering
DOC	Dissolved organic carbon
DOM	Dissolved organic matter
EDXA	Energy-dispersive X-ray analysis
$f$	Friction coefficient of component
$F$	External field force
$f_c$	Rotation frequency of the SdFFF channel (= rpm/60)
FCS	Fluorescence correlation spectroscopy
FFF	Field-flow fractionation
FLD	Fluorescence detector
FIFFF	Flow field-flow fractionation
aFIFFF	Asymmetric FIFFF
sFIFFF	Symmetrical FIFFF
GF-AAS	Graphite furnace atomic absorption spectrometry
HS	Humic substances
ICP-MS	Inductively coupled plasma mass spectrometry
Q-ICP-MS	Quadrupole-based ICP-MS
HPLC	High-performance liquid chromatography
HR-ICP-MS	High-resolution ICP-MS (with sector field MS)
ICP-AES	Inductively coupled plasma atomic emission spectrometry
$k$	Boltzmann constant
$l$	Mean cloud thickness (of the component in the channel)
LIBD	Laser-induced breakdown detection
$M$	Molar mass
$M_1$	First moment of a distribution
MALLS	Multi-angle laser light scattering (variant of SLS)
$m_e$	Effective mass
MWCO	Molecular weight cut-off
NOM	Natural organic matter
PSD	Particle size distribution
$R$	Retention ratio
$r_c$	Radius of SdFFF channel
$r_g$	Root mean square radius of gyration (RMS radius)
$r_h$	Hydrodynamic radius
RMS	Root mean square
$r_v$	Volumetric radius (radius of a sphere with equivalent volume)
SEC	Size-exclusion chromatography

SEM	Scanning electron microscopy
SdFFF	Sedimentation field-flow fractionation
SLS	Static light scattering
SUVA	Specific UV absorbance
$T$	Absolute temperature
$t_r$	Retention time
$t_v$	Void time
TEM	Transmission electron microscopy
TXRF	Total reflection X-ray fluorescence
UV-VIS	Ultraviolet-visible
$V^0$	Channel volume
$V_{in}$	Volumetric flow-rate at channel inlet
$V_{out}$	Volumetric flow-rate at channel outlet
$V_c$	Volumetric cross-flow rate
$V_p$	Particle volume
$w$	Channel height
$x$	Distance from the accumulation wall

## REFERENCES

- McCarthy, J. F. and Zachara, J. M. (1989). Subsurface transport of contaminants, *Environ. Sci. Technol.*, **23**, 496–502.
- Honeyman, B. D. and Santchi, P. H. (1989). A Brownian-pumping model for oceanic trace metal scavenging: evidence from Th isotopes, *Deep Sea Res.*, **47**, 951–992.
- Lead, J. R., Davison, W., Hamilton-Taylor, J. and Buffle, J. (1997). Characterizing colloidal material in natural waters, *Aquat. Geochem.*, **3**, 212–232.
- Giddings, J. C. (1966). A new separation concept based on a coupling of concentration and flow nonuniformities, *Sep. Sci.*, **1**, 123–125.
- Thompson, G. H., Myers, M. N. and Giddings, J. C. (1969). Thermal field-flow fractionation of polystyrene samples, *Anal. Chem.*, **41**, 1219–1222.
- Giddings, J. C., Yang, F. J. F. and Myers, M. N. (1975). Application of sedimentation field-flow fractionation to biological particles – molecular weights and separation, *Sep. Sci.*, **10**, 133–149.
- Giddings, J. C., Yang, F. J. and Myers, M. N. (1976). Theoretical and experimental characterization of flow field-flow fractionation, *Anal. Chem.*, **48**, 1126–1132.
- Caldwell, K. D., Giddings, J. C., Myers, M. N. and Kesner, L. F. (1972). Electrical field-flow fractionation of proteins, *Science*, **176**, 296–298.
- Caldwell, K. D. and Gao, Y.-S. (1993). Electrical field-flow fractionation in particle separation. 1. Monodisperse standards, *Anal. Chem.*, **65**, 1764–1772.
- Karauskakis, G., Graff, K. A., Caldwell, K. D. and Giddings, J. C. (1982). Sedimentation field-flow fractionation of colloidal particles in river water, *Int. J. Environ. Anal. Chem.*, **12**, 1–15.
- Beckett, R., Nicholson, G., Hart, B. T., Hansen, M. and Giddings, J. C. (1988). Separation and size characterization of colloidal particles in river water by sedimentation field-flow fractionation, *Water Res.*, **22**, 1535–1545.
- Beckett, R., Jue, Z. and Giddings, J. C. (1987). Determination of molecular weight distributions of fulvic and humic acids using flow field-flow fractionation, *Environ. Sci. and Technol.*, **21**, 289–295.
- Beckett, R., Nicholson, G., Hotchin, D. M. and Hart, B. T. (1992). The use of sedimentation field-flow fractionation to study suspended particulate matter, *Hydrobiologia*, **235**, 697–710.

14. Murphy, D. M., Garbarino, J. R., Taylor, H. E., Hart, B. T. and Beckett, R. (1993). Determination of size and element composition distributions of complex colloids by sedimentation field-flow fractionation inductively-coupled plasma-mass spectrometry, *J. Chromatogr.*, **642**, 459–467.
15. Giddings, J. C. (1973). Conceptual basis of field-flow fractionation, *J. Chem. Educ.*, **50**, 667–669.
16. Caldwell, K. D. (1988). Field-flow fractionation, *Anal. Chem.*, **60**, 959A–971A.
17. Giddings, J. C. (1993). Field-flow fractionation: analysis of macromolecular, colloidal, and particulate matter, *Science*, **260**, 1456–1465.
18. Schimpf, M., Caldwell, K. and Giddings, J. C., eds (2000). *Field-flow Fractionation Handbook*. John Wiley & Sons, Inc., New York.
19. Beckett, R. and Hart, B. T. (1993). Use of field-flow fractionation techniques to characterise aquatic particles, colloids, and macromolecules. In *Environmental Particles*, eds Buffe, J. and van Leeuwen, H. P. IUPAC Series on Analytical and Physical Chemistry of Environmental Systems, Vol. 2. Lewis, Boca Raton, FL, pp. 165–205.
20. von der Kammer, F. (2005). Characterization of environmental colloids applying field-flow fractionation–multi-detection analysis with emphasis on light scattering Techniques. *Ph.D Thesis*, Hamburg University of Technology, p. 254.
21. Giddings, J. C. and Myers, M. N. (1978). Steric field-flow fractionation: a new method for separating 1–100 µm particles, *Sep. Sci. Technol.*, **13**, 637–645.
22. Ratanathanawongs, S. K. and Giddings, J. C. (1992). Dual-field and flow-programmed lift hyperlayer field-flow fractionation, *Anal. Chem.*, **64**, 6–15.
23. Ratanathanawongs, S. K. and Giddings, J. C. (1994). Rapid size characterization of chromatographic silicas by flow field-flow fractionation, *Chromatographia*, **38**, 545–554.
24. Barman, B. N., Ashwood, E. R. and Giddings, J. C. (1993). Separation and size distribution of red blood cells of diverse size, shape, and origin by flow/hyperlayer field-flow fractionation, *Anal. Biochem.*, **212**, 35–42.
25. Hoffstetter-Kuhn, S., Rosler, T., Ehrat, M. and Widmer, H. M. (1992). Characterization of yeast cultivations by steric sedimentation field-flow fractionation, *Anal. Biochem.*, **206**, 300–308.
26. Moon, M. H. and Giddings, J. C. (1993). Rapid separation and measurement of particle size distribution of starch granules by sedimentation/steric field-flow fractionation, *J. Food Sci.*, **58**, 1166–1171.
27. Hassellöv, M., Lyven, B., Bengtsson, H., Jansen, R., Turner, D. R. and Beckett, R. (2001). Particle size distributions of clay-rich sediments and pure clay minerals: a comparison of grain size analysis with sedimentation field-flow fractionation, *Aquat. Geochem.*, **7**, 155–171.
28. Giddings, J. C., Moon, M. H., Williams, P. S. and Myers, M. N. (1991). Particle size distribution by sedimentation/steric FFF: development of a calibration procedure based on density compensation, *Anal. Chem.*, **63**, 1366–1372.
29. Beckett, R., Jiang, Y., Liu, G., Moon, M. H. and Giddings, J. C. (1994). Separation and behaviour of nonspherical particles in sedimentation/steric field-flow fractionation, *Part. Sci. Technol.*, **12**, 89–113.
30. Wahlund, K.-G. and Giddings, J. C. (1987). Properties of an asymmetrical flow field-flow fractionation channel having one permeable wall, *Anal. Chem.*, **59**, 1332–1339.
31. Wahlund, K. G. (2000). Asymmetrical flow field-flow fractionation. In *Field-flow Fractionation Handbook*, eds Schimpf, M., Caldwell, K. and Giddings, J. C. John Wiley & Sons, Inc., New York, pp. 279–294.
32. van Bruijnsvoort, M., Tijssen, R. and Kok, W. T. (2001). Assessment of the diffusional behavior of polystyrene sulfonates in the dilute regime by hollow-fiber flow field flow fractionation, *J. Polym. Sci. B Polym. Phys.*, **39**, 1756–1765.
33. Lee, W. J., Min, B. R. and Moon, M. H. (1999). Improvement in particle separation by hollow fiber flow field-flow fractionation and the potential use in obtaining particle size distribution, *Anal. Chem.*, **71**, 3446–3452.
34. Litzen, A. and Wahlund, K. G. (1991). Zone broadening and dilution in rectangular and trapezoidal asymmetrical flow field-flow fractionation channels, *Anal. Chem.*, **63**, 1001–1007.

35. Buffle, J., Perret, J. and Newman, J. (1992). The use of filtration and ultrafiltration for size fractionation of aquatic particles, colloids and macromolecules. In *Environmental Particles*, eds Buffle, J. and van Leeuwen, H. P. IUPAC Series on Analytical and Physical Chemistry of Environmental Systems, Vol. 1. Lewis, Boca Raton, FL, pp. 171–230.
36. Gimbert, L. J., Haygarth, P. M., Beckett, R. and Worsfold, P. J. (2005). Comparison of centrifugation and filtration techniques for the size fractionation of colloidal material in soil suspensions using sedimentation field-flow fractionation, *Environ. Sci. Technol.*, **39**, 1731–1735.
37. Hassellöv, M., Lyven, B., Haraldsson, C. and Sirinawin, W. (1999). Determination of continuous size and trace element distribution of colloidal material in natural water by on-line coupling of flow field-flow fractionation with ICPMS, *Anal. Chem.*, **71**, 3497–3502.
38. Amarasiriwardena, D., Siripinyanond, A. and Barnes, R. M. (2000). Flow field-flow fractionation–inductively coupled plasma-mass spectrometry (flow-FFF–ICP-MS): a versatile approach for characterization of trace metals complexed to soil-derived humic acids. In *Humic Substances: Versatile Components of Plants, Soil and Water*, eds Ghabbour, E. A. and Davies, G. Royal Society of Chemistry, Cambridge, pp. 214–226.
39. Lyvén, B., Hassellöv, M., Turner, D. R., Haraldsson, C. and Andersson, K. (2003). Competition between iron- and carbon-based colloidal carriers for trace metals in a freshwater assessed using flow field-flow fractionation coupled to ICPMS, *Geochim. Cosmochim. Acta*, **67**, 3791–3802.
40. Stolpe, B., Hassellöv, M., Andersson, K. and Turner, D. R. (2005). High resolution ICPMS as an on-line detector for flow field-flow fractionation; multi-element determination of colloidal size distributions in a natural water sample, *Anal. Chim. Acta*, **535**, 109–121.
41. Petteys, M. P. and Schimpf, M. E. (1998). Characterization of hematite and its interaction with humic material using flow field-flow fractionation, *J. Chromatogr. A*, **816**, 145–158.
42. von der Kammer, F., Baborowski, M. and Friese, K. (2005). Field-flow fractionation coupled to multi-angle laser light scattering detectors: applicability and analytical benefits for the analysis of environmental colloids, *Anal. Chim. Acta*, **552**, 166–174.
43. von der Kammer, F., Baborowski, M. and Friese, K. (2005). Application of HPLC fluorescence detector as a nephelometric turbidity detector following field-flow fractionation to analyse size distributions of environmental colloids, *J. Chromatogr. A*, **1100**, 81–89.
44. Lyvén, B., Hassellöv, M., Haraldsson, C. and Turner, D. R. (1997). Optimisation of on-channel preconcentration in flow field-flow fractionation for the determination of size distributions of low molecular weight colloidal material in natural waters, *Analyt. Chim. Acta*, **357**, 187–196.
45. Bouby, M., Geckes, H., Manh, T. N., Yun, J. I., Dardenne, K., Schafer, T., Walther, C. and Kim, J. I. (2004). Laser-induced breakdown detection combined with asymmetrical flow field-flow fractionation: application to iron oxi/hydroxide colloid characterization, *J. Chromatogr. A*, **1040**, 97–104.
46. Hassellöv, M., Lyven, B. and Beckett, R. (1999). Sedimentation field-flow fractionation coupled online to inductively coupled plasma mass spectrometry – new possibilities for studies of trace metal adsorption onto natural colloids, *Environ. Sci. Technol.*, **33**, 4528–4531.
47. Thielking, H. and Kulicke, W. M. (1998). Determination of the structural parameters of aqueous polymer solutions in the molecular, partially aggregated, and particulate states by means of FFFF/MALLS, *J. Microcol. Sep.*, **10**, 51–56.
48. Magnuson, M. L., Lytle, D. A., Frietch, C. M. and Kelty, C. A. (2001). Characterization of submicrometer aqueous iron(III) colloids formed in the presence of phosphate by sedimentation field flow fractionation with multiangle laser light scattering detection, *Anal. Chem.*, **73**, 4815–4820.
49. Thang, N. M., Knopp, R., Geckes, H., Kim, J. I. and Beck, H. P. (2000). Detection of nanocolloids with flow-field flow fractionation and laser-induced breakdown detection, *Anal. Chem.*, **72**, 1–5.
50. Reszat, T. N. and Hendry, M. J. (2005). Characterizing dissolved organic carbon using asymmetrical flow field-flow fractionation with on-line UV and DOC detection, *Anal. Chem.*, **77**, 4194–4200.

51. Beckett, R. (1987). The application of field-flow fractionation techniques to the characterization of complex environmental samples, *Environ. Technol. Lett.*, **8**, 339–354.
52. Contado, C., Blo, G., Fagioli, F., Dondi, F. and Beckett, R. (1997). Characterisation of River Po particles by sedimentation field-flow fractionation coupled to GFAAS and ICP-MS, *Colloids Surf. A*, **120**, 47–59.
53. van Berkel, J. and Beckett, R. (1996). Determination of adsorption characteristics of the nutrient orthophosphate to natural colloids by sedimentation field-flow fractionation, *J. Chromatogr. A*, **733**, 105–117.
54. Saal, C. and von der Kammer, F. (2002). Vergleich verschiedener Filtrationstechniken zur Aufkonzentrierung natürlicher kolloidaler Dispersionen für die Feld-Fluß-Fraktionierung (FFF), *Wasser*, **98**, 193–202.
55. Hassellöv, M. (2005). Relative molar mass distributions of chromophoric colloidal organic matter in coastal seawater determined by flow field-flow fractionation with UV absorbance and fluorescence detection, *Mar. Chem.*, **94**, 111–123.
56. Dahlqvist, R., Benedetti, M. F., Andersson, K., Turner, D., Larsson, T., Stolpe, B. and Ingri, J. (2004). Association of calcium with colloidal particles and speciation of calcium in the Kalix and Amazon rivers, *Geochim. Cosmochim. Acta*, **68**, 4059–4075.
57. Caldwell, K. D., Steven, L. B., Gao, Y. and Giddings, J. C. (1988). Sample overloading effects in polymer characterization by field-flow fractionation, *J. Appl. Polym. Sci.*, **36**, 703–719.
58. Giddings, J. C., Williams, P. S. and Benincasa, M. A. (1992). Rapid breakthrough measurement of void volume for field-flow fractionation channels, *J. Chromatogr.*, **627**, 23–35.
59. Litzen, A. (1993). Separation speed, retention, and dispersion in asymmetrical flow field-flow fractionation as functions of channel dimensions and flow-rates, *Analyt. Chem.*, **65**, 461–470.
60. Botana, A. M., Ratanathanawongs, S. K. and Giddings, J. C. (1995). Field-programmed flow field-flow fractionation, *J. Microcol. Sep.*, **7**, 395–402.
61. Moon, M. H., Williams, P. S., Kang, D. J. and Hwang, I. (2002). Field and flow programming in frit-inlet asymmetrical flow field-flow fractionation, *J. Chromatogr. A*, **955**, 263–272.
62. Williams, P. S. and Giddings, J. C. (1987). Power programmed field-flow fractionation – a new program form for improved uniformity of fractionating power, *Anal. Chem.*, **59**, 2038–2044.
63. Assemi, S., Newcombe, G., Hepplewhite, C. and Beckett, R. (2004). Characterization of natural organic matter fractions separated by ultrafiltration using flow field-flow fractionation, *Water Res.*, **38**, 1467–1476.
64. Newcombe, G., Drikas, M., Assemi, S. and Beckett, R. (1997). Influence of characterised natural organic material on activated carbon adsorption. 1. Characterisation of concentrated reservoir water, *Water Res.*, **31**, 965–972.
65. Hartmann, R. L. and Williams, S. K. R. (2002). Flow field-flow fractionation as an analytical technique to rapidly quantitate membrane fouling, *J. Membr. Sci.*, **209**, 93–106.
66. Geckeis, H., Manh, T. N., Bouby, M. and Kim, J. I. (2003). Aquatic colloids relevant to radionuclide migration: characterization by size fractionation and ICP-mass spectrometric detection, *Colloids Surf. A*, **217**, 101–108.
67. Wells, M. L. (2004). The colloidal size spectrum of CDOM in the coastal region of the Mississippi plume using flow field-flow fractionation, *Mar. Chem.*, **89**, 89–102.
68. Exner, A., Theisen, M., Panne, U. and Niessner, R. (2000). Combination of asymmetric flow field-flow fractionation (AF(4)) and total-reflexion X-ray fluorescence analysis (TXRF) for determination of heavy metals associated with colloidal humic substances, *Fresenius J. Anal. Chem.*, **366**, 254–259.
69. Beckett, R., Bigelow, J. C., Jue, Z. and Giddings, J. C. (1989). Analysis of humic substances using flow field-flow fractionation. In *Aquatic Humic Substances: Influence on Fate and Treatment of Pollutants*, eds Suffet, I. H. and MacCarthy, P. American Chemical Society, Washington, DC, pp. 65–80.
70. Dycus, P. J. M., Healy, K. D., Stearman, K. and Wells, M. J. M. (1995). Diffusion coefficients and molecular weight distributions of humic and fulvic acids determined by flow field-flow fractionation, *Sep. Sci. Technol.*, **30**, 1435–1453.

71. Klein, N. and Niessner, R. (1998). Characterization of heavy-metal-containing seepage water colloids by flow FFF, ultrafiltration, ELISA and AAS, *Mikrochim. Acta*, **129**, 47–55.
72. Schimpf, M. E. and Wahlund, K. G. (1997). Asymmetrical flow field-flow fractionation as a method to study the behavior of humic acids in solution, *J. Microcol. Sep.*, **9**, 535–543.
73. von der Kammer, F. and Forstner, U. (1998). Natural colloid characterization using flow field-flow fractionation followed by multi-detector analysis, *Water Sci. Technol.*, **37**, 173–180.
74. van den Hoop, M. and van Leeuwen, H. P. (1997). Influence of molar mass distribution on the complexation of heavy metals by humic material, *Colloids Surf. A*, **120**, 235–242.
75. Zanardi-Lamardo, E., Clark, C. D. and Zika, R. G. (2001). Frit inlet/frit outlet flow field-flow fractionation: methodology for colored dissolved organic material in natural waters, *Anal. Chim. Acta*, **443**, 171–181.
76. Zanardi-Lamardo, E., Clark, C. D., Moore, C. A. and Zika, R. G. (2002). Comparison of the molecular mass and optical properties of colored dissolved organic material in two rivers and coastal waters by flow field-flow fractionation, *Environ. Sci. Technol.*, **36**, 2806–2814.
77. Schimpf, M. E. and Petteys, M. P. (1997). Characterization of humic materials by flow field-flow fractionation, *Colloids Surf. A*, **120**, 87–100.
78. Lead, J. R., Wilkinson, K. J., Balnois, E., Cutak, B. J., Larive, C. K., Assemi, S. and Beckett, R. (2000). Diffusion coefficients and polydispersities of the Suwannee river fulvic acid: comparison of fluorescence correlation spectroscopy, pulsed-field gradient nuclear magnetic resonance, and field-flow fractionation, *Environ. Sci. Technol.*, **34**, 3508–3513.
79. Coble, P. G. (1996). Characterization of marine and terrestrial DOM in seawater using excitation emission matrix spectroscopy, *Mar. Chem.*, **51**, 325–346.
80. Ratanathanawongs Williams, S. K. and Keil, R. G. (1997). Monitoring the biological and physical reactivity of dextran carbohydrates in seawater incubations using flow field-flow fractionation, *J. Liq. Chromatogr. Rela. Techniques*, **20**, 2815–2834.
81. Vaillancourt, R. D. and Balch, W. M. (2000). Size distribution of marine submicron particles determined by flow field-flow fractionation, *Limnolo. Oceanogr.*, **45**, 485–492.
82. Thang, N. M., Geckes, H., Kim, J. I. and Beck, H. P. (2001). Application of the flow field flow fractionation (FFFF) to the characterization of aquatic humic colloids: evaluation and optimization of the method, *Colloids Surf. A*, **181**, 289–301.
83. Gimbert, L. J., Andrew, K. N., Haygarth, P. M. and Worsfold, P. J. (2003). Environmental applications of flow field-flow fractionation (FIFFF), *T Trends Anal. Chem.*, **22**, 615–633.
84. Wijnhoven, J. E. G. J., Koorn, J. P., Poppe, H. and Kok, W. (1995). Hollow-fibre flow field-flow fractionation on polystyrene sulphonates, *J. Chromatogr. A*, **699**, 119–129.
85. Pelekani, C., Newcombe, G., Snoeyink, V. L., Hepplewhite, C., Assemi, S. and Beckett, R. (1999). Characterization of natural organic matter using high performance size exclusion chromatography, *Environ. Sci. Technol.*, **33**, 2807–2813.
86. Siripinyanond, A., Worapanyanond, S. and Shiowatana, J. (2005). Field-flow fractionation-inductively coupled plasma mass spectrometry: an alternative approach to investigate metal–humic substances interaction, *Environ. Sci. Technol.*, **39**, 3295–3301.
87. Tipping, E. and Hurley, M. A. (1992). A unifying model of cation binding by humic substances, *Geochim. Cosmochim. Acta*, **56**, 3627–3641.
88. Dzombak, D. A. and Morel, F. M. M. (1990). *Surface Complexation Modelling: Hydrous Ferric Oxide*. John Wiley, & Sons, Inc., New York.
89. Amarasiriwardena, D., Siripinyanond, A. and Barnes, R. M. (2001). Trace elemental distribution in soil and compost-derived humic acid molecular fractions and colloidal organic matter in municipal wastewater by flow field-flow fractionation–inductively coupled plasma mass spectrometry (flow FFF–ICP-MS), *J. Anal. At. Spectrom.*, **16**, 978–986.
90. von der Kammer, F., Baborowski, M., Tadjiki, S. and von Tunpling, W. (2003). Colloidal particles in sediment pore waters: particle size distributions and associated element size distribution in anoxic and re-oxidized samples, obtained by FFF–ICP-MS coupling, *Acta Hydrochim. Hydrobiol.*, **31**, 400–410.
91. Benedetti, M. F., Ranville, J. F., Allard, T., Bednar, A. J. and Menguy, N. (2003). The iron status in colloidal matter from the Rio Negro, Brasil, *Colloids Surf. A*, **217**, 1–9.

92. Zattoni, A., Melucci, D., Torsi, G. and Reschiglian, P. (2000). Quantitative analysis in field-flow fractionation using ultraviolet-visible detectors: an experimental design for absolute measurements, *J. Chromatogr. Sci.*, **38**, 122–128.
93. Zattoni, A., Piccolomini, E. L., Torsi, G. and Reschiglian, P. (2003). Turbidimetric detection method in flow-assisted separation of dispersed samples, *Analyt. Chem.*, **75**, 6469–6477.
94. McCarthy, J. F. and Degueldre, C. (1993). Sampling and characterization of colloids and particles in groundwater for studying their role in contaminant transport. In *Environmental Particles*, eds Buffe, J. and van Leeuwen, H. P. IUPAC Series on Analytical and Physical Chemistry of Environmental Systems, Vol. 2. Lewis, Boca Raton, FL, pp. 247–315.
95. Taylor, H. E., Garbarino, J. R., Murphy, D. M. and Beckett, R. (1992). Inductively coupled plasma mass-spectrometry as an element-specific detector for field-flow fractionation particle separation, *Analyt. Chem.*, **64**, 2036–2041.
96. Chen, B. L. and Beckett, R. (2001). Development of SdFFF–ETAAS for characterising soil and sediment colloids, *Analyst*, **126**, 1588–1593.
97. Schmitt, D., Taylor, H. E., Aiken, G. R., Roth, D. A. and Frimmel, F. H. (2002). Influence of natural organic matter on the adsorption of metal ions onto clay minerals, *Environ. Sci. Technol.*, **36**, 2932–2938.
98. Ranville, J. F., Chittleborough, D. J., Shanks, F., Morrison, R. J. S., Harris, T., Doss, F. and Beckett, R. (1999). Development of sedimentation field-flow fractionation–inductively coupled plasma mass-spectrometry for the characterization of environmental colloids, *Anal. Chim. Acta*, **381**, 315–329.
99. van Berkel, J. and Beckett, R. (1997). Estimating the effect of particle surface coatings on the adsorption of orthophosphate using sedimentation field-flow fractionation, *J. Liq. Chromatogr. Relat. Technologies*, **20**, 2647–2667.
100. Gajdos, L. J. and Brenner, H. (1978). Field-flow fractionation – extensions to nonspherical particles and wall effects, *Sep. Sci. Technol.*, **13**, 215–240.
101. Beckett, R. and Giddings, J. C. (1997). Entropic contribution to the retention of nonspherical particles in field-flow fractionation, *J. Colloid Interface Sci.*, **186**, 53–59.
102. Jennings, B. R. and Parslow, K. (1988). Particle-size measurement – the equivalent spherical diameter, *Proce. R. Soci. London, Ser. A*, **419**, 137–149.
103. Beckett, R., Murphy, D., Tadjiki, S., Chittleborough, D. J. and Giddings, J. C. (1997). Determination of thickness, aspect ratio and size distributions for platy particles using sedimentation field-flow fractionation and electron microscopy, *Colloids Surf. A*, **120**, 17–26.
104. Thielking, H., Roessner, D. and Kulicke, W.-M. (1995). On-line coupling of flow field-flow fractionation and multiangle laser light scattering for the characterization of polystyrene particles, *Anal. Chem.*, **67**, 3229–3233.
105. Baalousha, M., v.d.Kammer, F., Motelica-Heino, M. and Le Coustumer, P. (2005). Natural sample fractionation by FlFFF–MALLS–TEM: sample stabilization, preparation, pre-concentration and fractionation, *J. Chromatogr. A*, **1093**, 156–166.
106. Siripinyanond, A., Barnes, R. M. and Amarasinghe, D. (2002). Flow field-flow fractionation–inductively coupled plasma mass spectrometry for sediment bound trace metal characterization, *J. Anal. At. Spectrom.*, **17**, 1055–1064.

---

# 6 Modern Electrophoretic Techniques for the Characterisation of Natural Organic Matter

---

PHILIPPE SCHMITT-KOPPLIN AND JENS JUNKERS<sup>†</sup>

*GSF—National Research Center for Environment and Health, Institute for Ecological Chemistry, Molecular BioGeoanalysis, Ingolstädter Landstraße 1, D-85764 Neuherberg, Germany*

1	Introduction . . . . .	278
2	Historical Aspects . . . . .	279
2.1	Electrophoretic Separations Over Recent Centuries . . . . .	279
2.2	Classical Electrophoretic Separations of Natural Organic Matter . . . . .	281
2.2.1	Free Solution and Paper Electrophoresis . . . . .	281
2.2.2	Classical Polyacrylamide Gel Electrophoresis (PAGE) . . . . .	282
2.2.3	Isoelectric Focusing . . . . .	283
2.2.4	Combining Gel Electrophoresis and Isoelectric Focusing in 2D-PAGE .	285
2.3	Emergence of Capillary Electrophoresis Techniques . . . . .	285
3	The Capillary Electrophoresis Approach . . . . .	287
3.1	Specificities of Capillary Electrophoresis . . . . .	287
3.1.1	Hydrodynamic Sample Injection . . . . .	287
3.1.2	The Driving Force in the Capillary: Electroosmotic Flow (EOF) . . . .	289
3.2	Zone Electrophoresis for Polyelectrolytes and Charged Particles . . . .	289
4	Capillary Electrophoresis of Natural Organic Matter . . . . .	291
4.1	Literature Survey . . . . .	292
4.2	From Fingerprinting to Structural Information . . . . .	294
4.2.1	Capillary Zone Electrophoresis of NOM . . . . .	294
4.2.2	pH and Ionic Strength Effects on Capillary Zone Electrophoresis of NOM . . . . .	295
4.2.3	Capillary Gel Electrophoresis (CGE) of NOM . . . . .	298
5	Selected Preparative Electrophoresis Approaches for Natural Organic Matter .	298
5.1	Capillary IEF (CIEF) Versus Preparative Solution Isoelectric Focusing .	298
5.2	Free-Flow Electrophoresis (FFE) Versus CZE . . . . .	302
5.3	Free-Flow Electrophoresis Combined Off-Line with Electrospray Ionisation Mass Spectrometry (ESI-MS) Versus CZE Coupled With ESI-MS . . . .	303

<sup>†</sup>Deceased.

6 Conclusion . . . . .	305
List of Abbreviations . . . . .	305
References . . . . .	307

## 1 INTRODUCTION

Organic environmental colloids (OECs) all constitute refractory products of chemical and biological degradation and condensation reactions of plant or animal residues that play a crucial role in many biogeochemical processes. They are complex heterogeneous and polydisperse mixtures of non-stoichiometric composition. These functionalised polyelectrolytes are not only small entities presenting a huge exchange surface but they also have pH-dependent aggregation potentials, creating ‘compartments’ with their own specific architectures, charge, size and functions. The best examples of polyelectrolytes in living systems are macromolecules such as collagen, hyaluronic acids and lignin. Among the non-living organic systems in the environment, dissolved humic substances (HS) are the main constituents of dissolved organic carbon (DOC) in surface, ground and soil pore waters as part of the natural organic matter (NOM) pool. Although dissolved HS compose about 25% of the total organic carbon (TOC) on earth and 50% of the organic carbon in oceans and fresh waters [1], their structural chemistry is understood less than any other biopolymer of living origin [2]. Both the diagenesis and function of HS in ecologically relevant processes are closely intertwined. OECs form an important link between: the natural and anthropogenic cycling of elements and molecules; the organic and the mineral world; and the dissolved and particulate state. They interact with microbes and affect microbial diversity in soils, affecting not only soil fertility, but also the mode and rate of transformation of xenobiotic compounds. OECs control the migration and bioavailability of trace nutrients, toxic metal ions and organic analytes. In particular, structural characteristics such as their charge and size distribution (charge density) and their secondary/tertiary structures (hydrophobic/hydrophilic sites) will influence their mobility in the environment, thereby affecting their bioavailability and/or toxicity. Several general structural models have been proposed for humic substances [2–5, but they should be used to relate structural concepts in terms of their functions in the environment rather than as exact chemical formulae. The highly complex, polydisperse and irregular structures of HS pose specific and, as yet, unresolved analytical challenges in the field of structural and quantitative analysis and data interpretation.

A systematic, interdisciplinary and multi-analytical characterisation is therefore necessary [6]. The necessary techniques are, in large part, covered in this book series. Electrophoresis plays a key role as an analytical or preparative technique in the characterisation of natural organic matter because it gives information about the behaviour of molecular mixtures under controlled conditions. The electrophoretic separation depends on both the size and the charge distribution frequency of the analytes in the complex mixture. Among all of the environmental particles presented in the second chapter of this book, only natural organic matter obtained by reverse osmosis, HS obtained from chemical fractionation, dissolved organic matter (DOM) from soil water extracts or natural water samples and UDOM (ultrafiltered DOM) or solid-phase extraction (SPE) extracts

(e.g. methanol eluates from C<sub>18</sub> SPE) have been thoroughly analysed with electrophoretic techniques. To date, only a few studies have examined undisturbed environmental colloids. For this reason, selected techniques based on electrophoresis are presented in this chapter with a focus on their use for the structural characterisation of organic matter mixtures that can be used as good models for natural organic environmental colloids.

## 2 HISTORICAL ASPECTS

The first electrophoretic separations were conducted with environmental colloids. Over the years, techniques based on zone and gel electrophoresis and isoelectric focusing have been used in their different set-ups to analyse natural organic matter and, to a lesser extent, other environmental particles. A rapid overview is given in the next section on the classical electrophoretical techniques and their use with humic substances in the last century. In the subsequent section, a critical view on the advantages and limitations of modern capillary electrophoretic methods is presented.

### 2.1 ELECTROPHORETIC SEPARATIONS OVER RECENT CENTURIES

Electrophoretic separations of mixtures of charged and neutral components are based on the differences in electrophoretic velocity of these molecules or their charged adducts when placed in an electric field. Different electrophoretic migration modes such as *frontal* (moving boundary), *zonal* and *displacement* can be theoretically distinguished, but in practice the observed migrations are a combination of all these phenomena.

Electrophoresis (from the Greek, 'borne by electricity') was introduced in the early 19th century. The Russian physicist Ferdinand Friedrich Reuss (1778–1852) accomplished the first observations of electromigration and electroosmosis over 200 years ago [Reuss, F. F. (1809). Sur un nouvel effet de l'électricité galvanique, *Mémoires de la Société Impériale des Naturalistes de Moscou*, 2, 327–337], 10 years after Alessandro Volta (1745–1827) built his first voltaic cell. Even more relevant to this chapter is that his observations were with environmental colloids. In that work, two vertical glass tubes were placed over wet clay filled with water while a layer of sand was placed in the bottom of each tube. Wires from a voltaic cell were inserted into the tubes and, when the circuit was closed, fine particles of clay migrated through the sand layer toward the positive pole, resulting in a cloudy solution. Conversely, at the negative pole, the solution remained clear and an increase in volume was observed [7].

Michael Faraday performed his first studies on electrode reactions in 1833–34 and formulated his *Laws of electrolysis*, which stated that the quantitative amount of material expunged from or deposited at an electrode surface was proportional to the applied electric field and the chemical equivalent weights. Further important experiments in the 19th century led to a deeper understanding of electrophoretic mechanisms, electroosmosis, mobility of ions in electrical fields and of the influence of physical parameters such as ionic radii. Kohlrauch (electroconductive properties of electrolytes, migration of ions in electrolytes) [8], von Helmholtz (ion double layer at interfaces) and Hittorf (electricity-carrying capacity of charged atoms and molecules) were key to developments at this time. In the late 1850s, Weidman and Quincke quantitatively reported the movement of charged species in an electric field and determined that the rate of migration was proportional

to the potential gradient [9]. In 1892, Picton and Linder studied the electromigration of colloid particles and observed that certain particles migrated towards the positive electrode and others to the negative electrode [9]. This led to the theory that the direction of the migration of particles was determined by their acid or base characteristics.

In 1948, the Nobel Prize lecture of Tiselius was entitled ‘Electrophoresis and adsorption analysis as aids in investigations of large molecular weight substances and their breakdown products’. His work was one of the first electrophoretic experiments on proteins in solutions at the beginning of the 20th century. These experiments certainly set the groundwork for the first electrophoresis experiments in the 1950s to characterise humic-like substances. The main problems encountered were band broadening due to Joule effects (thermal effects), a problem solved partially by water cooling the system to 4 °C (Figure 1) [10].

Other efficient solutions included using buffers and a supporting medium such as paper, starch, agarose or polyacrylamide; not only was the diffusion reduced but also molecular sieving occurred, permitting an additional separation based on size [11,12]. The first paper electrophoresis systems of the early 1940s could only be used successfully on small molecules (amino acids, lipids, charged sugars). After the sample was applied to the middle of a paper strip, a potential difference of about 100 V cm<sup>-1</sup> was applied and the analytes could be separated on the paper according to their charge and size. Application of this technique on larger paper strips allowed the two-dimensional orthogonal separations of mixtures at two different pHs. Separations on agarose or polyacrylamide gels are also over 100 years old. Many interesting developments occurred about 30 years ago, when it was realised that these supports were ideal for the separation of proteins in denaturing agents such as urea or sodium dodecyl sulfate (SDS): polyacrylamide gel electrophoresis (PAGE) was born.

The next important electrophoretic separation technique that was developed was isoelectric focusing (IEF) [13], which was based on the existing gel systems that were impregnated with ampholytes, thus creating a pH gradient between the anode and cathode.

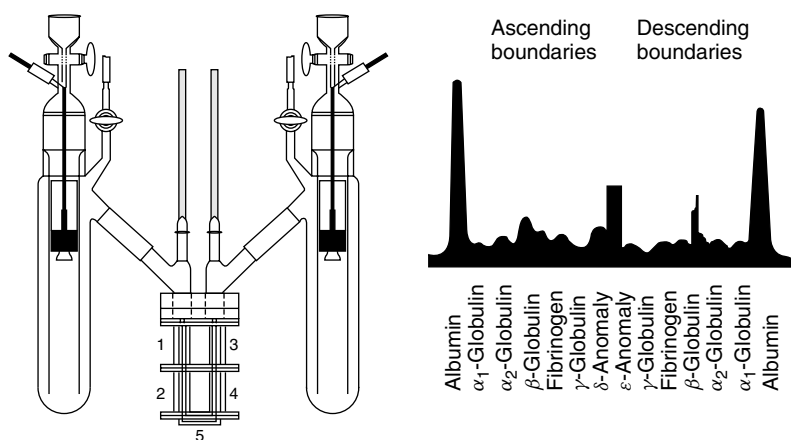


**Figure 1.** Electrophoresis U-tube assembled by Tiselius with electrode containers; Electrophoresis of normal human plasma and separation of albumin from  $\alpha$ -,  $\beta$ - and  $\gamma$ -globulins (from Tiselius’s Nobel Lecture, 1948 [10])

2D gel electrophoresis was created by combining orthogonal gel electrophoresis with isoelectric focusing. The technique has recently gained popularity as the basis for separations in modern *proteomics*. Also in the 1960s, Hjerten [14] performed the first separations using narrow-diameter tubes, which had the advantage of the best heat dissipation, thus limiting band broadening. In that case, capillaries had an inner diameter (i.d.) of 300 µm and the separated bands were detected by UV spectroscopy. Developments continued with the introduction of polyacrylamide gel-filled capillaries to separate proteins in the 1970s (450 µm i.d., 3 cm length; Pyrex® or even Teflon® capillaries) to separate small ions. Jorgenson and Lukacs [15,16] first demonstrated the possibility of using narrow-bore capillaries (<100 µm i.d.) at voltages of 30 kV combined with fluorescence detection to separate amino acids and peptides with up to 40 000 theoretical plates: this was the beginning of the success of the capillary electrophoresis technique, known that time as high-performance capillary electrophoresis (HPCE). Only in the late 1980s were the first HPCE instruments commercialised and other detection techniques introduced (*e.g.* UV, laser-induced fluorescence, electrochemical, mass spectrometry).

The reader will find thorough reviews of the technique in the current literature (electrophoresis [17] and capillary electrophoresis [18–21]). For specific reviews on the application of classical electrophoretic techniques to the characterisation of humic substances, the reader is referred to an excellent and critical overview by Duxbury [22], which covers work from the early 1950s to late 1980s. A tabulated review on the use of capillary electrophoresis techniques on natural organic matter (NOM) [23] covers most of the publications in the period from the early 1990s to 2003. In the present chapter, we will critically discuss the use and limitations of the above-mentioned methods with respect to the structural characterisation of natural organic matter and focus on the latest developments from 2000 to 2005 using analytical and preparative electrophoresis methods.

## 2.2 CLASSICAL ELECTROPHORETIC SEPARATIONS OF NATURAL ORGANIC MATTER

The goal of most of the electrophoretic studies on NOM over the years has been its fractionation, often directed toward the separation of specific biomolecules (polysaccharides, N-containing compounds, enzymes, *etc.*) that are potentially present in the mixtures. Methods have mainly been focused on the analysis of humic like materials (alkali extracts of soils) and, in most cases, electrophoresis was used as a fingerprinting method rather than a method to study quantitatively structural characteristics such as molecular size or charge. Free solution and paper electrophoresis, gel electrophoresis and isoelectric focusing (electrofocusing) were the most frequently used techniques from the 1950s to the late 1980s [22]. Since the early years of electrophoretic work, the main goal of most researchers was to obtain as many ‘bands’ as possible as was the case with the biomolecules. In most cases, bands are attributed to humic fractions having similar electrophoretic mobility. Even though artefacts due to the interactions of the humic substances with buffer components or separation matrices were already demonstrated in the early 1950s, these facts have often been neglected over the years.

### 2.2.1 Free Solution and Paper Electrophoresis

Following the experiments of Reuss in 1809, the second reported experiment on the use of electrophoresis with NOM date from 1925 by Ostwald [24] using the moving

boundary method. Stevenson, *et al.* subsequently experimented intensively with humic substances [25] using the Tiselius cooled U-tube system [9]. Most of the free solution experiments used paper or cellulose packed in powder as an additional stabilization medium [22]. Usually, the authors managed to separate one to three fractions in addition to an immobile fraction; fractions were detected with UV spectroscopy. The limitations of the early approaches may have been due to the fact that the UV signal was not necessarily correlated with the C content in the fractions. More detailed experiments involved the hydrolysis of the fractions and analysis of the amino acid and carbohydrate contents. Some important trends were observed [22]:

- the mobility increased with increasing pH, confirming the role of COOH and OH ionisation;
- the interactions of metals (Cu, Co, Ni, Fe) could in some cases alter the mobility;
- interactions between buffer components could also be responsible for mobility changes (*e.g.* borate ions);
- comparisons among results were often difficult since different samples (origin and extraction methods) were used by different authors.

These results demonstrated the importance of complexing agents and cations for the electrophoretic mobility and reflected associations of humic materials into intermolecular aggregates. For example, in 1953, Stevenson and Martin stated that the association of humic molecules could interfere with the separation process [26].

### 2.2.2 Classical Polyacrylamide Gel Electrophoresis (PAGE)

Polyacrylamide gel electrophoresis (PAGE) first found application with proteins in combination with denaturing agents (urea to reduce intermolecular H-bonds; sodium dodecyl sulfate (SDS) to give the proteins a similar charge density and thus to create a separation in the gel based only on sieving). It was first reported as an anticonvective matrix for humic materials in 1969 [27]. At the time it yielded comparable results to paper zone electrophoresis (at least visually in terms of the creation of ‘separation’ bands). SDS is not used with acidic proteins owing to its low binding resulting from charge repulsion. Its role with humic substances has been previously described as ‘*any disaggregating effect of SDS on humic substances would probably be due to displacement of polyvalent cations from humic substances and would therefore be a function of the purification procedure undertaken prior to electrophoresis*’ [22].

In terms of the separation of bands (fingerprinting without possible structural information), the PAGE approach certainly yields good results, but a direct correlation in terms of structural characteristics is difficult because of specific interactions with the buffer/gel components. Separations are caused by chemical interactions between fractions of the NOM and polyacrylamide, urea, SDS or buffer constituents that depend on the sample structure. Numerous recent papers from Trubetskoy and co-workers [28–34] have shown that this approach using complexing buffers may still be used; recent findings have shown that most fluorophores and a large proportion of photoinductive chromophores are located in the low molar mass fractions (C + D) of soil humic substances (Figure 2) and such a distribution of photochemically active constituents may be characteristic across different soil types [35].

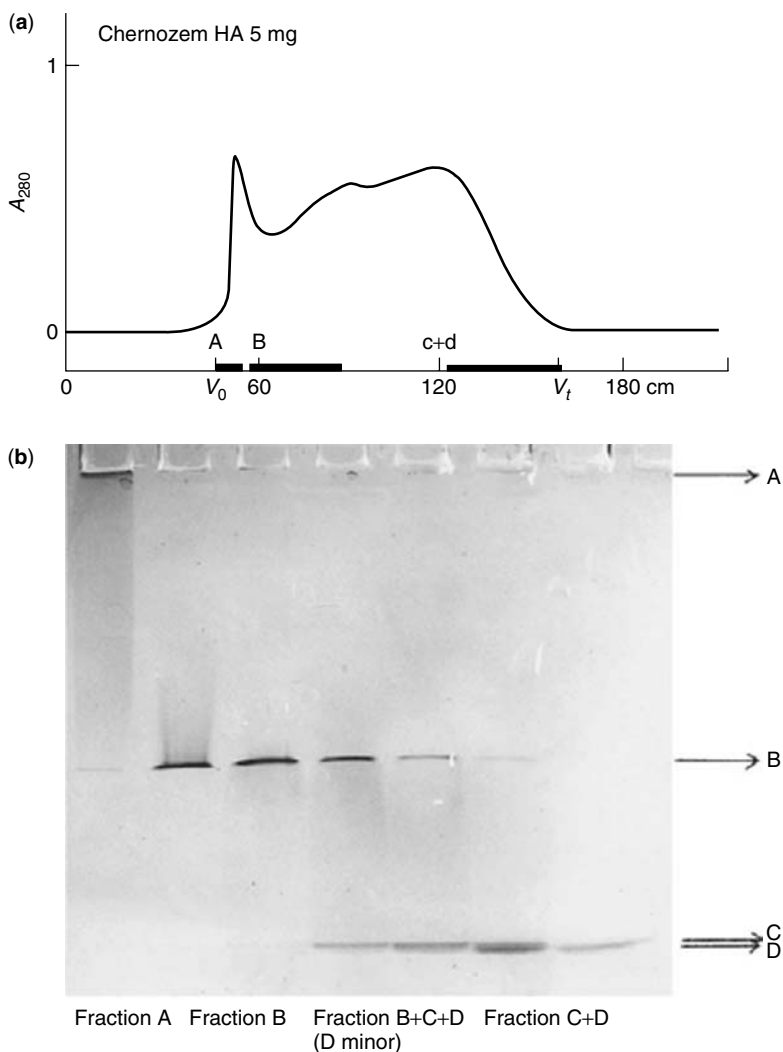


**Figure 2.** SEC–PAGE technique for the characterisation of humic acids; illustration adapted from [36]. (a) SEC of the humic acids with collection of the fractions A–D; (b) PAGE of the collected fractions A–D. Reprinted with permission from Richard, C., *et al.*, *Environmental Science and Technology*, **38**, 2052–2057. Copyright 2004 American Chemical Society

### 2.2.3 Isoelectric Focusing

Isoelectric focusing (IEF) has been used for biochemical separations since the mid-1960s [37]. The separation is carried out in a pH gradient created by the addition of zwitterionic substances called ampholytes to the separation solution or integrated in the gels (analytical agarose, Sephadex or polyacrylamide gels); the analytes migrate in the solution or the gel matrix to the pH where their positive charges balance their negative charges [isoelectric points ( $pI$ )]. IEF in gels of humic substances generates a series of

regular bands in the different isoelectric point domains, extending from a more diffuse area of increasing colour on going from lower pH (anode) to higher pH values (cathode).

Although results obtained with the IEF technique in gels are extremely dependent on the experimental conditions [38], it is one of the most commonly used classical electrophoretic techniques for the fingerprinting of NOM [39]. It has been used to fingerprint humic substances from different soils, composts [38,40,41] and fulvic and humic acids [42] and to differentiate phenol oxidase products [43], and it has also been employed to follow humification processes [39–41,44–48]. Govi *et al.* [49] used IEF to follow the transformation of leather meal fertilisers in soils.

Many authors attributed these bands to humic fractions having a specific isoelectric point; others attributed possible artefacts to the bands [22,42,50,51], based on several observations:

- IEF-refocusing of a given band may again deliver a series of bands around the position of the original band, especially towards lower pH ranges [22,50,52] (Figure 3);

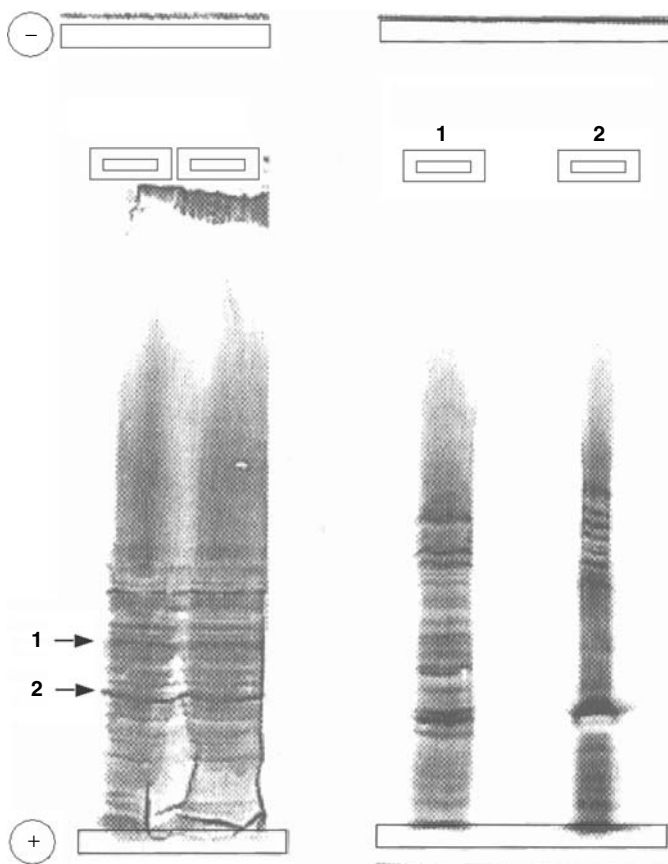


**Figure 3.** Refocusing of two extracted bands (1 and 2) from an IEF run of a leonardite humic acid (from U. Schoen, personal communication)

- In IEF in a gel, the band pattern obtained is strongly influenced by the prefocusing of the gel and the quality of the pH gradient that is obtained at the moment of contact between the NOM and the ampholytes (especially for the bands near the application zone [52]).
- The flocculation of acidic ampholytes in contact with NOM has often been described [39,50].
- Gjessing and Gjerdahl [53] described up to 85% flocculation of aquatic humic substances with Ampholine at low pH (pH 3) in a solution IEF column (without gel). In the pH gradient zone from pH 3 to 1, they observed three major bands with a major peak at pH 1.52. Comparable behaviour in flocculation and focusing was observed in preparative solution IEF by Schmitt *et al.* [54] using humic substances from soils, surface water and ground water.
- A major indication of interactions is the observation that when using the same sample and the same gel with different commercially available ampholytes, one obtains different band positions [51].

With ampholites in pH gradients from pH 3 to 10, several bands are formed in the acidic [55] and neutral pH range [56]. In the alkaline region, bands are mainly found at the position of application, confirming a sieving effect or immobilisation with respect to the polyacrylamide gel. The presence of humic substances with high ash contents due to clay residues often gives perturbed areas (precipitation) at the points where they are applied (cathode) (Figure 4). The nature of the interactions between humic acid fractions and different ampholyte systems in IEF has been investigated in detail [52].

With a median nitrogen content around 2% [57], NOM may contain only limited amounts of free positive charge (amino acids and peptide bonds play a minor role). In solution IEF, only limited amounts of carbon will be found in the  $pI$  range  $>4$ ; flocculation of about 60% of the carbon occurs at acidic pH (pH lower than 4) [54]. In addition, numerical simulations show that anionic molecules (such as organic acids) will not reach a steady state but will approach asymptotically a mobility minimum at a pH that is 2 units lower than their  $pK_a$ , resulting in an accumulation of analytes and potential band formation without the need for zwitterions (Figure 4).

## 2.2.4 Combining Gel Electrophoresis and Isoelectric Focusing in 2D-PAGE

Due to recent advances in proteomics, the 2D-PAGE technique has been modernised. The new methodology combines the sieving effects and size selectivity of polyacrylamide gels with the pH-dependent charge selectivity of IEF. For example, this approach has been used successfully to fractionate Th-binding polysaccharidic fractions from colloidal marine organic matter [59] and can thus be used as a fractionation tool for specific substance classes within complex NOM mixtures.

## 2.3 EMERGENCE OF CAPILLARY ELECTROPHORESIS TECHNIQUES

Capillary electrophoresis (CE) is a non-perturbing method allowing the electrophoretic separation of monodisperse or polydisperse mixtures [20] of small ions [60–62], macromolecules [63–66], polymers [67–70], colloids [71], nanoparticles [72–75], liposomes [76], bacteria [71,77] and viruses, using non-aqueous or aqueous buffers with coated or

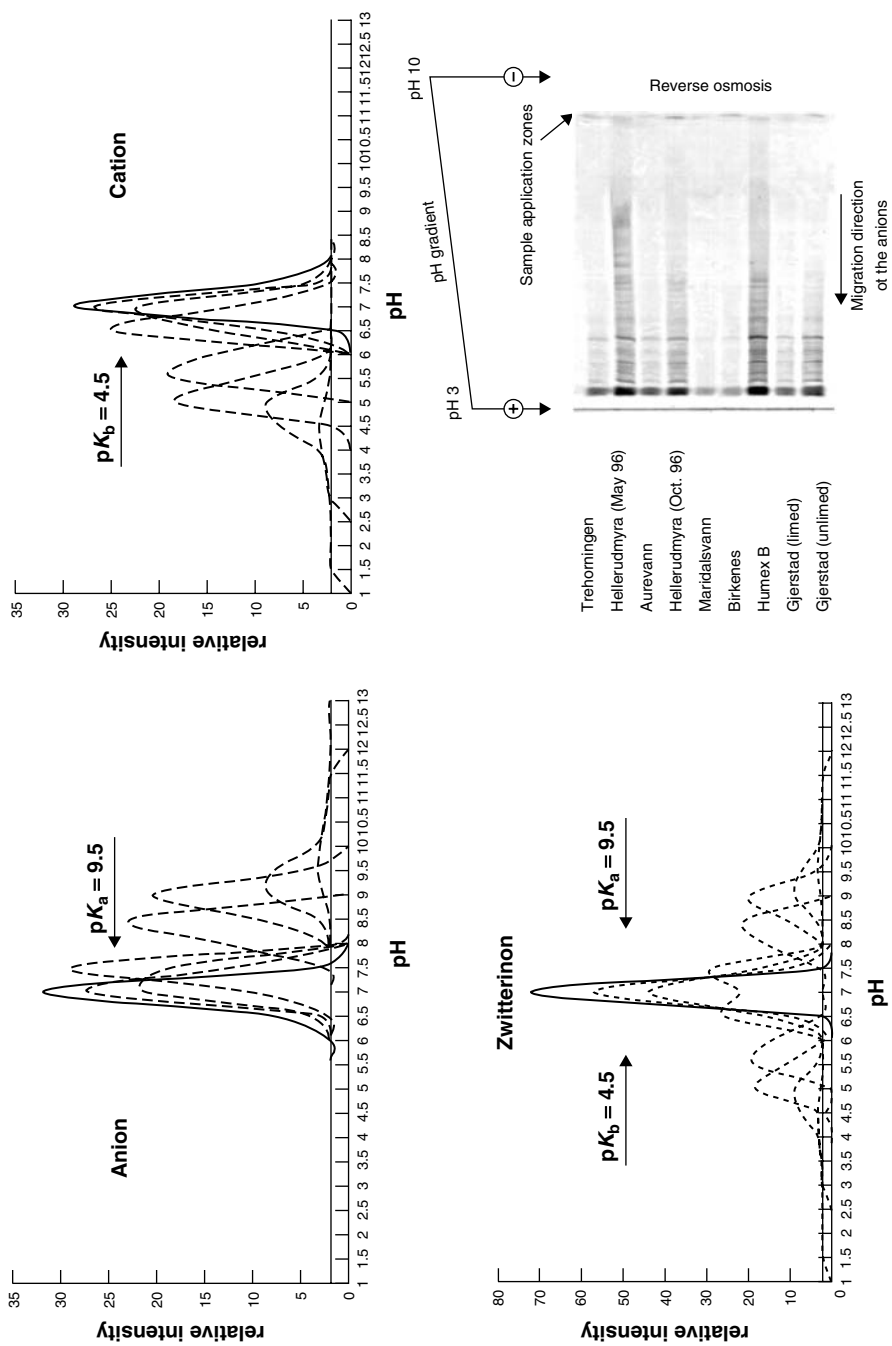


**Figure 4.** Zone electrophoretic simulation of the isoelectric focusing of an anion, cation and zwitterion in a pH gradient from 1 to 13 showing the concentration distributions as a function of time. At  $t = 0$ , an identical concentration of analyte is present all over the pH gradient. Only the ionised fractions at higher pH for acids ( $pK_a = 9.5$ ) and lower pH for the bases ( $pK_b = 4.5$ ) move with zone electrophoresis to form a moving boundary. Real gel IEF of Norwegian lake NOM from the NIVA Project [58] showing different bands in the gel

uncoated capillary columns [18,19]. The small volume of analyte needed in CE experiments makes it possible to measure cellular contents (*e.g.* native proteins [78] using fluorescently labelled or induced proteins [79], metabolites [80]) and to monitor the gene expression of single cells [81]. Different CE techniques such capillary gel electrophoresis (CGE) and capillary isoelectric focusing (CIEF) can currently be coupled into two-dimensional techniques (CGE–CIEF) in a similar manner to classical 2D gel electrophoresis in the fields of human genomics and proteomics [82–84]. CZE allows the separation of analytes based on their charge-to-size ratio and has established new possibilities for the characterisation of complex mixtures (including natural compounds [85–87] and natural organic matter (NOM) [88]). These strategies can from the basis of many studies designed to elucidate the molecular composition of mixtures such as in metabolomics [89], especially when combined with mass spectrometry (MS) using mild detection by ionisation techniques such as electrospray ionisation (ESI). The compiling of high-resolution separation techniques (CE and CEC) to high-precision mass measurements obtained with powerful MS systems {quadrupole time-of-flight mass spectrometry (Q-TOF) [90] or high-resolution Fourier transform ion cyclotron resonance mass spectrometry & (FT-ICR–MS) [91]} is another step towards understanding complex mixtures and answering important questions in chemical biology, cellular biochemistry [92] and environmental chemistry.

### 3 THE CAPILLARY ELECTROPHORESIS APPROACH

The main advantage of CE is its simple instrumentation, consisting of a high-voltage power supply, two buffer reservoirs, a fused-silica capillary and a detector. The basic set-up can be complemented with enhanced features such as multiple injection devices, autosamplers, sample and capillary temperature controls, programmable power supplies, multiple detectors, fraction collection and computer interfacing.

In CE, the separation is performed in a flexible fused-silica capillary (length 20–100 cm, i.d. 25–100 µm) that is filled with an appropriate buffer solution of defined pH and ionic strength (aqueous or non-aqueous). A small volume of sample (less than 3–4% of the column volume to maintain separation efficiency) is introduced hydrodynamically (or, less often, electrokinetically) into the capillary and an electrical potential is applied (Figure 5). Charged species in the sample exhibit different effective electrophoretic mobilities (field strength-reduced velocities) and are thereby separated. The detectors are based on UV–VIS, laser-induced fluorescence, electrochemical, conductivity and mass spectrometry. Different techniques are possible as a function of the type of capillary column and the buffer, allowing separations of charged, neutral, polar or hydrophobic analytes. Fraction collection is possible but yields only minuscule amounts of sample.

#### 3.1 SPECIFICITIES OF CAPILLARY ELECTROPHORESIS

Compared with chromatography, two main differences with CE are the technique of injection into the capillary and the means by which the sample is driven through the column, *i.e.* electroosmosis rather than hydrodynamic pumping [93,94].

##### 3.1.1 Hydrodynamic Sample Injection

For hydrodynamic sample injection, pressure forces a small portion of the sample into an open-tube capillary. A difference in pressure is applied across the capillary by pressurising

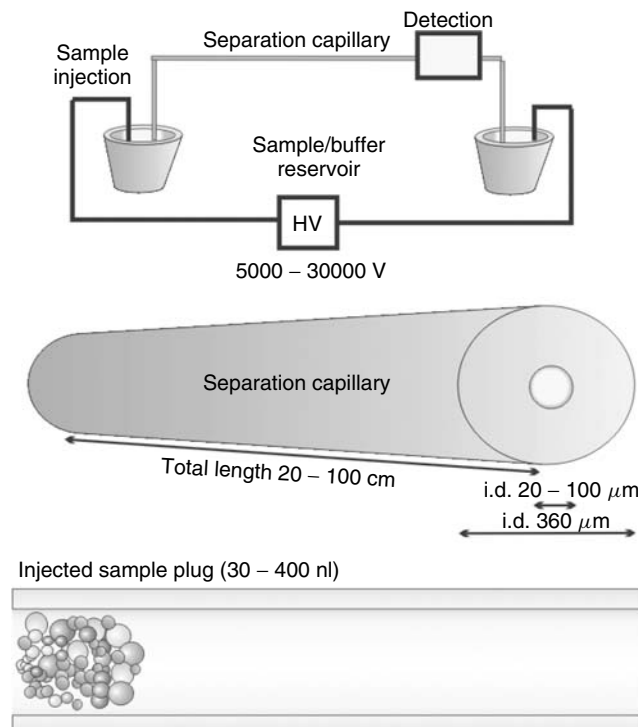


**Figure 5.** Simple set-up of capillary electrophoresis (the potential set-up is illustrated as generally used for NOM)

**Table 1.** Calculated total volumes, volumes injected when applying an identical 15 s hydrodynamic injection at 0.5 psi and 30 °C and the corresponding percentage of column lengths injected for different columns lengths and capillary internal diameter

Column $L_d/L_t^a$	Total capillary volume $\mu\text{l}$ and volume injected $\text{nl}$			% total length injected		
	I.d. 50 $\mu\text{m}$	I.d. 75 $\mu\text{m}$	I.d. 100 $\mu\text{m}$	I.d. 50 $\mu\text{m}$	I.d. 75 $\mu\text{m}$	I.d. 100 $\mu\text{m}$
30/37	0.7/27	1.3/135	2.9/429	4.6	10.3	18.2
50/57	1.1/18	2.5/88	4.4/278	1.8	4	7.1
70/77	1.5/13	3.4/65	6.0/206	0.9	2.1	3.7

<sup>a</sup>  $L_d$ , capillary length to detector;  $L_t$  capillary total length

the sample vial. The injected sample volume can be determined by taking account of the pressure difference across the capillary, the inner diameter of the capillary, the time of application of the pressure, the viscosity of the sample and the capillary length. Overly large sample zones may result in signal distortion because the sample zone will not reach equilibrium before being detected. A general rule in CE is that the sample plug should never exceed 5% of the total column length (Table 1). This rule is essential when adapting some methods from the literature to different instruments where the injection conditions and/or column lengths are not necessarily identical. It should be noted that identical

injection times with different column i.d.s or lengths not only lead to different column volumes but also to different local sample concentrations when passing the detector (as a function of the pH-dependent mobility profiles). This is particularly important when analysing samples with concentration-dependent aggregation properties such as polymeric materials and NOM.

### 3.1.2 The Driving Force in the Capillary: Electroosmotic Flow (EOF)

Electroosmosis is the fundamental driving force in CE that is a direct consequence of the surface charge on the walls of an uncoated fused-silica capillary. In most cases, the capillary surface has silanol groups ( $pK_a$ -3–5) that ionise as a function of the pH of the separation buffer [95]. The dissociation of  $\text{SiOH}$  groups to  $\text{SiO}^-$  produces a negatively charged surface on which an electrical double layer is generated to preserve electroneutrality. The counterions and their associated solvating water molecules migrate in the electric field, producing a flow towards or away from the detector called electroosmotic flow (EOF). The EOF is directly dependent on the chemistry of the separation buffer, its viscosity  $\eta$  and its dielectric constant  $\epsilon$  [especially important in the non-aqueous mode (NACE)]. For example, an increase in the ionic strength of the electrolyte or a decrease in pH can decrease the zeta potential and, as a consequence, the EOF (Figure 6). Strongly adsorbed ions will have the same effect. By coating the inside of the capillaries (e.g. neutral or charged polymers), it is possible to alter chemically the surface and thus regulate the EOF if required.

## 3.2 ZONE ELECTROPHORESIS FOR POLYELECTROLYTES AND CHARGED PARTICLES

In free solution, the electrophoretic mobility (i.e.  $\mu_{\text{elec}}$ , the particle velocity per unit applied electric field) is a function of the net charge, the hydrodynamic drag of a molecule and the

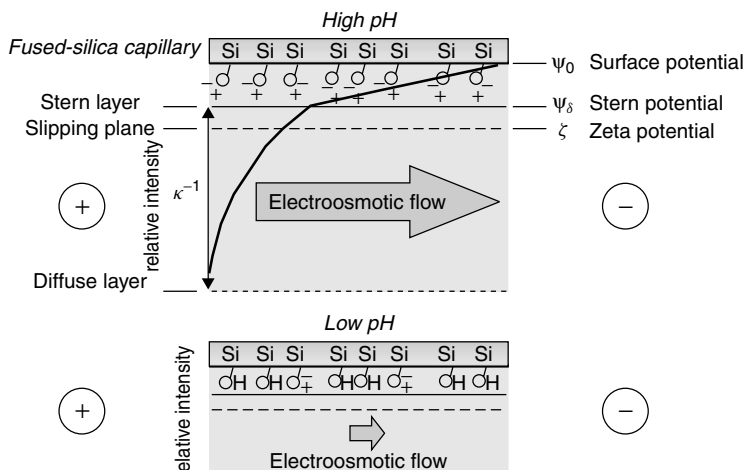


**Figure 6.** Schematic representation of the fused-silica capillary surface at high and low pH values and practical consequences for the electroosmotic flow when a difference of potential is applied across the capillary.  $\kappa^{-1}$  corresponds to the Debye length and is function of the ionic strength and the pH of the separation buffer. Reprinted with permission from Wiley-VCH

properties of the solution (viscosity, electrolyte ions – their concentration and mobility). It can be expressed as the ratio of the electric charge  $Z$  ( $Z = qe$ , where  $e$  is the charge of an electron and  $q$  the valence) to the electrophoretic friction coefficient. Different predictive models have been employed to interpret the data; most involve the size, flexibility and permeability of the molecules or particles.

The combination of Henry's theoretical model [96] of  $\mu_{\text{elec}}$  for colloids and Debye-Hückel theory predicts a linear relation between the mobility and the charge of a molecule:

$$\mu_{\text{elec}} = \frac{eZ}{6\pi\eta R_h} \frac{f_1(\kappa R_h)}{(1 + \kappa R_h)} \quad (1)$$

where  $R_h$  is the hydrodynamic radius of the analyte,  $\kappa$  is the inverse of the Debye length,  $\eta$  is the viscosity of the separation buffer,  $e$  is the fundamental unit of charge and  $f_1$  is a function that describes the effect of the molecule (or particle) on the electric field. This function is defined between two limits: (i) the Hückel limit,  $f_1 = 1$  when  $\kappa R_h < 1$  (when the hydrodynamic radius is smaller than the Debye length); and (ii) the Helmholtz-Smoluchovski limit,  $f_1 = \frac{3}{2}$  when  $\kappa R_h > 10$  (when the hydrodynamic radius is larger than the Debye length) (see also Figure 7). Between these limits,  $f_1$  can be calculated from following equation [96]:

$$f_1(\kappa R_h) = \left( 1 + \frac{\kappa^2 R_h^2}{16} - \frac{5\kappa^3 R_h^3}{48} - \frac{\kappa^4 R_h^4}{96} + \frac{\kappa^5 R_h^5}{96} + -\frac{11}{96} e^{\kappa R_h} \int_{\infty}^{\kappa R_h} \frac{e^{-r}}{r} dr \right) \quad (2)$$

For small molecules (metabolites, monomers and small oligomers), the mobility equation may be solved empirically using the Offord model (linear relation to charge to size ratio, the charge being obtained directly from the ionisation constants and the size being estimated from the molar mass,  $M$ ) [97]):

$$\mu_{\text{elec}} = a \frac{eZ}{M^\alpha} \quad (3)$$

where  $a$  and  $\alpha$  are two constants determined experimentally which vary as a function of the class of chemical compounds (DNA, peptides, organic acids) [98]. This empirical concept has been adapted to simulate the separation of a number of analytes, including DNA fragments, peptides and proteins [99], allowing the optimisation of their separation and the assignment of chemical structures and properties.

From oligomers to polymers, the theoretical and empirical approaches found in the electrophoresis literature often involve a parameterisation that includes the degree of polymerisation ( $N$ , number of monomer units) of the objects into their models [20]. This approach yields exact results but is not generally applicable to polydisperse polyelectrolytes such as NOM. Cottet and Gareil [100] developed a model for different polymeric materials that depends on the number of monomers and their frictional characteristics (charge distribution as a function of chemical substitution of the monomers to which the authors attributed relative frictional coefficients). Fairly good correspondence was obtained between predicted and observed electrophoretic mobilities for benzene polycarboxylic acids, dichondroitin, polyalanines, polyglycines, linear fatty acids, polystyrene

sulfonates (PSS) and polycytidines. The same approach was possible with PSS with various degrees of sulfonation [100]. Although the above electrophoretic models may be useful for well-defined polymers, they are more delicate to apply to NOM.

For colloids and particles, the electrophoretic mobility contains information on electric (surface charge) and hydrodynamic properties (size, conformation). For colloids and particles with dimensions in the lower nanometer range (*e.g.* polymers) to the lower micrometer range [*e.g.* living organisms or their fractions thereof (mitochondria, cells, cell wall fractions, *etc.*), the Poisson–Boltzmann equation, expressed in spherical coordinates for the distribution of ions around the sphere and the consequent potentials coupled to equations for forces as a result of electroosmotic flow [101], can be employed to interpret electrophoretic mobility measurements. Approximate solutions lead to a relatively complex picture of a balance of a number of forces on a particle: a driving force of electrical field on the charged particle, a frictional retarding force from moving a particle through a fluid, a retardation force due to the diffuse double layer on the particle surface (equivalent to an electroosmotic backflow from the charged particle surface) and a relaxation effect due to the polarisation of the diffuse double layer [101]. Many theoretical approaches have been developed with different geometric models and assumptions concerning the characteristics of the studied analytes ([102] and references therein). Mixed models that consider polymer coated particles [103] or stabilized colloids [104] have appeared recently.

For NOM and organic colloids, the models that have been proposed thus far generally involve hard sphere or cylinder models [105–108], permeable Donnan gel phases [109, 110], or branched [111] or linear [112] polyelectrolytes. For polyelectrolytes, the different limiting cases must be distinguished, *i.e.* impermeable hard spheres, semipermeable spherical colloids [113,114] and fully permeable electrolytes. The most recent model applied to NOM was presented by Duval *et al.* [115]. It involves an electrokinetic model for a soft particle and takes into account a hard (impermeable) core and a permeable diffuse polyelectrolyte layer (Figure 7). More recently, a unifying approach to combine potentiometric data with size information from SEC and pH-dependent electrophoretic mobilities should be available by the time this book is published (J. Ritchie, M. Perdue, Ph. Schmitt-Kopplin in preparation).

The development of all of the different electrophoretic models is beyond the scope of the present chapter as they all represent a projection of a theoretical model on experimental datasets obtained within the limitations of the experimental conditions. For these aspects, the reader should refer to the literature cited above and subsequent chapters in this book.

#### 4 CAPILLARY ELECTROPHORESIS OF NATURAL ORGANIC MATTER

In this section, many of the applications of CE that are found in the literature for the characterisation of NOM are presented with respect to their potential relative to the classical electrophoretic techniques and their limitations in terms of the structural information they can deliver. By far the most promising approach is the combination of CE with mass-selective detection via different interfaces. In all cases, adsorptive interactions between the capillary wall and the colloid particles can be nearly excluded in the case of NOM, because both the colloids and the capillary wall are negatively charged under most present experimental conditions (*i.e.* electrostatic repulsion rather than adsorption should occur [117]).

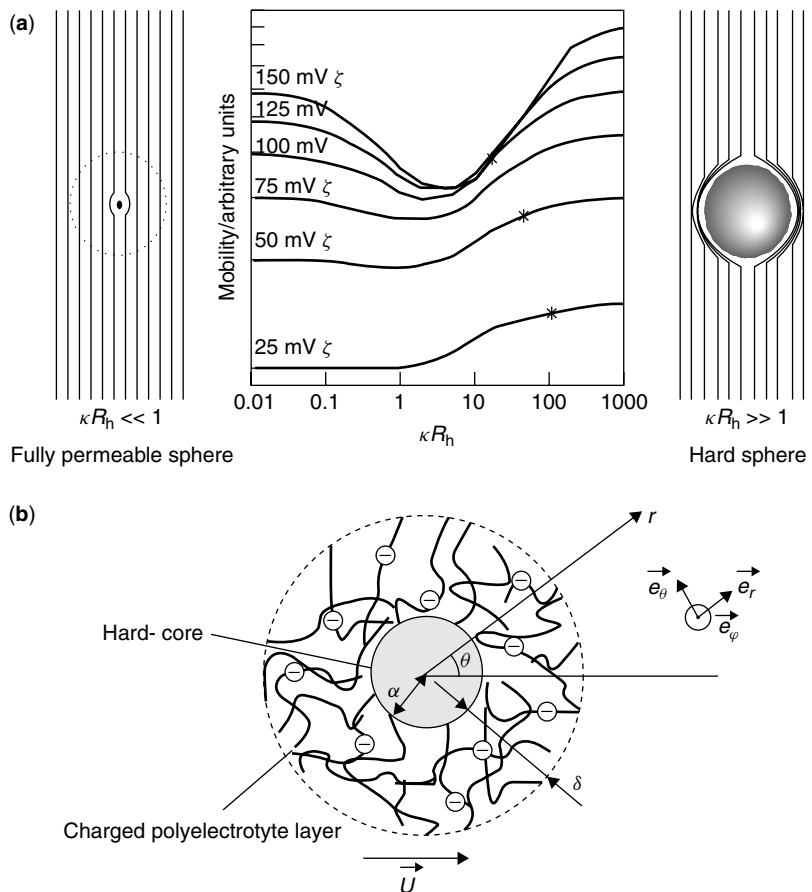


**Figure 7.** (a) Flow streamlines corresponding to the hydrodynamic flow around a NOM seen as a fully permeable sphere ( $R_h \gg \kappa^{-1}$ ) and as a hard sphere ( $R_h \ll \kappa^{-1}$ ); schematic representation of the dependence of electrophoretic mobility on  $\kappa R_h$  for different  $\zeta$  potential values. The stars represent the decrease in mobility of a particle of a given size due to a decrease in the electric double layer by changes in ionic strength. Humic substances were reported to have  $\zeta$  potentials ranging from  $-39$  to  $-69$  mV for the Suwannee River fulvic acid at pH 4.5 and 11, respectively [116]. (b) schematic representation of a charged NOM particle viewed as a semipermeable particle in [115]. Reprinted in part with permission from Duval, J., Wilkinson, K. J., Van Leeuwen, H. and Buffel, J., *Environmental Science and Technology*, **39**, 6435–6445. Copyright 2005 American Chemical Society

#### 4.1 LITERATURE SURVEY

About 100 articles have examined the separation of humic substances using CE [23]. In all studies, the electrophoretic signals (UV–VIS, fluorescence, electrospray ionisation mass spectrometry or total organic carbon in free flow electrophoresis) were observed in the anionic range and had very similar mobility patterns: a (Gaussian-like) distribution of charge density (described as a hump) and, in some cases, some singly resolved peaks corresponding to single molecules (polar and charged small molecules). The degree of

ionisation of phenolic and carboxylic groups is governed by the pH of the separation buffer. Fulvic acids exhibit a consistent and characteristic set of sharp peaks (partially characterised as being phenolic acids or lignin degradation products in soils) that extend from the humic 'hump' [118] (Figure 8). The average electrophoretic mobility (AEM) of the humps depends on the structure of the HS, the experimental conditions and the buffer composition [58,119,120]. Humic acids generally only show the 'hump' and sometimes multiple humps. Particulate fractions show up as spikes in the electropherograms. Most of the articles published up to 2003 were included in a review paper [23]; no significant 'new' results have been reported recently.

NOM is a mixture of constituents with a wide hydrophobic/hydrophilic range that behave as molecules and/or colloids depending on their concentration and the ionic

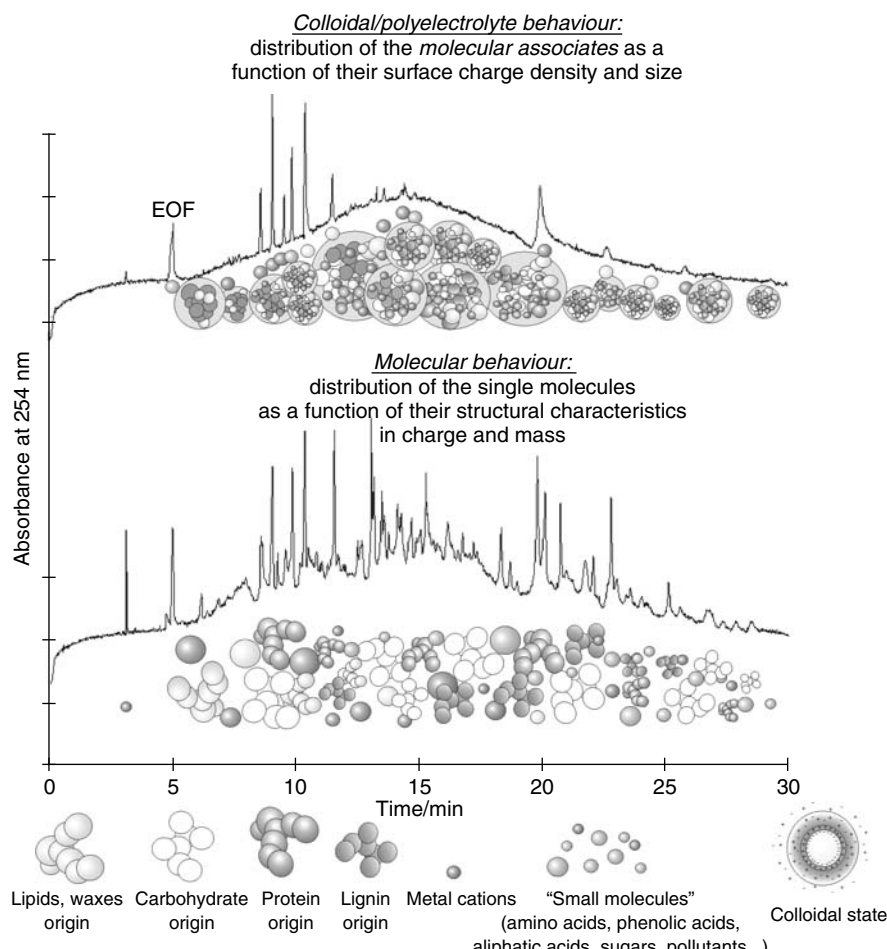


**Figure 8.** Illustrative cartoon representing the electrophoretic behaviour of NOM with a soil fulvic acid and solution isoelectric focusing fractions (see also Figures 14 and 15). Top: humic 'hump' corresponding to polyelectrolytic and colloidal properties of the NOM. Bottom: molecular electrophoretic behaviour showing a multitude of single peaks with individual mobilities

strength, pH, *etc.*, of the medium. These properties often make the comparison of results difficult and necessitate the normalisation/standardisation of experimental conditions. With this complexity in mind, a few comments can be made on the majority of reported applications of CE [23]:

- The main aim of most papers was *fingerprinting* of humic samples.
- Buffer interactions with the sample may lead to an increase in the number of reproducible signals (i.e. zwitterions). Possible CE artifacts due to interactions with phosphate or borate buffers have been described in early papers [118] although they did not catch the attention of many workers.
- The determination of metal–humic interactions with CE techniques remains problematic due to the complexity of the electropherograms.
- The investigation of humic samples or natural NOM in the absence of standard materials [i.e. from the International Humic Substance Society (IHSS)] makes inter-laboratory comparisons very difficult.

It is clear that the majority of the papers using CE to characterise NOM have remained at a very descriptive level.

## 4.2 FROM FINGERPRINTING TO STRUCTURAL INFORMATION

### 4.2.1 Capillary Zone Electrophoresis of NOM

The basic separation principle of all the CE techniques is *capillary zone electrophoresis* (CZE) [20]. Selectivity is governed by the effective charge and thus by the separation buffer pH and the electroosmotic flow (EOF). By changing the separation buffer system, optimised interactions of the sample with some buffer constituents may increase selectivity in the separation of charged or neutral analytes. CZE allows the separation of anions and cations as a direct function of their charge density (effective charge-to-size ratio) [95]. The addition of up to 100% solvents to the running buffer [non-aqueous CE (NACE)] can increase the selectivity and solubility of some analytes. CZE is often used for the separation of pharmaceuticals or plant secondary metabolites [87] and has frequently been used with NOM.

The definitions of apparent and effective electrophoretic mobility should be developed further. For an instrumental set-up where the anode is at the injection inlet and the cathode at the outlet, cations will move to the cathode first with the highest apparent velocity, neutral samples will move towards the detector with the velocity of the EOF and anions will move against the EOF with a reduced apparent velocity (apparently slower). The peaks are detected at increasing times in the electropherogram. The electrophoretic mobility is defined as being the field strength-reduced velocity of the ions in the capillary. With an applied field,  $E$ , across a capillary of total length  $L_t$ , the field strength is  $E/L_t$ . Following the injection, analytes (anions, neutrals, cations) will pass through the detector that is situated at a distance  $L_d$  from the inlet, their observed velocity ( $v$ ) being equal to  $L_d/t$ . Electrophoretic mobilities calculated from the observed velocity are called apparent electrophoretic mobilities ( $\mu_{ap}$ ) while the effective electrophoretic mobilities ( $\mu_{ef}$ ) take into account the velocity of the buffer towards the detector (EOF,  $\mu_{eo}$ ). In this manner, the EOF-normalised electrophoretic mobility is given by  $\mu_{ef} = \mu_{ap} - \mu_{eo}$ ;  $\mu_{ef}$  is zero for

neutral analytes, negative for anions and positive for cations. The effective electrophoretic mobility is an absolute parameter that is independent of the applied field or the column length and dependent only on the charge and size of the analyte [see equation (3)]. A conversion of the electropherograms from the time scale to the effective mobility scale ( $\mu$  scale) allows better reproducibility of separation patterns and of quantification parameters.

With NOM samples, the plot of UV absorbance versus effective mobility shows Gaussian-like distributions around average electrophoretic mobility (AEM) values. This representation of electrophoretic data takes into account the changes in electroosmotic flow that can occur from one measurement to the other (dependent on buffer chemistry – pH, ionic strength, buffer type) [88,94,120,121]. An electropherogram on this new scale can be considered as a frequency distribution of individual molecules or *molecular aggregates*. From the relationship between mobility with charge and size using model compounds (aliphatic and phenolic acids, polyacrylic acids, PSS), charge density information can be derived directly from mobility-scale electropherograms [122]. When the scale transformation is used to analyse single molecules, better peak tracking is possible from real matrices (qualitative improvement) and an increased reproducibility of quantitative data is achieved [94,123]. In addition, a direct linear relationship between the effective mobility ( $\mu$ ) and the charge-to-mass ratio can be verified ( $\mu$  is the field strength-reduced velocity of the ions that is independent of experimental set-up including voltage, capillary length, and EOF).

Mobility scaling (Figure 9) includes (i) the use of an internal standard (charged *p*-hydroxybenzoic acid, PSS or a neutral EOF marker such as mesityl oxide), (ii) a baseline correction, (iii) a scale transformation from migration time to effective mobility and (iv) the deletion of the internal standard peak. The sign of the mobility scale is negative for anions and positive for cations. Figure 9 gives results for a soil NOM separated by CZE in a pH 9.3 carbonate buffer with or without addition of 0.3% methylcellulose (CGE).

Changing the time scale to mobility scale can have effects on the shape of the electropherogram and the resulting interpretations when the samples are mixtures. Since data acquisition occurs with respect to the time (5–10 data points per second), the electropherogram is ‘compressed’ when converting to a mobility scale [mobility =  $f(\text{time}^{-1})$ ]. Peaks in the high-mobility region are defined by more data points than those near the EOF. As a consequence, the optimised description of analytes migrating near the EOF should be performed with a high data acquisition rate. The mobility scale represents well the mobility distribution in the sample whereas the time scale visually overestimates the contribution of high-mobility components. This approach allows the use of average statistical parameters similar to those used in polymer chemistry, such as those describing the molar mass distribution of a sample [124].

#### 4.2.2 pH and Ionic Strength Effects on Capillary Zone Electrophoresis of NOM

The observation of the mobility profile changes that are obtained as a function of pH certainly gives useful information on the changes in charge density that these materials undergo (changes in both charge and size). For example, Neihof and Loeb [125] reported electrophoretic measurements on particulate and dissolved organic matter from seawater by means of the microelectrophoresis technique in the early 1970s. These early studies

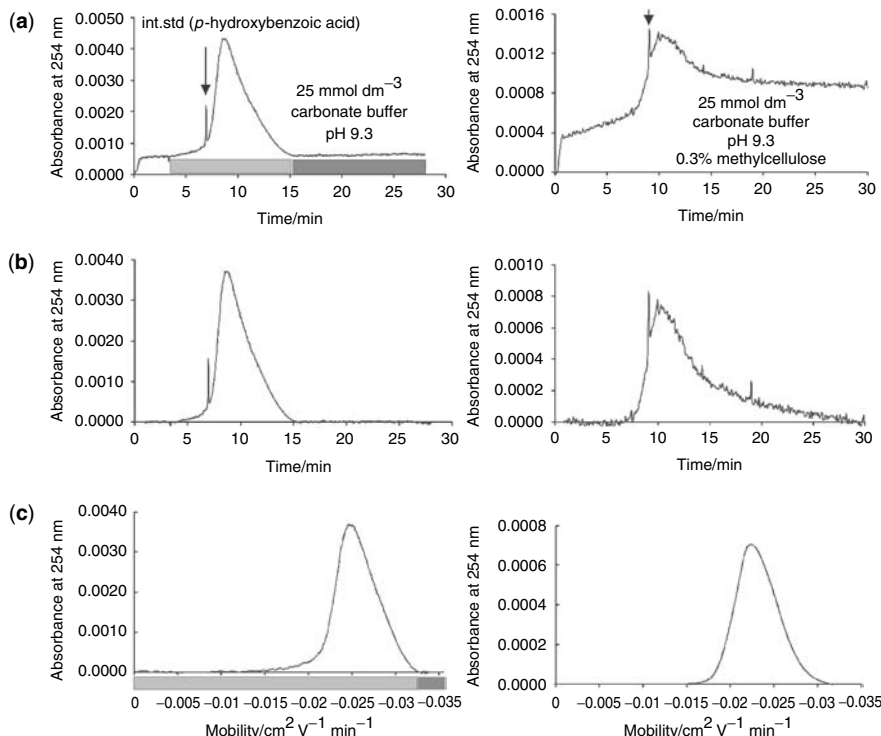


**Figure 9.** CZE (left) and corresponding CGE electropherograms (right) of a NOM measured with *p*-hydroxybenzoic acid as an internal standard; (a) raw data; (b) baseline correction; (c) mobility transformation and smoothing of the data from CGE

reported on organic–mineral interactions that were based on changes in surface potentials of the particulate matter in different water salinities [126]. The method was further developed and adapted by Hunter [127] to measure the pH-dependent electrophoretic mobilities of organic-coated minerals in marine systems. The author was able to show the importance of COOH and OH groups with respect to the binding of different metal ions. pH-dependent microelectrophoretic techniques have also been used to study metal and mineral binding to NOM [128].

Both average mobilities (as measured by taking the mobility value at the peak maximum) in addition to mobility distribution profiles need to be taken into consideration. From the example of the pH–CZE of Suwannee River NOM (Figure 10), one can see that from a Gaussian profile at high pH, a bimodal mobility distribution is obtained at lower pH, with some differentiation already observed at neutral pH. This result clearly indicates that within the sample mixture different populations having different distributions of charge to size migrate independently at the different pH values. For any other humic material, the shapes of the humps may differ as their composition is different. Nevertheless, (i) all the observable signals of NOM in CZE are found in the anionic range (including neutral molecules and cations) and (ii) the effective mobility distribution is very similar independent of its origin (terrestrial, limnic, marine) or structural

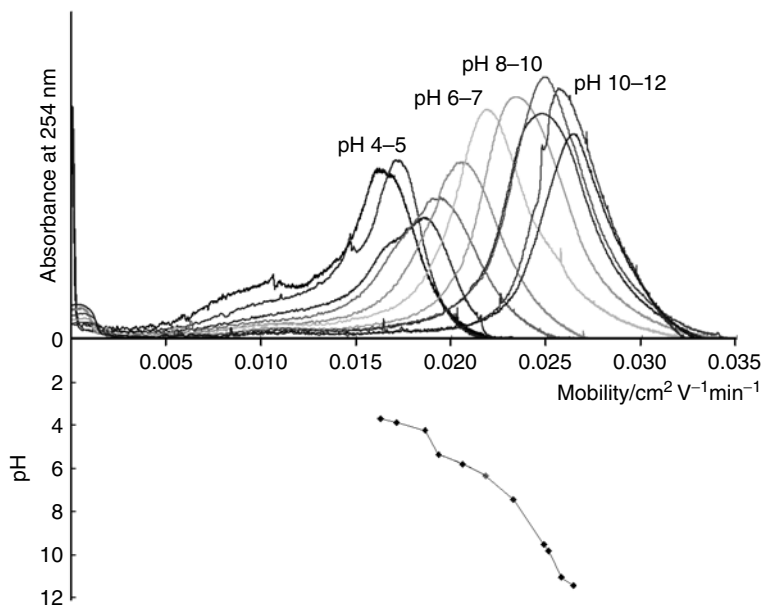


**Figure 10.** Effect of pH on the electrophoretic mobility profiles of the Suwannee River NOM

characteristics (measured by NMR). These data confirm the polyelectrolyte behaviour of NOM in aqueous zone electrophoresis. The trend is that high mobilities are found with highly charged and/or small molecules but that no (linear) correlation is observed with respect to effective charges as measured by potentiometric titrations of polyelectrolytes (*e.g.* PSS) in their free draining mode [100].

Hosse and Wilkinson [130,116,129] illustrated the additional effect of ionic strength on the electrophoretic mobility of a fulvic acid in the pH range 4–11 (Figure 11). They fitted their experimental mobility values with existing potentiometric titration data. These ionic

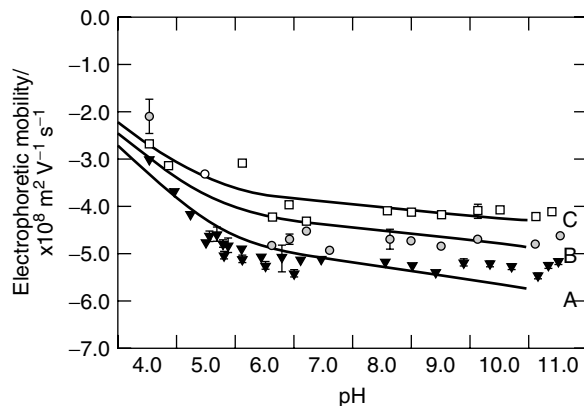


**Figure 11.** Changes in average electrophoretic mobility values by pH at ionic strength (A) 5, (B) 20 and (C) 40 mmol dm<sup>-3</sup> [129]

strength- and pH-dependent CZE data [116] were consistent with a model of semipermeable spheres, as demonstrated by Duval *et al.* [115].

#### 4.2.3 Capillary Gel Electrophoresis (CGE) of NOM

CGE allows the analysis of molecules based on their size. The separation is performed in entangled polymer solutions acting as replaceable physical gels (diluted polymer solutions such as methylcellulose, hydroxypropylcellulose, polyethylene glycols) in which molecular size and concentration determine the selectivity by sieving effects. This technique is the basis of the gene sequencing techniques used in modern molecular biology and genomics. Figure 12a shows the changes in the electrophoretic mobilities (mobility scale) for a mixture of six linear PSS with monomer contents from  $N = 36$  to 1900. Without the presence of methylcellulose, the PSS behave as if in free draining mode. The highest molar mass standard is affected to the greatest extent when increasing gel concentration due to the sieving effect.

CGE has historically been developed for the separation of proteins and DNA fragments. In the presence of anionic detergents such as SDS, proteins have a homogeneous charge density such that when in the sieving medium, the CGE migration times can directly be correlated with size. SDS cannot be used with NOM because strong interactions alter the electropherograms significantly [23]. When comparing systems with different charge densities, the linear relationship between mobility and size [131] is no longer verified and only the variation in effective mobility in presence of the gel is correlated with the size (Figure 12b). A physical gel composed of 0.3% methylcellulose in a 25 mmol dm<sup>-3</sup> carbonate buffer at pH 9.3 was used as a separation medium for NOM in CGE. Of the gels tested, polar polysaccharides were shown to be the best for the separation of NOM. Interactions were minimised but not suppressed. From changes in the mobility profile of an NOM in CGE (with gel) compared with CZE (without gel) (Figure 13), the PSS mass equivalents and corresponding hydrodynamic ratios of the fraction can be calculated from the experimental linearization illustrated in Figure 12b. Under these conditions, the average hydrodynamic radii of this NOM were in the range 2–3 nm (values found with an independent approach [122] and also illustrated several times in Chapter 11).

### 5 SELECTED PREPARATIVE ELECTROPHORESIS APPROACHES FOR NATURAL ORGANIC MATTER

Analytical electrophoresis using minimal sample quantities does not always allow the use of additional characterisation techniques (such as the powerful NMR or MS techniques). An adequate preparative approach with a reasonable scaling up is therefore necessary and is illustrated here with isoelectric focusing and zone electrophoresis.

#### 5.1 CAPILLARY IEF (CIEF) VERSUS PREPARATIVE SOLUTION ISOELECTRIC FOCUSING

CIEF separates analytes based on differences in their isoelectric points ( $pI$ ) using the same principles as in preparative solution IEF. After a focusing step that builds up a

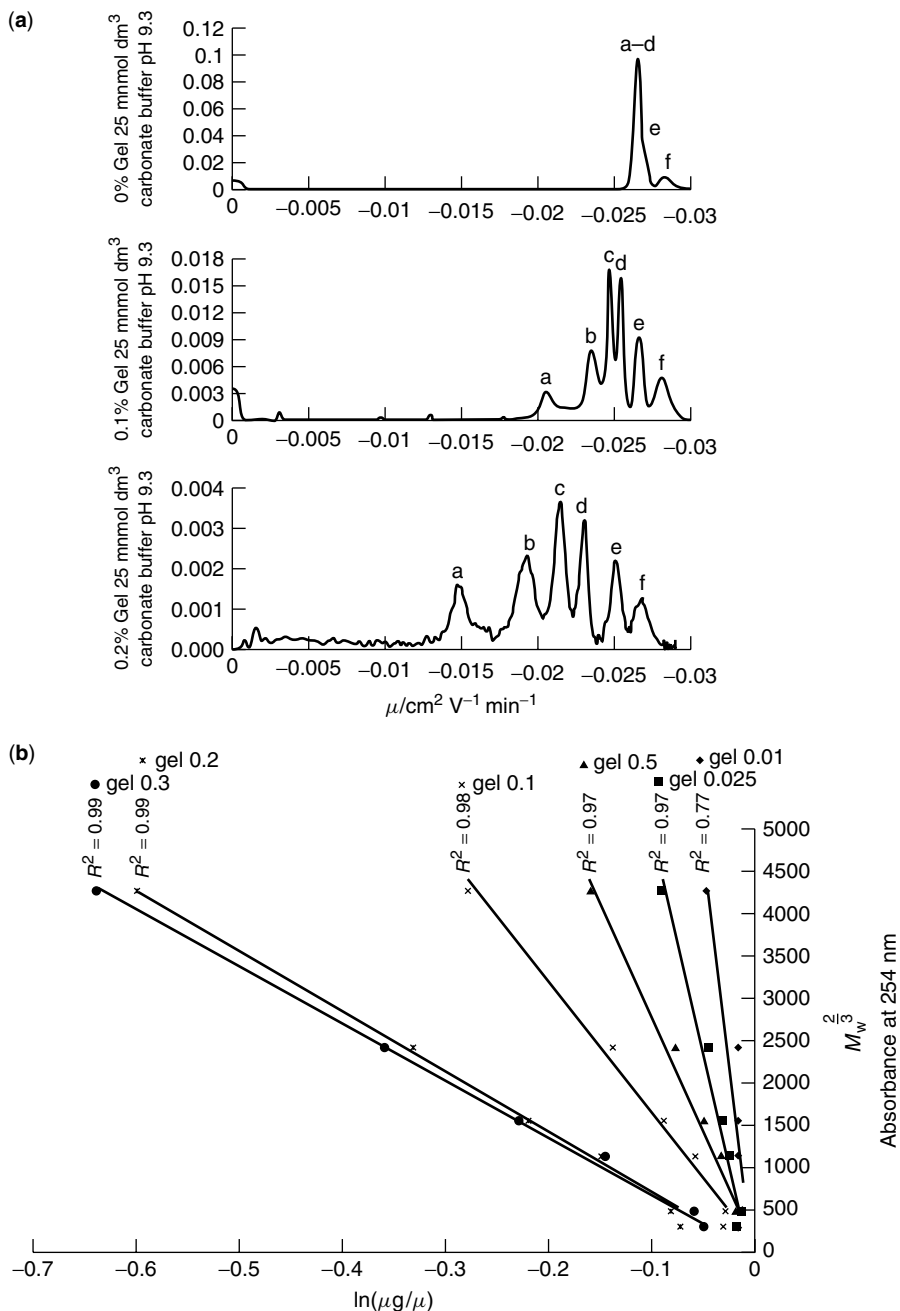


**Figure 12.** (a) Separation of PSS molar mass standards (a-f;  $N = 1900-36$ ) in CZE influenced by the concentration of the entangled polymer solutions in the separation buffer (without gel, 0.1 and 0.2% methylcellulose in carbonate buffer, pH 9.3). (b) Linear relationship between the logarithm of the effective mobility change in the gel [ $\ln(\mu_g/\mu)$ ] and the size parameter derived from the molecular mass ( $M_w^{2/3}$ ) at different gel concentrations as in (a). Best results were always obtained with 0.3% methylcellulose dissolved in the buffer

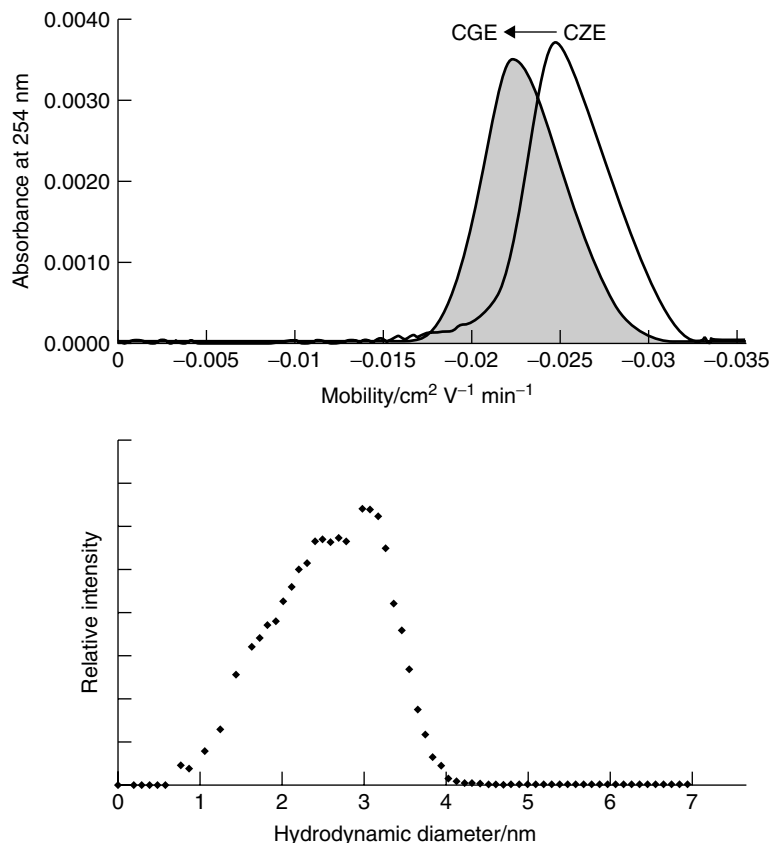


**Figure 13.** (a) Changes in the electrophoretic mobility profile (with versus without 0.3% methylcellulose in the 20 mmol dm<sup>-3</sup> carbonate buffer, pH 9.3) – data from mobility scale transformations in Figure 10. (b) Corresponding calculated distribution in hydrodynamic diameters based on the mobility changes in (a) and on Figure 8b

linear pH gradient in the capillary (controlled with zwitterionic internal markers), the analytes move as a function of their respective charge until they reach a position of zero charge (isoelectric point). The solution is then sent to the detector hydrodynamically (Figure 14a).

Preparative solution isoelectric focusing has been performed to fractionate NOM (sample load up to 50 mg). The 20 fractions harvested (Figure 14b) were characterised with UV–VIS spectroscopy, gel permeation chromatography and capillary zone electrophoresis (CZE). A molar mass distribution of the focused fulvic fractions in the created pH gradient was obtained. CZE of the fractions obtained (Figure 14c) showed a series of sharp peaks that resulted from the disaggregation of colloidal NOM after interaction with the ampholytes. In this case, some signals could even be observed in the cationic range [54,94]. In-column borate complexation was also used in CZE to compare fractions by fingerprinting. Only 32% of the total fulvic acids did not interact with the ampholytes

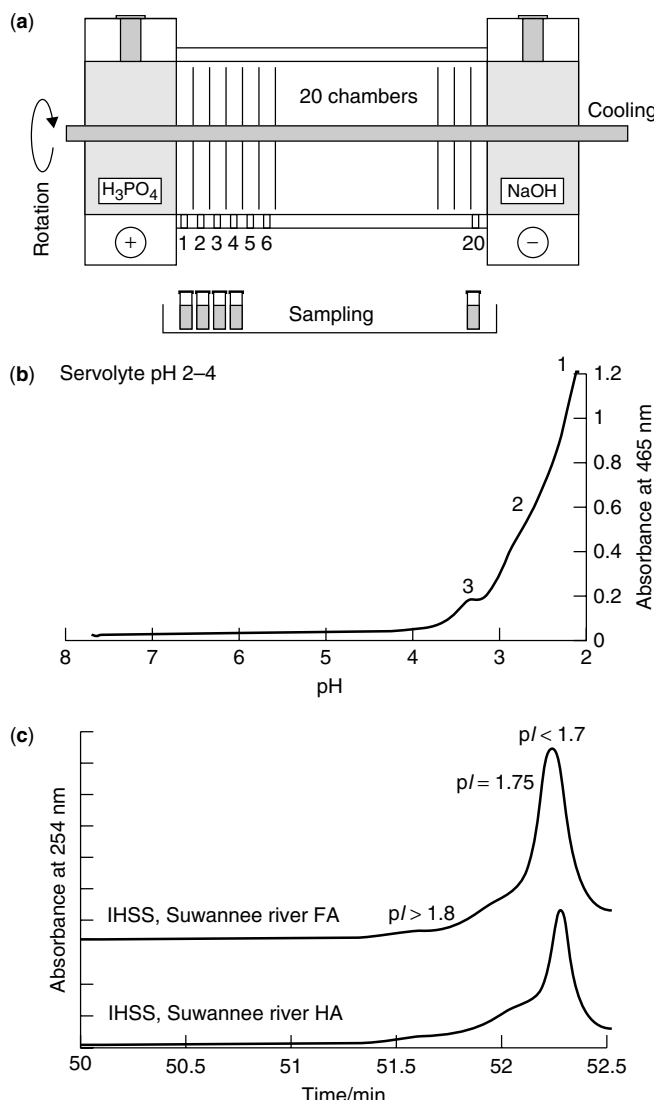


**Figure 14.** (a) Classical solution IEF (Rotofor, Bio-Rad) and (b) corresponding separation. (c) Separation of humic substances in CIEF showing the mobilisation to lower pH zone (apparent isoelectric points,  $pI$ ) with a pattern comparable to IEF [54]

that were used (precipitation) and this fulvic acid fraction was mainly composed of low molecular weight compounds (shown by CZE). Similarities were found in the distribution (at least three individualised fractions) of the low pH-focused NOM fractions in preparative IEF compared with CIEF (Figure 15). Due to the interactions between the NOM and the ampholytes, this method found only limited application, especially when the fractions needed to be analysed using mass or NMR spectrometry.

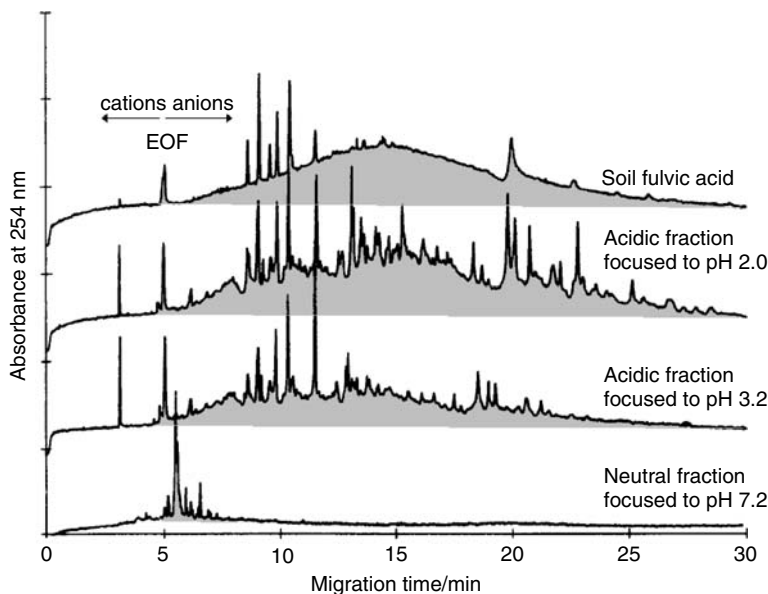


**Figure 15.** CZE of original soil fulvic acid (see Figure 9) and corresponding fractions obtained with solution IEF (presented in Figure 14); acidic fraction (moving towards lower pH) and neutral fractions

## 5.2 FREE-FLOW ELECTROPHORESIS (FFE) VERSUS CZE

An up-scaling of analytical CZE to preparative free-flow electrophoresis (FFE) has been described for humic materials [132]. The FFE device used in these experiments had a vertical separation chamber with a length of 500 mm, a width of 100 mm and a thickness of 0.5 mm, resulting in a total chamber volume of 25 cm<sup>3</sup>. The rear plate of the separation chamber was cooled during fractionation. The electrodes were separated from the electrophoretic chamber by filter membranes, which kept the electrode buffer from mixing with the separation medium. An electric field was applied perpendicularly to the direction of the flow across the width of the device. The separation medium was pumped continuously into the bottom of the chamber via three inlets, in order to create a laminar flow profile in the chamber. The analytes were pumped continuously into the bottom of the chamber, where they moved according to the separation medium speed (vertical direction) such that they were simultaneously separated according to their electrophoretic mobilities (horizontal direction). They reached an array of outlet tubes (every 1.06 mm, 96 fractions in all) at the top of the chamber after a time that depended on the flow-rate of the medium. The system is illustrated in Figure 16.

Since the separation medium is collected along with the fractionated sample, they are diluted during capillary electrophoresis, causing dilution of the fractions. It is therefore important to have sufficiently high sample concentrations at the outlet and, depending on the analytical steps that follow (MS, NMR, LC, CE, etc.), to keep the salt content in the fractions at the lowest possible level.

FFE allows for a fractionation that is based on charge density, and in larger amounts than in CZE, permitting further off-line analysis of the fractions. Model compounds

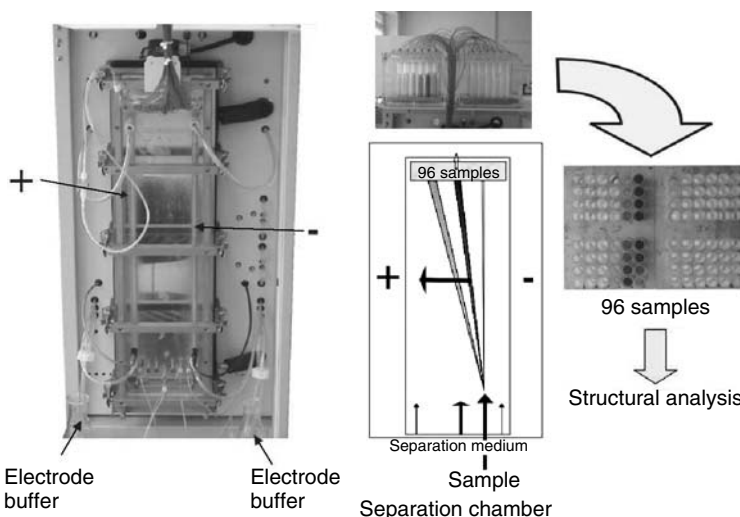


**Figure 16.** Preparative FFE system allowing the sampling of 96 charge density fractions that can be further characterised with UV–VIS, fluorescence, TOC, pH or conductimetry measurements, infusion ESI-MS, NMR techniques or classical chemical analysis of biomarkers (carbohydrates, amino acids). Reprinted with permission from Wiley-VCH

(carboxylic acids and PSS) showed a similar behaviour in FFE as in CZE. Diffusion and electrodynamic distortion effects are nonetheless more pronounced in FFE than in CZE. A comparison of the FFE fractions with CZE measurements of the same sample using the effective mobility scale showed good agreement between the two methods for NOM from soils, a surface water and marine systems [134]. Figure 17 shows the separation of a soil water extract (soil pore DOC) separated with CZE and with FFE. Good agreement in the separation profiles was found when comparing the CZE separation with UV–VIS detection and the FFE separation with total organic carbon analysis of all 96 collected fractions. The power of the method was verified by the possibility of using sensitive two-dimensional NMR experiments on the collected fractions ( $^1\text{H}$ ,  $^{13}\text{C}$ -HSQC,  $^1\text{H}$ ,  $^1\text{H}$ -COSY and  $^1\text{H}$ ,  $^1\text{H}$ -JRES in Figure 17). In the example shown in Figure 17, one can clearly recognise the high carbohydrate content of the neutral fraction and the higher aromaticity of high charge density fractions. Furthermore, mass spectrometry or other types of spectrometry are possible (UV–VIS, FTIR, fluorescence, *etc.*), allowing a detailed description of specific chemical structures that are involved in the charge density distribution.

### 5.3 FREE-FLOW ELECTROPHORESIS COMBINED OFF-LINE WITH ELECTROSPRAY IONISATION MASS SPECTROMETRY (ESI-MS) VERSUS CZE COUPLED WITH ESI-MS

Only limited structural information can be determined from mobility distribution profiles obtained by CZE using UV–VIS detection because they depend on both the charge and mass distributions within the NOM. Any kind of information on size or charge would reduce the possible combinations and thus greatly limit interpretation of the datasets.

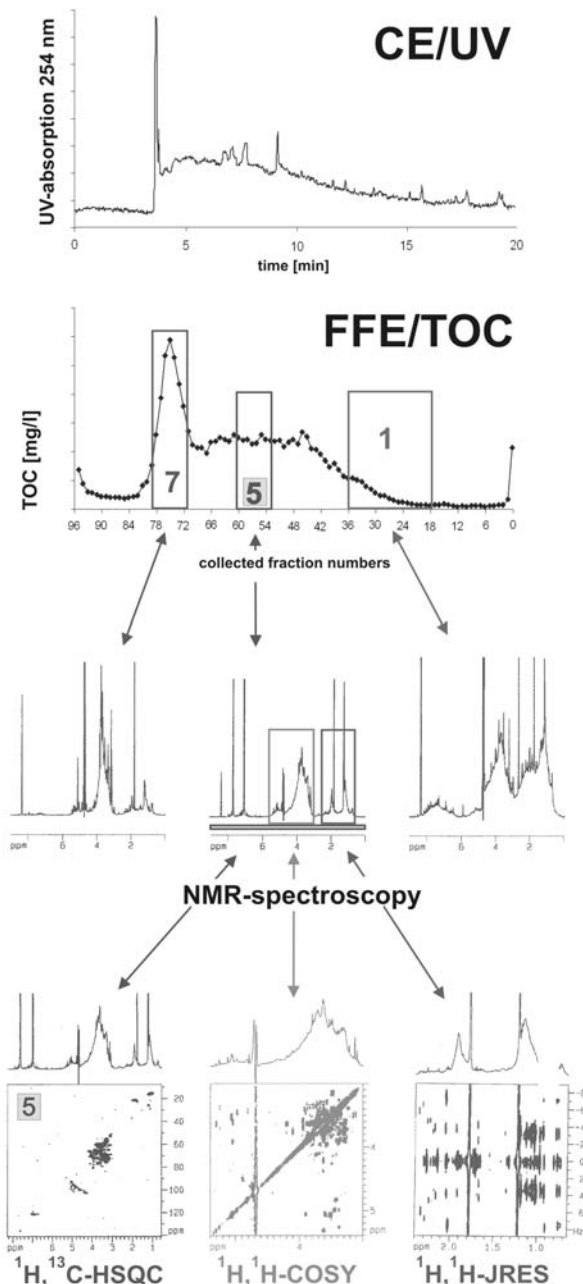


**Figure 17.** CZE-UV profile compared with FFE-TOC of a soil water extract and further characterisation of the charge density fractions with different proton and multidimensional NMR techniques [133]

A first option is the fractionation of sufficient material such that it could be analysed off-line by MS. This alternative is offered by FFE combined off-line with flow injection electrospray mass spectrometry (FI-ESI-MS) [134–136]. Another possibility is to measure mass distributions directly on-line after CZE. The coupling of CE with ESI-MS has been realised and the interface optimised [93,136]. Coupled CE–ESI-MS gives a continuous indication, as a function of the separation pH, of the relationships between effective mobility (relative to the charge-to-size ratio) and mass [expressed as the mass-to-charge ratio ( $m/z$ ) taking account of multiplicity of charges after ionisation in the ESI source]. Based on this relationship, theoretical approaches can be proposed and tested in experiments. For example, the reverse osmosis extract of a groundwater (GOHY 182 – Gorleben Location) is shown in Figure 18. The coupling of CE with MS techniques will certainly be a very promising research field in the near future, since the coupling of ultra-high-resolution FT-ICR-MS with CE could resolve the average structure of the different CE fractions (Figure 18) on a molecular level (information on the elemental composition of each mass signal is possible).

## 6 CONCLUSION

The use of electrophoresis to characterise environmental colloids is as old as the method itself and almost 200 years old. Among the modern electrophoretic approaches, capillary techniques including CZE are often used for both fingerprinting and structural investigations on NOM. Capillary electrochromatography (CEC) is a technology in full development that may be used for the specific sorption/separation of dissolved organic fractions. The design of on-line solid-phase extraction–CE separations will be an interesting field that will be useful for concentrating the analytes selectively prior to separation in the capillary. Such an application will be very important when analysing minute amounts of samples. In the near future, CE will provide enormous amounts of information when coupled with MS. In this case, developments are still required in the field of ionisation techniques (electrospray and photoionisation, new nanospray interfaces, ESI on a chip) and with respect to ion secondary fragmentations in the mass spectrometer (via laser technology). The coupling of CE with ultra-high-resolution MS (FT-ICR-MS) should provide elemental composition information on all ionisable molecules. The great potential of these methods has already been demonstrated when combined with NMR spectroscopy for the structural analysis of environmental organic colloids of different origins (terrestrial, limnic, marine or atmospheric).

## LIST OF ABBREVIATIONS

ACE	Affinity capillary electrophoresis
AEM	Average electrophoretic mobility
CD	Cyclodextrin
CE	Capillary electrophoresis
CEC	Capillary electrochromatography
CGE	Capillary gel electrophoresis
CIEF	Capillary isoelectric focusing

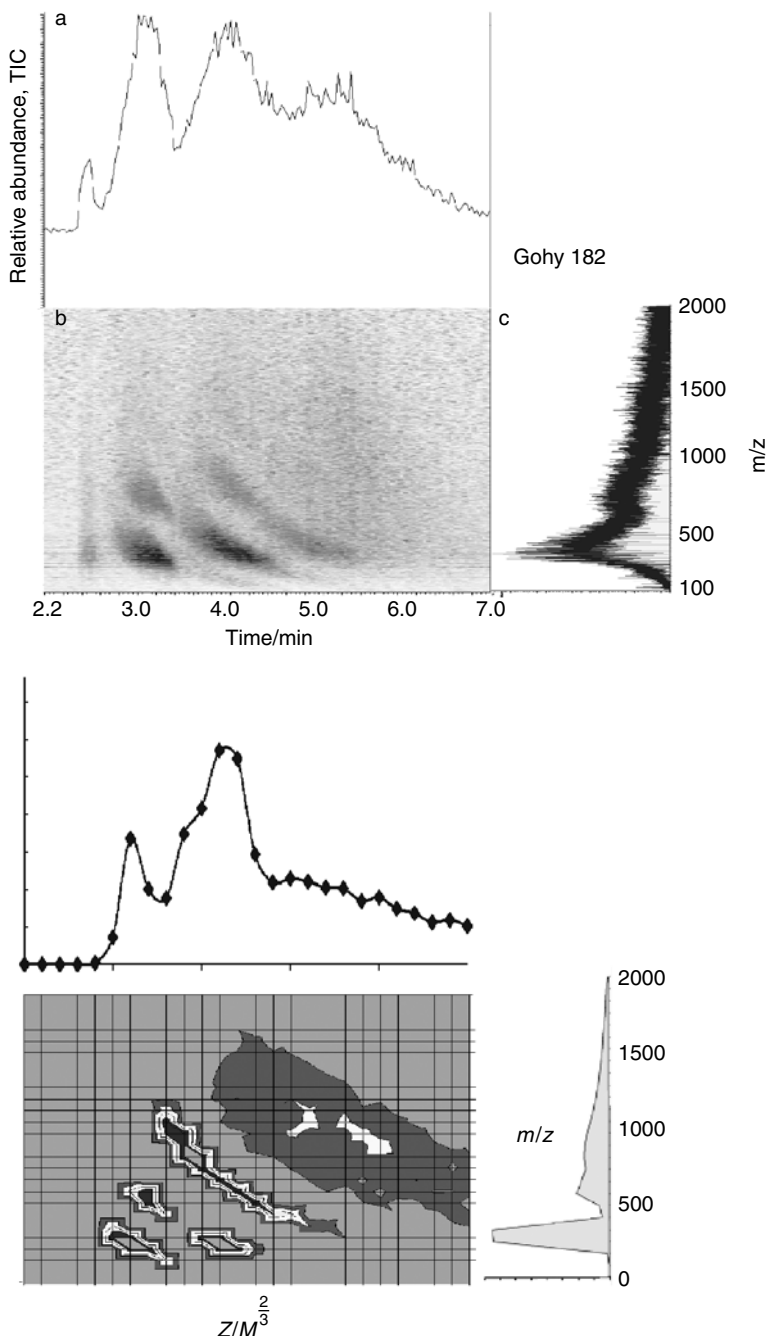


**Figure 18.** (a) CE-ESI-MS profile of a ground-water reverse osmosis extract (GOHY 182 – Gorleben Location) with corresponding TIC by time and summed  $m/z$  profiles. (b) Numerical simulation of the CE-ESI-MS profile constituted from five main populations with individual and independent distributions in size and charge

COSY	Homonuclear correlated spectroscopy
CZE	Capillary zone electrophoresis
DOC	Dissolved organic carbon
DOM	Dissolved organic matter
EOF	Electroosmotic flow (endoosmotic flow)
ESI	Electrospray ionisation
FFE	Free-flow electrophoresis
FI	Flow injection
FT-ICR	Fourier transform ion cyclotron resonance
FZE	Free zone electrophoresis
HPCE	High-performance capillary electrophoresis
HS	Humic substances
HSQC	Heteronuclear single quantum coherence
IEF	Isoelectric focusing
JRES	<i>J</i> -resolved spectroscopy
MS	Mass spectrometry
NACE	Non-aqueous capillary electrophoresis
NIC	Normalised intensity comparison
NMR	Nuclear magnetic resonance
NOM	Natural organic matter
OEC	Organic environmental colloid
PAGE	Polyacrylamide gel electrophoresis
PSS	Polystyrene sulfonates
SDS	Sodium dodecyl sulfate
SEC	Size-exclusion chromatography
SPE	Solid-phase extraction
TOC	Total organic carbon
UDOM	Ultrafiltered dissolved organic matter

## REFERENCES

1. Aiken, G. R. (1985). *Humic Substances in Soil, Sediment, and Water*. John Wiley & Sons, Inc., New York.
2. Shevchenko, S. M. and Bailey, G. W. (1996). Life after death: lignin–humic relationships reexamined, *Crit. Rev. Environ. Sci. Technol.*, **26**, 95–153.
3. Schulten, H.-R. (1998). Interactions of dissolved organic matter with xenobiotic compounds: molecular modeling in water, *Environ. Toxicol. Chem.*, **18**, 1643–1655.
4. Kubicki, J. D. and Apitz, S. E. (1999). Models of natural organic matter and interactions with organic contaminants, *Org. Geochem.*, **30**, 911–927.
5. Shin, H. S. and Moon, H. (1996). An “average” structure proposed for soil fulvic acid aided by dept/quat  $^{13}\text{C}$  NMR pulse techniques, *Soil Sci.*, **161**, 250–258.
6. Kögel-Knabner, I. (2000). Analytical approaches for characterizing soil organic matter, *Org. Geochem.*, **31**, 609–625.
7. Faraday, M. (1957). *On the Various Forces of Nature*. Thomas Y. Crowell, New York.
8. Kohlrausch, F. (1897). Ueber Konzentrations-Verschiebungen durch Electrolyse im Inneren von Lösungen und Lösungsgemischen, *Annal. Phys. Chem.*, **62**, 210–239.
9. Tiselius, A. (1937). A new apparatus for electrophoretic analysis of colloidal mixtures, *Trans. Faraday Soc.*, **33**, 524.

10. Tiselius, A. K. (1948). Electrophoresis and adsorption analysis as aids in investigations of large molecular weight substances and their breakdown products, *Nobel Lecture, December 13, 1948*.
11. Block, R. J. D., Durrum, E. L. and Zweig, G. (1958). *A Manual of Paper Chromatography and Paper Electrophoresis*. Academic Press, New York.
12. Tiselius, A. (1953). Zone electrophoresis in filter paper and other media, *Discuss. Faraday Soc.*, **29**, 39–33.
13. Swenson, H. (1961). Isoelectric fractionation, analysis and characterization of amphotytes in natural pH gradients, *Acta Chem. Scand.*, **15**, 325.
14. Hjerten, S. (1967). Free zone electrophoresis, *Chromatogr. Rev.*, **8**, 122.
15. Jorgenson, J. W. and Lukacs, K. D. (1981). Zone electrophoresis in open-tubular glass capillaries, *Anal. Chem.*, **53**, 1298–1302.
16. Jorgenson, J. W. and Lukacs, K. D. (1983). Capillary zone electrophoresis, *Science*, **222**, 266–272.
17. Deyl, Z. E. (1979). *Electrophoresis: a Survey of Techniques and Applications*. Elsevier, Amsterdam.
18. Khaledi, M. G. (1998). *High-performance Capillary Electrophoresis: Theory, Techniques, and Applications*. John Wiley & Sons, Ltd, Chichester.
19. Kuhn, R. and Hoffstetter-Kuhn, S. (1993). *Capillary Electrophoresis: Principles and Practise*. Springer, Berlin.
20. Schmitt-Kopplin, P. (2007). *Capillary Electrophoresis; from Small Ions to Macromolecules, book in the Serie Methods in Methods in Molecular Biology, Molecular Medicine and Biotechnology*. (Series Editor: John M. Walker), Humana Press, Totowa, NJ.
21. Schmitt-Kopplin, P. and Frommberger, M. (2003). Capillary electrophoresis–mass spectrometry: 15 years of developments and applications, *Electrophoresis*, **24**, 3837–3867.
22. Duxbury, J. M. (1989) In *Humic Substances II: In Serach of Structure*, eds Hayes, M. H. B., MacCarthy, P., Malcolm, R. L. and Swith, R. S. John Wiley & Sons, Inc., New York, pp. 594–618.
23. Schmitt-Kopplin, P. and Junkers, J. (2003). Capillary zone electrophoresis of natural organic matter, *J. Chromatogr. A*, **998**, 1–20.
24. Ostwald, W. S. A. (1925). Colloid chemistry of humus and peat, *Kolloidchem. Beih.*, **21**, 97–170.
25. Stevenson, F. J., van Winkle, Q. and Martin, W. P. (1952). Electrophoretic and chromatographic investigations of clay absorbed organic colloids I. Preliminary investigations, *Soil Sci. Soc. Am. Proc.*, **16**, 69–72.
26. Stevenson, F. J., van Winkle, Q. and Martin, W. P. (1953). Physicochemical investigations of clay absorbed organic colloids, *Soil Sci. Soc. Am. Proc.*, **17**, 31–34.
27. Stepanov, V. V. and Pakhonov, A. N. (1969). Electrophoresis of humus substances in polyacrylamide gel, *Pochvovedenie*, **12**, 48–56.
28. Trubetskoy, O. A., Trubetskaya, O. E., Reznikova, O. I. and Afanas'eva, G. F. (1999). Weight and optical differences between soil humic acids fractions obtained by coupling SEC–PAGE, *Geoderma*, **93**, 277–287.
29. Trubetskoy, O. A., Trubetskaya, O. E., Afanasieva, G. V., Reznikova, O. I., Hermosin, B. and Saiz-Jimenez, C. (1998). Tandem size exclusion chromatography polyacrylamide gel electrophoresis of humic acids, *Z. Pfanzenernähr. Bodenkd.*, **161**, 619–625.
30. Trubetskoy, O. A., Trubetskaya, O. E., Afanaseva, G. V., Reznikova, O. I. and Saiz-Jimenez, C. (1997). Polyacrylamide gel electrophoresis of soil humic acid fractionated by size-exclusion chromatography and ultrafiltration, *J. Chromatogr. A*, **767**, 285–292.
31. Trubetskoy, O. A., Trubetskaya, O. E., Reznikova, O. I., Afanas'eva, G. V. and Saiz-Jimenez, C. (2001). Electrophoretic analysis of humic acids and the products of their acid hydrolysis, *Euras. Soil Sci.*, **34**, 1097–1100.
32. Trubetskaya, O., Trubetskoy, O., Guyot, G., Andreux, F. and Richard, C. (2002). Fluorescence of soil humic acids and their fractions obtained by tandem size exclusion chromatography–polyacrylamide gel electrophoresis, *Org. Geochem.*, **33**, 213–220.
33. Trubetskaya, O. E., Trubetskoy, O. A., Afanas'eva, G. V., Reznikova, O. I., Markova, L. F. and Muranova, T. A. (1998). Amino acid composition of humic acids from different soil

- types fractionated by gel-chromatography complemented with electrophoresis amino acid composition, *Izv. Akad. Nauk Ser. Biol.*, 84–88.
34. Trubetskaya, O. E., Trubetskoj, O. A. and Saiz-Jimenez, C. (2001). Polyacrylamide gel electrophoresis of humic and fulvic acids after acid hydrolysis, *Fresenius Environ. Bull.*, **10**, 635–637.
  35. Richard, C., Trubetskaya, O., Tubetsko, O., Reznikova, O., Afanas'eva, Aguer, J. P. and Guyot, G. (2004). Key role of the low molecular size fraction of soil humic acids for fluorescence and photoinductive activity, *Environ. Sci. Technol.*, **38**, 2052–2057.
  36. Aguer, J. P., Richard, C., Trubetskaya, O., Trubetskoj, O., Leveque, J. and Andreux, F. (2002). Photoinductive efficiency of soil extracted humic and fulvic acids, *Chemosphere*, **49**, 259–262.
  37. Righetti, P. G. and Brown, R. P. (1978). Aggregation of ampholine on heparin and other acidic polysaccharides in isoelectric focussing, *Biochim. Biophys. Acta*, **542**, 232–244.
  38. Govi, M., Ciavatta, C. and Gessa, C. (1994). In *Humic Substances in the Global Environment and Implications on Human Health*, eds Senesi, N. and Miano, T. M., Elsevier, Amsterdam, pp. 1311–1316.
  39. Kutsch, H. and Schumacher, B. (1994). Isoelectric focusing of humic substances on ultrathin polyacrylamide gels: evidence of fingerprint performance, *Biol. Fertil. Soils*, **18**, 163–167.
  40. De Nobili, M. (1988). Electrophoretic evidence of the integrity of humic substances separated by means of electrofocusing, *J. Soil Sci.*, **39**, 437–445.
  41. Ciavatta, C., Govi, M., Bonoretti, G. and Gess, C. (1996). Identification of peat and leonardite using humification parameters and isoelectric focusing (IEF): a first approach, *Fert. Res.*, **44**, 225–230.
  42. Ceccanti, B., Bertolucci, M. T., Rustighi, G. and Calcina, M. (1986). Isoelectric focusing of soil humic substances in the presence of 8 M urea, *Biol. Fertil. Soils*, **2**, 71–75.
  43. Kutsch, H. and Schleich, C. (1989). Improved colorimetric determination of high-molecular weight hyaluronic acid from synovial fluids, *Fresenius' J. Anal. Chem.*, **333**, 810–817.
  44. Petrussi, F., De Nobili, M., Viotto, M. and Sequi, P. (1988). Characterization of organic matter from animal manures after digestion by earthworms, *Plant Soil*, **105**, 41–46.
  45. García, C., Hernández, T. and Ceccanti, B. (1995). Characterization by isoelectric focusing of the organic matter of a regenerated soil, *Commun. Soil Sci. Plant Anal.*, **26**, 3033–3041.
  46. García, C., Hernández, T., Costa, F., Ceccanti, B. and Dell' Amico, C. (1992). Characterization of the organic fraction of an uncomposted and composted sewage sludge by isoelectric focusing and gel filtration, *Biol. Fertil. Soils*, **13**, 112–118.
  47. Govi, M., Francisco, O., Ciavatta, C. and Sequi, P. (1992). Influence of long-term residue and fertilizer applications on soil humic substances: a study by electrofocusing, *Soil Sci. Plant Anal.*, **154**, 8–13.
  48. Ciavatta, C., Govi, M., Sitti, L. and Gessa, C. (1997). Influence of blood meal organic fertilizer on soil organic matter, *J. Plant Nutr.*, **20**, 1573–1591.
  49. Govi, M., Ciavatta, C., Sitti, L., Bonoretti, G. and Gessa, C. (1995). Influence of leather meal fertilizer on soil organic matter: a laboratory study, *Fert. Res.*, **44**, 65–72.
  50. Aak, O. V., Galynkin, V. A., Kashkin, A. P., and Yakovlev, V. I. (1984). Isoelectric focusing of high-molecular-weight shale and humic acids, *Appl. Biochem. Microbiol.*, **20**, 290–294.
  51. Govi, M., Bonoretti, G., Ciavata, C. and Sequi, P. (1994). Characterization of soil organic matter using isoelectric focusing: a comparison of six commercial carrier ampholytes, *Soil Sci.*, **157**, 91–96.
  52. Schoen, U. (1999). Erklärungsansatz zum Phänomen der isoelektrischen Fokussierung (IEF) von Huminstoffen auf Polyacrylamid Gelen in der Flachbett-Elektrophorese, Catolische Universität Eischstätt, Eischstätt, Germany.
  53. Gjessing, E. T. and Gjerdahl, T. (1972). Electromobility of aquatic humus: fractionation by the use of the isoelectric focusing technique, *Proc. Int. Meet. Humic Subst., Nieuwersluis, Pudoc*, 33–51.
  54. Schmitt, P., Garrison, A. W., Freitag, D. and Kettrup, A. (1997). Capillary isoelectric focusing (CIEF) for the characterization of humic substances, *Water Res.*, **31**, 2037–2049.
  55. Orioli, G. A. and Curvetto, N. R. (1980). Evaluation of extractants for soil humic substances. I. Isotachophoretic studies, *Plant Soil*, **55**, 353–361.

56. Ceccanti, B. and Nannipieri, P. (1978). In *Recent Developments in Chromatography and Electrophoresis*, eds Frigerio, A. and Renoz, L. J. I. Elsevier, Amsterdam, pp. 225–232.
57. Perdue, E. M. and Ritchie, J. D. (2003). In *Treatise on Geochemistry*, ed. Drever, J. I. Elsevier, Amsterdam, Vol. 5.
58. Schmitt-Kopplin, P., Freitag, D., Kettrup, A., Schoen, U. and Egeberg, P. K. (1999). Capillary zone electrophoretic studies on Norwegian surface water natural organic matter, *Environ. Int.*, **25**, 259–274.
59. Quigley, M. S., Santschi, P. H., Hung, C. C., Guo, L. and Honeyman, B. D. (2002). Importance of acid polysaccharides for  $^{234}\text{Th}$  complexation to marine organic matter, *Limnol. Oceanogr.*, **47**, 367–377.
60. Heinig, K., Vogt, C. and Werner, G. (1997). Separation of nonionic surfactants of the polyoxyethylene type by capillary electrophoresis, *Fresenius' J. Anal. Chem.*, **357**, 695–700.
61. Heinig, K., Vogt, C. and Werner, G. (1998). Separation of nonionic surfactants by capillary electrophoresis and high-performance liquid chromatography, *Anal. Chem.*, **70**, 1885–1892.
62. Hiermann, A. and Radl, B. (1998). Analysis of aromatic plant acids by capillary zone electrophoresis, *J. Chromatogr. A*, **803**, 311–314.
63. Hong, M., Sudor, J., Steffansson, M. and Novotny, M. V. (1998). High-resolution studies of hyaluronic acid mixtures through capillary gel electrophoresis, *Anal. Chem.*, **70**, 568–573.
64. Deyl, Z., Rohlicek, V. and Adam, M. (1989). Separation of collagens by capillary zone electrophoresis, *J. Chromatogr.*, **480**, 371–378.
65. Morneau, A., Pillai, V., Nigam, S., Winnik, F. M. and Ziolo, R. F. (1999). Analysis of ferrofluids by capillary electrophoresis, *Colloids Surf. A*, **154**, 295–301.
66. Stefansson, M. (1998). Characterization of cellulose derivatives and their migration behavior in capillary electrophoresis, *Carbohydr. Res.*, **312**, 45–52.
67. Bullock, J. (1993). Application of capillary electrophoresis to the analysis of the oligomeric distribution of polydisperse polymer, *J. Chromatogr.*, **645**, 169–177.
68. Clos, H. N. and Engelhardt, H. (1998). Separations of anionic and cationic synthetic polyelectrolytes by capillary gel electrophoresis, *J. Chromatogr. A*, **802**, 149–157.
69. Grosche, O., Bohrisch, J., Wendler, U., Jaeger, W. and Engelhardt, H. (2000). Characterization of synthetic polyelectrolytes by capillary electrophoresis, *J. Chromatogr. A*, **894**, 105–116.
70. Gao, J. Y., Dubin, P. L., Sato, T. and Morishima, Y. (1997). Separation of polyelectrolytes of variable compositions by free-zone capillary electrophoresis, *J. Chromatogr. A*, **766**, 233–236.
71. Glynn, J. R., Belongia, B. M., Arnold, R. G., Ogden, K. L. and Baygents, J. C. (1998). Capillary electrophoresis measurements of electrophoretic mobility for colloidal particles of biological interest, *Appl. Environ. Microbiol.*, **64**, 2572–2577.
72. Jones, H. K. and Ballou, N. E. (1990). Separations of chemically different particles by capillary electrophoresis, *Anal. Chem.*, **62**, 2484–2490.
73. Radko, S. P. and Chrambach, A. (1999). Capillary electrophoresis of subcellular-sized particles, *J. Chromatogr. B*, **722**, 1–10.
74. Radko, S. P., Stastna, M. and Chrambach, A. (2000). Capillary zone electrophoresis of sub- $\mu\text{m}$ -sized particles in electrolyte solutions of various ionic strengths: size-dependent electrophoretic migration and separation efficiency, *Electrophoresis*, **21**, 3583–3592.
75. Vanifatova, N. G., Spivakov, B. Y., Mattusch, J. and Wennrich, R. (2000). Separation of unmodified polystyrene nanosphere standards by capillary zone electrophoresis, *J. Chromatogr. A*, **898**, 257–263.
76. Radko, S. P., Stastna, M. and Chrambach, A. (2001). Polydispersity of liposome preparations as a likely source of peak width in capillary zone electrophoresis, *J. Chromatogr. B*, **761**, 69–75.
77. Pfetsch, A. and Welsch, T. (1997). Determination of the electrophoretic mobility of bacteria and their separation by capillary zone electrophoresis, *Fresenius' J. Anal. Chem.*, **359**, 198–201.
78. Krylov, S. N. and Dovichi, N. J. (2000). Single-cell analysis using capillary electrophoresis: influence of surface support properties on cell injection into the capillary, *Electrophoresis*, **21**, 767–773.

79. Malek, A. and Khaledi, M. G. (1999). Expression and analysis of green fluorescent proteins in human embryonic kidney cells by capillary electrophoresis, *Anal. Biochem.*, **268**, 262–269.
80. Zabzdyr, J. L. and Lillard, S. J. (2001). New approaches to single-cell analysis by capillary electrophoresis, *Trends Anal. Chem.*, **20**, 467–476.
81. Zabzdyr, J. L. and Lillard, S. J. (2001). Measurement of single-cell gene expression using capillary electrophoresis, *Anal. Chem.*, **73**, 5771–5775.
82. Patton, W. F. (1999). II. Protein subcellular redistribution: linking physiology to genomics via the proteome and separation technologies involved, *J. Chromatogr. B*, **722**, 203–223.
83. *Proceedings of the 14th International Symposium on Microscale Separations and Analysis, HPCE'01. J. Chromatogr. A*, Vol. 924, Special Issue. Elsevier, Amsterdam, 2001.
84. Lopez, M. F. (1999). Proteome analysis I. Gene products are where the biological action is, *J. Chromatogr. B*, **722**, 191–202.
85. Campa, C., Schmitt-Kopplin, P., Cataldi, T. R. I., Bufo, S. A., Freitag, D. and Kettrup, A. (2000). Analysis of cyanogenic glycosides by micellar capillary electrophoresis, *J. Chromatogr. B*, **739**, 95–100.
86. Bianco, G., Schmitt-Kopplin, P., Crescenzi, A., Comes, S., Kettrup, A. and Cataldi, T. R. I. (2003). Evaluation of glycoalkaloids in tubers of genetically modified virus Y-resistant potato plants (var. Desiree) by non-aqueous capillary electrophoresis coupled with electrospray ionization mass spectrometry (NACE-ESI-MS), *Anal. Bioanal. Chem.*, **375**, 799–804.
87. Bianco, G., Schmitt-Kopplin, P., De Benedetto, G., Kettrup, A. and Cataldi, T. R. (2002). Determination of glycoalkaloids and relative aglycones by nonaqueous capillary electrophoresis coupled with electrospray ionization-ion trap mass spectrometry, *Electrophoresis*, **23**, 2904–2912.
88. Schmitt-Kopplin, P., Garmash, A. V., Kudryavtsev, A. V., Perminova, I. V., Hertkorn, N., Freitag, D. and Kettrup, A. (1999). Mobility distribution description of synthetic and natural polyelectrolytes with capillary zone electrophoresis, *J. AOAC Int.*, **82**, 1594–1603.
89. Nicholson, J. K., Lindon, J. C. and Holmes, E. (1999). ‘Metabonomics’: understanding the metabolic responses of living systems to pathophysiological stimuli via multivariate statistical analysis of biological NMR spectroscopic data, *Xenobiotica*, **29**, 1181–1189.
90. Chernushevich, I. V., Loboda, A. V. and Thomson, B. A. (2001). An introduction to quadrupole-time-of-flight mass spectrometry, *J. Mass Spectrom.*, **36**, 849–865.
91. Marshall, A. G. (2000). Milestones in Fourier transform ion cyclotron resonance mass spectrometry technique development, *Int. J. Mass Spectrom.*, **200**, 331–356.
92. Hofstadler, S. A., Swanek, F. D., Gale, D. C., Ewing, A. G. and Smith, R. D. (1995). Capillary electrophoresis-electrospray ionization Fourier transform ion cyclotron resonance mass spectrometry for direct analysis of cellular proteins, *Anal. Chem.*, **67**, 1477–1480.
93. Schmitt-Kopplin Ph. and Frommberger, M. (2003). Capillary electrophoresis-electrospray ionization mass spectrometry: 15 years of development and applications, *Electrophoresis*, **24**, 3837–3867.
94. Schmitt-Kopplin, P., Menzinger, F., Freitag, D. and Kettrup, A. (2001). Improving the use of CE in a chromatographer’s world, *LC-GC Eur.*, **14**, 284–388.
95. Schmitt, P., Poiger, T., Simon, R., Garrison, A. W., Freitag, D. and Kettrup, A. (1997). Simultaneous ionization constants and isoelectric points determination of 12 hydroxy-s-triazines by capillary zone electrophoresis (CZE) and capillary electrophoresis isoelectric focusing (CIEF), *Anal. Chem.*, **69**, 2559–2566.
96. Henry, D. C. (1931). *Proc. Ro. Soc. London*, **133**, 106–140.
97. Offord, R. E. (1966). Electrophoretic mobilities of peptides on paper and their use in the determination of amide groups, *Nature*, **211**, 591.
98. Jalali-Heravi, M., Shen, Y., Hassanisadi, M. and Khaledi, M. G. (2005). Prediction of electrophoretic mobilities of peptides in capillary zone electrophoresis by quantitative structure-mobility relationships using the Offord model and artificial neural networks, *Electrophoresis*, **26**, 1874–1885.
99. Carbeck, J. D. and Negin, R. S. (2001). Measuring the size and charge of proteins using protein charge ladders, capillary electrophoresis, and electrokinetic models of colloids, *J. Am. Chem. Soc.*, **123**, 1252–1253.

100. Cottet, H. and Gareil, P. (2000). From small charged molecules to oligomers: a semiempirical approach to the modeling of actual mobility in free solution, *Electrophoresis*, **21**, 1493–1504.
101. Stokes, J. C. and Johnson, M. J. (2004). Resolution in sub-micrometer particle separations by capillary electrophoresis, *Microchem. J.*, **76**, 121–129.
102. Hoagland, D. A., Arvanitidou, E. and Welch, C. (1999). Capillary electrophoresis measurements of the free solution mobility for several model polyelectrolyte systems, *Macromolecules*, **32**, 6180–6190.
103. Ohshima, H. (2002). Electrophoretic mobility of a charged spherical colloidal particle covered with an uncharged polymer layer, *Electrophoresis*, **23**, 1993–2000.
104. Fritz, G., Schaedler, V., Willenbacher, N. and Wagner, N. J. (2002). Electrosteric stabilization of colloidal dispersions, *Langmuir*, **18**, 6381–6390.
105. De Wit, J. C., van Riemsdijk, W. H. and Koopal, L. K. (1993). Proton binding to humic substances. 1. Electrostatic effects, *Environ. Sci. Technol.*, **27**, 2005–2014.
106. Benedetti, M. F., Van Riemsdijk, W. H. and Koopal, L. K. (1996). Humic substances considered as a heterogeneous Donnan gel phase, *Environ. Sci. Technol.*, **30**, 1805–1813.
107. Avena, M. J., Koopal, L. K. and van Riemsdijk, W. H. J. (1999). Proton binding to humic acids: electrostatic and intrinsic interactions, *J. Colloid Interface Sci.*, **217**, 37–48.
108. Carballera, J. L., Antelo, J. M., Rey, F. and Arce, F. (1999). Modeling the effects of ionic strength on ionization parameters for a soil fulvic acid at low concentrations, *Anal. Chim. Acta*, **401**, 243–249.
109. Ephraim, J. H., Alegret, S., Mathuthu, A., Bicking, M., Malcom, R. L. and Marinsky, J. A. (1986). A unified physicochemical description of the protonation and metal ion complexation equilibria of natural organic acids (humic and fulvic acids). 2. Influence of polyelectrolyte properties and functional group heterogeneity on the protonation equilibria of fulvic acid, *Environ. Sci. Technol.*, **20**, 354–366.
110. Marinsky, J. A. and Ephraim, J. H. (1986). A unified physicochemical description of the protonation and metal ion complexation equilibria of natural organic acids (humic and fulvic acids). 1. Analysis of the influence of polyelectrolyte properties on protonation equilibria in ionic media: fundamental concepts, *Environ. Sci. Technol.*, **20**, 349–354.
111. Klein Wolterink, J., Leermakers, F. A. M., Fleer, G. J., Koopal, L. K., Zhulina, E. B. and Borisov, O. V. (1999). Screening in solutions of starbranched polyelectrolytes, *Macromolecules*, **32**, 2365–2377.
112. Gosh, K. and Schnitzer, M. (1980). Macromolecular structures of humic substances, *Soil Sci.*, **129**, 266–276.
113. Marinsky, J. A. and Ephraim, J. (1986). A unified physicochemical description of the protonation and metal ion complexation equilibria of natural organic acids (humic and fulvic acids). 1. Analysis of the influence of polyelectrolyte properties on protonation equilibria in ionic media: fundamental concepts, *Environ. Sci. Technol.*, **20**, 349–354.
114. Kinniburgh, D. G., Milne, C. J., Benedetti, M. F., Pinheiro, J. P., Filius, J., Koopal, L. K. and van Riemsdijk, W. H. (1996). Metal ion binding by humic acid: application of the NICA model, *Environ. Sci. Technol.*, **30**, 1687–1698.
115. Duval, J., Wilkinson, K. J., Van Leeuwen, H. and Buffle, J. (2005). Humic substances are soft and permeable: evidence from their electrophoretic mobilities, *Environ. Sci. Technol.*, **39**(17), 6435–6445.
116. Schmitt-Kopplin, P. (2002). Comment on “Determination of electrophoretic mobilities and hydrodynamic radii of three humic substances as a function of pH and ionic strength”, *Environ. Sci. Technol.*, **36**, 3041–3042.
117. Schnabel, U., Fischer, C. H. and Kenndler, E. (1997). Characterization of colloidal gold nanoparticles according to size by capillary zone electrophoresis, *J. Microcol. Sep.*, **9**, 529–534.
118. Garrison, A. W., Schmitt, P. and Kettrup, A. (1995). Capillary electrophoresis for the characterization of humic substances, *Water Res.*, **29**, 2149–2159.
119. Schmitt-Kopplin, P., Freitag, D., Kettrup, A., Hertkorn, N., Schoen, U., Klocking, R., Helbig, B., Andreux, F. and Garrison, A. W. (1999). Analysis of synthetic humic substances for medical and environmental applications by capillary zone electrophoresis, *Analisis*, **27**, 390–396.

120. Schmitt-Kopplin, P., Garrison, A. W., Perdue, E. M., Freitag, D. and Kettrup, A. (1998). Capillary electrophoresis in the analysis of humic substances – facts and artifacts, *J. Chromatogr. A*, **807**, 101–109.
121. Menzinger, F., Schmitt-Kopplin, P., Frommberger, M., Freitag, D. and Kettrup, A. (2001). Partial-filling micellar electrokinetic chromatography and non-aqueous capillary electrophoresis for the analysis of selected agrochemicals, *Fresenius' J. Anal. Chem.*, **371**, 25–34.
122. Schmitt-Kopplin, P., Freitag, D., Kettrup, A., Schoen, U. and Egeberg, P. (1999). Capillary zone electrophoretic studies on Norwegian surface water natural organic matter, *Environ. Int.*, **25**, 259–274.
123. Schmitt-Kopplin, P., Garmash, A. V., Kudryavtsev, A. V., Menzinger, F., Perminova, I. V., Hertkorn, N., Freitag, D., Petrosyan, V. S. and Kettrup, A. (2001). Quantitative and qualitative precision improvements by effective mobility-scale data transformation in capillary electrophoresis analysis, *Electrophoresis*, **22**, 77–87.
124. Belenkii, B. G. and Vilenchik, L. Z. (1983). *Modern Liquid Chromatography of Macromolecules*. Elsevier, Amsterdam.
125. Neihof, R. A. and Loeb, G. I. (1972). The surface of particulate matter in seawater, *Limnol. Oceanogr.*, **17**, 7–16.
126. Neihof, R. A. and Loeb, G. I. (1973). Dissolved organic matter in seawater and the electric charge of immersed surfaces, *J. Mar. Res.*, **32**, 5–11.
127. Hunter, K. A. (1980). Microelectrophoretic properties of natural surface-active organic matter in coastal seawater, *Limnol. Oceanogr.*, **25**, 807–822.
128. Tipping, E., ed. (2002). *Cation Binding by Humic Substances*. Cambridge University Press, Cambridge.
129. Hosse, M. and Wilkinson, A. E. (2002). Response to ‘Comment on “Determination of electrophoretic mobilities and hydrodynamic radii of three humic substances as a function of pH and ionic strength”’, *Environ. Sci. Technol.*, **36**, 3043–3044.
130. Hosse, M. and Wilkinson, K. J. (2001). Determination of electrophoretic mobilities and hydrodynamic radii of three humic substances as a function of pH and ionic strength, *Environ. Sci. & Technol.*, **35**, 4301–4306.
131. De Nobili, M., Bragato, G. and Mori, A. (1999). Capillary electrophoretic behaviour of humic substances in physical gels, *J. Chromatogr. A*, **863**, 195–204.
132. Junkers, J., Schmitt-Kopplin, P., Munch, J. C. and Kettrup, A. (2002). Up-scaling capillary zone electrophoresis separations of polydisperse anionic polyelectrolytes with preparative free-flow electrophoresis exemplified with a soil fulvic acid, *Electrophoresis*, **23**, 2872–2879.
133. Hertkorn, N., Schmitt-Kopplin, P., Junkers, J. and Kettrup, A. (2004). Die strukturrechemische Charakterisierung von natürlicher organischer Materie (NOM) und Huminstoffen (HS) mittels NMR-Spektroskopie und Kapillarelektrophorese/Massenspektrometrie – eine entscheidende Grundlage für das Verständnis ihrer molekularen Wechselwirkungsmechanismen in der Umwelt, *GIT Fachzeitschr. Lab.*, **5**, 487–491.
134. Junkers, J., Schmitt-Kopplin, P., Munch, J. C. and Kettrup, A. (2002). Up-scaling capillary zone electrophoresis (CZE) separations of polydisperse anionic polyelectrolytes with preparative free flow electrophoresis (FFE) exemplified with a soil fulvic acid, *Electrophoresis*, **23**, 2872–2879.
135. Schmitt-Kopplin, P. (2003). In *Humic Substances: Nature's Most Versatile Materials*, eds. Ghabbour, E. A. and Davies, E. Taylor and Francis, New York, pp. 9–30.
136. Schmitt-Kopplin, P., Kettrup, A. (2003). Capillary electrophoresis–electrospray ionization/mass spectrometry for the characterization of natural organic matter: an evaluation with free flow electrophoresis offline flow injection electrospray ionization mass spectrometry, *Electrophoresis*, **24**, 3057–3066.



---

# 7 Electrophoresis of Soft Colloids: Basic Principles and Applications

---

JÉRÔME F. L. DUVAL

*Laboratory Environment and Mineral Processing, Nancy-University, CNRS, 15 avenue du Charmois, B.P. 40, 54501 Vandoeuvre-lès-Nancy cedex, France*

1	Introduction	315
2	Electrophoresis of Soft Particles	319
2.1	Modelling the Surface Structure of a Charged Soft Particle	319
2.2	Fundamental Electrokinetic Equations*	321
2.3	Boundary Conditions	323
2.4	Characteristic Electrokinetic Features of Soft Particles	325
3	Applications	328
3.1	Determination of the Key Electrostatic and Hydrodynamic Model Parameters	328
3.1.1	Evaluation of the Distribution Function, $f$ , of the Soft, Polymeric Material	329
3.1.2	Evaluation of the Characteristic Size of the Particles	330
3.1.3	Evaluation of the Space Charge Density	330
3.2	Application to Biocolloids: The Case of Bacteria	332
3.3	Application to Environmental Colloids: The Case of the Humics	334
4	Conclusions	337
	List of Symbols	338
	References	340

## 1 INTRODUCTION

The electrophoretic mobility of a colloidal particle moving in a liquid under the action of an applied electric field is a key quantity that, given accurate interpretation, may provide valuable information on the electric and hydrodynamic properties of the particle that is under consideration. Whereas the electrophoresis of rigid, hard particles is now well understood [1–9], the situation for soft, permeable systems is much less established. Generally, the terms soft and ‘permeable’ relate to interfaces or to colloidal systems coated with hydrodynamically permeable and generally charged surface layers.

The development of electrokinetic theory for such systems [10–35] has been motivated by an increasing number of experimental determinations of the electro-hydrodynamic features of soft colloids including adsorbed polyelectrolytes [16,17,19,22,26–29,31–35], bacteria [13–15,19,36–44], human blood cells [18,45] and humic substances [46]. Knowledge of their electrostatic and hydrodynamic properties as a function of the physicochemical characteristics of their ionic environment (pH, ionic strength, nature of the ions and the solvent) is fundamental to understanding, at a microscopic level, a large number of environmentally relevant interfacial phenomena, including the formation of biofilms and bioadhesion [47–51], the binding of ions to natural organic matter [52–54], aggregation and heterocoagulation [55–57], the nanorheological properties of organisms [58,59] and the conformation, swelling or shrinking properties of soft macromolecules [60–65]. Soft, charged layers are of prime importance in the biological and environmental sciences.

Following the definition given by Ohshima [24], soft particles consist of a hard core, which is *stricto sensu* impermeable to fluid flow, and an adsorbed polyelectrolyte-type layer characterised by a three-dimensional spatial distribution of hydrodynamically stagnant, ionogenic groups (Figure 1). In the complete absence of a particle core, the soft particle becomes entirely porous. It has long been recognised that the electrophoretic behaviour of soft particles deviates substantially from that of hard (i.e. rigid) particles [10,11]. The main reasons for the deviations are twofold. In the interphase region,

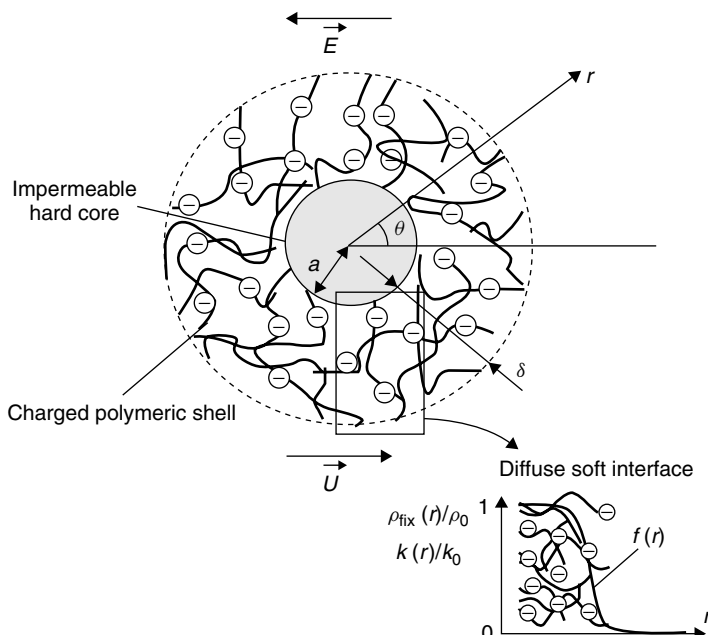


**Figure 1.** Schematic representation of a diffuse soft particle that is composed of a rigid hard-core and a permeable charged polymeric layer, moving with a velocity  $\vec{U}$  in an electrolyte and subjected to a d.c. electric field  $\vec{E}$ . The polar coordinate system relevant for the theoretical description of the electrophoretic migration of the particle is indicated. Reproduced with permission from Duval, J. F. L. and Ohshima, H., Electrophoresis of Diffuse Soft Particles, *Langmuir*, **22**, 3533–3546. Copyright 2006 American Chemical Society

the distribution of fixed charged groups in the ion-permeable layer takes place within distances that are comparable to, if not larger than, the Debye length, thus considerably modifying electric potential distributions as derived from hard-surface models. In addition, electroosmotic flow and/or penetration of hydrodynamic flow inside the permeable layer may lead to orders of magnitude discrepancies between the observed electrokinetic response and that expected on the basis of the classical approaches for hard surfaces. With hard particles, ion transport and hydrodynamics may be tackled using classical models. For example, hydrodynamic shear is located at the particle surface and the electrostatic potential at the surface of rigid particles can be assimilated to the electrokinetic potential or zeta-potential,  $\zeta$ , that is involved in every expression of the electrophoretic mobility,  $\mu$ . Electrokinetic models simply differ in their degree of approximation (treatment within the Debye–Hückel limit, inclusion or not of surface conduction phenomena, ability to account for the polarisation of the electric double layer by the applied electric field, etc.). Two expressions for the electrophoretic mobility of a rigid particle were proposed long ago [66–69] and remain valid [5] as limiting laws, one for  $\kappa a \gg 1$  and the other for  $\kappa a \ll 1$ , where  $1/\kappa$  is the classical Debye length and  $a$  denotes the radius of the supposedly spherical particle:

$$\mu = \frac{\varepsilon\zeta}{\eta} \quad (\kappa a \gg 1) \quad (1)$$

corresponding to the Helmholtz-Smoluchowski limit [66,67] and

$$\mu = \frac{2\varepsilon\zeta}{3\eta} \quad (\kappa a \ll 1) \quad (2)$$

corresponding to the Hückel–Onsager limit [68,69]. The quantity  $\varepsilon (= \varepsilon_0 \varepsilon_r)$  denotes the dielectric permittivity of the medium with  $\varepsilon_0$  the dielectric permittivity of vacuum and  $\varepsilon_r$  the relative dielectric permittivity of the medium considered of dynamic viscosity,  $\eta$ . Unlike for hard particles, it is impossible to define the location of the shear plane or slipping plane within a surface layer surrounding a soft particle. For that reason, all relevant theories dealing with the electrokinetics of permeable particles do not depend on the classical notion of zeta potential, a concept which is clearly inappropriate for soft systems [31,32].

To account for the electrophoretic mobility of soft particles, a variety of models have been adopted to mimic transport processes inside thin porous layers [4,70]. Most realistic are the treatments where the soft, charged layer is viewed as a continuous phase with a hydrodynamic permeability and an electric charge that reflects the density and the physicochemical properties of the soft material [23–30,39,46]. A large number of approximate analytical expressions for the electrophoretic mobility of soft particles have been developed but none has the generality of O’Brien and White’s numerical solution for the complete set of governing electrokinetic equations for hard particles [5]. For the sake of illustration, Brooks *et al.* derived an expression for the mobility of red blood cells using flat-plate geometry to represent the glycocalyx layer [18] Hermans and Fujita treated the electrophoresis of polyelectrolytic spheres within the Debye–Hückel approximation [10,11] and more recently Ohshima [24] developed a theory that generalised the preceding developments and derived a number of analytical solutions for practical situations.

Ohshima's analytical expressions are widely employed because they constitute a tractable model based on a limited number of unknown parameters. In this theory, the polarisation and relaxation of the electric double layer by the applied electric field are assumed to be negligible. The analysis of the electrophoretic mobility of a given system, as measured for various ionic strengths, is classically interpreted using the following analytical expression [24]:

$$\mu = \frac{\rho_0}{\eta \lambda_0^2} + \frac{\varepsilon}{\eta} \frac{\psi^0/\kappa_m + \psi^D/\lambda_0}{1/\kappa_m + 1/\lambda_0} \quad (3)$$

where  $\rho_0$  represents the space charge density of the soft surface layer of the system,  $\kappa_m$  the reciprocal Debye thickness of that layer and  $\lambda_0$  a softness parameter. The quantity  $1/\lambda_0$  corresponds to the characteristic penetration length of the flow within the soft surface structure. In the limit of  $1/\lambda_0 \rightarrow 0$ , the surface layer is impermeable to flow whereas the limit  $1/\lambda_0 \rightarrow \infty$  denotes a surface layer that exerts no significant frictional forces on the flow. In equation (3),  $\psi^0$  represents the surface potential, that is, the potential at the position corresponding to the location of the outer boundary of the surface layer and  $\psi^D$  the Donnan potential, i.e. the electrostatic potential attained within the bulk of that layer. The parameters  $\psi^D$ ,  $\psi^0$  and  $\kappa_m$  depend on the space charge density  $\rho_0$  according to the following expressions [24]:

$$\psi^D = \frac{RT}{F} \sinh^{-1} \left( \frac{\rho_0}{2Fc^\infty} \right) \quad (4)$$

$$\psi^0 = \psi^D - \frac{RT}{F} \tanh \left( \frac{F\psi^D}{2RT} \right) \quad (5)$$

$$\kappa_m = \kappa \left[ \cosh \left( \frac{F\psi^D}{RT} \right) \right]^{\frac{1}{2}} \quad (6)$$

where  $c^\infty$  is the bulk concentration of the 1:1 electrolyte that is considered,  $R$  the gas constant,  $T$  the absolute temperature and  $F$  the Faraday constant. The fitting of the mobility–ionic strength curves based on equations (3)–(6) is obtained after adjustment of the unknown variables  $\lambda_0$  and  $\rho_0$  according to a least-squares method.

As stated previously, Ohshima's model suffers from a number of assumptions underlying the derivation of equations (3)–(6). These assumptions are valid (i) within the restricted limits  $\kappa a \gg 1$ ,  $\kappa \delta \gg 1$  and  $\lambda^0 \delta \gg 1$ , where  $\delta$  corresponds to the thickness of the outer (permeable) surface layer of the particle, and (ii) for sufficiently low Donnan potentials, i.e. for sufficiently large electrolyte concentrations at which double-layer polarisation by the applied electric field is negligible. A more recent semi-analytical study [25] has demonstrated, however, the significant importance of these phenomena for soft particles. Furthermore, equations (3)–(6) do not take into account the necessary dependence of the space charge density  $\rho_0$  on the local potential distribution across the soft surface layer, or equivalently, on the electrolyte concentration,  $c^\infty$  [39]. This dependence has long been experimentally and theoretically demonstrated within the framework of the interfacial double-layer formalism for rigid particles [71], which may be regarded as soft particles with  $1/\lambda_0 \rightarrow 0$ . Finally, the derivation of equations (3)–(6) is performed

using the assumption that the soft surface layer is homogeneous, i.e. the space density of charged, soft material—which determines the parameters  $\lambda_0$  and  $\rho_0$ —is assumed to be constant throughout the surface layer. Sophisticated theories on the adsorption of polymers or polyelectrolytes at interfaces go beyond this approximation by computing the position-dependent profile for the density of polymer segments that gradually decays with increasing radius. In view of the complexity of environmental and biological surface structures [72–74], this approximation is further severe since it disregards the chemical and physical heterogeneities of the soft surface layer. The shortcomings of equations (3)–(6) in the quantitative interpretation of experimental data have been demonstrated in various recent studies, including those carried out on streptococcal strains [39], *Escherichia coli* mutants [40], stealth liposomes [45], human erythrocytes [45] and humic substances [46].

It should be recognised that the aforementioned analytical theories have been important in improving our understanding of the complex electrokinetic features of soft particles. However, if experimental results collected for significantly charged and heterogeneous soft systems are to be interpreted on a rigorous quantitative level over a broad spectrum of experimental conditions, exact evaluation of the fundamental electrostatic and transport equations without any restriction on the particle size, particle charge and ionic strength are necessarily required. Recent studies have included this consideration and provided numerical evaluations for the electrophoretic mobility over a wide range of particle charges, coatings and double-layer thicknesses [26–30,45]. Within the framework of most analytical and numerical theories for the electrophoresis of soft particles, with some exceptions [26,27,39], the density of the charged polymer segments within the surface layer is assumed to be constant (homogeneous layer), dropping sharply to zero at the interface formed with the electrolyte. This interfacial step-function modelling may be reasonable for soft systems verifying  $\delta \ll a$  and  $\kappa\delta \ll 1$  but needs to be revisited for  $\delta \geq a$  and/or  $\kappa\delta \geq 1$ .

In the following, the fundamental physical and chemical bases for the theoretical interpretation of the electrohydrodynamic properties of a soft particle are discussed. Subsequently, several concrete applications to biological and environmental systems are examined.

## 2 ELECTROPHORESIS OF SOFT PARTICLES

### 2.1 MODELLING THE SURFACE STRUCTURE OF A CHARGED SOFT PARTICLE

Consider a spherical, polymeric shell particle with a core of radius  $a$  that moves with a velocity  $\vec{U}$  in an electrolyte, for which a uniform d.c. electric field  $\vec{E}$  is applied (Figure 1). The origin of the spherical coordinate system  $(r, \theta, \varphi)$  is placed at the centre of the particle and the polar axis ( $\theta = 0$ ) is set parallel to  $\vec{E}$ . In the limit  $a \rightarrow 0$ , the particle core vanishes and the model reduces to that of a porous sphere, whereas for  $\delta \rightarrow 0$ , the limiting case of a hard sphere is approached. The electrolyte is composed of  $N$  types of ionic, mobile species with valences  $z_i$ , bulk concentrations  $c_i^\infty$  and limiting ionic conductivities  $\lambda_i^0 (i = 1, \dots, N)$ . Although differences in ion valences may be easily accounted for, fixed monovalent charges that are distributed throughout the polymer shell with a volume density  $\rho_{\text{fix}}$  are considered here.

For the sake of simplicity, the spatial dependence of the polymer segment density, denoted  $n_s$ , is chosen to be dependent on  $r$  only (radial profile):

$$n_s(r)/n_s^0 = f(r) \quad (7)$$

where  $n_s^0$  is the nominal segment density of the layer with homogeneously distributed chains and  $f$  a radial function satisfying

$$f(r \rightarrow \infty) \rightarrow 0 \quad (8)$$

which expresses the vanishing of the polymeric shell for  $r \rightarrow \infty$ . The model of Debye–Bueche [75] is used to describe the hydrodynamic properties of the surface layer. Within the framework of that classical model, the polymer segments that constitute the soft surface layer are regarded as resistance centres of radius  $a_s$ , exerting frictional forces on the liquid flowing in the charged layer. The corresponding friction coefficient is denoted  $k$ . The position-dependent hydrodynamic volume fraction of polymer segments,  $\phi$ , is given by  $\phi = 4n_s\pi a_s^3/3$ . Using equation (7), the dependence of  $\phi$  on  $r$  is given simply by  $\phi(r)/\phi_0 = f(r)$  with  $\phi_0 = 4n_s^0\pi a_s^3/3$ . To obtain the spatial distribution of  $k$ , the Brinkman equation is employed [76]. It relates  $k$  to  $\phi$  by considering the flux of fluid across a group of spheres of radius  $a_s$ . For sufficiently low volume fractions ( $\phi < 0.3$ ), one may show that it coincides with the limit predicted by the Stokes equation, i.e. [31]

$$k(r)/k_0 = f(r) \quad (9)$$

with  $k_0 (= 9\eta_w\phi_0/2a_s^2)$ , the friction coefficient of the polymeric shell for a homogeneous distribution of segments. In [26], the limit given by equation (9) was derived from a semi-empirical relationship that yields Brinkman theory at very low  $\phi$  and reproduces the results of numerical computations at higher  $\phi$ . In the following, equation (9), justified for the commonly reported water contents of soft surface layers ( $\phi < 0.05$ ), is adopted. By assuming that the ionogenic sites are uniformly distributed along the polymer chains, the local density of fixed charges,  $\rho_{\text{fix}}$ , satisfies the relationship

$$\rho_{\text{fix}}(r)/\rho_0 = f(r)g[\text{pH}, \psi^{(0)}(r)] \quad (10)$$

where  $\rho_0$  is the nominal charge density within the polymeric layer. Equation (10) takes into account the partial dissociation of the amphoteric groups in the polyelectrolyte layer due to pH and the local equilibrium potential, denoted  $\psi^{(0)}(r)$ . The function  $g$  represents the isotherm that describes the protolytic properties of the polyelectrolytic layer. If necessary, it may include the occurrence of specific interactions between the ionogenic sites and ions from the electrolyte [39]. These interactions depend on the chemical affinity of the ions for the sites and on the local potential within the polymeric shell. For a step function-like modelling of the interface,  $f(r) = 1$  for  $a < r < a + \delta$  and  $f(r) = 0$  for  $r > a + \delta$ . The quantity  $k$  then recovers its classical meaning within the framework of Ohshima's approach (constant bulk friction coefficient  $k_0$ ). If a complete dissociation of all ionogenic sites is assumed,  $\rho_{\text{fix}}$  will be equivalent to  $\rho_0$  [equation (3)]. The gradual transition of the (electrostatic and hydrodynamic) soft layer properties from the bulk surface layer to the

bulk electrolyte solution, as taken into account in the radial function  $f$ , has motivated the qualification of the interface between the soft particle and the electrolyte solution as ‘diffuse’ (Figure 1) and can be generally employed for the soft particle as a whole [31,32].

## 2.2 FUNDAMENTAL ELECTROKINETIC EQUATIONS\*

In the following, we consider the ability of the applied electric field to produce small distortions of the electrostatic potential distribution, ion concentrations and electrochemical potential of the electrolyte ions with respect to their equilibrium values (reached in the absence of the applied field). The determination of the equilibrium values is required prior to tackling the whole set of electrokinetic equations.

Assuming that Boltzmann statistics apply for the distribution of ions around and within the soft surface layer, the equilibrium electric potential distribution,  $\psi^{(0)}(r)$ , is given by the classical Poisson–Boltzmann equations, both being functions of only one spatial variable ( $r$ ):

$$\nabla^2 \psi^{(0)}(r) = -\frac{1}{\varepsilon_0 \varepsilon_r} [\rho_{el}^{(0)}(r) + \rho_{fix}(r)] \quad (11)$$

with

$$\rho_{el}^{(0)}(r) = F \sum_{i=1}^N z_i c_i^\infty \exp[-z_i e \psi^{(0)}(r)/k_B T] \quad (12)$$

where  $k_B$  is the Boltzmann constant. The term  $\rho_{el}^{(0)}$  denotes the local space charge density (at equilibrium) that stems from the mobile ionic species. The second term in brackets on the right-hand side of equation (11) originates from the charged, hydrodynamically fixed, ionogenic sites distributed throughout the soft surface layer.

The standard set of equations governing the dynamics of a soft particle with a discontinuous distribution of polymer chains has been extensively discussed in the literature [24,28,29]. Analysis is extended here to the case of diffuse soft particles where the distribution of soft polymeric material is a function of the radial position,  $r$  [26,27,39,46].

The Navier–Stokes equation that determines the flow velocity,  $\vec{u}(\vec{r})$ , at the position  $\vec{r}$  relative to the particle, is written in its general form

$$\eta \nabla \times \nabla \times \vec{u}(\vec{r}) + \nabla p(\vec{r}) + \rho_{el}(\vec{r}) \nabla \psi(\vec{r}) + k(r) \vec{u}(\vec{r}) = \vec{0} \quad (13)$$

where  $p(\vec{r})$  is the pressure,  $\rho_{el}(\vec{r})$  and  $\psi(\vec{r})$  the space charge density (resulting from the mobile ionic species) and the electrostatic potential in the presence of the applied electric field, respectively.  $k(r)$  is the position-dependent friction coefficient as given by equation (9). The quantity  $\rho_{el}(\vec{r})$  is related to the local ionic concentrations, denoted  $c_i(\vec{r})$ , by

$$\rho_{el}(\vec{r}) = F \sum_{i=1}^N z_i c_i(\vec{r}) \quad (14)$$

---

\* Based on Duval, J. F. L. and Ohshima, H. Electrophoresis of Diffuse Soft Particles, *Langmuir*, **22**, 3533–3546.

The continuity equation for a steady incompressible flow further imposes that

$$\nabla \cdot \vec{u}(\vec{r}) = 0 \quad (15)$$

The local velocity,  $\vec{v}_i(\vec{r})$ , of an ion  $i$  is determined by that of the liquid flow,  $\vec{u}(\vec{r})$  (convection), and by the gradient in electrochemical potential, denoted  $\mu_i(\vec{r})$  (diffusion), so that

$$\vec{v}_i(\vec{r}) = \vec{u}(\vec{r}) - \frac{1}{\bar{\lambda}_i} \nabla \mu_i(\vec{r}) \quad (16)$$

with  $\bar{\lambda}_i$  the drag coefficient of ion  $i$ .  $\bar{\lambda}_i$  is related to the limiting conductivity  $\lambda_i^0$  by the simple expression  $\bar{\lambda}_i = |z_i|eF/\lambda_i^0$ . The continuity equation written for an ion  $i$  leads to

$$i = 1, \dots, N : \quad \nabla \cdot [c_i(\vec{r}) \vec{v}_i(\vec{r})] = 0 \quad (17)$$

For sufficiently weak electric fields  $\vec{E}$ , as commonly considered within the framework of electrokinetic phenomena of the first kind, we may expand  $\rho_{\text{el}}(\vec{r})$ ,  $\psi(\vec{r})$ ,  $c_i(\vec{r})$  and  $\mu_i(\vec{r})$  as follows:

$$\rho_{\text{el}}(\vec{r}) = \rho_{\text{el}}^{(0)}(r) + \delta\rho_{\text{el}}(\vec{r}) \quad (18)$$

$$\psi(\vec{r}) = \psi^{(0)}(r) + \delta\psi(\vec{r}) \quad (19)$$

$$i = 1, \dots, N : \quad c_i(\vec{r}) = c_i^{(0)}(r) + \delta c_i(\vec{r}) \quad (20)$$

$$i = 1, \dots, N : \quad \mu_i(\vec{r}) = \mu_i^{(0)}(r) + \delta\mu_i(\vec{r}) \quad (21)$$

In equations (18)–(21), the quantities indicated by the superscript (0) refer to those at equilibrium (i.e. in the absence of the applied electric field) and the variables,  $\delta\rho_{\text{el}}(\vec{r})$ ,  $\delta\psi(\vec{r})$ ,  $\delta c_i(\vec{r})$  and  $\delta\mu_i(\vec{r})$  indicate small perturbations of the corresponding equilibrium values due to the presence of the applied field  $E$ .  $\rho_{\text{el}}^{(0)}(r)$  and  $\psi^{(0)}(r)$  are given by equations (11) and (12), whereas  $\mu_i^{(0)}(r)$  is related to  $c_i^{(0)}(r)$  via the relationship

$$i = 1, \dots, N : \quad \mu_i^{(0)}(r) = \mu_i^\infty + z_i e \psi^{(0)}(r) + k_B T \ln [c_i^{(0)}(r)] \quad (22)$$

where  $\mu_i^\infty$  is the electrochemical potential of ion  $i$  at some reference state. Using equations (18)–(21), one can show that the linearisation of the governing electrokinetic equations (13)–(17) with respect to the electric field  $E$  reduces to [46]

$$\begin{aligned} L_r L_r h(r) - \lambda_0^2 \left\{ f(r) L_r h(r) + \frac{df(r)}{dr} \left[ \frac{h(r)}{r} + \frac{dh(r)}{dr} \right] \right\} \\ = -\frac{F}{\eta r} \frac{dy(r)}{dr} \sum_{i=1}^N z_i^2 c_i^\infty \varphi_i(r) \exp [-z_i y(r)] \end{aligned} \quad (23)$$

$$i = 1, \dots, N : \quad L_r \varphi_i(r) = \frac{dy}{dr} \left[ z_i \frac{d\varphi_i(r)}{dr} - 2 \frac{\bar{\lambda}_i}{e} \frac{h(r)}{r} \right] \quad (24)$$

where the radial functions  $h$  and  $\varphi_i$  depend on  $\vec{u}(\vec{r})$  and  $\delta\mu_i(\vec{r})$  according to

$$\vec{u}(\vec{r}) = \left\{ -\frac{2}{r}h(r)E \cos \theta, \frac{1}{r}\frac{d[rh(r)]}{dr}E \sin \theta, 0 \right\} \quad (25)$$

and

$$\varphi_i(r) = -\delta\mu_i(r)/z_i e E \cos \theta \quad (26)$$

with  $L_r$  the differential operator defined by

$$L_r \equiv \frac{d^2}{dr^2} + \frac{2}{r}\frac{d}{dr} - \frac{2}{r^2}.$$

The quantity  $y(r)$  [ $= e\psi^{(0)}(r)/k_B T$ ] in equations (23) and (24) is the dimensionless equilibrium potential and  $e$  is the elementary charge. The (nominal) softness parameter  $\lambda_0$  of the permeable polymeric shell depends on the (nominal) friction coefficient  $k_0$  via the relationship

$$\lambda_0 = (k_0/\eta)^{\frac{1}{2}} \quad (27)$$

It should be emphasised that the permeability of the surface layer, denoted  $1/\lambda^2$ , is a function of the radial position  $r$  according to  $1/[\lambda(r)]^2 = 1/[\lambda_0^2 f(r)]$ , as inferred from equations (9) and (27).

### 2.3 BOUNDARY CONDITIONS

As a general comment, the boundary conditions for the governing electrokinetic equations are simpler when written for a diffuse interface than for a sharp interface [26,27,39,46]. The gradual transition from the surface layer to the electrolyte eliminates the necessity for introducing boundaries other than those found between the hard and soft components of the particle (i.e. at  $r = a$ ) or pertaining to the far-field domain (i.e. for  $r \rightarrow \infty$ ).

The hard component of the particle is strictly inaccessible for electrolyte ions so that, for the condition of zero velocity at  $r = a$ , where the slipping plane is rigorously located, one obtains from equation (25)

$$h(r = a) = 0 \quad (28)$$

and

$$\frac{dh}{dr}|_{r=a} = 0. \quad (29)$$

For  $r \rightarrow \infty$ , the velocity vector  $\vec{u}(\vec{r})$  of the liquid relative to the particle must be equal in magnitude but opposite in sign to the velocity of the particle, denoted  $\vec{U}$ . In turn, this leads to [24]

$$h(r \rightarrow \infty) \rightarrow \frac{\mu}{2}r \quad (30)$$

where  $\mu$  is the sought electrophoretic mobility defined by  $\mu = U/E$ . From the condition that the net force acting on the particle must be zero under steady-state conditions, one may refine equation (30) to [24]

$$h(r \rightarrow \infty) \rightarrow \frac{\mu}{2}r + O\left(\frac{1}{r}\right) \quad (31)$$

Equations (28)–(31) are the boundaries associated with the differential equation (23) of the fourth order in  $h$ . The two boundary conditions satisfied by the functions  $\varphi_i$  are written as

$$i = 1, \dots, N : \quad \left. \frac{d\varphi_i(r)}{dr} \right|_{r=a} = 0 \quad (32)$$

$$\varphi_i(r \rightarrow \infty) \rightarrow r \quad (33)$$

Equation (32) is a direct consequence of the slipping plane condition at  $r = a$ . Equation (33) is obtained after considering that far from the particle, perturbations of the local electric potential and local ion concentrations caused by the applied field become negligible. The boundaries relating to the (dimensionless) equilibrium potential distribution,  $y$ , reflect the bulk electroneutrality condition at large distances from the particle and the electrostatic state of the surface of the particle core. Depending on the system investigated, the latter may be written in terms of the surface potential,  $y^s$ , or surface charge density,  $\sigma^s$ . For the case of a porous sphere devoid of any hard core, the following condition is used:

$$\left. \frac{dy(r)}{dr} \right|_{r=0} = 0 \quad (34)$$

which attests to the symmetry of the potential distribution around the centre of the particle.

To compute the electrophoretic mobility, it is necessary to solve consistently the non-linear system composed of the coupled differential equations (11)–(12), (23) and (24) (of order 2, 4 and 2 in  $y$ ,  $h$  and  $\varphi_i$ , respectively) and obeying the appropriate boundary conditions, discussed previously. The complexity of the problem requires a numerical solution [46]. In recent years, several authors have proposed numerical schemes for solving the complete set of electrokinetic equations for soft particles. Some [28,29] are based on a network model that disregards the possibility of heterogeneous (or diffuse) soft layers, whereas others [26,27] offer the advantage of dealing with electrophoresis under oscillatory conditions.

The main assumptions of the model described above [24] are that: (a) the Reynolds numbers of the liquid flow inside and outside the polyelectrolyte layer are small so that the liquid may be considered as incompressible; (b) the electrophoretic velocity,  $\vec{U}$ , is proportional to the applied field,  $\vec{E}$ , which is correct for low  $E$  (terms in  $E$  of order higher than 1 may be neglected); (c) the relative permittivities,  $\varepsilon_r$ , inside and outside the polyelectrolyte layer are the same, which is reasonable for polymeric shells with sufficiently high water content; and (d) the slipping plane (at which the velocity of the fluid relative to the particle is zero) is located on the particle core ( $r = a$ ). Following assumption (c), we will consider that the mobilities or diffusion coefficients of electrolyte ions within the soft layer equate with those in the bulk electrolyte solution. This approximation is essentially true for rather loose layer structures but becomes necessarily questionable for more dense brushes where ionic correlations effects may further play a significant role.

In the next section, the typical dependences of the electrophoretic mobilities of environmental (soft) particles on the electrolyte concentration, the hydrodynamic permeability and the fixed charge density are discussed in relation to the model presented above.

## 2.4 CHARACTERISTIC ELECTROKINETIC FEATURES OF SOFT PARTICLES

For a porous particle of a given radius  $\delta$  and devoid of any hard core ( $a = 0$ ), dimensionless electrophoretic mobilities, denoted  $\bar{\mu}$  and given by  $\mu e\eta/\varepsilon k_B T$ , are reported as a function of the electrolyte concentration of a 1:1 electrolyte (NaCl) (Figure 2). The results are first presented for various nominal charge densities (constant throughout the particle volume),  $\rho_0$ , for the case of step-function modelling of the soft surface layer [i.e.  $f(r) = 1$  for  $0 < r < \delta$  and  $f(r) = 0$  for  $r > \delta$ ]. For the sake of simplicity, the dependence of the space charge density on the electrolyte concentration [i.e. equation (10)] is ignored, which is equivalent to writing  $g \equiv 1$ . Variations in the electrolyte concentration are expressed in terms of the dimensionless parameter  $\kappa\delta$ . Upon increase of  $\rho_0$  at constant  $\kappa\delta$ ,  $\bar{\mu}$  increases due to a corresponding increase in the local electrostatic potential,  $y$ . At sufficiently low electrolyte concentrations, i.e. when the double layer is much thicker than the coating thickness ( $\kappa\delta \ll 1$ ),  $\bar{\mu}$  is nearly proportional to the (quasi-uniform) potential within the surface layer. This result is expected based on analogy with Hückel's theory for hard particles,  $\bar{\mu} = 2\xi e/3k_B T$  [equation (2)], which is valid for low values of  $\xi$  and small particles [27]. Depending on the magnitude of the potentials at low  $\kappa\delta$ , polarisation of the double layer by the applied electric field may take place, which effectively lowers its electrophoretic mobility. In the other limiting regime reached at high electrolyte concentrations ( $\kappa\delta \gg 1$ ), the mobility  $\bar{\mu}$  asymptotically tends towards a constant value given by the general relationship

$$\bar{\mu} \rightarrow (\kappa\lambda_0^{-1})^2 \frac{\rho_0}{2Fc^\infty} \frac{\cosh(\lambda_0\delta) - 1}{\cosh(\lambda_0\delta)} \text{ for } \kappa^{-1} \rightarrow 0 \quad (35)$$

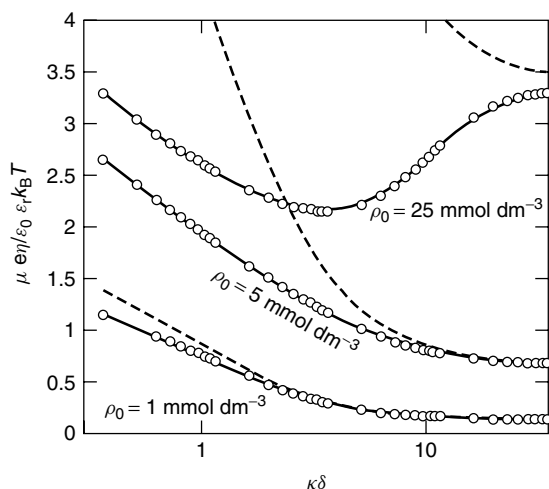


**Figure 2.** Dimensionless electrophoretic mobility,  $\bar{\mu}$ , for various values of fixed charge density  $\rho_0$  (indicated) for a porous sphere as a function of the electrolyte concentration (NaCl electrolyte at 298 K). Model parameters:  $\alpha \rightarrow 0$  (step-function interfacial modelling),  $\delta = 35$  nm,  $\lambda_0^{-1} = 5$  nm. The dashed lines are approximations of the soft particle mobility using the expressions of Hermans and Fujita [11]. Reproduced with permission from Duval, J. F. L. and Ohshima, H., Electrophoresis of Diffuse Soft Particles, *Langmuir*, **22**, 3533–3546. Copyright 2006 American Chemical Society

that can be reduced to the well known result  $\mu \rightarrow \rho_0/\eta_w \lambda_0^2$  provided that  $\lambda_0 \delta \gg 1$  [24]. In the limit given by equation (35), there are no hydrodynamic interactions among the polymer segments, the mobility being essentially that of a single resistance centre associated with a single polymer segment. This peculiar feature characterises soft interfaces and differentiates them from hard interfaces for which the electrokinetic response in concentrated electrolytes vanishes. For intermediate  $\kappa\delta$  values, a mobility minimum is eventually observed as a result of the balance between the electrostatic forces that tend to promote the migration of the particle (in the absence of polarisation of the double layer) and the electroosmotic drag that slows the migration of the particle due to the friction exerted by the polymer segments on the flow. As expected, mobilities may be well approximated by those obtained from the analytical expression for spherical polyelectrolytes at low potentials (i.e. for sufficiently large  $c^\infty$ ) [11]. A discrepancy gradually arises for lower values of  $\kappa\delta$ , i.e. when electrostatic potentials are sufficiently large for polarisation phenomena to be significant [25].

The impact of the softness parameter  $\lambda_0$  on the mobility of a soft particle is illustrated in Figure 3. Calculations were performed within the conditions of Figure 2 except that the particle also contained an uncharged hard component. When varying the penetration length,  $1/\lambda_0$ , of the fluid flow within the surface layer, the various  $\bar{\mu}-\kappa a$  plots all tended to the same limit at low  $\kappa a$  because the double layer was well outside the coating ( $\kappa\delta \ll 1$ ). In addition, the surface potential of the particle [i.e. at ( $r = a$ )], which essentially controls the magnitude of the mobility, remained unaffected. For a given  $\kappa a$ , upon increase of  $1/\lambda_0$ , the electroosmotic drag is reduced considerably, thus favouring an increase of the electrophoretic mobility. The mobility minimum that originates in the balance between hydrodynamic and electrostatic forces is shifted to lower  $\kappa a$  values. For

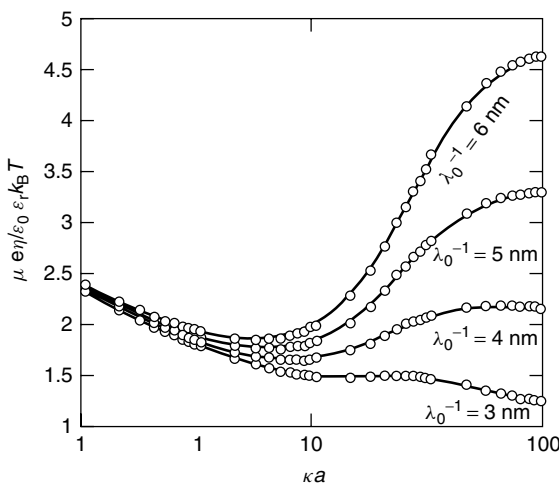


**Figure 3.** Impact of the softness parameter  $\lambda_0$  (indicated in terms of the characteristic hydrodynamic penetration length  $1/\lambda_0$ ) on the electrophoretic mobility of a soft particle as a function of the electrolyte concentration (NaCl electrolyte at 298 K). Model parameters:  $\alpha \rightarrow 0$  (step-function interfacial modelling),  $a = 100$  nm,  $\delta = 50$  nm,  $\rho_0 = 25$  mmol dm $^{-3}$ . Reproduced with permission from Duval, J. F. L. and Ohshima, H., Electrophoresis of Diffuse Soft Particles, *Langmuir*, **22**, 3533–3546. Copyright 2006 American Chemical Society

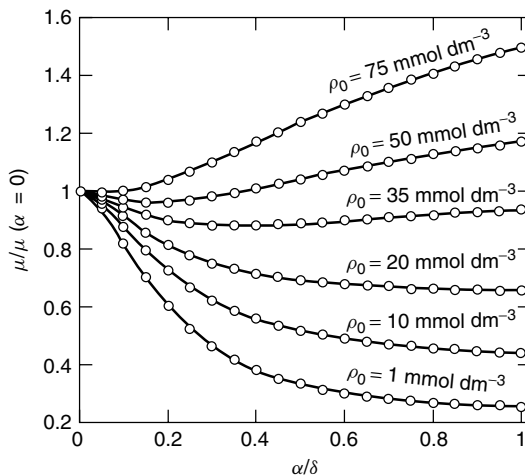


**Figure 4.** Influence of the diffuse character of the interface (indicated by the decay length  $\alpha$ ) on the electrophoretic mobility for various values of  $\rho_0$  (as indicated). Model parameters:  $a = 10 \text{ nm}$ ,  $\delta = 40 \text{ nm}$ ,  $\lambda_0^{-1} = 3 \text{ nm}$ ,  $c_\infty = 1 \text{ mmol dm}^{-3}$  (NaCl electrolyte at 298 K,  $\kappa^{-1} = 9.6 \text{ nm}$ ). Reproduced with permission from Duval, J. F. L. and Ohshima, H., Electrophoresis of Diffuse Soft Particles, *Langmuir*, **22**, 3533–3546. Copyright 2006 American Chemical Society

sufficiently large electrolyte concentrations where the polarisation of the double layer by the applied electric field is negligible,  $\bar{\mu}$  may be adequately described by Ohshima's general flat-plate theory [24]. At infinite  $c^\infty$ ,  $\bar{\mu}$  arrives at a constant finite value that is given by equation (35).

As a final illustration, the effect of heterogeneity of the surface layer on the electrophoretic mobility of the particle as a whole is reported (Figure 4). For that purpose, the following arbitrary form for the radial function  $f(r)$  can be adopted for sake of illustration:

$$f(r) = \frac{\omega}{2} \left\{ 1 - \tanh \left[ \frac{r - (a + \delta)}{\alpha} \right] \right\} \quad (36)$$

The parameter  $\alpha$  has a dimension of length that represents the degree of inhomogeneity of the distribution of the polymer segment density. For  $\alpha \rightarrow 0$ , the distribution is homogeneous whereas for increasing values of  $\alpha$ , the interface between the surface layer and the electrolyte becomes more diffuse with a gradual decay of the soft layer properties from the bulk soft layer to the bulk electrolyte (Figure 5). The dimensionless parameter  $\omega$  is determined in such a way that the total amount of polymer segments (and thus of charges) remains constant upon variation of  $\alpha$  and/or  $\delta$ , as required:

$$\omega = \frac{2}{3} [(a + \delta)^3 - a^3] / \int_a^\infty \left\{ 1 - \tanh \left[ \frac{r - (a + \delta)}{\alpha} \right] \right\} r^2 dr \quad (37)$$

In the light of Figure 4, it is obvious that the heterogeneous distribution of the resistance centres (or polymer segments) has a dramatic impact on the electrophoretic mobility. For sufficiently low space charge densities,  $\rho_0$ , a large decrease in the mobility is observed due to an increase in  $\alpha$ . At first sight, this result might appear surprising. Indeed, increasing  $\alpha$  is equivalent to increasing the local charge in the region  $r > a + \delta$  [see Figure 5 and

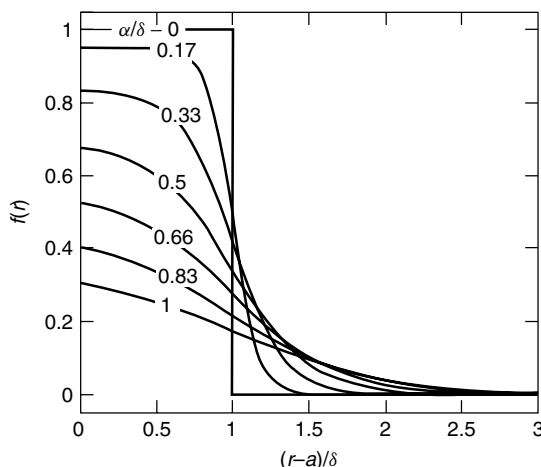


**Figure 5.** Representation of the spatial modelling of the interface for a diffuse soft particle [equations (36) and (37)]. The function  $f$  relates to the spatial distribution of the polymer segment density [equation (7)], to the distribution of the friction coefficients [equation (9)] and fixed charges [equation (10)] within the polymeric shell. Reproduced with permission from Duval, J. F. L. and Ohshima, H., Electrophoresis of Diffuse Soft Particles, *Langmuir*, **22**, 3533–3546. Copyright 2006 American Chemical Society

equation (10)], where the flow penetration within the coating is expected to be the most significant. On the other hand, an extension of the thickness of the diffuse interface also results in a local increase of the frictional forces [equation (9)] within the region where there is an excess of electrokinetically active counterions. This hydrodynamic effect overwhelms the electrostatic effect and is responsible for the overall decrease of the mobility when increasing  $\alpha$  at low  $\rho_0$ . Furthermore,  $d\mu/d\alpha$  gradually tends to zero with increasing  $\alpha$  due to the corresponding increase in the local charges at  $r > a + \delta$  resulting in potentials that are large enough to partially compensate for the increasing electroosmotic drag. At the other limit of large charge densities ( $\geq 75 \text{ mmol dm}^{-3}$  in the example given in Figure 4), the mobility increases with increasing values of  $\alpha$ . The latter situation is the mirror image of that discussed for low  $\rho_0$ . The increase of the local equilibrium potentials with  $\alpha$  for  $r > a + \delta$  now predominates the mobility increase. For intermediate values of  $\rho_0$ , the balance between the hydrodynamic and the electrostatic effects of a changing  $\alpha$  on the diffuse interface is eventually reflected by the presence of a mobility minimum.

The applicability of the theoretical framework of Section 2 will be demonstrated for the quantitative interpretation of electrophoretic mobility measurements on biological and environmental systems. Recent analyses performed on bacteria [39] and humic particles [46] will serve as illustrative examples.

### 3 APPLICATIONS

#### 3.1 DETERMINATION OF THE KEY ELECTROSTATIC AND HYDRODYNAMIC MODEL PARAMETERS

In the formalism that was described in the preceding sections, several model parameters are required to address the electrostatic and hydrodynamic characteristics of the soft

layer surrounding the particle under investigation. These parameters include the function  $f$  [equation (7)] that relates to the heterogeneous character of the polymeric shell, the function  $g$  [equation (10)] that describes the ionic specificity of the surface layer with respect to charge-determining ions and ions from the background electrolyte, the (nominal) softness parameter,  $\lambda_0$ , the (nominal) space charge density,  $\rho_0$ , and the sizes  $a$  and  $\delta$ .

### 3.1.1 Evaluation of the Distribution Function, $f$ , of the Soft, Polymeric Material

Rigorous determination of the distribution function for the density of charged chains in the soft surface layer requires an accurate knowledge of the interactions between the solvent molecules, the electrolyte ions and the soft material therein. Depending on the system that is considered, including the type of preparation chosen for the soft structure and the (possible) specificity with the boundary particle surface, those interactions may vary. It should be recalled that the polyelectrolyte-like chains that make up many surface layers show some degree of flexibility and their characteristic size and spatial arrangements depend strongly on their neighbouring environment and, in particular, are mediated by the local distributions of electrolyte. In polymer chemistry, self-consistent-field calculations, based on Scheutjens–Fleer theory, and molecular dynamic simulations are commonly used to determine the inhomogeneous spatial distribution of polymers adsorbed at a given interface [77–80]. Although such information may be obtained for relatively well-defined and uncharged soft layers, it is less accessible when dealing with charged biological or environmental systems such as bacteria, viruses, humics or polysaccharides. Mean-field calculations are feasible for soft particles of relatively simple and controlled structure but rapidly become intricate and elusive for complex soft systems due to the absence of rigorous model variables. Knowledge of the physicochemical properties of the system, including the polymer chain density, the thickness and permeability of the polymer layer, the polymer molar mass, absorbed quantities and the hydrodynamic layer thickness may turn out to be very advantageous for the interpretation of the electrokinetic data. This important point was first underscored by Hill and Saville [45]. If such details are not available, the diffuse soft layer approach, as presented here, is particularly powerful for analysing experimental data collected on systems with complex surface structures [39]. The analysis is able to mimic many practical situations by tuning a single adjustable parameter, in the present case the decay length,  $\alpha$ . Experimental indication of structural heterogeneity for a given particle may be obtained from size measurements (see Section 3.1.2) as a function of ionic strength or pH. Indeed, the electrostatic stiffening of charged chains, resulting in an expansion (swelling) of the particle, finds its origin in the building up of a significant osmotic pressure drop at the interface. The space dependence of the osmotic pressure, which is intrinsically related to that of the equilibrium potential, results in an anisotropic rearrangement of the chains leading to a heterogeneous distribution of the chain density [equation (7)] within the surface layer. Variations in temperature may also induce an important reorganisation of the polymer chains in the surface layers of hydrogel particles [60–65].

Given the above considerations, the quantitative interpretation of the electrophoretic mobility measurements for a given complex system can be performed initially by assuming that the soft surface layer is uniform (step-function representation of the interface). In a second step, discrepancies, if any, between theory and experiment may be corrected by an

appropriate choice of the distribution function  $f$  and accompanying decay length, denoted  $\alpha$  in our analysis. The values of the latter and the resulting effective particle size should then be discussed in relationship with independently measured sizes for the particle. It is emphasised that the formalism detailed in Section 2 may cope with any segment distribution, either empirical, analytical or computational. The above strategy has been successful in analysing the electrokinetic features of polyacrylamide gels in connection with their propensity to swell in relationship to the ionic strength of the solution [60].

### 3.1.2 Evaluation of the Characteristic Size of the Particles

The characteristic particle size may be determined using a wide range of analytical techniques. Among them, several provide direct images of the particles, including atomic force microscopy (AFM), transmission electron microscopy (TEM) and scanning electron microscopy (SEM). Since some of these techniques may alter the delicate surface structures of microorganisms, including bacteria, non-destructive, dynamic techniques including dynamic light scattering (DLS) and fluorescence correlation spectroscopy (FCS) are also employed [81]. These methods allow for the measurement of time-dependent fluctuations in the intensity of scattered light or fluorescence due to the random, Brownian motion of the particles. Analysis of the intensity fluctuations allows for the determination of diffusion coefficient distributions, which can then be converted into a size distribution using established theory. Some of the classical theoretical expressions used for that purpose, such as the Stokes–Einstein equation, yield hydrodynamic radii that are strictly valid for hard systems. As such, their application to soft materials, exhibiting significant permeability, may be questionable [46]. Indeed, the physical size of a particle differs from its effective size due to the hydrodynamic drag on the soft surface layer and charge effects. In the absence of the latter, the effective particle size might be assimilated to the experimentally measured hydrodynamic size. Hill and Saville have demonstrated how the hydrodynamic thickness may be obtained from a set of electrokinetic equations [45]. The proposed method neglects the impact of electro-viscous effects on the particle size and is therefore rigorously appropriate for an uncharged polymeric shell ( $\rho_{\text{fix}} = 0$ ) and an uncharged hard-component ( $\sigma^{\text{S}} = 0$ ). It therefore applies only within a restricted range of (high) electrolyte concentrations. Comparisons between theoretical and measured sizes become approximate (or qualitative) with decreases in the ionic strength or increases (in magnitude) of the surface layer charge.

### 3.1.3 Evaluation of the Space Charge Density

The (generally) amphoteric nature of the ionogenic sites distributed throughout the polymeric fringe of soft particles leads to a pH dependence for the local space charge density,  $\rho_{\text{fix}}$  [equation (10)]. The affinity of protons for those sites is mediated by a chemical contribution, which is determined by the molar Gibbs energies of protonation and an electrostatic contribution that leads to a dependence of  $\rho_{\text{fix}}$  on the electrolyte concentration (or equivalently on the local electrostatic potential,  $y$ ). In the following discussion, we will exclusively refer to soft particles with an uncharged hard component (*i.e.*  $\sigma^{\text{S}} = 0$ ). The classical method for evaluating the charge carried by a particle is by potentiometric

titration. Titrations allow for the measurement of an overall charge, denoted  $Q^0$ , which depends on  $\rho_{\text{fix}}$  according to the general relationship

$$Q^0 = \int_V \rho_{\text{fix}} \, dV \quad (38)$$

where  $V$  is the volume of the particle (or the surface layer). By assuming that the charge  $Q^0$  originates from proton exchange equilibria that operate on  $p$  types of ionogenic sites,  $\rho_{\text{fix}}$  may be expressed as a sum of Langmuir isotherms, written as

$$\rho_{\text{fix}} = f(r) \sum_p \rho_{\text{max},p}^0 \frac{1}{1 + 10^{pK_p - \text{pH}} \exp[-y(r)]} \quad (39)$$

where the constants  $\rho_{\text{max},p}^0/F$  denote the volume concentrations of the sites  $p$  and  $K_p$  are the affinity constants associated with each of the acid–base reactions. Equation (39) is valid under the condition that the distribution of the polymer chains is radial and the distribution of amphoretic sites along the chains is homogeneous (smeared-out). For certain systems, i.e. when operating with Langmuir–Freundlich-type isotherms [52,82], it is necessary to account for the chemical heterogeneity of the sites, which is reflected in a continuous distribution of the affinity constants around a median value. Depending on the chemical nature of the soft layer and the electrolyte considered, ions other than charge-determining ions, i.e. protons in equation (39), may specifically interact with the charged ionogenic sites. It is beyond the scope of this chapter to analyse these cases in detail and readers are referred to [39,55] for further information. The theoretical determination of the charge carried by the soft particle requires a consistent numerical determination of the potential distribution,  $y(r)$ , as given by equations (11) and (12) after substitution of  $\rho_{\text{fix}}$  by equation (39). Once the Poisson–Boltzmann equation has been solved, the integral (38) may be evaluated and the resulting charge  $Q^0$  compared with the experimental data. The parameters  $\rho_{\text{max},p}^0$  and  $pK_p$  are determined according to this procedure by a least-squares method. For purposes of accuracy, comparison between theory and experiment should necessarily be made over a wide range of pH values and electrolyte concentrations. Determination of the number of sites may be accomplished following analysis of the derivative of the experimental isotherm with respect to the pH at sufficiently high electrolyte concentrations, where the electrostatic contribution to ion-exchange processes is largely reduced. The number of different energetic domains or types of adsorption sites may then be assimilated to the number of peaks observed. For homogeneous and sufficiently thick polymeric shells, i.e. for  $\kappa\delta \gg 1$ , the electrostatic potential within the surface layer is nearly constant and one may consider  $y(r)$  to be equivalent to the Donnan potential difference,  $y^D$ , between the polymer layer phase and the surrounding electrolyte solution. This substantially simplifies the determination of the protolytic characteristics of the surface layer since it decouples equations (11) and (39). The Donnan potential  $y^D$  is resolved from the transcendental equation that reflects the balance in the bulk soft layer between the charges due to the mobile ionic species and those due to the fixed ionogenic sites, i.e.  $\rho_{\text{fix}}|_{y=y^D} + \rho_{\text{el}}^{(0)}|_{y=y^D} = 0$  with  $\rho_{\text{fix}}$  and  $\rho_{\text{el}}^{(0)}$  defined by equations (39) and (12), respectively. Based on the preceding theory, the hydrodynamic permeability can be

evaluated from electrophoretic mobilities once the parameters relative to the particle size (Section 3.1.2) and the particle charge distribution (Sections 3.1.1 and 3.1.3) are known.

### 3.2 APPLICATION TO BIOCOLLOIDS: THE CASE OF BACTERIA

Long-range electrostatic forces are of prime importance in the determination of bacterial interactions and bacterial adhesion processes during the preliminary steps of biofilm formation [51]. The strength of these forces depends strongly on the underlying structure of the biological surfaces that are investigated. Some important information on the structure can be obtained from an appropriate analysis of electrophoretic mobility measurements. Due to the permeable character of the cell wall and/or the surrounding polymeric layer, bacteria may be regarded as paradigms of soft bioparticles. The recent developments of electrokinetic theories for soft particles [26–30,39,46] now allows the rigorous evaluation of the degree of softness (i.e. the hydrodynamic permeability) and eventually the space charge density (if unknown) of the soft surface structure from the raw electrokinetic data. Numerous analyses of electrophoretic mobilities have been reported previously for bacterial cells on the basis of equations (3)–(6). As mentioned previously, those studies suffer from a number of limitations that are overcome by the theory reported in Section 2. To illustrate the issue, we shall re-examine an interpretation of the electrokinetics of two oral streptococcal strains, *Streptococcus salivarius* HB and *Streptococcus salivarius* HB-C12 [39]. These two strains are Gram-positive bacteria with a cell wall with a thickness,  $\delta_w$ , of around 23 nm. As indicated in Figure 6, HB-C12 is a ‘bald’ bacterium that is devoid of any fibrillar or capsular material whereas HB has a fibrillar surface covering of a thickness,  $\delta_F$ , of approximately 200 nm. Such observations have allowed for the modelling of the distribution function  $f$  (Figure 6). A detailed analysis of the titration data for these two bacterial strains was made along the lines of Section 3.1.3. It revealed that the ionogenic sites responsible for the negative charge of the cell wall were amino acids with alkaline side-chains and that the fibrillar layer also contained sugar entities. The amount of charges within the fibrillar layer was about eight times lower than that in the cell wall. Furthermore, some evidence for specific interactions between potassium ions and the cell wall was put forward. All these elements were in agreement with the known structure and composition of the peptidoglycan layer for Gram-positive bacteria [72,73] in addition to titration measurements made in various electrolytes [83]. It should be mentioned that, following the conclusions given by van der Wal *et al.* [84], titration experiments were carried out sufficiently fast to prevent any biological regulation (proton pumps) by the bacteria that would tend to modify their ionic environment. By integrating all of this information in a consistent way using the model presented in Section 2, the electrokinetic properties of the bacteria could be quantitatively interpreted (Figure 7). In particular, it was demonstrated that the softness (or, equivalently, the hydrodynamic permeability) of the fibrillar layer was more important than that of the cell wall, and that all electrokinetic data were satisfactorily described using a step-function representation for the distribution function  $f$  (see Figure 6). Such a representation excludes any significant swelling, shrinking or aggregation of the bacteria during variations in ionic strength or pH. This conclusion was consistent with size measurements, the low charge density obtained for the fibrillar layer (resulting in a small interfacial osmotic pressure) and the rigid nature of the cell wall that can withstand a considerable turgor pressure of the protoplast. In previous studies [85–87], electron microscopy using a negative-staining technique showed

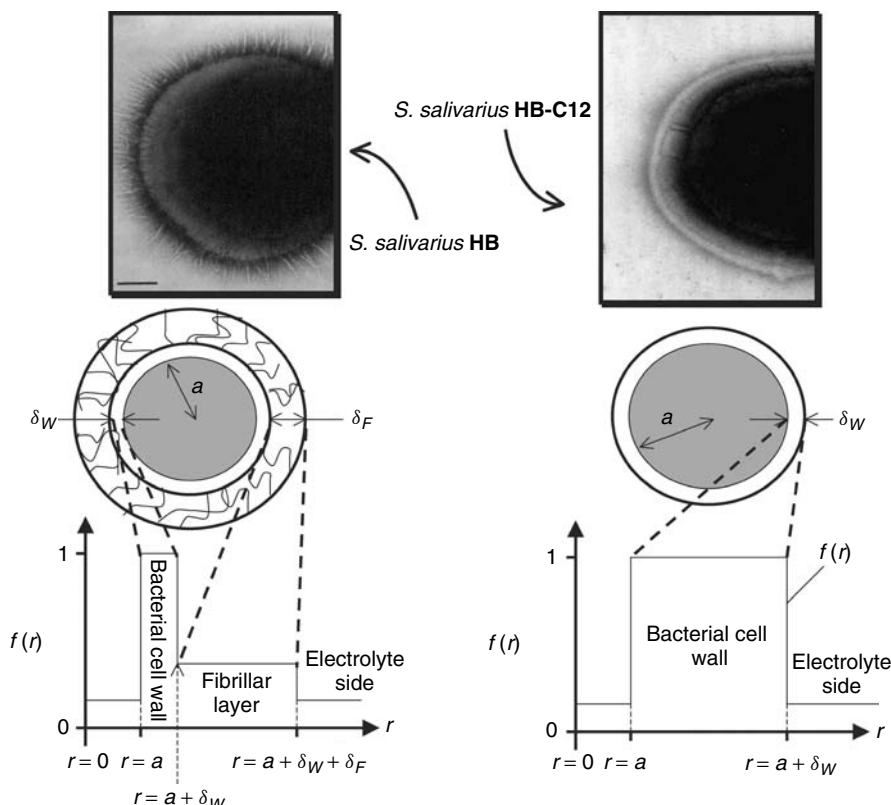


**Figure 6.** (Top) electron micrographs of a 1% methylamine tungstate-stained *S. salivarius* HB strain and of the completely bald, non-fibrillated variant, *S. salivarius* HB-C12. The bar denotes 100 nm. (Bottom) modelling of the fibrillated (HB) and non-fibrillated (HB-C12) oral streptococcal strains. For the sake of clarity, the schema are not to scale. The fibrils have a space charge density that is about 30 times lower than that of the bacterial cell wall, which explains the step in the density distribution function  $f$  for the HB strain variant at the position  $r = a + \delta_w$ . Reproduced with permission from Duval, J. F. L., Busscher, H. J., van de Belt-Gritter, B., van der Mei, H. C. and Norde, W., Analysis of the interfacial properties of fibrillated and non-fibrillated oral streptococcal strains from electrophoretic mobility and titration measurements: evidence for the shortcomings of the ‘classical soft particle approach’, *Langmuir*, **21**, 11268–11282. Copyright 2005 American Chemical Society

that four distinct fibril classes, with lengths of approximately 200, 100, 70 and 60 nm were detectable on *S. salivarius* HB. This spatial distribution of the fibrils around the bacteria should have led, *a priori*, to the definition of a diffuse representation for the bacterium–electrolyte solution interface. However, careful analysis of the electroosmotic flow profiles demonstrated that it was impossible to probe the heterogeneous distribution of the fibrillar material around the cells using electrophoresis. The argument was that the “slipping plane” was located within a spatial region corresponding to the outer tails of the longest bacterial fibrils ( $\lambda_0\delta_F \gg 1$ ) such that the longest fibrils alone were governing the electrokinetic features of the HB strain.

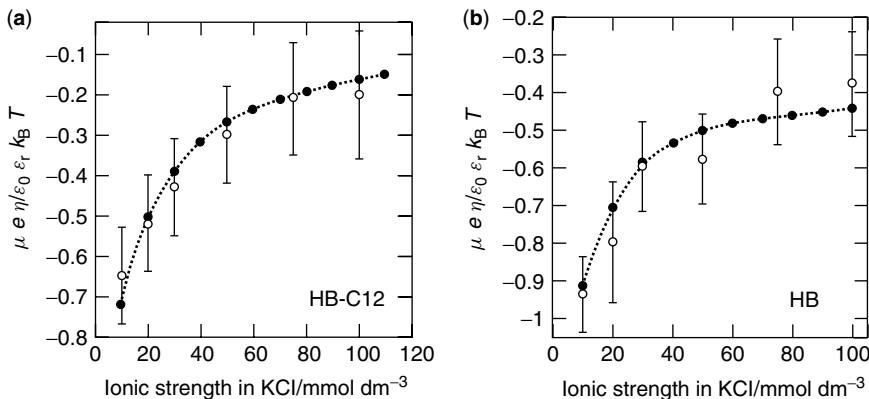


**Figure 7.** (Dimensionless) electrophoretic mobility as a function of KCl ionic strength (298 K) for the HB-C12 bald variant (a) and for the HB fibrillated strain (b) of *S. salivarius* [39]. Open circles, experimental data; filled circles, theoretical predictions with the dashed lines as guides for the eye. HB-C12,  $1/\lambda_0 \approx 1.2$  nm; HB,  $1/\lambda_0 \approx 1.9$  nm. See text and [39] for further details. Reproduced with permission from Duval, J. F. L., Busscher, H. J., van de Belt-Gritter, B., van der Mei, H. C. and Norde, W., Analysis of the interfacial properties of fibrillated and non-fibrillated oral streptococcal strains from electrophoretic mobility and titration measurements: evidence for the shortcomings of the ‘classical soft particle approach’, *Langmuir*, **21**, 11268–11282. Copyright 2005 American Chemical Society

### 3.3 APPLICATION TO ENVIRONMENTAL COLLOIDS: THE CASE OF THE HUMICS

It is now well recognised that humic substances (HS) play an important role in the transport and binding of trace metals in the environment [53,54]. For that reason, much attention has been devoted to understanding the ‘surface’ properties of the humics and relating them to the propensity of the particles to interact with multivalent metals. Recently [46], an integrated analysis of those properties was performed by interpreting consistently a large set of data obtained by FCS, protolytic titration and capillary electrophoresis over a broad range of pH and electrolyte concentration values. The strategy adopted was that explained in Sections 2 and 3.1. Although it is beyond the scope of this chapter to describe all of the results in detail, the main conclusions illustrate well the benefits of rigorously modelling the electrohydrodynamics of soft particles. Experimental details are thoroughly described in [46].

The dependence of the electrophoretic mobility on ionic strength at  $\text{pH} \approx 11$  for three different standard humic substances [Suwannee River fulvic (FA) and humic acids (HA) and a peat humic acid (PHA)] was consistent with the basic features that were expected for hydrodynamically permeable particles (Figure 8a) of constant size ( $\delta \approx 1$  nm). While it is clear that an individual humic particle cannot be regarded as a homogeneous entity, but rather as a combination of homologous molecules with similar (but not identical) nature, it nonetheless may behave in a way similar to that of an average polyelectrolyte with an internally homogeneous site distribution [74]. This feature, which certainly deserves further attention, was in line with the interfacial step-function representation (of the hydrodynamics and electrostatics [see equations (9) and (10), respectively]) and is consistent

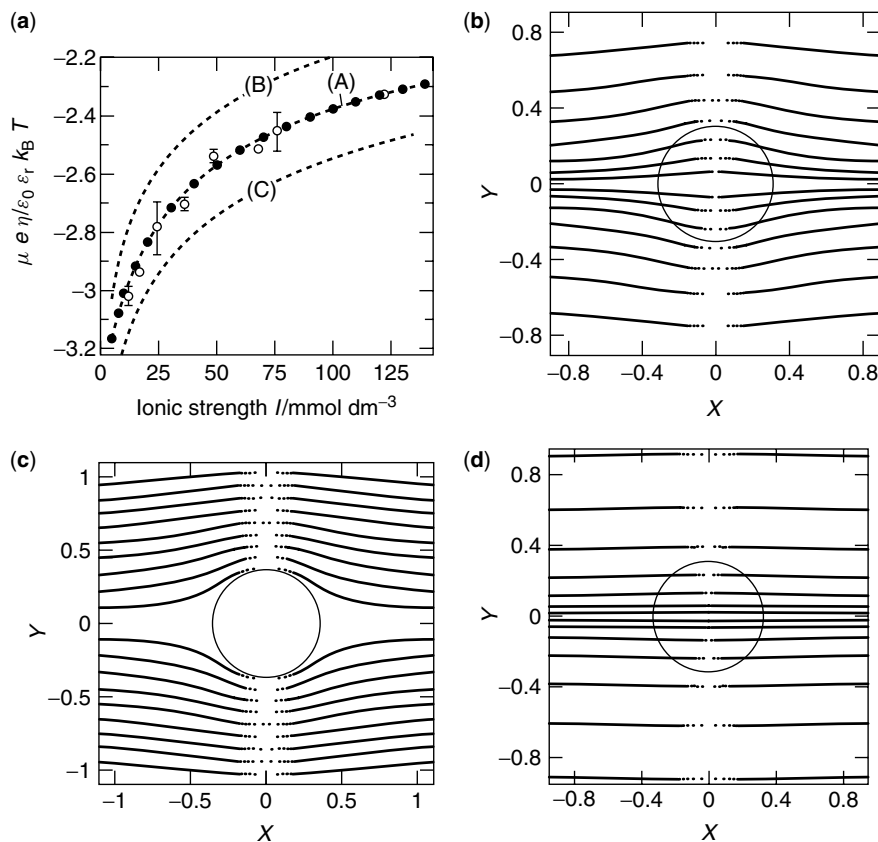


**Figure 8.** (a) Reduced electrophoretic mobilities as a function of total  $\text{Na}_2\text{CO}_3$  ionic strength (298 K) at pH 10.7 for Suwannee River fulvic acids. Open circles, experimental data; filled circles, theoretical predictions with the dashed line (curve A) as guide to the eye,  $1/\lambda_0 = 0.27 \text{ nm}$ . Curves B and C correspond to mobilities computed with  $1/\lambda_0 = 0.27 \text{ nm} \pm 10\%$ . See text and [46] for further details. (b)–(d) Flow streamlines corresponding to the hydrodynamic flow within and/or around a Suwannee River peat humic acid viewed as a semi-permeable (b), hard (c) and fully permeable (d) colloids ( $\text{Na}_2\text{CO}_3$  ionic strength  $10 \text{ mmol dm}^{-3}$ , pH 10.7). The circles represent the peat humic acid of normalised radius  $\kappa\delta$  ( $\delta = 0.94 \text{ nm}$ ). The flow streamlines are obtained from the numerical solution  $(r, \theta)$  of the equation  $\Psi(r, \theta) = \text{constant}$  with the stream function,  $\Psi$ , given by  $\Psi(r, \theta) = -h(r)E\{\sin\theta\}^2$  and the radial function,  $h$ , defined by equation (23). Reproduced with permission from Duval, J. F. L., Wilkinson, K. J., van Leeuwen, H. P. and Buffle, J., Humic substances are soft and permeable: evidence from their electrophoretic mobilities, *Environmental Science and Technology*, **39**, 6435–6445. Copyright 2005 American Chemical Society

with the electrokinetic data. Furthermore, the small size of the humic substances, which are at the limit of the ‘truly’ soluble molecules and small colloids, implies that very little spatial heterogeneity could be present.

The softness parameter that was obtained indicated a relatively large permeability as compared to the radius  $\delta$  of the particles ( $\lambda_0\delta \approx 3$ ). This point is illustrated in Figure 8b–d, where a plot of the flow streamlines computed from the radial function  $h$  [equation (23)]

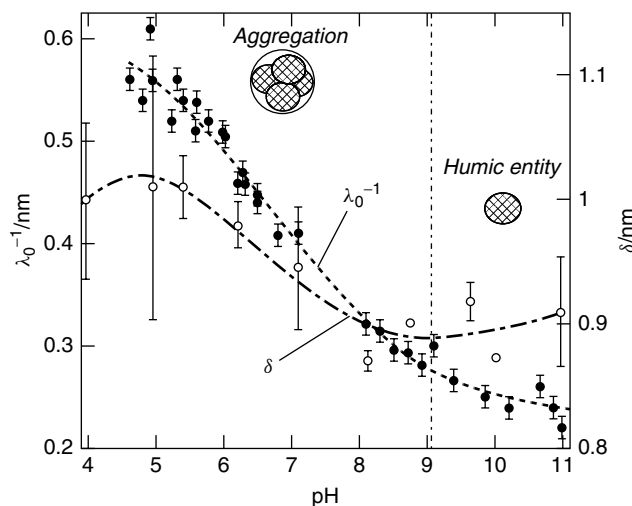


**Figure 9.** Permeability  $\lambda_0^{-1}$  and hydrodynamic radii  $\delta$  of humic acids as a function of pH at  $5 \text{ mmol dm}^{-3}$  ionic strength. The  $\delta$  values (open circles) are calculated from FCS measurements and the  $\lambda_0^{-1}$  values (filled circles) are obtained after numerical analysis of the electrophoretic mobilities. See text for further details. Reproduced with permission from Duval, J. F. L., Wilkinson, K. J., van Leeuwen, H. P. and Buffle, J., Humic substances are soft and permeable: evidence from their electrophoretic mobilities, *Environmental Science and Technology*, **39**, 6435–6445. Copyright 2005 American Chemical Society

is given for  $\lambda_0\delta \approx 3$  and compared with those for  $\lambda_0 \rightarrow 0$  (completely permeable particle) and  $\lambda_0 \rightarrow \infty$  (hard sphere). Following a decrease in the solution pH at fixed ionic strength, FCS data revealed that aggregation was taking place as a result of the decrease in intermolecular repulsion between the humic particles. Taking into account the (experimentally determined) size  $\delta$  and space charge density  $\rho_{\text{fix}}$  of the humic particles for each pH value, it was possible to reconstruct the electrophoretic data after an adjustment of  $\lambda_0$  (Figure 9). The obtained increase in the hydrodynamic penetration length  $1/\lambda_0$ , which compounds that observed for the size  $\delta$ , could be explained by referring to the notion of hydrodynamic path. For a given aggregate composed of several, probably entangled, humic particles, the fluid can flow not only through the permeable units, but also among them via (hydrodynamic) paths. As the number of units increases during aggregation, the number of hydrodynamic paths increases in parallel, as does the overall permeability. The increase of the calculated penetration length  $1/\lambda_0$  upon variation of the measured size  $\delta$  is shown in Figure 10. The observed linear dependence between these quantities is in line with that expected on the basis of the Brinkman equation and other empirical relationships [88,89]. The corresponding slope reveals crucial information on the physicochemical properties of the investigated aggregates/particles. In particular, variations of  $1/\lambda_0$  at constant  $\delta$  yielded the sequence of decreasing permeability FA > HA  $\gg$  PHA. This result was consistent with the known ramified structure and the high degree of hydrophobicity of the PHA, as compared with the FA and HA. In addition, the slope of  $1/\lambda_0$  versus  $\delta$  ‘quantifies’ the change in permeability for a given increment in  $\delta$ , i.e. for a given aggregate growth. It revealed the same sequence of decreasing compactness FA > HA  $\gg$  PHA. This implied

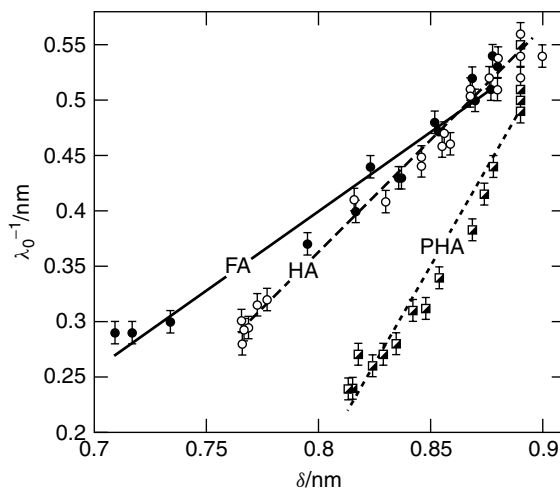


**Figure 10.** Dependences of  $\lambda_0^{-1}$  on the size  $\delta$  of the FA, HA and PHA (indicated) within the pH region that corresponds to the occurrence of aggregation ( $I = 5 \text{ mmol dm}^{-3}$ ). Reproduced with permission from Duval, J. F. L., Wilkinson, K. J., van Leeuwen, H. P. and Buffle, J., Humic substances are soft and permeable: evidence from their electrophoretic mobilities, *Environmental Science and Technology*, **39**, 6435–6445. Copyright 2005 American Chemical Society

that the probability of H-bridging between FA particles within an aggregate was more important for the FA than for the HA and PHA, i.e. the larger particles with a lower density of ionogenic sites. H-bonds are likely to render the aggregate structure more compact and consequently limit the number of hydrodynamic paths or permeability, a result consistent with the observed variation of the permeabilities with the aggregate size.

#### 4 CONCLUSIONS

A review of the literature dealing with the electrophoresis of soft particles has been provided. After demonstrating the necessity to go beyond the approximate ‘classical soft particle analysis’ as first proposed by Ohshima, we have reported the complete set of fundamental transport and electrostatic equations. These must be solved numerically in order to derive the electrophoretic mobilities without any restriction on particle size, particle charge or double-layer thickness. The model also integrates the partial dissociation of surface amphoteric sites, the possibility of a heterogeneous distribution of the polymeric chains within that layer and the polarisation and relaxation phenomena that are as important for soft particles as for bare, rigid colloidal entities. The impact of the softness parameter, the space charge density, the electrolyte concentration and the physically diffuse character of the soft particle on its electrophoretic motion are illustrated on the basis of a few simulation results. The peculiar features underlying the electrophoresis of soft (environmental) particles as compared with their hard counterparts are discussed and illustrated by applications to real systems such as bacteria and humic particles. It is stressed that the combined analysis of the electrokinetic parameters with size and proton

titration data is particularly helpful for addressing the electrostatic, hydrodynamic and aggregation properties of the colloidal system. The intrinsic complexity of biological and environmental systems necessarily requires a consistent and quantitative interpretation of data obtained from several independent techniques. The possibility of coupling information from molecular dynamics or Monte Carlo simulations [90] with more classical electrokinetic models is very attractive in its ability to account, at a nanoscopic scale, for the intrinsic polydisperse nature of complex systems. The development of models for understanding the electrophoresis of permeable particles that are exposed to oscillatory electric fields [27,29] is also promising for addressing the dynamic properties of the surrounding soft polymeric layer.

## LIST OF SYMBOLS

$a$	Radius of the impermeable particle core
$a_s$	Radius of the resistance centres distributed throughout the polymer shell of the particle
$c^\infty$	Bulk concentration of a 1:1 electrolyte
$c_i^\infty$	Bulk concentration of ion $i$ present in the electrolyte solution
$c_i(\vec{r})$	Concentration of ion $i$ at the position $\vec{r}$
$c_i^{(0)}(r)$	Concentration of ion $i$ at the radial position $r$ at equilibrium (i.e. in the absence of an applied electric field)
$e$	Elementary charge
$\vec{E}$	Applied electric field
$f$	Function that specifies the spatial distribution of the polymer segment density within the permeable shell of the particle
$F$	Faraday constant
$g$	Function that specifies the protolytic characteristics of the ionogenic sites distributed throughout the polymer shell of the particle
$h$	Radial function defined by equation (23)
$k$	Friction coefficient (position dependent)
$k_B$	Boltzmann constant
$k_0$	Nominal friction coefficient (position independent)
$K_p$	Affinity constant associated with the acid–base reaction where the ionogenic site of type $p$ —within the polymer shell of the particle—is involved
$n_s$	Polymer segment density in the permeable shell of the particle (position dependent)
$n_s^0$	Nominal polymer segment density in the permeable shell of the particle (position independent)
$N$	Number of different types of ions $i$ present in the electrolyte solution ( $i = 1, \dots, N$ )
$Q^0$	Total amount of charges within the polymer shell of the particle, as probed by potentiometric titration
$(r, \theta, \varphi)$	Spherical coordinate system. A position $(r, \theta, \varphi)$ is equivalently defined by the vectorial entity $\vec{r}$
$R$	Gas constant

$T$	Temperature
$\vec{u}(\vec{r})$	Velocity of the fluid at the position $\vec{r}$ relative to the particle
$\vec{U}$	Electrophoretic velocity
$y(r)$	Dimensionless equilibrium potential at the radial position $r$
$y^D$	Dimensionless Donnan potential
$y^S$	Dimensionless potential at the surface of the particle core
$z_i$	Valence of ion $i$
$\alpha$	Characteristic length that describes the diffuseness of the interface between the particle and the electrolyte solution [equation (36)]
$\delta$	Nominal thickness of the polymer shell of the particle
$\delta_F$	Thickness of the fibrillar layer of <i>Streptococcus salivarius</i> HB bacterial strain
$\delta_w$	Thickness of the cell wall of <i>Streptococcus salivarius</i> HB and HB-C12 bacterial strains
$\delta c_i(\vec{r})$	Deviation of the concentration $c_i(\vec{r})$ of ion $i$ from its equilibrium value, due to the applied electric field
$\delta \mu_i(\vec{r})$	Deviation of the electrochemical potential $\mu_i(\vec{r})$ of ion $i$ from its equilibrium value, due to the applied electric field
$\delta \psi(\vec{r})$	Deviation of the electrostatic potential $\psi(\vec{r})$ from its equilibrium value due to the applied electric field
$\delta \rho_{el}(\vec{r})$	Deviation of the space charge density $\rho_{el}(\vec{r})$ from its equilibrium value due to the applied electric field
$\varepsilon (= \varepsilon_0 \varepsilon_r)$	Dielectric permittivity of the medium
$\varphi_i$	Radial function pertaining to ion $i$ and defined by equation (24)
$\phi$	Hydrodynamic volume fraction of polymer segments within the permeable shell of the particle (position dependent)
$\phi_0$	Nominal hydrodynamic volume fraction of polymer segments within the permeable shell of the particle (position independent)
$\kappa$	Reciprocal screening Debye length
$\kappa_m$	Reciprocal screening Debye length within the permeable shell of the particle
$\lambda_i^0$	Limiting conductivity of ion $i$
$\overline{\lambda}_i$	Drag coefficient of ion $i$
$\lambda_0$	Nominal softness parameter (position independent)
$\overline{\mu}$	Dimensionless electrophoretic mobility
$\mu_i(\vec{r})$	Electrochemical potential of ion $i$ at the position $\vec{r}$
$\mu_i^{(0)}(r)$	Electrochemical potential of ion $i$ at the radial position $r$ at equilibrium (in the absence of an applied electric field)
$\mu_i^\infty$	Electrochemical potential of ion $i$ at some reference state
$\eta$	Dynamic viscosity of the medium
$\psi(\vec{r})$	Electrostatic potential at the position $\vec{r}$
$\psi^D$	Donnan potential
$\psi^0$	Surface potential (valid within the framework of step-function modelling of the interface between a soft particle and an electrolyte solution)
$\psi^{(0)}(r)$	Electrostatic potential at the radial position $r$ in the absence of an applied electric field (equilibrium situation)

$\rho_{\text{el}}(\vec{r})$	Space charge density – that stems from the mobile ionic species in the electrolyte – at the position $\vec{r}$
$\rho_{\text{el}}^{(0)}(r)$	Space charge density – that stems from the mobile ionic species in the electrolyte – at the radial position $r$ in the absence of an applied electric field (equilibrium situation)
$\rho_{\text{fix}}$	Space charge density in the polymer shell of the particle (position dependent)
$\rho_{\text{max},p}^0/F$	Volume concentrations of the sites of type $p$ within the polymer shell of the particle
$\rho_0$	Nominal space charge density due to the fixed ionogenic sites distributed throughout the polymer shell of the particle (position-independent)
$\sigma^s$	Surface charge density of the particle core
$\zeta$	Electrokinetic potential (valid for rigid particles)
$\omega$	Parameter that ensures the constancy of the total amount of charges within the particle shell when varying $\alpha$ and/or $\delta$ [equation (37)]

## REFERENCES

- Overbeek, J. Th. G. (1943). Theorie der elektrophorese, *Kolloid-Beih.*, **54**, 287–364.
- Booth, F. (1950). The cataphoresis of spherical, solid non-conducting particles in a symmetrical electrolyte, *Proc. R. Soc. London*, **203**, 533–551.
- Wiersema, P. H., Loeb, A. L. and Overbeek, J. Th. G. (1966). Calculation of the electrophoretic mobility of a spherical colloid particle, *J. Colloid Interface Sci.*, **22**, 78–99.
- Dukhin, S. S. and Seminikhin, N. M. (1970). Theory of double layer polarization and its effect on the electrokinetic and electrooptical phenomena and the dielectric permeability of dispersed systems, *Kolloid Zh.*, **32**, 360–368.
- O'Brien, R. W. and White, L. R. (1978). Electrophoretic mobility of a spherical colloidal particle, *J. Chem. Soc., Faraday Trans. 2*, **74**, 1607–1626
- DeLacey, E. H. B. and White, L. R. (1981). Dielectric response and conductivity of dilute suspensions of colloidal particles, *J. Chem. Soc., Faraday Trans. 2*, **77**, 2007–2039.
- O'Brien, R. W. and Hunter, R. J. (1981). The electrophoretic mobility of large colloidal particles, *Can. J. Chem.*, **59**, 1878–1887.
- Dukhin, S. S. (1993). Non-equilibrium electric surface phenomena, *Adv. Colloid Interface Sci.*, **44**, 1–134.
- Lyklema, J. (1995). Electrokinetics and related phenomena. In *Fundamentals of Colloid and Interface Science*. Academic Press, New York, pp. 4.1–4.135.
- Hermans, J. J. (1955). Sedimentation and electrophoresis of porous spheres, *J. Polym. Sci.*, **18**, 527–534.
- Hermans, J. J. and Fujita, H. (1955). Electrophoresis of charged polymer molecules with partial free drainage, *Koninkl. Ned. Akad. Wetenschap. Proc.*, **B58**, 182–187.
- Overbeek, J. Th. G. and Stigter, D. (1956). Electrophoresis of polyelectrolytes with partial drainage, *Recl. Trav. Chim. Pays-Bas*, **75**, 543–554.
- Donath, E. and Pastuschenko, V. (1980). Electrophoretical study of cell surface properties. Theory and experimental applicability, *Bioelectrochem. Bioenerg.*, **7**, 31–40.
- Pastuschenko, V. and Donath, E. (1976). Potential distribution near the cell coated with a charged glycoprotein layer, *Stud. Biophys. (Berlin)*, **56**, 9–10 (and B8–C2).
- Donath, E. and Pastuschenko, V. (1979). Electrophoretical study of cell surface properties. The influence of the surface coat on the electric potential distribution and on general electrokinetic properties of animal cells, *Bioelectrochem. Bioenerg.*, **6**, 543–554.
- Jones, I. S. (1979). A theory of electrophoresis of large colloid particles with adsorbed poly-electrolyte, *J. Colloid Interface Sci.*, **68**, 451–461.

17. Wunderlich, R. W. (1982). The effects of surface structure on the electrophoretic mobilities of large particles, *J. Colloid Interface Sci.*, **88**, 385–397.
18. Levine S., Levine, M., Sharp, K. A. and Brooks, D. E. (1983). Theory of the electrokinetic behavior of human erythrocytes, *Biophys. J.*, **42**, 127–135.
19. Sharp, K. A. and Brooks, D. E. (1985). Calculation of the electrophoretic mobility of a particle bearing bound polyelectrolyte using the non-linear Poisson Boltzmann equation, *Biophys. J.*, **47**, 563–566.
20. Ohshima, H. and Ohki, S. (1985). Donnan potential and surface potential of a charged membrane, *Biophys. J.*, **47**, 673–678.
21. Ohshima, H. (2002). Electrophoretic mobility of a charged spherical colloidal particle covered with an uncharged polymer layer, *Electrophoresis*, **23**, 1995–2000.
22. Ohshima, H. and Kondo, T. (1990). Electrokinetic flow between two parallel plates with surface charge layers: electro-osmosis and streaming potential, *J. Colloid Interface Sci.*, **135**, 443–448.
23. Ohshima, H. (1994). Electrophoretic mobility of soft particles, *J. Colloid Interface Sci.*, **163**, 474–483.
24. Ohshima, H. (1995). Electrophoresis of soft particles, *Adv. Colloid Interface Sci.*, **62**, 189–235.
25. Saville, D. A. (2000). Electrokinetic properties of fuzzy colloidal particles, *J. Colloid Interface Sci.*, **222**, 137–145.
26. Hill, R. J., Saville, D. A. and Russel, W. B. (2003). Electrophoresis of spherical polymer-coated particles, *J. Colloid Interface Sci.*, **258**, 56–74.
27. Hill, R. J., Saville, D. A. and Russel, W. B. (2003). Polarizability and complex conductivity of dilute suspensions of spherical colloidal particles with charged (polyelectrolyte) coatings, *J. Colloid Interface Sci.*, **263**, 478–497.
28. Lopez-Garcia, J. J., Grosse, C. and Horno, J. (2003). Numerical study of colloidal suspensions of soft spherical particles using the network method: 1. DC electrophoretic mobility, *J. Colloid Interface Sci.*, **265**, 327–340.
29. Lopez-Garcia, J. J., Grosse, C. and Horno, J. (2003). Numerical study of colloidal suspensions of soft spherical particles using the network method: 2. AC electrokinetic and dielectric properties, *J. Colloid Interface Sci.*, **265**, 341–350.
30. Hill, R. J. (2004). Hydrodynamics and electrokinetics of spherical liposomes with coatings of terminally anchored poly(ethylene glycol): numerically exact electrokinetics with self-consistent mean-field polymer, *Phys. Rev. E*, **70**, /1-051046/16.
31. Duval, J. F. L. and van Leeuwen, H. P. (2004). Electrokinetics of diffuse soft interfaces. I. Limit of low Donnan potentials, *Langmuir*, **20**, 10324–10336.
32. Duval, J. F. L. (2005). Electrokinetics of diffuse soft interfaces. II. Analysis based on the non-linearized Poisson–Boltzmann equation, *Langmuir*, **21**, 3247–3258.
33. Starov, V. and Solomentsev, Y. E. (1993). Influence of gel layers on electrokinetic phenomena: 1. Streaming potential, *J. Colloid Interface Sci.*, **158**, 159–165.
34. Starov, V. and Solomentsev, Y. E. (1993). Influence of gel layers on electrokinetic phenomena: 2. Effect of ions interaction with the gel layer, *J. Colloid Interface Sci.*, **158**, 166–170.
35. Donath, E. and Voigt, A. (1986). Streaming current and streaming potential on structured surfaces, *J. Colloid Interface Sci.*, **109**, 122–139.
36. Van der Wal, A. (1996). Electrochemical characterization of the bacterial cell surface. *Ph.D Thesis*, Wageningen University.
37. Poortinga, A. T. (2001). Electric double layer interactions in bacterial adhesion and detachment. *Ph.D Thesis*, Rijksuniversiteit Groningen.
38. Bos, R., van der Mei, H. C. and Busscher, H. J. (1998). ‘Soft-particle’ analysis of the electrophoretic mobility of a fibrillated and non-fibrillated oral streptococcal strain: *Streptococcus salivarius*, *Biophys. Chem.*, **74**, 251–255.
39. Duval, J. F. L., Busscher, H. J., van de Belt-Gritter, B, van der Mei, H. C. and Norde, W. (2005). Analysis of the interfacial properties of fibrillated and non-fibrillated oral streptococcal strain from electrophoretic mobility and titration measurements: evidence for the shortcomings of the ‘classical soft particle approach’, *Langmuir*, **21**, 11268–11282.
40. de Kerchove, A. J. and Elimelech, M. (2005). Relevance of electrokinetic theory for ‘soft’ particles to bacterial cells: Implications for bacterial adhesion, *Langmuir*, **21**, 6462–6472.

41. Morisaki, H., Nagai, S., Ohshima, H., Ikemoto, E. and Kogure, K. (1999). The effect of motility and cell-surface polymers on bacterial attachment, *Microbiology*, **145**, 2797–2802.
42. Dague, E., Duval, J. F. L., Jorand, F., Thomas, F. and Gaboriaud, F. (2006). Probing surface structures of *Shewanella* spp. by microelectrophoresis, *Biophys. J.*, **90**, 2612–2621.
43. Okuda, S., Igarashi, R., Kusui, Y., Kasahara, Y. and Morisaki, H. (2003). Electrophoretic mobility of *Bacillus subtilis* knockout mutants with and without flagella, *J. Bacteriol.*, **185**, 3711–3717.
44. Kiers, P. J. M., Bos, R., van der Mei, H. C. and Busscher, H. J. (2001). The electrophoretic softness of the surface of *Staphylococcus epidermidis* cells grown in a liquid medium and on a solid agar, *Microbiology*, **147**, 757–762.
45. Hill, R. J. and Saville, D. A. (2005). ‘Exact’ solutions of the full electrokinetic model for soft spherical colloids: electrophoretic mobility, *Colloids Surf. A*, **267**, 31–49.
46. Duval, J. F. L., Wilkinson, K. J., van Leeuwen, H. P. and Buffel, J. (2005). Humic substances are soft and permeable: evidence from their electrophoretic mobilities, *Environ. Sci. Technol.*, **39**, 6435–6445.
47. Bakker, D. P., Busscher, H. J. and van der Mei, H. C. (2002). Bacterial deposition in a parallel plate and a stagnation point flow chamber: microbial adhesion mechanisms depend on the mass transport conditions, *Microbiology*, **148**, 597–603.
48. McClaine, J. W. and Ford, R. M. (2002). Reversal of flagellar rotation is important in initial attachment of *Escherichia coli* to glass in a dynamic system with high- and low-ionic-strength buffers, *Appl. Environ. Microbiol.*, **68**, 1280–1289.
49. Vigeant, M. A.-S., Ford, R. M., Wagner, M. and Tamm, L. K. (2002). Reversible and irreversible adhesion of motile *Escherichia coli* cells analyzed by total internal reflection aqueous fluorescence microscopy, *Appl. Environ. Microbiol.*, **68**, 2794–2801.
50. Thomas, W. E., Trintchchina, E., Forero, M., Vogel, V. and Sokurenko, E. (2002). Bacterial adhesion to target cells enhanced by shear-force, *Cell*, **109**, 913–923.
51. Rutter, P. R. and Vincent, B. (1980). The adhesion of microorganisms to surfaces: physico-chemical aspects. In *Microbial Adhesion to Surfaces*, eds Berkeley, R. C. W., Lynch, J. M., Melling, J., Rutter, P. R. and Vincent, B. Ellis Horwood, Chichester, pp. 79–91.
52. Koopal, L. K., Saito, T., Pinheiro, J. P. and van Riemsdijk, W. H. (2005). Ion binding to natural organic matter: general considerations and the NICA–Donnan model, *Colloids Surf. A*, **265**, 40–54.
53. Buffel, J. (1988). *Complexation Reactions in Aquatic Systems. An Analytical Approach*. Ellis Horwood, Chichester.
54. Buffel, J. (1984). Natural organic matter and metal–organic interactions in aquatic systems. In *Metal Ions in Biological Systems*, ed. Sigel, H. Marcel Dekker, New York, pp. 165–221.
55. Lyklema, J. and Duval, J. F. L. (2005). Hetero-interaction between Gouy–Stern double layers: charge and potential regulation, *Adv. Colloid Interface Sci.*, **114–115**, 27–45.
56. Fernandez-Nieves, A., van Duijneveldt, J. S., Fernandez-Barbero, A., Vincent, B. and de Las Nieves, F. J. (2001). Structure formation from mesoscopic soft particles, *Phys. Rev. E*, **64**, /1-051603/10.
57. Vadillo-Rodriguez, V., Busscher, H. J., Norde, W., de Vries, J., Dijkstra, R. J., Stokroos, I. and van der Mei, H. C. (2004). Comparison of atomic force microscopy interaction forces between bacteria and silicon nitride substrata for three commonly used immobilization methods, *Appl. Environ. Microbiol.*, **70**, 5441–5446.
58. Touhami, A., Nysten, B. and Dufrêne, Y. F. (2003). Nanoscale mapping of the elasticity of microbial cells by atomic force microscopy, *Langmuir*, **19**, 4539–4543.
59. Gaboriaud, F., Bailet, S., Dague, E. and Jorand, F. (2005). Surface structure and nanomechanical properties of *Shewanella putrefaciens* bacteria at two pH values (4 and 10) determined by atomic force microscopy, *J. Bacteriol.*, **187**, 3864–3868.
60. Yezek, L., Duval, J. F. L. and van Leeuwen, H. P. (2005). Electrokinetics of diffuse soft interfaces. III. Interpretation of data on the polyacrylamide/water interface, *Langmuir*, **21**, 6220–6227.
61. Makino, K., Yamamoto, S., Fujimoto, K., Kawaguchi, H. and Ohshima, H. (1994). Surface structure of latex particles covered with temperature-sensitive hydrogel layers, *J. Colloid Interface Sci.*, **166**, 251–258.

62. Taylor, L. D. and Cerankowski, L. D. (1975). Preparation of films exhibiting a balanced temperature dependence to permeation by aqueous solution. Lower consolute behavior, *J. Polym. Sci. Polym. Chem.*, **13**, 2551–2570.
63. Kawaguchi, H., Fujimoto, K. and Mizuhara, Y. (1992). Hydrogel microspheres 3. Temperature-dependent adsorption of proteins on poly(*N*-isopropylacrylamide) hydrogel microspheres, *Colloid Polym. Sci.*, **270**, 53–57.
64. Gao, C., Leporatti, S., Moya, S., Donath, E. and Mohwald, H. (2003). Swelling and shrinking of polyelectrolyte microcapsules in response to changes in temperature and ionic strength, *Chem. Eur. J.*, **9**, 915–920.
65. Garcia-Salinas, M. J., Romero-Cano, M. S. and de Las Nieves, F. J. (2001). Electrokinetic characterization of poly(*N*-isopropylacrylamide) microgel particles: effect of electrolyte concentration and temperature, *J. Colloid Interface Sci.*, **241**, 280–285.
66. Von Helmholtz, H. (1879). Studies of electric boundary layers. *Wied. Ann.*, **7**, 337–382.
67. Von Smoluchowski, M. (1917). Mathematical theory of the kinetics of the coagulation of colloidal solutions, *Z. Phys. Chem.*, **92**, 129–168.
68. Hückel, E. (1924). Die kataphorese der kugel. *Phys. Z.*, **25**, 204–210.
69. Onsager, L. (1926). Zur theorie der elektrolyte I. *Phys. Z.*, **27**, 388–392.
70. Rosen, L. A., Baygents, J. C. and Saville, D. A. (1993). The interpretation of dielectric response measurements on colloidal dispersions using the dynamic stern layer model, *J. Chem. Phys.*, **98**, 4183–4194.
71. Lyklema, J. (1995). Electric double layers. In *Fundamentals of Colloid and Interface Science*, Academic Press, New York, pp. 3.1–3.232.
72. Hammond, S. M., Lambert, P. A. and Rycroft, A. N. (1984). *The Bacterial Cell Surface*. Croom Helm, London.
73. Wicken, A. J. (1985). Bacterial cell walls and surfaces. In *Bacterial Adhesion, Mechanisms and Physiological Significance*, eds Savage, D. C. and Fletcher, M. Plenum Press, New York, pp. 45–70.
74. Buffle, J. and Filella, M. (1995). Physico-chemical heterogeneity of natural complexants: clarification, *Anal. Chim. Acta*, **313**, 144–150.
75. Debye, P. and Bueche, A. (1948). Intrinsic viscosity, diffusion and sedimentation rate of polymers in solution, *J. Chem. Phys.*, **16**, 573–579.
76. Brinkman, H. C. (1949). Problems of fluid through swarms of particles and through macromolecules in solution, *Research*, **2**, 190–194.
77. van Male, J. (2003). Self-consistent-field theory for chain molecules: extensions, computational aspects, and applications. *Ph.D Thesis*, Wageningen University.
78. Scheutjens, J. M. H. M. and Fleer G. J. (1979). Statistical theory of the adsorption of interacting chain molecules. 1. Partition function, segment density distribution, and adsorption isotherms, *J. Phys. Chem.*, **83**, 1619–1635.
79. Van der Gucht, J. (2004). Equilibrium polymers in solution and at interfaces. *Ph.D Thesis*, Wageningen University.
80. Zhulina, E. B., Klein Wolterink, J. and Borisov, O. V. (2000). Screening effects in a polyelectrolyte brush: self-consistent-field theory, *Macromolecules*, **33**, 4945–4953.
81. Fatin-Rouge, N. and Buffle, J. (2007). Study of environmental systems by means of fluorescence correlation spectroscopy. In *Environmental Colloids: Behaviour, Structure and Characterisation*, eds Wilkinson, K. J. and Lead, J. R. IUPAC Series on Analytical and Physical Chemistry of Environmental Systems, Vol. 10. John Wiley & Sons, Ltd, Chichester, Chapter 11.
82. Umpleby, R. J., II, Baxter, S. C., Chen, Y., Shah, R. N. and Shimizu, K. D. (2001). Characterization of molecularly imprinted polymers with the Langmuir–Freundlich isotherm, *Anal. Chem.*, **73**, 4584–4591.
83. van der Mei, H. C., Meinders, J. M. and Busscher, H. J. (1994). The influence of ionic strength and pH on diffusion of micro-organisms with different structural surface features, *Microbiology*, **140**, 3413–3419.
84. van der Wal, A., Norde, W., Zehnder, A. J. B. and Lyklema, J. (1997). Determination of the total charge in the cell walls of Gram-positive bacteria, *Colloids Surf. B*, **9**, 81–100.

85. Weerkamp, A. H., Handley, P. S., Baars, A. and Slot, J. W. (1986). Negative staining and immunoelectron microscopy of adhesion-deficient mutants of *Streptococcus salivarius* reveal that the adhesive protein antigens are separate classes of cell surface fibril, *J. Bacteriol.*, **165**, 746–755.
86. Weerkamp, A. H. and Jacobs, T. (1982). Cell wall-associated protein antigens of *Streptococcus salivarius*: purification, properties, and function in adherence, *Infect. Immun.*, **38**, 233–242.
87. van der Mei, H. C., Weerkamp, A. H. and Busscher, H. J. (1987). Physico-chemical surface characteristics and adhesive properties of *Streptococcus salivarius* strains with defined cell surface structures, *FEMS Microbiol.*, **40**, 15–19.
88. Carman, P. C. (1937). Fluid flow through granular beds, *Trans. Inst. Chem. Eng. London*, **15**, 150–166.
89. Cohen-Stuart, M. A., Waagen, F. H. W. H., Cosgrove, T.; Vincent, B. and Crowley, T. L. (1984). Hydrodynamic thickness of adsorbed polymer layers, *Macromolecules*, **17**, 1825–1830.
90. Starkweather, M. E., Muthukumar, M. and Hoagland, D. A. (1998). Single chain entanglement: a Monte Carlo simulation of dilute solution capillary electrophoresis, *Macromolecules*, **31**, 5495–5501.

---

# 8 Strategies and Advances in the Characterisation of Environmental Colloids by Electron Microscopy

---

**DENIS MAVROCORDATOS<sup>†</sup>**

*Swiss Federal Institute for Environmental Science and Technology, EAWAG Urban Water Management, 133 Überlandstrasse, CH-8600 Dübendorf, Switzerland*

**DIDIER PERRET**

*School of Chemistry and Biochemistry, University of Geneva, 30 quai Ernest Ansermet CH-1211 Geneva 4, Switzerland*

**GARY G. LEPPARD**

*National Water Research Institute, 867 Lakeshore Road, PO Box 5050, Burlington, Ontario, Canada L7R 4A6*

1	Introduction . . . . .	346
2	Sampling of Environmental Colloids for Electron Microscopic Investigation . . . . .	350
2.1	Sampling of Aerosols and Atmospheric Colloids . . . . .	350
2.2	Sampling of Soil and Sediment Colloids . . . . .	352
2.3	Sampling of Aquatic Colloids . . . . .	353
3	Specimen Preparation . . . . .	354
3.1	Ultramicrotomy . . . . .	356
3.2	Whole Mounts . . . . .	357
3.3	Ultracentrifugation . . . . .	359
3.4	Cryotechniques: Freeze-etching and Vitrification . . . . .	361
3.5	Focused Ion Beam Sectioning . . . . .	362
3.6	Staining and Labelling of Organic-rich Colloids . . . . .	363
3.7	Potential Artefacts Related to Specimen Preparation . . . . .	364

<sup>†</sup> Dr Denis Mavrocordatos tragically disappeared in Lake Geneva on 6 December 2003. This chapter is written in his memory by his friends and fellows, holding as much as possible to the spirit of his work in electron microscopy, and relying as much as possible on the chapter structure that he had prepared for this book.

*Homme libre, toujours tu chériras la mer!*

Charles Baudelaire

4	Morphometric Analysis of Particles and Colloids . . . . .	364
4.1	Qualitative Observations . . . . .	365
4.2	Quantitative Analysis and Particle Size Distribution . . . . .	367
4.3	Image Analysis . . . . .	369
5	Element Analysis of Particles and Colloids . . . . .	373
5.1	Energy-dispersive Spectroscopy (X-EDS) and Related Techniques . . . . .	373
5.2	Electron Energy-loss Spectroscopy (EELS) and Related Techniques . . . . .	377
6	Applications of EM and AEM for the Understanding of Physicochemical Pathways in the Environment . . . . .	378
6.1	Selected Case Studies Relating Particle Characterisation to Contaminant Transport . . . . .	378
6.2	Nano- and Microparticles Characterised by TEM and AEM . . . . .	380
6.2.1	Humic Substances . . . . .	380
6.2.2	Polysaccharide Fibrils . . . . .	380
6.2.3	Iron Oxyhydroxides . . . . .	381
6.2.4	Viruses and Refractory Cell Debris . . . . .	381
6.2.5	Nanoscale Mineral Agglomerates on Cell Surfaces and on the Surfaces of Extracellular Polymers . . . . .	381
6.3	Microparticles as Natural Aggregates of Nanoparticles . . . . .	382
6.4	Selected Case Studies Relating Particle Characterisation to Water Treatment Problems . . . . .	383
6.5	Correlative Use of TEM with AFM and STXM . . . . .	383
6.6	Accurate Selection of Target Species and Fingerprinting of Biomineralisation . . . . .	385
6.7	Aggregation and Sedimentation of Organic Matter in Lake Water . . . . .	385
6.8	Copper Scavenging from Roof Runoff . . . . .	388
7	Conclusion . . . . .	388
	List of abbreviations . . . . .	390
	References . . . . .	391

## 1 INTRODUCTION

The significant work of Louis de Broglie in 1923 on wave mechanics established that electrons and other subatomic particles behave like waves. With this insight, Ruska invented transmission electron microscopy (TEM) in 1931, replacing the visible light source of a conventional photon (optical) microscope by a source of focused electrons operated under a vacuum and guided by a series of magnetic lenses. Owing to their intrinsic properties [ $\lambda_{\text{electron}} = (\approx 10^{-3} - 10^{-5}) \times \lambda_{\text{visible light}}$ ], electrons are able to convey information about incident objects with much smaller dimensions than is achievable with visible light. With his microscope, Ruska was able to identify micrometre-sized biological objects with a resolution never before attained. For his seminal work in electron optics that opened the doors to the atomic scale, Ruska finally received the Nobel Prize in 1986, sharing it with Binnig and Rohrer for their invention in the late 1970s of scanning tunnelling microscopy (STM).

The first publications reporting the use of electron microscopy (EM) in the environmental sciences were released long after Ruska's invention, owing to the need for reliable magnetic lenses and appropriate specimen preparation schemes. Soil particles were first described in 1940, airborne particles in 1946 (magnifications up to  $2 \times 10^5 \times$ ), and finally non-living aquatic particles not earlier than the mid-1970s. Since Ruska's time, new opportunities for the observation and characterisation of environmental particles and colloids over a large range of sizes and compositions have arisen, closely matching the successive progress in technological development: scanning-transmission electron microscopy (STEM) in the late 1930s, scanning electron microscopy (SEM) in the early 1950s, high-voltage microscopy, analytical electron microscopy (AEM), X-ray energy-dispersive spectroscopy (X-EDS), electron energy-loss spectroscopy (EELS) and brighter electron sources [LaB<sub>6</sub>; field emission gun (FEG)] in the 1960s and 1970s. Although still in their infancy for the study of environmental samples, environmental scanning electron microscopes (ESEM), available in the late 1980s, have finally allowed new possibilities for the observation of (sub-)micrometric entities in their hydrated state [1].

To date, more than 1000 papers have been published on the characterisation of environmental particles and colloids by techniques of electron microscopy. Historically, EM has been exploited for the documentation of the morphotypes, textures and sizes of living and non-living colloidal and particulate entities. Until recently, most studies on electron microscopy were published for merely illustrative purposes, underexploiting the analytical performances of the existing techniques. AEM has now come to maturity, and sensational electron micrographs are frequently supplemented by quantitative measurements aimed at demonstrating the presence of well-characterised species down to the nanometre scale, or even to assess relationships between the formation or existence of specific types of particles or colloids at the microscopic scale and the evolution of their natural macroscopic milieu. Indeed, the detailed characteristics, activities and behaviours of particles and colloids in natural systems must still be better understood in order to model their life cycle and impact, and to design more cost-effective treatment facilities when dealing with problems of pollution control.

Hydrated colloids provide a nanoscale medium into and on to which dissolved contaminants and nutrients can move from the bulk liquid, without significant gravitational settling [2]. At the nanoscale, large numbers of small colloids and suspended macromolecules are likely to influence water quality and particle separation processes. New nanoscale observations should contribute to our understanding of the environmental cycling of chemicals [2–5], aggregation processes [6,7], the interactions of natural organic matter with microorganisms [8] and the deposition from solution of nanoscale mineral aggregates on to microbial cell surfaces [9–15].

Electron optical analyses which correlate morphological data with data from both physical and molecular probes will further facilitate the development of colloid 'speciation' at the nanoscale. Such nanoscale data are already leading to improved characterisations of the following particles and phenomena:

1. contaminant and biogeochemical transport agents in surface waters [3–5, 15–19];
2. specific events in the biogenesis of minerals by bacteria [9–11, 14, 20, 21];
3. immobilisation sites at molecular and nanoscale ranges for heavy metals in lacustrine sediments [13, 22] and wastewater flocs [23];

4. pollutant source associated with trace element carriers which are discharged into aquatic ecosystems by combined sewer overflows [3];
5. colloidal promoters of biofouling in membrane filters used for water purification [24];
6. colloidal flocculants used in water treatment [25].

For heterogeneous aggregation processes, new speciation information should allow one to determine the extent to which colloids are major contributors to:

1. engineered aggregation processes;
2. contaminant binding in water treatment facilities;
3. biofouling of immersed surfaces; and
4. the transfer of toxic chemicals to environmental sinks.

Also, a better understanding of mineral nucleation on organic templates might yield a list of characteristics which could become very helpful in the search for biosignatures in ancient environments on Earth and other planets [11].

Correlated multi-method interdisciplinary approaches to water analysis, which include AEM and which use independent methods to provide chemical, biological and environmental context for electron optical observations, are increasingly likely to yield practical information on both nano- and microparticle activities [4,5,13,15,20,22,23,26–28]. Confocal laser scanning microscopy (CLSM), used correlative with TEM and Scanning-transmission X-ray microscopy (STXM) is contributing to this multi-method interdisciplinary approach [27]; see also Chapter 10, covering confocal laser scanning microscopy.

Over the last decade, TEM has improved drastically and its adaptation for the characterisation of colloidal particles has progressed well. The technique is now considered to be reliable, quantitative and efficient among water scientists [4,12,28–38]. TEM is a remarkable tool and an essential technique for the morphological characterisation of fine hydrated colloids and particles, as it allows the direct observation of individual entities as well as aggregates at the nanometre to micrometre scale, yielding descriptions of size, shape, native associations and internal differentiation on a ‘per colloid’ basis. The technique complements other more conventional techniques used for sizing, which usually address average signals recorded at the level of the bulk suspension. When utilised under appropriate conditions, *e.g.* in conjunction with accessory techniques and with optimised specimen preparation, TEM may give clues and yield information on the *in situ* processes leading to the formation, transport, function and behaviour of colloids and their aggregates in situations involving complex and heterogeneous species, with an unprecedented level of accuracy [4,6,13,19,23,29–31,33,36,39–41]. Nevertheless, TEM should not be the technique of choice when only simple, rapid, qualitative or semi-quantitative assessments of colloid characteristics are required, because the TEM approach, from sampling to data analysis, is costly and time consuming and requires skilled and experienced staff.

The major accessory techniques applicable to preselected individual colloids are: X-ray energy-dispersive spectroscopy (X-EDS), selected-area electron diffraction (SAED), electron energy-loss spectroscopy (EELS), energy-filtered TEM (EF-TEM), and electron-opaque selective probes. Figure 1a schematises the construction and function of transmission and scanning electron microscopes. The electron–matter interactions within the specimen that give rise to the spectrometric signals used in AEM are shown in Figure 1b.

Detailed discussions of electron optics and the physics of electron microscopy can be found elsewhere [42–50]. Used correlative in parallel and used in conjunction with the ever-improving atomic force microscopy (AFM), these accessory techniques provide a powerful suite of AEM techniques for studying hydrated environmental particles [4–6,12,15,33,37,41,51,52].

The characterisation of airborne colloids and aerosols, combustion and fly-ash particles, ambient air and vehicle emission particles in the 10 nm–10 µm range also benefits from combined analytical protocols, mostly TEM–X-EDS or SEM–X-EDS, but sometimes TEM–EELS and TEM–SAED, with other micrometric (AFM), semi-micrometric

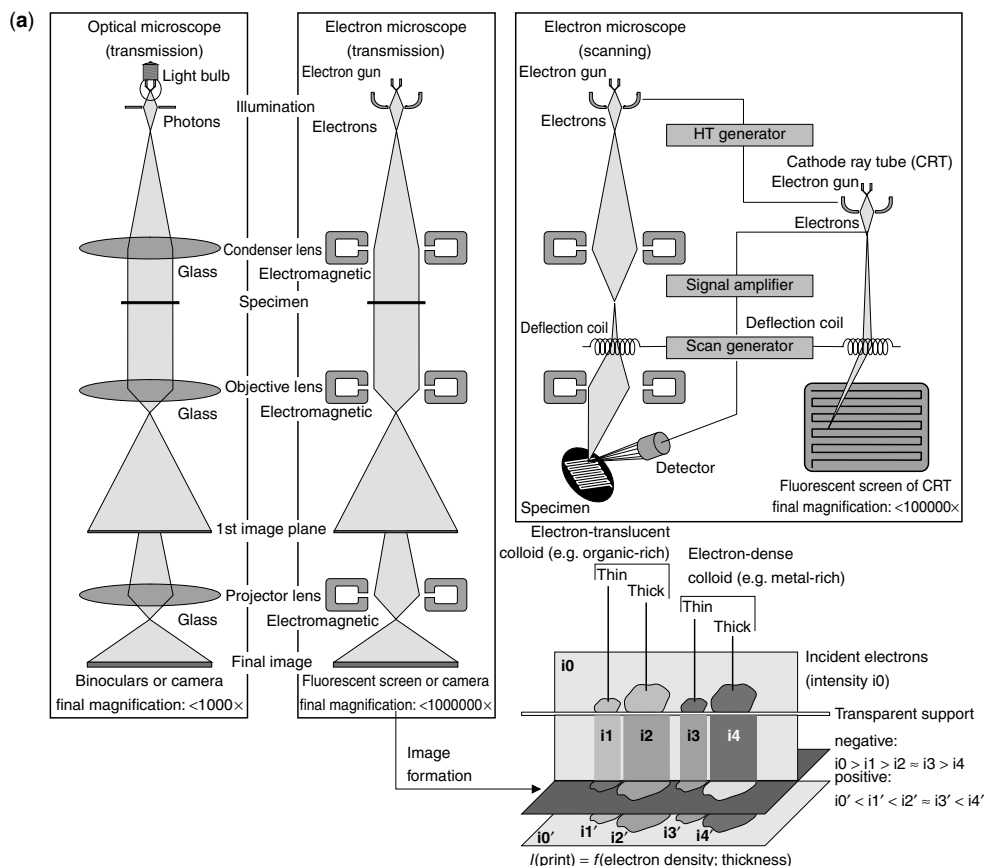


**Figure 1.** (a) Comparison of an optical microscope (left) and a transmission electron microscope (middle), showing the similarities in their construction, and a scanning electron microscope (right). The scheme below the TEM instrument shows that the final image from a mixture of colloids is a complex function of the composition of colloids and their thickness. For example, a 'thick' organic-rich entity may appear with the same grey level as a 'thin' metal-rich entity. (b) Analytical electron microscopy can be performed in the transmission electron microscope mostly by means of X-EDS (X-ray energy-dispersive spectroscopy; measurement of the X-rays emitted during the electronic rearrangement of a target element when one of its electrons is ejected by the incident electron beam), or EELS (electron energy-loss spectrometry; measurement of the energy being lost by the incident electron beam during an inelastic event with a target element)

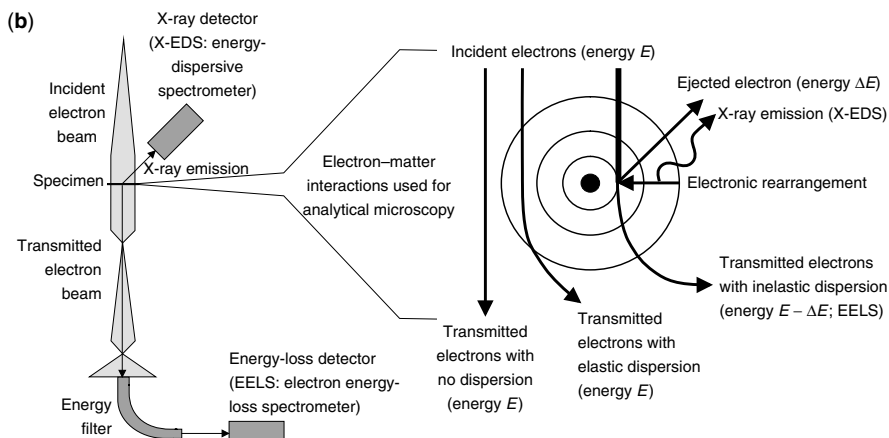


**Figure 1.** (continued)

[proton-induced X-ray emission (PIXE)] or bulk [X-ray fluorescence (XRF), X-ray diffraction (XRD), inductively coupled plasma atomic emission spectroscopy (ICP-AES) or mass spectrometry (ICP-MS), *etc.*] analytical devices [53–67]. Because of the weak hydration state of these ‘dry’ particles, specimen preparation is usually less sophisticated than is necessary for aquatic entities.

## 2 SAMPLING OF ENVIRONMENTAL COLLOIDS FOR ELECTRON MICROSCOPIC INVESTIGATION

Particulate matter consists of living entities (bacteria, algae, fungi, protozoa) and non-living ones (refractory macromolecular organics, viruses, recognisable cell fragments, crystalline or amorphous mineral phases). Its unbiased investigation by electron microscopy in either a hydrated or dry state requires a blend of dedicated sample collection schemes and specimen preparation techniques. Figure 2 highlights the most appropriate approaches to be used, from specimen preparation to particle characterisation.

Whatever investigations are to be performed on a given type of sample, it must be kept in mind that every step of the protocol should be designed to avoid artefacts due to alteration of the native physicochemical characteristics of the sample (*e.g.* precipitation, coagulation or dissolution due to variations in particle concentration, ionic strength, pH, redox potential, temperature or uncontrolled dehydration of the sample).

The sections below discuss the specific measures that have to be taken when aerosol and atmospheric colloids, soil and sediment colloids, or aquatic colloids are to be investigated. Indeed, sampling of suspended matter should take into account the nature of the medium in which these colloids are dispersed. It must be borne in mind, however, that each particular situation usually requires optimisation of the generic procedure if satisfactory results are to be obtained.

### 2.1 SAMPLING OF AEROSOLS AND ATMOSPHERIC COLLOIDS

Atmospheric particles are probably the most straightforward to sample, as a variety of collectors, in which particulate material can be size fractionated, have been devised

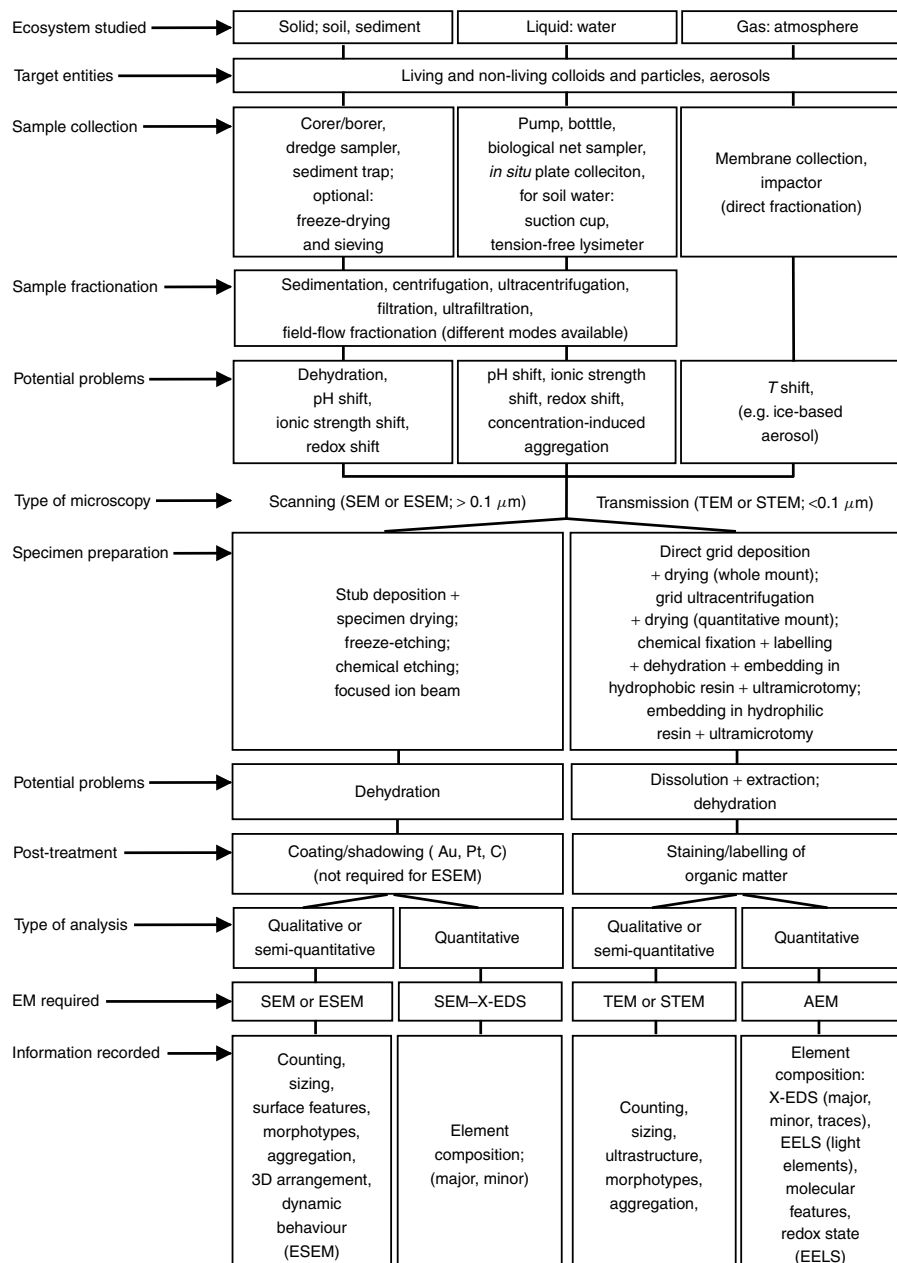


**Figure 2.** Overview of the recommended approaches, crucial steps and possible artefacts relevant to the physicochemical characterisation of particulate material in environmental systems by electron microscopies. This scheme does not take into account precautions required for conventional bulk physicochemical analyses

and optimised over the past half century or more. Sampling of aerosol particles, unlike aquatic ones, is less sensitive to physicochemical changes, although biased size fractionation may occur owing to particle hydrophilicity/hydrophobicity or surface charges. For instance, filtration of aerosols may be just as problematic for air as for water samples. The most commonly used procedures are briefly summarised below; critical discussions of the collection and characterisation of atmospheric particles have been published elsewhere [68–74].

For indoor particles (*e.g.* asbestos fibres, industrial particles, soot or combustion smoke of health concern), direct sampling by air pumping through collecting membranes (smooth/flat neutron-impacted Nuclepore-type filters) without size fractionation is the optimal sampling method [71,75]. Outdoor atmospheric or plume particles can be size fractionated and collected by cascade impactors, charged-particle collectors, thermal precipitators, filters or nephelometers [67,76–80]. Particles have to be transferred by contact from the sampling device to the specimen holder, be it a stub for SEM or a grid for TEM.

The collection of aerosols requires special procedures that are aimed at maintaining the original temperature and hydration status of the sample. This is especially important for studies involving wet or frozen entities for which the mechanisms of cloud or ice formation are driven by the complex interaction of water, inorganic condensation nuclei, dissolved salts and organics acting as hygroscopic agents [81–86]. In these cases, microscopic examination of specimens with a cold stage should be carried out with minimal delay. TEM (for the smallest colloids) and SEM (for larger particles) in imaging or element analysis modes are used indiscriminately for the characterisation of atmospheric entities. ESEM, which allows imaging under various conditions of temperature, hydration and pressure, and which also allows energy-dispersive spectroscopy, is especially useful for water-containing particles larger than 50 nm [71,87].

## 2.2 SAMPLING OF SOIL AND SEDIMENT COLLOIDS

Soil and sediment colloids have been the subject of numerous publications concerned with the identification of the phases which constitute the soil or the sediment matrix, and with the formation of soils or sediments and their stratification. To a lesser extent, scientists have examined the role of colloids as scavengers and contaminant carriers. For these reasons, sampling and specimen preparation protocols for soil or sediment particles are usually less sophisticated than protocols for aquatic particles, provided that one considers soil and sediment particles as static entities having a limited mobility in their surrounding water. A detailed discussion of the collection and characterisation of soil particles is given elsewhere [88].

While the majority of soil samples are characterised by slow reactivities and thus require fewer precautions, hydromorphic soils subjected to rapid hydration and dehydration are highly sensitive to redox changes and must be sampled with care in order to avoid precipitation of dissolved species (*e.g.*  $\text{Fe}^{2+}$  and  $\text{Mn}^{2+}$ ) through accidental aeration. Otherwise, soils are usually dried, sieved and ground before being resuspended in an electrolyte for the selective isolation of various constituents (*e.g.* organic matter, clay, silt, and sand) by sedimentation or centrifugation. These approaches are, however, not recommended for the identification of trace metals, as drastic morphological and compositional modifications can be expected at each step of the protocol. Because of their size, soil particulates

are most frequently analysed by SEM, but the ultrastructural analysis of clay micelles or other finely divided components (*e.g.* iron oxides and humic substances) requires TEM examination [89–105].

The particulate phases in hydrated sediments represent an intermediate situation between soil particles and suspended aquatic particles. Except for deeply buried, highly consolidated sediments, the water content of sediments is large and their reactivity is comparable to, or even larger than, that of hydromorphic soils. Sediments are sampled by means of vertical corers, from which the different season- or event-dependent strata must be subsampled by slicing in a glove-box under controlled atmosphere. Textural analysis of sediment particles can be performed by SEM [106], but more detailed investigations will require dilution of the samples in an electrolyte of composition similar to the interstitial water, prior to specimen preparation for TEM.

### 2.3 SAMPLING OF AQUATIC COLLOIDS

The study of suspended solids, whether as individual particles or as aggregations of particles, encompasses a wide variety of matrices (marine and fresh waters, surface and ground waters, gravitational and capillary water of soils, engineered particles in water treatment facilities, *etc.*), particle types and sizes (nanometre to millimetre, living, non-living, organic, organomineral and mineral), and phenomena (structure–composition–function relationships, contaminant transport, mechanisms of formation and dissolution, *etc.*). The sampling of aquatic particles is thus a complex task which requires systematic adaptation of generic protocols to the specific type of material under investigation. However, the most relevant investigations usually employ correlative EM techniques, namely the use of scanning and transmission electron microscopes to examine in parallel whole mounts and resin-embedded specimens (see below), to embrace the broadest and most accurate physicochemical fingerprints of particles.

Sampling and handling of natural waters for TEM must be performed with the greatest care in order to avoid physical, chemical and microbial alteration of the native state of colloids and particles. As much as possible, the partial pressure of dissolved gases (*e.g.* low O<sub>2</sub> in anoxic waters or high CO<sub>2</sub> in carbonated ground waters) should be maintained in order to avoid redox or pH drifts during sample storage. Temperature is also an important parameter that should be kept constant, whenever feasible.

Furthermore, preservatives (*e.g.* acids, organic solvents, NaN<sub>3</sub> or HgCl<sub>2</sub>) must not be added to the samples, as they may produce artefacts owing to coagulation and sedimentation, or dissolution of colloids, photosynthetic activity, or microbial production of extracellular polymeric substances [40]. When visually identifiable, particulates larger than several tens of micrometers should be discarded from the sample, either by gentle sieving (*e.g.* with a 50–100 µm nylon mesh), by flotation (for light organic debris) or by brief sedimentation/centrifugation (for dense mineral debris).

To avoid rapid modification of the physicochemical and microbiological characteristics of natural water samples due to dissolution, precipitation, coagulation, sedimentation, microbial growth or shifts in chemical equilibria affecting colloids and particles brought about by changes in temperature, pH, depth, dissolved O<sub>2</sub> or CO<sub>2</sub>, light, and convection, aquatic samples should be processed for EM without delay (in <1 day), as is also the case for conventional bulk chemical analyses. Prefractionation of aquatic particles and

colloids to divide them into narrower classes can be performed by gravitational sedimentation in thermostated columns, by single or cascade centrifugation/ultracentrifugation or by single or cascade filtration/ultrafiltration. Samples treated by either fractionation approach are subject to artefacts, but these can be minimised by careful control of conditions. For example, centrifugation must be performed with relatively dilute suspensions to avoid problems of differential settling. Similarly, tangential-flow filtration at low flow-rates usually yields no, or less, polarisation concentration and membrane clogging than uncontrolled/unstirred cross-flow filtration. Centrifugation and filtration are usually performed to eliminate the fractions containing the largest particles, although they may be used instead to collect appreciable amounts of particulate material from waters with low concentrations of suspended solids (*e.g.* ground water or pristine waters), with possible biases caused by apparent coagulation of particles. It is clear that the structural features of physically unstable, well-hydrated aggregates of colloids in their native state can be altered by treatments and apparatus so as to confound analysis [107]. However, exquisite attention to the details of sample preparation can overcome even the most subtle of artefacts.

Particulate material can also be sampled from natural waters by direct collection on vertical or horizontal plates (Teflon, glass, plastics) inserted for periods of a few days to weeks in the water column [108]. Horizontal plates collect sedimenting particles without the drawbacks of conventional sediment traps (shifts in biological activity and redox conditions due to the absence of mixing at the bottom of the trap); vertical plates selectively collect those entities exhibiting a certain affinity for the plate (*e.g.* adhering bacteria, polysaccharides, humic substances and iron and manganese oxyhydroxides).

Particles suspended in soil water require different sampling approaches, depending on the type of water to be sampled [93,97,109]. Gravitational water is better collected by means of tension-free lysimeters; as these devices integrate the sampled water over time, the particles should be recovered without delay to avoid modifications in their size distribution or chemistry. It must be stressed however, that tension-free lysimeters may exhibit fairly low collection efficiencies (as low as 10% of the gravitational water, depending on soil texture and porosity). On the other hand, the capillary water of soils can be recovered by means of suction cups made of a porous material (ceramic or plastic), which are inserted in the soil and connected to a syringe or pump. Owing to their porosity (*ca.* 10–100  $\mu\text{m}$ ), these devices inevitably fractionate the particulate matter, and tend to clog with time. In addition, the nature of the porous material may result in selective adsorption of colloids.

### 3 SPECIMEN PREPARATION

This section will be confined to colloids and particles suspended in an aquatic medium, whatever their origin (soil, sediment or natural waters). After appropriate sampling, suspensions of particulate and colloidal material have to be converted to specimens for SEM or TEM investigation. Consider on the one hand a natural aquatic system containing living entities, such as bacteria, algae, fungi and protozoa, and non-living ones such as viruses, debris and macromolecular aggregates in their native medium (freshwater or saline, environmentally stressed or not, in still or running water, oxic or anoxic, *etc.*). The suspension may contain  $10^8$ – $10^{13}$  entities  $\text{dm}^{-3}$  over a 1– $10^5$  nm range, with a broad diversity of

morphotypes (*e.g.* fibrillar or compact, ill-defined and amorphous or crystalline). Be that as it may, however, conventional EM requires that the particulates of interest be analysed under high vacuum, i.e. in the absence of water.

The criteria for a successful and accurate TEM study is its ability to overcome this dilemma, transforming a given volume containing billions of entities into an unbiased specimen of colloids and aggregates evenly dispersed on a small supporting grid (3.05 mm diameter). Under controlled and appropriate conditions, the characterisation of *ca.* 100–1000 entities (individual colloids and aggregates) per grid can be expected to yield statistically relevant results, which can then be quantitatively extrapolated back to the original suspension.

Specimen preparation for SEM [43,47] requires the collection of particles on stubs (either directly or after precollection on Nuclepore-type membranes), followed by coating, most frequently with an Au or Pt film (for imaging) or a C film (for analysis). On the other hand, specimens for ESEM require no prior coating or treatment, but the spatial resolution of ESEM is usually limited when operated in wet mode (*ca.* 30–100 nm) [110]. The maximum achievable resolution that one can expect for SEM of complex heterogeneous environmental particles is *ca.* 10–50 nm, even for high-intensity FEG-SEM.

For morphological and sizing aims, the most useful TEM grids are made of 200-mesh Cu (square holes: *ca.* 80 × 80 µm) with alpha-numeric labels (Figure 3). More exotic (and expensive) grids (*e.g.* Be, Au or Pt) should be reserved for AEM (*e.g.* element analysis by energy-dispersive spectrometry, TEM-X-EDS). To ensure the most transparent and stable support possible, TEM grids must be coated with a flexible ultra-thin (10–50 nm) supporting film of Formvar or Parlodion for strength, then carbon-sputtered (3–10 nm) for thermal and electrical conductivity. When ultrastructural analysis is required, the plastic film can be dissolved, at the expense of specimen strength.

The choice of the grid type and supporting film is critical for analytical TEM/STEM (AEM in X-EDS or EELS modes). It is important to bear in mind that the X-rays produced by the analyte under the focused electron beam are emitted in a spherical region of the sample and will induce secondary X-rays of the materials they hit (*e.g.* the supporting grid or the pole pieces of the EM column). These secondary X-rays may be emitted in the direction of the detector, generating artefact peaks.

While Formvar- or Parlodion-coated, carbon-sputtered copper grids are the best choice from the standpoint of price and ease of operation for imaging purposes, element analysis requires supporting materials which will not mask the elements of interest. For example, gold grids are preferred for the X-EDS analysis of trace transition metals.

For the identification of carbon-rich entities prepared as whole mounts or quantitative mounts (i.e. without resin embedding), the supporting film should be substituted by a carbon-free 5–15 nm SiO film (not useful for Si-rich entities) or Be film (expensive). Large-scale entities (*e.g.* 3D networks or organic–mineral mixtures) can be collected on holey or Quantifoil (supporting film with controlled and repetitive holes) or lacey carbon films for the analysis of their unsupported portions (Figure 3), with the risk of a weaker mechanical and electrical stability under the electron beam. Whichever grid is used, the alpha-numeric styles are generally preferred in order to keep track of the particles of interest over time.

Depending on the information to be extracted, different methods are available for the optimal specimen preparation for TEM investigation: ultramicrotomy (preparation

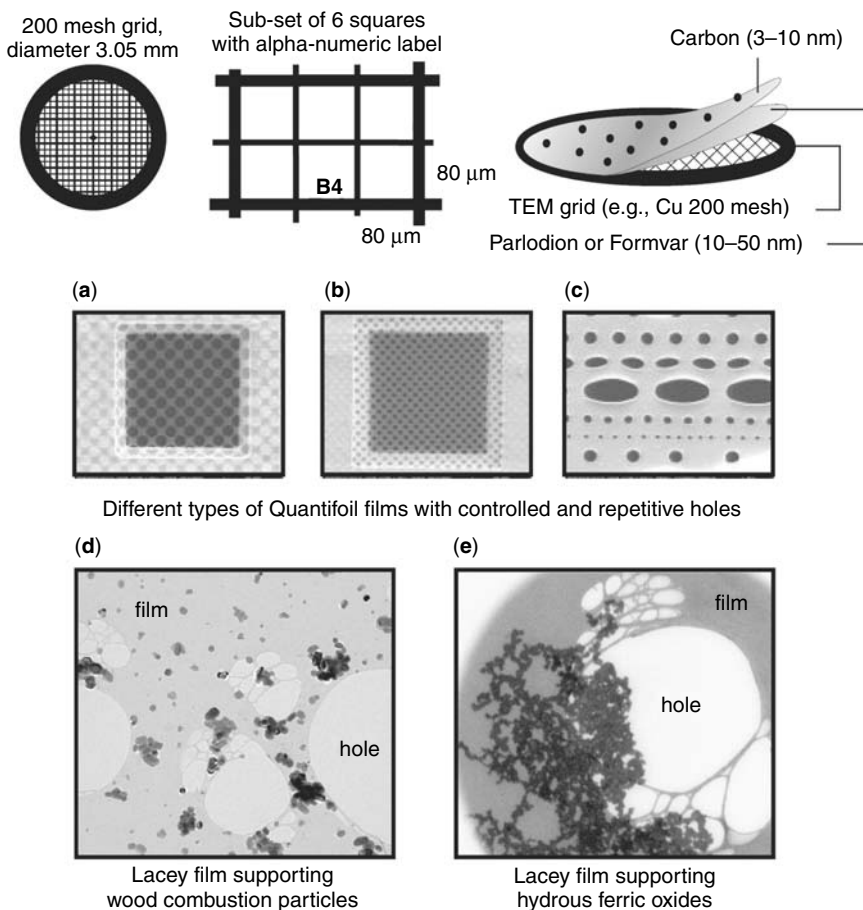


**Figure 3.** Specimen grids used to collect colloids and particles for TEM investigation. Supporting films with holes [*e.g.* Quantifoil with repetitive holes, micrographs (a)–(c), or lacey films, micrographs (d) and (e)] are recommended when supporting film-free element analysis of entities larger than the hole size (*e.g.* aggregates or fibrillar material) is required. In micrograph (d), wood combustion particles are too small to be analysed without a contribution from the supporting film; in micrograph (e), the aggregate of hydrous ferric oxides is large enough to cover the unsupported portion of the film and is thus prone to film-free element analysis

of ultra-thin sections of colloids embedded in plastic resin), preparation of whole mounts (deposition of the suspension on TEM grids), ultracentrifugation (direct and quantitative collection of colloids on grids), freeze-etching or vitrification (direct fixation of colloidal material at low temperature) and focused ion beam milling (microsectioning of material in the electron microscope). These techniques are described in full below.

### 3.1 ULTRAMICROTOMY

Ultrastructural investigations require the preparation of ultra-thin sections (*ca.* 50–100 nm), while thicker sections (which are much easier to obtain but should not exceed

150–200 nm) are amenable to element analysis, even when performing EELS, which theoretically requires the thinnest possible specimens.

For the extraction of ultrastructural information (in particular from bacteria, algae and three-dimensional networks of polymers in organic flocs), large entities (i.e. >1 µm) should be examined by TEM after preparation of thin sections obtained by resin embedding and ultramicrotomy (Figure 4). To avoid artefacts, the choice of an appropriate embedding medium is crucial. A hydrophilic resin (Nanoplast), rather than one of the more conventional hydrophobic ones (*e.g.* Spurr, Epon or Araldite) is appropriate because the latter require stepwise dehydration of the sample in organic solvents (acetone, methanol, ethanol or propylene oxide). These dehydration steps are potentially disturbing, as they may cause dissolution of particulate organic moieties and modifications of the morphology of complex three-dimensional networks containing organic entities. As Nanoplast produces water molecules during the permeation and polymerisation step, it readily infiltrates porous specimens (*e.g.* loose and amorphous colloids) and biological entities (*e.g.* bacteria), maintaining their fine morphological features [111,112].

For aquatic samples rich in microorganisms, one may require additional contrast of the cellular ultrastructure. This can be done as part of a fixation protocol prior to embedding or as part of a counterstaining protocol applied directly to ultrathin sections [113–115]. The most effective ‘morphological stains’ for microbiota are based on compounds which contain Os, U or Pb, or all three used in sequence [113–117]. Unfortunately, the stain technology that has been well developed for samples embedded in hydrophobic resins is underdeveloped for samples embedded in the hydrophilic Nanoplast resin. One solution to this dilemma is to split the sample and embed it in both kinds of resin [118]. In principle, Nanoplast-embedded specimens yield images in which individual colloids within aggregates retain their true three-dimensional disposition, whilst images of specimens embedded in a hydrophobic resin [117] reveal essential details of microbial ultrastructure.

Ultramicrotomy of the resin-embedded material should be performed exclusively with a diamond knife to overcome the hardness of mineral particles or biogenic minerals such as silica frustules, which quickly damage conventional glass knives. Diamond knives must be used with great caution, since they are expensive and can be chipped by hard minerals in the true particle size range. The ‘chipping’ is related less to particle hardness than to particle size, the result of the very slender shape of the diamond at its cutting edge. Nanoparticles of extremely hard materials are usually not problematic for the diamond knife, although such particles may sometimes ‘pop out’ of the embedding matrix during cutting, leaving a hole in the ultrathin section.

### 3.2 WHOLE MOUNTS

TEM offers a broad palette of protocols for specimen preparation. The most important procedures are illustrated schematically in Figure 4. Qualitative investigations are best served by direct deposition of a suspension on TEM grids (whole mounts), followed by evaporation (air drying). This rapid procedure may, nonetheless, induce (a) crystallisation of undesirable electrolytes (*e.g.* salt crystals in marine samples, which can be avoided by rapid rinsing of the grid in ultra-pure water), (b) shrinkage of aggregates of flexible organic materials (*e.g.* extracellular polymeric substances) or (c) coagulation of small colloids.

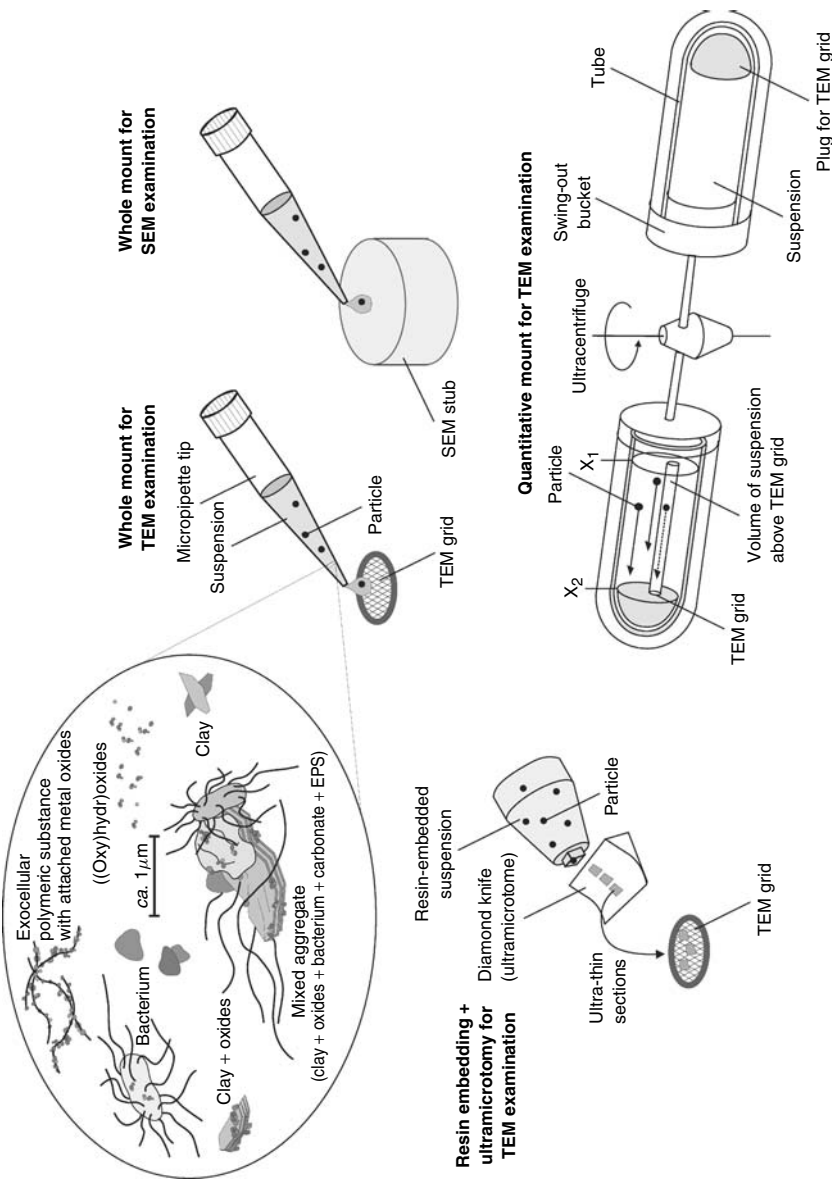


**Figure 4.** Scheme of the most useful qualitative and quantitative specimen preparation schemes for the SEM/TEM examination of colloids and particles present in aquatic samples. The preparation of whole mounts (on grids for TEM; on stubs for SEM) is the most rapid and easy to perform, but subsequent EM observation is usually biased by artefacts produced due to the evaporation of water from the specimen and support. Resin embedding is time consuming and requires operator skill but is well suited for ultrastructural analysis of specimens rich in biota. Ultracentrifugation is generally the most quantitative approach, as there is a direct relationship between the number of colloids impacted onto the grid and their concentration in the sampled medium.

### 3.3 ULTRACENTRIFUGATION

Whenever quantitative results are expected [*e.g.* particle size distribution (PSD)], colloids and particles must be deposited on the grid in a quantitative way. For this reason, the usual preparation of direct whole mounts is strongly discouraged, as it leads to shrinking and aggregation of entities during dehydration. Probably the most successful approach to prepare specimens for quantitative analysis by TEM is based on their controlled deposition by direct ultracentrifugation of the particles on TEM grids [31,94]. This procedure (Figure 4) yields quantitative whole mounts with evenly distributed particles. For a given suspension, the final coverage of the grid can be fine-tuned by varying the centrifuged volume, allowing a fairly accurate estimation of the particle concentration in the initial sample, while avoiding the excessively high concentration of particles that is commonly seen in whole mounts. Entities sensitive to dehydration or redox modifications can be post-protected by horizontally spinning an ultrathin film of hydrophilic Nanoplast resin. Indeed, the preparation of quantitative mounts can be coupled to sequential fractionation schemes to narrow further the number of particle types that are collected on the grids.

For this specimen preparation scheme, TEM grids are fixed with a light adhesive (one contact point at the periphery of the grid is sufficient), carbon side up, on the flat surface of a hemispherical plug which is inserted in a centrifuge tube (the plug having been moulded from epoxy resin to fit the tubes). A known volume of suspension is poured in the tube, which is then mounted in the swing-out bucket of an ultracentrifuge rotor. The duration and the speed of the centrifugation, together with the optimal volume of the suspension to be centrifuged, rely on the types of colloids to be collected and on the initial concentration of particulates in the suspension.

According to Stokes' law, the time  $t$ (s) required for a spherical particle of diameter  $d$ (cm) and density  $\rho$ ( $\text{g cm}^{-3}$ ) to settle from the top  $x_1$  (cm) of the suspension with density  $\rho_0$  ( $\text{g cm}^{-3}$ ) and viscosity  $\eta$  ( $\text{Pa s}$ ) to the surface of the grid  $x_2$  (cm) when subjected to an angular rotation speed  $\omega$  ( $\text{rad s}^{-1}$ ) is given by

$$t = [18\eta \ln(x_2/x_1)]/[d^2(\rho - \rho_0)\omega^2] \quad (1)$$

For example, an inorganic colloid ( $\rho = 2.0 \text{ g cm}^{-3}$ ) with  $d = 20 \text{ nm}$  would be collected on the TEM grid after *ca.* 1 h of centrifugation at *ca.*  $1.25 \times 10^5 \text{ g}$ , whereas an equivalent organic colloid ( $\rho = 1.1 \text{ g cm}^{-3}$ ) would require *ca.* 14 h of centrifugation. On the other hand, a large and dense mineral colloid ( $d = 450 \text{ nm}$ ;  $\rho = 2.0 \text{ g cm}^{-3}$ ) would reach the TEM grid after merely 0.5 h at *ca.* 520 g. Strictly, however, these approximations apply only to ideal rigid spherical colloids; most natural colloids (*e.g.* tabular clay crystals or fibrillar polysaccharides) deviate very far from this ideal.

The key factor for optimal centrifugation is the fraction of the TEM grid covered with particles. Ideally, a coverage of *ca.* 1–5% will minimise the probability of ‘apparent aggregates’, *i.e.* of individual entities occupying the same position on the grid (see sketch in Figure 5). In practice, turbid waters (*e.g.* sediment–water interfaces, wastewaters or waters from eutrophic lakes) require either the centrifugation of a very small volume (*i.e.* a thin layer of suspension above the grid) or predilution of the suspension with an electrolyte that is as similar as possible to the natural water (*e.g.* ultrafiltered carbonated water of pH 6–8 with ionic strength  $I = (1–5) \times 10^{-3} \text{ mol dm}^{-3}$  for a continental water). In the latter case, however, there is a risk of producing unexpected modifications of the original particle

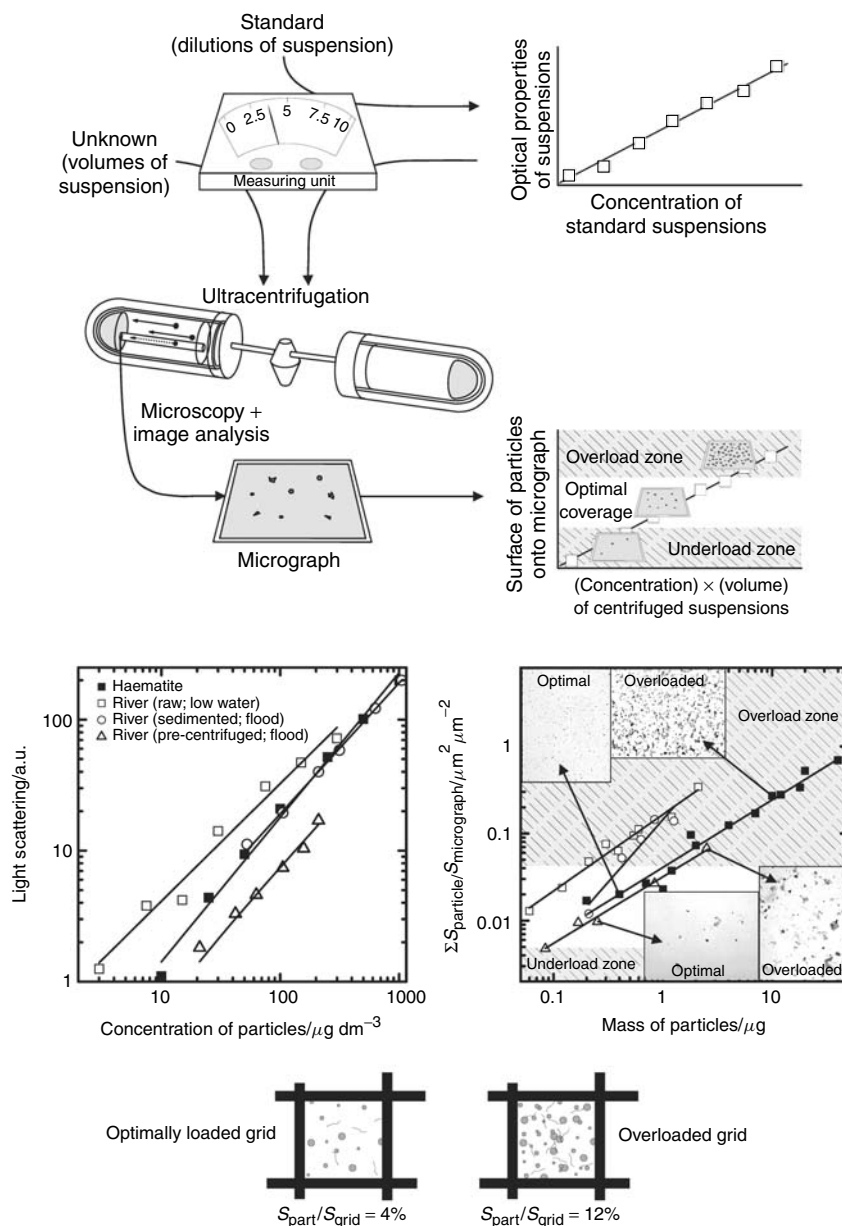


**Figure 5.** Scheme of a quantitative specimen preparation by the direct ultracentrifugation of colloids onto TEM grids. Optimal preparation of grids is performed in two steps: precalibration of the method with different dilutions of a standard colloid or of the suspension to be studied (for an optimal guess of the relative colloid concentration in the samples to be studied), followed by ultracentrifugation of the volume-optimised samples to avoid over- or underloading of TEM grids. Examples of optimally covered (few entities, homogeneously spread) and overloaded grids (too many colloids, apparently coagulated) are given for standard colloids (synthetic haematite particles) and for a real suspension (precentrifuged river during a flood event). The ratio of surface of TEM grid covered by colloidal entities to surface of TEM grid visualised determines the optimal coverage range (in general,  $\leq 10\%$  coverage is a maximum)

size distribution. For unknown samples, the conditions of specimen preparation can be optimised empirically by centrifuging a large set of different volumes and dilutions. On an *ad hoc* basis, the experimenter may measure some optical parameter of the suspension (*e.g.* turbidity, nephelometric data, light scattering or optical density) in order to estimate the concentration of particles, and thus the best combination of centrifugation conditions, to avoid overloaded or underloaded TEM grids [31].

Replicate grids are positioned in the same tube, and suspension volumes between *ca.*  $10^{-3}$  and  $3 \times 10^{-2} \text{ dm}^3$  should be centrifuged. Nonetheless, the crucial parameter for optimal grid coverage is the height of the suspension above the grid, not the volume of suspension. Thus, centrifuge tubes of small diameter are preferred for small volumes (*i.e.* very low heights of suspension). For example, a suspension containing *ca.*  $10^{11}$  particles  $\text{dm}^{-3}$  will result in *ca.* 6400 particles spread over a TEM grid square ( $80 \times 80 \mu\text{m}$ ) when a 1 cm high suspension is centrifuged.

For specific purposes, the direct ultracentrifugation of colloids on to TEM grids can be performed with appropriately selected sequences of increasing centrifugal forces and durations, new grids being inserted in the tube at each step. In such cases, the suspension is depleted in particles with high density and size, and the recovered TEM grids exhibit increasing proportions of colloids with low density and size. This specimen preparation scheme can also be performed for the AFM study of aquatic colloids and particles (see Chapter 9).

Labile specimens, *i.e.* ones prepared from redox-sensitive waters or from samples containing flexible fibrils that may shrink during dehydration, can be protected after centrifugation with an ultrathin film of TEM-transparent hydrophilic Nanoplast [35]. The resin is spun over a grid placed on a horizontal rotating disc. Particulate entities are then embedded during a controlled polymerisation. Rigid, resistant specimens (*e.g.* silica particles) are simply air-dried prior to TEM examination; in this case, shrinking and aggregation of colloids are not observed, as the entities are firmly fixed to the supporting grid by the centrifugal force.

### 3.4 CRYOTECHNIQUES: FREEZE-ETCHING AND VITRIFICATION

Cryotechniques offer an alternative preparatory technology that complements chemical fixation and embedding, producing aggregates whose 3D relationships are spatially ‘fixed’ by physical means (*e.g.* vitrification). The cryotechnique that most faithfully preserves the original structure is freeze-etching, which consists of freezing an hydrated sample rapidly enough to vitrify it (*i.e.* ultra-fast freezing of the suspension to obtain colloids embedded in vitreous water), mechanically generating a fracture plane through it and then making a metallic replica of the fracture surface, while maintaining the vitrified sample below the recrystallisation temperature. The product of the freeze-etch technique is a replica which presents a topographical image of a colloid or aggregate, untouched by chemical agents and amenable to analysis by TEM. In any case, given the complexity (*i.e.* need for dedicated technical skills) and cost of freeze-etching, well developed by cell biologists for analyses of intracellular structure, it has been essentially unexploited by scientists who examine hydrated colloids despite its potential as a confirmatory technique [29].

Indeed, vitrification should be the best specimen preparation scheme [119–125]. Unfortunately, this technique is not adapted to colloids and particles because of the fairly high

cost and need for dedicated technical skills. In addition, the large differences in thermal conductivities between particulate material and the surrounding water matrix make it difficult to obtain purely vitrified colloid–water interfaces for entities larger than several nanometres, thus resulting in local crystallisation of ice and damage to the morphology of colloids.

### 3.5 FOCUSED ION BEAM SECTIONING

Focused ion beam (FIB) sectioning, an emerging technique for the microscopic analysis of environmental samples, was described in the late 1980s for the preparation of specimens from semiconductor devices [126]. The technique is highly versatile, because it provides the user with the ability to control visually, in real time, a preselected portion of a massive environmental sample (*e.g.* a bacterial mat, a large aggregate, a filtration membrane, a fraction of soil, a specimen preembedded in resin) that is to be transformed into a thin (or even ultrathin) section for TEM observation. The FIB approach consists in cross-sectioning a sample in a dedicated SEM equipped with a beam of charged elements (*e.g.*  $\text{Ga}^+$ ,  $\text{Ne}^+$  or  $\text{Ar}^+$  ions at energies down to 100 eV) that are focused to a small spot size (typically 10 nm) and rastered across the sample. The thin section that is produced can be transferred by micromanipulator to a TEM grid for examination at high resolution (Figure 6).

FIB milling can be applied to hard (*e.g.* materials science [127]) and soft (*e.g.* biological [128, 129]) samples, and even to complex materials that include hard and soft counterparts (*e.g.* [130]). Very limited beam damage is reported, even for high-resolution

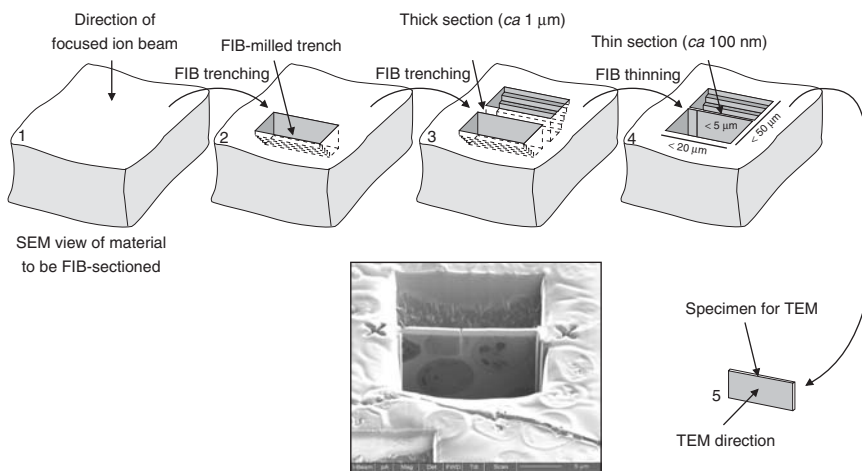


**Figure 6.** Scheme of the steps required for the preparation of a thin section for TEM examination in an SEM equipped with an FIB. A cross-section is milled by the ion beam on the sample surface; a similar cross-section is then milled in the vicinity in order to produce a preliminary thick section, which is ion-thinned from both sides until it becomes electron transparent. The thin section is finally cut free and removed for TEM investigation. The whole process is monitored in the SEM. The micrograph shown is a typical example of the operator's control over the preparation and thinning of a FIB section of algae; cross-sections of cells are visible at the freshly milled surface of the thin section; the layer above the specimen is a protective platinum coating

TEM, provided that the energy and the incidence angle of the beam are carefully controlled [131–133]. FIB sections of material of known composition and controlled thickness can be prepared and used to standardise the TEM–X-EDS signals [134]. For a review of the technique and details related to FIB, the reader is referred to a special publication on ion beams [135] and references therein.

### 3.6 STAINING AND LABELLING OF ORGANIC-RICH COLLOIDS

Staining procedures designed for biological or medical applications can be applied to environmental specimens (in particular in soils, sediments and natural waters) either to enhance the contrast of poorly electron-opaque organic material (salts of heavy elements, amongst which the most commonly employed are uranyl acetate, lead citrate, phosphotungstate, and Alcian Blue; see Figure 7) or to stain extracellular polymeric substances selectively [136–138]. For instance, Thiéry [139,140] described an elegant multi-step reaction with silver proteinate yielding nanometre-sized Ag grains on polysaccharides embedded in a Spurr resin (Figure 7). This selective identification method was

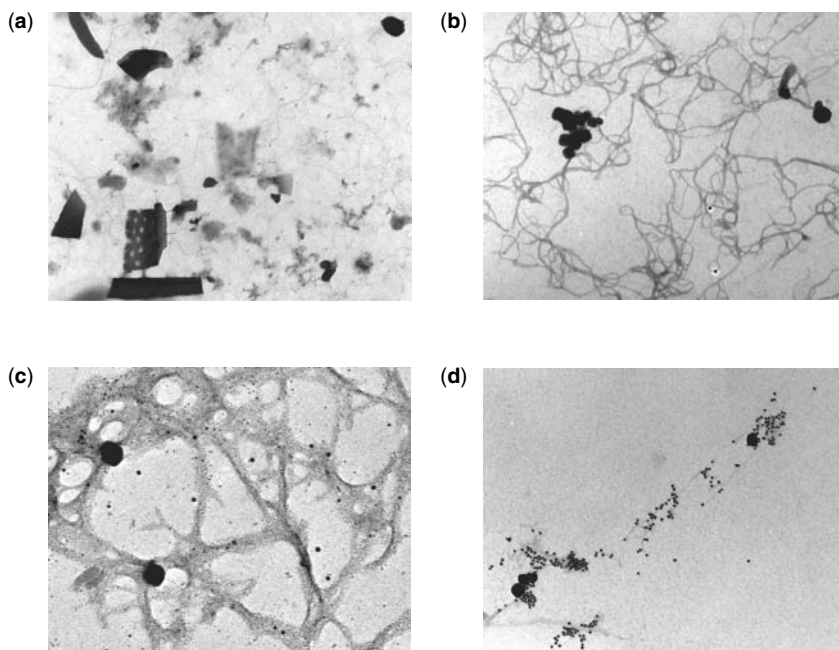


**Figure 7.** Examples of natural and synthetic polysaccharides. (a) Unstained heterogeneous lacustrine sample (Paul Lake, USA); the barely visible exocellular polymeric substances are ‘naturally stained’ by the major ions (mostly  $\text{Ca}^{2+}$ ) present in the system. (b) Mixture of alginates (produced by *Macrocystis pyrifera*) and 50 nm haematite nanoparticles; the polysaccharides were post-stained with uranyl acetate (i.e. after deposition of colloids on the grid and recovery of the latter), and appear as uniformly dark. (c) Mixture of xanthans (produced by *Xanthomonas campestris*) and haematite; the polysaccharides were selectively post-labelled by reaction with silver proteinate, and appear as dark networks carrying small black dots (Ag grains). (d) Xanthans were specifically post-labelled by reaction with a lectin–gold conjugate (lectin: UEA<sub>1</sub>, *Ulex europaeus*); the 10 nm black spheres are the gold colloids. All specimens were prepared by quantitative ultracentrifugation

later applied to soil extracellular polymeric substances (EPS) that cement clay particles together [141] and to bacterially produced polysaccharides in freshwaters [5,142].

At present, it is not easy to identify clearly colloidal and macromolecular humic/fulvic substances, which constitute an important proportion of natural organic materials. On the other hand, highly sophisticated labelling techniques using ultraspecific markers (*e.g.* gold–lectin conjugates that bind specifically to given carbohydrate moieties of polysaccharides (Figure 7) [143–158]) that were developed for the study of macromolecules in plants, animals and fungi should, in the near future, prove to be extremely useful for distinguishing similar natural organic macromolecules (*e.g.* neutral vs acidic polysaccharidic moieties produced by bacteria and algae) in aquatic samples.

The development of ultraspecific markers for TEM is progressing so well that it is now possible to label individual protein species selectively within a microdomain inside an individual bacterial cell [159] and specific polysaccharide molecules within the mucilage matrix of a biofilm [27,160].

In many environmental situations, colloidal organic matter is naturally stained by the major ions present in the electrolyte and therefore requires no staining for simple visualisation purposes. It must be noted, however, that most existing staining protocols were not designed for environmental specimens (whole mounts or resin-embedded ones) and necessitate careful optimisation before they can be used on a routine basis.

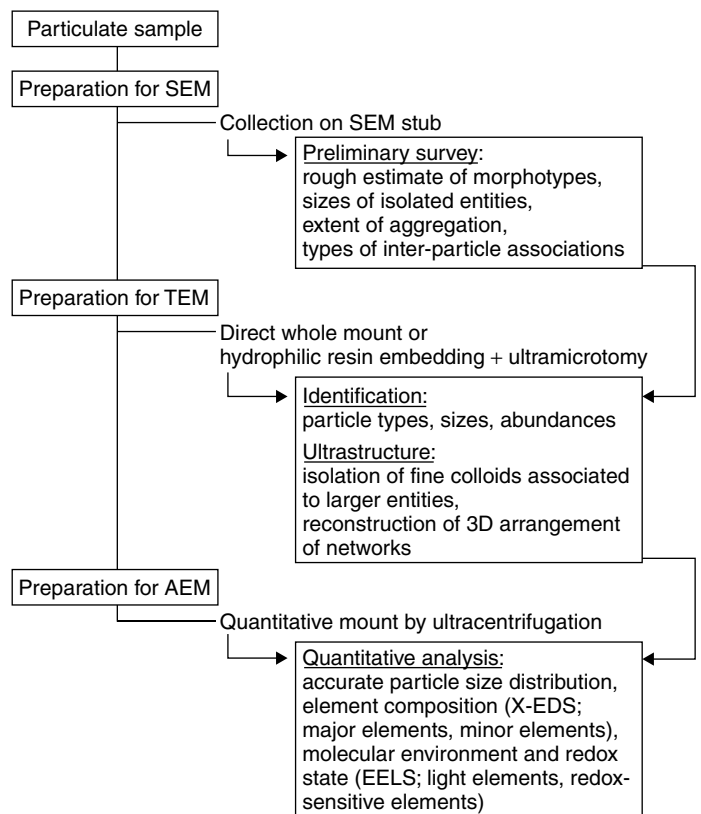
### 3.7 POTENTIAL ARTEFACTS RELATED TO SPECIMEN PREPARATION

Protocols recommended for obtaining ultrathin sections and optimally prepared whole mounts have been discussed elsewhere [35,118], as have procedures for analysing the three-dimensional architecture of readily deformed water-rich flocs [161,162]. The principal artefacts to consider in the production of sections and whole mounts for analysis are those caused by dehydration and shrinkage, extraction being a potential but soluble problem in the case of sections. These artefacts are well understood and readily minimised for many kinds of samples [29,30,40]. AEM (TEM, STEM–X-EDS, EELS, EF-TEM) techniques and rationales for the selection of representative images as related to the artefact problem have been treated at some length in the literature [4,23].

For the optimal preparation of native wet colloids prior to AEM analyses, a detailed treatment of the detection, assessment and minimisation of artefacts was given by Leppard and Buffle [40]. Artefacts include those inherent in preparatory protocols and those created before analysis (*e.g.* sample mishandling at time of sampling, unnecessary fractionation, alteration during storage, exposure to chemical agents that cause perturbation and excessive preconcentration). Leppard and Buffle [40] recommend (i) avoiding sample storage, (ii) minimising the number of steps in water sample preparation, (iii) paying exquisite attention to detail in the use of any fractionation procedure and (iv) adapting the prefractionation steps (if necessary) to take account of particle size polydispersity.

## 4 MORPHOMETRIC ANALYSIS OF PARTICLES AND COLLOIDS

Over recent decades, the investigation of environmental samples by EM was traditionally performed for merely illustrative purposes, although the spatial resolving power and analytical capabilities of modern electron microscopes presented unique features with the



\* Step performed on the basis of the results of the previous step in the correlative scheme

**Figure 8.** Idealised correlative electron microscopic procedure for the examination and physico-chemical characterisation of environmental colloids and particles. Examples of micrographs, spectra and plots can be found in the other figures

potential to supply qualitative and quantitative methods for providing unequivocal answers to complex problems in which colloids and particles play a central role.

Although the qualitative and quantitative aspects of this sort of investigation are discussed separately in the following sections, they should be considered as being intimately interrelated within the framework of every correlative electron microscopic investigation, as illustrated in an idealised hypothetical investigation outlined in Figure 8.

#### 4.1 QUALITATIVE OBSERVATIONS

SEM and ESEM are particularly well suited for the imaging and quantification of surface and textural features of large particulate entities (*ca.*  $>1\text{ }\mu\text{m}$ ) and for a rough estimate of the particle size distribution. Qualitative three-dimensional morphological information is readily extracted from SEM, operated in either the secondary electron mode or backscattered electron mode. The extent of aggregation among particles (provided that the aggregation is not an artefact produced by overloaded specimen stubs) can be documented

with a resolution down to *ca.* 50 nm without difficulty. Because of its ease of operation, SEM should be selected for the routine gross-scale survey of samples, in particular for atmospheric and soil particles. Preliminary qualitative surveys should help the operator to focus on either the general trends (*e.g.* major classes of particle types, sizes or associations) or the significant specificities of the sample (*e.g.* characteristic aggregation between two types of particles or prevalence of a narrow size class for a given type of entity). On the other hand, ESEM is useful for looking at wetting and drying processes involving highly flexible organic polymers and aggregates, eventually avoiding perturbation of their structure, as can be the case for microscopy performed under high vacuum. Under controlled conditions, it is even possible to determine particle size distributions, fractal dimensions and element maps by ESEM [110].

When carried out in the context of conventional bulk experiments and analyses employed in research on ecosystems, qualitative SEM/ESEM may yield significant supplementary information, affording increased understanding of the ecosystems. For example, visualisation of the microscopic features of humic and fulvic substances, as affected by changes in the pH or ionic strength of the surrounding milieu, has contributed greatly to our knowledge of conformational changes in these dominant organic substances in soils. Thus, humic colloids with shapes from spheroids to flexible extended fibrils or densely networked three-dimensional systems have been observed [163–167]. Similarly, the systematic SEM–X-EDS identification of the general features of particles transported through a complex peat–river–karst–spring aquifer has highlighted the ubiquity of a well defined Fe–Ca–C-rich class of globules and the role of humic substances in their formation and behaviour [4,168,169]. In a similar manner, the role of associations between clays and fibrillar polysaccharide networks on the stabilisation of soil structures has been assessed mainly by means of SEM. Nonetheless, such investigations require careful specimen preparation techniques (*e.g.* freeze-drying instead of air-drying) to minimise artefactual changes in conformation which may occur at any step of the preparation.

Accurate qualitative or semi-quantitative investigations on colloidal entities (*ca.* <500 nm) are better performed by means of TEM or STEM, with a resolving power down to the nanometre scale even for complex heterogeneous entities (a claimed sub-ångstrom resolution being achievable using TEM with aberration-corrected electron optics [170–172]). Whole mounts and quantitative mounts (Figure 4) are appropriate for semi-routine TEM investigations on colloidal entities, provided that TEM grids are not too densely covered with large particles and aggregates. In addition, inorganic entities can be verified for their potential crystallinity (Figure 9) by qualitative electron diffraction, either in selected area mode or in convergent beam mode. This is particularly useful for ill-defined particles (*e.g.* ferrihydrites or partly amorphous oxides) that may reveal locally ordered domains of their atoms, or to distinguish between particles exhibiting approximately the same morphology and composition but representing different stages of ageing.

Ultrastructural TEM characterisation of ultrathin resin sections is recommended for the detection of structures such as microscopic mineral deposits on bacterial cells, which would be obscured by the thickness-related opacity of bacteria prepared as whole mounts. This method is also recommended for the study of complex large-scale networks of fibrillar extracellular polymers, which retain their natural conformation when embedded in an appropriate resin. The reconstruction of their three-dimensional architecture is

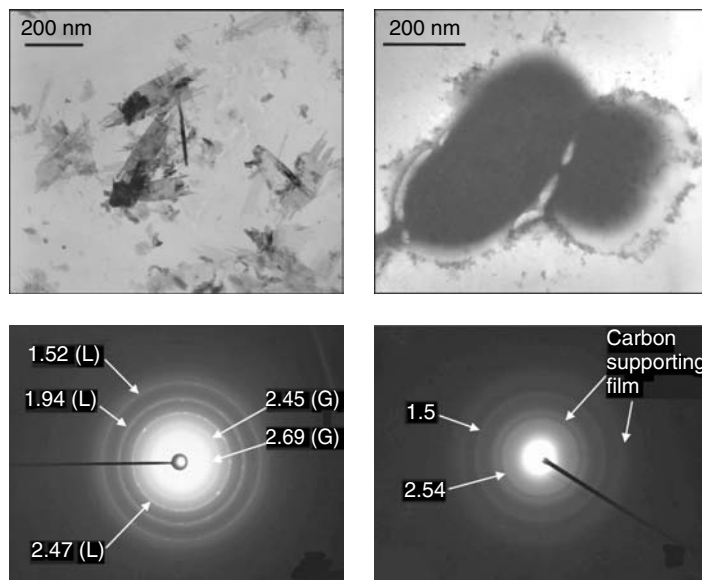


**Figure 9.** Examples of electron diffraction patterns (SAED) obtained on an abiotic mixture of goethite (G) and lepidocrocite (L) (left side), and on hydrous ferric oxides formed in the presence of *Bacillus subtilis* (right side). The  $d$ -spacings are given in Å. Whereas goethite and lepidocrocite are highly diffractive, the biotic hydrous ferric oxide can be identified as a two-line ferrihydrite [287]

theoretically achievable by imaging successive serial sections, but this requires tedious and extensive image analysis.

#### 4.2 QUANTITATIVE ANALYSIS AND PARTICLE SIZE DISTRIBUTION

Automated particle detection systems have been described [66,173–182], but their use is rather limited. This discussion will therefore focus on the conventional use of TEM for the recording of micrographs which are later processed by image analysis to extract information on particle size distributions (PSDs) and other useful morphological parameters.

Quantitative PSDs (either for all types of particles and aggregates present in the specimen or for a specific type of particle identified either by morphological criteria or by routine X-EDS element mapping) must be performed on quantitative whole mounts. High-quality micrographs can then be digitised for mathematical morphometry using image analysis software. The accurate determination of the PSD of atmospheric, aquatic, soil or sediment entities may yield information on the processes driving their behaviour (*e.g.* formation, dissolution, coagulation and sedimentation). It is also possible to estimate the mechanisms of colloid aggregation by measuring the fractal dimension of the aggregates. Provided that micrographs are obtained under carefully controlled conditions of illumination, estimates on the volume of non-spherical particles of known composition can also be obtained by image analysis (thickness-dependent opacity of the particles).

Owing to the physicochemical processes involved, such as the formation, coagulation and sedimentation of particulate material in aquatic systems, PSDs usually appear to

follow some kind of power law (*e.g.* Pareto's distribution; [183]), *e.g.*

$$d(N_{\text{part}})/d(d_{\text{part}}) = ad_{\text{part}}^{-b} \quad (2)$$

where  $d(N_{\text{part}})$  is the number of particles in a given interval of particle sizes  $d(d_{\text{part}})$ , and  $a$  and  $b$  are characteristic constants of the system. The constants can be linked to the colloidal transformation process in the water column (Figure 10).

In other words, the number of particles tends to decrease when their size becomes larger. This consideration must be kept in mind when dealing with TEM, as the human eye is a subjective tool. The experimenter can easily miss significant numbers of small colloids when they are in the presence of much larger, more conspicuous entities, such as diatoms, algae, clusters of bacteria and mineral particles which obviously monopolise the attention of the observer. To avoid such biases, TEM sessions for the determination of PSD must always be planned in a rigorous, systematic and objective way.

As a first step, TEM grids should be previsualised at very low magnification in order to control the quality of the sample preparation protocol. At nominal magnifications  $<10^3 \times$  (*i.e.* magnifications corresponding to the image projected on the fluorescent screen of the TEM, not taking into account further magnification when a digital camera is installed), only large particles ( $>1 \mu\text{m}$ ) are identifiable; they should be evenly distributed on the grid.

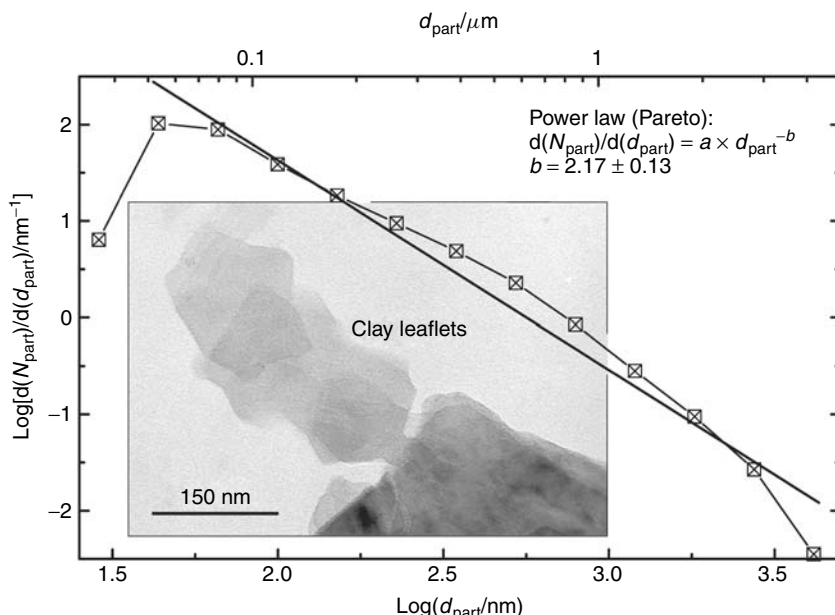


**Figure 10.** Example of a particle size distribution (PSD) obtained on colloids in a deep marl ground water. Colloids, as small as 30 nm, consist mainly of clays (see micrograph) in roughly equal proportions of chlorite, illite and smectite. The low concentration of colloids ( $<0.5 \text{ mg dm}^{-3}$ ) and the reducing conditions ( $E_h = -310 \text{ mV}$ ) required careful sampling and specimen preparation; approximately 9600 individual colloids were analysed to yield an unbiased PSD, the slope of which ( $b = 2.2$ ) indicated that clay entities were subjected to elimination from the ground water by orthokinetic coagulation

As the recovery of TEM grids following centrifugation requires considerable skill, broken portions of the supporting film are not uncommon. Nonetheless, they do not impair further observations, as they are discarded from the set of 2–3 potentially interesting zones (i.e. assemblies of 2 × 3 squares with alpha-numeric label). A rapid previsualisation of a replicate grid can ascertain whether the centrifugation step was performed under optimal conditions.

In a second step the zones of interest have to be accurately surveyed at higher magnification in order to record micrographs of the colloidal and particulate entities. A nominal magnification factor of *ca.*  $(2.5\text{--}5) \times 10^4\times$  is a good compromise to avoid underestimation of very small colloids (at  $5 \times 10^4\times$ , entities  $<20$  nm appear as  $<1$  mm) or very large particles (at  $5 \times 10^4\times$ , entities  $>2\text{--}5$   $\mu\text{m}$  cannot be entirely recorded). Nonetheless, even at this magnification, huge numbers of micrographs can be generated (at  $5 \times 10^4\times$ ,  $>10^3$  micrographs of a single grid square could be recorded).

Surveys of the zones to be micrographed can be performed either randomly or statistically. The random survey consists of recording micrographs at different randomly selected positions of the zone. This procedure is recommended when colloids exhibit a fairly narrow PSD and are homogeneously distributed on the supporting film. The statistical approach consists of recording micrographs at predetermined nodes of an imaginary grid; this approach ensures less bias in the selection of micrographs.

As far as possible, the recording of micrographs, either on negatives or with a digital camera, should be performed under reproducible conditions. Experimental parameters of the TEM, such as apertures, magnification, beam current, beam spreading and homogeneity, underfocus, exposure time and development process (for negatives), should be kept constant in order to guarantee that identical electron densities (i.e. similar types of materials for a given particulate size) in the specimen will translate into identical grey levels from micrograph to micrograph. Of course, additional magnification factors from the fluorescent screen to the camera must be taken into account, and digital micrographs should be recorded in TIFF format to avoid loss of data during handling of the files.

#### 4.3 IMAGE ANALYSIS

Once recorded, micrographs are generally processed by means of image analysis. There are a number of software programs available for image treatment (*e.g.* Photoshop with dedicated plug-ins and macros for PC, or the shareware NIH-Image for Mac), but the professional (and usually expensive) ones dedicated to image analysis are recommended, as they are fitted with a number of routines and macros relevant for mathematical morphometry, *i.e.* the recognition of objects and their characterisation [184–203]. Digital archiving of micrographs is convenient, as it allows storage of keywords and other relevant information for further retrieval [204].

Micrographs recorded on negatives must be digitised at a high resolution (*e.g.* 1000 pixels per inch, to record subtle details) prior to image analysis. For example, for a TEM magnification of  $5 \times 10^4\times$  on the negative, the diameter of a 10 nm colloid translates into 20 pixels at a resolution of 1000 pixels per inch. Transfer from the negative to the final print is not recommended, as it may induce distortions in the palette of grey levels, the dynamic properties (*i.e.* the ability to separate shades of very dark or very light greys) of the final print being much narrower than those of the original negative.

Although digitised micrographs may be binarised by selecting a threshold range (meaning that shades of grey are converted to black and white pixels, where certain grey levels

are considered as objects and others as background), it is recommended to work directly on the original files, in order to extract relevant information on the grey levels of each entity.

Figure 11 shows a simplified sketch of the steps that must be taken before measurements are started. Specific digital filters (*e.g.* shade correction or differential contrast enhancement) can, under certain circumstances, correct variations in the background (as, for instance, when one side of the micrograph is dimmer) when micrographs are obtained in an inhomogeneous electron beam.

After such preliminary corrections, a threshold has to be imposed on micrographs or regions of interest (ROIs) to limit the morphometric analysis to the colloids and particles of interest. Accurate scaling (in  $X$ ,  $Y$  and  $Z$  if required) of the micrographs must also be applied in order to measure morphometric parameters in real sizes. Of course, these crucial preliminary operations must be performed and adjusted with care on each micrograph or ROI, but the procedure should be facilitated when all micrographs are recorded under constant conditions.

It must be emphasised that  $Z$  calibrations are possible only for clearly identifiable colloids and particles of simple morphology. For instance, spheroids (*e.g.* crystalline iron or manganese oxides), tabular entities (*e.g.* clay leaflets) or fibrillar entities (*e.g.* extracellular polymeric substances) and their aggregates are predisposed to  $Z$  calibration. In contrast, the  $Z$  calibration of ill-shaped entities and multi-type aggregates or very thick objects cannot be extracted from grey levels, which are a complex function of thickness and electron density.

Among parameters of interest for particle sizing, the following should be measured for each entity: area, minimum and maximum diameter, perimeter and grey levels. Other derived parameters, such as mean diameter, centre of gravity, radius of gyration, mean grey value, equivalent circle diameter [ $ECD = 2(\text{area}/\pi)^{0.5}$ ], shape factor ( $SF = 4\pi \times \text{area}/\text{perimeter}^2$ ;  $0 \leq SF \leq 1$ ) and volume (provided that the grey levels can be accurately calibrated in units of thickness), are easily calculated for an exhaustive description of the morphology of an entity. As a rule, particles on the border of the ROI and also particles with holes in them should be excluded from the analysis to avoid biases in the final description of the morphological characteristics of a population.

Of course, the determination of a PSD is not feasible in every circumstance. For instance, the mean size of an entity with a shape factor  $SF \ll 1$  (*e.g.* fibrillar material or an irregular aggregate or ill-defined porous colloid; see examples in Figure 12) may have no physical meaning. For such entities, the determination of other parameters, in particular their minimum and maximum diameter or shape factor, is more relevant.

Under optimal conditions (*i.e.* when assemblages of colloids in the specimen present a realistic picture of assemblages in the initial suspension), information on the degree of coagulation and the processes leading to aggregation may also be extracted. For instance, discrimination between reaction-limited and diffusion-limited colloid aggregation [205–217] can be highlighted for colloidal systems by means of their fractal dimension,  $Df$ :

$$V_{\text{aggr}} \propto (RG_{\text{aggr}}/r_{\text{unit}})^{Df} \quad (3)$$

where  $V_{\text{aggr}}$  and  $RG_{\text{aggr}}$  are the volume and radius of gyration of the aggregate, respectively,  $r_{\text{unit}}$  is the radius of the elementary colloids within the aggregate and  $Df$  is the computed fractal dimension.

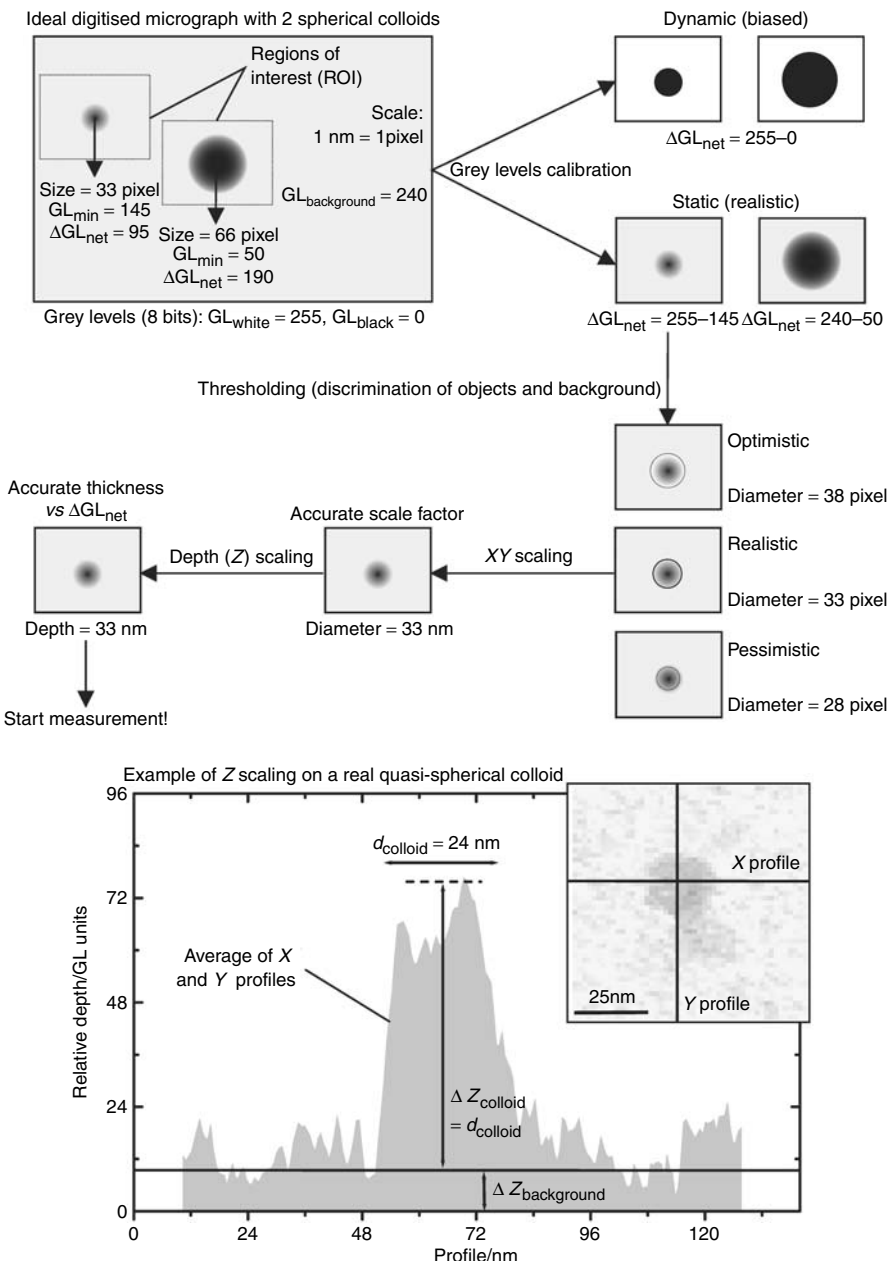


**Figure 11.** Steps required prior to the morphometric analysis of colloids. The schematised micrograph contains ideally spherical and homogeneous colloids. An accurate grey-level calibration and thresholding is a prerequisite to the least unbiased determination of the colloidal characteristics. An example of the calibration of the thickness of colloids (Z calibration) as a function of their grey levels is given in the bottom graph for a real quasi-spherical colloid (inset). Knowing the size of the colloid and by assuming a spherical shape, one can convert the grey values into real thicknesses

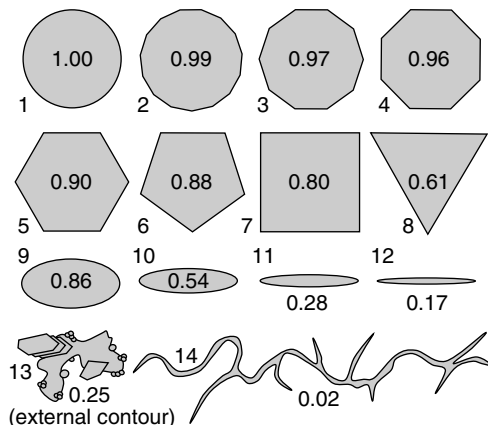


**Figure 12.** Examples of the variation of the shape factor ( $SF = 4\pi \times \text{area}/\text{perimeter}^2$ ) of geometric objects. Whereas the SF is close to 1 for objects with a high symmetry (objects 1–8), it decreases rapidly for elongated objects (9–12), aggregates (object 13) and fibrillar material (object 14)

Similarly, orthokinetic and perikinetic aggregation of colloids can be differentiated by means of a PSD expressed in terms of the Pareto power law (Figure 10 [183,218]).

For quantifying individual native colloid ‘species’ (as defined by a combination of size and compositional and morphological criteria), a practical electron-optical technology is now available [31], for use in combination with the quantitative ultracentrifugation of colloids on to TEM grids. User-friendly image analysis has become available [219] to facilitate TEM-based colloid quantification efforts.

Computerised image analysis has become a powerful means for extracting quantitative data from EM-based information, and there are many parameters whereby valuable information on environmental particles can be acquired that is not measurable with bulk techniques [29]. For example, with a representative specimen, size distributions of nanoscale particles from a heterogeneous suspension, which are not measurable when bulk techniques are used, can be quantified in a statistically meaningful manner. Such measurements can be evaluated with respect to bulk measurements when the particle population is homogeneous. Recent advances in the analysis of many kinds of particles are relevant to the image analysis of nano- and microparticles.

The accurate determination of the particle size distribution of colloidal entities may yield information on the processes driving their behaviour in the environment (*e.g.* formation, dissolution, coagulation and sedimentation). For instance, Couture *et al.* [220] performed image analysis on *ca.* 9000 individual colloids collected under state-of-the-art conditions from a deep ground water of a potential site for the repository of nuclear wastes in Switzerland. It was demonstrated that clay minerals (mainly chlorite, illite, and smectite with *ca.* 30–4000 nm mean size) were subject to elimination from the waters by orthokinetic (fluid shear-induced) coagulation (slope of the particle size distribution being expressed as a Pareto power law:  $b = -2.2$ ; Figure 10).

In addition, the aggregation regime of particles can be determined. The fractal dimension of an aggregate as determined by image analysis [221–224] provides information about the mechanisms of aggregation. According to Lin *et al.* [206] and Jullien [225],

$Df \approx 1.8$  corresponds to an aggregation controlled by Brownian motion [diffusion-limited colloid aggregation (DLCA)], whereas when  $Df \approx 2.1$ , owing to electrostatic repulsions, the aggregation rate is limited by the low collision efficiency between colloidal entities [reaction-limited colloid aggregation (RLCA)]. Such calculations have been used by Fatin-Rouge *et al.* [226] to determine the aggregation mechanism of nanoparticles analysed by TEM. In the same manner, Mavrocordatos *et al.* [58] showed that the  $Df$  of wood combustion particles could be determined by AFM. Results obtained on 1200 particles correlated very significantly with data obtained by STEM-X-EDS, scanning mobility particle sizer (SMPS) and bulk chemical analyses, and were coherent with previous work on combustion particles.

## 5 ELEMENT ANALYSIS OF PARTICLES AND COLLOIDS

Quantitative investigations of natural particulate matter entail special requirements. First, the specimen must be representative of the original medium. For example, all particle types initially present in the natural sample must be present in the proper proportions, unless the sample has intentionally undergone controlled fractionation to remove certain particle classes. The aggregates present in the specimen must not be artefactual expressions of an overloaded TEM grid or of a sample whose conditions of handling and preparation favoured coagulation of existing entities or precipitation of dissolved species. In that respect, the preparation of quantitative whole mounts (see Figure 5) by direct ultracentrifugation of suspended particles on to TEM grids is the most appropriate approach for quantitative measurements, provided that it is performed without delay. Most samples extracted from natural waters, sediments or soils can be prepared in this manner. In addition, quantitative investigations need to be performed on a statistically significant number of entities in order to yield sound measurements. Depending on the expected confidence of the final results and on the type of suspension (*e.g.* fairly homogeneous classes of colloids vs highly heterogeneous samples), the measurements of size and composition should be performed on a sufficiently large sampling of particles, *i.e.* between  $10^2$  (for simple suspensions) and  $10^4$  entities (for heterogeneous suspensions; Figure 13).

Characteristic X-ray fluorescence (X-EDS analysis) and energy-loss (EELS analysis) features of environmentally relevant elements are given in Figure 14. When dealing with element composition, the measured X-EDS peak intensities must be calibrated against representative standards. These standards may have to be synthesised in the laboratory under the conditions encountered in the ecosystem under investigation, because the mechanisms of X-ray production are influenced by the matrix of the sample material. Standardless analysis [49] is feasible in X-EDS (Figure 15), but it requires accurate measurement of element- and microscope-related parameters. A guide to obtaining quantitative X-EDS results from ultrathin sections of resin-embedded particles has been provided by Russ [227]. For EELS analysis, relative quantification (*i.e.* the ratio of one element to another one in the particle of interest) is readily obtained by calculation without the need for standards.

### 5.1 ENERGY-DISPERSIVE SPECTROSCOPY (X-EDS) AND RELATED TECHNIQUES

Over the past two decades, the clever and non-artefactual determination of the composition of environmental particles and colloids by X-EDS has transformed EM into a unique and

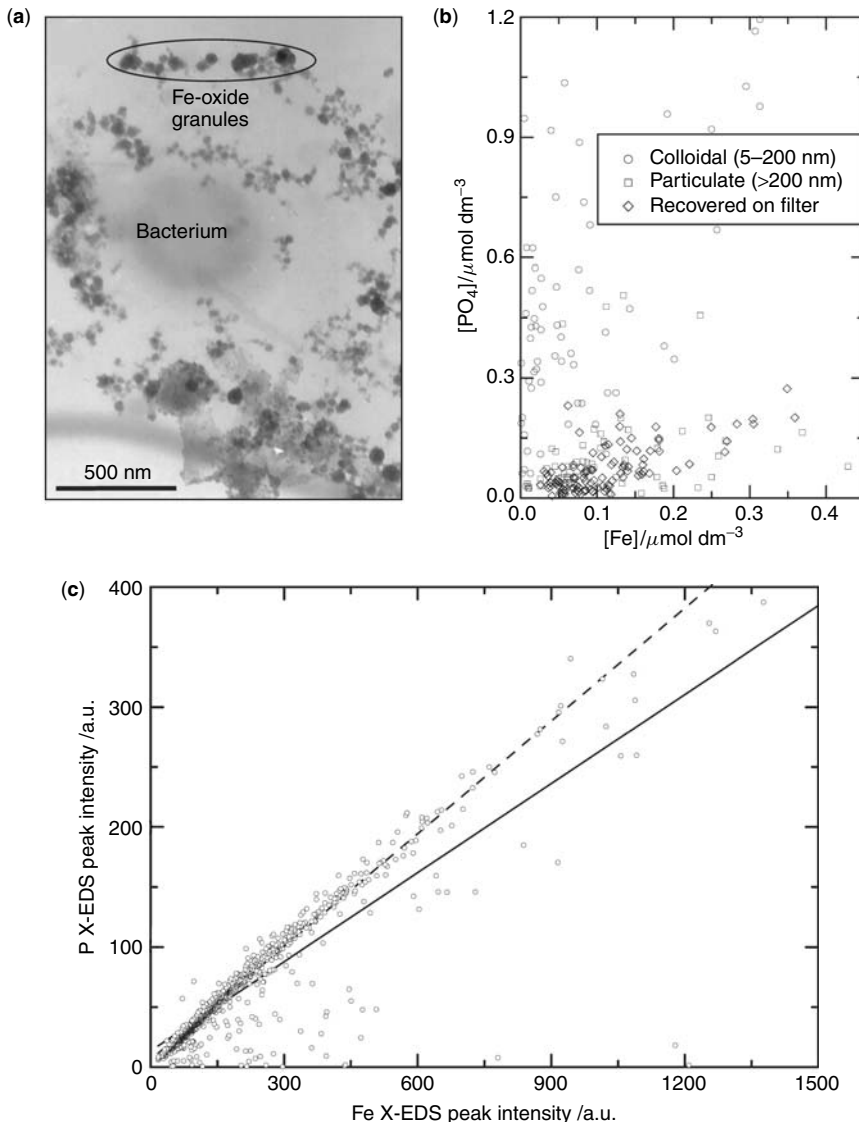


**Figure 13.** The stoichiometric nature of the association between iron and phosphorus in iron-rich nanogranules isolated from a large lake [234] cannot be expressed in terms of bulk chemical analyses, but requires the TEM–X-EDS analysis on a large set of individual entities. **(a)** Ubiquitous assemblage of Fe-rich nanogranules attached to polysaccharides of biotic origin. **(b)** Bulk chemical analyses of  $Fe_{tot}$  and  $PO_4_{tot}$  in different size fractions of the lake column (obtained by filtration and ultrafiltration). Because of the high heterogeneity of particle types in the water samples, there is no apparent correlation between the two elements, suggesting that phosphorus is not specifically bound to Fe-rich particles. **(c)** TEM–X-EDS analysis of 1096 individual Fe-rich granules (probe size: 50–400 nm). Owing to the visual ‘separation’ that can be applied during TEM analysis (i.e. only particles exhibiting specific morphological characteristics are analysed by X-EDS), the strong correlation between the two elements indicates that phosphorus is indeed stoichiometrically bound to Fe-rich granules (after conversion of X-EDS peak intensities into element concentrations,  $[Fe_{part}]/[P_{part}] = 0.5 \pm 0.04$  for 90% of the granules)

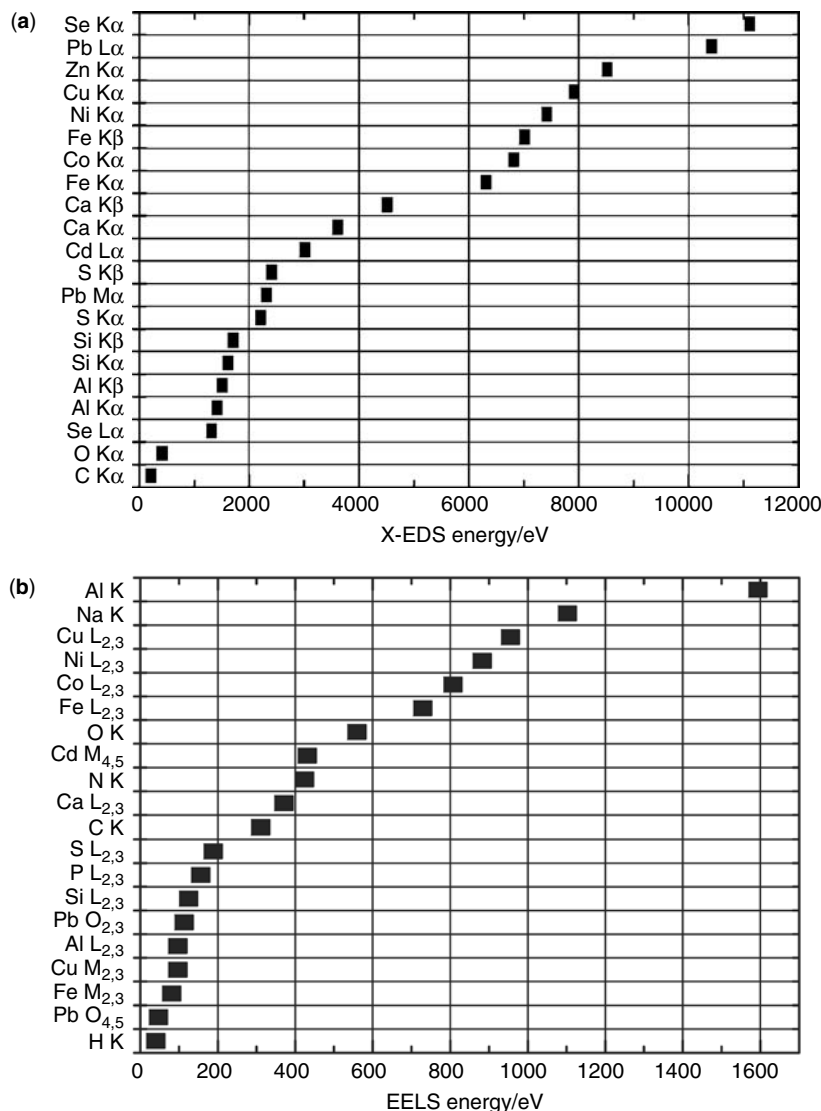


**Figure 14.** Energies of X-EDS peaks (a) and EELS edges (b) of some of the most relevant environmental elements; only the most prominent peaks and edges are shown

powerful analytical tool [42,44,45,50,228–233]. Under optimal conditions employing an X-EDS detector equipped with an ultrathin window (and with a parallel beam using the nano mode, if available on the apparatus), even carbon can be quantified, and the detection limits for trace metals can be as low as 500–1000 mg kg<sup>-1</sup>, even for sub-micrometric particles, provided that the peaks of trace elements of interest are not overlapped by those of other elements (Figure 15).

The X-EDS method is particularly well suited for elements emitting  $K\alpha$  peaks in the sensitive 0–10 keV energy range, but L-emitting elements can also be measured in

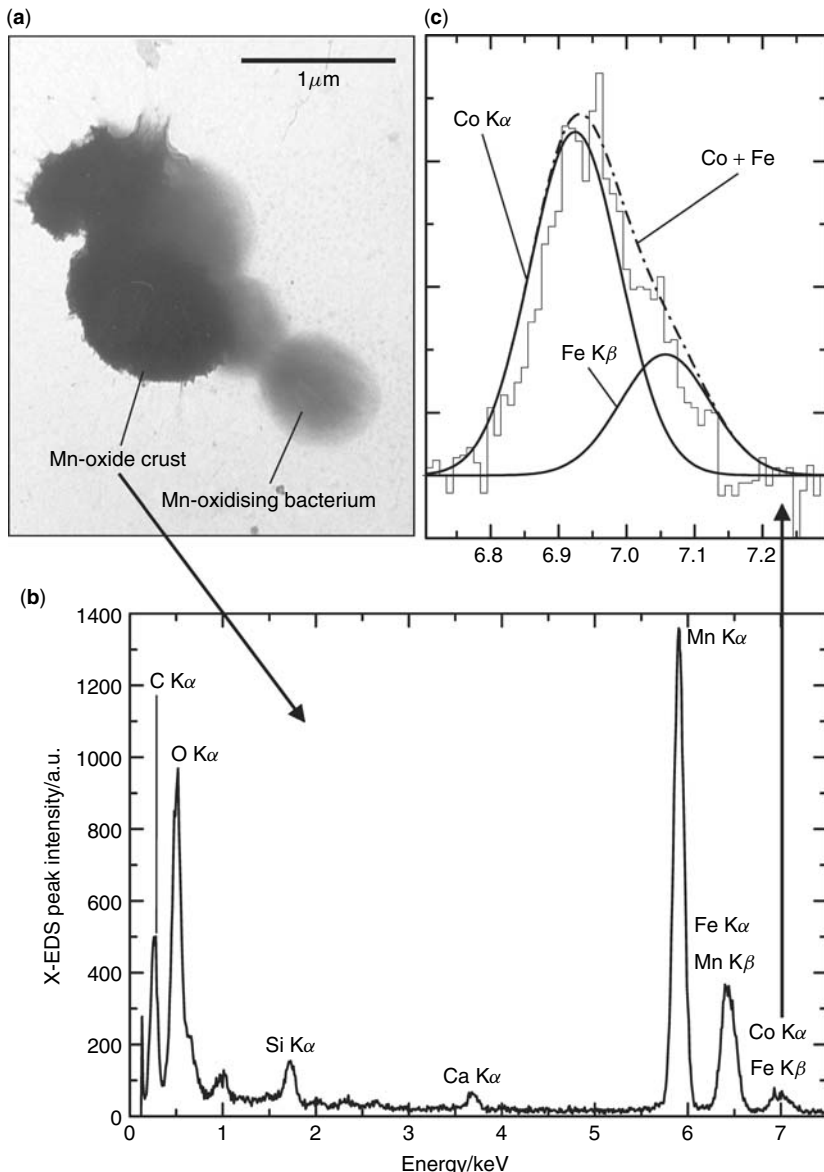


**Figure 15.** TEM–X-EDS analyses can be performed to highlight the presence of trace elements associated with elements constituting the bulk matrix of the particle of interest. (a) Manganese-oxidising bacteria isolated from the oxic–anoxic interface of a small lake [19]. The dark component is a crust of manganese oxide. (b) X-EDS spectrum (2 nm spot) of the Mn-rich crust shown in the micrograph. The crust contains mostly  $MnO_x(OH)_y$  with impurities of Si, Ca and Fe in non-stoichiometric proportions. The K $\alpha$  peak of iron (6.398 keV) overlaps the K $\beta$  peak of manganese (6.489 keV). (c) A detailed observation of the weak contribution around 7 keV indicates that traces of cobalt (K $\alpha$  = 6.924 keV) overlap the weak K $\beta$  peak of iron (7.057 keV). Standardless analysis and spectral deconvolution of the Fe K $\alpha$  + Mn K $\beta$  peaks around 6.4 keV and of the Co K $\alpha$  + Fe K $\beta$  peaks around 7 keV reveal that the manganese oxide crust contains approximately 2% cobalt

this range, provided that they are not present as trace elements. Quantitative X-EDS analysis is currently an excellent method (and probably the method of choice, provided that the sensitivity is sufficient) for the quasi-routine detection of trace elements bound by particles and the search for stoichiometric relationships between different elements in similar morphotypes [4,34,234].

## 5.2 ELECTRON ENERGY-LOSS SPECTROSCOPY (EELS) AND RELATED TECHNIQUES

EELS techniques [228,231,232,235–257], employed in either imaging or spectrum modes, are capable of detecting single atoms with energy resolutions as low as 0.2 eV in the useful 0–1000 eV energy range (Figure 14). In comparison, high-resolution X-EDS is achieved at not less than *ca.* 150 eV. This ability has been clearly demonstrated in materials science and even in biological science. Regrettably, however, EELS is not commonly used in environmental science, although several researchers have developed specific methods for the utilisation of EF-TEM and TEM–EELS in the aquatic sciences [19,258,259]. It has to be said, moreover, that the interpretation of spectra is not as clear-cut as in X-EDS, because (i) the technique is best suited for light elements (although transition metals yield valuable spectral information), (ii) the extraction of the EELS K- or L- or even M-edges of elements requires a careful and substantial stripping of the background (in accordance with the power law  $I = aE^{-b}$ ), (iii) the region below *ca.* 100 eV (plasmons region) is difficult to model with accuracy, (iv) there remain uncertainties in the determination of the cross-sections of the M-edges used for absolute quantification purposes and (v) EELS is theoretically best suited for specimens with thicknesses below 20–50 nm. Although it has been demonstrated that the technique can be used to quantify thicker (<500 nm) environmental particles [67], accuracy drops as specimen thickness increases.

In its simplest expression, EELS can be performed in energy-filtered (EF-TEM [33]) or electron spectroscopic imaging (ESI) mode, i.e. to generate element maps, but EELS in spectroscopic mode is better suited for quantitative analysis, with a high energy and lateral resolution (Figure 16).

The main advantage of EELS over X-EDS is its ability to yield molecular information in the form of specific features at and beyond the edges (Figure 17). Energy-loss near-edge structure (ELNES; which extends up to 50–100 eV beyond the edge) is the counterpart of X-ray absorption near-edge structure (XANES) in X-ray spectroscopy. Its features provide qualitative information about the molecular environment of the element giving rise to an EELS edge. For instance, the shape of an EELS–ELNES spectrum is different for aromatic, aliphatic or amorphous organic carbon centres or inorganic carbon centres. EELS spectra acquired with a high energy resolution (<0.5–1 eV) may also reveal the electronic configuration of redox-sensitive elements (*e.g.*  $\text{Fe}^{2+}$  vs  $\text{Fe}^{3+}$ , or mixtures of these two oxidation states in the same entity;  $\text{Mn}^{2+}$  vs  $\text{Mn}^{3+}$  vs  $\text{Mn}^{4+}$ ; Figure 17). Although exemplary results have already been obtained on pure crystalline iron and manganese minerals, the approach is, as yet, far from routine for complex heterogeneous environmental particles. Similarly, the use of EELS for the redox discrimination of elements of environmental concern such as  $\text{Cr}^{3+}/\text{Cr}^{6+}$ ,  $\text{Cu}^+/ \text{Cu}^{2+}$ ,  $\text{As}^{3-}/\text{As}^{3+}/\text{As}^{5+}$ ,  $\text{Sb}^{3-}/\text{Sb}^{3+}/\text{Sb}^{5+}$  or  $\text{Se}^{2-}/\text{Se}^{4+}/\text{Se}^{6+}$  has not yet been reported.

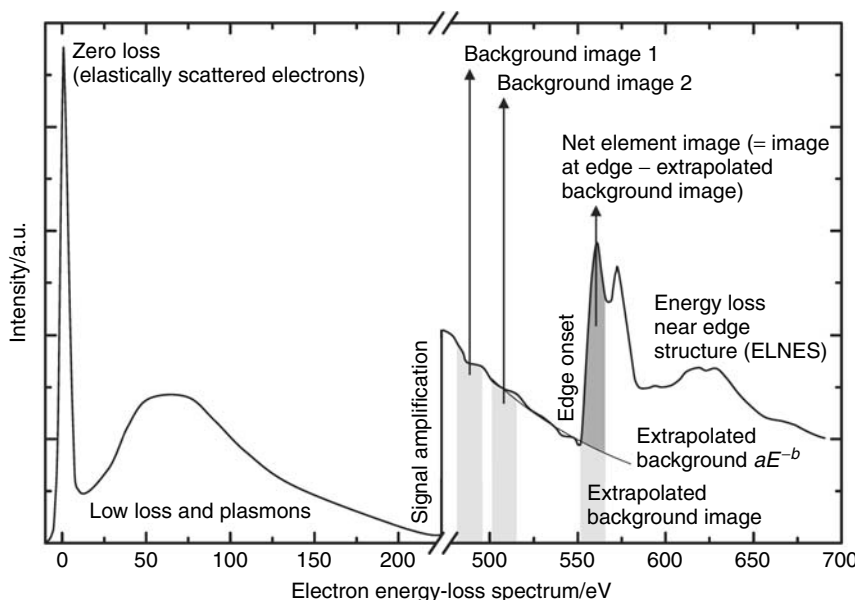


**Figure 16.** Scheme of a typical EELS spectrum showing several regions of interest. The image that can be obtained at the zero loss is roughly similar to the conventional bright-field image, but with sharper and more contrasted details because aberrations due to inelastically scattered electrons are stripped out. Electron spectroscopic imaging (ESI), i.e. element mapping, requires the recording of two images over a given window at different energies prior to the absorption edge and a third image at the absorption edge of the element of interest. The third image is used to strip the extrapolated background image from the gross image at the edge, and to extract specifically the net image of the element. ESI in the low-loss and plasmons region is feasible, but background extrapolation is more difficult. The ELNES region is used for qualitative molecular information (fingerprint of the molecular environment of the element)

## 6 APPLICATIONS OF EM AND AEM FOR THE UNDERSTANDING OF PHYSICOCHEMICAL PATHWAYS IN THE ENVIRONMENT

### 6.1 SELECTED CASE STUDIES RELATING PARTICLE CHARACTERISATION TO CONTAMINANT TRANSPORT

Using a multi-method approach with TEM, Campbell *et al.* [8] demonstrated the accumulation of nanoparticles of natural organic matter on the surfaces of living cells (two algal species and cells isolated from fish gills). Using environmentally relevant pH values and organic matter concentrations, they produced data consistent with the idea that the nanoparticles might exert a *direct* effect on organism physiology at the interface between living cell and aquatic environment. They also presented some interesting and unconventional implications of their findings regarding the interactions of toxic solutes with aquatic biota.

In 1998, Leppard *et al.* [17] isolated microparticles and flocs from the surface waters of Hamilton Harbor (Ontario, Canada) by size class (in ranges from <0.02 to >80 µm), and then analysed each size class for polycyclic aromatic hydrocarbons (PAHs), which presented a serious contamination problem in the harbour. Using TEM, SEM and STEM-

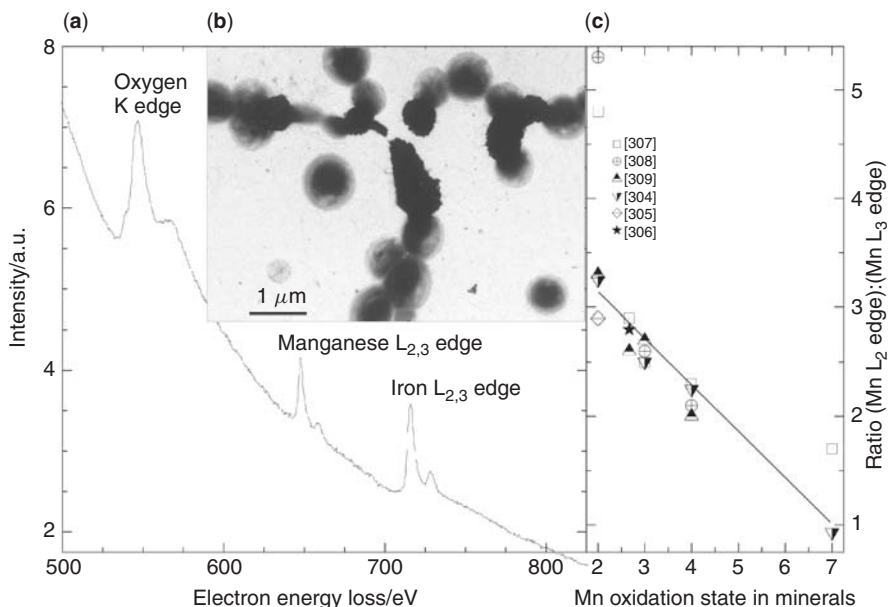


**Figure 17.** (a) EELS spectrum of a complex mixture of manganese oxides and iron oxides at the surface of colonies of Mn-oxidising bacteria (b) (see also Figure 15) at the oxicline of a eutrophic lake [19,142]. The presence of iron on the manganese crust is due to aggregation in the water column during sedimentation of the  $\text{MnO}_x(\text{OH})_y$  bacteria in the Fe-rich layers. The exclusive features of the  $L_{2,3}$  absorption edges of the redox-sensitive elements Mn and Fe allow clues on their oxidation states. (c) The ratio of the  $L_2$  and  $L_3$  absorption edges of manganese changes with the oxidation state of Mn [304–309]. This ratio is, however, highly dependent on the conditions of specimen preparation and EELS measurement

X-EDS in tandem, they found that the microparticles and flocs consisted mainly of aggregated colloids, among them numerous nanoparticles [260] of minerals (clays, iron oxyhydroxides, manganese-rich colloids and biogenic silica) and organic matter (cell debris, fibrils and humic substances). Heterogeneous porous flocs larger than 20  $\mu\text{m}$  accounted for 98% of phenanthrene binding, 89% of fluoranthene binding and 85% of pyrene binding.

In 2000, Mavrocordatos *et al.* [4] used AEM in an interdisciplinary investigation of individual colloids in successive compartments of a complex peat–karst–spring ecosystem (Vallée-des-Ponts, Switzerland). Their results revealed that globules rich in humic matter (identifiable by their characteristic morphology) formed intimate associations with colloidal iron and then underwent specific physicochemical transformations during their transport through a karstic aquifer, eventually turning into entities with drastically different properties. The investigation focused on the nanoscale characteristics of reactive particulate entities upstream and downstream from the karstic aquifer. The authors pointed out that their analytical approach should have major consequences for estimating the vulnerability of karstic aquifers to pollution events.

Also in 2000, Taillefert *et al.* [5] employed a suite of analytical techniques in conjunction with TEM to study the chemical speciation of iron and lead in the water column of a lake characterised by biogenic meromixis (Paul Lake, MI, USA). The primary goal was

to determine the effect of iron oxyhydroxides and natural organic matter on the speciation of lead, so as to understand better the cycling of lead in a natural lacustrine ecosystem. The results indicated that iron oxyhydroxides and organic fibrils aggregated together to form complex microparticles, which then became enriched in lead. Such a process would not have been accurately described by surface adsorption models.

Previously, Lienemann *et al.* [19,261] showed that sub-micrometre manganese-rich crusts produced by manganese-oxidising bacteria at the oxic–anoxic interface of this highly stratified lake had selectively preconcentrated cobalt ions with respect to the water column. As the manganese-rich and iron-rich layers partially overlapped at depth, classical bulk chemical analyses of the particulate material had to be supplemented by TEM–X-EDS measurements at the ‘per particle’ level to yield unambiguous insight into the selective scavenging of Pb by particulate iron and of Co by particulate manganese. Their approach, although time consuming, opened up new perspectives for documenting the speciation of toxic trace metals at the solid–solution interface.

## 6.2 NANO- AND MICROPARTICLES CHARACTERISED BY TEM AND AEM

### 6.2.1 Humic Substances

Marvin *et al.* [18] described a refined adjustable methodology for fractionating lake water contaminated by PAHs and polychlorinated biphenyls (PCBs), using TEM, STEM–X-EDS and standard images from the literature to characterise the major nano- and microparticles in the fractions richest in PAHs and PCBs. The results showed that the organic contaminants were preferentially associated with fractal aggregates of humic substances. Humic substances have also been shown to influence the formation and behaviour of iron-rich globular colloids [4,34,168,258,262]. Thus, it has been shown that acidic/anoxic peat waters slowly release into the river globule-shaped humic material (<500 nm) and stable complexes of  $\text{Fe}^{2+}$ , whereupon the  $\text{Fe}^{2+}$  is oxidised and precipitated at the surfaces of the globules when the pH,  $\text{O}_2$  content and ionic strength of the river increase; eventually these particles scavenge quasi-stoichiometric amounts of Ca. Myneni and co-workers [263–265] used high-resolution X-ray spectromicroscopy (in conjunction with standard TEM images from the literature) to demonstrate that macromolecular structures of humic substances vary with the origin of the humic matter, the chemical composition of the ambient solution and the nature of associated minerals. Wilkinson *et al.* [37] characterised humic substances by correlative TEM and AFM, Leppard *et al.* [266] revealed morphological evidence for a fibril-to-humic substance evolution and Senesi [267] explored a fractal approach using TEM images to derive quantitative descriptions of humic substance aggregation patterns and macromolecular morphology.

### 6.2.2 Polysaccharide Fibrils

Leppard [268,269] provided reviews of multi-method descriptions of polysaccharide fibrils sampled from diverse aquatic ecosystems, which included TEM descriptions of fibril morphotypes and complex aggregates. Wilkinson and co-workers [37,270,271] characterised fibrils using TEM in multi-method investigations, as did Santschi *et al.* [51]. Moreover, Lienemann *et al.* [272] demonstrated a means for the enhanced visualisation of polysaccharides from aqueous suspensions and devised a method for optimal preparation of water samples for TEM examinations of colloids, including fibrils [31].

### 6.2.3 Iron Oxyhydroxides

Colloidal iron oxyhydroxides and their role in the biogeochemical cycling of various elements have been characterised with the aid of TEM and STEM–X-EDS in a multi-disciplinary, multi-method investigation [4,34,234,273–275]. This major research effort, which was undertaken by different teams working on a wide range of various aquatic environments, led Perret *et al.* [36] to propose a general scheme for the formation of iron oxyhydroxides. They concluded that the various morphotypes of these colloidal species in a given aquifer can be explained and predicted in terms of the physicochemical conditions (pH, ionic strength, oxic/anoxic conditions, presence of humic or fulvic acids or non-humic organic matter, *e.g.* polysaccharides, and concentrations of reacting species) prevailing in the surrounding medium. In addition, this work puts forward a new paradigm for incorporation into geochemical speciation models dealing with surface adsorption. It is generally accepted that natural organic matter has a strong tendency to coat the outer surface of particulate material and to induce globally negative surface charges in water, but a careful EM examination of iron oxyhydroxides revealed that natural organic matter may also act as a heterogeneous template on whose surface the oxidation/precipitation of iron-rich material is favoured.

### 6.2.4 Viruses and Refractory Cell Debris

Many viruses are readily identified by TEM because of their unique combination of morphology and nanoscale size. This aspect of virology is of paramount interest, since viral populations can numerically dominate natural waters, with a potential as predators to alter the species composition of microbial communities whose individual activities, in turn, dominate aquatic biogeochemistry.

In 1990, Borsheim *et al.* [276] detailed a TEM-based procedure for the enumeration and biomass estimation of aquatic viruses. Proctor and Fuhrman [277–279] extended this work by relating virus population size to bacterial mortality rate. Weinbauer and Peduzzi [280–282] added important details, relating virus morphology to morphological correlations of the infection process. Danovaro *et al.* [283] employed TEM in a multi-method research initiative to determine virus abundance in sediments.

Leppard and co-workers [266,284] have provided TEM descriptions of abundant distinctive cell debris from marine waters and surface/ground waters. The latter study was related to plutonium contamination near a nuclear weapons production facility.

### 6.2.5 Nanoscale Mineral Agglomerates on Cell Surfaces and on the Surfaces of Extracellular Polymers

The genesis of minerals by bacteria and their extracellular polymers has become a central theme in biogeochemistry. This phenomenon has far-reaching implications and has aroused intense interest among geologists, chemists and microbiologists. A number of advances in our understanding of the microbial biogenesis of minerals which have been made with the aid of TEM and AEM analyses have been reported in the literature [9,11,12,14,15,20,21,285–287].

At present there is keen interest in natural associations of organic fibrils of EPS with other colloids, including iron oxyhydroxides in aquatic environments. Such heterogeneous

associations of abundant nanoparticles with other nanoparticles must be better understood for the sake of improving our understanding of global water processes. It is noteworthy that careful preparation of fragile hydrated specimens is helping to unravel the complexity of interactions between fibrils and other biotic or abiotic entities, such as the abundant ones prevailing in marine snow [31,288] and in wastewater flocs [7,23,118], and elucidate their biogeochemical functions. When the weak electron opacity of organic matter lacking metal-rich markers is an obstacle to its identification by TEM, nanoscale fibrils can still be visualised by means of EF-TEM at the carbon K-edge [272]. In addition, the polysaccharide character of EPS fibrils can be ascertained unambiguously by reaction with specific probes (*e.g.* Ag-proteinate [142], or oligosaccharide-specific lectins labelled with colloidal gold [27]).

For iron oxyhydroxides and their heterogeneous associations, which are virtually ubiquitous in freshwater environments, Perret *et al.* [36] demonstrated specific morphotypes whose structure is mainly a function of (i) the type of macromolecular organic matter present in the water and (ii) the relative concentrations of total iron and natural organic matter (NOM). In the presence of aquagenic EPS, which can form three-dimensional networks of fibrils, Fe–NOM associations tend to lead to the formation of iron oxide nanogranelles attached to the surfaces of fibrils, especially when the ionic strength of the ambient water is high and the  $\text{Fe}_{\text{tot}}:\text{NOM}$  ratio is low. In contrast, ill-defined Fe–NOM mixtures are favoured at lower ionic strength and high  $\text{Fe}_{\text{tot}}:\text{NOM}$  ratios. In the presence of terrestrial humic/fulvic-rich materials, the final Fe–NOM entities are spherical globules made of a C-rich core surrounded by amorphous iron oxyhydroxides. It has also been shown by Lienemann *et al.* [234] that the lacustrine oxidation of Fe(II) may lead to the formation of iron oxyhydroxides which bind phosphates and have a stoichiometric quantity of phosphate and iron, and that this nutrient-scavenging process is an efficient barrier against the upward diffusion of phosphates in the water column of Lake Lugano (Switzerland), a stratified eutrophic lake. In the case of iron–humic complexes formed during the oxygenation of acidic, anoxic Fe(II)-rich peat waters [34], it has been shown by high-resolution TEM–PEELS (EELS in parallel mode) measurements of individual 100 nm globules that the abrupt rise in pH, O<sub>2</sub> and ionic strength in the drainage waters leads to the formation of a compact outer crust of *ca.* 2–4 nm amorphous Fe–Ca-rich granules at the surface of shrunken humic spheroids, the shape of the latter being dictated mostly by pH and ionic strength constraints.

### 6.3 MICROPARTICLES AS NATURAL AGGREGATES OF NANOPARTICLES

Many of the microparticles found in surface waters and engineered aquatic ecosystems are heterogeneous aggregates of microbes and nanoparticles [7,15,17,18,23,118,162]. A generalised description of colloidal interactions in water (leading potentially to the formation of microparticles) has been published by Buffe *et al.* [6], who demonstrated that the concentration of stable colloids in a given aquatic ecosystem depends on the proportions of three general classes of native colloids (compact inorganic colloids; large rigid biopolymers; and fulvic acids and similar substances). Micelle-like microparticles can form from the self-organisation of dissolved organic matter in river water [289]. For biota-rich flocs, Liao *et al.* [7] proposed a conceptual model of aggregate structure whereby the gel-like matrix consists of two physically distinct regions defined by the arrangement of

nanoscale EPS, which cross-connect individual cells of the microbiota. The physically distinct regions are likely to be differentially affected by agents applied to manipulate floc integrity. AEM and selective extraction methods have revealed heterogeneity in the packing and specific chemical composition of EPS, apparently reflecting floc stability. For marine biota-rich flocs, Heissenberger *et al.* [288] suggested a scheme (based on TEM observations) for the growth and development of marine snow and the occasional subsequent buildup of the economically undesirable mucilage in the water [268]. Heissenberger *et al.* [288] related the growth of suspended marine snow flocs to (i) secretion of nanoscale fibrils by microorganism communities and (ii) a large number of environmental processes that modulate the cross-linking activities of fibrils and the developing flocs.

#### 6.4 SELECTED CASE STUDIES RELATING PARTICLE CHARACTERISATION TO WATER TREATMENT PROBLEMS

Liss *et al.* [118] used TEM and CLSM in parallel to describe the nano- and microscale architecture of engineered flocs sampled from an activated sludge effluent system (Thunder Bay, Ontario, Canada). At a practical resolution of 0.001 µm, they described bacteria and other colloid-sized particles embedded in a complex matrix of extracellular polymeric substances (EPS). This matrix was rich in EPS fibrils (4–6 nm diameter) which (i) acted as bridges between the diverse colloidal particles within a floc and (ii) formed the tenuous boundaries of an extensive intra-floc pore structure. Liss *et al.* [290] then used optical microscopy, TEM, STEM-X-EDS and ESEM to demonstrate correlatively that EPS at the bulk water–floc interface can aggregate so as to form a ‘skin’ which decreased the surface roughness of the floc. The induced formation of this ‘nanoscale skin’, which is highly relevant to economically important floc settling problems in water treatment tanks, was achieved by a laboratory manipulation that is potentially capable of being scaled up to an industrial treatment system. Liao *et al.* [7] employed a variety of physicochemical techniques including TEM, to analyse interparticle interactions affecting the stability of sludge flocs sampled from laboratory scale sequencing batch reactors. Focusing on the three-dimensional arrangement and packing of fibrils, they proposed a conceptual model of floc architecture which relates EPS nanoparticles to floc stability in engineered water treatment systems. Since this model was proposed, an interdisciplinary AEM study of contaminated wastewater flocs has demonstrated that various nanoscale flocs immobilise heavy metals differentially [23]. This finding has implications for heavy metal recovery from activated sludge and reuse of the metals.

#### 6.5 CORRELATIVE USE OF TEM WITH AFM AND STXM

Correlative TEM and AFM analyses of aquatic organic nanoparticles (especially aggregated polysaccharides and humic substances) are being conducted to ascertain better the activities and behaviour of organic macromolecules in natural waters. On examining water samples from different marine environments, estuarine and surface and deep waters, Santschi *et al.* [51] found that an important fraction of the colloidal organic matter dispersed in the water consisted of fibrils rich in polysaccharides. Although both techniques were subject to potential artefacts (which could be minimised), the two used in tandem were found to be complementary, especially when used in a multi-method context with standard techniques. Wilkinson *et al.* [266] have developed multi-method approaches to

the characterisation of the supramolecular microscopic structure of humic substances and polysaccharides, whose roles in aquatic biogeochemistry and ecology are largely dependent on their supramolecular structure, and which cannot be determined by bulk chemical methods alone.

Verdugo *et al.* [291] endorsed the correlative use of AFM and TEM to analyse ‘oceanic gel phase’, polymer gel particles, which are abundant and important in biogeochemical cycling, sedimentation processes, the microbial loop (cycling of elements by microbes), marine carbohydrate chemistry and particle dynamics in the oceans. These gel particles are mainly three-dimensional colloidal networks of biopolymers suspended in sea water, and they range in size from the nanoscale (single macromolecules entwined), to the microscale (networks of colloids), and on to the gross scale (aggregated polymer networks of near millimetre overall size). Regarding the investigation of colloidal environmental particles in general (both aquatic and atmospheric), Mavrocordatos *et al.* [292] discussed the advantages of combining AFM and TEM observations, in a correlative multi-method approach, with data from STEM–X-EDS, TEM–EELS, SEM, FIB and TEM–SAED (selected-area electron diffraction). They provided general guidelines for the effective use of microscopy and presented examples of diverse analyses (including analyses of biofilms, combustion particles, biofouled membranes, biogenic minerals and particle/contaminant associations).

Correlative TEM, STXM and CLSM analyses of colloidal extracellular organic polymeric substances comprising the mucilaginous matrix of a microbial biofilm were described by Lawrence *et al.* [27]. Their goals were to achieve a better understanding of the three-dimensional configurations of the major classes of organic macromolecules within the colloidal matrix structure serving as a habitat for the microbial communities of the biofilms. CLSM and fluorescent probes were used initially on a fresh sample to ascertain the gross architecture of the biofilm matrix and to map out the overall distribution of several abundant extracellular polysaccharides as related to the density and nature of microbe associations. The same fresh sample was subjected to a synchrotron analysis for confirmation of the gross architecture by STXM at a higher spatial resolution; the known abundant macromolecules were used as probes. The different major classes of macromolecules (polysaccharides, proteins, lipids and nucleic acids) were localised and distinguished from each other in a given image, on the basis of their interactions with soft X-rays. Details of the important features were then examined by TEM at much higher resolution, with identification of key nanoscale features.

Chan *et al.* [20] examined the growth of (sub-micrometre) iron oxyhydroxide filaments by combining data from TEM and STXM to yield novel observations of a biological process relevant to biominerallisation. SEM was used for orientation to show fibrils and mineralised filaments protruding from a microbial cell, high-resolution TEM was used to examine nanoscale morphological details within the growing mineralised filaments, and both STXM and X-PEEM (X-ray photoemission electron microscopy) were used to obtain chemical data. Chan *et al.* [20] infer that cells synthesised and then extruded polysaccharide macromolecules in the form of nanoscale-size fibrillar packets (insofar as the smallest diameter was concerned), with the polysaccharide fibrils subsequently localising FeOOH precipitation in proximity to the cell membrane, and thus harnessing a proton gradient for energy production. An organic template coupled to metabolic activity thus generated an iron-rich filament having a specific mineralogy and nanoscale morphology.

Hitchcock *et al.* [293] reviewed the most recent advances in STXM describing instrumentation and acquisition protocols and outlining methods for conversion of image sequences to quantitative maps of chemical components. Moreover, they discuss an example of the correlation of STXM data with CLSM data taken from an identical region of a biofilm. The work also integrated the use of STXM and TEM to characterise selected morphological features of the biofilms with nanoscale resolution (1–3 nm), which is not currently obtainable with STXM [27]. Through the application of adjustable soft X-rays and appropriate analysis of X-ray absorption spectra in the form of NEXAFS image sequences, quantitative chemical mapping at a spatial scale below 50 nm is now achievable [293,294]. To supplement the progress being made with STXM in the analysis of environmental materials, Lerotic and co-workers [295,296] described a method to find natural groupings of spectromicroscopic data without prior knowledge of the spectra of all components. Their approach permits visualisation of nanoscale speciation in complex specimens.

## 6.6 ACCURATE SELECTION OF TARGET SPECIES AND FINGERPRINTING OF BIOMINERALISATION

Cyanobacteria are important agents of calcite ( $\text{CaCO}_3$ ) precipitation in natural waters, but the detailed mechanisms of nucleation of  $\text{CaCO}_3$  and the influence of abiotic and biotic factors are still debatable. Laboratory experiments employing cultures of specific cyanobacteria under strictly controlled conditions, performed in combination with AEM of selected specimens, may allow an insight into the initial stages of  $\text{CaCO}_3$  precipitation. Experiments performed by Dittrich and co-workers [297–300] have shown that the picocyanobacterium *Synechococcus* accelerates the nucleation and growth of  $\text{CaCO}_3$  crystals in waters with low alkalinity ( $<2 \text{ mmol dm}^{-3}$ ), high saturation ( $[\text{Ca}^{2+}][\text{CO}_3^{2-}] / K_{\text{sp}} = 5–7$ ) and a high  $\text{Ca}^{2+}/\text{CO}_3^{2-}$  ratio. While SEM reveals that calcite crystals are almost systematically attached to *Synechococcus* (Figure 18a) and even embedded in the cells at later stages of growth (Figure 18b), the FIB preparation of targeted specimens (Figure 18c and d) for TEM observation (Figure 18e) and TEM–EELS fingerprinting (Figure 18f) have proved to be an efficient way to elucidate the chemical bonds at the cell–crystal interface.  $\text{CaCO}_3$  crystals are intimately bound to the surface of the *Synechococcus* cell, and the cell–crystal interface can be clearly discriminated by EELS owing to the specific features of the EELS near-edge structure of  $\text{C}_{\text{org}}$  (cell fraction; C–C and C=C bonds) and  $\text{C}_{\text{inorg}}$  (crystal fraction; C=O bond). In this example, an ingenious combination of high-resolution AEM techniques (FIB + TEM + EELS) may allow conclusions to be drawn at the molecular level.

## 6.7 AGGREGATION AND SEDIMENTATION OF ORGANIC MATTER IN LAKE WATER

Natural organic matter (NOM) in lakes strongly influences the fate and behaviour of toxic substances and nutrients. Depending on its nature (*e.g.* whether it is humic matter of terrestrial origin or is made up of non-humic compounds, such as polysaccharides of aquatic origin), NOM will follow different pathways of biophysicochemical transformation that will influence its aggregation and sedimentation properties, which, in turn, will affect

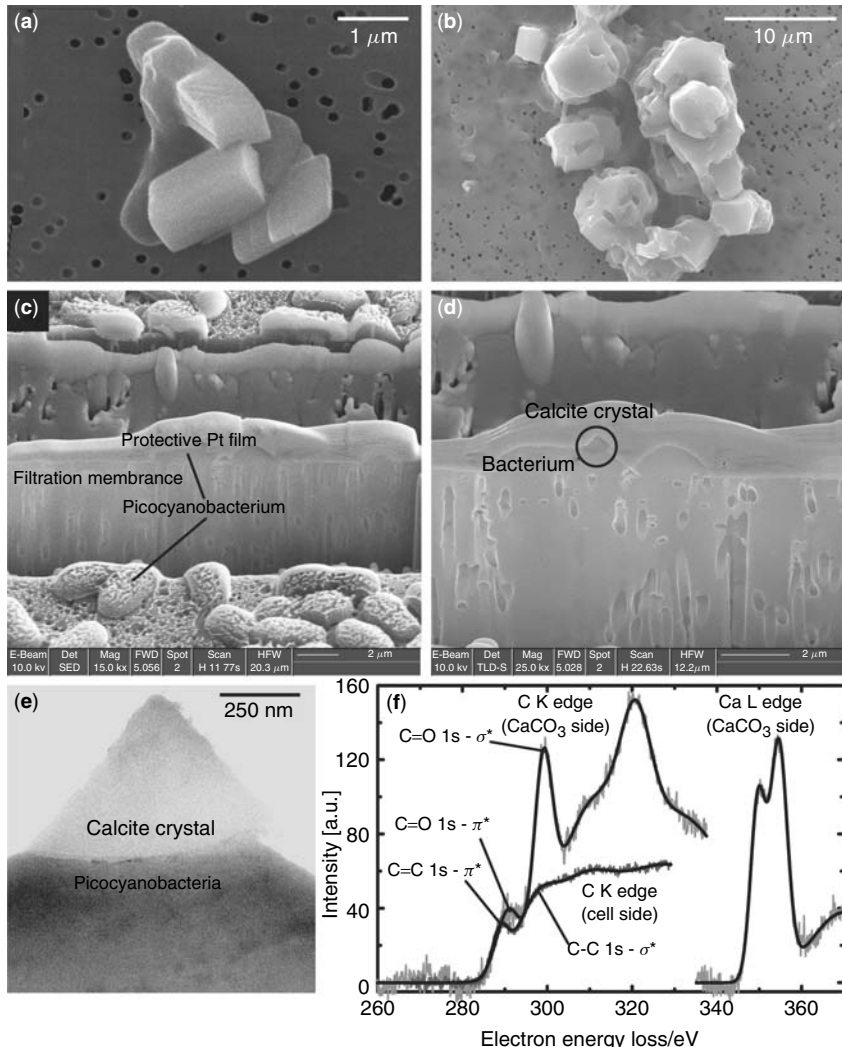


**Figure 18.** *Synechococcus* picocyanobacteria cells catalyse the growth of calcite crystals onto their surface (a) and may even become embedded in calcite at a later stage of precipitation (b). (c) FIB is used to mill a selected portion of a cell specimen being prepared by filtration on to Nuclepore membranes. The SEM micrograph (d) of the FIB-prepared section reveals the presence of a calcite crystal (circle; the layer above the cell-crystal interface is a protective platinum coating). The equivalent TEM micrograph (e) highlights the interface between the cell surface and the calcite crystal. (f) EELS of the cell and the crystal shown in (d) and (e), revealing the different patterns of the carbon K-edge for the cell (organic carbon) and the crystal (inorganic carbon)

the distribution of the toxic substances and nutrients it transports. In a survey of the water column of Lake Geneva (Switzerland), Mavrocordatos and Wilkinson [301] distinguished colloidal organic substances from inorganic colloids by their poorly developed electron diffraction patterns, sizes, low electron density and ill-defined shapes when viewed by TEM. The micrographs of organic colloids were digitised, thresholded and binarised with

care to minimise image analysis artefacts. Two mathematical models were applied to calculate the fractal dimension,  $Df$ , of the resulting objects: the Minkowski model based on the contour of the object (Figure 19a), and the Witten–Sanders model based on the center of mass of the object (Figure 19b).

The absolute values of  $Df$  were different for the two mathematical operations (Minkowski,  $Df = 1.22\text{--}1.1$ ; Witten–Sanders,  $Df = 1.9\text{--}1.75$ ), and no clear conclusion

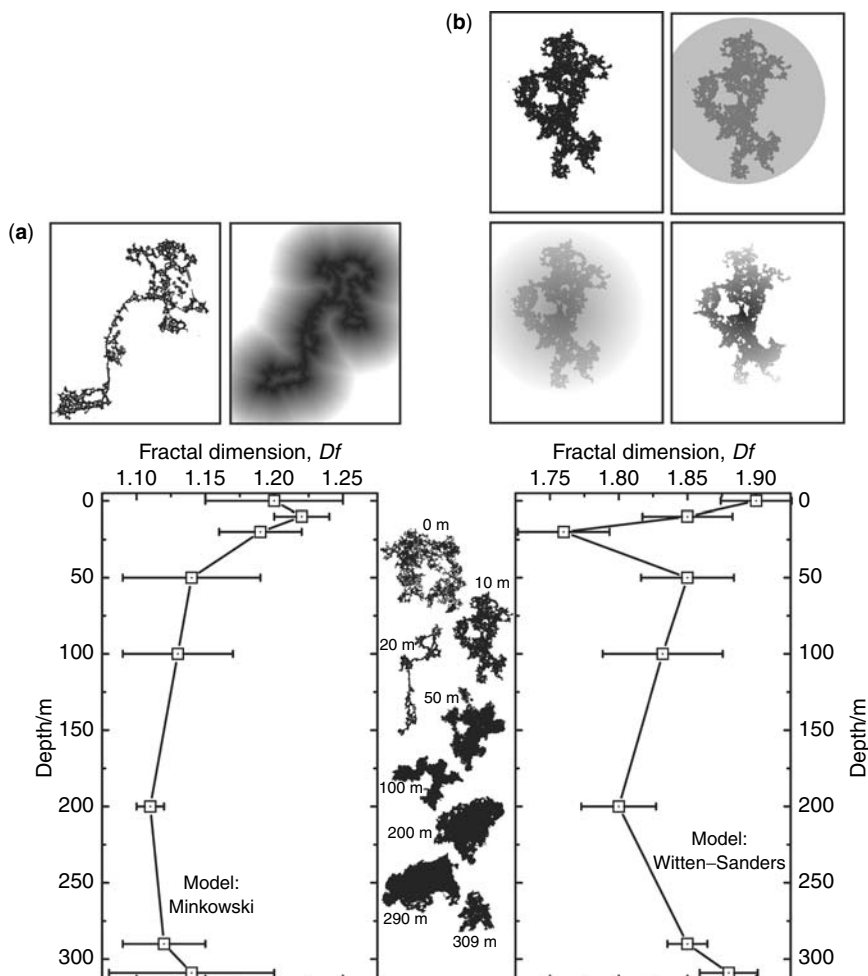


**Figure 19.** (a) The two images at top left show the binarised TEM image of an organic colloid in the water column of a deep lake and the corresponding Euclidean distance map used to calculate the fractal dimension ( $Df$ ) of the colloid by the Minkowski approach, which gives an estimate of the compactness of the object. (b) The four images at top right schematise the Witten–Sanders approach, which consists in drawing concentric circles centered on the binarised colloid, to determine the number of intersections between the circles and the object.  $Df$  is derived from the relationship between the number of intersections and distance. The two profiles at the bottom show the evolution of  $Df$  with depth in the lake. Typical examples of binarised organic colloids found at different depths are given between the two plots

could be drawn regarding the conditions that typically promote aggregation of NOM in the water column, or whether the phenomenon is diffusion-limited or reaction-limited, owing to the heterogeneous nature of the polysaccharide–humic matter complexes that constituted the colloids. The two models demonstrated a gradual decrease in the fractal dimension of the objects with depth, followed by a weak increase in  $Df$  at the water–sediment interface, reflecting both compaction of refractory NOM as it settles and heterogeneity of colloidal NOM at the sediment–water interface.

## 6.8 COPPER SCAVENGING FROM ROOF RUNOFF

Among heavy metal contaminants in the environment, copper is ubiquitous owing to its wide use in human activities. Cu in runoff may originate in large part from corroding copper surfaces on roofs. For example, up to 50% of the Swiss copper load in sewer systems can be related to roof runoff. These potentially dangerous fluxes (Figure 20) can be limited by selective on-site filter/adsorbent systems, consisting of impacted iron oxides (5–500 nm), through which roof runoff is passed. Mavrocordatos *et al.* [302] tested the scavenging efficiency of the iron oxide filter by means of quantitative ultracentrifugation, SEM–FIB sectioning and TEM–EELS identification of the adsorbing material. They observed that up to 95–99% of the copper present in roof runoff was retained by the iron oxide adsorbent. As shown in Figure 20, high-resolution EF-TEM maps of the granular iron oxides revealed that Cu was evenly distributed within the impacted filter/adsorbent particles as a result of their high permeability and surface area (water diffuses through nanochannels in the porous iron oxide). In addition, iron oxides are effective scavengers of heavy metals such as  $\text{Cu}^{2+}$ , because they have many sites where metal ions can be strongly bound by surface complexation.

Moreover, iron oxides were shown to be surrounded by a relatively thick layer of Cu (up to 20 nm), which may be attributed to a carbonate form,  $\text{Cu}_2(\text{OH})_2\text{CO}_3$ , in agreement with the physicochemical conditions of the ambient medium ( $\text{pH} = 7.5$ ) and the EELS correlations between copper and carbon at the nanometre scale. For the sake of fine adjustment of the chemical behaviour of the filter/adsorbent material with respect to copper, Mavrocordatos *et al.* [303] synthesised hydrous ferric oxides and reacted them with solutions containing  $\text{Cu}^{2+}$  at various concentrations; using a combination of optimal specimen preparation (ultracentrifugation on to holey carbon film) and high-resolution parallel EELS (PEELS; see Figure 20), they were able to demonstrate that EELS yields quantitative information even for trace metals.

## 7 CONCLUSION

The above selection of applications of analytical electron microscopy in water science exemplifies the progress achieved during the past decade in the development of highly efficient morphological and chemical techniques for characterisation of living and non-living microscopic entities in the natural environment on the micro- and nanometre scales.

Having progressed beyond its infancy, correlative AEM has become part of an integrated characterisation process applicable to raw or treated waters, from initial sampling to final quantitative results. At every step of the complete process, biases have been identified

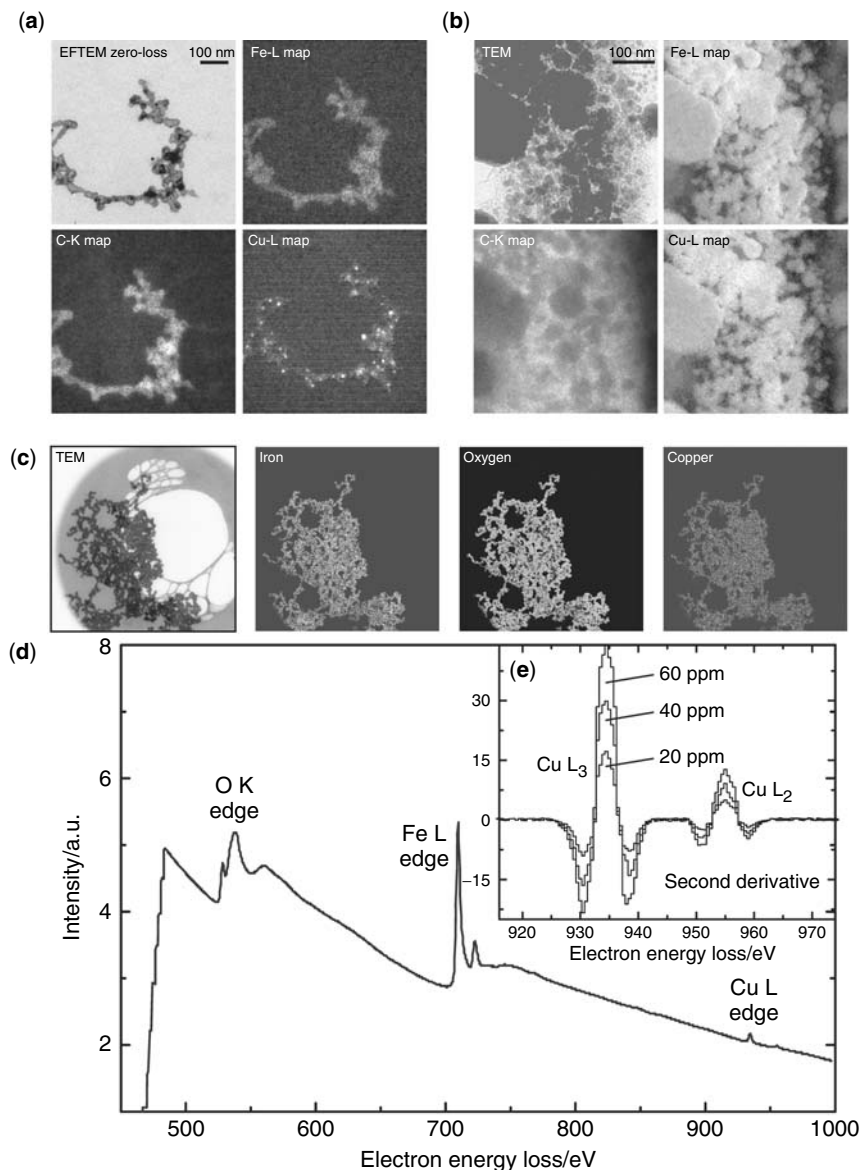


**Figure 20.** (a) Roof runoffs typically transport aggregates containing carbon, iron oxides and traces of copper; EFTEM element maps show that Cu is unevenly distributed in the aggregate and forms individual nanogranules. (b) The impacted iron oxide filter/adsorbent retains most of the copper in the runoffs. EFTEM element maps of this FIB section show that Cu is evenly distributed within the filter/adsorbent. (c) Laboratory experiments on synthetic hydrous ferric oxides (HFO) reacted with copper and mimic the filter/adsorbent. (d) The high-resolution EELS spectrum of Cu–HFO indicates the presence of copper, even at relatively high electron energy-losses. (e) The inset shows that the intensity of the Cu L<sub>2,3</sub> edge (second derivative for correct analysis) is directly linked to the concentration of Cu reacted with synthetic HFO

and overcome, while quantitative and representative specimen preparation schemes have been developed. The most suitable techniques of microscopy have been pinpointed and optimised in accordance with the specific requirements of the samples and finally, thanks to the power of image analysis software, representative and quantitative morphological and compositional parameters can be measured.

These days, microscopic techniques are no longer used merely to produce representative qualitative images of particulate matter in natural waters. They are also used very profitably to complement conventional bulk measurements and analyses, producing a wealth of information about variations in physical and chemical properties of sample materials on a microscopic scale, information that is far beyond the reach of the conventional methods.

## LIST OF ABBREVIATIONS

AEM	Analytical electron microscopy
AFM	Atomic force microscopy
CLSM	Confocal laser scanning microscopy
<i>Df</i>	Fractal dimension
DLCA	Diffusion-limited colloid aggregation
ECD	Equivalent circle diameter
X-EDS	Energy-dispersive X-ray spectroscopy
EELS	Electron energy-loss spectrometry
EF-TEM	Energy-filtered transmission electron microscopy
ELNES	Energy-loss near-edge structure
EM	Electron microscopy
EPS	Extracellular polymeric substances (exocellular polysaccharides)
ESEM	Environmental scanning electron microscopy
ESI	Electron spectroscopic imaging
FEG	Field emission gun
FIB	Focused ion beam
ICP-AES	Inductively coupled plasma atomic emission spectrometry
ICP-MS	Inductively coupled plasma mass spectrometry
NOM	Natural organic matter
PAH	Polycyclic aromatic hydrocarbon
PCB	Polychlorinated biphenyl
PEELS	Parallel electron energy-loss spectrometry
PIXE	Proton-induced X-ray emission
PSD	Particle size distribution
RG	Radius of gyration
RLCA	Reaction-limited colloid aggregation
ROI	Region of interest
SAED	Selected-area electron diffraction
SEM	Scanning electron microscopy
SF	Shape factor
SMPS	Scanning mobility particle sizer
STEM	Scanning-transmission electron microscopy

STM	Scanning tunnelling microscopy
STXM	Scanning-transmission X-ray microscopy
TEM	Transmission electron microscopy
XANES	X-ray absorption near-edge structure
X-EDS	X-ray energy-dispersive spectroscopy
XRF	X-ray fluorescence
XRD	X-ray diffraction

## REFERENCES

- Doucet, F. J., Maguire, L. and Lead, J. R. (2004). Size fractionation of aquatic colloids and particles by cross-flow filtration: analysis by scanning electron and atomic force microscopy, *Anal. Chim. Acta*, **522**, 59–71.
- Gustafsson, O. and Gschwend, P. M. (1997). Aquatic colloids: concepts, definitions, and current challenges, *Limnol. Oceanogr.*, **42**, 519–528.
- El Samrani, A. G., Lartiges, B. S., Ghanbaja, J., Yvon, J. and Kohler, A. (2004). Trace element carriers in combined sewer during dry and wet weather: an electron microscope investigation, *Water Res.*, **38**, 2063–2076.
- Mavrocordatos, D., Mondi-Couture, C., Atteia, O., Leppard, G. G. and Perret, D. (2000). Formation of a distinct class of Fe–Ca( $-C_{org}$ )-rich particles in a complex peat–karst system, *J. Hydrol.*, **237**, 234–247.
- Taillefert, M., Lienemann, C. P., Gaillard, J. F. and Perret, D. (2000). Speciation, reactivity, and cycling of Fe and Pb in a meromictic lake, *Geochim. Cosmochim. Acta*, **64**, 169–183.
- Buffle, J., Wilkinson, K. J., Stoll, S., Filella, M. and Zhang, J. (1998). A generalized description of aquatic colloidal interactions: the three-colloidal component approach, *Environ. Sci. Technol.*, **32**, 2887–2899.
- Liao, B. Q., Allen, D. G., Leppard, G. G., Droppo, I. G. and Liss, S. N. (2002). Interparticle interactions affecting the stability of sludge flocs, *J. Colloid Interface Sci.*, **249**, 372–380.
- Campbell, P. G. C., Twiss, M. R. and Wilkinson, K. J. (1997). Accumulation of natural organic matter on the surfaces of living cells: implications for the interaction of toxic solutes with aquatic biota, *Can. J. Fish. Aquat. Sci.*, **54**, 2543–2554.
- Chatellier, X., Fortin, D., West, M. M., Leppard, G. G. and Ferris, F. G. (2001). Effect of the presence of bacterial surfaces during the synthesis of Fe oxides by oxidation of ferrous ions, *Eur. J. Miner.*, **13**, 705–714.
- Chatellier, X., West, M. G., Rose, J., Fortin, D., Leppard, G. G. and Ferris, F. G. (2004). Characterization of iron-oxides formed by oxidation of ferrous ions in the presence of various bacterial species and inorganic ligands, *Geomicrobiol. J.*, **21**, 99–112.
- Fortin, D. (2004). Geochemistry: what biogenic minerals tell us, *Science*, **303**, 1618–1619.
- Jackson, T. A. and Leppard, G. G. (2002). Energy dispersive X-ray microanalysis and its applications in biogeochemical research, *Dev. Soil Sci.*, **28A**, 219–260.
- Jackson, T. A., West, M. M. and Leppard, G. G. (1999). Accumulation of heavy metals by individually analyzed bacterial cells and associated nonliving material in polluted lake sediments, *Environ. Sci. Technol.*, **33**, 3795–3801.
- Schultze-Lam, S., Fortin, D., Davis, B. S. and Beveridge, T. J. (1996). Mineralization of bacterial surfaces, *Chem. Geol.*, **132**, 171–181.
- Webb, S. M., Leppard, G. G. and Gaillard, J. F. (2000). Zinc speciation in a contaminated aquatic environment: characterization of environmental particles by analytical electron microscopy, *Environ. Sci. Technol.*, **34**, 1926–1933.
- Lartiges, B. S., Deneux-Mustin, S., Villemin, G., Mustin, C., Barres, O., Chamerois, M., Gerard, B. and Babut, M. (2001). Composition, structure and size distribution of suspended particulates from the Rhine River, *Water Res.*, **35**, 808–816.

17. Leppard, G. G., Flannigan, D. T., Mavrocordatos, D., Marvin, C. H., Bryant, D. W. and McCarry, B. E. (1998). Binding of polycyclic aromatic hydrocarbons by size classes of particulate in Hamilton Harbor water, *Environ. Sci. Technol.*, **32**, 3633–3639.
18. Marvin, C. H., Leppard, G. G., West, M. M., Stern, G. A., Boden, A. R. and McCarry, B. E. (2004). Refined tunable methodology for characterization of contaminant–particle relationships in surface water, *J. Environ. Qual.*, **33**, 2132–2140.
19. Lienemann, C. P., Taillefert, M., Perret, D. and Gaillard, J. F. (1997). Association of cobalt and manganese in aquatic systems: chemical and microscopic evidence, *Geochim. Cosmochim. Acta*, **61**, 1437–1446.
20. Chan, C. S., De Stasio, G., Welch, S. A., Girasole, M., Frazer, B. H., Nesterova, M. V., Fakra, S. and Banfield, J. F. (2004). Microbial polysaccharides template assembly of nanocrystal fibers, *Science*, **303**, 1656–1659.
21. Fortin, D., Ferris, F. G. and Beveridge, T. J. (1997). Surface-mediated mineral development by bacteria, *Rev. Miner.*, **35**, 161–180.
22. Leppard, G. G. and Dropo, I. G. (2003). The need and means to characterize sediment structure and behavior prior to the selection and implementation of remediation plans, *Hydrobiologia*, **494**, 313–317.
23. Leppard, G. G., Dropo, I. G., West, M. M. and Liss, S. N. (2003). Compartmentalization of metals within the diverse colloidal matrices comprising activated sludge microbial flocs, *J. Environ. Qual.*, **32**, 2100–2108.
24. Liao, B. Q., Bagley, D. M., Kraemer, H. E., Leppard, G. G. and Liss, S. N. (2004). A review of biofouling and its control in membrane separation bioreactors, *Water Environ. Res.*, **76**, 425–436.
25. He, Q. H., Leppard, G. G., Paige, C. R. and Snodgrass, W. J. (1996). Transmission electron microscopy of a phosphate effect on the colloid structure of iron hydroxide, *Water Res.*, **30**, 1345–1352.
26. Dropo, I. G., Leppard, G. G., Flannigan, D. T. and Liss, S. N. (1997). The freshwater floc: a functional relationship of water and organic and inorganic floc constituents affecting suspended sediment properties, *Water Air Soil Pollut.*, **99**, 43–54.
27. Lawrence, J. R., Swerhone, G. D. W., Leppard, G. G., Araki, T., Zhang, X., West, M. M. and Hitchcock, A. P. (2003). Scanning transmission X-ray, laser scanning, and transmission electron microscopy mapping of the exopolymeric matrix of microbial biofilms, *Appl. Environ. Microbiol.*, **69**, 5543–5554.
28. Perret, D., Newman, M. E., Negre, J. C., Chen, Y. and Buffle, J. (1994). Submicron particles in the Rhine River—I. Physico-chemical characterization, *Water Res.*, **28**, 91–106.
29. Leppard, G. G. (1992). Evaluation of electron microscope techniques for the description of aquatic colloids. In *Environmental Particles*, eds Buffe, J. and van Leeuwen, H. P. IUPAC Series on Analytical and Physical Chemistry of Environmental Systems, Vol.1. Lewis, Boca Raton, FL, pp. 231–289.
30. Leppard, G. G. (1992). Size, morphology and composition of particulates in aquatic ecosystems: solving speciation problems by correlative electron microscopy, *Analyst*, **117**, 595–603.
31. Lienemann, C. P., Heissenberger, A., Leppard, G. G. and Perret, D. (1998). Optimal preparation of water samples for the examination of colloidal material by transmission electron microscopy, *Aquat. Microb. Ecol.*, **14**, 205–213.
32. Mavrocordatos, D. and Perret, D. (1998). Quantitative and qualitative characterization of aquatic iron oxyhydroxide particles by EF-TEM, *J. Microsc.*, **191**, 83–90.
33. Mavrocordatos, D., Lienemann, C. P. and Perret, D. (1994). Energy filtered transmission electron microscopy for the physico-chemical characterization of aquatic submicron colloids, *Mikrochim. Acta*, **117**, 39–47.
34. Mondi, C., Leifer, K., Mavrocordatos, D. and Perret, D. (2002). Analytical electron microscopy as a tool for accessing colloid formation process in natural waters, *J. Microsc.*, **207**, 180–190.
35. Perret, D., Leppard, G. G., Mueller, M., Belzile, N., De Vitre, R. and Buffe, J. (1991). Electron microscopy of aquatic colloids: non-perturbing preparation of specimens in the field, *Water Res.*, **25**, 1333–1343.

36. Perret, D., Gaillard, J. F., Dominik, J. and Atteia, O. (2000). The diversity of natural hydrous iron oxides, *Environ. Sci. Technol.*, **34**, 3540–3546.
37. Wilkinson, K. J., Balnois, E., Leppard, G. G. and Buffe, J. (1999). Characteristic features of the major components of freshwater colloidal organic matter revealed by transmission electron and atomic force microscopy, *Colloids Surf. A*, **155**, 287–310.
38. Xhoffer, C., Wouters, L. and Van Grieken, R. (1992). Characterization of individual particles in the North Sea surface microlayer and underlying seawater: comparison with atmospheric particles, *Environ. Sci. Technol.*, **26**, 2151–2162.
39. Perret, D., Mavrocordatos, D. and Lienemann, C.-P. (1994). Natural microparticles–macromolecules interactions: an EFTEM approach. In *Electron Microscopy 1994, Proc. 13th Int. Congr. Electr. Microsc.*, Paris, 17–22 July 1994, pp. 1277–1278.
40. Leppard, G. G. and Buffe, J. (1998). Aquatic colloids and macromolecules: effects on analysis. In *Encyclopedia of Environmental Analysis and Remediation*, Vol. 1, ed. Meyers, R. A. John Wiley & Sons, Inc., New York, 349–377.
41. Perret, D., Leppard, G. G. and Mavrocordatos, D. (2005). Microscopy: environmental applications. In *Encyclopedia of Analytical Science*, eds Worsfold, P. J., Townsend, A. and Poole, C. F. Elsevier, Oxford, pp. 65–74.
42. Goldstein, J. I. and Yakowitz, H. (1975). *Practical Scanning Electron Microscopy: Electron and Ion Microprobe Analysis*. Plenum Press, New York.
43. Holt, D. B., Muir, M. D., Grant, P. R., and Boswarva, I. M. (1974). *Quantitative Scanning Electron Microscopy*. Academic Press, New York. 570 pp.
44. Kiss, K. (1987). Industrial problem solving with microbeam analysis, *Scanning Microsc.*, **1**, 1515–1538.
45. Murr, L. E. (1991). *Electron and Ion Microscopy and Microanalysis. Principles and Applications, Optical Engineering*. Marcel Dekker, New York.
46. Reimer, L. (1984). Scanning electron microscopy, *Comm. Eur. Commun. Rep.*, EUR8824, 141–168.
47. Wells, O. C., Boyde, A., Lifshin, E. and Rezanowich, A. (1974). *Scanning Electron Microscopy*. McGraw-Hill, New York.
48. Hawkes, P. W., Mulvey, T. and Kazan, B. (2002). *Advances in Imaging and Electron Physics*, Vol. 121. Academic Press, San Diego, CA.
49. Reed, S. J. B. (1993). *Electron Microprobe Analysis*. Cambridge University Press, Cambridge.
50. Rossiter, B. W. and Hamilton, J. F. (1991). *Physical Methods of Chemistry*, Vol. 4, *Microscopy*. Wiley-Interscience, New York.
51. Santschi, P. H., Balnois, E., Wilkinson, K. J., Zhang, J., Buffe, J. and Guo, L. (1998). Fibrillar polysaccharides in marine macromolecular organic matter as imaged by atomic force microscopy and transmission electron microscopy, *Limnol. Oceanogr.*, **43**, 896–908.
52. Webb, S. M., Gaillard, J. F. and Leppard, G. G. (2000). Analytical electron microscopy characterization of zinc speciation in a contaminated system, *Abstr. 220th ACS Nat. Meet.*, Washington, DC, 20–24 August 2000, ENVR-271.
53. Berube, K. A., Jones, T. P., Williamson, B. J., Winters, C., Morgan, A. J. and Richards, R. J. (1999). Physicochemical characterization of diesel exhaust particles: factors for assessing biological activity, *Atmos. Environ.*, **33**, 1599–1614.
54. Chabas, A. and Lefevre, R. A. (1999). Chemistry and microscopy of atmospheric particulates at Delos (Cyclades, Greece), *Atmos. Environ.*, **34**, 225–238.
55. Conner, T. L., Norris, G. A., Landis, M. S. and Williams, R. W. (2001). Individual particle analysis of indoor, outdoor, and community samples from the 1998 Baltimore particulate matter study, *Atmos. Environ.*, **35**, 3935–3946.
56. Hueglin, C., Gaegauf, C., Kuenzel, S. and Burtscher, H. (1997). Characterization of wood combustion particles: morphology, mobility, and photoelectric activity, *Environ. Sci. Technol.*, **31**, 3439–3447.
57. Kaegi, R. and Holzer, L. (2003). Transfer of a single particle for combined ESEM and TEM analyses, *Atmos. Environ.*, **37**, 4353–4359.
58. Mavrocordatos, D., Kaegi, R. and Schmatloch, V. (2002). Fractal analysis of wood combustion aggregates by contact mode atomic force microscopy, *Atmos. Environ.*, **36**, 5653–5660.

59. Naoe, H. and Okada, K. (2001). Mixing properties of submicrometer aerosol particles in the urban atmosphere – with regard to soot particles, *Atmos. Environ.*, **35**, 5765–5772.
60. Osan, J., Alfoldy, B., Torok, S. and Van Grieken, R. (2002). Characterisation of wood combustion particles using electron probe microanalysis, *Atmos. Environ.*, **36**, 2207–2214.
61. Rietmeijer, F. J. M. and Janeczek, J. (1997). An analytical electron microscope study of airborne industrial particles in Sosnowiec, Poland, *Atmos. Environ.*, **31**, 1941–1951.
62. Shi, J. P., Harrison, R. M. and Brear, F. (1999). Particle size distribution from a modern heavy duty diesel engine, *Sci. Total. Environ.*, **235**, 305–317.
63. Shukla, S., Seal, S., Akesson, J., Oder, R., Carter, R. and Rahman, Z. (2001). Study of mechanism of electroless copper coating of fly-ash cenosphere particles, *Appl. Surf. Sci.*, **181**, 35–50.
64. Watt, J. (1998). Automated characterization of individual carbonaceous fly-ash particles by computer controlled scanning electron microscopy: analytical methods and critical review of alternative techniques, *Water Air Soil Pollut.*, **106**, 309–327.
65. Xhoffer, C., Jacob, W., Buseck, P. R. and Van Grieken, R. (1995). Problems in quantitatively analyzing individual salt aerosol particles using electron energy loss spectroscopy, *Spectrochim. Acta B*, **50**, 1281–1292.
66. Maura de Miranda, R., Andrade, M. d. F., Worobiec, A. and Van Grieken, R. (2002). Characterisation of aerosol particles in the São Paulo Metropolitan Area, *Atmos. Environ.*, **36**, 345–352.
67. Jones, T. P., Williamson, B. J., Berube, K. A. and Richards, R. J. (2001). Microscopy and chemistry of particles collected on TEOM filters: Swansea, south Wales, 1998–1999, *Atmos. Environ.*, **35**, 3573–3583.
68. Bang, J. J. and Murr, L. E. (2002). Collecting and characterizing atmospheric nanoparticles, *J. Miner. Metals Mater. Soc.*, **54**, 28–30.
69. Buffat, P. A. (1999). Electron microscopy for the characterisation of atmospheric particles, *Analisis*, **27**, 340–346.
70. Harrison, R. and Van Grieken, R. (1998). *Atmospheric Particles*. John Wiley & Sons, Inc., New York.
71. Micic, M., Markovic, D., Vukelic, N., Radu, A., Milosevic, B. and Leblanc, R. M. (2000). Environmental scanning electron microscopy study of commonly used filters substrates for the active sampling of atmospheric aerosols, *Fresenius' Environ. Bull.*, **9**, 193–200.
72. Pooley, F. D., de Mille, M. G., (1999). Microscopy and the characterization of particles. In *Particulate Matter: Properties and Effects Upon Health*, eds Maynard, R. L. and Howard, C. V. BIOS Scientific Publishers, Oxford, pp. 19–37.
73. Russel, P. A. (1990). The analysis of anthropogenic atmospheric particulates by electron microscopy, *Microbeam Anal.*, **25**, 445–448.
74. Schlaegle, S. F. and Doerr, A. (2000). Approaches to the collection and analysis of nuisance dust using a combination of old and new sampling methods and analytical techniques. In *Proc. 93rd Air Waste Manag. Ass. Annu. Conf. Exhib.*, Salt Lake City, 18–22 June 2000, pp. 215–223.
75. Ormstad, H., Gaarder, P. I. and Johansen, B. V. (1997). Quantification and characterisation of suspended particulate matter in indoor air, *Sci. Total Environ.*, **193**, 185–196.
76. Ali, A. E. and Bacso, J. (1996). Investigation of different types of filters for atmospheric trace elements analysis by three analytical techniques, *J. Radioanal. Nucl. Chem.*, **209**, 147–155.
77. Eleftheriadis, K. and Colbeck, I. (2000). The fractionation of atmospheric coarse aerosol by a tunnel sampler employing single stage impactors, *J. Aerosol Sci.*, **31**, 321–334.
78. Kronholm, D. F. and Howard, J. B. (2000). Analysis of soot surface growth pathways using published plug-flow reactor data with new particle size distribution measurements and published premixed flame data, *Proc. Combust. Inst.*, **28**, 2555–2561.
79. Lu, R., Turco, R., Stolzenbach, K., Friedlander, S., Xiong, C., Schiff, K., Tiefenthaler, L. and Guangyu, W. (2003). Dry deposition of airborne trace metals on the Los Angeles Basin and adjacent coastal waters, *J. Geophys. Res.*, **108**, AAC11–AAC24.
80. Thurmer, H. and Kersten, N. (2001). Measurement of ultrafine aerosols by a thermal precipitator, *Gefahrstoffe Reinhalt. Luft*, **61**, 275–279.

81. Chen, Y. L., Kreidenweis, S. M., McInnes, L. M., Rogers, D. C. and Demott, P. J. (1998). Single particle analyses of ice nucleating aerosols in the upper troposphere and lower stratosphere, *Geophys. Res. Lett.*, **25**, 1391–1394.
82. Delzeit, L. and Blake, D. (2001). A characterization of crystalline ice nanoclusters using transmission electron microscopy, *J. Geophys. Res.*, **106**, 33371–33379.
83. Okada, K. (1983). Nature of individual hygroscopic particles in the urban atmosphere, *J. Meteorol. Soc. Jpn.*, **61**, 727–736.
84. Posfai, M., Xu, H. F., Anderson, J. R. and Buseck, P. R. (1998). Wet and dry sizes of atmospheric aerosol particles: An AFM–TEM study, *Geophys. Res. Lett.*, **25**, 1907–1910.
85. Rogers, D. C., Demott, P. J. and Kreidenweis, S. M. (2001). Airborne measurements of tropospheric ice-nucleating aerosol particles in the Arctic spring, *J. Geophys. Res.*, **106**, 15053–15063.
86. Rogers, D. C., Demott, P. J., Kreidenweis, S. M. and Chen, Y. L. (2001). A continuous-flow diffusion chamber for airborne measurements of ice nuclei, *J. Atmos. Ocean. Technol.*, **18**, 725–741.
87. Ebert, M., Inerle-Hof, M. and Weinbruch, S. (2002). Environmental scanning electron microscopy as a new technique to determine the hygroscopic behaviour of individual aerosol particles, *Atmos. Environ.*, **36**, 5909–5916.
88. Huang, P. M., Senesi, N. and Buffle, J. (1998). *Structure and Surface Reactions of Soil Particles*. John Wiley & Sons, Ltd, Chichester.
89. Chen, Y. and Schnitzer, M. (1976). Water adsorption on soil humic substances, *Can. J. Soil Sci.*, **56**, 521–524.
90. Chen, Y., Banin, A. and Schnitzer, M. (1976). Use of the scanning electron microscope for structural studies on soils and soil components, *Scanning Electron Microsc.*, **9**, 425–432.
91. Chen, Y. and Schnitzer, M. (1976). Scanning electron microscopy of a humic acid and a fulvic acid and its metal and clay complexes, *Soil Sci. Soc. Am. J.*, **40**, 682–686.
92. Chenu, C., Hassink, J. and Bloem, J. (2001). Short-term changes in the spatial distribution of microorganisms in soil aggregates as affected by glucose addition, *Biol. Fert. Soils*, **34**, 349–356.
93. Keller, C. and Mavrocordatos, D. (1997). Particulate matter and transfer of K, Cu, Al and Fe in the soil solutions of a podzol: preliminary results on semi-quantitative and qualitative approaches, *Coll. Inst. Nat. Rech. Agron.*, **85**, 373–382.
94. Mavrocordatos, D. and Perret, D. (1995). Non-artifacted specimen preparation for transmission electron microscopy of submicron soil particles, *Comm. Soil Sci. Plant Anal.*, **26**, 2593–2602.
95. Chen, Y. and Banin, A. (1975). Scanning electron microscope (SEM) observations of soil structure changes induced by sodium–calcium exchange in relation to hydraulic conductivity, *Soil Sci.*, **120**, 428–436.
96. Chen, Y. (1998). *Electron Microscopy of Soil Structure and Soil Components*. John Wiley & Sons, Ltd, Chichester.
97. Citeau, L., Lamy, I., van Oort, F. and Elsass, F. (2001). Nature of soils and nature of mobile colloids in gravitational water: a field study, *C. R. Acad. Sci. A*, **332**, 657–663.
98. Golchin, A., Oades, J. M., Skjemstad, J. O. and Clarke, P. (1994). Study of free and occluded particulate organic matter in soils by solid-state C-13 CP/MAS NMR-spectroscopy and scanning electron-microscopy, *Aust. J. Soil Res.*, **32**, 285–309.
99. Huber, K. and Deniaux, L. (2000). Genesis and transfer of colloids in gravitational waters of an alpine podzol, *C. R. Acad. Sci. A*, **330**, 251–258.
100. Laird, D. (2001). Nature of clay–humic complexes in an agricultural soil: II. Scanning electron microscopy analysis, *Soil Sci. Soc. Am. J.*, **65**, 1419–1425.
101. Elsass, F., van Oort, F., Le Mot, Y. and Jaunet, A. M. (2002). Identification minéralogique des polluants par microscopies électroniques. In *Les Éléments Traces Métalliques dans les Sols: Approches Fonctionnelles et Spatiales*, eds Baize, D. and Tercé, M. Editions INRA, Versailles, pp. 331–350.
102. Righi, D., Elsass, F. and Lapeyronnie, J. P. (1999). Clay minerals in soils: global characterization by X-ray diffraction in the study of particles with analytical electron microscopy.

- In *Structure et Ultrastructure des Sols et des Organismes Vivants*, eds Elsass, F. and Jaunet, A. M. Colloques de l'INRA, Versailles, pp. 79–92.
- 103. Seaman, J. C. (2000). Thin-foil SEM analysis of soil and groundwater colloids: reducing instrument and operator bias, *Environ. Sci. Technol.*, **34**, 187–191.
  - 104. Southard, R. J., Shainberg, I. and Singer, M. J. (1988). Influence of electrolyte concentration on the micromorphology of artificial depositional crust, *Soil Sci.*, **145**, 278–288.
  - 105. Tiessen, H. and Stewart, J. W. B. (1988). Light and electron microscopy of stained microaggregates – the role of organic matter and microbes in soil aggregation, *Biogeochemistry*, **5**, 312–322.
  - 106. de Boer, D. H. and Crosby, G. (1995). Evaluating the potential of SEM/EDS analysis for fingerprinting suspended sediment derived from two contrasting topsoils, *Catena*, **24**, 243–258.
  - 107. Buffle, J. and Leppard, G. G. (1995). Characterization of aquatic colloids and macromolecules. 2. Key role of physical structures on analytical results, *Environ. Sci. Technol.*, **29**, 2176–2184.
  - 108. Belzile, N., De Vitre, R. R. and Tessier, A. (1989). *In situ* collection of diagenetic iron and manganese oxyhydroxides from natural sediments, *Nature*, **340**, 376–377.
  - 109. Citeau, L., Lamy, I., van Oort, F. and Elsass, F. (2002). Role of colloids in the metal mobilisation in soils: a field study, *Geochim. Cosmochim. Acta*, **66**, A142.
  - 110. Redwood, P. S., Lead, J. R., Harrison, R. M., Jones, I. P. and Stoll, S. (2005). Characterization of humic substances by environmental scanning electron microscopy, *Environ. Sci. Technol.*, **39**, 1962–1966.
  - 111. Froesch, D. and Westphal, C. (1985). Choosing the appropriate section thickness in the melamine embedding technique, *J. Microsc.*, **137**, 177–183.
  - 112. Froesch, D. and Westphal, C. (1989). Melamine resins and their application in electron microscopy, *Electron Microsc. Rev.*, **2**, 231–255.
  - 113. Lewis, P. R. and Knight, D. P. (1992). Introduction to cytochemical staining methods for electron microscopy. In *Cytochemical Staining methods for Electron Microscopy*, eds Lewis, P. R and Knight, D. P. Practical Methods in Electron Microscopy, Vol. 14. Elsevier, Amsterdam, 1–29.
  - 114. Knight, D. and Lewis, P. (1992). General cytochemical methods. In *Cytochemical Staining Methods for Electron Microscopy*, eds Lewis, P. R and Knight, D. P. Practical Methods in Electron Microscopy, Vol. 14. Elsevier, Amsterdam, 79–145.
  - 115. Lewis, P. (1992). Other cytochemical methods for enzymes. In *Cytochemical Staining Methods for Electron Microscopy*, eds Lewis, P. R and Knight, D. P. Practical Methods in Electron Microscopy, Vol. 14. Elsevier, Amsterdam, 237–298.
  - 116. Spurr, A. R. and Galle, P. (1979). Localization of elements in botanical materials by secondary ion mass spectrometry, *Springer Ser. Chem. Phys.*, **9**, 252–255.
  - 117. Spurr, A. R. (1969). A low-viscosity epoxy resin embedding medium for electron microscopy, *J. Ultrastruct. Res.*, **26**, 31–43.
  - 118. Liss, S. N., Droppo, I. G., Flannigan, D. T. and Leppard, G. G. (1996). Floc architecture in wastewater and natural riverine systems, *Environ. Sci. Technol.*, **30**, 680–686.
  - 119. Dubochet, J., Booy, F. P., Freeman, R., Jones, A. V. and Walter, C. A. (1981). Low temperature electron microscopy, *Annu. Rev. Biophys. Bioeng.*, **10**, 133–149.
  - 120. Dubochet, J., Alba, C. M., MacFarlane, D. R., Angell, C. A., Kadiyala, R. K., Adrian, M. and Teixeira, J. (1984). Glass-forming microemulsions: vitrification of simple liquids and electron microscope probing of droplet-packing modes, *J. Phys. Chem.*, **88**, 6727–6732.
  - 121. Dubochet, J. and Lepault, J. (1984). Cryo-electron microscopy of vitrified water, *J. Phys. (Paris)*, **9**, 85–94.
  - 122. Dubochet, J., Bednar, J., Furrer, P. and Stasiak, A. (1994). Cryo-electron microscopy of DNA, *Nucleic Acids Mol. Biol.*, **8**, 41–55.
  - 123. Dubochet, J., Adrian, M. and Vogel, R. H. (1983). Amorphous solid water obtained by vapor condensation or by liquid cooling: a comparison in the electron microscope, *Cryo-Letters*, **4**, 233–240.
  - 124. Dubochet, J. (1987). Life, liquids and cryo-electron microscopy, *Europhys. News*, **18**, 54–56.
  - 125. Dubochet, J., Adrian, M., Dustin, I., Furrer, P. and Stasiak, A. (1992). Cryoelectron microscopy of DNA molecules in solution, *Methods Enzym.*, **211**, 507–518.

126. Kirk, E. C. G., Williams, D. A. and Ahmed, H. (1989). Cross-sectional transmission electron microscopy of precisely selected regions from semiconductor devices, *Inst. Phys. Conf. Ser.*, **100**, 501–506.
127. Phaneuf, M. W., Rowlands, N., Carpenter, G. J. C. and Sundaram, G. (1997). Focused ion beam sample preparation of non-semiconductor materials, *Mater. Res. Soc. Symp. Proc.*, **480**, 39–47.
128. Tanaka, A., Shimizu, T., Kikuchi, M., Kobayashi, Y., Yamashita, T. and Watanabe, H. (1997). Biological effect of penetration controlled irradiation with ion beams. In *Proc. 7th Int. Symp. Adv. Nucl. Energy Res.* JAERI-Conf 97-003, pp. 323–326.
129. Tanaka, A., Watanabe, H., Shimizu, T., Inoue, M., Kikuchi, M., Kobayashi, Y. and Tano, S. (1997). Penetration controlled irradiation with ion beams for biological study, *Nucl. Instrum. Methods Phys. Res. B*, **129**, 42–48.
130. Loos, J., van Duren, J. K. J., Morrissey, F. and Janssen, R. A. J. (2002). The use of the focused ion beam technique to prepare cross-sectional transmission electron microscopy specimen of polymer solar cells deposited on glass, *Polymer*, **43**, 7493–7496.
131. Barna, A., Pecz, B. and Menyhard, M. (1998). Amorphization and surface morphology development at low-energy ion milling, *Ultramicroscopy*, **70**, 161–171.
132. Barna, A., Menyhard, M., Zsolt, G., Koos, A., Zalar, A. and Panjan, P. (2003). Interface broadening due to  $\text{Ar}^+$  ion bombardment measured on Co/Cu multilayer at grazing angle of incidence, *J. Vac. Sci. Technol. A*, **21**, 553–557.
133. Barna, A., Menyhard, M., Zalar, A. and Panjan, P. (2005). Ion bombardment induced interface broadening in Co/Cu system as a function of layer thickness, *Appl. Surf. Sci.*, **242**, 375–379.
134. Longo, D. M., Howe, J. M. and Johnson, W. C. (1999). Experimental method for determining Cliff–Lorimer factors in transmission electron microscopy (TEM) utilizing stepped wedge-shaped specimens prepared by focused ion beam (FIB) thinning, *Ultramicroscopy*, **80**, 85–97.
135. Labar, J. L. and Egerton, R. (1999). Special issue on ion beam techniques, *Micron*, **30**, 195–196.
136. Hall, J. L. (1978). *Electron Microscopy and Cytochemistry of Plant Cells*. Elsevier/North-Holland Biomedical Press, Amsterdam.
137. Newman, G. R. and Hobot, J. A. (2001). *Resin Microscopy and On-Section Immunocytochemistry*. Springer, Berlin.
138. Bullock, G. R. and Petrusz, P. (1983). *Techniques in Immunocytochemistry*. Academic Press, London.
139. Thiery, J. P. and Ovtracht, L. (1980). Ultrastructural chemistry on isolated molecules. Technique applied to some biological macromolecules. Study of metachromasy, *C. R. Soc. Biol.*, **174**, 584–597.
140. Thiery, J. P. (1967). Demonstration of polysaccharides in thin sections by electron microscopy, *J. Microsc. (Paris)*, **6**, 987–1018.
141. Chenu, C. (1993). Clay- or sand-polysaccharide associations as models for the interface between microorganisms and soil: water related properties and microstructure, *Geoderma*, **56**, 143–156.
142. Lienemann, C. P. (1997). Associations entre phases minérales de fer et de manganèse, polluants anthropogéniques et biota en milieu lacustre: mise en évidence par microscopie électronique. *Ph.D Thesis*, University of Lausanne.
143. Beesley, J. E. (1987). Colloidal gold. A modern, high resolution immunocytochemical marking system of wide applicability, *Int. Analyst*, **1**, 20–25.
144. Beesley, J. E. and Dougan, G. (1991). Detection of surface antigens by immunogold labeling, In *Microbial Cell Surface Analysis*, Mozes, N. ed., VCH, New York, 151–69.
145. Beesley, J. E. (1992). Preparation of gold probes. In *Immunochemical Protocols, Methods in Molecular Biology*, Vol. 10, ed. Manson M. M. Humana Press, Totowa, NJ, pp. 163–168.
146. Beesley, J. E. (1993). *Immunocytochemistry: a Practical Approach*. Oxford University Press, Oxford.

147. Benhamou, N. and Ouellette, G. B. (1986). Use of pectinases complexes to colloidal gold for the ultrastructural localization of polygalacturonic acids in the cell walls of the fungus *Ascocalyx abietina*, *Histochem. J.*, **18**, 95–104.
148. Benhamou, N., Chamberland, H., Ouellette, G. B. and Pauze, F. J. (1987). Ultrastructural localization of  $\beta$ -(1,4)-D-glucans in two pathogenic fungi and in their host tissues by means of an exoglucanase–gold complex, *Can. J. Microbiol.*, **33**, 405–417.
149. Benhamou, N., Gilboa-Garber, N., Trudel, J. and Asselin, A. (1988). A new lectin–gold complex for ultrastructural localization of galacturonic acids, *J. Histochem. Cytochem.*, **36**, 1403–1411.
150. Benhamou, N., Chamberland, H., Ouellette, G. B. and Pauze, F. J. (1988). Detection of galactose in two fungi causing wilt diseases and in their plant host tissues by means of gold-complexed *Ricinus communis* agglutinin I, *Physiol. Mol. Plant Pathol.*, **32**, 249–266.
151. Benhamou, N., Chamberland, H., Noel, S. and Ouellette, G. B. (1990). Ultrastructural localization of  $\beta$ -1,4-glucan-containing molecules in the cell walls of some fungi: a comparative study between spore and mycelium, *Can. J. Microbiol.*, **36**, 149–158.
152. Benhamou, N. (1992). Ultrastructural detection of  $\beta$ -1,3-glucans in tobacco root tissues infected by *Phytophthora parasitica* var. *nicotianae* using a gold-complexed tobacco  $\beta$ -1,3-glucanase, *Physiol. Mol. Plant Pathol.*, **41**, 351–370.
153. Dumasgaudot, E., Tahirialaoui, A. and Benhamou, N. (1992). Cytochemical localization of some polysaccharidic components in the cell-walls of *Chalara elegans* during its life-cycle, *Can. J. Microbiol.*, **38**, 828–837.
154. Horisberger, M. (1992). Applications of colloidal gold in cytochemistry. An overview, *Recent Adv. Cell. Mol. Biol.*, **4**, 263–269.
155. Horisberger, M. (1992). Colloidal gold and its application in cell biology, *Int. Rev. Cytol.*, **136**, 227–287.
156. Hayat, M. A. (1989). *Colloidal Gold: Principles, Methods, and Applications*, Vol. 1. Academic Press, San Diego, CA.
157. Hayat, M. A. (1989). *Colloidal Gold: Principles, Methods, and Applications*, Vol. 2. Academic Press, San Diego, CA.
158. Hayat, M. A. (1991). *Colloidal Gold: Principles, Methods, and Applications*, Vol. 3. Academic Press, San Diego, CA.
159. Rosch, J. and Caparon, M. (2004). A microdomain for protein secretion in Gram-positive bacteria, *Science*, **304**, 1513–1515.
160. Lawrence, J. R., Hitchcock, A. P., Leppard, G. G. and Neu, T. R. (2005). Mapping biopolymer distributions in microbial communities. In *Flocculation in Natural and Engineered Environmental Systems*, eds Leppard, G. G., Liss, S. N. and Milligan, T. G. CRC Press, Boca Raton, pp. 121–141.
161. Droppo, I. G., Flannigan, D. T., Leppard, G. G. and Liss, S. N. (1996). Microbial floc stabilization and preparation for structural analysis by correlative microscopy, *Water Sci. Technol.*, **34**, 155–162.
162. Droppo, I. G., Flannigan, D. T., Leppard, G. G., Jaskot, C. and Liss, S. N. (1996). Floc stabilization for multiple microscopic techniques, *Appl. Environ. Microbiol.*, **62**, 3508–3515.
163. Ghosh, K. and Schnitzer, M. (1981). Effect of pH and neutral electrolyte concentration on free radicals in humic substances, *Soil Sci. Soc. Am. J.*, **45**, 831.
164. Ghosh, K. and Schnitzer, M. (1980). Macromolecular structures of humic substances, *Soil Sci.*, **129**, 266–276.
165. Ghosh, K. and Schnitzer, M. (1982). A scanning electron microscopic study of effects of adding neutral electrolytes to solutions of humic substances, *Geoderma*, **28**, 53–56.
166. Stevenson, I. L. and Schnitzer, M. (1982). Transmission electron microscopy of extracted fulvic and humic acids, *Soil Sci.*, **133**, 179–185.
167. Stevenson, I. L. and Schnitzer, M. (1984). Energy-dispersive X-ray microanalysis of saturated fulvic acid–iron and–copper complexes, *Soil Sci.*, **138**, 123–126.
168. Atteia, O., Perret, D., Adatte, T., Kozel, R. and Rossi, P. (1998). Characterization of natural colloids from a river and spring in a karstic basin, *Environ. Geol.*, **34**, 257–269.
169. Couture-Mondi, C., Mavrocordatos, D., Perret, D. and Atteia, O. (1999). Interactions between iron and organic matter in a peaty zone. In *Structure et Ultrastructure des Sols et des*

- Organismes Vivants*, eds Elsass, F. and Jaunet, A. M. Colloques de l'INRA, Versailles, pp. 183–192.
- 170. Batson, P. E., Dellby, N. and Krivanek, O. L. (2002). Sub-Å resolution using aberration corrected electron optics, *Nature*, **419**, 94.
  - 171. Krivanek, O. L., Dellby, N. and Lupini, A. R. (1999). Towards sub-Å electron beams, *Ultramicroscopy*, **78**, 1–11.
  - 172. Krivanek, O. L., Nellist, P. D., Dellby, N., Murfitt, M. F. and Szilagyi, Z. (2003). Towards sub-0.5 Å electron beams, *Ultramicroscopy*, **96**, 229–237.
  - 173. Bernard, P. C., Van Grieken, R. E. and Eisma, D. (1986). Classification of estuarine particles using automated electron-microprobe analysis and multivariate techniques, *Environ. Sci. Technol.*, **20**, 467–473.
  - 174. Bruynseels, F., Storms, H., Van Grieken, R. and Vanderauwera, L. (1988). Characterization of North-Sea aerosols by individual particle analyses, *Atmos. Environ.*, **22**, 2593–2602.
  - 175. Jambers, W., De Bock, L. and Van Grieken, R. (1996). Applications of microanalysis to individual environmental particles, *Fresenius' J. Anal. Chem.*, **355**, 521–527.
  - 176. Jambers, W. and Van Grieken, R. (1996). Single particle characterization of inorganic North Sea suspension, *Bull. Soc. R. Sci. Liege*, **65**, 115–117.
  - 177. Jambers, W., Smekens, A., Van Grieken, R., Shevchenko, V. and Gordeev, V. (1997). Characterization of particulate matter from the Kara Sea using electron probe X-ray micro analysis, *Colloids Surf. A*, **120**, 61–75.
  - 178. Raeymaekers, B., Van Espen, P. and Adams, F. (1984). The morphological characterization of particles by automated scanning electron microscopy, *Mikrochim. Acta*, **2**, 437–454.
  - 179. Raeymaekers, B., Van Espen, P., Adams, F. and Broekaert, J. A. C. (1988). A characterization of spark-produced aerosols by automated electron probe microanalysis, *Appl. Spectrosc.*, **42**, 142–150.
  - 180. Raeymaekers, B. J., Liu, X., Janssens, K. H., Van Espen, P. J. and Adams, F. C. (1987). Determination of thickness of flat particles by automated electron microprobe analysis, *Anal. Chem.*, **59**, 930–937.
  - 181. Raeymaekers, B. J. M. (1986). Characterization of particles by automated electron probe microanalysis. *Ph.D Thesis*, University of Antwerp.
  - 182. Wouters, L., Bernard, P. and Van Grieken, R. (1988). Characterization of individual estuarine and marine particles by LAMMA and EPXMA, *Int. J. Environ. Anal. Chem.*, **34**, 17–29.
  - 183. Lerman, A. (1979). *Geochemical Processes: Water and Sediment Environments*. John Wiley & Sons, Inc., New York.
  - 184. Beddow, J. K. (1987). Size, shape, and texture analysis. In: *Particle Size Distribution: Assessment and Characterization* (Provder, T. ed). ACS Symp. Series 332. ACS, Washington. 2–29.
  - 185. Beddow, J. K. (1987). Morphological analysis, *Adv. Ceram.*, **21**, 747–757.
  - 186. Beddow, J. K. (1984). *Particle Characterization in Technology, Vol. 1: Applications and Microanalysis*. CRC Press, Boca Raton, FL.
  - 187. Beddow, J. K. (1984). *Particle Characterization in Technology, Vol. 2: Morphological Analysis*. CRC Press, Boca Raton, FL.
  - 188. Dougherty E. (1993). *Mathematical Morphology in Image Processing*. Marcel Dekker, New York.
  - 189. Gonzalez, R., Woods, R. and Swain, W. (1986). Digital image processing: an introduction, *Digit. Des.*, **16**, 15–20.
  - 190. Jain, A. K. (1983). Digital image processing: problems and practice, *KINAM Rev. Fis.*, **5**, 41–70.
  - 191. Jain, A. K. (1981). Advances in mathematical models for image processing, *Proc. IEEE*, **69**, 502–528.
  - 192. Jain, A. K. (1986). Image processing, *J. Opt. Soc. Am. A*, **3**, 4.
  - 193. Kindratenko, V. V., Treiger, B. A. and Van Espen, P. J. M. (1996). Chemometrical approach to the determination of the fractal dimension(s) of real objects, *Chemom. Intell. Lab. Syst.*, **34**, 103–108.

194. Kindratenko, V. V., Van Espen, P. J. M., Treiger, B. A. and Van Grieken, R. E. (1996). Characterization of the shape of microparticles via fractal and fourier analyses of scanning electron microscope images, *Mikrochim. Acta*, **13**, 355–361.
195. Pitas, I. (1993). *Digital Image Processing Algorithms*. Prentice Hall, Englewood Cliffs, NJ.
196. Russ, J. C. and Russ, J. C. (1986). Shape and surface roughness characterization for particles and surfaces viewed in SEM, *Microbeam Anal.*, **21**, 509–512.
197. Russ, J. C. and Russ, J. C. (1986). Image processing for the location and isolation of features, *Microbeam Anal.*, **21**, 501–504.
198. Russ, J. C. (1988). Computers in stereology and image analysis, *Microbeam Anal.*, **23**, 14–17.
199. Russ, J. C. (1991). Computer-aided quantitative microscopy, *Mater. Charact.*, **27**, 185–197.
200. Russ, J. C. (1992). Imaging the three-dimensional microstructure of materials, *Adv. X-Ray Anal.*, **35B**, 1219–1226.
201. Serra, J. (1978). Quantitative analysis of images, *Recherche*, **9**, 247–256.
202. Serra, J. (1979). Biomedical image analysis by mathematical morphology, *Pathol. Biol.*, **27**, 205–207.
203. Serra, J. (1987). Morphological optics, *J. Microsc.*, **145**, 1–22.
204. Frey, J., Pinvidic, J. J., Botet, R. and Jullien, R. (1988). Light scattering by fractal aggregates: a numerical investigation, *J. Phys. (Paris)*, **49**, 1969–1976.
205. Lin, M. Y., Lindsay, H. M., Weitz, D. A., Ball, R. C., Klein, R. and Meakin, P. (1989). Universality of fractal aggregates as probed by light scattering, *Proc. R. Soc. London, Ser. A*, **423**, 71–87.
206. Lin, M. Y., Lindsay, H. M., Weitz, D. A., Ball, R. C., Klein, R. and Meakin, P. (1989). Universality in colloid aggregation, *Nature*, **339**, 360–362.
207. Lin, M. Y., Klein, R., Lindsay, H. M., Weitz, D. A., Ball, R. C. and Meakin, P. (1990). The structure of fractal colloidal aggregates of finite extent, *J. Colloid Interface Sci.*, **137**, 263–280.
208. Lin, M. Y., Lindsay, H. M., Weitz, D. A., Ball, R. C., Klein, R. and Meakin, P. (1990). Universal reaction-limited colloid aggregation, *Phys. Rev. A*, **41**, 2005–2020.
209. Meakin, P. (1984). Diffusion-limited aggregation in three dimensions: results from a new cluster–cluster aggregation model, *J. Colloid Interface Sci.*, **102**, 491–504.
210. Meakin, P. (1984). Computer simulation of cluster–cluster aggregation using linear trajectories: results from three-dimensional simulations and a comparison with aggregates formed using Brownian trajectories, *J. Colloid Interface Sci.*, **102**, 505–512.
211. Meakin, P. (1991). Fractal aggregates in chemistry, *Trends Chem. Phys.*, **1**, 303–347.
212. Meakin, P., Feder, J. and Jossang, T. (1991). Growth of adaptive networks in a modified diffusion-limited-aggregation model, *Phys. Rev. A*, **44**, 5104–5110.
213. Meakin, P., Feder, J. and Jossang, T. (1991). Radially biased diffusion-limited aggregation, *Phys. Rev. A*, **43**, 1952–1964.
214. Meakin, P. (1992). Aggregation kinetics, *Phys. Scr.*, **46**, 295–331.
215. Meakin, P. (1992). Simplified diffusion-limited aggregation models, *Physica A*, **187**, 1–17.
216. Meakin, P. (1994). What do we know about DLA?, *Heterocycl. Chem. Rev.*, **1**, 99–102.
217. Meakin, P. (1999). The diffusion-limited aggregation model and geological pattern formation. In *Proc. 11th Kongsberg Sem. Growth Dissol. Pattern Form. Geosyst.*, Kongsberg, Norway, pp. 177–188.
218. Albarede, F. (2003). *Geochemistry: an Introduction*. Cambridge University Press, Cambridge.
219. Leppard, G. G. and Arsenault, A. L. (2003). Quantification of individual native biocolloids in natural waters: assessing indicators of aquatic events, by using transmission electron microscopy with a modified approach to image analysis, *Arch. Hydrobiol.*, **156**, 565–573.
220. Couture, C., Lienemann, C. P., Mavrocordatos, D. and Perret, D. (1996). New directions towards the understanding of physico-chemical processes in aquatic systems, *Chimia*, **50**, 625–629.
221. Cheng, S., Lin, J., Wu, J. R. and Gentry, J. W. (1994). Test cases for examination of fractal dimension, *J. Aerosol Sci.*, **25**, S379–S380.

222. Chevalier, J. P., Colliex, C. and Tence, M. (1985). Annular dark-field imaging in a STEM: application to the calculation of the fractal dimension of aggregates of iron particles, *J. Microsc. Spectrosc. Electr.*, **10**, 417–424.
223. Clark, N. N., Diamond, H., Gelles, G., Bocoum, B. and Meloy, T. P. (1987). Polygonal harmonics of silhouettes: shape analysis, *Part. Charact.*, **4**, 38–43.
224. Orford, J. D. and Whalley, W. B. (1983). The use of the fractal dimension to quantify the morphology of irregular-shaped particles, *Sedimentology*, **30**, 655–668.
225. Jullien, R. (1990). The application of fractals to investigations of colloidal aggregation and random deposition, *New J. Chem.*, **14**, 239–253.
226. Fatin-Rouge, N., Toth, E., Perret, D., Backer, R. H., Merbach, A. E. and Buenzli, J. C. (2000). Lanthanide podates with programmed intermolecular interactions: luminescence enhancement through association with cyclodextrins and unusually large relaxivity of the gadolinium self-aggregates, *J. Am. Chem. Soc.*, **122**, 10810–10820.
227. Russ, J. C. (1973). Obtaining quantitative information from an SEM (scanning electron microscope) equipped with an energy-dispersive X-ray analyzer. In *Proc. Conf. Scanning Electr. Microsc. Syst. Appl.*, pp. 238–241.
228. Budd, P. M. and Goodhew, P. J. (1988). *Light-element Analysis in the Transmission Electron Microscope: WDX and EELS*. Oxford Science Publications, Oxford.
229. Eberhart, J. P. (1991). *Structural and Chemical Analysis of Materials: X-ray, Electron and Neutron Diffraction, X-ray, Electron and Ion Spectrometry, Electron Microscopy*. John Wiley & Sons, Ltd, Chichester.
230. Goldstein, J. I., Newbury, D. E. and Echlin, P., Joy, D. C., Fiori, C. and Lifshin, E. (1984). *Scanning Electron Microscopy and X-Ray Microanalysis*. Plenum Press, New York.
231. Reimer, L. (1998). Energy-filtering imaging and diffraction, *Mater Trans.*, **39**, 873–882.
232. Reimer, L. (1995). *Introduction to Energy-filtering Transmission Electron Microscopy*. Springer, Berlin.
233. Reimer, L. (1997). *Transmission Electron Microscopy: Physics of Image Formation and Microanalysis*. Springer, Berlin.
234. Lienemann, C. P., Monnerat, M., Dominik, J. and Perret, D. (1999). Identification of stoichiometric iron–phosphorus colloids produced in a eutrophic lake, *Aquat. Sci.*, **61**, 133–149.
235. Egerton, R. F. (1980). An automated system for energy-loss microanalysis, In *Proc. 38th Annu. Meeting Electr. Microsc. Soc. Am.*, pp. 130–131.
236. Egerton, R. F. (1980). Instrumentation and software for energy-loss microanalysis, *Scanning Electron Microsc.*, pp. 41–52.
237. Egerton, R. F. (1980). Electron energy-loss analysis: theory and instrumentation, *Conf. Ser. Inst. Phys.*, **52**, 323–328.
238. Egerton, R. F. (1981). Applications of energy-loss microanalysis. In *Proc. Workshop Anal. Electron Microsc.*, pp. 154–160.
239. Egerton, R. F. (1981). Some general principles of EELS parallel detection. In *Proc. Workshop Anal. Electron Microsc.*, pp. 211–213.
240. Egerton, R. F. (1981). The range of validity of EELS microanalysis formulas, *Ultramicroscopy*, **6**, 297–300.
241. Egerton, R. F. (1981). Chemical analysis by energy-loss spectroscopy. In *Proc. 8th Microsc. Soc. Can.*, pp. 40–41.
242. Egerton, R. F. (1981). An introduction to EELS, *Bull. Microsc. Soc. Can.*, **9**, 4–8.
243. Egerton, R. F. (1982). Electron energy loss analysis in biology, *Pap. 10th Int. Congr. Elect. Microsc.*, **1**, 151–158.
244. Egerton, R. F. (1982). Principles and practice of quantitative electron energy-loss spectroscopy, *Microbeam Anal.*, **17**, 43–53.
245. Egerton, R. F. (1982). Electron energy-loss spectroscopy for elemental analysis, *Philos. Trans. R. Soc. London, Sec. A*, **305**, 521–533.
246. Egerton, R. F. and Egerton, M. (1983). An electron energy-loss bibliography, *Scanning Electron Microsc.*, 119–142.
247. Egerton, R. F. (1984). Electron energy-loss spectroscopy. In *Proc. 25th Scottish Univ. Summer School Phys.*, pp. 273–304.

248. Egerton, R. F. (1984). Quantitative microanalysis by electron energy-loss spectroscopy: the current status, *Scanning Electron Microsc.*, **505–512**.
249. Egerton, R. F., Crozier, P. A. and Rice, P. (1987). Electron energy-loss spectroscopy and chemical change, *Ultramicroscopy*, **23**, 305–312.
250. Egerton, R. F. (1989). Quantitative analysis of electron-energy-loss spectra, *Ultramicroscopy*, **28**, 215–225.
251. Egerton, R. F. (1993). Electron energy-loss spectroscopy (EELS). In *Proc. 40th Scottish Univ. Summer School Phys.*, pp. 145–168.
252. Egerton, R. F. (1996). *Electron Energy-loss Spectroscopy in the Electron Microscope*. Plenum Press, New York.
253. Egerton, R. F. (2003). New techniques in electron energy-loss spectroscopy and energy-filtered imaging, *Micron*, **34**, 127–139.
254. Egerton, R. F. and Malac, M. (2005). EELS in the TEM, *J. Electron Spectrosc. Relat. Phenom.*, **143**, 43–50.
255. Reimer, L. (1992). Transmission electron microscopy. In *Proc. Int. Summer Sch. Diagn. Appl. Thin Films*, pp. 1–20.
256. Reimer, L., Fromm, I., Hirsch, P., Plate, U. and Rennekamp, R. (1992). Combination of EELS modes and electron spectroscopic imaging and diffraction in an energy-filtering electron microscope, *Ultramicroscopy*, **46**, 335–347.
257. Reimer, L. (1998). Energy-filtering imaging and diffraction, *Mater. Trans.*, **39**, 873–882.
258. Mavrocordatos, D. (1997). Développement de la microscopie électronique analytique pour la caractérisation physico-chimique de colloïdes aquatiques. *Ph.D Thesis*, University of Lausanne.
259. Perret, D., Lienemann, C.-P. and Mavrocordatos, D. (1995). EELS–ESI identification of heterogeneous suspensions of aquatic microparticles, *Microsc. Microanal. Microstruct.*, **6**, 41–51.
260. Leppard, G. G., Mavrocordatos, D. and Perret, D. (2004). Electron-optical characterization of nano- and micro-particles in raw and treated waters: an overview. *Water Sci. Technol.*, **50**, 1–8.
261. Lienemann, C.-P., Taillefert, M., Perret, D. and Gaillard, J.-F. (1997). Cobalt and manganese oxide ( $MnO_x$ ) association at an oxic/anoxic interface, *Abstr. 213th ACS Nat. Meet.*, San Francisco, 13–17 April 1997, ENVR-040.
262. Couture, C., Mavrocordatos, D., Atteia, O. and Perret, D. (1998). The genesis and transformation of organo-mineral colloids in a drained peatland area, *Phys. Chem. Earth*, **23**, 153–157.
263. Myneni, S. C. B., Brown, J. T., Martinez, G. A. and Meyer-Ilse, W. (1999). Imaging of humic substance macromolecular structures in water and soils, *Science*, **286**, 1335–1337.
264. Myneni, S. C. B., Brown, J. T., Meyer-Ilse, W. and Martinez, G. A. (1999). Macromolecular structures of humic substances in water and soils under varying solution conditions, *Abstr. 217th ACS Nat. Meet.*, Anaheim, 21–25 March 1999, ENVR-078.
265. Myneni, S. C. B. (2002). Soft X-ray spectroscopy and spectromicroscopy studies of organic molecules in the environment, *Rev. Miner. Geochem.*, **49**, 485–579.
266. Leppard, G. G., West, M. M., Flannigan, D. T., Carson, J. and Lott, J. N. A. (1997). A classification scheme for marine organic colloids in the Adriatic Sea: colloid speciation by transmission electron microscopy, *Can. J. Fish. Aquat. Sci.*, **54**, 2334–2349.
267. Senesi, N. (1999). Aggregation patterns and macromolecular morphology of humic substances: a fractal approach, *Soil Sci.*, **164**, 841–856.
268. Leppard, G. G. (1995). The characterization of algal and microbial mucilages and their aggregates in aquatic ecosystems, *Sci. Total Environ.*, **165**, 103–131.
269. Leppard, G. G. (1997). Colloidal organic fibrils of acid polysaccharides in surface waters: electron-optical characteristics, activities and chemical estimates of abundance, *Colloids Surf. A*, **120**, 1–15.
270. Wilkinson, K. J., Stoll, S. and Buffle, J. (1995). Characterization of NOM–colloid aggregates in surface waters: coupling transmission electron microscopy staining techniques and mathematical modeling, *Fresenius' J. Anal. Chem.*, **351**, 54–61.

271. Wilkinson, K. J., Joz-Roland, A. and Buffe, J. (1997). Different roles of pedogenic fulvic acids and aquagenic biopolymers on colloid aggregation and stability in freshwaters, *Limnol. Oceanogr.*, **42**, 1714–1724.
272. Lienemann, C. P., Mavrocordatos, D. and Perret, D. (1997). Enhanced visualization of polysaccharides from aqueous suspensions, *Mikrochim. Acta*, **126**, 123–129.
273. Buffe, J., De Vitre, R. R., Perret, D. and Leppard, G. G. (1989). Physico-chemical characteristics of a colloidal iron phosphate species formed at the oxic–anoxic interface of a eutrophic lake, *Geochim. Cosmochim. Acta*, **53**, 399–408.
274. Leppard, G. G., Buffe, J., DeVitre, R. R. and Perret, D. (1988). The ultrastructure and physical characteristics of a distinctive colloidal iron particulate isolated from a small eutrophic lake, *Arch. Hydrobiol.*, **113**, 405–424.
275. Pizarro, J., Belzile, N., Filella, M., Leppard, G. G., Negre, J. C., Perret, D. and Buffe, J. (1995). Coagulation–sedimentation of submicron iron particles in a eutrophic lake, *Water Res.*, **29**, 617–632.
276. Borsheim, K. Y., Bratbak, G. and Heldal, M. (1990). Enumeration and biomass estimation of planktonic bacteria and viruses by transmission electron microscopy, *Appl. Environ. Microbiol.*, **56**, 352–356.
277. Proctor, L. M. and Fuhrman, J. A. (1990). Viral mortality of marine bacteria and cyanobacteria, *Nature*, **343**, 60–62.
278. Proctor, L. M. and Fuhrman, J. A. (1991). Roles of viral infection in organic particle flux, *Mar. Ecol. Prog. Ser.*, **69**, 133–142.
279. Proctor, L. M. and Fuhrman, J. A. (1992). Mortality of marine bacteria in response to enrichments of the virus size fraction from seawater, *Mar. Ecol. Prog. Ser.*, **87**, 283–293.
280. Weinbauer, M. G. and Peduzzi, P. (1994). Frequency, size and distribution of bacteriophages in different marine bacterial morphotypes, *Mar. Ecol. Prog. Ser.*, **108**, 11–20.
281. Weinbauer, M. G. and Peduzzi, P. (1995). Effect of virus-rich high molecular weight concentrates of seawater on the dynamics of dissolved amino acids and carbohydrates, *Mar. Ecol. Prog. Ser.*, **127**, 245–253.
282. Weinbauer, M. G. and Peduzzi, P. (1995). Significance of viruses versus heterotrophic nanoflagellates for controlling bacterial abundance in the Northern Adriatic Sea, *J. Plankt. Res.*, **17**, 1851–1856.
283. Danovaro, R., Dell’anno, A., Trucco, A., Serresi, M. and Vanucci, S. (2001). Determination of virus abundance in marine sediments, *Appl. Environ. Microbiol.*, **67**, 1384–1387.
284. Roberts, K. A., Santschi, P. H., Leppard, G. G. and West, M. M. (2004). Characterization of organic-rich colloids from surface and ground waters at the actinide-contaminated Rocky Flats Environmental Technology Site (RFETS), Colorado, USA, *Colloids Surf. A*, **244**, 105–111.
285. Ferris, F. G., Fyfe, W. S. and Beveridge, T. J. (1987). Bacteria as nucleation sites for authigenic minerals in a metal-contaminated lake sediment, *Chem. Geol.*, **63**, 225–232.
286. Fortin, D. and Beveridge, T. J. (2000). Mechanistic routes to biomimetic surface development. In *Biomimetic mineralization*, Baierlein, E., ed., Wiley-VCH, Weinheim, 7–24.
287. Mavrocordatos, D. and Fortin, D. (2002). Quantitative characterization of biotic iron oxides by analytical electron microscopy, *Am. Mineral.*, **87**, 940–946.
288. Heissenberger, A., Leppard, G. G. and Herndl, G. J. (1996). Ultrastructure of marine snow. II. Microbiological considerations. *Mar. Ecol. Prog. Ser.*, **135**, 299–308.
289. Kerner, M., Hohenberg, H., Ertl, S., Reckermann, M. and Spitz, A. (2003). Self-organization of dissolved organic matter to micelle-like microparticles in river water, *Nature*, **422**, 150–154.
290. Liss, S. N., Liao, B. Q., Droppo, I. G., Allen, D. G. and Leppard, G. G. (2002). Effect of solids retention time on floc structure, *Water Sci. Technol.*, **46**, 431–438.
291. Verdugo, P., Alldredge, A. L., Azam, F., Kirchman, D. L., Passow, U. and Santschi, P. H. (2004). The oceanic gel phase: a bridge in the DOM–POM continuum, *Mar. Chem.*, **92**, 67–85.
292. Mavrocordatos, D., Pronk, W. and Boller, M. (2004). Analysis of environmental particles by atomic force microscopy, scanning and transmission electron microscopy, *Water Sci. Technol.*, **50**, 9–18.

293. Hitchcock, A. P., Morin, C., Tyliszczak, T., Koprinarov, I. N., Ikeura-Sekiguchi, H., Lawrence, J. R. and Leppard, G. G. (2002). Soft X-ray microscopy of soft matter-hard information from two softs, *Surf. Rev. Lett.*, **9**, 193–201.
294. Jacobsen, C., Wirick, S., Flynn, G. and Zimba, C. (2000). Soft X-ray spectroscopy from image sequences with sub-100 nm spatial resolution, *J. Microsc.*, **197**, 173–184.
295. Lerotic, M., Jacobsen, C., Schafer, T. and Vogt, S. (2004). Cluster analysis of soft X-ray spectromicroscopy data, *Ultramicroscopy*, **100**, 35–57.
296. Lerotic, M., Jacobsen, C., Gillow, J. B., Francis, A. J., Wirick, S., Vogt, S. and Maser, J. (2005). Cluster analysis in soft X-ray spectromicroscopy: finding the patterns in complex specimens, *J. Electron Spectrosc. Relat. Phenom.*, **144–147**, 1137–1143.
297. Obst, M., Dittrich, M., Mavrocordatos, D. and Wehrli, B. (2002). Calcite formation by picoplankton, *Geochim. Cosmochim. Acta*, **66**, A566.
298. Obst, M., Dittrich, M., Mavrocordatos, D. and Gasser, P. (2003). Cyanobacterial calcite precipitation: laboratory study on different spatial scales, *EOS Trans. AGU, Fall Meeting 2003 Suppl.*, San Francisco, **84**, B12C-0799.
299. Obst, M., Gasser, P., Mavrocordatos, D. and Dittrich, M. (2005). TEM-specimen preparation of cell/mineral interfaces by focused ion beam milling, *Am. Mineral.*, **90**, 1270–1277.
300. Dittrich, M., Kurz, P. and Wehrli, B. (2004). The role of autotrophic picocyanobacteria in calcite precipitation in an oligotrophic lake, *Geomicrobiol. J.*, **21**, 45–53.
301. Mavrocordatos, D. and Wilkinson, K. J. (2003). Personal communication.
302. Mavrocordatos, D., Steiner, M. and Boller, M. (2003). Analytical electron microscopy and focused ion beam: complementary tool for the imaging of copper sorption onto iron oxide aggregates, *J. Microsc.*, **210**, 45–52.
303. Mavrocordatos, D., Leupin, O., Perret, D. and Glotter, A. (2003). Intimate interaction of Cu and hydrous ferric oxides determined by analytical electron microscopy, *Abstr. Pap. 225th ACS Nat. Meeting*, New Orleans, 23–27 March 2003, GEOC-198.
304. de Vries, J. and Waser, R. (1991). Grain boundary and lattice diffusion of Mn in ATiO<sub>3</sub> (A = Ba, Sr). In *7th IEEE Int. Symp. Appl. Ferroelectr.*, pp. 557–561.
305. Paterson, J. H. and Krivanek, O. L. (1990). ELNES of 3d transition-metal oxides. II. Variations with oxidation state and crystal structure, *Ultramicroscopy*, **32**, 319–325.
306. Ravikumar, V., Rodrigues, R. P. and Dravid, V. P. (1996). An investigation of acceptor-doped grain boundaries in SrTiO<sub>3</sub>, *J. Phys. D*, **29**, 1799–1806.
307. Sparrow, T. G., Williams, B. G., Rao, C. N. R. and Thomas, J. M. (1984). L<sub>3</sub>/L<sub>2</sub> white-line intensity ratios in the electron energy-loss spectra of 3d transition metal oxides, *Chem. Phys. Lett.*, **108**, 547–550.
308. Vollmann, M. and Waser, R. (1997). Grain boundary defect chemistry of acceptor-doped titanates: high field effects, *J. Electroceram.*, **1**, 51–64.
309. Daniels, J., Von Festenberg, C., Raether, H., and Zeppenfeld, K. (1970). Optical constants of solids by electron spectroscopy. *Springer Tracts in Modern Physics*, **54**, 77–135.

---

# 9 Force Microscopy and Force Measurements of Environmental Colloids

---

**ERIC BALNOIS**

*Laboratoire Polymères, Propriétés aux Interfaces et Composites (L2PIC), Université de Bretagne Sud, rue de St Maudé, BP 92116, F-56321 Lorient Cedex, France*

**GEORG PAPASTAVROU**

*Laboratory of Colloid and Surface Chemistry (LCSC), Department of Inorganic, Analytical and Applied Chemistry, University of Geneva, Sciences II, 30 quai Ernest Ansermet, CH-1211 Geneva 4, Switzerland*

**KEVIN J. WILKINSON**

*Department of Chemistry, University of Montreal, CP 6128, Succ. Centre-Ville, Montreal, Canada H3C 3J7*

1	Introduction . . . . .	406
2	Basic Principles of Atomic Force Microscopy . . . . .	407
3	Sample Preparation for AFM Measurements of Environmental Colloids . . . . .	411
3.1	Choice of Substrate for AFM Imaging . . . . .	412
3.2	Sample Deposition Techniques . . . . .	413
3.3	Sample Immobilisation Techniques . . . . .	415
4	Quantitative Determinations of Colloidal Dimensions Using AFM . . . . .	416
4.1	Lateral Dimensions . . . . .	416
4.2	Vertical Dimensions . . . . .	418
4.3	Molecular/Aggregate Conformations . . . . .	418
5	Application of AFM to the Imaging of Natural Aquatic Colloids . . . . .	422
5.1	Inorganic Colloids . . . . .	422
5.2	Biopolymers Excluding Humic Substances . . . . .	424
5.3	Humic Substances . . . . .	425
5.4	Heterogeneous Samples of Environmental Colloids . . . . .	426
6	Quantitative Determinations of Forces by AFM . . . . .	428
6.1	Instrumentation for Force Measurements . . . . .	429
6.2	Measurement of Force–Distance Curves . . . . .	430
6.3	Tip Sample Geometry and Colloidal Probes . . . . .	432
6.4	Determination of the Cantilever Spring Constant . . . . .	433
6.4.1	Cleveland or Added Mass Method . . . . .	433
6.4.2	Hutter–Bechhoefer or Thermal Noise Method . . . . .	434

6.4.3	Sader's Method . . . . .	435
6.4.4	Static Loading Using Two Cantilevers . . . . .	435
7	Forces Between (Colloidal) Surfaces and Their Measurement . . . . .	435
7.1	DLVO Forces . . . . .	435
7.2	Measurements of Interaction Forces Between Environmental Surfaces . .	437
7.3	Non-DLVO Forces . . . . .	440
7.4	Adhesion Forces . . . . .	441
7.5	Measurements of Adhesion Forces Applied to Environmental Systems . .	444
7.6	Force Spectroscopy: Stretching of Single Polymers . . . . .	446
7.7	Single Molecule Extensions . . . . .	448
8	Conclusions and Future Perspectives . . . . .	450
	Acknowledgements . . . . .	451
	List of Symbols and Abbreviations . . . . .	451
	References . . . . .	453

## 1 INTRODUCTION

Aquatic colloids are known to play a significant role in modifying the bioavailability and transport of trace elements due to their high reactive surface area and large interaction forces [1,2]. Colloids and their associated organic and inorganic trace compounds are generally stable in the water column and can thus be transported over long distances. Depending upon the nature and strength of the intermolecular colloidal forces, they may also be eliminated from the water column by sedimentation, most often following coagulation or flocculation. In order to predict the exact role of colloidal particles in aquatic systems, it is therefore of prime importance to determine their supramolecular properties, including size, shape and electric charge [2,3]. Whereas chemical compositions of the colloids have been largely documented in the literature, the determination of their structural parameters remains much more difficult, mainly due to the complexity and heterogeneity of the natural colloids and the lack of appropriate characterisation techniques, especially those that work well under the physicochemical conditions most closely resembling those of the natural environment (i.e. circumneutral pH, low concentrations, variable ionic strength, *etc.*).

Atomic force microscopy (AFM) is a powerful technique for studying (adsorbed) environmental colloids since it provides an extremely high spatial resolution in three dimensions. Furthermore, it is possible to observe all colloid types, including conductive and non-conductive materials, under near *in situ* conditions. The focus of this chapter will be to provide a critical review of the capabilities of AFM, both as an imaging technique and as a technique to measure intermolecular colloidal forces. Since its inception, considerable progress has been made due to the improvement of AFM instrumentation and probes, imaging conditions and sample preparation techniques. The first part of the chapter will therefore describe the AFM technique, review sample preparation methods for environmental colloids, describe the quantitative data that can be obtained from AFM imaging and finally review recent applications that have been made on environmental colloids. The second half of the chapter will review the general principles of the force technique

followed by environmentally relevant examples that illustrate potential (mainly) future applications of the technique. The rapid development of AFM force measurements is perhaps most impressively illustrated by the fact that a 10-year-old review dealing with the applications of AFM to the environmental sciences [4] barely mentioned force measurements. By contrast, recent examinations of the literature have indicated an ever-increasing number of environmentally motivated studies using AFM force measurements.

## 2 BASIC PRINCIPLES OF ATOMIC FORCE MICROSCOPY

The invention of scanning tunnelling microscopy (STM) [5] in 1982 led to the development of a class of microscopy known as scanning probe microscopy (SPM), capable of measuring a variety of physical properties at local scales including interaction forces (AFM), friction forces (FFM, friction force microscopy), magnetic forces (MFM, magnetic force microscopy), electrical properties (EFM, electrostatic force microscopy) and chemical properties (CFM, chemical force microscopy). Among the family of SPMs, AFM has developed the most rapidly since it can be applied to non-conductive samples in a wide range of media, including gases and liquids. Indeed, the field of biology has greatly driven the rapid development of AFM, due to its unique capacity to observe and measure biomolecules under physiological conditions.

All SPM techniques are based on measurements of the interactions between the sample and a probe separated by a small distance. In AFM, a sharp (nanometre range) tip, attached to a cantilever, scans an object using a piezoelectric scanner [6]. Interactions between the atoms of the tip and those of the sample vary according to Hooke's law:

$$F_z = k_c Y_z \quad (1)$$

where  $F_z$  is the force,  $k_c$  the cantilever spring constant and  $Y_z$  the deflection of the extremity of the cantilever. Cantilevers (Figure 1a) are produced by micro-fabrication techniques with lengths from 0.5 to 300  $\mu\text{m}$ . A short overview of the production process and some properties of the cantilevers can be found in a review [7]. Their spring constants vary according to their shape, size and composition, typically ranging from 0.01 to 100  $\text{N m}^{-1}$ . Due to the fabrication process, the exact value of the spring constant varies from one probe to another and therefore must be determined for each AFM probe that is used, a process that is crucial for quantitative force measurements but not for imaging (see Section 6.4).

AFM tips (Figure 1b) are typically made of  $\text{Si}_3\text{N}_4$  or single-crystal silicon, although metal (*e.g.* tungsten) or metal-coated (Pt/Ir) silicon nitride tips are employed for specialised applications such as EFM and conductive AFM. The size and shape of the tip apex are important parameters that determine the resolution of the AFM. Although the typical radius of curvature of an AFM tip is between 5 and 50 nm [8], it is now possible to purchase a large number of AFM probes of variable spring constants, tip radii, shapes and coatings. The correct choice and quality of the AFM tip will greatly influence the image quality for a given sample and sample conditions.

Deflections of the cantilever are monitored by a simple optical device in which a laser light is reflected from the back of a cantilever on to a highly sensitive photodiode (optical

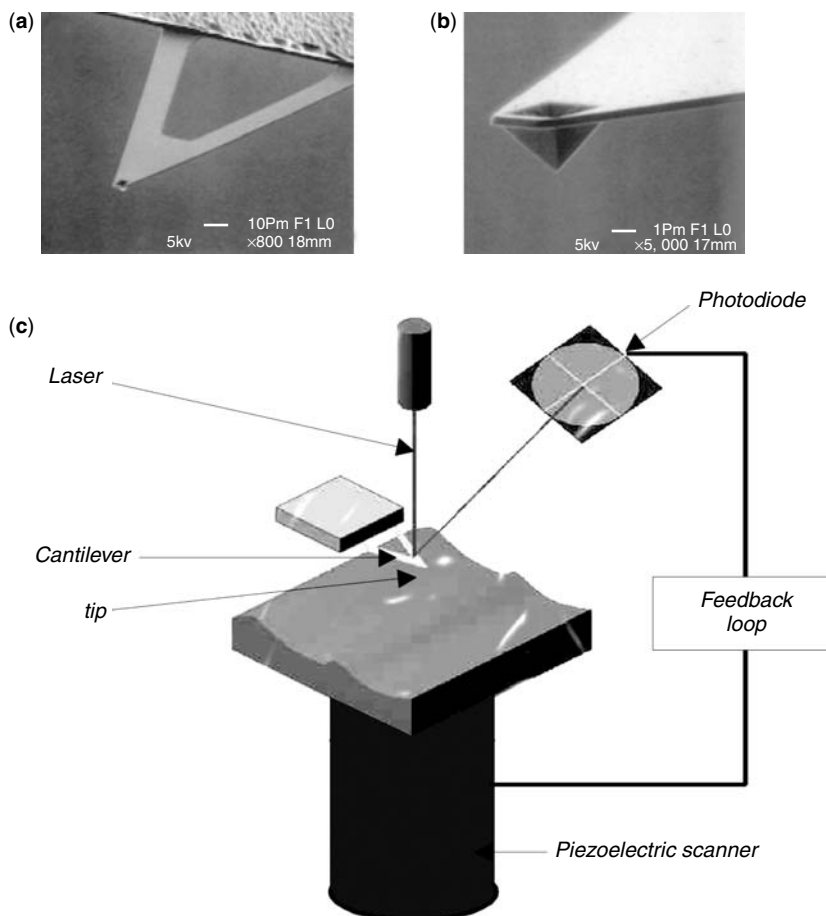


**Figure 1.** Scanning electron micrographs of (a) an AFM cantilever and (b) a pyramidal AFM tip. Reprinted from Drummond, C. J. and Senden, T. J., Examination of the geometry of long-range tip–sample interactions in atomic force microscopy, *Colloids and Surfaces A*, **87**, 217–234, Copyright 1994, with permission from Elsevier. (c) Schema of the important components of an atomic force microscope

lever technique). The signal of the photodiode can be used to control the movement of the piezoelectric translation stage via a feedback mechanism between the photodiode and the scanner. In AFM imaging mode, the piezoceramic scanner, which moves the sample in the  $x$  and  $y$  directions, typically adjusts the height of the sample in order to maintain a constant cantilever deflection. For each pair of  $x$  and  $y$  coordinates, the resulting movements of the scanner in the  $z$  direction are used to reconstruct a three dimensional image of the sample. Additionally, tip deflections can be recorded by maintaining the sample at a constant height. This second mode of imaging is principally used for obtaining atomic resolution of flat and hard surfaces.

Several interaction forces between the tip and the sample cause a deflection of the AFM cantilever. The most commonly measured forces in AFM are well described by a

Lennard Jones potential:

$$U(r) = \frac{\alpha}{r^{12}} - \frac{\beta}{r^6} \quad (2)$$

where  $r$  is the distance between the atoms and  $\alpha$  and  $\beta$  are constants. At small distances ( $\sim 1/r^{12}$ ), the potential is positive and corresponds mainly to repulsive forces, i.e. due to the exclusion of the electronic clouds surrounding the atoms as they start to overlap (Pauli principle), whereas at larger distances ( $\sim 1/r^6$ ), an attractive potential appears due primarily to van der Waals dispersion forces. A typical resulting force-distance curve is shown in Figure 2.

By applying a triangular voltage to the piezoelectric translator, the cantilever will initially move towards the sample. In the region of large separation distances where the probe and sample do not measurably interact, the cantilever is not deflected by external forces. This part of the force-distance curve defines the non-contact line or the baseline deflection signal,  $Y_0$ , (usually measured in volts). When the probe and sample reach sufficiently small separations, the probe is deflected (resulting in a photodiode signal,  $\tilde{Y}_z$ ) that is due to the forces of interaction between the probe and the sample. The velocity of vertical movement towards and away from the sample has to be appropriate to allow for a quasi-static deflection of the cantilever. In liquids, hydrodynamic limits also apply [11]. When the attractive force between probe and sample overcomes a threshold, an instability occurs which results in a jump of the probe towards the sample ('jump in'). For hard, incompressible surfaces, the probe and sample remain in contact and the deflection of the cantilever follows the movement of the piezoelectric translation stage. This part of the deflection versus displacement curve corresponds to a straight line that is referred to as the 'constant compliance region'. In the absence of elastic deformations, the deflection observed during retraction of the piezoelectric stage will follow the constant compliance region of the approach. Generally, an adhesion hysteresis, for which the probe remains in contact with sample surface, is observed in the brief period where adhesion forces

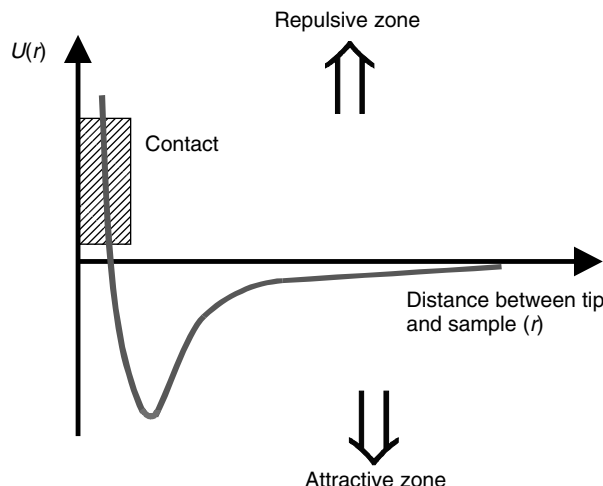


**Figure 2.** Schematic representation of a force-distance curve in raw format [10]

overcome the restoring force of the deflected cantilever. Subsequently, the tip pulls back from the surface to its next equilibrium position.

Both the attractive and repulsive regions on the force–distance curves (Figure 2) can be used to produce topographic images of sample surfaces. The most conventional imaging mode in AFM is *contact* mode, in which the tip is in close contact with the surface in the repulsive force regime. In this mode, forces are typically in the range of  $10^{-7}$ – $10^{-9}$  N when the AFM is operated in air and as small as  $10^{-12}$  N in liquids. The lower forces can be probed under liquid conditions due to the elimination of the strong capillary forces that are present between the AFM probe and the surface when the imaging is performed in air. The main limitation of the contact mode imaging is due to the significant lateral forces, created by the dragging motion of the tip across the sample, which can displace or damage poorly attached objects [12]. To overcome this limitation, other modulation modes have been developed: the *intermittent* mode (also called *tapping* mode) [13] and *non-contact* mode [14]. In the tapping mode, the cantilever is oscillated at its resonance frequency,  $\omega_0$ , with a given free amplitude,  $A_0$ , that is typically in the range 10–100 nm. As the probe is brought into contact with the surface, i.e. in the repulsive regime of the force curve, the tip–sample interaction will alter the tip oscillation. By maintaining the oscillation at constant amplitude (set point amplitude) via a feedback signal based on the tip to sample distance, it is possible to generate a topographical image of the surface from the required movements of the piezoelectric scanner. The set point amplitude is typically 90–95% of the free amplitude in the light tapping mode. Since the tip only briefly interacts with the surface, this imaging mode reduces shear forces that are applied to the sample and consequently can be used to study weakly immobilised molecules. Although surface forces and long-range forces can also play an important role in the oscillatory behaviour, they will not be discussed here; reviews are available elsewhere [15]. The non-contact mode relies on a similar principle to the tapping mode except that the cantilever is oscillated above the surface at distances at which the tip is in the attractive regime of the intermolecular force curve (Figure 2). In this case, the tip to sample distance and the oscillation amplitude are of the order of 1 and 10 nm, respectively. Due to the relatively large tip to sample distances and the correspondingly small forces that are exerted on the sample, this mode is non-invasive, making it ideal for imaging soft and fragile samples. On the other hand, due to the relatively large separation of the tip and the sample, the resolution of the non-contact mode is necessarily lower than that obtained in the contact or tapping mode. Furthermore, the non-contact mode is more difficult to operate than the tapping mode due to the instability of the attractive signal with respect to jumps on the surface, especially when the AFM is operated under ambient conditions.

In addition to topographical imaging, changes in the phase angle of the resonance frequency can produce a second image, a technique called phase imaging. The phase change

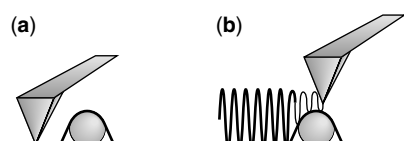


**Figure 3.** Schematic representation of two principal AFM scanning modes: (a) contact mode and (b) tapping mode

of the cantilever oscillation will depend on the energy dissipation of the sample, which can be related to its mechanical properties, including adhesion, stiffness or viscoelastic properties [16–20]. Although the properties measured by such images are only qualitative, the images are often more contrasted than topographical images and are thus complementary. For example, in a recent study, tapping mode AFM phase imaging was used to visualise the amount of condensed water vapour and surface changes occurring on organic coatings of environmental nanoparticles [21].

The potential uses of AFM have increased many-fold owing to the use of novel operation modes. The EFM, MFM and CFM techniques all have great potential for the characterisation of environmental colloids. Furthermore, it is relatively simple to adapt these techniques to commercial AFM instruments simply by equipping them with technique-specific tips, i.e. magnetic, conductive or chemically functional tips. In EFM, an analogue circuit maps the electric field gradient between a conductive tip and the sample. MFM uses magnetic tips that are sensitive to magnetic domains on the surface. CFM techniques use AFM tips that are coated with self-assembled organic monolayers containing specific chemical functional groups to probe chemical forces. The EFM and MFM techniques are operated using a variation on the tapping and non-contact modes called the lift mode. In that case, a first scan in tapping mode records the surface features and sample topography. In a second scan, the tip is lifted 1–2 nm from the surface where an analogue circuit probes the electric or magnetic forces. Although these techniques have rarely been used for the study of environmental colloids to date, they are very likely to be employed in the future.

### 3 SAMPLE PREPARATION FOR AFM MEASUREMENTS OF ENVIRONMENTAL COLLOIDS

As for other microscopic techniques, the ability of AFM to image sorbed environmental colloids depends greatly on the use of appropriate, minimally perturbing, sample preparation techniques. Considerable attention must be given to the preparation step because aquatic (especially colloidal) systems are always dynamic: pH, ionic strength, colloid concentrations, *etc.*, often vary over short periods of time. Several considerations are therefore essential for the correct preparation of colloidal matter for microscopic observation, including [22,23] (i) the preservation of molecular conformations and aggregate structure and (ii) the absence of an induced coagulation or flocculation due to the sample preparation technique. Previously, the most frequently used AFM sample preparation techniques were those adapted from the literature on electron microscopy for biological samples. The use of such techniques ignores the fact that a major interest of AFM is to study specimens under natural conditions. Nonetheless, while the imaging of environmental samples in water is clearly a desirable capability of the AFM, it is not yet always practical or feasible. Indeed, in spite of the potential of the technique for the observation of sorbed environmental species in aqueous solutions, there are relatively few examples [24] for which the samples are strongly enough adsorbed so that they are not perturbed by the scan conditions. When such observation is possible, sample preparation is generally straightforward, in most cases consisting of the introduction of the colloidal solution into a liquid cell. In another commonly used method, the substrate is introduced into a

colloidal solution for a controlled period. The adsorbed sample is subsequently rinsed with a colloid-free solution in order to remove any non-adsorbed materials. Imaging is then performed under the same colloid-free solution. This second procedure is generally employed in order to minimise the adsorption of colloids on the AFM tip.

Nonetheless, observation in the liquid cell is clearly not adapted to all samples. Indeed, some early experiments have highlighted the difficulties of imaging heterogeneous environmental colloids under liquid conditions. For example, both Maurice and Namjesnik-Dejanovic [25] and Plaschke *et al.* [26] have presented AFM images of humic substances (HS) that were obtained in water. Although both studies were promising, the results were dissimilar, with both papers concluding that further investigations were still needed to improve the resolution and reproducibility. In the latter paper [26], the authors clearly demonstrated that the molecules were easily swept away by the AFM tip and/or the AFM tip was easily contaminated due to adsorption of HS, two explanations for the lack of reproducibility and difficulty in obtaining well-resolved images in the liquid cell. For this particular type of colloid (HS), there is a continuing debate on whether TM-AFM is best under ambient or liquid cell conditions. Although HS have also been successfully imaged under ambient conditions (i.e. following gentle evaporation, without drying at 50–60% humidity), (e.g. [27]), the observed minimal perturbation was likely due to the small size of the HS with respect to the hydration water present on the surface of the substrate (1–2 nm on mica at 90% humidity) [28]. For other environmental colloids, more efforts are probably still necessary in order to ensure minimal sample perturbation prior to AFM observation. For all imaging techniques, including AFM, this step is vital and the subject of the next section.

### 3.1 CHOICE OF SUBSTRATE FOR AFM IMAGING

Several important factors must be considered when selecting a substrate for AFM imaging:

- The ideal substrate will have a surface roughness that is much lower than the height of the macromolecules/colloids being studied.
- The observed specimens should be attached/adsorbed sufficiently strongly so as not to be removed or displaced by the tip during the scan.
- The substrate should not undergo any physical or chemical alteration during the time frame of the experiment.

Mica, silicon wafers, glass and highly oriented pyrolytic graphite (HOPG) are the most popular substrates used in AFM due to their low roughness (Table 1). Mica is particularly well suited to the study of environmental colloids due to its large, flat surface area (roughness of ca 0.1 nm over several  $\mu\text{m}^2$ ); the facility by which it can be cleaned by simple cleavage with adhesive tape and the fact that it mimics the clay surfaces that are naturally present in aquatic systems. Other hydrophilic and flat substrates, such as silicon wafers and glass, are commonly used in spite of their structural irregularities in the nanometre range and the requirement for rigorous cleaning procedures prior to their use. For example, silicon wafers must typically be cleaned in an acid bath containing  $\text{H}_2\text{SO}_4$  and  $\text{H}_2\text{O}_2$  by heating to 80 °C (15 min), rinsing thoroughly with deionised water and then drying with a filtered gas. Among hydrophobic substrates, HOPG is a convenient surface

**Table 1.** Characteristics of several typical substrates used in AFM studies. Reproduced from Droz, E., Taborelli, M., Wells, T. N. and Descouts, P., 1993. Preparation of isolated biomolecules for SFM observation T4 bacteriophage as a test sample, *Biophysical Journal*, **65**, 1180–1187, with permission of the Biophysical Society

Substrate	Roughness	Structure and properties
Muscovite mica	~0.1	Crystalline–hydrophilic
Silicon wafer	~0.3	Amorphous – hydrophilic
Glass	>0.8	Amorphous–hydrophilic
HOPG	<0.1	Crystalline–hydrophobic
Gold-coated mica	~0.2	Crystalline–hydrophilic

for AFM that is atomically flat over several  $\mu\text{m}^2$ . Gold is also a suitable substrate for AFM which has found many applications due its metallic properties (suitable for electrochemical applications and for deposition under controlled potential [30]) and its easy to functionalise surface [31,32]. For example, Hegner *et al.* [33] developed a method in which micrometre-sized gold surfaces with atomically flat areas are produced by their epitaxial growth on freshly cleaved mica. The mica is subsequently chemically stripped in tetrahydrofuran.

The charge of the substrate will influence its capacity to maintain the colloids in place during scanning. In aqueous solution, mica is always negatively charged due to the dissolution of  $\text{K}^+$ . For example, in 1 mmol  $\text{dm}^{-3}$  KCl, Nishimura *et al.* [34] determined negative zeta potentials for muscovite mica across a wide pH range (*e.g.* –80 to –60 mV for pH 2–3). Silicon wafers and glass contain silanol groups (Si–OH) with a surface charge that depends on the pH of the solution ( $\text{pH}_{\text{zpc}} \approx \text{pH } 2 \text{ or } 3$ ) [35]. With such substrates, the adsorption of negatively charged colloids and macromolecules (*i.e.* the majority of environmental colloids [36]) will not be favoured (see Section 3.2). Thus, immobilisation techniques using partial drying, bridging cations to enhance the interaction between the object and the substrate or the modification of the substrate to allow chemical or electrostatic bonds to form between the samples and substrates is often necessary to ensure sufficient specimen attachment (see Section 3.3).

### 3.2 SAMPLE DEPOSITION TECHNIQUES

In all microscopy techniques, especially those involving environmental colloids, the optimisation of the sample preparation techniques accounts for the majority of the effort required. In AFM, the most common deposition techniques are drop deposition, ultracentrifugation, spraying, spin-coating and adsorption, techniques that, for the most part, were initially developed for the deposition of biopolymers on TEM grids [37–39]. The drop deposition, ultracentrifugation and adsorption techniques have been compared for model natural colloids [40] (Figure 4). The authors concluded that the drop deposition best allowed for the observation of all particles in solution; ultracentrifugation selectively concentrated the largest particles and aggregates on the mica whereas the adsorption method selectively showed small (*i.e.* rapidly diffusing), chemically active particles. Their work did not conclude that one technique was optimal for the observation of aquatic colloids, rather the authors insisted on the complementary nature of the different sample preparation

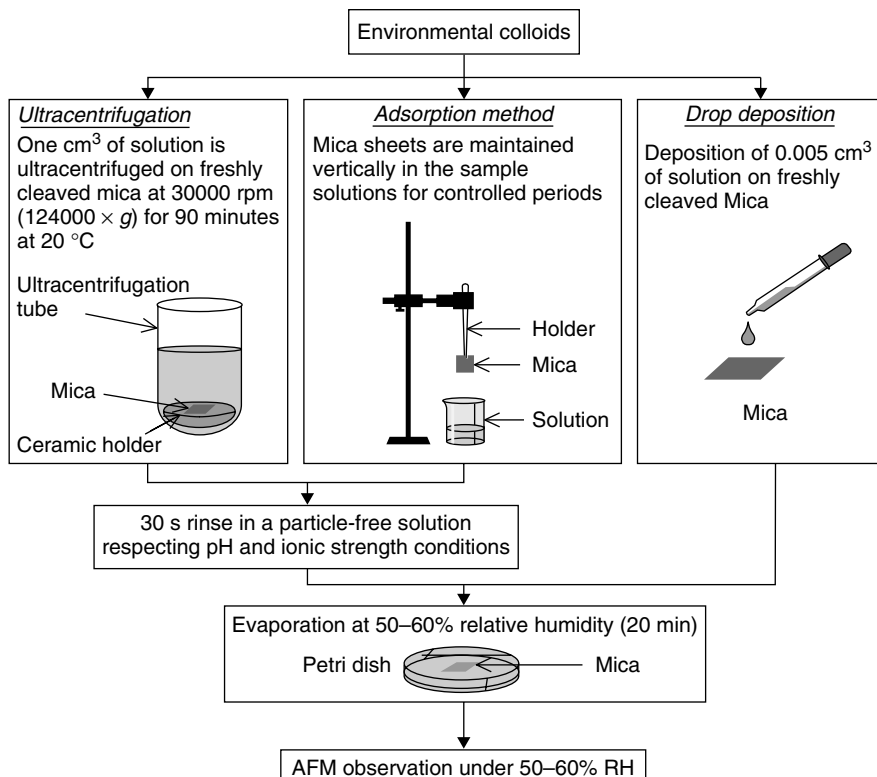


**Figure 4.** Schematic diagrams of three common sample preparation techniques for AFM: ultracentrifugation, drop deposition and adsorption [40], RH = relative humidity

techniques. Indeed, when used in parallel, several techniques are most likely to provide the greatest insight into the true nature of the colloidal sample, a conclusion that is similar to that reached in the electron microscopy literature [41,42]. Other deposition techniques including the spraying or spin coating techniques have also been used for the deposition of natural organic colloids [39,43–45]. For example, spray deposition of aqueous solutions of xanthan or of samples containing 50% aqueous glycerol gave a relatively uniform distribution of the sample over the droplet area and introduced less aggregation than the drop deposition technique [46]. The spin coating method, in which a homogeneous thin film in the nanometre to micrometre range is deposited over several  $\text{cm}^2$  of substrate, has also given a uniform sample distribution and showed minimal perturbation for the AFM imaging of polysaccharides [46,47] and humic substances [44]. Indeed, Mertig *et al.* [44] reported that the spin coating technique allowed the preparation of HS films that were free of lateral mass gradients, thus giving a homogeneous distribution of the molecules on the substrate and a reduction of artefacts during drying. Nonetheless, for the spin coating of collagen on HOPG, artefacts occurred occasionally due to substrate de-wetting [48]. The above examples demonstrate that there is no unique solution for AFM sample preparation: the choice of the technique is highly system dependent (sample, substrate, matrix)

and must be evaluated for each set of conditions with a goal of obtaining minimal perturbation. Confidence in the results can be increased by the use of several methods in parallel.

### 3.3 SAMPLE IMMOBILISATION TECHNIQUES

AFM image quality is very dependent upon whether or not the sample is well immobilised on the substrate during the AFM scan. Although partial drying is an effective means to immobilise the sample, great caution must be exercised in order to avoid molecular conformational changes, colloidal aggregation or sample ordering. Parameters such as the nature of the particle and substrate, particle polydispersity, drying rate, colloidal concentrations and the solution physicochemistry will govern the structure of the deposited layer [49–52]. For example, Denkov *et al.* [53] have shown that, due to capillary forces, non-adhering particles were organised into 2D arrays upon drying. In contrast, Johnson and Lenhoff [54] observed no modifications of the adsorbed layer upon drying for strongly adsorbed (positively charged) amidine latex beads on (negatively charged) mica under conditions of low particle concentration and low ionic strength. Under these conditions, the particles were presumably too widely spaced for capillary attractions to overcome the molecular forces holding the particle to the substrate. At high particle concentrations (i.e. near surface saturation) and higher ionic strength (i.e. ionic strengths leading to a reduction of the electrostatic repulsion among the particles), AFM images both in air and in a liquid cell revealed aggregation. Indeed, Balnois and Wilkinson [40] tested the role of particle concentration on the AFM imaging of two organic colloids, a neutral polysaccharide and a humic substance, deposited on mica and partially dried. No evidence of aggregation occurred for dilute colloidal solutions ( $10 \text{ mg dm}^{-3}$ ) whereas widespread aggregation and gel formation were observed for colloid concentrations of 100 and  $1000 \text{ mg dm}^{-3}$ . Although aggregation could result from the action of capillary forces during drying, the occurrence of a 2D *in situ* aggregation due to the lateral migration of the particles cannot be excluded [55]. Nonetheless, for weakly adhering alumina particles on mica, Thill and Spalla [51,52] concluded that colloidal aggregation was uniquely due to drying since even for alumina particles that were weakly adhered on the mica (obtained by tuning the charge of the colloids), surface mobility was not observed. The above examples demonstrate that aggregation upon drying is a potentially important artefact that needs to be controlled, or at least identified. Nonetheless, it is not systematic but specific to the sample, substrate and solutions that are being investigated.

It should be noted that sample drying in AFM is not as drastic as sample drying in a classical electron microscope. When AFM is performed under ambient conditions, a thin, adsorbed water layer is generally present on the hydrophilic substrates. For example, using ellipsometry, Beaglehole and Christenson [28] measured the thickness of the adsorbed water layer on mica as a function of the relative humidity (RH). They found a film thickness of ca 0.1 nm at 20% RH that increased to 1.5–2 nm at 95% RH. While the water layer will reduce image resolution due to an increase of the applied force on the specimen with increasing RH [8,56,57], the layer will also help maintain small colloids in their hydrated state if they are of similar size to the water layer thickness. Indeed, for humic substances and aquatic polysaccharides, no measurable differences in polymer conformation or morphology were observed for RH values ranging from 5 to 95% [40].

In summary, it is probably safe to work under ambient conditions (50–60% RH) for small (<2 nm in vertical dimension) environmental colloids and macromolecules at (very) dilute concentrations. To our knowledge, the role of drying has not been systematically examined for larger colloids and macromolecules. Finally, other methods such as imaging the sample under alcohol (propanol or butanol) have been used for polysaccharides [58–60]. In this case, the alcohol acts both as a precipitant for the polysaccharides and to minimise adsorption on the AFM tip.

Another approach is to form covalent bonds between the substrate and the sample, either by substrate or sample functionalisation. In both cases, one of the advantages of AFM over TEM, i.e. lack of sample pretreatment, is lost. There are only a few reports where natural colloids have been observed following a modification of the AFM substrate. Among the possible surface treatments, poly-L-lysine can be used for coating glass and mica (*e.g.* DNA fixation [61,62]). At neutral pH, its basic side-chains render the coated surface positively charged. The chemical modification of freshly cleaved mica using 3-aminopropyltriethoxysilane (APTES) [63] (*i.e.* AP-mica) has also been used extensively to image DNA, including its AFM imaging under water [64,65]. In comparison with untreated mica, AP-mica is positively charged with an estimated surface potential of about 7 mV in 0.01 mol dm<sup>-3</sup> electrolyte and 2 mV in 0.1 mol dm<sup>-3</sup> electrolyte [66]. Finally, a monolayer coverage of polyethylenimine (PEI) on mica ( $\text{pH}_{\text{zpc}} \approx 9.9$ ) has been shown to be useful for immobilising clay particles [67].

Metallic substrates, such as gold, may be also be used to enhance immobilisation of the sample by electrochemical fixation. For example, Lindsay *et al.* [30] describe a procedure for the adsorption of DNA on a gold electrode by applying a controlled electrochemical potential. Another immobilisation technique is cryo-AFM, where thermal fluctuations are reduced and the mechanical stability of biological samples enhanced under the cryogenic temperatures required for sample observation [68]. Clearly, for some of the above immobilisation strategies, the studies are not carried out under ‘natural’ conditions.

In conclusion, although it is desirable to perform AFM under liquid conditions, it is not yet always feasible, especially for environmental colloids. Indeed, most natural colloids have been imaged under ambient conditions of atmospheric humidity. Although partial drying of the sample can improve image quality through sample immobilisation, it can also lead to aggregation or conformational modifications. In all cases, the quality of AFM images of environmental colloids will depend on optimisation of the minimally perturbing techniques that allow the visualisation of nanometre-sized molecules in their (partially) hydrated state.

## 4 QUANTITATIVE DETERMINATIONS OF COLLOIDAL DIMENSIONS USING AFM

### 4.1 LATERAL DIMENSIONS

AFM resolution is limited by the ability of the AFM tip to probe two successive points on the sample in the  $x$  and  $y$  directions. Atomic resolution is generally achieved on flat crystallised surfaces such as mica, HOPG or even soft matter (*e.g.* proteins). Indeed, for tips that are much (<2×) sharper than the surface features, the surface is generally accurately tracked whereas convolution effects are likely to occur for relatively small molecular or

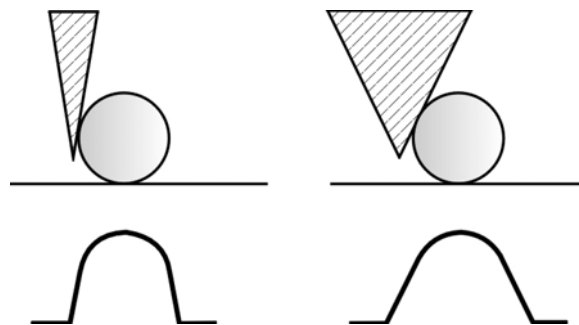


**Figure 5.** Schematic representation of how molecular dimensions can be overestimated due to the size and geometry of the AFM tip. Such effects are mainly observed when the AFM tip has a radius of curvature of the order of or larger than the object being visualised

colloidal features [69]. For example, for molecules such as DNA, the often measured thickness of ca 3 nm overestimates the known crystallographic diameter of 2 nm [66]. Such overestimations of the molecular dimensions can be attributed, in large part, to the size and geometry of the AFM tip. This effect is illustrated in Figure 5 for a tip with a radius of curvature of the order of (or larger than) the object being scanned. In principle, the convolution effect can be accounted for quantitatively by calibration of the shape and size of the AFM tip [70,71]. Colloidal gold particles [72], DNA [73], the tobacco mosaic virus [74] and T4-bacteriophages [73,74] have been employed as calibration standards. Calibration standards should be of a simple geometry with a size and nature that resemble the specimen that is to be observed. Simple mathematical models (*e.g.* [75,76]) can be used to obtain corrected surface lateral distances. Classical geometric features, such as spheres, rectangles or spherical caps, are used to correct the AFM tip distortion effect (Figure 5b). Nonetheless, the models are often imprecise due to uncertainties in either the size or the presumed geometry of the calibration materials. Furthermore, the deconvolution models only consider geometric effects without considering interaction distances between the tip and the substrate/sample that cannot be neglected for nanometre-sized objects. For environmental colloids of an (often) ill-defined nature, tip corrections are therefore difficult to perform. For example, lateral distances, even after correction, were largely overestimated for an HS due to the large repulsion between the AFM tip and the humic macromolecule under operating conditions where both the tip and the sample were negatively charged [40]. On the other hand, for a neutral polysaccharide, schizophyllan [40], correct lateral dimensions (*i.e.* contour length,  $L_c$ ) have been obtained following calibration. In some cases, the unexpected presence of atomic asperities at the end of the AFM tip may result in an atomically fine tip that gives correct lateral dimensions without the need for deconvolution models [66,77].

Image reconstruction programs have been developed to back out the original shape and size of the sample (“blind tip reconstruction”; [76,78,79]). Typically, these programs restore the original specimen image by deconvoluting the tip and the sample using an etching algorithm [76]. The tip size and geometry must have been previously determined on a standard. The main disadvantage of the surface reconstruction methods is that it is impossible to reconstruct the contours of surface areas that are not probed by the AFM tip due to its finite size and thus ‘black holes’ are created. Several examples can be found in

the literature of improved AFM imaging using the reconstruction procedures; nonetheless, the techniques are still being developed and are not yet completely reliable for complex systems such as those containing environmental particles.

#### 4.2 VERTICAL DIMENSIONS

In addition to providing valuable lateral information, one of the advantages of AFM over TEM is its ability to measure vertical distances quantitatively. In contrast to the measurement of lateral dimensions, AFM height measurements are not affected by the shape and size of the tip and are generally recognised to be accurate to a sub-nanometre precision. Nonetheless, some height anomalies have been reported for various materials and biomaterials, irrespective of the operation mode (i.e. contact or tapping mode) or the imaging conditions (ambient or liquid). DNA is probably the best-documented example of a biomolecule for which heights have been systematically obtained under a variety of conditions. Nonetheless, DNA heights obtained in liquid or in air vary from 0.5 to 1.8 nm (*e.g.* [66,80–86]), consistently smaller than the accepted diameter of 2 nm. In this case, the height anomalies have been attributed to several factors, including possible deformation of the sample due to the force exerted by the AFM tip [87,88], the presence of water or salt layers on the substrate adjacent to the deposited object [86,89] or the possible dehydration of the macromolecule when the AFM is operated under ambient conditions [90]. The last argument is often evoked when criticising AFM observations of biomolecules under ambient conditions; however, given that the height of DNA is systematically underestimated, even in the liquid cell, it is unlikely to be an argument that can be applied in all cases. When the AFM is operated in the tapping mode under ambient conditions, Van Noort *et al.* [91] have shown that height anomalies could be attributed to a damping of the amplitude of the cantilever due to adhesive capillary forces between the tip and the water layer on the mica. The use of small tip amplitudes was proposed to reduce this effect. Finally, Muller and co-workers [92,93] have demonstrated that electrostatic interactions between the AFM tip, the substrate and the sample could be responsible for height variations on the order of a fraction of a nanometre (Figure 6).

#### 4.3 MOLECULAR/AGGREGATE CONFORMATIONS

The function of environmental biopolymers is largely dependent on their supramolecular nature, characterised by their contour lengths ( $L_c$ ) and their flexibility as quantified by the persistence length ( $L_p$ ) and the molecular end-to-end distance ( $R_{ee}$ ). Determinations of chain stiffness using AFM imaging are only possible on semi-rigid and rigid polymers for which the entire individual molecules are visible. Determination of the chain persistence length can be determined from statistical changes in the tangent direction  $\theta(\ell)$  of the polymer chain as a function of the segment separation,  $\ell$ , along the chain [94]:

$$\langle \theta^2(\ell) \rangle_{3D} = \ell/L_p \quad (3)$$

and

$$\langle \cos \theta(\ell) \rangle_{3D} = e^{-\ell/L_p} \quad (4)$$

This analysis is based on a worm-like chain model (WLC) that has introduced the notion of continuously curved chain morphology where the angle between two consecutive segments can be described by a Gaussian distribution. Frontali *et al.* [95] determined DNA

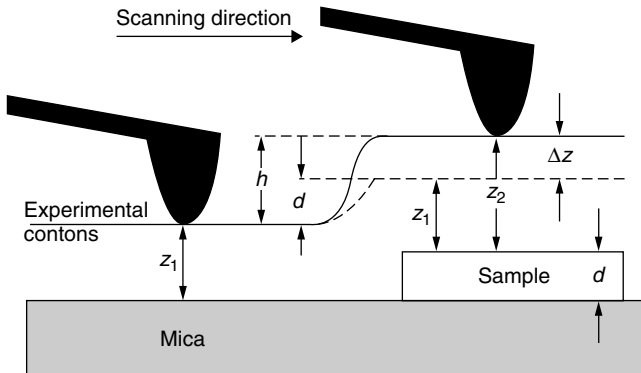


**Figure 6.** Schematic diagram of the electrostatic height contribution measured with the AFM operated in the constant force mode in solution. The surface charge densities  $\sigma$  of support ( $\sigma_{\text{support}}$ ) and object ( $\sigma_{\text{object}}$ ) are assumed to be different. Consequently, at constant force, the distance between tip and support,  $z_1$ , and object,  $z_2$ , must also be different ( $\Delta z \neq 0$ ). Because the measured height  $h$ , is a composite of the structural height,  $d$ , and the difference in the tip–sample distances,  $\Delta z$ , a systematic error occurs with each height measurement,  $h = d + \Delta z$ . Reproduced by permission of the Biophysical Society from Müller, D. J. and Engel, A. (1997). The height of biomolecules measured with the atomic force microscope depends on electrostatic interactions, *Biophysical Journal*, **73**, 1633–1644

persistence lengths by modifying the above relationship to take into account the loss of one degree of freedom due to the interaction of the molecules with a surface:

$$\langle \cos \theta(\ell) \rangle_{2D} = e^{-\ell/2L_p} \quad (5)$$

The assumption of a Gaussian distribution of the measured angles can be tested by calculating the ratio between higher moments of the angular distribution. For a symmetrical Gaussian distribution, the ratios of all odd moments should be zero:

$$\langle \theta(\ell) \rangle_{2D} = 0 \quad (6)$$

whereas the distribution of even moments should be 3:

$$\frac{\langle \theta^4(\ell) \rangle_{2D}}{\langle \theta^2(\ell) \rangle_{2D}^2} = 3 \quad (7)$$

This method has been adapted to determine the conformation of several polymers, including DNA [96,97], polysaccharides [98,99], intermediate filaments [100] and mucins [101] from their AFM images. Polymer surface conformations can be compared with the theoretical conformations using the equations [97]:

$$\langle R_{ee}^2 \rangle_{2D} = 4L_p L_c \left[ 1 - 2 \frac{L_p}{L_c} \left( 1 - e^{-\frac{L_c}{2L_p}} \right) \right] \quad (8)$$

and

$$\langle R_{ee}^2 \rangle_{\text{proj}} = \frac{4}{3} L_p L_c \left[ 1 - \frac{L_p}{L_c} \left( 1 - e^{-\frac{L_c}{L_p}} \right) \right] \quad (9)$$

where  $\langle R_{ee} \rangle_{2D}$  and  $\langle R_{ee} \rangle_{proj}$  are the 2D and projected mean square end-to-end distances, respectively. For macromolecule chains that have reached thermodynamic equilibrium with the surface, their conformation and thus their measured end-to-end distances are expected to correspond to the 2D conformation of the macromolecules rather than a 3D projection. For any given experiment, observed 2D conformations may be projected or equilibrated structures depending on the physicochemistry of the medium and the nature of the sample and substrate. For example, DNA molecules deposited on freshly cleaved mica equilibrated with the surface as an ideal two-dimensional conformation with a  $L_p$  of 53 nm, in good agreement with the  $L_p$  of the molecules in solution. In addition, measured  $\langle R_{ee} \rangle$  values corresponded well with calculated  $\langle R_{ee} \rangle_{2D}$  values. In that study, molecular conformations obtained by 2D imaging were representative of conformations obtained in the bulk solution. In contrast, DNA molecules that were deposited on glow discharged mica did not equilibrate with the surface. In a study examining the conformations of a polysaccharide as a function of the ionic strength, Balnois *et al.* [99] showed that experimental values of the mean square end-to-end distances for succinoglycan deposited in 0.01 mol dm<sup>-3</sup> KCl were reasonably close to the projected 3D  $\langle R_{ee} \rangle$  values, indicating that the molecules may have been trapped on the mica prior to their equilibration due to a reduction in the electrostatic repulsion between the macromolecule and the mica in the presence of salt. In the absence of KCl, two populations of succinoglycan molecules were observed. A proportion of succinoglycan molecules had a slightly extended conformations ( $L_p \approx 19$  nm with respect to 5 nm in solution) due to significant charge repulsion between the anionic polymer and the negatively charged mica. In this case, the observed  $\langle R_{ee} \rangle$  was different from both the projected  $\langle R_{ee} \rangle_{3D}$  and  $\langle R_{ee} \rangle_{2D}$  values. On the other hand, for the same conditions, some of the succinoglycan molecules formed dimers ( $L_p \approx 105$  nm) that were at equilibrium with the mica surface due to their higher polymer rigidity. In that case, molecular conformations obtained by 2D imaging could be considered to be representative of the conformations obtained in bulk solution.

These results and others (*e.g.* [102]) have shown that with appropriate sample preparation, AFM can provide information on the conformational changes of macromolecules under variable physicochemical conditions. For example, Kirwan *et al.* [103] have used AFM observations to demonstrate a coil-to-globule conformational transition of a weak synthetic polyelectrolyte, polyvinylamine, that was adsorbed on mica under ambient conditions.

In summary, it is possible to obtain AFM images with a resolution down to the sub-nanometre range, in both the lateral and vertical directions; nonetheless, images must be thoroughly standardised and interpreted, with caution, since in some cases the substrate can play an important, if not predominant, role in polymer conformation. The critical role of the substrate is well illustrated by the adsorption of poly(methacryloyloxyethylidemethylbenzylammonium chloride) (PMB) on mica (Figure 7). In that case, a decrease in pH from 7 to 3 had little effect on the polymer conformation in solution, but had a highly significant effect on the AFM observations of polymer end-to-end lengths. At present, AFM imaging cannot be used for quantitative determinations of the conformations of flexible macromolecules. Nonetheless, the technique has a unique ability to record the conformational changes of chemically heterogeneous and polydisperse macromolecules such as those found in natural systems.

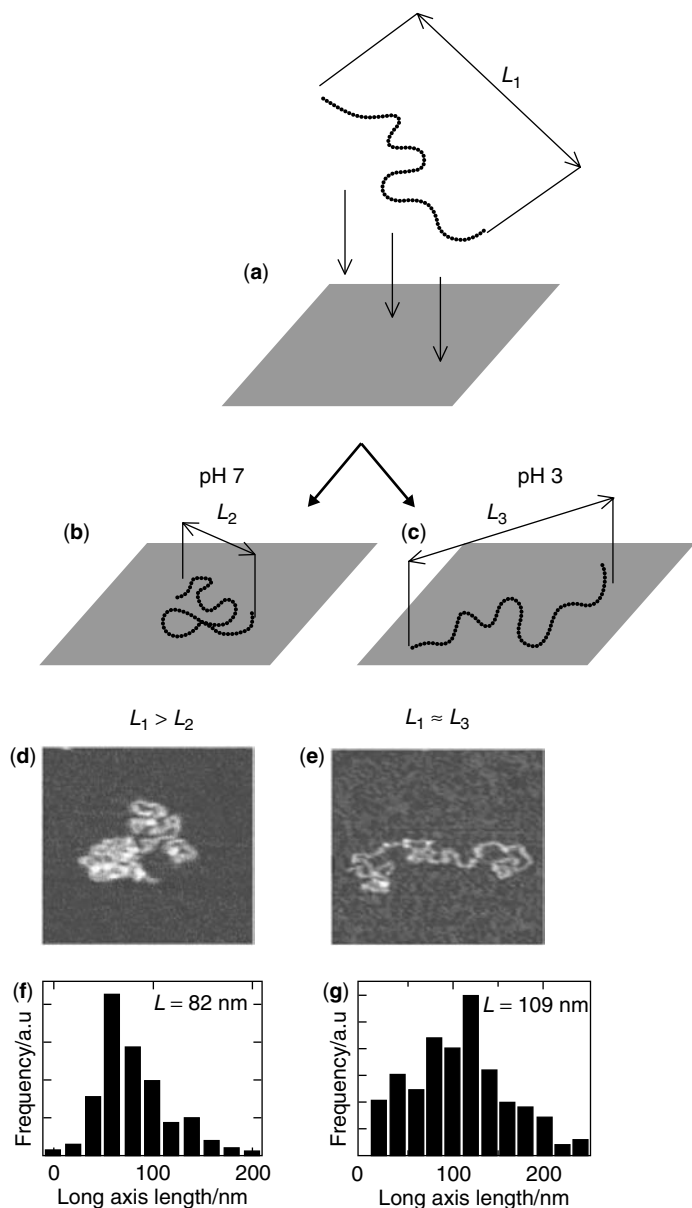


**Figure 7.** Adsorption of molecules of poly(methacryloyloxyethyltrimethylbenzylammonium chloride) (PMB) on mica. Outline of two cases where PMB is either (b, d, f) adsorbed and trapped with a dramatic change of conformation or (c, e, g) adsorbed with dimensions that are very similar to the molecule in solution. AFM images were acquired at a pH corresponding to a negatively charged ( $-28 \text{ mV}$ ) mica at pH 7 (d) or on mica at its isoelectric point (pH 3) (e). The histograms represent the average end-to-end lengths at pH 7 (f) and pH 3 (g). Reprinted with permission from Kiriy, A., Gorodyska, G., Minko, S., Jaeger, W., Stepanek, P. and Stamm, M., Cascade of coil–globule conformation transactions of single flexible polyelectrolyte molecules in a poor solvent, *Journal of the American Chemical Society*, **124**, 13454–13462, Copyright 2002 American Chemical Society

Finally, AFM can also be used to monitor aggregation processes *in situ*. Aggregation can be quantified from a fractal analysis of the resulting structures [104–107]. Measurements of the fractal dimension can be obtained from direct microscopic (generally TEM) observations. Fractal dimensions have been determined for aggregates of smoke particles [104], colloidal hematite [108] and humic substances [109]. AFM images have also been used to characterise aggregates or to monitor aggregation (e.g. [110–112]). For example, Grohens *et al.* [110] found that the aggregation of isotactic and syndiotactic poly(methyl methacrylate) polymers, in different solvents and on different surfaces, could be well described by a diffusion-limited aggregation model as determined by the invariability of the fractal dimension. Yan and Iwasaki used AFM to reveal the fractal nature of DNA aggregates after thermal denaturation [111].

## 5 APPLICATION OF AFM TO THE IMAGING OF NATURAL AQUATIC COLLOIDS

This section presents documented applications of the AFM technique for the characterisation of environmental colloids, organised into four subsections. The first three subsections are dedicated to the study of the major aquatic colloidal components as classified by Buffe *et al.* [2]: inorganic colloids, recalcitrant biopolymers and humic substances. This classification is mainly based on the observation that natural colloidal aggregates are primarily composed of these three components. In the last sub-section, examples of the application of AFM to the imaging of natural water samples will be given.

### 5.1 INORGANIC COLLOIDS

The major inorganic colloids in natural waters include clays, silica, iron and aluminium oxides and calcium carbonate [1,36] and whose chemical surface properties control such important phenomena as nutrient and contaminant element release and uptake, pH buffering, water quality, and soil rheological properties [113]. Most of these materials have been studied with AFM, including bentonite [114], hectorite [115], illite/smectite [116], montmorillonite [117] and iron oxides [118,119]. These materials have been mainly examined for their morphology, particle size distribution and surface heterogeneity. Early studies were mainly dedicated to exploring the mineral surfaces in order to provide a precise and complete description of the particle and aggregate morphologies. In this sense, AFM provides direct observations of individual particles and aggregates, in contrast with averaging techniques such as light scattering. In addition, the technique is able to evaluate the surface heterogeneity of the particles at the nanometric scale. For example, Plaschke *et al.* [114] have investigated the morphology of bentonite particles using AFM and several other colloidal characterisation techniques: laser-induced breakdown detection (LIBD) [120], photon correlation spectroscopy (PCS) and flow field-flow fractionation coupled to inductively coupled plasma mass spectrometry (FIFFF–ICP-MS) [121]. AFM revealed that the particles were disk-like platelets with an average diameter of 73 nm and an aspect ratio of ~1/10. Furthermore, a broad size distribution was observed by AFM, in agreement with PCS and FIFFF–ICP-MS. The mean particle size, deduced from FIFFF–ICP-MS and LIBD, was around 70 nm, in agreement with the AFM result, whereas a larger diameter (intensity-weighted size distribution of the hydrodynamic particle diameter of *ca.* 200 nm) was found by PCS. Studies of synthetic laponite clay colloids by AFM revealed that the

particles were not disk shaped, as previously reported from small-angle X-ray and neutron scattering experiments, but rather ellipses [77].

It is also possible to use AFM to investigate the surface reactivity of various minerals *in situ*, including their dissolution/growth mechanisms, adsorption, precipitation or aggregation. For example, AFM has been used to study the growth mechanisms of barite [122], gypsum [123,124], calcite [125] and the dissolution of barite [126], chlorite [127], Fe oxides [128], calcite [129–131] and aluminosilicates [114,132]. At pH 2, the dissolution of hectorite colloids occurred exclusively at the edge surface, whereas the basal surface was shown to be non-reactive over several hours [119] (Figure 8). A dissolution rate that was normalised to the reactive edge surface of  $7.3 \times 10^{-9}$  mol hectorite  $\text{m}^{-2} \text{s}^{-1}$  area was calculated from the AFM data. Bickmore *et al.* [132] compared the dissolution mechanisms of hectorite and nontronite particles in acid solution using AFM and observed that the dissolution of the (001) faces was six times slower than for the lath ends, whereas for nontronite the (010), (110) and (110) faces were very resistant to dissolution. More complex systems, including the interaction between metals and colloids or particles, have also been examined by AFM [128]. Weaver *et al.* [133] showed that the interactions of Cr(III)<sub>aq</sub> and manganite ( $\gamma\text{-MnOOH}$ ) were highly heterogeneous: whereas localised microprecipitation and/or dissolution was observed on some manganite surfaces, other, adjacent areas showed no evidence for any reactivity. In these examples,

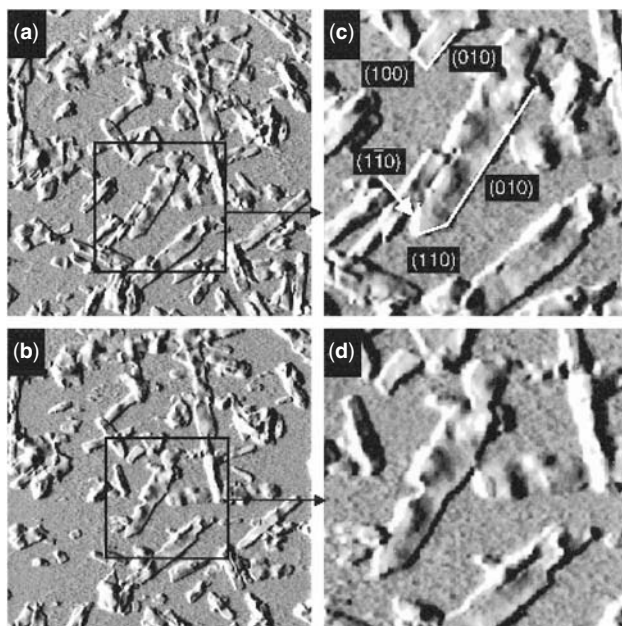


**Figure 8.** *In situ* imaging of hectorite particles on mica substrate in an aqueous solution at pH 2. Images were acquired using contact mode AFM over a scan area of  $1.5 \times 1.5 \mu\text{m}$  (a, b) or  $400 \times 400 \text{ nm}$  (c, d). Images (b) and (d) correspond to the particles after 40 min. Lateral dimensions of the particles decreased due to the dissolution of the particle edges. Reprinted from Bosbach, D., Charlet, L., Bickmore, B. and Hochella, M. F., The dissolution of hectorite: *in situ*, real-time observations using atomic force microscopy, *American Mineralogist*, **85**, 1209–1216, 2000, with permission from the Mineralogical Society of America

kinetic investigations were used to deduce the reactivity of individual particles, *in situ*. To understand the fate of inorganic colloids, it is certainly advantageous to couple AFM measurements with classical macroscopic approaches [134].

## 5.2 BIOPOLYMERS EXCLUDING HUMIC SUBSTANCES

The fibrillar (rigid) biopolymers include mainly the aquagenic polysaccharides and peptidoglycans, accounting for ca 5–50% of the organic matter in aquatic systems [2,135]. A large number of AFM studies have been devoted to the characterisation of polysaccharides originating from bacteria (*e.g.* xanthan or succinoglycan), plants (*e.g.* cellulose, alginate) or fungi (*e.g.* scleroglucan) (for a recent review, see [136]) (Figure 9). In these studies, AFM and image analysis were used in combination to obtain quantitative molecular dimensions including heights (diameters), contour lengths, end-to-end distances and persistence lengths [99,136]. From these molecular dimensions, a good estimation of the molar mass distributions is possible if the polymer mass per unit length is known. For example, Sheiko *et al.* [137] used a combination of AFM and the Langmuir–Blodgett technique to determine number-average molar masses and molar mass distributions of macromolecules. In comparison with other analytical techniques classically used in polymer science (*e.g.* size exclusion chromatography, scattering techniques and NMR), AFM is uniquely able to provide local information that is especially helpful when probing heterogeneous and polydisperse samples. For example, AFM was shown to be well suited to revealing heterogeneities such as the coexistence of circular and linear conformations of scleroglucan following denaturation in solvent [89] or the incomplete renaturation of the xanthan triple helices after its heating [138].

The self-assembly and gelling properties of polymers, principally polysaccharides and proteins can also be investigated by AFM (*e.g.* [134,140–142]). The gelling mechanism

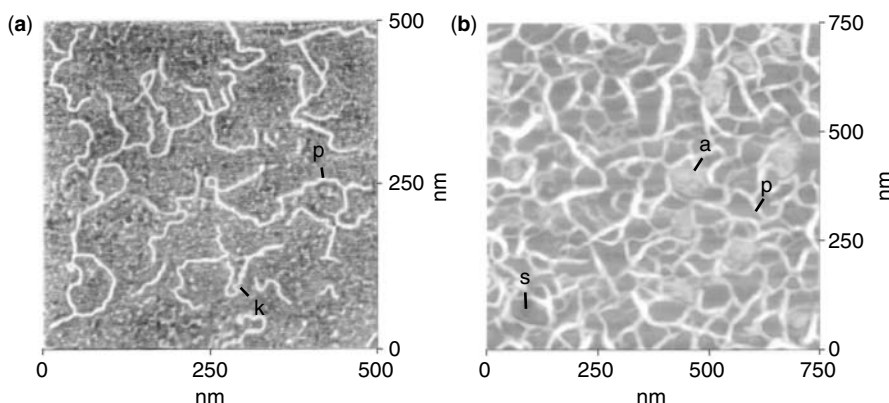


**Figure 9.** (a) An enlarged AFM image of alginate molecules (image size 500 × 500 nm) sorbed on a freshly prepared mica surface. Note the abrupt angled changes or ‘kinks’ (k) in the molecular shape of polymers (p). (b) An enlarged AFM image of an alginate gel (2%) in seawater (30 parts per 1000 salinity). s, Solvent cavity; p, polymer; a, artifact. Reprinted from Decho, A. W., Imaging an alginate polymer gel matrix using atomic force microscopy, *Carbohydrate Research*, **315**, 330–333, Copyright 1999, with permission from Elsevier

of biopolymers has been studied both in presence of cations [143,144] and in biopolymer mixtures [145–147]. From their AFM images, Ikeda and Morris [148] suggested that the heat-induced gelation of curdlan involved a first step where single molecular chains partially dissociated from heterogeneous microfibrils and then interacted with the parent microfibrils through the formation of triple-stranded helices. The proposed structural model was in good agreement with the fibrous model, which indicates that the gel network is predominantly composed of microfibrillar aggregates at the supramolecular level [140,149]. AFM therefore has good potential to obtain information on the early stages of the aggregation/gellation process.

In a recent paper, Verdugo *et al.* [150] discussed the importance of studying organic gels in marine systems in order to understand organic carbon cycling in environmental systems. Polymer gel particles in the ocean were shown to be abundant and involved in several processes, including the microbial loop, sedimentation processes, biogeochemical cycling, marine carbohydrate chemistry and particle dynamics [151]. Using AFM and a controlled sample preparation, Zutic and co-workers [152,153] were able to visualise directly the 3D structure of a marine gel formed episodically in the Adriatic Sea. By diluting or by reducing the ionic strength, they were able to dissociate the macrogel into its primary fibrils, suggesting that the gel was held together by fairly weak bonds [152–154].

### 5.3 HUMIC SUBSTANCES

In the literature, HS have alternately been described as flexible, linear chains with a poly-electrolytic character, as micelles or as compact spheres [155–159]. Furthermore, data on the molecular sizes of the HS vary from fractions of nanometres to several hundred nanometres. Indeed, although many techniques have been used to determine the structure and size of humic macromolecules, due to their chemical heterogeneity and physical polydispersity, no consensus has yet emerged on their supramolecular structure (for reviews, see [2,135]). For the most part, differences have been attributed to the different sources of HS employed, the sample preparation techniques, the observation conditions (pH, *I*, concentration) and the inherent bias of the analytical techniques that were employed. Namjesnik-Dejanovic and Maurice [160] were the first to apply AFM to the analysis of fulvic acids from soils and streams under ambient conditions. At relatively low concentrations ( $50 \text{ mg dm}^{-3}$ ), they observed small spheres (10–50 nm in diameter, 2–10 nm in height) and sponge-like, ring structures. On the other hand, for concentrations between 500 and  $1000 \text{ mg dm}^{-3}$ , aggregates of spheres (heights  $>9.5 \text{ nm}$ ) and chain-like assemblies were observed. Several other papers on the characterisation of HS by AFM followed shortly after [25–27,44,45,161,162] and it now seems well established that the smallest particles that are observed by AFM (typical heights  $<5 \text{ nm}$  and found under either ambient or liquid conditions) can be classified as individual humic acid macromolecules. Indeed, their sizes are generally in reasonable agreement with those obtained by fluorescence correlation spectroscopy, pulsed field gradient nuclear magnetic resonance or flow field-flow fractionation [44,161,163]. Nonetheless, further work is required to understand how the solution physicochemistry can affect the conformations of the HS. On the one hand, decreasing heights of an HS with increasing pH was interpreted by a random coil model, i.e. elongated molecules that lie flat on mica at high pH due to their deprotonation [164]. On the other hand, height increases of a hydrophobic HS were attributed

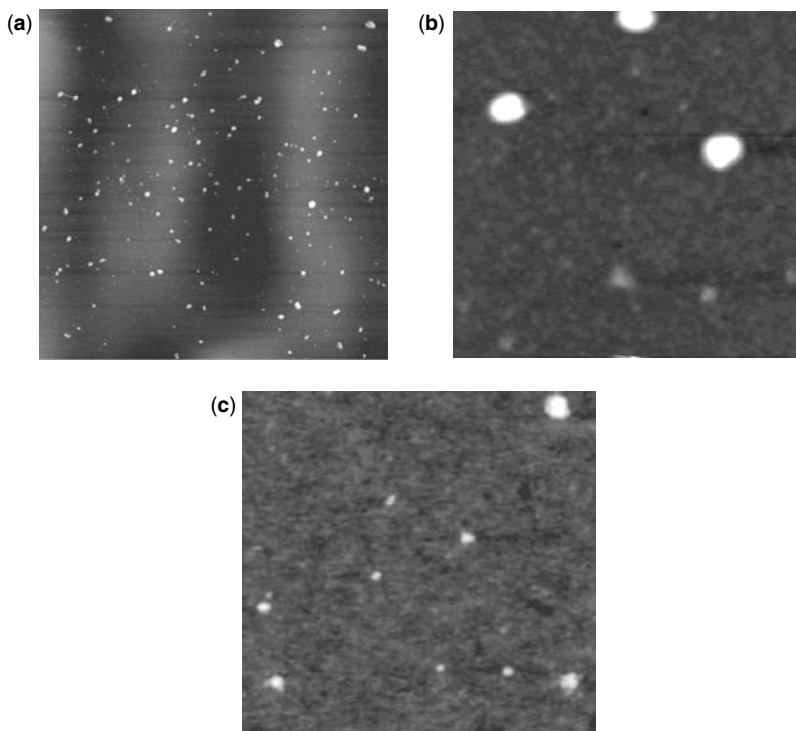


**Figure 10.** (a) AFM image of the International Humic Substances Society Suwannee River fulvic acid ( $10 \text{ mg dm}^{-3}$ ,  $50 \text{ mmol dm}^{-3}$  NaCl, pH 5.5) adsorbed on mica. Scan size  $600 \times 600 \text{ nm}$ . The image shows mainly isolated points (as opposed to aggregates) with adsorbed heights that averaged  $0.8 \pm 0.3 \text{ nm}$ . Adapted from [27] with permission from the American Chemical Society. Parts (b) and (c) correspond to tapping mode atomic force microscopy (TM-AFM) images of the UK Geological Survey peat humic acid (PHA). Scan size  $2 \times 2 \mu\text{m}$ . (b)  $10 \text{ mg dm}^{-3}$  solution adsorbed on mica at pH 3.2,  $5 \text{ mmol dm}^{-3}$  NaCl. (c)  $10 \text{ mg dm}^{-3}$  PHA solution adsorbed on mica at pH 6.8,  $5 \text{ mmol dm}^{-3}$  NaCl

to its aggregation at low pH (<5) and high ionic strength ( $I \approx 500 \text{ mmol dm}^{-3}$  NaCl) whereas no differences in molecular dimension were observed as a function of pH (3–10) and ionic strength ( $I = 5\text{--}50 \text{ mmol dm}^{-3}$  NaCl) for a more hydrophilic HS (Suwannee River humic acid) [27] (Figure 10). No consensus has yet emerged with respect to the nature of HS aggregates which have been described as sponge-like ring structures, chain-like assemblies, networks (gels) and large compact aggregates [25–27]. In this case, more research is required to determine whether the different conclusions that have been reached in the literature are due to the different nature of HS that have been examined or whether they are a consequence of the sample preparation techniques.

#### 5.4 HETEROGENEOUS SAMPLES OF ENVIRONMENTAL COLLOIDS

In contrast to the relatively important number of AFM publications on polysaccharides and humic acids, there are, to the best of our knowledge, only a few AFM studies on natural aquatic (heterogeneous) systems. Santschi *et al.* [165] used AFM, in parallel with TEM

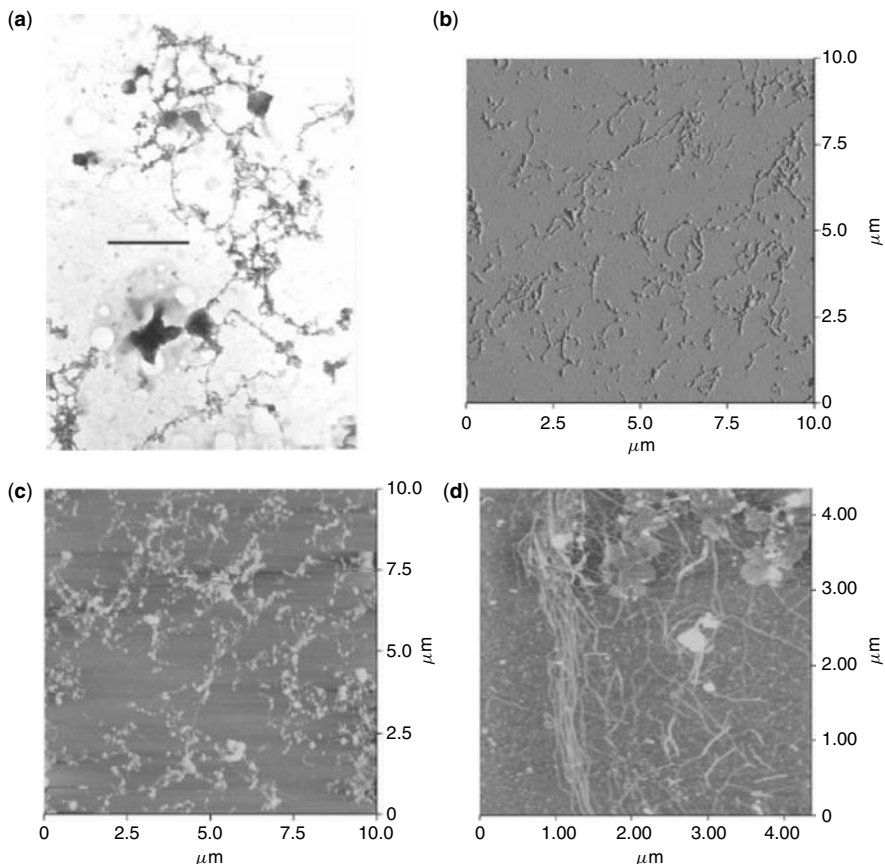


**Figure 11.** Fibrillar network of colloidal particles and fibrils, arranged in a pearl-on-necklace fashion. (a) TEM of stained fibrillar network, embedded in a hydrophilic resin, which is part of the colloidal organic matter (COM, ultrafilter size range 1–400 nm), sampled from the Middle Atlantic Bight surface waters. (b) AFM from Middle Atlantic Bight surface water COM; fibrils were also identified by AFM, albeit at lower abundance, in nepheloid layers at 2500 m but not in midwaters. (c) AFM of COM from Galveston Bay waters. (d) AFM image of COM from the surface waters of the Gulf of Mexico, which shows the potential for gel formation of fibrillar macromolecules at the edge of the mica support plate, where the gel-like aggregates are probably formed as a consequence of drying. Reprinted from Santschi, P. H., Balnois, E., Wilkinson, K. J., Zhang, J., Buffle, J. and Guo, L., Fibrillar polysaccharides in marine macromolecular organic matter as imaged by atomic force microscopy and transmission electron microscopy, *Limnology and Oceanography*, **43**, 896–908, 1998, with permission from American Society of Limnology and Oceanography

and spectrophotometric analysis, to explore marine and estuarine colloids (Figure 11). The analysis clearly revealed that an important fraction of colloidal organic matter from estuarine, surface and deep-water marine samples consisted of fibrillar materials, rich in polysaccharides. Aggregated fibrils and more processed organic colloids were observed in the deeper waters, an observation that was explained by the rapid aggregation and sedimentation of these fibrils. Using a similar methodology, both fibrillar and globular colloids were identified in freshwaters, including an urbanised watershed [166] and freshwater

streams [167]. A limitation of the AFM technique has nonetheless been identified [165] for the imaging of mixed organic and inorganic colloidal aggregates. Due to pronounced height differences in this system, small organic colloids were probably masked due to the deflection of the AFM tip by large inorganic colloids. The imaging of highly polydisperse natural samples using AFM can thus be improved by a preliminary sample fractionation [165] and by employing several characterisation techniques simultaneously [161]. In comparison, TEM is generally biased towards the observation of the larger (more electron dense) particles.

## 6 QUANTITATIVE DETERMINATIONS OF FORCES BY AFM

The ability to measure directly the interaction forces between surfaces has played an important role in advancing our understanding of colloid and adhesion science, where progress has been due, in a large part, to the development of new techniques [168]. The recent, widespread use of AFM, not solely as an imaging technique but also as a tool to measure surface forces, has made it possible for an increasing number of laboratories to obtain a complementary physicochemical characterisation of their systems by direct force measurements. This development is of particular interest for environmental systems, where long-range interaction or adhesive properties can often not be predicted *a priori* due to their complexity.

Initially, the development of direct force measurements by AFM was motivated by the need to quantify precisely the interaction forces between the tip and sample in order to achieve reproducible images [169,170]. The determination of such forces was previously only possible using the surface force apparatus (SFA) [171,172]. In contrast to AFM, the SFA requires smooth, macroscopic surfaces that must be semi-transparent in order to act as mirrors for a Fabry–Perrot type of interferometer. These restrictions strongly reduce the number of materials that can be examined, especially for surfaces that are commonly encountered in the environmental sciences. While the SFA does not have a higher absolute sensitivity for force measurements than the AFM ( $\sim 10^{-9}$  N for the SFA vs  $\sim 10^{-12}$  N for AFM), it provides a much larger interaction area than AFM due to its macroscopic mica cylinders. Additionally, it allows for the independent determination of distances between surfaces. For these reasons, use of the SFA is still the method of choice to examine the steric forces involved in solvent layering or the interactions that occur between highly compressible surfaces. In contrast, AFM can be used for any type of material as long as it is sufficiently flat, in microscopic terms. For example, measurements on bacterial surfaces or on isolated molecules are currently only possible using AFM. Furthermore, in addition to greater versatility, AFM can laterally resolve interaction forces and sample properties.

A significant improvement in quantitative force measurements was obtained with the development of the colloidal probe technique by Ducker *et al.* [173,174] and Butt [175]. By attaching a micrometre-sized particle ('colloidal probe') to the end of an AFM cantilever, it was possible to overcome restrictions due to the nature of the tip material (typically Si or  $\text{Si}_3\text{N}_4$ ) and obtain well-defined tip–sample geometry and higher force resolution. Additional improvements resulted from novel methods to determine the cantilever spring constant [176,177]. Another landmark in the measurement of AFM interaction forces was due to the work of Gaub and co-workers [178,179], in which the superior force resolution of AFM was exploited to measure extension forces between a sample

and a tip that were bridged by a single polymer. The novelty of measuring the forces exerted by a single molecule rather than those obtained for a large number of molecules has created a lot of excitement in the fields of biochemistry and biophysics. In an environmental context, single molecule force measurements have been used to probe the role of extracellular polymers in bacterial adhesion [136,180], among other topics.

Finally, other techniques such as optical tweezers (OT) [181,182] and total internal reflection microscopy (TIRM) [183] have been employed to measure interaction forces between colloidal particles. These techniques can resolve forces in the sub-piconewton regime ( $\sim 10^{-14}$  N) and allow interaction forces to be probed in the regime of the thermal energy. The emerging use of OT and TIRM in the colloidal domain will surely stimulate numerous future applications of environmentally oriented research.

## 6.1 INSTRUMENTATION FOR FORCE MEASUREMENTS

The terminology for force measurement determinations has evolved in recent years. Measurements that focus on the extension of single molecules or the unbinding forces between ligand–receptor pairs are often referred to as ‘force spectroscopy’, whereas measurements that concentrate on long- or short-range interaction forces are described as ‘direct force measurements’. Measurements that examine general adhesion phenomena between the probe and the sample are often called ‘adhesion force measurements’. In any case, the basic instrumental requirements are the same in all cases and, for the most part, can be fulfilled by commercially available AFM systems.

During force measurements, the sample or the tip holder is moved vertically by a piezoelectric scanner, while the other components remain in place. Deflection of the cantilever is recorded during the vertical piezo movement, generally by the optical lever technique (see Section 2). When a force is exerted on the probe (i.e. AFM tip or colloidal probe), the cantilever bends and the reflected light beam changes its position on the quadrant photodiode, which acts as a position sensor. The signal detected by the optical lever technique is not proportional to the deflection,  $Y$ , of a cantilever of length,  $l$ , but rather to its end-slope ( $\tan\alpha$ ); those quantities are related by [184]:

$$Y = \frac{2}{3} \ell \tan \alpha \quad (10)$$

Theoretically, the deflection resolution of the optical lever technique can approach ca 0.01 nm. For all practical purposes, this limit is not relevant, since the thermal vibrations of cantilevers with low spring constants (i.e. those most often used for force measurements) commonly exceed this value. For example, for typical spring constants of  $0.01\text{--}1\text{ N m}^{-1}$ , a thermal noise of  $0.07\text{--}0.7\text{ nm}$  is obtained at room temperature [184]. Since both the spring constant and the overall dimensions influence the resonance frequency and viscous damping, current efforts are focused on developing smaller cantilevers [185,186]. Cantilevers employed for force measurements are generally made from silicon or silicon nitride.

There are a number of factors that can affect the suitability of AFM for force measurements. The piezoelectric ceramics used for the vertical movement of the sample or cantilever holder exhibit hysteresis and creep [187]; therefore, the absolute distance

over which the piezo element travels is not exactly proportional to the applied voltage. In imaging, such effects result in a non-linear distortion of the sample features, whereas in force measurements, a false separation distance between sample and probe is obtained. New generations of home-made set-ups and commercially available instruments have overcome most of the problems related to the non-linear effects of the piezoceramics by using piezoelectric translators that work on a feedback mechanism. In this manner, the reproducibility and accuracy of the force-distance curves can be greatly enhanced. Interferences between the sample and cantilever due to the laser illumination can be used to calibrate the piezoelectric translator in order to determine its non-linear movement [188]. These interferences can also lead to an apparent distortion of the cantilever deflection when the cantilever approaches the sample. The problem can be overcome by using non-coherent laser diodes. Instrumental developments are continuing by measuring changes in thermal noise [189], by combining sophisticated single-molecule optical microscopy techniques with imaging or force measurements [190] and by using magnetic cantilevers whose deflection can be controlled by an external magnetic field [191,192]. The aforementioned instrumental developments, although not currently applicable for all systems, will continue to improve detection limits for both distance and force measurements.

## 6.2 MEASUREMENT OF FORCE–DISTANCE CURVES

A typical force–distance curve, with an arbitrary attractive potential between the tip and the sample, is shown in Figure 12. Since photodiode signals are measured rather than cantilever deflections, the slope  $(dV/dz)|_{cc}$  of the constant compliance (cc) region is used to convert photodiode signals,  $V_z$ , to cantilever deflections,  $Y_z$ :

$$Y_z = (V_z - V_0)/(dV/dz)|_{cc} \quad (11)$$

where  $V_0$  is the photodiode signal at large separation distances where no external forces are acting on the cantilever.  $(dV/dz)|_{cc}$  is often referred to as the inverse optical lever sensitivity (InvOLS). The force acting on the cantilever is given by Hooke's law [equation (1)]. A determination of the absolute distance,  $D_i$ , between the probe and sample must take into account the deflection,  $Y_i$ , of the cantilever at each position,  $z_i$ , of the piezoelectric translator:

$$D_i = (z_i - z_0) + Y_i \quad (12)$$

where  $z_0$  is the beginning of the constant compliance line. The conversion of force curves can be automated using appropriate algorithms, an example of which is given by Senden [193].

A major disadvantage of AFM with respect to the SFA is that no absolute distance scale between the probe and sample is currently available. In this respect, the constant compliance region of the force–distance curves is of crucial importance. From this part of the force curve, the optical lever sensitivity and the point of zero separation is extracted. For hard, incompressible surfaces, the problem is relatively straightforward, but the situation is more complicated when elastic surfaces are involved. For example, in the case of very

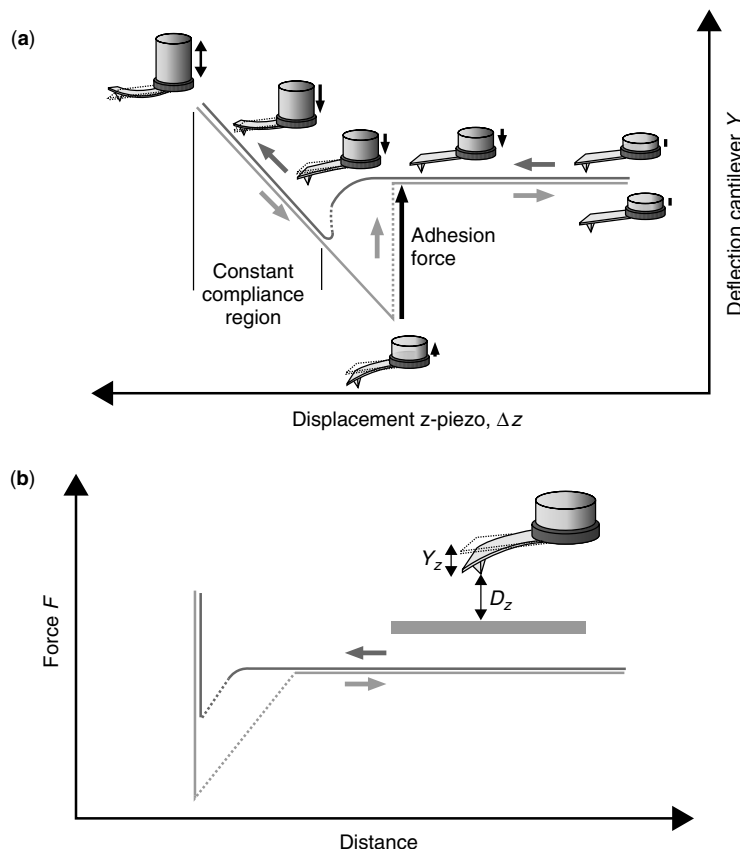


**Figure 12.** Schematic representation of a force profile in raw format (cantilever deflection versus piezo displacement) (a) and after conversion to force versus distance curve (b)

thin (less than a few nanometres) polymer layers, one can safely assume that a region of incompressibility is reached after applying high forces [194], which is not the case for thicker films [195]. Although it is possible to observe a linear constant compliance region, the slope does not correspond to the optical lever sensitivity [196]. If the interaction potential can be measured independently, the point of zero separation can be determined, even for highly elastic surfaces [197,198]. Common practices in determining the zero separation have been critically reviewed by Gillies *et al.* [197,198]. Whenever possible, the optical lever sensitivity should also be determined on a hard, incompressible substrate. A well-established practice is to employ cantilevers with different spring constants in order to detect differences in interaction forces, which are due to the improper determination of either the optical lever sensitivity or the zero distance due to short-range forces [199]. Nonetheless, in some cases, it might not be possible to separate surface elasticity from interaction forces, especially when measuring interaction forces, *in situ*, on soft, biological samples (*e.g.* bacteria). Some recent work provides indications of possible solutions in these cases [200–202].

### 6.3 TIP SAMPLE GEOMETRY AND COLLOIDAL PROBES

A quantitative knowledge of tip–sample geometry is crucial in order to extract quantitative information from the measured interaction forces between two surfaces. Measured forces,  $F(D)$ , should be compared with the interaction free energy,  $W(D)$ , between two plates separated by a distance  $D$ . Fortunately, a simple relationship, the Derjaguin approximation [172,203], exists for the sphere–sphere geometries commonly encountered in an AFM experiment:

$$F(D)_{\text{sphere-sphere}} = 2\pi R_{\text{eff}} W(D) \quad (13)$$

where  $R_{\text{eff}}$  is the effective radius, i.e.  $R_{\text{eff}}^{-1} = R_1^{-1} + R_2^{-1}$  and  $R_1, R_2$  are the radii of the two spheres.  $R_{\text{eff}}$  is generally estimated from the radii of the (presumably spherical) AFM tip and sample, although this approximation might not always be valid [204,205]. The Derjaguin approximation holds as long as the range of interaction and the separation distance are much smaller than the radii of the spheres. For many AFM direct force measurements, a sphere–plane geometry (i.e. colloidal probe and flat sample) is assumed such that the effective radius can be estimated from the radius of the probe.

Although the diameters of normal tips of silicon fabricated cantilevers can be increased in a controlled manner beyond the typical 10–100 nm [8], a more defined surface geometry can be obtained by the colloidal probe technique [173–175,206]. In this case, individual colloidal spheres are attached to the end of an AFM cantilever using an etched tungsten wire attached to a micromanipulator and a small amount of suitable glue (Figure 13). The precise radius of the colloidal probe can be determined by electron microscopy. Handling is monitored by light microscopy. This technique allows for a probe with a well-defined surface geometry and surface chemistry. Raiteri *et al.* [207] have described a simpler set-up.

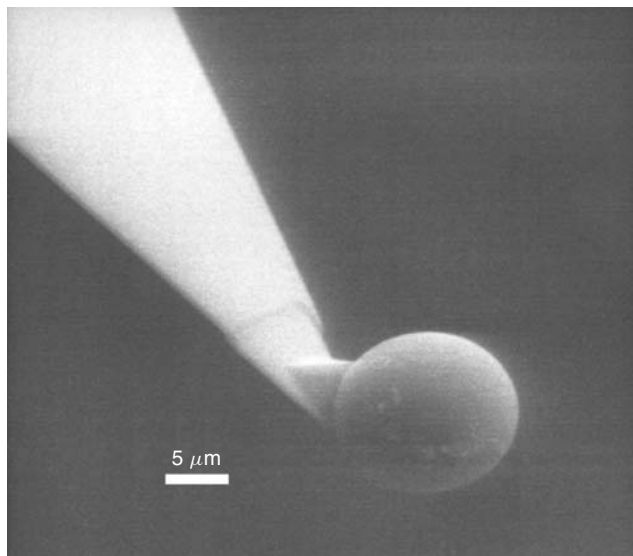


**Figure 13.** A typical colloidal probe obtained by attaching a borosilicate glass particle ( $\sim 15 \mu\text{m}$ ) to the end of an  $\text{Si}_3\text{N}_4$  cantilever

The colloidal probe technique is not limited to sphere–plane geometries. Several groups have measured interaction forces between spherical particles of polystyrene latex [208–210] or ZnS [211]. It has also been possible to measure forces between  $\alpha$ -alumina fibres by the colloidal probe technique in a crossed cylinder geometry, similar to the geometry of a SFA set-up [212]. With respect to their long-range interaction forces, biological samples such as bacteria can also be considered particle-like when the colloidal particle and biological object have comparable dimensions [213]. Nonetheless, even when the tip–sample geometry is well defined, surface roughness can have a pronounced influence on the interaction forces, especially at small separation distances [214–216]. A comprehensive treatment of the role of surface heterogeneities can be found in a review by Walz [217].

#### 6.4 DETERMINATION OF THE CANTILEVER SPRING CONSTANT

Quantitative analysis of the direct force measurements requires an accurate knowledge of the cantilever spring constant in order to convert a cantilever deflection to a corresponding force value. Typically, cantilevers used for direct force measurements have lengths of 100–450  $\mu\text{m}$  and widths of 25–50  $\mu\text{m}$ . For a single-beam cantilever, the resonance frequency,  $v_c$ , and the spring constant,  $k_c$ , are described by

$$v_c = \frac{t}{4\pi l^2} \sqrt{\frac{E}{0.24\rho_c}} \quad (14)$$

$$k_c = \frac{Ewt^3}{4l^3} \quad (15)$$

where  $t$  is the thickness of a single beam cantilever with length  $l$  and width  $w$ . The elastic modulus,  $E$ , and the density,  $\rho$ , are material constants. Unfortunately, it is difficult to control the cantilever thickness during the production process and therefore it is often subject to significant variations. Since the spring constant is directly proportional to  $t^3$ , even small variations in cantilever thickness will have a pronounced influence on the measured force. In addition, for cantilevers fabricated from silicon nitride, the material constants vary due to slight differences in composition within a single wafer. It is therefore essential to calibrate cantilevers that are used in direct force measurements. Unfortunately, due to their small dimensions, a straightforward calibration of the cantilever spring constant is difficult. Instead of applying methods with analogues in the macroscopic world, such as the measurement of the static deflection of a loaded cantilever [218], the frequency and power spectrum of the thermally excited cantilever are determined. Due to the central importance of this topic for quantitative force measurements some current methods are described in detail below. In addition, the search for novel calibration methods of the cantilever spring constant is continuing [219–221]. Of special interest are studies that compare the accuracy of the different techniques [221–223].

##### 6.4.1 Cleveland or Added Mass Method

This commonly used method to calibrate the spring constant is based on a shift of the cantilever resonance frequency when the end of the cantilever is loaded with a small

additional mass [177]. The resonance frequency,  $\nu_M$ , of a simple beam cantilever with a mass  $M$  attached to its end is given by

$$\nu_M = \frac{1}{2\pi} \sqrt{\frac{k_c}{M + m^*}} \quad (16)$$

where  $m^*$  is the effective mass of the cantilever beam. The equation can be rearranged to give

$$M = k_c(2\pi\nu_M)^{-2} - m^* \quad (17)$$

From a plot of equation (17), the slope of  $M$  versus  $(2\pi\nu_M)^{-2}$  corresponds to the spring constant of the cantilever and the intercept gives its effective mass. The mass is adjusted by using colloidal particles of a known density (*e.g.* tungsten spheres) whose diameter has been determined by light microscopy. Sader *et al.* [224] demonstrated that the position of the additional mass is crucial to the accuracy of the method and provided practical equations to correct for non-ideal positioning of the end-loaded masses. The great advantage of this method is that the resonance frequencies ( $\nu_c$ ,  $\nu_M$ ) of the cantilever can be measured with high precision by practically all AFM instruments without the need for further equipment. The method has the disadvantage of requiring a time-consuming micromanipulation of colloidal particles for each calibration.

#### 6.4.2 Hutter–Bechhoefer or Thermal Noise Method

The thermal noise method is based on the equipartition theorem, which states that, at thermal equilibrium, any harmonic energy term with one degree of freedom has an energy equal to  $\frac{1}{2}k_B T$  [176], where  $k_B$  is the Boltzmann constant and  $T$  is the temperature (K). For an AFM cantilever:

$$\frac{1}{2}k_c\langle Y^2 \rangle = \frac{1}{2}k_B T \quad (18)$$

where  $k_c$  is the spring constant of the cantilever and  $\langle Y^2 \rangle$  is its mean square deflection in the vertical direction due to thermal motion. The thermal noise spectrum is obtained by transforming time series data of the cantilever deflection into frequencies using a fast Fourier transformation. It is convenient to plot the thermal noise curve as a power spectral density where the thermally excited cantilever spectrum has the shape of a Lorentzian curve and the area under the curve corresponds to  $\langle Y^2 \rangle$  once the white and  $1/f$  noise have been subtracted. Optical lever sensitivity is determined by an additional measurement from the constant compliance region on a hard surface using exactly the same laser alignment as was used as for the acquisition of the power spectrum. In order to obtain quantitatively correct results by the Hutter–Bechhoefer method, all modes of cantilever vibration must be considered [225]. Furthermore, it is necessary to take into account that most AFM measure the inclination of the cantilever beam rather than its deflection [225]. Due to technical (bandwidth limitations) and practical reasons, it is often more convenient to evaluate only the first resonance peak. Nonetheless, Butt and Jaschke [225] derived expressions for the mean cantilever deflection in each mode after considering the effect of the cantilever inclination. In this case, under sole consideration of the first vibration mode, the spring constant is given by

$$k_c = 0.82k_B T/\langle Y_1^{*2} \rangle \quad (19)$$

where  $\langle Y_1^{*2} \rangle$  is the area under the first resonance peak as measured by the light lever technique.

#### 6.4.3 Sader's Method

This method allows for the determination of the cantilever spring constant for rectangular, single-beam cantilevers by measuring the easily accessible top-view dimensions and by evaluating the quality factor,  $Q$ , and resonance frequency,  $\nu$ , from the thermal noise spectrum [226,227]. The method is non-destructive and can be used for soft colloidal probes or modified cantilevers. Furthermore, the spring constants can be obtained without knowledge of the optical lever sensitivity [177]. Sader's method eliminates the requirement for an *a priori* knowledge of  $\rho$  and  $E$  for a given cantilever and accounts for the effects of the surrounding medium [227]. The spring constant,  $k_c$ , is given by

$$k_c = 0.1906l Q (w 2\pi\nu)^2 \rho_f \Gamma_i(\nu_c) \quad (20)$$

where  $w$  is the width (top view) of the cantilever,  $Q$  is the quality factor,  $\rho_f$  is the density of the fluid in which the cantilever is immersed and  $\Gamma_i(\nu)$  is the imaginary part of a hydrodynamic function, which depends on the Reynolds number of the cantilever in the medium. The quality factor  $Q$  is a measurement of the sharpness of the noise peak and is defined by  $Q = \nu/\Delta\nu$ , where  $\Delta\nu$  is its full width at half-maximum (FWHM) in the power spectrum. An analytical expression describing the hydrodynamic function  $\Gamma(\nu)$  has been provided by Sader [226]. The great advantage of this method results from the fact that the cantilever spring constant can be determined without a time-consuming attachment of colloidal particles or the necessity to determine the optical lever sensitivity, which depends critically on the accuracy of the piezo calibration and the elasticity of the sample.

#### 6.4.4 Static Loading Using Two Cantilevers

This method uses the fact that the slope in the constant compliance region depends on the spring constant of the sample [228,229]. By replacing the sample by a cantilever with a known spring constant,  $k_{std}$ , the spring constant of the cantilever under investigation can be obtained by

$$k_c = k_{std} \frac{1 - S_{cc}}{S_{cc}} \quad (21)$$

where  $S_{cc}$  is the slope of the constant compliance region. The accuracy of this technique depends critically on the calibration of the reference cantilever, which should have approximately the same spring constant as the undefined cantilever. In addition, the precise positioning of the cantilevers, one with respect to the other, is extremely important.

## 7 FORCES BETWEEN (COLLOIDAL) SURFACES AND THEIR MEASUREMENT

### 7.1 DLVO FORCES

In water, most surfaces are charged due to the dissociation of surface groups or the adsorption of ions from the bulk solution. Surface charges are compensated by oppositely

charged counterions from the bulk solution. A fraction of these counterions bind to the surface within the diffuse double layer [172,230]. If their diffuse double layers overlap, similarly charged surfaces will repel each other. The resulting force is referred to as the electrical or electrostatic double-layer repulsion or force, although, in reality, the repulsion is due to the entropic confinement of the counterions. In the electrical double layer, the concentration of counterions decays exponentially with distance.

The electrostatic potential,  $\psi(x)$ , within the diffuse layer is described by the Poisson–Boltzmann equation, which for two flat, identical surfaces is given by the following non-linear, differential equation [172]:

$$\frac{d^2\psi}{dx^2} = -\frac{e}{\varepsilon\varepsilon_0} \sum_i \tilde{z}_i n_{\infty i} \exp\left(\frac{-\tilde{z}_i e \psi}{k_B T}\right) \quad (22)$$

where  $e$  is the elementary charge,  $n_{\infty i}$  is bulk number density of the ions  $i$  with a valency  $\pm\tilde{z}_i$  and  $\varepsilon\varepsilon_0$  is the dielectric permittivity of water. The Debye length,  $\kappa^{-1}$ , also referred to as the double-layer thickness [172]:

$$\kappa = \sqrt{\sum_i \frac{n_{\infty i} e^2 \tilde{z}_i^2}{\varepsilon \varepsilon_0 k_B T}} \quad (23)$$

The Debye length depends solely on the properties of the liquid and not on the properties of the surface. For an aqueous solution of a monovalent salt at 25 °C,  $\kappa^{-1} = 0.304/\sqrt{c}$  (nm), where  $c$  is the concentration of the 1:1 salt (mol dm<sup>-3</sup>) [172]. The free energy per unit area can be calculated from the pressure  $\Pi$  between the surfaces, which, for two plates in a symmetrical electrolyte, is given by [231]

$$\Pi = 2n_{\infty} k_B T \left[ \cosh(\Phi) - \frac{1}{2} \left( \frac{d\Phi}{\kappa dx} \right)^2 - 1 \right] \quad (24)$$

where  $\Phi = ze\psi/k_B T$  and  $\psi$  denotes the potential at a distance  $x$  from the plate. By integrating the pressure (i.e. force per unit area) over the separation distance,  $D$ , it is possible to obtain the interaction free energy per unit area  $W_{DL}$  for two plates:

$$W_{DL}(D) = \int_D^\infty \Pi(x) dx \quad (25)$$

The force profile  $F(D)$  for two interacting surfaces can then be readily calculated using the Derjaguin approximation [see equation (13)]. In the case of low potentials ( $\psi_0 < 25$  mV), the Poisson–Boltzmann (PB) equation can be linearised to obtain the Debye–Hückel approximation [172], leading to a simple expression for the interaction free energy in a 1:1 electrolyte:

$$W_{DL}(D) \approx \varepsilon \varepsilon_0 \kappa \psi_0 e^{-\kappa D} \approx \sigma^2 e^{-\kappa D} / \kappa \varepsilon \varepsilon_0 \quad (26)$$

Equation (26) only applies to surface separations that are beyond one Debye length. In order to obtain the interaction energies for smaller separation distances or higher surface potentials, the full non-linear PB equation must be solved using numerical methods

and appropriate boundary conditions, i.e. constant charge (CC) and constant potential (CP). For example, when both surfaces are made from the same material (symmetric combination), algorithms are readily available [232,233]. For asymmetric combinations, more computational effort is required [234,235]. Note that the aforementioned boundary conditions (CC, CP) are not fulfilled by most surfaces. Indeed, the interaction forces between surfaces with dissociating surfaces groups are likely to fall between the CC and CP boundary conditions. A good example of charge regulation is given by the interaction forces between silica surfaces (Figure 14).

The free interaction energy of two surfaces in a solution contains contributions not only from the electrical double layers but also from the van der Waals interactions. The van der Waals forces follow a power law [equation (27)] and will always exceed the double-layer forces at small distances. In aqueous solutions, the van der Waals forces (Debye, Keesom and London) are, in large part, not sensitive to the properties of the bulk electrolyte. Given knowledge of the Hamaker constant,  $A$ , their contributions to the free energy per unit area can be summarised by

$$W(D)_{\text{vdW}} = -\frac{A}{6D} \quad (27)$$

Hamaker constants are readily available in the literature for many systems (*e.g.* inorganic materials [88]). Classical DLVO theory [237,238] is often used to describe the interactions in colloidal suspensions, is obtained by the additive combination of electrostatic,  $W_{\text{DL}}$ , and van der Waals,  $W_{\text{vdW}}$ , contributions:

$$W(D) = W_{\text{DL}}(D) + W_{\text{vdW}}(D) \quad (28)$$

## 7.2 MEASUREMENTS OF INTERACTION FORCES BETWEEN ENVIRONMENTAL SURFACES

Interaction forces between surfaces have been characterised using the colloidal probe technique, most often using a silica particle [236,239–242]. For example, the electrostatic interaction between colloidal silica and an oxidised silicon wafer has been investigated as a function of the bulk electrolyte concentration and pH [174]. In addition to obtaining good agreement between the measured and calculated Debye lengths as a function of the bulk electrolyte concentration, Ducker *et al.* clearly demonstrated the expected decrease in surface potential with pH [174]. Hartley *et al.* [236] found excellent agreement between surface potentials obtained by DLVO fits of force curves and values derived from electrophoretic mobility and streaming potential measurements (see Figure 14). Zhmud *et al.* [239] determined the surface ionisation parameters of silica by fitting a comprehensive set of force curves obtained at different pH values using a colloidal probe. Charge regulation could only be accounted for by excluding interaction forces in the final 1–5 nm, which is the region where surface roughness and non-DLVO forces can dominate the interaction, *i.e.* for nearly all surfaces, the applicability of the constant charge and constant potential boundary conditions is limited to large separation distances.

In addition to silica, a great number of oxide or organic surfaces have been examined by the colloidal probe technique. A comprehensive treatment can be found in a number of reviews [184,243–245]. Even in the very first papers using the colloidal probe

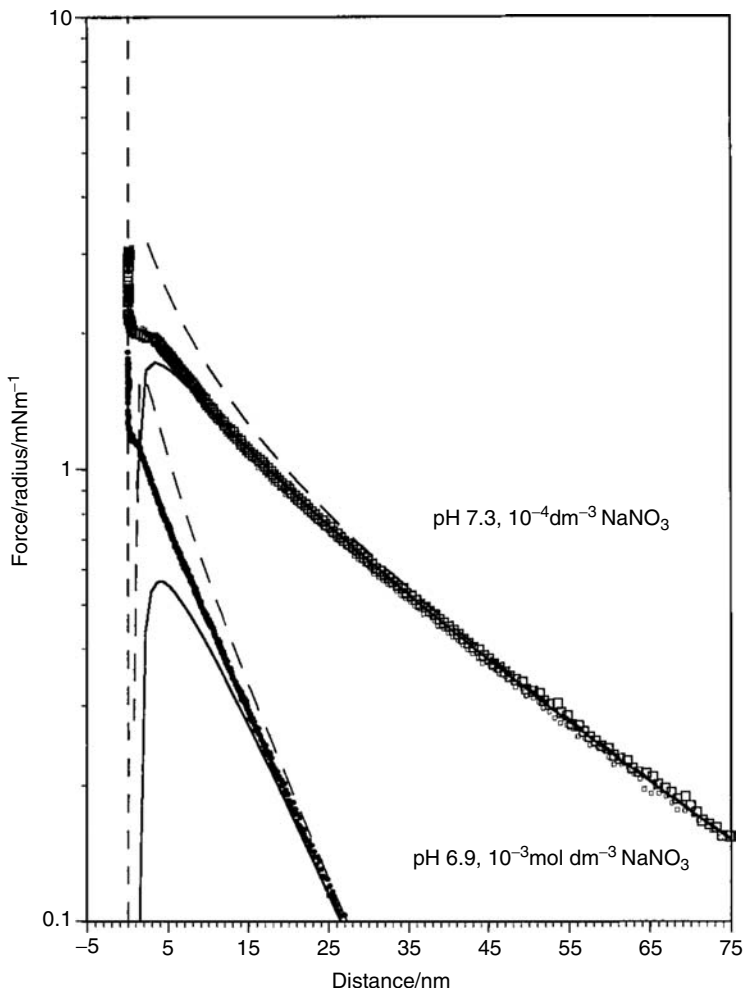


**Figure 14.** Interaction forces between a silica colloidal probe and a silica wafer. The interaction forces are normalised to the particle radius ( $F/R$ ) and are plotted on a logarithmic scale, so that the long-range part of the interaction force has a linear slope, which corresponds to the Debye length. The fits for two identical surface potentials are shown for the constant charge and the constant potential boundary condition. Reprinted with permission from Hartley, P.G., Larson, I. and Scales, P.J., Electrokinetic and direct force measurements between silica and mica surfaces in dilute electrolyte solutions, *Langmuir*, **13**, 2207–2214, Copyright 1997 American Chemical Society

technique, the versatility of the AFM set-up was demonstrated by measuring electrostatic interaction forces between dissimilar surfaces (e.g. [206]). Most often, the interaction between colloidal spheres and a flat surface such as titanium oxide [246], aluminium oxide [247,248] or mica [236] was probed. In some cases, the surface and the colloidal probe have been independently characterised by other techniques (e.g. streaming potential or electrophoretic mobility measurements) [236]. For interaction forces in asymmetric

systems, the points of zero charge of the two surfaces are useful for determining, in advance, whether the interaction will be attractive or repulsive [234,248].

Force measurements by AFM have also been used to study the electrostatic surface properties of membranes, in particular membrane–colloid interactions and hence membrane fouling. Until recently, these properties were generally evaluated by electrokinetic techniques such as streaming potential measurements, for which a value that is averaged over the entire surface is obtained. In contrast, a main advantage of the AFM technique is that surface roughness and chemical inhomogeneity effects can be probed directly and resolved laterally. Since in most cases the sample and probe constitute an asymmetric system, a quantitative evaluation of their interaction forces requires comparison with the non-linear PB equation. For example, Bowen *et al.* [249] measured the long-range electrostatic forces between a silica particle and a Desal nanofiltration membrane in electrolyte solutions of varying ionic strength. The experimental data were fitted to the constant charge and constant potential boundary conditions for the non-linear PB equation with dissimilar surfaces (Figure 15). At lower ionic strength, good agreement between the experimental data and the constant charge conditions was obtained since calculated surface potentials were in the range expected from zeta-potential measurements. On the other hand, with increasing ionic strength, increasing discrepancies with values predicted by DLVO calculations were observed. The authors attributed this observation to effects of the surface roughness of the membrane, in particular when the Debye length approached values of

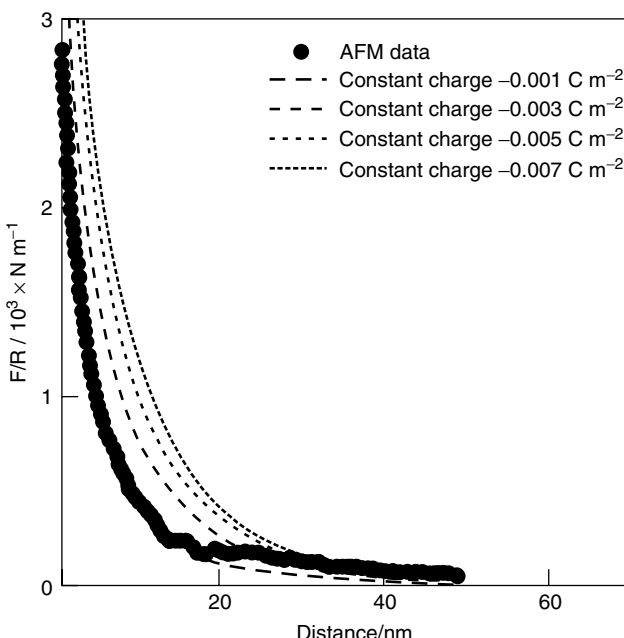


**Figure 15.** Interaction forces between silica colloidal probe and a Desal membrane in  $10^{-3}$  mol dm $^{-3}$  NaCl with the corresponding DLVO calculation for the constant charge boundary condition. Reprinted from Bowen, W. R., Doneva, T. A. and Stoton, J. A. G., The use of atomic force microscopy to quantify membrane surface electrical properties, *Colloids and Surfaces A*, **201**, 73–83, Copyright 2002, with permission from Elsevier

similar lengths to the membrane inhomogeneities. In a similar study [250], the long-range interaction forces between different types of colloidal particles (silica, aluminium and polystyrene) and two different types of membranes were determined in order to evaluate the significance of polar interactions at small separation distances. Surface energy components (acid–base, hydrophobicity) were characterised by means of zeta-potential and contact angle measurements. Experimental data were compared with DLVO theory and an extended model that accounted for non-DLVO short-range interactions. Although the data qualitatively followed the sequence predicted by the extended model, pronounced differences between the standard and extended DLVO models were demonstrated.

The origin and nature of interparticle forces between colloidal surfaces in natural waters have been examined by precipitating a film of iron oxide on silica surfaces that constituted the colloidal probe as well as the sample [251]. Natural organic matter (NOM) from riverside and marine environments strongly adsorbed to the modified surfaces. By measuring interaction forces in electrolyte solutions and in natural waters, Mosley *et al.* [251] demonstrated several important contributions to the interaction forces. The long-range interactions were dominated by an electrostatic repulsion arising from the negative functional groups on the NOM. For small separations, steric interactions (see also Section 7.3) due to the adsorbed NOM were also detected. At low pH or high ionic strength (*e.g.* sea-water), a steric repulsion predominated. By using a poly(methacrylic acid), a synthetic polymer with a comparable COOH group density to NOM, a similar trend was observed, although the pH effect on steric interactions was less pronounced. This and the previous examples illustrate how direct force measurements can be applied to environmentally relevant systems. Although a complete quantitative description has not yet been obtained and will be difficult to accomplish for most real-world systems, the combination of AFM with other techniques will certainly facilitate the measurement of properties that are not easily accessible by other techniques.

### 7.3 NON-DLVO FORCES

While classical DLVO theory considers electrostatic long-range and van der Waals short-range forces, a number of other forces can be important in environmental systems (for a review, see [252]). Indeed, hydrophobic surfaces have a greater tendency to aggregate than predicted by DLVO theory alone. Nonetheless, there is no clear consensus about the origin of many non-DLVO forces. For example, evidence has been presented that the long-range part of hydrophobic forces is due to the coalescence of micro-bubbles [208,253–255]. For hydrophilic surfaces, hydration effects are possible due to the reorganisation of surface-bound water upon approach of the colloidal particles [175,256]. They are of primary importance to the interaction of molecularly smooth surfaces [175,256]. Steric forces may arise in the presence of diffuse interfaces, such as those occurring when biopolymers protrude from the interface. These forces are well known in classical colloid chemistry, where they are of great importance in the stabilisation of colloidal suspensions (for a recent review, see [135]). Nonetheless, steric forces are not restricted to organic layers. For example, Virgil *et al.* [257] demonstrated the formation of a silicic acid gel layer on silica surfaces, which could account for an additional steric contribution at small separation distances.

The first direct measurements of steric interaction forces were performed with the SFA [258–260] and several SFA studies have dealt with their more fundamental aspects

[261–264]. Measurements of steric interaction forces can be made using AFM either for polymers that are adsorbed or grafted to a solid surface [265–267] or those present on biological cells [201,268]. For steric interactions, the surface coverage of the adsorbed or grafted chains is an important parameter. At low coverage, there is no overlap between neighbouring chains so that each chain can interact with the opposite surface in an independent manner. In that case, the layer thickness,  $L$ , corresponds reasonably to the radius of gyration,  $R_g$ , of a single polymer molecule. In the case of high coverage, the neighbouring chains are so close to each other that  $L$  is much larger than  $R_g$ . Once the polymer brushes are separated by less than  $2L$ , a repulsive force occurs. Alexander–deGennes theory [172,269] can be used to describe interaction forces between uncharged polymer brushes and the interaction energy per unit area:

$$W(D) = 8 \frac{k_B T}{35s^3} \left[ 7 \left( \frac{2L}{D} \right)^{\frac{5}{4}} + 5 \left( \frac{D}{2L} \right)^{\frac{7}{4}} - 12 \right] \quad (29)$$

where  $s$  is the average distance between the anchor points of the chains. Although the above theory is only strictly valid for end-grafted polymers, it has also been successfully applied to physi-sorbed polyampholytes [262]. For most of the interaction range, equation 29 can be approximated by an exponential equation [172]. In the case of polyelectrolytes, a more complex behaviour is observed that depends on both the grafting density ( $1/s$  [2]) and the fraction of charged monomers [270,271]. Some expressions for the interaction force that are based on the scaling theory of Pincus [272] can be found in the work of Abraham *et al.* [261]. Using the SFA, they found that the interaction forces were given solely by the osmotic pressure due to the counterions (low salt concentration). Using AFM, the measurement of steric forces has been performed on the bacterium *Pseudomonas putida* [268] and the oocyst *Cryptosporidium parvum* [201]. In these cases, a quantitative interpretation is much more difficult to obtain since the grafting density is not known *a priori* and since the extracellular polymers may have a significant polydispersity. Nevertheless, for the extracellular biopolymers of *Pseudomonas putida*, Abu-Lail and Camesano [268] were able to show a clear dependence of the brush thickness on the salt concentration up to a critical concentration at which the ionic brush collapsed.

#### 7.4 ADHESION FORCES

During the approach of the AFM tip, long-range forces generally result from interactions among a large number of molecules of the tip and sample and thus are fairly representative of the general behaviour of the surface. On the other hand, when the probe is withdrawn from the sample, the force curves can show a more complex behaviour. Often, hysteresis ('jump out' instability) due to adhesion between the probe and sample is observed (Figure 16a). The contact area between the tip and the surface is of central importance to the adhesion. If no other interaction forces are important, the contact area can be given by Hertzian contact mechanics where only the geometric dimensions and elastic properties of probe and sample determine the deformation. Under ambient conditions, the main contributions to the adhesion forces are due to capillary forces. Due to the adsorption of a thin water layer on most hydrophilic surfaces, a meniscus forms upon contact of the

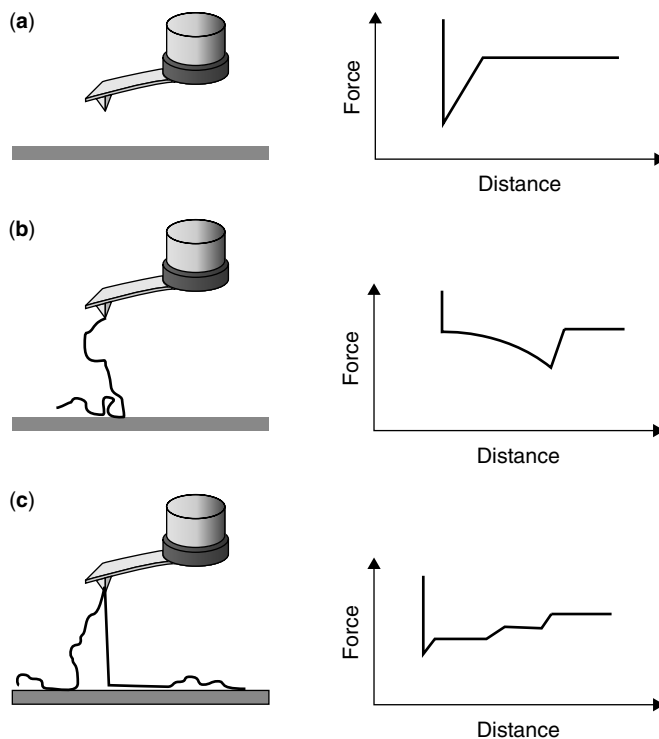


**Figure 16.** Schematic representation of different forms of adhesion resulting in (a) a single unspecific adhesion peak, (b) the bridging of a single polymer chain between the AFM probe and sample and (c) the desorption of a polymer adsorbed in a train-like conformation

tip, resulting in large adhesion forces due to the surface tension of the liquid. In this case, adhesion depends on the free surface energies of the tip and sample, the humidity and the tip radius.

In typical studies on environmental colloids, an adhesion force is determined between two solid objects in an aqueous phase. It is evaluated from the interfacial tensions,  $\gamma$ , of the three interfaces [sample (1), tip (2), liquid (3)]. The work necessary to separate the two surfaces from contact to infinite separation is given by [172]

$$W_{132} = \gamma_{13} + \gamma_{23} - \gamma_{12} \quad (30)$$

The adhesion force between two rigid (incompressible) spheres can be related to their work of adhesion by the Derjaguin approximation [172] using  $R_{eff} = R_1 R_2 / (R_1 + R_2)$  as the effective radius.

Contrary to the above long-range behaviour, where most surfaces can be regarded as non-deformable, the elastic properties of the tip and/or sample have to be taken explicitly into account when relating the work of adhesion with measured adhesion forces. Two models are commonly applied to describe adhesion behaviour: that of Johnson, Kendall and Robertson (JKR model [273]) and the model based on the work of Derjaguin, Müller and Toporov (DMT model [203]). These two models represent the extreme boundaries of

the more general Maugis theory [274], which cannot be solved analytically and is thus seldom considered for practical applications.

In JKR theory, the radius of the contact area,  $a$ , between two spheres of effective radius  $R$  (i.e.  $1/R = 1/R_1 + 1/R_2$ ) and elastic modulus,  $E$ , under an external loading force,  $F$ , can be given by [172]:

$$a_{\text{JKR}}^3 = \frac{R}{E} \left[ F + 3\pi RW_{132} + \sqrt{6\pi RW_{132}F + (3\pi RW_{132})^2} \right] \quad (31)$$

An important consequence of equation (31) is that even under small negative loads, the solids still adhere. At a critical negative adhesion force, the surfaces separate abruptly, corresponding to

$$F_{\text{adh|JKR}} = -\frac{3}{2}\pi RW_{132} \quad (32)$$

with a finite contact radius at the moment of separation that is given by

$$a_{\text{sep|JKR}} = \sqrt[3]{6\pi \frac{R^2}{E} W_{132}} \quad (33)$$

An interesting consequence of these equations is that while the elastic modulus determines the contact area, it has no influence on the adhesion force [172]. The JKR model assumes that the attractive forces between the two surfaces act solely over the contact area. This leads to physically impossible conditions at the outer rim of the contact area, *e.g.* infinite stress. On the other hand, in the DMT model, the attractive interaction forces are assumed to act only outside the contact area such that the adhesion force can be described by

$$F_{\text{adh|DMT}} = -2\pi RW_{132} \quad (34)$$

In this case, the tip–sample geometry remains Hertzian and the contact area at the moment of separation is zero, i.e. the DMT model tends to underestimate the contact radius. Therefore, the DMT model is generally applied to rigid surfaces and systems with low adhesion and long-range interaction forces whereas the JKR model does a better job of describing elastic surfaces with high surface energies. In addition to their theoretical limitations, it is also often difficult to distinguish between the simple adhesion models (JKR, DMT) due to uncertainties in the determination of the cantilever spring constant and the tip radius. The latter problem can be overcome by applying the colloidal probe technique for adhesion force measurements (a comprehensive review is given by Kappl and Butt [275]). As described above (Section 7.2), the primary limitation arises from the surface roughness of most colloidal particles. Indeed, pronounced deviations from the theoretically expected values have been found when measuring micrometre-sized particles (*e.g.* [214,215]). The limitations of both adhesion models have nonetheless led to a series of more sophisticated adhesion theories (for a comprehensive overview, see [274,276,277]).

While a ‘clean’ jump out of contact is often observed for adhesion between oxide surfaces, this is generally not the case for surfaces that are covered with (bio)polymers. Due to the discrete character of the single polymer chains, they can often bridge the sample and the tip, leading to a more complex adhesion behaviour that cannot always be split

into its individual contributions. For example, for many polymeric surfaces, in addition to the ‘jump out’ at zero distance (see Figure 16a), it is possible to observe additional adhesion events further out from the surface (see Figure 16b for a single polymer). In this case, one or several polymers are adsorbed to the probe, stretched, then finally detached from the probe surface at distances that depend primarily on the polymer contour lengths. Since the polymer molecules bridge the sample and the probe, the configurational freedom of the polymer is increasingly limited with increasing distance between the two entropic forces (see Section 7.7) leading to a non-linear force behaviour (Figure 16c). In spite of the multiple adhesion events, it is possible to determine the distribution of the adsorbed polymer loops [278–280]. Most often, experiments to measure desorption forces are designed where the polymer is covalently bound to one surface so that the measured force distribution can be attributed to the weakest polymer–surface interaction. For synthetic polyelectrolytes, values of the order of 75–200 pN are found, whereas for biopolymers, values of up to a few nanonewtons have been reported. Interpretation is nonetheless difficult due to limited information on the interfacial conformation of the polymer. An instructive example on a living diatom was provided by Higgins and co-workers [202,281,282], who showed pronounced differences in the adhesion forces that were measured following contact between the tip and mucilage on the surface of the organism ( $>1$  nN) and those measured ( $>200$  pN) when the tip was brought in the vicinity of the surface in order to pick up only polymer chains protruding into the solution. In the latter technique, often referred to as *fly-fishing*, the tip is brought towards the substrate so that polymer segments may adsorb. Increased contact times are used to compensate for low adsorption probabilities that favour the bridging of single segments.

The use of AFM to measure the external forces required to desorb polyelectrolytes or polysaccharides that are in extended conformations on the surface (train-like conformations) is a special case of an adhesion measurement [283,284]. In contrast to the desorption of short polymer segments, where a single sharp peak and subsequent instability are observed after polymer stretching, a long plateau is measured at constant force for long polymers [284] (Figure 16c). For example, values corresponding to constant forces were typically observed for the desorption of polyvinylamines (PVA) from silica [283]. For PVA molecules of two linear charge densities (varied by hydrolysis), a clear dependence of the desorption plateau force was observed as a function of the ionic strength of the electrolyte, in good agreement with a simple Debye–Hückel model of polymer desorption [283].

## 7.5 MEASUREMENTS OF ADHESION FORCES APPLIED TO ENVIRONMENTAL SYSTEMS

The measurement of adhesion forces is a valuable means to determine the properties of environmental surfaces. Applications range from the examination of ultrafiltration membrane properties to the determination of biological adhesion to substrates. In this respect, the colloidal probe technique can either mimic surface properties by using model particles (*e.g.* latex) with suitable functional groups or by directly measuring the interaction forces in the system of interest (*e.g.* between a silica particle and a immobilised bacterium). In the following short overview, a number of representative studies have been selected to illustrate several important concepts, such as the dependence of the adhesion force on the interfacial energy [See equations (30) and (32)] or the influence of ions on adhesion.

The adhesion of hydrophobic contaminants to soil particles is a key factor that controls the efficiency of soil decontamination processes [285]. A thermal or chemical (i.e. adsorption of alkanes) treatment of silica can be used to increase its hydrophobicity, as determined by contact angle measurements. Adhesion forces between treated silica wafers and polyethylene colloidal particles have been measured in water and compared with values calculated using JKR theory and the Fowkes–van Oss–Chaudhury–Good surface tension model [286–288]. In the latter model, surface tension is separated into two components related to dispersion forces (LW) and the Lewis acid and base (AB) properties of the surface such that the total surface tension can be described by

$$\gamma_{\text{tot}} = \gamma^{\text{LW}} + \gamma^{\text{AB}} = \gamma^{\text{LW}} + 2\sqrt{\gamma^+ \gamma^-} \quad (35)$$

Following thermal treatment of the silica, the silicic acid component,  $\gamma_{\text{silica}}^-$ , became the determining component for the adhesion. Good agreement was found between theoretical calculations based on the surface tensions of water, silica and polyethylene and the measured adhesion forces (Figure 17). Nalaskowski *et al.* [285] proposed that the observed increases in adhesion were related to a decreased efficiency of oil removal from the contaminated soil.

The role of different functional groups on the sample surface and thus interfacial energies can be probed in a more defined manner by chemical force microscopy (CFM), in which a self-assembled monolayer is covalently bound to the AFM tip [289–295]. By modifying the tips, surface properties such as hydrophobicity or surface charge [180,296] can be probed with a lateral resolution on the nanometre scale [297]. For example, the influence of solvent properties and functional groups was studied using thiol compounds

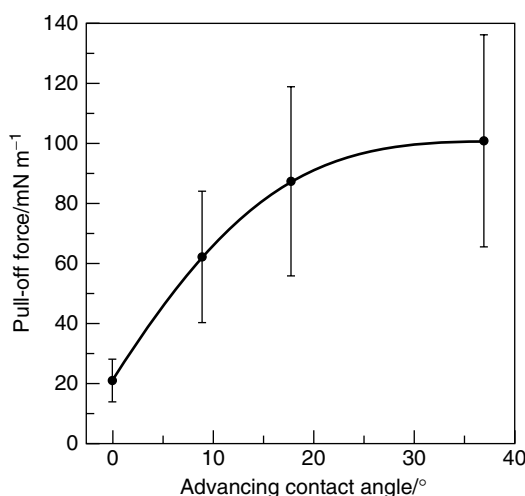


**Figure 17.** Adhesion force measured between a polyethylene colloidal probe and a thermally treated silica wafer in water as a function of the contact angle measured on the silica wafer. Reprinted with permission from Nalaskowski, J., Drelich, J., Hupka, J. and Miller, J. D., Adhesion between hydrocarbon particles and silica surfaces with different degrees of hydration as determined by the AFM colloidal probe technique, *Langmuir*, **19**, 5311–5317, Copyright 2003 American Chemical Society

with the same alkane spacer length but different end groups. Adhesion forces obtained with different tip–sample combinations and measured in different solvents were described quantitatively [298–300] using the Fowkes–van Oss–Chaudhury–Good surface tension model [286–288]. In addition, surfaces of unknown or heterogeneous composition such as flat polymeric substrates [301] or the surface of biological organisms [302] have been characterised by CFM (reviewed in [297]), although quantitative information may be limited due to surface roughness [303].

Li and Elimelech [304] elegantly combined batch techniques and force measurements in order to investigate the organic fouling and chemical cleaning of nanofiltration membranes. A colloidal probe, consisting of a carboxylate latex particle, was used as a surrogate for a humic acid. Adhesion forces under various solution conditions (concentrations of monovalent and divalent ions, surfactants) were very well correlated with the nanofiltration membrane fluxes. The efficiency of the chemical cleaning of the nanofiltration membranes was also examined by varying pH and surfactant concentrations. Adhesion measurements demonstrated that  $\text{Ca}^{2+}$  bridging stabilised the interaction of the organic fouling molecules with the nanofiltration membranes. Effective cleaning occurred when Ca complexation of the organic fouling molecules was inhibited.

Closely related to the adhesion of particles are their sticking coefficients, which can be used to predict particle removal from solution. Indeed, sticking coefficients derived from DLVO theory rarely match values found experimentally, *e.g.* in column adhesion experiments. Cail and Hochela [305] recently determined the sticking coefficients of small colloidal particles to a collector using colloidal probe measurements. They measured the interfacial potential energy by integrating the approach forces over the separation distance, as a means to calculate the sticking coefficient using the interaction force boundary layer model. They obtained results that were much nearer to theory than those obtained by other experimental techniques. The approach of comparing force measurements with column adsorption experiments is not limited to abiotic colloidal particles but can also be applied to biological organisms [306,307].

Lipopolysaccharides (LPS) in the outer cell membrane of Gram-negative bacteria are known to have an important role in bacterial cell adhesion. Adhesion between an  $\text{Si}_3\text{N}_4$  tip and *Escherichia coli* JM109 was measured in water and in a  $0.01 \text{ mol dm}^{-3}$  PBS buffer [308] before and after treatment of the bacteria with ethylenediaminetetraacetic acid (EDTA). When desorption events were plotted against the distance at which the corresponding pull-off force was detected (Figure 18), it became clear that the EDTA treatment reduced the observed average length of the extracellular LPS molecules, both in water and in PBS. This difference was also observed for steric interactions during the approach of the tip. The distribution of adhesion forces was unimodal, in contrast to that observed for *Pseudomonas putida*, where different polysaccharides were present on the bacterial surface [308].

## 7.6 FORCE SPECTROSCOPY: STRETCHING OF SINGLE POLYMERS

Force spectroscopy examines the properties of a single molecule that is bridged between the tip and the sample [136,309–312]. Although to date this technique has been used primarily for biological and synthetic polymers, its potential applications to the study of environmental colloids are extremely promising. Indeed, the high force resolution and the small diameter of the tip make the AFM an ideal tool to measure forces at a molecular

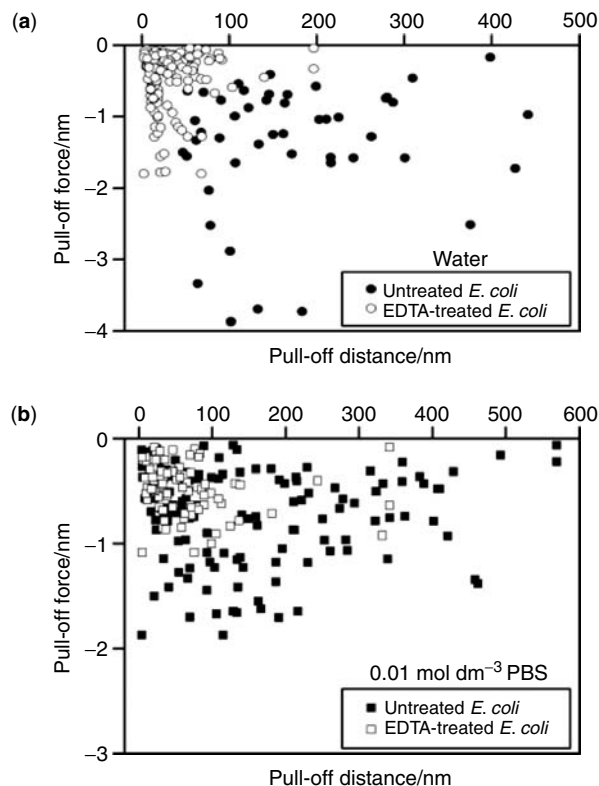


**Figure 18.** Distribution of the adhesion forces between *E. coli* and an  $\text{Si}_3\text{N}_4$  tip in (a) water and (b) PBS buffer [308]. For both solutions, the distribution of the adhesion forces and the observed pull-off distance changed significantly after EDTA treatment, indicating a reduction in the length of the extracellular polysaccharides. Reprinted with permission from *Environmental Science and Technology*, **37**, 2173–2183, Abu-Lail, N. I. and Camesano, T. A., Role of lipopolysaccharides in the adhesion, retention, and transport of *Escherichia coli* JM 109, Copyright 2003 American Chemical Society

level. Nonetheless, these experiments can require a complex experimental design in order to ensure that the stretching of single molecules dominates the interaction forces during the retraction of the probe. Often, the sample and tip preparation need to be optimised in order to favour the adsorption of polymer segments and to minimise the adhesion peak at zero separation. The number density of the adsorbed polymer can be reduced in order to increase the probability of single molecule stretching events. Another possibility is the use of the ‘fly-fishing’ technique in which the tip is positioned slightly above, or directly on, a polymer-bearing surface and then retracted. In this manner, single polymer segments are stretched by continuously increasing the separation distance between the tip and the sample. When the ends of the polymer segments are sufficiently strongly bound to the sample, it is possible to measure the entropic restoring force for a large extension range (Figure 16b). For some polymers, including proteins and polysaccharides, changes in the secondary structure of the polymer segments can be observed at sufficiently high forces.

For example, for the muscle protein titin, a saw-tooth pattern that indicated the unfolding of single domains at well-defined forces was observed [179].

## 7.7 SINGLE MOLECULE EXTENSIONS

If the contour length of a linear polymer is sufficiently high, it will adopt a random coil conformation in solution that is subject to Brownian motion. If the molecule, or a sufficiently long segment, is attached by its ends to two surfaces, an increase in distance between the surfaces will result in a loss of conformational freedom and entropy of the polymer. The simplest case is given by a Gaussian chain in the low force regime where the restoring force  $F$  is proportional to the extension ( $R_{ee}$ ) of the polymer chain with the contour length  $L_c$ :

$$F(R_{ee}) = 3 \frac{k_B T}{\ell_K} \frac{R_{ee}}{L_c} \quad (36)$$

where  $\ell_K$  is the Kuhn length. In the case of a polymer segment bridged between the tip and the substrate, the end-to-end distance,  $R_{ee}$ , corresponds to the separation distance,  $D_{po}$  between the tip and the sample. At higher forces, the single segments of the chains are no longer oriented in a random fashion and different models have to be employed. The most commonly used models describing the entropic restoring forces of a stretched polymer chain are the freely jointed chain model (FJC model) and the worm-like chain model (WLC model). The FJC model has been applied to synthetic [278,313,314] and natural polymers, such as dextran [179] and single-stranded DNA [315]. The worm-like chain or Kratky–Porod model describes the polymer chain as a continuous sequence, neglecting any discrete chain structure [316]. The characteristic length scale for this model is the persistence length,  $L_p$ , which corresponds to the characteristic decay length of any directional correlation along the polymer chain. For small forces (extensions) and flexible chains ( $L_c \gg L_p$ ), the persistence length is equal to half of the Kuhn length in the FJC model. For higher forces/greater extensions, the WLC model predicts a stiffer behaviour of the polymer chain because the single segments can move in an independent manner in the FJC model. The exact dependence for the force versus extension curve  $F(D_{po})$  can only be calculated numerically for the WLC model [317]. An approximation, which is exact in the limits  $R_{ee} \rightarrow 0$  and  $R_{ee} \rightarrow \infty$ , has been given [318]:

$$F(D_{po}) = \frac{k_B T}{L_p} \left[ \frac{D_{po}}{L_c} + \frac{1}{4(1 - D_{po}/L_c)^2} - \frac{1}{4} \right] \quad (37)$$

This analytical approximation is very helpful when analysing experimental data, but it should be kept in mind that deviations on the order of 10% for the forces in the intermediate regions from  $0.2k_e T/L_p$  to  $0.9k_B T/L_p$  are typically encountered [319]. Further details can be found in comprehensive reviews on this subject [309–312]. The model that is applied depends to a large extent on the nature of the polymer that is examined. For synthetic polymers, both the FJC [320,321], the WLC [283,322,323] or both [313,314] models have been applied. Recent theoretical findings of Livadaru *et al.* [324] have shown why the extension of more rigid biopolymers (high intrinsic persistence length) such as double-stranded DNA is well described by the WLC model whereas this is not the case for many polymers with a low intrinsic  $L_p$  (e.g. synthetic polyelectrolytes). Livadaru

*et al.* [324] have demonstrated that semi-flexible polymer chains may show a crossover from the standard WLC behaviour to a discrete chain (DC) behaviour for forces of approximately 100 pN, exactly in the force range that is probed by AFM experiments.

In the context of environmentally motivated research, the extension behaviour is especially important in connection with natural polymers, in particular polysaccharides. Polysaccharides are a major constituent of the cell walls and external layers of a number of organisms (*e.g.* bacteria, green algae and fish). They are also present in the aqueous environment as organic colloids, where they are involved in contaminant transport, aggregation and nutrient bioavailability. In particular, the role of polysaccharides in the bioadhesion process has received a great deal of attention since AFM can measure the properties of single exopolymer strands, *in situ*, directly on bacterial surfaces.

Polysaccharides were among the very first macromolecules whose extension, due to external forces, was examined by AFM-based force spectroscopy. In pioneering work, Rief *et al.* [178] examined a native and carboxymethylated dextran (CM-dextran). Molecular elasticity was examined for high (up to 1000 pN) stretching forces using either streptavidin-modified tips (native dextran tethered to a gold substrate and modified by biotin) or hydrophobic tips (CM-dextran). In the low extension regime (<500 pN), the force response of both dextran molecules was well described by the extended FJC model ( $\ell_K \approx 0.6$  nm,  $K_c \approx 60$  N m<sup>-1</sup>). At forces of ca 500 pN (ca 300 pN for CM-dextran), the extension curves exhibited shoulder-like plateaus that corresponded to an increase in the stiffness of the polysaccharide chains due to a transition in the C-5–C-6 bond of the pyranose rings. Amylose, pullan and pectin have also shown pronounced deviations from the entropic elasticity [325–328]. In addition, extension curves have been used to ‘fingerprint’ single polysaccharide molecules in a polysaccharide mixture [328].

Polysaccharides can also form intermolecular suprastructures. For example, the extension behaviour of  $\kappa$ ,  $\iota$ ,  $\lambda$ -carrageenan isolated from a marine red alga was related to differences in the rotational freedom of the pyranose ring structure [329]. Native carrageenan exhibited a complex random coil–helix–gel transition with a conformation that depended on the nature and concentration of the counterion as well as the temperature. When measurements were performed in NaI, a long plateau was observed for an external force of ca 300 pN that was ascribed to the unwinding of the helical structure [330]. A similar behaviour has been observed for native xanthan [331].

In addition to the measurement of single polymers that are adsorbed or tethered to solid substrates, extension measurements can be made for biopolymers that are on the cell surface. Naturally, these measurements are more complex since it is more difficult to define the zero-separation. Furthermore, tip modification techniques are more limited since the same tip has to be used to pick up the polymer chains and localise the cell position. Thus, for biological samples, preparation protocols have a pronounced influence, not only on the elasticity and long-range interaction forces [332,333] but also on the nature and concentration of the extracellular polymers [308]. In spite of these difficulties, several groups have measured the extension behaviour of extracellular polymers on cell surfaces [202,268,308,334,335]. For example, for polymers on the spores of *Aspergillus oryzae*, extension curves could be described by an extended FJC model with a Kuhn length of ca 3.2 nm, contour lengths of 20–500 nm and a segment elasticity of ca 3.9 N m<sup>-1</sup> [334]. The elasticity of the surface of *Pseudomonas putida* has been examined by varying systematically a number of parameters including solvent

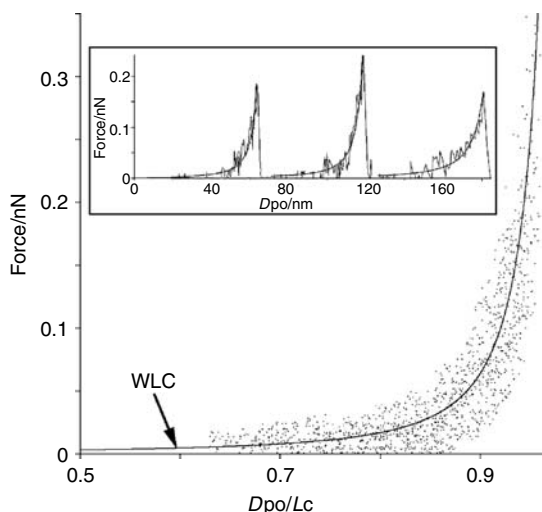


**Figure 19.** Stretching of the surface polymer chains of *Craspedostauros australis*. The normalised force versus extension curves (composed of 45 different measurements) are shown as a master curve with the corresponding fit to the experimental data. The inset shows an example of the different extension curves with different contour lengths. Reprinted from Higgins, M. J., Sader, J. E., Mulvaney, P. and Wetherbee, R. (2003). Probing the surface of living diatoms with atomic force microscopy: the nanostructure and nanomechanical properties of the mucilage layer, *Journal of Phycology*, **39**, 722–734, with permission from Blackwell Publishing Ltd

composition, ionic strength and the influence of an EDTA treatment [268,308,335,336]. Among other important results, these experiments demonstrated that ionic strength had an important effect on surface elasticity and adhesion.

Diatoms are known to glide on their substrate, leaving behind a trail of adhesive mucilage. For example, for the mucilage of *Craspedostauros australis*, the contour length distribution measured by single force microscopy was broad [202,281] (Figure 19). Experimental force extension plots were fitted to the WLC model, resulting in a persistence length of  $\sim 1.8$  nm. Single molecule probing measurements were in agreement with topographic images, taken by tapping mode AFM in fluid, revealing different morphologies for a number of diatoms [202]. The use of AFM for the study of biological organisms, *in situ*, will certainly be an application that is greatly exploited in the future. By using modified AFM tips, it is already possible to probe various cell properties, *in situ*, following a given external stimulus [180].

## 8 CONCLUSIONS AND FUTURE PERSPECTIVES

AFM is a powerful technique that offers high-resolution images, down to the sub-nanometre level, of complex and individual biomolecules. The technique has had and will continue to have an enormous impact on understanding problems as different as biological adhesion or colloidal aggregation. Furthermore, it also allows their study under relevant and minimally perturbing conditions. In the field of environmental sciences, the possibility of measuring the conformation and distribution of environmental colloids under natural conditions is extremely promising. Nonetheless, despite efforts that have

been made to optimise sample preparation, many challenges still need to be resolved, such as improvements in the resolution and reproducibility obtained for the observation of colloids in liquid cells. The present situation can be compared with the early years of electron microscopy. While the technique has reached a certain degree of maturity, future progress will now depend on refining sample preparation techniques and on the advancement of data analysis. At the present time, the best results are obtained by using several deposition methods, substrates and sample conditions in parallel.

Although the list of examples that was presented on the single molecule force spectroscopy of biological cells was rather short and by no means complete, it should nonetheless have given an impression of the enormous potential of the technique. AFM imaging and force measurements have already provided new insights into the understanding of the structure of colloids, biomacromolecules and supramolecular assemblies that is complementary with more conventional averaging techniques, since they provide information at the level of the individual molecules/particles. Future combination of classical batch techniques with locally resolved image or force measurements will allow insight into the environmental colloids that is not currently accessible in other manners. We expect that this approach will be highly fruitful for both the microscopic and macroscopic domains. Novel force techniques such as electrical and chemical force microscopy certainly have enormous, as of yet unexploited, potential in the field of environmental colloids. Clearly, the technique is still in its infancy with much potential for growth.

## ACKNOWLEDGEMENTS

The authors would like to thank the Swiss national science foundation for providing partial funding for this work. Critical comments by M. Kleijn and several anonymous reviewers were greatly appreciated.

## LIST OF SYMBOLS AND ABBREVIATIONS

<i>a</i>	Contact radius
<i>A</i>	Hamaker constant
<i>c</i>	Ion concentration
<i>D</i>	Probe–sample distance
<i>D</i> <sub>po</sub>	Extension of polymer bridged between sample and probe
<i>E</i>	Elastic modulus of AFM cantilever
<i>F</i>	Force
<i>k</i> <sub>c</sub>	Spring constant of AFM cantilever
<i>k</i> <sub>B</sub>	Boltzmann constant
<i>l</i>	Segment length along a polymer chain
<i>l</i> <sub>K</sub>	Kuhn length of a polymer
<i>l</i>	Length of AFM cantilever
<i>L</i> <sub>c</sub>	Contour length of a polymer
<i>L</i> <sub>p</sub>	Persistence length of a polymer
<i>m</i> <sup>*</sup>	Effective mass of cantilever beam
<i>M</i>	Mass attached to the end of a cantilever
<i>n</i> <sub>∞i</sub>	Bulk number density of ionic species <i>i</i>

$Q$	Quality factor of cantilever beam
$r$	Tip–sample distance
$R$	Probe radius
$R_{ee}$	End-to-end distance for a polymer
$R_{\text{eff}}$	Effective probe radius
$R_g$	Radius of gyration of a polymer
$s$	Average distance between anchor points of polymer chains
$t$	Thickness of AFM cantilever
$T$	Temperature
$V$	Deflection signal
$w$	Width of AFM cantilever
$W$	Interaction free energy
$Y_z$	cantilever deflection
$z$	Piezo displacement
$\tilde{z}_i$	Valency of ion
$\gamma^{ij}$	Interfacial tension between phase $i$ and phase $j$
$\gamma^{\text{LW}}$	Lifshitz–van der Waals component of the interfacial tension
$\gamma^{\text{AB}}$	Lewis acid base component of the interfacial tension
$\kappa^{-1}$	Debye length
$\nu_c$	Resonance frequency of AFM cantilever
$\nu_M$	Resonance frequency of AFM cantilever with added mass
$\rho$	Density of material for AFM cantilever
$\rho_f$	Density of medium
$\Pi$	Pressure
$\psi$	Diffuse layer potential
$\theta(l)$	Angle between two consecutive segments, $l$ , along a polymer chain
AFM	Atomic force microscopy
CFM	Chemical force microscopy
EFM	Electrical force microscopy
FFM	Friction force microscopy
FJC	Freely jointed chain
HOPG	Highly oriented pyrolytic graphite
HS	Humic substances
LIBD	Laser-induced breakdown detection
MFM	Magnetic force microscopy
NOM	Natural organic matter
PCS	Photon correlation spectroscopy
RH	Relative humidity
SFA	Surface force apparatus
SPM	Scanning probe microscopy
STM	Scanning tunnelling microscopy
TEM	Transmission electron microscopy
TIRM	Total internal reflection microscopy
TM-AFM	Tapping mode atomic force microscopy
OT	Optical tweezers
WLC	Worm-like chain

## REFERENCES

1. Filella, M. (2006). Colloidal properties of submicron particles in natural waters. In *Environmental Colloids: Behaviour, Structure and Characterisation*, eds Wilkinson, K. J. and Lead, J. R. IUPAC Series on Analytical and Physical Chemistry of Environmental Systems, Vol. 10, John Wiley & Sons, Ltd, Chichester, Chapter 2.
2. Buffle, J., Wilkinson, K. J., Stoll, S., Filella, M. and Zhang, J. (1998). A generalized description of aquatic colloidal interactions: the three-colloidal component approach, *Environ. Sci. Technol.*, **32**, 2887–2899.
3. Wells, M. L. (1998). Marine colloids: a neglected dimension, *Nature*, **391**, 530–531.
4. Maurice, P. A. (1996). Applications of atomic-force microscopy in environmental colloid and surface chemistry, *Colloids Surf. A*, **107**, 57–75.
5. Binnig, G., Rohrer, H., Gerber, C. and Weibel, E. (1982). Surface studies by scanning tunneling microscopy, *Phys. Rev. Lett.*, **49**, 57–61.
6. Binnig, G., Quate, C. F. and Gerber, C. (1986). Atomic force microscope, *Phys. Rev. Lett.*, **56**, 930–933.
7. Tortonese, M. (1997). Cantilevers and tips for atomic force microscopy, *IEEE Eng. Med. Biol. Mag.*, **16**, 28–33.
8. Thundat, T., Zheng, X.-Y., Chen, G. Y. and Warmack, R. J. (1993). Role of relative humidity in atomic force microscopy imaging, *Surf. Sci. Lett.*, **294**, L939–L943.
9. Drummond, C. J. and Senden, T. J. (1994). Examination of the geometry of long-range tip–sample interaction in atomic force microscopy, *Colloids Surf. A*, **87**, 217–234.
10. Jalili, N. and Laxminarayananais, K. (2004). A review of atomic force microscopy imaging systems: application to molecular metrology and biological sciences, *Mechatron.*, **14**, 907–945.
11. Vinogradova, O. I., Butt, H. J., Yakubov, G. E. and Feuillebois, F. (2001). Dynamic effects on force measurements. I. Viscous drag on the atomic force microscope cantilever, *Rev. Sci. Instrum.*, **72**, 2330–2339.
12. Keller, D. and Bustamante, C. (1993). Attaching molecules to surfaces for scanning probe microscopy, *Biophys. J.*, **64**, 896–897.
13. Zhong, Q., Innis, D., Kjoller, K. and Elings, V. B. (1993). Fractured polymer/silica fiber surface studied by tapping mode atomic force microscopy, *Surf. Sci. Lett.*, **290**, L688–L692.
14. Albrecht, T. R., Grütter, P., Horne, D. and Rugar, D. (1991). Frequency modulation detection using high- $q$  cantilevers for enhanced force microscope sensitivity, *J. Appl. Phys.*, **69**, 668–673.
15. Garcia, R. and Perez, R. (2002). Dynamic atomic force microscopy methods, *Surf. Sci. Rep.*, **47**, 197–301.
16. Magonov, S. N., Elings, V. and Whangbo, M.-H. (1997). Phase imaging and stiffness in tapping-mode atomic force microscopy, *Surf. Sci.*, **375**, L385–L391.
17. Tamayo, J. and Garcia, R. (1996). Deformation, contact time, and phase contrast in tapping mode scanning force microscopy, *Langmuir*, **12**, 4430–4435.
18. Tamayo, J. and Garcia, R. (1997). Effects of elastic and inelastic interactions on phase contrast images in tapping-mode scanning force microscopy, *Appl. Phys. Lett.*, **71**, 2394–2396.
19. Whangbo, M. H., Bar, G. and Brandsch, R. (1998). Qualitative relationships describing height and phase images of tapping mode atomic force microscopy. An application to micro-contact-printed patterned self-assembled monolayers, *Appl. Phys. A*, **66**, S1267–S1270.
20. Bar, G., Brandsch, R. and Whangbo, M.-H. (1999). Effect of tip sharpness on the relative contributions of attractive and repulsive forces in the phase imaging of tapping mode atomic force microscopy, *Surf. Sci.*, **422**, L192–L199.
21. Dong, R. and Yu, L. E. (2003). Investigation of surface changes of nanoparticles using TM-AFM phase imaging, *Environ. Sci. Technol.*, **37**, 2813–2819.
22. Buffle, J. and Leppard, G. G. (1995). Characterization of aquatic colloids and macromolecules. 1. Structure and behavior of colloidal material, *Environ. Sci. Technol.*, **29**, 2169–2175.
23. Buffle, J. and Leppard, G. G. (1995). Characterization of aquatic colloids and macromolecules. 2. Key role of physical structures on analytical results, *Environ. Sci. Technol.*, **29**, 2176–2184.

24. Arita, T., Kanda, Y. and Higashitani, K. (2004). *In situ* observation of single polymers adsorbed onto mica surfaces in water, *J. Colloid Interface Sci.*, **273**, 102–105.
25. Maurice, P. A. and Namjesnik-Dejanovic, K. (1999). Aggregate structures of sorbed humic substances observed in aqueous solution, *Environ. Sci. Technol.*, **33**, 1538–1541.
26. Plaschke, M., Römer, J., Klenze, R. and Kim, J. I. (1999). *In situ* AFM study of sorbed humic acid colloids at different pH, *Colloids Surf. A*, **160**, 269–279.
27. Balnois, E., Wilkinson, K. J., Lead, J. R. and Buffle, J. (1999). Atomic force microscopy of humic substances: effects of pH and ionic strength, *Environ. Sci. Technol.*, **33**, 3911–3917.
28. Beaglehole, D. and Christenson, H. K. (1992). Vapor adsorption on mica and silicon: entropy effects, layering, and surface forces, *J. Phys. Chem.*, **96**, 3395–3403.
29. Droz, E., Taborelli, M., Wells, T. N. and Descouts, P. (1993). Preparation of isolated biomolecules for SFM observations: T4 bacteriophage as a test sample, *Biophys. J.*, **65**, 1180–1187.
30. Lindsay, S. M., Tao, N. J., DeRose, J. A., Oden, P. I., Lyubchenko, Y. L., Harrington, R. E. and Shlyakhtenko, L. (1992). Potentiostatic deposition of DNA for scanning probe microscopy, *Biophys. J.*, **61**, 1570–1584.
31. Wagner, P. (1998). Immobilization strategies for biological scanning probe microscopy, *FEBS Lett.*, **430**, 112–115.
32. Wagner, P. and Hegner, M. (1998). A general method for immobilizing biomolecules on gold for SPM in aqueous buffers. In *Procedures in Scanning Probe Microscopy*, eds Colton, R. J., Engel, A., Frommer, J. E., Gaub, H. E., Gewirth, A. A., Guckenberger, R., Rabe, J., Heckl, W. M., and Parkinson, B., John Wiley & Sons, Inc., New York, pp. 481–484.
33. Hegner, M., Wagner, P. and Semenza, G. (1993). Ultralarge atomically flat template-stripped Au surfaces for scanning probe microscopy, *Surf. Sci.*, **291**, 39–46.
34. Nishimura, S., Tateyama, H., Tsunematsu, K. and Jinrai, K. (1992). Zeta potential measurement of muscovite mica basal plane–aqueous solution interface by means of plane interface technique, *J. Colloid Interface Sci.*, **152**, 359–367.
35. Iler, R. K. (1979). *The Chemistry of Silica*. John Wiley & Sons, Ltd, Chichester.
36. Buffle, J. (1988). *Complexation Reactions in Aquatic Systems: an Analytical Approach*. Ellis Horwood, Chichester.
37. Tyler, J. M. and Branton, D. (1980). Rotary shadowing of extended molecules dried from glycerol, *Ultrastruct. Res.*, **71**, 95–102.
38. Stokke, B. T., Smidsrød, O. and Elgsaeter, A. (1989). Electron microscopy of native xanthan and xanthan exposed to low ionic strength, *Biopolymers*, **28**, 617–637.
39. Wilkins, M. J., Davies, M. C., Jackson, D. E., Mitchell, J. R., Roberts, C. J., Stokke, B. T. and Tendler, S. J. B. (1993). Comparison of scanning tunneling microscopy and transmission electron microscopy image data on a microbial polysaccharide, *Ultramicroscopy*, **48**, 197–201.
40. Balnois, E. and Wilkinson, K. J. (2002). Sample preparation techniques for the observation of environmental biopolymers by atomic force microscopy, *Colloids Surf. A*, **207**, 229–242.
41. Liss, S. N., Droppo, I. G., Flannigan, D. T. and Leppard, G. G. (1996). Floc architecture in wastewater and natural riverine systems, *Environ. Sci. Technol.*, **30**, 680–686.
42. Droppo, I. G., Flannigan, D. T., Leppard, G. G., Jaskot, C. and Liss, S. N. (1996). Floc stabilization for multiple microscopic techniques, *Appl. Environ. Microbiol.*, **62**, 3508–3515.
43. Leggett, G. J., Davies, M. C., Jackson, D. E. and Tendler, S. J. B. (1996). Scanning probe microscopy of biomolecules and polymeric biomaterials, *J. Electron Spectrosc. Relat. Phenom.*, **81**, 249–268.
44. Mertig, M., Klemm, D., Zänker, H. and Pompe, W. (2002). Scanning force microscopy of two-dimensional structure formation in thin humic acid films, *Surf. Interface Anal.*, **33**, 113–117.
45. Mertig, M., Klemm, D., Pompe, W., Zänker, H. and Böttger, M. (1999). Scanning force microscopy of spin-coated humic acid, *Surf. Interface Anal.*, **27**, 426–432.
46. Wilkins, M. J., Davies, M. C., Jackson, D. E., Roberts, C. J. and Tendler, S. J. B. (1993). An investigation of substrate and sample preparation effects of scanning tunnelling microscopy studies on xanthum gum, *J. Microsc.*, **172**, 215–221.
47. McIntire, T. M. and Brant, D. A. (1997). Imaging of individual biopolymers and supramolecular assemblies using noncontact atomic force microscopy, *Biopolymers*, **42**, 133–146.

48. Mertig, M., Thiele, U., Bradt, J., Leibiger, G., Pompe, W. and Wendrock, H. (1997). Scanning force microscopy and geometric analysis of two-dimensional collagen network formation, *Surf. Interface Anal.*, **25**, 514–521.
49. Yamaki, M., Higo, J. and Nagayama, K. (1995). Size-dependent separation of colloidal particles in two-dimensional convective self-assembly, *Langmuir*, **11**, 2975–2978.
50. Rakers, S., Chi, L. F. and Fuchs, H. (1997). Influence of the evaporation rate on the packing order of polydisperse latex monofilms, *Langmuir*, **13**, 7121–7124.
51. Thill, A. and Spalla, O. (2002). Capillary against adhesion forces during drying of particle submonolayers on a solid substrate, *Langmuir*, **18**, 4783–4789.
52. Thill, A. and Spalla, O. (2003). Aggregation due to capillary forces during drying of particle submonolayers, *Colloids Surf. A*, **217**, 143–151.
53. Denkov, N., Velev, O., Kralchevski, P., Ivanov, I., Yoshimura, H. and Nagayama, K. (1992). Mechanism of formation of two-dimensional crystals from latex particles on substrates, *Langmuir*, **8**, 3183–3190.
54. Johnson, C. A. and Lenhoff, A. M. (1996). Adsorption of charged latex particles on mica studied by atomic force microscopy, *J. Colloid Interface Sci.*, **179**, 587–599.
55. Spalla, O. and Dessen, S. (2000). Direct evidence of lateral migration of mineral colloids adsorbed at a solid–water interface, *Langmuir*, **16**, 2133–2140.
56. Yang, J. and Shao, Z. (1993). Effect of probe force on the resolution of atomic force microscopy of DNA, *Ultramicroscopy*, **50**, 157–170.
57. Thundat, T., Allison, D. P., Warmack, R. J. and Ferrell, T. L. (1992). Imaging isolated strands of DNA molecules by atomic force microscopy, *Ultramicroscopy*, **42–44**, 1101–1106.
58. Kirby, A. R., Gunning, A. P. and Morris, V. J. (1995). Imaging xanthan gum by atomic force microscopy, *Carbohydr. Res.*, **267**, 161–166.
59. Kirby, A. R., Gunning, A. P., Morris, V. J. and Ridout, M. J. (1995). Observation of the helical structure of the bacterial polysaccharide acetan by atomic force microscopy, *Biophys. J.*, **68**, 360–363.
60. Gunning, A. P., Kirby, A. R., Morris, V. J., Wells, B. and Brooker, B. E. (1995). Imaging bacterial polysaccharides by AFM, *Polym. Bull.*, **34**, 615–619.
61. Woolley, A. T. and Kelly, R. T. (2001). Deposition and characterization of extended single-stranded DNA molecules on surfaces, *Nano Lett.*, **1**, 345–348.
62. Bussiek, M., Mucke, N. and Langowski, J. (2003). Polylysine-coated mica can be used to observe systematic changes in the supercoiled DNA conformation by scanning force microscopy in solution, *Nucleic Acids Res.*, **31**, 137–147.
63. Lyubchenko, Y. L. and Lindsay, S. M. (1998) In *Procedures in Scanning Probe Microscopy*, eds Colton, R. J., Engel, A., Frommer, J. E., Gaub, H. E., Gewirth, A. A., Guckenberger, R., Rabe, J., Heckl, W. M., and Parkinson, B., John Wiley & Sons, Ltd, Chichester, pp. 493–496.
64. Lyubchenko, Y. L., Gall, A. A., Shlyakhtenko, L. S., Harrington, R. E., Jacobs, B. L., Oden, P. I. and Lindsay, S. M. (1992). Atomic force microscopy imaging of double stranded DNA and RNA, *Biomol. Struct. Dyn.*, **10**, 589–606.
65. Shlyakhtenko, L. S., Gall, A. A., Weimer, J. J., Hawn, D. D. and Lyubchenko, Y. L. (1999). Atomic force microscopy imaging of DNA covalently immobilized on a functionalized mica substrate, *Biophys. J.*, **77**, 568–576.
66. Lyubchenko, Y. L. and Shlyakhtenko, L. S. (1997). Visualization of supercoiled DNA with atomic force microscopy *in situ*, *Proc. Natl. Acad. Sci. USA*, **94**, 496–501.
67. Bickmore, B. R., Hochella, M. F., Bosbach, D. and Charlet, L. (1999). Methods for performing atomic force microscopy imaging of clay minerals in aqueous solutions, *Clays Clay Miner.*, **47**, 573–581.
68. Czajkowsky, D. M. and Shao, Z. (1998). Submolecular resolution of single macromolecules with atomic force microscopy, *FEBS Lett.*, **430**, 51–54.
69. Westra, K. L., Mitchell, A. W. and Thomson, D. J. (1993). Tip artifacts in atomic force microscope imaging of thin film surfaces, *J. Appl. Phys.*, **74**, 3608–3610.
70. Villarrubia, J. S. (1997). Algorithms for scanned probe microscope image simulation, surface reconstruction, and tip estimation, *J. Res. Natl. Inst. Stand. Technol.*, **102**, 425–454.

71. Dongmo, S., Vautrot, P., Bonnet, N. and Troyon, M. (1998). Correction of surface roughness measurements in spm imaging, *Appl. Phys. A Mater. Sci. Process.*, **66**, S819–S823.
72. Xu, S. and Arnsdorf, M. F. (1994). Calibration of the scanning (atomic) force microscope with gold particles, *J. Microsc.*, **173**, 199–210.
73. Thundat, T. A., Zheng, X.-Y., Sharp, S. L., Allison, D. P., Warmack, R. J., Joy, D. C. and Ferrell, T. L. (1992). Calibration of atomic force microscope tips using biomolecules, *Scanning Microsc.*, **6**, 903–910.
74. Zenhausern, F., Adrian, M., Emch, R., Taborelli, M., Jobin, M. and Descouts, P. (1992). Scanning force microscopy and cryo-electron microscopy of tobacco mosaic virus as a test specimen, *Ultramicroscopy*, **42–44**, 1168–1172.
75. Keller, D. (1991). Reconstruction of STM and AFM images distorted by finite-size tips, *Surf. Sci.*, **253**, 353–364.
76. Markiewicz, P. and Goh, M. C. (1994). Atomic force microscopy probe tip visualization and improvement of images using a simple deconvolution procedure, *Langmuir*, **10**, 5–9.
77. Balnois, E., Durand-Vidal, S. and Levitz, P. (2003). Probing the morphology of laponite clay colloids by atomic force microscopy, *Langmuir*, **19**, 6633–6637.
78. Keller, D. J. and Franke, F. S. (1993). Envelope reconstruction of probe microscope images., *Surf. Sci.*, **294**, 409–419.
79. Markiewicz, P. and Goh, M. C. (1994). Simulation of atomic force microscope tip–sample/ sample–tip reconstruction, *J. Vac. Sci. Technol. B*, **13**, 1115–1118.
80. Vesenka, J., Guthold, M., Tang, C. L., Keller, D., Delaine, E. and Bustamante, C. (1992). Substrate preparation for reliable imaging of DNA molecules with the scanning force microscope, *Ultramicroscopy*, **42–44**, 1243–1249.
81. Bustamante, C., Vesenka, J., Tang, C. L., Rees, W., Guthold, M. and Keller, D. (1992). Circular DNA molecules imaged in air by scanning force microscopy, *Biochemistry*, **31**, 22–26.
82. Thundat, T., Allison, D. P. and Warmack, R. J. (1994). Stretched DNA structures observed with atomic force microscopy, *Nucleic Acids Res.*, **22**, 4224–4228.
83. Lyubchenko, Y., Shlyakhtenko, L., Harrington, R., Oden, P. and Lindsay, S. (1993). Atomic force microscopy of long DNA: imaging in air and under water, *Proc. Natl. Acad. Sci. USA*, **90**, 2137–2140.
84. Thomson, N. H., Kasas, S., Smith, B. L., Hansma, H. G. and Hansma, P. K. (1996). Reversible binding of DNA to mica for AFM imaging, *Langmuir*, **12**, 5905–5908.
85. Margeat, E., Le Grimellec, C. and Royer, C. A. (1998). Visualization of trp repressor and its complexes with DNA by atomic force microscopy, *Biophys. J.*, **75**, 2712–2720.
86. Moreno-Herrero, F., Colchero, J. and Baro, A. M. (2003). DNA height in scanning force microscopy, *Ultramicroscopy*, **96**, 167–174.
87. Fritz, M., Radmacher, M., Cleveland, J. P., Allersma, M. W., Stewart, R. J., Giesemann, R., Janmey, P., Schmidt, C. F. and Hansma, P. K. (1995). Imaging globular and filamentous proteins in physiological buffer solutions with tapping mode atomic force microscopy, *Langmuir*, **11**, 3529–3535.
88. Weisenhorn, A. L., Khorsandi, M., Kasas, S., Gotzos, V. and Butt, H.-J. (1993). Deformation and height anomaly on surfaces studied with an AFM, *Nanotechnology*, **4**, 106–113.
89. McIntire, T. M., Penner, R. M. and Brant, D. A. (1995). Observations of a circular, triple-helical polysaccharide using noncontact atomic force microscopy, *Macromolecules*, **28**, 6375–6377.
90. Bolshakova, A. V., Kiselyova, O. I., Filonov, A. S., Frolova, O. Y., Lyubchenko, Y. L. and Yaminsky, I. V. (2001). Comparative studies of bacteria with an atomic force microscopy operating in different modes, *Ultramicroscopy*, **86**, 121–128.
91. Van Noort, S. J. T., Van der Werf, K. O., De Groot, B. G., Van Hulst, N. F. and Greve, J. (1997). Height anomalies in tapping mode atomic force microscopy in air caused by adhesion, *Ultramicroscopy*, **69**, 117–127.
92. Muller, D. J., Schabert, F., Buldt, G. and Engel, A. (1995). Imaging purple membranes in aqueous solutions at sub-nanometer resolution by atomic force microscopy, *Biophys. J.*, **68**, 1681–1686.

93. Müller, D. J. and Engel, A. (1997). The height of biomolecules measured with the atomic force microscope depends on electrostatic interactions, *Biophys. J.*, **73**, 1633–1644.
94. Flory, P. J. (1969). *Statistical Mechanics of Chain Molecules*, Interscience New York.
95. Frontali, C., Dore, E., Ferrauto, A., Gratton, E., Bettini, A., Porzzan, M. R. and Valdevit, E. (1979). An absolute method for the determination of the persistence length of native DNA from electron micrographs, *Biopolymers*, **18**, 1353–1373.
96. Rivetti, C., Walker, C. and Bustamante, C. (1998). Polymer chain statistics and conformational analysis of DNA molecules with bends or sections of different flexibility, *J. Mol. Biol.*, **280**, 41–59.
97. Rivetti, C., Guthold, M. and Bustamante, C. (1996). Scanning force microscopy of DNA deposited onto mica: equilibration versus kinetic trapping studied by statistical polymer chain analysis, *J. Mol. Biol.*, **264**, 919–932.
98. Camesano, T. A. and Wilkinson, K. J. (2001). Single molecule study of xanthan conformation using atomic force microscopy, *Biomacromolecules*, **2**, 1184–1191.
99. Balnois, E., Stoll, S., Wilkinson, K. J., Buffle, J., Rinaudo, M. and Milas, M. (2000). Conformations of succinoglycan as observed by atomic force microscopy, *Macromolecules*, **33**, 7440–7447.
100. Mücke, N., Kreplak, L., Kirmse, R., Wedig, T., Herrmann, H., Aeby, U. and Langowski, J. (2004). Assessing the flexibility of intermediate filaments by atomic force microscopy, *J. Mol. Biol.*, **335**, 1241–1250.
101. Round, A., Berry, M., McMaster, T. J., Stoll, S., Gowers, D., Corfield, A. P. and Miles, M. J. (2002). Heterogeneity and persistence length in human ocular mucins, *Biophys. J.*, **83**, 1661–1670.
102. Minko, S., Kiriy, A., Gorodyska, G. and Stamm, M. (2002). Single flexible hydrophobic polyelectrolyte molecules adsorbed on solid substrate: transition between a stretched chain, necklace-like conformation and a globule, *J. Am. Chem. Soc.*, **124**, 3218–3219.
103. Kirwan, L. J., Papastavrou, G., Borkovec, M. and Behrens, S. H. (2004). Imaging the coil-to-globule conformational transition of a weak polyelectrolyte by tuning the polyelectrolyte charge density, *Nano Lett.*, **4**, 149–152.
104. Forest, S. and Witten, T. (1979). Long-range correlations in smoke-particle aggregation, *J. Phys. A Math. Gen.*, **12**, L109–L117.
105. Weitz, D. A. and Oliveria, M. (1984). Fractal structures formed by kinetic aggregation of aqueous solutions, *Phys. Rev. Lett.*, **52**, 1433–1437.
106. Meakin, P. (1983). Formation of fractal clusters and networks by irreversible diffusion-limited aggregation, *Phys. Rev. Lett.*, **51**, 1119–1122.
107. Meakin, P. (1984). Diffusion-limited aggregation in three dimensions: results from a new cluster-cluster aggregation model, *J. Colloid Interface Sci.*, **102**, 491–504.
108. Zhang, J. and Buffle, J. (1996). Multi-method determination of the fractal dimension of hematite aggregates, *Colloids Surf. A*, **107**, 175–187.
109. Rizzi, F. R., Stoll, S., Senesi, N. and Buffle, J. (2004). A transmission electron microscopy study of fractal properties and aggregation processes of humic acids, *Soil Sci.*, **169**, 765–775.
110. Grohens, Y., Castelein, G., Carriere, P., Spevacek, J. and Schultz, J. (2001). Multiscale aggregation of pmma stereocomplexes at a surface: an atomic force microscopy investigation, *Langmuir*, **17**, 86–94.
111. Yan, L. and Iwasaki, H. (2004). Fractal aggregation of DNA after thermal denaturation, *Chaos Solutions Fractals*, **20**, 877–881.
112. Mavrocordatos, D., Kaegi, R. and Schmatloch, V. (2002). Fractal analysis of wood combustion aggregates by contact mode atomic force microscopy, *Atmos. Environ.*, **36**, 5653–5660.
113. Brown, G. E., Henrich, V. E., Casey, W. H., Clark, D. L., Eggleston, C., Felmy, A., Goodman, D. W., Gratzel, M., Maciel, G., McCarthy, M. I., Nealson, K. H., Sverjensky, D. A., Toney, M. F. and Zachara, J. M. (1999). Metal oxide surfaces and their interactions with aqueous solutions and microbial organisms, *Chem. Rev.*, **99**, 77–174.
114. Plaschke, M., Schäfer, T., Bundschuh, T., Ngo Manh, T., Knopp, R., Geckeis, H. and Kim, J. I. (2001). Size characterization of bentonite colloids by different methods, *Anal. Chem.*, **73**, 4338–4347.

115. Lindgreen, H., Garnaes, J., Hansen, P. L., Besenbacher, F., Laegsgaard, E., Stensgaard, I., Gould, S. A. C. and Hansma, P. K. (1991). Ultrafine particles of north sea illite/smectite clay minerals investigated by STM and AFM, *Am. Mineral.*, **76**, 1218–1222.
116. Hartman, H., Sposito, G., Yang, A., Manne, S., Gould, S. A. C. and Hansma, P. K. (1990). Molecular-scale imaging of clay mineral surfaces with the atomic force microscope, *Clays Clay Miner.*, **38**, 337–342.
117. Rakovan, J., Becker, U. and Hochella, M. F. (1999). Aspects of goethite surface microtopography, structure, chemistry, and reactivity, *Am. Mineral.*, **84**, 884–894.
118. Johnson, P. A., Eggleston, C. M. and Hochella, M. F. (1991). Imaging molecular scale structure and microtopography of hematite with the atomic force microscope, *Am. Mineral.*, **76**, 1442–1445.
119. Bosbach, D., Charlet, L., Bickmore, B. and Hochella, M. F. (2000). The dissolution of hectorite: *in-situ*, real-time observations using atomic force microscopy, *Am. Mineral.*, **85**, 1209–1216.
120. Kim, J.-I. and Walther, C. (2006). Laser induced breakdown detection. In *Environmental Colloids: Behaviour, Separation and Characterisation*, eds Wilkinson, K. J. and Lead, J. R. IUPAC Series on Analytical and Physical Chemistry of Environmental Systems, Vol. 10. John Wiley & Sons, Ltd, Chichester, Chapter 5.
121. Hassellöv, M., von der Kammer, F. and Beckett, R. (2006). Characterisation of aquatic colloids and molecules by field-flow fractionation. In *Environmental Colloids: Behavior, Structure and Characterisation*, eds Wilkinson, K. J. and Lead, J. R. IUPAC Series on Analytical and Physical Chemistry of Environmental Systems, Vol. 10. John Wiley & Sons, Ltd, Chichester, Chapter 5.
122. Pina, C. M., Bosbach, D., Prieto, M. and Putnis, A. (1998). Microtopography of the barite (001) face during growth: AFM observations and PBC theory, *J. Cryst. Growth*, **187**, 119–125.
123. Bosbach, D., Junta-Rosso, J. L., Becker, U. and Hochella, M. F. (1996). Gypsum growth in the presence of background electrolytes studied by scanning force microscopy, *Geochim. Cosmochim. Acta*, **60**, 3295–3304.
124. Bosbach, D. and Hochella, M. F. (1996). Gypsum growth in the presence of growth inhibitors: a scanning force microscopy study, *Chem. Geol.*, **132**, 227–236.
125. Teng, H. H., Dove, P. M. and De Yoreo, J. J. (2000). Kinetics of calcite growth: surface processes and relationships to macroscopic rate laws, *Geochim. Cosmochim. Acta*, **64**, 2255–2266.
126. Bosbach, D., Hall, C. and Putnis, A. (1998). Mineral precipitation and dissolution in aqueous solution: *in-situ* microscopic observations on barite (001) with atomic force microscopy, *Chem. Geol.*, **151**, 143–160.
127. Brandt, F., Bosbach, D., Krawczyk-Bärsch, E., Arnold, T. and Bernhard, G. (2003). Chlorite dissolution in the acid pH range: a combined microscopic and macroscopic approach, *Geochim. Cosmochim. Acta*, **67**, 1451–1461.
128. Stipp, S. L. S., Hansen, M., Kristensen, R., Hochella, M. F., Bennedsen, L., Dideriksen, K., Balic-Zunic, T., Leonard, D. and Mathieu, H.-J. (2002). Behaviour of Fe-oxides relevant to contaminant uptake in the environment, *Chem. Geol.*, **190**, 321–337.
129. Perry, T. D., Duckworth, O. W., McNamara, C. J., Martin, S. T. and Mitchell, R. (2004). Effects of the biologically produced polymer alginic acid on macroscopic and microscopic calcite dissolution rates, *Environ. Sci. Technol.*, **38**, 3040–3046.
130. Dove, P. M. and Hochella, M. F. (1993). Calcite precipitation mechanisms and inhibition by orthophosphate: *in situ* observations by scanning force microscopy, *Geochim. Cosmochim. Acta*, **57**, 705–714.
131. Jordan, G. and Rammensee, W. (1998). Dissolution rates of calcite obtained by scanning force microscopy: microtopography-based dissolution kinetics on surfaces with anisotropic step velocities, *Geochim. Cosmochim. Acta*, **62**, 941–947.
132. Bickmore, B. R., Bosbach, D., Hochella, M. F., Charlet, L. and Rufe, E. (2001). *In situ* atomic force microscopy study of hectorite and nontronite dissolution: implications for phyllosilicate edge surface structures and dissolution mechanisms, *Am. Mineral.*, **86**, 411–423.

133. Weaver, R. M., Hochella, M. F. and Ilton, E. S. (2002). Dynamic processes occurring at the Cr(III) aq–manganite ( $\gamma$ -MnOOH) interface: simultaneous adsorption, microprecipitation, oxidation/reduction, and dissolution, *Geochimica et Cosmochimica Acta*, **66**(23), 4119–4132.
134. Scheidegger, A. M. and Sparks, D. L. (1996). A critical assessment of sorption–desorption mechanisms at the soil mineral/water interface, *Soil Sci.*, **161**, 813–831.
135. Wilkinson, K. J. and Reinhardt, A. (2005) Contrasting roles of natural organic matter on colloidal stabilization and flocculation in freshwaters. In *Flocculation in Natural and Engineered Environmental Systems*, eds Droppo, I. G., Leppard, G. G., Liss, S. N., and Milligan, T., CRC Press, Boca Raton, FL, pp. 143–170.
136. Abu-Lail, N. I. and Camesano, T. A. (2003). Polysaccharide properties probed with atomic force microscopy, *J. Microsc. (Oxford)*, **212**, 217–238.
137. Sheiko, S. S., da Silva, M., Shirvaniants, D., LaRue, I., Prokhorova, S., Moeller, M., Beers, K. and Matyjaszewski, K. (2003). Measuring molecular weight by atomic force microscopy, *J. Am. Chem. Soc.*, **125**, 6725–6728.
138. McIntire, T. M. and Brant, D. A. (1998). Observations of the (1  $\rightarrow$  3)- $\beta$ -D-glucan linear triple helix to macrocycle interconversion using noncontact atomic force microscopy, *J. Am. Chem. Soc.*, **120**(28), 6909–6919.
139. Decho, A. W. (1999). Imaging an alginate polymer gel matrix using atomic force microscopy, *Carbohydr. Res.*, **315**, 330–333.
140. Gunning, A. P., Kirby, A. R., Ridout, M. J., Brownsey, G. J. and Morris, V. J. (1996). Investigation of gellan networks and gels by atomic force microscopy, *Macromolecules*, **29**, 6791–6796.
141. Linder, A., Bergman, R., Bodin, A. and Gatenholm, P. (2003). Mechanism of assembly of xylan onto cellulose surfaces, *Langmuir*, **19**, 5072–5077.
142. Ikeda, S. and Shishido, Y. (2005). Atomic force microscopy studies on heat-induced gelation of curdlan, *J. Agric. Food Chem.*, **53**, 786–791.
143. Ikeda, S., Nitta, Y., Temsiripong, T., Pongsawatmanit, R. and Nishinari, K. (2004). Atomic force microscopy studies on cation-induced network formation of gellan, *Food Hydrocolloids*, **18**, 727–735.
144. Lin, W., Zhou, Y., Zhao, Y., Zhu, Q. and Wu, C. (2002). Cr<sup>3+</sup>/COO<sup>−</sup> complexation induced aggregation of gelatin in dilute solution, *Macromolecules*, **35**, 7407–7413.
145. Ikeda, S., Nitta, Y., Kim, B. S., Temsiripong, T., Pongsawatmanit, R. and Nishinari, K. (2004). Single-phase mixed gels of xyloglucan and gellan, *Food Hydrocolloids*, **18**, 669–675.
146. Roesch, R., Cox, S., Compton, S., Happek, U. and Corredig, M. (2004).  $\kappa$ -Carrageenan and  $\beta$ -lactoglobulin interactions visualized by atomic force microscopy, *Food Hydrocolloids*, **18**, 429–439.
147. Maurstad, G., Danielsen, S. and Stokke, B. T. (2003). Analysis of compacted semiflexible polyanions visualized by atomic force microscopy: influence of chain stiffness on the morphologies of polyelectrolyte complexes, *J. Phys. Chem. B*, **107**, 8172–8180.
148. Ikeda, S. and Morris, V. J. (2002). Fine-stranded and particulate aggregates of heat-denatured whey proteins visualized by atomic force microscopy, *Biomacromolecules*, **3**, 382–389.
149. Gunning, A. P. and Morris, V. J. (1990). Light scattering studies of tetramethylammonium gellan, *Int. J. Biol. Macromol.*, **12**, 338–341.
150. Verdugo, P., Alldredge, A. L., Azam, F., Kirchman, D. L., Passow, U. and Santschi, P. H. (2004). The oceanic gel phase: a bridge in the DOM–POM continuum, *Mar. Chem.*, **92**, 67–85.
151. Chin, W. C., Orellana, M. V. and Verdugo, P. (1998). Spontaneous assembly of marine dissolved organic matter into polymer gels, *Nature*, **391**, 568–571.
152. Zutic, V., Svetlicic, V., Radic, T., Malfatti, F., Degobbis, D. and Azam, F. (2004). Controlled ecosystem carbon flow experiment in the northern adriatic sea, *Period. Biol.*, **106**, 106.
153. Svetlicic, V., Balnois, E., Zutic, V., Chevalet, J., Hozic Zimmermann, A., Kovac, S. and Vdovic, N. (2006). Electrochemical detection of gel microparticles in seawater, *Croat. Chem. Acta.*, **79**, 107–113.
154. Azam, F. and Worden, A. Z. (2004). Oceanography: microbes, molecules, and marine ecosystems, *Science*, **303**, 1622–1624.

155. Piccolo, A. (2001). The supramolecular structure of humic substances, *Soil Sci.*, **166**, 810–832.
156. Swift, R. (1999). Macromolecular properties of soil humic substances: fact, fiction, and opinion, *Soil Sci.*, **164**, 790–802.
157. Clapp, C. E. and Hayes, M. H. B. (1999). Sizes and shapes of humic substances, *Soil Sci.*, **164**, 777–789.
158. Ghosh, K. and Schnitzer, M. (1980). Macromolecular structures of humic substances, *Soil Sci.*, **129**, 266–276.
159. Guetzloff, T. F. and Rice, J. A. (1994). Does humic acid form a micelle, *Sci. Total Environ.*, **152**, 31–35.
160. Namjesnik-Dejanovic, K. and Maurice, P. A. (1997). Atomic force microscopy of soil and stream fulvic acids, *Colloids Surf. A*, **120**, 77–86.
161. Lead, J. R., Balnois, E., Hosse, M., Menghetti, R. and Wilkinson, K. J. (1999). Characterization of norwegian natural organic matter. Size, diffusion coefficients, and electrophoretic mobilities, *Environ. Int.*, **25**, 245–258.
162. Liu, A., Wu, R. C., Eschenazi, E. and Papadopoulos, K. D. (2000). Afm on humic acid adsorption on mica, *Colloids Surf. A*, **174**, 245–252.
163. Lead, J. R., Wilkinson, K. J., Balnois, E., Cutak, B. J., Larive, C. K., Assemi, S. and Beckett, R. (2000). Diffusion coefficients and polydispersities of the Suwannee River fulvic acid: comparison of fluorescence correlation spectroscopy, pulsed-field gradient nuclear magnetic resonance, and flow field-flow fractionation, *Environ. Sci. Technol.*, **34**, 3508–3513.
164. Zänker, H., Mertig, M., Böttger, M., Hüttig, G., Pompe, S., Pompe, W. and Nitsche, H. (1998). Photon correlation spectroscopy and scanning force microscopy on humic acid, *Forschungszent. Rossendorf*, **218**, 78–80.
165. Santschi, P. H., Balnois, E., Wilkinson, K. J., Zhang, J., Buffle, J. and Guo, L. (1998). Fibrillar polysaccharides in marine macromolecular organic matter as imaged by atomic force microscopy and transmission electron microscopy, *Limnol. Oceanogr.*, **43**, 896–908.
166. Muirhead, D. and Lead, J. R. (2003). Measurement of the size and structure of natural aquatic colloids in an urbanised watershed by atomic force microscopy, *Hydrobiologia*, **464**, 65–69.
167. Hannah, D. M., Muirhead, D. and Lead, J. R. (2003). Imaging of suspended macromolecules and colloids in glacial and alpine streams by atomic force microscopy, *J. Glaciol.*, **49**, 607–609.
168. Claesson, P. M., Ederth, T., Bergeron, V. and Rutland, M. W. (1996). Techniques for measuring surface forces, *Adv. Colloid Interface Sci.*, **67**, 119–183.
169. Weisenhorn, A. L., Hansma, P. K., Albrecht, T. R. and Quate, C. F. (1989). Forces in atomic force microscopy in air and water, *Appl. Phys. Lett.*, **54**, 2651–2653.
170. Weisenhorn, A. L., Maivald, P., Butt, H. J. and Hansma, P. K. (1992). Measuring adhesion, attraction, and repulsion between surfaces in liquids with an atomic-force microscope, *Phys. Rev. B*, **45**, 11226–11232.
171. Israelachvili, J. and Tabor, D. (1973). Van der Waals Forces: Theory and Experiment, *Prog. Surf. Membr. Sci.*, **7**, 1–55.
172. Israelachvili, J. (1992). *Intermolecular and Surface Forces*. Academic Press, London.
173. Ducker, W. A., Senden, T. J. and Pashley, R. M. (1991). Direct measurement of colloidal forces using an atomic force microscope, *Nature*, **353**, 239–241.
174. Ducker, W. A., Senden, T. J. and Pashley, R. M. (1992). Measurement of forces in liquid using a force microscope, *Langmuir*, **8**, 1831–1836.
175. Butt, H. J. (1991). Measuring electrostatic, van der Waals, and hydration forces in electrolyte solutions with an atomic force microscope, *Biophys. J.*, **60**, 1438–1444.
176. Hutter, J. L. and Bechhoefer, J. (1993). Calibration of atomic-force microscope tips, *Rev. Sci. Instrum.*, **64**, 1868–1873.
177. Cleveland, J. P., Manne, S., Bocek, D. and Hansma, P. K. (1993). A nondestructive method for determining the spring constant of cantilevers for scanning force microscopy, *Rev. Sci. Instrum.*, **64**, 403–405.
178. Rief, M., Oesterhelt, F., Heymann, B. and Gaub, H. E. (1997). Single molecule force spectroscopy on polysaccharides by atomic force microscopy, *Science*, **275**, 1295–1297.

179. Rief, M., Gautel, M., Oesterhelt, F., Fernandez, J. M. and Gaub, H. E. (1997). Reversible unfolding of individual titin immunoglobulin domains by AFM, *Science*, **276**, 1109–1112.
180. Dufrene, Y. F. (2004). Using nanotechniques to explore microbial surfaces, *Nat. Rev. Microbiol.*, **2**, 451–460.
181. Ashkin, A. (1992). Forces of a single-beam gradient laser trap on a dielectric sphere in the ray optics regime, *Biophys. J.*, **61**, 569–582.
182. Walz, J. Y. and Prieve, D. C. (1992). Prediction and measurement of the optical trapping forces on a microscopic dielectric sphere, *Langmuir*, **8**, 3073–3082.
183. Prieve, D. C. (1999). Measurement of colloidal forces with TIRM, *Adv. Colloid Interface Sci.*, **82**, 93–125.
184. Butt, H. J. (2003) Analyzing electric double layers with the atomic force microscope. In *Encyclopedia of Electrochemistry*, Vol. 1, eds Bard, A. J. and Stratmann, M., Wiley-VCH, Weinheim, pp. 225–252.
185. Walters, D. A., Cleveland, J. P., Thomson, N. H., Hansma, P. K., Wendman, M. A., Gurley, G. and Elings, V. (1996). Short cantilevers for atomic force microscopy, *Rev. Sci. Instrum.*, **67**, 3583–3590.
186. Viani, M. B., Schaffer, T. E., Chand, A., Rief, M., Gaub, H. E. and Hansma, P. K. (1999). Small cantilevers for force spectroscopy of single molecules, *J. Appl. Phys.*, **86**, 2258–2262.
187. Howland, R. and Benatae, L. (2000). *A Practical Guide to Scanning Probe Microscopy*. ThermoMicroscopes, Santa Barbara, CA.
188. Jaschke, M. and Butt, H. J. (1995). Height calibration of optical lever atomic-force microscopes by simple laser interferometry, *Rev. Sci. Instrum.*, **66**, 1258–1259.
189. Heinz, W. F., Antonik, M. D. and Hoh, J. H. (2000). Reconstructing local interaction potentials from perturbations to the thermally driven motion of an atomic force microscope cantilever, *J. Phys. Chem. B*, **104**, 622–626.
190. Noy, A. and Huser, T. R. (2003). Combined force and photonic probe microscope with single molecule sensitivity, *Rev. Sci. Instrum.*, **74**, 1217–1221.
191. Schemmel, A. and Gaub, H. E. (1999). Single molecule force spectrometer with magnetic force control and inductive detection, *Rev. Sci. Instrum.*, **70**, 1313–1317.
192. Ashby, P. D., Chen, L. W. and Lieber, C. M. (2000). Probing intermolecular forces and potentials with magnetic feedback chemical force microscopy, *J. Am. Chem. Soc.*, **122**, 9467–9472.
193. Senden, T. J. (2001). Force microscopy and surface interactions, *Curr. Opin. Colloid Interface Sci.*, **6**, 95–101.
194. Hartley, P. G. and Scales, P. J. (1998). Electrostatic properties of polyelectrolyte modified surfaces studied by direct force measurement, *Langmuir*, **14**, 6948–6955.
195. Domke, J. and Radmacher, M. (1998). Measuring the elastic properties of thin polymer films with the atomic force microscope, *Langmuir*, **14**, 3320–3325.
196. Ducker, W. A., Xu, Z. G. and Israelachvili, J. N. (1994). Measurements of hydrophobic and DLVO forces in bubble-surface interactions in aqueous solutions, *Langmuir*, **10**, 3279–3289.
197. Gillies, G., Prestidge, C. A. and Attard, P. (2001). Determination of the separation in colloid probe atomic force microscopy of deformable bodies, *Langmuir*, **17**, 7955–7956.
198. Gillies, G., Prestidge, C. A. and Attard, P. (2002). An AFM study of the deformation and nanorheology of cross-linked PDMS droplets, *Langmuir*, **18**, 1674–1679.
199. Milling, A., Mulvaney, P. and Larson, I. (1996). Direct measurement of repulsive van der Waals interactions using an atomic force microscope, *J. Colloid Interface Sci.*, **180**, 460–465.
200. Considine, R. F., Drummond, C. J. and Dixon, D. R. (2001). Force of interaction between a biocolloid and an inorganic oxide: complexity of surface deformation, roughness, and brushlike behavior, *Langmuir*, **17**, 6325–6335.
201. Considine, R. F., Dixon, D. R. and Drummond, C. J. (2002). Oocysts of *Cryptosporidium parvum* and model sand surfaces in aqueous solutions: an atomic force microscope (AFM) study, *Water Res.*, **36**, 3421–3428.
202. Higgins, M. J., Sader, J. E., Mulvaney, P. and Wetherbee, R. (2003). Probing the surface of living diatoms with atomic force microscopy: the nanostructure and nanomechanical properties of the mucilage layer, *J. Phycol.*, **39**, 722–734.

203. Derjaguin, B. V. (1934). Untersuchungen über die Reibung und Adhäsion, *Kolloid Z.*, **69**, 155–164.
204. Hartmann, U. (1991). Vander Waals interactions between sharp probes and flat sample surfaces, *Phys. Rev. B*, **43**, 2404–2407.
205. Todd, B. A. and Eppell, S. J. (2004). Probing the limits of the Derjaguin approximation with scanning force microscopy, *Langmuir*, **20**, 4892–4897.
206. Butt, H. J. (1991). Electrostatic interaction in atomic force microscopy, *Biophys. J.*, **60**, 777–785.
207. Raiteri, R., Preuss, M., Grattarola, M. and Butt, H. J. (1998). Preliminary results on the electrostatic double-layer force between two surfaces with high surface potentials, *Colloids Surf. A*, **136**, 191–197.
208. Considine, R. F., Hayes, R. A. and Horn, R. G. (1999). Forces measured between latex spheres in aqueous electrolyte: non-DLVO behavior and sensitivity to dissolved gas, *Langmuir*, **15**, 1657–1659.
209. Vinogradova, O. I., Yakubov, G. E. and Butt, H. J. (2001). Forces between polystyrene surfaces in water–electrolyte solutions: long-range attraction of two types?, *J. Chem. Phys.*, **114**, 8124–8131.
210. Li, Y. Q., Tao, N. J., Pan, J., Garcia, A. A. and Lindsay, S. M. (1993). Direct measurement of interaction forces between colloidal particles using the scanning force microscope, *Langmuir*, **9**, 637–641.
211. Toikka, G., Hayes, R. A. and Ralston, J. (1996). Surface forces between spherical ZnS particles in aqueous electrolyte, *Langmuir*, **12**, 3783–3788.
212. Meagher, L., Franks, G. V., Gee, M. L. and Scales, P. J. (1999). Interaction forces between alpha-alumina fibres in aqueous electrolyte measured with an atomic force microscope, *Colloids Surf. A*, **146**, 123–137.
213. Considine, R. F., Dixon, D. R. and Drummond, C. J. (2000). Laterally-resolved force microscopy of biological microspheres–oocysts of *Cryptosporidium parvum*, *Langmuir*, **16**, 1323–1330.
214. Cooper, K., Ohler, N., Gupta, A. and Beaudoin, S. (2000). Analysis of contact interactions between a rough deformable colloid and a smooth substrate, *J. Colloid Interface Sci.*, **222**, 63–74.
215. Heim, L. O., Ecke, S., Preuss, M. and Butt, H. J. (2002). Adhesion forces between individual gold and polystyrene particles, *J. Adhes. Sci. Technol.*, **16**, 829–843.
216. Considine, R. F. and Drummond, C. J. (2001). Surface roughness and surface force measurement: a comparison of electrostatic potentials derived from atomic force microscopy and electrophoretic mobility measurements, *Langmuir*, **17**, 7777–7783.
217. Walz, J. Y. (1998). The effect of surface heterogeneities on colloidal forces, *Adv. Colloid Interface Sci.*, **74**, 119–168.
218. Senden, T. J. and Ducker, W. A. (1994). Experimental determination of spring constants in atomic force microscopy, *Langmuir*, **10**, 1003–1004.
219. Maeda, N. and Senden, T. J. (2000). A method for the calibration of force microscopy cantilevers via hydrodynamic drag, *Langmuir*, **16**, 9282–9286.
220. Notley, S. M., Biggs, S. and Craig, V. S. J. (2003). Calibration of colloid probe cantilevers using the dynamic viscous response of a confined liquid, *Rev. Sci. Instrum.*, **74**, 4026–4032.
221. Burnham, N. A., Chen, X., Hodges, C. S., Matei, G. A., Thoreson, E. J., Roberts, C. J., Davies, M. C. and Tendler, S. J. B. (2003). Comparison of calibration methods for atomic-force microscopy cantilevers, *Nanotechnology*, **14**, 1–6.
222. Gibson, C. T., Watson, G. S. and Myhra, S. (1997). Scanning force microscopy – calibrative procedures for ‘best practice’, *Scanning*, **19**, 564–581.
223. Levy, R. and Maaloum, M. (2002). Measuring the spring constant of atomic force microscope cantilevers: thermal fluctuations and other methods, *Nanotechnology*, **13**, 33–37.
224. Sader, J. E., Larson, I., Mulvaney, P. and White, L. R. (1995). Method for the calibration of atomic-force microscope cantilevers, *Rev. Sci. Instrum.*, **66**, 3789–3798.
225. Butt, H. J. and Jaschke, M. (1995). Calculation of thermal noise in atomic-force microscopy, *Nanotechnology*, **6**, 1–7.

226. Sader, J. E. (1998). Frequency response of cantilever beams immersed in viscous fluids with applications to the atomic force microscope, *J. Appl. Phys.*, **84**, 64–76.
227. Sader, J. E., Chon, J. W. M. and Mulvaney, P. (1999). Calibration of rectangular atomic force microscope cantilevers, *Rev. Sci. Instrum.*, **70**, 3967–3969.
228. Gibson, C. T., Watson, G. S. and Myhra, S. (1996). Determination of the spring constants of probes for force microscopy/spectroscopy, *Nanotechnology*, **7**, 259–262.
229. Torii, A., Sasaki, M., Hane, K. and Okuma, S. (1996). A method for determining the spring constant of cantilevers for atomic force microscopy, *Meas. Sci. Technol.*, **7**, 179–184.
230. Hunter, R. J. (1992). *Foundations of Colloid Science*. Oxford University Press, Oxford.
231. Langmuir, I. (1938). The role of attractive and repulsive forces in the formation of tactoids in thixotropic gels, protein crystals and coacervates, *J. Chem. Phys.*, **6**, 873–896.
232. Chan, D. Y. C., Pashley, R. M. and White, L. R. (1980). A simple algorithm for the calculation of the electrostatic repulsion between identical charged surfaces in electrolyte, *J. Colloid Interface Sci.*, **77**, 283–285.
233. Chan, D. Y. C. (2002). A simple algorithm for calculating electrical double layer interactions in asymmetric electrolytes – Poisson–Boltzmann theory, *J. Colloid Interface Sci.*, **245**, 307–310.
234. Hillier, A. C., Kim, S. and Bard, A. J. (1996). Measurement of double-layer forces at the electrode/electrolyte interface using the atomic force microscope: Potential and anion dependent interactions, *J. Phys. Chem.*, **100**, 18808–18817.
235. McCormack, D., Carnie, S. L. and Chan, D. Y. C. (1995). Calculations of electric double-layer force and interaction free-energy between dissimilar surfaces, *J. Colloid Interface Sci.*, **169**, 177–196.
236. Hartley, P. G., Larson, I. and Scales, P. J. (1997). Electrokinetic and direct force measurements between silica and mica surfaces in dilute electrolyte, solutions, *Langmuir*, **13**, 2207–2214.
237. Derjaguin, B. V. and Landau, L. (1941). Theory of the stability of strongly charged lyophobic sols and of the adhesion of strongly charged particles in solutions of electrolytes, *Acta Physicochim. URSS*, **14**, 633–662.
238. Verwey, E. J. W. and Overbeek, J. T. G. (1948). *Theory of Stability of Lyophobic Colloids*. Elsevier, Amsterdam.
239. Zhmud, B. V., Meurk, A. and Bergström, L. (1998). Evaluation of surface ionization parameters from AFM data, *J. Colloid Interface Sci.*, **207**, 332–343.
240. Zhmud, B. V., Meurk, A. and Bergström, L. (2000). Application of charge regulation model for evaluation of surface ionization parameters from atomic force microscopy (AFM) data, *Colloids Surf. A*, **164**, 3–7.
241. Giesbers, M., Kleijn, J. M. and Stuart, M. A. C. (2002). The electrical double layer on gold probed by electrokinetic and surface force measurements, *J. Colloid Interface Sci.*, **248**, 88–95.
242. Hu, K. and Bard, A. J. (1997). Use of atomic force microscopy for the study of surface acid-base properties of carboxylic acid-terminated self-assembled monolayers, *Langmuir*, **13**, 5114–5119.
243. Cappella, B. and Dietler, G. (1999). Force-distance curves by atomic force microscopy, *Surf. Sci. Rep.*, **34**, 1–104.
244. Butt, H. J., Jaschke, M. and Ducker, W. (1995). Measuring surface forces in aqueous-electrolyte solution with the atomic-force microscope, *Bioelectrochem. Bioenerg.*, **38**, 191–201.
245. Hartley, P. G. (1999). Measurement of colloidal interactions using the atomic force microscope. In *Colloid-Polymer interactions: from Fundamentals to Practice*, eds Farantino, R. S. and Dubin, P. L. John Wiley & Sons, Ltd, New York, 253–286.
246. Larson, I., Drummond, C. J., Chan, D. Y. C. and Grieser, F. (1995). Direct force measurements between dissimilar metal-oxides, *J. Phys. Chem.*, **99**, 2114–2118.
247. Larson, I., Drummond, C. J., Chan, D. Y. C. and Grieser, F. (1997). Direct force measurements between silica and alumina, *Langmuir*, **13**, 2109–2112.

248. Veeramasuneni, S., Yalamanchili, M. R. and Miller, J. D. (1996). Measurement of interaction forces between silica and alpha-alumina by atomic force microscopy, *J. Colloid Interface Sci.*, **184**, 594–600.
249. Bowen, W. R., Doneva, T. A. and Stoton, J. A. G. (2002). The use of atomic force microscopy to quantify membrane surface electrical properties, *Colloids Surf. A.*, **201**, 73–83.
250. Brant, J. A. and Childress, A. E. (2002). Membrane–colloid interactions: comparison of extended DLVO predictions with AFM force measurements, *Environ. Eng. Sci.*, **19**, 413–427.
251. Mosley, L. M., Hunter, K. A. and Ducker, W. A. (2003). Forces between colloid particles in natural waters, *Environ. Sci. Technol.*, **37**, 3303–3308.
252. Grasso, D. (2002). A review of non-DLVO interactions in environmental colloidal systems, *Re/Views Environ. Sci. Bio/Technol.*, **1**, 17–38.
253. Christenson, H. K. and Claesson, P. M. (2001). Direct measurements of the force between hydrophobic surfaces in water, *Adv. Colloid Interface Sci.*, **91**, 391–436.
254. Yakubov, G. E., Butt, H. J. and Vinogradova, O. I. (2000). Interaction forces between hydrophobic surfaces. Attractive jump as an indication of formation of ‘Stable’ submicrocavities, *J. Phys. Chem. B*, **104**, 3407–3410.
255. Attard, P. (2003). Nanobubbles and the hydrophobic attraction, *Adv. Colloid Interface Sci.*, **104**, 75–91.
256. Leikin, S., Parsegian, V. A., Rau, D. C. and Rand, R. P. (1993). Hydration forces, *Annu. Rev. Phys. Chem.*, **44**, 369–395.
257. Vigil, G., Xu, Z. H., Steinberg, S. and Israelachvili, J. (1994). Interactions of silica surfaces, *J. Colloid Interface Sci.*, **165**, 367–385.
258. Klein, J. and Luckham, P. (1982). Forces between 2 adsorbed polyethylene oxide layers immersed in a good aqueous solvent, *Nature*, **300**, 429–431.
259. Luckham, P. F. (1991). Measurement of the interaction between adsorbed polymer layers – the steric effect, *Adv. Colloid Interface Sci.*, **34**, 191–215.
260. Patel, S. S. and Tirrell, M. (1989). Measurement of forces between surfaces in polymer fluids, *Annu. Rev. Phys. Chem.*, **40**, 597–635.
261. Abraham, T., Giasson, S., Gohy, J. F. and Jerome, R. (2000). Direct measurements of interactions between hydrophobically anchored strongly charged polyelectrolyte brushes, *Langmuir*, **16**, 4286–4292.
262. Kamiyama, Y. and Israelachvili, J. (1992). Effect of pH and salt on the adsorption and interactions of an amphoteric polyelectrolyte, *Macromolecules*, **25**, 5081–5088.
263. Ruths, M., Sukhishvili, S. A. and Granick, S. (2001). Static and dynamic forces between adsorbed polyelectrolyte layers (quaternized poly-4-vinylpyridine), *J. Phys. Chem. B*, **105**, 6202–6210.
264. Balastre, M., Li, F., Schorr, P., Yang, J. C., Mays, J. W. and Tirrell, M. V. (2002). A study of polyelectrolyte brushes formed from adsorption of amphiphilic diblock copolymers using the surface forces apparatus, *Macromolecules*, **35**, 9480–9486.
265. Biggs, S. (1996). Non-equilibrium interaction forces between adsorbed polymer layers, *J. Chem. Soc., Faraday Trans.*, **92**, 2783–2789.
266. Biggs, S. (1995). Steric and bridging forces between surfaces fearing adsorbed polymer – an atomic-force microscopy study, *Langmuir*, **11**, 156–162.
267. Butt, H. J., Kappl, M., Mueller, H., Raiteri, R., Meyer, W. and Ruhe, J. (1999). Steric forces measured with the atomic force microscope at various temperatures, *Langmuir*, **15**, 2559–2565.
268. Abu-Lail, N. I. and Camesano, T. A. (2003). Role of ionic strength on the relationship of biopolymer conformation, DLVO contributions, and steric interactions to bioadhesion of *Pseudomonas putida* kt2442, *Biomacromolecules*, **4**, 1000–1012.
269. Degennes, P. G. (1987). Polymers at an interface – a simplified view, *Adv. Colloid Interface Sci.*, **27**, 189–209.
270. Netz, R. R. and Andelman, D. (2003). Polyelectrolytes in solution and at surfaces. In *Encyclopedia of Electrochemistry*, Vol. 1, eds Bard, A. J. and Stratmann, M. Wiley-VCH, Weinheim, pp. 282–325.
271. Ruhe, J., Ballauff, M., Biesalski, M., Dziezok, P., Grohn, F., Johannsmann, D., Houbenov, N., Hugenberg, N., Konradi, R., Minko, S., Motornov, M., Netz, R. R., Schmidt, M., Seidel,

- C., Stamm, M., Stephan, T., Usov, D. and Zhang, H. N. (2004). Polyelectrolyte brushes, *Advances in Polymer Science*, **165**, 79–150.
272. Pincus, P. (1991). Colloid stabilization with grafted polyelectrolytes, *Macromolecules*, **24**, 2912–2919.
273. Johnson, K. L., Kendall, K. and Roberts, A. D. (1971). Surface energy and contact of elastic solids, *Proc. R. Soc. London, Ser. A*, **324**, 301–313.
274. Maugis, D. (1992). Adhesion of spheres – the JKR–DMT transition using a Dugdale model, *J. Colloid Interface Sci.*, **150**, 243–269.
275. Kappl, M. and Butt, H. J. (2002). The colloidal probe technique and its application to adhesion force measurements, *Part. Part. Syst. Charact.*, **19**, 129–143.
276. Derjaguin, B. V. (1994). Problems of adhesion, *Prog. Surf. Sci.*, **45**, 223–231.
277. Burnham, N. A. and Kulik, A. J. (1999) Surface forces and adhesion. In *Handbook of Micro/nanotribology*, ed. Bhushan, B. CRC Press, Boca Raton, FL, 247–71.
278. Senden, T. J., di Meglio, J. M. and Auroy, P. (1998). Anomalous adhesion in adsorbed polymer layers, *Eur. Phys. J. E*, **3**, 211–216.
279. Senden, T. J., Di Meglio, J. M. and Silberzan, I. (2000). The conformation of adsorbed polyacrylamide and derived polymers, *C. R. Acad. Sci., Ser. IV: Phys. Astrophys.*, **1**, 1143–1152.
280. Haschke, H., Miles, M. J. and Koutsos, V. (2004). Conformation of a single polyacrylamide molecule adsorbed onto a mica surface studied with atomic force microscopy, *Macromolecules*, **37**, 3799–3803.
281. Higgins, M. J., Crawford, S. A., Mulvaney, P. and Wetherbee, R. (2002). Characterization of the adhesive mucilages secreted by live diatom cells using atomic force microscopy, *Protist*, **153**, 25–38.
282. Higgins, M. J., Molino, P., Mulvaney, P. and Wetherbee, R. (2003). The structure and nanomechanical properties of the adhesive mucilage that mediates diatom–substratum adhesion and motility, *J. Phycol.*, **39**, 1181–1193.
283. Hugel, T., Grosholz, M., Clausen-Schaumann, H., Pfau, A., Gaub, H. and Seitz, M. (2001). Elasticity of single polyelectrolyte chains and their desorption from solid supports studied by AFM based single molecule force spectroscopy, *Macromolecules*, **34**, 1039–1047.
284. Chatellier, X., Senden, T. J., Joanny, J. F. and di Meglio, J. M. (1998). Detachment of a single polyelectrolyte chain adsorbed on a charged surface, *Europhys. Lett.*, **41**, 303–308.
285. Nalaskowski, J., Drelich, J., Hupka, J. and Miller, J. D. (2003). Adhesion between hydrocarbon particles and silica surfaces with different degrees of hydration as determined by the AFM colloidal probe technique, *Langmuir*, **19**, 5311–5317.
286. van Oss, C. J., Good, R. J. and Chaudhury, M. K. (1988). Additive and nonadditive surface-tension components and the interpretation of contact angles, *Langmuir*, **4**, 884–891.
287. van Oss, C. J., Chaudhury, M. K. and Good, R. J. (1988). Interfacial Lifshitz–van der Waals and polar interactions in macroscopic systems, *Chem. Rev.*, **88**, 927–941.
288. van Oss, C. J. (1994). *Interfacial Forces in Aqueous Media*. Marcel Dekker, New York/CRC Press, Boca Raton, FL.
289. Nakagawa, T., Ogawa, K. and Kurumizawa, T. (1994). Atomic-force microscope for chemical sensing, *J. Vac. Sci. Technol. B*, **12**, 2215–2218.
290. Noy, A., Frisbie, C. D., Rozsnyai, L. F., Wrighton, M. S. and Lieber, C. M. (1995). Chemical force microscopy – exploiting chemically-modified tips to quantify adhesion, friction, and functional-group distributions in molecular assemblies, *J. Am. Chem. Soc.*, **117**, 7943–7951.
291. Sinniah, S. K., Steel, A. B., Miller, C. J. and Reutt-Robey, J. E. (1996). Solvent exclusion and chemical contrast in scanning force microscopy, *J. Am. Chem. Soc.*, **118**, 8925–8931.
292. Vezenov, D. V., Noy, A., Rozsnyai, L. F. and Lieber, C. M. (1997). Force titrations and ionization state sensitive imaging of functional groups in aqueous solutions by chemical force microscopy, *J. Am. Chem. Soc.*, **119**, 2006–2015.
293. Noy, A., Vezenov, D. V. and Lieber, C. M. (1997). Chemical force microscopy, *Annu. Rev. Mater. Sci.*, **27**, 381–421.
294. vanderVege, E. W. and Hadzioannou, G. (1997). Acid–base properties and the chemical imaging of surface-bound functional groups studied with scanning force microscopy, *J. Phys. Chem. B*, **101**, 9563–9569.

295. vanderVegte, E. W. and Hadzioannou, G. (1997). Scanning force microscopy with chemical specificity: an extensive study of chemically specific tip–surface interactions and the chemical imaging of surface functional groups, *Langmuir*, **13**, 4357–4368.
296. Dufrene, Y. F., Boonaert, C. J. P., van der Mei, H. C., Busscher, H. J. and Rouxhet, P. G. (2001). Probing molecular interactions and mechanical properties of microbial cell surfaces by atomic force microscopy, *Ultramicroscopy*, **86**, 113–120.
297. Takano, H., Kenseth, J. R., Wong, S. S., O'Brien, J. C. and Porter, M. D. (1999). Chemical and biochemical analysis using scanning force microscopy, *Chem. Rev.*, **99**, 2845–2890.
298. Papastavrou, G., Akari, S. and Mohwald, H. (2000). Interactions between hydrophilic and hydrophobic surfaces on microscopic scale and the influence of air bubbles as observed by scanning force microscopy in aqueous and alcoholic mediums, *Europhys. Lett.*, **52**, 551–556.
299. Warszynski, P., Papastavrou, G., Wantke, K. D. and Mohwald, H. (2003). Interpretation of adhesion force between self-assembled monolayers measured by chemical force microscopy, *Colloids Surf. A*, **214**, 61–75.
300. Vezenov, D. V., Zhuk, A. V., Whitesides, G. M. and Lieber, C. M. (2002). Chemical force spectroscopy in heterogeneous systems: intermolecular interactions involving epoxy polymer, mixed monolayers, and polar solvents, *J. Am. Chem. Soc.*, **124**, 10578–10588.
301. Schonherr, H., Hruska, Z. and Vancso, G. J. (2000). Toward high resolution mapping of functional group distributions at surface-treated polymers by AFM using modified tips, *Macromolecules*, **33**, 4532–4537.
302. Dufrene, Y. F. (2000). Direct characterization of the physicochemical properties of fungal spores using functionalized AFM probes, *Biophys. J.*, **78**, 3286–3291.
303. McKendry, R., Theoclitou, M. E., Abell, C. and Rayment, T. (1998). Role of surface perfection in chemical force microscopy, *Langmuir*, **14**, 2846–2849.
304. Li, Q. and Elimelech, M. (2004). Organic fouling and chemical cleaning of nanofiltration membranes: measurements and mechanisms, *Environ. Sci. Technol.*, **38**, 4683–4693.
305. Cail, T. L. and Hochella, M. F. (2005). Experimentally derived sticking efficiencies of microparticles using atomic force microscopy, *Environ. Sci. Technol.*, **39**, 1011–1017.
306. Cail, T. L. and Hochella, M. F. (2005). The effects of solution chemistry on the sticking efficiencies of viable *Enterococcus faecalis*: an atomic force microscopy and modeling study, *Geochim. Cosmochim. Acta*, **69**, 2959–2969.
307. Tong, M. P., Camesano, T. A. and Johnson, W. P. (2005). Spatial variation in deposition rate coefficients of an adhesion-deficient bacterial strain in quartz sand, *Environ. Sci. Technol.*, **39**, 3679–3687.
308. Abu-Lail, N. I. and Camesano, T. A. (2003). Role of lipopolysaccharides in the adhesion, retention, and transport of *Escherichia coli* JM109, *Environ. Sci. Technol.*, **37**, 2173–2183.
309. Hugel, T. and Seitz, M. (2001). The study of molecular interactions by AFM force spectroscopy, *Macromol. Rapid Commun.*, **22**, 989–1016.
310. Merkel, R. (2001). Force spectroscopy on single passive biomolecules and single biomolecular bonds, *Phys. Rep. Rev. Sec. Phys. Lett.*, **346**, 344–385.
311. Zhang, W. and Zhang, X. (2003). Single molecule mechanochemistry of macromolecules, *Prog. Polym. Sci.*, **28**, 1271–1295.
312. Janshoff, A., Neitzert, M., Oberdorfer, Y. and Fuchs, H. (2000). Force spectroscopy of molecular systems – single molecule spectroscopy of polymers and biomolecules, *Angew. Chem. Int. Ed.*, **39**, 3213–3237.
313. Bemis, J. E., Akhremitchev, B. B. and Walker, G. C. (1999). Single polymer chain elongation by atomic force microscopy, *Langmuir*, **15**, 2799–2805.
314. Ortiz, C. and Hadzioannou, G. (1999). Entropic elasticity of single polymer chains of poly(methacrylic acid) measured by atomic force microscopy, *Macromolecules*, **32**, 780–787.
315. Smith, S. B., Cui, Y. J. and Bustamante, C. (1996). Overstretching  $\beta$ -DNA: the elastic response of individual double-stranded and single-stranded DNA molecules, *Science*, **271**, 795–799.
316. Kratky, O. and Porod, G. (1949). Röntgenuntersuchung gelöster Fadenmoleküle, *Recl. Trav. Chim. Pays-Bas J. Roy. Neth. Chem. Soc.*, **68**, 1106–1122.
317. Marko, J. F. and Siggia, E. D. (1995). Stretching DNA, *Macromolecules*, **28**, 8759–8770.

318. Bustamante, C., Marko, J. F., Siggia, E. D. and Smith, S. (1994). Entropic elasticity of lambda-phage DNA, *Science*, **265**, 1599–1600.
319. Bouchiat, C., Wang, M. D., Allemand, J. F., Strick, T., Block, S. M. and Croquette, V. (1999). Estimating the persistence length of a worm-like chain molecule from force-extension measurements, *Biophys. J.*, **76**, 409–413.
320. Kikuchi, H., Yokoyama, N. and Kajiyama, T. (1997). Direct measurements of stretching force-chain ends elongation relationships of a single polystyrene chain in dilute solution, *Chem. Lett.*, 1107–1108.
321. Zhang, W. K., Zou, S., Wang, C. and Zhang, X. (2000). Single polymer chain elongation of poly(*N*-isopropylacrylamide) and poly(acrylamide) by atomic force microscopy, *J. Phys. Chem. B*, **104**, 10258–10264.
322. Li, H. B., Zhang, W. K., Xu, W. Q. and Zhang, X. (2000). Hydrogen bonding governs the elastic properties of poly(vinyl alcohol) in water: single-molecule force spectroscopic studies of PVA by AFM, *Macromolecules*, **33**, 465–469.
323. Yamamoto, S., Tsujii, Y. and Fukuda, T. (2000). Atomic force microscopic study of stretching a single polymer chain in a polymer brush, *Macromolecules*, **33**, 5995–5998.
324. Livadaru, L., Netz, R. R. and Kreuzer, H. J. (2003). Stretching response of discrete semi-flexible polymers, *Macromolecules*, **36**, 3732–3744.
325. Marszalek, P. E., Oberhauser, A. F., Pang, Y. P. and Fernandez, J. M. (1998). Polysaccharide elasticity governed by chair-boat transitions of the glucopyranose ring, *Nature*, **396**, 661–664.
326. Marszalek, P. E., Pang, Y. P., Li, H. B., El Yazal, J., Oberhauser, A. F. and Fernandez, J. M. (1999). Atomic levers control pyranose ring conformations, *Proc. Natl. Acad. Sci. USA*, **96**, 7894–7898.
327. Li, H. B., Rief, M., Oesterhelt, F., Gaub, H. E., Zhang, X. and Shen, J. C. (1999). Single-molecule force spectroscopy on polysaccharides by AFM – nanomechanical fingerprint of alpha-(1,4)-linked polysaccharides, *Chem. Phys. Lett.*, **305**, 197–201.
328. Marszalek, P. E., Li, H. B. and Fernandez, J. M. (2001). Fingerprinting polysaccharides with single molecule atomic force microscopy, *Nature Biotechnology*, **19**(3), 258–262.
329. Xu, Q. B., Zhang, W. and Zhang, X. (2002). Oxygen bridge inhibits conformational transition of 1,4-linked  $\alpha$ -D-galactose detected by single-molecule atomic force microscopy, *Macromolecules*, **35**, 871–876.
330. Xu, Q. B., Zou, S., Zhang, W. K. and Zhang, X. (2001). Single-molecule force spectroscopy on carrageenan by means of AFM, *Macromol. Rapid Commun.*, **22**, 1163–1167.
331. Li, H., Rief, M., Oesterhelt, F. and Gaub, H. E. (1999). Force spectroscopy on single xanthan molecules, *Appl. Phys. A: Mater. Sci. Process.*, **68**, 407–410.
332. Velegol, S. B. and Logan, B. E. (2002). Contributions of bacterial surface polymers, electrostatics, and cell elasticity to the shape of AFM force curves, *Langmuir*, **18**, 5256–5262.
333. Burks, G. A., Velegol, S. B., Paramonova, E., Lindenmuth, B. E., Feick, J. D. and Logan, B. E. (2003). Macroscopic and nanoscale measurements of the adhesion of bacteria with varying outer layer surface composition, *Langmuir*, **19**, 2366–2371.
334. van der Aa, B. C., Michel, R. M., Asther, M., Zamora, M. T., Rouxhet, P. G. and Dufrene, Y. F. (2001). Stretching cell surface macromolecules by atomic force microscopy, *Langmuir*, **17**, 3116–3119.
335. Abu-Lail, N. I. and Camesano, T. A. (2002). Elasticity of *pseudomonas putida* kt2442 surface polymers probed with single-molecule force microscopy, *Langmuir*, **18**, 4071–4081.
336. Camesano, T. A. and Abu-Lail, N. I. (2002). Heterogeneity in bacterial surface polysaccharides, probed on a single-molecule basis, *Biomacromolecules*, **3**, 661–667.



---

# 10 Laser Scanning Microscopy for Microbial Flocs and Particles

---

**JOHN R. LAWRENCE**

*National Water Research Institute, 11 Innovation Boulevard, Saskatoon, Saskatchewan,  
Canada S7N 3H5*

**THOMAS R. NEU**

*Department of River Ecology, UFZ Centre for Environmental Research Leipzig-Halle,  
Brueckstrasse 3a, D-39114 Magdeburg, Germany*

1	Introduction . . . . .	470
2	Sample Preparation Options . . . . .	471
3	Base Microscope and Objective Lenses . . . . .	472
3.1	2P-Non-Linear and 1P-Confocal Instrumentation . . . . .	473
3.2	Fluorophores and Fluorophore Conjugates for LSM . . . . .	474
4	Imaging Techniques . . . . .	474
4.1	Scan Modes . . . . .	474
4.1.1	2D Imaging . . . . .	475
4.1.2	3D Imaging . . . . .	476
4.1.3	4D Imaging . . . . .	476
5	Sequential and Simultaneous Image Acquisition . . . . .	477
6	Other LSM Imaging Options . . . . .	478
6.1	Selective Treatment of Subregions Within Imaged Areas . . . . .	478
6.2	Transmission Imaging . . . . .	480
6.3	Reflection Imaging . . . . .	480
7	Quantitative Imaging . . . . .	481
7.1	Ratiometric Imaging . . . . .	481
7.2	Dynamic Measurements . . . . .	482
7.2.1	Fluorescence Recovery after Photobleaching . . . . .	482
7.2.2	Fluorescence Lifetime Imaging . . . . .	483
7.2.3	Fluorescence Resonance Energy Transfer . . . . .	483
8	Applications to Imaging of Specific Particle Properties . . . . .	485
8.1	Cell Identity . . . . .	485
8.2	Structural Chemistry . . . . .	486
8.3	Physical Properties . . . . .	487
8.4	Environmental Chemistry . . . . .	488
8.5	Dynamic Processes/Metabolic State . . . . .	489

9	Image Processing and 3D Visualisation . . . . .	491
10	Image Analysis Packages for Quantification of LSM Images . . . . .	495
	10.1 Digital Image Analysis (DIA) – Methodology and Limitations . . . . .	496
11	Future Applications and Directions . . . . .	497
	Acknowledgements . . . . .	498
	Glossary . . . . .	498
	References . . . . .	499

## 1 INTRODUCTION

Although there are a number of options for the visualisation of microorganisms in their habitat, one-photon and two-photon-laser scanning microscopy (1p- and 2p-LSM) have become the benchmark for the visualisation and analysis of both biofilms and flocs. 1P- and 2P-LSM are truly non-perturbing methodologies based on the use of a scanned laser beam and detector system to obtain optical thin sections through living and preserved biological materials. The roots of confocal laser scanning microscopy or 1P-LSM technology lie in the work of Minsky [1]. However, it took until 1982 for the first 1P-LSM instrumentation to appear. The first commercial 1P-LSM systems used reflection imaging and were designed for use in the semiconductor industry. With the arrival of commercial reflection and fluorescence instruments in 1987, applications proliferated in the life sciences particularly in the biomedical fields. 2P-LSM has its origins in 1931 with Maria Göppert-Mayer [2]. However, it was not until the efforts of Webb's group that it was effectively used in a microscopy application [3], with commercial instruments becoming available in 1996.

The first applications of fluorescence and reflection 1P-LSM in environmental microbiology were reported by Caldwell's group at the University of Saskatchewan, where it was demonstrated that the approach was particularly useful for quantitative structural analyses of bacterial biofilms [4]. From these early applications, LSM has become an effective tool for examination of the delicate, complex structures of microbial biofilms and flocs. There are a number of groups worldwide that now use 1P-LSM as a major tool in their investigations in environmental microbiology. Applications of 2P-LSM in environmental microbiology have also occurred comparatively rapidly, with publications by Vroom *et al.* [5] and Neu and co-workers [6,7] demonstrating its potential for the imaging of bacterial biofilm and floc materials. LSM is well suited to the examination of environmental particles and colloids over a wide range of sizes and compositions. In particular, LSM allows the examination of the living biological properties of fully hydrated particles, their aggregates and flocs. This is an important and understudied aspect of environmental particles and a major control on the dynamics of environmental contaminants. Other approaches such as transmission electron microscopy (TEM) provide remarkable morphological characterisation and may give clues to *in situ* processes (see Chapter 8); however, LSM in conjunction with fluorescent reporters offers the potential to observe the dynamics of these processes. One reason for the success of laser scanning microscopy

(LSM) techniques is their versatility. LSM has many different modes: reflection, fluorescence and transmission, single- and multi-channel, one- and two-photon. In addition, the user has the option of looking at either the intensity or lifetime of the fluorescent signal. Concurrent with the development of LSM technology has been the development of a wide range of fluorescent probes such as target-specific and/or environmentally sensitive probes that are now commercially available. Application of these fluorescent reporters in conjunction with LSM allows the acquisition of data on a wide range of parameters, including: diffusion [8], redox conditions and ion concentrations including pH, heavy metals [9], cell viability, taxonomic affiliation [10], the structure and chemistry of the exopolymeric matrix [11,12] and even the metabolic condition [7] and growth rates [13] of microorganisms.

The ultimate goal in the application of LSM is to study and integrate structural, physiological, biochemical and molecular aspects of living microbial systems including both their cellular and extracellular aspects. There have been several reviews on the confocal laser scanning microscopy (CLSM) of microbiological samples. The basics of analytical microscopy and general technical requirements of a suitable LSM system and fluorescence staining techniques have been described in detail by Lawrence and co-workers [14–16] (see also [17]). These overviews describe how to get started, possible applications in microbiology and the basics for the analysis of three-dimensional image data. Although some of these techniques have only been demonstrated in biofilms, by extension, with appropriate sampling and handling, they may be realistically applied to a range of environmental particles and their aggregates. This chapter is intended to provide overview of LSM with specific illustrations relevant to biofilms, flocs, aggregates and particles, with suggestions for developments in the field.

## 2 SAMPLE PREPARATION OPTIONS

The fine structure of flocs is virtually impossible to examine under *in situ* conditions; therefore, we are reliant on careful sampling and rapid examination of fresh materials. Analysis of particles and flocs is thus extremely time sensitive. For example, aggregation can occur with time or with treatments during preparation and concentration, resulting in significant errors in floc analyses [18]. In general, storage for longer than 24 h may result in worthless samples. Typical treatments, such as drying, freezing, washing and centrifuging, all disrupt floc structure and properties. Leppard and co-workers [18–21] explained the best procedures for handling and preservation of flocs. Details regarding sampling are also provided by Mavrocordatos *et al.* [22]. In general, careful evaluation must be carried out to determine what protocol will work effectively for the floc being examined. For example, we have found that [*e.g.* 23]:

1. Placing the water sample with contained flocs and particles in a settling chamber with a cover-slip bottom such as those provided by NalgeNunc International (Denmark), or collecting lotic aggregates directly in cover-slip chambers and allowing them to settle, can be used as a first step to prepare material for LSM.
2. Staining may be carried out by the careful addition and withdrawal of stain and water using tissues or small sponges, followed by subsequent replacement and washing with sterile medium or environmental water (3–5 times).

3. In some cases, removal of excess stain must be carried out by centrifugation of the floc and resuspension in stain/probe-free water (with risk of artefacts).
4. For observation of flocs or other water-rich particles an inverted microscope (see below) may be the preferred method of analysis with 1P-LSM, 2P-LSM or conventional fluorescence microscopy for observation and recording.
5. Note that if an inverted microscope is used, access to the sample for imaging using water-immersible lenses is not possible and the presence of a cover-slip and the working distance of the objective lens may further limit examination of the material.

Preservation and preparation of flocs or particles for examination with LSM can be carried out using a variety of approaches, including embedding and sectioning. Mavrocordatos *et al.* [22] discuss in detail aspects of sample handling, embedding, staining and ultramicrotomy for transmission electron microscopy. If serial dehydration is used in the protocol, a concern that may arise is the loss of original material and resulting artefacts. Relatively fragile materials such as flocs and particles may be embedded using a variety of embedding materials, including Epon, Periplast and TissueTek. A number of authors recommend the use of hydrophilic resins such as Nanoplast, which has been used to stabilise structures for observation using LSM [23,24–26]. Less complicated approaches to the problem of stabilising flocs and granules for examination include the use of paraffin [27], cryosectioning, in which the samples are frozen and then sectioned prior to staining [28], 0.1% (w/v) agarose [29] or 20% (w/v) DNA sequencing-grade acrylamide [30]. This gel embedding allows the use of dehydrated or hydrated materials and, although fragile, they are relatively simple to handle and stain for LSM.

### 3 BASE MICROSCOPE AND OBJECTIVE LENSES

The base microscope for 1P or 2P instruments is usually a standard epifluorescence-equipped microscope. Phase contrast and other conventional light microscopy options can also be very helpful in the assessment of samples prior to or in conjunction with LSM. Epifluorescence is highly recommended for the preliminary assessment of samples, focusing, alignment and selection of regions of interest (ROI). The microscope selected must be one that offers a simple, clean light path with minimal opportunity for loss of transmitted light in the system. The fundamental choices are an inverted or a standard microscope, each with several advantages. Although we have previously favoured the standard microscope in our work [14], for floc and particle work the inverted microscope can have major advantages. These include sample settling, access to the sample for micro-electrodes and options to physically manipulate the sample from above. Due to its critical nature, the selection of microscope objective lenses should be considered carefully, especially in relation to the required application. For most applications in LSM, the objective should be corrected from ~350 to 1000 nm, should have a high numerical aperture (NA) (oil or water immersion lenses have an NA of 1.2–1.4) and have an optimum working distance. Working distances can range from 10 µm or less for planapochromat lenses to 220 µm for lenses optimised for LSM such as the water immersion 63 × 1.2 NA lens. These high-NA planapochromat objectives also have a large corrected central region such as in the 60 × planapochromat 1.4 NA that ensures high quality over the maximum

image area. The operational rule is that as NA increases, the working distance of the objective lens decreases. One critical consideration regarding objective lenses and applications in LSM is that the NA in conjunction with the instrument's pinhole size controls the thickness of the optical section. For example, if the NA = 0.2, the optical section is approximately 10  $\mu\text{m}$ . For NA  $\geq 0.6$ , section thickness decreases to  $<1 \mu\text{m}$ .

Water-immersible lenses are also highly useful for 1P- and 2P-LSM [16]. These so-called dipping lenses offer many advantages (*e.g.* long working distance, eliminating the need for cover-slips or fixation, leaving the sample open for further staining and manipulation) for examination of delicate biological structures that must be kept fully hydrated for study. There are a variety of high-NA water-immersible objectives supplied by the major manufacturers (Leica, Nikon, Olympus and Zeiss). An example is the 63  $\times$  /0.9 NA water-immersible lenses that have been used in combination with standard microscopes for the examination of flocs. Since no cover-slip is required, free-floating or partially stabilised flocs may be imaged. Vibration, heating currents and other factors that create motion in the sample must be minimised to allow successful imaging using this approach. Additional details regarding the selection of microscope objectives may be found elsewhere [14,16].

### 3.1 2P-NON-LINEAR AND 1P-CONFOCAL INSTRUMENTATION

Conventional optical microscopes form an image using all the light passing through the specimen or emanating from it. The resulting image includes light from above and below the focal plane, leading to degradation of image quality and interfering with a true three-dimensional (3D) impression of the object. LSM systems eliminate this stray light, thereby improving the clarity of the image. LSM can be divided into 1P- and 2P-LSM or multi-photon systems based on their mode of excitation. In these cases, the resultant image is an optical thin section. The optical thin section is created through a combination of a laser light source, optical elements to determine excitation and emission wavelengths, scanning mirrors, a pinhole system to restrict returning light to that from the focal plane of the objective in 1P-LSM, a photomultiplier or other light-sensitive detector and a computer system to control the apparatus and facilitate collection of the digital image. In 2P-LSM, the optical thin section is obtained by the two-photon effect, wherein excitation of the fluorophore occurs only in the focal plane of the objective. In brief, the creation of the two-photon effect requires a light source that can produce photons which arrive at the focal plane such that two photons are absorbed by the fluorophore within 1 fs. The system usually consists of three lasers, a laser diode bar, a pump laser and an infrared laser, usually a pulsed titanium–sapphire laser, the combination of which produces very short pulses of infrared light. In addition, the nature of the effect is also dependent on the incident light intensity, which decreases with the square of the distance from the focal plane, resulting in only fluorophore molecules in the focal plane being excited and fluorescing, thereby creating the optical thin section.

For CLSM or 1P-LSM, visible and ultraviolet continuous-wave lasers (these may be diode or gas-phase laser sources) are used for excitation of fluorochromes, whereas for two-photon excitation a pulsed titanium–sapphire laser producing infrared light is employed. The excitation light can be used to image via reflection or fluorescence in 1P-LSM, whereas 2P-LSM is for fluorescence imaging only. Typically, fluorescence is collected as an intensity signal giving rise to a typical 1P or 2P image. However, fluorescence may also be collected as a lifetime signal. When the fluorescence lifetime is

recorded, the technique is called fluorescence lifetime imaging microscopy (FLIM). LSM excitation may be employed for intensity imaging or through the addition of specialised equipment at the same instrument, for lifetime imaging. At this point, two-photon imaging, 2P-LSM and in particular FLIM have only been used in a limited number of microbiological studies [5–7,24,25,31–33]. In contrast, there have already been several reviews on 1P-LSM of microbiological samples [14–16,34].

Despite their many advantages, LSM approaches still suffer from major limitations, including: those unique to one-photon: bleaching and cell damage in out-of-focus areas, limited depth of laser penetration, fluorescence of the background and large differences in fluorescence emission intensity. Disadvantages unique to 2P-LSM include the non-uniformity of two-photon intensity output for excitation, two-photon emission signal intensity and difficulty imaging infrared-absorbing samples. Both 1P- and 2P-LSM techniques may suffer from low resolution in the axial (XZ) direction, large differences in fluorescence emission intensity and, although reduced in 2P systems, light scattering in thick ( $>100\text{ }\mu\text{m}$ ) biological specimens. The advantages of 2P-LSM are excitation in the focal plane only, deeper penetration of infrared light into scattering samples, i.e. less scattering, and higher resolution in deep areas of the sample, making it suitable for thicker light-scattering materials [35]. Some of these benefits have been demonstrated for microbial systems by Neu and co-workers [6,7,31] and Vroom *et al.* [5].

### 3.2 FLUOROPHORES AND FLUOROPHORE CONJUGATES FOR LSM

Fluorescence is an extremely sensitive and useful tool for the exploration of biological colloids and particles, including flocs. However, there are a range of considerations and concerns regarding its use. For a fluorophore alone or a fluorophore conjugated to a probe such as a lectin, antibody or a dextran, it should (i) have excitation and emission wavelengths matched to the sample (i.e. check for autofluorescence); (ii) not interact with other fluorophores present in the sample (the order of addition in multiple staining may be a concern, i.e. lectins may become a target for subsequent lectins); (iii) be stable and resist photobleaching and produce visible light throughout the experimental interval; (iv) be able to access binding sites in the sample (i.e. does not sorb non-specifically which is a concern for antibodies, lectins and dextrans; non-specific binding in environmental samples is always a major concern; in some cases the use of correlative microscopy can provide validation, see *e.g.* [36]); (v) not be toxic to the biological material being examined (CTC is an example of a fluorescent probe where toxicity to living cells is a concern [14,37]; (vi) be highly specific in its response and, in the case of fluorophore conjugates, it should not alter the binding pattern of the probe (a concern for lectins [11]). The reader should also consult Fatin-Rouge and Buffle [17] for an additional useful discussion of fluorescent dyes, their photochemical properties and applications in fluorescence correlation spectroscopy.

## 4 IMAGING TECHNIQUES

### 4.1 SCAN MODES

The user may collect single images in the XY, XZ planes or a series of XY or XZ images, thereby creating an image stack for 3D reconstruction and/or digital image analyses. Time

series may also be collected for a single depth and wavelength or for multiple depths and wavelengths of light, allowing 4D imaging of multiple parameters. It is also possible to collect images using combinations of one, two, three or more excitation and emission wavelengths, using 1P (including UV) or 2P systems. These images may be collected sequentially or simultaneously, depending on the LSM system in use and the suitability of the fluorophores and fluorophore-conjugated probes selected. One may also collect images using fluorescence, reflection (i.e. colloidal gold, particulates) and non-confocal transmission modes. See Figures 15 and 16 for examples of the combination of reflection and fluorescence imaging.

#### 4.1.1 2D Imaging

Although substantially improved over conventional light microscopy, 1P and 2P or multi-photon microscopy are still subject to the limits imposed on all optical techniques, thus the spatial resolution in the focal or XY plane is at best 180 nm. In practical terms, this limit is  $>200$  nm, versus  $<1$  nm for TEM. Nonetheless, this limit does not prevent the detection of specific molecules and biologically relevant information when imaging microbial samples. Assuming that the LSM system has been aligned and the correct staining has been carried out, there are a number of options available for imaging. The most common is the single XY image where the beam is scanned over a defined area. A single image showing a floc stained with the nucleic acid stain Syto 9 is shown in Figure 1a.

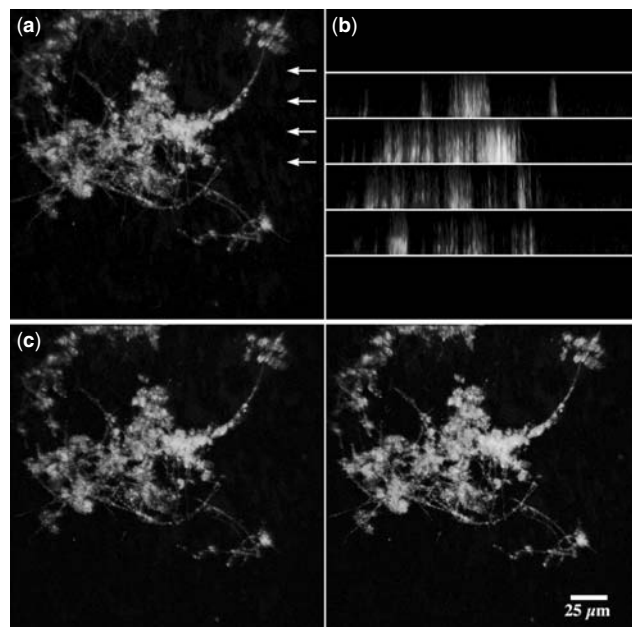


**Figure 1.** A single image showing a floc stained with Syto 9 is shown in (a). Part (b) illustrates the XZ images taken through the floc (at arrows) shown in plan view in (a). Part (c) illustrates a 3D image created from an image stack of the floc shown in (a) and (b). The resulting stereo pair (c) allows spatial examination of the floc architecture (best viewed with stereo glasses)

As indicated above, during an *XY* scan the laser beam is scanned over a defined area; however, the beam can also scan along a single line extending into the specimen (*XZ*-scan). When a line scan is repeated at many *Z* levels, the resulting image (*Z*-scan) is a sagittal or *XZ* section through the sample. It is also possible to calculate *XZ* images from *XY* serial sections using various software packages. However, a major limitation in LSM is the *XZ* spatial resolution, which is of the order of 500–800 nm. Hence *Z*-scan images lack the resolution of *XY* images due to the nature of the corrections in standard objectives and the point spread function error of the lens. The net effect is that *XZ* images are exaggerated in the *Z* dimension and a point or object will appear to have an elongated *Z* axis. Figure 1b illustrates the *XZ* image taken through the floc shown in plan view in Figure 1a and in 3D projection in Figure 1c.

#### 4.1.2 3D Imaging

The major advantage of LSM is the capacity to collect a series of images that allow the user to obtain 3D spatial information. This capability follows from the optical sectioning capacity and the creation of a *Z* series in perfect register. This series of *XY* images is referred to as a *Z* series since it is taken along the *Z* axis or commonly as an image stack. Serial optical sections can be used for a variety of three-dimensional reconstruction techniques (see below). Figure 1c shows a typical stereo pair that allows spatial examination of the floc architecture (the images are best viewed with stereo glasses). During the collection of 3D stacks, whether single or time series, the images should be collected (i) non-destructively, i.e. photobleaching is not a significant factor, (ii) without oversampling or undersampling error, i.e. selection of the correct sectioning interval, (iii) operating within the working distance of the objective lens, (iv) with an absence of heterogeneity such as vignetting, (v) so that images are aligned and in register, (vi) calibrated so that image grey levels accurately represent the features being investigated and (vii) *XY* pixels should correspond to the *Z* dimension. Assuming that the above assumptions are met, a variety of image collection options can be considered, such as *XYT*-scans where a single optical plane is repeatedly imaged over time, or *XYZ* collection at multiple *Z* positions in the sample. Some manufacturers offer the capacity to execute so-called lambda or wavelength scans, *XYλ* or *XZλ*, which allow the collection of emission spectra at specified locations within the sample in either the *XY* or *XZ* axis. Figure 2 illustrates the result of a lambda scan of a photosynthetic biofilm (the sample is shown as a maximum projection) showing the optimum excitation emission combination for imaging the sample.

#### 4.1.3 4D Imaging

In order to appreciate the nature of highly dynamic complex structures, it may be necessary to record data in three spatial dimensions and over time (4D). The current LSM equipment offered by commercial manufacturers is able repeatedly to acquire complete volumes, i.e. *XYZT* or 3D time-lapse imaging. The fundamentals are relatively straightforward, although as noted by Gerlich and Ellenberg [38], one must keep the specimen or material under study ‘alive’ and in a normal state. The other challenges are maintaining a signal over repeated scans without photobleaching, photodamage or toxic effects. The 3D imaging constraints listed above should also be met for each time interval. Other constraints include the capacity to move the specimen repeatedly through the *XZ*; this requires a

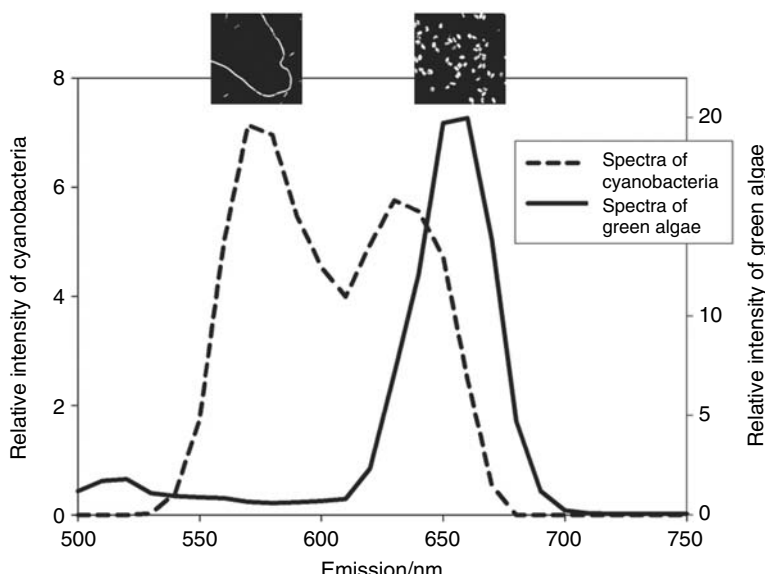


**Figure 2.** Lambda scan of photosynthetic biofilms indicating the optimum excitation emission combination for detection and imaging of cyanobacteria and algae in the sample

precision stepper motor to move either the objective or the stage. Experiments that monitor biological activity may occur over several days. For example, we have monitored biofilm formation at specific locations in porous media for up to 7 consecutive days. There are many potential applications for time course imaging, including dynamic events in flocs, such as enzyme activities, metabolic rates and sorption kinetics.

## 5 SEQUENTIAL AND SIMULTANEOUS IMAGE ACQUISITION

One of the key advantages to the LSM approach is the capacity to collect multiple emission signals and, for example, show the identities and locations of bacterial cells, bacterial macromolecules and enzyme and metabolic activities. For example, a microbial sample may be stained with fluorophore-conjugated lectins, nucleic acid stains and fluorescein diacetate to assess and localise metabolic activity. A major decision must be made on whether to collect these signals simultaneously or sequentially. Although simultaneous excitation with image acquisition for double or triple staining may be desirable, there can be bleed-through from one channel to the next and interference between fluorophores or from autofluorescence. Fine tuning of the laser power/gain/pinhole settings can only overcome these problems to a certain extent. Therefore, the best option is often sequential scanning, in which the user optimises the application of the fluorophore, the laser power, the pinhole, the excitation–emission wavelengths and the gain and the offset for each channel, and saves these settings prior to performing the sequential image stack collection. This methodology eliminates the risk of false-positive signals being detected in any channel. The instrument must be properly aligned and the correct objective used with appropriate corrections, magnification and working distance. The user should also realise

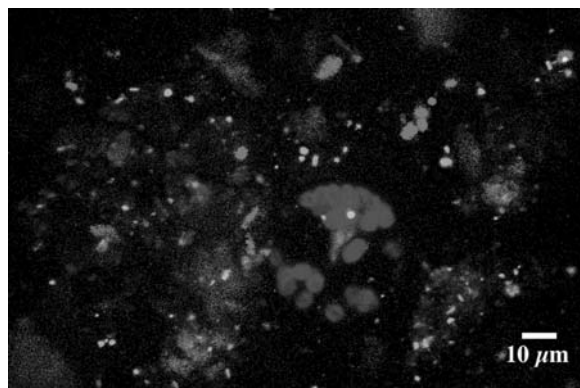


**Figure 3 (Plate 1).** LSM imaging showing the results of an optimised three channel scan with autofluorescence (red) showing the distribution of photosynthetic organisms based on detection of chlorophyll, *Triticum vulgaris*-TRITC lectin staining (blue) used to detect exopolymers in the biofilm matrix and nucleic acid staining with Syto 9 (green) to detect bacteria within a Saskatchewan River floc

that the longer the wavelength of light, the thicker is the optical section, and conversely, the shorter the wavelength, the thinner is the section and the higher the resolution. For example, green (488 nm excitation) wavelength images are of higher quality than far-red ones (640 nm excitation). Inherent errors such as field curvature and lateral aberration in the image will also impact on the quality at the edges of the image; as indicated above, this is best minimised through selection of the correct objective lens. Although rarely applied, the process of adding probes sequentially to the sample under the microscope may also improve the result. Figure 3 shows the results of an optimised sequential three-channel scan using autofluorescence (shown in red) to detect photosynthetic organisms based on the presence of chlorophyll, *Triticum vulgaris*-TRITC lectin staining, which is used to detect glycoconjugates in the exopolymeric matrix (shown in blue), and nucleic acid staining with Syto 9 to detect bacterial cells (shown in green) in a biological floc or particle from the South Saskatchewan River. Lawrence *et al.* [16] described in detail the procedure for this approach to three-channel imaging, which also allows the quantification of the algal, bacterial and exopolymer biomass through the application of digital image analyses to the image stacks. Excellent multi-channel images of flocs and other microbial systems can be found in the literature [14,16,23,36,39,40].

## 6 OTHER LSM IMAGING OPTIONS

### 6.1 SELECTIVE TREATMENT OF SUBREGIONS WITHIN IMAGED AREAS

This function is available on most commercial 1P- and 2P-LSM systems and is useful for selective imaging and for use in combination with selective bleaching techniques such as fluorescence recovery after photobleaching (FRAP) to determine sorption, metabolic or diffusion rates (see below). Caged probes or selected objects within a field of view can be imaged without illuminating the rest of the field and individual regions of the specimen can be excited with different wavelengths and intensities. Spot bleaching can

be achieved by keeping the laser at a particular spot overtime to bleach the fluorophore over the smallest possible area. The size of the induced damage depends on the laser intensity and duration of radiation. This type of scanning has been used to monitor some of the dynamic processes in microbial systems using the FRAP process [8]. Figure 4a shows an ROI and bleaching of that region, which is then monitored to observe and quantify recovery times and kinetics of sorption of the herbicide diclofop methyl by the biofilm (see Section 7.2.1).

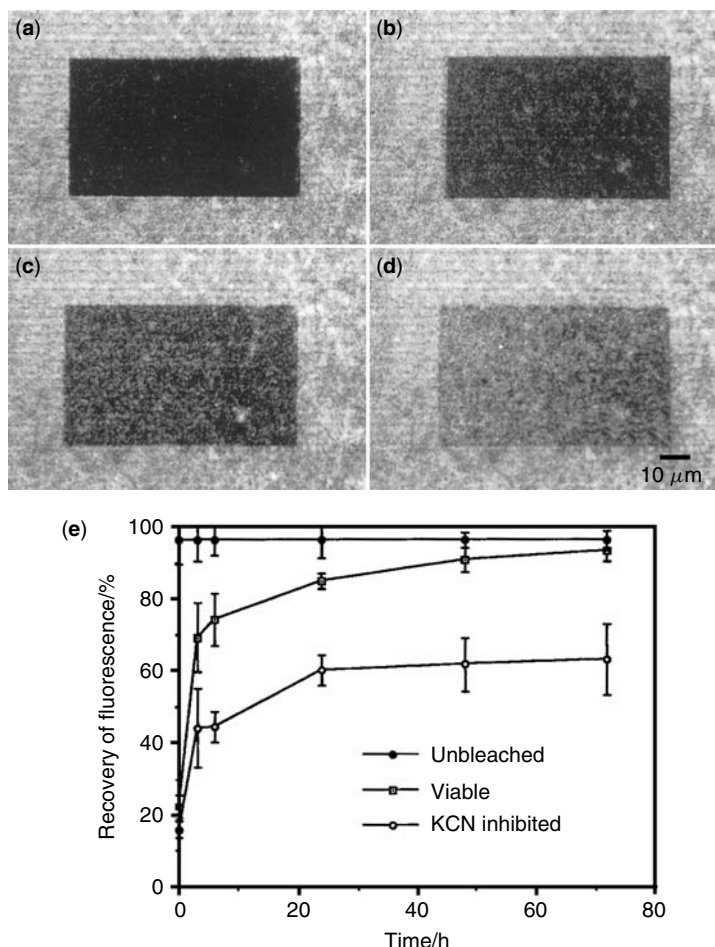


**Figure 4.** CLSM photomicrographs showing FRAP measurements to compare the rates of accumulation of the herbicide diclofop methyl in a mixed species degradative biofilm. Shown here is a typical example of fluorescence recovery in a viable biofilm immediately (a), 3 h (b), 6 h (c) and 24 h (d) after photobleaching. Part (e) shows the recovery rates after FRAP in viable and inhibited biofilms. The fluorescence intensities in photobleached areas are represented as percentages of the average intensity in unbleached areas. Reprinted with permission of ASM Press from Wolfaardt, G. M., Lawrence, J. R., Robarts R. D., and Caldwell, D. E. (1995). Bioaccumulation of the herbicide diclofop in extracellular polymers and its utilisation by a biofilm community during starvation. *Appl. Environ. Microbiol.*, **61**, 152–158

## 6.2 TRANSMISSION IMAGING

Both 1P- and 2P-LSM systems may be equipped with a non-confocal detector system for scanned transmitted light imaging. The detector may be either a photodiode or a fibre optic connection below the condenser. This is an inexpensive add-on that is extremely useful for the documentation of specimens and obtaining a variety of relevant images. When a microscope is equipped for dark-field, phase-contrast and Nomarski DIC, all of these images may be digitised using the transmission option. This approach can be used to provide multiple comparative data sets for the same sample materials. This can be useful for tracking organisms which do not stain readily or for the confirmation of numbers of stained and unstained populations or regions in some samples. Figure 5 shows dual channel images of the same location in a biofilm collected using phase contrast and confocal fluorescence imaging of a protozoan in a river biofilm. Packroff *et al.* [41] used this approach extensively in a study of fluorescent probes for the staining and detection of protozoa in microbial biofilms.

## 6.3 REFLECTION IMAGING

Confocal reflection imaging may also be performed using 1P-LSM systems. In this type of imaging, the scattering or reflection of the incident light by the sample provides what is detected to form the image. Scattering may originate from reflective particles associated with a microbiological sample or from the cellular constituents themselves (sulfur granules, silica, diatom frustules, other geogenic signals). The scattering signal has also been used to visualise mineral and metal surfaces covered by microbial biofilms [39].

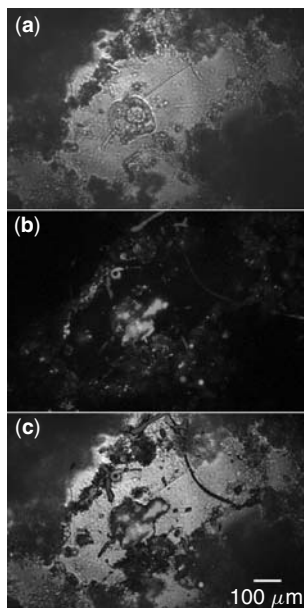


**Figure 5.** Dual channel images of the same location in a biofilm collected using phase contrast and confocal fluorescence imaging of a protozoan in a river biofilm

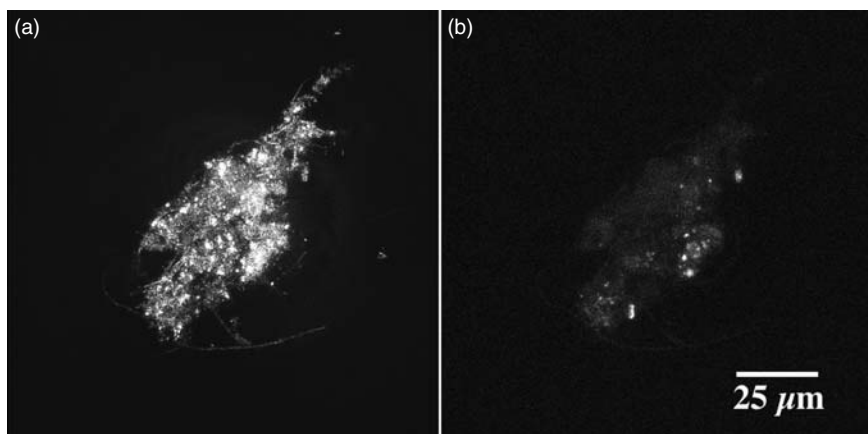


**Figure 6.** Dual-channel image of a floc imaged using reflection to visualise the largely inorganic reflective particles (a) and Syto 9 staining of nucleic acids to detect bacterial cells (b)

Confocal reflection contrast images may be obtained using 1P-LSM and can provide superior images to conventional interference microscopy. The combination of reflectance imaging with colloidal gold labelling also has been used in cell biology [42], but not yet in the examination of biofilms. Figure 6 provides an illustration of reflectance imaging performed in combination with nucleic acid staining using Syto 9 (Molecular Probes, Eugene, OR, USA). The side-by-side presentation of the two channels clearly illustrates the two types of signal originating in the sample (Figure 6).

## 7 QUANTITATIVE IMAGING

### 7.1 RATIO METRIC IMAGING

Ratiometric imaging is a microscopic technique that allows the determination of ion concentrations based on their impact on the fluorescence of a reporter molecule or molecules. Ratio imaging can be performed using emission, excitation or lifetime signals. The concept of ratio measurements is that they preclude potential artefacts due to variations in dye concentration. Fluorescent probes, such as fluorescein, 5- and 6-carboxyfluorescein, dual-labelled fluorescein–rhodamine dextrans, *etc.*, exhibit pH-sensitive fluorescence, and consequently have potential for *in situ* measurements. Carboxyfluorescein is a ratiometric pH probe that exhibits no pH sensitivity when it is excited at 435 nm and maximum sensitivity when it is excited at 490 nm. In general, a fluorescence signal is obtained at each excitation wavelength; a concentration-independent ratio between pH-sensitive and pH-insensitive signals calculated and related to a range of pH values. Calculation of pH from the ratio images is based on ratiometric imaging of killed pH-equilibrated cells, biofilm or other specimens which have been stained in the same fashion as those under investigation. The cells used for equilibration may first be fixed in 70% (v/v) ethanol or rendered permeable using valinomycin and nigericin, which act to equilibrate potassium and proton gradients across the cell membrane. These materials are then placed in appropriate

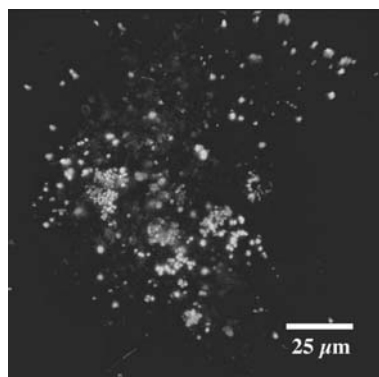


**Figure 7 (Plate 2).** LSM dual-channel image of fluorescence intensity when a 10 kDa molecular weight dextran conjugated to pH-sensitive fluorescein and pH-insensitive rhodamine was added to a waste water treatment system floc and the images taken using 1P-LSM. The image represents the ratio of the pH-sensitive and pH-insensitive signals, eliminating variations due to concentration. A standard curve was created using fixed floc material equilibrated with buffered pH solutions containing the 10 kDa dextran probe and imaged using the same LSM settings. Based on this calibration, the green regions have pH around 7.0 whereas the red regions have pH around 5, indicating differences in pH over small distances associated with microcolonies within the floc material

buffers (pH 5.0–8.0) with the fluorophore to obtain pH-equilibrated specimens that are analysed using LSM and digital image analysis to establish a standard calibration. This calibration procedure is the major drawback for ratiometric imaging since it is relatively time consuming. However, this method has been used successfully to measure internal pH values in populations of bacteria [43–45]. In Figure 7, a 10 kDa molecular weight dextran conjugated to pH-sensitive fluorescein and pH-insensitive rhodamine was added to a floc and the images were taken using 1P-LSM. The green regions have  $\text{pH} \approx 7.0$  whereas the red regions have  $\text{pH}$  near 5, indicating differences in  $\text{pH}$  over small distances associated with microcolonies within the floc material. This interpretation is based on a standard curve created using fixed floc material equilibrated with buffered pH solution containing the 10 kDa dextran probe and the flocs imaged using the same LSM settings.

## 7.2 DYNAMIC MEASUREMENTS

### 7.2.1 Fluorescence Recovery after Photobleaching

Fluorescence recovery after photobleaching (FRAP) is an analytical imaging method that is used to assess a wide range of dynamic biological processes; as the name implies, it is based on an initial destruction of the fluorophore in a location and subsequent observation of the rate of replacement by new fluorescent molecules. It was developed more than two decades ago expressly for the study of the diffusion of molecules in living cells [46]. The method has been markedly enhanced by the application of fluorescent proteins such as GFP in the area of cell biology. Lippincott-Schwartz *et al.* [47] provide a current overview of photobleaching and photoactivation techniques as applied in cell biology. These two approaches have considerable potential for examination of kinetic processes in microbial systems such as flocs or particles. Photoactivation is the light activation of a molecule;

this may be used for caged compounds that are released by ultraviolet radiation or the use of genetically encodable photoactivated proteins [47]. Three main steps are performed in FRAP: (i) acquisition of the image prior to photobleaching, (ii) photobleaching of an area of interest with a high laser power and (iii) re-imaging over time under the original laser settings to monitor fluorescence recovery. The analyses provide information about the dynamic behaviour of macromolecules in the cell, exopolymeric substances (EPS), particle matrices, *etc.* (see Figure 4a and b). In microbial systems this approach has mainly been used with 1P-LSM to examine diffusion [8]. Two-photon excitation may also be used to carry out FRAP for measuring diffusion coefficients taking advantage of its superior penetration versus 1P-LSM in deep biofilm regions. Bryers [33] applied this approach in order to determine *in situ* the diffusion coefficients of fluorescein, dextran and BSA. However, attempts have also been made to the track metabolism and sorption of compounds using FRAP [48]. The image in Figure 4a illustrates an application of photobleaching and time-lapse imaging to track the sorption of diclofop methyl by a complex biofilm community; sorption kinetic data are shown in Figure 4e.

### 7.2.2 Fluorescence Lifetime Imaging

Fluorescence lifetime imaging was introduced about 10 years ago as an alternative method for achieving contrast in fluorescence images. It is based on detecting differences in the fluorescence decay of a molecule or its lifetime. Lifetime imaging approaches have several advantages: (i) the lifetime of a fluorochrome ( $\tau_f$ ) is independent of its concentration and the laser intensity used for excitation, (ii) the lifetime of a specific fluorochrome is sensitive to its micro-environment; and (iii) fluorochromes with an identical emission wavelength can be distinguished based on their specific lifetime characteristics. Booth and Wilson [49] present an overview and describe a system for both fluorescence lifetime and intensity imaging with confocal microscopy. Either 1P- or 2P-LSM may be used to perform FLIM measurements. The use of the time domain is a common way to record lifetimes where the excitation is done with a pulsed two-photon laser combined with time-correlated single-photon counting (TCSPC) [50,51]. FLIM devices are either available commercially as stand-alone instruments or attachments can be obtained and added to an existing 2P-LSM system. The major advantage of FLIM is related to the simplicity of calibration relative to the ratiometric imaging techniques (see above) as shown for pH determinations [52,53]. Some applications of FLIM include the acridine orange imaging of oral biofilms [32] and the imaging of diffusion in biofilms [54]. A number of publications have shown that this approach can also be applied for the determination of ion concentrations in bacterial cells [55] and pH gradients in biofilms by monitoring the pH-sensitive probe carboxyfluorescein [5]. The nucleic acid-specific fluorochrome Syto 13 has been applied to FLIM imaging in order to distinguish metabolic rates based on the bacterial cells having a different DNA/RNA ratio [7]. Figure 8 illustrates the appearance of the FLIM imaging and mapping of metabolic activity of bacterial cells as demonstrated by Neu *et al.* [7].

### 7.2.3 Fluorescence Resonance Energy Transfer

Fluorescence resonance energy transfer (FRET) is based on a distance-dependent interaction between the electronic excited states of two dye molecules in which excitation

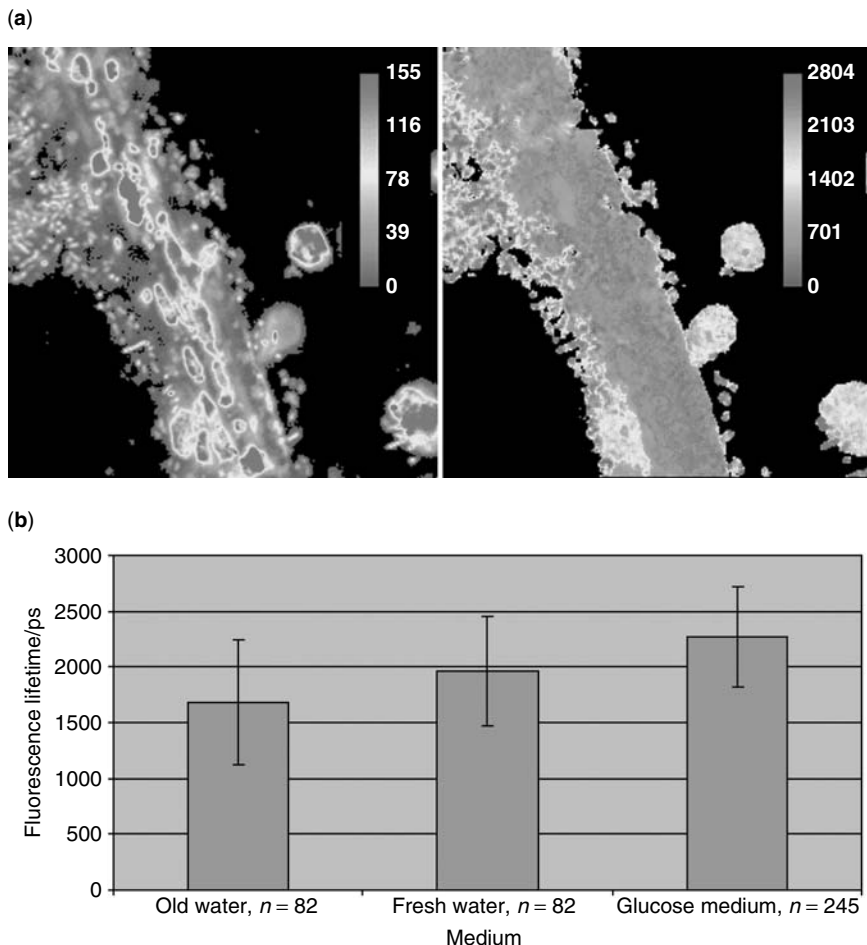


**Figure 8.** Comparison between two-photon intensity imaging versus two-photon lifetime imaging. Image (a) shows a Syto 13-stained lotic biofilm sample. The image should contain a diatom, inorganic granules and associated bacteria. From the intensity image (left) it is not possible to allocate a signal to a specific object or cell. However, the lifetime image (right) clearly differentiates between the signal of the diatom, the Syto 13 signal of the bacteria and the signal originating from inorganic granules. (b) Fluorescence lifetime of Syto 13-stained lotic biofilms growing on polycarbonate slides in Petri dishes. Effect of nutrient conditions on Syto 13 lifetime  $\tau_f$  in picoseconds. Left: biofilm after 70 h of incubation with Saale river water. Due to starvation conditions, the bacteria show a short lifetime. Middle: biofilm supplied with fresh river Saale water; FLIM measurement was done after 24 h. Due to natural nutrients, the cells continue to grow slowly resulting in a longer lifetime. Right: biofilm supplied with glucose medium ( $1.5 \text{ g dm}^{-3}$  glucose,  $1 \text{ g dm}^{-3}$   $\text{MgSO}_4$ ,  $0.4 \text{ g dm}^{-3}$   $\text{CaCl}_2$ ); FLIM measurement was done after 24 h. Due to high nutrient concentration, the fast-growing bacterial cells show a longer lifetime.  $n$  = Number of bacteria evaluated. Reprinted from Neu, T. R., Walczysko, P. and Lawrence, J. R. (2004). Two-photon imaging for studying the microbial ecology of biofilm systems, *Microbes and Environments*, **19**, 1–6, with permission from the Japanese Society of Microbial Ecology/Japanese Society of Soil Microbiology

is transferred from a donor molecule to an acceptor molecule without the emission of a photon. The result is a decrease in donor emission and an enhancement of acceptor emission. Overviews of the methods and applications have been provided [56–58]. FRET allows the monitoring of biological or chemical processes in which (i) the spatial distance between donors and acceptors is less than 10 nm, (ii) the absorption spectrum of the acceptor overlaps with the fluorescence emission spectrum of the donor and (iii) donor and acceptor transition dipole orientations must be approximately parallel. Using fluorophore-tagged (lanthanide chelates, quantum dots, Cy3–Cy5) macromolecules, it is possible to observe a variety of biological phenomena that produce changes in molecular proximity, including co-localisation of proteins and other molecules. The processes can be imaged with spatial resolution beyond the limits of conventional optical microscopy. Although not extensively applied in microbiology in relation to biofilms and flocs, Derdowski *et al.* [59] demonstrated that FRET is a powerful tool for the detection of protein–protein interactions involved in retrovirus assembly. Although applications to complex environmental samples are speculative in nature, there is potential for this approach alone or in combination with other imaging techniques including standard LSM, FLIM and FRAP.

## 8 APPLICATIONS TO IMAGING OF SPECIFIC PARTICLE PROPERTIES

### 8.1 CELL IDENTITY

The combination of LSM and fluorescent probes offers a wide range of potential *in situ* analyses of hydrated microbial systems. Although probes are most frequently conjugated to fluorophores, a range of colloidal reflective conjugates (gold, silver) may also be used in LSM applications [14]. A new reporter is the quantum dot (QD), a semiconductor nanocrystal whose photoluminescence emission wavelength is proportional to the size of the crystal [60]. However, most commonly, fluorescent nucleic acid probes such as Syto 9 are used to detect and visualise bacterial cells *in situ* [23,40,61]. Figure 9 shows an LSM

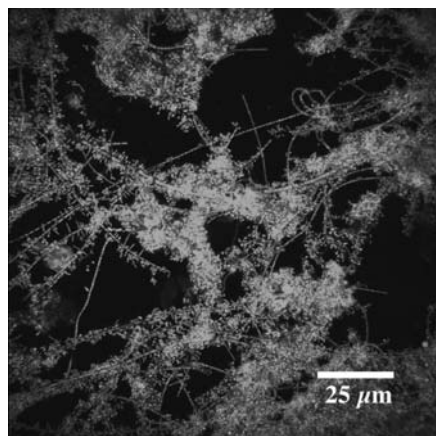


**Figure 9.** LSM micrograph of a formalin-fixed waste water treatment floc stained with the nucleic acid stain SYTOX, allowing visualisation of the bacterial cells and illustrating typical architecture of the floc

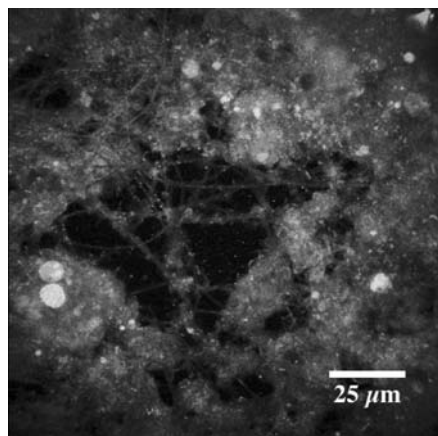


**Figure 10 (Plate 3).** Dual-channel colour image of the result of a combined fluorescent *in situ* hybridisation (FISH) of a waste water treatment floc with the 16S RNA probe for eubacteria (EUB 338) (green) and a FISH probe specific for archaea ARC915 (red), revealing the distribution of eubacteria and archaea, respectively, in the floc

micrograph of a floc stained with SYTOX, a nucleic acid stain for fixed cells, illustrating a typical floc architecture and distribution of cells within the floc. The use of fluorescent Gram staining (Molecular Probes) has also been successfully applied to microbial communities to localise members in each of the Gram-positive or -negative groups [62]. Cell-specific probes such as fluorophore-conjugated rRNA-targeted oligonucleotides may be used to detect bacterial groups at various levels of resolution from kingdom to subspecies. Figure 10 illustrates the combined probing of a floc with the EUB 338 and ARC 915 probes, showing the distribution of eubacteria and archaea, respectively, in the floc.

Although autofluorescence is often a concern or even a problem in imaging microbial systems, it can be used to detect and identify photosynthetic organisms such as algae and cyanobacteria in biofilms. Lawrence *et al.* [16] demonstrated the fundamental approach in 1P-LSM, and in a subsequent paper, Neu *et al.* [31] established the utility of 2P-LSM for detection, localisation and quantification of photosynthetic organisms in microbial systems. In this case, wavelength or lambda scans may be useful to optimise the excitation and emission wavelengths for a given sample (see Figure 2).

## 8.2 STRUCTURAL CHEMISTRY

Probes may also be targeted towards the various macromolecules that are abundant in microbial systems including polysaccharides, proteins, lipids or nucleic acids. Probes for specific macromolecules include fluorophore-conjugated lectins for glycoconjugates and fluorescent protein stains such as SYPRO Orange (Molecular Probes). Kloepfer *et al.* [60] indicated that quantum dots conjugated to lectins worked well to detect glycoconjugates on microbial cells. As a general protein stain, Hoechst 2495 has been used to label ‘footprints’ of bacteria on surfaces [63,64]. Similarly, this dye may be used to probe for proteins in biofilms [36]. In addition, there is a range of reactive probes which can be linked to certain groups of amino acids, amines, proteins and thiols (Molecular Probes). Newer stains such as the SYPRO Ruby protein gel stain, Pro-Q Diamond phosphoprotein

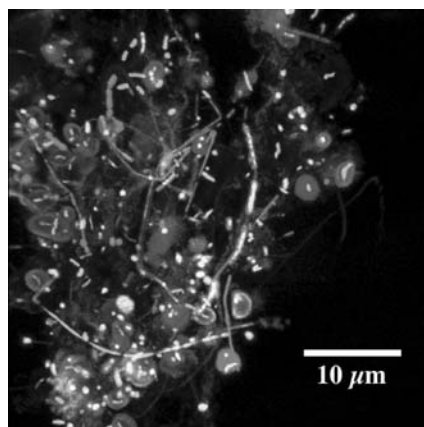


**Figure 11 (Plate 4).** Three-channel LSM overlay image showing the result of the sequential imaging of a triple-labelled microbial sample using the nucleic acid stain Syto 9 (green), the hydrophobic lipid sensitive stain Nile Red (red) and polysaccharide using the lectin of *Ulex europaeus*-CY5 (blue)

gel stain and the Pro-Q Emerald glycoprotein stain can be used individually or in series to detect total protein, phosphoproteins and glycoproteins, respectively. However, with the exception of the SYPRO series dyes, these latter stains have not yet been applied directly to microbial systems with subsequent examination by 1P- or 2P-LSM. Various stains may also be used in combination to co-localise major structural polymers in biofilms and flocs. The combination of nucleic acid, lipid and polysaccharide staining is demonstrated in the three-channel image shown in Figure 11. Lawrence and co-workers [11,36,65] describe specific techniques for the detection and quantification of cellular and polymeric compounds in biofilms using fluorescent probes. Probes for extracellular macromolecules may also be combined with nucleic acid probes or rRNA probes resulting in simultaneous identification and co-localisation of cells and EPS. Böckelmann *et al.* [66] demonstrated the effectiveness of a fluorescent lectin binding assay in combination with fluorescent *in situ* hybridisation for the detection of both glycoconjugates of the EPS and cell identity.

### 8.3 PHYSICAL PROPERTIES

There is a wide range of fluorescent probes such as dextrans, ficolls and surface-modified polystyrene beads to assess cell and EPS properties such as charge, hydrophobicity, diffusion or permeability [8,14,67]. Fluorophore-conjugated dextrans used in conjunction with 1P-LSM allow the micro-scale determination of positively and negatively charged residues in biofilms. They are relatively inert, have low toxicity and are suitable for *in situ* determinations of charge and particle mobility. Fluorophore-conjugated dextrans are commercially available with molecular weights ranging between 3000 and  $1.0 \times 10^6$ . Protocols for their application in conjunction with LSM have been published by Lawrence and co-workers [8,14]. Ficolls are synthetic polymers made by copolymerisation of sucrose and epichlorohydrin; these polymers may be obtained size fractionated and fluorophore conjugated for use in penetration and diffusion studies. For studies of diffusion or permeability, the size-fractionated probe (beads, dextrans or ficolls) may

be added as a point source via a micropipette [67], injected or pulsed in using laminar flow [8,14] and observed in time series using LSM. The resultant image series may be analysed for spatial distribution or fluorescent intensity changes versus time, allowing mapping or calculation of permeability and diffusion coefficients (see, *e.g.*, Lawrence and co-workers [8,14]). Major limitations of these approaches include non-specific binding to the matrix, photobleaching and signal loss and deviation from the assumption of being spherical, a problem particularly for the calculation of diffusion coefficients.

Fluorescent polystyrene beads with sulfated or carboxylated surface chemistry for the determination of hydrophobicity and hydrophilicity of bacterial cells have been used to analyse the surface properties of filamentous bacteria in flocs [68]. Figure 12 presents LSM micrographs which illustrate the application of microbeads to assess the sorption and penetration of bacterial microcolony EPS and determination of hydrophobicity and permeability. This is based on the interpretation of relative penetration of size-fractionated beads and their localisation in the biofilm. The figure shows bacterial structures to which three types of beads were applied, 20 nm carboxylate surface chemistry (hydrophilic) (blue), 20 nm aldehyde surface chemistry (hydrophobic) (green) and 100 nm sulfate surface chemistry (hydrophobic) (red). Their distribution indicates both the permeability and relative hydrophobicity of colonies and filaments. In general, these images are limited to mapping or, through application of image analysis, to the determination of the relative abundance of the specific binding sites.

#### 8.4 ENVIRONMENTAL CHEMISTRY

In general, one of the major goals in the application of LSM has been the visualisation of gradients within microbial biofilms and flocs. This goal has been accomplished to some

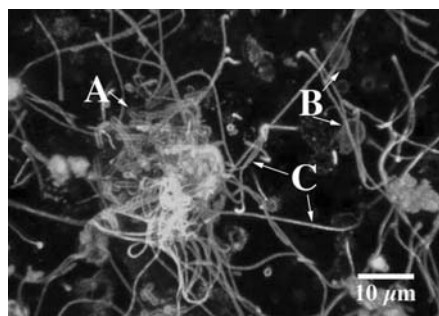


**Figure 12 (Plate 5).** An LSM micrograph which illustrates the application of microbeads to assess the sorption and penetration of bacterial microcolony EPS and determination of relative hydrophobicity and permeability. The following beads were applied: 20 nm carboxylate surface chemistry (hydrophilic) (blue), 20 nm aldehyde surface chemistry (hydrophobic) (green) and 100 nm sulphate surface chemistry (hydrophobic) (red). Note that in many cases regions of the biofilm bind only one of the bead types, and that in some cases the beads are restricted to the outside of the microcolony or structure; these indicate differences in the surface chemistry and also variations in permeability. Arrows at A, green sulfate hydrophobic on surface of cells in a microcolony, around the cells are 20 nm blue carboxylate hydrophilic beads; at B, microcolony with red 100 nm hydrophobic beads sorbed to the exterior, with the interior having the 20 nm blue carboxylate hydrophilic beads showing differential permeability of the colony boundary, and at C, microcolonies and filaments which bind the 100 nm hydrophobic beads on their surfaces as well as the 20 nm green hydrophobic beads

extent for pH using LSM and 5,6-carboxyfluorescein as described by Caldwell *et al.* [34]. The major problems with the use of free or bound dyes to determine microenvironmental conditions are (i) non-specific interactions with biomolecules resulting in quenching, (ii) effects of *Eh* on probe response, (iii) effects of ionic composition on probe response and (iv) the general problem of independent validation for quantitative measurements. However, Vroom *et al.* [5] used ratiometric and lifetime imaging to provide a more quantitative determination of pH and changes in pH with microbial biofilms overcoming many of the concerns indicated above.

LSM can also be applied in conjunction with specific probes such as antibodies or metal-sensitive fluorochromes to detect and localize specific molecules with a microbial system. For example, Lawrence *et al.* [69] localised the herbicide atrazine within river biofilms using antibody staining. In this instance atrazine was found to be associated with a particular bacterial colony type, rather than generally distributed in the biofilm. In general, this approach allows localisation but is not amenable to quantification. Wuertz *et al.* [9] applied ion- or metal-sensitive probes such as Newport Green to detect the presence of metals in biofilms and within the EPS matrix. Newport Green staining is illustrated in Figure 13a and b, which show LSM micrographs of a control and a cadmium-treated biofilm stained with Newport Green and imaged using LSM to show the increase in Cd in the biofilm. The major issue here, as noted by Wuertz *et al.* [9], was an inability to quantify metals through this approach, which they concluded was limited to detection. In addition, both sensitivity and specificity are problematic with interferences occurring from other metals and cations. However, there remains considerable opportunity to explore various aspects of the chemistry of microbial systems through combinations of fluorescent probes and various lifetime and intensity imaging approaches which have not been fully explored to date.

## 8.5 DYNAMIC PROCESSES/METABOLIC STATE

Although FRAP, FLIM, FRET and ratiometric analyses allow the investigation of dynamic processes, gradients and cellular metabolism, there are a range of other 1P- and 2P-LSM

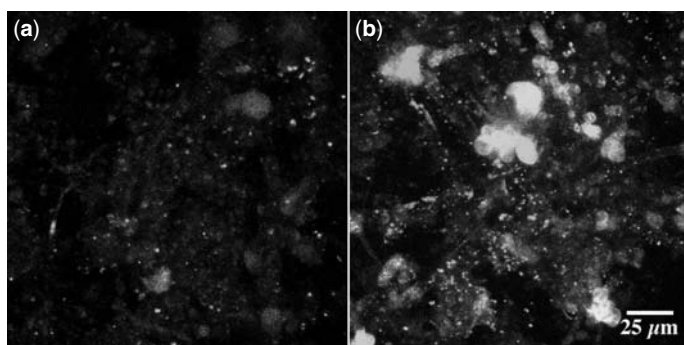


**Figure 13.** LSM micrograph of control and cadmium-treated (exposed to 1 ppm Cd for 24 h) river biofilm stained with Newport Green following the manufacturer's instructions and imaged using LSM. The presence of cadmium in the treated sample is indicated by increased fluorescence. Sensitivities for fluorescent indicators of metals in solution are generally in the micromolar concentration range. Confirmation using X-ray microprobe analyses is recommended

methods that can be usefully applied to answer questions about the nature, levels and sites of biological activity in microbial communities. LSM allows the user to assess various levels of activity within the microbial community, including enzymes, specific metabolic activities and metabolic state (live–dead). Probes used for these applications have been based on the detection of cytoplasmic redox potential, electron transport chain activity, cell membrane potential, membrane integrity and specific enzymatic activity (see below). Their application is complicated by a variety of factors: (i) a difficulty in obtaining verification, (ii) the impact of microenvironmental conditions such as redox or pH on the probe and (iii) the fact that flocs and biofilms are open systems in which non-specific binding and other interactions may cause significant problems. Another option for activity determination is the application of compounds such as bromodeoxyuridine, an analogue of thymidine, which after incubation is detected in active cells via fluorescent antibody staining. This approach provides another alternative for the examination of general metabolic activity in biofilms [70]. Cyanoditolyltetrazolium chloride (CTC) [71] has proven useful for detecting viable bacterial cells; however, toxicity and other questions have arisen [34,72]. The dyes rhodamine 123, propidium iodide and oxonol and the membrane-potential sensitive dye 3,3'-dihexyloxacarbocyanine [73,74] have all been recommended for the assessment of bacterial viability. In addition, the fluorogenic enzyme substrates (fluorescein and carboxyfluorescein diacetate, calcine AM), the probes sensitive to DNA damage (Hoechst 33342) and the commercial fluorescent staining kit (BacLight Live/Dead stain, Molecular Probes) are extremely useful. Figure 14 shows the results obtained with this Live/Dead viability kit when applied to a floc system and imaged using LSM. The kit uses Syto 9, a nucleic acid stain, to distinguish living cells (which fluoresce green), having a functional plasma membrane, and from propidium iodide-stained dead cells (which fluoresce red), having a compromised membrane. Although in natural communities we have found that errors may arise due to autofluorescence (plant material,

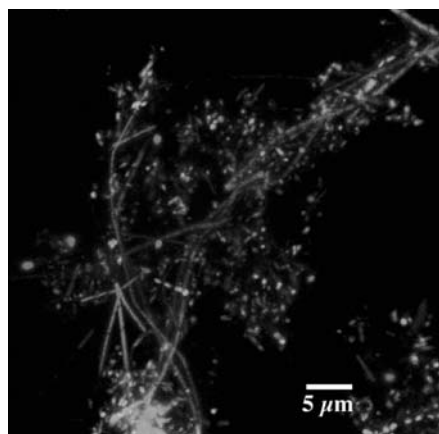


**Figure 14 (Plate 6).** Results obtained with the Live/Dead viability kit from Molecular Probes when applied to a waste water treatment floc system and imaged using LSM. The kit uses Syto 9 a nucleic acid stain, to distinguish living cells (which fluoresce green) and have a functional plasma membrane and dead cells (which fluoresce red) when stained with propidium iodide due to a compromised membrane

cyanobacteria, algae) in the red and far-red regions, we have applied the system successfully in a variety of studies. These studies have shown the distribution of live-dead cells in biofilms, shifting ratios of live:dead cells with environmental stress and other effects [40,61].

Enzyme activities may also be visualised *in situ* at the microscale using fluorescent reporters. Perhaps the best example of this approach is the ELF-precipitating fluorescent reporter, which overcomes the problem of diffusion of the fluorophore away from the site of production and consequent loss of signal. Christensen *et al.* [30] provided detailed protocols for the application of ELF for detection of phosphatase and Van Ommen Kloek and Geesey [75] illustrated an *in situ* application to sewage flocs. Gene expression may be monitored using fluorogenic substrates including  $\beta$ -galactosidase,  $\beta$ -glucuronidase, chloramphenicol acetyl transferase and luciferase. An excellent example of this approach is that of Davies and co-workers [76,77], who through direct visualisation demonstrated that *P. aeruginosa* upregulated algC genes during attachment to the surface and growth in a biofilm. Although this approach is still very useful, the application of green fluorescent protein (GFP) and a host of derivatives of this fluorescent protein to monitor gene expression has become favoured. The applications, advantages and disadvantages of GFP may be found elsewhere [30,78]. Excellent examples of the use of GFP in conjunction with 1P-LSM to monitor gene expression were given by Møller and co-workers [79,80]. The use of GFP to monitor gene transfer was demonstrated by Hausner and Wuertz [81]. Additional information about genes and gene expression may be obtained by *in situ* polymerase chain reaction (PCR). The details and examples of this visualisation technique were first presented by Hodson *et al.* [82]. An emerging and very important combination of techniques is that of microautoradiography in combination with fluorescence *in situ* hybridisation. This allows the determination of both physiological activity and phylogenetic identity of microorganisms and has been used in a range of studies over the last 5 years [83–87].

## 9 IMAGE PROCESSING AND 3D VISUALISATION

The simplest presentation of LSM images is the image gallery, where the stack is arranged in panels as a series of optical sections. This can be useful for the selection of images or presentation of trends observed in image stacks. Another option uses maximum intensity projection (MIP), which simply projects the image stack into one optical plane with varying degrees of transparency. This approach may be combined with XYZ presentations showing the image as a combination of XY and XZ orientations. Variations on this include ortho slices, where subsets of the 3D data set are calculated and presented at any angle or location in the specimen. Pseudo-3D may be created by ‘shadow effects’ using an imaginary light source or ‘simulated fluorescence’ whereby the material is viewed as though it were illuminated from an oblique angle and the surface layer was fluorescent. However, there are a range of true 3D presentation methods that should be considered to exploit maximally the information content of the image stack. The image stack created by LSM imaging allows the user to create a variety of 3D reconstructions using as few as 12 optical sections. In general, an optimal stack as defined above is a prerequisite for effective 3D visualisation of the material under study. For the basic presentation, the user constructs two extended focus images at the same location in the specimen, shifts one of

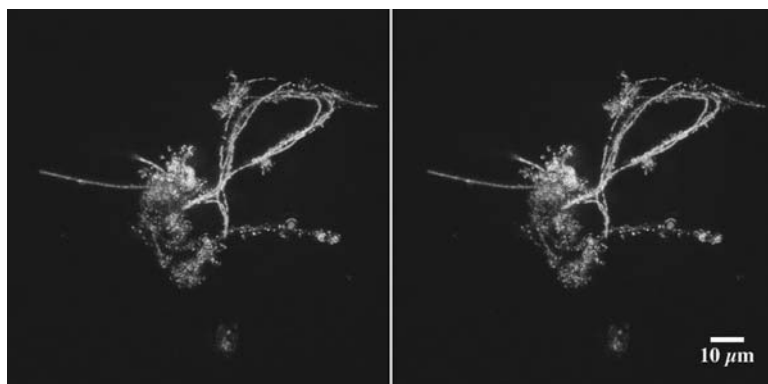


**Figure 15 (Plate 7).** Three-channel images stack combined to create a three-colour stereo image of a river floc integrating the reflectance (reflective mineral, colloidal materials), autofluorescence (cyanobacteria and algae) and Syto 9 nucleic acid stained bacteria signals (best viewed using stereo glasses)

the images to create an oblique view and finally the two images are then aligned to create a stereo pair. Selection of the degree of offset is very important since if the shift is too large the image will have poor contrast and a poor depth effect. A suggested total offset is in the range of 15 pixels for the entire image stack, or 5° offset. These stereo data sets may then be presented as side-by-side stereo pairs (grey-scale or coded multicolour images) (see Figure 1c) or as red/green anaglyph projections. Colour coding may also be used to create three-colour stereo pairs in which materials of the same type or those that bind the same fluorescent probe appear in the same colour. A range of colour stereo presentations may be found in publications by Lawrence and co-workers [14,16,36,40]. Figure 15 provides a three-colour image of a river floc showing the reflectance, autofluorescence and Syto 9 nucleic acid signals.

Most of the presentation methods listed above are available as tools with commercial LSM systems. However, there are many more advanced 3D visualisation software packages available, including AMIRA (TGS), a highly advanced 3D visualisation package with many options including deconvolution, IMARIS (Bitplane), which is well suited to measurements, co-localisation and deconvolution, VOXBLAST (Vaytek), which also offers advanced 3D visualisation in combination with deconvolution; VELOCITY (Improvision), a freeware package which offers basic image handling and 3D visualisation, and IMAGE-PRO PLUS (MediaCybernetics), which also has three-dimensional rendering and deconvolution. A 3D rendering of an Elbe River floc integrating signals for reflectance, autofluorescence, EPS, as well as bacteria shows the data set as a 3D isosurface (Figure 16).

Deconvolution is necessary in some applications, particularly as part of rendering 3D data sets. This is carried out through various deconvolution exercises which sharpen an image through mathematical removal of out-of-focus information [88–90]. Specialised software is also available for the removal of out-of-focus haze by mathematical deconvolution. Deconvolution software such as EPR is available from Scanalytics (Billerica, MA, USA) and its utility was demonstrated by Manz *et al.* [90]. A UNIX-based deconvolution

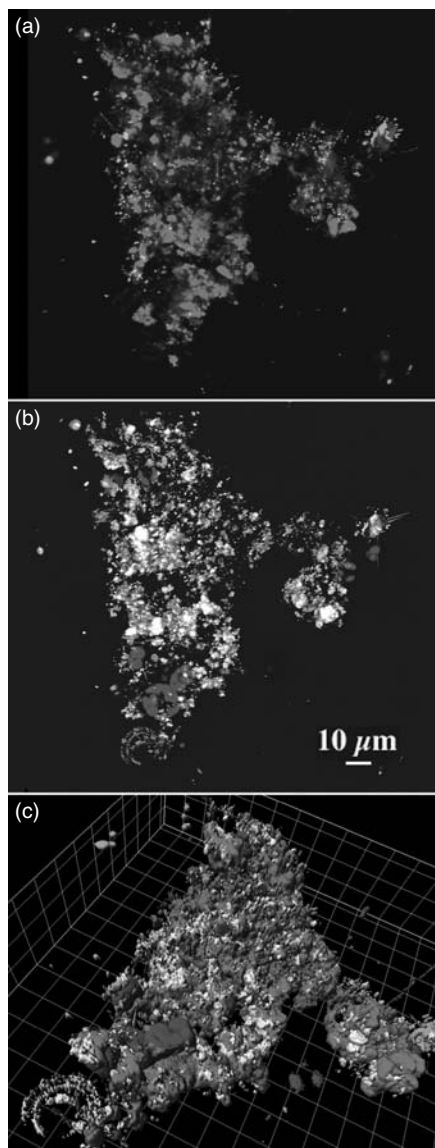


**Figure 16.** A series of image stacks of an Elbe River floc integrating (a) the reflectance (reflective mineral, colloidal materials) and autofluorescence (cyanobacteria and algae), as well as (b) lectin (exopolymeric substances) and Syto 9 (nucleic acid stained bacteria) signals. (c) The same aggregate projected as 3D isosurface image

package is available over the Internet and may be applied to any fluorescent image (see <http://ibc.wustl.edu/bcl/xcosm/xcosm.html>, now available for the SGI, DEC and Sun platforms). The Huygens system (Scientific Volume Imaging, Hilversum, The Netherlands) runs on Silicon Graphics computers and includes many image processing features, including deconvolution.

**Table 1.** Fluorescent compounds and applications

Fluor	Application
<b>Probe labels (/indicates excitation maximum)</b>	Fluors suitable for conjugation to protein linkers on dextrans, lectins, nucleotides, oligonucleotides, peptides, etc., creating fluor-conjugated reporter molecules
Alexa series	
Oregon Green/488 (diluorofluorescein)	
Fluorescein isothiocyanate/494 nm	
BODIPY FL/503 nm	
Carboxytetramethylrhodamine/550 nm	
Texas Red/596 nm	
Cyanine dyes (CY2, CY3/550 nm, CY5/649 nm)	
<b>Nucleic acid stains</b>	Fluors which become fluorescent after binding to nucleic acids allowing visualisation of cells
DAPI (4',6-diamidino-2-phenylindole)	Live cells
AO (Acridine Orange)	Live cells
Hoechst 33258	Live cells
Hoechst 33342	Live cells
SYTO series stains	Live cells
PicoGreen	Live cells
TOTO-1/TO-PRO-1	Live cells
YOYO-1/YO-PRO-1	Live cells
POPO-3	Live cells
SYBR-Green I/II	Live cells
ChemChrome V6	Live cells
SYTOX series stains	For fixed cells
Propidium iodide	For fixed cells
<b>Probes for other biomolecules</b>	Target
Nile Red	Lipids
Sypro Orange	Proteins
Lectins (8 out of 70 commercially available used to characterise glycoconjugates in microbial communities:	Major target glycoconjugates of lectins [11]
<i>Canavalia ensiformis</i>	Methyl α-D-mannopyranoside, D-(+)-mannose
<i>Helix pomatia</i>	N-Acetylgalactosamine
<i>Limulus polyphemus</i>	Glucuronic acid
<i>Arachis hypogaea</i>	D-(+)-Galactose
<i>Canavalia ensiformis</i>	Methyl α-D-mannopyranoside, D-(+)-mannose
<i>Erythrina cristagalli</i>	N-Acetyl-D-galactosamine, D-galactose
<i>Ulex europaeus</i>	L-(–)-Fucose
<i>Triticum vulgaris</i>	<i>N, N'</i> -Diacetylchitobiose, <i>N, N', N''</i> -Triacetylchitobiose
<b>Identification</b>	
FISH fluorescence <i>in situ</i> hybridisation	Fluor-labelled oligonucleotide probes/hybridisation [66]
BacLight fluorescent Gram stain	<i>In situ</i> Gram reaction (pure cultures, mixed biofilms [62])

**Table 1.** (*continued*)

Fluor	Application
GFP green fluorescent protein Immunostaining	Tracking GFP-labelled cells [30,78] fluorescent label antibody recognition of antigen
<b>Activity/viability</b>	
RH-795	Cell membrane integrity, membrane potential
Rhodamine 123	Cell membrane integrity, membrane potential [73]
Live/Dead BacLight (propidium iodide/SYTO 9)	Integrity of individual cell membrane/cell viability [40,61]
FISH fluorescence <i>in situ</i> hybridisation	Cellular activity/ribosome content [13]
FISH–MAR fluorescence <i>in situ</i> hybridisation	Ribosomal content and response to substrate addition [84]
Microautoradiography <i>in situ</i> PCR	Detection of specific mRNA activity [82]
<b>Fluorescent enzyme assays</b>	
ELF97	Alkaline phosphatase activity [75]
SFDA (sulfofluorescein diacetate)	Esterase activity
CFDA (carboxyfluorescein diacetate)	Esterase activity
TTC (triphenyltetrazolium chloride)	Respiratory activity (dehydrogenase)
CTC (5-cyano-2,3-ditolytetrazolium chloride)	Respiratory activity (dehydrogenase) [72]
<i>gfp</i> gene green fluorescent protein	Gene expression of individual cells [15,79,80]
<b>Environmental reporters</b>	
BCECF-AM	pH responsive
SNAFL-1	pH responsive
5- and 6-carboxyfluorescein	pH responsive [5,43]
Newport Green	Sensitive to nickel (metal) concentrations [9]

## 10 IMAGE ANALYSIS PACKAGES FOR QUANTIFICATION OF LSM IMAGES

Image analysis is a critical tool for use in conjunction with the 2D, 3D and 4D data sets that can be created by 1P- or 2P-LSM imaging (see also a discussion of digital imaging and image analyses applied to transmission electron microscopy [22]). For many applications freeware packages are available from a number of websites. The most versatile and popular programs in this class are available for a number of platforms: NIH Image (<http://rsb.info.nih.gov/nih-image/>), ScionImagePC ([www.scioncorp.com](http://www.scioncorp.com)) and ImageJ (<http://rsbinfo.nih.gov/ij/>). These software packages (i) are specifically designed for use with LSM image stacks, (ii) they have many built-in functions for image analyses and (iii) they allow the development of macros for specific applications. Neu *et al.* [11] gave an example of the application of NIH image and specially developed macros to the quantification of lectin binding in microbial biofilms. Another freeware package is Image-Tool (<http://ddsdx.uthscsa.edu/dig/itdesc.html>), which, although not designed for image stacks, can be very useful when applications call for object recognition and analysis. For example, it has been used to enumerate up to 11 different bacterial populations in a community using phase contrast microscopy [91]. Macros or plug-ins for this program are available from a number of websites. There are also programs which are ‘free’ but require the purchase of additional software in order to make them fully functional. In this category

are Comstat [92], which is good for some 2D structural and feature analyses but requires the purchase of MATLAB, and the programs ISA [93], CLSM tool box and PHLIP [94], which also require MATLAB. The programs IA [95], Microstat [96] and ConAn [97] are all applicable to microbial systems and allow thresholding, quantification, object property extraction, co-localisation and multichannel image analyses and can be automated or semi-automated. A number of commercial software suppliers are listed by Lawrence *et al.* [14] or can be obtained via the Internet. In general, no system will provide all the functions and flexibility desired; however, careful assessment will allow the selection of the most appropriate package. Examples of suitable commercial systems include the Quantimet System offered by Leica (Heidelberg, Germany), which has been used to analyse CLSM images of bacteria [98]. PC-based three-dimensional imaging/image analysis systems include MicroVoxel (Indec Systems, Sunnyvale, CA, USA), VoxelView (Vital Images, Fairfield, IA, USA) and VoxBlast (VayTek, Fairfield, IA, USA). Other systems which allow image handling, processing and analysis include Huygens (SVI), AutoDeblur (AutoQuant), Microtome (Vaytek), Volocity Restoration (Improvision), 3D Deconvolution (Zeiss) and AMIRA (TGS) (see above).

### 10.1 DIGITAL IMAGE ANALYSIS (DIA) – METHODOLOGY AND LIMITATIONS

Current imaging techniques using LSM result in digital images consisting of pixels (2D, XY direction) or voxels (3D, plus Z direction) at a certain resolution. As the images are not continuous, their quantitative analysis is affected by a range of different parameters to be selected, first during microscopic recording and second during the DIA procedure. A primary issue is the quality of staining and the resulting signal-to-noise ratio, which have a dramatic effect on DIA. A related problem is the decreasing signal intensity in axial (Z) direction. The decrease in intensity is due to scattering in the biological material and the size, thickness and density of the sample. Hardly any program addresses this problem in biofilm research [99]. Another issue is the proper setting of photomultiplier voltage and gain during recording of the images. For this purpose, specific look-up tables are available which support the correct setting; however, there is still a range of different correct settings possible. A further aspect to be considered is the selection of an appropriate lens, not only in terms of magnification but even more importantly the numerical aperture (NA). The NA significantly affects the resolution in the axial (Z) direction. The higher the NA, the better is the axial resolution. For confocal images, the NA should be at least 0.9 or higher; however, working distance is inversely related to the NA and may be critical with some sample types.

The next issue is the resolution of the images on the computer screen. The older CLSM instruments started with  $256 \times 256$  pixels; nowadays,  $512 \times 512$  is the normal resolution for fast image recording. The newest instruments are able to collect images at  $1024 \times 1024$  or even  $2048 \times 2048$  pixels, but at a slow speed. This decision has, of course, an effect on DIA, first in terms of file size and consequently computing time and second in terms of the detailed settings for subsequent DIA. In this respect, one important point is the size of the smallest objects to be imaged (*e.g.* eukaryotic cell organelles, small bacteria, viruses) in comparison with the size of so-called one-pixel or one-voxel objects. For example, with a  $63 \times$  NA 1.2 lens and a pixel resolution of  $512 \times 512$ , the pixel size will be 310 nm. The size of viruses or virus-like particles is in the range 50–200 nm. Hence the resolution has to be increased to at least  $1024 \times 1024$  pixels in order to resolve the viruses with a pixel size of 155 nm.

The next parameter to be considered is the step size in the axial (*Z*) direction for collecting images. Again the step size should be controlled by the size of the smallest objects. In addition, the step size in the *Z* direction is highly important if deconvolution software is intended to be used. For deconvolution, in general, a step size of about 170 nm is needed. Ideally the step size should result in a voxel of a cubic shape, but usually this is never the case and the voxels mostly have a long cuboid shape extended in the *Z* direction. This *XZ* direction error will determine the accuracy of the result of quantitative DIA.

Apart from the microscope settings, the actual DIA settings will, of course, have an effect on the quality of DIA. One of the first decisions to be made is whether to filter and, if so, what type of filter and which kernel size to apply. Again, whether a filter has to be used is dependent on the quality and content of the original image data set, *e.g.* size and structure of single objects and background.

The next most critical step in DIA is thresholding. By thresholding, the image series having a pixel intensity of 0 (black) to 255 (white) is transferred into a binary image series with only black and white pixels. A threshold can be set on one side of the intensity range, *e.g.* at 51 pixel intensity (= 20%), then every pixel with an intensity of 50 or lower is removed from the data set [97]. However, the threshold may also be set on both sides of the intensity range. As a result, the very bright pixels are also cut out. Thus, by means of thresholding, a decision is made regarding what is real signal and what is background signal or signal from non-specific staining. As thresholding is extremely critical, many different approaches have been tested and applied in biofilm analysis [100–102]. Thresholding methods are available as either automatic user-independent thresholds or set manually by the operator after examination of the images. Which method is the most accurate depends very much on the type of images to be analysed, simple or complex. A further point to consider is the type of DIA software applied to the data set. There is software which does a straight calculation of pixels and voxels which is very fast. Examples are the software NIH Image (Mac), Scion Image (PC) and recently ImageJ (Java). However, there is other more advanced software which first defines objects in three-dimensional space using specific algorithms and then does the calculation of volumetric data for each single object. This procedure requires a lot of computing time, *e.g.* the analysis of one medium-sized two-channel data set or image stack (20 optical slices) will take about 20 min.

In conclusion, there are many parameters affecting the result of quantitative DIA. In most cases the results from different laboratories cannot be compared as data sets have been recorded under different microscope settings and for the subsequent quantitative DIA different softwares and procedures were employed.

## 11 FUTURE APPLICATIONS AND DIRECTIONS

LSM provides a wide range of imaging options for application in microbial systems. However, there is still room for far more extensive applications to understand the nature of microbial communities, their structure, composition and specifically activity. Conventional design of LSM systems still allows considerable room for improvement in the areas of speed, acquisition, efficiency and sensitivity. In particular, the dynamic range of detectors requires improvement to allow a linear response over a broader range of signal intensity. Faster, higher resolution (theoretical 200 nm), real-time imaging should also be

possible to allow the determination of metabolic events and microenvironmental dynamics. Although we have commented on this often, the objective lens is the key element in LSM imaging and although improvements have been made there remains room to rethink the conventional objective in terms of LSM imaging. Here there must be room to think beyond lenses optimised for human vision to those optimised for specific wavelengths, working distances, numerical aperture and sensitivities relevant to environmental applications. The progress in fluorescent, reflective and quantum dot reporters has been rapid, as has that for probes directed at specific molecular targets, and this should continue for the foreseeable future.

One major challenge particularly in the application of LSM techniques to microbial ecology is that of independent calibration and quantification. Although correlative microscopy has offered considerable reassurance, the puzzle of ‘what you probe is what you see’ remains incompletely solved [12]. Additional discussion of correlative microscopy combining multiple microscopic examinations of particles and other biological samples has been provided by Mavrocordatos *et al.* [22]. There is also considerable excitement regarding emerging techniques based on two-photon excitation which are becoming commercially available, *e.g.* second harmonic imaging microscopy (SHIM) and coherent anti-Stokes Raman scattering (CARS) microscopy. The last decade has seen a resurgence of optical imaging and microvisualisation in microbiology, which is reflected in a proliferation of books and reviews on the current state of the art.

## ACKNOWLEDGEMENTS

The authors gratefully acknowledge the excellent technical assistance of Ute Kuhlicke (Germany) and George D. W. Swerhone (Canada). The studies reported here were supported by the Canada–Germany Agreement on Scientific Research (1995–2003), Health Canada through the Toxic Substances Research Initiative of Health Canada, the National Water Research Institute, Environment Canada, the National Research Council of Canada, Natural Sciences and Engineering Research Council of Canada and the UFZ Centre for Environmental Research Leipzig-Halle, Germany.

## GLOSSARY

**1-Photon LSM** conventional confocal laser scanning microscopy wherein a pinhole or system of pinholes is used to limit the light returning to a detector to that from the focal plane of the objective lens creating an optical thin section.

**2-Photon LSM** laser scanning microscopy that utilises the effect of rapid interactions of two photons with fluorophores to limit the excitation zone to that of focal plane of the objective lens creating an optical thin section.

**Anaglyph** a pair of superimposed pictures produced in red and green or red and blue, which when viewed through complementary coloured glasses produces a stereoscopic image in one colour. A percentage of the population may not be able to perceive the effect.

**Apochromatic objective lens** a lens designed to provide the same focal length and freedom from spherical aberration for two wavelengths of light.

*Axial resolution* resolution of an objective lens in the *Z* dimension of a 3D volumetric image as compared with the lateral *X-Y* resolution of a 2D image. Axial resolution is half to one-third of the lateral resolution.

*Deconvolution* a mathematical process of removing haze due to diffraction from a series or stack of digital images obtained by fluorescence microscopy. Deconvolution is also used to improve the axial resolution.

*Depth of field* the distance between the closest and furthest objects in focus within a scene when viewed with a lens.

*Depth of focus* the range of distances between a lens and image plane for which the image formed is clearly focused.

*Lifetime imaging* detecting the fluorescence decay of a molecule which is expressed as its lifetime, rather than the intensity of the fluorescence signal.

*Numerical aperture (NA)* in microscopy the half angle of the cone of light accepted by the objective lens  $\times$  the refractive index of the medium between the specimen and the lens. The light-gathering capacity of the lens.

*Pixel* the picture element defined by its *X* and *Y* dimensions and its grey level; it is the single finite element of a digital image.

*Pinhole* in confocal microscopy an aperture placed at a position in the light path such that only light returning from the focal plane of the objective lens reaches the detector, reducing haze from above and below the focal plane and creating an optical thin section through the specimen.

*Plan apochromatic lens* high numerical aperture objective lens, corrected for spherical aberration in the dark blue, blue, green and red, and for chromatic aberration and for flatness of field.

*Point spread function* a mathematical representation of the way a hypothetical point-like object (usually a fluorescent bead) is imaged by a given microscope system under defined settings (e.g. lens); the point spread function error accounts for the reduced resolution in the *Z* dimension observed in confocal microscopy.

*Region of interest (ROI)* a sub-area of an image selected for special treatment.

*Signal-to-noise ratio* ratio of the peak signal to the root mean square of the noise; the higher the ratio, the cleaner is the signal or image produced.

*Thresholding (segmentation, object recognition, discrimination)* the definition of what is an object in a digital image for the purpose of image analyses. Simply, pixels above a specified brightness are set to white and those below are set to black. Creating a binary image, with either white objects on a black background or black objects on a white background.

*Vignetting* shaded loss of the edges of an image or picture.

*Voxel* the smallest volume element in a digital 3D image. Each voxel is a hypothetical cube or cuboid with a defined length, depth, width and volume. The size is defined by the selected pixel resolution and the step size in the axial direction.

## REFERENCES

1. Minsky, M. (1988). Memoir on inventing the confocal microscope, *Scanning*, **10**, 128–138.
2. Göppert-Mayer, M. (1931). Über Elementarakte mit zwei Quantensprüngen, *Ann. Phys.*, **9**, 273–295.

3. Denk, W., Strickler, J. H. and Webb, W. W. (1990). Two-photon laser scanning fluorescence microscopy, *Science*, **248**, 73–76.
4. Lawrence, J. R., Korber, D. R., Hoyle, B. D., Costerton, J. W. and Caldwell, D. E., (1991). Optical sectioning of microbial biofilms, *J. Bacteriol.*, **173**, 6558–6567.
5. Vroom, J. M., Grauw, C. J., Gerritsen, H. C., Bradshaw, A. M., Marsh, P. D., Watson, G. K., Birmingham, J. J. and Allison, C. (1999). Depth penetration and detection of pH gradients in biofilms by two-photon excitation microscopy, *Appl. Environ. Microbiol.*, **65**, 3502–3511.
6. Neu, T. R., Kuhlicke, U. and Lawrence, J. R. (2002). Assessment of fluorochromes for two-photon laser scanning microscopy of biofilms, *Appl. Environ. Microbiol.*, **68**, 901–909.
7. Neu, T. R., Walczysko, P. and Lawrence, J. R. (2004). Two-photon imaging for studying the microbial ecology of biofilm systems, *Microbes Environ.*, **19**, 1–6.
8. Lawrence, J. R., Wolfaardt, G. M. and Korber, D. R. (1994). Monitoring diffusion in biofilm matrices using scanning confocal laser microscopy, *Appl. Environ. Microbiol.*, **60**, 1166–1173.
9. Wuertz, S., Mueller, E., Spaeth, R., Pfleiderer, P. and Flemming, H.-C. (2000). Detection of heavy metals in bacterial biofilms and microbial flocs with the fluorescent complexing agent Newport Green, *J. Ind. Microbiol. Biotechnol.*, **24**, 116–123.
10. Amann, R. I., Ludwig, W. and Schleifer, K.-H. (1995). Phylogenetic identification and *in situ* detection of individual microbial cells without cultivation, *Microbiol. Rev.*, **59**, 143–169.
11. Neu, T. R., Swerhone, G. D. W. and Lawrence, J. R. (2001). Assessment of lectin-binding analysis for *in situ* detection of glycoconjugates in biofilm systems, *Microbiology*, **147**, 299–313.
12. Neu, T. R. and Lawrence, J. R. (2002). Laser scanning microscopy in combination with fluorescence techniques for biofilm study. In *The Encyclopedia of Environmental Microbiology*, ed. Bitton, G. John Wiley & Sons, Inc., New York, pp. 1772–1788.
13. Poulsen, L. K., Ballard, G. and Stahl, D. A. (1993). Use of rRNA fluorescence *in situ* hybridization for measuring the activity of single cells in young and established biofilms, *Appl. Environ. Microbiol.*, **59**, 1354–1360.
14. Lawrence, J. R., Korber, D. R., Wolfaardt, G. M., Caldwell, D. E. and Neu, T. R. (2002). Analytical imaging and microscopy techniques. In *Manual of Environmental Microbiology*, 2nd edn, eds Hurst, C. J., Crawford, R. L., Knudsen, G. R., McInerney, M. and Stetzenbach, L. D. American Society for Microbiology Press, Washington, DC, pp. 39–61.
15. Lawrence, J. R. and Neu, T. R. (1999). Confocal laser scanning microscopy for analysis of microbial biofilms, *Methods Enzymol.*, **310**, 131–144.
16. Lawrence, J. R., Neu, T. R. and Swerhone, G. D. W. (1998). Application of multiple parameter imaging for the quantification of algal, bacterial and exopolymer components of microbial biofilms, *J. Microb. Methods*, **32**, 253–261.
17. Fatin-Rouge, N. and J. Buffle. (2007). Study of environmental systems by means of fluorescence correlation spectroscopy. In *Environmental Colloids: Behaviour, Structure and Characterization*, eds Wilkinson K. J. and Lead J. R. IUPAC Series on Analytical and Physical Chemistry of Environmental Systems, Vol. 10. John Wiley and Sons, Ltd, Chichester, Chapter 11.
18. Leppard, G. G. (1993). Organic flocs in surface waters: their native state and aggregation behavior in relation to contaminant dispersion. In *Particulate Matter and Aquatic Contaminants*, ed. Rao S. S. Lewis, Boca Raton, FL, pp. 169–195.
19. Leppard, G. G. (1992). Evaluation of electron microscope techniques for the description of aquatic colloids. In *Environmental Particles*, eds Buffle, J. and van Leeuwen, H. P. IUPAC Series on Analytical and Physical Chemistry of Environmental Systems, Vol. 1. Lewis, Boca Raton, FL, pp. 231–289.
20. Leppard, G. G., Burnison, B. K. and Buffle, J. (1990). Transmission electron microscopy of the natural organic matter of surface waters, *Anal. Chim. Acta*, **232**, 107–121.
21. Droppo, I. G., Flannigan, D. T., Leppard, G. G., Jaskot, C. and Liss, S. N. (1996). Floc stabilization for multiple microscopic techniques, *Appl. Environ. Microbiol.*, **62**, 3508–3515.
22. Mavrocordatos, D., Perret, D. and Leppard, G. G. (2007). Strategies and advances in the characterisation of environmental colloids by electron microscopy. In *Environmental Colloids:*

- Behaviour, Structure and Characterization*, eds Wilkinson, K. J. and Lead, J. R., IUPAC Series on Analytical and Physical Chemistry of Environmental Systems, Vol. 10. John Wiley & Sons, Ltd, Chichester, Chapter 8.
- 23. Neu, T. R. (2000). *In situ* cell and glycoconjugate distribution of river snow as studied by confocal laser scanning microscopy, *Aquat. Microb. Ecol.*, **21**, 85–95.
  - 24. Decho, A. W. and Kawaguchi, T. (1999). Confocal imaging of *in situ* natural microbial communities and their extracellular polymeric secretions using Nanoplast resin, *BioTechniques*, **27**, 1246–1252.
  - 25. Kawaguchi, T. and Decho, A. (2002). *In situ* microspatial imaging using two-photon and confocal laser scanning microscopy of bacteria and extracellular polymeric secretions (EPS) within marine stromatolites, *Mar. Biotechnol.*, **4**, 127–131.
  - 26. Perret, D., Leppard, G. G., Muller, M., Belzile, N., De Vitre, R. and Buffle, J. (1991) Electron microscopy of aquatic colloids: non-perturbing preparation of specimens in the field, *Water Res.*, **25**, 1333–1343.
  - 27. Rocheleau, S., Greer C. W., Lawrence, J. R., Cantin C., Laramee, L. and Guiot S. R. (1999). Differentiation of *Methanosaeta concilii* and *Methanosarcina barkeri* in anaerobic mesophilic granular sludge by fluorescent *in situ* hybridization and confocal scanning laser microscopy, *Appl. Environ. Microbiol.*, **65**, 2222–2229.
  - 28. Yu, F. P., Callis, G. M., Stewart, P. S., Griebel, T. and McFeters, G. A. (1994). Cryosectioning of biofilms for microscopic examination, *Biofouling*, **8**, 85–91.
  - 29. Massol-Deya, A., Whallon, J., Hickey, R. F. and Tiedje, J. (1995). Channel structures in aerobic biofilms of fixed film reactors treating contaminated groundwater, *Appl. Environ. Microbiol.*, **61**, 767–777.
  - 30. Christensen, B. B., Sternberg, C., Andersen, J. B., Eberl, L., Møller, S., Givskov, M. and Molin, S. (1999). Molecular tools for study of biofilm physiology, *Methods Enzymol.*, **310**, 20–42.
  - 31. Neu, T. R., Woelfl, S. and Lawrence, J. R. (2004). Three-dimensional differentiation of photo-autotrophic biofilm constituents by multi-channel laser scanning microscopy (single-photon and two-photon excitation), *J. Microbiol. Methods*, **56**, 161–172.
  - 32. Sytsma, J., Vroom, J. M., Grauw, C. J. and Gerritsen, H.-C. (1998). Time-gated fluorescence lifetime imaging and microvolume spectroscopy using two-photon excitation, *J. Microsc.*, **191**, 39–51.
  - 33. Bryers, J. D. (2001). Two-photon excitation microscopy for analyses of biofilm processes, *Methods Enzymol.*, **337**, 259–269.
  - 34. Caldwell, D. E., Korber, D. R. and Lawrence, J. R. (1992). Confocal laser microscopy and digital image analysis in microbial ecology, *Adv. Microb. Ecol.*, **12**, 1–67.
  - 35. Denk, W., Piston, D. W. and Webb, W. W. (1995). Two-photon molecular excitation in laser-scanning microscopy. In *Handbook of Biological Confocal Microscopy*, ed. Pawley, J. B. Plenum Press, New York, pp. 445–458.
  - 36. Lawrence, J. R., Swerhone, G. D. W., Leppard, G. G., Araki, T., Zhang, X., West, M. M. and Hitchcock, A. P. (2003). Scanning transmission x-ray, laser scanning, and transmission electron microscopy mapping of the exopolymeric matrix of microbial biofilms, *Appl. Environ. Microbiol.*, **69**, 5543–5554.
  - 37. Ulrich, S., Karrasch, B., Hoppe, H. G., Jeskulke, K. and Mehren, M. (1996). Toxic effects on bacterial metabolism of the redox dye 5-cyano-2,3-ditolyl tetrazolium chloride, *Appl. Environ. Microbiol.*, **62**, 4587–4593.
  - 38. Gerlich, D. and Ellenberg, J. (2003). 4D imaging to assay complex dynamics in live specimens. *Nat. Cell Biol., Suppl.*, **5**, S14–S19.
  - 39. Lawrence, J. R., Kwong, Y. T. J. and Swerhone, G. D. W. (1997). Colonization and weathering of natural sulfide mineral assemblages by *Thiobacillus ferrooxidans*, *Can. J. Microbiol.*, **43**, 68–78.
  - 40. Lawrence, J. R., Chenier, M. R., Roy, R., Beaumier, D., Fortin, N., Swerhone, G. D. W., Neu, T. R. and Greer C. W. (2004). Microscale and molecular assessment of the impacts of nickel, nutrients and oxygen level on structure and function of river biofilm communities, *Appl. Environ. Microbiol.*, **70**, 4326–4339.

41. Packroff, G., Lawrence, J. R. and Neu, T. R. (2002). *In situ* confocal laser scanning microscopy of protozoans in pure cultures and complex communities, *Acta Protozool.*, **41**, 245–253.
42. Shotton, D. M. (1989). Confocal scanning optical microscopy and its applications for biological specimens, *J. Cell Sci.*, **94**, 175–206.
43. Breeuwer, P., Drocourt, J.-L., Rombouts, F. M. and Abee T. (1996). A novel method for continuous determination of the intracellular pH in bacteria with the internally conjugated fluorescent probe 5- (and 6-)carboxyfluorescein succinimidyl ester, *Appl. Environ. Microbiol.*, **62**, 178–183.
44. Molenaar, D., Abee, T. and Konings, W. N. (1991). Continuous measurement of the cytoplasmic pH in *Lactococcus lactis* with a fluorescent pH indicator, *Biochim. Biophys. Acta*, **1115**, 75–83.
45. Siegumfeldt, H., Bjornrechinger, K. and Jakobsen, M. (2000). Dynamic changes of intracellular pH in individual lactic acid bacterium cells in response to a rapid drop in extracellular pH, *Appl. Environ. Microbiol.*, **66**, 2330–2335.
46. Axelrod, D., Koppel, D. E., Schlessinger, J., Elson, E. and Webb, W. W. (1976). Mobility measurements by analysis of fluorescence photobleaching recovery kinetics, *Biophys. J.*, **16**, 1055–1069.
47. Lippincott-Schwartz, J., Altan-Bonnet, N. and Patterson, G. H. (2003). Photobleaching and photoactivation: following protein dynamics in living cells, *Nat. Cell Biol., Suppl.*, **5**, S7–S14.
48. Wolfaardt, G. M., Lawrence, J. R., Robarts, R. D. and Caldwell, D. E. (1995). Bioaccumulation of the herbicide diclofop in extracellular polymers and its utilization by a biofilm community during starvation, *Appl. Environ. Microbiol.*, **61**, 152–158.
49. Booth, M. J. and Wilson, T. (2004). Low-cost, frequency-domain, fluorescence lifetime confocal microscopy, *J. Microsc.*, **214**, 36–42.
50. Clegg, R. M., Holub, O. and Gohlke, C. (2003). Fluorescence lifetime-resolved imaging: measuring lifetimes in an image, *Methods Enzymol.*, **360**, 509–542.
51. Gadella, T. W. J. Jr. (1999). Fluorescence lifetime imaging microscopy (FLIM): instrumentation and applications. In *Fluorescent and Luminescent Probes for Biological Activity*, ed. Mason, W. T. B. Academic Press, San Diego, CA, pp. 467–479.
52. Sanders, R., Draaijer, A., Gerritsen, H. C., Houpt, P. M. and Levine, Y. K. (1995). Quantitative pH imaging in cells using confocal fluorescence lifetime imaging microscopy, *Anal. Biochem.*, **227**, 302–308.
53. Lin, H.-J., Herman, P., Kang, J. S. and Lakowicz, J. R. (2001). Fluorescence lifetime characterization of novel low-pH probes, *Anal. Biochem.*, **294**, 118–125.
54. Guiot, E., Georges, P., Brun, A., Fontaine, M. P., Bellon-Fontaine, M.-N. and Briandet, R. (2002). Heterogeneity of diffusion inside microbial biofilms determined by fluorescence correlation spectroscopy under two photon excitation, *Photochem. Photobiol.*, **75**, 570–578.
55. Szmacinski, H. and Lakowicz, J. R. (1993). Optical measurements of pH using fluorescent lifetimes and phase-modulation fluorometry, *Anal. Chem.*, **65**, 1668–1674.
56. Jares-Erijman, E. A. and Jovin, T. M. (2003). FRET imaging, *Nat. Biotechnol.*, **21**, 1387–1395.
57. Clegg, R. M. (1996). Fluorescence resonance energy transfer (FRET). In *Fluorescence Imaging Spectroscopy and Microscopy*, eds Wang, X. F. and Herman, B. J. John Wiley & Sons, Inc., New York, pp. 179–252.
58. Centonze, V. E., Sun, M., Masuda, A., Gerritsen, H. C. and Herman, B. (2003). Fluorescence resonance energy transfer imaging microscopy, *Methods Enzymol.*, **360**, 542–560.
59. Derdowski, A. A., Ding, L. and Spearman, P. (2004). A novel fluorescence resonance energy transfer assay demonstrates that the human immunodeficiency virus type 1 Pr55<sup>Gag</sup> I domain mediates Gag–Gag interactions, *J. Virol.*, **78**, 1230–1242.
60. Kloepper, J. A., Mielke, R. E., Wong, M. S., Nealon, K. H., Stucky, G. and Nadeau, J. L. (2003). Quantum dots as strain- and metabolism-specific microbiological labels, *Appl. Environ. Microbiol.*, **69**, 4205–4213.
61. Neu, T. R. and Lawrence, J. R. (1997). Development and structure of microbial biofilms in river water studied by confocal laser scanning microscopy, *FEMS Microb. Ecol.*, **24**, 11–25.

62. Wolfaardt, G. M., Lawrence, J. R., Robarts, R. D. and Caldwell, D. E. (1998). *In situ* characterization of biofilm exopolymers involved in the accumulation of chlorinated organics, *Microbiol. Ecol.*, **35**, 213–223.
63. Paul, J. H. and Jeffrey, W. H. (1985). Evidence for separate adhesion mechanisms for hydrophilic and hydrophobic surfaces in *Vibrio proteolytica*, *Appl. Environ. Microbiol.*, **50**, 431–37.
64. Neu, T. R. and Marshall, K. C. (1991). Microbial ‘footprints’ – a new approach to adhesive polymers, *Biofouling*, **3**, 101–112.
65. Neu, T. R. and Lawrence, J. R. (1999). *In situ* characterization of extracellular polymeric substances (EPS) in biofilm systems. In *Microbial Extracellular Substances*., eds Wingender, J., Neu, T. R. and Flemming, H.-C. Springer, Berlin, pp. 21–48.
66. Böckelmann, U., Manz, W., Neu, T. R. and Szewzyk, U. (2002). A new combined technique of fluorescent *in situ* hybridization and lectin-binding-analysis (FISH–LBA) for the investigation of lotic microbial aggregates, *J. Microbiol. Methods*, **49**, 75–87.
67. De Beer, D., Stoodley, P. and Lewandowski, Z. (1997). Measurement of local diffusion coefficients in biofilms by microinjection and confocal microscopy, *Biotechnol. Bioeng.*, **53**, 151–8.
68. Nielsen, J. L., Mikkelsen, L. H. and Nielsen, P. H. (2000). *In situ* detection of cell surface hydrophobicity of probe-defined bacteria in activated sludge, *Water Sci. Technol.*, **43**, 97–103.
69. Lawrence, J. R., Kopf, G., Headley, J. V. and Neu, T. R. (2001). Sorption and metabolism of selected herbicides in river biofilm communities, *Can. J. Microbiol.*, **47**, 634–641.
70. Steward, G. F. and Azam, F. (1999). Bromodeoxyuridine as an alternative to H-thymidine for measuring bacterial productivity in aquatic samples, *Aquat. Microb. Ecol.*, **19**, 57–66.
71. Rodrigues, G. G., Phipps, D., Ishiguro, K. and Ridgway, H. F. (1992). Use of a fluorescent redox probe for direct visualization of actively respiring bacteria, *Appl. Environ. Microbiol.*, **58**, 1801–1808.
72. Choi, J.-W., Sherr, B. F. and Sherr, E. B. (1999). Dead or alive? A large fraction of ETS-inactive marine bacterioplankton cells, as assessed by reduction of CTC, can become ETS-active with incubation and substrate addition, *Aquat. Microb. Ecol.*, **18**, 105–115.
73. Lopez-Amoros, R., Comas, J. and Vives-Rego, J. (1995). Flow cytometric assessment of *Escherichia coli* and *Salmonella typhimurium* starvation–survival in seawater using rhodamine 123, propidium iodide and oxonol, *Appl. Environ. Microbiol.*, **61**, 2521–2526.
74. Muller, M., Loffhagen, N., Bley, T. and Babel, W. (1996). Membrane-potential-related fluorescence intensity indicates bacterial injury, *Microbiol. Res.*, **151**, 127–31.
75. Van Ommen Kloeke, F. and Geesey, G. G. (1999). Localization and identification of populations of phosphatase-active bacterial cells associated with activated sludge flocs, *Microb. Ecol.*, **38**, 201–214.
76. Davies, D. G., Chakrabarty, A. and Geesey G. G. (1993). Exopolysaccharide production in biofilms: substratum activation of alginic gene expression by *Pseudomonas aeruginosa*, *Appl. Environ. Microbiol.*, **59**, 1181–1186.
77. Davies, D. G. and Geesey G. G. (1995). Regulation of the alginic biosynthesis gene algC in *Pseudomonas aeruginosa* during biofilm development in continuous culture, *Appl. Environ. Microbiol.*, **61**, 860–87.
78. Errampali, D., Leung, K., Cassidy, M. B., Kostrzynska, M., Blears, M., Lee, H. and Trevors, J. T. (1999). Applications of the green fluorescent protein as a molecular marker in environmental microorganisms, *J. Microbiol. Meth.*, **35**, 187–199.
79. Møller, S., Sternberg, C., Andersen, J.-B., Christensen, B. B., Ramos, J. L., Givskov, M. and Molin, S. (1998). *In situ* gene expression in mixed-culture biofilms: evidence of metabolic interactions between community members, *Appl. Environ. Microbiol.*, **64**, 721–732.
80. Christensen, B. B., Haagensen, J. A. J., Heydorn, A. and Molin, S. (2002). Metabolic commensalism and competition in a two-species microbial consortium, *Appl. Environ. Microbiol.*, **68**, 2495–2502.
81. Hausner, M. and Wuertz, S. (1999). High rates of conjugation in bacterial biofilms as determined by quantitative *in situ* analysis, *Appl. Environ. Microbiol.*, **65**, 3710–3713.

82. Hodson, R. E., Dustman, W. A., Garg, R. P. and Moran M. A. (1995). *In situ* PCR for visualization of microscale distribution of specific genes and gene products in prokaryotic communities, *Appl. Environ. Microbiol.*, **61**, 4074–4082.
83. Gray, N. D., Howarth, R., Pickup, R. W., Jones, J. G. and Head, I. M. (2000). Use of combined microautoradiography and fluorescence *in situ* hybridization to determine carbon metabolism in mixed natural communities of uncultured bacteria from the genus *Achromatium*, *Appl. Environ. Microbiol.*, **66**, 4518–4522.
84. Lee, N., Nielsen, P. H., Andreasen, K. H., Juretschko, S., Nielsen, J. L., Schleifer, K. and Wagner, M. (1999). Combination of fluorescent *in situ* hybridisation and microautoradiography – a new tool for structure–function analyses in microbial ecology, *Appl. Environ. Microbiol.*, **65**, 1289–1297.
85. Nielsen, J. L., Juretschko, S., Wagner, M. and Nielsen, P. H. (2002). Abundance and phylogenetic affiliation of iron reducers in activated sludge as assessed by fluorescence *in situ* hybridization and microautoradiography, *Appl. Environ. Microbiol.*, **68**, 4629–4636.
86. Nielsen, J. L., Christensen, D., Kloppenborg, M. and Nielsen, P. H. (2003). Quantification of cell-specific substrate uptake by probe-defined bacteria under *in situ* conditions by microautoradiography and fluorescence *in situ* hybridization, *Environ. Microbiol.*, **5**, 202–211.
87. Ouvroney, C. C. and Fuhrman, J. A. (1999). Combined microautoradiography – 16sRNA probe technique for determination of radioisotope uptake by specific microbial cell types *in situ*, *Appl. Environ. Microbiol.*, **65**, 1746–1752.
88. Agard, D. A. (1984). Optical sectioning microscopy: cellular architecture in three dimensions, *Annu. Rev. Biophys. Bioeng.*, **13**, 191–219.
89. Gorby, G. L. (1994) Digital confocal microscopy allows measurements and three-dimensional multiple spectral reconstructions of *Neisseria gonorrhoea*/epithelial cell interactions in the human fallopian tube organ culture model, *J. Histochem. Cytochem.*, **42**, 297–306.
90. Manz, W., Arp, G., Schumann-Kindel, G., Szewzky, U. and Reitner J. (2000). Widefield deconvolution epifluorescence microscopy combined with fluorescence *in situ* hybridization reveals the spatial arrangement of bacteria in sponge tissue, *J. Microbiol. Methods*, **40**, 125–134.
91. Liu, J., Dazzo, F. B., Glagoleva, O., Yu, B. and Jain A. K (2001). CMEIAS: a computer-aided system for the image analysis of bacterial morphotypes in microbial communities, *Microb. Ecol.*, **41**, 173–194.
92. Heydorn, A., Nielsen, A. T., Hentzer, M., Sternberg, C., Givskov, M., Ersböll, B. K. and Molin, S. (2000). Quantification of biofilm structures by the novel computer program COMSTAT, *Microbiology*, **146**, 2395–2407.
93. Beyenal, H., Donovan, C., Lewandowski, Z. and Harkin, G. (2004). Three-dimensional biofilm structure quantification, *J. Microbiol. Methods*, **59**, 395–413.
94. Xavier, J. B., White, D. C. and Almeida, J. S. (2003). Automated biofilm morphology quantification from confocal laser scanning microscopy imaging, *Water Sci. Technol.*, **47**, 31–37.
95. Rodenacker, K., Hausner, M. and Gorbushina, A. A. (2003). Quantification and spatial relationship of microorganisms in sub-aquatic and subaerial biofilms. In *Fossil and Recent Biofilms*, eds Krumbein, W. E., Paterson, D. M. and Zavarzin, G. A. Kluwer, Dordrecht, pp. 387–399.
96. Bergner, S., Pohle, R., Al-Zubi, S., Toennies, K., Eitner, A. and Neu, T. R. (2002). Segmenting microorganisms in multi-modal volumetric datasets using a modified watershed transform. In *Lecture Notes in Computer Science*, ed. Van Gool, L., Springer, Heidelberg, pp. 429–437.
97. Staudt, C., Horn, H., Hempel, D. C. and Neu, T. R. (2004). Volumetric measurements of bacterial cells and extracellular polymeric substance glycoconjugates in biofilms, *Biotechnol. Bioeng.*, **88**, 585–592.
98. Bloem, J., Veninga, M. and Shepherd, J. (1995). Fully automatic determination of soil bacterium numbers, cell volumes and frequency of dividing cells by confocal laser scanning microscopy and image analysis, *Appl. Environ. Microbiol.*, **61**, 926–936.
99. Rodenacker, K., Hausner, M., Kühn, M., Wuertz, S. and Purkayastha, S. (2001). Depth intensity correction of biofilm volume data from confocal laser scanning microscopes, In *Proceedings of 8th ECS and Image Analysis*, Bordeaux, pp. 556–560.

100. Yang, X., Beyenal, H., Harkin, G. and Lewandowski, Z. (2001). Evaluation of biofilm image thresholding methods, *Water Res.*, **35**, 1149–1158.
101. Yang, X., Beyenal, H., Harkin, G. and Lewandowski, Z. (2000). Quantifying biofilm structure using image analysis, *J. Microbiol. Methods*, **39**, 109–119.
102. Xavier, J. B., Schnell, A., Wuertz, S., Palmer, R., White, D. C. and Almeida, J. S. 2001. Objective threshold selection procedure (OTS) for segmentation of scanning laser confocal microscope images, *J. Microbiol. Methods*, **47**, 169–180.



---

# 11 Study of Environmental Systems by Means of Fluorescence Correlation Spectroscopy

---

**NICOLAS FATIN-ROUGE**

*Laboratoire de Chimie des Matériaux et Interfaces, 16 route de Gray, F-25030 Besançon cedex, France*

**JACQUES BUFFLE**

*Analytical and Biophysical Environmental Chemistry (CABE), Department of Inorganic, Analytical and Applied Chemistry, University of Geneva, 30 quai Ernest Ansermet, CH-1211 Geneva 4, Switzerland*

1	Introduction . . . . .	508
2	Basic Description of FCS . . . . .	510
2.1	Principle of the Technique . . . . .	510
2.2	Basic Applications of FCS . . . . .	513
2.2.1	Shape Factors, Size and Conformational Changes . . . . .	514
2.2.2	Molecular Interactions and Aggregation . . . . .	514
2.2.3	Spatial Resolution and Diffusion in Heterogeneous Environments . . . . .	516
2.3	Advantages and Limitations for Applications to Environmental Systems . . . . .	516
3	Non-perturbing Labelling of Environmental Colloids and Polymers . . . . .	518
3.1	Labelling Strategies . . . . .	518
3.1.1	Applications to Complex Environmental Samples . . . . .	519
3.1.2	Single-Versus Multi-labelling per Compound . . . . .	519
3.2	Conditions for Labelling by Adsorption of Fluorophore . . . . .	520
3.3	Conditions for the Covalent Labelling of Fluorophores . . . . .	521
3.3.1	Chemical Conditions for Covalent Labelling . . . . .	521
3.3.2	Major Artefacts . . . . .	523
3.4	Choice of the Dye: Spectroscopic Properties . . . . .	525
3.4.1	Photophysical Properties . . . . .	525
3.4.2	Quenching . . . . .	525
3.5	Specific Examples . . . . .	526
4	Applications of FCS to the Study of Properties of Environmental Macromolecules . . . . .	528
4.1	Humic Substances (HS) . . . . .	528
4.2	High Molecular Weight Polysaccharides . . . . .	532

5	Study of Colloid and Macromolecule Aggregation by FCS . . . . .	533
5.1	Aggregation of Small Colloids and Comparatively Large Biopolymers . . . . .	533
5.2	Disaggregation of Humic Substances . . . . .	534
6	Applications of FCS to the Study of Reaction/Transport in Gels . . . . .	537
6.1	Reaction/Diffusion of Organic and Inorganic Ions in Porous Media: Role of Electrostatic Effects and Specific Binding . . . . .	537
6.2	Diffusion of Colloids and Macromolecules Within Gels . . . . .	540
7	Summary and Perspectives . . . . .	544
	Acknowledgements . . . . .	545
	List of Symbols and Abbreviations . . . . .	545
	References . . . . .	547

## 1 INTRODUCTION

The key role of submicron colloids and biopolymers in the transport of trace metals and organic pollutants in waters and soils is now well documented [1–4] (see also Chapter 1). Through covalent, electrostatic or hydrophobic interactions [5,6] (see also Chapter 1), a large proportion (often 40–90%) of trace compounds may be adsorbed on aquatic colloids [7,8]. Subsequently, the associated trace compounds can be transported over long distances on stable colloids, or quickly settle down on flocculating colloids and biopolymers. In addition, the structure and function of natural porous media such as biofilms, soils and sediments largely result from the characteristics and interactions of natural organic or inorganic colloids and microorganisms. A clear understanding of the physicochemical properties of the major groups of colloids is therefore essential to make predictions on pollutant circulation and impact on aquatic and terrestrial ecosystems, and also to optimise water treatment or soil remediation processes.

A large number of sophisticated and sensitive techniques have been developed to determine the *chemical* composition of inorganic colloids [*e.g.* atomic absorption spectrometry (AAS), X-ray fluorescence, inductively coupled plasma mass spectrometry (ICP-MS), laser-induced breakdown detection (LIBD) (see Chapter 12)] and organic biopolymers [high-performance liquid chromatography (HPLC), mass spectrometry, matrix-assisted laser desorption/ionisation mass spectrometry (MALDI)]. On the other hand, the number of sophisticated tools to study *supramolecular physical* properties such as the size, conformation or fractal dimensions of the submicron colloids, large biopolymers or their aggregates is limited. In particular, static and dynamic light scattering is usually not selective or sensitive enough for the measurement of environmentally relevant concentrations of the submicron colloids and polymers in natural systems [9,10], even though improvements have been made in the last decade. Microscopic techniques such as transmission electron microscopy and atomic force microscopy are informative but require significant skill and time in order to obtain representative results [11,12]. In that respect, fluorescence correlation spectroscopy (FCS) offers significant potential advantages for environmental systems (see Section 2.3 for a detailed discussion), in particular for the study of very

small colloids and polymers at very low concentrations, including their behaviour in gels or other porous media. Until recently, FCS was mainly applied to biochemical and pharmaceutical systems, and only rarely to environmental systems [13]. This chapter will focus on aspects which are particularly relevant for and/or specific to environmental systems, i.e. very low concentrations of colloids and biopolymers, a large size polydispersity, chemical heterogeneity of colloids and polymers, a strong tendency to aggregate and the importance of diffusion/reaction in porous media.

The nature of natural colloids and polymers is described in more detail in Chapter 2 and only a very brief overview of the major groups of colloids is given here. In the rest of this chapter, the word *colloid* will be used for any organic or inorganic entity large enough to have supramolecular structure and properties (*e.g.* possibility of modification of the conformation or surface properties) but small enough so as not to sediment quickly (hours–days) in the absence of aggregation. Colloids are thus typically in the size range 1 nm–1 µm. Most organic and inorganic colloids are negatively charged [5,14]. The major aquatic and terrestrial colloids include the following components [15] (see also Chapter 2):

- *The inorganic colloids* in freshwaters and soils consist primarily of aluminosilicates (clays), silica and iron oxyhydroxides. Aluminosilicates are angular sheet-like particles, whereas iron oxyhydroxides and silica colloids are often near spherical, although silica can also be found as irregularly shaped diatom debris. Calcium carbonate is also present in aquatic systems but is generally found in the larger size fraction. Therefore, as a first approximation, the inorganic colloids, despite their variable shapes, can be treated as compact entities with a negative surface charge [15]. Two important characteristics of inorganic colloids are (i) their irregular shape and physico-chemical heterogeneity and (ii) their large size distribution that follows a Pareto power law distribution [16,17] over 2–4 orders of magnitude in water, sediments and soils.
- *The polysaccharides and peptidoglycans* are high molecular weight ( $10^4$ – $10^6$  Da) refractory biopolymers that are released from the cell walls of plankton [14,15]. They are generally neutral or slightly negatively charged due to carboxylate groups. They often form structurally rigid fibrils, due to their association into double or triple helices stabilised by hydrogen or calcium bridges [18]. In many cases, the total length of the fibrils may be 1 µm or greater whereas their thickness is not more than a few nanometres [15]. These rigid biopolymers may represent 10–30% of surface water natural organic matter (NOM) [14]. More flexible large biopolymers, such as the alginates in sea water, might also be important but their role is currently poorly known.
- The last major group of aquatic colloids includes *the humic substances (HS)*, which originate from the degradation of higher plants and microorganisms, followed by their recombination into chemically heterogeneous small polymers (molar mass typically in the range 500–5000 Da). These compounds may be distinguished into two main groups [14,15]: (i) those produced by the degradation of plankton in the water column, which are largely aliphatic with a lower charge density ( $-2$  to  $-5$  meq g $^{-1}$ ), and (ii) the soil-derived fulvics which are largely aromatic, have a high proportion of carboxylic and phenolic groups and a higher charge density ( $-6$  to  $-11$  meq g $^{-1}$ ). The soil-derived fulvics are ubiquitous in surface freshwaters, where they often represent 40–80% of NOM. They are the most studied of the aquatic NOM, generally resembling 1–3 nm small spheres (see Figures 5 and 6; Section 4). Furthermore, they are

highly hydrated and can self-aggregate due to the presence of hydrophobic moieties (Section 5.2). Due to their aromatic structure, they are naturally fluorescent, which allows for their direct study by FCS, without the need for labelling (Section 4).

## 2 BASIC DESCRIPTION OF FCS

### 2.1 PRINCIPLE OF THE TECHNIQUE

Like other fluorescence based-techniques, FCS allows the detection of solutes at very dilute concentrations ( $10^{-8}$ – $10^{-15}$  mol dm $^{-3}$ ). The use of confocal optics allows the measurements to be made in a very small, well-defined volume (the confocal volume,  $\sim 10^{-15}$  dm $^3$ ) such that single molecules can be detected. The basis of FCS is presented in Figure 1. In practice, FCS measures both the absolute value of fluorescence intensity and the intensity of fluctuations emitted in the confocal volume (Figures 1a and b [19]), i.e. the original fluorescence intensity is correlated at different delay times. Under the

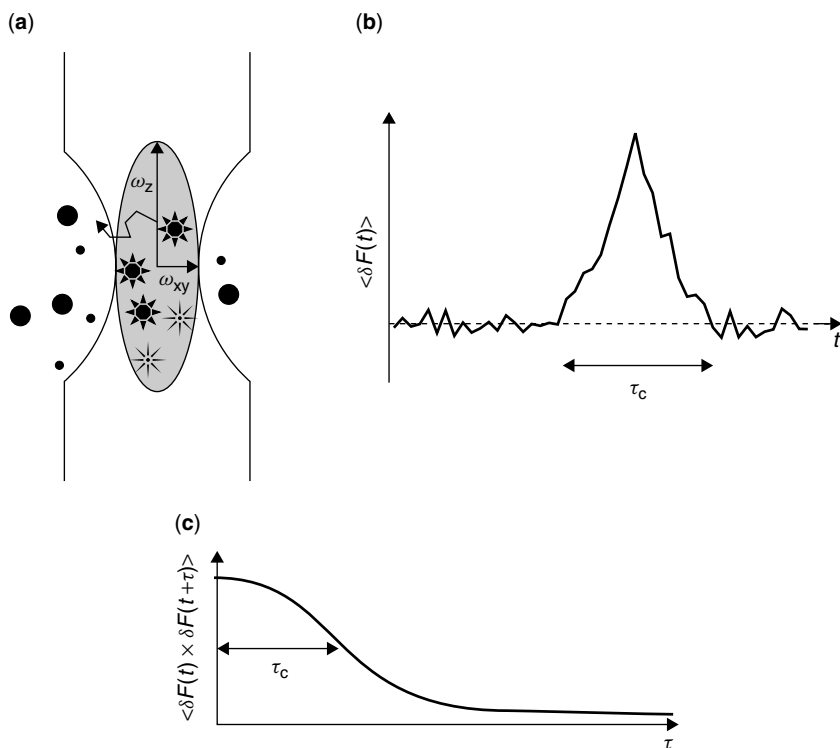


**Figure 1.** (a) Emitted light from two different kinds of mobile fluorescent particles (represented by small and large dots) is collected from the illuminated confocal volume. (b) Fluctuations of intensity  $\delta F$  are inversely proportional to the number of fluorescent particles (assuming they have the same brightness) within the confocal volume. Correlation of intensity vs time gives the autocorrelation as a function of delay time ( $\tau$ ) and then the dynamic parameters of the emitting dye.  $\tau_c$  represents a correlation time which is the time that the particle spends within the confocal volume. (c) ACF obtained from equations (1) and (2)

conditions of non-interacting species, for sample absorbance  $<0.05$ , and provided there is no fluorescence saturation due to an elevated excitation power, the fluorescence intensity will be proportional to, and allow the measurement of, the number or concentration of fluorescent molecules in the confocal volume, i.e. in a volume of *ca.*  $1 \mu\text{m}^3$ . When the detection is coupled to high-resolution motors, the mapping of fluorescent compounds can be realised at  $1 \mu\text{m}$  resolution or less, in non-homogeneous media. Intensity fluctuations result from input/output of fluorophores in/from the confocal volume and from physicochemical processes that affect the fluorescent molecules (time-scales from  $10^{-7}$  to  $>10^2$  s). When the frequency and intensity of fluctuations are recorded versus time, an autocorrelation function (ACF) can be computed (Figure 1c), which is related to the dynamic parameters of the system as expressed by the fluctuation–dissipation theorem. Optimal autocorrelation measurements occur for about five solutes [20] in the confocal volume at any given time so that the contribution of each is substantial, yielding a good signal-to-noise ratio. Local average concentrations, mobility coefficients (diffusion, convection), binding and rate constants of fluorescent molecules involved in chemical reactions or photochemical processes may be extracted from the ACF.

The first FCS instrument was built in the 1970s [21], but recent technological developments using, in particular, confocal optics [22] and lasers have greatly improved its efficiency. Until now, most of the systems were based on single-photon excitation (Figure 2). An excitation beam provided by a stable laser source is collimated into a confocal microscope objective and focused into a sample cell via an excitation filter and a dichroic mirror. The role of the dichroic mirror is to reflect selectively the exciting light to the sample cell while allowing the passage of emitted light. The emission filter (Figure 2) is needed to reduce Rayleigh and Raman scattering of the solvent, which is the major source of noise. A high numerical aperture immersion (water) objective is used to focus the laser beam into the sample cell. All light emitted outside the confocal volume is blocked by the pinhole in the image plane. The pinhole serves as the detection aperture and provides

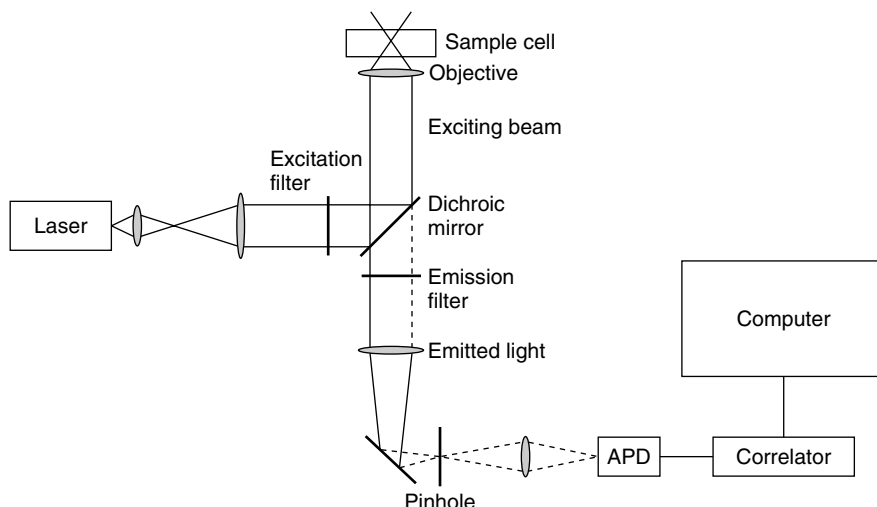


**Figure 2.** Schematic diagram of a one-photon FCS set-up

the axial resolution. The light passing the pinhole is then measured by an avalanche photodiode (APD) before being analysed with a sub-microsecond time resolution correlator. In an alternative set-up, excitation is produced by the absorption of two photons, each having half the absorption energy [23]. The probability of such an excitation is fairly low and high-power laser sources are needed. The two-photon excitation systems have advantages and limitations when damage to biological samples is concerned: they use larger excitation wavelengths but higher power lasers. They do not require a pinhole to collect the light selectively from the confocal volume. Photobleaching is also minimised in the two-photon excitation mode, because the energy required for dye excitation is present only at the cross-point of the two laser sources, whereas with one-photon excitation, all the dyes residing in the illuminated volume are excited and possibly bleached out. Further developments of FCS have led to cross-correlation techniques [24]. Here, two interacting species are labelled separately with different dyes and each is selectively excited with two laser beams of different wavelengths. Information is thus obtained on their interactions.

The normalised autocorrelation function,  $G(\tau)$ , is obtained as follows (Figure 1b and c) [25]:

$$G(\tau) = \frac{\langle \delta F(t) \times \delta F(t + \tau) \rangle}{\langle F(t) \rangle^2} \quad (1)$$

where  $t$  is the acquisition time,  $\tau$  is the delay time,  $F(t)$  is the fluorescence intensity at time  $t$  and the temporal fluctuation intensity  $\delta F(t)$  is defined as

$$\delta F(t) = F(t) - \langle F(t) \rangle \quad (2)$$

where  $\langle \cdot \rangle$  refers to average values. Physically,  $G(\tau)$  corresponds to the probability of detecting, on average, a photon at a delay shift,  $\tau$ , when a photon is detected at zero time.

The ACF contains dynamic information about the fluorescent species, in particular the diffusion coefficient, chemical and photophysical rate constants and the equilibrium concentration and molecular brightness. The temporal intensity fluctuation,  $\delta F(t)$ , is proportional to the temporal fluctuation of the number,  $N$ , of fluorescent molecules in the confocal volume, assuming they have the same brightness. The zero-time autocorrelation function value,  $G(0)$ , for a homogeneous dye solution is [26]

$$G(0) = 1/\langle N \rangle \quad (3)$$

$G(\tau)$  depends on the confocal volume profile  $O(r, z)$ , which describes the spatial distribution of emitted light in cylindrical coordinates. Its rigorous determination is not possible and it is usually approximated by a 3D Gaussian function decaying to  $1/e^2$  at  $r = \omega_{xy}$  in the transverse direction and  $z = \omega_z$  in the longitudinal direction [27]:

$$O(r, z) \approx \exp \left[ -2 \left( \frac{r^2}{\omega_{xy}^2} + \frac{z^2}{\omega_z^2} \right) \right] \quad (4)$$

The above approximation holds for the two-photon excitation mode. For a one-photon excitation mode, it is essential to use a small pinhole and an under-filled objective back-aperture in order to avoid experimental artefacts [28]. Under these conditions, at low

fluorescence intensity and for a single fluorescent species,  $G(\tau)$  is given by [29]

$$G(\tau) = \frac{1}{N} \left(1 + \frac{\tau}{\tau_c}\right)^{-1} \left(1 + \frac{\tau}{p^2 \tau_c}\right)^{-0.5} \quad (5)$$

where  $p$  is the ratio between longitudinal and transverse radius of the confocal volume (see Figure 1,  $p = \omega_z/\omega_{xy}$ ) and  $\tau_c$  is the diffusion time of the fluorescent species in the confocal volume. In a fully isotropic micro-environment within and around the confocal volume, and for a particle radius smaller than  $\omega_{xy}/10$ , the diffusion coefficient of a particle can be estimated by

$$\omega_{xy}^2 = 4D\tau_c \quad (6)$$

Values of  $p$ ,  $\omega_{xy}$  and  $\omega_z$  are obtained by calibration with a dye such as Rhodamine 6G (R6G), which has a well-known diffusion coefficient,  $(2.8 \pm 0.7) \times 10^{-10} \text{ m}^2 \text{ s}^{-1}$  for R6G in water at  $25^\circ\text{C}$  [21]. The value of  $p$  should lie between 5 and 10, depending on the optics, with a value of  $\omega_{xy}$  of about 250 nm. Based on equation (4), the confocal volume can be estimated by [30]

$$V_{\text{conf}} = \pi^{\frac{3}{2}} \omega_{xy}^2 \omega_z \quad (7)$$

Using equation (3), the average concentration of fluorescent particles in the confocal volume:

$$\langle C \rangle = [V_{\text{conf}} G(0)]^{-1} \quad (8)$$

can be easily determined from the calibration parameters and  $G(0)$ .

Phosphorescence must also be considered when interpreting FCS–ACF curves. As for fluorescence, phosphorescence is a radiative process of deactivation. Because it is forbidden in quantum mechanics, it usually occurs on much longer time-scales than fluorescence. The corresponding excited molecule is no longer light absorbing and it appears as non-emitting on the fluorescence time-scale. The ACF contains an additional exponential factor [31]:

$$G(\tau) = \frac{1}{N} \frac{1 - F_T + F_T \times \exp(-\tau/\tau_T)}{1 - F_T} \left(1 + \frac{\tau}{\tau_c}\right)^{-1} \left(1 + \frac{\tau}{p^2 \tau_c}\right)^{-0.5} \quad (9)$$

where  $F_T$  is the triplet fraction and  $\tau_T$  is the triplet lifetime.

Other mathematical expressions of the ACF are reported elsewhere for cases of active transport and free 2D diffusion on membrane surfaces [27]. An analysis of the ACF for a single fluorescent species is showed in Figure 3.

## 2.2 BASIC APPLICATIONS OF FCS

Once the apparatus has been calibrated, one can measure the diffusion times of fluorescent particles. Diffusion coefficients,  $D$ , are subsequently calculated using equation (6).  $D$  is related to the shape-dependent friction coefficient,  $f$ , of the particle through the Stokes–Einstein relationship:

$$f = \frac{k_B T}{D} \quad (10)$$

where  $k_B$  is the Boltzmann constant and  $T$  is the absolute temperature.

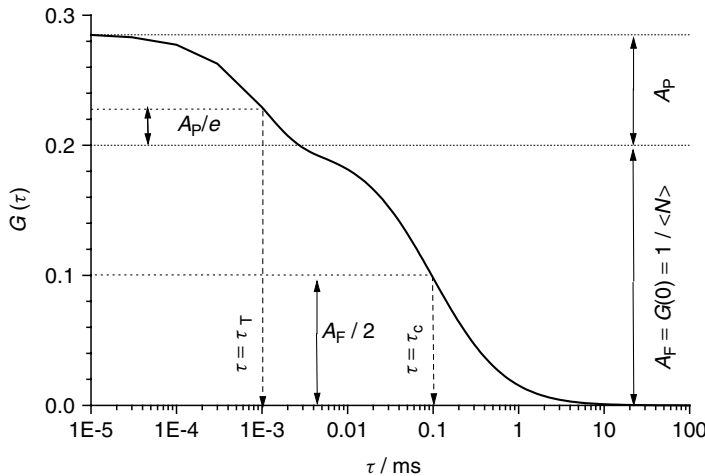


**Figure 3.** Analysis of a typical FCS–ACF for a single fluorescent species.  $A_F$ , amplitude of fluorescence;  $A_P$ , amplitude of phosphorescence. The triplet fraction  $F_T = A_P/A_F$

Assuming a spherical-shaped particle of hydrodynamic radius  $R_h$ , the friction coefficient is given by

$$f_{sp} = 6\pi\eta R_h \quad (11)$$

where  $\eta$  is the solution viscosity. Relations (10) and (11) allow the estimation of the hydrodynamic radii of a globular particle.

### 2.2.1 Shape Factors, Size and Conformational Changes

The friction and diffusion coefficients of a particle depend on its shape [32–35]. For shapes other than spheres,  $f$  is obtained by multiplying  $f_{sp}$  by a shape factor,  $S_F$ , which has been calculated for several morphologies (Table 1) [36–38]. FCS has been used, for example, as a complementary tool to AFM, to investigate the diffusivity and size of different natural polysaccharides [39,40]. At high dilution and constant viscosity, the solute's diffusion coefficient may be affected by conformational changes, especially for flexible and ionic polymers. FCS offers a means to follow the equilibrium and dynamic properties of large molecular reorganisations of biopolymers [41] and model molecules [42] at the individual scale. Such studies are more efficiently performed in combination with AFM and/or computational chemistry. FCS is poorly sensitive to small conformational changes for which competitive macroscopic techniques are available, *e.g.* fluorescence anisotropy (for small reorganisations) or intramolecular luminescent resonant energy transfer (LRET), for which the resolution is better than 1 nm for sizes ranging from 1 to 10 nm).

### 2.2.2 Molecular Interactions and Aggregation

Molecular interactions may be investigated by different means in FCS. In classical FCS, a substantial change is required, either in the molar mass,  $M$ , (by at least a factor of 4) or in brightness of the labelled species, to discriminate unambiguously between two

**Table 1.** Mathematical expression of shape factor for some geometries

Prolate ellipsoid with major radius  $a$  and minor radius  $b$ :

$$S_F = \frac{\sqrt{1 - b^2/a^2}}{(b/a)^{\frac{2}{3}} \ln \left[ \left( 1 + \sqrt{1 - b^2/a^2} \right) / (b/a) \right]}$$

Oblate ellipsoid with major radius  $a$  and minor radius  $b$ :

$$S_F = \frac{\sqrt{a^2/b^2 - 1}}{(a/b)^{\frac{2}{3}} \arctan \left( \sqrt{a^2/b^2 - 1} \right)}$$

Cylinder of length  $l$  and radius  $a$ :

$$S_F = \frac{(1/2a)^{\frac{2}{3}}}{\left(\frac{3}{2}\right)^{\frac{1}{3}} [2 \ln(1/a) - 0.11]}$$

diffusing compounds. In homogeneous media, assuming that the densities of all organic compounds are similar, it is possible to estimate  $M$  of a spherical polymer diffusing with a diffusion coefficient  $D$  by the following relationship:

$$D \sim \frac{k_B T}{18\eta} \left( \frac{6^2 N_A d}{\pi^2 M} \right)^{\frac{1}{3}} \quad (12)$$

where  $N_A$  is Avogadro's constant,  $d$  the density of the substance and  $\eta$  the viscosity of the solution.

Variations in the diffusion times of a small dye, when bound to increasing concentrations of a polymeric compound, are shown in Figure 4 [43]. If the brightnesses of the free and bound dye are identical, the global ACF is simply expressed as the sum of ACFs for each pure species balanced by their fraction. Aggregation processes can also be followed: for example, disaggregation rates of the naturally fluorescent humic acids have been investigated as a function of time, pH, ionic strength ( $I$ ) and concentration [44]. In contrast to classical FCS, cross-correlation is more sensitive to molecular interactions. Using this technique, it is possible to follow a lysis reaction by determining the fractions of intact and lysed molecules as a function of time [45]. Here, the most important parameter is the cross-correlation amplitude, which is related to the concentration of doubly labelled molecules. Thus, the cross-correlation amplitude focuses on the occurrence of coincident fluctuations induced by concerted motions.

Very bright species could dominate the autocorrelation decay, even when they are few in number. In order to minimise the brightness differences between free and associated particles, it is important to label only a small fraction of interacting species since in a mixture the relative contribution of each species is proportional to the square of its brightness (see Section 3.1). Brightness enhancement of labelled particles due to aggregation effects implies performing a brightness distribution analysis for which the recent method of photon counting histogram analysis [46] is the most adapted. Based on photon counting statistics, even molecules with the same diffusion times can be distinguished as long as their individual fluorescence intensities differ.

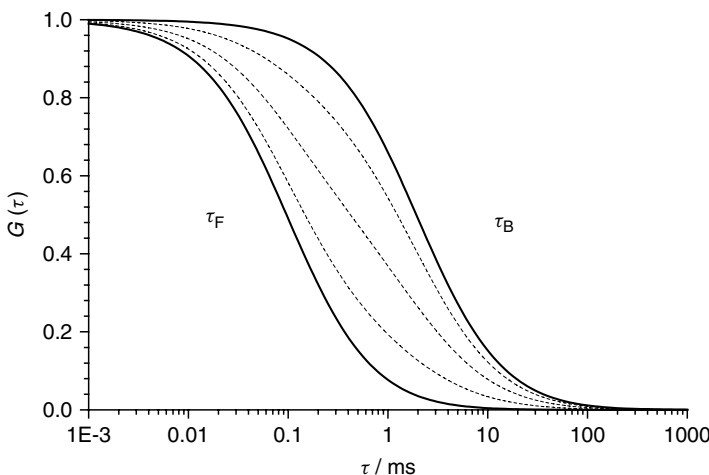


**Figure 4.** Normalised ACF from a typical FCS titration experiment with a small substrate by a large host. The diffusion time of the small labelled substrate increases upon binding, from  $\tau_F$  to  $\tau_B$ . In extreme cases (large binding constants and large difference in  $M$ ), two distinct sigmoidal curves are observed, for intermediate proportions of bound substrate

### 2.2.3 Spatial Resolution and Diffusion in Heterogeneous Environments

Due to its sub-micrometre resolution, FCS is a powerful technique to probe particle mobility in different micro-environments as long as the sample is optically translucent. Associated with a piezo-table, FCS can offer now a nanometric resolution (down to about 50 nm [47]) to probe interfaces such as bacterial films and cells. Heterogeneous media such as gels may also be investigated by classical FCS when 1  $\mu\text{m}$  resolution is sufficient (see Section 6). Hence, FCS provides the ability to probe local interactions, density, heterogeneity and connectivity in porous material.

## 2.3 ADVANTAGES AND LIMITATIONS FOR APPLICATIONS TO ENVIRONMENTAL SYSTEMS

A major advantage of FCS is the combination of a very high sensitivity (sub-nanomolar concentrations), high spatial resolution (micrometre scale or even below) with mapping capabilities and its non-destructive characteristics. Therefore, it can offer a wealth of information about heterogeneous environmental samples and more detailed information than global techniques. Another major feature of FCS for environmental applications is that it can provide not only equilibrium chemical information, but also data on dynamic physicochemical processes, i.e. information related to the structure–function relationships of a heterogeneous medium. Only very few techniques have such capabilities.

The high sensitivity of FCS allows the investigation of aquatic natural systems under realistic conditions. This holds especially for aquatic colloids, which due to their small particle size (down to nm) and concentration ( $<1 \text{ mg dm}^{-3}$  [10]), cannot be analysed easily using light scattering techniques (static and dynamic light scattering = PCS). In particular, the low- $M$  compounds such as fulvic acids are nearly impossible to detect by PCS, but are easily studied by FCS, especially since they are naturally fluorescent [48]

in the near-UV region. Fluorescent amino acids such as tyrosine and tryptophan should also be efficiently detected.

The sub-micrometre spatial resolution of FCS offers the possibility of investigating natural systems such as biofilms and biological or environmental interfaces, provided that the material is translucent. Media and interfaces can be probed with a resolution of  $\sim 80$  nm. The ability to probe inside a particular phase without penetration of a physical sensor will guarantee a minimum of artefacts. Hence, long-range interactions, organisation, transport processes, *etc.*, can be locally investigated (see Section 6). For comparison, the technique of fluorescence recovery after photobleaching (FRAP) [49] requires much higher fluorophore concentrations than FCS and uses a high-power laser source to bleach the dyes. This procedure may stress living organisms and/or the processes under study due to local warming or unwanted photoreactions. In addition, the temporal resolution of FRAP is limited to the millisecond-time scale, whereas time-scales of  $0.1\text{--}1\ \mu\text{s}$  can be reached with FCS. Nonetheless, FRAP has been used to study the diffusion of dextran, DNA, proteins and latex beads in agarose gels [50]. For more discussion about advantages and disadvantages of FCS over other techniques in gels, see Section 6.2.

The high sensitivity of FCS may lead to experimental difficulties. Indeed, at the very low concentrations of fluorophores used, their adsorption on cell walls may significantly affect the results, due to the loss of an important fraction of fluorophore. This effect, however, can usually be minimised by using carefully selected conditions.

A more important difficulty is the need to label the studied compound specifically, uniformly and under appropriate conditions (see Section 3.1), since most natural colloids and molecules are non-fluorescent when excited with a wavelength between the near-UV and near-IR regions. This may be a major task, especially for environmental colloids, which are often very dilute, chemically heterogeneous and without a single specific reactive site to attach the dye. Moreover, some natural materials, in particular iron oxyhydroxides, are efficient quenchers. In such cases, specific strategies must be found to allow efficient tagging, that do not perturb the composition and conformation of the compound being studied. Labelling is discussed in Section 3.

Classical FCS theory has generally been developed for particles smaller than  $\omega_{xy}/10$ .  $\omega_{xy}$  is usually a fraction of a micrometre, so that for particles  $>50$  nm, interpretation of data cannot be based on this simple theory. For larger particles, with radii up to  $2\omega_{xy}$ , it has been shown both theoretically and experimentally [51,52] that a correction of the mathematical expression of the autocorrelation function can be applied in order to obtain a correct value of the diffusion coefficient from the experimental ACF. The expressions of the ACF at zero time,  $G(0)$ , and of the diffusion time are given by the equations

$$G_R(0) = G_0(0)/(1 + R_h^2/\omega_{xy}^2) \quad (13a)$$

$$\tau_R = \tau_O(\omega_{xy}^2 + R_h^2)/4D \quad (13b)$$

where the subscripts R and O refer to particles with either an infinitely small (O) or a finite (R) hydrodynamic radius  $R_h$ , respectively. Diffusion properties of particles larger than  $2\omega_{xy}$  cannot be determined by FCS.

A major characteristic of environmental compounds is their size polydispersity. The mathematical function of an FCS-ACF is not simple and rigorous interpretation of polydispersity is not straightforward, although major advances have recently been made to

overcome this problem [53,54]. The simplest case is that of a discrete system containing particles of a few different sizes, with each component having identical quantum yields. In such cases, they may be discriminated from each other when their diffusion times differ by a factor of 1.6 [55].

The size distribution of environmental compounds, however, is usually broad and includes an infinite number of different sizes. In such a case, an average size can be given by any physicochemical technique sensitive to particle size; however, each of the techniques provides a different average value depending on its operating principle (Chapter 1). For example, dynamic light scattering (DLS) provides *z*-average diffusion coefficients, static light scattering (SLS) provides weight-average  $M$  and membrane osmometry provides number-average  $M$ . The combination of these values can be used to determine the sample polydispersity [56]. Thompson [57] has pointed out that a weight-average  $M$  can be calculated from the zero-time FCS autocorrelation function. However, this is only valid when the fluorescence yield of each detected molecule is proportional to its  $M$ . This is likely to be the case when the environmental colloids are labelled by attaching dyes to 'non-specific' reactive groups of the colloids (*e.g.*  $\equiv M-OH$  surface groups of metal oxyhydroxides, alcohol groups of polysaccharides). If the fluorophore is attached to a site that is unique in the macromolecule (*e.g.* terminal aldehydic group in polysaccharide or SH group in proteins), the fluorescence will be independent of  $M$ , and for polydisperse samples, a number-average  $M$  is obtained. In an unknown sample, the forced fitting of the ACF with an average diffusion time is therefore not recommended because the average value of  $\tau$  thus obtained is ill-defined. Furthermore, the method of cumulants proposed for PCS [58] is not applicable to FCS because of the strong non-linearity of the FCS autocorrelation function, even for monodisperse samples. To interpret FCS data of polydisperse samples, the best approach is the determination of the full size distribution by the method of histograms [53], for which the FCS diffusion time-scale is divided into a finite number of intervals. The corresponding fraction of fluorescent particles in each interval (represented by a bar height) is then calculated by varying all these fractions in order to minimise the differences between the calculated and experimental ACF. For such an approach to converge successfully, a number of conditions should be fulfilled [13]. A detailed example of the application of this approach to the measurement of polydispersity of fulvic acids and a comparison between different techniques have been given [59].

### 3 NON-PERTURBING LABELLING OF ENVIRONMENTAL COLLOIDS AND POLYMERS

#### 3.1 LABELLING STRATEGIES

Apart from a very few compounds, such as humic substances (HS), which are naturally fluorescent [60], most environmental compounds, including polysaccharides, peptides, proteins and inorganic colloids, need to be fluorescently labelled in order to be investigated by FCS. As will be discussed below, two types of chemical reactions can be used for labelling a particular compound: (i) equilibrium adsorption of the dye on the colloid/polymer surface resulting in a distribution between free and bound dye in solution or (ii) covalent binding of a fluorophore. The advantages and limitations of these two labelling modes are discussed below with respect to the reactivity and stability of the labelled compound.

### 3.1.1 Applications to Complex Environmental Samples

The two labelling strategies have different capabilities for the study of real environmental samples (water, biofilms, *etc.*) under minimally perturbing conditions. Even under mild conditions, in particular pH and ionic strength (*I*), the synthesis conditions for the formation of covalent bonds are usually too perturbing to be applied directly to the natural sample. Hence the colloid or polymer of interest must be first isolated, labelled and then introduced in the test sample with minimal perturbation. This approach is more perturbing than the adsorption mode, but the labelling is also more selective. In some cases, adsorption can be performed directly by adding the fluorophore to an unperturbed sample, provided that a fluorophore can be found that is selectively and strongly adsorbed on the test compound. Perfect selectivity is difficult to find in complex environmental samples, but perturbation due to this latter labelling procedure is likely to be minimal. In some cases, the adsorption properties of the naturally fluorescent HS [14,61] can also be used to follow the diffusion properties of the colloids on which they adsorb.

So far, FCS has not yet been applied to complete environmental samples, although it has been used to study the properties of environmental components such as HS, silica and alumina colloids, polysaccharides and peptidoglycans, organic gels, and their interactions (Sections 4–6).

### 3.1.2 Single-Versus Multi-labelling per Compound

Adsorption and covalent binding also have different capabilities in terms of the number of fluorophores bound to each test compound. This is an important issue for the interpretation of polydispersity (Section 2.3). Adsorption reactions usually lead to the binding of several fluorophores per polymer or colloidal particle (Section 3.2) [62], due to insufficient selectivity. This is particularly true with chemically heterogeneous environmental compounds, whose site reactivity may change in a continuous manner. On the other hand, covalent binding may be much more specific. For instance, linear polysaccharides or DNA molecules may be tagged at a specific moiety present at the end of the polymeric chain.

When possible, it is preferable to bind only one fluorophore per studied macromolecule or colloid. In such a case, the size/conformation of the colloid or macromolecule is minimally perturbed and the analysis of the FCS–ACF (see Section 2.3) is simplified. When the number of fluorophores bound to the colloid/macromolecule is larger than 1, the  $G(0)$  value is the sum of the  $G_i(0)$  values for each fluorescent species *i* (including the free fluorophore and each differently labelled colloid), weighted by the square of the fractional intensity [57]:

$$G(0) = \frac{\sum_{i=1}^J \langle F_i \rangle^2 \times G_i(0)}{\left\langle \sum_{j=1}^J F_j \right\rangle^2} = \frac{\sum_{i=1}^J (\varepsilon_i \overline{N}_i)^2 \times G_i(0)}{\left\langle \sum_{j=1}^J F_j \right\rangle^2} \quad (14)$$

where  $\langle F \rangle$  is the average fluorescence intensity in counts s<sup>-1</sup>, *J* is the number of different fluorescent species (i.e. free fluorophore plus the labelled colloids),  $\varepsilon_i$  is the molecular brightness (in count s<sup>-1</sup>) and  $\overline{N}_i$  is the average number of fluorescent species, *i*, in the confocal volume. For cases where the brightnesses of the fluorophores bound to a given colloid are different,  $G(0)$  will depend on the brightness and number distributions of these

fluorophores. The brightness of each fluorophorescent species can be obtained either by measuring the ACF of each pure species under identical physicochemical conditions or, if they are in equilibrium with each other, through a titration experiment [63]. Usually, as a result of their different chemical environments, the brightness of a fluorophore is different in free and bound states. When there are several binding sites on a colloid, different brightnesses may also occur. An example of such a case is discussed in Section 5.1.

The above considerations permit a comparison of the intensity distribution of ACF due to sample size polydispersity. When there is only one binding site per colloid/macromolecule (*e.g.* polysaccharide tagged at the end), the intensity distribution from the ACF is not skewed by the molecular size distribution. On the other hand, for chemically homogeneous spherical colloids tagged by adsorption, the number of adsorbed dyes increases with the surface area, which introduces a different brightness of the particles [equation (14)].

### 3.2 CONDITIONS FOR LABELLING BY ADSORPTION OF FLUOROPHORE

An advantage of labelling by adsorption is that it is rapidly performed. Labelling conditions, however, must be carefully chosen. In addition to the criteria linked to wavelength and quantum yield (Section 3.5), the major factor to consider is the binding equilibrium constant,  $K$ , of the dye (D) and sites (S) of the colloid or polymer:

$$K = \frac{\{DS\}}{[D]\{S\}} \quad [15a]$$

where  $\{DS\}$  and  $\{S\}$  denote the surface concentrations ( $\text{mol m}^{-2}$ ) of the bound dye and the free sites, respectively, and  $[D]$  is the bulk concentration of the free dye in solution. Conditions are optimised to obtain  $\{DS\}/\{S\} \ll 1$ , and

$$\{S\} \sim \{S\}_t \quad [15b]$$

where  $\{S\}_t$  is the total surface concentration of sites. Simultaneously, the FCS–ACF can be readily interpreted only [equation (14)] when

$$\frac{\varepsilon_{DS}[DS]}{\varepsilon_D[D]} \gg 1 \quad [15c]$$

where  $[DS]$  is the average concentration of DS in  $\text{mol dm}^{-3}$  and the  $\varepsilon_{DS}$  and  $\varepsilon_D$  are the brightness of DS or D, respectively. Combining equations (15a)–(15c) leads to

$$K \gg \frac{\varepsilon_D}{\varepsilon_{DS} c A \{S\}_t} \quad [15d]$$

where  $c$  is the concentration of colloids ( $\text{g dm}^{-3}$ ) and  $A$  is the specific surface area ( $\text{m}^2 \text{ g}^{-1}$ ). Equation (15d) shows that the stability constant of the dye that is employed depends on the possible quenching of the fluorescence of D by the labelled particle (Section 3.4). The relative brightness of the free and adsorbed dye should be determined before choosing the right label.

Typical values of  $A$  and  $\{S\}_t$  of metal oxides relevant for inorganic colloids are in the ranges  $10\text{--}700 \text{ m}^2\text{g}^{-1}$  and  $5\text{--}15 \text{ sites nm}^{-2}$  [i.e.  $(1\text{--}3) \times 10^{-5} \text{ mol sites sm}^{-2}$ ] respectively, while typical concentrations of inorganic colloids in waters are  $0.1\text{--}10 \text{ mg dm}^{-3}$  [14]. Using  $A = 100 \text{ m}^2\text{g}^{-1}$ ,  $\{S\}_t = 2 \times 10^{-5} \text{ mol of sites sm}^{-2}$ ,  $c = 10^{-3} \text{ g dm}^{-3}$  and  $\varepsilon_D = \varepsilon_{DS}$ , one obtains  $K \gg 10^{5.7}$ , or  $K \geq 10^7 \text{ dm}^3 \text{ mol}^{-1}$ . Leng *et al.* [62,64] for instance, studied the labelling of alumina and silica nanoparticles, as model inorganic colloids, by adsorption of the fluorescent dyes Rhodamine 6G and calcein. In that case,  $K$  values were in the range  $10^8\text{--}3 \times 10^9 \text{ dm}^3 \text{ mol}^{-1}$ . The former binds through electrostatic and van der Waals interactions, whereas the latter forms a chemical bond with surface  $\text{Si}^{\text{IV}}$  or  $\text{Al}^{\text{III}}$  by elimination of a water molecule between  $\equiv\text{Si-OH}$  (or  $\equiv\text{Al-OH}$ ) groups and the carboxylate groups of the dye [5].

To obtain a completely negligible fraction of free dye, even at low dye concentrations, inorganic colloids have to be tagged with ligands that have strong anchoring properties such as polydentate moieties. Phosphates, polyphosphonates [65] and polycarboxylates [66] are known to be strong binders of metal oxides. They can also be used as spacers between the surface and the fluorophore, to minimise quenching. In order to favour surface binding compared with colloidal dissolution, it is probably better to choose a polydentate anchoring moiety without chelating effect, *e.g.* polyacrylic acid may be preferable to EGTA derivatives. In such a case, the length of the chain is important (typically 5–20 monomers): it should be long enough for strong adsorption, but sufficiently short to avoid colloid coagulation by bridging [67]. Polymeric dyes may have strong association constants with the test macromolecule/colloid, but their large size is usually a limiting factor. For instance, avidin interacts strongly with the protein biotin ( $K \approx 10^{15} \text{ dm}^3 \text{ mol}^{-1}$ ) but it also strongly affects the activity of biotin due to its size (67 kDa) and the fact that it binds to four different sites [68]. Perturbation of the stability of DNA by the intercalation of the fluorophore YOYO-1 [69], and the need for relatively high concentrations of fluorophores for the labelling of DNA [70] have also been reported.

### 3.3 CONDITIONS FOR THE COVALENT LABELLING OF FLUOROPHORES

#### 3.3.1 Chemical Conditions for Covalent Labelling

Compared with labelling by adsorption, hydrolysis-resistant covalent labelling provides labels that are not released upon dilution and that have improved yields and better control on the location and number of tags per molecule. On the other hand, purification of the labelled molecule is nearly always required to remove unwanted reactants and products (usually by HPLC, gel chromatography, centrifugation or precipitation). More than one step is therefore usually required for covalent labelling.

Table 2 summarises many of the types of reactions that are used to couple a fluorophore to a target macromolecule or colloid. Most dyes are poorly soluble in water, hence they generally need to be dissolved in a small volume of methanol or dimethyl formamide (DMF) prior to their addition to the reactive medium. Dimethyl sulfoxide (DMSO) is usually not recommended, because it is known to induce phase transitions in biopolymers and reacts with sulfonyl chloride-activated dyes. Many dyes have primary amine [Rhodamine 123 (R123), Nile Blue, *etc.*] or carboxylate [Rhodamine B (RB)] functions that allow covalent tagging through an amide bond. Some of them (*e.g.* R123 and RB)

**Table 2.** Main coupling reactions to tag biomolecules

Class of reagents	Reactive functions on reagents	Bond/product
Aldehyde-reactive: Amine		
Amine-reactive: Carboxylic acid derivatives		
Sulfonyl chlorides		
Isothiocyanates	$R=N=C=S$	
Thiol-reactive: Iodoacetamides		
Maleimides		

preserve their fluorescence properties upon transformation, but others (*e.g.* Nile Blue) do not. The synthesis of dyes bearing a chemically reactive functions which do not influence fluorescent properties is now an important field of development.

Fluorescent reagents with primary amines are frequently used to label polysaccharides or glycoproteins. For the former class of molecule, the amine group reacts with the free aldehyde function at one end of the biomolecule to produce an imine at pH 4–9. To prevent hydrolysis, the imine is reduced to an amine, with a soft and specific reagent such as NaCNBH<sub>3</sub> [40]. This reduction reagent is not effective in basic medium.

Acid derivatives are used to label H<sub>2</sub>N-containing biomolecules, such as peptides and proteins. The covalent tagging through an amide bond is frequently used in water because

it is resistant to hydrolysis. Two major activated acid derivatives are used for the labelling. The first group includes isothiocyanates (ITC), sulfonyl chlorides (SC) and succinimidyl esters (SE) that can be used to combine with amines in water, even though the latter reagent is fairly easily hydrolysable. The second group includes acid chloride (AC), acid anhydride (AA) and imidazolides (IM) that are used in non-protic solvents. The use of a non-protic solvent generally leads to much better yields compared with water, but the risks of denaturation of the test macromolecule are much greater.

In water, labelling yields are strongly dependent on pH. Only the proton free amine groups are reactive. On the other hand, acid derivatives rapidly hydrolyse as the pH is increased. Therefore, tagging is usually carried out in the pH range 7.5–10. Buffers containing free amines must be avoided and phosphate or carbonate buffers are commonly used. Because SE are not very soluble in water, it may be useful to prepare *in situ* the activated reagent from the carboxylic acid in buffered water by using 1-ethyl-3-(3-dimethylaminopropyl)carbodiimide (EDC). Addition of *N*-hydroxysulfosuccinimide (NHSS) in catalytic amounts can enhance the yield of the carbodiimide-mediated conjugation [71].

Iodoacetamides and maleimides are used to label proteins and nucleic acids by reactions with their free thiols. In proteins and nucleic acids, free thiols are not very common, which provides a certain selectivity. The thioether bond is fairly stable to hydrolysis.

### 3.3.2 Major Artefacts

Two major types of artefacts must be considered in relation to covalent labelling. First, photophysical properties (excitation wavelength, absorptivity and quantum yield) of the free dye may be significantly modified by its coupling to the labelled molecule/colloid, due to the electronic reorganisation of the dye subsequent to its covalent attachment. In particular, its optimal excitation wavelength may be shifted by more than 20 nm (possibly out of the excitation wavelength of the laser beam), and its absorptivity or its quantum yield may be lowered, making the dye inefficient for applications with FCS. For example, free Nile Blue is efficiently excited by an He–Ne laser at 633 nm (Tables 3 and 4), but when its primary amine is transformed into an amide by reaction with a carboxylic acid derivative, the quantum yield is lowered by more than 90% [72]. For that reason, a substantial market for the production of reactive fluorescent dyes has been developed recently [73]. In particular, less perturbing labels can be produced by adding spacers between the dye and the reactive moiety.

Another possible major artefact is the unwanted modification of the target molecule. This is particularly true when many fluorophores are fixed by molecules (as may happen with absorption labelling), when the size of the dye is large compared with the

**Table 3.** Main laser sources and spectral lines (bold) used for excitation in FCS

Laser source	$\lambda_{\text{em}}/\text{nm}$
Argon ion	458, 477, <b>488, 514.5</b>
Helium–neon	<b>543</b> , 594, 604, 612, <b>633</b>
Argon–krypton	488, 568, <b>647</b>
Titanium–sapphire	<b>770</b>

**Table 4.** Some excitation wavelength(s) of few fluorochromes suitable for FCS<sup>a</sup>

Dyes	$\lambda_{\text{ex}}^{\max}/\text{nm}$
Alexas (from near-UV to NIR dyes) [74]	<b>488</b> , 500, <b>514</b> , 532, <b>546</b> , 555, 568, 594, 610, <b>633</b> , <b>635</b> , <b>647</b> , 660, 680, 700, <b>750</b>
Calcein	<b>495</b>
Rhodamines	502 (Green), <b>507</b> (R123), <b>519</b> (R6G), <b>541</b> (TMR), <b>555</b> (RB), 570 (Red)
Bodipy	503
Texas Red	590
Nile Blue	<b>633</b>
DY 630 and 635 [75]	<b>630</b> <b>635</b>
YOYO-1, TOTO-1	491 509
Fluorescent proteins	<b>489</b> (GFP), <b>514</b> (YFP), <b>555</b> (DsRed), 573 (ArRed)
Allophycocyanin	<b>650</b>
R-phycoerythrin	<b>480/565</b>

<sup>a</sup> Values in bold match laser spectral lines. TMR = tetramethylrhodamine.

target molecule (see Section 3.2) or when the dye tends to favour coagulation of the target macromolecules/colloids. This often happens when the surface charge is significantly decreased by the labelling, leading to a decreased colloidal stability. Preserving molecular integrity during the labelling process is not trivial, since the conformation and also equilibrium and dynamic chemical properties of the tested macromolecule/colloid must not be perturbed. For a macromolecule with well-defined activity, the activity of the labelled molecule should be compared with that of the non-labelled molecule. In any case, the use of mild labelling conditions is essential. Whenever possible, the covalent labelling of a single fluorophore, at a well-defined specific site of a given macromolecule, is recommended. For example, in molecular biology, genetic engineering can be used to produce proteins that are labelled at a specific location by a small fluorescent protein (size ~6–7 nm) from the family of the ‘green fluorescent proteins’ (GFP), originally produced by jellyfish. GFP is a 27 kDa protein (238 amino acids) with a barrel-like structure containing the fluorescent group in its centre. Several molecules of the same family but with different colours can be produced [76]. GFP can be fixed within the test protein far from its surface [77] and thus carry a permanently fluorescent tag [78], which then affects few of its surface properties. GFP may nonetheless perturb the conformation of the test molecule because of its rather large size. To overcome this difficulty, small molecules that are useful for specific covalent labelling have been synthesised. They contain As<sup>III</sup>, which binds strongly to the thiol group of cysteine [79], and they have the advantage of being non-fluorescent in the free state but highly fluorescent when combined with a cysteine moiety. Another example of the labelling of a macromolecule by a single fluorophore has been shown for linear polysaccharides. By using a small amine reagent, the open aldehydic end of the polysaccharide was tagged during the hemiacetal conversion. The imine that was produced was then converted to an amine through a soft reduction

by means of  $\text{NaCNBH}_3$ . Such a synthesis is non-perturbing [40] and the position of the fluorophore does not hinder the properties of the polysaccharide, whose interactions with other compounds occur mainly laterally, *e.g.* by hydrogen bonds.

### 3.4 CHOICE OF THE DYE: SPECTROSCOPIC PROPERTIES

#### 3.4.1 Photophysical Properties

These criteria are essential because the number of photons emitted per dye should be large enough ( $>10$  kHz) to ensure that the signal-to-noise ratio of the ACF is sufficiently large. Until now, laser diodes have not been used as excitation sources. Commercial FCS devices use the sharp lines of  $\text{Ar}^+$ , He–Ne and Ti–Sapphire laser sources (see Table 3). Excitation bands of organic dyes are typically 50–100 nm. A good selection of the dye requires that :

1. Its excitation spectrum matches the wavelength of the light emitted by the laser source (see Table 4 for some examples of excitation maxima).
2. The quantum yield of the fluorophore is large (typically  $\geq 0.5$ ) at the excitation wavelength employed. If possible, it should be larger in the bound state than in the free state. Many fluorescent dyes are not suitable for FCS because their quantum yield is too low. For example, Rhodamine 123 and Rhodamine 6G are preferable to free ethidium bromide, eosin and erythrosin for this reason.
3. Photobleaching of the dye is as low as possible under the intense power ( $\sim 1$  mW  $\mu\text{m}^{-2}$ ) of the laser focus. A fluorescent dye molecule is excited from a ground to an excited state about  $10^9$  s $^{-1}$  and, to be suitable, it must emit more than  $10^5$  photons before photobleaching. Fluorescein and its conjugates [80] have a high quantum yield but also a high rate of photobleaching and therefore are not suitable for FCS. Other examples of photobleached dyes are the hydroxycoumarins and SNARFL. The photobleaching of fluorophores by FCS can be identified by an important decrease in the count rate as a function of excitation time. In such a case, the average number of dye molecules in the confocal volume will decrease continuously. Such a process will dramatically skew the ACF analysis if a kinetic term corresponding to photobleaching process is not added to equation (5).
4. The fluorescence properties of the dyes are independent of pH. For example, a fluorescein based dye is not suitable for work with a natural water sample, because its  $pK_a$  is 6.4 [81]. If the pH of the sample varies around that value, the photophysical properties of the dye may change significantly, resulting in a more difficult analysis of the ACF.
5. The fraction of triplet state versus singlet state of the excited dye is as low as possible. For a significant fraction of the molecules in the triplet state (see Section 2.1), the ACF must be analysed either for delay times larger than  $\sim 0.01$  ms in water for classical organic dyes, or using equation (9) by accounting for phosphorescence.  $\text{Ru}^{II}\text{--tris(phenanthroline)}$  is a typical example of an unsuitable dye, due to its large triplet fraction.

#### 3.4.2 Quenching

Any other type of energy conversion of the excited singlet state (collisional, vibrational, singlet–triplet transition and intersystem crossing) is competitive with fluorescence

and may lead to a decrease in fluorescence yield. In particular, the presence of heavy metal ions [82], such as those present in certain colloidal metal oxides, may have a dramatic effect on fluorescence. In addition, if the absorption spectrum of the test macromolecule/colloid matches the fluorescence spectrum of the dye, emitted light may be quenched by absorption. Magnetite (iron oxide) has a very broad absorption spectrum, which quenches the fluorescence of any adsorbed dyes. The efficiency of the energy transfer follows the Forster mechanism and is very sensitive to the distance between the donor and the acceptor. It drops dramatically at distances smaller than  $d_0$ , the distance at which the energy transfer efficiency is 50% [83]. Note that for typical small molecules,  $d_0$  is about 1 nm, but it is larger for colloids. In the case of magnetite, fluorescence quenching can be prevented by maintaining the dye a few nanometres away from the particle surface using a rigid spacer or a fluorescent protein. In many cases, such problems may be overcome with the right choice of the dye; for instance, haematite (iron oxide) nanoparticles absorb up to 630 nm, so that quenching can be prevented by using a near-infrared (NIR)-emitting dye (see Table 4) chemically connected to a surface binder. In scattering media, long-wavelength-emitting dyes are also better for a maximum photon collection efficiency. Nonetheless, it is important to keep in mind that water absorbs at around 730 nm.

### 3.5 SPECIFIC EXAMPLES

Examples for the labelling of natural and model colloids and macromolecules are given in Table 5. Among the inorganic colloids, clays and silica are widely encountered in natural samples. They are negatively charged particles under most environmental conditions, and fluorescent cationic dyes are readily adsorbed on their surfaces. On the other hand, coupling agents such as (3-aminopropyl)triethoxysilane (APTES) may be used to connect amine-reactive dyes, *e.g.* TRITC, to the silanol groups of the colloidal surface. Adsorption of humic acids on TiO<sub>2</sub> particles has been reported under acidic and neutral conditions (humic acids are naturally fluorescent and may be excited at 488 nm with an Ar<sup>+</sup> laser (see Section 4). This adsorption process involves electrostatic interactions, but it is not excluded that carboxylate or phenol groups present in the structure of humic acids may bind Ti<sup>4+</sup> ions on the TiO<sub>2</sub> surface, increasing the strength of adsorption. Co-adsorption of humic acids and cationic dyes including methylene blue have been reported to change the colour of haematite. Haematite is positively charged up to pH 7–8 and most NIR dyes are cationic. The direct adsorption of NIR dyes has not been reported so far; however, it is certainly feasible.

The covalent labelling of polysaccharides and derivatives using the aldehyde moiety present during the hemiacetal interconversion was discussed in Section 3.3. In addition to this specific and recommended labelling, boronic acids are known to bind sugars through the formation of boronic esters. These esters are sensitive to hydrolysis and usually the binding constant is not very large ( $\log K \approx 3$  [83]), but the strength of the binding can be increased by increasing the number of boronic esters formed between the sugar and polyboronic acid molecule or by shifting the equilibrium using a borate buffer.

**Table 5.** Some labelling possibilities of natural and model particles<sup>a</sup>

Inorganic colloids	Molecules/polymers		
	Polysaccharides	Peptides/proteins	Model polymers
<b>Clays<sup>(-)</sup><sup>b</sup> and silica<sup>(-)</sup></b> Ads. R6G [64], R123, Nile Blue, ... Cov. [84] TRITC-APS	<i>Cov.:</i> 1. <i>Specific to the terminal free aldehyde</i> R123, pH = 5, Imine reduction, e.g. dextrans, agarose, bacterial polysaccharides, schizophyllan [40]	<b>Proteins</b> <i>Cov. specific</i> GFP fusion at NH <sub>2</sub> - or CO <sub>2</sub> H- terminus [77,78]	<b>PAA<sup>(-)</sup></b> [85] <i>Cov. non-specific (amide bond)</i>
<b>TiO<sub>2</sub></b> (IEP ≈ 7) Ads. Humic acids [62] Cov. Carboxylated porphyrins [86]		As <sup>III</sup> thiol bond [79] Rhodamine–iodoacetamide for thiol groups [87]	For M < 4 × 10 <sup>5</sup> Da: solvent=DMF, (i) DCC, (ii) R123
<b>Iron hydroxides</b>	2. <i>Hydrolysable and non-specific</i>	<b>Protein and peptide</b>	For larger M: solvent = water/DMF, (i) EDC, (ii) R123
<b>haematite</b> Ads. Humic acids + cationic dyes [88]	Boronic acids [89] Ads. R6G, borate buffer [39] <sup>c</sup>	Cov. Non-specific at NH <sub>2</sub> - or CO <sub>2</sub> H- terminus [90,91]	<b>Amine-terminated dendrimers<sup>(+)</sup></b> [92] <i>Cov. (amide bond)</i> <i>Organic or water solvents</i> Activated RB <sup>d</sup>

<sup>a</sup> Usual charge of the compound is given in parentheses. Adsorption tagging (*Ads.*); covalent tagging (*Cov.*). *Reagents:* (3-aminopropyl)triethoxysilane (APTES); H, N'-dicyclohexylcarbodiimide (DCC); Rhodamine B (RB); Rhodamine 6G (R6G); Rhodamine 123 (123); tetramethylrhodamine isothiocyanate (TRITC); polyacrylic acids (PAA). IEP = isoelectric point, M=molar mass, DMF=dimethyl formamide.

<sup>b</sup> Kaolinite is the most stable of the aluminosilicates in acidic conditions.

<sup>c</sup> The use of a borate buffer may be detrimental for the preservation of the polysaccharide structure, because many boronic esters are formed that may disturb lateral interactions.

<sup>d</sup> Acid chloride and succinimidyl ester derivatives of Rhodamine B have been used.

The boronic ester being negatively charged, subsequent adsorption of cationic dyes can be achieved [39].

Model polymers have been employed to understand the reactivity of natural polymers. For example, polyacrylic acids (PAA) have been labelled with R123 and amine terminated-dendrimers with RB for use as diffusion probes in porous media [42,92]. With polymers, dramatic solubility changes are observed with increasing molar mass. In addition, covalent labelling in water is usually characterised by a low yield so that it is necessary to work with large excesses of reactants in order to obtain reasonable yields. Such a procedure might be limiting with respect both to the labelling control and to the preservation of

the polymer structure. Fortunately, in some cases, synthetic polymers can recover their spatial structure when dried and reintroduced in water. In such cases, anhydrous DMF could be used to label polymers efficiently in sizeable amounts using a low ratio of dye to polymer. The purification of labelled polymers by precipitation or centrifugation in aqueous media is easy for high molecular weight polymers, whereas for low and medium molecular weight polymers, extraction or separation in gel column is more efficient.

## 4 APPLICATIONS OF FCS TO THE STUDY OF PROPERTIES OF ENVIRONMENTAL MACROMOLECULES

### 4.1 HUMIC SUBSTANCES (HS)

Knowledge of the diffusion coefficients of HS [which include fulvic acids (FA) and humic acids (HA)] is essential to understanding their role in the transport of associated trace compounds in water, soils and sediments and in their biouptake by microorganisms, in addition to the interpretation of the signal of a number of analytical speciation techniques based on diffusion in gels, such as diffusive gradient in thin films (DGT [93]) or voltammetry with gel-integrated microelectrodes (GIME) [94,95]. Until recently, diffusion coefficients of FA and HA were not well known, partly because of their complexity and polydispersity and partly because of the limitations of the available techniques. Dynamic light scattering [96] requires very high concentrations and is selective for the larger sized fractions of polydisperse samples. Voltammetry requires that a metal is bound to the HS [97]. In size-exclusion chromatography, interactions with the solid phase may lead to important artefacts [14]. More recent techniques such as flow field-flow fractionation (FFFF) and pulsed-field gradient NMR (PFG-NMR) are discussed elsewhere (Chapter 5, [98]). The major advantages of FCS for studies of HS is that it can be used at very low concentrations (down to  $\sim 0.5 \text{ mg dm}^{-3}$ ), i.e. in concentration ranges where aggregation is minimised (see below). It can also be used under wide ranges of solution pH and  $I$ , and there is no interaction with a solid phase, which is often a major problem with HS, due to their rather strong adsorption properties. The major problems to consider are the photobleaching of HS and the fact that the measured fluorescence may be representative of only a small fraction of HS, as discussed below.

Systematic studies of FCS to determine diffusion coefficients of HS have been reported [48]. As far as the photobleaching effect is concerned, no changes in the absorption spectra of HS were detected after an exposure to  $18.7 \text{ J cm}^{-2}$  irradiation at 488 nm. On the other hand, a decrease in fluorescence emission was observed for an irradiation time of 4 h, equivalent to conditions of higher excitation intensity for shorter times used in FCS. A maximum decrease of 40% was observed at pH 8, for irradiation doses  $> 18.7 \text{ J cm}^{-2}$ , whereas decrease of 20% was observed for  $9.4 \text{ J cm}^{-2}$  at  $\lambda = 488 \text{ nm}$ . Under the irradiation conditions used in FCS, photobleaching of HS should have a negligible effect on the determination of diffusion coefficients, as has been confirmed by varying the irradiation intensity and by comparing the results with other methods (see below). The appropriateness of the irradiation wavelength used in FCS (488 or 514 nm) has also been tested [48]. This wavelength is fixed by the laser of the instrument, *e.g.* 488 or 514 nm, far from the maximum excitation wavelengths of the HS ( $\sim 350 \text{ nm}$  [99]). In addition, HS have a broad excitation band (main part of the band in the range 300–450 nm [99,100]), reflecting the

presence of many fluorophores or fluorophore molecular environments, although it is known that only a small fraction of the fulvic and humic molecules are fluorescent [100] and the precise nature of fluorescent molecules is unknown. Thus excitation with a laser at 488 or 514 nm might lead to systematic errors in the determination of  $D$  if fluorophores are not distributed homogeneously throughout the humic mixture, since very few fluorophores will be excited. On the other hand, the use of such high wavelengths has the advantage that photobleaching is less likely to occur due to the lower energies involved. Although the FCS optics used in the above study [48] did not allow the use of lower wavelengths for comparison, other results suggested that the use of these high wavelengths had negligible effects on the measurements of  $D$ . Indeed, (i) separation of FA and HA by capillary electrophoresis using laser induced fluorescence detectors with excitation wavelength at 325 and 514 nm gave similar results and (ii) no difference in diffusion coefficients measured by FCS was observed using lasers at 488 and 514 nm.

Lead *et al.* [48] reported a systematic study of the diffusion coefficients of Suwannee River fulvic acids (FA) and humic acids (HA) measured by FCS, as function of pH,  $I$  and  $\text{Ca}^{2+}$  concentration. Figure 5 shows that, as expected,  $D$  values of FA are larger than those of HA although the difference is fairly small. Based on these results, it is likely that the much smaller values of  $D$  (and much larger sizes) reported for HA, *e.g.* in the 1970s and 1980s [101], are due to artefacts, in particular aggregation occurring with the much less sensitive techniques (thus requiring higher concentrations) available at that time. Figure 5 shows that, for both FA and HA,  $D$  increased with pH in the range 3–8, while a slight decrease of  $D$  might occur for pH > 8. Hydrodynamic diameters,  $d_h$ , computed from  $D$  values were 1.5 and 1.7 nm for FA and HA at pH ≈ 8 and 2.1 nm for both the FA and HA at pH = 3–4. Two opposite effects may explain the dependence of  $D$  on pH. As pH is lowered, aggregation is favoured and thus size increases ( $D$  decreases). As pH increases, the carboxylate (and phenolic) groups dissociate and the negative charge of FA and HA increases; intramolecular repulsions are thus favoured such that the size increases ( $D$  decreases). Figure 5 suggests that the aggregation effect predominates over molecular expansion, except possibly at pH > 8. The relatively small decrease in  $D$  (30% on average for FA) on passing from pH = 8 to 3 suggested that aggregation was also weak: only dimers or trimers would be formed. This result is also supported by AFM and recent NMR and FFFF results [59,102] and is in agreement with other observations which suggest that the XAD extraction procedure, used for the purification of Suwannee River FA and HA, eliminates the hydrophobic compounds which can strongly adsorb or aggregate [14].

From Figure 5, it can be estimated that unaggregated molecules are present at pH > 6. By using the empirical relationship (where  $d_h$  is given in nm) [14,56]:

$$d_h = 0.054M^{0.5} \quad (16)$$

valid for globular, not necessarily spherical, polymers, the values of  $M = 1650$  and 2300 were obtained for FA and HA, respectively at pH = 8, which is consistent with literature data (*e.g.* values for FA range between 730 and 2300 [14,103]).

Variations of ionic strength ( $I$ ),  $\text{Ca}^{2+}$  concentration and FA and HA concentrations [48] showed that an increase in ionic strength between 1 and 100  $\text{mmol dm}^{-3}$  had very little effect on  $D$  values, at both pH 4.5 and 6.8. Considering that FA and HA are highly

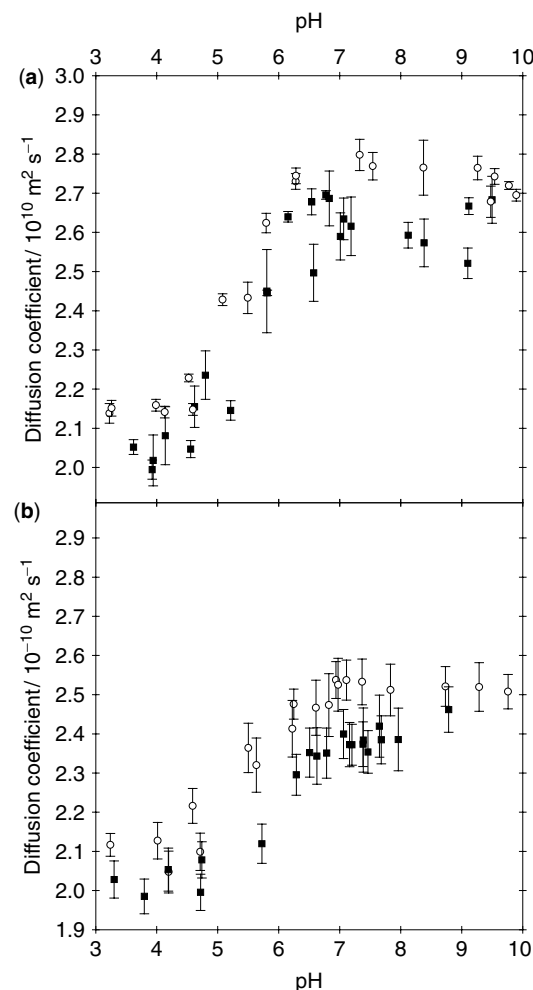


**Figure 5.** (a) Variation of diffusion coefficient with pH of SRFA for two ionic strengths: 5 (○) and 50 mmol dm<sup>-3</sup> (■). (b) Variation of diffusion coefficient with pH of SRHA for two ionic strengths: 5 (○) and 50 mmol dm<sup>-3</sup> (■). In both cases, the ionic strength was adjusted with NaCl. Concentration of SRFA = 10 mg dm<sup>-3</sup>. Adapted with permission from Lead, J., Wilkinson, K. J., Startchev, K., Canonica, S. and Buffle, J., Diffusion coefficients of humic substances as determined by fluorescence correlation spectroscopy: role of solution conditions, *Environ. Sci. Technol.*, **34**, 1365–1369. Copyright 2000 American Chemical Society

charged at pH 6.8, an increase of  $I$  could be expected to reduce the electrostatic repulsion and therefore decrease the size of the molecule, through the screening of charged groups. The very small influence of  $I$  suggests an important intrinsic rigidity of FA and HA. This point has been confirmed by AFM measurements [102], which also confirmed FCS data suggesting that FA and HA can be considered as spherical in solution.

Interestingly, a detailed inter-comparison of diffusion coefficient data obtained by FCS, FFFF and PFG-NMR at different pH and  $I$  has been published for Suwannee River

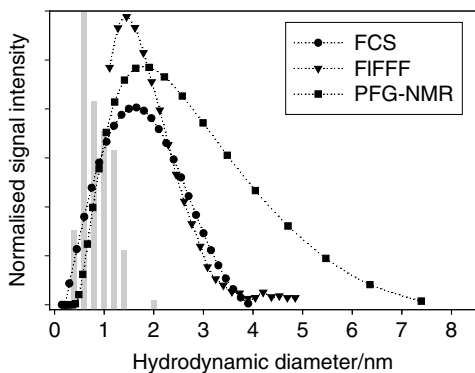


**Figure 6.** Hydrodynamic diameters of the SRFA calculated from the diffusion coefficients measured at pH 8.5 and low ionic strength ( $5\text{--}27 \text{ mmol dm}^{-3}$ ) using the Stokes–Einstein equation. Heights of the SRFA as measured by AFM are presented as a histogram ( $N = 100$ ). Reprinted with permission from Lead, J. R., Wilkinson, J. W., Balnois, E., Cutak, B. J., Larive, C. R., Assemi, S. and Beckett, R., Diffusion coefficients and polydispersities of Suwannee River fulvic acid: comparison of fluorescence correlation spectroscopy, pulses-field gradient nuclear magnetic resonance, and flow field-flow fractionation, *Environ. Sci. Technol.*, 34, 3508–3513. Copyright 2000 American Chemical Society

FA [59]. Values of  $D$  and polydispersities were given at various pH. Good agreement was obtained between the three techniques, both for the average value of  $D$  and for the polydispersity and size distribution, as shown in Figure 6. The advantages and limitations of each technique were discussed. In brief, FCS proved to be a sensitive and selective technique for studying fluorescent components. PFG-NMR allowed the selective determination of the  $D$  values of specific chemical fractions of the FA (e.g. the aromatic or aliphatic components), but it was not a sensitive technique as it requires higher concentrations. FFFF provides direct measurement of  $D$  without the need for calibration and had a reasonable sensitivity, but losses of the smaller molecules through the membrane may skew the results towards larger values of  $D$ . The good coherence of the results of these three techniques is very encouraging and suggests that artefacts have been reasonably limited.

FCS has also been used to compare systematically the diffusion coefficients of a large number of fulvic samples originating from different rivers, lakes and ponds [60,104]. Very similar values to those obtained for the Suwannee River FA were obtained, suggesting that these values were applicable to a large number of soil-derived, aquatic FA. The diffusion of Suwannee River FA in agarose gel has also been studied [60]. The  $D$  value of FA in agarose is only 10–20% smaller than that in water (see Figure 13), probably because the diameter of the FA ( $\sim 2 \text{ nm}$ ) is much smaller than the critical pore diameter of agarose ( $\sim 140 \text{ nm}$ , Figure 13). In addition, both electrostatic and steric retention effects are weak (see Section 6). Furthermore, as both agarose and Suwannee River FA are largely hydrophilic, their chemical interactions are minimised. The decrease in  $D$  in gel compared with aqueous solution was larger at pH 3–4 (20%) than at pH 7–8 (10%), which might be due either to the larger size of the FA (due to aggregation) at low pH (see above) or to the greater interaction between the FA and agarose due to the neutralisation of negative charges on both the FA and the agarose at pH < 4 (see also Section 6).

## 4.2 HIGH MOLECULAR WEIGHT POLYSACCHARIDES

Fibrillar polysaccharides may be a major fraction (up to 20–30%) of organic matter of natural waters [14]. The capability of FCS to study these compounds has been demonstrated by a study of the size and conformation of native and denatured schizophyllan [39]. This polysaccharide, secreted by the fungus *Schizophyllum commune*, consists of a main chain composed of (1 → 3)- $\beta$ -linked D-glucose units, with one (1 → 6)- $\beta$ -linked glucosyl side-chain for every three D-glucose units. At room temperature, in water, in the pH range 3–13, schizophyllan is a stable triple helix forming a semi-rigid rod. At pH > 13, at higher temperatures or in DMSO, the triple helix is denatured and schizophyllan is found as a random coil. Its average molar mass is 437 kDa, but smaller fragments, denatured or not, can be obtained by sonication.

The size and conformation of schizophyllan, as for many other polysaccharides, have been studied by various techniques, including light scattering, X-ray diffraction, electric birefringence and viscosimetry. Nonetheless, the sensitivity of these techniques is low and the concentrations used are typically not lower than 0.1 g dm<sup>-3</sup>. At that level, complicating secondary processes such as aggregation may occur. A major advantage of FCS is that it can be used at much lower concentrations, e.g. reliable FCS results have been obtained for solutions of 0.001 g dm<sup>-3</sup> schizophyllan ( $\sim 2 \times 10^{-9}$  mol dm<sup>-3</sup>) corresponding to the concentration of polysaccharides in natural waters (0.1–1.0 mg dm<sup>-3</sup>) [14].

On the other hand, polysaccharides are not fluorescent, which is a major difficulty for their investigation by FCS, particularly for conformational studies. A number of non-perturbing labelling techniques are compared in Section 3. A very mild labelling procedure has been reported [39] that can be applied only to polysaccharides with alcoholic groups close enough to form a complex with borate anion  $[B(OH)_4^-]$ . The negatively charged schizophyllan–borate complex itself can then react with the positively charged fluorescent dye R6G<sup>+</sup> to form a fluorescent complex. These reactions are reversible and the complex is stable only at pH > 8 and at temperature that is not too high. It has been shown, however, that FCS measurements of diffusion coefficients are feasible at 25 °C.

Figure 7 shows the size of non-denatured (triangles) and denatured molecules (squares) as function of their molar mass. Open symbols are data obtained by FCS [39] and black symbols are data obtained by other techniques, including viscosimetry. Clearly, FCS data provide coherent results for any type of conformation: for the non-denatured schizophyllan, the diffusion coefficient measured by FCS can be related to the diffusive behaviour of rigid rods giving a length,  $L$ , of rod that is proportional to its molar mass (slope of 1.0 in Figure 7). The values of  $L$  obtained were confirmed by AFM measurements. For the denatured schizophyllan, the FCS data suggested that it behaved as a random coil that was swollen by an excluded volume, and the measured diffusion coefficient is directly dependent, through Stokes law, on its radius of gyration. The slope of 0.59 in Figure 7 is consistent with this interpretation and with computer simulations.

In conclusion, FCS is a very useful tool for determining the conformation and size of naturally fluorescent or non-fluorescent colloids and macromolecules, under environmental conditions, in particular at low concentrations. A major limitation of FCS is that unambiguous interpretation is possible only in solutions containing one or a few different compounds. In order to apply FCS to complicated mixtures, the components studied should be selectively labelled and sophisticated labelling strategies must be developed in such cases.

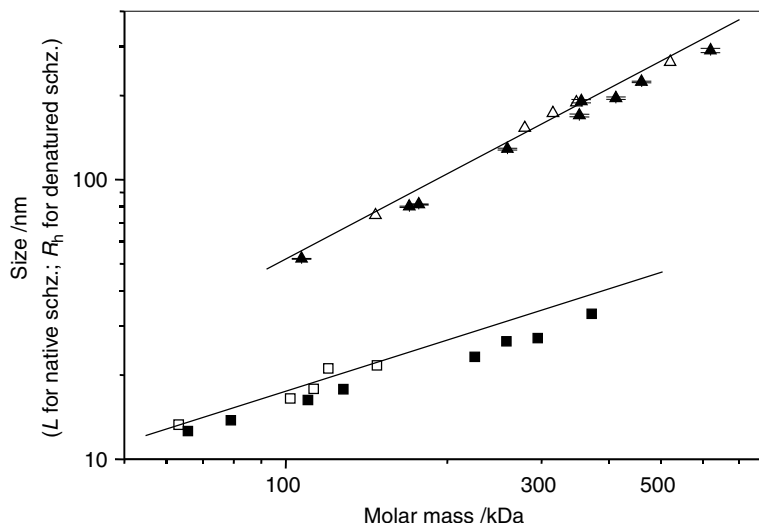


**Figure 7.** Comparison of size data for native and denatured schizophyllan.  $\Delta$ , Lengths,  $L$ , of non-denatured schizophyllan determined in [39];  $\square$ , radius,  $R_h$ , of denatured schizophyllan determined in [39];  $\blacktriangle$ , lengths of non denatured schizophyllan extracted from [91];  $\blacksquare$ , radius of denatured scleroglucan from the work of Yanaki and Norisuye [105]

## 5 STUDY OF COLLOID AND MACROMOLECULE AGGREGATION BY FCS

There are only a few environmentally relevant aggregation studies that have been performed by FCS. For such studies, the advantages of FCS are (i) its high sensitivity, which allows for aggregation studies to be performed at environmentally realistic concentrations ( $0.001\text{--}10 \text{ mg dm}^{-3}$  [14]) of aquatic colloids and macromolecules, (ii) its capability to follow the dynamics of very small colloids, macromolecules ( $\geq 1 \text{ nm}$ ) or aggregates and (iii) its selectivity to specific colloids or macromolecules labelled with specific dyes. The combination of these characteristics in a single technique is unique. An important limitation of FCS is that particles or aggregates larger than the laser beam size are not measurable (Section 2.3). This implies that FCS will be a unique technique for studying small aggregates (typically  $< 1 \mu\text{m}$ ), in particular during the initial steps of aggregation, but it will not be useful when following the evolution of large aggregates. A few examples of applications of FCS in aggregation studies are briefly described below.

### 5.1 AGGREGATION OF SMALL COLLOIDS AND COMPARATIVELY LARGE BIOPOLYMERS

The capability of FCS to study the aggregation of nanometre particles with comparatively much longer rod-like biopolymers has been demonstrated [106]. The flocculation of schizophyllan (length = 188 nm; uncharged molecule) with latex [ $R_h = 15 \text{ nm}$ ; zeta-potential ( $\zeta$ ) =  $-34 \text{ mV}$ ] and alumina ( $R_h = 25 \text{ nm}$ ;  $\zeta = 32 \text{ mV}$ ) particles has been studied separately and compared. In these systems, schizophyllan was not labelled, whereas latex was covalently labelled and alumina was labelled by the adsorption of calcein

(Section 3.2). It was shown that the autocorrelation function curves could be interpreted on the basis of equation (14), applied either to a two-component system (labelled free colloids and labelled aggregates) for the schizophyllum–latex interaction or to a three-component system (free dye, labelled free colloids and labelled aggregates) for the schizophyllum–alumina interactions. A major interest of FCS is that two characteristic parameters of the aggregates can be obtained: their diffusion coefficient, i.e. hydrodynamic radius,  $R_h$ , and the ratio of fluorescence intensities,  $F_f/F_p$ , of a single floc and a free colloidal particle. When the fluorescence quantum yields of the dye in the free and bound states are equal, as for the schizophyllum–latex system,  $F_f/F_p$  provides directly the number of colloidal particles per floc. Similar information could be obtained for the number of biopolymers per floc, by labelling the polymer. In addition, the comparison of  $R_h$  and  $F_f/F_p$  gave information on the looseness or compactness of the floc.

The interactions between schizophyllum and latex are very rapid: stabilisation is obtained within a few minutes, as shown by the invariance of FCS autocorrelation curves. Figure 8a and b show the changes in  $R_h$  and  $F_f/F_p$  with the number concentration ratio,  $q$ , of schizophyllum over the colloids in suspension. For  $q < 1$ ,  $R_h$  corresponds to that of latex particles. For  $q > 1$ , flocs are formed and their size increases abruptly and then decreases slowly for larger  $q$ .  $F_f/F_p$  follows a similar trend and Figure 8b shows that flocs include a maximum of five latex particles per floc. For large  $q$  ( $q > 10$ ), the number of latex particles per floc tends again to 1, but  $R_h$  remains about 15 times larger than that of the individual latex particles. This suggests that latex adsorbs several schizophyllum helices, to form a loose aggregate with one latex particle as nucleus.

Schizophyllum also reacts with alumina particles but more weakly and slowly [106]. Since, contrary to latex particles, alumina particles are positively charged, and since schizophyllum is neutral, its aggregation with both latex and alumina suggests that van der Waals forces are the major driving forces for the interaction. With alumina,  $R_h$  also increases for  $q > 1$ , but  $F_f/F_p = 1$ , irrespective of  $q$ . This suggests that only flocs with several schizophyllum and one alumina particle are formed, and that multi-particle flocs are not stable. The difference in behaviour between latex and alumina particles has been interpreted based on their different electrostatic repulsions.

The kinetics of aggregation of schizophyllum with alumina can also be followed by FCS. It was shown that the rates obtained by FCS and PCS were in good agreement with each other. Optimisation of FCS conditions is delicate, however. Indeed in a closed system such as an FCS cell, the aggregate size increases with time whereas the aggregate number decreases. Hence the number of aggregates which pass through the laser beam per time unit decreases with aggregation time, and the statistics of photon counting becomes poorer and poorer. This can be overcome by increasing the acquisition time. However, the latter parameter should always be maintained as a small fraction of the aggregation time. In spite of these limitations, FCS remains a unique tool for studying the aggregation kinetics of nano-sized particles.

## 5.2 DISAGGREGATION OF HUMIC SUBSTANCES

Aggregation of naturally extracted fulvic and humic compounds has been demonstrated previously [107], by surface tension measurements, ultrafiltration experiments and electron microscopy. Chemically purified fulvics and humics often adsorb and aggregate less

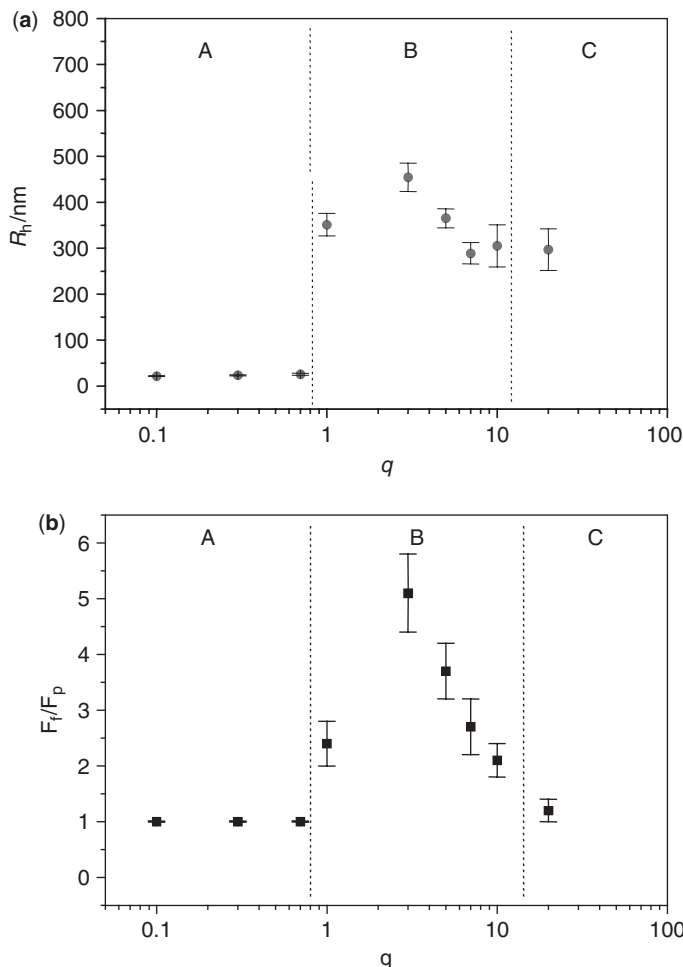


**Figure 8.** (a) Evolution of the hydrodynamic radius  $R_h$  of schizophyllum-latex floc versus the number ratio of schizophyllum/particles  $q$  in solution at pH 5.6,  $[NaCl] = 1 \text{ mmol dm}^{-3}$ ,  $T = 22 \pm 0.5^\circ\text{C}$ . (b) Evolution of the fluorescence intensity ratio  $F_f/F_p$  of schizophyllum-latex floc vs the number concentration ratio of schizophyllum/particles  $q$  in solution at pH 5.6,  $[NaCl] = 1 \text{ mmol dm}^{-3}$ ,  $T = 22 \pm 0.5^\circ\text{C}$ . Zones A, B, C correspond to the formation of different kind of aggregates (see original reference for details). Reprinted from Leng, X., Startcher, K. and Buffle, J., Application of fluorescence correlation spectroscopy: a study of flocculation of rigid rod-like biopolymer (Schizophyllum) and colloidal particles, *J. Coll. Interface Sci.* **251**, 64–72, Copyright 2002, with permission from Elsevier

strongly than naturally extracted ones, due to the specific elimination of surface-active molecules during the chemical purification process (see Section 4). However, peat humic substances (PHA) are usually more strongly surface active than water- or soil-derived HA, and detailed disaggregation studies of chemically purified peat humic substances have been performed by FCS [44]. This is an example of the unique capabilities of FCS: the radius of humic monomers is  $\sim 1 \text{ nm}$  (Section 4), and, although the sizes of

the aggregates formed are large (*ca.* 300 nm), only nanometre to submicrometre particles are present in solution, which are very difficult to study by other techniques. Only a small fraction of PHA monomers are fluorescent, but since aggregates include up to  $10^6$  monomers, all aggregates can be considered as fluorescent.

Disaggregation kinetics were studied by following the autocorrelation curves (ACF) as a function of time, by diluting a stock solution of chemically purified peat humic substances ( $5.28 \text{ g dm}^{-3}$  at pH 3.2) to  $30 \text{ mg dm}^{-3}$  at various pH (ionic strength maintained at  $0.005 \text{ mol dm}^{-3}$ ). Examples of ACF curves at three different times (Figure 9; similar curves were obtained for other conditions) clearly show two inflection points: the first at  $\tau_{c1} = 0.04 \text{ ms}$ , is completely independent of conditions and time and corresponds to a value of  $D = 2.5 \times 10^{-10} \text{ m}^2 \text{ s}^{-1}$ , i.e. to the diffusion coefficient of the free PHA monomer (Section 4). The second, which corresponds to aggregates, is initially located at  $\tau_{c2} = 14 \text{ ms}$ , but this value tends to decrease with disaggregation time. The corresponding values of  $D$  increase from  $7 \times 10^{-13} \text{ m}^2 \text{ s}^{-1}$  to  $1.6 \times 10^{-12} \text{ m}^2 \text{ s}^{-1}$ , i.e. the average radii decrease from 300 to 135 nm. Thus, the simple observation of the ACF curves shows that there are only two populations of species in solution, the PHA monomers and the aggregates whose sizes slowly decrease with time. This allowed a quick disintegration of aggregates into small fragments to be excluded as the disaggregation mechanism upon dilution. Rather, these observations suggested an attrition mechanism, where the monomers were progressively dissociated from the surface of the aggregates, leading to aggregates of smaller and smaller sizes.

Based on these observations, systematic FCS measurements allowed the determination of the disaggregation rate,  $r$ , of the chemically purified peat humic substances as function of pH;  $r$  is the rate (in size/time units) at which the radius of hypothetical spherical aggregates is decreasing, and can be computed from the experimental curve of the increase in monomer concentration with time, as measured by FCS [44]. By plotting  $\log(r)$  as function of pH, two linear segments are obtained with a change of slope at pH 4.6. Thus  $r$  can be written as

$$\log(r/k_1) = -n \times \text{pH} \quad \text{at pH} < 4.6 \quad (17a)$$

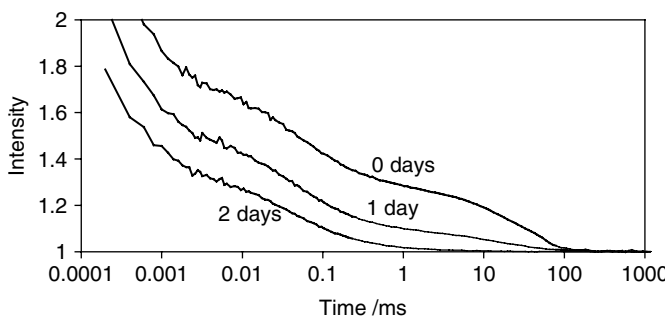


**Figure 9.** Autocorrelation curves obtained for a  $30 \text{ mg dm}^{-3}$  PPHA solution at pH 4.90. The time shown on each curve corresponds to the time elapsed since initiation of the disaggregation process.  $I = 0.005 \text{ mol dm}^{-3}$ ,  $T = 25^\circ\text{C}$ . Reprinted with permission from Avena, M. and Wilkinson, K. J., Disaggregation kinetics of a peat humic acid: mechanism and pH effects, *Environ. Sci. Technol.*, **36**, 5100–5105. Copyright 2002 American Chemical Society

$$\log(r/k_2) = -m \times \text{pH} \quad \text{at pH} > 4.6 \quad (17\text{b})$$

The values of the constants are  $k_1 = 0.19 \text{ nm day}^{-1}$ ,  $k_2 = 6 \times 10^{-16} \text{ nm day}^{-1}$ ,  $n = -0.35$  and  $m = -3.5$ . These results fit with other information in the literature and suggest that the first process corresponds to a loss of protons which stabilise the aggregate by hydrogen bonding, whereas the second process corresponds to the loss of protons of carboxylate groups. This process favours dissociation by creating negative charges on the monomers. This example clearly shows how the characteristics of FCS can help to elucidate the mechanism and kinetics of aggregation/disaggregation mechanisms of submicrometre aggregates.

## 6 APPLICATIONS OF FCS TO THE STUDY OF REACTION/TRANSPORT IN GELS

The bioavailability of metabolites for microorganisms is strongly affected by the surrounding materials inside biofilms, flocs or other porous media. In particular, biofilms and flocs are made of polysaccharide entanglements that are characterised by a large spatial heterogeneity. On the one hand, an accumulation of metabolites within these phases is often observed, due to the presence of binding moieties along the polysaccharide backbone. On the other hand, their transport rate inside the gel is highly selective due to the binding properties, electric field and steric effects of the gel. For instance the steric effect allows quasi-free diffusion of small non-reactive solutes, but prevents incoming colloidal and particulate species. The study of transport processes in polysaccharide gels is thus essential to understand the function(s) of biofilms and flocs. It is also important for a rigorous development of *in situ* environmental analytical techniques such as diffusive gradient in thin films (DGT) [93] and voltammetry on gel integrated microelectrodes (GIME) [94,95], in addition to analytical separation techniques (electrophoresis, gel chromatography) based on the controlled diffusion of solutes in organic hydrogels.

### 6.1 REACTION/DIFFUSION OF ORGANIC AND INORGANIC IONS IN POROUS MEDIA: ROLE OF ELECTROSTATIC EFFECTS AND SPECIFIC BINDING

Under non-steady-state conditions, the diffusion of solutes may be significantly affected by their specific and non-specific interactions with the gel itself. Until recently, the available information on diffusion in gels was very limited because of the lack of techniques allowing the study of reaction and transport processes at the microscale level. Hirota *et al.* [108] highlighted the effects of intrinsic charges and electrostatic interactions on the diffusion of solutes within highly charged gels such as  $\lambda$ -carrageenan. Comparatively, agarose gels are representative of weakly charged, porous gels and previous studies performed with more global techniques did not reach clear conclusions [109,110]. Recently, this gel has been studied in detail by FCS in order to determine the relative importance of steric, chemical and electrostatic interactions that may occur between a solute and the gel [111]. It is discussed below, to demonstrate some of the capabilities of FCS for the characterisation of porous media.

Agarose is a linear polysaccharide consisting of repeating units of agarobiose (1,3-linked  $\beta$ -D-galactopyranose and 1,4-linked 3,6-anhydro- $\alpha$ -L-galactopyranose); it is isolated from

agar, obtained itself from marine red algae (*Rhodophyta*). Even the best purified biopolymer is weakly charged, because of the presence of chemical ionic side-groups in the backbone structure, in particular sulfonate, ester sulfate, ketal pyruvate and carboxyl groups located at the 2- and 6-positions of the  $\beta$ -D-galactopyranose [112,113]. The amount of these groups can affect the physicochemical properties of the agarose hydrogels [114]. By cooling a hot solution of agarose in water, double helices [115] are formed by association of the polymer chains resulting in the formation of rigid fibres. Those fibres aggregate in a three-dimensional strongly hydrated network, producing a gel [116] stabilised by hydrogen bonding and hydrophobic interactions. The bulk structure of the agarose gel has been studied by small-angle neutron scattering (SANS) and reveals a broad distribution of pore diameters ranging from 0 to more than 120 nm, centred coarsely around 50–70 nm [117].

For the agarose studied recently [111], systematic measurements of partitioning and diffusion of small organic and inorganic ions into the agarose gel equilibrated with water have been performed by FCS and other techniques. From chemical analysis, it was shown that binding sites are mainly pyruvates (90%) and sulfates (10%), and that the latter are fully deprotonated at pH > 2. It was also observed that the distribution of solutes between the agarose gel phase and the aqueous solution can be described by a global partition coefficient, which is the product of the partition coefficients due to steric, chemical and electrostatic interactions only. Steric effects can be mathematically modelled based on the excluded volume of the solute and the pore radius,  $R_p$ . The electrostatic interactions can be described classically by a Donnan potential at the gel–water interface. The chemical interactions of cations and gel take into account their binding by pyruvate groups. Each interaction was studied and modelled separately. In particular, electrostatic ones could

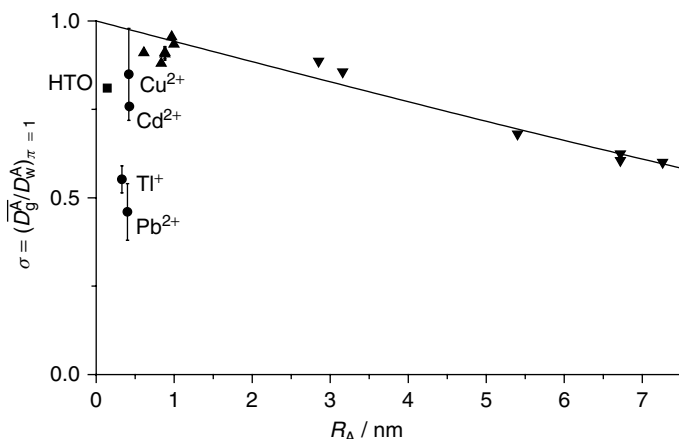


**Figure 10.** Ratio  $\sigma = \overline{D}_g^A / D_w^A$  in the absence of electrostatic interactions ( $\pi = 1$ ) as a function of the hydrodynamic radius  $R_A$  for  $\text{Cd}^{2+}$ ,  $\text{Cu}^{2+}$ ,  $\text{Tl}^+$  and  $\text{Pb}^{2+}$  ( $\bullet$ ), and for  $\text{R6G}^{2+}$ ,  $\text{NB}^{2+}$ , calcein $^{3-}$ , HA, peat HA ( $\blacktriangle$ ) and proteins ( $\blacktriangledown$ ). The line is the theoretical prediction, in the absence of electrostatic and chemical interaction, with  $R_p = 37 \text{ nm}$ . Reprinted with permission from Fatin-Rouge, Milon, A., Buffle, J., Goulet, R. R. and Tessier, A., Diffusion and partitioning of solutes in agarose hydrogels: the relative influence of electrostatic and specific interactions, *J. Phys. Chem. B.* **107**, 12126–12137. Copyright 2003 American Chemical Society

be eliminated experimentally, by increasing the salt concentration. For ionic strengths  $\geqslant 10^{-2}$  mol dm $^{-3}$ , the partition coefficient is linearly related to the radius of the solute,  $R_A$ . Under such conditions, the points not located on the line in Figure 10 correspond to chemical interactions (complexation for metals). Thus the values of equilibrium constants,  $K_A^{\text{in}}$ , for the complexation of Cu<sup>II</sup>, Cd<sup>II</sup>, Pb<sup>II</sup> and Tl<sup>I</sup> by pyruvate groups bound to the gel can be computed with

$$(\overline{D}_g^A / D_w^A)_{\pi=1} = \sigma / (1 + K_A^{\text{in}}[S]) \quad (18)$$

where  $\sigma$  is computed for steric effects only (see below) and [S] is the concentration of complexing sites in the gel. For the above metals, values of  $\log K_A^{\text{in}}$  in the range 2.7 to 3.5 were obtained.

The diffusion of solutes inside agarose gels was probed locally, at the micrometre scale, by FCS. The roles of steric, chemical and electrostatic interactions, and also that of heterogeneity of the gel structure on diffusion properties were also evaluated [111]. Steric interactions were modelled (Figure 10) using the Renkin model [118], which describes the restricted diffusion of spherical molecules of radius  $R_A$ , within cylindrical pores of mean effective radius  $R_p$ . The ratio of the diffusion coefficient of solute A in the gel and in water, in the absence of electrostatic ( $\pi = 1$ ) and chemical interactions,  $\sigma = (\overline{D}_g^A / D_w^A)_{\pi=1}$ , varies fairly linearly with  $R_A$ .

Under conditions where the electric charges of the gel are not screened (low ionic strength, Figures 11 and 12), diffusive transport may be affected in two ways: (i) the partitioning of any ionic solute between the solution and the gel is influenced by the

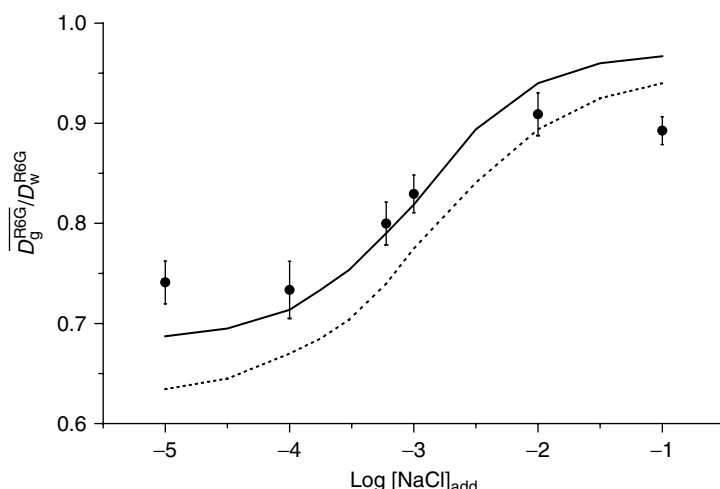


**Figure 11.** Ratio  $D_g^{\text{R6G}} / D_w^{\text{R6G}}$  vs  $[\text{NaCl}]_{\text{add}}$  (in mol dm $^{-3}$ ) in agarose gel. The lines are the predictions of the Schmoluchowsky–Poisson–Boltzman (SPB) theory, using either a cylindrical cell (full line) or a spherical cell (dotted line) (see [111] for details).  $T = 20^\circ\text{C}$ ;  $[R6G]_{\text{tot}} = 2 \times 10^{-8}$  mol dm $^{-3}$ ;  $[S]_{\text{tot}} = 8.2 \times 10^{-4}$  mol dm $^{-3}$ ; pH = 6. Reprinted with permission from Fatin-Rouge, Milon, A., Buffle, J., Goulet, R. R. and Tessier, A., Diffusion and partitioning of solutes in agarose hydrogels: the relative influence of electrostatic and specific interactions, *J. Phys. Chem. B* **107**, 12126–12137. Copyright 2003 American Chemical Society

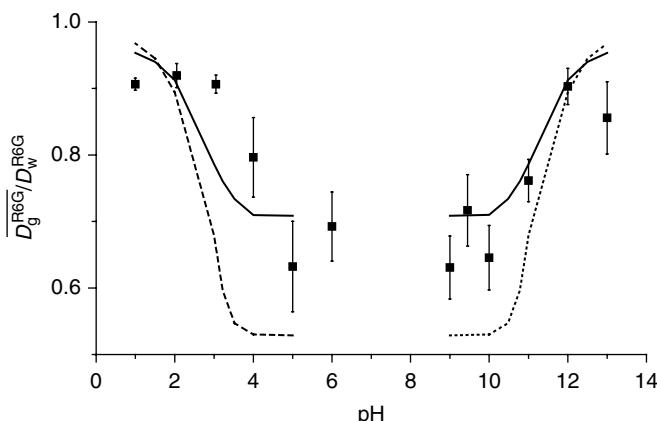


**Figure 12.** Ratio  $\overline{D_g^{R6G}}/\overline{D_w^{R6G}}$  vs pH in agarose gel equilibrated with aqueous solution. The lines are the theoretical predictions of the SPB model, using either a cylindrical cell (full line) or a spherical cell (dotted line).  $T = 293\text{ K}$ ;  $[R6G]_{\text{tot}} \approx 2 \times 10^{-8}\text{ mol dm}^{-3}$ ;  $[S]_{\text{tot}} = 8.2 \times 10^{-4}\text{ mol dm}^{-3}$ ;  $V_w/V_g = 1$ . Reprinted with permission from Fatin-Rouge, Milon, A., Buffle, J., Goulet, R. R. and Tessier, A., Diffusion and partitioning of solutes in agarose hydrogels: the relative influence of electrostatic and specific interactions, *J. Phys. Chem. B*, **107**, 12126–12137. Copyright 2003 American Chemical Society

Donnan potential formed between the water and the gel; it influences the concentration gradients and thus the diffusive transport in the gel; and (ii) in the case of low charge density gels such as agarose, the non-uniform electric field inside the gel may significantly influence the value of the average diffusion coefficient of solute A in the gel,  $\overline{D_g^A}$ , even in the absence of steric or chemical interaction. FCS is a unique technique to measure effect (ii) locally, inside the gel, in the absence of gradients and under conditions where effect (i) does not exist. This is shown in Figures 11 and 12, where the electric field inside the gel (due to pyruvate deprotonation) has been modified by changing the pH and ionic strength. FCS is much more appropriate for such studies than macroscopic techniques based on flux measurements which are strongly influenced by effect (i). In particular, in the latter techniques, correction for the partition coefficients may be a significant source of error.

## 6.2 DIFFUSION OF COLLOIDS AND MACROMOLECULES WITHIN GELS

Gel structures have been studied for several decades but are still the subject of debate. FCS has been used to observe aggregates and inhomogeneities [119,120] in agarose gels, and several techniques have been used to try to elucidate their complicated structure, such as SLS [121], X-ray scattering [115], SANS [122,123], transmission electron microscopy (TEM) [124], AFM [125] and NMR [126]. However, these techniques have led to a number of contradictory interpretations because they are sensitive to structures at different scales. Information on the gel structure can also be obtained from the diffusive behaviour of colloids and macromolecules. Unfortunately, there are only a few appropriate techniques to perform such studies over a large range of tracer and pore sizes. Pulse field gradient spin echo (PGSE) NMR has been used to study the diffusion of myoglobin in agarose and  $\lambda$ -carrageenan gels [127], but it provides an average signal for the whole gel.

PCS is not suitable, because of the strong background scattering and the large amount of diffusing particles required, which in turn may perturb the gel structure. Diffusing wave spectroscopy (DWS) [128,129] extends the range of application of traditional light-scattering techniques to systems which exhibit strong multiple scattering. Unfortunately, it is not selective and the size range of probes that can diffuse remains small. Single particle tracking (SPT) [130–132]) can be used, but in only a limited length range (0.2–15 µm) due to the low resolution of optical microscopy. In addition, the technique is time consuming and the reproducibility is poor. Methods based on fluorescence detection such as FRAP and FCS are advantageous because very local measurements, in dilute solutions, can be made. FRAP has been used to study the diffusion of dextran, DNA, proteins and latex beads in agarose gels [50]. In that case, it was shown that globular proteins and latex particles have a very similar diffusive behaviour. FCS is highly selective since only fluorescently labelled diffusing particles are observed. It can be used with compounds in a size range of 1–150 nm and hence large gel pore size distributions can be investigated. It has been used, in particular, for biochemical investigations of so-called anomalous diffusion in cell cytoplasm and membranes [133,134]. Anomalous diffusion [135,136] of particles (i.e. diffusion which cannot be described by Fick's first law) occurs in inhomogeneous porous fractal media, because in that case the diffusion process depends on the polydispersity of pore sizes, on their connectivity as a function of the size of the diffusing particle and on the scale (time or length) of observation. The agarose gel structure has been described as a mass fractal [137] and the corresponding diffusion properties of solutes as anomalous [138]. FCS is one of the very few appropriate techniques to study such systems because it can not only measure diffusion at the micrometre scale, but also enables mapping of diffusion properties to be performed on much larger surface areas, under minimally perturbing conditions.

The fractal structure does not affect the diffusion law in classical macroscopic observations, because of the averaging of data over large scales. However, at the scale of the test fractal structure, diffusion is anomalous. It may have a strong impact on solute transport across films or membranes with thicknesses comparable to the fractal structure. As shown below, FCS is unique in being able to determine such effects.

The diffusion behaviour of a particle within any medium can be characterised by its mean square displacements  $\langle r^2(t) \rangle$  vs time,  $t$ , which are as follows [135]:

$$\langle r^2(t) \rangle = \Gamma t^{\frac{2}{d_w}} \quad (19)$$

where  $\Gamma$  is the transport coefficient and  $d_w$  is defined as the fractal dimension of diffusion. When  $d_w = 2$ , the classical relationship,  $\langle r^2(t) \rangle \sim t$ , is obtained. When  $d_w \neq 2$ , because of the obstructions sensed by the particles, diffusion is considered to be ‘anomalous’. However, anomalous diffusion is not necessarily caused by a fractal matrix and can also be due to non-elastic interactions between the network and the diffusing particles [139]. Anomalous diffusion is different from trapped diffusion, where the particles are permanently trapped in holes without issue. In such cases, when  $t \rightarrow \infty$  the mean square displacements tend to a constant value. In the case of anomalous diffusion,  $D$  depends on the time-scale of the measurement [139]:

$$D(t) = \frac{1}{4} \Gamma t^{\frac{2}{d_w}-1} \quad (20)$$

and so  $d_w$  is a better parameter than  $D$  to characterise anomalous diffusion. Netz and Dorfmüller *et al.* [140] discussed the role of time and spatial scales in which anomalous diffusion applies. They investigated the diffusion processes by means of a 3D Monte Carlo (MC) simulation of hard spheres in random media approximating the topology of organic gels. They showed that normal, anomalous [141] or trapped [142] diffusion can occur in the same gel with heterogeneous structure, depending on the size ratio of particles and pores.

For anomalous diffusion, equation (5) is not applicable to the interpretation of FCS data. Schwille *et al.* [134] reported a more general equation, where the term  $\tau/\tau_c$  in equation (5) is replaced by  $(\tau/\tau_c)^\alpha$ , with  $\alpha = 2/d_w$  [see equation (19)]. The validity of introducing a fractal exponent in the analytical formula of the FCS–ACF for fractal gels is supported by the typical broadening of the corresponding FCS–ACF, which results from the heterogeneity of the porous medium and the reduced pore connectivity. This broadening cannot be modelled by equation (5). Qian *et al.* [143] studied the diffusion of fluorescent beads in actin gel and found a large broadening of the ACF. Guiot *et al.* [144] investigated the diffusion of latex particles and dextrans in microbial biofilms by FCS and fitted their data with an anomalous diffusion model. The mechanisms of anomalous diffusion are still not completely clear and theoretical equations need to be validated by experimental investigations.

The diffusive properties of solutes A introduced within agarose gel with varying sizes have been investigated by means of FCS [92], at infinite dilution to avoid coagulation of the colloids in the gel, and at high ionic strength to eliminate electrostatic effects (Section 6.1 [111]). The sizes of solutes varied from about 50 times less to two times more than the average pore size, and the data were interpreted with anomalous diffusion equations. The results were compared with the aforementioned MC simulations [140] in order to be validated. At first, the reduced diffusion coefficient,  $\sigma = \overline{D}_g^A / D_w^A$ , of a particle A within the gel was measured as a key parameter to characterise the porous material. Plots of  $\sigma$  values versus the hydrodynamic radius of the particle A,  $R_A$  (Figure 13), allowed for an estimation of (i) an average pore size of the gel by fitting  $\sigma$  vs  $R_A$  using the Johansson–Clague theories [145,146], (ii) the minimum size,  $R_c$ , of trapped, immobile, particles (which in turn gives an estimation of the largest pore size) and (iii) the nature of particles which interact chemically with the polymer fibres. This is observed for all compounds for which  $\sigma$  falls below the dotted line in Figure 13. Such a behaviour is different from anomalous diffusion. In Figure 13, the diffusing particles can be separated into two groups. A first group of compounds includes the organic dyes, the proteins and the latex beads: they have the upper values of  $\sigma$ , with small or negligible interactions with fibres, probably due to their relatively hydrophobic properties. The second group of compounds is composed of more hydrophilic compounds (silica, dendrimers, trace metals), which exhibit a clear affinity for the agarose network. From the first group of particles,  $R_c$  was estimated as 70 nm for a 1.5% agarose gel. This value is in good agreement with SANS analysis obtained with the same agarose gel ( $R_c \approx 80$  nm [117]). To compare the experimental data with theoretical MC computations [140], a reduced hydrodynamic radius for solutes A,  $R_A/R_c$ , was introduced (Figure 14). Values of  $d_w$  were obtained, for each colloid, by curve fitting of the ACF modified for fractal media [92]. The experimental results for the change of  $d_w$  with  $R_A/R_c$  were very similar to the theoretical predictions [140] (Figure 14) although, when  $R_A/R_c \rightarrow 0$ , experimental values of  $d_w$  tended to

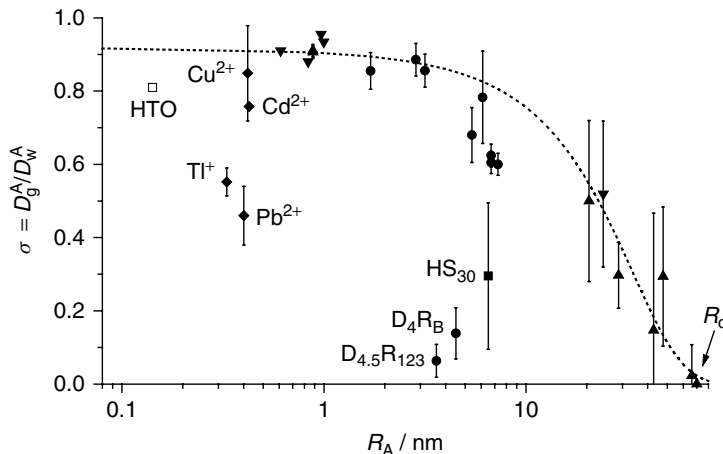


**Figure 13.**  $\sigma$  ( $I \geq 10^{-2}$  mol dm $^{-3}$ ) as a function of the hydrodynamic radius  $R_A$  for HTO (□), trace metals (◆), R6G, Nile Blue, R123, humic acids (▼), proteins (●), latex beads (▲), Ludox silica (HS<sub>30</sub>■), NH<sub>2</sub>- or CO<sub>2</sub>H-dendrimers (D<sub>4</sub>R<sub>B</sub> and D<sub>4.5</sub>R<sub>123</sub>, respectively) (■). The dashed line shows the compounds displaying only steric interactions with the gel. Reprinted from Fatin-Rouge, N., Starcher, K. and Buffle, J., Size effects on diffusion processes within agarose gels, *Biophysical J.*, 2004, **86**, 2710–2719, with permission from the Biophysical Society

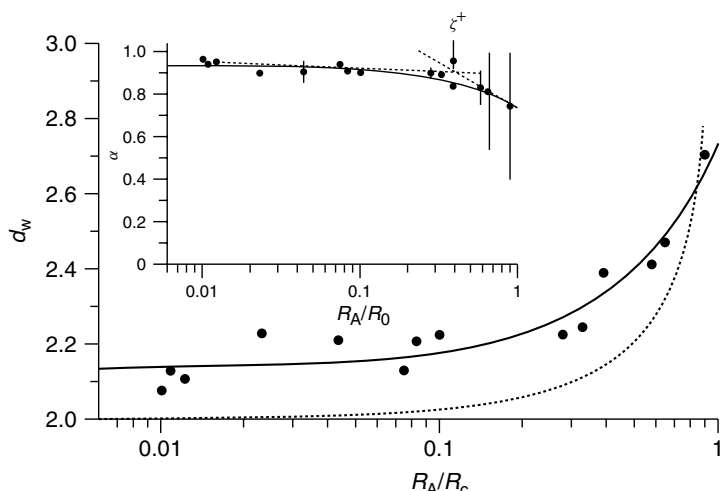


**Figure 14.** Plot of the fractal dimension of diffusion  $d_w$  as a function of the reduced particle size,  $R_A/R_c$ . Full line is simulated with the empirical equation (10) in [92]. Dashed line shows the MC simulations of beads diffusion in fractal polyacrylamide networks [140]. The inset is a plot of the fractal exponent  $\alpha$  dependence on reduced particle size. The reduced critical size,  $\xi^*$ , of agarose pores has been estimated as the intercept of tangent dotted lines (arrow). Phosphate-buffered solutions; pH = 7.0;  $I \geq 10^{-2}$  mol dm $^{-3}$ ;  $T = 20^\circ\text{C}$ . Reprinted from Fatin-Rouge, N., Starcher, K. and Buffle, J. (2004). Size effects on diffusion processes within agarose gels, *Biophysical J.*, **86**, 2710–2719, with permission from the Biophysical Society

2.1, whereas MC simulations converge to 2. Measurements conducted with various fibre fractions suggest that the difference in  $d_w$  values is the result of non-specific collisions of the diffusing particles with the polymer network. Nonetheless, an important observation is that both MC simulations [140] and experimental results [92] show that  $d_w$  varies little for  $R_A/R_c \leq 0.4\text{--}0.6 = \xi^*$ . Around  $\xi^*$  (see arrow in Figure 14), a transition step from anomalous to trapped diffusion is suggested by the rapid evolution of  $d_w$ . Above this value, the connectivity of the pores decreased rapidly and the movement of particles is entrapped in a limited volume. For  $R_A \geq R_c$ , particles are so tightly entrapped that their movement is forbidden. This suggests that free anomalous diffusion of particles only occurs over a limited range of length, because connectivity depends on reduced particle size.

## 7 SUMMARY AND PERSPECTIVES

From the discussion in this chapter, it should be clear that the major advantages of FCS for the measurement of the diffusion coefficients of molecules, macromolecules and colloids in environmental media are the following:

- It permits determinations of values of diffusion coefficients over several orders of magnitude, and it can provide information on the polydispersity of the sample.
- It is a very sensitive technique which requires very low concentrations of test compound.
- FCS can also be very selective through the appropriate choice of labelling procedures and the spectroscopic properties of the dyes.
- It allows the measurement of the diffusion coefficient of compounds in a very small volume ( $\sim 10^{-15}$  dm<sup>3</sup>) and with the capability of mapping values of diffusion coefficient over a surface with high spatial resolution.
- Finally, it is intrinsically a non-destructive method which is not limited to homogeneous solutions, but is also applicable to certain porous media.

All these characteristics are major advantages for applications in environmental media, which are physically and chemically heterogeneous systems, where the solutes of interest are often at very low concentrations, and mixed with many other compounds. In particular, as shown in Sections 5 and 6, on the basis of the above characteristics, FCS is a very powerful tool for studying not only the diffusion characteristics of a solute, but above all, the relationships between its physical transport properties, its chemical reactivity with other components of the medium and the physical structure of this medium. It is very likely that applications of this technique to environmental studies will develop more and more in the future.

At present, a major limitation of the technique is linked to the lack of well-tested procedures for non-denaturing labelling of environmental macromolecules and colloids. However, it is likely that this field will develop since it is also required for applications in biology and medicine. Another limitation is the small number of excitation wavelengths available. In particular, lasers in the near-UV region would be most useful for environmental applications. The development of lasers, however, is a fast-growing field and it is likely that the possible choice of lasers will improve in the near future. Finally, the

resolving power of FCS for distributions of diffusion coefficients should also be improved, as it may be an important limitation, particularly in environmental systems.

In general, the environmental applications of FCS seem very promising, also due to the new technical developments which have recently become commercially available. For instance, cross-correlation, in which two laser beams of different wavelengths cross to excite 'their' molecules in the same sample volume, allows the simultaneous measurement of the behaviours of each of the two components of a chemical reaction or of a hetero-coagulation process. The combination of FCS and fluorescence lifetime imaging spectroscopy (FLIM) will allow the diffusion/reaction of a compound to be studied at a well-defined location (*e.g.* reactive site of a plasma membrane, specific face of a clay particle). The use of time-resolved fluorescence or polarisation light in FCS may also be most useful to improve selectivity and promote applications in heterogeneous media.

## ACKNOWLEDGEMENTS

The Swiss National Foundation is gratefully acknowledged for its support of several projects on the development of FCS for environmental applications over the past 7 years.

## LIST OF SYMBOLS AND ABBREVIATIONS

A	Specific area ( $\text{m}^2 \text{ g}^{-1}$ )
AA	Acid anhydride
AAS	Atomic absorption spectrometry
AC	Acid chloride
ACF	Autocorrelation function
AFM	Atomic force microscopy
APD	Avalanche photodiode
$d_0$	Distance for 50% energy transfer (m)
$d_f$	Mass fractal dimension
$d_w$	Fractal exponent of diffusion
$c$	Concentration of species ( $\text{mol dm}^{-2}$ or $\text{mol dm}^{-3}$ )
$D_g^A$	Diffusion coefficient of particle A within the gel ( $\text{m}^2 \text{ s}^{-1}$ )
$D_w^A$	Diffusion coefficient of particle A in water ( $\text{m}^2 \text{ s}^{-1}$ )
DGT	Diffusive gradient in thin films
DLS	Dynamic light scattering
DWS	Diffusing wave spectroscopy
EDC	1-Ethyl-3-(3-dimethylaminopropyl)carbodiimide
$f$	Frictional coefficient
$f_{sp}$	Frictional coefficient of a sphere
$F$	Fluorescence intensity
FCS	Fluorescence correlation spectroscopy
FLIM	Fluorescence lifetime imaging spectroscopy
$F_p, F_f$	Fluorescence intensity of free particles or flocs respectively
FFFF	Flow field-flow fractionation

$F_T$	Triplet fraction
FRAP	Fluorescence recovery after photobleaching
$G$	Normalised autocorrelation function
GFP	Green fluorescent protein
GIME	Gel integrated microelectrode
HS	Humic substances
HPLC	High-performance liquid chromatography
$I$	Ionic strength ( $\text{mol dm}^{-3}$ )
ICPMS	Inductively coupled plasma mass spectrometry
IM	Imidazolidine
IR	Infrared
ITC	Isothiocyanate
$J$	Number of different fluorescent species
$k$	Kinetic rate constant
$K$	Equilibrium formation constant
$K_A^{\text{int}}$	Intrinsic equilibrium formation constant for solute A
$L$	Linear size
LIBD	Laser-induced breakdown dissociation
$\langle m \rangle$	Ensemble average of the number of empty holes
MALDI	Matrix-assisted laser desorption/ionisation mass spectrometry
$M$	Molar mass ( $\text{g mol}^{-1}$ )
MC	Monte Carlo
$N$	Mean number of particles in the confocal volume
NHSS	<i>N</i> -Hydroxysulfosuccinimide
NIR	Near-infrared
NOM	Natural organic matter
$O$	Confocal volume profile ( $\text{m}^3$ )
$p$	FCS structure parameter of the confocal volume
PAA	Polyacrylic acid
PCS	Photon correlation spectroscopy
PGSE	Pulsed-field gradient spin echo
$q$	number concentration ratio
$r$	Disaggregation rate
$R_c$	Critical radius (m)
$R_h, R_A$	Hydrodynamic radius of diffusing particle (m)
RB	Rhodamine B
R6G	Rhodamine 6G
R123	Rhodamine 123
$R_c$	Critical radius, i.e. the minimum size of completely trapped particles within the gel (m)
$R_p$	Average pore radius of a porous material (m)
SANS	small-angle neutron scattering
SC	Sulfonyl chloride
SE	Succinimidyl ester
$S_F$	Shape factor
SLS	Static light scattering

$SV$	FCS sample volume ( $\text{dm}^3$ )
$t$	Time (s)
TEM	Transmission electron microscopy
UV	Ultraviolet
$V_{\text{conf}}$	Confocal volume ( $\text{m}^3$ )
$\alpha$	Anomalous exponent
$\delta_F$	Fluctuation of fluorescence intensity
$\varepsilon$	Molar absorptivity ( $\text{dm}^2 \text{ mol}^{-1}$ )
$\phi$	Volume fraction of fibres in the gel
$\lambda$	Wavelength of light (m)
$\sigma$	Reduced diffusion coefficient in a porous medium
$\tau$	Delay time (s)
$\tau_c$	Diffusion time (s)
$\tau_f, \tau_p$	Diffusion times of the free label and the non-covalently labelled particles, respectively
$\tau_T$	Triplet time (s)
$\xi$	Correlation length or network mesh size (m)
$\xi^*$	Reduced correlation length
$\omega_z, \omega_{xy}$	Longitudinal and transverse radii of the SV, respectively
$\Gamma$	Transport coefficient ( $\text{m}^2 \text{ s}^{-1}$ )

## REFERENCES

1. Buffle, J. and van Leeuwen, H. P., eds (1992). *Environmental Particles*. Vol. 1, IUPAC Series on Analytical and Physical Chemistry of Environmental Systems, Series eds. Buffle, J and van Leeuwen, H. P., Lewis Publishers, Michigan.
2. Buffle J. and van Leeuwen H. P., eds. (1993). *Environmental Particles*. IUPAC Series on Analytical and Physical Chemistry of Environmental Systems, Vol. 2. J Lewis, Boca Raton, FL.
3. Huang, P. M., Senesi, N. and Buffle, J., eds (1998). *Structure and Surface Reactions of Soil Particles*. IUPAC Series on Analytical and Physical Chemistry of Environmental Systems, Vol. 4. John Wiley & Sons, Ltd, Chichester.
4. Huang, P. M., Bollag, J.-M. and Senesi, N., eds (2002). *Interactions Between Soil Particles and Microorganisms*. IUPAC Series on Analytical and Physical Chemistry of Environmental Systems, Vol. 8. John Wiley & Sons, Ltd, Chichester.
5. Stumm, W. and Morgan, J. J. (1996). *Aquatic Chemistry. Chemical Equilibria and Rates in Natural Waters*, 3rd edn. John Wiley & Sons, Inc., New York.
6. Stumm, W. (1992). *Chemistry of the Solid-Water Interface*. Wiley-Interscience, New York.
7. Guo, L. and Santschi, P. H. (1997). Composition and cycling of colloids in marine environments, *Rev. Geophys.*, **35**, 17–40.
8. Martin, J. M. and Dai, M. H. (1995). Significance of colloids in the biogeochemical cycling of organic carbon and trace metals in a coastal environment: example of the Venice Lagoon (Italy), *Limnol. Oceanogr.*, **40**, 119–131.
9. Buffle, J. and Leppard, G. G. (1995). Characterization of aquatic colloids and macromolecules. Part I: structure and behaviour of colloidal material, *Environ. Sci. Technol.*, **29**, 2169–2175.
10. Filella, M., Zhang, J., Newman, M. and Buffle, J. (1997). Analytical applications of photon correlation spectroscopy for size distribution measurements of natural colloidal suspensions: capabilities and limitations, *Colloids Surf. A*. **120**, 27–46.

11. Buffle, J. and Leppard, G. G. (1995). Characterization of aquatic colloids and macromolecules. Part II: the key role of physical structures on analytical results, *Environ. Sci. Technol.*, **29**, 2176–2184.
12. Wilkinson, K. J., Balnois, E. G., Leppard, G. G. and Buffle, J. (1999). Characteristic features of the major components of freshwater colloidal organic matter revealed by transmission electron and atomic force microscopy, *Colloids Surf. A*, **155**, 287–310.
13. Startchev, K., Wilkinson, K. and Buffle J. (2001). Application of FCS to study of environmental systems. In *Fluorescence Correlation Spectroscopy*, eds Rigler, R. and Elson, E. S. Springer, Berlin, pp. 251–275.
14. Buffle, J. (1998). *Complexation Reactions in Aquatic Systems: an Analytical Approach*. Ellis Horwood, Chichester.
15. Buffle, J., Wilkinson, K. J., Stoll, S., Filella, M. and Zhang, J. (1998). A generalized description of aquatic colloidal interactions: the three-colloidal component approach, *Environ. Sci. Technol.*, **32**, 2887–2899.
16. Filella, M. and Buffle, J. (1993). Factors controlling the stability of submicron colloids in natural waters, *Colloids Surf.*, **73**, 255–273.
17. Buffle, J. and van Leeuwen, H. P. eds. (1992). Foreword. In *Environmental Particles*, eds Buffle, J. and van Leeuwen, H. P. IUPAC Series on Analytical and Physical Chemistry of Environmental Systems, Vol. 1, Lewis, Boca Raton, FL.
18. Morris, E. R., Rees, D. A. and Robinson, G. (1980). Cation-specific aggregation of carrageenan helices: domain model of polymer gel structure, *J. Mol. Biol.*, **138**, 349–362.
19. Madge, D., Elson, E. L. and Webb, W. W. (1972). Thermodynamic fluctuations in a reacting system measurement by fluorescent correlation spectroscopy, *Phys. Rev. Lett.*, **29**, 705–708.
20. Maiti, S., Haupt, U. and Webb, W. W. (1997). Fluorescence correlation spectroscopy: diagnostics for sparse molecules, *Proc. Natl. Acad. Sci. USA*, **94**, 11753–11757.
21. Madge, D., Elson, E. L. and Webb, W. W. (1974). Fluorescence correlation spectroscopy. II. An experimental realization, *Biopolymers*, **13**, 29–61.
22. Eigen, M. and Rigler, R. (1994). Sorting single molecules application to diagnostics and evolutionary biotechnology, *Proc. Natl. Acad. Sci. USA*, **91**, 5740–5747.
23. Berland, L. M., So, P. T. C. and Gratton, E. (1995). Two-photon fluorescence correlation spectroscopy: method and application to the intracellular environment, *Biophys. J.*, **68**, 694–701.
24. Schwille, P. (2001). In *Fluorescence Correlation Spectroscopy. Theory and Applications*, eds Elson, E. L. and Rigler, R. Springer, Berlin, 360–370.
25. Webb, W. W. (1976). Applications of fluorescence correlation spectroscopy, *Q. Rev. Biophys.*, **9**, 49–68.
26. Schwille, P., Oehlenschläger, F. and Walter, N. G. (1996). Quantitative hybridization kinetics of DNA probes to RNA in solution followed by diffusional fluorescence correlation analysis, *Biochemistry*, **35**, 10182–10193.
27. Schwille, P., Haupt, U., Maiti, S. and Webb, W. W. (1999). Molecular dynamics in living cells observed by fluorescence correlation spectroscopy with one- and two-photon excitation, *Biophys. J.*, **77**, 2251–2265.
28. Hess, S. and Webb, W. W. (2002). Focal volume optics and experimental artifacts in confocal fluorescence correlation spectroscopy, *Biophys. J.*, **83**, 2300–2317.
29. Aragon, S. R. and Pecora, R. (1976). Fluorescence correlation spectroscopy as a probe of molecular dynamics, *J. Phys. Chem.*, **64**, 1791–1803.
30. Schwille, P., Meyer-Almes, J. F. and Rigler, R. (1997). Dual-color fluorescence cross-correlation spectroscopy for multicomponent diffusional analysis in solution, *Biophys. J.*, **72**, 1878–1886.
31. Widengren, J., Mets, U. and Rigler, R. (1995). Fluorescence correlation spectroscopy of triplet states in solution: a theoretical and experimental study, *J. Phys. Chem.*, **99**, 13368–13379.
32. Boersma, S. (1960). Rotational diffusion constant of a cylindrical particle, *J. Chem. Phys.*, **32**, 1626–1631.
33. Boersma, S. (1960). Viscous force constant for a closed cylinder, *J. Chem. Phys.*, **32**, 1632–1635.

34. Hearst, J. E. and Stockmayer, W. H. (1962). Sedimentation constants of broken chains and wormlike coils, *J. Chem. Phys.*, **37**, 1425–1433.
35. Yamakawa, H. (1971). *Modern Theory of Polymer Solutions*. Harper and Row, New York.
36. Van Holde, K. E. (1971). *Physical Biochemistry*. Prentice-Hall, Englewood Cliffs, NJ.
37. Cantor, C. R. and Schimmel, P. R. (1980). *Biophysical Chemistry, Part I. The Conformation of Biological Macromolecules*. Freeman, San Francisco.
38. Ortega, A. and Garcia de la Torre, J. T. (2003). Hydrodynamic properties of rodlike and disklike particles in dilute solution, *J. Chem. Phys.*, **119**, 9914–9919.
39. Leng, X., Startchev, K. and Buffle, J. (2001). Applications of fluorescence correlation spectroscopy: measurement of size–mass relationship of native and denatured schizophyllan, *Biopolymers*, **59**, 290–299.
40. Meunier, F. and Wilkinson, K. J. (2002). Non-perturbing fluorescent labelling of polysaccharides, *Biomacromolecules*, **3**, 857–864.
41. Börsch, M., Turina, P., Eggeling, C., Fries, J. R., Seidel, C. A. M., Labahn, A. and Gräber, P. (1998). Conformational changes of the H<sup>+</sup>-ATPase from *Escherichia coli* upon nucleotide binding detected by single molecule fluorescence, *FEBS Lett.*, **437**, 251–254.
42. Labille, J., Fatin-Rouge, N. and Buffle, J. Local and average diffusion of nanosolutes in agarose gel: the effect of the gel/solution interface structure. *Langmuir*. To print.
43. Haustein, E. and Schwille, P. (2003). Ultrasensitive investigations of biological systems by fluorescence correlation spectroscopy, *Methods*, **29**, 153–166.
44. Avena, M. and Wilkinson, K. J. (2002). Disaggregation kinetics of a peat humic acid: mechanism and pH effects, *Environ. Sci. Technol.*, **36**, 5100–5105.
45. Kettling, U., Koltermann, A., Schwille, P. and Eigen, M. (1998). Real-time enzyme kinetics monitored by dual-color fluorescence cross-correlation spectroscopy, *Proc. Natl. Acad. Sci. USA*, **95**, 1416–1420.
46. Müller, J. D., Chen, Y. and Gratton, E. (2000). Resolving heterogeneity on the single molecular level with the photon-counting histogram, *Biophys. J.*, **78**, 474–486.
47. Confocor 2. Zeiss, Carl Zeiss, 07740, Jena, Germany. 2004
48. Lead, J., Wilkinson, K. J., Startchev, K., Canonica, S. and Buffle, J. (2000). Diffusion coefficients of humic substances as determined by fluorescence correlation spectroscopy: role of solution conditions, *Environ. Sci. Technol.*, **34**, 1365–1369.
49. Petersen, N. O. and Elson, E. L. (1986). Measurements of diffusion and chemical kinetics by fluorescence photobleaching recovery and fluorescence correlation spectroscopy, *Methods Enzymol.*, **130**, 454–484.
50. Pluen, A., Netti, P. A., Rakesh, K. J. and Berk, D. A. (1999). Diffusion of macromolecules in agarose gels: comparison of linear and globular configurations. *Biophys. J.*, **77**, 542–552.
51. Startchev, K., Zhang, J. W. and Buffle, J. (1998). Applications of fluorescence correlation spectroscopy–particle size effect, *J. Colloid. Interface Sci.*, **203**, 189–196.
52. Vaz, W. L. C., Criado, M., Madeira, V. M. C., Schoellmann, G. and Jovin, T. M. (1982). Size dependence of the translational diffusion of large integral membrane proteins in liquid-crystalline phase lipid bilayers: a study using fluorescence recovery after photobleaching, *Biochemistry*, **21**, 5608–5612.
53. Startchev, K., Buffle, J. and Perez, E. (1999). Applications of fluorescence correlation spectroscopy – polydispersity measurements, *J. Colloid Interface Sci.*, **213**, 479–487.
54. Sengupta, P., Garai, K., Balaji, J., Periasamy, N. and Maiti, S. (2003). Measuring size distribution in highly heterogeneous systems with fluorescence correlation spectroscopy, *Biophys. J.*, **84**, 1977–1984.
55. Meseth, U., Wohland, T., Riegler, R. and Vogel, H. (1999). Resolution of fluorescence correlation measurements, *Biophys. J.*, **76**, 1619–1631.
56. Tanford, C. (1961). *Physical Chemistry of Macromolecules*. John Wiley & Sons, Inc., New York.
57. Thompson, N. L. (1991). Fluorescence correlation spectroscopy. In *Topics in Fluorescence Spectroscopy, Techniques*, Vol. 1, ed. Lakowicz, J. R. Plenum Press, New York, pp. 337–378.
58. Koppel, D. (1972). Analysis of macromolecular polydispersity in intensity correlation spectroscopy: the method of cumulants. *J. Chem. Phys.*, **57**, 4814–4820.

59. Lead, J. R., Wilkinson, K. W., Balnois, E., Cutak, B. J., Larive, C. R., Assemi, S. and Beckett, R. (2000). Diffusion coefficients and polydispersities of the Suwannee River fulvic acid: comparison of fluorescence correlation spectroscopy, pulsed-field gradient nuclear magnetic resonance, and flow field-flow fractionation, *Environ. Sci. Technol.*, **34**, 3508–3513.
60. Lead, J. R., Starchev, K. and Wilkinson, K. J. (2003). Diffusion coefficients of humic substances in water and through agarose gel, *Environ. Sci. Technol.*, **37**, 482–487.
61. Uyguner, C. S. and Bekbolet, M. (2004). Evaluation of humic acid, chromium(VI) and TiO<sub>2</sub> ternary system in relation to adsorptive interactions, *Appl. Catal. B*, **49**, 267–275.
62. Leng, X., Starchev, K. and Buffe, J. (2002). Adsorption of fluorescent dyes on oxide nanoparticles studied by fluorescence correlation spectroscopy, *Langmuir*, **18**, 7602–7608.
63. Chen, Y., Müller, J. D., Tetin, S. Y., Tyner, J. D. and Gratton, E. (1999). Probing ligand binding equilibria with fluorescence fluctuation spectroscopy, *Biophys. J.*, **76**, 1619–1631.
64. Leng, X. (2001). Application of fluorescence correlation spectroscopy to the study of particles and polymers interactions in model environmental systems, *Ph.D Thesis*, University of Geneva.
65. Novack, B. and Stone, A. T. (1999). The influence of metal ions on the adsorption of phosphonates onto Goethite, *Environ. Sci. Technol.*, **33**, 3627–3633.
66. Mak, S. Y. and Chen, D. H. (2004). Fast adsorption of methylene blue on polyacrylic acid-bound iron oxide magnetic nanoparticles, *Dyes Pigm.*, **61**, 93–98.
67. Ferretti, R. (1999). Mécanisme de floculation de particules d'hématite en présence d'acide polyacrylique et de schizophyllane, *Ph.D Thesis*, University of Geneva.
68. De Wolf, F. A. and Brett, G. M. (2000). Ligand-binding proteins: their potential for application in systems for controlled delivery and uptake of ligands, *Pharmacol. Rev.*, **52**, 207–236.
69. Larsson, A., Carlsson, C., Jonsson, M. and Albinsson, B. (1994). Characterization of the binding of the fluorescent dyes YO and YOYO to DNA by polarized light spectroscopy, *J. Am. Chem. Soc.*, **116**, 8459–8465.
70. Gaugain, B., Barbet, J., Capelle, N., Roquesand, B. P. and Le Pecq, J. B. (1978). DNA bifunctional intercalators. II. Fluorescence properties and DNA binding interaction of an ethidium homodimer and an acridine ethidium heterodimer, *Biochemistry*, **17**, 5078–5088.
71. Staros, J. V. (1986). Enhancement by *N*-hydroxysulfosuccinimide of water-soluble carbodiimide-mediated coupling reaction, *Anal. Biochem.*, **156**, 220–222.
72. Rahavendran, S. V. and Karnes, H. T. (1997). Visible diode laser-induced fluorescence detection of phenylacetic acid in plasma derivatized with Nile Blue and using precolumn phase transfer catalysis, *Anal. Chem.*, **69**, 3022–3027.
73. *Technical Literature: Reactive Fluorescent Dyes*. Molecular Probes, Eugene, OR; Hilyte Biosciences, San Jose, CA.
74. Panchuk-Voloshina, N., Haugland, R. P., Bishop-Stewart, J., Bhalgat, M. K., Millard, P. J., Mao, F., Leung, W. Y. and Haugland, R. P. (1999). Alexa dyes, a series of new fluorescent dyes that yield exceptionally bright, photostable conjugates, *J. Histochem. Cytochem.*, **47**, 1179–1188.
75. Czerney, P., Lehmann, F., Wenzel, M., Buschmann, V., Dietrich, A. and Mohr, G. (2001). Tailor-made dyes for fluorescence correlation spectroscopy, *Biol. Chem.*, **382**, 495–498.
76. Labas, Y. A., Gurskaya, N. G., Yanushevich, Y. G., Fradkov, A. F., Lukyanov, K. A., Lukyanov, S. A. and Matz, M. V. (2002). Diversity and evolution of the green fluorescent protein family, *Proc. Natl. Acad. Sci. USA*, **99**, 4256–4261.
77. Chalfie, M. and Kain, S. R. (1998). *GFP: Green Fluorescent Protein – Strategies and Applications*. John Wiley & Sons, Inc., New York.
78. Tsien, R. Y. (1998). The green fluorescent protein, *Annu. Rev. Biochem.*, **67**, 509–544.
79. Griffin, A. B., Adams, S. R. and Tsien, R. Y. (1998). Specific covalent labelling of recombinant protein molecules inside live cells, *Science*, **281**, 269–272.
80. Song, L., Hennink, E. J., Young, I. T. and Tanke, H. J. (1995). Photobleaching kinetics of fluorescein in quantitative fluorescence microscopy, *Biophys. J.*, **68**, 2588–2600.
81. Sjöback, R., Nygren, J. and Kubista, M. (1995). Absorption and fluorescence properties of fluorescein, *Spectrochim. Acta, Part A*, **51**, L7–L21.

82. Shin, H. S., Hong, K. H., Lee, M. H., Cho, Y. H. and Lee, C. W. (2001). Fluorescence quenching of three molecular weight fractions of a soil fulvic acid by UO<sub>2</sub>(II), *Talanta*, **53**, 791–799.
83. Förster, Th. (1948). Intermolecular energy migration and fluorescence, *Ann. Phys.*, **2**, 55–75.
84. Eiden-Assmann, S., Lindlar, B. and Maret, G. (2004). Synthesis and characterization of colloidal fluorescent mesoporous silica particles, *J. Colloid Interface Sci.*, **271**, 120–123.
85. Laguecir, A., Ulrich, S., Labille, J., Fatin-Rouge, N., Stoll, S. and Buffle, J. (2006) Size and pH effect on electrical and conformational behavior of poly(acrylic acid). Simulation and experiment. *European Polymer Journal*, **42**, 1135–1144.
86. Koehorst, R. B. M., Boschloo, G. K., Savenije, T. J., Goossens, A. and Schaafsma, T. J. (2000). Spectral sensitization of TiO<sub>2</sub> substrates by monolayers of porphyrin heterodimers, *J. Phys. Chem. B*, **104**, 2371–2377.
87. Pitschke, M., Fels, A., Schmidt, B., Heiliger, L., Kuckert, E. and Riesner, D. (1995). Polymeric fluorescent dyes for labelling of proteins and nucleic acids, *Colloid Polym. Sci.*, **273**, 740–752.
88. Janos, P. (2003). Sorption of basic dyes onto iron humate, *Environ. Sci. Technol.*, **37**, 5792–5798.
89. Davis, A. P. and Wareham, R. S. (1999). Carbohydrate recognition through noncovalent interactions: a challenge for biomimetic and supramolecular chemistry, *Angew. Chem. Int. Ed.*, **38**, 2978–2996.
90. Guthaus, E., Bürgle, M., Schmiedeberg, N., Hocke, S., Eickler, A., Kramer, M. D., Sweep, C. G. J. F., Magdolen, V., Kessler, H. and Schmitt, M. (2002). uPA-silica-particles (SP-uPA): a novel analytical system to investigate uPA–uPAR interaction and to test synthetic uPAR antagonists as potential cancer therapeutics, *Biol. Chem.*, **383**, 207–216.
91. Kashiwagi, Y., Norisuye, T. and Fujita, H. (1981). Triple helix of *Schizophyllum commune* polysaccharide in dilute solution. 4. Light scattering and viscosity in dilute aqueous sodium hydroxide, *Macromolecules*, **14**, 1220–1225.
92. Fatin-Rouge, N., Starchev, K. and Buffle, J. (2004). Size effects on diffusion processes within agarose gels, *Biophys. J.*, **86**, 2710–2719.
93. Davison, W. and Zhang, H. (1994). *In situ* speciation measurements of trace components in natural waters using thin-film gels, *Nature*, **367**, 546–548.
94. Tercier, M. L. and Buffle, J. (1996). Antifouling membrane-covered voltammetric microsensor for *in situ* measurements in natural waters, *Anal. Chem.*, **68**, 3670–3678.
95. Belmont-Hébert, C., Tercier, M. L. and Buffle, J. (1998). Gel-integrated microelectrode arrays for direct voltammetric measurements of heavy metals in natural waters and other complex media, *Anal. Chem.*, **70**, 2949–2956.
96. Pinheiro, J. P., Mota, A. M., Simões Gonçalves, M. L. S. and van Leeuwen, H. P. (1998). The pH effect in the diffusion coefficient of humic matter: influence in speciation studies using voltammetric techniques, *Colloids Surf. A*, **137**, 165–170.
97. Greter, F.-L. Buffle, J. and Haerdi, W. (1979). Voltammetric study of fulvic and humic substance. I. Behaviour of fulvic and humic complexes of lead on the mercury electrode. *J. Electroanal. Chem.*, **101**, 211–229.
98. Price, W. S. (1997). Pulsed field gradient nuclear magnetic resonance as a tool for studying translational diffusion: Part I. Basic theory, *Concepts Magn. Reson.*, **9**, 299–336.
99. Buffle, J., Deladoey, P., Zumstein, J. and Haerdi, W. (1982). Analysis and characterization of natural organic matter in freshwaters. I. Study of analytical techniques, *Schweiz. Z. Hydrol.*, **44**, 325–362.
100. Senesi, N. (1990). Molecular and quantitative aspects of the chemistry of fulvic acid and its interaction with metal ions and organic chemicals. II. The fluorescence spectroscopy approach, *Anal. Chim. Acta*, **232**, 77–106.
101. Cameron, R. S., Swift, R. S., Thornton, B. K. and Posner, A. M. (1972). Calibration of gel permeation chromatography materials for use with humic acid, *J. Soil Sci.*, **23**, 342–349.
102. Balnois, E., Wilkinson, K. J., Lead, J. R. and Buffle, J. (1999). Atomic force microscopy of humic substances. Effects of pH and ionic strength, *Environ. Sci. Technol.*, **33**, 3911–3917.

103. Leenheer, J. A., McKnight, D. M., Thurman, E. M. and McCarthy, P. (1995). *Humic Substances in the Suwannee River, Georgia: Interactions, Properties and Proposed Structures*. USGS Water Supply Paper 2373. US Geological Survey, Boulder, CO.
104. Lead, J. R., Balnois, E., Hosse, M., Menghetti R. and Wilkinson, K. J. (1999). Characterization of Norwegian natural organic matter: size, diffusion coefficients and electrophoretic mobilities, *Environ. Int.*, **25**, 245–258.
105. Yannaki, T. and Norisuye, T. (1983). Triple helix and random coil of scleroglucan in dilute solution, *Polym. J.*, **15**, 389–396.
106. Leng, X., Startchev, K. and Buffle, J. (2002). Application of fluorescence correlation spectroscopy: a study of flocculation of rigid rod-like biopolymer (schizophyllan) and colloidal particles, *J. Colloid Interface Sci.*, **251**, 64–72.
107. Leppard, G. G., Buffle, J. and Baudat, R. (1986). A description of the aggregation properties of aquatic pedogenic fulvic acids. Combining physico-chemical data and microscopic observations, *Water Res.*, **20**, 185–196.
108. Hirota, N., Kumaki, Y., Narita, T., Gong, J. P. and Osada, Y. (2000). Effect of charge on protein diffusion in charged hydrogels, *J. Phys. Chem. B*, **104**, 9898–9908.
109. Zhang, S. and Sun, Y. (2002). Ionic strength dependence of protein adsorption to dye-ligand adsorbents, *AIChE J.*, **48**, 178–186.
110. Johnson, E. M., Berk, D. A., Rakesh, K. J. and Deen, W. M. (1995). Diffusion and partitioning of proteins in charged agarose gels, *Biophys. J.*, **68**, 1561–1568.
111. Fatin-Rouge, N., Milon, A., Buffle, J., Goulet, R. R. and Tessier, A. (2003). Diffusion and partitioning of solutes in agarose hydrogels: the relative influence of electrostatic and specific interactions, *J. Phys. Chem. B*, **107**, 12126–12137.
112. Dumitau, S. (1998). *Polysaccharides – Structural Diversity and Functional Versatility*. Marcel Dekker, New York.
113. FMC (1982). *The Agarose Monograph*. FMC Corporation.
114. Araki, C. and Arai, K. (1967). Studies on the chemical constitution of agar-agar. XXIV. Isolation of a new disaccharide as a reversion product from acidic hydrolyzate, *Bull. Chem. Soc. Jpn.*, **40**, 12–1456.
115. Arnott, S., Fulmer, A., Scott, W. E., Dea, C. M., Moorhouse, R. and Rees, D. A. (1974). Agarose double helix and its function in agarose gel structure, *J. Mol. Biol.*, **90**, 269–284.
116. Rees, D. A. (1969). Structure, conformation, and mechanism in the formation of polysaccharide gels and networks, *Carbohydr. Chem. Biochem.*, **24**, 267–332.
117. Fatin-Rouge, N., Wilkinson, K. and Buffle, J. (2006) J. Phys. Chem. B. Combining SANS and FCS measurements to relate diffusion in agarose gels to their structure. In press.
118. Renkin, E. M. (1954). Filtration, diffusion, and molecular sieving through porous cellulose membranes, *J. Gen. Physiol.*, **38**, 225–243.
119. Stellwagen, J. and Stellwagen, N. (1994). Transient electric birefringence of agarose gels. I. Unidirectional electric fields, *Biopolymers*, **34**, 187–201.
120. Waki, S., Harvey, J. D. and Bellamy, A. R. (1982). Study of agarose gels by electron microscopy of freeze-fractured surfaces, *Biopolymers*, **21**, 1909–1926.
121. Manno, M. and Palma, M. (1997). Fractal morphogenesis and interacting processes in gelation, *Phys Rev. Lett.*, **79**, 4286–4289.
122. Krueger, S., Plopis, A. and Nossal, A. (1994). Small angle neutron scattering studies of structural characteristics of agarose gels, *Biophys. Chem.*, **53**, 85–94.
123. Jaecques, S. V., Helsen, J. A. and Teixeira, J. J. (1996). SANS and swelling assessment of the structural properties of the thermoplastic elastomers Santoprene<sup>TM</sup> and Sarlink<sup>TM</sup>, *J. Appl. Polym. Sci.*, **61**, 819–826.
124. Attwood, T. K., Nelmes, B. J. and Sellen, D. B. (1988). Electron-microscopy of beaded agarose gels, *Biopolymers*, **27**, 201–212.
125. Pernodet, N., Maaloum, M. and Tinland, B. (1997). Pore size of agarose gels by atomic force microscopy, *Electrophoresis*, **18**, 55–58.
126. Chui, M. M., Phillips, R. J. and McCarthy, M. J. (1995). Measurement of the porous Microstructure of hydrogels by nuclear magnetic resonance, *J. Colloid Interface Sci.*, **174**, 336–344.
127. Hirota, N., Kumaki, Y., Narita, T., Gong, J. P. and Osada, Y. (2000). Effect of charge on protein diffusion in hydrogels, *J. Phys. Chem. B*, **104**, 9898–9903.

128. Urban, C., Romer, S., Scheffold, F. and Schurtenberger P. (2000). Structure, dynamics and interactions in concentrated colloidal suspensions and gels, *Prog. Colloid Polym. Sci.*, **115**, 270–274.
129. Pine, D. J., Weitz, D. A., Chaikin, P. M. and Herbolzheimer, E. (1988). Diffusing-wave spectroscopy, *Phys. Rev. Lett.*, **60**, 1134–1137.
130. Ghosh, R. N. and Webb, W. W. (1988). Results of automated tracking of low density lipoprotein receptors on cell surfaces, *Biophys. J.*, **53**, 352.
131. Starchev, K., Sturm, J., Weill, G. and Brogren, C.-H. (1997). Brownian motion and electrophoretic transport in agarose gels studied by epifluorescence microscopy and single particle tracking analysis, *J. Phys. Chem.*, **101**, 5659–5663.
132. So, P. T., Konig, K., Berland, K., Dong, C. Y., French, T., Buhler, C., Ragan, T. and Gratton, E. (1998). New time-resolved techniques in two-photon microscopy, *Cell Mol. Biol.*, **44**, 771–793.
133. Berland, K. M., So, P. T. C. and Gratton, E. (1995). Two-photon fluorescence correlation spectroscopy: method and application to the intracellular environment, *Biophys. J.*, **68**, 694–701.
134. Schwille P., Korlach, J. and Webb, W. W. (1999). Fluorescence correlation spectroscopy with single-molecule sensitivity on cell and model membranes, *Cytometry*, **36**, 176–182.
135. Havlin, S. (1989). Molecular diffusion and reactions. In *The Fractal Approach to Heterogeneous Chemistry*, ed. Avnir, D. John Wiley & Sons, Ltd, Chichester, pp. 251–269.
136. Havlin, S. and Ben-Avraham, D. (1987). Diffusion in disordered media, *Adv. Phys.*, **36**, 695–798.
137. Manno, M., Emanuelle, A., Martorana, V., Bulone, D., San Biagio, P. L., Palma-Vittorelli, M. B. and Palma, M. (1999). Fractal morphology and interacting processes in gelation, *Phys. Rev. E*, **59**, 4286–4289.
138. Harder, H., Havlin, S. and Bunde, A. (1987). Diffusion on fractals with singular waiting-time distribution, *Phys. Rev. B*, **36**, 3874–3879.
139. Saxton, M. J. (2001). Anomalous subdiffusion in fluorescence photobleaching recovery: a Monte Carlo study, *Biophys. J.*, **81**, 2226–2240.
140. Netz, P. A. and Dorfmuller, T. (1995). Computer simulation studies of anomalous diffusion in gels: structural properties and probe-size dependence, *J. Phys. Chem. B*, **103**, 9074–9082.
141. Saxton, M. J. (1994). Anomalous diffusion due to obstacles: a Monte Carlo study, *Biophys. J.*, **66**, 394–401.
142. Kerstein, A. R. (1985). Diffusion in a medium with connected traps, *Phys. Rev. B*, **32**, 3361–3363.
143. Qian, H., Elson, E. and Frieden, C. (1992). Studies on the structure of actin gels using time correlation spectroscopy of fluorescent beads, *Biophys. J.*, **63**, 1000–1010.
144. Guiot, E., Georges, P., Brun, A., Fontaine-Aupart, M. P., Bellon-Fontaine, M. N. and Brian-det, R. (2002). Heterogeneity of diffusion inside microbial biofilms determined by fluorescence correlation spectroscopy under two-photon excitation, *Photochem. Photobiol.*, **75**, 570–578.
145. Johansson, L., Elvingsson, C. and Löfroth, J. E. (1991). Diffusion and interaction in gels and solutions. 3. Theoretical results on the obstruction effect. *Macromolecules*, **24**, 6024–6029.
146. Clague, D. S. and Phillips, R. J. (1996). Hindered diffusion of spherical macromolecules through dilute fibrous media, *Phys. Fluids*, **8**, 1720–1731.



---

# 12 Laser-induced Breakdown Detection

---

JAE-IL KIM AND CLEMENS WALTHER

*Institut für Nukleare Entsorgung, Forschungszentrum Karlsruhe, PO 3640, D-76021  
Karlsruhe, Germany*

1	Introduction . . . . .	556
2	The Development of LIBD . . . . .	556
3	The Physics Behind the Technique . . . . .	559
3.1	Multi-Photon Ionisation of Atoms . . . . .	559
3.2	Flux Density Distribution in a Laser Focus and ‘Focal Volume’ . . . . .	562
3.3	From the Electron Number to the Breakdown Probability . . . . .	567
4	Experimental Approaches . . . . .	573
4.1	Bubble Detection . . . . .	573
4.2	Detection by Thomson Scattering . . . . .	573
4.3	Optical Detection . . . . .	574
4.4	Laser-Induced Breakdown Spectroscopy . . . . .	578
4.5	Acoustic Detection . . . . .	579
4.6	Comparison of Optical and Acoustic LIBD . . . . .	580
4.7	Measurement of Size Distribution by Acoustic LIBD . . . . .	581
5	Applications . . . . .	584
5.1	Aquatic Colloids in Drinking Water . . . . .	585
5.2	Colloid Formation and Thermodynamic Equilibria . . . . .	585
5.3	Aluminosilicate Colloids . . . . .	587
5.4	Migration of Aquatic Colloids . . . . .	588
5.5	Colloids in Deep Underground Waters . . . . .	590
5.6	Aggregation of Bentonite Colloids . . . . .	592
5.7	LIBD on Organic Colloids . . . . .	594
5.8	LIBD and LIBS on Aerosols . . . . .	595
5.9	LIBS on Aquatic Colloids . . . . .	595
6	Practical Remarks when using LIBD . . . . .	596
7	Conclusions and Future Perspectives . . . . .	598
Symbols . . . . .		599
Glossary . . . . .		602
References . . . . .		605

## 1 INTRODUCTION

Laser-induced breakdown detection (LIBD) is a colloid detection method utilising plasma formation in the high field of a focused laser beam. Size distributions of colloids between 5 and 1000 nm of mass concentrations down to  $10^{-9}$  g dm $^{-3}$  can be measured, often without sample pretreatment, both in the laboratory and in field experiments. The method is ‘non-invasive’ in the sense that the detected colloid itself is destroyed in the plasma of the microprobe, but since only a marginal fraction of the total colloid number is used for characterisation, the sample is virtually unaffected. This allows repeated measurements of a single sample, for instance when studying time resolved colloid stability.

This chapter starts with a historical overview of LIBD development and applications (Section 2) followed by details of the breakdown process and a short mathematical treatment (Section 3). Since LIBD is not yet a commercial method, this section instructs readers on how to build a machine and evaluate LIBD data themselves. Existing LIBD instrumentations are described (Section 4) and cross-referenced to the respective theoretical grounds of (Section 3). Selected applications are discussed (Section 5) and some important remarks on how to use LIBD in practice and in day-to-day operations follow (Section 6). The chapter closes with conclusions, future perspectives, a list of all variables and symbols used in this chapter and a glossary where the most important technical terms are explained.

## 2 THE DEVELOPMENT OF LIBD

The first laser-induced breakdown spectroscopy (LIBS) experiments were reported for the microanalysis of solids [1], shortly after the development of the ruby laser [2]. The analysis of liquids and gases followed (see, *e.g.* review by Rusak *et al.* [3]). In spite of the closely related principle, the investigation of colloids by LIBD required a different approach. In the late 1980s, Kitamori and co-workers tried to quantify the very low colloidal contamination of process liquids in semiconductor manufacturing. They made use of the photoacoustic effect, first observed by A. G. Bell in 1880: matter that absorbs light heats up, expands and generates an acoustic signal. Historically, the method was investigated first for bulk solids. However, the most important application in aquatic chemistry is laser-induced photoacoustic spectroscopy (LPAS) for the detection and speciation of solvated ions [4]: the signal scales linearly with the intensity of the light source, hence the intense light of a laser in combination with a very sensitive microphone results in very low detection limits. A similar principle was applied for colloid detection. The acoustic wave is picked up by a piezo-receiver, and particles in the sub-micrometre size range are detected at very low concentrations. Kitamori *et al.* [5] tried to lower the detection limit by focusing the laser beam. A continual increase in flux density lead to breakdown (BD) and plasma formation in water, which was a well known local phenomenon by that time [6]. Kitamori *et al.* were the first to ascertain the breakdown process on colloids in the laser focal region [7]. The expansion of the hot plasma gave rise to a shock wave which was easily detected by a piezo-receiver (Figure 1).

The number of BD events relative to the total number of laser pulses (breakdown probability, BDP) turned out to be directly proportional to the particle number density of colloids with a detection limit down to  $10^4$  particles cm $^{-3}$  [8]. More detailed investigations

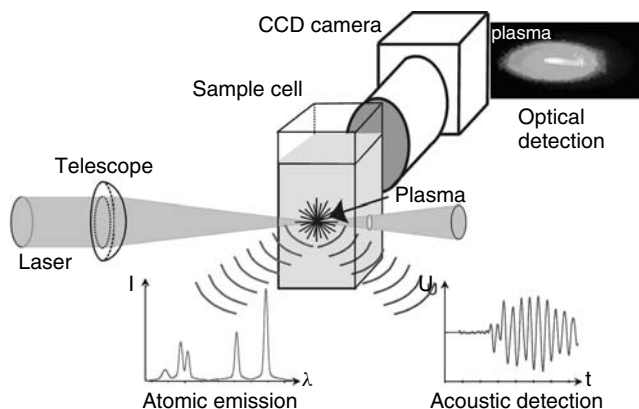


**Figure 1.** The plasma created by a pulsed laser causes an acoustic wave, which is detected by a piezoelectric receiver. In addition, the emitted light can be detected by a spectrometer or spatially resolved by a microscope lens and a CCD camera. Adapted from Walther, C. (2003). Comparison of colloid investigation by single particle analytical techniques – a case study on thorium-oxyhydroxides, *Colloids and Surfaces A*. **217**, 81–92, with permission from Elsevier

followed: an increase in detection volume and laser pulse energy led to a further improvement in sensitivity down to  $10^{-11}$  g dm $^{-3}$ , corresponding to only 100 particles cm $^{-3}$  of 38 nm polystyrene particles [8]. Theoretical treatments of the breakdown process were based on previous work on plasma formation in pure water [9,10]. A size dependence of the BD threshold was reported shortly thereafter, allowing an appraisal of the mean particle size in addition to the number concentration [11]. The second part of this work focused on the optical emission. The plasma which typically is heated to 15 000–20 000 K, emits both blackbody radiation and atomic emission and, due to the high density of electrons, absorbs and scatters the late part of the laser pulse (Section 3). As observed by a streak camera, the time period between laser pulse and plasma emission was found to decrease with increasing particle size. However, the inherent scattering of data was very large and the size resolution too low to apply this correlation for particle sizing. The same holds for a functional dependence of the emission intensity on the delay time [12].

Even though the spectroscopic signal cannot be applied to particle sizing, it is possible to use it to gain information on the elemental composition of colloids. Kitamori *et al.* observed emission from CaCO<sub>3</sub> [13] and Ito *et al.* detected colloidal iron at concentrations below 10 $^{-3}$  g dm $^{-3}$  with a coaxial nozzle arrangement, where a thin stream of liquid is surrounded by an atmosphere of argon [14]. The detection limit was lowered to  $1.6 \times 10^{-5}$  g dm $^{-3}$  by using a second laser pulse for plasma heating [15], a technique well known for bulk solids [16] and taken up again by Pu *et al.* [17] for detection of PbCO<sub>3</sub> colloids down to  $1.4 \times 10^{-5}$  g dm $^{-3}$ . Generally, the presence of colloids strongly enhances the LIBS signal. Knopp *et al.* demonstrated that Er<sup>3+</sup> could not be detected as dissolved ion, even at g dm $^{-3}$  concentrations. However, ErBa<sub>2</sub>Cu<sub>3</sub>O<sub>x</sub> colloids of 200 nm diameter gave rise to strong Er lines down to concentrations below 10 $^{-3}$  g dm $^{-3}$  [18]. Yun *et al.* performed spectroscopy on europium(III) oxide and hydroxide colloids. The atomic emission intensity of the Eu<sub>2</sub>O<sub>3</sub> suspension was about two orders of magnitude higher than that of the Eu<sup>3+</sup> aquo ion and allowed spectroscopy down to  $2 \times 10^{-7}$  mol dm $^{-3}$  [19].

The higher sensitivity facilitates selective detection for the colloids even in the presence of bulk ionic species. This principle is used for solubility measurements (see below and Section 5). The emission signal can even be enhanced by the presence of colloids of different composition, as reported for Eu ions sorbed on  $\text{TiO}_2$  particles [19]. Plasma emission spectroscopy in liquids suffers from various line broadening effects and thus spectral resolution is typically limited to about 1 nm. However, Nakamura *et al.* showed that even the very small plasma generated on colloids can act as an ‘optical gain medium’ allowing amplified atomic emission [20]. They showed that laser action takes place in a plasma of polystyrene particles by measuring the isotope shifts of the hydrogen and deuterium Balmer  $\text{H}\alpha$  lines with a resolution of 0.1 nm [21].

The majority of work on laser-induced breakdown in colloidal suspensions has focused on particle sizing. Scherbaum *et al.* [22] published a statistical model, which described the BD probability as a function of the pulse energy using polystyrene beads of various sizes at different concentrations. Data gained by an excimer–dye system and acoustic detection corroborate this approach. In addition, the material dependence of the breakdown process has been investigated for polystyrene, thoria ( $\text{ThO}_2$ ) and alumina ( $\text{Al}_2\text{O}_3$ ) [22]. This technique was applied amongst others to investigate natural systems such as drinking waters, ground waters and water in waste repositories [23] as well as contaminants in the primary cooling circuit of a nuclear power reactor [24]. With the approach based on the same physical concept as given in [11], but with acoustic detection, Izumida *et al.* [25] made use of the variation in delay time between the laser pulse and acoustic wave for the appraisal of the size and composition of the colloids, namely for silica, polystyrene, iron ( $\text{Fe}_2\text{O}_3$ ) and gold particles. In this study, gold and iron colloids were significantly smaller than both polystyrene and silica particles, as known from electron microscopy. Whereas polystyrene and silica particles behaved similarly, gold and iron colloids showed considerably lower thresholds. The authors explained this effect by the lower breakdown threshold of metal surfaces compared with optically transparent media. Saito *et al.* [26] suggested a further enhancement in detection efficiency: by the use of standing acoustic plane waves, colloids were accumulated in the nodes. When the laser focus was located inside one of these ‘particle bands’, the probability of particle detection was strongly enhanced over simple diffusion into the focal volume by Brownian motion.

The effect of various laser parameters on the detection efficiency was investigated by Bundschuh *et al.* [27], who compared an Nd:YAG-based system with an excimer–dye apparatus with various focusing optics. They claimed a detection limit of colloids as small as  $0.64 \pm 0.33$  nm, based on model calculations. Partin [28] announced their intention to combine the LIBD and LIBS techniques in a single mobile apparatus that could be sold commercially; however, to our knowledge, such an instrument is not yet available.

Another approach for particle sizing, using spatially resolved imaging of the optical plasma emission, was reported in 1991 and patented in 1994 [29]. The focal region of the laser beam is imaged by a lens onto a two-dimensional array photodetector and the position of a plasma plume along the laser beam axis is recorded for every single breakdown. Small particles create plasma events solely in the centre region, whereas the events of large particles are spread over an extended volume, described as a large ‘ignition length’ or large ‘effective focal length’ ( $l_Z$ ). This quantity can be calibrated versus particle size with some 20% precision. Bundschuh *et al.* [30] demonstrated a power law dependence of  $l_Z$  versus the colloid diameter between 20 nm and 1  $\mu\text{m}$ , which is only weakly dependent

on the colloidal material (Section 3.3). The BDP increases roughly linearly with colloid concentration (Section 4). They applied the method for the characterisation of granitic ground water. Based on the same technique, Hauser *et al.* [31] built a mobile LIBD, which was used in field measurements. The groups of Hauser and Moeri reported real time, *in situ* observations of the colloid-mediated migration of trace elements in underground laboratories in Grimsel (Switzerland) [31,32] and Äspö (Sweden) [33]. The results were in agreement with off-line measurements (ICP-MS, light scattering and gamma-ray detection). Using a diode-pumped TEM<sub>00</sub>-Nd:YAG laser<sup>1</sup>, an optimal Gaussian profile in the focal region was realised [34], which is a prerequisite to verifying mathematical predictions on the BD probability and position. In order to locate the plasma in three dimensions, an image of the BD position in the laser focal volume was obtained by two CCD cameras, perpendicular to each other.

Recent applications of LIBD (Section 5) have included characterisation of bentonite colloids in ground water [35], the determination of particle contents of drinking water (Section 5.1) before and after purification [36,37] and *in situ* observation of ZrO<sub>2</sub>–colloid aggregation down to  $2 \times 10^6$  particles cm<sup>-3</sup> [38]. Within the framework of nuclear waste disposal safety assessment, thermodynamic solubility data of actinides were gained by investigating colloid formation in oversaturated solutions, in particular plutonium(IV) [39–42], neptunium(IV) [43] (Section 5.2) and thorium [93,44–46]. Detection and spectroscopy of americium(III)–colloids was reported [47], and interaction of actinides (americium and curium) with nascent aluminosilicate colloids investigated in great detail [48,49] (Section 5.3). A combination of laser-induced fluorescence and LIBD has been applied for the sorption of curium(III) on cement and formation of curium-containing colloids [50].

In addition to the ‘stand-alone’ applications, LIBD has been used for sensitive detection in combination with a size fractionating method. This is particularly useful, when no reference colloids of a certain size fraction are available, *e.g.* in the range below 20 nm. Manh *et al.* [51] reported a three orders of magnitude sensitivity enhancement when LIBD replaced the light-scattering detector of a commercial flow field-flow fractionation (FFFF) instrument (Chapter 5). A multiple combination of UV–VIS, ICP-MS, LIBD and FFFF facilitated the characterisation of humic colloids in ground water in detail [52].

### 3 THE PHYSICS BEHIND THE TECHNIQUE

It is obvious from the name of the method, ‘laser-induced breakdown detection’, that breakdown plays a central role in the underlying physical processes [53]. But how do we define a ‘breakdown’? The expression originates from the breakdown of classical dielectric properties of a given medium due to the presence of free charge carriers. As a common convention in the literature, the minimum density of electrons needed to speak of a breakdown is chosen to be  $10^{18}$  electrons cm<sup>-3</sup> [16]. In the following, the generation processes will be examined in a short overview in order to understand how LIBD works and provide sufficient information to apply correctly and understand the limitations of the method.

#### 3.1 MULTI-PHOTON IONISATION OF ATOMS

When matter interacts with light of a pulsed laser beam, there are several possibilities of producing electrons. Direct photo-ionisation is a very efficient process as long as the

---

<sup>1</sup> Basic transverse mode; see Glossary.

photon energy  $E_{\text{Ph}} = h\nu$  ( $h$  is Planck's constant,  $\nu$ - is the frequency of light) exceeds the energy to liberate one electron (ionisation energy,  $E_I$ ). However, for visible light ( $h\nu = 1.5 - 3 \text{ eV}$ ) this is not the case, since most materials have an ionisation energy (work function, or band gap for solids<sup>2</sup>) between 6 and 10 eV [54]. The simultaneous absorption of  $m > 1$  photons is required and one speaks of multiphoton ionisation (MPI) of order  $m$  [55,56].

In general this is a non-resonant process, which scales proportionally to the  $m$ th order of the photon flux-density and is very unlikely for 'long-pulse' lasers (nanoseconds and longer). This can be depicted as follows: in order to excite one electron of a molecule above the ionisation energy, all  $m$  photons have to be absorbed 'simultaneously', i.e., before the energy is dissipated on a picosecond time-scale. Below saturation, an increase in electron number  $N_e$ , equation (1), can be expressed in terms of the number of (neutral) molecules in the focal volume  $N_M$  [56], the power density  $I$  of the laser and the MPI cross-section  $\mu_m$  [in general all quantities may depend on space coordinate and time (Section 4)].

$$\left( \frac{\partial N_e}{\partial t} \right)_{\text{MPI}} = -\frac{\partial N_M}{\partial t} = N_M(t) \mu_m I(t)^m \quad (1)$$

For nanosecond pulses, this process is very unlikely and can generate only a few electrons per laser shot. The majority of charge carriers have to be provided by a second process, cascade multiplication, which is also referred to as inverse bremsstrahlung<sup>3</sup> (IB) (Figure 2). Once free electrons are present in the focus, they will be accelerated by the

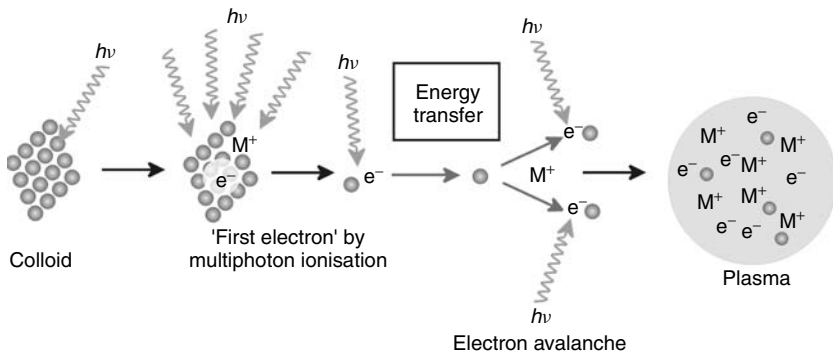


**Figure 2.** Nanosecond-laser induced plasma formation can be understood by the following model: a few 'first' electrons are produced by non-resonant multiphoton ionisation during the laser pulse. These electrons gain energy in the electric field of the laser by inverse bremsstrahlung which then produce further electrons via collisions with constituents of the colloid (atoms or molecules). Within a few nanoseconds, more than  $10^{18} \text{ electrons cm}^{-3}$  are generated and a dense, hot (15 000–20 000 K) plasma is formed. Drawing from [57]

<sup>2</sup> In the case of atoms or molecules in the gas phase, the energy to free one electron is referred to as ionisation energy (former expression: ionisation potential). For solids, this energy is named electron work function and in the case of (semi-)conductors the respective quantity is the gap between valence and conduction bands. In this chapter we will use the term *ionisation energy* irrespective of the medium.

<sup>3</sup> See glossary.

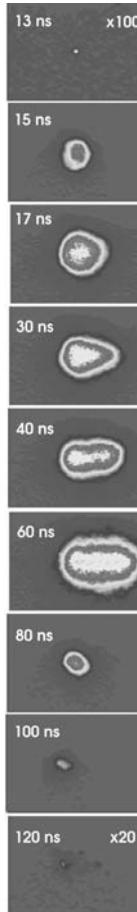


**Figure 3.** Evolution of the plasma plume induced by ns-laser pulses (532 nm), imaged by an ultrafast CCD camera

electric field of the laser and a few of them will gain energy that is greater than the ionisation energy of neighbouring atoms or molecules. In this case, a collision can ionise a molecule and detach one additional electron, which in turn is accelerated and may ionise further molecules. This repeated effect leads to an avalanche-like increase in the electron density within a few nanoseconds (Figure 3) and is the dominant electron production process for nanosecond pulses [58]. For gases [59], liquids [9] and solids [60], multiphoton ionisation and avalanche ionisation have been investigated in great detail and are well understood.

An increase of the electron density with time can be expressed by the following differential equation:

$$\frac{\partial N_e}{\partial t} = \left( \frac{\partial N_e}{\partial t} \right)_{MPI} + \eta(E)N_e - \left( \frac{\partial N_e}{\partial t} \right)_{loss} \quad (2)$$

where  $\eta(E)$  is the rate at which an electron of energy  $E$  undergoes an ionising collision. The third term represents a decrease in electron number due to diffusion out of the focal region and recombination or trapping processes. The relative importance of these terms depends strongly on the laser pulse duration [58,61,62]. For nanosecond-laser pulses, diffusional loss can be neglected and the electron density increases exponentially, once some ‘seed’ electrons are generated by MPI. Two important conclusions drawn from this model should be noted:

1. The generation of the first electron represents the ‘bottleneck’ of plasma formation in the case of very pure materials without ‘free’ electrons, due to the polynomial dependence of equation (1) and a small value of the cross-section  $\mu_m$ .
2. The cascade multiplication process has to be initiated early enough in the laser pulse to generate a high density of electrons. Only then will the plasma absorb laser light efficiently and become hot enough to be detected.

Both effects give rise to a *threshold behaviour* [63]. Below the lowest pulse energy, no plasma can be detected. The precise value of this threshold depends on the mechanism and efficiency of plasma detection, which are the most important criteria for LIBD, and on the plasma ignition material.

### 3.2 FLUX DENSITY DISTRIBUTION IN A LASER FOCUS AND ‘FOCAL VOLUME’

Equations (1) and (2) are valid for a homogeneous distribution of molecules and a homogeneous photon flux. Unfortunately, the latter cannot be achieved by focusing a laser beam with refractive optics. Holographic elements, on the other hand, cannot handle the small spot size (typically  $\lesssim 10 \mu\text{m}$ ) required for breakdown generation. Hence one has to deal with photon flux that varies within the focal volume. The power density  $I$  and the absolute molecule and electron numbers ( $N_M$  and  $N_e$ ) in equation (1) are replaced by the space-dependent power density  $I(\vec{r}, t)$  and the respective number densities ( $\rho_M$  and  $\rho_e$ ). Absolute electron numbers are calculated later on by integration over space [see equation (26)]:

$$\frac{\partial \rho_M(t)}{\partial t} = -\rho_M(t)\mu_m I(\vec{r}, t)^m \quad (3)$$

The power density in the focus must first be calculated. As detailed treatments can be found in basic textbooks [64,65], only a short description is given here in order to define the technical terms needed later on.

A laser pulse of energy  $E_0$  and duration  $t_0$  has a mean power of

$$P_0 = \frac{E_0}{t_0} \quad (4)$$

When the area of the spot is  $A$ , the mean power density is

$$I = \frac{E_0}{A t_0} \quad (5)$$

A common quantity for the treatment of linear processes is the photon flux density<sup>4</sup>:

$$\phi = \frac{\text{number of photons}}{\text{time area}} = \frac{E_0}{h\nu t_0 A} \quad (6)$$

where  $h\nu$  is the energy of one photon. Focusing a TEM<sub>00</sub> laser beam by a spherical lens (neglecting aberration effects) results in a diffraction-limited Gaussian focus, which is parameterised as follows:  $r_0$  is the radius perpendicular to the laser axis (*radial dimension r*), where the power density decreases to 1/e of the peak value:

$$P_0 := \int_0^{2\pi} \int_0^\infty I(r, \varphi) r d\varphi dr = I_0 \int_0^{2\pi} \int_0^\infty r e^{-\frac{r^2}{r_0^2}} d\varphi dr \quad (7)$$

$$= I_0 \frac{2\pi r_0^2}{2} \quad \text{and} \Rightarrow I_0 = \frac{P_0}{\pi r_0^2} \quad (8)$$

with the peak power density  $I_0$ . Since the 1/e-radius varies with the position along the laser beam axis,  $r_0 = r_0(z)$ , the power density can be written as

$$I(r, z) = \frac{P_0}{\pi r_0^2(z)} e^{-\frac{r^2}{r_0^2(z)}} \quad (9)$$

with the *longitudinal* dependence of the 1/e-radius  $r_0(z)$ , as given in [65, p. 27, equation (I.79)]

$$r_0(z) = r_0(0) \left[ 1 + \left( \frac{z\lambda}{n\pi r_0^2(0)} \right)^2 \right]^{\frac{1}{2}} \quad (10)$$

where  $\lambda$  is the wavelength of light and  $n$  the refractive index of the medium into which the beam is focused [in general  $n = n(\lambda)$ ]. The calculated  $r_0(z)$  are compared with measured data (■) [34] in Figure 4.

Scherbaum *et al.* [22] approximated the focal volume by an ellipsoid with volume

$$V_{\text{el}} = \frac{4}{3}\pi r_C^2 z_C \quad (11)$$

where  $r_C$  is the critical radius, i.e. the radius at  $z = 0$  (perpendicular to the laser beam), where the power density decreases to a value below the breakdown threshold for a given particle. At the same time,  $r_C$  is the short half-axis of the (prolate) ellipsoid (Figure 5). By analogy,  $z_C$  is the critical distance from the focal centre along the laser axis, where the power density decreases below the breakdown threshold. The quantities are calculated as a function of the total power  $P_0$  and the critical power density  $I_C$ , which in general depend on particle size and composition.

---

<sup>4</sup> Photon flux and photon flux density are used ambiguously in the literature. In this chapter, photon flux means number of photons per second and photon flux density is the differential quantity with respect to area. Some authors use photon flux for the number of photons per second and area, whereas photon flux density is the corresponding differential quantity with respect to the emission angle.

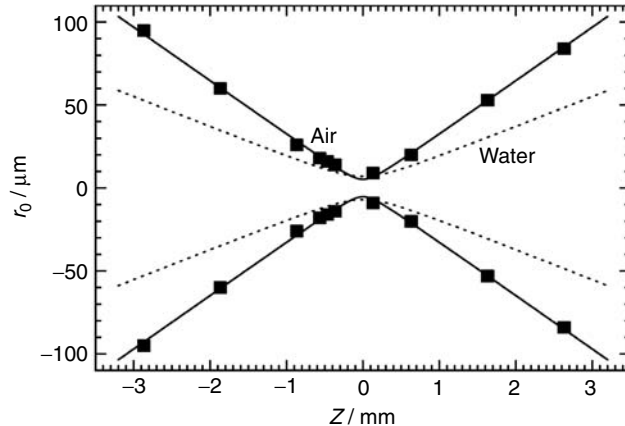


**Figure 4.** Measured data in air for the 1/e intensity isolines [ $r_0(z)$ ] of a focused Gaussian laser beam ( $\lambda = 532$  nm, total focal length of telescope ( $f_{\text{tot}} = 80$  mm) and calculation for water ( $n_{\text{H}_2\text{O}} = 1.33$ ). Reprinted from Walther, C., Bitea, C., Hauser, W., Kim, J. I. and Scherbaum, F. J., (2002). Laser induced breakdown detection for the assessment of colloid mediated radionuclide migration, *Nuclear Instruments and Methods in Physics Research B*, **195**, 374–388, with permission from Elsevier

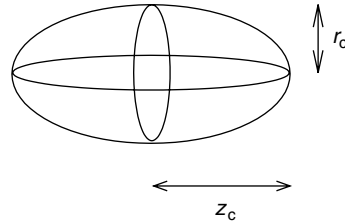


**Figure 5.** Approximation of the focal volume for a Gaussian beam, focused by a spherical lens without aberration as used in [22]

Inverting equation (9) yields

$$r_C = r_0(0) \sqrt{\ln \left[ \frac{P_0}{I_C \pi r_0^2(0)} \right]} \Big|_{z=0} \quad (12)$$

By substituting equation (10) into equation (9) at  $r = 0$  we obtain

$$I_C = \frac{P_0}{\pi r_0^2(0)} \frac{1}{1 + \left[ \frac{z_C \lambda}{n \pi r_0^2(0)} \right]^2} \Bigg|_{r=0} \quad (13)$$

which is inverted in order to obtain the critical distance along the laser axis,  $z_C$ :

$$z_C = \frac{n \pi r_0^2(0)}{\lambda} \left[ \frac{P_0}{I_C \pi r_0^2(0)} - 1 \right]^{\frac{1}{2}} \quad (14)$$

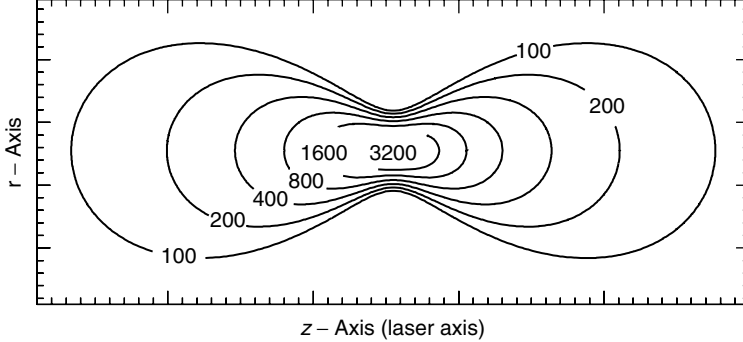


**Figure 6.** Contour plot of isoflux lines (regions of equal photon flux density or equal power area-density, respectively). The numbers indicate the relative photon flux density

The focal volume is then calculated as

$$V_{\text{el}} = \frac{4}{3} \frac{n\pi^2 r_0^2(0)}{\lambda} r_0^2(0) \ln \left[ \frac{P_0}{I_C \pi r_0^2(0)} \right] \left[ \frac{P_0}{I_C \pi r_0^2(0)} - 1 \right]^{\frac{1}{2}} \quad (15)$$

The volume scales with increasing power according to

$$V_{\text{el}} \propto P_0^{\frac{1}{2}} \ln P_0 \quad (16)$$

The above simple treatment only holds in the limit of small laser pulse energy or high breakdown threshold. Outside this limit one has to take into account the non-elliptical (butterfly) shape of the breakdown region depicted in Figure 6. The mathematical treatment for spherical focus conditions is given in [66] and is briefly summarised below.

Equation (11) can be substituted by the more general formula in cylindrical coordinates:

$$V_{\text{foc}} = 4\pi \int_0^{z_C} \int_0^{r_C(z)} r \, dr \, dz \quad (17)$$

and equation (12) is generalised by including the  $z$ -dependence of  $r_0$ :

$$r_C(z) = r_0(z) \sqrt{\ln \left[ \frac{P_0}{I_C \pi r_0^2(z)} \right]} \quad (18)$$

Integration over  $r$  yields

$$V_{\text{foc}} = \frac{4\pi}{2} \int_0^{z_C} r_0^2(z) \ln \left[ \frac{P_0}{I_C \pi r_0^2(z)} \right] dz \quad (19)$$

By introducing constants  $a$  and  $b$ , equation (10) can be written as follows:

$$r_0(z) = r_0(0) \sqrt{1 + b^2 z^2} \quad | \quad a = \frac{P_0}{I_C \pi r_0^2(0)}; \quad b = \frac{\lambda}{n \pi r_0^2(0)} \quad (20)$$

and equation (19) becomes

$$V_{\text{foc}} = 2\pi \int_0^{z_c} r_0^2(0)(1 + b^2 z^2) \ln \left( a \frac{1}{1 + b^2 z^2} \right) dz \quad (21)$$

which is solved by integration by parts and simple integral calculus ([67], p. 156):

$$V_{\text{foc}} = \frac{4\pi^2 r_0^4(0)n}{9\lambda} \left[ \frac{P_0}{I_C \pi r_0^2(0)} - 1 \right]^{\frac{3}{2}} \quad (22)$$

The solid curve in Figure 7 is a fit of equation (22) to the calculated data of the ‘butterfly’ in the top of the figure. The isoflux areas are transformed well to isoflux volumes by weighting each area segment with its radius.<sup>5</sup>

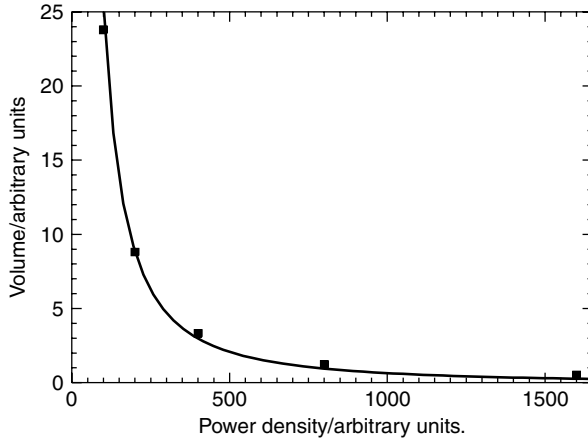


**Figure 7.** Cumulative relative volumes of the focal region, more precisely of the three-dimensional isoflux object depicted in Figure 6

---

<sup>5</sup> It is interesting to compare this exact result with the approximation of equation (15). At  $\alpha = 1$ , the  $\ln$  can be approximated as a Taylor series:

$$\ln \alpha = (\alpha - 1) - \frac{(\alpha - 1)^2}{2} + \frac{(\alpha - 1)^3}{3} - \dots$$

When the approximation is truncated at the second order term, we obtain the exact solution:

$$\begin{aligned} \ln \left[ \frac{P_0}{I_C \pi r_0^2(0)} \right] &\approx \frac{P_0}{I_C \pi r_0^2(0)} - 1 - \frac{1}{2} \left[ \frac{P_0}{I_C \pi r_0^2(0)} \right] - 1^2 + \dots \\ V_{\text{el}} &\propto \left[ \frac{P_0}{I_C \pi r_0^2(0)} \right] - 1^{\frac{3}{2}} - \frac{1}{2} \left[ \frac{P_0}{I_C \pi r_0^2(0)} \right] - 1^{\frac{5}{2}} + \dots \end{aligned}$$

### 3.3 FROM THE ELECTRON NUMBER TO THE BREAKDOWN PROBABILITY

When the breakdown probability of colloids, i.e. the probability of igniting a plasma integrated over the total focal volume, is calculated, the temporal evolution of the electron density must be considered. It is assumed that the plasma formation is preceded by the generation of only *one* first free electron via non-resonant multiphoton ionisation (MPI). In the case of nanosecond-pulses, this process presents a bottleneck in plasma formation and its rate determines the total plasma generation. In due time, electrons are multiplied by inverse bremsstrahlung and the plasma is heated until it can be detected either by light emission or by the acoustic shockwave produced during expansion.

The power density at a fixed coordinate within the focal region is not constant but varies in time:  $I = I(\vec{r}, t)$ . For calculation of the MPI rate, equation (3) is used initially. In the following, a laser pulse of single transverse mode is assumed. In this case,  $I(\vec{r}, t)$  can be separated into a spatial and a temporal part,  $g(\vec{r})$  [equation (9)] and  $h(t)$ , respectively:

$$I(\vec{r}, t) = E_0 g(\vec{r}) \cdot h(t) \quad (23)$$

where  $E_0$  is the total energy of the pulse (*e.g.* in joules). The combination of equations (3) and (23) and integration over time yield the number-density of electrons,  $\rho_e$ :

$$\frac{\rho_e}{\rho_M} = 1 - \exp \left\{ \int_{-\infty}^{\infty} dt \mu_m \left[ E_0 \frac{1}{\sqrt{\pi} \tau} e^{-\frac{t^2}{\tau^2}} \frac{1}{\pi r_0^2} e^{-\frac{r^2}{r_0^2}} \right]^m \right\} \quad (24)$$

where  $\rho_{-\infty}$  is the density of educts before irradiation ( $t = -\infty$ ). For the sake of simplicity, the temporal profile is approximated by a Gaussian with a ‘1/e lifetime’ of  $\tau$ . However, the mathematical treatment is valid for an *arbitrary* temporal dependence, since the time integration is independent of the space coordinates and yields a constant factor  $c_t$ . In the case of the temporal Gaussian,  $c_t$  amounts to:

$$c_t = \int_{-\infty}^{\infty} dt \left[ \frac{1}{\sqrt{\pi} \tau} e^{-\frac{t^2}{\tau^2}} \right]^m = \frac{1}{\sqrt{m} (\tau \sqrt{\pi})^{m-1}} \quad (25)$$

In order to calculate the number of electrons  $N_e$ , the number-density  $\rho_e$  has to be integrated over space. One should note the  $z$ -dependence of the 1/e radius  $r_0(z)$  [equation (10)] which, for the sake of readability, is not always written explicitly. In cylindrical coordinates, we obtain:

$$N_e = 2\pi \int_{-\infty}^{\infty} dz \int_0^{\infty} r dr \rho_M \left( 1 - \exp \left\{ -\mu_m c_t \left[ E_0 \frac{1}{\pi r_0(z)^2} e^{-\frac{r^2}{r_0(z)^2}} \right]^m \right\} \right) \quad (26)$$

By two-fold substitution:

$$u = m \frac{r^2}{r_0^2(z)} \text{ and } v = a e^{-u} \quad (27)$$

we have

$$N_e = -\frac{2\pi\rho_M}{m} \int_0^\infty dz r_0^2(z) \int_a^0 dv \left( \frac{1}{v} - \frac{1}{v} e^{-v} \right) \quad (28)$$

which is solved by using an integral table (e.g. [68], 8.21) to give

$$N_e = \frac{2\pi\rho_M}{m} \int_0^\infty dz r_0^2(z) [\ln a + C - \text{Ei}(-a)] \quad (29)$$

$$a = \mu_m c_t \frac{P_0^n}{\pi^n r_0^{2n}(z)}$$

where  $C = 0.57721566490153$ , i.e. Euler's constant, and  $\text{Ei}(-x)$  is the exponential-integral function<sup>6</sup>.

Both  $\ln a$  and  $-\text{Ei}(-a)$  diverge as  $a \rightarrow 0$  ( $z \rightarrow \infty$ ), but it can be shown ([68], 8.214) that

$$\lim_{a \rightarrow 0} \ln a - \text{Ei}(-a) = -C \quad (30)$$

and hence the second part of the integrand of equation (29) approaches 0.<sup>7</sup>

Equation (29) is visualised by an example with a set of parameters, which are typical for the experimental set-up of [34] (Table 1). The MPI cross-section [69] of polystyrene particle molecules were approximated by the measured value of toluene in the gas phase [70].

The transition from a free molecular gas to colloids in water is made by considering the following:

- ‘Clustered’ targets: one colloid consists of  $N_m = \left[ \frac{4}{3}\pi(\frac{d}{2})^3 \right] / V_{\text{mol}}$  molecules, with an MPI cross-section of  $\mu_m^1$  each. Under the assumption that the colloids are perfectly transparent, the cross-section of ionising at least *one* molecule inside the colloid amounts to  $\mu_m = N_m \mu_m^1$ . If colloids are not transparent and have a penetration depth for light  $d_p$ , only an outer layer with thickness  $d_p$  facing the laser beam contributes to electron production during the initial ionisation stage until vaporisation destroys the particle.
- The number density of colloids replaces the number density of gas molecules, with the important difference that having one colloid within a volume element means that there are  $N_m$  absorbers at a time. The absorption cross-section of the colloid is given by the sum of absorption cross-sections of clustered constituents justifying the introduction of the mesoscopic cross-section  $\mu_m$ .

---

<sup>6</sup>  $\text{Ei}(x) = \int_0^x e^t^2 dt$ .

<sup>7</sup> Note that  $\lim_{z \rightarrow \infty} r_0(z) = \infty$ .

**Table 1.** Set of parameters used in Example 1

Parameter	Value	Comment
$d_{\text{coll}}$	0.1	Diameter of colloid in $\mu\text{m}$
$\rho_C$	$4 \times 10^5$	Number of colloids $\text{cm}^{-3}$
$m$	4	Order of process
$r_0(0)$	6.7	Radius at Gaussian focus in $\mu\text{m}$
$n_{\text{H}_2\text{O}}$	1.334	Index of refraction
$\lambda$	0.532	Wavelength in $\mu\text{m}$
$\mu_m^1$	$1.4 \times 10^{-10}$	MPI cross-section of one molecule in $\mu\text{m}^8\text{W}^{-4}\text{s}^{-1}$
$V_{\text{mol}}$	$1.7 \times 10^{-10}$	Volume of one molecule in $\mu\text{m}^3$
$\tau$	$1 \times 10^{-8}$	1/e pulse duration in s
$\rho_{C\mu\text{m}^3}$	$\rho_{\text{cm}^3}/10^{12}$	Colloids $\mu\text{m}^{-3}$
$C_C$	$\rho_{C\mu\text{m}^3}\delta\left(\frac{4\pi}{3}r_{\text{coll}}^3\right) \times 10^{12}$	Concentration in $10^{-9}\text{g dm}^{-3}$ (density colloid = $\delta \text{ g cm}^{-3}$ )
$\mu_m$	$\mu_m^1\left(\frac{4\pi}{3}r_{\text{coll}}^3\right)/V_{\text{mol}}$	Cross-section of colloid
$c_t$	$[\sqrt{m}(\tau\sqrt{\pi})^{m-1}]^{-1}$	Integral over time dependence in $\text{s}^{m-1}$ [equation (25)]

- Although the total number of molecules may still be large, the number of colloids per unit volume is considerably lower, due to clustering. Hence saturation effects occur already at moderate pulse energies (see below).
- Since colloids are suspended in water, light propagation is determined by the ratio of the respective indices of refraction  $n_{\text{H}_2\text{O}}/n_{\text{Coll}} \approx n_{\text{H}_2\text{O}}$  in the present work (polystyrene spheres:  $n_{\text{Coll}} = 1.59$ ).
- It is assumed that every electron that is generated by MPI is multiplied by avalanche generation, which is a good approximation for high pulse energies and small particles (see later).
- In the following example, we do not include focusing and field enhancement effects inside the colloid, which may become important for large particles of size  $d \gtrsim \lambda$  (wavelength of the laser light) [71–73].

Figure 8 displays the inner function of equation (29), namely

$$\frac{\partial N_e}{\partial z} = \frac{2\pi\rho_M}{m} r_0^2(z) [\ln a + C - \text{Ei}(-a)] \quad \Big| \quad a = \mu_m c_t \frac{P_0^m}{\pi^m r_0^{2m}(z)} \quad (31)$$

i.e. the number density of electrons per unit  $z$ -axis which equals the number density of ionised molecules per unit  $z$ -axis as a function of the  $z$ -axis position ( $\partial N_c/\partial z$  has the one dimensional unit  $\text{cm}^{-1}$ ). This quantity is observed directly by optical LIBD (Section 4, Figure 12), when the position of plasma plumes is imaged by one or two CCD cameras, and the relative number of events is plotted versus position along the laser beam ( $z$ -axis). Due to the small number of ‘targets’, a saturation effect occurs, most prominently in the focal area of high photon flux (central regions, Figure 6). At a certain level of photon flux density, an additional increase in pulse energy does not cause a higher number of events in the central region, because every colloid diffusing therein is ionised with a probability of 1. An increase can only be achieved at the outer regions due to the ‘growth’ of the effective

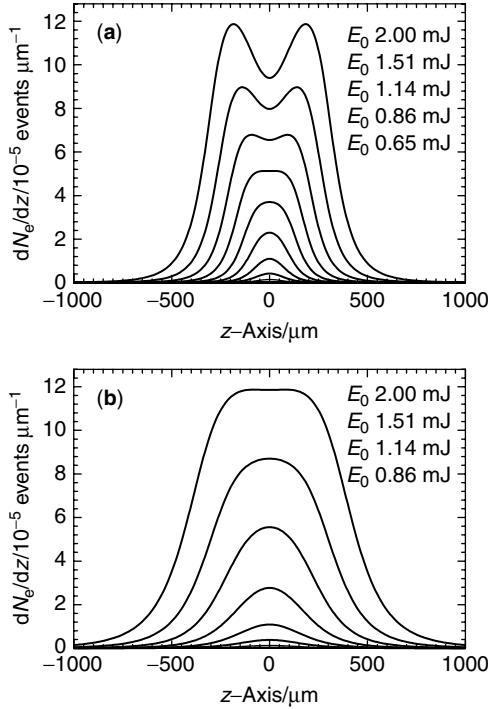


**Figure 8.** The number density of ionised molecules as a function of the  $z$ -axis (along the laser beam). This quantity is observed directly by optical LIBD (Section 4, Figure 12). (a) The higher the pulse energy  $E_0$  (given in mJ), the more prominent is the saturation, causing a flat top or even ‘hole burning’ in the central region of the distribution. (b) The hole burning effect decreases as the radius of the Gaussian focus increases from 6.7 to 10  $\mu\text{m}$

focal volume at large  $z$ , as described earlier [equation (22)]. This effect causes a flattening of the distribution function of Figure 8 at the centre and can lead to a local minimum of breakdown events at  $z = 0$  at very high pulse energies. For a given pulse energy, this effect is less pronounced for a laser beam of larger diameter in the Gaussian focal plane, because a larger focal volume contains more ‘targets’ and, accordingly, saturation does not play a role until the pulse energy is increased further.

The ‘event density’ equation (31) of Figure 8a is integrated numerically according to equation (29) and yields the total event number  $N_e(z)$ , which is plotted as a function of laser pulse energy  $E_0$  on a double logarithmic scale in Figure 9a. The set of parameters for Example 1 (Table 1) and the pulse energies of Figure 8a were used again here. Deviating from the previous example, the number density of colloids was increased by a factor of 100 from  $\rho_C = 4 \times 10^5$  to  $4 \times 10^7$  particles  $\text{cm}^{-3}$ . At low pulse energy, in the absence of saturation, the curve has a slope  $m = 4$ , i.e. the order of the process. As the pulse energy increases and the central region no longer contributes to an event enhancement, the curve merges continuously differentiable into the characteristic growth dependence of the focal volume with a slope  $s = 1.5$  [equation (22)] [66].

In the case of ‘acoustic LIBD’, i.e. the detection by a piezo-detector, the number of events for a single laser shot is not resolved. A single plasma cannot be discriminated

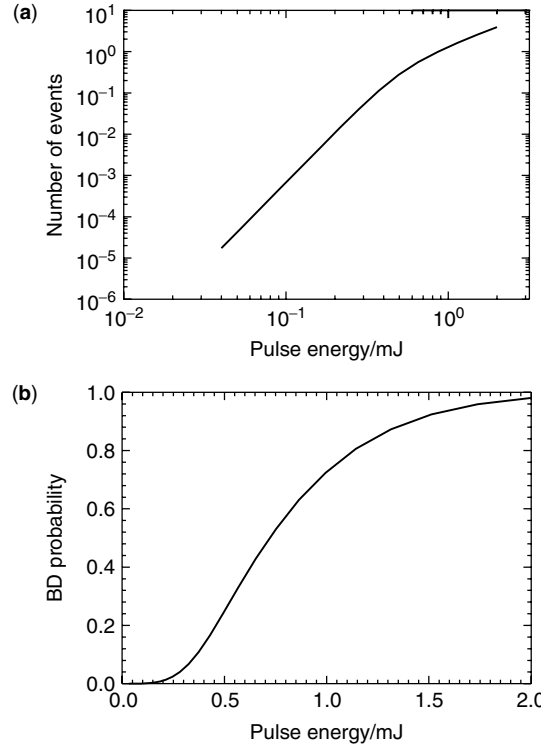


**Figure 9.** (a) Number of breakdown events versus laser pulse energy (log–log plot), taken from the limit as  $z \rightarrow \infty$  of equation (29). (b) The probability of measuring at least one event per laser shot as a function of the laser pulse energy, the so called ‘s-curve’ according to equation (35). These are the data achieved by an acoustic LIBD experiment

from multiple events (two or more plasma plumes ignited by the same laser pulse). Hence the inverse probability, i.e. the probability of having no event, is taken as an unequivocal measure. Given a ‘true’ number of events  $\bar{\mu}$ , the probability ( $p_N$ ) of measuring a value of  $N$  events can be calculated, according to Poisson statistics, as

$$p_N = \frac{\bar{\mu}^N}{N!} e^{-\bar{\mu}} \quad (32)$$

In the present case, the probability of measuring  $N = 0$  events, when the ‘true’ number should be  $\bar{\mu}$ , is given by

$$p_0 = e^{-\bar{\mu}} \quad (33)$$

and the BD probability, which of course is the inverse of measuring *no* event, is

$$p_{BD} = 1 - e^{-\bar{\mu}}, \quad \text{with } \bar{\mu} = N_e \quad (34)$$

Figure 9b shows the breakdown probability  $p_{BD}$  as a function of the laser pulse energy  $E_0$ :

$$p_{BD}(E_0) = 1 - e^{-N_e(E_0)} \quad (35)$$

This is the so called s-curve, the direct data one obtains with an acoustic LIBD apparatus (section 4).

Some remarks can be given for the applicability of this model and the restrictions formulated above.

- In the presence of electron donors [74], for particles with a large number of electrons in shallow states (low ionisation energy) [75], or for particles with a large total MPI cross-section ( $\gtrsim 300$  nm, depending on composition) ‘first electrons’ might be produced at a pulse energy not yet sufficient to sustain the avalanche process of electron multiplication. In these cases, the bremsstrahlungs term  $\eta(E)N_e$  of equation (2) is added in equation (3) and an additional condition is introduced. After the first electron is generated, at least the threshold energy for detection has to be absorbed during the remaining laser pulse. A transition from MPI-dominated to avalanche-dominated breakdown is described for these cases [9]. Detailed investigations on electron multiplication and plasma growth [76] and heating processes [77,78] in aqueous media has been reported [63], mainly in the framework of eye surgery with short pulse lasers [79].
- The photon flux distribution of Figure 6 is only achieved when a perfect Gaussian beam is focused without diffraction by an aberration-free ideal lens. In the literature, most pulsed lasers used for LIBD do not deliver a satisfactory beam quality. In addition, as soon as spherical aberrations and diffraction become relevant, the profile changes drastically and small regions of higher photon flux density occur. Detailed calculations for plane and Gaussian wavefronts and various lens configurations have been discussed [53,80,81]. Within these regions, the probability for MPI is strongly enhanced due to the nonlinear character of the process [equation (1)] and the distribution of events observed by optical LIBD is altered (Section 4, Figure 14) [82].
- Of equal relevance is the evolution of the photon flux density with time. Some lasers do not have a smooth temporal profile but rather exhibit a peak structure enveloped by some kind of Gaussian function (see, for instance, Figure 10). The number and width of these peaks are, determined by the (longitudinal) mode structure of the laser. The strong enhancement of photon flux during the spikes of typically  $< 100$  ps leads to an increase in  $c_t$  [equation (25)] by up to  $m!$  ( $m$  factorial,  $m$ -order of process = number of photons needed for ionisation) depending on coherence and whether or not these modes are locked [83].
- Self-focusing is an additional mechanism of flux density increase which must be considered. For laser pulses of high energy, the refractive index of matter,  $n_L$ , is no longer constant. It depends on the strength of the electric field  $\mathcal{E}$ :  $n_L = n + \gamma_L |\mathcal{E}|^2$ ;  $\gamma_L$  is a material-dependent constant, which amounts to  $0.5 \times 10^{-22} \text{ m}^2 \text{ V}^{-2}$  in the case of water [65]. For Gaussian beams, the electric field is higher in the centre than outside, which gives rise to a more pronounced refractive index enhancement in the centre and an overall focusing of the light. It can be shown [65] that the focusing becomes important above a so-called ‘critical power’ of the beam  $L_C$ :

$$L_C = \frac{\varepsilon_0 c_0 \lambda_0^2}{8\pi\gamma_L} \quad (36)$$

where  $\varepsilon_0$  is the electric permittivity,  $c_0$  the velocity and  $\lambda_0$  the wavelength of light in vacuum. The relevance of self focusing even for nanosecond lasers is demonstrated in Section 4, Figure 14.

## 4 EXPERIMENTAL APPROACHES

In the preceding section, we determined that a molecule of ionisation energy  $E_I$  can be ionised by the simultaneous absorption of  $m = \text{MOD}(E_I/h\nu) + 1$  photons of energy  $h\nu$ , a process that scales with the  $m$ th power of the photon flux density. A typical electron ionisation energy (work function) of a solid ranges from 6 to 10 eV [54], and hence  $m = 3\text{--}5$  for visible light. This process describes the ionisation of a single atom or molecule<sup>8</sup>. For a system of many atoms, the probability of an ionisation process occurring scales linearly with the total number of atoms available. In addition, the efficiency of ionisation depends on the material properties, as does the electron multiplication process by inverse bremsstrahlung. For a dense solid, the process begins much more easily than for a liquid. This point is made use of for particle detection. The pulse energy is chosen to be just below the breakdown threshold of pure water [74]. Whenever a colloid enters the focal region, the threshold for a solid phase applies (which is exceeded) and a plasma is ignited. Because each plasma event corresponds to a single colloid, the relative number of events per predefined number of laser shots (breakdown probability) provides a measure of the colloid number density. The plasma generation mechanism becomes more efficient with increasing colloid size, leading to a pronounced size dependence<sup>9</sup>, which is exploited for appraising the colloid size: *Small colloids require a higher photon flux density to ignite breakdown than larger ones, i.e. they have a higher ‘breakdown threshold’.*

### 4.1 BUBBLE DETECTION

The plasma ignition causes different observable signals which can be conveniently used for detection (Figure 1). The first (and most sensitive, especially for ultra-short pulses) is the generation of gas bubbles due to the thermal expansion [77,84], which can be visualised by shining an additional light source through the breakdown area in order to display the shadow of the bubble [75]. In the case of plasmas created by nanosecond-pulses, the gas bubble effect is not used routinely, since the information is only rough.

### 4.2 DETECTION BY THOMSON SCATTERING

The second detection method is based on the extinction of laser light during the breakdown process. A plasma of electron density  $\rho_e$  is translucent for light above the critical (plasma) frequency:

$$\nu_C = \frac{1}{2\pi} \sqrt{\frac{\rho_e e^2}{m_e \varepsilon_0}} \quad (37)$$

---

<sup>8</sup> More precisely, this depends on the number of electrons in a valence band or, if the bond character of constituents within the particle does not permit delocalisation of electrons, this depends on the number of outer shell electrons in the individual atoms or molecules involved.

<sup>9</sup> This is valid for colloids of different size and similar chemical composition. For limitations, see Section 6.

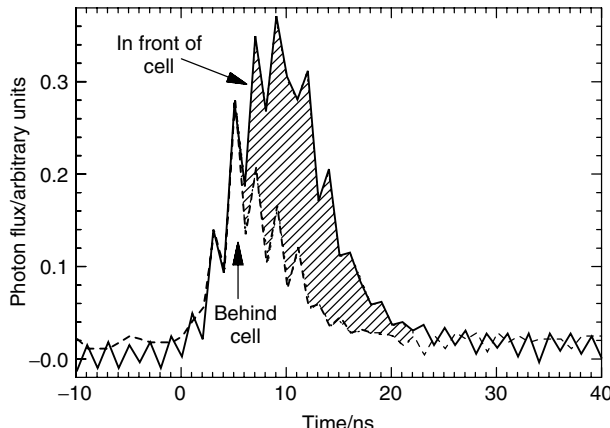


**Figure 10.** Shadowing of the laser pulse due to Thomson scattering of the incident laser beam at the plasma electrons. Reprinted from Walther, C., Bitea, C., Hauser, W., Kim, J. I. and Scherbaum, F. J. (2002). Laser induced breakdown detection for the assessment of colloid mediated radionuclide migration, *Nuclear Instruments and Methods in Physics Research B*, **195**, 374–388. with permission from Elsevier

where  $e$  and  $m_e$  denote the electron charge and mass, respectively, and  $\epsilon_0$  is the permittivity of free space. In other words, light of frequency  $\nu < \nu_C$  undergoes Thomson scattering [85] and cannot pass the plasma region. By comparing the temporal pulse shapes in front of and behind the quartz cell, as recorded by two photodiodes, this shadowing can be observed directly (Figure 10). During the first few nanoseconds of the laser pulse, no significant extinction of light takes place. When the plasma has evolved to a higher electron density, Thomson scattering [85] weakens the light transmission [86] and the integral of the difference between both curves (hatched area, Figure 10) is a measure of the total extinction. As shown by François *et al.* [87], such an ‘induced optical density’ contains information on the size and chemical composition of colloids.

#### 4.3 OPTICAL DETECTION

In a third approach, we make use of the photon flux density distribution inside the focal volume (see Section 3). The flux density increases as the beam diameter  $r(z)$  decreases. Within the Gaussian laser focus, the isolines of flux distribution resemble a double club with a cylindrical symmetry or peanut-like shape as discussed in Section 3.2. Figure 11a shows a section through the three-dimensional distribution along a plane containing the laser beam axis (see also Figure 6). The focal region typically has a radius of  $\sim 5\text{--}10\text{ }\mu\text{m}$  and a length of  $1\text{--}2\text{ mm}$  along the laser axis, much larger than the colloids of interest for LIBD investigations ( $<100\text{ nm}$  in diameter). Therefore, the flux density is constant within the total volume of the colloid, to a very good approximation, and determined exclusively by the position of the colloid within the laser focus. In other words, different values of photon flux density are present within the focal volume for *fixed* pulse energy and the respective flux density to which a colloid is exposed depends on its position inside the focal volume. By using a microscope lens and a CCD camera, the exact position of the plasma plume can be imaged on a pulse-to-pulse basis for several thousand laser shots and a spatial distribution of BD events can be obtained. This detection scheme is referred to

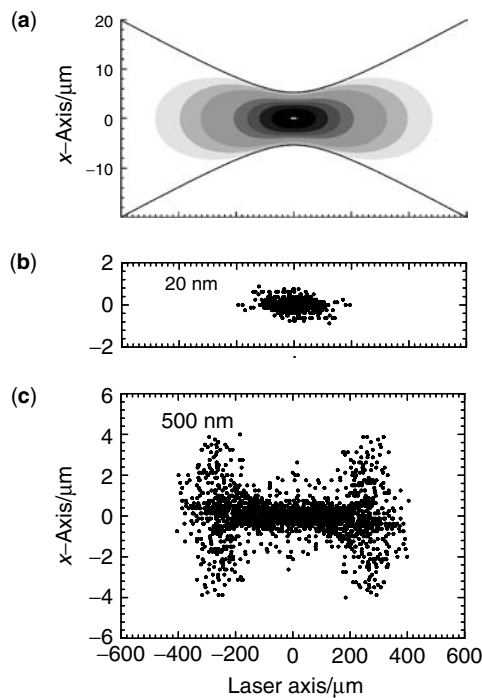


**Figure 11.** (a) Photon flux density distribution in the central region of the laser focus. The grey contour scales indicate a two-dimensional cut through the three-dimensional double-club-like distribution (flux increases from light to dark). Reprinted from Walther, C., Betea, C., Hauser, W., Kim, J. I. and Scherbaum, F. J. (2002). Laser induced breakdown detection for the assessment of colloid mediated radionuclide migration, *Nuclear Instruments and Methods in Physics Research B*, **195**, 374–388, with permission from Elsevier. (b) Small colloids (polystyrene, 20 nm) are exclusively detected in the central region of high flux, whereas (c) large colloids (polystyrene, 500 nm) ignite also along the edges at lower flux (pulse energy 0.6 mJ)

as ‘optical detection’. Typically, the plasma plume is observed with one camera which is mounted perpendicular to the beam axis [27]. A recent observation by two cameras from directions perpendicular to each other was also reported, allowing a true three-dimensional assignment of position and photon flux [34]. As discussed above, the smaller the colloids, the higher is the breakdown threshold, i.e. the higher is the photon flux density required for plasma formation. Applied to the spatially resolved observation, small particles are exposed to sufficiently high photon flux density only in the central region, whereas for large colloids the low flux density at the ‘wings’ of the focal area still suffices to ignite a plasma. Figure 11 illustrates this behaviour on polystyrene spheres of different diameters recorded at the same laser pulse energy (0.6 mJ). All events of 20 nm spheres are centred tightly around the Gaussian focus with a rather small spread along the laser axis. The plasma plumes ignited on 500 nm colloids are distributed over a much wider region along the iso-flux lines. For the same data, the number of events per unit length along the laser axis is shown in Figure 12. Adapting the evaluation method of [30], the 20 nm particles (a) are fitted by a Gaussian of  $l_z = 92 \mu\text{m}$  width (denoted ‘ignition length’), whereas the 500 nm particles (b) result in an ignition length of  $l_z = 334 \mu\text{m}$ . The Gaussian function

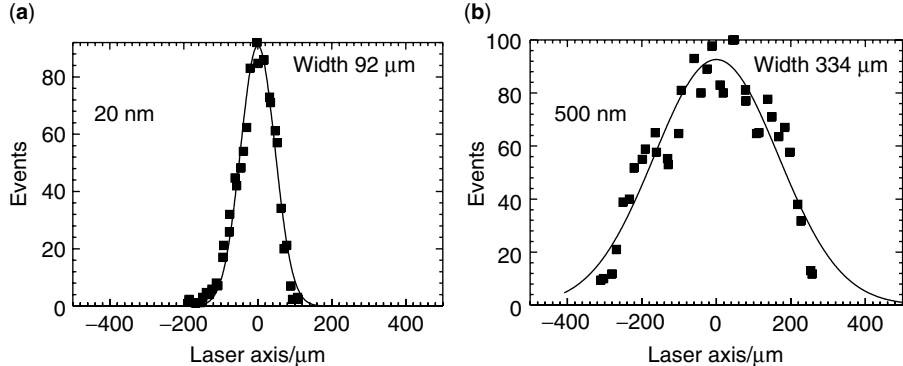


**Figure 12.** For the data of Figure 11, the number of events per unit length along the laser axis is shown. (a) The 20 nm particles are fitted by a Gaussian of 92  $\mu\text{m}$  width (denoted ‘effective focal length’), whereas the 500 nm particles (b) result in a focal length of 334  $\mu\text{m}$

was used for a convenient approximation in [30]. Since this plot represents the experimental counterpart of Figure 8, the distribution is more exactly described by equation (31). After an appropriate calibration with reference particles, the ignition length can serve as a measure of average particle size (for material dependence, see Section 6). The colloid concentration scales linearly proportional to the BD probability.

An example of an optical LIBD apparatus is the mobile version used for deep underground *in situ* measurements (Section 5.5). The light emission of each plasma event is recorded two-dimensionally (Figure 13a) and the ‘centres of gravity’ of these intensity profiles are plotted versus their position along the laser axis (*cf.* Figure 12). The resulting distribution can be approximated by a Gaussian curve of full width at half-maximum (FWHM)  $l_z$  (ignition length) (Figure 13b).  $l_z$  increases monotonously with the average size of colloids [30] and allows for the calibration of ignition length versus size (Figure 13c).

It is essential to preserve the spatial Gaussian profile of the laser beam. When using refractive optics, a major source of beam disturbance are spherical aberrations of the focusing lens(es). Morgan [53] calculated the isophotes (lines of equal photon flux density) for different values of the so called ‘aberration function’,  $\Phi_{\max}$  [64]. This function depends on focal length, refractive index and the ratio of unfocused beam diameter to lens diameter. Simplified, the aberration becomes stronger as the unfocused beam becomes larger relative to the size of the lens and the focal length becomes shorter. Hence the focusing of a large beam at short distances into the sample should be avoided. Figure 14 shows the calculation for  $\Phi_{\max} = 0.5\lambda$  [53]. Since for polystyrene the BDP depends on the fourth power of the power density,  $I^4$ , the fourth power of the isophotes is plotted and compared with respective measurements on 500 nm polystyrene particles (Figure 14a). For illustration purposes, an unfavourable optics configuration is chosen. The distribution of BD events reflects the asymmetry of the flux profile and the additional region of high flux at  $z \approx -500 \mu\text{m}$  results in additional events at the respective positions.

With increasing pulse energy, self-focusing can become important. As discussed above [equation (36)], this process depends on the power (energy/time) during the laser pulse. For the parameters given in Table 1, the critical power is  $L_C = 6 \times 10^5 \text{ J s}^{-1}$ . For a smooth Gaussian temporal pulse profile, this corresponds to 6 mJ. In the case of short spikes due

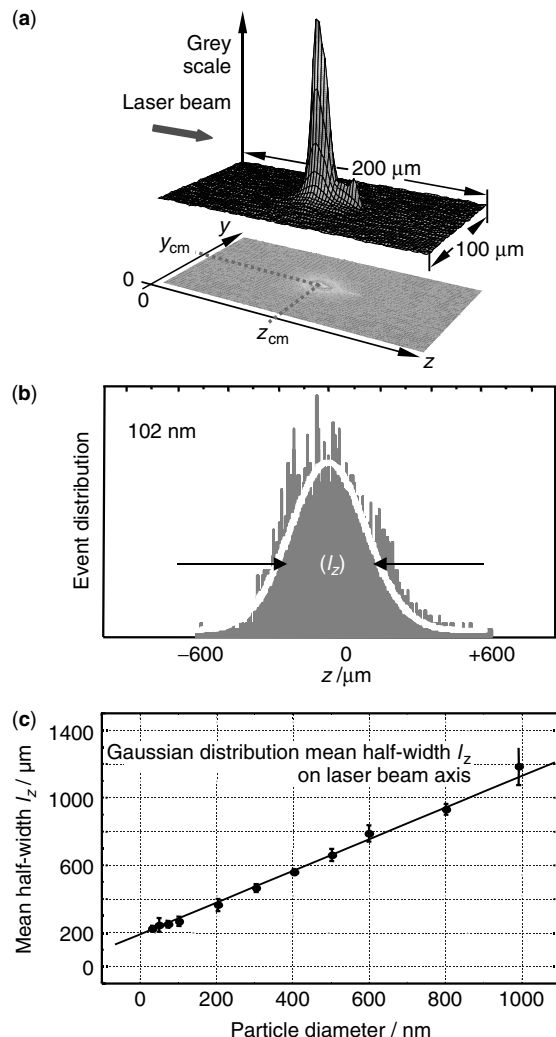


**Figure 13.** (a) A single particle breakdown event in a three-dimensional visualisation. (b) Breakdown events accumulated in the laser focus volume as they appear in a Gaussian distribution. (c) Calibration of FWHM (full width at half-maximum) values  $l_z$  (ignition length) as a function of particle diameter. Reprinted from Hauser, W., Geckeis, H., Kim, J.I. and Fierz, Th., A mobile laser-induced breakdown detection system and its application for the *in situ* monitoring of colloid migration, *Colloids and Surfaces A*, **203** 37–45, Copyright 2002, with permission from Elsevier

to coherence effects of the laser (see Figure 10 and the respective discussion), the temporary power, however, might be much higher: a 100 ps spike of 100 μJ energy corresponds to  $P = 10^6$  W. The focal length of the self-focusing is calculated according to

$$z_f = \frac{\pi r_0^2}{\lambda_0 \sqrt{(P/L_C) - 1}} \quad (38)$$

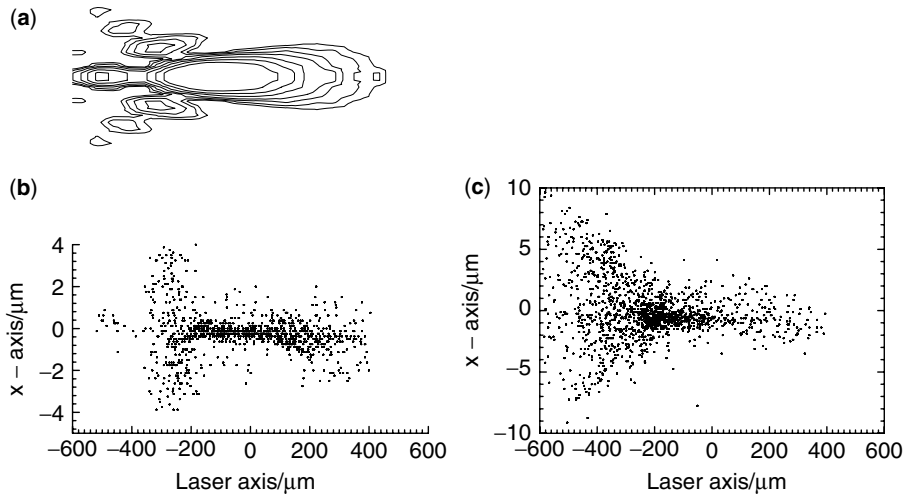


**Figure 14.** The position of plasma events within the focal volume, observed directly by a CCD camera as in Figure 12. (a) Spherical aberration disturbs the ideal flux profile of Figure 6 (according to Morgan, C. G. (1975). Laser-induced breakdown of gases, *Rep. Prog. Phys.*, **38**, 621–665.) and, as a consequence, the distribution of BD events is deformed (b) (polystyrene, 500 nm,  $E_0 = 0.7$  mJ). (c) With increasing pulse energy of the laser, self-focusing occurs, which becomes prominent for the system of Table 1 at  $E_0 = 2.6$  mJ (polystyrene, 500 nm)

Figure 14 shows the results of an experiment at  $P = 1.1L_C$ , which should lead to a focal length  $z_f = 500 \mu\text{m}$ . This is in accordance with the shift of breakdown events towards the laser.

Aberration and self-focusing complicate the determination of the ignition length and of the effective focal volume where a breakdown is generated. The optical layout, focusing conditions and pulse energies should be chosen in such a way as to minimise these effects when using LIBD as a quantitative tool for colloid detection.

#### 4.4 LASER-INDUCED BREAKDOWN SPECTROSCOPY

In addition to detecting the position of a breakdown event, the optical emission can be analysed spectroscopically. For bulk samples, LIBS is well established as a standard method for quantitative element analysis [16]. Colloidal suspensions can be analysed in the same way [88], as discussed in the Introduction. The emission signal from the particles is well discriminated against the background from ionic species. By use of double pulse techniques and excitation of the evaporated material in the gas bubble, the detection limit is lowered to the  $10^{-6} \text{ g dm}^{-3}$  range. However, no true ‘single-colloid spectroscopy’ has been reported. In order to achieve a good background-to-noise ratio, many colloids have to be present either in the focal volume at a time, or the signals of many single events have to be averaged. While multi-element analysis of solids by LIBS has become a routine method, various line-broadening mechanisms (up to several nanometres) complicate speciation in aqueous media. LIBS on colloids in suspension is hence limited to samples of well-defined and homogeneous composition. For examples, see Section 5.9.

#### 4.5 ACOUSTIC DETECTION

The fourth approach uses the shock wave caused by thermal plasma expansion [84], which creates a strong sound in the case of nanosecond-laser excitation, audible even to the human ear, that can easily be detected by a piezo crystal [89] attached to a quartz cell perpendicular to the laser beam. The BDP is measured by counting the number of shock waves [7,8,22,27,34] relative to the total number of laser shots (if 100 shock waves occur for 1000 laser shots, the BDP is 10%). In contrast to optical detection, BD events are not recorded with a spatial resolution and no information on the photon flux density of a single plasma is obtained. The weighted average flux density of the total focal volume is, however, known. When probing BD at different flux densities, the average pulse energy has to be varied by the use of devices such as crossed Glan polarisers [34]. The pulse energy is monitored by a pyroelectric detector and the energy is recorded along with the acoustic signal for every single laser shot by a transient recorder. In such a case, the BDP as a function of pulse energy  $E_0$  results in an ‘s-curve’, as discussed in Section 3 [equation (35)]. The total cross-sections for MPI and IB increase proportionally to the particle volume (proportional to the number of valence electrons in the particle) and hence the breakdown threshold  $E_T$  decreases with increasing particle size (Figure 15a) [25,34]. The slope of the curve scales with the particle concentration (Figure 15b); see also equation (39) and detailed discussion thereafter. At very low concentrations (50 ppt), the BDP increases strongly when the background due to the ultrapure water becomes effective (here  $\sim 3$  mJ). The use of reference colloids of well-defined diameters provides a calibration for relating breakdown thresholds to particle size. For an unknown sample, the threshold is determined by recording the s-curve and subsequently converted to the particle diameter. If the sample contains colloids of more than one size (size distribution), the single ‘diameter’ obtained by this method is of limited value and should only be regarded as a mean diameter for fast comparative measurements (*e.g.* if one observes aggregation of colloids time resolved). It is highly recommended to use the multimodal evaluation instead (Section 4.7).

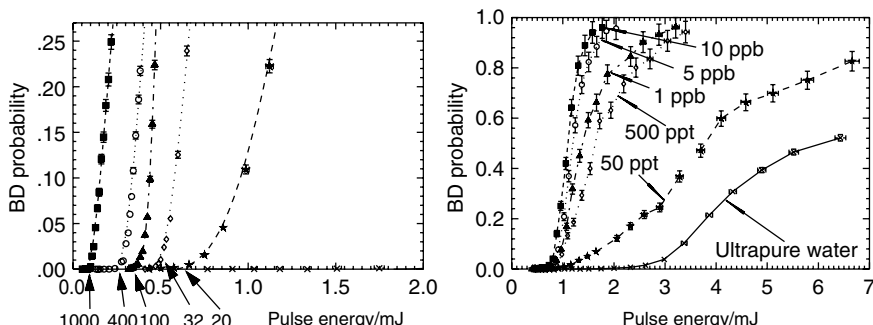


**Figure 15.** Acoustic detection: the breakdown probability (BDP) is plotted as a function of the laser pulse energy. **(a)** The threshold  $E_T$  of the so-called ‘s-curves’ increases with decreasing particle size (polystyrene reference spheres). **(b)** While the threshold remains constant, the slope changes with colloid concentration (polystyrene, 20 nm). Reprinted from Walther, C., Bitea, C., Hauser, W., Kim, J. I. and Scherbaum, F. J., Laser induced breakdown detection for the assessment of colloid mediated radionuclide migration, *Methods in Physics Research B*, **195**, 374–388. 2002, with permission from Elsevier

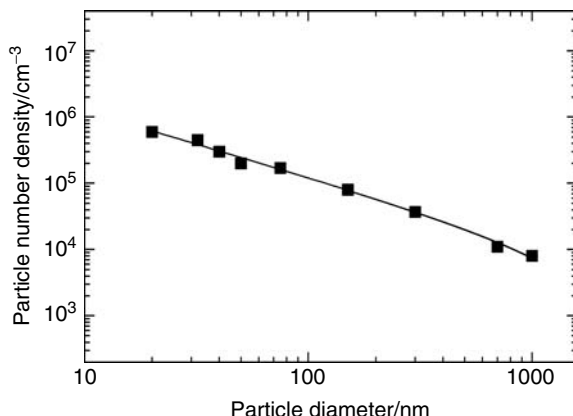


**Figure 16.** LIBD is capable of detecting particles with diameters between  $\sim 10$  and  $1000$  nm. The limit of detection (LOD), plotted as particle number density versus diameter, scales almost linearly with size, allowing detection in the  $10^{-9}$  g dm $^{-3}$  concentration range. Reprinted from Walther, C. (2003). Comparison of colloid investigations by single particle analytical techniques – a case study on thorium-oxyhydroxides, *Colloids and Surfaces A*, **217**, 81–92, with permission from Elsevier

The limit of detection (for both optical and acoustic detection) is only weakly size dependent and determined by the probability of finding a colloid in the laser focal volume [22], crudely estimated by  $\pi r^2 z \approx 10^{-6}$  cm $^3$  for small colloids. Since the effective focal length increases with increasing particle size, the effective focal volume for 1000 nm particles is 10-fold greater than for 20 nm colloids. Assuming a photon flux that is sufficient to induce a breakdown for every colloid entering the focal volume, we expect a BDP  $p_{BD} = 0.1$  for a particle number density of  $10^5$  particles cm $^{-3}$  (Figure 16). In the range  $<50$  nm, the detection efficiency is comparable to that of fluorescence correlation spectroscopy (FCS, Chapter 11), which, however, requires fluorescing particles or the addition of dyes. For small colloids, the sensitivity is clearly superior to the widely used dynamic light-scattering techniques. Single particle counting [90,91] and other static light-scattering [71,72,92] methods are more sensitive for colloids  $>100$  nm but the operational range becomes limited below *ca.* 80 nm [93,94] where concentrations are required which far exceed those of natural waters [95] (see also Section 6). Recently Particle Measuring Systems (PMS) [96] claimed to have reached a detection limit of 50 particles dm $^{-3}$  for 30 nm particles. However, to our knowledge, no applications in environmental science have been reported so far.

#### 4.6 COMPARISON OF OPTICAL AND ACOUSTIC LIBD

The acoustic set-up requires less equipment and is cheaper and easier to implement. In order to attain statistically sound measurements, a minimum of 1000 laser shots are needed for each of at least 20 different pulse energies. For a 20 Hz laser, this amounts to a total measurement time of  $>15$  min. An optical system, which allows shorter measurement cycles to be used, requires a camera, a frame grabber, software and a microscope lens, which increase substantially the price of the instrument. One thousand events are sufficient for a satisfactory measurement; BDP = 0.2 corresponds to 5000 laser shots or 4 min.

However, speed is paid for by limitations of the dynamic range. Whereas the acoustic detection is applicable for colloid concentrations from approximately  $10^{-9}$  g dm $^{-3}$  to several  $10^{-3}$  g dm $^{-3}$ , optical detection can only cover three orders of magnitude without changing pulse energy. This is evident from the fact that, to a first approximation, the BDP scales linearly with concentration. If, for instance, a suspension of 50% BDP is diluted by a factor of 1000, the BDP decreases to 0.05%. Two million lasershots or 1 day would then be needed to achieve 1000 events. Increasing the pulse energy solves the problem only partially. The number of events will increase and the time required for the measurement will decrease. However, since the effective focal volume depends on the pulse energy, any change in the pulse energy requires a renewed calibration of the system. In order to achieve maximum sensitivity, the working pulse energy is chosen just below the threshold of ultrapure water, i.e. below 0.1% BDP. In this manner, dilute suspensions (e.g.  $10^4$ – $10^7$  particles cm $^{-3}$ ) of size classes 10–1000 nm are accessible. In order to investigate more concentrated samples, the pulse energy should be lowered. Alternatively, for concentrations  $>10^8$  particles cm $^{-3}$ , complementary methods, e.g. photon correlation spectroscopy (PCS), can be applied, at least for particles larger than 100 nm.

#### 4.7 MEASUREMENT OF SIZE DISTRIBUTION BY ACOUSTIC LIBD

Thus far, ideal, monodisperse samples have been discussed. Although these might be of interest in the laboratory, they are of less relevance in nature where size distributions extend over several orders of magnitude. In the case of optical detection, each size corresponds to an ignition length  $l_z^{(i)}$  and for a given size distribution, one observes a superposition of various  $l_z^{(i)}$ . For the simple case of a bimodal distribution, a small Gaussian curve due to the small colloids is superimposed on a broad curve due to the large particles [29], much like summing the data of Figure 12a and b. So far, this effect has not been evaluated quantitatively for more than two size fractions. For polydisperse samples, an evaluation scheme based on s-curve detection has been developed recently [97].

In the following, the s-curves are described by a semi-empirical model with only two free parameters [equation (39)]. The breakdown threshold  $E_t$  is a measure of the particle size and the concentration determines the constant  $C$ :

$$p_{\text{mono}}(E_0) = 1 - \left\{ (1 + C(E_0 - E_t) - \frac{1}{2}[C(E_0 - E_t)]^2 + \frac{1}{6}[C(E_0 - E_t)]^3 \right\} \exp[-C(E_0 - E_t)] \quad (39)$$

In this case, the ‘first electron’ is generated by four-photon ionisation in the present case ( $h\nu = 2.3$  eV,  $IP_{\text{Polystyrene}} = 8.9$  eV) such that at low pulse energy  $E_0$ , a  $p_{\text{mono}} \propto E_0^4$  dependence is required [98]. If one expands equation (39) in a Taylor series, the first three terms up to  $(E_0 - E_t)^3$  cancel, which results in the  $\propto E^4$  dependence. The negative sign of the quadratic term causes a weak second-order ( $E^2$ ) dependence which approximates the increase in the effective focal volume  $V_{\text{eff}} \propto E^{\frac{3}{2}}$  as the pulse energy is increased [66]. Since the probability of detecting a colloid scales linearly with the focal volume, the breakdown probability also increases.  $p_{\text{BD}}(E_0)$  approaches unity asymptotically as  $E_0 \rightarrow \infty$ .

Strictly, equation (39) describes the BDP for a suspension containing colloids of only one size (monomodal). For a size distribution, it is possible to make use of the weak size dependence<sup>10</sup> of LIBD sensitivity (Figure 16). Whereas light scattering methods suffer from a decrease in signal proportional to  $d^{-6}$ , the detection limit of LIBD increases linearly with particle diameter from  $\sim 10^3$  particles  $\text{cm}^{-3}$  at 1000 nm to  $\sim 10^5$  particles  $\text{cm}^{-3}$  at 10 nm due to the increase in effective focal volume with increasing particle size [22]. As a consequence, size screening of small particles by the simultaneous presence of large ones is weak, a key to our approach of measuring size distributions. For a bimodal colloidal suspension containing particles of sizes  $d_1$  and  $d_2 < d_1$ , with thresholds  $E_t^{(2)} > E_t^{(1)}$ , the s-curve will be identical with a pure sample of the first fraction of the colloids below the threshold of the second fraction. As the pulse energy increases and exceeds the threshold of the smaller size class [ $E_t^{(2)}$ ], the latter will contribute to the sum curve. Each point of the s-curve represents a probability. ‘Adding’ two s-curves is the equivalent of determining the probability of either the fraction of colloids with  $d_1$  or the fraction of colloids with  $d_2$  generating an event (logical OR). Such a probability is defined as one minus the product of the probabilities of no breakdown occurring:

$$p_{Bi} = 1 - (1 - p_1)(1 - p_2) \quad (40)$$

Combining equations (39) and (40), we obtain

$$\begin{aligned} p_{Bi} = 1 - \prod_{i=1}^2 & \left\{ 1 + C^{(i)}[E_0 - E_t^{(i)}] - \frac{1}{2}[C^{(i)}(E_0 - E_t^{(i)})]^2 \right. \\ & \left. + \frac{1}{6}[C^{(i)}(E_0 - E_t^{(i)})]^3 \right\} \exp[-C^{(i)}(E_0 - E_t^{(i)})] \end{aligned} \quad (41)$$

where  $E_t^{(i)}$  and  $C^{(i)}$  are the threshold and the parameter of the colloid number density, respectively. Equation (11) is easily extended for any number of size classes. To appraise the size distribution of an unknown sample, the s-curve is measured and the above product of convoluted exponentials is fitted to the data.

In practice, it is necessary to limit the number of free fitting parameters. In the following example of six size classes, i.e. 20, 30, 40, 50, 70 and 100 nm, the thresholds  $E_t^{(i)}$  are obtained by calibration with monodisperse polystyrene reference spheres and remain fixed thereafter. Monomodal suspensions of varying concentration are measured to calibrate the slope parameter  $C^{(i)}$  versus the colloid number density per unit volume  $\rho_C$  according to the semi-empirical equation

$$\log C^{(i)} = a^{(i)} \log[b^{(i)} \rho_C^{(i)}] \quad (42)$$

To obtain the size distribution, the s-curve of a sample is measured with optimal statistics, especially in the low pulse energy region, i.e. the region that contains the size information. Increasing the particle size from 20 to 100 nm causes a decrease in threshold  $E_t^{(i)}$  by a factor of 2 (from 0.5 to 0.28 mJ for the present optics set-up), which is

---

<sup>10</sup> This is valid for colloids of similar chemical composition. For limitations, see Section 6.

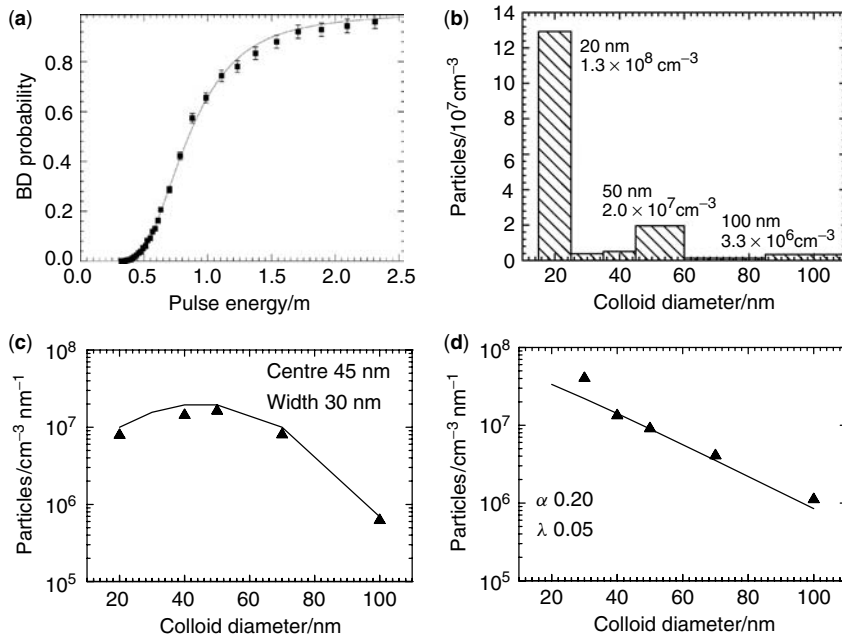


**Figure 17.** Particle size distribution (PSD) of polystyrene particles are reproduced typically within 20% error: (a) the relative number of breakdown events (BD probability) as a function of the laser pulse energy for a three modal colloid sample. (b) From the fitted curve the PSD is appraised. Reprinted with permission from Walther, C., Cho, H. R. and Fanghänel, Th. (2004). Measuring multimodal size distributions of aquatic colloids at trace concentrations. *Appl. Phys. Lett.*, **85**, 6329–6331. Copyright 2004, American Institute of Physics. Synthetic distributions (solid lines) following a Gaussian function (c) and a gamma function (d) are compared with the measured values ( $\blacktriangle$ )

small compared with the typical energy interval of a complete ‘s-curve’ (as depicted in Figure 17a). Equation (41) is then fitted to the data. The threshold parameters,  $E_t^{(i)}$ , remain fixed, since they determine the size classes, and only the concentration parameters  $C^{(i)}$  are varied. In spite of six parameters being fitted simultaneously, the fit turns out to be robust. The parameters hardly affect one another, but rather each parameter is sensitive to a unique region of the s-curve.  $C^{(1)}$  is determined solely in the region below  $E_t^{(2)}$ , the threshold of the second size class;  $C^{(2)}$  is most sensitive at energies  $E_t^{(2)} < E_0 < E_t^{(3)}$ , and so forth. The size classes need to be separated sufficiently that several different pulse energies can be measured between  $E_t^{(i)}$  and  $E_t^{(i+1)}$ . Typically the mean values of neighbouring size classes differ by at least 25%. Figure 17 illustrates the case of a trimodal sample of polystyrene reference beads:  $1.5 \times 10^8$  particles  $\text{cm}^{-3}$  of 20 nm diameter,  $2.0 \times 10^7$  particles  $\text{cm}^{-3}$  of 50 nm and  $2.7 \times 10^6$  particles  $\text{cm}^{-3}$  of 100 nm. They are combined in order to simulate a Pareto-like particle size distribution as is found in natural waters. The differential number density of different sizes  $\partial\rho_C(d)/\partial d$  scales as a power law of the particle diameter  $d$ :

$$\frac{\partial\rho_C(d)}{\partial d} \propto d^{-\beta}; \quad 3 < \beta < 5 \quad (43)$$

In Figure 17a, the raw data, i.e. the number of breakdown events as a function of the laser pulse energy, are plotted. Note the high quality of the data at low pulse energies, which is crucial to achieve meaningful results. All six concentration parameters  $C^{(i)}$  are varied and the results displayed in the histogram in Figure 17b.  $C^{(1)}$ ,  $C^{(4)}$  and  $C^{(6)}$  yield finite values, whereas  $C^{(2)}$ ,  $C^{(3)}$  and  $C^{(5)}$  remain close to zero, which demonstrates that little crosstalk<sup>11</sup> to lower channels exists. The particle number concentrations are reproduced with an approximately 20% error down to  $\sim 10^8$  particles cm<sup>-3</sup>, which is about two orders of magnitude more sensitive than the combination of FFFF and LIBD [51]. The method is applicable to continuous distributions with a size resolution of approximately 20% (i.e. 40 and 50 nm particles can be distinguished), as shown for the case of a synthetic gaussian distribution (Figure 17c):

$$dN(d)/dd \propto \exp[(d - \mu_G)^2/\sigma_G^2], \mu_G = 45 \text{ nm}, \sigma_G = 30 \text{ nm} \quad (44)$$

and for a gamma distribution (Figure 17d)

$$dN(d)/dd \propto d^{\alpha_\gamma} \exp[-d\lambda_\gamma], \alpha_\gamma = 0.2, \lambda_\gamma = 0.06 \quad (45)$$

If, however, a sample contains a predominant fraction of large colloids, some size-screening effects may occur. Colloids do not contribute to the sum curve below their specific threshold  $E_t^{(i)}$ . In order for the contribution of small colloids (at comparatively high energy) to be of measurable relevance, the signal caused by the large colloids must remain sufficiently low. As the s-curve  $p(E_0)$  approaches unity, an additional increase due to a fraction of very small sizes can no longer be resolved.<sup>12</sup>

## 5 APPLICATIONS

This chapter deals mainly with the characterisation of aquatic colloids by LIBD. In addition, some interesting applications of LIBD to aerosols will be mentioned briefly. As discussed in Chapters 1 and 2, colloids are ubiquitous in all kinds of natural waters [23,27,48, 90,99–101]. Variations of their size distribution, chemical composition and stability are attributed to their biogeochemical origin, either by nucleation or by dispersion. Natural aquatic colloidal systems generally contain very small particles at relatively low concentrations [48,49,91,102–107], and their detection may be complicated by the simultaneous presence of larger particles that have no enduring stability and hence may precipitate over time. The advent of LIBD [3,5–16,22,93] has made it possible to visualise such small and stable aquatic colloids. It is less well known that also in laboratory systems, even in chemicals of ultra-high purity, there are always colloids present [8–10]. Their presence is increasingly relevant when working in very dilute systems [39,41,43–45]. On the other hand, nanoscopic chemical reactions of actinides under environmental conditions can be masked by the presence of aquatic colloids [31,32,48,49]. LIBD is therefore applied to study the environmental significance of aquatic colloids [27–37].

<sup>11</sup> This crosstalk, i.e. a phantom signal in small size classes which results from large colloids, is a severe problem in the case of static light scattering [91].

<sup>12</sup> Recently, an increase of the size range and number of channels has been reported [82,84]. By taking into account the effects of spherical aberrations, size distributions from 15–400 nm can be measured by LIBD.

## 5.1 AQUATIC COLLOIDS IN DRINKING WATER

LIBD allows the size and concentration of aquatic colloids present in potable water to be investigated. As the present book treats environmental colloids, it is appropriate to comment on the amount of aquatic colloids that we consume. LIBD facilitated the investigation of purified Bodensee waters (drinking water) with respect to their low colloid contents [108–110]. Bundschuh *et al.* measured the breakdown probability of several waters and found that river water (Hirschbach, Frauenau, Germany) contained far more colloids than mineral waters, which in turn had a higher colloid content than tap waters [27]. Figure 18 shows a similar comparison of different commercial mineral waters, laboratory tap water and ultrapure water (MilliQ). Their particle size range is measured as less than 200 nm, as equivalent to spherical diameter, and the predominant number density is in the range below 50 nm. Corresponding mass-weighted mean number densities varied from  $10^{11}$  to  $10^{14}$  particles  $\text{dm}^{-3}$  (Figure 18). Particle size distributions could not be measured by that time [27]. On average, water in plastic bottles contained less colloids than sparkling water in glass bottles. Carbonate may augment colloids but also glass leaching probably caused higher colloid concentrations.

## 5.2 COLLOID FORMATION AND THERMODYNAMIC EQUILIBRIA

An interesting application of LIBD in laboratory systems is in the determination of the solubility of sparingly soluble metal hydroxides [39,41,43–46]. Metal ions of higher oxidation state with  $Z \geq 3+$  readily undergo hydrolysis in the acidic pH region and polynucleation leads to colloid formation with increasing pH. LIBD can be applied to monitor the pH edge at which such colloid formation begins [43–45]. If the hydrolysis constants of the metal ion are known, the solid–liquid equilibrium reaction can be evaluated from the pH edge of colloid formation.

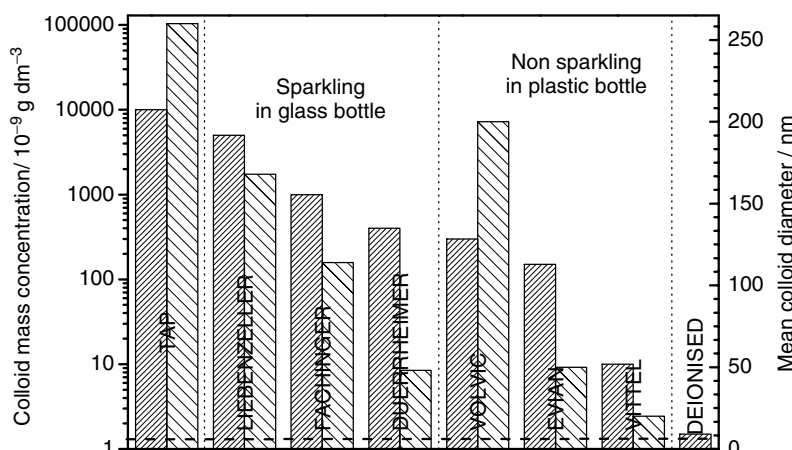


**Figure 18.** Aquatic colloids present in different kinds of drinking water as observed by LIBD. The mass concentration is estimated to be  $10^{-5} \text{ g dm}^{-3}$  in tap water down to  $10^{-8} \text{ g dm}^{-3}$  in Vittel bottled water (left bars) with average sizes range <200 nm in diameter (right bars). The horizontal dashed line indicates the detection limit of LIBD

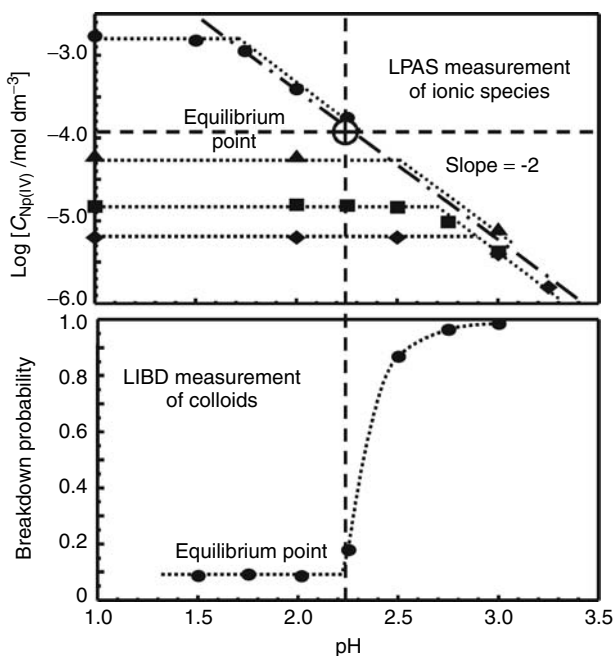
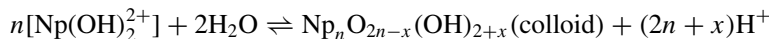


**Figure 19.** A combination of LPAS and LIBD experiments: the abundance of ionic Np(IV) relative to total Np concentration in solution shows a threshold-like decrease at a certain pH as measured by LPAS. The pH threshold depends on the total Np concentration (**a**). It is shown by LIBD that at the pH threshold colloids form, which explains the decrease in ionic Np(IV) (**b**) [ $3 \times 10^{-5}$  mol dm<sup>-3</sup> Np(IV)]. Reproduced from Neck, V., Kim, J. I., Seidel, B. S., Marquardt, C. M., Dardenne, K., Jensen, M. P. and Hauser, W. (2001). A spectroscopic study of the hydrolysis, colloid formation and solubility of Np(IV). *Radiochim. Acta*, **89**, 439–446, by permission of Oldenbourg Wissenschaftsverlag GmbH

A typical example is demonstrated in Figure 19 for the hydrolysis of  $\text{Np}^{4+}$  either in  $\text{H}_2\text{O}$  or in  $\text{D}_2\text{O}$  [43]. The speciation of Np(IV) was performed by LPAS (laser-induced photoacoustic spectroscopy) as a function of pH (Figure 19a). The absorbance of Np(IV) at 724 nm ( $143 \text{ dm}^3 \text{ mol}^{-1} \text{ cm}^{-1}$ ) was observed with varying pH. A region of constant absorbance is followed by a sharp decrease at a pH edge. Simultaneously, the colloid content of the Np(IV) solution at  $3 \times 10^{-5}$  mol dm<sup>-3</sup> was measured by LIBD as a function of pH (Figure 19b). With increasing pH, only the background signals of LIBD were observed up to pH 2. The first colloid signal appeared at pH 2.25, which then increased further with increasing pH. This pH edge coincided with the absorptivity decrease of LPAS measurements at  $(3.0 \pm 0.5) \times 10^{-5}$  mol dm<sup>-3</sup>. In previous studies, the absorptivity decrease was attributed to the formation of hydrolysed species, which were supposed to have a lower molar extinction coefficient than the free Np(IV) ion. However, in [43] the co-occurrence of an absorptivity decrease and colloid formation at the same pH edge suggested that all  $\text{Np(OH)}_n^{4-n+}$ ,  $n = 0-2$  have equal absorption coefficients and the decrease in absorptivity is rather due to the formation of (non-absorbing) polynuclear species.

The edges of colloid formation were shifted to higher pH with decreasing Np(IV) concentrations and led to a slope of 2 for all measurements, which showed that the

colloids were formed from the hydrolysed species  $\text{Np}(\text{OH})_2^{2+}$ :



According to this reaction, the colloids may have evolved with time and formed precipitates such as  $\text{NpO}(\text{OH})_2$  or  $\text{Np}(\text{OH})_4$ , or a mixture of both, depending on the pH. The solubility product of such a mixture was estimated to be  $\log K_{\text{sp}} = -54.4 \pm 0.4$ , obtained by use of the known hydrolysis constant for  $\text{Np}(\text{OH})_2^{2+}$ . Similar work has been performed for Th(IV) [44–46], Pu(IV) [39,41] and Zr(IV) [117]. A comparable experiment for Eu(III) employing LIBS has also been published [19] (Section 5.9).

### 5.3 ALUMINOSILICATE COLLOIDS

Silicon and aluminium are omnipresent in natural water, the former in near  $\text{mmol dm}^{-3}$  concentrations and the latter in  $\mu\text{mol dm}^{-3}$  concentrations. Both elements are known as major components of various clay minerals in any geological environment and hence are present in all natural aquatic systems [48,49]. They readily form polynuclear species that may act as crystallisation cells (kernels) of larger aquatic colloids. In the course of the formation of such hydroxyl aluminosilicate colloids, many trace metal ions of high oxidation state (in particular actinides) can be incorporated [48,49]. The process results in the formation of actinide pseudo-colloids. Therefore, aquatic colloids may play a carrier role to facilitate the migration of metals (and other pollutants) in aquifer systems [105]. Consequently, the migration behaviour of colloid-borne metals is of environmental significance. Although the mass concentration of aquatic colloids is very low, their number density is in general high, particularly for small (<50 nm) colloids. The long-term safety assessment of nuclear waste repositories represents one example [111,112], where the possible migration of colloid-borne actinides in the course of time from a nuclear waste disposal site can be, for obvious reasons, of radiological importance.

A heterogeneous nucleation of aluminosilicate colloids with trace actinides has been investigated systematically [48,49] with LIBD and also other methods. A particular part of such an investigation is illustrated in Figure 20 [48]. Mixing of an acidic Al solution ( $10^{-5} \text{ mol dm}^{-3}$ ) containing  $5 \times 10^{-8} \text{ mol dm}^{-3}$  Am with alkaline Si ( $10^{-3} \text{ mol dm}^{-3}$ ) resulted in a three-phase equilibrium: ionic phase, colloidal phase and an aluminosilicate precipitate. In order to separate solute species and small colloids from the precipitate, a 450 nm filtration was performed. The amount of Am found in the filtrate showed a minimum at pH 6 (Figure 20a), where the aluminosilicate solubility was the lowest. Am was found both in the colloidal and in the solute fraction. For  $\text{pH} > 5$ , most of the Am was incorporated into colloids (Figure 20b).

The formation of aluminosilicate colloids was examined under non-perturbed conditions (Figure 20c). Many laboratory chemicals of even the highest purity grade contain colloids typically at concentrations of the order of  $10^{-6} \text{ g dm}^{-3}$ . In particular, strong bases suffer from colloidal contaminations. In the present case this was true for one of the stock solutions for titration, i.e. Si in  $0.03 \text{ mol dm}^{-3}$  NaOH. In contrast, the second stock solution, i.e. Al in  $0.03 \text{ mol dm}^{-3}$  HCl, was prepared colloid free. Three titrations were performed. The Al–HCl mixture was titrated with NaOH to higher pH (Figure 20c, ‘Al’). HCl was

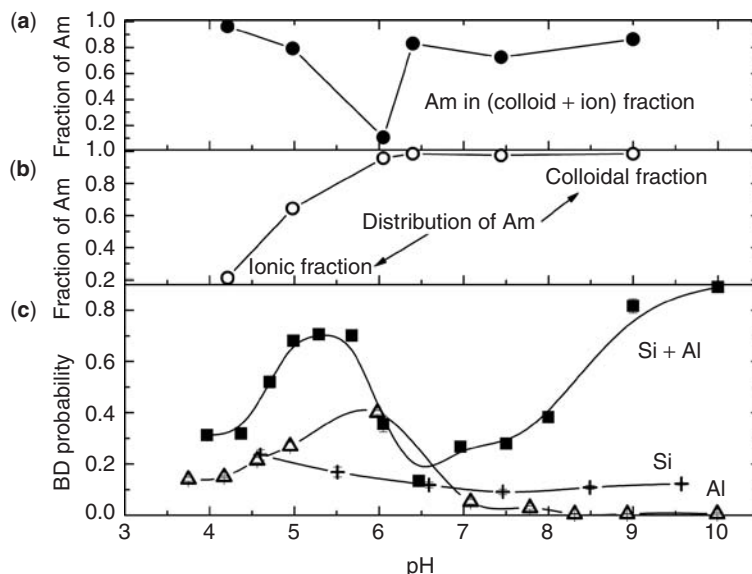


**Figure 20.** Formation of aluminosilicate colloids and colloid-borne Am in a mixture of  $10^{-3}$  mol dm $^{-3}$  Si,  $10^{-5}$  mol dm $^{-3}$  Al and  $10^{-8}$  mol dm $^{-3}$  Am. Am is distributed into three phases: ions, colloid and precipitate. (a) The amount of Am in either colloidal or ionic phase shows a minimum around pH 6. (b) Within the (colloid + ion) fraction, most Am is found incorporated or attached to colloids at pH > 5. (c) Colloid formation is observed in pure Si ( $10^{-3}$  mol dm $^{-3}$ ) and Al ( $10^{-3}$  mol dm $^{-3}$ ) solutions but is most pronounced in the mixture of both ( $C_{\text{Si}} 10^{-3}$  mol dm $^{-3}$ ,  $C_{\text{Al}} 10^{-5}$  mol dm $^{-3}$ ). Reprinted from Kim, M. A., Panak, P. J., Yun, J. I., Kim, J. I., Klenze, R. and Kohler, K., Interaction of actinides with aluminosilicate colloids in *statu nascendi*. Part I: generation and characterisation of actinide (III)-pseudocolloids, *Colloids and Surfaces A*, 97–108, Copyright 2003, with permission from Elsevier

titrated with the Si–NaOH mixture towards higher pH ('Si') and finally the Al–HCl solution was titrated with the Si–NaOH solution ('Si + Al'). LIBD showed the formation of colloids in all three mixtures. However, in the third titration, where both Si and Al are present, the colloid generation was most pronounced. At pH < 5, the dissolution of aluminosilicates decreased the colloid formation, whereas the lowest solubility region at pH 6.5 also provided a minimal amount of colloids. The formation of aluminosilicate colloids was pronounced at pH 5.5 and at pH > 7. The concordance among Figure 20a,b and c is direct evidence for the formation of aluminosilicate colloid-borne Am. This is further corroborated by chemical speciation with TRLFS (time-resolved laser fluorescence spectroscopy), replacing Am by Cm. As confirmed further by LIBD, the mass concentration of aluminosilicate colloids formed under the given conditions ranged from  $1 \times 10^{-5}$  to  $5 \times 10^{-5}$  g dm $^{-3}$  in the particle size range 10–50 nm. The corresponding number density varied in the range  $10^{11}$ – $10^{14}$  particles dm $^{-3}$  water.

#### 5.4 MIGRATION OF AQUATIC COLLOIDS

To understand further the migration of colloid-borne actinides, a field experiment was conducted in the Grimsel underground laboratory in Switzerland by using LIBD for *in situ*

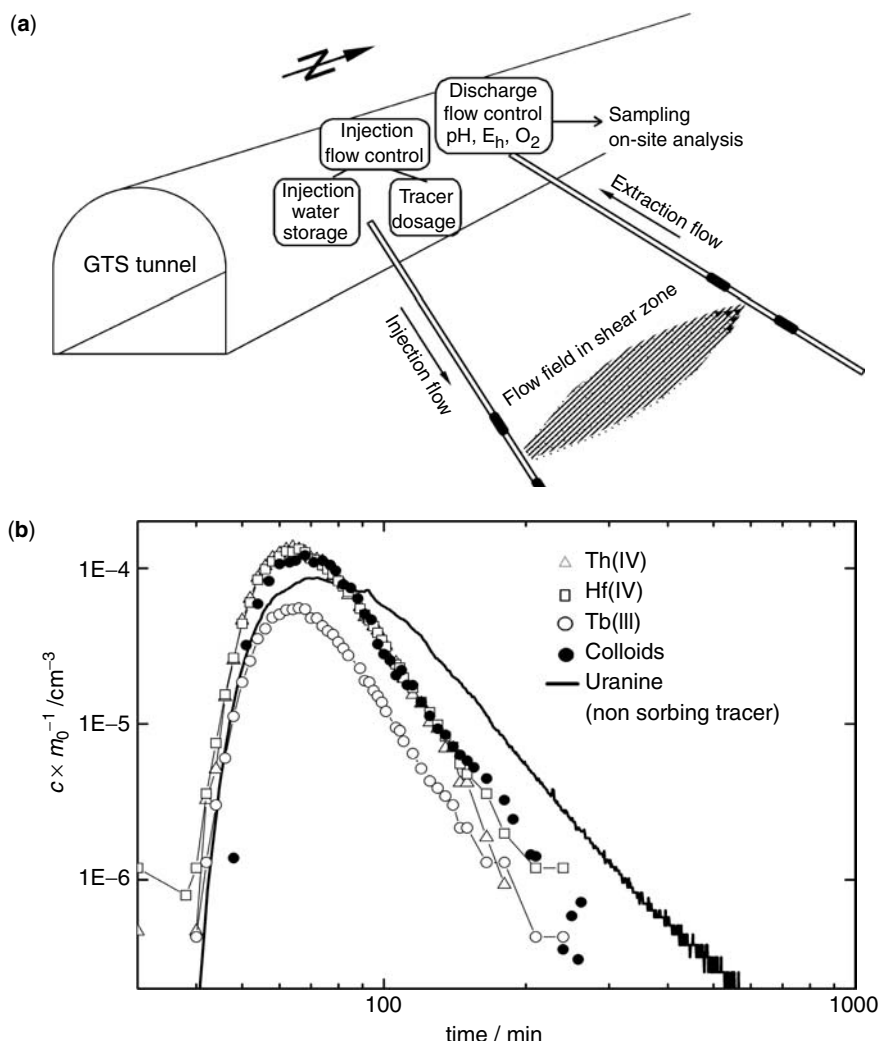


**Figure 21.** (a) Bentonite colloid migration through a 5 m long granite fracture was studied at the Grimsel test site (GTS). (b) An extraction profile of migrated colloids and colloid-borne trace elements. Colloids and uranine were monitored *in situ* by LIBD and fluorescence detection, respectively. The metals were analysed off-line by ICP-MS. Reprinted from Hauser, W., Geekeis, H., Kim, J. I. and Fierz, Th., A mobile laser-induced breakdown detection system and its application for the *in situ* monitoring of colloid migration, *Colloids and Surfaces A*, 37–45, Copyright 2002, with permission from Elsevier

monitoring [31,32,113]. For this purpose, a granite fracture of 5 m length was localised for a dipole aquifer flow path (Figure 21a) [31]. Bentonite colloids (smectite type) of concentration of  $2 \times 10^{-2} \text{ g dm}^{-3}$  in about  $100 \text{ cm}^3$  were injected into the fracture. The colloids showed a distribution between ca. 100 and 180 nm with a mean colloid size of 150 nm. The colloid content of the outflow of the dipole path was measured by time-resolved

LIBD. A background colloid level of  $5 \times 10^{-6}$  g dm $^{-3}$  was found at an average size of 200 nm. After extracting 400 times the injection volume (100 cm $^3$ ), the injected colloid recovery was 55% in mass concentration and the average size of the extracted colloids decreased to 120 nm. From the mass concentration and the mean colloid diameter, the total colloidal surface area was calculated. Since mainly large colloids (with a lower surface to mass ratio) were lost [31] in the course of migration, the recovered colloidal surface area exceeded the mass recovery and appeared to be about 70%.

A further experiment was conducted with a cocktail of bentonite colloids spiked with about 10 $^{-7}$  mol dm $^{-3}$  each of Th(IV), Hf(IV) and Tb(III). The mass concentration of the colloids exceeded the trace metal content by about 670-fold. This time colloid recovery was 55%, similar to the previous one. The extraction profile of all metals was the same as for the colloids (Figure 21b) [31]; radionuclide and colloid concentrations in the figure are normalised to the injected mass or activity ( $m_0$ ). The peak maxima of the colloid and metal breakthrough curves appeared about 10 min ahead of the non-sorbing (conservative) tracer uranine. The shift suggested the existence of size and/or charge exclusion effects typical of colloid migration. The recovery was  $78 \pm 8\%$  for both Th(IV) and Hf(IV) and  $33 \pm 3\%$  for Tb(III). The tetravalent element recovery was related to the recovery of bentonite-colloid surface area ( $\sim 70\%$ )<sup>13</sup>. The agreement between surface recovery and trace recovery implied the surface-bound incorporation of tracers to colloids. The lower recovery of Tb suggested a rapidly reversible sorption on colloids and thus partial retention at surfaces of tubings or rock minerals.

## 5.5 COLLOIDS IN DEEP UNDERGROUND WATERS

Closely related to the investigations described in the previous section is the Äspö Hard Rock Laboratory (HRL) project of the Svensk Kärnbränslehantering AB (SKB) in Oskarshamn, Sweden. A granitic rock formation was assessed for the suitability of building a nuclear waste repository [114]. In contrast to the Swiss project in the Grimsel mountains, the Swedish Hard Rock Laboratory is located underneath the island of Äspö in the Baltic sea close to the Oskarshamn nuclear power plant. The rock formation contains several granitic shear zones, penetrated by aquifers of different origin (Figure 22) [33].

The laboratory is accessible via a tunnel 3.5 km long that descends 450 m below sea level, which allows one to measure *in situ* the ground waters at selected boreholes (depicted as 1–8 in Figure 22). The natural conditions of the water prior to and during the measurement have been conserved carefully; in particular, a high pressure LIBD cell was built which withstands the hydrostatic pressure up to 416 m below sea level (Table 2). The pressures given in the table reflect the heights of the water columns of the respective aquifers, which do not necessarily equal the total vertical depths of the sampling locations.

The variation in colloid content is remarkably high [34] (Figure 23), even considering the large difference in metal ion concentrations (up to three orders of magnitude). The water from the uppermost site at –69 m (borehole 1) contains large colloids (mean size 600 nm) at high concentrations. This large amount of colloids is found in concert with low salinity and a high content of organic substances (DOC 16 mg dm $^{-3}$ ). LIBD has a low sensitivity to pure humic/fulvic acids (see section 5.7), but these substances

<sup>13</sup> As defined previously, the surface area recovery is the ratio of total colloidal surface of recovered colloids to total colloidal surface of injected colloids.

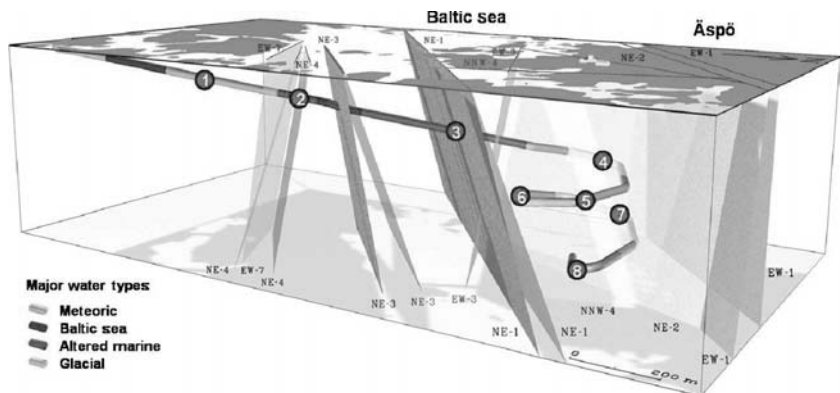


**Figure 22.** Sampling locations for LIBD. Different shades correspond to different origins of waters (meteoric water, seawater, altered marine water and glacial water). For parameters, see Table 2. Reprinted from *Äspö progress Report IPR 03-38*, 2003, with permission from Swedish Nuclear Fuel and Waste Management Company

**Table 2.** Borehole locations and water pressure

Location	Elevation/m	Pressure/ $10^5$ Pa
1	-69	5.9
2	-168	12.9
3	-182	$\geq 8.0$
4	-235	14.4
5	-282	21.3
6	-306	16.2
7	-370	14.3
8	-416	32.8

nevertheless might play an important modifying role towards the inorganic colloid concentrations [115,116]. The stability of inorganic or lignite particles is strongly enhanced by the formation of mixed complexes and at low ionic strength (which prevents further aggregation followed by precipitation) where even large particles are stable on long time-scales.

Borehole (4) at  $-235$  m contains a very pure water of high salinity ( $\text{Cl}^-$  concentration  $11 \text{ g dm}^{-3}$ ) with colloidal contamination similar to that observed for filtered ultrapure deionised water shown as the detection limit ('Ultra-Pure water'). Colloids were smaller than 20 nm with a concentration in the region of  $10^{-8} \text{ g dm}^{-3}$ , five orders of magnitude lower than in the case of borehole (1). The data below a  $\text{Cl}^-$  concentration of  $12 \text{ g dm}^{-3}$  followed a systematic decrease in colloid concentration with increasing salinity, suggesting a decrease in stability due to colloid aggregation and subsequent precipitation or sedimentation. Only the colloid content of borehole (7) deviated from this trend as it was too high by almost three orders of magnitude. However, the water of borehole (7) originated from a region disturbed by the tunnel driving. It is known that additional iron hydroxide colloids may be generated by oxygen permeation into these so called 'excavation disturbed zones'. In a more recent experiment, the water of the same aquifer

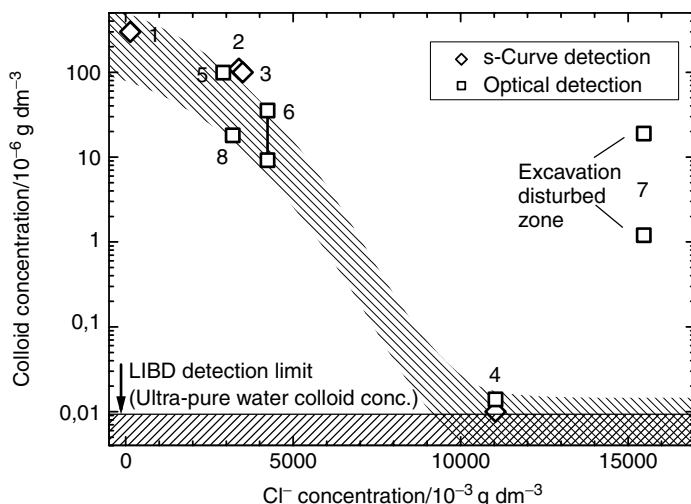


**Figure 23.** LIBD analysed colloid concentration as a function of the  $\text{Cl}^-$  concentration as an indicator for salinity (data points connected by bars indicate varying colloid concentrations due to pressure fluctuations). Reprinted from Åspö progress Report IPR 03-38, 2003, with permission from Swedish Nuclear Fuel and Waste Management Company

was sampled at a different position away from the disturbed zone and a colloid content close to the detection limit was found.

The change in colloid formation with experimental conditions was observed by varying the ground-water flow-rate and length of the tubing. Oxygen permeated the polyethylene (PE) tubing, which led to colloid formation in waters that were rich in Fe(II). The apparent colloid content increased with increasing length of the tubing (up to 100 m) and decreasing flow-rate. Sampling was hence performed as close to the boreholes as possible. Nonetheless, the flow-rate still is a critical parameter. Whereas at borehole (4) at  $4 \text{ cm}^3 \text{ min}^{-1}$  the 'natural' colloid content of  $10^{-8} \text{ g dm}^{-3}$  was measured, the colloid concentration increased 50-fold ( $5 \times 10^{-7} \text{ g dm}^{-3}$ ) at a flow-rate of  $1400 \text{ cm}^3 \text{ min}^{-1}$ . This effect was caused by the erosion of the backfill material.

Since the transport capacity for colloid-mediated migration scales proportionally to the total specific surface area of suspended particles, a water containing high concentrations of colloids such as (1) increases the risk of radionuclide release into the environment. Even the low colloidal water (4) contains a large number of colloids ( $\sim 10^9 \text{ particles dm}^{-3}$ ), resulting in a large total surface area due to the small diameter. The importance attributed to colloid-mediated transport becomes apparent from the fact that Sweden is about to make LIBD measurements an integral part of future repository assessments.

## 5.6 AGGREGATION OF BENTONITE COLLOIDS

The multimode s-curve method discussed in section 4.7 is especially suited to observe changes in size distributions as a function of time, *e.g.* in the case of particle aggregation. Figure 24 shows the behaviour of bentonite colloids.

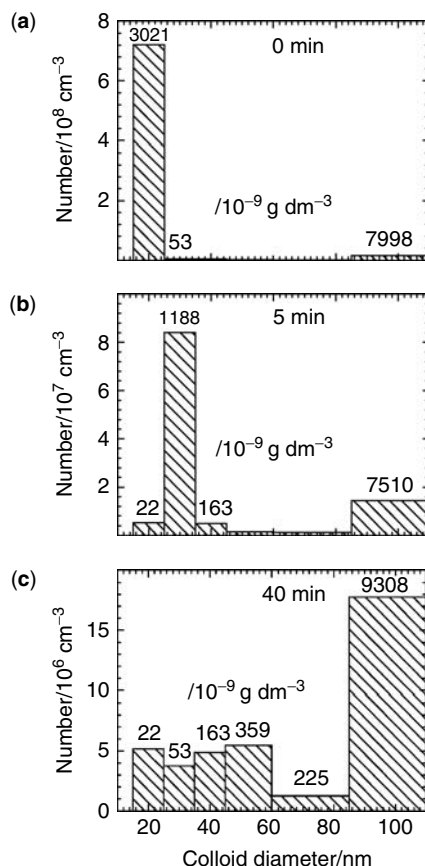


**Figure 24.** Time-resolved observation of aggregation in a multimodal bentonite colloid suspension ( $10^{-5}\text{ g dm}^{-3}$ ): (a) at pH 6 and (b) 5 min after the pH was adjusted to 2 and (c) 40 min after pH adjustment. Reprinted with permission from Walther, C., Cho, H. R. and Fanghänel, Th. (2004). Measuring multimodal size distributions of aquatic colloids at trace concentrations. *Appl. Phys. Lett.*, **85**, 6329–6331. Copyright 2004, American Institute of Physics

Figure 24a reflects the original, bimodal, size distribution at pH 6. The 100 nm size class<sup>14</sup> contains two-thirds of the total colloidal mass ( $7 \times 10^{-6}\text{ g dm}^{-3}$ ); the rest ( $3 \times 10^{-6}\text{ g dm}^{-3}$ ) has a size of approximately 20 nm. Due to their small mass (only 0.8% of a 100 nm colloid), the small fraction contributes the dominant colloid *number*. At pH 2 in  $10\text{ mmol dm}^{-3}$  NaCl solution, the electric double layer of the colloids is neutralised and aggregation proceeds very fast, as can be seen from Figure 24b. The PSD is noticeably shifted to larger diameter after 5 min. The fraction of 100 nm particles remains constant (note the different scalings of Figure 24a and b) since collisions of two 100 nm particles are very unlikely due to their lower number density. After 40 min, practically all particles

<sup>14</sup> For non-spherical particles, the ‘size’ given by LIBD corresponds to a colloid of equal volume but spherical shape.

formed aggregates of 100 nm or larger (Figure 24c). The range for particle size distributions has now been extended from 15 to 400 nm. Combination with a single particle counter for the detection of colloids >100 nm [117] (Section 7) extends the size range from 15 nm to 2  $\mu\text{m}$  [82].

## 5.7 LIBD ON ORGANIC COLLOIDS

LIBD is not commonly used for the detection of organic particles due to inherent difficulties. The colloid detection mechanism is based on the different breakdown thresholds of pure water and solid particles. Colloids of very high water content are difficult to discriminate from the background. Nonetheless, there have been a few reports on successful application of LIBD to organic substances. A systematic study on natural humic acid (HA) and fulvic acid (FA) substances isolated from deep groundwaters of the Gorleben site (Germany) was performed by Monsallier *et al.* [118]. It is well known from gel permeation chromatography (GPC) [119,120] that natural HA typically contain two fractions of hydrodynamic size equivalent to 1.5 kDa (globular protein calibration) and >100 kDa ( $d \approx 6 \text{ nm}$ ). Synthetic HA and FA do not contain the larger size fraction and cannot be detected by LIBD. By means of carefully designed blank experiments, the authors excluded possible artefacts from inorganic colloids and showed that LIBD signals originated in the HA content of the samples. Whereas LIBD was blind for the smaller size class and did not detect any colloids in the FA, the larger (colloidal) fraction in natural HA was detected by LIBD and a size of approximately 10 nm  $m \approx 500 \text{ kDa}$  (according to a calibration with polystyrene particles) was assigned. The s-curves scaled correctly and reproducibly with increasing concentration. Aggregation and flocculation of HA was observed upon pH change from 3.5 to 9.3. Further proof that LIBD detected the large fraction only was given by centrifugation experiments. In a recent study [121], LIBD (called ‘nano-particle analyser’) was used to detect spores (*Bacillus subtilis*, 13–15% water content,  $0.8 \times 1.5 \mu\text{m}$ ) and two types of bacteria (*Enterococcus faecalis*, 70–85%, 1  $\mu\text{m}$ , and *Enterococcus durans*, 70–85%, 1–2  $\mu\text{m}$  [37]). However, it is not possible to distinguish bacteria from inorganic particles by LIBD and little information is given on how background contamination was avoided, especially in the case of the bacteria with high water content. Possibly only metabolites of the bacteria were detected. In addition, it is not clear why the optical detection set-up was used to record s-curves (of low statistical quality) instead of obtaining size information from the ignition length. Globular proteins of mass 669 kDa in water were detected, the concentrations ranging from  $10^{-6}$  to  $10^{-3} \text{ g dm}^{-3}$  [122]. The slope of the s-curves increased with increasing concentration, but no size information was obtainable from the thresholds due to poor reproducibility. Smaller proteins (<500 kDa) could not be discriminated against the background at all. Recently, particulate matter from diesel car engines was investigated by LIBD when the exhaust gas was bubbled through ultrapure water for 1 min [123]. Sooty particles of up to micrometre size were detected for conventional diesel engines, while only particles of <50 nm were found in the exhaust gas of a car with a particulate filter.

Although LIBD is sensitive to compact organic particles, it is evident from [118] that small or low-density proteins, FA and monomeric units of HA are not detectable. To our

knowledge, there are no systematic studies on how LIBD behaves in the transition region from compact organic particles to gelly particles and at what point the signal is lost.

## 5.8 LIBD AND LIBS ON AEROSOLS

In addition to colloid detection in aqueous media, LIBD has found applications in a variety of related research fields [124]. Particularly LIBD and LIBS have become standard methods in aerosol science, and have been used in this field longer than for the aquatic chemistry of colloids. The material and size of liquid aerosols were investigated for their breakdown thresholds [98]. A similar experimental and theoretical investigation followed [125,126] for plasma generation and evolution in droplets. By the use of intensified gated CCD cameras following a spectrograph, the elemental composition of aerosols could be determined by LIBS, since in air the perturbation of discrete emission lines is much less than in water. Various airborne particles have been analysed by a combination of LIBD and LIBS. Coal fire-ash particles [127] or seawater aerosols [128] were investigated and the size distribution of aerosols [129] or their chemical composition [88] was probed even in an *in situ* experiment [130]. Other examples include analyses of nanometre-sized carbon clusters [131], large biological aerosols [132] and spray droplets containing colloids [133]. This is an appealing scheme but it is hard to distinguish the contributions from true colloids and the signals from solvated species which form colloids during the evaporation process. Analyses by LIBS were also attempted on filtered colloids [134–136] and on aquatic colloids dispersed on the solid surface [137]. LIBS has been widely used mostly for solid surface characterisation [138–142] or performed on particulate material [143,144] and small particles [145,146], which is, however, outside the scope of this chapter.

## 5.9 LIBS ON AQUATIC COLLOIDS

It is well known that a colloid-borne element can be better recognised by LIBS than its ionic species [18,147,20], a fact that can be used for distinguishing the colloid formation of a particular element or for a solubility study (similar to section 5.2). An example for LIBS of aquatic colloids directly in suspension is the work of Yun *et al.* [19]. Figure 25a compares two different spectra of Eu in aqueous solution. Both samples contained an equal amount of Eu (concentration  $2 \times 10^{-4}$  mol dm<sup>-3</sup> each) [19]. Trace (A) refers to a colloidal Eu<sub>2</sub>O<sub>3</sub>(s) suspension in neutral water and trace (B) depicts the emission signal of the solvated Eu<sup>3+</sup><sub>aq</sub> ion in 0.7 mol dm<sup>-3</sup> nitric acid. The Eu(I) emission lines at 495.4, 462.7 and 466.1 nm are clearly visible for the particles in water and about 100-fold weaker for the solvated ion. The peak at 306 nm originates from the O–H rotation–vibration transition of water [148]. For solvated species, and also colloids, the emission intensity shows a linear relation with concentration (Figure 25b) but is much weaker for solvated ions. This enhanced sensitivity for colloids was applied for the determination of Eu<sup>3+</sup> solubility (Figure 25c). The pH of an Eu<sup>3+</sup> solution ( $1.3 \times 10^{-4}$  mol dm<sup>-3</sup>) was increased by titration with NaOH. At pH ≈ 7.1 the emission intensity increased strongly due to the formation of colloids. This provides a possibility of assessing the solubility products of Eu oxy-hydroxide.

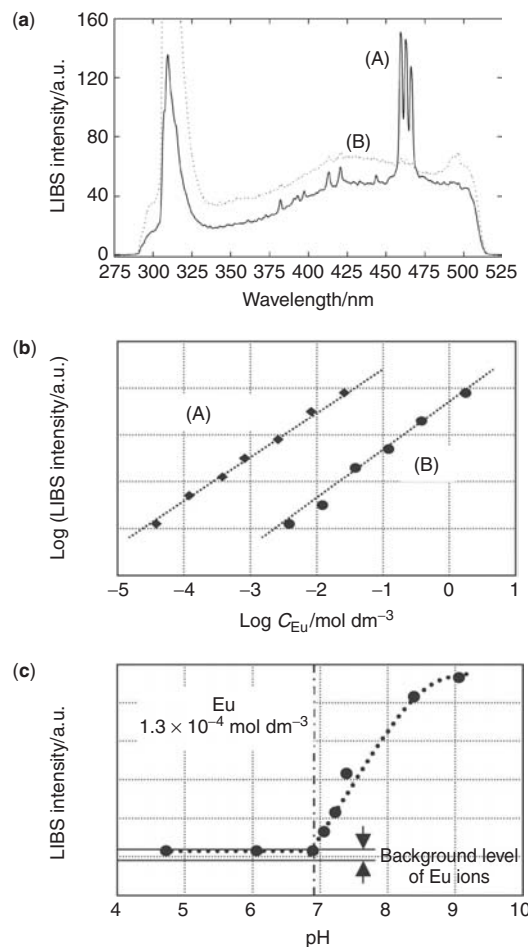


**Figure 25.** (a) LIBS spectra of samples with Eu concentrations of  $2 \times 10^{-4}$  mol dm<sup>-3</sup>. Trace (A) shows a suspension of Eu<sub>2</sub>O<sub>3</sub>(s) particles in water and (B) Eu<sup>3+</sup> in 0.7 mol dm<sup>-3</sup> nitric acid. (b) Calibration of the Eu concentration by LIBS in  $10^{-3}$  mol dm<sup>-3</sup> HClO<sub>4</sub> for ions or for solid suspension. (c) the pH edge of Eu colloid formation when an acidic ionic solution was titrated to higher pH. Reprinted from Yun, J. I., Bundschuh, T., Neck, V. and Kim, J.-I. (2001). Selective determination of europium(III) oxide and hydroxide colloids in aqueous solution by laser-induced breakdown spectroscopy. *Applied Spectroscopy* **55**, 273–278, with permission from the Society of Applied Spectroscopy

## 6 PRACTICAL REMARKS WHEN USING LIBD

Whereas the technical requirements on laser and optics are discussed in Sections 3.3 and 4, this section addresses some important issues for actual working with LIBD systems. It must be kept in mind that LIBD is an ultra-sensitive method for trace detection, inherently susceptible to contamination. Exposure of a dilute sample ( $10^{-9}$  g dm<sup>-3</sup> regime) to air for a few minutes leads to an input of aerosols which may significantly increase the colloidal background signal. For this reason, sample preparation should be performed in a clean

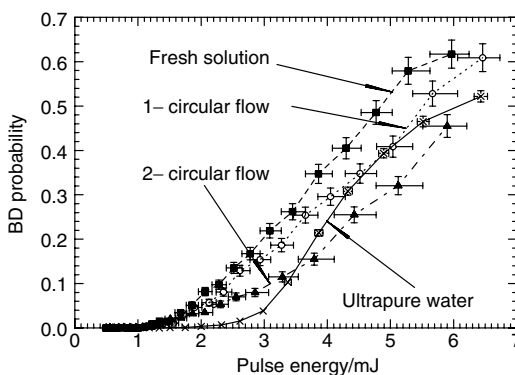


**Figure 26.** For very dilute samples (here polystyrene spheres, 20 nm,  $5 \times 10^{-8}$  g dm $^{-3}$ ), surface sorption plays an important role. In a closed-circle flow-through set-up, fresh sample is compared with once and twice recycled solutions. The colloid concentration decreased (lower slope) while the threshold as a measure of size remained unaffected. This effect can be avoided by proper choice of reactor and tubing material

air environment (laminar flow cabinet) and the colloid content of chemicals involved in the sample preparation has to be examined. If necessary, ultrafiltration, centrifugation or recrystallisation has to be applied for purification of the chemicals. Filters have to be soaked properly for cleaning and rinsed thoroughly prior to use. Containers and quartz cells have to be cleaned, *e.g.* in nitric acid, and rinsed thoroughly with colloid-free water.

On the other hand, the colloidal phase must not be perturbed and the usual care has to be taken for handling [99,100,104]. In particular, surface sorption has to be avoided. In a typical set-up, a sample is provided in a glass reactor, pumped through polyethylene tubing into the LIBD detection flow-through quartz cell and back into the reactor. Figure 26 shows s-curves of freshly prepared  $5 \times 10^{-8}$  g dm $^{-3}$  20 nm polystyrene suspensions along with measurements after the total volume has been pumped through once and twice. Whereas the threshold remains constant (the particle size, of course, does not change), the slope decreases, indicating colloid loss due to sorption. This problem is avoided by using Teflon-like materials, in particular PFA (perfluorinated alkoxy compounds) for containers and PEEK (polyether ether ketone) for capillaries.

The measurement cells are made of quartz (no metal tubing should be used, to avoid sorption) and the surface roughness has to remain below 100 nm in order not to alter the laser beam profile. Simple static cells (1–10 cm $^3$ ) with magnetic (Teflon-coated) stirrers are used for limited sample volume. If at least 20 cm $^3$  samples are available, flow-through measurements can be performed, with the optimum performance in a once-through cycle, where the sample is discarded after being exposed to the laser beam. LIBD is often referred to as being a non-invasive and non-destructive method. That is not true in an absolute sense. Of course, a colloid being detected by plasma ignition is completely destroyed and in addition a laser pulse of several GW cm $^{-2}$ , even for a period as short as nanoseconds, can induce photochemical reactions. Nonetheless, the measurement of a sample with total absolute number of colloids exceeding  $10^6$  will not be altered considerably by destroying a few thousand of them. However, this might be a problem for extremely dilute samples. The same holds for photochemically produced radicals. Systems of exceptionally high redox sensitivity might even be influenced by a tiny amount of radicals. In such cases, a

once-through cycle should be used. Finally, the hot expanding plasma creates gas bubbles of millimetre size, which obstruct the laser pulse and cause an apparent decrease in BDP if not removed in time. This limits the pulse repetition rate of the laser to about 20 Hz and requires a sufficient flow-rate in a flow-through regime. Static cells should not be completely filled in order to allow the gas bubbles to escape to the surface.

In order to counteract sedimentation, samples containing particles  $>100$  nm should be stirred. Nonetheless, care has to be taken not to abrade material from either stirrer or bottom of the cell or reactor. Even tiny fragments can contribute to the colloidal background considerably, hence stirring should be slow.

Further, the breakdown process depends on the material properties of the colloids [16, 22,38]. As shown above, the number of photons required to generate the first electron depends on the ionisation energy of the colloid [54,149]. Most materials, including the reference material polystyrene, require four photons of the frequency-doubled light (532 nm,  $h\nu = 2.3$  eV) of an Nd:YAG laser, corresponding to an ionisation energy of  $7 \text{ eV} < E_I < 9.3 \text{ eV}$ . The cross-section for multi-photon ionisation is of similar magnitude [55,69,70, 150]. There are, however, exceptions, such as thoria ( $\text{ThO}_2$ ) colloids [22], which are detected at lower sensitivity and require a calibration different from the four-photon case. Materials of high transparency (such as crystalline  $\text{SiO}_2$ ) or low density and high water content (organics, see section 5.7) [52] hinder the inverse bremsstrahlung and are detected at higher photon flux or above  $10^{-3} \text{ g dm}^{-3}$  concentration.

Recent modifications of the mobile LIBD apparatus [31] have allowed measurements in a flow-through cell up to  $3 \times 10^6$  Pa pressure and simultaneous recording of pH, redox potential (Eh), oxygen content and conductivity. Details on the technique are published and no restrictions apply to the use of LIBD for research purposes. For potential commercial use, it should be noted that LIBD detection is patented by Japanese inventors [29] and an additional German patent exists covering optical acquisition [151]. To date, no commercial system is available.

A concluding remark concerns light scattering. LIBD is many orders of magnitude more sensitive than light scattering for particles that are much smaller than the wavelength of light. However, for colloids larger than  $\sim 100$  nm, static light scattering techniques [152,153] (such as the single particle counter, SPC [94,154,155]) become more sensitive, and for  $\mu\text{m}$ -sized particles, or at high concentrations, dynamic scattering (PCS) [103,156] is the method of choice due to a much faster measurement time and a less delicate set-up (in addition, both methods are available commercially). Suspensions which scatter light effectively cannot be measured by LIBD. The threshold evaluation relies on well-defined photon flux conditions in the focal area. If, however, a large fraction of light is scattered along the light path, this is no longer the case. For natural waters, containing a considerable fraction of large organics ( $\gg 1 \mu\text{m}$ ) or strongly coloured substances, a fractionation prior to LIBD measurements may be inevitable.

## 7 CONCLUSIONS AND FUTURE PERSPECTIVES

LIBD is an essentially non-invasive method for measuring aquatic samples devoid of perturbation. Colloids submitted to breakdown processes are destroyed but for most natural samples the number is too small to be significant. The appraisal of colloid size distribution

by LIBD requires a large number of single measurements and subsequent statistical evaluation. Quantification of the colloid number density and the size distribution entails a proper calibration of the method. For this, there are not so many reference particles of wide size range available except for polystyrene particles which exist as well-defined monomodal particles, ranging from 20 to 1000 nm or greater. Therefore, an operational relationship of LIBD with respect to the material properties of the colloids has to be established.

Applications of LIBD can be made for laboratory experiments dealing with the presence of colloids or their formation and also for field experiments concerned with *in situ* monitoring of aquatic colloids or their migration behaviour. Recently, size dispersion effects were observed during colloid migration by means of multimodal s-curve evaluations [82]. Radioactive tracers may help to study the formation and dispersion of aquatic colloids with the help of LIBD. A combination of LIBD with LPAS or TRLFS (time-resolved laser fluorescence spectroscopy) allows speciation of metals in solution with respect to oxidation state (LPAS), chemical properties, binding states, complex formation or nature of ligands (TRLFS) and formation of polynuclear (LPAS) or colloidal (LIBD) species. A mobile LIBD facilitates the *in situ* monitoring of aquatic colloids under original natural conditions, without the need for colloidal sampling and transport, processes that perturb more often than not the original state of aquatic colloids.

Future developments are expected to take place in at least three fields. First, LIBD has already been applied to the sensitive detection of inorganic colloids following size fractionation by FFFF [51,52,157]. In these cases optical LIBD was used and, in addition to the size information obtained from FFFF, an evaluation of the BD event distribution presented a second independent size measurement (see Chapter 5). In order to lower the price and the complexity of the detection system, constant pulse energy acoustic detection can be used, acting as a 'yes/no' detector. Although the size information can be obtained from FFFF alone, the sensitivity can be enhanced by at least three orders of magnitude compared with light scattering. It should even be possible to commercialise such a system.

A second approach concerns size distributions. At present the evaluation of size distributions is limited to six channels in the size classes between 20 and 100 nm and only possible for acoustic detection. An analogue evaluation of the optical detection signal should be possible that could allow faster measurements. The size range could be extended and the number of size classes might be increased slightly. However, since the size information is not obtained from a single colloid but from the total distribution, the presence of many large particles will prevent the precise determination of the number of small colloids.

As a third development, LIBD can be combined with a single particle counter (SPC), as has been shown recently [117]. In a combined set-up, the sample can be measured in parallel by the SPC and LIBD in a flow-through cell. In such a case, the SPC detects large colloids ( $>100$  nm) with very high sensitivity and LIBD can contribute its superior detection limit for smaller sizes. By combining these complementary techniques, one is able to cover a size range from 15 nm up to micrometres at concentrations down to  $10\text{-}10^4$  particles  $\text{cm}^{-3}$  [83].

## SYMBOLS

$\alpha_\gamma$	Parameter of $\Gamma$ -distribution (dimensionless)
$\bar{\mu}$	Mean value of probability distribution (Poisson) (dimensionless)

$\delta$	Mass density of a colloid $\text{g cm}^{-3}$
$\varepsilon_0$	Electric permittivity of free space $= 8.854187 \times 10^{-12} \text{ F m}^{-1}$
$\eta(E)$	Rate of ionisation of electrons (energy $E$ ) by IB. $\text{s}^{-1}$
$\gamma_L$	Self focusing constant. Water: $\gamma_L = 0.5 \times 10^{-22} \text{ m}^2 \text{ V}^{-2}$
$\lambda$	Wavelength of light. nm
$\lambda_0$	Wavelength of light in vacuum. nm
$\lambda_\gamma$	Parameter of $\Gamma$ -distribution. arbitrary; here, $\text{nm}^{-1}$
$C$	Euler's constant $= 0.57721566490153$
$\mathcal{E}$	Electric field strength. $\text{Vm}^{-1}$
$\mu_m^1$	MPI cross-section of one molecule inside a colloid. $\mu\text{m}^{2m} \text{W}^{-m} \text{s}^{-1}$
$\mu_G$	Centre of Gaussian distribution. arbitrary; here, nm
$\mu_m$	MPI cross-section. $\mu\text{m}^{2m} \text{W}^{-m} \text{s}^{-1}$
$\nu$	Frequency of light. $\text{s}^{-1}$
$\nu_C$	Critical (plasma) frequency. $\text{s}^{-1}$
$\phi$	Photon flux density. $\text{cm}^{-2} \text{ s}^{-1}$
$\Phi_{\max}$	Optical aberration function (dimensionless)
$\rho_C$	Concentration (number density) of colloids. $\text{cm}^{-3}$
$\rho_e$	Number density of electrons. $\text{cm}^{-3}$
$\rho_M$	Number density of molecules. $\text{cm}^{-3}$
$\rho_M$	Number density of educts (neutral molecules) before laser irradiation. $\mu\text{m}^3$
$\sigma_G$	Width of Gaussian distribution. arbitrary; here nm
$\tau$	Pulse duration: 1/e width of the temporal laser profile. ns
$\varphi$	Azimuth angle of cylindrical coordinates (dimensionless)
$A$	Area. $\mu\text{m}^2$
$a$	Integration constant (dimensionless)
$a^{(i)}$	Calibration parameter for multimodal s-curve fitting (dimensionless)
$b$	Integration constant (dimensionless)
$b^{(i)}$	Calibration parameter for multimodal s-curve fitting (dimensionless)
$C$	Colloid concentration fit parameter (dimensionless)
$c_0$	Velocity of light in vacuum $= 299792458 \text{ ms}^{-1}$
$C_C$	Mass concentration of colloids. $\text{g cm}^{-3}$
$c_t$	Temporal integration constant. $\text{ns}^{-m+1}$
$d$	Diameter of colloid. nm
$d_p$	Penetration depth of light. nm
$E$	Energy eV, J
$e$	Electron charge: $1.602177 \times 10^{-19} \text{ C}$
$E_0$	Energy of a single laser pulse. mJ
$E_I$	Ionisation energy: see footnote 2, Section 3.1. eV
$E_t$	Threshold energy for breakdown. mJ
$E_{\text{Ph}}$	Photon energy. eV
$g(\vec{r})$	Spatial part of the power density: $I(\vec{r}, t = \text{constant})$ (dimensionless)
$h$	Planck's constant $= 6.626 \times 10^{-34} \text{ Js} = 4.135 \text{ eV fs}$
$h(\vec{r})$	Temporal part of the power density: $I(\vec{r} = \text{constant}, t)$ (dimensionless)

$h\nu$	Photon energy. eV
$I$	Power density. $\text{W } \mu\text{m}^{-2}$ ( $= P/A$ )
$I_0$	Peak power density. $\text{Wcm}^{-2}$
$I_C$	Critical power density. $\text{W cm}^{-2}$
$K_{\text{sp}}$	Solubility constant (dimensionless)
$L_C$	Critical power for self-focusing. W
$l_z$	Ignition length = effective focal length. $\mu\text{m}$
$m$	Order of $\rightarrow \text{MPI-process} \rightarrow \text{MPI-ionisation}$ by $m$ photons (dimensionless)
$m_0$	Total injected mass or activity. g or Bq
$m_e$	Electron mass: $9.109389 \times 10^{-31}$ kg
$N$	Number of colloids (dimensionless)
$n$	Refractive index (dimensionless)
$N_e$	Number of electrons (dimensionless)
$n_L$	Refractive index change during self-focusing (dimensionless)
$N_M$	Number of (neutral) molecules (dimensionless)
$N_m$	Number of molecules inside a colloid (dimensionless)
$P$	Power. W
$p$	Probability (dimensionless)
$P_0$	(Mean) power of a single laser pulse. W
$p_N$	Probability of measuring a value of $N$ events (dimensionless)
$P_t$	Threshold power for breakdown. W
$p_{\text{BD}}$	Probability of a breakdown (dimensionless)
$r, \vec{r}$	Spatial coordinate(s). $\mu\text{m}$
$r_0$	Radius where power $\sim$ /photon flux density decreased to 1/e of maximum. $\mu\text{m}$
$r_C$	Critical radius $\mu\text{m}$
$s$	Slope of growth of focal volume (dimensionless)
$t$	Time. s
$t_0$	Laser pulse duration. ns
$u$	Substitution variable (dimensionless)
$V$	Volume. $\text{cm}^{-3}$
$v$	Substitution variable (dimensionless)
$V_{\text{el}}$	Volume of ellipsoid. $\mu\text{m}^3$
$V_{\text{foc}}$	Focal volume of arbitrary shape. $\mu\text{m}^3$
$x$	1st axis perpendicular to laser beam propagation direction. $\mu\text{m}$
$y$	2nd axis perpendicular to laser beam propagation direction. $\mu\text{m}$
$Z$	Ionic charge. elementary charge e: $1.602177 \times 10^{-19}$ C
$z$	Axis along laser beam propagation direction. $\mu\text{m}$
$z_C$	Critical distance along laser beam propagation. $\mu\text{m}$
$z_f$	Focal length induced by self-focusing. m
$\text{BD}$	Breakdown
$\text{BDP}$	Breakdown probability (dimensionless)
$\text{Ei}(x)$	Exponential-integral function
$\text{IB}$	Inverse bremsstrahlung

## GLOSSARY

Cross-references are marked by an arrow ( $\rightarrow$ ) and *italic* font; ‘*cf.*’ hints at a complementary term.

**Absorption** The fraction of light that is lost and remains in a sample due to inelastic processes (*cf.* extinction).

**Acoustic detection** The breakdown is detected by means of a  $\rightarrow$  piezo detector, which picks up the acoustic signal caused by the expansion of the hot laser induced  $\rightarrow$  plasma.

**Amplified atomic emission** Prerequisite for laser action. In addition to spontaneous photon emission, an excited atom can be stimulated to emit a photon by the presence of a second photon of exactly the excitation energy. The emitted photon has the same properties as has the stimulating one, which results in monochromatic, coherent light.

**Atomic emission** Optical line spectra which are used for identifying elements quantitatively. In LIBS these are superimposed on and have to be discriminated against the background of  $\rightarrow$  blackbody radiation.

**Bimodal** A suspension which contains colloids of two distinct, well-defined sizes.

**Blackbody radiation** Continuous electromagnetic radiation spectra of a body with absorptivity = 1 (ideal absorber/radiator) and defined temperature. Due to the quantum nature of light emission the *b.r.* spectra exhibit maxima at  $\lambda = 0.2898 \text{ cm K}^{-1}$  (Wien’s law).

**Breakdown** Generation of a practically totally ionised gas ( $\rightarrow$  plasma) [16]. The experimental criterion generally used is the observation of a glow or flash or that the plasma becomes opaque for laser light ( $\rightarrow$  Thomson scattering) which corresponds to an electron density of  $10^{19} - 10^{21} \text{ cm}^{-3}$ .

**Breakdown probability** The number of BD events relative to the total number of laser pulses. E.g. if 100 laser pulses cause 10 breakdowns, the  $BDP = p_{BD} = 0.1$ .

**Breakdown threshold** The lowest power density  $I_t$  that suffices to initiate a breakdown for a colloid of certain properties (size,  $\rightarrow$  MPI cross-section,  $\rightarrow$  ionisation energy). *B.t.* is also equally used for the lowest mean power ( $P_t$ ) of a laser or the lowest pulse energy ( $E_t$ ) which initiates a breakdown.

**Cascade multiplication**  $\rightarrow$  Inverse bremsstrahlung

**Colloid concentration** The concentration of colloids in suspension is preferentially given in number per volume (particles  $\text{cm}^{-3}$ ). If available data only allow one to give the colloid content in mass concentration (if only average sizes, or no size information is available at all, for filtration experiments or in the case of quotations from the literature) this is explicitly stated by use of the units ( $\text{g cm}^{-3}$ ).

**Critical power density** See remark under *breakdown threshold*

**Critical radius** Critical distance from the focal centre along the laser axis, where the power density decreases below the  $\rightarrow$  breakdown threshold.

**Critical radius** Radius at  $z = 0$  (perpendicular to the laser beam), where the power density decreases to a value below the  $\rightarrow$  breakdown threshold for a given particle.

**Crosstalk** General: unwanted signals in a communication channel (as in a radio) caused by transfer of energy from another circuit (as by leakage or coupling). Here: phantom signal in size classes that are not populated, for instance when a monomodal suspension of 100 nm causes signals in size classes <100 nm.

*Destructive* A detection method is referred to being destructive if the single colloid under investigation is destroyed and cannot be subjected to future investigations. *cf. Invasive.*

*Detection limit* The lowest number of detectable species that can be discriminated from background. In the case of LIBD for small colloids (< 100 nm), the *d.l.* is determined by the remaining colloid contaminations of the purest water that can be supplied in the laboratory and for large colloids it is determined by the finite size of the → *effective focal volume*.

*Effective focal length* → *Ignition length* ( $l_Z$ )

*Effective focal volume* The volume within the laser focus where the power density suffices to ignite a breakdown. Since, the → *breakdown threshold* decreases with increasing particle size, the *e.f.v.* also depends on particle size.

*Extinction* The weakening of light on passing through a sample. Sum of → *absorption* and → *scattering*.

*Focal volume* → *Effective focal volume*

*Ignition length* The width of the spatial distribution of → *breakdown* (plasma-) events along the laser beam axis. The *i.l.* increases monotonously with increasing colloid size and is applied for size measurements in the → *optical detection* of LIBD. See also Section 4, Figure 12 and Figure 13.

*Invasive* A detection method is referred to being invasive if the total sample is altered considerably or is completely destroyed by the measurement and it cannot be used for subsequent investigations. *cf. Destructive.*

*Inverse bremsstrahlung* From German Bremsstrahlung: ‘Braking radiation’. Denotes electromagnetic radiation produced by a sudden slowing down or deflection of charged particles (especially electrons) passing through matter in the vicinity of the strong electric fields of atomic nuclei [158]. Inverse bremsstrahlung means the opposite—the acceleration of electrons by an electromagnetic field (here the laser field) in the presence of ions. For the sake of energy and momentum conservation, this needs to be a three-body process. Symbol  $\eta(E)$ .

*Ionisation energy* Energy to free one electron from an atom or molecule. See footnote 2, Section 3.1.

*Isophote* Line of equal photon flux density.

*Kernels* Oligomers or colloids which are too small to be detected by LIBD, but initiate crystallisation for formation of larger colloids.

*Laser-induced breakdown spectroscopy* See LIBS.

*Laser-induced photoacoustic spectroscopy* See LPAS.

*LIBS* Laser-induced breakdown spectroscopy. Technique used for the elemental analysis of solids, liquids and gases. The sample is heated and vaporised by the focused light of a pulsed laser. During the cooling of the hot (ionised) gas, recombination processes lead to the emission of ionic and → *atomic lines* (*cf.* atomic emission), which allow the quantitative determination of element content.

*LPAS* Laser-induced photoacoustic spectroscopy. Matter which absorbs light is heated, expands and causes an acoustic shock wave which can be detected by a sensitive microphone. The amplitude of the acoustic signal increases linearly proportionally with the concentration of absorbers and with the molar absorptivity (or photon absorption

cross-section). By scanning the excitation wavelength an optical absorption spectrum is obtained, which in turn is used to quantify the amount of species present in the sample. LPAS is applicable to solids and liquids. The detection limit depends on the absorptivity and is typically 1.5 orders of magnitude lower than for UV–VIS detection. In contrast to UV–VIS, the measurement is not disturbed by → scattering signals (*e.g.* due to colloids) since LPAS does not probe → extinction but → absorption.

*Material dependency* The → photon flux density required to generate a → breakdown depends on material properties such as → multi-photon absorption cross-section and → ionisation energy. Hence, the → breakdown threshold might be different for particles of the same size but different materials. See Section 3.1.

*Monomodal* A suspension which contains colloids of only one size.

*MPI* Ionisation of an atom or molecule by the ‘simultaneous’ (within picoseconds) absorption of several photons. This effect takes place when the → ionisation energy exceeds the energy of one photon. Depending on the → MPI cross-section, a very high → photon flux density is required.

*MPI cross-section* Cross-section for multiphoton ionisation. Symbol  $\mu_m$ . The product of MPI cross-section times the  $m$ th power of the → power density  $I^m$  gives the ionisation rate (per unit time). Therefore, the unit of the MPI cross-section is length $^{2m}$  power $^{-m}$  time $^{-1}$  (*e.g.*  $\mu\text{m}^{2m}\text{W}^{-m}\text{s}^{-1}$ ).

*Multi-photon ionisation* → MPI

*Multimodal* A suspension which contains colloids of many distinct sizes.

*Optical detection* Detection of the → plasma by means of its optical emission, which is observed by a microscope lens and a CCD camera. From the → ignition length, the particle size is appraised. The light originating from the hot → plasma is composed of → blackbody radiation, → atomic emission lines and → Thomson scattering. The very intense Thomson scattered light is filtered out by use of holographic notch filters. The blackbody emission is used for localising the plasma; the atomic emission lines can be used to measure the elemental composition of the colloid (*cf.* LIBS).

*Photo-ionisation* Ionisation of atoms or molecules by absorption of one or several photons. The former process is known as photoeffect and the latter as non-resonant → multi-photon ionisation.

*Photon flux density* Number of photons per second per unit area. Symbol  $\phi$ .

*Piezo receiver* Microphone based on the piezoelectric effect. A piezo-crystal generates a voltage which is linearly proportional to the applied pressure.

*Plasma* An electrically conducting medium in which there are roughly equal numbers of positively and negatively charged particles, produced when the atoms in a gas become ionised. It is sometimes referred to as the fourth state of matter, distinct from the solid, liquid and gaseous states. The negative charge is usually carried by electrons; the positive charge is typically carried by atoms or molecules that are missing those same electrons. [158].

*Power density* Energy per second per unit area. Symbol  $I$ .

*Pretreatment* Here, pretreatment exclusively refers to fractionation methods such as filtration, centrifugation or FFFF in order to lower the fraction of large particles which alter the LIBD signal due to light → scattering or due to their low → breakdown threshold.

*Scattering* The fraction of light that is lost in a sample due to elastic processes and typically leaves the sample in arbitrary direction (*cf.* extinction).

*Screening* In the context of this chapter (size-)screening is used for the suppression of a signal originating from small colloids due to the simultaneous presence of large particles.

*Size distribution* If a sample contains colloids of more than one size, the term size distribution is used. In this chapter, the number of colloids in a certain size class (*e.g.* 30–40 nm) is given. Since the size classes of LIBD are not arbitrarily small absolute numbers are sometimes preferred over the common differential expression  $dN/dVdd$ .

*Size-screening* → *Screening*.

*TEM<sub>00</sub>* The basic transverse electromagnetic mode in a laser resonator, which has a Gaussian intensity distribution perpendicular to the laser axis.

*Temporal profile* Change of laser → *power density* (→ *photon flux density*) in time. Idealised this is a Gaussian function, but especially single transversal, multi-longitudinal mode lasers show short (<100 ps) spikes, where the power density is very high.

*Thomson scattering* A → *plasma* of electron density  $\rho_e$  becomes opaque for light of frequency  $\nu < \nu_C(\rho_e)$  (critical plasma frequency). The light can no longer penetrate the plasma and is scattered effectively.

*Threshold* → Breakdown threshold

*Work function* Energy to free one electron from bulk material. See footnote 2, Section 3.1.

## REFERENCES

1. Brech, F. and Cross, L. (1962). Optical microemission stimulated by a ruby laser, *Appl. Spectrosc.*, **16**, 59–61.
2. Maiman, T. H. (1960). Stimulated optical emission in ruby, *Nature*, **187**, 493–494.
3. Rusak, D. A., Castle, B. C., Smith, B. W. and Winefordner, J. D. (1997). Fundamentals and applications of laser-induced breakdown spectroscopy, *Crit. Rev. Anal. Chem.*, **27**, 257–290.
4. Kim, J.-I., Stumpe, R. and Klenze, R. (1990). Laser-induced photoacoustic spectroscopy for the speciation of transuranic elements in natural aquatic systems, *Top. Curr. Chem.*, **157**, 131–179.
5. Kitamori, T., Fujii, M., Sawada, T. and Gohshi, Y. (1985). Linear response theory in photoacoustic spectroscopy and characterization of turbid particles, *Jpn. J. Appl. Phys., Part 1*, **24**, 210–213.
6. Arushanov, S. Z., Bebchuk, A. S., Kosolobov, V. N. and Lomonosov, V. L. (1978). Laser induced breakdown of aqueous solutions of electrolytes, *Sov. Phys. Dokl.*, **23**, 587–588.
7. Kitamori, T., Yokose, K., Suzuki, K., Sawada, T. and Goshi, Y. (1988). Laser breakdown acoustic effect of ultrafine particle in liquids and its application to particle counting, *Jpn. J. Appl. Phys.*, **27**, L983–L985.
8. Kitamori, T., Yokose, K., Sakagami, M. and Sawada, T. (1989). Detection and counting of ultrafine particles in ultrapure water using laser breakdown acoustic method, *Jpn. J. Appl. Phys.*, **28**, 1195–1198.
9. Sacchi, C. A. (1991). Laser-induced breakdown in water, *J. Opt. Soc. Am. B*, **8**, 337–345.
10. Docchio, F., Avigo, A. and Palumbo, R. (1991). Characteristics of optical breakdown in ultrapure water induced by nanosecond Nd:YAG laser pulses., *Europhys. Lett.*, **15**, 69–73.
11. Fujimori, H., Matsui, T., Ajiro, T., Yokose, K., Hsueh, Y. M. and Izumi, S. S. (1992). Detection of fine particles in liquids by laser breakdown method, *Jpn. J. Appl. Phys., Part 1*, **31**, 1514–1518.
12. Ajiro, T., Fujimori, H., Matsui, T. and Izumi, S. (1992). Particle size dependence of correlation between plasma emission delay time and plasma emission intensity of laser breakdown induced by a particle, *Jpn. J. Appl. Phys., Part 1*, **31**, 2760–2761.

13. Kitamori, T., Matsui, T. and Sakagami, M. (1989). Laser breakdown spectrochemical analysis of microparticles in liquids, *Chem. Lett.*, **89**, 2205–2208.
14. Ito, Y., Ueki, O. and Nakamura, S. (1995). Determination of colloidal iron in water by laser-induced breakdown spectroscopy, *Anal. Chim. Acta*, **299**, 401–405.
15. Nakamura, S., Ito, Y. and Sone, K. (1996). Determination of an iron suspension in water by laser-induced breakdown spectroscopy with two sequential laser pulses, *Anal. Chem.*, **68**, 2981–2986.
16. Radziemski, L. J. and Cremers, D. A. (1989). *Laser-induced Plasmas and Applications*. Marcel Dekker, New York.
17. Pu, X. Y., Ma, W. Y. and Cheung, N. H. (2003). Sensitive elemental analysis of aqueous colloids by laser-induced plasma spectroscopy, *Appl. Phys. Lett.*, **83**, 3416–3418.
18. Knopp, R., Scherbaum, F. J. and Kim, J.-I. (1996). Laser induced breakdown spectroscopy (libs) as an analytical tool for the detection of metal ions in aqueous solutions, *Fresenius' J. Anal. Chem.*, **355**, 16–20.
19. Yun, J. I., Bundschuh, T., Neck, V. and Kim, J.-I. (2001). Selective determination of europium(III) oxide and hydroxide colloids in aqueous solution by laser-induced breakdown spectroscopy, *Appl. Spectrosc.*, **55**, 273–278.
20. Nakamura, M., Kitamori, T. and Sawada, T. (1991). Size and element dependence of amplified atomic emissions from laser breakdown plasma of ultrafine particles, *Anal. Sci.*, **7**, 563–564.
21. Nakamura, M., Kitamori, T. and Sawada, T. (1993). Highly anisotropic light emission from laser breakdown of microparticles in water, *Nature*, **366**, 138–141.
22. Scherbaum, F. J., Knopp, R. and Kim, J.-I. (1996). Counting of particles in aqueous solutions by laser-induced photoacoustic breakdown detection, *Appl. Phys. B*, **63**, 299–306.
23. Kim, J. I., Klenze, R. and Scherbaum, F.-J. (1996). Hochempfindliche Quantifizierung von Aquatischen Kolloiden mit Hilfe der laser-induzierten Breakdown-Detektion, *FZK Nachr.*, **28**, 321–328.
24. Bolz, M., Hoffmann, W., Ruehle, W. and Becker, F. (1996). Characterization of colloids in primary coolant, *Water Chem. Nucl. React. Syst.*, **7**, 42–46.
25. Izumida, S., Onishi, K. and Saito, M. (1998). Estimation of laser-induced breakdown threshold of microparticles in water, *Jpn. J. Appl. Phys., Part 1*, **37**, 2039–2042.
26. Saito, M., Izumida, S., Onishi, K. and Akazawa, J. (1999). Detection efficiency of microparticles in laser breakdown water analysis, *J. Appl. Phys.*, **85**, 6353–6357.
27. Bundschuh, T., Knopp, R. and Kim, J. I. (2001). Laser-induced breakdown detection (LIBD) of aquatic colloids with different laser systems, *Colloids Surf. A*, **177**, 47–55.
28. Partin, J. (2002). New instruments reveals information about colloids, *INEEL Newslett.*, **4**, 1–2.
29. Fujimori, H., Matsui, T., Ajiro, T., Yokose, K. and Izumi, S. (1994). Apparatus for analysis of particulate material, analytical method for same, apparatus for production of ultrapure water, apparatus for manufacturing of semiconductor, and apparatus for production of pure gas, *US Patent*, 5316983.
30. Bundschuh, T., Hauser, W., Kim, J. I., Knopp, R. and Scherbaum, F. J. (2001). Determination of colloid size by two-dimensional optical detection of laser induced plasma, *Colloids Surf. A*, **180**, 285–293.
31. Hauser, W., Geckes, H., Kim, J. I. and Fierz, Th. (2002). A mobile laser-induced breakdown detection system and its application for the *in situ* monitoring of colloid migration, *Colloids Surf. A*, **203**, 37–45.
32. Mori, A., Alexander, W. R., Geckes, H., Hauser, W., Schafer, T., Eikenberg, J., Fierz, T., Degueldre, C. and Missana, T. (2003). The colloid and radionuclide retardation experiment at the Grimsel test site: influence of bentonite colloids on radionuclide migration in a fractured rock, *Colloids Surf. A*, **217**, 33–47.
33. Hauser, W., Götz, R., Geckes, H. and Kienzler, B. (2003). *In situ* colloid detection in granite groundwater along the Äspö hard rock laboratory access tunnel, *Äspö Progress report IPR*, 03–38, Swedish Nuclear Fuel and Waste Management Co..
34. Walther, C., Bitea, C., Hauser, W., Kim, J. I. and Scherbaum, F. J. (2002). Laser induced breakdown detection for the assessment of colloid mediated radionuclide migration, *Nucl. Instrum. Methods B*, **195**, 374–388.

35. Plaschke, M., Schäfer, T., Bundschuh, T., Thang, N. M., Knopp, R., Geckeis, H. and Kim J. I. (2001). Size characterization of bentonite colloids by different methods, *Anal. Chem.*, **73**, 4338–4347.
36. Bundschuh, T., Knopp, R., Winzenbacher, R., Kim, J. I. and Koster, R. (2001). Quantification of aquatic nano particles after different steps of Bodensee water purification with laser-induced breakdown detection (LIBD), *Acta Hydrochim. Hydrobiol.*, **29**, 7–15.
37. Wagner, T., Bundschuh, T., Schick, R., Schwartz, T. and Koster, R. (2003). Investigation of colloidal water content with laser-induced breakdown detection during drinking water purification, *Acta Hydrochim. Hydrobiol.*, **30**, 266–274.
38. Bitea, C., Walther, C., Kim, J. I., Geckeis, H., Rabung, T., Scherbaum, F. J. and Cacuci, D. (2003). Time resolved observation of ZrO<sub>2</sub>-colloid agglomeration, *Colloids Surf. A*, **215**, 55–66.
39. Knopp, R., Neck, V. and Kim, J. I. (1999). Solubility, hydrolysis and colloid formation of plutonium(IV), *Radiochim. Acta*, **86**, 101–108.
40. Romanovski, V. V., Brachmann, A., Palmer, C. E., Shaw, H. F., Bourcier, W. L. and Jaridine, L. J. (2000). Characterization of Pu colloidal and aqueous speciation in Yucca mountain groundwater surrogate, *Abstr. Pap. Am. Chem. Soc.*, **219**, U80.
41. Walther, C., Bitea, C., Yun, J. I., Kim, J. I., Fanghänel, Th., Marquardt, C. M., Neck, V. and Seibert, A. (2003). Nanoscopic approaches to the aquatic plutonium chemistry, *Actinide Res. Q.*, **3**, 12–16.
42. Rothe, J., Walther, C., Denecke, M. A. and Fanghänel, T. (2004). XAFS and LIBD investigation of the formation and structure of colloidal Pu(IV) hydrolysis products, *Inorg. Chem.*, **43**, 4708–4718.
43. Neck, V., Kim, J. I., Seidel, B. S., Marquardt, C. M., Dardenne, K., Jensen, M. P. and Hauser, W. (2001). A spectroscopic study of the hydrolysis, colloid formation and solubility of Np(IV), *Radiochim. Acta*, **89**, 439–446.
44. Bundschuh, T., Knopp, R., Müller, R., Kim, J. I., Neck, V. and Fanghänel, Th. (2000). Application of LIBD to the determination of the solubility product of thorium(IV)-colloids, *Radiochim. Acta*, **88**, 625–629.
45. Neck, V., Müller, R., Bouby, M., Altmaier, M., Rothe, J., Denecke, M. A. and Kim, J. I. (2002). Solubility of amorphous Th(IV) hydroxide—application of LIBD to determine the solubility product and EXAFS for aqueous speciation, *Radiochim. Acta*, **90**, 485–494.
46. Bitea, C., Müller, R., Neck, V., Walther, C. and Kim, J. I. (2003). Study of the generation and stability of thorium(IV) colloids by LIBD combined with ultrafiltration, *Colloids Surf. A*, **217**, 63–70.
47. Brachmann, A., Wruck, D. A., Palmer, C. E. A. and Terminello, L. J. (1998). Laser induced photoacoustic breakdown spectroscopy for colloid size distribution and colloid concentration analysis, *Abstr. Pap. Am. Chem. Soc.*, **216**, U634.
48. Kim, M. A., Panak, P. J., Yun, J. I., Kim, J. I., Klenze, R. and Kohler, K. (2003). Interaction of actinides with aluminosilicate colloids in statu nascendi. Part I: generation and characterization of actinide(III)-pseudocolloids, *Colloids Surf. A*, **216**, 97–108.
49. Panak, P. J., Kim, M. A., Yun, J. I. and Kim, J. I. (2003). Interaction of actinides with aluminosilicate colloids in statu nascendi. Part II: spectroscopic speciation of colloid borne actinides(III), *Colloids Surf. A*, **227**, 93–103.
50. Stumpf, T., Tits, J., Walther, C. and Fanghänel, Th. (2004). Uptake of trivalent actinides (Cm(III)) by cement: a time-resolved laser fluorescence spectroscopy (TRLFS) study, *J. Colloid Interface Sci.*, **276**, 118–124.
51. Manh, T. N., Knopp, R., Geckeis, H., Kim, J. I. and Beck, H. P. (2000). Detection of nano-colloide with flow-field flow fractionation and laser-induced breakdown detection, *Anal. Chem.*, **72**, 1–5.
52. Bouby, M., Manh, T. N., Geckeis, H., Scherbaum, F. J. and Kim, J. I. (2001). Characterization of aquatic colloids by a combination of LIBD and ICP-MS following size fractionation, *Radiochim. Acta*, **90**, 727–732.
53. Morgan, C. G. (1975). Laser-induced breakdown of gases, *Rep. Prog. Phys.*, **38**, 621–665.
54. Lide, D. R., ed. (1995). *Handbook of Chemistry and Physics*, 75th edn. CRC Press, Boca Raton, FL.

55. Keldysh, L. V. (1965). Ionization in the field of a strong electromagnetic wave, *Sov. Phys. JETP*, **20**, 1307–1314.
56. Chin, S. L. and Lambropoulos, P. (1984). *Multiphoton Ionisation of Atoms*. Academic Press, Toronto.
57. Walther, C., Hauser, W., Geckeis, H. and Fanghänel, Th. (2003). Die Laser induzierte Breakdown Detektion zur Analytik von aquatischen Kolloiden im Ultraspurenbereich, *FZK Nachr.*, **35**, 179–184.
58. Niemz, M. H. (1995). Threshold dependence of laser-induced optical-breakdown on pulse duration, *Appl. Phys. Lett.*, **66**, 1181–1183.
59. Zeldovich, Ya. B. and Raizer, Yu. P. (1965). Cascade ionization of a gas by a light pulse, *Sov. Phys. JETP*, **20**, 772–780.
60. Bloembergen, N. (1974). Laser induced electric breakdown in solids, *IEEE J. Quantum Electron.*, **10**, 375–386.
61. Kennedy, P. K. (1995). A first-order model for computation of laser-induced breakdown thresholds in ocular and aqueous media: Part I—theory, *IEEE J. Quantum Opt.*, **31**, 2241–2249.
62. Stuart, B. C., Feit, M. D., Herman, S. and Rubenchik, A. M. (1996). Nanosecond-to-femtosecond laser-induced breakdown in dielectrics., *Phys. Rev. B*, **53**, 1749–1761.
63. Noack, J. and Vogel, A. (1999). Laser-induced plasma formation in water at nanosecond to femtosecond time scales: calculation of thresholds, absorption coefficients and energy density, *IEEE J. Quantum Electron.*, **35**, 1156–1167.
64. Born, M. and Wolf, E. (1999). *Principles of Optics*, 7th edn. Cambridge University Press, Cambridge.
65. Bergmann, L. and Schaefer, C. (1999). *Optics*, 9th edn. Walter de Gruyter, Berlin.
66. Cervenan, M. R. and Isenor, N. R. (1975). Multiphoton ionization yield curves for gaussian laser beams, *Opt. Commun.*, **13**, 175–178.
67. Bronstein, I. N. and Semendjajew, K. A. (1996). *Taschenbuch der Mathematik*. Teubner, Leipzig.
68. Gradshteyn, I. S. and Ryzhik, I. M. (2000). *Table of Integrals Series and Products*, 6th edn. Academic Press, San Diego, CA.
69. Schwarz, J., Rambo, P. and Diels, J. C. (2001). Measurement of multiphoton ionization coefficients with ultrashort ultraviolet laser pulses, *Appl. Phys. B*, **72**, 343–347.
70. Walther, C., Herlert, A., Kim, J. I., Scherbaum, F. J., Schweikhard, L. and Vogel, M. (2001). Absolute cross-sections for the nonresonant multi-photon ionization of toluene and xylene in the gas phase, *Chem. Phys.*, **265**, 243–250.
71. Mie, G. (1908). Beiträge zur Optik trüber Medien, *Ann. Phys.*, **25**, 377–445.
72. Bohr, C. F. and Huffmann, D. R. (1998). *Absorption and Scattering of Light by Small Particles*. John Wiley & Sons, Inc., New York.
73. Mosbacher, M., Munzer, H. J., Zimmermann, J., Solis, J., Boneberg, J. and Leiderer, P. (2001). Optical field enhancement effects in laser-assisted particle removal, *Appl. Phys. A Mater. Sci. Proc.*, **72**, 41–44.
74. Schmidt-Kloiber, H., Paltauf, G. and Reichel, E. (1989). Investigation of the probabilistic behavior of laser-induced breakdown in pure water and in aqueous solutions of different concentrations, *J. Appl. Phys.*, **66**, 4149–4153.
75. Hammer, D. X., Thomas, R. J., Noojin, G. D., Rockwell, B. A., Kennedy, P. K. and Roach, W. P. (1996). Experimental investigation of ultrashort pulse laser-induced breakdown thresholds in aqueous media, *IEEE J. Quantum Electron.*, **32**, 670–678.
76. Noack, J., Hammer, D. X., Noojin, G. D. and Rockwell, B. A. (1998). Influence of pulse duration on mechanical effects after laser-induced breakdown in water, *J. Appl. Phys.*, **83**, 7488–7495.
77. Vogel, A., Noack, J., Nahen, K., Theisen, D., Busch, S., Parlitz, U., Hammer, D. X., Noojin, G. D., Rockwell, B. A. and Birngruber, R. (1999). Energy balance of optical breakdown in water at nanosecond to femtosecond time scales, *Appl. Phys. B*, **68**, 271–280.
78. Capitelli, M., Capitelli, F. and Eletskii, A. (2000). Non-equilibrium problems in laser-induced plasmas, *Spectrochim. Acta, Part B*, **55**, 559–574.

79. Feng, Q., Moloney, J. V., Newell, A. C. and Wright, E. M. (1997). Theory and simulation on the threshold of water breakdown induced by focused ultrashort laser pulses, *IEEE J. Quantum Electron.*, **33**, 127–137.
80. Evans, L. R. and Morgan, C. G. (1969). Lens aberration effects in optical-frequency breakdown of gases, *Phys. Rev. Lett.*, **22**, 1099–1102.
81. Evans, L. R. and Morgan, C. G. (1969). Intensity distribution of focussed laser beams in bio-medical studies, *Phys. Med. Biol.*, **14**, 205–212.
82. Walther, C., Buchner, S., Filella, M., Chanadel, V. Probing particle size distributions in natural surface waters from 15 nm to 2 µm by a combination of LIBD and single particle counting, *J. Coll. Int. Sci.* **301**, 532–537 (2006).
83. Mainfray, G. (1977). Resonance and laser temporal coherence effects in multiphoton ionisation of atoms. In *Multiphoton Processes*, eds Eberly, J. H. and Lambropoulos, P., John Wiley & Sons, Inc., New York, pp. 253–266.
84. Sobral, H., Villagran-Muniz, M., Navarro-Gonzalez, R. and Raga, A. C. (2000). Temporal evolution of the shock wave and hot core air in laser induced plasma, *Appl. Phys. Lett.*, **77**, 3158–3160.
85. Warner, K. and Hieftje, G. M. (2002). Thomson scattering from analytical plasmas, *Spectrochim. Acta, Part B*, **57**, 201–241.
86. Hammer, D. X., Jansen, E. D., Frenz, M., Noojin, G. D., Thomas, R. J., Noack, J., Vogel, A., Rockwell, B. A. and Welch, A. J. (1997). Shielding properties of laser-induced breakdown in water for pulse durations from 5 ns to 125 fs, *Appl. Opt.*, **36**, 5630–5640.
87. Francois, L., Mostafavi, M., Belloni, J., Delouis, J. F., Delaire, J. and Feneyrou, P. (2000). Optical limitation induced by gold clusters. 1. Size effect, *J. Phys. Chem. B*, **104**, 6133–6137.
88. Hahn, D. W., Flower, W. L. and Hencken, K. R. (1997). Discrete particle detection and metal emissions monitoring using laser-induced breakdown spectroscopy, *Appl. Spectrosc.*, **51**, 1836–1844.
89. Hauser, W. and Götz, R. (1999). Druckwellensensor, *German Patent*, DE-19602048.
90. Degueldre, C., Triay, I., Kim, J. I., Vilks, P., Laaksoharju, M. and Miekeley, N. (2000). Groundwater colloid properties: a global approach, *Appl. Geochem.*, **15**, 1043–1051.
91. Rosse, P. and Loizeau, J. L. (2003). Use of single particle counters for the determination of the number and size distribution of colloids in natural surface waters, *Colloids Surf. A*, **217**, 109–120.
92. Rayleigh, Lord (1871). On the light from the sky, its polarization and colour, *Philos. Mag.*, **41**, 107.
93. Walther, C. (2003). Comparison of colloid investigations by single particle analytical techniques—a case study on thorium-oxyhydroxides, *Colloids Surf. A*, **217**, 81–92.
94. Degueldre, C., Bilewicz, A., Hummel, W. and L. Loizeau, J. (2001). Sorption behaviour of Am on marl groundwater colloids, *J. Environ. Radioactivity*, **55**, 241–253.
95. Borkovec, M. (2002). Measuring particle size by light scattering. In *Handbook of Applied Surface and Colloid Chemistry*, vol. 2, Holmberg, K. ed. John Wiley & Sons, Inc., New York, pp. 357–370.
96. <http://www.pmeasuring.com/particleCounting/liquid/upw/ultraDI>, Ultra DI ultra pure water laser particle counter, (2004).
97. Walther, C., Cho, H. R. and Fanghänel, Th. (2004). Measuring multimodal size distributions of aquatic colloids at trace concentrations, *Appl. Phys. Lett.*, **85**, 6329–6331.
98. Chylek, P., Jarzembski, M. A., Chou, N. Y. and Pinnick, R. G. (1986). Effect of size and material of liquid spherical-particles on laser-induced breakdown, *Appl. Phys. Lett.*, **49**, 1475–1477.
99. Buffle, J. and Leppard, G. G. (1995). Characterization of aquatic colloids and macromolecules. 1. Structure and behavior of colloidal matter, *Environ. Sci. Technol.*, **29**, 2169–2175.
100. Buffle, J. and Leppard, G. (1995). Characterization of aquatic colloids 2. Key role of physical structures on analytical results, *Environ. Sci. Technol.*, **29**, 2176–2184.
101. Evans, D. F. and Wennerström, H. (2000). *The Colloidal Domain*. VCH, New York.
102. Kim, J. I. (1994). Actinide colloids in natural aquifer systems, *Mater Res. Soc. Bull.*, **19**, 47–53.

103. Ledin, A., Karlsson, S., Düker, A. and Allard, B. (1994). Measurements *in situ* of concentration and size distribution of colloidal matter in deep groundwaters by photon correlation spectroscopy, *Water Res.*, **28**, 1539–1545.
104. Ledin, A., Karlsson, S., Dueker, A. and Allard, B. (1995). Characterization of the submicrometer phase in surface waters: a review, *Analyst*, **120**, 603–608.
105. Ryan, J. N. and Elimelech, M. (1996). Colloid mobilization and transport in groundwater, *Colloids Surf.*, **107**, 1–56.
106. Degueldre, C. (1997). Groundwater colloid properties and their potential influence on radionuclide transport, *Mater. Res. Symp. Proc.*, **465**, 835–846.
107. Filella, M., Zhang, J., Newman, M. and Buffle, J. (1997). Analytical applications of photon correlation spectroscopy for size distribution measurements of natural colloidal suspensions: capabilities and limitations, *Colloids Surf., A*, **120**, 27–46.
108. Wachter, U. (2004). *Die Schwebstofffracht des Bodenseetrinkwassers*. Diploma, University of Konstanz.
109. Wagner, T., Bundschuh, T., Schick, R. and Koster, R. (2004). Detection of aquatic colloids in drinking water during its distribution via a water pipeline network, *Water Sci. Technol.*, **50**, 27–37.
110. Bundschuh, T., Wagner, T., Weber, M. and Koster, R. (2004). Method of laser-induced breakdown detection and application examples, *Chem. Eng. Tech.*, **27**, 377–382.
111. Honeyman, B. D. (1999). Colloidal culprits in contamination, *Nature*, **397**, 23–24.
112. Kersting, A. B., Efurd, D. W., Finnegan, D. L., Rokop, D. J., Smith, D. K. and Thompson, J. L. (1999). Migration of plutonium in ground water at the Nevada test site, *Nature*, **397**, 56–59.
113. Geckeis, H., Schäfer, T., Hauser, W., Rabung, Th., Missana, T., Degueldre, C., Möri, A., Eikenberg, J., Fierz, Th. and Alexander, W. R. (2004). Results of the colloid and radionuclide retention experiment (CRR) at the Grimsel Test Site (GTS), Switzerland—impact of reaction kinetics and speciation on radionuclide migration, *Radiochim. Acta*, **92**, 9–11.
114. Laaksoharju, M. (2001). Åspö hard rock laboratory, project description of the Åspö project colloid with the aim to investigate the stability and mobility of colloids, *SKB International Progress Report IPR*, 3–38.
115. Tonner, B. P., Droubay, T., Denlinger, J., Meyer-Ilse, W., Warwick, T., Rothe, J., Kneedler, E., Pecher, K., Nealson, K. and Grundl, T. (1999). Soft x-ray spectroscopy and imaging of interfacial chemistry in environmental species, *Surf. Interface Anal.*, **27**, 247–258.
116. Rothe, J., Denecke, M. A. and Dardenne, K. (2000). Soft x-ray spectromicroscopy investigation of the interaction of aquatic humic acid and clay colloids, *J. Colloid Interface Sci.*, **231**, 91–97.
117. Cho, H. R., Walther, C., Rothe, J., Neck, V., Denecke, M. A., Dardenne, K. and Fanghänel, Th. (2005). Combined LIBD and EXAFS investigation of the formation and structure of Zr(IV) colloids, *Anal. Bioanal. Chem.*, **383**, 28–40.
118. Monsallier, J. M., Bitea, C., Scherbaum, F. J., Buckau, G. and Kim, J. I. (2000). Application of libd to humic size investigation, *Technical Report FZK*, Forschungszentrum Karlsruhe, PO 3640, 76021 Karlsruhe, Germany.
119. Artlinger, R., Buckau, G., Kim, J. I. and Geyer, S. (1999). Characterization of ground-water humic and fulvic acids of different origin by GPC with UV/VIS and fluorescence detection, *Fresenius' J. Anal. Chem.*, **364**, 737–745.
120. Artlinger, R., Buckau, G., Geyer, S., Fritz, P., Wolf, M. and Kim, J. I. (2000). Characterization of groundwater humic substances: influence of sedimentary organic carbon, *Appl. Geochem.*, **15**, 97–116.
121. Bundschuh, T., Wagner, T., Eberhagen, I., Hambach, B. and Koster, R. (2005). Detection of biocolloids in aquatic media by nano-particle analyzer, *Spectroscopy*, **19**, 69–78.
122. Manh, T. N., Walther, C., Geckeis, H. and Kim, J. I. (2000). Detection of proteins by LIBD, unpublished results.
123. Walther, C. and Geckeis, H. (2005). Feinstaub Analyse von Diesel Abgasen in wasser, in preparation.

124. Panne, U. (2003). Laser induced breakdown spectroscopy (LIBS) in environmental and process analysis. In *Lasers in Environmental and Life Sciences*, eds. Hering, P., Lay, J.P. and Stry, S., Jan Springer, Berlin, pp. 99–123.
125. Zheng, J. B., Hsieh, W. F., Chen, S. C. and Chang, R. K. (1991). Laser-induced breakout and detonation waves in droplets. I. experiments, *J. Opt. Soc. Am. B*, **8**, 319–328.
126. Carls, J. C., Seo, Y. and Brock, J. R. (1991). Laser-induced breakout and detonation waves in droplets, *J. Opt. Soc. Am. B*, **8**, 329–336.
127. Singh, J. P., Zang, H., Yueh, F. Y. and Cook, R. L. (1993). Laser-induced breakdown spectra in a coal-fired MHD facility. In *Intersoc. Energy Convers. Eng.*, Vol. 1. American Chemical Society, Washington, DC, pp. 1.995–1.1000.
128. Poulain, D. E. and Alexander, D. R. (1995). Influences on concentration measurements of liquid aerosols by laser-induced breakdown spectroscopy, *Appl. Spectrosc.*, **49**, 569–579.
129. Hahn, DW. (1998). Laser-induced breakdown spectroscopy for sizing and elemental analysis of discrete aerosol particles, *Appl. Phys. Lett.*, **72**, 2960–2962.
130. Carranza, J. E., Fisher, B. T., Yoder, G. D. and Hahn, D. W. (2001). On-line analysis of ambient air aerosols using laser-induced breakdown spectroscopy, *Spectrochim. Acta, Part B*, **56**, 851–864.
131. Andreev, A. and Ueda, T. (2001). Detection of carbon particle and cluster parameters by laser-induced plasma line radiation. In *Fullerenes and Atomic Clusters, IWFA' 2001*, St Petersburg, p. 288, <http://www.ioffe.rssi.ru/IWFA/2001/index.html>.
132. Hybl, J. D., Litngow, G. A. and Buckley, S. G. (2003). Laser-induced breakdown spectroscopy detection and classification of biological aerosols, *Appl. Spectrosc.*, **57**, 1207–1215.
133. Niida, T., Kousaka, Y. and Oda, S. (1988). Aerosol generation method for measuring particles suspended in water—detection of particulate impurities in ultrapure water and sizing of fine powders, *Part. Part. Syst. Charact.*, **5**, 139–143.
134. Panne, U., Haisch, C., Liermann, J. and Niessner, R. (1997). Characterization of aquatic colloids by laser-induced plasma spectroscopy (LIPS), *Wasser*, **88**, 227–241.
135. Haisch, C., Liermann, J., Panne, U. and Niessner, R. (1997). Characterization of colloidal particles by laser-induced plasma spectroscopy (LIPS), *Anal. Chim. Acta*, **346**, 23–35.
136. Haisch, C., Panne, U. and Niessner, R. (1998). Combination of an intensified charge coupled device with an echelle spectrograph for analysis of colloidal material by laser-induced plasma spectroscopy, *Spectrochim. Acta, Part B*, **53**, 1657–1667.
137. Wal, R. L. vander, Ticich, T. M., West, J. R. and Householder, P. A. (1999). Trace metal detection by laser-induced breakdown spectroscopy, *Appl. Spectrosc.*, **53**, 1226–1236.
138. Gornushkin, I. B., Ruiz-Medina, A., Anzano, J. M., Smith, B. W. and Winefordner, J. D. (2000). Identification of particulate materials by correlation analysis using a microscopic laser induced breakdown spectrometer, *J. Anal. At. Spectrom.*, **15**, 581–586.
139. Bulajic, D., Corsi, M., Cristoforetti, G., Legnaioli, S., Palleschi, V., Salvetti, A. and Tognoni, E. (2002). A procedure for correcting self-absorption in calibration free-laser induced breakdown spectroscopy, *Spectrochim. Acta, Part B*, **57**, 339–353.
140. Kim, T., Lin, C. I. and Yoon, Y. (1998). Compositional mapping by laser-induced breakdown spectroscopy., *J. Phys. Chem B*, **102**, 4284–4287.
141. Bauer, H. E., Leis, F. and Niemax, K. (1998). Laser induced breakdown spectrometry with an echelle spectrometer and intensified charge coupled device detection, *Spectrochim. Acta, Part B*, **53**, 1815–1825.
142. Beddows, D. C. S., Samek, O., Liska, M. and Telle, H. H. (2002). Single-pulse laser-induced breakdown spectroscopy of samples submerged in water using a single-fibre light delivery system, *Spectrochim. Acta, Part B*, **57**, 1461–1471.
143. Castle, B. C., Talabardon, K., Smith, B. W. and Winefordner, J. D. (1998). Variables influencing the precision of laser-induced breakdown spectroscopy measurements, *Appl. Spectrosc.*, **52**, 649–657.
144. Gornushkin, I. B., Smith, B. W., Potts, G. E. and Omenetto, N. (1999). Some considerations on the correlation between signal and background in laser-induced breakdown spectroscopy using single-shot analysis, *Anal. Chem.*, **71**, 5447–5449.

145. Huang, J.-S., Ke, C. B., Huang, L. S. and Lin, K. C. (2002). The correlation between ion production and emission intensity in the laser induced breakdown spectroscopy of liquid droplets, *Spectrochim. Acta, Part B*, **57**, 35–48.
146. Huang, J.-S., Ke, C.-B. and Lin, K. C. (2004). Matrix effect on emission/current correlated analysis in laser-induced breakdown spectroscopy of liquid droplets, *Spectrochim. Acta, Part B*, **59**, 321–326.
147. Hotokozaka, H., Tanaka, S., Suzuki, A. and Nagasaki, S. (2000). Speciation analysis on europium(III) using laser-induced breakdown spectroscopy, *Radiochim. Acta*, **88**, 645–648.
148. Pearse, R. W. B. and Gaydon, A. G. (1976). *The Identification of Molecular Spectra*. Chapman and Hall, London.
149. Burtscher, H., Mueller, U. and Schmidt-Ott, A. (1989). Monitoring adsorption on small particles, *Z. Phys. D*, **12**, 563–565.
150. Uiterwaal, C. J., Gebhardt, C. R., Schröder, H. and Kompa, K.-L. (2001). Analysis of non-linear ionization of atoms and molecules based on their photoabsorption spectra in the ionization continuum, unpublished results.
151. Hauser, W. and Bundschuh, T. (1998). Verfahren zur Bestimmung der Größe von Partikein in einer Lösung, *German Patent*, DE-19833339.
152. März, F., Scheer, R. and Graf, E. (1990). Use of a laser diffraction particle counter to monitor integrity of reverse osmosis membranes and its inefficiency to detect bacteria in product water, *Int. J. Pharm.*, **61**, 57–66.
153. Takanashi, S., Ishikawa, M. and Ohbayashi, K. (1998). Detection of submicron particles in water using Fabry-Perot interferometer, *Jpn. J. Appl. Phys., Part 1*, **37**, 2708–2711.
154. Alder, H. P., Degueldre, C. and Schenker, E. (1996). Non-invasive monitoring of corrosion in the light water reactor by optical methods, *Water Chem. Nucl. Reactor Syst.*, **7**, 272–276.
155. Degueldre, C., Pfeiffer, H. R., Alexander, W., Wernli, B. and Bruetsch, R. (1996). Colloid properties in granitic groundwater systems. I. Sampling and characterisation, *Appl. Geochem.*, **11**, 677–695.
156. Rees, T. F. (1987). A review of light scattering techniques for the study of colloids in natural waters, *J. Cont. Hydr.*, **1**, 425–439.
157. Bouby, M., Geckeis, H., Manh, T. N., Yun, J.-I., Dardenne, K., Schäfer, Th., Walther, C. and Kim, J.-I. (2004). Laser-induced breakdown detection combined with asymmetrical flow field-flow fractionation: application to iron oxy/hydroxide colloid characterization, *J. Chromatogr. A*, **1040**, 97–104.
158. DVD-ROM (2001). *Encyclopaedia Britannica*. [www.Britannica.co.uk](http://www.Britannica.co.uk), London.

---

# 13 Probing Environmental Colloids and Particles with X-rays

---

JEAN-FRANÇOIS GAILLARD

*Northwestern University, Departments of Civil and Environmental Engineering, 2145  
Sheridan Road, Evanston, IL 60208-1309, USA*

1	Introduction . . . . .	614
2	Interactions of X-rays with Matter . . . . .	615
3	Around the Edge: X-Ray Absorption Spectroscopy . . . . .	616
3.1	Rudiments of XAS . . . . .	617
3.1.1	Extended X-ray Absorption Fine Structure (EXAFS) . . . . .	618
3.1.2	X-ray Absorption Near-edge Structure . . . . .	620
3.1.3	Data Analysis and Calculations Based on First Principles . . . . .	621
3.2	Experimental Protocols . . . . .	624
3.2.1	Measurements in Transmission and Fluorescence . . . . .	625
3.2.2	Sample Preparation and Stability Under the Beam . . . . .	626
3.3	Applications . . . . .	629
3.3.1	Sorption of Elements by Environmental Particles . . . . .	629
3.3.2	Metal Complexation with Humic Substances . . . . .	630
3.3.3	Formation of Precipitates . . . . .	633
3.3.4	Metal Speciation . . . . .	635
4	Imaging and Spectro-microscopy . . . . .	639
4.1	Hard X-ray Spectro-Microscopy . . . . .	640
4.2	Soft X-ray Spectro-Microscopy . . . . .	641
4.3	Computed Microtomography . . . . .	643
5	X-ray Scattering . . . . .	646
5.1	Scattering at Small and Wide Angles: SAXS and WAXS . . . . .	647
5.2	Applications . . . . .	650
5.3	Total Scattering: Pair Distribution Function (PDF) . . . . .	651
6	Conclusions . . . . .	652
	Acknowledgements . . . . .	653
	List of Symbols and Abbreviations . . . . .	653
	References . . . . .	654

## 1 INTRODUCTION

The discovery of X-rays by Röntgen, in 1895, as a novel form of radiation is just over a century old. At first, X-rays were primarily used in the medical field for imaging purposes, but soon became a prevalent mode of structural determination when von Laue and collaborators, in 1912, showed that their electromagnetic properties could be used to study the three-dimensional periodic properties of crystals. Later, following the development of particle accelerators for probing the structure of matter, physicists noticed that these rings produced a parasitic ‘synchrotron’ radiation providing energetic X-rays [1,2]. This discovery stimulated the growth and development of new and more powerful rings dedicated to the production of synchrotron light [3]. Nowadays, scientists can use this light at a wide variety of facilities across the world, not only as sources of X-rays but also as sources of infrared light. There are 75 storage rings providing synchrotron radiation currently available today, and a further handful of storage rings that are planned or in construction. Within the last 10 years, synchrotron light experiments have experienced a renaissance with the advent of new and more powerful sources that are now capable of producing a flux density of X-ray photons that is more than 10 orders of magnitude greater than with conventional X-ray tubes used in the laboratory. This increase in flux density has opened up the possibility of performing new types of experiments, that were not achievable in the past, and acquiring data on shorter time-scale. The recent development of research initiatives in nano-technology and the nano-sciences has also been instrumental in promoting the use of X-rays since they are particularly well suited for interrogating structure–function relationships at an atomic/molecular scale. Ultimately, all of these developments will benefit chemists who are characterising environmental colloids and particles.

The recent development of ‘molecular environmental science’ beamlines at various synchrotron light sources demonstrates the growing field of the application of X-rays in the environmental sciences. However, most of these facilities are overbooked and there is constant pressure from the community to obtain more experimental time and to build new and dedicated facilities. A large fraction of the work performed at synchrotron radiation (SR) facilities has been centred on the use of X-ray absorption spectroscopy (XAS). This stems from the unique ability of this spectroscopic method to probe specific elements in complex chemical and physical matrices that characterise environmental samples [4]. No other spectroscopic method is as general and as element specific as XAS. Synchrotron radiation can be used to perform a wide variety of other experiments on either model or natural systems. From an analytical point of view, it is important to stress that SR-based methods often need to be complemented by other techniques, even in model laboratory systems, limitations that are inherent to many spectroscopic and microscopic methods. Actually, XAS is still poorly perceived as a structural tool because of early pitfalls linked to over-interpretation of data [5]. In environmental applications, an important development of XAS has focused on determining the chemical speciation of metals in environmental systems (*e.g.* [4,6–15]).

The objectives of this chapter are (1) to present a selection of experimental approaches that can be used to probe environmental particles using SR-based methods, (2) to discuss their application domain and their limitations within an environmental framework, (3) to provide key references for environmental chemists new to these methods and (4) to

demonstrate that these methods have a bright future in environmental research. This chapter will focus on the use of SR methods to probe samples in natural systems, since this is one of the primary tasks of the environmental chemist. However, as mentioned above, it is important to remember that, in numerous cases, these methods work best on model and/or simple systems. There remains a lot of work to be done in order to apply these techniques to complex environmental systems. A number of excellent reviews have been published recently on the use of SR in environmental science and low-temperature geochemistry [16]. This chapter will not repeat this previous information – it is impossible to provide the level of detail presented in the above contributions in a single book chapter – but rather provide an overview of the possibilities offered by SR to environmental chemists.

## 2 INTERACTIONS OF X-RAYS WITH MATTER

As with any type of electromagnetic radiation, *X-rays interact only in two meaningful ways with matter: they can either be scattered or be absorbed*. Therefore, all the methods that use X-rays for performing structural determinations are directly related to these two modes of interaction. Furthermore, in the case of an absorption event, most of the information of interest results from the scattering of an ejected photoelectron; this can be viewed as a local scattering experiment.

Synchrotron light results from the movement of an electric charge on a curved trajectory. It is a natural phenomenon in the universe, and it can be produced in the laboratory by moving electrons or positrons in a circular orbit. When the particles move at relativistic velocities, which is the case in most synchrotron light sources, the photons are emitted in a narrow cone in the forward direction, tangential to the orbit. The emitted photons have energies ranging from the infrared to energetic X-rays [3]. In the most recent synchrotron light sources, i.e. third-generation sources that started in the 1990s, synchrotron light is produced not only by bending magnets but also by insertion devices where electrons oscillate over short distances between a series of magnets of alternating polarity. These insertion devices, or undulators, produce a highly collimated beam of high intensity. Synchrotron radiation is highly polarised and is emitted in very short pulses of less than 1 ns.

*X-ray photons interact primarily with electrons.* A schematic diagram of the various processes resulting from the interactions of X-rays with matter is presented in Figure 1. With the exclusion of pair formation, that occurs significantly only at energies above 1 MeV, the usual characteristic energy range for absorption and scattering experiments starts from a few hundred electronvolts for soft X-rays, e.g. 280 eV for probing C, to about 40 keV for Ba, although recent experiments have also been performed at higher energies. Of the various interactions, one possible event is that the energy of the photon is lost within the target, with the net result being one photon in and no photons out. However, if the energy of the incoming X-ray photon is located in proximity of the energy required to excite core shell electrons, the absorption event leads to the emission of a photoelectron. This photoelectron can either move to an unoccupied bound state or be ejected into the continuum, where it can be backscattered by the surrounding atoms. These interactions also produce the emission of secondary electrons and X-ray fluorescence. This summarises the principle of XAS that is based on the photoelectric effect for which

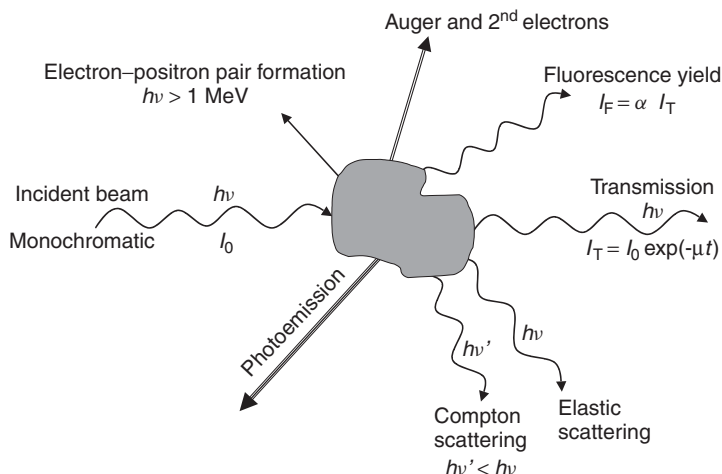


**Figure 1.** Schematic representation of the various phenomena related to the interaction of photons with matter. See List of symbols and Abbreviations for the terminology used

Einstein received the Nobel Prize, which can be represented by one photon in and one photon out. Finally, the X-ray photon can be scattered either elastically, i.e. Thompson scattering, or by inelastic Compton scattering. In the case of elastic scattering, the photon conserves its energy, i.e. same wavelength, whereas in the case of inelastic scattering the photon loses energy. Since photons interact primarily with electrons, the net result of an elastic collision with an electron is a change in the direction of the incoming photon. At wide angles, in the presence of matter that has a periodic structure, i.e. in crystalline solids, the scattered intensity leads to diffraction peaks characteristic of the inter-atomic spacing. At small angles, scattering events can be used to probe variations in electron densities on larger scales. If one is primarily interested in using X-ray absorption, the probability of electron scattering is usually small and adds only a rather constant background that shows little energy dependence.

At any synchrotron facility, the most critical aspect is the ability to select the energy or wavelength of the incoming photons. The typical wavelength of the X-rays produced is of the order of 1 Å, corresponding to an energy of about 12 keV. These wavelengths are therefore particularly well suited for obtaining information about the size and spatial distribution of atoms since they are within the range of inter-atomic bond distances. Because of its wide use in the environmental sciences, a significant fraction of this chapter will be devoted to X-ray absorption spectroscopy. To understand better the prospects and the limitations of the method, we will present a short description that emphasises this spectroscopic method with some applications. As stressed above, the intended audience is the environmental chemist with no, or little, experience with the method.

### 3 AROUND THE EDGE: X-RAY ABSORPTION SPECTROSCOPY

X-ray absorption spectroscopy is one of the most powerful methods available for probing the local coordination environment of metals and other elements in a variety of samples.

It is a short-range order method that can be used regardless of the physical state of the sample. The samples can be either crystalline, amorphous, in solution or in a gas phase. In contrast to other spectroscopic methods, it is an element-specific technique that works with virtually every element in the periodic table, with the exception of hydrogen. It requires little sample preparation, which provides the possibility of using it as a direct probe. Consequently, it has become a popular method of investigation in the environmental community since samples are often complex chemical mixtures containing multiple elements. In this section, the physical principles of XAS are presented together with its experimental layout and some recent applications in studying environmental particles and colloids.

### 3.1 RUDIMENTS OF XAS

X-ray photons of sufficient energy can eject core shell electrons via the photoelectric effect. Since each element has core shell electrons of well-defined binding energy, XAS is element specific. When one scans the energy of the incoming X-ray photons from below to above the binding energy of the core shell electrons of a selected element, one observes an abrupt increase in the absorption coefficient. This jump corresponds to the characteristic absorption edge of the element, also called the white line. Edges are named according to the electron that is excited, i.e. K for 1s, L<sub>I</sub> for 2s, L<sub>II</sub>, L<sub>III</sub> for 2p, and so on. The specificity of XAS resides in the fine structure that is superimposed on the absorption edge, hence it is also referred to as X-ray absorption fine structure (XAFS). This fine structure is often, and to some extent arbitrarily, divided into two regions: the X-ray absorption near-edge structure (XANES), also referred to as near-edge X-ray absorption fine structure (NEXAFS) in the case of low-Z elements, and the extended X-ray absorption fine structure (EXAFS), as shown in Figure 2. The physical principles

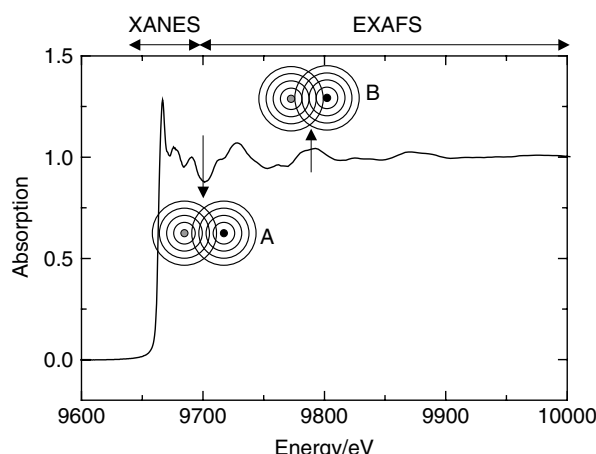


**Figure 2.** Schematic representation of X-ray absorption spectrum at the K-edge of Zn. The concentric circles show the destructive (A) and constructive (B) interferences leading to the modulation of the absorption coefficient. Also shown is the somewhat arbitrary distinction between the XANES and the EXAFS part of the spectrum. Reprinted from Penner-Hahn, J. E., X-ray absorption spectroscopy in coordination chemistry, *Coordination Chemistry Reviews*, **192**, 1101–1123, Copyright 1999, with permission from Elsevier

and the theory of XAS have been described in detail [17–19] and require advanced quantum mechanical concepts. Here, a gentler introduction will be presented, starting with the EXAFS region of the spectrum, since in its simplest form it best exemplifies the basic phenomenon responsible for the spectroscopic features observed.

### 3.1.1 Extended X-ray Absorption Fine Structure (EXAFS)

The nature of the fine structure comes from the scattering of the excited photoelectrons by surrounding atoms. In the EXAFS region, as one increases the energy of the incoming X-rays, the kinetic energy of the photoelectron, i.e. the excess energy beyond the binding threshold, increases. The presence of neighbouring atoms leads to a modulation of the absorption coefficient because of the interference between outgoing and backscattered photoelectron waves. The net result is a decreasing wavelength of the photoelectron and the modulation of the signal because of alternating destructive and constructive interferences (Figure 2). In essence, EXAFS is a spectroscopically detected scattering process [20]. These interferences produce sinusoidal oscillations in the absorption coefficient that are extracted and reported as a function of  $k$ , the photoelectron wavevector:  $k = \sqrt{2m_e(E - E_0)/\hbar^2}$ ; where  $m_e$  is the mass of the electron,  $E$  is the energy,  $E_0$  is the binding energy of the photoelectron and  $\hbar$  is Planck's constant.

Conventional EXAFS analysis, aimed at determining the coordination environment of the central absorber, relies on interpreting the fractional modulation of the X-ray absorption coefficient:

$$\chi(k) = \frac{\mu(E) - \mu_0(E)}{\Delta\mu_0(E)} \quad (1)$$

where  $\mu(E)$  is the coefficient of absorption that is measured,  $\mu_0(E)$  is a smooth background function representing the absorption of an isolated atom and  $\Delta\mu_0(E)$  is the jump in the absorption coefficient at the edge energy.  $\chi(k)$  can be described as the sum of the various oscillations created by the presence of surrounding atoms after the ejection of the photoelectron. These oscillations can be written as [21]

$$\chi(k) = -S_0^2 \sum_i \frac{N_i}{kR_i^2} |f_i(k)| e^{-2\sigma_i^2 k^2} e^{-\frac{2R_i}{\lambda(k)}} \sin[2kR_i + \phi_{ij}(k)] \quad (2)$$

where  $S_0^2$  is the passive electron reduction factor, an amplitude reduction term that is due to multi-electronic effects,  $N_i$  is the number of neighbours  $i$  at an average distance  $R_i$ ,  $R_i$  is average distance between the central atom and the neighbours of type  $i$ ,  $f_i(k)$  is the amplitude of the backscattering wave from the neighbour of type  $i$ ,  $\sigma_i$  is a Debye–Waller factor that describes both the static and dynamic (thermal agitation) disorder in a Gaussian distribution approximation,  $\lambda(k)$  is free mean path of the photoelectron and is a phenomenological term that accounts for inelastic losses and  $\phi_{ij}(k)$  is the phase shift between the central ion  $j$  and its neighbours  $i$ .

In a simpler manner, looking at a single photoelectron that scatters from a single atom, this equation can be decomposed into three contributions that can be related to:

- the photoelectron wave:

$$\frac{f_i(k)}{R_i^2} [\sin 2kR_i + \phi_{ij}(k)] \quad (3)$$

- the lifetime of the photoelectron and the core hole:

$$\text{lifetime} = e^{-\frac{2R_i}{\lambda(k)}} \quad (4)$$

- the passive electron reduction factor:  $S_0^2$ .

Equation (2) can be used to determine the parameters that are important for characterising the coordination environment of a metal, chiefly the type of neighbours, the coordination numbers and the bond distances. These parameters are related to the amplitude and the frequency of the EXAFS signal. Figure 3 presents a simplified view of the information content available from an EXAFS spectrum. It is limited in that it does not provide any information about bond angles, although in some instances the modelling of multiple scattering peaks can provide some additional constraints. However, in order to obtain this information, it is necessary to define all the other parameters. The most important are the energy dependence of the amplitude of the photoelectron backscattering,  $f_i(k)$ , and the phase shift of the photoelectron,  $\phi_{ij}(k)$ . These functions contain information that is characteristic of the scattering atom. They are only weakly dependent on the scattering atom identity so that in practice it is not possible to distinguish between atoms that are close together in the periodic table. For example, it is not possible to distinguish between O and N, whereas the difference between O and S is clear. This is a serious limitation in environmental applications when one deals with ill-defined ligands such as natural organic matter that contains both O and N. On the other hand, in model systems where the composition of the medium is well established, the interpretation of EXAFS spectra is greatly facilitated. Nonetheless, since EXAFS is a bulk measurement, it provides averaged

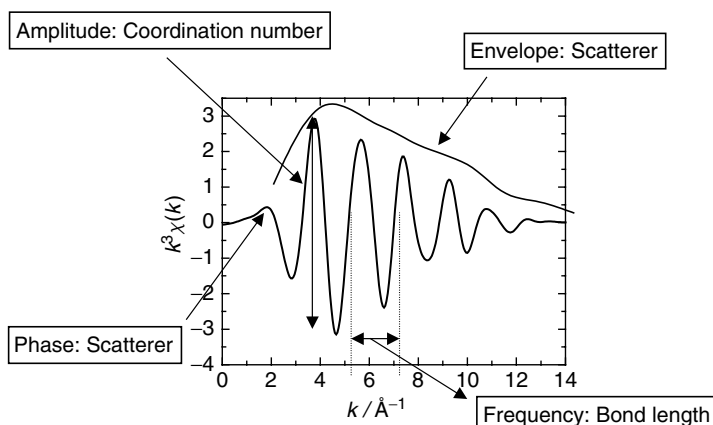


**Figure 3.** Schematic representation of the information obtained from an EXAFS spectrum of a single shell. EXAFS spectra are usually a combination of different shells. Qualitatively the spectrum is limited to the amplitude, the frequency and the phase of the EXAFS oscillations. To a first approximation, the amplitude is proportional to the coordination number, the frequency is inversely related to bond length and the phase to the envelope of the oscillations allowing the type of scatterer to be determined. Reprinted from Penner-Hahn, J. E., X-ray absorption spectroscopy in coordination chemistry, *Coordination Chemistry Reviews*, **192**, 1101–1123, Copyright 1999, with permission from Elsevier

information. The question of the presence of an absorber in a unique type of coordinative environment therefore becomes very central to the precise interpretation of the structural information obtained. A very challenging case is when the sample contains the element of interest bound to the same nearest neighbour in two or more different coordinative environments.

Another limitation of the method is that since the amplitude of the EXAFS signals falls as  $1/R^2$ , only atoms close to the central absorber contribute to the signal – in the best cases up to 8 Å, but more realistically about 5 Å. Three additional factors are present: the passive electron reduction factor  $S_0^2$ , which usually falls between 0.7 and 1, and two exponential damping factors. The first arises from the mean free path of the electron and the second from the Debye–Waller factor. All these contribute to an EXAFS signal that decays approximately as  $1/k^3$ . It is therefore common to multiply the EXAFS oscillations by various powers of  $k$ , up to  $k^3$ , to compensate for this decrease.

Because of the sinusoidal nature of the signal, a Fourier transform (FT) of the EXAFS signal provides a very convenient way to visualise the electronic shells surrounding the central observer. The application of this mathematical treatment was pioneered by Sayers *et al.* [21] in 1971, and it revolutionised the way in which EXAFS data were analysed. Using reciprocal space, one obtains a pseudo-radial distribution function (RDF) that provides the position of the different scatterers. It is a pseudo-RDF because of the various damping factors that affect the amplitude of the FT, and also because the distances are shifted by about 0.5 Å due to the phase shift in  $\phi_{ij}(k)$ . This transformation provides a quick way of determining qualitatively the potential type of surrounding atoms. As mentioned above, the presence of ligands such as O and S can easily be distinguished since S is a larger scatterer that will be located further away from the absorber than O. However, one needs to remember that discrete Fourier transforms of a limited data set may lead to various truncation errors, *e.g.* multiple shells may not give multiple peaks but just a broad peak, and the peaks can appear at non-physical distances because of improper sampling of the signal. In any case, the RDF should not be used for quantitative analysis and one should instead rely on  $\chi(k)$  and the EXAFS equation (2) to adjust the parameters of interest.

### 3.1.2 X-ray Absorption Near-edge Structure

The same physical principles apply in the XANES region; however, the XANES region is more sensitive to a large range of absorber – scatterer distances since at low kinetic energy the electron mean free path increases drastically. As a result, XANES is more prone to multiple scattering events and the calculation of all the various resonances observed is complicated. This means that this part of the spectrum will be sensitive to the geometry of the absorber. For example, metals in octahedral or tetrahedral coordination will present different spectral signatures in the XANES. In addition, the position of the edge is a function of the oxidation state of the element. This can be understood easily, since an element in an oxidised state will have lost valence shell electrons and therefore core shell electrons will be more energetically bound to the nucleus. The chemical effect is small, about 2 eV per  $e^-$ , but combined with other factors, such as changes in site geometry, the shift in the edge position can be significant. The XANES region is actually valuable for determining valence states, provided that the element remains in a similar geometry

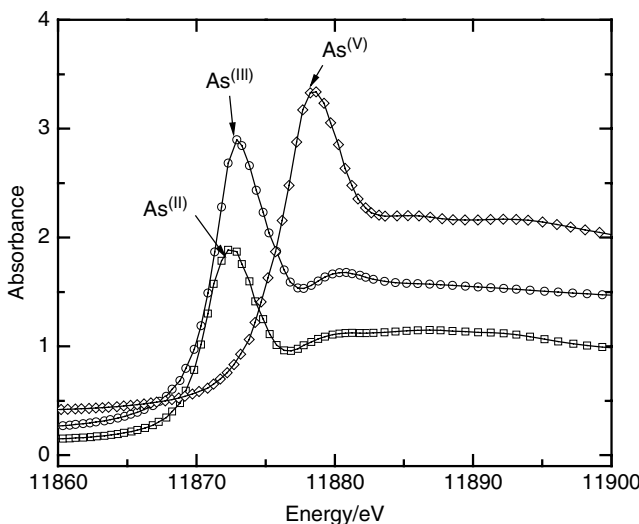


**Figure 4.** Changes in the XANES with region for various oxidation states and site geometry. The difference in the various resonance features are observable, although the spectra have not been normalised. The spectra presented are those of ( $\square$ )  $\text{As}_2\text{S}_2$ , ( $\circ$ )  $\text{As}_2\text{O}_3$  and ( $\diamond$ )  $\text{As}_2\text{O}_5$

for the valence state considered. As an illustration, Figure 4 presents XANES spectra for As compounds that have different oxidation states.

Since the XANES region is sensitive to the site geometry of the metal, it can provide valuable qualitative information when seeking to differentiate among compounds coordinated to the same ligand. For example, Webb *et al.* [22] showed that certain microbial cells that demonstrate metal resistance actively complex Zn. In these live cells, Zn is bound to S not as an inorganic ZnS precipitate, that usually forms on the cell walls, but more likely as an organic moiety (Figure 5). The characteristic resonances present in the XANES region of the inorganic ZnS (sphalerite) reference are absent from the spectrum taken from the microbial cells. In this case, the EXAFS shows that Zn is in a fourfold coordination with Zn, as in sphalerite, but the XANES suggest that it is bound to S as an asymmetric sulfur product – possibly thiol groups – that is intra- or extracellular. This example shows that the XANES investigations can provide valuable qualitative information. Recently, numerous computational efforts have been undertaken in order to provide more quantitative, albeit difficult [23,24], interpretations.

In addition, in the XANES region, pre-edge features can be present that can also be used to study the oxidation state of elements. These peaks arise from bound-state transitions [24] and are indicative of geometry-sensitive crystal-field splitting. Wilke *et al.* [25] reported a very interesting study of Fe oxidation in various mineral phases that allowed them to discuss, in detail, the coordination of Fe in these minerals.

### 3.1.3 Data Analysis and Calculations Based on First Principles

The interpretation of XAS spectra during the last 10 years has benefited tremendously from the development of computer programs and packages that provide convenient and

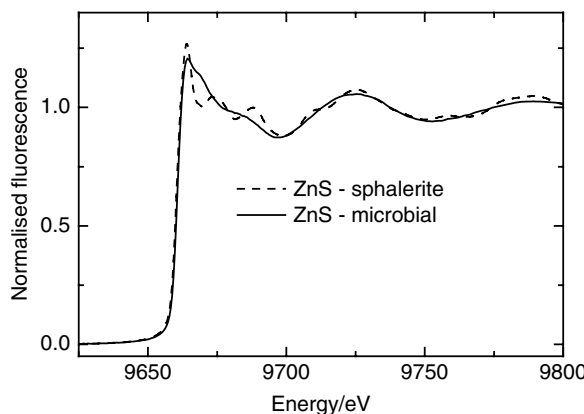


**Figure 5.** XANES signatures at the Zn K-edge of an inorganic precipitate: ZnS (sphalerite) that shows distinct resonances in contrast to Zn complexed certainly to thiol groups inside a microbial cell. Reproduced from Webb, S. M., Gaillard, J. F., Jackson, B. E. and Stahl, D. A., *J. Synchrotron Radiation*, **8**, 943–945, with permission from the International Union of Crystallography (Crystallography Journals Online, <http://www.journals.iucr.org/>)

robust ways of extracting the signal and simulating it using first principles [19,26,27]. With the development of the curve-wave approximation for the movement of the photo-electron [19,28–30], significant theoretical advances have been made from to allow the precise calculation of the EXAFS region. Calculation of the entire XAS spectrum [30], in particular the XANES region, has progressed recently but remains difficult and limited to simple cases.

In order to interpret the EXAFS part of the spectrum, experimental data are background corrected to remove the contribution of the ‘atomic XAS’ and normalised to unit absorption, corresponding to one photon in and one photon out – see Chapter 6 by Sayers and Bunker in [17] for more details. Isolation of the fine structure oscillations is a critical part of the process and many approaches can be used, such as using a simple arctangent or using various cubic spline functions, resulting in some variability in the  $\chi(k)$  data. Newville *et al.* [31] pioneered the use of an automatic technique that is now often applied and incorporated into a few data interpretation programs. It is important to emphasise, however, that this step can be critical in the interpretation of the data, and that it is essential to examine carefully the background function that is produced. In some instances, this process turns out to be more an art than a science. Recently, a normalisation procedure has been proposed that provides a more consistent way of treating a set of samples with the goal of looking at the speciation of elements or key features in the XANES [32]. Depending on the goal of the XAS experiments, it is crucial to select the best and most appropriate method for extracting the desired information.

After the extraction of  $\chi(k)$ , a discrete Fourier transform can be applied in order to obtain a pseudo-radial distribution function providing the distance between the absorber and the various scatterers [21]. Given the linearity of the Fourier transformation, specific shells can be isolated, and the corresponding Fourier-filtered oscillations can be studied independently. In practice however, it is important to explain the whole EXAFS spectrum. The experimental data are usually fitted to a selected cluster of atoms containing the

absorber and the scatterers. This cluster is constructed based either on previous information about the structure of the site or by trial and error. This model may not be unique and one can find several instances in the literature where authors re-interpret the data of others. The EXAFS equation presented above shows that numerous parameters have to be adjusted and that some functions such as the backscattering amplitude and the phase shift need to be evaluated. Before the availability of computer codes based on first principles, these functions were obtained from the EXAFS spectra of reference compounds that were fully characterised and where the coordination of the absorber was thought to be similar to the compound studied. This was not always possible and other options consisted in using tabulated values such as those calculated by McKale *et al.* [33]. These calculations seriously limited the interpretation of the data to the first two coordination shells without addressing the issue of multiple scattering that can be of importance in the interpretation of EXAFS data. Nowadays, several programs are available for performing these calculations that do not require *a priori* the use of reference compounds, although it is still good practice to use these compounds as controls to ensure that the calculations are performed correctly. In addition, they permit more complex calculations to be performed that account for full multiple scattering (MS) effects that arise from the fact that the photoelectron can travel to more than one atom before returning to the absorber. In the Fourier transform of the EXAFS, this effect can be observed by the presence of significant peaks at pseudo-radial distances around or longer than 5 Å. This effect is linked to the relative alignment of the atoms in space since the scattering of an electron by an atom is strongly focused in the forward direction. Each multiple scattering path is therefore defined by an angle, the effect being maximised when the angle between two atoms is 180° and decaying rapidly when the angle becomes less than 150°. The complexity of full MS calculations can be enormous, although the availability of *ab initio* programs has made these calculations more tractable [34]. Although it was stated earlier that EXAFS does not provide any angular information, this is only partially true since the modelling of multiple scattering effects can provide limited information. These effects are much more pronounced in the XANES region of the spectrum, which is the most difficult to simulate precisely.

The main codes that are used for performing these complex calculations are FEFF [29] with the recent FEFF8 version that allows full multiple scattering calculations [27,35], GNXAS [36] and EXCURVE [30]. In addition, TT-Multiplet [37] uses another approach to perform electronic calculations in the soft X-ray region. The principles of *ab initio* calculations have been reviewed in detail by Rher and Alberts [19], and the interested reader should consult their paper. One should note that it is not necessary to understand all of the details of these calculations since some of these codes are fairly user friendly. Nonetheless, it is necessary to have a good background knowledge of inorganic chemistry and a good working knowledge of quantum mechanics. Calculations performed with FEFF are now accessible from a number of data analysis programs that are freely available on the Internet.

To assist the experimentalist, a series of data analysis programs have been developed to help interpret XAS data in the case of either the structural determination of pure compounds, the investigation of specific coordination environments or the interpretation of mechanical mixtures of compounds (see below). A list of the available programs can be found on the website of the International X-ray Absorption Spectroscopy Society (<http://www.xafs.org/>). One of the most recent developments has been spearheaded by

Newville [38] and Ravel [39], who are freely distributing a number of programs that are interfaced with FEFF to fit EXAFS data. These programs are available for various computer platforms and the community of users is constantly testing the newly added features (see <http://cars9.uchicago.edu/ifeffit/>). In addition, this website provides access to a list of frequently asked questions that it is extremely useful to consult. Finally, the package SIXPACK, that is part of this distribution, and developed by Webb, uses the same fitting engine for conventional EXAFS analyses, but also includes the possibility of performing speciation calculations as discussed below.

### 3.2 EXPERIMENTAL PROTOCOLS

The key to any successful spectroscopic investigation is to obtain good spectral information. The primary limitation of the XAS applications is the concentration level of the element studied in the sample. If the element is concentrated, i.e. a few weight percent, it is fairly easy to obtain good data. For many environmental situations, however, the concentration of the element of interest may be too low such that an XAS experiment may not be possible. As a rule of thumb, experimenters have been able to obtain interpretable data when the concentration of the element is above a few ppm – although this value ultimately depends on the matrix. At these concentration levels, the experiment is challenging and may require data collection for long periods – 6 or more. As we shall see later, this may cause stability problems for the sample under an intense beam of X-ray photons.

The layout of an XAS experimental set-up is presented in Figure 6. XAS measures the energy dependence of the X-ray absorption coefficient  $\mu(E)$  and this signal can be measured in transmission, fluorescence and, in some instances, using total electron yield – although this technique is more suited for metallic samples. The white radiation produced by the synchrotron ring is monochromatised using a pair of parallel silicon crystals according to the Bragg diffraction law:  $n\lambda = 2d \sin \theta$ , where  $n$  is an integer,  $\lambda$  the wavelength,  $d$  the distance between atomic layers in the crystal and  $\theta$  the angle of incidence. Typically, the resolution is  $\Delta E/E = 10^{-4}$  for Si(111), a common crystal

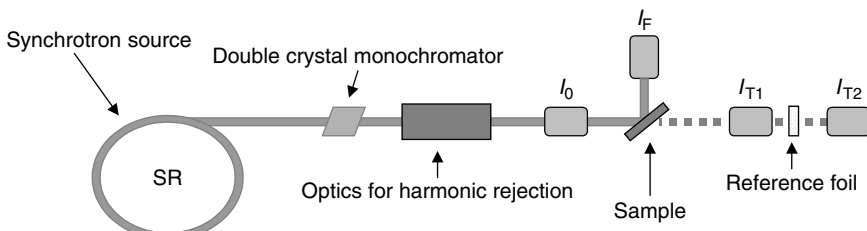


**Figure 6.** Schematic representation of an experimental station designed for performing XAS experiments in either transmission or fluorescence mode. The beam produced either by a bending magnet or by an undulator is monochromatised using two crystals that are parallel. The harmonics produced by Bragg diffraction are rejected using mirrors. Usually, ion chambers are used to measure the incident beam energy ( $I_0$ ), and the transmitted beams ( $I_{T1}$  and  $I_{T2}$ ). The fluorescence detection mode is used when the samples are dilute and is measured best at  $90^\circ$  from the incident beam. A reference foil of the element of interest is placed between the two last ionisation chambers to allow calibration of the energy scale at all times

cut used at many beamlines, and it can be improved slightly by using other cuts. The actual resolution depends on the collimation of the incident beam, which is optimal in third-generation synchrotron rings. The harmonics produced by this set-up are removed preferably using X-ray mirrors that will cut off higher energies or by detuning the second crystal. Since the monochromator may drift over time, it is best to calibrate the energy by measuring a reference sample such as a metal foil of the element investigated. This is accomplished by positioning the foil between two transmission detectors, usually ion chambers, located after the sample.

### 3.2.1 Measurements in Transmission and Fluorescence

In the transmission mode, the flux of X-ray photons is conveniently measured using ion chambers [40] or Si photodiodes [41] by collecting photons scattered off a target. Fluorescence coming off the sample can be collected at 90° to the incident beam by various detectors such as a Stern Heald ‘Lytle’ cell [42], Si photodiodes [43] or a multi-element solid-state detector that provides energy resolution. In order to obtain good fluorescence data, the major constraint is to collect sufficient X-ray emission from the element of interest. Since the EXAFS signal represents a modulation of the absorption coefficient that can be about 1% of the signal, it is important to measure a signal with an error around or better than 0.1%. Given that the detectors are counting devices following Poisson distribution statistics, a signal with a 0.1% error requires at least  $10^6$  events, so that  $\sigma = \sqrt{n}/n = 10^{-3}$ . This entails the collection of at least 1 million ‘usable’ X-ray photons, i.e., the fluorescent photons emitted by the absorber. This requirement imposes drastic constraints on the collection of XAS data and requires some form of energy resolution in order to select the ‘good’ photons. Such energy resolution is required on order to remove ‘parasitic’ or background photons, i.e. X-ray photons scattered off the sample, and also fluorescent X-rays produced by elements with edges of lower energy than the element investigated. This is particularly crucial when looking at trace concentrations of elements in environmental samples that are inherently chemically complex. Among the detectors that provide energy resolution, solid-state detectors of 7, 13, 30 or even 100 elements are used now routinely at various beamlines. However, since they collect all the photons coming off the sample, they can saturate easily – especially at the most powerful synchrotron light sources – and thus lose efficiency. The development of fast electronics has improved the situation but, depending on the sample matrix, detector dead time can be a limiting factor when good energy resolution is required. For example, if one wants to study the adsorption of  $\text{Co}^{2+}$  at the surface of iron oxide, the Co fluorescence signal is affected by the presence of a large fluorescence signal coming from the Fe. In addition, the energy of the K-M<sub>3</sub> ( $K\beta$ ) of Fe is a few tens of electronvolts from the K-L<sub>3</sub> ( $K\alpha$ ) of Co that will be used to collect XAS data. Typically, a solid-state detector, such as a high-purity Ge element, which provides about 140 eV resolution, is not good enough.

One of the best options is to use detectors that provide better energy resolution through crystal optics. One alternative is to use wavelength-dispersive X-ray (WDX) spectrometers that provide energy resolution of around a few electronvolts. On the other hand, this type of detector, used primarily in quantitative X-ray analyses, accepts only a very small solid angle, *ca.*  $10^{-4}$  sr, and becomes rapidly count limited. To solve this problem, two types of new detectors that can accept larger solid angles have been designed recently, which

are likely to be key in future environmental studies. The first detector uses a multilayer assembly that rejects most of the photons that are not within a small energy window around the fluorescence line of interest [44]. The other is based on log-spiral bent crystal optics in Laue geometry [45,46]. The bent Laue crystals seem to provide the best approach available so far with an energy resolution that can be comparable to that of WDX detectors. They are designed for various specific X-ray energies. However, XAS data can also be collected for elements contiguous in the periodic table –  $Z - 1$  and  $Z + 1$  – by merely changing the collection angle by translation.

Finally, it is worth mentioning dispersive EXAFS. Dispersive EXAFS uses a different layout of the instrumentation in which all the energy range required for obtaining an XAS spectrum is analysed at simultaneously [47]. This method is based on the use of mirrors that select a specific energy window. The excitation beam is thus multi-chromatic and dispersive optics allow for its analysis after it has interacted with the sample. In essence, it is the equivalent of a diode-array detector but in the X-ray region. This technique is by far the fastest way to produce a spectrum, and it has been used in catalysis to perform time-resolved analyses of surface species [48]. The energy resolution is a problem with the current instrumentation. However, the development of the next generation of synchrotron sources, known as free electron lasers, will increase photon fluxes by orders of magnitude and provide short pulses of radiation of 50–100 fs. Under these conditions, most samples will be relatively unstable. This will necessitate developing very fast acquisition protocols where a spectrum could be acquired during the duration of a pulse.

### 3.2.2 Sample Preparation and Stability Under the Beam

In contrast to other techniques such as transmission electron microscopy (TEM), the strength of XAS is its ability to measure samples in various physical forms with little preparation. Nevertheless, it is important to stress that the signal can be distorted, especially in transmission mode, if the sample is not prepared properly. In transmission mode, it is extremely important to have a homogeneous sample, with no pinholes, of optimised and constant thickness [17]. It is also important that the size of the particles in the sample is not much larger than one absorption length. This implies that the sample needs to be finely ground and homogeneous. Solutions produce the best transmission samples. In the case of environmental samples, these conditions may rarely be encountered, especially in the case of sensitive samples where the speciation of an element can change on exposure to air or drying. In addition, since the concentration of the element is usually small for transmission, i.e. less than 10%, most of the spectra are acquired in fluorescence mode. However, it is important to remember to prepare carefully transmission samples, especially if they are used as reference compounds. To obtain the best results in transmission mode, the total absorption of the sample should be between 2 and 3, and the change in absorption at the edge,  $\Delta\mu$ , should be greater than 0.1 and ideally close to 1 [49,50].

On the other hand, fluorescent measurements put fewer restrictions on sample preparation. The most important criterion is that the concentration of the element of interest is less than 10%. If it is greater, fluorescent measurements can still be performed at grazing angle, *e.g.* when the sample is positioned perpendicular to the incident beam and the fluorescent detector is oriented at a small angle of the plane defined by the sample [51]. One restriction, which is often ignored, however, is that the particle size distribution and

also solid packing in thick complex samples influence fluorescence. The heterogeneity of the sample affects the quality of the spectra obtained in fluorescence, a phenomenon that was recently documented by Tannazi and Bunker [52,53].

The potential for X-ray photons to cause significant chemical changes within the sample is also seldom reported in the literature. Manceau *et al.* [54] reported the reduction of Mn(IV) to Mn(II) as a result of beam exposure. We have also observed similar reactions when investigating biogenic Mn oxides suspended in solution under the high flux intensity of an insertion device (Figure 7). These types of reactions induced by the beam are more obvious with electrons in TEM since the blurring of the image happens in real time during the observation. In this case, the beam is highly focused and one does not usually seek to obtain any spectral information that could be altered. However, the SR community has been increasingly aware of these potential problems with third-generation sources. These light sources offer highly collimated beams that can deposit in the order of  $10^{11}$ – $10^{13}$  photons per second within a highly focused area – down to a few square micrometres in some applications. Secondary electrons emitted from the sample can lead to further reactions such as the breaking of chemical bonds, the creation of radicals and the reduction of redox-sensitive species. These effects are particularly enhanced in the presence of water since X-ray photons will lead to water hydrolysis. In general, the extent of beam damage remains difficult to assess since it can occur within an extremely short exposure time, given no time to document them unless fast scanning methods are used or control experiments performed. Biochemists are well aware of these potential problems during the study of

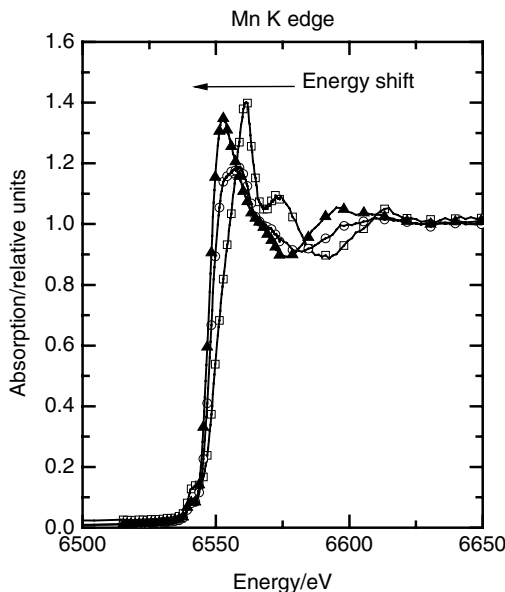


**Figure 7.** Effect of beam exposure on the redox speciation of Mn oxide formed by biogenic precipitation. The first spectrum recorded is represented by the open squares; the second (open circles) was collected after approximately 20 min of beam exposure, and the last (filled triangles) after 40 min of beam exposure. A clear energy shift in the position of the absorption edge – the white line – and changes in the XAS spectra indicate that Mn is reduced as a result of the exposure to the beam. Data obtained by the author and collaborators at the APS

metal centres within proteins in solution and now prefer to operate at beamlines that are equipped with cryogenic sample containment and quick and continuous energy scanning methods [22,48,55]. This scanning mode provides the possibility of acquiring a spectrum within a few milliseconds to 1–2 min, in contrast to the conventional method where the monochromator is moved step by step, which produces significant overhead time leading to scan times of about 20 min or more. In order to convert the data acquired on the fly to discrete energy levels in the EXAFS range, it is necessary to bin it (Figure 8).

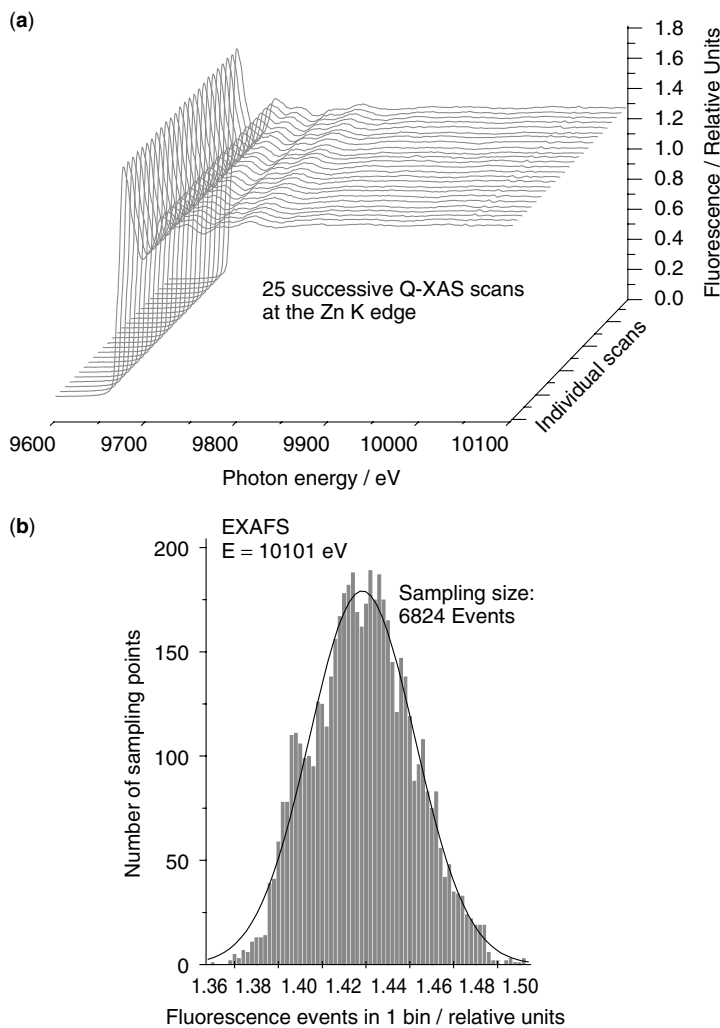


**Figure 8.** Example of the collection of multiple data set in the continuous scanning mode. **(a)** A series of 25 spectra were collected in less than 1 h at a rate of approximately 120 s per spectrum. **(b)** The results of the binning of multiple events that correspond to one data point at a specific energy for one of the curves are shown. The width of the bins is adjusted with respect to the various energy scales used in the different parts of one spectrum, i.e. pre-edge, XANES and EXAFS. This approach allows the determination of the experimental errors associated with the data

At beamlines equipped with quick, continuous scanning possibilities and new detectors, such as those relying on log-spiral bent Laue crystals, spectra on dilute solutions of good quality can now be acquired in about 1 min over large  $k$  values (Penner-Hahn, J. E., personal communication).

### 3.3 APPLICATIONS

The use of EXAFS as a means of determining the speciation of metals in the environment is a recent promising development [6,7,56]. The legacy of industrial activities has greatly perturbed the chemical composition of numerous natural environments and a critical point in assessing the environmental fate of metal is the determination of their chemical speciation. For these purposes, chemists first devised extraction procedures based on the differential release of metals, *e.g.* Tessier *et al.* [57]. Although there are now several metal extraction procedures, they are all indirect methods subject to potential artefacts such as early dissolution, reprecipitation reactions, or redistribution of metals, to name just a few [58]. In contrast, the explosion of direct speciation methods based on XAS has been observed over the past 10 years. Because of its selectivity, XAS speciation provides a good method to test sequential extraction procedures [9,59–63]. It can also be used in conjunction with a sequential extraction scheme, in order to increase the abundance of selected compounds, and allow a more detailed determination of chemical speciation [64].

Overall, two types of approaches have been used to investigate the speciation of metals with XAS. The first approach consists in establishing how metal species attach or are included in environmental particles using model systems. This is best achieved by performing experiments in the laboratory, where specific metals will interact with well-characterised mineral phases or classes of organic compounds. In order to understand the assembly of colloidal particles, one can also rely on XAS to examine the different steps in the formation of new mineral phases, the ageing of the precipitate and the final product. Another approach is to use XAS as a means to determine directly the speciation of metals in complex environmental matrices. We review here briefly some of these applications of XAS.

#### 3.3.1 Sorption of Elements by Environmental Particles

The ability of XAFS to study the average local coordination environment of a specific element makes it a powerful probe for investigating how metals are bound to environmental particles of a size range of a few millimetres down to a few nanometres. Independent of the size and chemistry of the particles, the basic principles that govern the sorption mechanisms of trace elements are thought to be similar. They are divided into (1) adsorption of elements as either outer-sphere or inner-sphere surface complexes, (2) formation of surface precipitates such as multinuclear surface overgrowths and (3) incorporation of the metal into the solid phase either by ionic substitution or by filling up of atomic vacancies [4]. Numerous studies have been performed on model systems to understand how elements interact with particles and their surfaces. During the past 10 years, a significant number of papers have provided new information about specific metal surface interactions. Brown and Sturchio [65] provided an exhaustive list of papers ( $>300$ ) that addressed this issue. Among the recently published papers, we can cite adsorption studies of As, Cd,

Hg, Pb, Se, Sr and Zn at the surface of iron or manganese oxides [66–80], sorption of Co and Pb on aluminium oxides and clays [81–90] and of U at the surface of calcite [91], the effect of organic ligands on the adsorption of metals at surfaces [79,92,93] and sorption reactions at the surface of bacterial cells [94]. In addition to these studies, EXAFS served as a key probe to show that under specific circumstances mixed-cation hydroxide phases can form during sorption reaction. This was evidenced in the landmark studies of Scheidegger *et al.* [95]. Even with the capabilities of XAFS as a local probe, the characterisation of the interactions between a selected metal and a single surface is not always an easy task. The challenges come from the fact that when the element is present at trace levels, the collection of an XAS spectrum necessitates long acquisition times in fluorescence mode and that the metal from the solid matrix, *e.g.* Fe or Mn in oxides, will be a major contributor to the total fluorescence signal if the energy of the edge of the element is above those of Fe and Mn. This situation is the case with many metals of interest in environmental applications.

Over the past 10 years, a large number of publications have sought to determine the coordination of metal species at the surface of environmental particles. The strength of XAS is its ability to measure bond distances with relatively good precision, allowing easy discrimination between outer- and inner-sphere complexes. In the majority of environmental examples, the first ligand is oxygen, either an oxygen atom from the water molecules surrounding the ions or an oxygen atom from the surface of the substrate. In the case of outer-sphere complexation, the coordination number is likely to reflect the coordinative environment of the ions in solution, and the first two shells will be oxygen layers. The metal is then at least 4.5 Å from the surface [81]. This corresponds to a situation in which the metal is likely to be labile as soon as changes in the composition of the background electrolyte will lead to ion-exchange reactions. This type of metal binding is thought to occur frequently in aquatic systems, especially for clay particles. In a complex matrix, it is often difficult to distinguish whether the metal is in the aqueous form or bound to a surface simply by electrostatic interactions. Changes in the coordination environment of metals such as Pb at the surface of montmorillonite or Zn at the surface of hectorite have been observed with time or due to variations in ionic strength or pH (Figure 9). For example, Strawn and Sparks [88] have shown that at low ionic strength ( $I = 0.006$ ) and  $4.5 < \text{pH} < 6.4$ , Pb was bound as an outer-sphere complex, whereas in equilibrated samples at  $I = 0.006$ , pH 6.77 and  $I = 0.1$ , pH 6.31, EXAFS results suggested that Pb formed both inner- and outer-sphere complexes.

### 3.3.2 Metal Complexation with Humic Substances

Numerous investigations of the association of metals with humic substances (HS) in either natural settings or laboratory experiments have benefited from the use of XAS as a local probe of the metal coordinative environment. Overall, the desired outcomes of these studies are (i) to understand better which atoms are primarily responsible for the binding of metals in HS; (ii) to assess whether outer- or inner-sphere complexes are formed, since this will control, in part, the bioavailability of the metal; (iii) to investigate the geometry of the metal site and compare it with well-defined ligation environments in the case of simple ligands; and (iv) to characterise the role of the interactions of inorganic particles with HS in controlling the speciation of metals. The predominant ligands that are likely

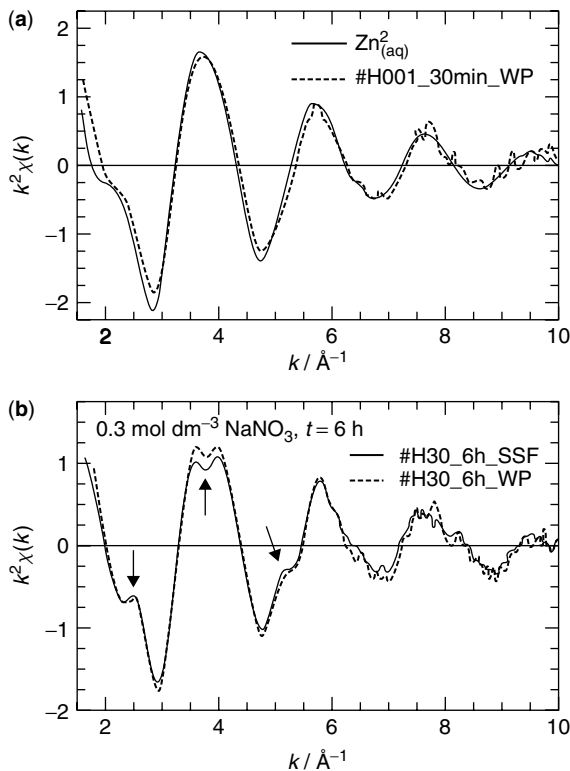


**Figure 9.** Comparison of different EXAFS spectra obtained as a function of time during the sorption of Zn on hectorite. (a) The spectrum of Zn reacted with hectorite after 30 min of contact in an aqueous solution of  $\text{NaNO}_3$  ( $0.0015 \text{ mol dm}^{-3}$ ) closely matches that of Zn in solution indicating an outer-sphere complexation. (b) After 6 h of reaction in  $\text{NaNO}_3$  ( $0.3 \text{ mol dm}^{-3}$ ), the spectra show resonance features that are characteristic of the development of inner-sphere binding sites for Zn. Reprinted from Schlegel, M. L., Manceau, A., Charlet, L. and Hazemann, J. L. (2001). Adsorption mechanisms of Zn on hectorite as a function of time, pH, and ionic strength, *American Journal of Science*, **301**, 798–830, by permission of the American Journal of Science

responsible for the binding of metals in HS are O, N and, to a lesser extent, S in the first shell, whereas C is expected in the second shell. As emphasised above, it is not possible to distinguish between O and N because of their similar scattering properties. Therefore, since the metal is likely to retain a similar geometry when bound to HS or when present as a free metal ion in solution, most of the spectroscopic analysis will focus on bond length variations and the presence or absence of a second neighbour. The signature of S in the first ligation shell should be expected in S-rich compounds since thiol groups are known to be good ligands for B-type metals [96].

The characterisation of the binding environment of metals associated with structurally ill-defined organic moieties such as HS is challenging because metals are usually present at trace levels in the environment. Since metals must be present at a concentration level high enough to obtain interpretable data, numerous studies of metal–HS interactions are performed at high metal loading on material that sometimes has been freeze-dried before

analysis [97]. The only exception is in the case of Fe, since it can be present in the colloidal size range at high concentration. Rose *et al.* [98] used this feature to study the association of Fe with colloidal natural organic matter by combining Fe EXAFS and pyrolysis–gas chromatography–mass spectrometry (PY–GC–MS) to characterise the organic fraction. They collected different colloidal fractions within an African river using tangential flow ultracentrifugation and examined the 20–300 kDa range by EXAFS. The results of this study showed that Fe was poorly polymerised, since it is predominantly complexed by the organic matter, forming monodentate and bidentate complexes with carboxylic groups present in the NOM. The absence of a signature of double corner sharing between iron octahedrons suggests that natural organic matter hinders the hydrolysis of Fe.

Xia *et al.* [97] investigated the coordinative environment of Co, Ni, Cu and Zn with aquagenic and soil-derived organic matter on freeze-dried samples. They used bond network analyses of the XANES features and also EXAFS to determine that Co, Ni and Zn are bound in octahedral geometry, whereas Cu sits in a tetragonally distorted octahedral environment. The presence of C in the second coordination shell indicates that these metals form inner-sphere complexes with HS. Similar results were reported for Cu in other studies by Frenkel and co-workers [99–101], who collected XAS spectra on liquid samples and provided detailed analyses of Cu complexation by HS relying on FEFF simulations. They were able to reproduce the distortion of the octahedral Cu site, show evidence that Cu was unlikely to be bound to carboxylic groups attached to furan rings and to parameterise Cu XANES features, showing their polarisation dependence. In addition, their results supported the view that nitrogen groups bound Cu preferentially at low metal loadings [99]. The coordination environment of Cu and Pb did not appear to be affected by a change in pH between 4 and 6 [102]. In contrast to the first-row transition element, Xia *et al.* [102] reported that Pb was bound to four O atoms, suggesting either square-planar or tetrahedral geometry. Sarret *et al.* [103] studied the complexation of Zn with two different natural humic acids using a wide range of metal concentrations. They found that Zn could exist in either octahedral or tetrahedral sites at low metal concentrations ( $<5000\text{ mg kg}^{-1}$ ). At medium concentrations (*ca.* 32 g kg $^{-1}$ ), most of the sites were octahedral. However, in natural soil samples where the metal can bind to a variety of ligands, the situation became less clear [104] unless the organic fraction was predominant. Using a fingerprinting approach, Manceau *et al.* [7] determined that the most likely functional groups that were binding Pb in soil organic matter were salicylic- and catechol-like. Since the characterisation of multiple binding environments for metals in natural samples is difficult, many investigations have focused on model systems containing a reduced set of relevant components. For example, Dubin *et al.* [105] investigated the complexation of Cu with a herbicide and the interaction of the complex with gibbsite. Their results suggest the formation of ternary surface complexes. Alcacio *et al.* [106] showed that Cu was bound to both organic (HS) and inorganic sites (goethite,  $\alpha$ -FeOOH). At low HS coverage of the goethite surface, Cu formed ternary surface complexes, whereas at high coverage, Cu was primarily bound to the organic fraction sorbed on the goethite surface. In other studies, Nachtegaal and Sparks [107] considered the influence of HS on the formation of surface precipitates on kaolinite, Liu *et al.* [108] investigated the complexation of Cd by HS and showed that it was six-fold coordinated to humic acids and Collins *et al.* [79] looked at the influence of humate during the sorption of Cd at the surface of goethite.

So far, little evidence has been reported on the involvement of sulfur present in NOM as a preferential ligand for binding metals, with the exception of some work on Hg [109–113]. However, S K-edge data can be used to determine the different sulfur species present in HS [114]. By combining S K-edge XANES information and Hg L<sub>III</sub>-edge EXAFS, Hesterberg *et al.* [111] showed that as the S:Hg ratio increased, the fraction of mercury bound to S increased relative to the fraction bound to O. These results suggested that in environmental situations, where Hg concentrations are low, thiol groups present in the NOM bind Hg preferentially. These same groups seem to be responsible for the binding of CH<sub>3</sub>–Hg<sup>+</sup> [112,113].

The potential role of humic substances in the transport of radionuclide in the sub-surface has also been recognised [115,116]; however, little information was available on the binding of these elements until the recent work of Denecke and co-workers [117–121]. These studies showed that carboxylic groups were primarily responsible for uranium complexation with HS in either natural or synthetic compounds. These groups formed predominantly monodentate complexes with the uranyl group. In some of these studies, EXAFS analysis of the U L<sub>III</sub>-edge was complemented with other methods such as infrared spectroscopy to define the binding site better [117,118,122], or time-resolved laser-induced fluorescence spectroscopy [123] to study the interactions of Eu(III), Tb(III) and Cm(III) with HS. In addition, the interactions of Hf(IV) and Th(IV) with HS were probed by EXAFS, showing similar involvement of the carboxylic groups in the binding of these metals. Finally, the introduction of <sup>99</sup>TcO<sub>4</sub><sup>−</sup> under reducing conditions in model groundwater solutions containing various mineral phases and HS led to similar EXAFS signatures [124]. This suggested that, at the relatively high concentrations of the experiment, Tc was reduced to form small Tc(IV) colloids that could interact with the humic substances.

### 3.3.3 Formation of Precipitates

The characterisation of individual particles of Fe and Mn oxides present in natural waters by analytical electron microscopy shows that these entities contain often, if not always, a variety of other elements such as Ca, Si and P [125–131]. In addition, these natural oxides form complex moieties with natural organic matter and play an important role in the fate of metals and toxic organic substances [132]. In fact, the precise nature of the structure of either Fe or Mn oxides in natural systems remains poorly characterised because of the diversity of the assemblages formed [126]. XAS is particularly suited for probing these structures and thus facilitating better understanding of the type of structure that can form upon hydrolysis of the metal. However, it is difficult to obtain spectroscopic information at concentration levels encountered in natural waters because of the intrinsic limitations of the method. On the other hand, experiments performed at high concentrations can provide valuable clues to the various products formed during or after hydrolysis of metals in solution, and the effects of the solution composition on the final assemblies.

The delineation of the various structures formed during the hydrolysis of Fe and the influence of foreign ions in solution was investigated early on in concentrated solutions using X-rays [133,134], and later by coupling XAS and SAXS experiments (*e.g.* [135,136]). The polyhedral approach, initiated by Combes and co-workers [137,138] and reviewed in detail in the first book on environmental particles [139], provides an excellent method for determining the structure of various hydrous oxides by

XAS, especially Al, Fe and Mn oxides. This approach, which consists in determining how metal octahedra assemble, has also been used to understand how foreign ions can affect the structure of oxides [135,140–142]. Recently, *ab initio* programs such as FEFF allowed a more detailed interpretation by including multiple scattering calculations. Nonetheless, most of the experimental evidence was gathered at high Fe concentrations ( $1\text{--}0.1 \text{ mol dm}^{-3}$ ) and low pH. These conditions are rarely encountered in an environmental media, with the exception of acid mine drainage waters.

XAS studies showed that the rapid hydrolysis of  $\text{Fe}^{3+}$  in either chloride or nitrate aqueous solutions forms Fe oxyhydroxide polynuclear species that consist of  $\text{Fe(O/OH/H}_2\text{O)}_6$  octahedra linked either by their edges or by two corners [143,144]. This process is exemplified in Figure 10, showing how Bottero *et al.* [143] used the radial distribution function to determine the different species that formed as a result of the hydrolysis of Fe(III) chloride by NaOH. The different inter-atomic distances observed in the Fourier transform and the coordination numbers obtained from fitting the EXAFS signal indicated edge-sharing octahedra. Subsequently, about 50 min after the start of the hydrolysis, trimeric species with edge- and corner-sharing octahedra were detected. After 1 h,  $\text{Fe}_{24}$ ,  $\beta\text{-FeOOH}$ -like, polycations were also detected. Upon ageing, these species are thought to be the basic units leading to the formation of a variety of iron oxides (*e.g.* 2L-ferrihydrite, goethite, akageneite).

Following the same principles, the nucleation of Fe oxides was investigated in the presence of silicate [135,141,142], phosphate [140,145] and organic matter [146]. All these species modified the hydrolysis kinetics and affected the assemblies of  $\text{Fe(O/OH/H}_2\text{O)}_6$  octahedra. These results are in agreement with TEM observations of natural iron oxides

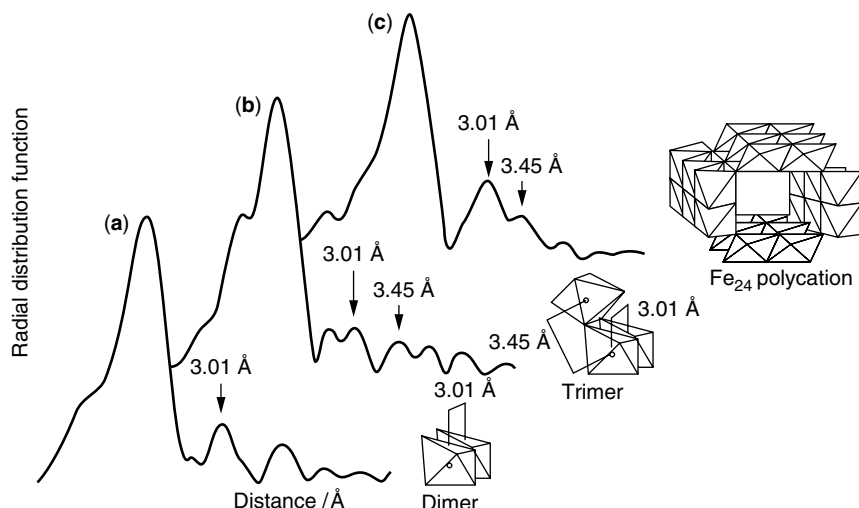


**Figure 10.** Radial distribution function versus ageing time  $t$ : (a)  $t = 10 \text{ min}$ ; (b)  $60 \text{ min}$ ; (c) 16 days. Arrows indicate  $\text{Fe}-(\text{OH})_2-\text{Fe}$  pairing at  $3.01 \text{ \AA}$  (edge linkages) and  $\text{Fe}-\text{O}-\text{Fe}$  ones at  $3.45 \text{ \AA}$  (corner linkages). Structural models of dimers, trimers and  $\text{Fe}_{24}$  polycations are shown on the right. Reprinted with permission from Bottero, J. Y., Manceau, A., Villieras, F. and Tchoubar, D., structure and mechanisms of formation of  $\text{FeOOH}(\text{NO}_3)_2$  polymers, *Langmuir*, **10**, 316–319. Copyright 1994 American Chemical Society

that form at oxic/anoxic interfaces and have shown the presence of multiple foreign ions [125,126]. For example, Rose and co-workers [140,145] investigated the nucleation and growth of Fe oxyhydroxide in the presence of phosphate by interpreting both Fe and the P K-edge EXAFS data. They reported that the growth of Fe–PO<sub>4</sub> colloids was dependent on the initial Fe:P ratio. The presence of phosphate ions affected the hydrolysis process by forming multiple subunits consisting of two or three iron dimers associated with one phosphate tetrahedron. These subunits were linked together through Fe–Fe corner sharing. In studies that looked at the influence of silicate on the formation of iron oxides, the difficulty of obtaining direct spectral evidence of the presence of Si is often emphasised [142,147]. However, Pokrovski *et al.* [148], working at lower Fe concentration of *ca.* 0.01 mol dm<sup>-3</sup>, reported the signature of Si in the second coordination shell of Fe. Their study indicated that under some experimental conditions, one Si tetrahedron was linked to two Fe octahedra by corner sharing. At high dissolved silica concentration, they saw the disappearance of Fe–Fe bonds in favour of Fe–Si linkages, indicating that Fe could be replaced by Si in the tetrahedral network.

Finally, XAS has also been used in studying the formation of Th [149] and Pu [150] colloids from solutions. In the case of Th, a study performed at low pH (up to 3.7) showed the presence of large quantities of polynuclear species or small colloids presenting a distorted Th–O coordination. In the case of Pu, the solubility of Pu was measured by LIBD, and XAS showed that the colloidal Pu particles formed were cubic face-centred with cation defects.

### 3.3.4 Metal Speciation

XAS offers very definitive advantages for assessing the speciation of metals in environmental samples. It is a method that is element selective; all the metals of environmental relevance and even some organic compounds can be probed in all of their forms. The main advantage of XAS is that the speciation can be determined directly, one just needs to condition the sample – taking care, for example, to avoid contact with the atmosphere if reduced species are present – and expose it directly to the beam. The principle that makes XAS an ideal method for speciation measurement is based on the linear nature of the signal. That is, the XAS spectrum of a mixture of a number of metal species is the linear combination of all XAS spectra of the species that are present. Hence

$$XAS_{(sample)} = \sum_{i=1}^n f_i XAS_{(i)} \quad (5)$$

where  $XAS_{(sample)}$  and  $XAS_{(i)}$  refer to the X-ray absorption spectra of the sample and the individual components  $i$ , respectively, and  $f_i$  is the fraction of component  $i$  in the mixture. This principle was first used by Jaklevic *et al.* [6], and revisited 10 years later [15,56], and has often been applied [9–14,54,59,151–158] beginning with the work of Manceau *et al.* [7]. Therefore, if one knows the number of species present and their respective identities, it is easy to establish the speciation of the sample by simple linear deconvolution. In that case, one collects the reference spectra of the compounds present in the mixture and solves for  $f_i$ . Spectral decompositions can be performed using the entire spectrum but, for reasons that are related to the nature of the signal, they are preferentially performed

using either the EXAFS and/or the XANES regions. In the XANES region, this approach aims primarily at determining the redox speciation of the element in the sample, a determination that can be difficult to perform by other means. The EXAFS region is more appropriate for determining the different coordination environments of the metal.

A necessary condition for the application of this method is that the individual components present in the mixture demonstrate unique features in their respective spectra. In mathematical terms, all the spectral references must form a mathematical basis set. That is,

$$XAS_{(0)} = \sum_{i=1}^n f_i XAS_{(i)} \text{ with unique solution } f_i = 0 \dots \forall i \quad (6)$$

where  $XAS_{(0)}$  represents a null spectrum. This relationship is generally well verified in the case of common mineral phases. For example, EXAFS spectra of carbonate, oxides, phosphates and sulfides clearly present distinct and unique oscillations. In addition, various polymorphs present distinct EXAFS features that can allow, in the most favourable cases, detailed speciation information to be obtained. This is a definitive plus compared with the sequential extraction procedures that usually regroup all these components into a single group.

In practice, however, this approach is limited by a number of compounding factors. The primary limitation remains the concentration level of the metal in the sample, since it will directly affect the quality of the spectroscopic information and our ability to determine the chemical speciation. A poor and noisy signal will provide poorly quantitative results, although it can still provide some qualitative information. As discussed previously, the acquisition of good data necessitates the noise level to be about  $10^{-3}$  since  $\chi(k)$  is about  $10^{-2}$ . Because we are limited by counting statistics, this means that one needs to spend long collecting times at high  $k$  values. A solution to this problem is to make multiple measurements since the noise level is decreased by  $1/\sqrt{N_{\text{repeat}}}$ , where  $N_{\text{repeat}}$  is the number of repeats. Another limitation results from the heterogeneity of the sample that can introduce non linear behaviour because of the absorption of the fluorescence by the matrix [52,53].

Wet chemical methods can be extremely sensitive, down to the ppt range, whereas the best report so far for XAS speciation in environmental samples is *ca.* tens of ppm in simple matrices. These limitations are primarily due to the sensitivity of the fluorescence signal and should improve with the use of more energy-selective detectors. In any case, efforts should be made to assess the confidence intervals that can be achieved. Second, it is clear that the presence of a minor component will not contribute significantly to the overall signal. In this case, one may want to consider combining XAS speciation with chemical extractions for removing the major chemical phases – although, as discussed above, this may introduce some artefacts [64]. Third, it is not always possible to build a comprehensive library of reference spectra because the mineral phases are physically and chemically complex and because the specificity of the chemical phase may reside in surrounding atomic structures that are not probed by XAS. For instance, it would be very difficult to obtain detailed speciation for a metal that is involved in solid solutions, as could be the case for carbonate minerals. The same will hold for phyllosilicate minerals that can accommodate a wide variety of cations in their structure under various geometries. Luckily, the most critical metal speciation information for an environmental

chemist can be well assessed by this method, i.e. one can obtain the overall fraction of the metal bound to carbonates. It is also important to note that the relative sensitivity will vary according to the strength of the oscillations in the EXAFS region. Obviously, a compound where the metal has a low coordination number and is bound to a weak scatterer is not a favourable case. Further, in most instances the metal species present environmental samples are *a priori* unknown. This turns out to be a serious limitation since, in combination with the inevitable noise problem; it will directly impact on our ability to be absolutely sure that the determined speciation is close to the true chemical distribution. One may find a mathematical solution to the problem, but there is no guarantee that this is the correct answer. This problem is common to most fitting techniques, but tends to be rarely recognised. In most instances, one requires additional information about the sample in order to constrain the results better.

One recent approach in the XAS community has been to use multivariate analysis, in particular principal component analysis, to assess the number of chemical species present in the sample [12,159–162]. Since the method has been presented in detail in a recent review article [4], only a brief description will be presented here. This approach is based on the collection of as many different spectra as possible of the same sample or samples presenting some relatedness. Then, using an eigenvalue analysis of the matrix constituted by these spectra, the number of mathematical components that explain most of the variance in the data [163] are selected. In this way, one seeks to determine orthogonal functions that explain the entire data set if recombined in the proportions given by their associated eigenvalues. In the domain whose dimension is defined by the number of available spectra, the calculation is derived from the singular-value decomposition theorem. The method is also known as empirical orthogonal functions, and it has been used fairly extensively in processing large data sets in fields as diverse as astronomy, climatic studies, and social science. Usually, one fixes the number of necessary orthogonal functions by looking at the proportion of variance explained by the so-called principal axes or ‘components’. Malinowski [163] presented a criterion to fix the best number of functions to use. Nonetheless, the number of functions is selected based on mathematical rather than chemical criteria, since in the suite of spectra collected it is possible for two chemical species to be linearly dependent. It is then necessary to establish a collection of reference spectra, i.e. a library that contains an exhaustive list of the potential spectra from which the functions can be reconstructed, and identify them by target transformation [163]. Once the reference spectra have been selected, the speciation can be determined by a least-squares approach or linear programming. Gaillard *et al.* [14] used an augmented least-squares minimisation approach in which the minimisation of the fractions  $f_i$  were subject to the constraints

$$\forall i, f_i \geq 0 \dots \text{and } \dots \sum_{i=1}^n f_i = 1 \quad (7)$$

This calculation was performed in parallel with an error analysis in order to determine the confidence intervals for each of the different fractions. The approach consisted in acquiring multiple spectra of the same sample so that an average spectrum could be computed and its confidence envelope characterised by the standard deviations calculated at each point in the spectrum (Figure 11). Subsequently, by a Monte Carlo process, the errors were propagated across the normalisation, background removal and EXAFS

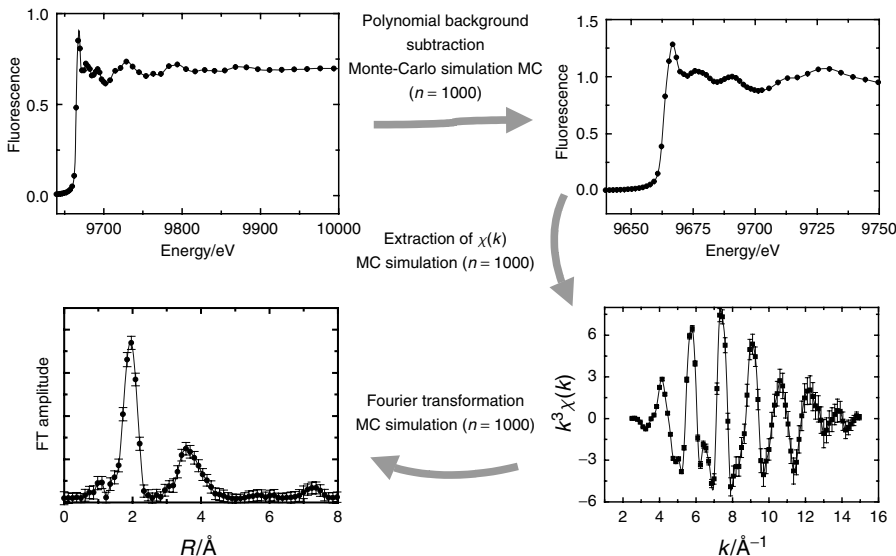


**Figure 11.** Schematic representation of the propagation of experimental errors by means of a pseudo Monte Carlo simulation. The errors calculated for each spectrum are sampled randomly and carried through the normalisation, background subtraction and extraction of the EXAFS signal. This operation is performed here on a ‘perfect’ sample collected in transmission mode. The data obtained from environmental samples are more noisy

extraction step of the data analysis. A Monte Carlo approach is necessary since these various steps use non-linear functions for obtaining the EXAFS (Figure 11). To extract finally the errors on the fractions  $f_i$ , the Monte Carlo process is repeated for the constrained linear least-squares fitting. Using this approach, it is possible to determine an experimental error on the chemical speciation of the metal (Figure 12). A modification of this approach is implemented in SIXPACK and relies instead on the use of penalty functions. As one can see from some spectra of the in the literature, the level of noise in the data can be significant in the high- $k$  region, depending on the concentration level of the metal and the complexity of the matrix [9].

In many instances, determination of the speciation of metals by XAS in environmental samples is facilitated by the use of complementary methods. For example, using AEM, Webb *et al.* [164] were not able to say unambiguously that small particles ( $\sim 100$  nm) present in contaminated sediments and containing Zn and S were zinc sulfide particles. On the other hand, XAS results provided clear evidence that the particles were indeed zinc sulfide, the overall signal closely matching the one of spharelite [165]. In the same lake and in different particles, Zn was associated with Fe and P as was confirmed by the EXAFS speciation. Because of the intrinsic limitations of AEM, Webb *et al.* [164] were unable to observe two significant fractions: Zn bound as an outer-sphere complex to the clay fraction and Zn present in carbonates. XAS speciation was sufficiently sensitive, but without the observation of the Zn–P relationship by AEM, it would have been difficult to envision that a zinc phosphate coordination shell could have been prevalent. Recently, a growing number of studies have reported the role of colloids in metal transport. For example, Zanker

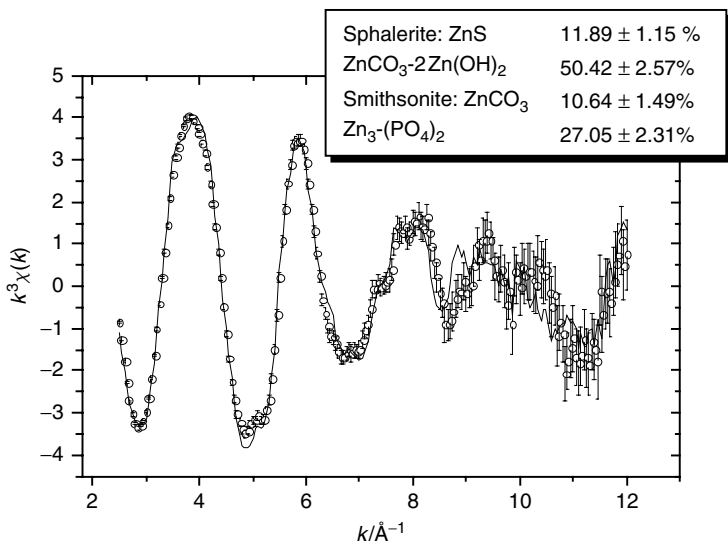


**Figure 12.** XAS speciation of Zn in the sediments of a contaminated lake performed using a spectral decomposition based on least-squares fitting under constraints. Note that in this result, one can discriminate between an amorphous Zn carbonate hydroxide and a crystalline form of Zn carbonate. The percentage deviation in the relative fractions is estimated through error propagation via a Monte Carlo calculation. Reproduced from Gaillard, J. F., Webb, S. M. and Quintana, J. P. G. (2001). *Journal of Synchrotron Radiation*, **8**, 928–930, with permission from the International Union of Crystallography (Crystallography Journals Online, <http://www.journals.iucr.org/>)

*et al.* [166] showed that As was scavenged by nanometre-sized jarosite–schwermanite particles in a mining area in Germany. Lowry *et al.* [167] showed that Hg was released in colloidal form as HgS in mine waste piles in California.

#### 4 IMAGING AND SPECTRO-MICROSCOPY

The need to interrogate samples at the micro- or nanometre scale is important in environmental applications of synchrotron radiation because samples are often heterogeneous and contain multiple species present in a complex matrix. XAS provides only average information. However, if one focuses the beam down to a small spot size, spatially resolved spectroscopic information can be obtained. In contrast to electrons, the focusing of X-ray photons is more challenging since it cannot be achieved using magnetic or electrostatic lenses as in electron microscopy; rather it is necessary to use conventional optics such as mirrors or interference lenses. The spatial resolution of the instrument and its capacity to perform in spectroscopic studies are limited since the focusing plan may change with the energy of the incoming X-ray photons. When using X-rays produced by synchrotron rings, two types of spectro-microscopy can be performed. Spectro-microscopy in the soft X-ray region uses a different instrumental set-up than spectro-microscopy in the hard X-ray region (above 4 keV). One of the primary reasons is that in the soft X-ray region the experiment must be performed under vacuum, because of the absorption of X-ray photons by the air. In addition, the production of secondary electrons is favoured compared with fluorescence for low-Z elements.

In contrast to X-ray microscopes available in the laboratory, the use of synchrotron radiation enhances the spatial resolution that can be obtained because of the polarised nature of the radiation. By controlling the geometry of the experiment, one can optimise signal-to-noise ratios. With the high flux of photons produced by synchrotron rings, the limits of detection are improved by orders of magnitude compared with laboratory instruments.

Although it has seldom been used to study the fate of environmental particles or colloids in environment, X-ray computed microtomography offers great potential. This technique is used to examine the internal structure of objects, providing an unprecedented opportunity to study the distribution of colloidal-sized particles in environmental media. In addition, it is possible to perform element-specific 3D mapping of particles.

#### 4.1 HARD X-RAY SPECTRO-MICROSCOPY

Multiple microbeam facilities designed for hard X-rays have become available at various synchrotron rings worldwide. The best spatial resolution that can be achieved is *ca.* 1 µm for Kirkpatrick–Baez (KB) focusing mirrors [168] and 100 nm for optics based on Fresnel zone plates (FZP) [169]. Other beam focusing options exist, such as tapered capillaries and multi-capillary assemblies known also as Kumakhov lenses [170], but they cannot achieve the same versatility or spatial resolution as the other two optics.

Currently, one can image objects with a spatial resolution in the upper limit of the colloidal range, whereas in the near future, observations will be possible on a nanometre scale that challenges electron microscopy, as is the case for soft X-ray spectro-microscopes. However, these experiments will not be easy to perform since minute movements in the beam or in the sample will be problematic. The positioning of the sample requires precise mounting stages with optics that ideally have a focal point that is independent of the beam energy. X-ray fluorescence is the method of choice for inspecting the chemical distribution and association of elements within a given sample. The sensitivity of the method is about or better than 1 mg kg<sup>-1</sup> when using a wavelength dispersive X-ray (WDX) detector. It is important to remember that it has a local sensitivity, i.e. the bulk concentration of the element can be less if it is concentrated in a few particles that can be probed independently. This detection limit is far better than those that can be achieved with an electron microscope equipped with an energy-dispersive spectrometer – about 0.1% in favourable cases. For x-ray spectroscopy, the detection limits are higher, *ca.* 10<sup>6</sup> atoms, since one needs to observe the fine structure within the signal. For µXANES a local concentration of about 10 mg kg<sup>-1</sup> is necessary, while for EXAFS, concentrations of 100–1000 mg kg<sup>-1</sup> are required in order to obtain interpretable spectral information. Somogyi and co-workers [171,172] provide a good theoretical description of the use of XRF for performing the analysis of single particles.

Among the methods of focusing the beam mentioned above, KB mirrors offer the possibility to perform µEXAFS measurements since the focal point shows little dependence with respect to energy. This contrasts with the case of zone plates, where the focal point of the beam moves with the energy. The effect is relatively weak in the XANES region and therefore FZP have been mostly used for collecting near-edge data [173]. In recent years, the number of microbeam applications has increased sharply and the construction of various nanoprobe should provide a unique opportunity to probe matter at the micro/nano-scale.

The applications of X-ray microprobes are recent [174,175], and have been reviewed by Bertsch and Hunter [176], Sutton *et al.* [177] and Manceau *et al.* [4]. In addition to XRF and XAS, it is possible to perform X-ray diffraction determinations on small particles [4]. The combined use of XRD, XRF and XAS provides unprecedented detail on the chemical make-up of complex environmental samples. Manceau *et al.* [54] used this approach to document the fate of Zn in a pristine clay horizon of a soil where its bulk concentration was about 130 mg kg<sup>-1</sup>. They were able to determine that Zn was present as sphalerite (ZnS), zincochromite (ZnCr<sub>2</sub>O<sub>4</sub>), Zn-containing phyllosilicate and lithiophorite and Zn-sorbed to either ferrihydrite or a phosphate. Duff *et al.* [178] used fluorescence mapping to show that Pu was primarily associated with manganese oxides and smectites, but not with iron oxides. The further inspection of Pu XANES spectra in the region where Pu was the most concentrated showed that this element was present either as Pu(V) or as Pu(VI), indicating redox reactions of Pu with the soil matrix. Strawn *et al.* [179] looked at As, Se and Fe in micrometre-sized particles from an acid sulfate soil. Using XRF and XAS, they were able to distinguish different locations where Fe was present either as an oxide or as iron sulfate (jarosite) and showed that As and Se were preferentially associated with the Fe oxides. The oxidation state of As remained As(V), whereas Se was present as either Se(IV) or Se(VI), Se(VI) being the major form of Se in the jarosite. The composition of atmospheric particles, particles generated by combustion engines and suspended particles in river water have also been characterised by combined XRF and XAS approaches [180–183]. Finally, the elemental mapping of and the determination of their oxidation state is now possible inside single bacterial cells [184].

#### 4.2 SOFT X-RAY SPECTRO-MICROSCOPY

Soft X-ray microscopy uses X-rays in the energy range 100–1200 eV, which correspond to wavelengths on the order of 1–10 nm [185–191]. This provides the spatial resolution to investigate particles in the colloidal range. These photon energies are characteristic of the inner-shell electronic transitions of low-Z elements such as the 1s (K-edge absorption) of C, O, and N and the 2s and 2p (L<sub>I</sub>, L<sub>II</sub>, and L<sub>III</sub> absorption edges) of P, S and some metals of environmental relevance such as Mn and Fe. At these energies, there is a good intrinsic contrast between organic matter and water. In essence, soft X-ray microscopy is particularly well suited for investigating in colloidal systems the interactions between organic and inorganic colloids. Various types of instruments for performing this type of microscopy are present at synchrotron rings dedicated to the production of soft X-rays, and their characteristic designs are presented in Figure 13. With the exception of the photoemission electron microscope (PEEM), all of these instruments use zone plates and translation stages to raster scan the sample in the beam. The primary requirement of the PEEM is that it necessitates relatively flat samples over a few tens of nanometres, so that the electrons emitted can be uniquely traced back to a precise location [191]. In the best cases, some of these instruments can achieve spatial resolutions of ~20 nm [189].

These microscopes were developed primarily for looking at polymers [186], surface phenomena and also for medical research applications [192]. However, more recently they have been used to study organic matter [193] and soil colloids [194]. The environmental structure of humic compounds under changing chemical conditions of pH, ionic strength and Ca and Fe<sup>3+</sup> additions was investigated *in situ* by X-ray microscopy by Myneni

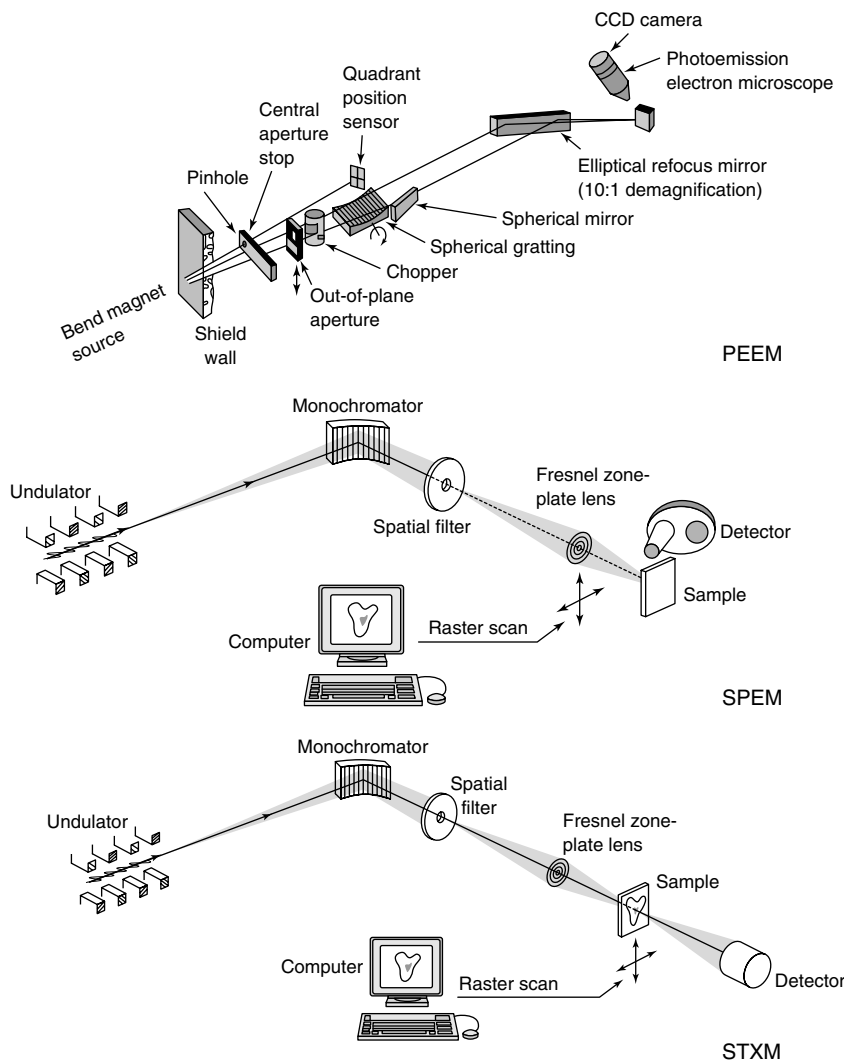


**Figure 13.** Various designs for soft X-ray microscopy. PEEM, photoemission electron microscopy; SPEM, scanning photoemission microscopy; STXM, scanning transmission X-ray microscopy (from <http://www-als.lbl.gov/>)

*et al.* [193] (Figure 14). This study demonstrated that the conformation of natural organic matter changes with changes in the bulk chemistry. The study also presented the first visualisation of these conformational changes with microscopic resolution *in situ*.

An important advantage of some of these microscopes is their ability to obtain spectroscopic information. For example, by changing the energy of the incoming beam it becomes possible to collect stacks of images corresponding to each of the different inner-shell processes at spot size resolution. By plotting the intensity of the signal at one sample location, it is possible to obtain an XAS spectrum. The operation can be

Publisher's Note:  
Permission to reproduce this image  
online was not granted by the  
copyright holder. Readers are kindly  
requested to refer to the printed version  
of this chapter.

**Figure 14.** X-ray transmission microscope images taken at the carbon K-edge at the Advanced Light Source showing the macromolecular structure of the Suwannee River fulvic acid (from the International Humic Substance Society) in aqueous solution as a function of pH and ionic strength: (a) pH = 3.0; (b) pH = 9.0; (c) pH = 4.0 and  $[Ca^{2+}] = 0.018 \text{ mol dm}^{-3}$ ; (d) pH = 4.0 and  $[Fe^{3+}] = 0.001 \text{ mol dm}^{-3}$ ). The scale bar, which applies to all of the micrographs, is shown in (d) and is 500 nm. Reprinted with permission from Myneni, S. C. B., Brown, J. T., Martinez, G. A. and Meyer-Ilse, W., Imaging of humic substance macromolecular structures in waters and soils, *Science*, **286**, 1335–1337. Copyright 1999 AAAS

repeated at other spots to determine, for example, how the carbon K-edge changes. This information can be very useful since it allows for the tracking of certain compounds, or even speciation studies within a radius of a few nanometres. All this information is appropriate for multivariate analysis such as PCA in order to tease out the different molecular contributions to the signal. For example, Schmidt *et al.* [194] looked at sulfur compounds present in a soil and identified amino acids such as methionine and cysteine produced by bacterial activity. An example of the richness of the information that can be obtained is presented in Figure 15, where near-edge X-ray absorption of S-containing compounds shows remarkable differences in their XAS spectra [195].

#### 4.3 COMPUTED MICROTOMOGRAPHY

The use of X-rays to obtain 3D reconstructions of the internal physical structure of objects was developed originally for medical applications, *e.g.* CAT scanners. Synchrotron-based microtomography [196] uses the same principles but the high collimation and intensity

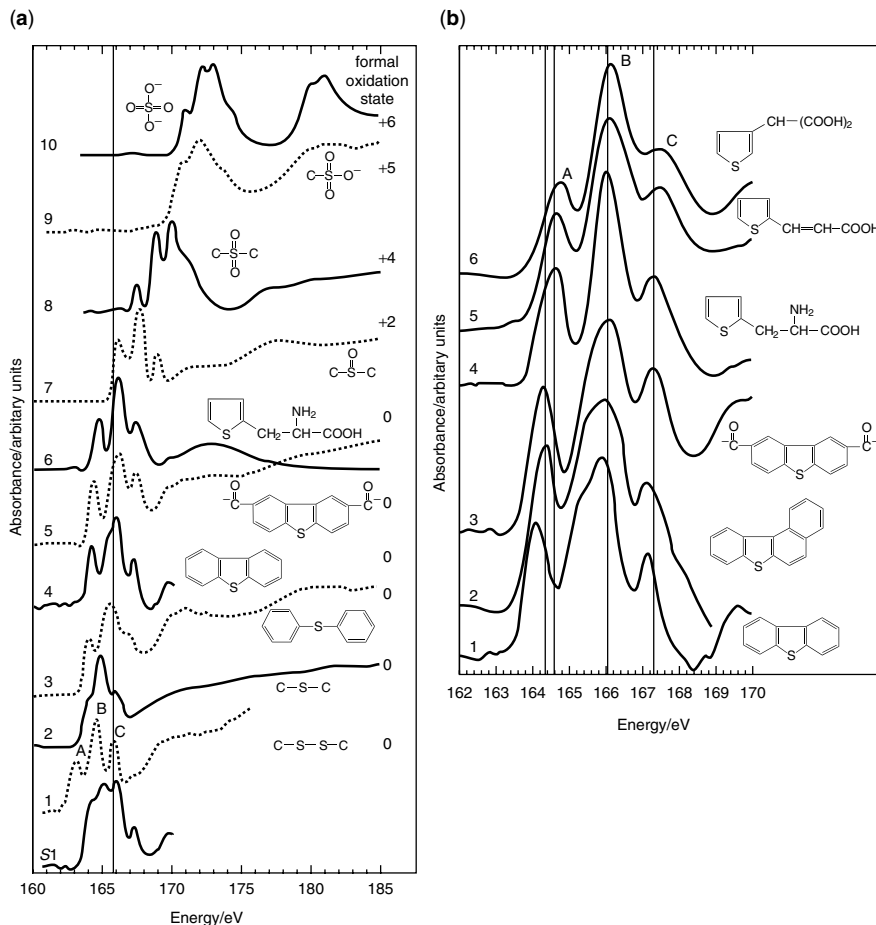


**Figure 15.** S L-edge XANES spectra for some reference compounds. **(a)** (1) DL-cystine, (2) DL-methionine, (3) poly(phenylene sulfide), (4) DBT, (5) tilorone analogue [2,8-bis(dimethylaminoacetyl)dibenzothiophene dihydrochloride trihydrate], (6) 3-(2-thienyl)-DL-alanine, (7) DL-methionine sulfoxide, (8) DBT sulfone, (9) anthraquinone-2-sulfonic acid, sodium salt, (10) sodium sulfate, [S(I)] synthesised spectrum using compounds 2 and 4 (50% each). **(b)** (1) DBT, (2) tilorone analogue, (3) benzonaphthothiophene, (4) 3-(2-thienyl)-DL-alanine, (5) 3-(2-thienyl)-DL-acrylic acid, (6) 3-thiophenemalonic acid. Reprinted from Sarret, G., Connan, J., Kasrai, M., Bancroft, G. M., Charrie-Duhaut, A., Lemoine, S., Adam, P., Albrecht, P. and Eybert-Berard, L., Chemical forms of sulfur in geological and archaeological asphaltenes from Middle East, France, and Spain determined by sulfur K- and L-edge X-ray absorption near-edge structure spectroscopy, *Geochimica et Cosmochimica Acta*, **63**, 3767–3779, Copyright 1999, with permission from Elsevier

of the X-ray beam provides better spatial resolution. In addition, because the X-ray beam can be monochromatic, X-ray synchrotron tomography is not plagued with beam hardening problems that need to be corrected for in laboratory instruments. At present, computed microtomography at synchrotron sources allows objects to be observed with sub-micrometre resolution [177], opening the door for investigations in the colloidal range [197].

Conventionally, tomographic reconstructions can be performed using three different approaches: (1) using X-rays transmitted through the sample, (2) using X-rays fluoresced by the sample and (3) using X-rays diffracted by the sample. The last technique is of little interest for looking at particles and will not be addressed in this section. The basic approach is to measure a large number of projections of either transmitted or emitted photons through the sample and to reconstruct the internal structure of the sample. These projections are obtained by rotating the sample in the beam (Figure 16). In transmission mode, the images obtained are shadowgrams that describe the attenuation of the intensity of a wide beam, whereas in fluorescence mode one collects data for a specific element using a beam that is as thin as possible. In the former case, the dimension of the beam defines the spatial resolution that one can achieve, whereas in the latter the resolution is directly related to the number of pixels available on the CCD camera. In transmission tomography, the width of the sample must, at all times, be contained within the dimension of the beam. Therefore, in order to observe spatial distributions with  $1\text{ }\mu\text{m}$  resolution, one needs to position the sample in a beam that has a width of 1 mm, or less, if the CCD camera has a chip of  $1000 \times 1000$  pixels. An important condition for good tomographic reconstruction is that the X-ray thickness of the sample be about two absorption lengths. Given the electron density of the sample, one needs to tune the energy in order to meet this criterion so that the shadowgrams recorded provide the best contrast. In the case of fluorescence tomography, the beam must be very thin, ideally with a diameter of about  $1\text{ }\mu\text{m}$ . Fluorescence tomography can achieve element specificity since it collects the fluorescence from the element of interest with a detector that is not position sensitive. The major drawback of the method is the re-absorption of the fluorescent photons emitted

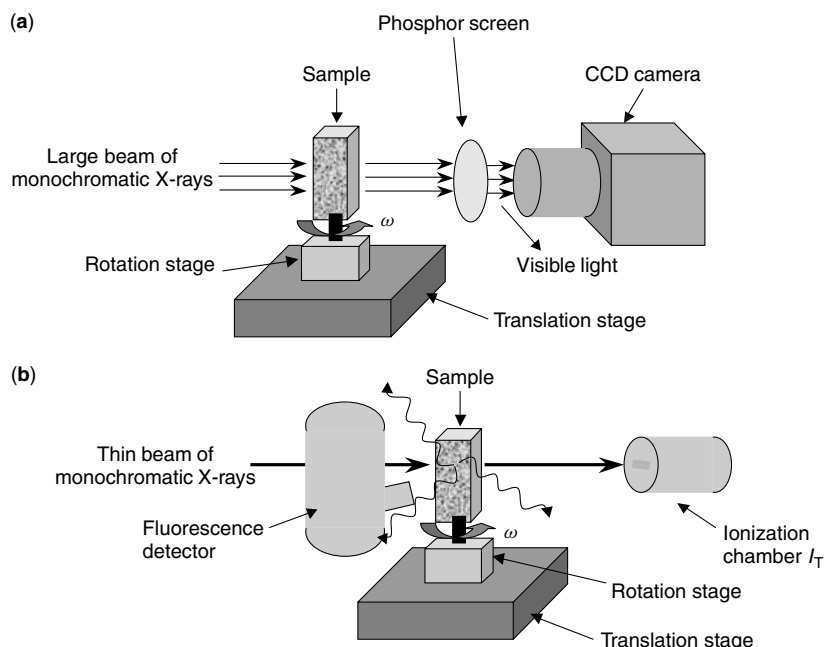


**Figure 16.** Schematic diagrams showing how tomographic sections can be collected in (a) transmission mode and (b) fluorescence mode

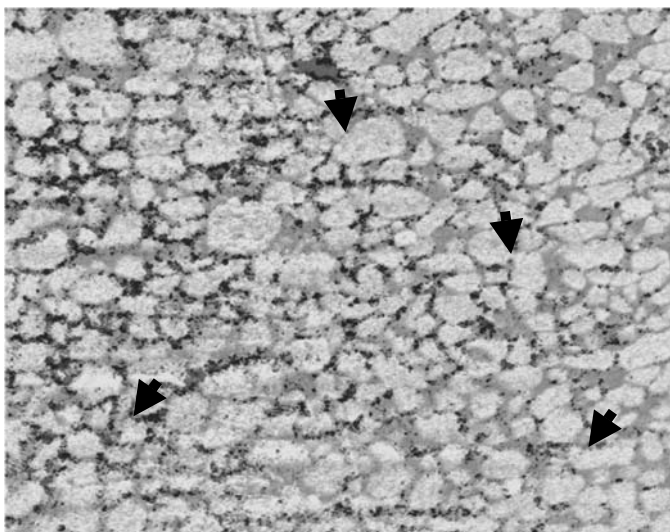


**Figure 17.** A Z-contrast tomographic section through the centre of a column packed with fine sand particles that shows the deposition pattern of colloidal ZrO<sub>2</sub> particles. The image is a composite of the tomogram slice that shows the structure of the porous medium and the difference tomogram obtained from the Zr K-edge. A few colloidal ZrO<sub>2</sub> particle aggregates are indicated by the black arrows

within the sample. This point must be taken into account during the processing of the data. One advantage is that multiple elements can be imaged simultaneously, provided that the energy resolution of the detector is good enough to discriminate them. Element-specific tomograms can also be obtained in transmission mode by collecting two sets of data, one below and one above the edge of the element of interest. By calculating the difference between the two tomograms, the three-dimensional distribution of the element can be reconstructed. In this case, the size of the sample must be controlled in order to maintain the absorbance criterion mentioned above.

The first applications of synchrotron X-ray tomography in environmental sciences addressed the structure of porous media [198,199]. In sandy material, the particles are large enough to be characterised easily [198]. Tomographic reconstructions are usually computer intensive and require the use of computer clusters [200]. They can also be combined with X-ray absorption to provide the location of the element in addition to its oxidation state [201,202]. Recently, we performed a study of the migration of colloidal ZrO<sub>2</sub> particles in a small sand column using Z-contrast absorption tomography (Figure 17). One can clearly see the accumulation of the zirconium oxide colloids within the porous medium.

## 5 X-RAY SCATTERING

A wide range of methods, such as light scattering, sedimentation and microscopy, can be used to determine the properties of small particles. Static light scattering (SLS) and dynamic light scattering (DLS) methods, which were reviewed in Volume 2 of this

series [203], present some limitations when dealing with colloidal systems. SLS measures the scattered intensity of visible light. The resulting diffraction patterns are then compared with a model to determine the particle size. Because of the lack of structure in the scattering pattern for radii below about 120 nm, it is limited to the rather large colloidal fraction, and it cannot provide any information about the internal structure of the particles. DLS is based on measuring the Doppler shifts due to Brownian motion of particles in a liquid. This method provides in essence a diffusion constant from which a radius can be predicted using the Stokes–Einstein approximation if one knows the viscosity of the liquid and the shape of the particles. Whether this is the true radius or a slightly larger ‘hydrodynamic’ radius depends on the composition of the medium and the volume fraction of colloidal particles. In addition to the radius, the size polydispersivity can be determined from DLS measurements, but again, by the inherent nature of the method, DLS is not sensitive to the internal structure of the spheres. Among the microscopic methods, only electron microscopy can provide some information at the scale required for probing colloidal systems, since optical microscopy lacks the resolving power [204]. Unfortunately, TEM is an ultra-high vacuum (UHV) method and samples need to be dried or embedded in a resin potentially affecting sample integrity. The recent development of cryo-TEM, especially for biological applications that are plagued with similar problems to those seen in colloidal science, presents one alternative, as does the use of the environmental cell TEM [205,206]. Nonetheless, beam damage from electrons can degrade the particles, a phenomenon often encountered when dealing with organic compounds. All these effects can seriously hamper the accurate determination of sizes and structures.

## 5.1 SCATTERING AT SMALL AND WIDE ANGLES: SAXS AND WAXS

To overcome these difficulties, small-angle X-ray scattering (SAXS), which was pioneered by Guinier in 1930 [207], offers an interesting alternative for probing, *in situ*, either inside colloids or within aggregates of colloidal sized particles. For these objectives, it is necessary to use a wavelength that is shorter than the average diameter of the particles, which is easily achieved with hard X-rays. Scattering will therefore be predominantly in the forward direction, thus defining the term small-angle scattering. Small-angle neutron scattering (SANS) is often used in conjunction with SAXS since the two methods are complementary [208]. The most important requirement for a good SAXS experiment is the availability of a well-collimated X-ray beam with a small cross-section. Synchrotron radiation sources with their intense brightness and natural collimation are ideal for this purpose. They also provide excellent angular resolution. The potential of SAXS for the study of colloidal systems such as polymers has been clearly demonstrated and reviewed by Ballauff in 2001 [209].

SAXS experiments probe the fluctuation of electronic densities in matter as a result of the interaction of X-ray photons with electrons. The technique is thus useful to describe the size and shape of colloids and the formation of aggregates. However, a detailed quantitative interpretation of the data requires that the objects are well characterised and of simple shapes, such as spherical or cylindrical particles [210,211]. *Ab initio* methods have been proposed to study proteins in solution [212]. Overall, SAXS experiments are more tailored to investigations of carefully designed model systems from which one wants to retrieve structural information. Heterogeneous environmental samples are far too

complex, although the method has been employed to look at humic substances [213–216] and the formation of precipitates and aggregates [217–221]. On the other hand, its use in biochemistry is flourishing since it allows scientists to probe the structure of large biomolecules in solution and to study directly structure–function relationships.

At some dedicated SAXS beamlines, wide-angle X-ray scattering (WAXS) data are collected in parallel. An analysis of the X-ray photons that are elastically scattered at wide angles, between 7 and 60°, provides information on the crystalline nature of the sample. The high flux produced by synchrotron rings allows time-resolved experiments to be performed where the evolution of the sample can be monitored [222]. WAXS probes the long-range order periodicity in the structure of the particles whereas SAXS covers the range from 2 nm to a few micrometres at ultra-small angles (USAXS). A schematic diagram of the two methods is presented in Figure 18 with the respective domains of application of SAXS and WAXS in Figure 19.

In a SAXS experiment, a monochromatic beam of incident wave vector  $k_i$  impacts the sample and the scattered X-ray photons are collected as a function of the scattering angle  $2\theta$ . Since elastic interactions are characterised by zero energy transfers, the final wavevector  $k_f$  is equal in modulus to  $k_i$ . In a typical SAXS experiment, all the photons are collected at once using a CCD camera, and then the intensity of the scattered electrons is determined by integrating the signal along concentric rings originating from the centre of the beam. The relevant parameter that characterises this interaction is the momentum transfer or scattering vector  $Q = k_i - k_f$ , defined by  $Q = 4\pi \sin \theta / \lambda$ . The standard unit for  $Q$  is Å<sup>-1</sup>. One can show that the scattered intensity  $I(Q)$  is the Fourier transform of  $G(r)$ , the correlation function of the electronic density  $\rho(r)$  which corresponds to the probability of finding a scatterer at a distance  $r$  from another scatterer.

In short, elastic X-ray scattering experiments reveal spatial correlations within the sample. Small-angle scattering experiments are designed to measure  $I(Q)$  at very small

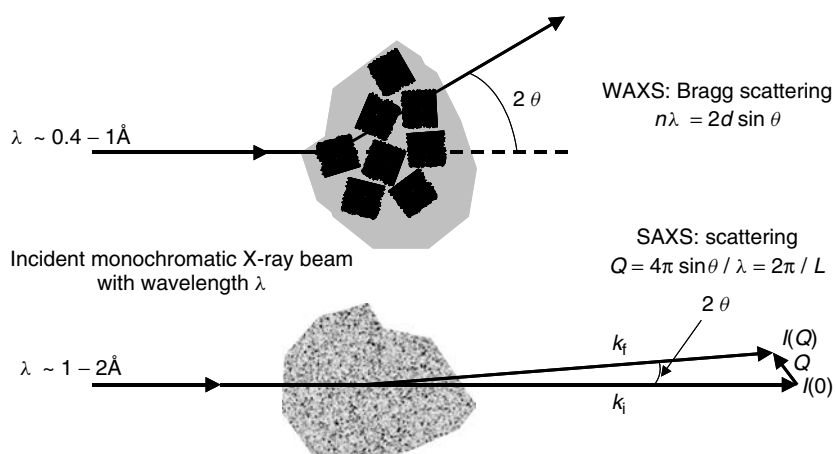


**Figure 18.** Schematic representation of WAXS and SAXS. The WAXS signal results from the Bragg scattering off particles that possess a long-range order with a periodicity  $d$  in their electron density. The intensity of the SAXS signal  $I(Q)$  corresponding to  $Q = 2\pi/L$  results from variations in electron density with a correlation length  $L$

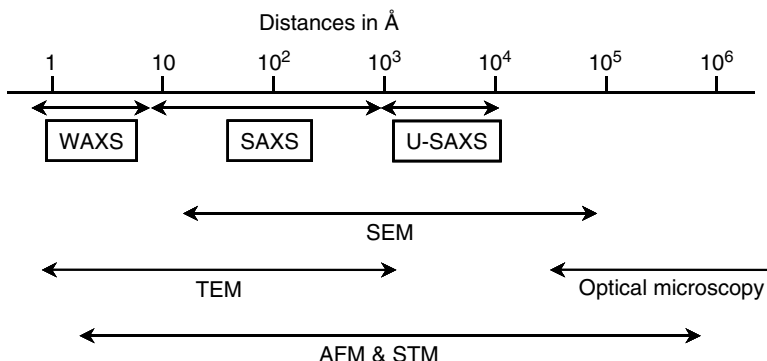


**Figure 19.** Schematic representation of the domain range of the SAXS and WAXS methods compared with other microscopic techniques

scattering vectors  $Q \approx (4\pi\theta/\lambda)$ , with  $2\theta$  ranging from a few microradians to 0.1 rad. This allows the investigation of systems with characteristic sizes ranging from crystallographic distances (a few ångstroms) to colloidal sizes (up to a few micrometres). To achieve these different scales, one varies the distance between the sample and the detector. Short distances (<1–2 m) correspond to larger solid angles and to smaller length scales, whereas long distances of 10 m and above interrogate larger length scales. For studies of colloidal suspensions, one can therefore look at inter-particle distances at small distances and the organisational behaviour of the aggregates at larger distances.

The other key aspects to consider are the electronic contrast of the sample and the need to measure absolute intensities for quantitative predictions. The electronic contrast is due to the difference in electron density between the scattering objects and the solution since the entire sample volume scatters X-ray photons. The greater the contrast, the better the signal will be. Therefore, inorganic colloids of high-Z elements will be ideal, whereas organic molecules such as humic substances will have an electronic contrast that will make the experiment more difficult. The measurement of the absolute intensity of the signal is needed for determining physical properties of the particles. This is achieved by measuring the amount of absorption by the sample in order to normalise the signal.

The data are interpreted by plotting the scattering intensity  $I(Q)$  as a function of the modulus of the scattering vector  $Q$ , the range of  $Q$  being determined by the geometry of the experiment. Conceptually, the width of the spatial window is inversely proportional to  $Q$ , and the distances probed are equivalent to  $2\pi/Q$ .

The interpretation of SAXS and WAXS data can be very difficult, unless the sample closely resembles idealised systems that have been studied previously. WAXS provides the location of Bragg peaks that help in identifying the lattice structures. Bragg peaks can also be observed in SAXS, although they correspond to periodic structures that are on the order of hundreds of ångstroms. The plot of  $I(Q)$  versus  $Q$  for the SAXS data provides three types of information. At very small angles, the Guinier region, the shape of the scattering curve can be used to determine the radius of gyration of the particles. At larger angles, if one investigates a relatively monodisperse system of non-interacting particles – the dilute case – one can observe broad peaks that are related to the morphology of the particles. For example, in the case of spherical particles one can measure, with

good precision, the radius of the particles [223]. Finally, at still larger angles, in the Porod region, the shape of the curve provides information about the surface-to-volume ratio of the scattering objects reflecting the particle dimension. All these interpretations are based on well-defined assumptions that assume uniform density within the particles and in the background, i.e. the solution, and a good contrast between the particles and solution. When these assumptions do not apply, the Fourier transform of the signal can be used to gain real space information. If one has little information on which to base the analysis, one can assume a strongly disordered structure and use fractal analysis.

To conclude, SAXS is very well suited for the characterisation of colloidal particles of simple geometry. For example, the size of colloidal spheres can be determined *in situ* and with high accuracy. Usually, the radii are in excellent agreement with those determined by SLS, whereas TEM consistently reports smaller radii and DLS consistently larger radii than SAXS [224].

## 5.2 APPLICATIONS

Environmental applications of SAXS to the study of colloidal particles have focused on the investigation of the hydrolysis of Al [219–221,225] and Fe [136,217,218,226], clay suspensions, the characterisation of humic substances [213,214,227,228] and the coagulation of organic matter in the presence of inorganic precipitates [225].

One of the first studies of humic substances by SAXS dates from 1967 [213], when Wershaw *et al.* used a laboratory SAXS instrument to characterise the colloidal particles present in the humic fraction of a sandy soil. They estimated the molecular weight, molecular volume, radius of gyration and a shape factor for the sodium humate. They interpreted their data by proposing that either the humic extract consisted of two or more different particle sizes or that the particles were of the same size but had a dense core surrounded by a less dense outer shell. The authors already noted the need to obtain a monodisperse system in order to acquire a precise measurement of particle size. Later investigations focused on determining the size of the particles [214], which was better assessed by SANS, which offers the possibility of increasing the contrast by using deuterated water. The studies of Osterberg and co-workers [215,229] determined that the largest particles present in humic matter were about 110 nm in length with a mean radius of gyration varying between about 20 and 30 nm. Their results also suggested that the colloidal particles investigated had a central core with different scattering properties. Pranzas *et al.* [216] combined SAXS with SANS and X-ray microscopy to study aquatic humic substances. In contrast with soil HS, they found that the particles tended to be spherical, in a quasi-'monomeric' state, and that they were stable to pH and ionic strength variations. At higher concentrations, they can form chain-like aggregates with sizes up to 2  $\mu\text{m}$ .

Masion *et al.* [225] studied the formation of NOM flocs with Al. Modelling of the SAXS data suggested that Al, whose polynuclear species are dissociated by the NOM, was present as monomers that are evenly distributed within the floc and separated by about 8–9 Å. This indicated that Al was bound at specific sites within the NOM in an ordered distribution. They also determined that the fractal dimension of the aggregates is pH dependent and varies from 2.3 at pH = 6 to 2.1 at pH = 8.

### 5.3 TOTAL SCATTERING: PAIR DISTRIBUTION FUNCTION (PDF)

We have seen that XAS provides us with a local probe for determining the structure of particles or the average coordination environment of metals within colloids and at their surfaces. On the other hand, X-rays can be used to probe the periodic structure of matter (XRD–WAXS) or the structure of aggregates using SAXS. However, there remains a gap between the EXAFS range – up to 5 Å – and the crystallographic methods that require periodicity on distances above 200 Å. A method that has been recently promoted and rediscovered, as a result of the construction of new and more powerful synchrotron light sources such as the European Synchrotron Radiation Facility (ESRF) and the Advanced Photon Source (APS), is based on the analysis of the total scattering of particles. The method bridges the gap between local probes such as EXAFS and NMR and conventional XRD approaches and is called the pair distribution function (PDF) method. It was pioneered and has been used for many years by crystallographers who were interested in the non-periodic structure of matter in non-crystalline materials [230]. The PDF method [231,232] is based on an idea originally formulated by Debye that aims at defining the distribution of distances between two atoms. The distribution can be obtained from the total scattering structure function  $S(Q)$ , where  $Q$  is the diffraction vector that is equal to  $4\pi \sin \theta / \lambda$  by a simple Fourier transformation. In theory, the Fourier integral needs to be determined at infinity, but in practice the wavelength used defines the upper limit:  $Q < 4\pi / \lambda$ . This method can be applied either with X-ray photons or with neutrons produced at spallation sources. Prior to the construction of SR facilities able to reach high energies, i.e. low wavelengths, the method suffered severe limitations because of its lack of resolution. For example, in the laboratory, using Mo K-L<sub>3</sub> data could only extend to about  $Q = 9.8 \text{ \AA}^{-1}$  with poor accuracy. Nowadays, PDF are collected on materials to  $Q > 40 \text{ \AA}^{-1}$  using X-ray photons of 100 keV corresponding to wavelengths of  $\lambda = 0.12 \text{ \AA}$  [232].

The atomic PDF,  $G(r)$ , is defined by  $G(r) = 4\pi r[\rho(r) - \rho_0]$ , where  $\rho_0$  is the average atomic number density,  $\rho(r)$  is the atomic pair density and  $r$  is the radial distance. It is experimentally accessible by measuring the scattering intensity from a sample and correcting this intensity for background and inelastic processes to obtain the coherent part of the total diffracted intensity,  $I^{\text{coh}}(Q)$ . By calculating the total scattering structure function,  $S(Q)$ , that is normalised by the flux and number of atoms in the sample:

$$S(Q) = \frac{I^{\text{coh}}(Q) - \sum c_i |f_i(Q)|^2}{\sum c_i |f_i(Q)|^2} + 1 \quad (8)$$

where  $c_i$  and  $f_i$  are the atomic concentrations and X-ray atomic form factors respectively. One obtains  $G(r)$ :

$$G(r) = \frac{2}{\pi} \int_{Q=0}^{Q=Q_{\max}} Q[S(Q) - 1] \sin(Qr) dQ \quad (9)$$

From these equations, one can see that  $G(r)$  provides another way of looking at diffraction in real space. It includes not only the Bragg peaks but also the local structural variations

Publisher's Note:  
Permission to reproduce this image  
online was not granted by the  
copyright holder. Readers are kindly  
requested to refer to the printed version  
of this chapter.

**Figure 20.** Pair distribution functions of bulk ZnS (sphalerite, dashed grey curve), bulk ZnS following truncation by the shape factor for a 3.4 nm diameter sphere (grey curve), and mercaptoethanol-coated ZnS nanoparticles of an average diameter of 3.4 nm (black curve). Reprinted with permission from Gilbert, B., Huang, F., Zhang, H. Z., Waychunas, G. A. and Banfield, J. F., Nanoparticles: Strained and stiff, *Science*, **305**, 651–654. Copyright 2004 AAAS

that are present in the diffuse components of the diffraction patterns that are usually regarded as background in conventional XRD methods [232].

It becomes also clear that the limitation of this approach in environmental systems resides in the precise characterisation of the sample, since one needs to know the detailed chemical composition of the particles in order to calculate  $G(r)$ . Since the chemical composition needs to be constant, this precludes the idea of using this approach on a collection of heterogeneous particles. However, if one could focus the beam on individual particles whose elemental composition were assessed by another means, such as nano-XRF, the approach could be very useful for understanding the structure of colloidal systems.

Under controlled experimental conditions in the laboratory, this method allows us to gain insights into the structure and transformation of colloidal size particles [233]. A recent example has been presented in the study of the transformation of ZnS colloidal particles prepared in the presence of methanol after exposure to water [234,235] (Figure 20). The structural transformations were seen first by PDF analysis and then later explained by combining SAXS, WAX, XAS and molecular dynamic simulations by Gilbert *et al.* [236].

## 6 CONCLUSIONS

This brief overview demonstrates the breadth and depth that one can achieve by probing environmental colloids and particles with X-rays produced at synchrotron light sources. The techniques presented above allow one to determine the structure of environmental particles from a molecular scale (ångstroms) by XAS to the formation of large aggregates (a few micrometres) by SAXS. Indeed, the techniques cover the entire colloidal range. In addition, they are, for the most part, direct methods where little sample preparation is required. Hence a number of processes can be observed in close to *in situ* conditions.

The constant development of new instrumentation and new methods for probing matter with X-rays has benefited from the construction of the latest generation of synchrotron

light sources that offer high fluxes of photons. The next generation of sources, based on free electron lasers, is already on the horizon, even though the full potential of the current facilities has not yet been entirely explored. The major advantage of these light sources is that they provide a unique opportunity to perform spatial- and time-resolved investigations of colloidal systems. Nonetheless, to exploit these techniques fully it is essential to understand the limitations of these methods. In particular, in many instances they can only be applied to model systems, or to systems that need to be characterised using complementary techniques.

## ACKNOWLEDGEMENTS

I would like to thank my former students and postdoc, Sam Webb, Ted Peltier, Pablo Pasten, Amy Dahl and Peter Wightman, for their help, contributions and useful discussions about XAS, and Ian Saratovsky for his comments on the manuscript. Thanks are due to Susa Stone, who prepared the tomographic reconstruction shown in Figure 17. I am also immensely grateful for the support of the staff of DND-CAT – more particularly John Quintana, Denis Keane, John Kulpin and Qing Ma – where we performed all of our experiments. The DuPont-Northwestern-Dow Collaborative Access Team (DND-CAT) is a Synchrotron Research Center located at Sector 5 of the Advanced Photon Source. DND-CAT is supported by E. I. DuPont de Nemours & Co., Dow Chemical Company, the US National Science Foundation through Grant DMR-9304725 and the State of Illinois through the Department of Commerce and the Board of Higher Education Grant IBHE HECA NWU 96. Use of the Advanced Photon Source was supported by the US Department of Energy, Office of Science, Office of Basic Energy Sciences, under Contract No. W-31-109-Eng-38. I thank Jerome Rose, Kevin Wilkinson and Jamie Lead for their thorough review of the manuscript. This work was supported by the National Science Foundation under Grant BES-0237624. This chapter is dedicated to the memory of Jerome Cohen, without whom I would not have learned about all these techniques.

## LIST OF SYMBOLS AND ABBREVIATIONS

AEM	Analytical electron microscopy
$\chi(k)$	EXAFS function, the fractional modulation of the X-ray absorption coefficient
EXAFS	Extended X-ray absorption fine structure
$E$	Beam energy
$I_0$	Intensity of the incoming X-ray beam
$I_F$	Intensity of the fluorescence
$I_T$	Intensity of the transmitted X-ray beam
$k$	Modulus of the photoelectron wavevector
$\mu(E)$	X-ray absorption coefficient that varies with the energy
MS	Multiple scattering of the photoelectron
$\mu\text{EXAFS}$	Micro-EXAFS
$\mu\text{XANES}$	Micro-XANES

NEXAFS	Near-edge X-ray absorption fine structure
PCA	Principal component analysis
PEEM	Photoemission electron microscopy
PDF	Pair distribution function or $G(r)$
$Q$	Scattering vector
RDF	Radial distribution function
SR	Synchrotron radiation
SAXS	Small-angle X-ray scattering
$S(Q)$	Scattering structure function
WDX	Wavelength-dispersive X-ray
WAXS	Wide-angle X-ray scattering
XAS	X-ray absorption spectroscopy, also called XAFS: X-ray absorption fine structure
XANES	X-ray absorption near edge structure
XRF	X-ray fluorescence
XRM	X-ray microscopy
X-CMT	X-ray computed microtomography
XRD	X-ray diffraction
Z	Atomic number

## REFERENCES

1. Pollock, H. C. (1983). The discovery of synchrotron radiation, *Am. J. Phys.*, **51**, 278.
2. Blewett, J. P. (1946). Radiation loss in the induction electron accelerator, *Phys. Rev.*, **69**, 87–95.
3. Margaritondo, G. (1988). *Introduction to Synchrotron Radiation*. Oxford University Press, Oxford.
4. Manceau, A., Marcus, M. A. and Tamura, N. (2002). Quantitative speciation of heavy metals in soils and sediments by synchrotron X-ray techniques, *Rev. Mineral. Geochem.*, **49**, 341–428.
5. Young, N. A. and Dent, A. J. (1999). Maintaining and improving the quality of published XAFS data: a view from the UK XAFS user group, *J. Synchrotron Radiat.*, **6**, 799–799.
6. Jaklevic, J. M., Kirby, J. A., Ramponi, A. J. and Thompson, A. C. (1980). Chemical characterization of air particulate samples using X-ray absorption-spectroscopy, *Environ. Sci. Technol.*, **14**, 437–441.
7. Manceau, A., Boisset, M. C., Sarret, G., Hazemann, R. L., Mench, M., Cambier, P. and Prost, R. (1996). Direct determination of lead speciation in contaminated soils by EXAFS spectroscopy, *Environ. Sci. Technol.*, **30**, 1540–1552.
8. O'Day, P. A., Carroll, S. A., Randall, S., Martinelli, R. E., Anderson, S. L., Jelinski, J. and Knezovich, J. P. (2000). Metal speciation and bioavailability in contaminated estuary sediments, Alameda Naval Air Station, California, *Environ. Sci. Technol.*, **34**, 3665–3673.
9. Ostergren, J. D., Brown, G. E., Parks, G. A. and Tingle, T. N. (1999). Quantitative speciation of lead in selected mine tailings from Leadville, CO, *Environ. Sci. Technol.*, **33**, 1627–1636.
10. Sarret, G., Balesdent, J., Bouziri, L., Garnier, J. M., Marcus, M. A., Geoffroy, N., Panfili, F. and Manceau, A. (2004). Zn speciation in the organic horizon of a contaminated soil by micro-X-ray fluorescence, micro- and powder-EXAFS spectroscopy, and isotopic dilution, *Environ. Sci. Technol.*, **38**, 2792–2801.
11. Manceau, A., Lanson, B., Schlegel, M. L., Harge, J. C., Musso, M., Eybert-Berard, L., Hazemann, J. L., Chateigner, D. and Lamble, G. M. (2000). Quantitative Zn speciation in smelter-contaminated soils by EXAFS spectroscopy, *Am. J. Sci.*, **300**, 289–343.

12. Isaure, M. P., Laboudigue, A., Manceau, A., Sarret, G., Tiffreau, C., Trocellier, P., Lamble, G., Hazemann, J. L. and Chateigner, D. (2002). Quantitative Zn speciation in a contaminated dredged sediment by  $\mu$ -PIXE,  $\mu$ -SXRF, EXAFS spectroscopy and principal component analysis, *Geochim. Cosmochim. Acta*, **66**, 1549–1567.
13. Foster, A. L., Brown, G. E., Tingle, T. N. and Parks, G. A. (1998). Quantitative arsenic speciation in mine tailings using X-ray absorption spectroscopy, *Am. Mineral.*, **83**, 553–568.
14. Gaillard, J. F., Webb, S. M. and Quintana, J. P. G. (2001). Quick X-ray absorption spectroscopy for determining metal speciation in environmental samples, *J. Synchrotron Radiat.*, **8**, 928–930.
15. Neils, T. L. and Burlitch, J. M. (1990). Determination of minor components in mixtures using EXAFS, *Anal. Chim. Acta*, **233**, 229–234.
16. Fenter, P. A., Rivers, M. L., Sturchio, N. C. and Sutton, S. R., eds (2002). *Applications of Synchrotron Radiation in Low-temperature Geochemistry and Environmental Science*. Mineralogical Society of America, Washington, DC. Rev. Mineral. Geochem., 49.
17. Koningsberger, D. C. and Prins, R., eds (1988). *X-ray Absorption: Principles, Applications, Techniques of EXAFS, SEXAFS and XANES*. John Wiley & Sons, Inc., New York.
18. Fontaine, A. (1993). Interactions of X-rays with matter: X-ray absorption spectroscopy. In *Neutron and Synchrotron Radiation for Condensed Matter Studies*, Vol. 1, eds Baruchel, J., Hodeau, J. L., Lehmann, M. S. Regnard J. R. and Schlenker, C., Les Editions de Physique, Les Ulis and Springer, Berlin.
19. Rehr, J. J. and Albers, R. C. (2000). Theoretical approaches to x-ray absorption fine structure, *Rev. Mod. Phys.*, **72**, 621–654.
20. Penner-Hahn, J. E. (1999). X-ray absorption spectroscopy in coordination chemistry, *Coord. Chem. Rev.*, **192**, 1101–1123.
21. Sayers, D. E., Stern, E. A. and Lytle, F. W. (1971). New technique for investigating non-crystalline structures – Fourier analysis of extended X-ray absorption fine structure, *Phys. Rev. Lett.*, **27**, 1204–1207.
22. Webb, S. M., Gaillard, J. F., Jackson, B. E. and Stahl, D. A. (2001). An EXAFS study of zinc coordination in microbial cells, *J. Synchrotron Radiat.*, **8**, 943–945.
23. Waychunas, G. A., Fuller, C. C., Davis, J. A. and Rehr, J. J. (2003). Surface complexation and precipitate geometry for aqueous Zn(II) sorption on ferrihydrite: II. XANES analysis and simulation, *Geochim. Cosmochim. Acta*, **67**, 1031–1043.
24. Westre, T. E., Kennepohl, P., DeWitt, J. G., Hedman, B., Hodgson, K. O. and Solomon, E. I. (1997). A multiplet analysis of Fe K-edge 1s→3d pre-edge features of iron complexes, *J. Am. Chem. Soc.*, **119**, 6297–6314.
25. Wilke, M., Farges, F., Petit, P. E., Brown, G. E. and Martin, F. (2001). Oxidation state and coordination of Fe in minerals: an FeK-XANES spectroscopic study, *Am. Mineral.*, **86**, 714–730.
26. Filippioni, A., Dicicco, A., Tyson, T. A. and Natoli, C. R. (1991). *Ab initio* modeling of X-ray absorption-spectra, *Solid State Commun.*, **78**, 265–268.
27. Ankudinov, A. L. and Rehr, J. J. (2003). Development of XAFS theory, *J. Synchrotron Radiat.*, **10**, 366–368.
28. Zabinsky, S. I., Rehr, J. J., Ankudinov, A., Albers, R. C. and Eller, M. J. (1995). Multiple scattering calculations of X-ray absorption spectra, *Phys. Rev. B*, **52**, 2995–3009.
29. Rehr, J. J., Deleon, J. M., Zabinsky, S. I. and Albers, R. C. (1991). Theoretical X-ray absorption fine-structure standards, *J. Am. Chem. Soc.*, **113**, 5135–5140.
30. Binsted, N. and Hasnain, S. S. (1996). State-of-the-art analysis of whole X-ray absorption spectra, *J. Synchrotron Radiat.*, **3**, 185–196.
31. Newville, M., Livins, P., Yacoby, Y., Rehr, J. J. and Stern, E. A. (1993). Near edge X-ray absorption fine structure of Pb – a comparison of theory and experiment, *Phys. Rev. B*, **47**, 14126–14131.
32. Weng, T. C., Waldo, G. S. and Penner-Hahn, J. E. (2005). A method for normalization of X-ray absorption data, *J. Synchrotron Radiat.*, **12**, 506–510.
33. McKale, A. G., Veal, B. W., Paulikas, A. P., Chan, S. K. and Knapp, G. S. (1988). Improved *ab initio* calculations of amplitude and phase functions for extended X-ray absorption fine structure spectroscopy, *J. Am. Chem. Soc.*, **110**, 3763–3768.

34. Oday, P. A., Rehr, J. J., Zabinsky, S. I. and Brown, G. E. (1994). Extended X-ray absorption fine structure (EXAFS) analysis of disorder and multiple scattering in complex crystalline solids, *J. Am. Chem. Soc.*, **116**, 2938–2949.
35. Ankudinov, A. L., Ravel, B., Rehr, J. J. and Conradson, S. D. (1998). Real-space multiple-scattering calculation and interpretation of x-ray-absorption near-edge structure, *Phys. Rev. B*, **58**, 7565–7576.
36. Westre, T. E., Dicicco, A., Filipponi, A., Natoli, C. R., Hedman, B., Solomon, E. I. and Hodgson, K. O. (1995). GNXAS, a multiple scattering approach to EXAFS analysis – methodology and applications to iron complexes, *J. Am. Chem. Soc.*, **117**, 1566–1583.
37. de Groot, F. (2001). High resolution X-ray emission and X-ray absorption spectroscopy, *Chem. Rev.*, **101**, 1779–1808.
38. Newville, M. (2001). EXAFS analysis using FEFF and FEFFIT, *J. Synchrotron Radiat.*, **8**, 96–100.
39. Ravel, B. (2001). ATOMS: crystallography for the X-ray absorption spectroscopist, *J. Synchrotron Radiat.*, **8**, 314–316.
40. Pettifer, R. F., Borowski, M. and Loeffen, P. W. (1999). The physics of ionization chambers – or how to improve your signal-to-noise ratio for transmission EXAFS measurements, *J. Synchrotron Radiat.*, **6**, 217–219.
41. Bouldin, C. E., Forman, R. A., and Bell, M. I. (1987). Silicon photodiode detector for fluorescence EXAFS, *Rev. Sci. Instrum.*, **58**, 1891–1894.
42. Stern, E. A. and Heald, S. M. (1979). X-ray filter assembly for fluorescence measurements of X-ray absorption fine structure, *Rev. Sci. Instrum.*, **50**, 1579–1582.
43. Manceau, A., Schlegel, M. L., Musso, M., Sole, V. A., Gauthier, C., Petit, P. E. and Trolard, F. (2000). Crystal chemistry of trace elements in natural and synthetic goethite, *Geochim. Cosmochim. Acta*, **64**, 3643–3661.
44. Zhang, K., Rosenbaum, G. and Bunker, G. (1998). Energy-resolving X-ray fluorescence detection using synthetic multilayers, *J. Synchrotron Radiat.*, **5**, 1227–1234.
45. Zhong, Z., Chapman, D., Bunker, B., Bunker, G., Fischetti, R. and Segre, C. (1999). A bent Laue analyzer for fluorescence EXAFS detection, *J. Synchrotron Radiat.*, **6**, 212–214.
46. Kropf, A. J., Finch, R. J., Fortner, J. A., Aase, S., Karanfil, C., Segre, C. U., Terry, J., Bunker, G. and Chapman, L. D. (2003). Bent silicon crystal in the Laue geometry to resolve x-ray fluorescence for x-ray absorption spectroscopy, *Rev. Sci. Instrum.*, **74**, 4696–4702.
47. Pellicer-Porres, J., San Miguel, A. and Fontaine, A. (1998). High-focusing Bragg-crystal polychromator design for energy-dispersive X-ray absorption spectroscopy, *J. Synchrotron Radiat.*, **5**, 1250–1257.
48. Dent, A. J. (2002). Development of time-resolved XAFS instrumentation for quick EXAFS and energy-dispersive EXAFS measurements on catalyst systems, *Top. Catal.*, **18**, 27–35.
49. Stern, E. A. and Kim, K. (1981). Thickness effect on the extended X-ray absorption fine structure amplitude, *Phys. Rev. B*, **23**, 3781–3787.
50. Lee, P. A., Citrin, P. H., Eisenberger, P. and Kincaid, B. M. (1981). Extended X-ray absorption fine-structure – its strengths and limitations as a structural tool, *Rev. Mod. Phys.*, **53**, 769–806.
51. Pfalzer, P., Urbach, J. P., Klemm, M., Horn, S., denBoer, M. L., Frenkel, A. I. and Kirkland, J. P. (1999). Elimination of self-absorption in fluorescence hard-x-ray absorption spectra, *Phys. Rev. B*, **60**, 9335–9339.
52. Tannazi, F. (2004). Studies of heterogeneous samples and material composition by fluorescence XAFS. *Thesis*, Illinois Institute of Technology, Chicago.
53. Tannazi, F. and Bunker, G. (2005). Determination of chemical speciation by XAFS, *Phys. Scr.*, **T115**, 953–956.
54. Manceau, A., Marcus, M. A., Tamura, N., Proux, O., Geoffroy, N. and Lanson, B. (2004). Natural speciation of Zn at the micrometer scale in a clayey soil using X-ray fluorescence, absorption, and diffraction, *Geochim. Cosmochim. Acta*, **68**, 2467–2483.
55. Frahm, R. (1988). Quick scanning EXAFS – 1st experiments, *Nucl. Instrum. Methods Phys. Res. A*, **270**, 578–581.

56. Gordon, B. M. and Jones, K. W. (1991). Synchrotron radiation and its application to chemical speciation, *ACS Symp. Ser.*, **445**, 290–305.
57. Tessier, A., Campbell, P. G. C. and Bisson, M. (1979). Sequential extraction procedure for the speciation of particulate trace-metals, *Anal. Chem.*, **51**, 844–851.
58. Tipping, E., Hetherington, N. B., Hilton, J., Thompson, D. W., Bowles, E. and Hamiltontaylor, J. (1985). Artifacts in the use of selective chemical extraction to determine distributions of metals between oxides of manganese and iron, *Anal. Chem.*, **57**, 1944–1946.
59. Welter, E., Calmano, W., Mangold, S. and Troger, L. (1999). Chemical speciation of heavy metals in soils by use of XAFS spectroscopy and electron microscopical techniques, *Fresenius' J. Anal. Chem.*, **364**, 238–244.
60. Kim, C. S., Brown, G. E. and Rytuba, J. J. (2000). Characterization and speciation of mercury-bearing mine wastes using X-ray absorption spectroscopy, *Sci. Total Environ.*, **261**, 157–168.
61. Kim, C. S., Bloom, N. S., Rytuba, J. J. and Brown, G. E. (2003). Mercury speciation by X-ray absorption fine structure spectroscopy and sequential chemical extractions: a comparison of speciation methods, *Environ. Sci. Technol.*, **37**, 5102–5108.
62. Peltier, E. F., Dahl, A. L., and Gaillard, J. F. (2005). Metal speciation in anoxic sediments: when sulfides can be construed as oxides, *Environ. Sci. Technol.*, **39**, 311–316.
63. Calmano, W., Mangold, S. and Welter, E. (2001). An XAFS investigation of the artefacts caused by sequential extraction analyses of Pb-contaminated soils, *Fresenius' J. Anal. Chem.*, **371**, 823–830.
64. Scheinost, A. C., Kretzschmar, R. and Pfister, S. (2002). Combining selective sequential extractions, x-ray absorption spectroscopy, and principal component analysis for quantitative zinc speciation in soil, *Environ. Sci. Technol.*, **36**, 5021–5028.
65. Brown, G. E. and Sturchio, N. C. (2002). An overview of synchrotron radiation applications to low temperature geochemistry and environmental science, *Rev. Mineral. Geochem.*, **49**, 1–115.
66. Manceau, A. (1995). The mechanism of anion adsorption on iron-oxides – evidence for the bonding of arsenate tetrahedra on free  $\text{Fe}(\text{O},\text{OH})_6$  edges, *Geochim. Cosmochim. Acta*, **59**, 3647–3653.
67. Bargar, J. R., Brown, G. E. and Parks, G. A. (1997). Surface complexation of Pb(II) at oxide–water interfaces 2. XAFS and bond-valence determination of mononuclear Pb(II) sorption products and surface functional groups on iron oxides, *Geochim. Cosmochim. Acta*, **61**, 2639–2652.
68. Axe, L., Bunker, G. B., Anderson, P. R. and Tyson, T. A. (1998). An XAFS analysis of strontium at the hydrous ferric oxide surface, *J. Colloid Interface Sci.*, **199**, 44–52.
69. Bargar, J. R., Persson, P. and Brown, G. E. (1997). XAFS studies of Pb(II)–chloro and Hg(II)–chloro ternary complexes on goethite, *J. Phys. IV*, **7**, 825–826.
70. Arai, Y., Sparks, D. L. and Davis, J. A. (2004). Effects of dissolved carbonate on arsenate adsorption and surface speciation at the hematite–water interface, *Environ. Sci. Technol.*, **38**, 817–824.
71. Bargar, J. R., Brown, G. E. and Parks, G. A. (1998). Surface complexation of Pb(II) at oxide–water interfaces: III. XAFS determination of Pb(II) and Pb(II)–chloro adsorption complexes on goethite and alumina, *Geochim. Cosmochim. Acta*, **62**, 193–207.
72. Foster, A. L., Brown, G. E. and Parks, G. A. (2003). X-ray absorption fine structure study of As(V) and Se(IV) sorption complexes on hydrous Mn oxides, *Geochim. Cosmochim. Acta*, **67**, 1937–1953.
73. Manceau, A. and Charlet, L. (1994). The mechanism of selenate adsorption on goethite and hydrous ferric-oxide, *J. Colloid Interface Sci.*, **168**, 87–93.
74. Manning, B. A., Fendorf, S. E., Bostick, B. and Suarez, D. L. (2002). Arsenic(III) oxidation and arsenic(V) adsorption reactions on synthetic birnessite, *Environ. Sci. Technol.*, **36**, 976–981.
75. Randall, S. R., Sherman, D. M. and Ragnarsdottir, K. V. (1998). An extended X-ray absorption fine structure spectroscopy investigation of cadmium sorption on cryptomelane ( $\text{KMn}_8\text{O}_{16}$ ), *Chem. Geol.*, **151**, 95–106.

76. Waychunas, G. A., Rea, B. A., Fuller, C. C. and Davis, J. A. (1993). Surface chemistry of ferrihydrite. 1. EXAFS studies of the geometry of coprecipitated and adsorbed arsenate, *Geochim. Cosmochim. Acta*, **57**, 2251–2269.
77. Waychunas, G. A., Fuller, C. C. and Davis, J. A. (2002). Surface complexation and precipitate geometry for aqueous Zn(II) sorption on ferrihydrite I: X-ray absorption extended fine structure spectroscopy analysis, *Geochim. Cosmochim. Acta*, **66**, 1119–1137.
78. Collins, C. R., Sherman, D. M. and Ragnarsdottir, K. V. (1999). Surface complexation of Hg<sup>2+</sup> on goethite: mechanism from EXAFS spectroscopy and density functional calculations, *J. Colloid Interface Sci.*, **219**, 345–350.
79. Collins, C. R., Ragnarsdottir, K. V. and Sherman, D. M. (1999). Effect of inorganic and organic ligands on the mechanism of cadmium sorption to goethite, *Geochim. Cosmochim. Acta*, **63**, 2989–3002.
80. Roberts, D. R., Ford, R. G. and Sparks, D. L. (2003). Kinetics and mechanisms of Zn complexation on metal oxides using EXAFS spectroscopy, *J. Colloid Interface Sci.*, **263**, 364–376.
81. Schlegel, M. L., Manceau, A., Charlet, L. and Hazemann, J. L. (2001). Adsorption mechanisms of Zn on hectorite as a function of time, pH, and ionic strength, *Am. J. Sci.*, **301**, 798–830.
82. Bargar, J. R., Brown, G. E. and Parks, G. A. (1997). Surface complexation of Pb(II) at oxide–water interfaces 1. XAFS and bond-valence determination of mononuclear and polynuclear Pb(II) sorption products on aluminum oxides, *Geochim. Cosmochim. Acta*, **61**, 2617–2637.
83. Bargar, J. R., Towle, S. N., Brown, G. E. and Parks, G. A. (1997). XAFS and bond-valence determination of the structures and compositions of surface functional groups and Pb(II) and Co(II) sorption products on single-crystal alpha-Al<sub>2</sub>O<sub>3</sub>, *J. Colloid Interface Sci.*, **185**, 473–492.
84. Oday, P. A., Parks, G. A. and Brown, G. E. (1994). Molecular structure and binding sites of cobalt(II) surface complexes on kaolinite from X-ray absorption spectroscopy, *Clays Clay Miner.*, **42**, 337–355.
85. Schlegel, M. L., Charlet, L. and Manceau, A. (1999). Sorption of metal ions on clay minerals – II. Mechanism of Co sorption on hectorite at high and low ionic strength and impact on the sorbent stability, *J. Colloid Interface Sci.*, **220**, 392–405.
86. Schlegel, M. L., Manceau, A., Chateigner, D. and Charlet, L. (1999). Sorption of metal ions on clay minerals I. Polarized EXAFS evidence for the adsorption of Co on the edges of hectorite particles, *J. Colloid Interface Sci.*, **215**, 140–158.
87. Strawn, D. G., Scheidegger, A. M. and Sparks, D. L. (1998). Kinetics and mechanisms of Pb(II) sorption and desorption at the aluminum oxide water interface, *Environ. Sci. Technol.*, **32**, 2596–2601.
88. Strawn, D. G. and Sparks, D. L. (1999). The use of XAFS to distinguish between inner- and outer-sphere lead adsorption complexes on montmorillonite, *J. Colloid Interface Sci.*, **216**, 257–269.
89. Zhang, P. C., Brady, P. V., Arthur, S. E., Zhou, W. Q., Sawyer, D. and Hesterberg, D. A. (2001). Adsorption of barium(II) on montmorillonite: an EXAFS study, *Colloids Surf. A*, **190**, 239–249.
90. Oday, P. A., Brown, G. E. and Parks, G. A. (1994). X-ray absorption spectroscopy of cobalt(II) multinuclear surface complexes and surface precipitates on kaolinite, *J. Colloid Interface Sci.*, **165**, 269–289.
91. Elzinga, E. J., Tait, C. D., Reeder, R. J., Rector, K. D., Donohoe, R. J. and Morris, D. E. (2004). Spectroscopic investigation of U(VI) sorption at the calcite-water interface, *Geochim. Cosmochim. Acta*, **68**, 2437–2448.
92. Bargar, J. R., Persson, P. and Brown, G. E. (1999). Outer-sphere adsorption of Pb(II)EDTA on goethite, *Geochim. Cosmochim. Acta*, **63**, 2957–2969.
93. Redden, G., Bargar, J. and Bencheikh-Latmar, R. (2001). Citrate enhanced uranyl adsorption on goethite: an EXAFS analysis, *J. Colloid Interface Sci.*, **244**, 211–219.

94. Boyanov, M. I., Kelly, S. D., Kemner, K. M., Bunker, B. A., Fein, J. B. and Fowle, D. A. (2003). Adsorption of cadmium to *Bacillus subtilis* bacterial cell walls: a pH-dependent X-ray absorption fine structure spectroscopy study, *Geochim. Cosmochim. Acta*, **67**, 3299–3311.
95. Scheidegger, A. M., Lamble, G. M. and Sparks, D. L. (1997). Spectroscopic evidence for the formation of mixed-cation hydroxide phases upon metal sorption on clays and aluminum oxides, *J. Colloid Interface Sci.*, **186**, 118–128.
96. Stumm, W. and Morgan, J. J. (1996). *Aquatic Chemistry: Chemical Equilibria and Rates in Natural Waters*. Wiley-Interscience, New York.
97. Xia, K., Bleam, W. and Helmke, P. A. (1997). Studies of the nature of binding sites of first row transition elements bound to aquatic and soil humic substances using X-ray absorption spectroscopy, *Geochim. Cosmochim. Acta*, **61**, 2223–2235.
98. Rose, J., Vilge, A., Olivie-Lauquet, G., Masion, A., Frechou, C. and Bottero, J. Y. (1998). Iron speciation in natural organic matter colloids, *Colloids Surf. A*, **136**, 11–19.
99. Frenkel, A. I., Korshin, G. V. and Ankudinov, A. L. (2000). XANES study of  $\text{Cu}^{2+}$  binding sites in aquatic humic substances, *Environ. Sci. Technol.*, **34**, 2138–2142.
100. Frenkel, A. I. and Korshin, G. V. (2001). Studies of Cu(II) in soil by X-ray absorption spectroscopy, *Can. J. Soil Sci.*, **81**, 271–276.
101. Korshin, G. V., Frenkel, A. I. and Stern, E. A. (1998). EXAFS study of the inner shell structure in copper(II) complexes with humic substances, *Environ. Sci. Technol.*, **32**, 2699–2705.
102. Xia, K., Bleam, W. and Helmke, P. A. (1997). Studies of the nature of  $\text{Cu}^{2+}$  and  $\text{Pb}^{2+}$  binding sites in soil humic substances using X-ray absorption spectroscopy, *Geochim. Cosmochim. Acta*, **61**, 2211–2221.
103. Sarret, G., Manceau, A., Hazemann, J. L., Gomez, A. and Mench, M. (1997). EXAFS study of the nature of zinc complexation sites in humic substances as a function of Zn concentration, *J. Phys. IV*, **7**, 799–802.
104. Strawn, D. G. and Sparks, D. L. (2000). Effects of soil organic matter on the kinetics and mechanisms of Pb(II) sorption and desorption in soil, *Soil Sci. Soc. Am. J.*, **64**, 144–156.
105. Dubbin, W. E., Sposito, G. and Zavarin, M. (2000). X-ray absorption spectroscopic study of Cu–glyphosate adsorbed by microcrystalline gibbsite, *Soil Sci.*, **165**, 699–707.
106. Alcacio, T. E., Hesterberg, D., Chou, J. W., Martin, J. D., Beauchemin, S. and Sayers, D. E. (2001). Molecular scale characteristics of Cu(II) bonding in goethite–humate complexes, *Geochim. Cosmochim. Acta*, **65**, 1355–1366.
107. Nachtegaal, M. and Sparks, D. L. (2003). Nickel sequestration in a kaolinite–humic acid complex, *Environ. Sci. Technol.*, **37**, 529–534.
108. Liu, C., Frenkel, A. I., Vairavamurthy, A. and Huang, P. M. (2001). Sorption of cadmium on humic acid: mechanistic and kinetic studies with atomic force microscopy and X-ray absorption fine structure spectroscopy, *Can. J. Soil Sci.*, **81**, 337–348.
109. Skyllberg, U., Xia, K., Bloom, P. R., Nater, E. A. and Bleam, W. F. (2000). Binding of mercury(II) to reduced sulfur in soil organic matter along upland-peat soil transects, *J. Environ. Qual.*, **29**, 855–865.
110. Xia, K., Skyllberg, U. L., Bleam, W. F., Bloom, P. R., Nater, E. A. and Helmke, P. A. (1999). X-ray absorption spectroscopic evidence for the complexation of Hg(II) by reduced sulfur in soil humic substances, *Environ. Sci. Technol.*, **33**, 257–261.
111. Hesterberg, D., Chou, J. W., Hutchison, K. J. and Sayers, D. E. (2001). Bonding of Hg(II) to reduced organic sulfur in humic acid as affected by S/Hg ratio, *Environ. Sci. Technol.*, **35**, 2741–2745.
112. Qian, J., Skyllberg, U., Frech, W., Bleam, W. F., Bloom, P. R. and Petit, P. E. (2002). Bonding of methyl mercury to reduced sulfur groups in soil and stream organic matter as determined by X-ray absorption spectroscopy and binding affinity studies, *Geochim. Cosmochim. Acta*, **66**, 3873–3885.
113. Skyllberg, U., Qian, J., Frech, W., Xia, K. and Bleam, W. F. (2003). Distribution of mercury, methyl mercury and organic sulphur species in soil, soil solution and stream of a boreal forest catchment, *Biogeochemistry*, **64**, 53–76.
114. Beauchemin, S., Hesterberg, D. and Beauchemin, M. (2002). Principal component analysis approach for modeling sulfur K-XANES spectra of humic acids, *Soil Sci. Soc. Am. J.*, **66**, 83–91.

115. McCarthy, J. F. and Zachara, J. M. (1989). Subsurface transport of contaminants – mobile colloids in the subsurface environment may alter the transport of contaminants, *Environ. Sci. Technol.*, **23**, 496–502.
116. Marley, N. A., Gaffney, J. S., Orlandini, K. A. and Cunningham, M. M. (1993). Evidence for radionuclide transport and mobilization in a shallow, sandy aquifer, *Environ. Sci. Technol.*, **27**, 2456–2461.
117. Denecke, M. A., Pompe, S., Reich, T., Moll, H., Bubner, M., Heise, K. H., Nicolai, R. and Nitsche, H. (1997). Measurements of the structural parameters for the interaction of uranium(VI) with natural and synthetic humic acids using EXAFS, *Radiochim. Acta*, **79**, 151–159.
118. Denecke, M. A., Reich, T., Pompe, S., Bubner, M., Heise, K. H., Nitsche, H., Allen, P. G., Bucher, J. J., Edelstein, N. M., Shuh, D. K. and Czerwinski, K. R. (1998). EXAFS investigations of the interaction of humic acids and model compounds with uranyl cations in solid complexes, *Radiochim. Acta*, **82**, 103–108.
119. Denecke, M. A., Reich, T., Bubner, M., Pompe, S., Heise, K. H., Nitsche, H., Allen, P. G., Bucher, J. J., Edelstein, N. M. and Shuh, D. K. (1998). Determination of structural parameters of uranyl ions complexed with organic acids using EXAFS, *J. Alloys Compd.*, **271**, 123–127.
120. Denecke, M. A., Bublitz, D., Kim, J. I., Moll, H. and Farkes, I. (1999). EXAFS investigation of the interaction of hafnium and thorium with humic acid and Bio-Rex70, *J. Synchrotron Radiat.*, **6**, 394–396.
121. Pompe, S., Bubner, M., Denecke, M. A., Reich, T., Brachmann, A., Geipel, G., Nicolai, R., Heise, K. H., and Nitsche, H. (1996). A comparison of natural humic acids with synthetic humic acid model substances: characterization and interaction with uranium(VI), *Radiochim. Acta*, **74**, 135–140.
122. Schmeide, K., Sachs, S., Bubner, M., Reich, T., Heise, K. H. and Bernhard, G. (2003). Interaction of uranium(VI) with various modified and unmodified natural and synthetic humic substances studied by EXAFS and FTIR spectroscopy, *Inorg. Chim. Acta*, **351**, 133–140.
123. Monsallier, J. M., Artinger, R., Denecke, M. A., Scherbaum, F. J., Buckau, G. and Kim, J. I. (2003). Spectroscopic study (TRLFS and EXAFS) of the kinetics of An(III)/Ln(III) humate interaction, *Radiochim. Acta*, **91**, 567–574.
124. Maes, A., Geraedts, K., Bruggeman, C., Vancluysen, J., Rossberg, A., and Hennig, C. (2004). Evidence for the interaction of technetium colloids with humic substances by X-ray absorption spectroscopy, *Environ. Sci. Technol.*, **38**, 2044–2051.
125. Taillefert, M., Lienemann, C. P., Gaillard, J. F. and Perret, D. (2000). Speciation, reactivity, and cycling of Fe and Pb in a meromictic lake, *Geochim. Cosmochim. Acta*, **64**, 169–183.
126. Perret, D., Gaillard, J. F., Dominik, J. and Atteia, O. (2000). The diversity of natural hydrous iron oxides, *Environ. Sci. Technol.*, **34**, 3540–3546.
127. Perret, D., Lienemann, C. P. and Mavrocordatos, D. (1995). EELS–ESI identification of heterogeneous suspensions of aquatic microparticles, *Microsc. Microanal. Microstruct.*, **6**, 41–51.
128. Taillefert, M., MacGregor, B. J., Gaillard, J. F., Lienemann, C. P., Perret, D. and Stahl, D. A. (2002). Evidence for a dynamic cycle between Mn and Co in the water column of a stratified lake, *Environ. Sci. Technol.*, **36**, 468–476.
129. Mondi, C., Leifer, K., Mavrocordatos, D. and Perret, D. (2002). Analytical electron microscopy as a tool for accessing colloid formation process in natural waters, *J. Microsc.*, **207**, 180–190.
130. Mavrocordatos, D., Mondi-Couture, C., Atteia, O., Leppard, G. G. and Perret, D. (2000). Formation of a distinct class of Fe–Ca(–C–org)-rich particles in a complex peat–karst system, *J. Hydrol.*, **237**, 234–247.
131. Lienemann, C. P., Monnerat, M., Dominik, J. and Perret, D. (1999). Identification of stoichiometric iron–phosphorus colloids produced in a eutrophic lake, *Aquat. Sci.*, **61**, 133–149.
132. Tessier, A., Fortin, D., Belzile, N., DeVitre, R. R. and Leppard, G. G. (1996). Metal sorption to diagenetic iron and manganese oxyhydroxides and associated organic matter: narrowing the gap between field and laboratory measurements, *Geochim. Cosmochim. Acta*, **60**, 387–404.

133. Magini, M. (1977). Structural relationships between colloidal solutions and hydroxide gels of iron(III) nitrate, *J. Inorg. Nucl. Chem.*, **39**, 409–412.
134. Magini, M. (1979). Solute structuring in aqueous iron(III) sulfate solutions – evidence for the formation of iron(III) sulfate complexes, *J. Chem. Phys.*, **70**, 317–324.
135. Doelsch, E., Rose, J., Masion, A., Bottero, J. Y., Nahon, D. and Bertsch, P. M. (2000). Speciation and crystal chemistry of iron(III) chloride hydrolyzed in the presence of SiO<sub>4</sub> ligands. 1. An Fe K-edge EXAFS study, *Langmuir*, **16**, 4726–4731.
136. Masion, A., Doelsch, E., Rose, J., Moustier, S., Bottero, J. Y. and Bertsch, P. M. (2001). Speciation and crystal chemistry of iron(III) chloride hydrolyzed in the presence of SiO<sub>4</sub> ligands. 3. Semilocal scale structure of the aggregates, *Langmuir*, **17**, 4753–4757.
137. Combes, J. M., Manceau, A., Calas, G. and Bottero, J. Y. (1989). Formation of ferric oxides from aqueous-solutions – a polyhedral approach by X-ray absorption-spectroscopy. 1. Hydrolysis and formation of ferric gels, *Geochim. Cosmochim. Acta*, **53**, 583–594.
138. Combes, J. M., Manceau, A. and Calas, G. (1990). Formation of ferric oxides from aqueous-solutions – a polyhedral approach by X-ray absorption-spectroscopy. 2. Hematite formation from ferric gels, *Geochim. Cosmochim. Acta*, **54**, 1083–1091.
139. Charlet, L. and Manceau, A. (1993). Structure, formation and reactivity of hydrous oxides particles: insights from X-ray absorption spectroscopy. In *Environmental Particles*, eds Buffle, J. and van Leeuwen, H. P., IUPAC Series an Analytical and Physical Chemistry of Environmental Systems, Vol. 2. Lewis, Ann Arbor, Boca Raton, FL, pp. 117–164.
140. Rose, J., Manceau, A., Bottero, J. Y., Masion, A. and Garcia, F. (1996). Nucleation and growth mechanisms of Fe oxyhydroxide in the presence of PO<sub>4</sub> ions. 1. Fe K-edge EXAFS study, *Langmuir*, **12**, 6701–6707.
141. Doelsch, E., Rose, J., Masion, A., Bottero, J. Y., Nahon, D. and Bertsch, P. M. (2002). Hydrolysis of iron(II) chloride under anoxic conditions and influence of SiO<sub>4</sub> ligands, *Langmuir*, **18**, 4292–4299.
142. Doelsch, E., Masion, A., Rose, J., Stone, W. E. E., Bottero, J. Y. and Bertsch, P. M. (2003). Chemistry and structure of colloids obtained by hydrolysis of Fe(III) in the presence of SiO<sub>4</sub> ligands, *Colloids Surf. A*, **217**, 121–128.
143. Bottero, J. Y., Manceau, A., Villieras, F. and Tchoubar, D. (1994). Structure and mechanisms of formation of FeOOH(Cl) polymers, *Langmuir*, **10**, 316–319.
144. Rose, J., Manceau, A., Masion, A. and Bottero, J. Y. (1997). Structure and mechanisms of formation of FeOOH(NO<sub>3</sub>) oligomers in the early stages of hydrolysis, *Langmuir*, **13**, 3240–3246.
145. Rose, J., Flank, A. M., Masion, A., Bottero, J. Y. and Elmerich, P. (1997). Nucleation and growth mechanisms of Fe oxyhydroxide in the presence of PO<sub>4</sub> ions. 2. P K-edge EXAFS study, *Langmuir*, **13**, 1827–1834.
146. Vilge-Ritter, A., Rose, J., Masion, A., Bottero, J. Y. and Laine, J. M. (1999). Chemistry and structure of aggregates formed with Fe-salts and natural organic matter, *Colloids Surf. A*, **147**, 297–308.
147. Manceau, A., Ildefonse, P., Hazemann, J. L., Flank, A. M. and Gallup, D. (1995). Crystal chemistry of hydrous iron silicate scale deposits at the Salton Sea geothermal field, *Clays Clay Miner.*, **43**, 304–317.
148. Pokrovski, G. S., Schott, J., Farges, F. and Hazemann, J. L. (2003). Iron(III)–silica interactions in aqueous solution: insights from X-ray absorption fine structure spectroscopy, *Geochim. Cosmochim. Acta*, **67**, 3559–3573.
149. Rothe, J., Denecke, M. A., Neck, V., Muller, R. and Kim, J. I. (2002). XAFS investigation of the structure of aqueous thorium(IV) species, colloids, and solid thorium(IV) oxide/hydroxide, *Inorg. Chem.*, **41**, 249–258.
150. Rothe, J., Walther, C., Denecke, M. A. and Fanghanel, T. (2004). XAFS and LIBD investigation of the formation and structure of colloidal Pu(IV) hydrolysis products, *Inorg. Chem.*, **43**, 4708–4718.
151. Hunter, D. B., Bertsch, P. M., Kemner, K. M. and Clark, S. B. (1997). Distribution and chemical speciation of metals and metalloids in biota collected from contaminated environments by spatially resolved XRF, XANES, and EXAFS, *J. Phys. IV*, **7**, 767–771.

152. Allard, T., Ildefonse, P., Beaucaire, C. and Calas, G. (1999). Structural chemistry of uranium associated with Si, Al, Fe gels in a granitic uranium mine, *Chem. Geol.*, **158**, 81–103.
153. Morin, G., Juillot, F., Ildefonse, P., Calas, G., Samama, J. C., Chevallier, P. and Brown, G. E. (2001). Mineralogy of lead in a soil developed on a Pb-mineralized sandstone (Largentiere, France), *Am. Mineral.*, **86**, 92–104.
154. Juillot, F., Morin, G., Ildefonse, P., Trainor, T. P., Benedetti, M., Galoisy, L., Calas, G. and Brown, G. E. (2003). Occurrence of Zn/Al hydrotalcite in smelter-impacted soils from northern France: evidence from EXAFS spectroscopy and chemical extractions, *Am. Mineral.*, **88**, 509–526.
155. Manceau, A., Tamura, N., Celestre, R. S., MacDowell, A. A., Geoffroy, N., Sposito, G. and Padmore, H. A. (2003). Molecular-scale speciation of Zn and Ni in soil ferromanganese nodules from loess soils of the Mississippi Basin, *Environ. Sci. Technol.*, **37**, 75–80.
156. Peltier, E. F., Webb, S. M. and Gaillard, J. F. (2003). Zinc and lead sequestration in an impacted wetland system, *Adv. Environ. Res.*, **8**, 103–112.
157. O'Day, P. A., Rivera, N., Root, R. and Carroll, S. A. (2004). X-ray absorption spectroscopic study of Fe reference compounds for the analysis of natural sediments, *Am. Mineral.*, **89**, 572–585.
158. Pinzani, M. C. C., Ansell, S., Somogyi, A., Steenari, B. M. and Lindqvist, O. (2004). Micro-extended X-ray absorption fine structure studies of cadmium speciation within single municipal solid waste fly ash particles, *Anal. Chem.*, **76**, 1596–1602.
159. Wasserman, S. R. (1997). The analysis of mixtures: application of principal component analysis to XAS spectra, *J. Phys. IV*, **7**, 203–205.
160. Wasserman, S. R., Allen, P. G., Shuh, D. K., Bucher, J. J. and Edelstein, N. M. (1999). EXAFS and principal component analysis: a new shell game, *J. Synchrotron Radiat.*, **6**, 284–286.
161. Ressler, T., Wong, J., Roos, J. and Smith, I. L. (2000). Quantitative speciation of Mn-bearing particulates emitted from autos burning (methylcyclopentadienyl)manganese tricarbonyl-added gasolines using XANES spectroscopy, *Environ. Sci. Technol.*, **34**, 950–958.
162. Bazin, D. and Rehr, J. J. (2003). Limits and advantages of x-ray absorption near edge structure for nanometer scale metallic clusters, *J. Phys. Chem. B*, **107**, 12398–12402.
163. Malinowski, E. R. (2002). *Factor Analysis in Chemistry*. John Wiley & Sons, Inc., New York.
164. Webb, S. M., Leppard, G. G. and Gaillard, J. F. (2000). Zinc speciation in a contaminated aquatic environment: characterization of environmental particles by analytical electron microscopy, *Environ. Sci. Technol.*, **34**, 1926–1933.
165. Webb, S. M. (2001). The chemistry of zinc–microbe interactions in the sediments of Lake DePue, IL. *Ph.D Thesis*, Northwestern University, Evanston, IL.
166. Zanker, H., Moll, H., Richter, W., Brendler, V., Hennig, C., Reich, T., Kluge, A. and Huttig, G. (2002). The colloid chemistry of acid rock drainage solution from an abandoned Zn–Pb–Ag mine, *Appl. Geochem.*, **17**, 633–648.
167. Lowry, G. V., Shaw, S., Kim, C. S., Rytuba, J. J. and Brown, G. E. (2004). Macroscopic and microscopic observations of particle-facilitated mercury transport from new idria and sulphur bank mercury mine tailings, *Environ. Sci. Technol.*, **38**, 5101–5111.
168. Kirkpatrick, P. and Baez, A. V. (1948). Formation of optical images by X-rays, *J. Opt. Soc. Am.*, **38**, 766–774.
169. Chevallier, P., Dhez, P., Legrand, F., Idir, M., Soullie, G., Mirone, A., Erko, A., Snigirev, A., Snigireva, I., Suvorov, A., Freund, A., Engstrom, P., Nielsen, J. A. and Grubel, A. (1995). First test of the scanning-X-ray microprobe with Bragg–Fresnel multilayer lens at ESRF beam line, *Nucl. Instrum. Methods Phys. Res. A*, **354**, 584–587.
170. Kumakhov, M. A. (2000). Capillary optics and their use in x-ray analysis, *X-Ray Spectrom.*, **29**, 343–348.
171. Somogyi, A., Janssens, K., Vincze, L., Vekemans, B., Rindby, A. and Adams, F. (2000). Interpretation and use of inter-element correlation graphs obtained by scanning X-ray fluorescence micro-beam spectrometry from individual particles. Part II – application, *Spectrochim. Acta, Part B*, **55**, 1039–1049.

172. Somogyi, A., Vincze, L., Janssens, K., Vekemans, B., Rindby, A. and Adams, F. (2000). Interpretation and use of inter-element correlation graphs obtained by scanning X-ray fluorescence micro-beam spectrometry from individual particles. Part I – theory, *Spectrochim. Acta, Part B*, **55**, 75–89.
173. Kemner, K. M., Yun, W., Cai, Z., Lai, B., Lee, H. R., Maser, J., Legnini, D. G., Rodrigues, W., Jastrow, J. D., Miller, R. M., Pratt, S. T., Schneegurt, M. A. and Kulpa, C. F. (1999). Using zone plates for X-ray microimaging and microspectroscopy in environmental science, *J. Synchrotron Radiat.*, **6**, 639–641.
174. Dhez, P., Chevallier, P., Lucatorto, T. B. and Tarrio, C. (1999). Instrumental aspects of x-ray microbeams in the range above 1 keV, *Rev. Sci. Instrum.*, **70**, 1907–1920.
175. Marcus, M. A., MacDowell, A. A., Celestre, R., Manceau, A., Miller, T., Padmore, H. A. and Sublett, R. E. (2004). Beamline 10.3.2 at ALS: a hard X-ray microprobe for environmental and materials sciences, *J. Synchrotron Radiat.*, **11**, 239–247.
176. Bertsch, P. M. and Hunter, D. B. (2001). Applications of synchrotron-based X-ray microprobes, *Chem. Rev.*, **101**, 1809–1842.
177. Sutton, S. R., Bertsch, P. M., Newville, M., Rivers, M. L., Lanzirotti, A. and Eng, P. (2002). Microfluorescence and microtomography analyses of heterogeneous earth and environmental materials, *Rev. in Mineral. Geochem.*, **49**, 429–483.
178. Duff, M. C., Hunter, D. B., Triay, I. R., Bertsch, P. M., Reed, D. T., Sutton, S. R., Shear-McCarthy, G., Kitten, J., Eng, P., Chipera, S. J. and Vaniman, D. T. (1999). Mineral associations and average oxidation states of sorbed Pu on tuff, *Environ. Sci. Technol.*, **33**, 2163–2169.
179. Strawn, D., Doner, H., Zavarin, M. and McHugo, S. (2002). Microscale investigation into the geochemistry of arsenic, selenium, and iron in soil developed in pyritic shale materials, *Geoderma*, **108**, 237–257.
180. Toyoda, M., Kaibuchi, K., Nagasano, M., Terada, Y., Tanabe, T., Hayakawa, S. and Kawai, J. (2004). X-ray analysis of a single aerosol particle with combination of scanning electron microscope and synchrotron radiation X-ray microscope, *Spectrochim. Acta, Part B*, **59**, 1311–1315.
181. Bobrov, V. A., Granina, L. Z., Kolmogorov, Y. P. and Melgunov, M. S. (2001). Minor elements in aeolian and riverine suspended particles in Baikal Region, *Nucl. Instrum. Methods Phys. Res. A*, **470**, 431–436.
182. Molders, N., Schilling, P. J., Wong, J., Roos, J. W. and Smith, I. L. (2001). X-ray fluorescence mapping and micro-XANES spectroscopic characterization of exhaust particulates emitted from auto engines burning MMT-added gasoline, *Environ. Sci. Technol.*, **35**, 3122–3129.
183. Huggins, F. E., Shah, N., Huffman, G. P. and Robertson, J. D. (2000). XAFS spectroscopic characterization of elements in combustion ash and fine particulate matter, *Fuel Process. Technol.*, **65**, 203–218.
184. Kemner, K. M., Kelly, S. D., Lai, B., Maser, J., O'Loughlin, E. J., Sholto-Douglas, D., Cai, Z. H., Schneegurt, M. A., Kulpa, C. F. and Nealson, K. H. (2004). Elemental and redox analysis of single bacterial cells by X-ray microbeam analysis, *Science*, **306**, 686–687.
185. Urquhart, S. G., Hitchcock, A. P., Smith, A. P., Ade, H. W., Lidy, W., Rightor, E. G. and Mitchell, G. E. (1999). NEXAFS spectromicroscopy of polymers: overview and quantitative analysis of polyurethane polymers, *J. Electron Spectrosc. Relat. Phenom.*, **100**, 119–135.
186. Hitchcock, A. P. (2001). Soft X-ray spectromicroscopy of polymers and biopolymer interfaces, *J. Synchrotron Radiat.*, **8**, 66–71.
187. Hitchcock, A. P., Morin, C., Tyliszczak, T., Koprinarov, I. N., Ikeura-Sekiguchi, H., Lawrence, J. R. and Leppard, G. G. (2002). Soft X-ray microscopy of soft matter – hard information from two softs, *Surf. Rev. Lett.*, **9**, 193–201.
188. Ade, H., Kilcoyne, A. L. D., Tyliszczak, T., Hitchcock, P., Anderson, E., Harteneck, B., Rightor, E. G., Mitchell, G. E., Hitchcock, A. P. and Warwick, T. (2003). Scanning transmission X-ray microscopy at a bending magnet beamline at the Advanced Light Source, *J. Phys. IV*, **104**, 3–8.
189. Myneni, S. C. B. (2002). Soft X-ray spectroscopy and spectromicroscopy studies of organic molecules in the environment, *Rev. Mineral. Geochem.*, **49**, 485–579.

190. DeStasio, G., Lorusso, G. F., Droubay, T., Kohli, M., Muralt, P., Perfetti, P., Margaritondo, G., Kelly, T. F. and Tonner, B. P. (1996). An electron imaging approach to soft-x-ray transmission spectromicroscopy, *Rev. Sci. Instrum.*, **67**, 737–741.
191. Margaritondo, G. and DeStasio, G. (1997). Synchrotron spectromicroscopy for the life sciences: general considerations and special procedures, *Int. J. Imag. Syst. Technol.*, **8**, 188–203.
192. DeStasio, G. and Margaritondo, G. (1997). Photoelectron spectromicroscopy with synchrotron radiation: applications to neurobiology, *J. Electron Spectrosc. Relat. Phenom.*, **84**, 137–147.
193. Myneni, S. C. B., Brown, J. T., Martinez, G. A. and Meyer-Ilse, W. (1999). Imaging of humic substance macromolecular structures in water and soils, *Science*, **286**, 1335–1337.
194. Schmidt, C., Thieme, J., Neuhausler, U., Jacobsen, C., Kaulich, B., Salome, M. and Susini, J. (2003). Spectromicroscopy of soil colloids, *J. Phys. IV*, **104**, 405–408.
195. Sarret, G., Connan, J., Kasrai, M., Bancroft, G. M., Charrie-Duhaut, A., Lemoine, S., Adam, P., Albrecht, P. and Eybert-Berard, L. (1999). Chemical forms of sulfur in geological and archeological asphaltenes from Middle East, France, and Spain determined by sulfur K- and L-edge X-ray absorption near-edge structure spectroscopy, *Geochim. Cosmochim. Acta*, **63**, 3767–3779.
196. Kinney, J. H. and Nichols, M. C. (1992). X-ray tomographic microscopy (XTM) using synchrotron radiation, *Annu. Rev. Mater. Sci.*, **22**, 121–152.
197. Jennesson, P. M., Luggar, R. D., Morton, E. J., Gundogdu, O. and Tuzun, U. (2004). Examining nanoparticle assemblies using high spatial resolution x-ray microtomography, *J. Appl. Phys.*, **96**, 2889–2894.
198. Spanne, P., Thovert, J. F., Jacquin, C. J., Lindquist, W. B., Jones, K. W. and Adler, P. M. (1994). Synchrotron computed microtomography of porous media – topology and transports, *Phys. Rev. Lett.*, **73**, 2001–2004.
199. Wildenschild, D., Hopmans, J. W., Vaz, C. M. P., Rivers, M. L., Rikard, D. and Christensen, B. S. B. (2002). Using X-ray computed tomography in hydrology: systems, resolutions, and limitations, *J. Hydrol.*, **267**, 285–297.
200. Ashbridge, D. A., Thorne, M. S., Rivers, M. L., Muccino, J. C. and O'Day, P. A. (2003). Image optimization and analysis of synchrotron X-ray computed microtomography (C mu T) data, *Comput. Geosci.*, **29**, 823–836.
201. Schroer, C. G., Kuhlmann, M., Gunzler, T. F., Lengeler, B., Richwin, M., Griesbock, B., Lutzenkirchen-Hecht, D., Frahm, R., Ziegler, E., Mashayekhi, A., Haefner, D. R., Grunwaldt, J. D. and Baiker, A. (2003). Mapping the chemical states of an element inside a sample using tomographic x-ray absorption spectroscopy, *Appl. Phys. Lett.*, **82**, 3360–3362.
202. Hansel, C. M., La Force, M. J., Fendorf, S. and Sutton, S. (2002). Spatial and temporal association of As and Fe species on aquatic plant roots, *Environ. Sci. Technol.*, **36**, 1988–1994.
203. Schurtenberger, P. and Newman, M. E. (1993). Characterization of biological and environmental particles using static and dynamic light scattering. In *Environmental Particles*, eds Buffe, J. and van Leeuwen, H. P., IUPAC Series on Analytical and Physical Chemistry of Environmental Systems, Vol. 2. Lewis, Boca Raton, FL, pp. 37–115.
204. Mavrocordatos, D., Perret, D. and Leppard, G. G. (2007). Strategies and advances in the characterisation of environmental colloids by electron microscopy. In *Environmental Particles and Colloids: Behaviour, Structure, and Characterisation*, eds Wilkinson, K. J. and Lead, J. R., IUPAC Series on Analytical and Physical Chemistry of Environmental Systems, Vol. 10. John Wiley & Sons, Ltd, Chichester, Chapter 8.
205. Daulton, T. L., Little, B. J., Lowe, K. and Jones-Meehan, J. (2001). *In situ* environmental cell-transmission electron microscopy study of microbial reduction of chromium(VI) using electron energy loss spectroscopy, *Microsc. Microanal.*, **7**, 470–485.
206. Kim, J. W., Furukawa, Y., Daulton, T. L., Lavoie, D. and Newell, S. W. (2003). Characterization of microbially Fe(III)-reduced nontronite: environmental cell-transmission electron microscopy study, *Clays Clay Miner.*, **51**, 382–389.
207. Guinier, A. and Fournet, G. (1955). *Small Angle Scattering of X-rays*. John Wiley & Sons, Inc., New York.
208. Feigin, L. A. and Svergun, D. I. (1987). *Structure Analysis by Small Angle X-ray and Neutron Scattering*. Plenum Press, New York.

209. Ballauff, M. (2001). SAXS and SANS studies of polymer colloids, *Curr. Opin. Colloid Interf. Sci.*, **6**, 132–139.
210. Svergun, D. I. (1991). Mathematical methods in small-angle scattering data analysis, *J. Appl. Crystallogr.*, **24**, 485–492.
211. Svergun, D. I. (1993). A direct indirect method of small-angle scattering data treatment, *J. Appl. Crystallogr.*, **26**, 258–267.
212. Svergun, D. I. (2000). Advanced solution scattering data analysis methods and their applications, *J. Appl. Crystallogr.*, **33**, 530–534.
213. Wershaw, R. L., Burcar, P. J., Sutula, C. L. and Wiginton, B. J. (1967). Sodium humate solution studied with small-angle X-ray scattering, *Science*, **157**, 1429–1431.
214. Lindqvist, I. (1970). Small angle X-ray scattering study of sodium humate solutions, *Acta Chem. Scand.*, **24**, 3068–3069.
215. Osterberg, R. and Mortensen, K. (1992). Fractal dimension of humic acids – a small-angle neutron scattering study, *Eur. Biophys. J. Biophys. Lett.*, **21**, 163–167.
216. Pranzas, P. K., Willumeit, R., Gehrke, R., Thieme, J. and Knochel, A. (2003). Characterisation of structure and aggregation processes of aquatic humic substances using small-angle scattering and X-ray microscopy, *Anal. Bioanal. Chem.*, **376**, 618–625.
217. Bottero, J. Y., Tchoubar, D., Arnaud, M. and Quienne, P. (1991). Partial hydrolysis of ferric nitrate salt – structural investigation by dynamic light-scattering and small-angle X-ray scattering, *Langmuir*, **7**, 1365–1369.
218. Tchoubar, D., Bottero, J. Y., Quienne, P. and Arnaud, M. (1991). Partial hydrolysis of ferric chloride salt – structural investigation by photon correlation spectroscopy and small-angle X-ray scattering, *Langmuir*, **7**, 398–402.
219. Masion, A., Tchoubar, D., Bottero, J. Y., Thomas, F. and Villieras, F. (1994). Chemistry and structure of Al(OH)/organic precipitates – a small-angle X-ray-scattering study. 1. Numerical procedure for speciation from scattering curves, *Langmuir*, **10**, 4344–4348.
220. Masion, A., Bottero, J. Y., Thomas, F. and Tchoubar, D. (1994). Chemistry and structure of Al(OH)/organic precipitates – a small-angle X-ray scattering study. 2. Speciation and structure of the aggregates, *Langmuir*, **10**, 4349–4352.
221. Masion, A., Thomas, F., Tchoubar, D., Bottero, J. Y. and Tekely, P. (1994). Chemistry and structure of Al(OH)/organic precipitates – a small-angle X-ray scattering study. 3. Depolymerization of the Al<sub>13</sub> polycation by organic ligands, *Langmuir*, **10**, 4353–4356.
222. Bolze, J., Peng, B., Dingenouts, N., Panine, P., Narayanan, T. and Ballauff, M. (2002). Formation and growth of amorphous colloidal CaCO<sub>3</sub> precursor particles as detected by time-resolved SAXS, *Langmuir*, **18**, 8364–8369.
223. Park, S. J., Lazarides, A. A., Storhoff, J. J., Pesce, L. and Mirkin, C. A. (2004). The structural characterization of oligonucleotide-modified gold nanoparticle networks formed by DNA hybridization, *J. Phys. Chem. B*, **108**, 12375–12380.
224. Rieker, T., Hanprasopwattana, A., Datye, A. and Hubbard, P. (1999). Particle size distribution inferred from small-angle X-ray scattering and transmission electron microscopy, *Langmuir*, **15**, 638–641.
225. Masion, A., Vilge-Ritter, A., Rose, J., Stone, W. E. E., Teppen, B. J., Rybacki, D. and Bottero, J. Y. (2000). Coagulation–flocculation of natural organic matter with Al salts: speciation and structure of the aggregates, *Environ. Sci. Technol.*, **34**, 3242–3246.
226. Masion, A., Rose, J., Bottero, J. Y., Tchoubar, D. and Elmerich, P. (1997). Nucleation and growth mechanisms of iron oxyhydroxides in the presence of PO<sub>4</sub> ions. 3. Speciation of Fe by small angle X-ray scattering, *Langmuir*, **13**, 3882–3885.
227. Kawahigashi, M., Fujitake, N., Azuma, J., Takahashi, T., Kajiwara, K. and Urakawa, H. (1995). The shape of humic acid in solution as observed by small-angle X-ray scattering, *Soil. Sci. Plant Nutr.*, **41**, 363–366.
228. Hubler, J. C., and Bloch, J. M. (1972). Determination of molar mass of monodispersed sodium humate, *C. R. Acad. Sci., Ser. C*, **274**, 514–516.
229. Osterberg, R., Lindqvist, I. and Mortensen, K. (1993). Particle size of humic acid, *Soil Sci. Soc. Am. J.*, **57**, 283–285.
230. Warren, B. E. (1990). *X-ray Diffraction*. Dover, New York.

231. Billinge, S. J. L. (2004). The atomic pair distribution function: past and present, *Z. Kristallogr.*, **219**, 117–121.
232. Billinge, S. J. L. and Kanatzidis, M. G. (2004). Beyond crystallography: the study of disorder, nanocrystallinity and crystallographically challenged materials with pair distribution functions, *Chem. Commun.*, 749–760.
233. Waychunas, G. A. (2001). Structure, aggregation and characterization of nanoparticles. *Rev. Mineral. Geochem.*, **44**, 105–166.
234. Zhang, H. Z., Gilbert, B., Huang, F. and Banfield, J. F. (2003). Water-driven structure transformation in nanoparticles at room temperature, *Nature*, **424**, 1025–1029.
235. Gilbert, B., Huang, F., Zhang, H. Z., Waychunas, G. A. and Banfield, J. F. (2004). Nanoparticles: strained and stiff, *Science*, **305**, 651–654.
236. Gilbert, B., Zhang, H. Z., Huang, F., Banfield, J. F., Ren, Y., Haskel, D., Lang, J. C., Srager, G., Jurgensen, A. and Waychunas, G. A. (2004). Analysis and simulation of the structure of nanoparticles that undergo a surface-driven structural transformation, *J. Chem. Phys.*, **120**, 11785–11795.

---

# Index

---

Note: references to Figures and Tables are indicated by italic page numbers

- $\mu$ EXAFS *see* micro-extended X-ray absorption structure  
 $\mu$ XANES *see* micro-X-ray absorption near edge structure  
1p-LSM *see* one-photon laser scanning microscopy  
2D imaging, LSM 475–476, 475  
2p-LSM *see* two-photon laser scanning microscopy  
3D imaging, LSM 475, 476, 477, 491–493, 492, 493  
4D imaging, LSM 476–477  
aberrations, in optical laser-induced breakdown detection 576, 578  
absorption edges, in X-ray absorption spectroscopy 617  
accessory techniques, used with TEM 348–349  
ACF *see* autocorrelation function  
acid polysaccharides (APS) 124–125, 136–137, 136  
acoustic signals 556, 557, 570–571, 571, 579–584, 592, 602  
actinides 202–205, 203, 204, 587–590, 588  
added mass method 433–434  
adhesion forces, in AFM 428, 441–446, 442  
adsorption  
    of humic substances at inorganic colloid surfaces 109  
    of labels for FCS 518, 519, 520–521, 526, 527  
    of samples for AFM samples 413, 414  
    *see also* binding  
adsorptive stripping voltammetry (AdSV) 120  
AEM *see* analytical electron microscopy  
aerosols 349–350, 352, 595  
aFlFFF *see* asymmetric flow field-flow fractionation  
AFM *see* atomic force microscopy  
agarose gels 531, 537–544, 538, 539, 540, 543  
aggregation  
    AFM 420, 422, 425–426  
    colloid–trace element binding 101  
    electron microscopy 370, 372–373, 385–388  
    electrophoresis interference 282  
    exudate structure 106–107  
    FCS 514–515, 533–537, 534–535, 534–537, 536  
    field-flow fractionation 254  
    of humic substances 254, 425–426, 534–537, 536  
    of organic matter in lake water 385–388  
    process analysis 370, 372–373, 420, 422  
    of schizophyllan 533–535, 534–535  
aggregation artefacts, in AFM samples 415  
alginate, AFM 424, 424  
aluminium 196, 197–199, 533, 534–535, 650  
aluminosilicate colloids, LIBD 587–588, 588  
americium 203–205, 204  
amplitude, of extended X-ray absorption structure signal 619, 619  
analytical electron microscopy (AEM)  
    applications of 378–390  
    combined with X-ray absorption spectroscopy 638  
    correlative procedures 365  
    techniques 347–349, 349–350  
antibody fluorophore conjugates 474  
apparent electrophoretic mobility 294  
apparent surface complexation constants 118  
APS *see* acid polysaccharides  
aquatic colloids  
    AFM 422–428  
    definitions 162, 163, 164  
    FCS 516–517  
    field-flow fractionation 223–269

- aquatic colloids (*continued*)  
 LIBD 588–592, 589, 590–592, 591, 592  
 mass concentrations 160  
 sampling techniques for electron microscopy 353–354  
 trace element interactions 95–140, 588–592, 589, 590–592, 591, 592  
 ultrafiltration 159–206, 165–167  
*see also* natural waters  
 archaea 486, 486  
 arsenic 641  
 artefacts  
   in AFM 414, 415  
   in electron microscopy 357, 364  
   in FCS 523–525  
   filtration 97  
   secondary X-rays from AEM 355  
 Äspö Hard Rock Laboratory project 559, 590–592, 591, 592  
 asymmetric flow field-flow fractionation (aFFF) 235–238, 235–238, 243  
 atmospheric colloids 349–350, 352  
 atomic force microscopy (AFM) 405–451  
   aqueous colloids 163, 164, 422–428  
   basic principles of 407–411, 408, 409, 410  
   cantilever spring constant 433–435  
   colloidal probe technique 428, 432–433, 432  
   correlative use of TEM with AFM and STXM 383–385  
   instrumentation for 407–408, 408, 429–430  
   natural samples 11, 422–428  
   particle size distribution 5–6, 8  
   quantitative determination of colloid dimensions 416–422  
   sample preparation for 411–416, 413, 414  
   surface force measurement 428–450  
 autocorrelation function (ACF), for FCS 511, 512–513, 514, 515, 516  
 autofluorescence 486  
 avalanche ionisation *see* cascade multiplication
- bacteria  
 adhesion force measurements 446, 447  
 colloid–trace element interactions 107–108  
 cyanobacteria 385, 386, 477  
 electrophoresis of soft colloids 332–333, 333, 334  
 LSM 469–498, 486
- cadmium  
 in aquatic colloids 196, 197–199  
 bacterial surfaces 107, 108  
 distribution coefficients 114–115  
 goethite surface complexes 104, 105  
 humic substances interaction with 632  
 marine colloid pools 132, 133  
 mussel uptake studies 101
- metabolic states 489–491  
 barium 177, 179  
 base microscopes, for LSM 472–473  
 BDP *see* breakdown probability  
 beam damage, in X-ray absorption spectroscopy 627, 627  
 Beer's law 240  
 bent Laue crystals 625, 629  
 bentonite 422, 588–590, 589, 592–594, 593  
 binding  
   freshwater colloid–metals binding strength 112–113  
   of humic substances to inorganic colloid surfaces 109  
   of organic colloids to metals 105–107  
   trace element fate and behaviour 100–102  
   trace element–colloid interactions 117–122  
 binding sites 107, 110–111, 124  
 binning multiple events, in XAS 628, 628  
 bioavailability, of trace elements 100  
 biofilms 125, 470, 477, 517  
 biomineralisation 385, 386  
 biopolymers  
   adhesion force study 442, 443–444  
   AFM 418–422, 421, 422, 424–425, 424, 442, 443–444, 448–450, 450  
   aggregation study 533–537, 534–535  
   contour lengths 418–420, 421  
   extension measurements 448–450, 450  
   FCS 533–537, 534–535  
 boundary conditions, soft colloid electrokinetic equations 323–324  
 breakdown events *see* laser-induced breakdown detection  
 breakdown probability (BDP), LIBD 556, 558–559, 566–572, 571, 579, 581  
 breakthrough volume method, of field-flow fractionation 245  
 Brownian mode separation principle 227, 228, 230, 231, 231, 232  
 bubble detection, in LIBD 573

- particle concentration effect 114  
ultrafiltration permeation behaviour of 177, 178, 179  
XAS 632  
calcite precipitation by cyanobacteria 385, 386  
calcium  
concentration calculations for colloidal fraction 116  
marine colloids 124  
size distributions in river water 258  
ultrafiltration permeation behaviour of 181–183, 182  
Caldwell, Karin 225  
calibration  
AFM 407, 417  
field flow fractionation channel dimensions 244–245  
ultrafiltration membranes 169, 171  
cantilevers, AFM 407–411, 408  
cantilever spring constants 407, 433–435  
capillary electrophoresis (CE)  
electroosmotic flow 289, 289  
history of 281, 285, 287  
literature survey 292–294  
natural organic matter 291–298  
sample plug volumes 288, 288  
simple set-up 288  
structural information 294–298  
technique 287–291, 288  
capillary gel electrophoresis (CGE) 298, 299, 300  
capillary isoelectric focusing (CIEF) 298, 299, 300, 300, 301, 301, 302  
capillary zone electrophoresis (CZE)  
combined off-line with ESI-MS 303, 305  
CZE–UV profile comparison with FFE–TOC 304  
ionic strength effects 295–298  
natural organic matter 300, 301  
pH effects 295–298  
polyelectrolytes/charged particles 289–291  
soil fulvic acid 302  
technique 294–298  
carbon-based colloid size distributions 257  
carbon–iron mass ratio, of Pacific Ocean waters 134  
carrier phases 132–137, 250, 252  
CARS *see* coherent anti-Stokes Raman scattering microscopy  
cascade multiplication, in LIBD 560–562, 560, 561, 567, 603  
cathodic stripping voltammetry 120  
CCD cameras, in LIBD 557, 559, 569, 574–575  
CE *see* capillary electrophoresis cells  
accumulation of nanoparticles 378  
debris contamination study by electron microscopy 381  
identity analysis by LSM 485–486, 485, 486  
nanoscale mineral agglomerates studied by electron microscopy 381–382  
surface biopolymer extension measurements by AFM 449–450  
trace element–colloid binding 107–108  
zinc complexes, X-ray absorption near edge structure 621, 622  
*see also* bacteria  
centrifugation  
for AFM 413, 414  
for electron microscopy 354, 358, 359, 360, 361  
CF *see* concentration factor  
CFF *see* cross-flow filtration  
CFM *see* chemical force microscopy  
CFUF *see* cross-flow ultrafiltration  
CGE *see* capillary gel electrophoresis  
channel cross-flow *see* flow field-flow fractionation  
charged particles 289–291, 316, 319–321  
chemcentric perspective 124, 162  
chemical force microscopy (CFM) 407, 411, 445–446  
chlorides 181–183, 182  
chlorophyll 478, 478  
chromium 196, 197–199  
CIEF *see* capillary isoelectric focusing  
classical electrophoretic separations 281–287  
classification of natural organic matter 109  
Cleveland method 433–434  
CLSM *see* confocal laser scanning microscopy  
clustered targets, for LIBD 568–569  
C/N molar ratios 193, 194  
coagulation 370  
cobalt 177, 179, 196, 197–199, 199, 632  
COC *see* colloidal organic carbon  
coherent anti-Stokes Raman scattering (CARS) microscopy 489

- colloidal fraction concentration  
calculations 116, 116
- colloidal organic carbon (COC) 160, 185, 186–189, 190–192, 192
- colloidal organic matter (COM) 160, 193–195, 193, 195, 426–428, 427  
*see also* macromolecules; organic colloids
- colloidal pools 96–99, 124
- colloidal probe technique, in AFM 428, 432–433, 432, 437–440, 438, 439
- colloidal pumping concept 101
- colloid–ion comparison, LIBD 595
- colloid–solution partitioning 133
- COM *see* colloidal organic matter
- computerised image analysis 367, 369–373
- concentration factor (CF)  
macromolecular permeation  
behaviour 173–178, 179, 180, 181  
optimum 183–185  
trace metals and radionuclides 177, 178, 180
- ultrafiltration permeation models 172–173  
variable 171
- confocal laser scanning microscopy (CLSM)  
in correlated multi-method approaches 348, 383, 384–385
- fluorescence recovery after  
photobleaching 479
- instrumentation for 473–474
- microbiological samples 471  
*see also* one-photon laser scanning  
microscopy
- confocal optics, FCS 510, 510, 511
- confocal reflection contrast imaging 481, 481
- confocal reflection imaging, LSM 480–481, 481
- ‘constant compliance region’, displacement  
curve in AFM 409
- constant field runs, FFF 246
- contact mode, of AFM 410, 410
- contaminant localisation in biofilms, LSM 489, 489
- contaminant transport, electron  
microscopy 378–380
- contamination of samples, LIBD 596–597
- continuous energy scanning methods, in  
XAS 628, 628
- continuous molecular weight-specific NIC  
analysis (NIC<sub>c</sub>) 250
- coordination environment  
determination 618–620, 619, 636
- copper  
in aquatic colloids 196, 197–199, 199  
distribution coefficients 114–115  
humic substances interaction with 632  
marine colloid interaction with 131–132, 133
- roof runoff scavenging study by electron  
microscopy 388, 389
- size distributions in soil using  
FIFFF–ICP–MS 257, 259
- ultrafiltration permeation behaviour of 177, 178, 179
- XAS 632
- correlative methods, in electron  
microscopy 347–348, 365, 383–385
- covalent bonds  
immobilisation techniques in AFM 416  
labelling methods for FCS 518, 519, 521–525, 522, 526, 527
- Craspedostaurus australis* 450, 450
- cross correlation, in FCS 545
- cross-flow filtration (CFF) 20, 121
- cross-flow ratios 171, 183
- cross-flow ultrafiltration (CFUF) 164, 165–167, 183–185, 248–249
- crosstalk, in LIBD 584, 602
- cryotechniques 361–362, 416, 631–632
- cyanobacteria 385, 386, 477
- CZE *see* capillary zone electrophoresis
- damping factors, in extended X-ray absorption  
structure 620
- Darling River 265
- Debye–Hückel limit 290, 317
- deconvolution, of LSM images 492–493
- deep underground aquatic colloids 590–592, 591, 592
- definitions  
apparent/effective electrophoretic  
mobility 294  
aqueous colloids 162, 163, 164  
colloidal dispersions 18  
colloids 224  
environmental colloids 1–3  
IUPAC definitions 2, 19  
particles 226  
soft colloids 316, 316
- dehydration *see* drying
- Derjaguin/Müller/Toporov (DMT)  
model 442–443

- desorption of train-like polymer  
conformations 442, 444
- detection limits 580, 580, 640
- detection systems, for FFF 240–244, 241, 242, 261
- devices  
for ultrafiltration 164, 165–167, 168  
*see also* instrumentation
- dextran–fluorophore conjugates 474, 482, 482
- Df *see* fractal dimension
- DGT *see* diffusive gradients in thin films
- DIA *see* digital image analysis
- diameter *see* particle size
- diatoms 450, 450
- diffusion, FCS 537–540, 538, 539, 540–544, 540, 543
- diffusion coefficients  
FCS 513, 515  
fulvic acids, technique  
comparison 530–531, 531  
humic substances, FCS 528–531, 530, 531  
importance of 9–10  
Suwannee River 10, 11, 531
- diffusion times, FCS 513, 515, 516
- diffusive gradients in thin films (DGT) 9, 120, 121, 122–123
- digital image analysis (DIA) 496–497
- digital micrographs from electron microscopy 367, 369–373, 371
- dimensionless electrophoretic mobility 325–328, 325, 334
- direct photo-ionisation, LIBD 559–560
- disaggregation, of humic substances 534–537, 536
- dispersive extended X-ray absorption structure 625
- dissolution, of inorganic colloids 423, 423
- dissolved organic carbon (DOC) 174, 185, 187, 188, 189
- dissolved organic matter (DOM) 164, 193–195
- dissolved phase comparison with colloids 99
- distribution coefficients ( $K_D$ ) 113–115
- distribution function 329–330, 332–333, 333
- DLS *see* dynamic light scattering
- DLVO forces 435–440, 439
- DMT *see* Derjaguin/Müller/Toporov model
- DNA  
AFM 417, 418–422  
*see also* nucleic acids
- DOC *see* dissolved organic carbon
- DOM *see* dissolved organic matter
- drinking water colloids 585, 585
- drop deposition, of AFM samples 413, 414
- drying  
of AFM samples 412, 414, 415  
of electron microscopy specimens 355, 357, 364
- dual channel imaging, in LSM 480–481, 480, 481, 482
- dyes *see* fluorophores; labelling; staining
- dynamic light scattering (DLS) 646–647
- dynamic processes  
FCS 511  
LSM 482–485, 484, 489–491, 497–498
- EDXA *see* energy-dispersive X-ray analysis
- EELS *see* electron energy-loss spectroscopy
- EFM *see* electrical force microscopy
- EF-TEM *see* energy-filtered transmission electron microscopy
- Elbe River flocs 492, 493
- electrical field-flow fractionation (electrical FFF) 225
- electrical force microscopy (EFM) 407, 411
- electrokinetics 292, 316, 317, 321–328, 325
- electron diffraction 366, 367
- see also* selected-area electron diffraction
- electron energy-loss spectroscopy (EELS)  
electron microscopy 347, 348, 349–350  
element analysis 373, 375, 377, 378, 379
- electron microscopy (EM) 345–390  
applications of 378–390  
development 346–347  
element analysis 373–377, 374, 375, 376, 378, 379
- instrumentation for 349–350
- physicochemical characterisation techniques 351
- qualitative observations 365–367
- quantitative analysis 367–369, 368
- sampling techniques 350, 352–354
- specimen preparation for 354–364, 373
- see also* analytical electron microscopy;  
environmental scanning electron microscopy; photoemission electron microscopes; scanning electron microscopy; transmission electron microscopy
- electron number calculations, in LIBD 566–572
- electron-opaque selective probes 348

- electron spectroscopic imaging (ESI) 377  
 electron/X-ray interactions 615  
 electroosmotic flow (EOF) 289, 289  
 electrophoresis  
     bacterial soft colloids 332–333, 333, 334  
     capillary electrophoresis 287–294  
     capillary IEF 299, 300, 300, 301, 301  
     capillary zone electrophoresis 294–298,  
         302–303, 302, 304, 305  
     classical separations 281–287  
     free-flow electrophoresis 302–303, 303,  
         304, 305  
     history of 279–287  
     humic substances 334–337, 335  
     natural organic matter  
         characterisation 277–306  
     NOM preparative techniques 298–305  
     soft colloids 315–338  
     soft particles 319–328  
     Tiselius U-tube 280, 280  
 electrophoretic mobility  
     apparent/effective 294  
     humic substances 334–337, 335  
     scaling 295, 296  
     soft particles 317–319, 324, 325–328, 325  
 electrospray ionisation mass spectrometry  
     (ESI-MS) 303, 305  
 electrostatic forces 436–440, 537–540, 538  
 element analysis  
     by electron microscopy 373–377, 374, 375,  
         376, 378, 379  
     by FFF 247  
     by XAS 617, 619  
 element atomic ratio distributions 247  
 element-based size distributions 264  
 element molar ratio 265  
 ELNES *see* energy-loss near-edge structure  
 elution modes, in FFF 228, 230, 231, 231  
 EM *see* electron microscopy  
 embedding media 357, 359, 361, 472  
 energy-dispersive spectroscopy *see* X-ray  
     energy-dispersive spectroscopy  
 energy-dispersive X-ray analysis (EDXA) 225  
 energy-filtered transmission electron  
     microscopy (EF-TEM) 348, 377  
 energy-loss near-edge structure (ELNES) 377,  
     378  
 environmental scanning electron microscopy  
     (ESEM) 6, 7, 11  
 atmospheric samples 352  
 development 347  
 particle size distributions 5–6  
 qualitative observations 365–366  
 specimen preparation for 355  
 enzyme activities 491  
 EOF *see* electroosmotic flow  
 epifluorescence 472  
 EPS *see* extracellular polymeric substances  
 equilibrium adsorption of fluorophores 518,  
     519, 520–521  
 equivalent diameter measurements 265  
 ESEM *see* environmental scanning electron  
     microscopy  
 ESI *see* electron spectroscopic imaging  
 ESI-MS *see* electrospray ionisation mass  
     spectrometry  
 estuarine waters 122–138, 163, 164, 165–166,  
     188  
 europium 557, 595  
 EXAFS *see* extended X-ray absorption  
     structure  
 exopolymeric substances *see* extracellular  
     polymeric substances  
 experimental error propagation 637–638, 638,  
     639  
 extended X-ray absorption structure (EXAFS)  
     data analysis 622–624  
     principles of 617, 617, 618–620, 619  
     spectral decompositions 636  
     trace element sorption 630, 631, 632  
     X-ray spectro-microscopy 640  
 extension behaviour of polymers 446–450,  
     450  
 extracellular polymeric substances  
     (EPS) 124–125, 381–382, 383–385, 487  
 exudates, role in aggregation of  
     colloids 106–107  
 FA *see* fulvic acids  
 Faraday, Michael 279  
 FCS *see* fluorescence correlation spectroscopy  
 FEFF codes 623–624  
 FFE *see* free-flow electrophoresis  
 FFF *see* field-flow fractionation  
 FFFF *see* flow field-flow fractionation  
 FFM *see* friction force microscopy  
 FIB *see* focused ion beam  
 fibrillar biopolymers  
     AFM 424–425, 424, 427  
     electron microscopy 380  
 FCS 532, 533

- Gram-positive bacteria 332–333, 333, 334  
polysaccharides 380, 424–425, 424, 532,  
533
- field-flow fractionation (FFF) 223–269  
back calculation using standard of known  
size 245  
breakthrough volume method of 245  
calibration of channel dimensions 244–245  
colloidal size effects on 4, 6  
constant field runs 246  
detection systems for 240–244, 241, 242  
element-based size distributions 264  
element content distributions 247  
FIFFF–ICP–MS method 254, 256, 257,  
258, 259, 260  
inorganic particles 261–267  
membrane operating conditions for 250–252  
NOM macromolecules size fractionation  
by 247–260  
non-spherical particles 264–265, 265  
operating conditions for 250–252  
prefractionation of steric particles 239–240  
retention modes 230–233, 231, 232, 233  
retention theory 228–230, 228, 230  
sample recovery 247  
separation principle 226–228, 227  
subtechniques in 233–239  
validation of 253–254  
void volume 245
- field studies 185–205  
filtration  
colloid size measurement 99–100  
inappropriateness of 140  
nanofiltration membrane adhesion force  
measurements 446  
phase definition 3  
of submicron particles 18  
of trace elements in colloidal pools 97–98  
*see also* ultrafiltration
- fingerprinting 284, 293, 293, 294
- FISH *see* fluorescent *in situ* hybridisation
- FJC *see* freely jointed chain
- FIFFF *see* flow field-flow fractionation
- FLIM *see* fluorescence lifetime imaging  
microscopy
- flocculation of schizophyllan 533–535,  
534–535
- flocs  
aluminium in NOM by small-angle X-ray  
scattering 650
- LSM 469–498, 475, 485, 486, 490, 492,  
493
- river water study 492, 493
- sample preparation 471–472
- waste water treatment studies 485–486,  
485, 486, 490
- flow field-flow fractionation (FIFFF) 6, 10, 11  
FCS comparison 530–531, 531
- fields applied 227
- FIFFF–ICP–MS method 254, 256, 257,  
258, 259, 260
- history of 225
- LIBD 242
- metal speciation studies 121
- molar mass/size distributions 249–250
- operating conditions 250–252
- separation principle 226–227
- size studies in trace element  
complexation 100
- technique 233–238
- flow through measurements, LIBD 597, 597,  
598
- fluorescence, of X-rays 615, 616
- fluorescence correlation spectroscopy (FCS) 6,  
10, 11, 507–545  
basic applications of 513–516, 516  
environmental applications of 516–518,  
519, 528–537
- gel diffusion 537–544, 538, 539, 540, 543
- high molecular weight polysaccharides 532,  
533
- humic substances (HS) 509–510, 518, 519,  
528–531, 530, 531
- labelling for 517, 518–528, 522, 523, 524,  
527, 532
- principles of 510–513, 510, 511, 514
- technique comparisons 508, 517, 530–531,  
531, 540–541
- fluorescence lifetime imaging microscopy  
(FLIM) 473–474, 483, 484, 545
- fluorescence mode  
of XAS 624, 624, 625–626  
of X-ray computed microtomography 645,  
645
- of X-ray spectro-microscopy 640
- fluorescence recovery after photobleaching  
(FRAP) 478–479, 479, 482–483, 517
- fluorescence resonance energy transfer  
(FRET) 483, 485
- fluorescent *in situ* hybridisation (FISH) 486,  
487, 494, 495

- fluorescent materials  
for FCS 518, 519–525, 522, 524  
for LSM 470–471, 474, 482, 482, 486–488,  
488, 494–495
- fluoride 181–183, 182
- flux density distribution in laser  
focus 562–566, 564, 565, 566, 603
- focal volume, in LIBD 562–567, 564, 603
- focused ion beam (FIB) 362–363, 362
- force measurements 405–407, 428–450
- force microscopy *see* AFM
- force spectroscopy 446–448
- force–distance curves 409, 410, 430–431, 431
- Fourier transformations (FT) 620, 622, 623,  
651
- fractal dimension (Df) from electron  
microscopy 370, 387–388, 387
- fractionation artefacts, in electron microscopy  
specimens 364
- fractograms 246–247, 259, 260, 262
- FRAP *see* fluorescence recovery after  
photobleaching
- free electron lasers 625
- free-flow electrophoresis (FFE) 302–303, 303,  
305
- freely jointed chain (FJC) model 448
- free molecular gases, transition to colloids in  
water 568–569
- free solution electrophoresis 281–282
- freeze-dried samples, for XAS 631–632
- freeze etching, for TEM 361
- freezing samples, for AFM 416
- frequency of extended X-ray absorption  
structure signal 619, 619
- fresh waters  
aggregation and sedimentation of organic  
matter 385–388
- colloidal actinides in 202–205, 203, 204
- colloid-trace element binding in 110–122
- electron microscopy 385–388
- element molar ratio versus particle  
diameter 264, 265
- lake contamination studies 121, 121,  
122–123, 379–380
- molecular distribution of DOC 185–186,  
187, 188
- particle diameter versus element molar  
ratio 265
- river floc images from LSM 492, 493
- size distributions of colloids in 257, 257,  
258, 258, 259
- see also* Suwannee River
- Fresnel zone plates (FZP) 640
- FRET *see* fluorescence resonance energy  
transfer
- friction coefficients, for FCS 514
- friction force microscopy (FFM) 407
- frit-outlet system 244
- FT *see* Fourier transformations
- full width at half-maximum (FWHM) 576,  
577
- fulvic acids (FA)  
electrophoresis 293, 293, 302, 334, 335  
FCS 516–517, 518, 528–531, 530, 531  
LIBD 594  
membrane adsorption 251
- FWHM *see* full width at half-maximum
- FZP *see* Fresnel zone plates
- gases transition to colloids in water 568–569
- Gaussian functions 563, 564, 567, 570, 572,  
605
- gels  
diffusion of ions in 537–540, 538, 539, 540  
diffusion of macromolecules/colloids  
in 540–544, 543
- electric focusing, colloidal binding phases  
evaluation 119, 119
- electrostatic effects on ion  
diffusion 537–540, 538
- FCS 537–544, 538, 539, 540, 543
- gelling properties of polymers 424–425,  
424
- geometric factors  
in AFM 417, 417, 432–433, 432  
in FFF 264–265, 265  
in XAS 620, 621, 621, 632
- geometry-sensitive crystal-field splitting 621
- GFP *see* green fluorescent proteins
- Giddings, Calvin 225
- glass substrates 412–413, 413
- global properties of submicron particles  
21–37
- goethite surface complexes 103, 104, 104, 105
- gold substrates 413, 413, 416
- gold–lectin conjugate markers 363, 364
- Göpperet-Mayer, Maria 470
- green algae 477
- green fluorescent proteins (GFP) 524
- grid types for TEM 355, 356
- Grimsel test site (GTS) 559, 588–590, 589

- HA *see* humic acids  
hard X-ray spectro-microscopy 639, 640–641  
Hauser, W. 559, 589  
hectorite 423, 423, 630, 631  
Helmholtz–Smoluchowski limit 317  
Henry's model 290  
highly oriented pyrolytic graphite  
    (HOPG) 412–413, 413, 414  
high molecular weight (HMW)  
    colloidal thorium-234 201  
    definition 161  
    polysaccharides 532, 533–535, 533,  
        534–535  
        *see also* fibrillar polysaccharides  
    ultrafiltration permeation  
        behaviour 173–176  
history  
    capillary electrophoresis 281, 285, 287  
    electron microscopy 346–347  
    electrophoresis of NOM 279–287  
    environmental scanning electron  
        microscopy 347  
    FFF 225–226  
    isoelectric focusing 280, 283–285  
    LIBD 556–559  
    polyacrylamide gel electrophoresis 282, 283  
    scanning tunnelling microscopy 407  
    TEM 346  
HMW *see* high molecular weight  
Hooke's law in AFM 407  
HOPG *see* highly oriented pyrolytic graphite  
HS *see* humic substances  
Hückel–Onsager limit 317  
humic acids (HA)  
    FCS 528–530, 534–537, 536  
    hydrodynamic diameter distributions 255  
    hydrodynamic radii 336  
    LIBD 594  
    membrane adsorption 251  
    permeability 336, 336, 337  
humic substances (HS)  
    AFM 412, 414, 425–426, 426  
    aggregation study 254  
    for analysis of colloids 11  
    contamination study 379, 380  
    diffusion coefficients of 528–531, 530, 531  
    disaggregation study 534–537, 536  
    electron microscopy 379, 380  
    electrophoretic behaviour of 293–294, 293,  
        302, 334–337, 335  
    FCS 509–510, 518, 519, 528–531, 530,  
        531, 534–537, 536  
    field flow fractionation 254  
    FIFFF–ICP–MS 257  
    Humic Ion Binding Model VI 105, 106, 107  
    laboratory metal-binding studies 105–107,  
        106, 107  
    laboratory trace element binding studies  
        102  
    metal binding studies 105, 106, 107,  
        630–633  
    organic–inorganic interaction  
        studies 108–109, 109  
    size distributions in soil 257  
    small-angle X-ray scattering 650  
    Suwannee River 529–531, 530, 531  
    XAS 630–633  
    X-ray spectro-microscopy 641–642, 643  
Hutter–Bechhoefer method 434–435  
hydrated environmental matter, for electron  
    microscopy 347, 349, 353  
hydrodynamic aspects  
    diameter in humic acids 255  
    model parameters in soft colloids 328–332  
    radii in humic acids 336  
    sample injection for CE 287–289  
hydrolysis-resistant covalent labelling 521  
hydromorphic soils 352  
hydrophilic media 357, 359, 361, 412–413,  
    413, 472  
hydrophobic forces 440  
hydrophobic media 357, 412–413, 413  
hydrophobic soil contaminants 445, 445  
  
ICP–MS elemental analyser 225–226, 243  
IEF *see* isoelectric focusing  
ignition length 576, 577, 603  
IHSS *see* International Humic Substance  
    Society  
image analysis  
    AFM 417–418  
    electron microscopy 369–373, 371  
    LSM 491–493, 492, 493, 495–497  
        particle size distribution measurements 367  
imaging techniques 474–477, 639–646  
inner/outer sphere complexes 630  
inorganic colloids  
    AFM 422–424, 423  
    FCS 509, 526, 527

- inorganic particles  
FFF 261–267
- laboratory trace element binding  
studies 102–105
- organic–inorganic interaction  
studies 108–110, 109
- instrumentation  
AFM 407–408, 408, 429–430  
asymmetric FIFFF 236  
confocal LSM 473–474  
electron microscopy 349–350  
FFF 226–228, 227  
LSM 472–474  
sedimentation FFF 239  
symmetrical FIFFF 235, 236, 237
- interaction forces between environmental surfaces 435–437
- interdisciplinary multi-method approaches 347–348
- intermittent mode, of AFM 410, 410
- International Humic Substance Society (IHSS) 426  
*see also* Suwannee River
- International Union of Pure and Applied Chemistry (IUPAC) definitions 2, 19
- intramolecular suprastructures, extension force measurements 449
- intrinsic equilibrium constants 103
- inverse bremsstrahlung 560–562, 560, 561, 567, 603
- inverted microscopes 472
- ionic substances  
average concentrations in marine colloids 126, 127, 127  
diffusion in gels 537–540, 538, 539, 540  
ionic strength effects 252, 295–298, 297  
LIBD 557, 595  
ultrafiltration permeation behaviour of 181–183, 182
- ionisation, LIBD 559–562
- iron  
in aquatic colloids 196, 197–199  
electron microscopy 380, 381, 382  
humic substances interaction with 632  
hydrolysis 633–635  
in lake water 121, 121, 122–123  
marine colloid interactions 130–131  
partitioning in NOM 255  
pH effects on oxides 104  
phosphorus association with 374
- size distributions in iron-based colloids 257, 257, 258, 259
- TEM–X-EDS analysis 374
- ultrafiltration permeation behaviour of 179
- XAS 621, 632, 633–635
- X-ray spectro-microscopy 641
- isoelectric focusing (IEF)  
colloidal binding phases evaluation by 119, 119  
development of 180, 283–285  
preparative versus capillary 298, 299, 300, 300, 301, 301, 302  
zone electrophoretic simulation of 286
- isoelectric points 135
- isoflux regions, in LIBD 565, 566
- IUPAC definitions 2, 19
- Johnson/Kendall/Robertson (JKR) model of adhesion forces 442–443
- karstic aquifers 379
- KB *see* Kirkpatrick–Baez
- $K_D$  *see* distribution coefficients
- kinetics  
electrokinetics 292, 316, 317, 321–328, 325  
of inorganic colloids from AFM 423–424, 423  
of metal–colloid reactions 111–112, 111, 112  
removal rate constants for surface-active colloidal ligands 137–138  
thorium-234 removal rate constants 138  
zinc sorption on gibbsite/amorphous silica 111, 112
- Kirkpatrick–Baez (KB) focusing mirrors 640
- labelling  
for FCS 517, 518–528, 522, 523, 524, 527, 532  
for TEM 363–364, 363
- laboratory studies 101–111
- lake waters  
aggregation of organic matter 385–388  
metal contamination studies 121, 121, 122–123, 379–380  
studies by electron microscopy 379–380, 385–388
- lambda scans from LSM 476, 477, 486
- laponite clay colloids 422
- laser-induced breakdown detection (LIBD) 555–599

- applications of 584–595  
development 556–559  
experimental approaches in 573–584  
FFF 241, 241, 242, 242, 261, 269  
physics of 559–572  
practical issues in 595–598  
laser-induced breakdown spectroscopy  
(LIBS) 557, 557, 578, 595, 603  
laser-induced photoacoustic spectroscopy  
(LPAS) 556, 603–604  
laser scanning microscopy (LSM) 469–498  
applications of 485–491  
future directions in 497–498  
image analysis 495–497  
image processing 491–493, 492, 493  
imaging techniques 474–477  
instrumentation for 472–474  
microorganisms 469–498  
quantitative imaging 481–485, 484  
sample preparation for 471–472  
selective treatment of subregions 478–479  
sequential and simultaneous  
imaging 477–478, 478  
laser sources, for FCS 523  
lateral colloid dimensions, from  
AFM 416–418, 417  
latex–schizophyllan aggregation  
study 533–535, 534–535  
Laue crystals 625, 629  
lead  
in aquatic colloids 196, 197–199  
contamination study by electron  
microscopy 379–380  
cycling in Paul Lake 121, 121  
distribution coefficients 114–115  
humic substances interaction by XAS 632  
marine colloid pools 132, 133  
particle concentration effect 114  
size distributions in soil using  
FIFFF–ICP–MS 257, 259  
ultrafiltration permeation behaviour of 177,  
178  
lectin–fluorophore conjugates 474, 486  
lectin–gold conjugates 363, 364  
Lennard Jones potential 409  
LIBD *see* laser-induced breakdown detection  
LIBS *see* laser-induced breakdown  
spectroscopy  
lift/hyperlayer mode 230, 231  
light scattering  
dynamic 646–647  
FFF detection systems 240  
LIBD 598  
multi-angle 266–267, 266, 268  
static 646–647  
limit of detection (LOD) 580, 580, 640  
lipids, staining for LSM 487, 487  
liquid cells, for AFM 411–412  
Live/Dead viability kit 490, 490, 495  
LMW *see* low molecular weight  
LOD *see* limit of detection  
log-spiral bent Laue crystals 625, 629  
low molecular weight (LMW)  
materials 173–177  
LPAS *see* laser-induced photoacoustic  
spectroscopy  
LSM *see* laser scanning microscopy
- macromolecules  
diffusion in gels 540–544, 543  
FCS 540–544, 543  
FFF 247–260, 262–263, 262  
inorganic particle differentiation 262–263,  
262  
LSM 486–487  
trace element associations 254–260  
ultrafiltration permeation behaviour  
of 173–176  
*see also* organic molecules; polymers  
magnesium 181–183, 182  
magnetic force microscopy (MFM) 407, 411  
M/Al atomic ratios 128  
MALLS *see* multi-angle laser light scattering  
manganese 122–123, 177, 178, 179, 196,  
197–199  
manganese oxide 376, 379, 627, 627  
marine waters  
colloidal pool constituents 124  
colloid–trace metal interactions 122–138  
DOC size distribution 189, 191–192, 192  
estuarine waters 122–138, 163, 164,  
165–166, 188  
organic gels under AFM 425  
thorium isotopes colloidal residence  
times 200–205, 200  
ultrafiltration applications 165–166, 189,  
191–192, 192  
ultrafiltration behaviour 173, 174, 175, 176  
mass balance of ultrafiltration membranes 171,  
183, 184  
mass concentrations of aquatic colloids 160

- mass distribution measurements 9  
maximum intensity projection (MIP) 491  
M/C atomic ratios 129  
membranes 439–440, 439, 446  
*see also* FFF membranes; ultrafiltration membranes  
mercury 196, 197–199, 199  
metabolic states of microbial samples 489–491  
metal/aluminium atomic ratios 128  
metal/organic carbon atomic ratios 129  
metals  
colloid interactions  
binding reaction kinetics 111–112, 111, 112  
binding strength in natural systems 112–113  
carrier phases 132–137  
electron microscopy 349  
in estuarine waters 122–138  
in natural waters 98, 98  
XAS 638–639  
LIBD 558  
oxides  
adsorption of organic acids 111  
electron microscopic analysis 376, 379, 380, 381, 382  
FCS 521, 526  
mixed oxide future study directions 139  
pH as important variable 104  
XAS 627, 627, 633–635  
X-ray computed microtomography 646, 646  
sorption on environmental particles 629–630  
speciation study 120–122, 629–639  
substrates for AFM 413, 413, 416  
*see also individual metals; trace elements*  
MFM *see* magnetic force microscopy  
mica, AFM substrate 412–413, 413  
microbiological particles, LSM 469–498  
micro-extended X-ray absorption structure ( $\mu$ EXAFS) 640  
microorganisms *see* bacteria; biofilms; cells; flocs  
microparticles, as nanoparticle aggregates 382–383  
micro-X-ray absorption near edge structure ( $\mu$ XANES) 640  
migration *see* transport  
MIP *see* maximum intensity projection  
mixed oxides, future study of 139  
mobile apparatus, for LIBD 559, 576  
mobility equation, for zone electrophoresis 290  
mobility scaling, for electrophoresis 295, 296  
‘model’ phases, in trace element binding studies 101–110  
model polymers, for FCS 527–528, 527  
Model V/VI 105, 106, 107, 139  
molar mass  
calibration for FFF 252–253, 253  
of colloidal organic matter used in FIFFF 249–250, 251  
equations 8  
molar mass cutoff *see* molecular weight cutoff  
molecular conformations  
AFM 418–422, 421  
train-like polymer desorption 442, 444  
worm-like chain model 418–419, 448–449  
molecular integrity preservation, in FCS 524  
molecular probes, for LSM 486  
molecular weight cutoff (MWCO)  
optimum concentration factor 184–185  
preconcentration of organic matter for FFF 248  
ultrafiltration membranes 164, 168–169, 168, 169, 170  
molecular weight (MW)  
optimum concentration factor 183–185  
ultrafiltration permeation behaviour 168–169, 169, 173–176  
*see also* particle size  
Monte Carlo calculations 637–638, 638, 639  
MPI *see* ultiphoton ionisation  
MS *see* multiple scattering  
multi-angle laser light scattering (MALLS) 266–267, 266, 268  
multi-labelling, for FCS 519–520  
multi-method interdisciplinary approaches 347–348  
multiphoton ionisation (MPI) 559–562, 567, 604  
multiple scattering (MS), in extended X-ray absorption structure 623  
multivariate analysis, in XAS 637  
mussels, Cd/Zn uptake study in 101  
MW *see* molecular weight  
MWCO *see* molecular weight cutoff  
Myers, Marcus 225  
nanofiltration membranes, adhesion force measurements of 446

- nanoparticles, aggregation to microparticles 382–383  
nanophases 254–260  
Nanoplast resin 357, 359, 361  
nanoscale mineral agglomerates 381–382  
nanosecond laser-induced plasma formation 560–562, 560, 561, 567  
natural organic matter (NOM) aggregation and sedimentation 385–388  
capillary electrophoresis 291–298, 299  
classical electrophoretic separations 281–287  
electrokinetic model 292  
electron microscopy study 385–388  
electrophoretic preparative techniques 298–305  
electrophoretic separation techniques 277–306  
FFF for size fractionation 247–260, 267  
organic–inorganic interactions in 108–109  
preconcentration of 248–249  
size distribution in 185–192  
submicron particles in 19  
ultrafiltration use in field studies 185–195  
natural waters colloids in 18, 20, 422–428  
percentage of colloidally bound metals in 98  
submicron particles in 17–93  
ultrafiltration applications to 165–167  
*see also* estuarine waters; fresh waters; marine waters  
Navier–Stokes equation 321  
near-edge X-ray absorption structure (NEXAFS) 617  
Newport Green stain, for LSM 489, 489, 495  
NEXAFS *see* near-edge X-ray absorption structure  
NIC *see* normalised intensity comparison  
NIC<sub>c</sub> *see* continuous molecular weight-specific NIC analysis  
NICCA model 105, 106, 107, 139  
nickel 177, 178, 196, 197–199, 199, 632  
NMWCO *see* nominal molecular weight cutoff  
NOM *see* natural organic matter  
nominal molecular weight cutoff (NMWCO) 168–169  
non-contact mode, for AFM 410  
non-DLVO forces, in AFM 437, 440–441  
non-invasiveness, of LIBD 556, 597  
non-linear laser scanning microscopy *see* two-photon laser scanning microscopy  
normalised intensity comparison (NIC) 249, 250  
nuclear waste colloid associations with 587–588, 590, 592  
*see also* radionuclides  
nucleic acids AFM of 417, 418–422  
LSM of 475, 475, 487, 487, 494  
number density of ionised molecules, LIBD 569, 570  
objective lenses, for LSM 472–473, 498  
OECs *see* organic environmental colloids  
Offord model 290  
Ohshima's model 317–318, 327  
on-channel preconcentration approach, for FFF 243, 244  
one-photon FCS 511–512, 511  
one-photon laser scanning microscopy (1p-LSM) 470, 473–474, 480–481  
*see also* confocal laser scanning microscopy  
on-line DOC detectors, for FFF 242, 249  
optical microscopy, electron microscopy comparison with 349  
optical signals, LIBD by 574–578, 575, 576, 577, 578, 580–581  
optical tweezers 429  
optimum concentration factor, in ultrafiltration 183–185  
organic environmental colloids (OECs) 278  
organic molecules acids adsorption by oxides 111  
carbon-based colloid size distributions 257  
correlative use of TEM with AFM and STXM 383–385  
dissolved organic matter 164, 185, 187, 188, 189, 193–195  
inorganic differentiation in FIFFF 262–263, 262  
inorganic interactions in surface studies 108–110, 109  
particulate organic matter 160, 185  
persistent organic pollutant ultrafiltration studies 205  
*see also* colloidal organic carbon; colloidal organic matter; natural organic matter

- organic-rich colloids  
 AFM of 424–428, 424, 427  
 appearance under electron microscopy 349  
 LIBD of 594  
 staining and labelling for TEM 363–364, 363  
 trace element binding to 105–107  
 oxidation states, determination of 620–621, 621  
 oxygen isotopes 183, 184
- Pacific Ocean 134
- PAGE *see* polyacrylamide gel electrophoresis
- PAHs *see* polycyclic aromatic hydrocarbons
- pair distribution function (PDF) 651–652, 652
- paper electrophoresis 281–282
- Pareto distribution 6, 8, 368, 372
- particle concentration effect (p.c.e.) 113, 114, 115
- particles  
 particulate phases–colloid comparison 99  
 rigid/soft distinctions 316–317  
 suspended particulate matter 117–118, 118, 160  
 use of term 226
- particle size  
 AFM 416–422, 417, 419  
 characteristic for soft particles 330  
 Darling River colloids 265  
 diameter calculations 8, 264, 265, 265  
 differentiation of particles from colloids by size 100–101  
 FCS 514, 517–518, 532, 533  
 flow-field fractionation 247–260, 265  
 fractionation of air samples for electron microscopy 352  
 global properties 21–22  
 importance of 3–9, 99–100  
 LIBD 557, 558, 579, 580, 581–584  
 limits for colloids 2  
 in trace element complexation 99–100
- particle size distributions (PSDs) 3–8, 4–5  
 acoustic LIBD 581–584, 583, 605  
 in carbon-based colloids 257  
 chemical species in aquatic systems 162, 163  
 colloidal radionuclides in natural waters 203, 204  
 colloids in natural waters 20
- DOC in estuarine environments 188
- electron microscopic quantitative analysis 367–369, 368
- element-based in FFF 264
- FFF fractogram conversion 246–247
- of iron-based colloids 257, 257, 258, 259
- of natural organic matter 185–192
- organic carbon in freshwater system 187  
 in Skagerrak sediment sample 268
- particle–water partition coefficients 137–138
- particulate organic carbon (POC) 185
- particulate organic matter (POM) 160
- partitioning  
 importance of the colloidal phase 115–116  
 metal-selective organic ligands 133  
 organic and iron-rich phases 255  
 particle–water partition  
 coefficients 137–138  
 thorium-234 in dissolved/colloidal/particulate phases 202  
 thorium to marine colloids 130  
*see also* distribution coefficients
- passive electron reduction factors 620
- Paul Lake, USA 121, 121
- $P_c$  *see* permeation coefficients
- PCBs *see* polychlorinated biphenyls
- p.c.e. *see* particle concentration effect
- PDF *see* pair distribution function
- peak deconvolution method 255, 257
- peat humic acids (PHA) 334, 336, 337, 337, 534–537, 536
- PEEM *see* photoemission electron microscopes
- permeation  
 of dissolved organic carbon 169  
 of radionuclides 177, 179, 180, 181  
 of trace metals 177, 178, 181  
 in ultrafiltration 172–173
- permeation coefficients ( $P_c$ ) 169, 172–173
- persistence lengths, of biopolymers 418–420
- persistent organic pollutants (POPs) 205
- perturbation minimisation, in FCS 519, 524
- PFG-NMR, FCS comparison with 530–531, 531
- PHA *see* peat humic acids
- phase, of extended X-ray absorption structure signal 619, 619
- phase definition, filtration steps 3
- phase imaging, AFM 410–411
- pH effects  
 capillary zone electrophoresis of NOM 295–298, 296

- on colloid formation, LIBD 585–586, 586  
distribution coefficient trends 115  
FCS labels 523  
metal binding to biological cells 108  
on surface complexes 104–105  
pH gradients 283–285, 488–489  
phosphorescence 513  
phosphorus 374  
photoelectric effects, of X-rays 615–616, 616,  
  617, 618  
photoemission electron microscopes  
  (PEEM) 641, 642  
photo-ionisation, LIBD 559–562, 604  
photon flux density, in LIBD 563, 565,  
  574–578, 575, 604  
photophysical properties, of fluorescent  
  dyes 523, 524, 525–527  
physicochemical parameters  
  electron microscopy determination 351  
  of marine colloidal organic matter 135  
physicochemical pathways, EM and AEM  
  applications 378–388  
 $pK_a$  values, of marine colloidal matter 135  
planapochromatic lenses 472  
plasma, in LIBD 556–557, 557, 604  
plutonium 203–205, 204, 641  
PMB *see* poly(methacryloyloxyethylidemethyl-  
  benzylammonium chloride)  
POC *see* particulate organic carbon  
Poisson–Boltzmann equation 291, 292, 321,  
  331  
polyacrylamide gel electrophoresis  
  (PAGE) 282, 283  
polychlorinated biphenyls (PCBs) 380  
polycyclic aromatic hydrocarbons  
  (PAHs) 378–379, 380  
polydentate anchoring moieties 521  
polyelectrolytes  
  in zone electrophoresis 289–291  
  *see also* natural organic matter  
polymers  
  adhesion force study of 442, 443–444  
  AFM 418–422, 424–425, 424, 442,  
    443–444, 448–450, 450  
  aggregation study 418–422, 533–537,  
    534–535  
  desorption in train-like conformations 442,  
    444  
  extension behaviour of 446–450, 450  
  FCS 527–528, 527, 533–537, 534–535  
  force spectroscopy 446–448  
gels, AFM 424–425, 424  
molecular conformations 418–420  
shells on charged soft particles 316,  
  319–321, 328, 329–330  
poly(methacryloyloxyethylidemethylbenzyl-  
  ammonium chloride) (PMB) 420, 421  
polysaccharides  
  acid 124–125, 136–137, 136  
contamination study by electron  
  microscopy 380  
extension behaviour study by AFM 449  
FCS 509, 522, 524–525, 526, 527  
fibrillar 380, 424–425, 424, 532, 533  
gels for FCS 537–544, 538, 539, 540, 543  
high molecular weight study by FCS 532,  
  533–535, 533, 534–535  
imaging by AFM 414, 416  
labelling for FCS 522, 524–525, 526, 527,  
  532  
staining for LSM 487, 487  
staining for TEM 363, 363, 364  
thorium-234/POC ratio carbohydrate  
  correlation 136–137, 136  
polystyrene particles  
  in LIBD 558, 598, 599  
  in LSM 487, 488, 488  
polystyrene sulfonate (PSS)  
  capillary gel electrophoresis 299  
  FFF 252–253, 253  
POM *see* particulate organic matter  
POPs *see* persistent organic pollutants  
porous media 537–540, 538, 646, 646  
  *see also* gels  
potassium 181–183, 182  
power density, in LIBD 563, 565, 566, 567  
power laws, of particle size distribution 368,  
  372  
precipitate formation 633–635  
  *see also* aggregation; sedimentation  
preconcentration of colloidal organic matter,  
  for FFF 248–249, 263, 263, 264  
preparative electrophoretic  
  techniques 298–305  
principal component analysis 637–638  
probes, for LSM 470–471, 486, 494  
propagation of experimental errors 637–638,  
  638, 639  
proteins 486–487, 522–523, 524, 527  
PSDs *see* particle size distributions  
PSS *see* polystyrene sulfonate

- pure phases, relevance to colloidal systems 110–113
- purified peat humic substances *see* peat humic acid
- pyrolysis–GC–MS 195, 195
- QD** *see* quantum dot
- qualitative observations, by electron microscopy 365–367
- Quantifoil films 356
- quantitative analysis
- AFM 416–422, 428–450
  - electron microscopy 367–369, 368, 373–378
  - LSM 481–485, 495–497
  - surface force apparatus 428
- quantum dot (QD) 485, 498
- quenching, in FCS 517, 520, 525–526
- R** *see* retention ratio
- radial distribution functions (RDFs) 620
- radionuclides
- $^{147}\text{Sm}$  FIFFF–HR–ICP–MS fractogram 260
  - LIBD 587–588, 590, 592
  - mobility in surface and subsurface waters 101
  - plutonium 203–205, 204, 641
  - transport, LIBD 587–588, 590, 592
  - ultrafiltration permeation behaviour of 177, 179, 180, 181
  - ultrafiltration studies in aquatic systems 200–205, 200
  - uranium 177, 180, 181, 202–203, 203
  - XAS 633
- ratiometric imaging, by LSM 481–482, 482
- $R_c$**  *see* retention coefficient
- RDFs *see* radial distribution functions
- reflection imaging, by LSM 480–481, 481
- rejection rates, ultrafiltration membranes 169, 170
- relative humidity (RH), AFM conditions 412, 414, 415–416
- resin embedding media, for TEM 357
- retention coefficient ( $R_c$ ) 169, 173
- retention modes, FFF 230–233, 231, 232
- retention ratio ( $R$ ), FFF 229, 230–233, 230, 232
- retention theory, FFF 228–230, 228, 230, 234
- Reuss, Ferdinand Friedrich 279, 281
- RH *see* relative humidity
- Rhodospirillum rubrum* 108
- rigid particles, soft particle distinctions 316–317
- river water 265, 492, 493
- see also* Suwannee River
- RMS *see* root mean square
- roof runoff, copper scavenging 388, 389
- root mean square (RMS), particle radii calculations 266–267, 266
- Ruska, Ernst 346–347
- Sadler's method 435
- SAED *see* selected-area electron diffraction
- sample injection 236, 236, 237, 237, 287–289
- sample preparation
- for AFM 411–416, 413, 414
  - for electron microscopy 354–364
  - for LIBD 596–598
  - for LSM 471–472
  - for XAS 625–629, 627
- sample recovery, for FFF 247
- sampling
- aquatic colloids 96, 159–206
  - for electron microscopy 350, 352–354
  - electrophoresis 277–306
  - FFF 223–269
  - preconcentration 263, 263, 264
  - ultrafiltration 159–207
- SANS, combined with SAXS and X-ray microscopy 650
- saturation, LIBD 569–570, 570
- SAXS *see* small-angle X-ray scattering
- scanning, *see also* laser scanning microscopy
- scanning electron microscopy (SEM)
- correlative procedures 365
  - environmental samples 352–353
  - instrumentation for 349
  - particle size distributions 5–6
  - qualitative observations 365–366
  - specimen preparation for 354–355, 358, 373
  - Tamar estuary sample 7
- scanning probe microscopy (SPM) 407
- scanning transmission electron microscopy (STEM) 366, 378–379, 380
- scanning transmission X-ray microscopy (STXM) 348, 383–385
- scanning tunnelling microscopy 407
- scattering elements, in extended X-ray absorption structure signal 619, 619
- Scheutjens–Fleer theory 329

- schizophyllan 532, 533–535, 533, 534–535  
SCM *see* surface complexation model  
s-curves, in acoustic LIBD 571, 572, 579, 579,  
  581–584  
SdFFF *see* sedimentation field-flow  
  fractionation  
SDS–PAGE electrophoresis 119, 119  
SEC *see* size exclusion chromatography  
second harmonic imaging microscopy  
  (SHIM) 498  
sedimentation 101, 354, 385–388  
sedimentation field-flow fractionation (SdFFF)  
  detection systems 243–244  
  fields applied 227  
  history of 225  
  LIBD 242  
  particle shapes 266  
  retention modes in 232  
  separation principle of 226–227  
  technique 238–239, 239  
sedimentation flow field-flow fractionation  
  (sFlFFF) 249  
sediment samples 268, 352–353, 638, 639  
selected-area electron diffraction (SAED) 348,  
  349, 366, 367  
selective treatment of subregions, in  
  LSM 478–479  
selenium 641  
self-focusing, in optical LIBD 576–578, 578  
SEM *see* scanning electron microscopy  
semi-quantitative investigations, by TEM 366  
sequential imaging, in LSM 477–478, 478  
SFA *see* surface force apparatus  
sFlFFF *see* sedimentation flow field-flow  
  fractionation  
shape factors (SFs)  
  electron microscopy 370, 372  
  FCS 514, 515  
  FFF measurements 264–265, 265, 266  
SHIM *see* second harmonic imaging  
  microscopy  
silicon wafer substrate, for AFM 412–413,  
  413  
silver, in aquatic colloids 196, 197–199, 199  
simultaneous imaging, by LSM 477–478  
single molecule study, by AFM 429, 448–450,  
  450  
sinks, marine metal-binding colloids 136–137,  
  136  
size, *see also* particle size  
size-based definitions 1–2  
size exclusion chromatography (SEC) 254  
size fractionation 247–260, 352  
Skagerrak sediment sample 268  
SLS *see* static light scattering  
small-angle X-ray scattering  
  (SAXS) 647–650, 648, 649  
smart stream splitting, in asymmetric  
  FlFFF 237  
 $\text{SO}_4^{2-}$ , ultrafiltration permeation behaviour  
  of 182, 183  
sodium, ultrafiltration permeation behaviour  
  of 181–183, 182  
soft colloids  
  bacterial 332–333, 333  
  biologically relevant examples of 316, 319,  
    332–333  
boundary conditions of electrokinetic  
  equations 323–324  
characteristic electrokinetic features  
  of 325–328, 325, 326  
characteristic particle size of 330  
definition 316, 316  
distribution function evaluation 329–330  
electrokinetic equations 321–323  
electrophoresis 315–338  
electrostatic and hydrodynamic model  
  parameters 328–332  
space charge density 330–332  
surface structure modelling of 316, 319–321  
softness parameter 326, 326  
soft X-ray spectro-microscopy 639, 641–643,  
  642, 643, 644  
soils  
  colloid sampling techniques for electron  
    microscopy 352–353, 354  
copper bound to 257, 259  
electrophoretic behaviour of 293–294, 293  
fulvic acid CZE 302  
humic substances 257  
hydrophobic contaminants 445, 445  
lead bound to 257, 259  
particle size distributions using  
  FlFFF–ICP–MS 257, 259  
qualitative observations by SEM/ESEM 366  
zinc in 257, 641  
solution-phase speciation, of colloidal trace  
  metals and ligands 125–132  
sorption kinetics, of metal–colloid  
  reactions 111–112, 111, 112  
space charge density 330–332  
spacers, for FCS 521, 526

spatial resolution, of FCS 516  
 speciation information, by electron microscopy 347–348  
 specific surface area (SSA), in colloid–trace element interactions 98–99  
 specific UV absorbance (SUVA) 249  
 specimen grid types, for TEM 355, 356  
 spectral decompositions, XAS 635–636  
 spectral lines, FCS 523, 524  
 spectroscopic properties, of fluorescent dyes 524, 525–527  
 sphalerite 621, 622, 640, 652, 652  
 spin coating techniques, for AFM samples 414, 414  
 split thin-flow fractionation (SPLITT) 100  
 SPM *see* scanning probe microscopy;  
 suspended particulate matter  
 spray deposition techniques, for AFM samples 414, 414  
 SR *see* synchrotron radiation  
 SSA *see* specific surface area  
 stable isotopes, colloidal organic matter 193–195, 193, 195  
 staining  
   for LSM 471, 472, 475, 475, 478, 478, 481, 481, 485, 486–487, 487  
   for TEM 357, 363–364, 363  
 standards, for FFF calibration 245  
 standing acoustic plane waves 558  
 static light scattering (SLS) 646–647  
 static loading method 435  
 STEM *see* scanning transmission electron microscopy  
 steric forces 440–441  
 steric/hyperlayer mode 228, 230, 231, 232  
 steric inversion diameter 233  
 steric inversion point 230, 231, 232, 233  
 steric particles, prefractionation of 239–240  
 sticking coefficients, in AFM 446  
 stoichiometry, of iron and phosphorus associations 374  
 Stokes diameter 265  
 Stokes' law 359  
 Stokes–Einstein relationship 513, 531  
*Streptococcus salivarius* 332  
 strong ligands 120, 127, 131  
 STXM *see* scanning transmission X-ray microscopy  
 submicron particles, in natural waters 17–93  
 substrates, for AFM 412–413, 413, 416  
 sulphur/metal interactions 631, 633

supporting media, for samples 280, 355  
 supramolecular physical properties, FCS 508  
 surface-active colloidal ligands 137–138  
 surface coatings, of humic substances 113  
 surface complexation constants 118  
 surface complexation model (SCM) 102–103, 103, 107–108, 111, 113  
 surface force apparatus (SFA) 428, 430  
 surface forces, AFM 428–450  
 surface layer heterogeneity, of soft particles 327, 327, 328, 329–330  
 surface sorption  
   of metals 629–630  
   of samples for LIBD 597, 597  
 surface structure modelling, of charged soft particles 316, 319–321  
 suspended particulate matter (SPM) 117–118, 118, 160  
 SUVA *see* specific UV absorbance  
 Suwannee River  
   diffusion coefficients 10, 11  
   electrophoretic electrokinetic model 292  
   humic substances  
     AFM 426  
     diffusion coefficient measurement techniques 530–531, 531  
     electrophoretic mobility 334, 335  
     FCS 529–531, 530, 531  
     soft X-ray spectro-microscopy 643  
     pH effects on CZE 296, 297  
 symmetrical flow FFF (sFFFF) 234–235, 235  
 synchrotron radiation (SR) 614–616  
   imaging and spectro-microscopy 639–646  
   XAS 616–639  
   X-ray scattering 646–652  
*Synechococcus* 385, 386  
 SYPRO staining 486–487  
 Syto 9 staining 475, 475, 478, 478, 481  
 SYTOX staining 485, 486  
 $t^0$  *see* void time  
 Tamar Estuary 7  
 tapping mode, in AFM 410, 410  
 TEM *see* transmission electron microscopy  
 temporal resolution, of FCS 517  
 TEP *see* transparent exopolymeric particles  
 ternary interactions 108–110, 109  
 thermal noise method 434–435  
 thermodynamic equilibria, of colloid formation 585–586, 586

- thickness of colloids, appearance under electron microscopy 349  
thiols, as marine metal-binding colloid sinks 136–137, 136  
Thompson scattering detection 573–574, 574, 605  
thorium-234  
  carbohydrates/uronic acids percentage calculations 136–137, 136  
  colloidal residence times in marine waters 200–205, 200  
  kinetic removal rate constants 138  
  in marine colloids 125–126  
  partitioning in dissolved/colloidal/particulate phases 202  
  ultrafiltration permeation behaviour of 177, 180, 181  
thorium 127, 129, 130, 130, 131, 200–205, 200  
threshold behaviour, LIBD 562, 602  
time-lapse imaging, in LSM 476  
Tiselius U-tube assembly 280, 280, 282  
topographical imaging, by AFM 410, 416–428  
total internal reflection microscopy 429  
total particle scattering *see* pair distribution function  
trace elements  
  binding to biological cells 107–108  
  carrier phases 132–137  
  colloidal phase importance 115–116  
  colloid interactions 95–140  
  colloid size importance in complexation 99–100  
  freshwater environments 110–122, 196, 197–199  
  laboratory binding studies 101–110  
  macromolecular organic matter associations 254–260  
  marine environments 122–138, 196, 197–199  
  ‘model’ phase binding studies 101–110  
  organic colloid interactions 105–107  
  reversibility/irreversibility of interactions 134–135  
  solution-phase speciation 125–132  
  ultrafiltration permeation behaviour of 177, 179, 180, 181  
  XAS studies 629–630  
transmission electron microscopy (TEM)  
  accessory techniques 348  
  applications of 378–388  
artefacts 357, 364  
in correlated multi-method approaches 348, 365, 383–385  
development 346  
element analysis 373–378  
environmental samples 352, 353  
instrumentation for 349  
particle size distribution  
  measurements 367–369, 368  
physicochemical pathway analysis 378  
qualitative observations 366–367  
quantitative analysis 367–369, 368  
specimen preparation for 354–364, 358, 360  
value to water scientists 348–349  
transmission imaging, by LSM 480, 480  
transmission mode  
  of XAS 624, 624, 625–626  
  of X-ray computed microtomography 645, 645  
transparent exopolymeric particles (TEP) 124, 125  
transport  
  of contaminants studied by electron microscopy 378–380  
migration, of trace elements, LIBD 588–590, 589  
of radionuclides studied by LIBD 587–588, 590, 592  
trace element uptake rates by aquatic bacteria 108  
*Triticum vulgaris*-TRITC lectin staining, for LSM 478, 478, 494  
two-dimensional PAGE 285  
two-photon FCS 512  
two-photon laser scanning microscopy (2p-LSM) 470, 473–474  
UDOM *see* ultrafiltered dissolved organic matter  
ultracentrifugation  
  for AFM 413, 414  
  for electron microscopy 354, 358, 359, 360, 361  
ultrafiltered dissolved organic matter (UDOM) 185  
ultrafiltration  
  applications of 185–206  
  aqueous colloids in field studies 185–205  
  chemical species behaviour 172–185

- ultrafiltration (*continued*)  
 colloidal trace metals in natural waters 196,  
 197–199, 203, 204  
 devices 164, 165–167, 168  
 permeation models 172–173  
 persistent organic pollutants in natural  
 waters 205  
 radionuclides in aquatic colloids 200–205,  
 200, 203, 204  
 typical system 167
- ultrafiltration membranes 168  
 adhesion force measurements 446  
 calibration 169, 171  
 integrity check 183  
 mass balance 171, 183, 184  
 MWCO 164, 168–169, 168, 169, 169, 170  
 permeation/retention coefficients 169
- ultramicrotomy, for TEM 356–357, 358
- ultra-small-angle X-ray scattering  
 (USAXS) 648
- ultraspecific markers, for TEM 363, 364
- ultrastructural characterisation, by  
 TEM 366–367
- uranium-238 177, 180, 181
- uranium 202–203, 203
- uronic acids 136–137, 136
- USAXS *see* ultra-small-angle X-ray scattering
- UV  
 detectors for FFF 240, 241, 242  
 specific UV absorbance 249  
 UV–VIS detection for FFF 261, 262, 262
- validation, of molar mass distribution by  
 FFF 253–254
- vanadium 103, 104
- van der Waals forces 437
- vertical colloid dimensions, determination by  
 AFM 418, 419
- viability of microbial cells, LSM 490–491,  
 490
- viruses 381
- vitrification, for TEM 361–362
- void time ( $t^0$ ), aFIFFF analysis 237
- waste water treatment flocs, LSM 485–486,  
 485, 486, 490
- water-immersible lenses, for LSM 473
- water treatment problems, electron microscopy  
 study 383
- wavelength-dispersive X-ray (WDX)  
 spectrometers 625, 640
- wavelength (lambda) scans, LSM 476, 477,  
 486
- WAXS *see* wide-angle X-ray scattering
- WDX *see* wavelength-dispersive X-ray
- weighted average flux density, acoustic  
 LIBD 579
- WHAM-V computer program 255
- whole mounts, for TEM 357, 358, 373
- wide-angle X-ray scattering  
 (WAXS) 647–650, 648, 649
- worm-like chain (WLC) model 418–419,  
 448–449
- XAES *see* X-ray absorption fine structure
- XANES *see* X-ray absorption near edge  
 structure
- XAS *see* X-ray absorption spectroscopy
- X-EDS *see* X-ray energy-dispersive  
 spectroscopy
- X-ray absorption fine structure (XAES) 617
- X-ray absorption near edge structure  
 (XANES)  
 data analysis 622, 623  
 metal/humic substances interaction 632  
 principles of 617, 617, 620–621, 621,  
 622  
 spectral decompositions 636  
 X-ray spectro-microscopy 640, 641, 644
- X-ray absorption spectroscopy  
 (XAS) 614–639  
 applications of 629–639  
 complementary methods 638  
 data analysis 621–624  
 experimental protocols 624–629, 624  
 principles of 615, 617–624, 617  
 sample preparation/stability 625–629, 627  
 sensitivity 636–637  
 soft X-ray spectro-microscopes 642–643  
*see also* extended X-ray absorption structure;  
 X-ray absorption near edge structure
- X-ray computed microtomography 640,  
 643–646, 645, 646
- X-ray energy-dispersive spectroscopy  
 (X-EDS)  
 applications of 379  
 electron microscopy 347, 348, 349–350  
 element analysis 373–377, 374, 375, 376  
 secondary X-ray artefacts 355
- X-rays  
 analysis techniques 613–653

- interactions with matter 615–616, 616  
synchrotron radiation 614–615
- X-ray scattering 646–652, 648, 649  
applications of 650  
pair distribution function 651–652  
small and wide angles 647–650, 648, 649
- X-ray spectro-microscopy 639–646
- Z-average, equations 8
- zinc  
in aquatic colloids 196, 197–199, 199  
bacterial surfaces 107, 108  
distribution coefficients 114–115  
FICFF–ICP–MS 257  
humic substances interaction with 632  
mussel uptake studies 101  
pair distribution function 652, 652
- sediment contamination 638, 639  
in soil 257, 641
- sorption on hectorite 630, 631  
sorption kinetics on gibbsite/amorphous  
silica 111, 112
- sphalerite 177, 179, 640, 652, 652
- ultrafiltration permeation behaviour of 177, 179
- X-ray absorption near edge structure 621, 622
- X-ray absorption spectroscopy 630, 631, 632, 638, 639
- X-ray spectro-microscopy 640, 641
- zirconium oxide 646, 646
- zone electrophoresis *see* capillary zone  
electrophoresis

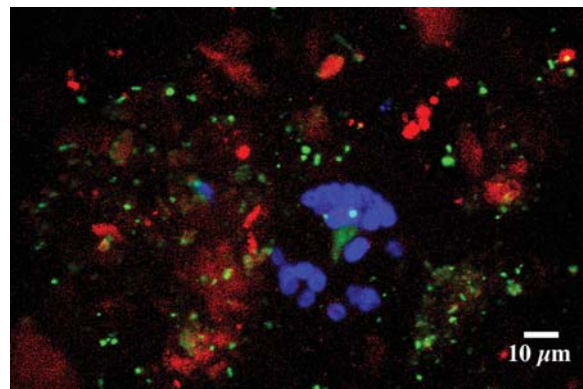


**Plate 1 (Figure 3, Chapter 10, p. 478).** LSM imaging showing the results of an optimised three channel scan with autofluorescence (red) showing the distribution of photosynthetic organisms based on detection of chlorophyll, *Triticum vulgaris*-TRITC lectin staining (blue) used to detect exopolymers in the biofilm matrix and nucleic acid staining with Syto 9 (green) to detect bacteria within a Saskatchewan River floc

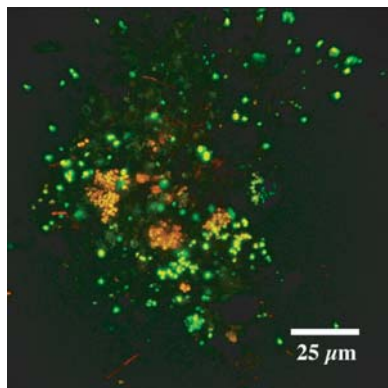


**Plate 2 (Figure 7, Chapter 10, p. 482).** LSM dual-channel image of fluorescence intensity when a 10 kDa molecular weight dextran conjugated to pH-sensitive fluorescein and pH-insensitive rhodamine was added to a waste water treatment system floc and the images taken using 1P-LSM. The image represents the ratio of the pH-sensitive and pH-insensitive signals, eliminating variations due to concentration. A standard curve was created using fixed floc material equilibrated with buffered pH solutions containing the 10 kDa dextran probe and imaged using the same LSM settings. Based on this calibration, the green regions have pH around 7.0 whereas the red regions have pH around 5, indicating differences in pH over small distances associated with microcolonies within the floc material

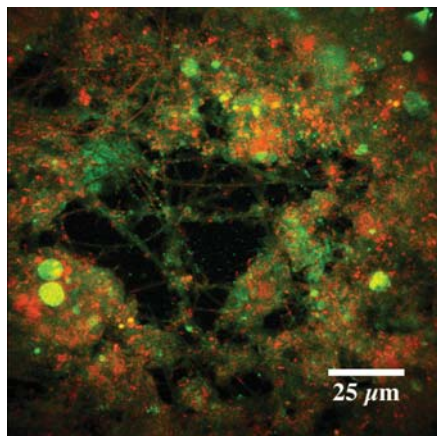


**Plate 3 (Figure 10, Chapter 10, p. 486).** Dual-channel colour image of the result of a combined fluorescent *in situ* hybridisation (FISH) of a waste water treatment floc with the 16S RNA probe for eubacteria (EUB 338) (green) and a FISH probe specific for archaea ARC915 (red), revealing the distribution of eubacteria and archaea, respectively, in the floc

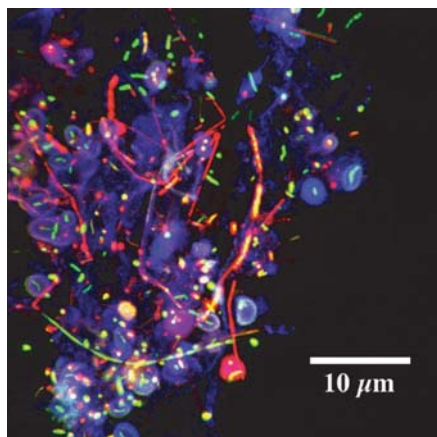


**Plate 4 (Figure 11, Chapter 10, p. 487).** Three-channel LSM overlay image showing the result of the sequential imaging of a triple-labelled microbial sample using the nucleic acid stain Syto 9 (green), the hydrophobic lipid sensitive stain Nile Red (red) and polysaccharide using the lectin of *Ulex europaeusus*-CY5 (blue)

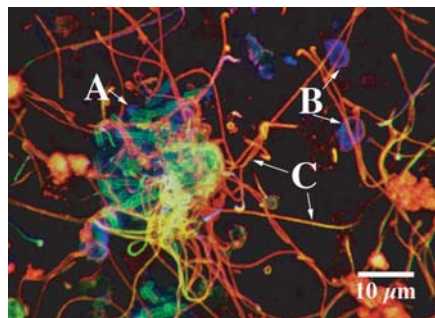


**Plate 5 (Figure 12, Chapter 10, p. 488).** An LSM micrograph which illustrates the application of microbeads to assess the sorption and penetration of bacterial microcolony EPS and determination of relative hydrophobicity and permeability. The following beads were applied: 20 nm carboxylate surface chemistry (hydrophilic) (blue), 20 nm aldehyde surface chemistry (hydrophobic) (green) and 100 nm sulphate surface chemistry (hydrophobic) (red). Note that in many cases regions of the biofilm bind only one of the bead types, and that in some cases the beads are restricted to the outside of the microcolony or structure; these indicate differences in the surface chemistry and also variations in permeability. Arrows at A, green sulfate hydrophobic on surface of cells in a microcolony, around the cells are 20 nm blue carboxylate hydrophilic beads; at B, microcolony with red 100 nm hydrophobic beads sorbed to the exterior, with the interior having the 20 nm blue carboxylate hydrophilic beads showing differential permeability of the colony boundary, and at C, microcolonies and filaments which bind the 100 nm hydrophobic beads on their surfaces as well as the 20 nm green hydrophobic beads

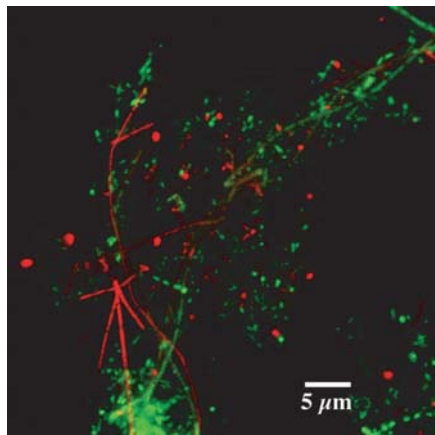


**Plate 6 (Figure 14, Chapter 10, p. 490).** Results obtained with the Live/Dead viability kit from Molecular Probes when applied to a waste water treatment floc system and imaged using LSM. The kit uses Syto 9 a nucleic acid stain, to distinguish living cells (which fluoresce green) and have a functional plasma membrane and dead cells (which fluoresce red) when stained with propidium iodide due to a compromised membrane

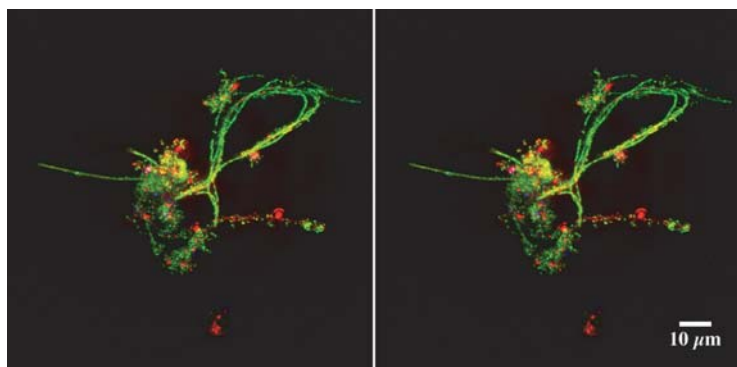


**Plate 7 (Figure 15, Chapter 10, p. 492).** Three-channel images stack combined to create a three-colour stereo image of a river floc integrating the reflectance (reflective mineral, colloidal materials), autofluorescence (cyanobacteria and algae) and Syto 9 nucleic acid stained bacteria signals (best viewed using stereo glasses)